FUSION ENERGY 1996

SIXTEENTH CONFERENCE PROCEEDINGS
MONTREAL, CANADA
7-11 OCTOBER 1996

IAEA

Vol.2

The cover picture shows the top view of the Tokamak de Varennes (TdeV) and its diagnostics. By courtesy of the Centre canadien de fusion magnétique (CCFM), Varennes, Quebec, Canada.

FUSION ENERGY 1996

VOLUME 2

The following States are Members of the International Atomic Energy Agency:

AFGHANISTAN
ALBANIA
ALGERIA
ARGENTINA
AUSTRALIA
ARMENIA
AUSTRIA
BANGLADESH
BELARUS
BELGIUM
BOLIVIA
BOSNIA AND HERZEGOVINA
BRAZIL
BULGARIA
CAMBODIA
CAMEROON
CANADA
CHILE
CHINA
COLOMBIA
COSTA RICA
COTE D'IVOIRE
CROATIA
CUBA
CYPRUS
CZECH REPUBLIC
DEMOCRATIC REPUBLIC OF THE CONGO
DENMARK
DOMINICAN REPUBLIC
ECUADOR
EGYPT
EL SALVADOR
ESTONIA
ETHIOPIA
FINLAND
FRANCE
GABON
GEORGIA
GERMANY
GHANA
GREECE
GUATEMALA
HAITI
HOLY SEE
HUNGARY
ICELAND
INDIA
INDONESIA
IRAN, ISLAMIC REPUBLIC OF
IRAQ
IRELAND
ISRAEL
ITALY
JAMAICA
JAPAN
JORDAN
KAZAKHSTAN
KENYA
KOREA, REPUBLIC OF
KUWAIT
LATVIA
LEBANON
LIBERIA
LIBYAN ARAB JAMAHIRIYA
LIECHTENSTEIN
LITHUANIA
LUXEMBOURG
MADAGASCAR
MALAYSIA
MALI
MARSHALL ISLANDS
MAURITIUS
MEXICO
MONACO
MONGOLIA
MOROCCO
MYANMAR
NAMIBIA
NETHERLANDS
NEW ZEALAND
NICARAGUA
NIGER
NIGERIA
NORWAY
PAKISTAN
PANAMA
PARAGUAY
PERU
PHILIPPINES
POLAND
PORTUGAL
QATAR
ROMANIA
RUSSIAN FEDERATION
SAUDI ARABIA
SENEGAL
SIERRA LEONE
SINGAPORE
SLOVAKIA
SLOVENIA
SOUTH AFRICA
SPAIN
SRI LANKA
SUDAN
SWEDEN
SWITZERLAND
SYRIAN ARAB REPUBLIC
THAILAND
THE FORMER YUGOSLAV REPUBLIC OF MACEDONIA
TUNISIA
TURKEY
UGANDA
UKRAINE
UNITED ARAB EMIRATES
UNITED KINGDOM OF GREAT BRITAIN AND NORTHERN IRELAND
UNITED REPUBLIC OF TANZANIA
UNITED STATES OF AMERICA
URUGUAY
UZBEKISTAN
VENEZUELA
VIET NAM
YEMEN
YUGOSLAVIA
ZAMBIA
ZIMBABWE

The Agency's Statute was approved on 23 October 1956 by the Conference on the Statute of the IAEA held at United Nations Headquarters, New York; it entered into force on 29 July 1957. The Headquarters of the Agency are situated in Vienna. Its principal objective is "to accelerate and enlarge the contribution of atomic energy to peace, health and prosperity throughout the world".

Printed by the IAEA in Austria
September 1997
STI/PUB/1004

PROCEEDINGS SERIES

FUSION ENERGY 1996

PROCEEDINGS OF THE
SIXTEENTH INTERNATIONAL CONFERENCE
ON FUSION ENERGY
ORGANIZED BY THE
INTERNATIONAL ATOMIC ENERGY AGENCY
AND HELD IN MONTREAL, 7–11 OCTOBER 1996

In three volumes

VOLUME 2

INTERNATIONAL ATOMIC ENERGY AGENCY
VIENNA, 1997

VIC Library Cataloguing in Publication Data

International Conference on Fusion Energy (16th : 1996 : Montreal, Canada)
Fusion energy 1996 : proceedings of the sixteenth International Conference on Fusion Energy / organized by the International Atomic Energy Agency and held in Montreal, 7–11 October 1996. — Vienna : The Agency, 1997.
3 v. ; 24 cm. — (Proceedings series, ISSN 0074–1884)
Contents: v.2.
STI/PUB/1004
ISBN 92–0–102997–7
"Formerly called the International Conference on Plasma Physics and Controlled Nuclear Fusion Research."
Includes bibliographical references.

1. Nuclear fusion—Congresses. 2. Controlled fusion—Congresses. 3. Plasma (Ionized gases)—Congresses. I. International Atomic Energy Agency. II. Title. III. Title: International Conference on Plasma Physics and Controlled Nuclear Fusion Research. IV. Series: Proceedings series (International Atomic Energy Agency).

VICL 97-00174

FOREWORD

The 16th International Atomic Energy Agency Fusion Energy Conference (formerly called the International Conference on Plasma Physics and Controlled Nuclear Fusion Research) was held in Montreal, Canada, from 7 to 11 October 1996. This series of meetings, which began in 1961, has been held biennially since 1974.

In addition to these biennial conferences, the IAEA organizes co-ordinated research projects, technical committee meetings, advisory group meetings and consultants meetings on fusion research topics. The objectives of the IAEA activities related to fusion research are to:

—Promote fusion energy development and worldwide collaboration;
—Support developing Member State activities in fusion research;
—Emphasize the safety and environmental advantages of fusion energy;
—Encourage the utilization of plasmas and fusion technology in industry;
—Provide auspices for the International Thermonuclear Experimental Reactor (ITER).

This conference, which was attended by some 500 participants from over thirty countries and two international organizations, was organized by the IAEA in co-operation with the Centre canadien de fusion magnétique and the Canadian National Fusion Program, to which the IAEA wishes to express its gratitude. Some 270 papers were presented in 19 oral and 8 poster sessions on magnetic and inertial confinement systems, plasma theory, computer modelling, alternative confinement approaches, fusion technology and future experiments. The opening session was designated the Artsimovich Memorial Session, in honour of Academician Lev Andreevich Artsimovich.

Fusion research is continuing to make excellent progress. Since the previous conference (Seville, 1994) over 10 MW of fusion power has been produced in the Tokamak Fusion Test Reactor, plasma conditions equivalent to breakeven have been demonstrated in the JT-60U experiment, the reversed shear mode has been demonstrated, low aspect ratio tokamaks have produced promising results and plans have been drawn up for powerful new inertial confinement fusion experiments. We can look forward to further encouraging results at the next conference (Yokohama, 1998), when the Joint European Torus will have employed a 50:50 mix of deuterium–tritium fuel, the Large Helical Device will be operating and the ITER Engineering Design Activities will be complete.

EDITORIAL NOTE

The Proceedings have been edited by the editorial staff of the IAEA to the extent considered necessary for the reader's assistance. The views expressed remain, however, the responsibility of the named authors or participants. In addition, the views are not necessarily those of the governments of the nominating Member States or of the nominating organizations.

Although great care has been taken to maintain the accuracy of information contained in this publication, neither the IAEA nor its Member States assume any responsibility for consequences which may arise from its use.

The use of particular designations of countries or territories does not imply any judgement by the publisher, the IAEA, as to the legal status of such countries or territories, of their authorities and institutions or of the delimitation of their boundaries.

The mention of names of specific companies or products (whether or not indicated as registered) does not imply any intention to infringe proprietary rights, nor should it be construed as an endorsement or recommendation on the part of the IAEA.

The authors are responsible for having obtained the necessary permission for the IAEA to reproduce, translate or use material from sources already protected by copyrights.

Material prepared by authors who are in contractual relation with governments is copyrighted by the IAEA, as publisher, only to the extent permitted by the appropriate national regulations.

CONTENTS OF VOLUME 2

HELICAL SYSTEMS (Session C1)

ALTERNATIVE SYSTEMS EXPERIMENTS (Session C2)

HELICAL SYSTEMS AND ALTERNATIVE SYSTEMS (Poster Session CP)

TRANSPORT THEORY (Session D1)

MHD AND ENERGETIC PARTICLE THEORY (Session D2)

DIVERTOR EDGE PHYSICS AND ALTERNATIVES (Session D3)

THEORY (Poster Session DP)

ITER (Poster Session FP)

HELICAL SYSTEMS

(Session C1)

Chairperson

F. WAGNER
Germany

EDGE PLASMA CONTROL BY A LOCAL ISLAND DIVERTOR IN THE COMPACT HELICAL SYSTEM

A. KOMORI, N. OHYABU, S. MASUZAKI, T. MORISAKI,
H. SUZUKI, C. TAKAHASHI, S. SAKAKIBARA,
K. WATANABE, T. WATANABE, T. MINAMI,
S. MORITA, K. TANAKA, S. OHDACHI, S. KUBO,
N. INOUE, H. YAMADA, K. NISHIMURA, S. OKAMURA,
K. MATSUOKA, O. MOTOJIMA, M. FUJIWARA,
A. IIYOSHI
National Institute for Fusion Science,
Nagoya, Japan

C.C. KLEPPER, J.F. LYON, A.C. ENGLAND,
D.E. GREENWOOD, D.K. LEE, D.R. OVERBEY, J.A. ROME,
D.E. SCHECHTER, C.T. WILSON
Oak Ridge National Laboratory,
Oak Ridge, Tennessee,
United States of America

Abstract

EDGE PLASMA CONTROL BY A LOCAL ISLAND DIVERTOR IN THE COMPACT HELICAL SYSTEM.

A local island divertor (LID) experiment was performed on the Compact Helical System (CHS) to demonstrate the principle of the LID. It was clearly demonstrated that the particle flow is controlled by adding a resonant perturbation field to the CHS magnetic configuration, and is guided to the back of an m/n = 1/1 island which is created by the perturbation field. The particles recycled there were pumped out with a pumping rate in the range from a few per cent to about 10%. As a result, the line averaged core density was reduced by a factor of about 2 in comparison with non-LID discharges at the same gas puffing rate. In addition to the demonstration of these fundamental divertor functions, a modest improvement of energy confinement was observed, which could be attributed to the edge plasma control by the LID.

1. INTRODUCTION

The Large Helical Device (LHD) is a superconducting heliotron type device under construction at the National Institute for Fusion Science at Toki, Japan [1]. One of the key research issues in the LHD programme is to enhance helical plasma performance through edge plasma control. The edge plasma behaviour is important in determining heat and particle fluxes to the wall and enhancing core plasma confinement. This control of the LHD edge plasma will primarily be done with a closed

full helical divertor which utilizes a natural separatrix in the edge region [2]. However, the closed full helical divertor will not be ready in the early stage of the LHD experiment. Instead we plan to use a local island divertor (LID) for the LHD edge plasma control [3]. The LID is a closed divertor that uses an m/n = 1/1 island. The advantage of the LID over the closed full helical divertor is the technical ease of hydrogen pumping because the hydrogen recycling is toroidally localized. The experimental study to demonstrate the principle of the LID was done in detail on the Compact Helical System (CHS) in Nagoya, Japan. The results obtained are described in this paper. The LID experiment on CHS has provided critical information on the edge plasma behaviour in the heliotron type device, and helped us to optimize the design of the LID and the closed full helical divertor on LHD. It has also influenced the divertor design of W7-AS [4] and W7-X [4, 5], and helped us to explore advanced divertor concepts.

2. EXPERIMENTAL APPARATUS

For the CHS experiment, a resonant perturbation field $\tilde{b}$ necessary for an m/n = 1/1 island was generated by 16 small perturbation coils located above and below the CHS vacuum vessel. The outward heat and particle fluxes crossing the the island separatrix flow along the field lines to the back of the island, where carbon (or stainless steel) target plates of 10 mm (2 mm) thickness are placed on a divertor head, as shown in Fig. 1(a) [3]. Figure 1(b) shows the relation between the divertor head and the island separatrix. The particles recycled there are pumped out by a cryogenic pump with a hydrogen pumping speed of 21 000 L/s. The divertor head consists of 18 small planar plates, although ideally they should be three dimensional curved tiles which match the magnetic surface. The geometric shapes of the divertor head and the pumping duct are designed to form a closed divertor configuration with high pumping efficiency [3]. The gap between the divertor head and the pumping duct was fixed at 4 cm in our experiment. For the standard LID configuration, the leading edges of the divertor head, i.e. those of the target plates, are located well inside the island, thereby being protected from the outward heat flux from the core [3].

The CHS device was operated with a toroidal magnetic field B_0 of 0.9 T and a magnetic axis position R_{ax} of 99.5 cm [6]. The $\iota/2\pi = 1$ flux surface is well inside the vacuum vessel wall when $R_{ax} > 97.4$ cm. The plasma was produced by ion Bernstein wave (IBW) and/or second harmonic electron cyclotron heating and was heated by 0.82 MW tangential neutral beam injection (NBI) at 38 keV. The following instruments were used as the key diagnostic systems of this experiment: an IR TV camera for surface temperature measurements, a CCD TV camera with an optical filter for H_α measurements, Langmuir probes for edge plasma measurements and an ASDEX style fast ion gauge system [7] for measurements of the neutral hydrogen pressure in the pumping duct.

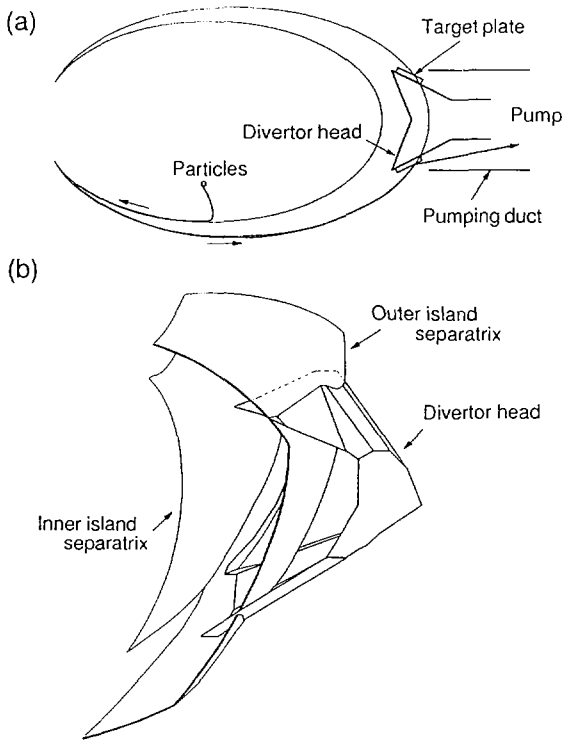

FIG. 1. LID concept. (a) LID configuration and particle flow to target plates; (b) relation between divertor head and island separatrix.

3. EXPERIMENTAL RESULTS AND DISCUSSION

The m/n = 1/1 island geometryof the LID was confirmed by mapping the magnetic surfaces. The mapping was carried out by the fluorescent method, using an electron gun with a W filament and a fluorescent mesh which emits light if the electron beam collides with it. The arrangement of the mapping apparatus is shown in Fig. 2. The fluorescent mesh is situated at the same toroidal position as the divertor head. The magnetic surfaces were measured by taking pictures of the beam positions on the fluorescent mesh while changing the radial position of the electron gun. The mapping was performed in a steady state operation at low field (B_0 = 0.0875 T) and a clear picture of the m/n = 1/1 island was obtained [8]. The island is located at the radial position that is predicted theoretically. However, the width of the island is a little greater than the expected value, and the island is not symmetrical with respect to the equatorial plane. This is because a 'natural' m/n = 1/1 island exists even without $\tilde{b}$. The natural island remains even at the operating field B_0 = 0.9 T, and

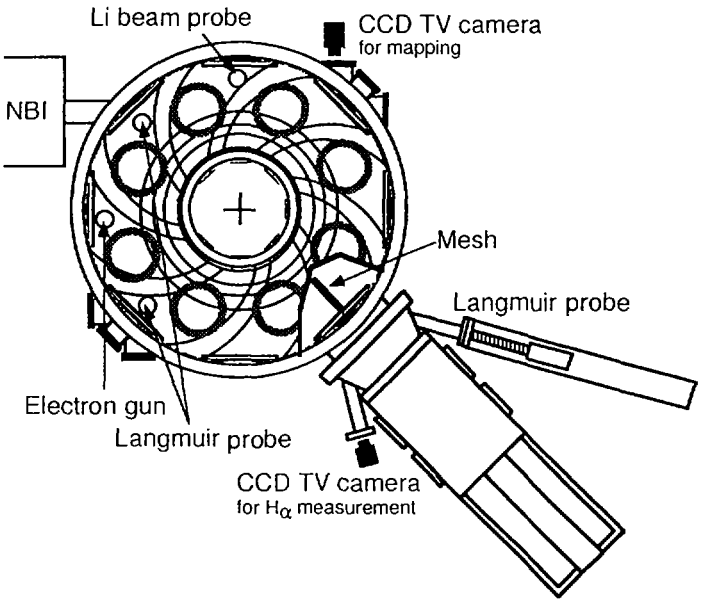

FIG. 2. Experimental apparatus.

this will be discussed elsewhere in detail. The poloidal phase of the natural island happens to be almost the same as that of the externally generated island. Thus the obtained configuration can be used for the LID experiment, although the divertor head was designed for the ideal island configuration without error fields. It was shown that there is an inherently high flexibility of the island configuration. By varying $\iota/2\pi$, the vertical field or the perturbation coil current I_{pert}, both island size and position can be modified. In our experiment, however, we mainly used the standard island configuration, whose external condition was utilized for the design of the divertor head.

We found that the plasma parameters change significantly when the island is formed. The line averaged electron density n_e and the OV radiation intensity decrease significantly with $\tilde{b}$ on, as shown in Figs 3(a) and (b), where a comparison between discharges with $\tilde{b}$ on and off is made at a fixed level of gas puffing. Figure 3 depicts temporal evolutions of n_e, the OV radiation intensity and the stored energy W_{dia} with and without $\tilde{b}$. The stored energy W_{dia}, measured by a diamagnetic loop, also decreases with $\tilde{b}$ on, but its reduction rate is much smaller than that of n_e because T_e increases, as shown in Fig. 4(a). Figure 4(a) depicts the radial T_e profiles with and without $\tilde{b}$ after the gas puffing, observed by a YAG Thomson scattering system. On the basis of these data, the temporal evolution of the energy confinement time τ_E is estimated. Figure 4(b) depicts the energy confinement time τ_E normalized by that of the LHD scaling law, $\tau_{LHD} = 0.17a^{2.0}R_m^{0.75}B_0^{0.84}n_e^{0.69}P_{tot}^{-0.58}$,

where a, R_m and P_{tot} are the averaged plasma radius, the major radius and the total absorbed power. We found that τ_E/τ_{LHD} with $\tilde{b}$ is greater than unity and that without $\tilde{b}$ mostly less than unity, especially after the gas puffing. There is a little uncertainty in estimating P_{tot} with $\tilde{b}$ on because of lower n_e. To avoid this uncertainty, we compared W_{dia} with and without $\tilde{b}$ at a fixed level of n_e. We found that W_{dia} in the discharge with $\tilde{b}$ is about 20% higher than that without $\tilde{b}$. These experimental results confirm that the energy confinement is improved with $\tilde{b}$ on.

An IR TV camera was used to measure the temperature profile of the target surface, and it was found that the position of the maximum temperature rise changes as the position of the divertor head is changed. The position of the maximum temperature rise is situated about 1 cm away from the leading edges when these are well inside the island. This indicates that the outward heat flux from the core is guided to the back of the divertor head along the island separatrix. Thus there will be no leading edge problem in the LID configuration even if the input power is increased significantly. The maximum temperature rise on the target plates during the discharge was observed to be about 5°C.

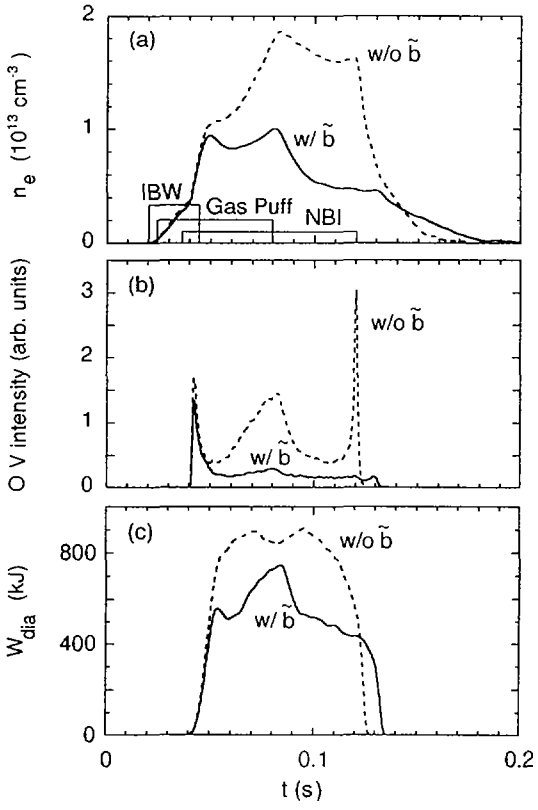

FIG. 3. Comparison of temporal evolutions of (a) averaged electron density n_e, (b) OV radiation intensity, and (c) stored energy W_{dia} between two discharges with and without $\tilde{b}$.

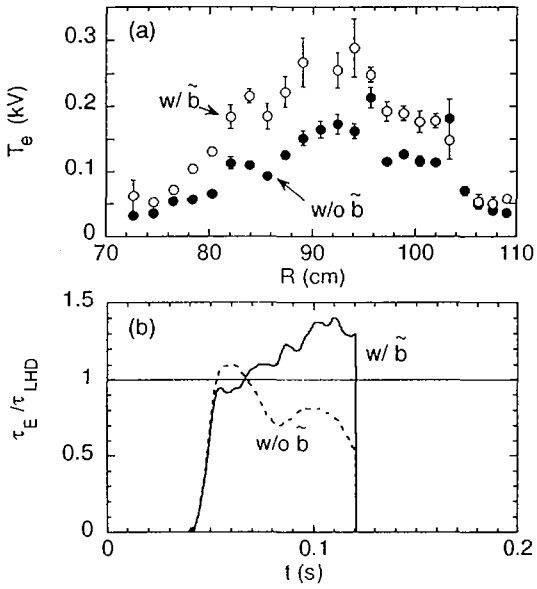

FIG. 4. (a) Radial T_e profiles with and without $\tilde{b}$, measured at $t = 0.1085$ s after the gas puffing (R is radial position from the major axis). (b) Energy confinement time τ_E normalized by that of the LHD scaling law, τ_{LHD}.

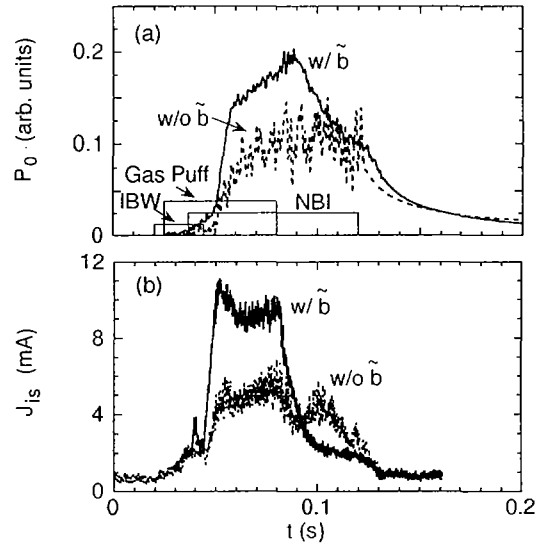

FIG. 5. Comparison of temporal evolutions of (a) neutral hydrogen pressure P_0, and (b) ion saturation current J_{is} behind the divertor head between two discharges with and without $\tilde{b}$.

The neutral particle pressure P_0 in the pumping duct was measured with a fast ion gauge [7] located just behind the divertor head. The pressure P_0 with a divertor head position $r_h = 0$ cm is shown in Fig. 5(a). Here the axis r_h is $R_{hs} - R_h$, where R_h is the major radial location of the divertor head and R_{hs} is that optimized in the design phase. When $\tilde{b}$ is turned on, P_0 becomes a factor of 1.5–2 higher than that without $\tilde{b}$ despite lower core density with $\tilde{b}$ on, as shown in Fig. 5(a). Figure 5(b) shows the ion saturation current J_{is}, which was measured with the Langmuir probe located behind the divertor head. It is clear that J_{is} with $\tilde{b}$ is a factor of 1.5–2 larger than that without $\tilde{b}$, and this is consistent with the fast ion gauge result. It should be noted that J_{is} without $\tilde{b}$ is kept almost constant even after the gas puff is turned off, while J_{is} with $\tilde{b}$ on decreases rapidly after the gas puffing. This suggests that efficient pumping of the recycled neutral particles takes place with the LID. On the basis of the particle flux calculated using J_{is} behind the divertor head, the pumping rate of the LID is roughly estimated to be in the range from a few per cent to about 10%. The radial T_e profiles behind the divertor head were also measured with the Langmuir probe. The temperature T_e during the gas puffing with $\tilde{b}$ is higher than that without $\tilde{b}$ by a factor of 2, and T_e after the gas puffing is also higher by a factor of 3 near the leading edge, whereas J_{is} is lower than that without $\tilde{b}$.

The dependence of P_0 and n_e on the island configuration was investigated by changing the perturbation coil current I_{pert} at a fixed position of the divertor head, as shown in Fig. 6(a). The size of the island was confirmed to change with I_{pert} by the mapping mentioned above. The position of the island O point is not affected by I_{pert}. When I_{pert} is gradually increased from 0 kA, P_0 increases abruptly at about 0.3 kA and is kept almost constant or decreases gradually until about 0.9 kA. A further increase in I_{pert} leads to an abrupt decrease in P_0. The pressure P_0 at $I_{pert} = 1.1$ kA is almost equal to that at $I_{pert} = 0$ kA. The pressure P_0 normalized by n_e has a clear peak at about 0.65 kA. On the other hand, n_e decreases gradually when I_{pert} is increased from 0 kA, and has a minimum at about 0.65 kA, corresponding to the value of I_{pert} for the maximum of P_0/n_e. This is an experimental demonstration that the LID function is sensitive to the LID geometry (island size, and position and shape of the head). When the geometry is optimized, the pumping efficiency is maximized, as evidenced by the maximum P_0/n_e, leading to the minimum n_e. The standard island configuration corresponds to that with $I_{pert} = 0.6$ kA.

To clarify the I_{pert} dependence of P_0, the plasma behind the divertor head was studied in detail with fixed Langmuir probes, which are mounted directly on the divertor head. The fixed probes are located radially 1 cm away from the leading edges of the divertor head. The radial J_{is} profiles at $t = 0.08$ s during the gas puffing with and without $\tilde{b}$ are shown in Fig. 6(b). They were measured by changing the head position r_h, so the horizontal axis shows the radial position r_h of the divertor head. The ion saturation current J_{is} without $\tilde{b}$ increases monotonically with r_h. When $\tilde{b}$ is turned on, J_{is} becomes larger for $r_h < 0$ cm, and J_{is} at $r_h = 1$ cm becomes smaller than that at $r_h = 0$ cm, as shown in Fig. 6(b). The peak of the profile at $r_h = 0$ cm corresponds to the outer island separatrix. Lower J_{is} at $r_h = 1$ cm

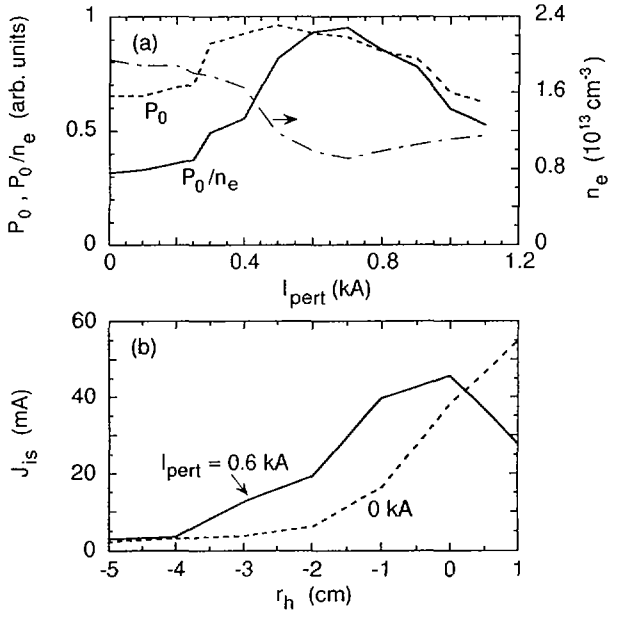

FIG. 6. Dependence of edge plasma parameters on LID geometry. (a) Dependence of P_0, n_e and P_0/n_e on perturbation coil current I_{peri}; (b) radial J_{is} profiles with and without $\tilde{b}$ at t = 0.08 s during the gas puffing, measured with a Langmuir probe fixed on the divertor head.

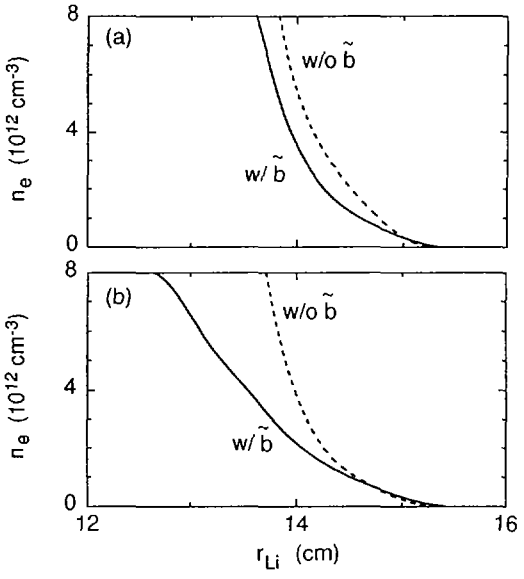

FIG. 7. Electron density profiles with and without $\tilde{b}$, measured with a thermal lithium beam probe. (a) Profiles during the gas puffing; (b) profiles after the gas puffing. The r_{Li} axis points towards the wall, and the separatrix is located at $r_{Li} \approx 14.3$ cm.

means that the plasma density just inside the outer separatrix is lower than that at the outer separatrix, because part of the divertor head is located inside the separatrix. As I_{pert} and hence the size of the island are increased, the peak position in the radial J_{is} profile moves towards the outside. The gap between the divertor head and the pumping duct, through which the edge plasma enters the duct, is fixed spatially, and hence the change in the peak position of the J_{is} profile explains well the I_{pert} dependence of P_0 shown in Fig. 6(a).

A CCD TV camera with an optical filter was used to measure the H_α radiation intensity near the target plates. The CCD TV camera is set behind the divertor head, as shown in Fig. 2, since the edge plasma enters the pumping duct and strikes the target plates. We found that the H_α radiation intensity behind the divertor head is higher with $\tilde{b}$ than without $\tilde{b}$. The H_α radiation intensity behind the divertor head behaves similarly to P_0 in the pumping duct.

The edge plasma behaviour with and without $\tilde{b}$ was measured with Langmuir probes and a thermal lithium beam probe [9], depicted in Fig. 2. Figure 7 shows the radial profiles of the electron density with and without $\tilde{b}$, measured with the lithium beam probe. The density profiles depicted in Fig. 7(a) were measured at $t = 0.09$ s during the gas puffing, whereas the profiles in Fig. 7(b) were obtained at $t = 0.11$ s after the gas puffing. The edge density with $\tilde{b}$ is found to decrease slightly during the gas puffing compared with that without $\tilde{b}$, and to decrease significantly after the gas puff is turned off. The J_{is} profiles, obtained with the Langmuir probes, are very similar [8]. The Langmuir probe measurement also yields the electron temperature T_e, which is higher when $\tilde{b}$ is turned on than without $\tilde{b}$, especially just after the gas puff is turned off and before the edge density becomes too low. This is consistent with the result obtained with the Langmuir probe behind the divertor head. The high temperature, low density edge plasma realized to some extent in our experiment suggests the feasibility of a low recycling operational mode in LHD that could lead to a significant energy confinement improvement [2]. The low recycling mode of operation will be pursued in the LHD experiment, combined with highly efficient pumping and core fuelling. The lithium beam probe was also used to measure the broadband density fluctuations in the edge region, and a correlation dimension and the largest Lyapunov exponent [10] were obtained. This study aims to achieve an understanding of the effect of chaos on particle transport, which could be helpful in substantially improving energy confinement in the LHD experiment.

4. SUMMARY

The fundamental functions of the LID have been clearly demonstrated in the experiment described. The leading edges of the divertor head, located inside the island, are protected from the outward heat flux from the core. The particle flow is guided to the back of the divertor head by the island magnetic field structure, and a high pumping efficiency can be realized to some extent even in CHS. A much

higher pumping rate will be achieved in LHD, because the majority of the outward plasma flux is expected to be guided to the target plates on the divertor head without diffusing to the wall owing to the smaller diffusion coefficient and larger size of LHD. The LID has also been found to affect the core plasma parameters significantly, and especially to improve the energy confinement.

We have not yet completed the experimental analysis, but the results analysed so far are very encouraging in terms of the effectiveness of the LID. The LID experiment has provided critical information on the edge plasma behaviour, and helped us to optimize the design of the LID and the closed full helical divertor on LHD.

REFERENCES

[1] IIYOSHI, A., et al., Fusion Technol. **17** (1990) 169.
[2] OHYABU, N., et al., Nucl. Fusion **34** (1994) 387.
[3] KOMORI, A., et al., in Plasma Physics and Controlled Nuclear Fusion Research 1994 (Proc. 15th Int. Conf. Seville, 1994), Vol. 2, IAEA, Vienna (1995) 773.
[4] SARDEI, F., et al., J. Nucl. Mater. (in press).
[5] GRIEGER, G., et al., in Plasma Physics and Controlled Nuclear Fusion Research 1990 (Proc. 13th Int. Conf. Washington, DC, 1990), Vol. 3, IAEA, Vienna (1991) 525.
[6] MATSUOKA, K., et al., in Plasma Physics and Controlled Nuclear Fusion Research 1988 (Proc. 12th Int. Conf. Nice, 1988), Vol. 2, IAEA, Vienna (1989) 411.
[7] HAAS, G., et al., J. Nucl. Mater. **121** (1984) 151.
[8] KOMORI, A., et al., J. Nucl. Mater. (in press).
[9] KOMORI, A., et al., Nucl. Fusion **28** (1988) 1460.
[10] KOMORI, A., et al., Phys. Rev. Lett. **73** (1994) 660.

DISCUSSION

K. LACKNER: You described low density operation in your divertor experiments. Do you also plan high density divertor operation in LHD, and do you plan to do pre-experiments also on CHS in this regime?

A. KOMORI: Yes, we plan both high density and low density divertor operation in LHD. In CHS, we have finished all the LID experiments, so we cannot do pre-experiments in the high density regime.

EFFECTS OF ECH ON NBI PLASMA IN HELIOTRON E

T. OBIKI, F. SANO, K. KONDO[1], H. ZUSHI[1], K. HANATANI,
T. MIZUUCHI, S. BESSHOU[1], H. OKADA, K. NAGASAKI,
M. WAKATANI[1], Y. NAKAMURA[1], M. NAKASUGA[1],
C. CHRISTOU, Y. IJIRI[1], T. SENJU, K. YAGUCHI, S. KOBAYASHI,
K. TOUSHI, K. SAKAMOTO, Y. KURIMOTO, H. FUNABA,
T. HAMADA, S. SUDO[2], M. SATO[2], K. IDA[2], B.J. PETERSON[2],
K. MURAOKA[3], S. KADO[3], H. SUGAI[4], H. TOYODA[4], K. SASAKI[4],
H. OKURA[4], K. MATSUO[5], G. DENISOV[6], A. GOLDENBERG[6],
V. KURBATOV[6], V. ORLOV[6], D. VINOGRADOV[6], V.Yu. SERGEEV[7],
K.V. KHLOPENKOV[7], V.V. CHECHKIN[8], V.S. VOJTSENYA[8]
Institute of Advanced Energy,
Kyoto University,
Uji, Japan

Abstract

EFFECTS OF ECH ON NBI PLASMA IN HELIOTRON E.

Propagation and absorption of second harmonic electron cyclotron resonance microwaves are investigated in Heliotron E. A highly focused beam with good single pass absorption allows a centrally peaked high electron temperature profile to be obtained. It is experimentally confirmed that the linearly polarized beam should be launched at a proper angle to the sheared field line and cross the resonance layer at the magnetic axis to obtain the best plasma production in heliotron/torsatron devices. The effects of ECH on NBI plasmas are studied by using two ECH systems with different absorption and resonance conditions. The superposition of ECH pulses on NBI plasmas has shown that $\Delta T_i > 0$ for ECH overlapping with a rather broad ECH power deposition profile but $\Delta T_i < 0$ for a centrally focused deposition profile. A key to an explanation of these different observations is the balance between the gain from $\Delta T_e > 0$ (and from $\Delta E_r > 0$, possibly) and the loss from the particle 'pump-out' and the resultant flattening of the density profile, both of which are caused by the ECH overlapping.

---

[1] Graduate School of Energy Science, Kyoto University, Uji, Japan.
[2] National Institute for Fusion Science, Nagoya, Japan.
[3] Interdisciplinary Graduate School of Engineering, Kyushu University, Kasuga, Japan.
[4] Faculty of Engineering, Nagoya University, Nagoya, Japan.
[5] Faculty of Engineering, Fukuoka Institute of Technology, Fukuoka, Japan.
[6] Institute of Applied Physics, Nizhnij Novgorod, Russian Federation.
[7] State Technical University, St. Petersburg, Russian Federation.
[8] Kharkov Institute of Physics and Technology, Kharkov, Ukraine.

1. INTRODUCTION

In helical systems, the transport phenomenon in the rare collision regime is one of the most important subjects in the reactor relevant physics. In recent Heliotron E experiments conditioned by the ECH boronization [1], we could study the confinement properties in low density high ion temperature plasmas whose collisionality ranges from the plateau to the helical ripple regime at half-radius [2]. In order to extend this study to regimes with lower collisionality it is necessary to raise the ion temperature further, under the restriction of the power source available. From the viewpoints of ion–electron energy transfer and power sharing of the NBI input power between electrons and ions, an increase in T_e by ECH during NBI is preferable to ion heating. Moreover, the positive radial electric field E_r, which is observed in ECH-only plasmas in Heliotron E [3], may reduce the loss cone for fast ions. Neoclassical theory predicts the improvement of ion heat transport in the 'electron root' scenario ($E_r > 0$). However, the degradation of particle confinement, which is usually observed during the ECH phase in many toroidal devices, may affect ion heating adversely. From these points of view, combined ECH and NBI heating was examined in this experimental campaign by changing the ECH power absorption profile.

As to ECH in heliotron/stellarator devices, it is important to examine the launching conditions for optimum electron heating. Because of the large poloidal field with strong radial dependence, wave propagation is not so simple as in a uniform field. Most plasma experiments in Heliotron E have been performed by using the 53 GHz ECH system (f_{ECH} = 53.2 GHz, $P_{ECH} \leq 0.5$ MW) [4]. Because of the TE_{02} mode and/or non-focused linearly polarized Gaussian beams and owing to the low O mode cut-off density, this system is not so effective in local plasma heating. In order to improve the controllability of the power deposition profile of microwaves, we have introduced a new 106 GHz second harmonic ECH system (f_{ECH} = 106.4 GHz, $P_{ECH} \leq 0.4$ MW) with a linearly polarized Gaussian beam [5]. The 1/e beam waist of this highly focused beam is less than 0.02 m (i.e. much smaller than the plasma radius a). The advantages of this system are: (1) accessibility to higher density regions (the cut-off density for the 106 GHz X mode is twice that for the 53 GHz O mode), (2) good single pass absorption of ~100% in usual Heliotron E plasmas, leading to local electron heating, and (3) the possibility of polarization control. By using this new system, we have experimentally studied the effect of the power deposition profile on electron heating and the effect of magnetic shear on wave propagation.

In this paper, the global properties of the 106 GHz second harmonic ECH plasma and the effects of the field structure on propagation and absorption of microwaves are described in Sections 2 and 3. In Sections 4 and 5, the effects of ECH on NBI plasma and on high energy ions produced by NBI are discussed. The conclusions are presented in Section 6.

2. GLOBAL PROPERTIES OF 106 GHz SECOND HARMONIC ECH

Second harmonic ECH experiments using the 106 GHz system are mainly performed at a magnetic field strength of 1.9 T, where the resonance layer crosses the magnetic axis. A comparison between the 106 GHz second harmonic ECH and the 53 GHz fundamental ECH cases indicates that the electron temperature, $T_e(r)$, in the 106 GHz case is much higher and has a peaked profile. Figure 1 shows the radial profiles of T_e for the 106 GHz ($P_{ECH} \sim 0.3$ MW) and 53 GHz ($P_{ECH} \sim 0.4$ MW) cases. Here, $T_e(r)$ is measured by a Thomson scattering system. The peaking factor, $\eta \equiv T_e(0)/T_e(a/2)$, is 2.6 ± 0.6 in this case, while it is 2.0 ± 0.5 in the 53 GHz case, suggesting that the single pass absorption of 106 GHz waves is effective and power deposition is localized in the central region (see Section 4). On the other hand, the electron density profile, $n_e(r)$, is very broad for both cases, as is shown in Fig. 1. This indicates that density pump-out has occurred in both cases.

The density dependence of the central electron temperature, $T_e(0)$, and the ion temperature, T_i, which is measured by a charge exchange (CX) neutral particle energy analyser in the equatorial plane, are shown in Fig. 2. The data for the 53 GHz fundamental ECH plasmas are also plotted. The accessible line averaged electron density for the 106 GHz ECH is extended to $\bar{n}_e = 5 \times 10^{19}$ m^{-3} at an ECH power of $P_{ECH} = 0.25$–0.3 MW, where $n_e(0)$ reaches the X mode cut-off density (7×10^{19} m^{-3}). Higher $T_e(0)$ than in the 53 GHz ECH case is observed over the whole operational density regime, and $T_e(0) \cong 2.8$ keV has been achieved so far in a low density plasma. As shown in Fig. 2, T_i seems to stay almost constant in ECH-only plasmas, which is in sharp contrast to the theoretical prediction of a collisional coupling between electrons and ions.

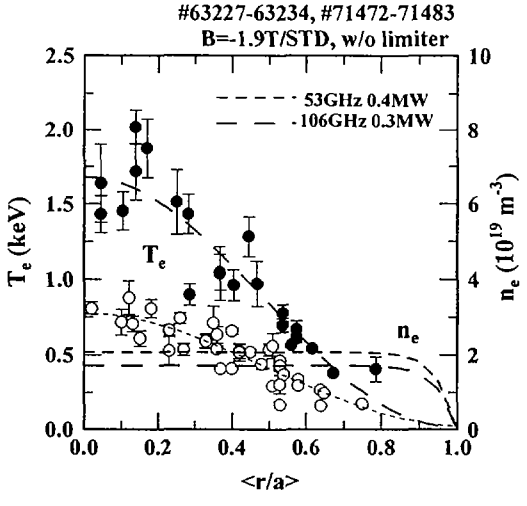

FIG. 1. T_e and n_e profiles for 53 GHz and 106 GHz ECH plasmas.

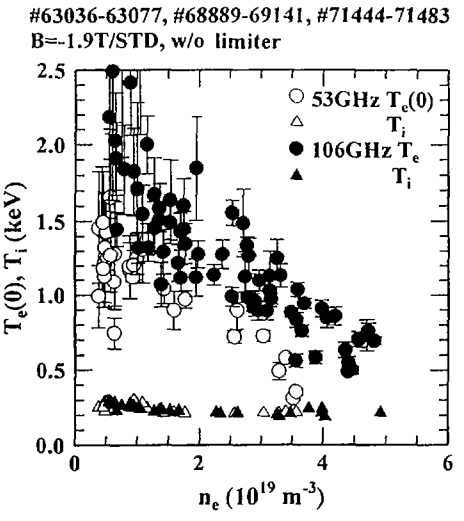

FIG. 2. Density dependence of $T_e(0)$ and T_i.

The global stored energy evaluated from measured profiles, W_p, increases with $\bar{n}_e$ up to 3.0×10^{19} m^{-3} and then seems to saturate at around 8 kJ. The apparent energy confinement time, $\tau_E = W_p/P_{ECH}$, is found to be improved by 10–50%, compared to the LHD scaling [6]. Since the density profile is very broad for all ECH plasmas, this improvement in energy confinement is attributed to the increase in electron temperature realized by the centrally focused ECH profile.

3. EFFECTS OF THE MAGNETIC FIELD CONFIGURATION ON THE 106 GHz SECOND HARMONIC ECH

From the viewpoint of plasma production, the second harmonic ECH has a narrower window in the magnetic field strength. This property is commonly observed for all examined frequencies of ECH, as is shown in Fig. 3 where the initially produced density is plotted as a function of the magnetic field strength, for several ECH methods but at the same filling gas pressure. In this figure, density and field strength are normalized by the cut-off density $n_{e,c}$ and the central resonance frequency f_h, respectively. The accessible field strength range is narrowest in the 106 GHz case. This is explained by the fact that the launched beam is well focused only in this case and that the mod-B pattern of Heliotron E is saddle shaped, where the resonance layer is rather remote from the beam as the field strength decreases. The density buildup is fastest when the resonance layer is placed on the magnetic axis. It is also interesting to note that breakdown first occurs in the central region

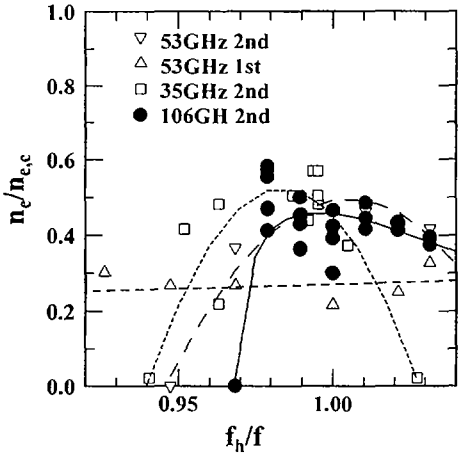

FIG. 3. Magnetic field dependence of plasma production for several ECH conditions. $n_{e,c}$, f_h and f are cut-off density, central resonance and wave frequencies, respectively.

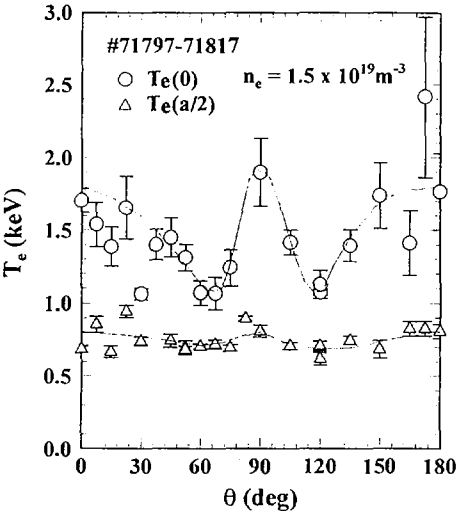

FIG. 4. Effect of rotation angle of polarizer on T_e of 106 GHz second harmonic ECH-only plasma.

in the second harmonic ECH, not only in the 106 GHz case but also in the non-focused 53 GHz ECH case at B = 0.94 T. Since non-linear interaction between cold electrons and microwaves plays an important role in the breakdown process in second harmonic ECH, this observation may be related to trapping of the accelerated electrons. These findings indicate that the launched beam should cross the resonance layer at the magnetic axis to ensure the most effective plasma production in heliotron/ torsatron devices.

When microwaves propagate across a magnetic field with magnetic shear, the power distribution between the X and O modes of the waves changes along the propagation path. A numerical calculation [7] shows that this shear effect cannot be neglected to obtain better single pass absorption in heliotron/torsatron devices in which the magnetic shear is higher than in tokamaks. The effect of magnetic shear is experimentally observed by using one of the mirrors in the waveguide transmission line as a linear polarizer [8]. By changing the rotation angle of the mirror, $T_e(0)$ changed drastically between 1 and 2 keV as is shown in Fig. 4, while $T_e(a/2)$ was almost constant. This suggests that local one pass absorption changes to uniform multipass absorption. The optimum mirror angle is in good agreement with the results of the calculations.

4. EFFECT OF ECH ON NBI PLASMA

Since the ratio of the injection energy to the theoretical 'critical energy' is about five for typical NBI plasmas in Heliotron E, an increase in the electron temperature is preferable to an increase in the input power to the ions, P^i_{NBI}. From the viewpoint of ion–electron energy transfer, higher T_e can also raise the input power to the ions. While ECH is one of the effective methods of electron heating, ECH and NBI plasmas have particle transport characteristics in Heliotron E that differ from each other substantially. The density profile of the ECH plasma is broad, as was shown in the previous section, but a rather peaked profile is usually observed in NBI plasmas. As to the radial electric field E_r in the edge region ($\langle r/a \rangle \sim 0.7$–$0.8$), a typical NBI plasma has $E_r < 0$ [3]. In the 53 GHz ECH-only plasmas, however, E_r is a function of $\bar{n}_e$ and $E_r > 0$ for the low density region ($\bar{n}_e \leq 2 \times 10^{19}$ m^{-3}).

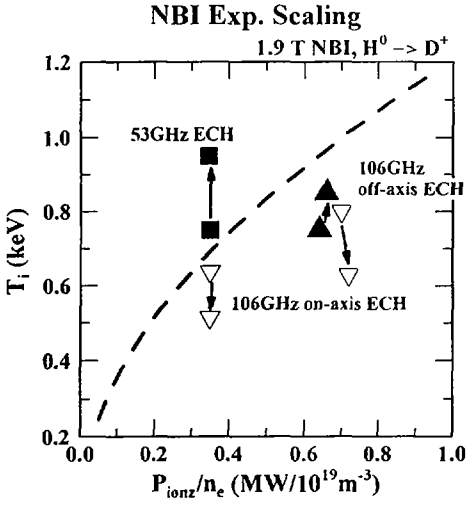

FIG. 5. Change of T_i caused by ECH superposition for several ECH conditions.

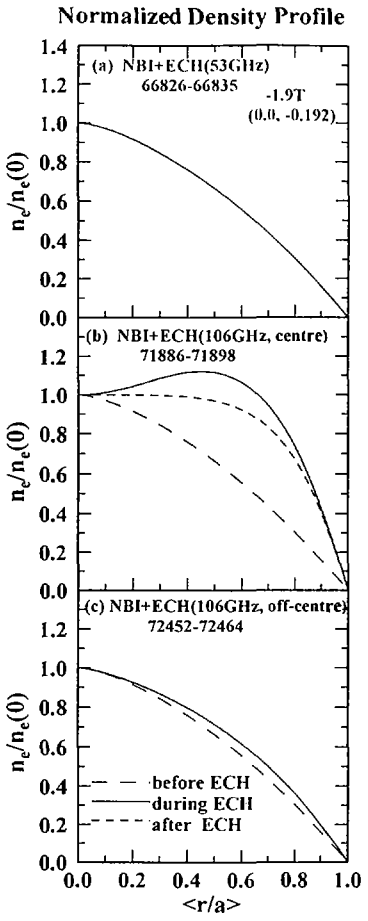

FIG. 6. Change of normalized density profile caused by superposition of ECH: (a) 53 GHz; (b) 106 GHz on-axis heating; (c) 106 GHz off-axis heating.

When the 53 GHz fundamental ECH ($P_{ECH} \sim 0.5$ MW) was superposed on the NBI plasma, both T_i and T_e rose [2]. The range of T_i can be scaled [4] as a function of $P_{ionz}/\bar{n}_e$ (the dashed line in Fig. 5), where P_{ionz} is the initially ionized neutral beam power injected through the port. The higher T_i during the 53 GHz ECH + NBI phase seems to exceed this scaling as shown in Fig. 5 (black squares). Although the increases in the H_α signal and the probe currents at the plasma edge or near the wall indicate a degradation of particle confinement, the ECH pulse does not flatten $n_e(r)$, as is shown in Fig. 6(a). Since the density profile is usually observed to steepen during NBI, we offer the interpretation that the density 'pump-out' by ECH is cancelled by this 'intrinsic' peaking effect of NBI.

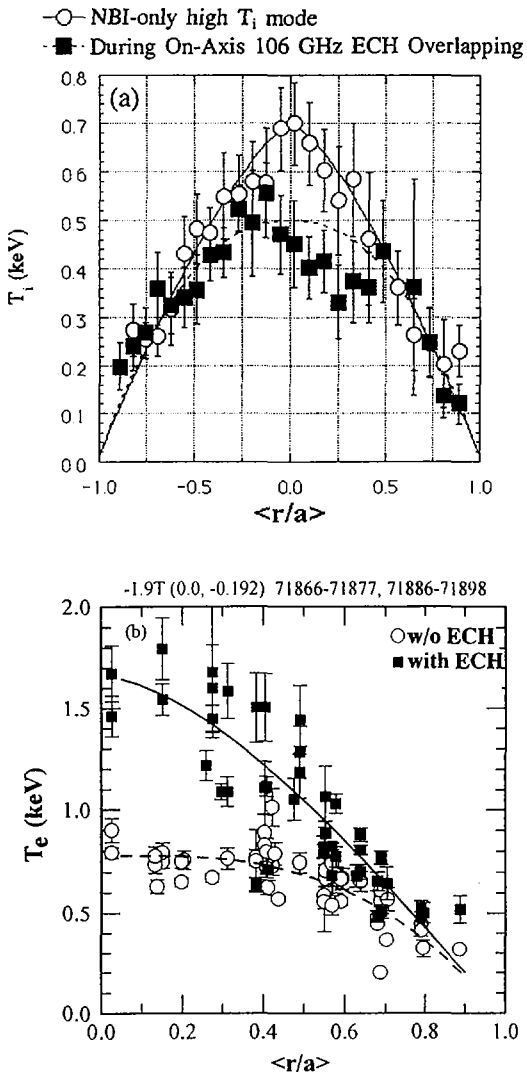

FIG. 7. (a) Comparison of T_i profiles in NBI plasma with and without 106 GHz on-axis ECH; (b) comparison of T_e profiles in NBI plasma with and without 106 GHz on-axis ECH.

According to the theory based on the Coulomb interactions between fast ions and bulk plasma particles, raising the electron temperature, with the same density profile, will increase P^i_{NBI}. Indeed, the observed increase in T_i lies in the expected range, which can be explained by this mechanism if no degradation of heat transport occurs during the combination heating phase.

As to the contribution of the radial electric field, an increase in E_r during the ECH pulse, $\Delta E_r \equiv E_r^{NBI+ECH} - E_r^{NBI} > 0$, is observed just inside the outermost magnetic surface by Langmuir probe measurements [9], and in the core region by rotation measurements of magnetic [10] and density fluctuation modes [11]. The change in the energy spectra of the charge exchange flux, which is considered to correspond to the modification of the loss structure for trapped beam ions (see Section 5), is also consistent with the buildup of $\Delta E_r \geq 0$ by ECH.

On the other hand, superposition of the 106 GHz second harmonic ECH ($P_{ECH} \sim 0.4$ MW) lowered T_i as is shown in Fig. 5 (inverted open delta). In contrast to the previous 53 GHz case, $\bar{n}_e$ was decreased and the density profile broadened during the ECH pulse (Fig. 6(b)) [12]. This means that the strong 'pump-out' in the core region is caused by this ECH overlapping. Figure 7(a) shows the radial profile of T_i measured by CX recombination spectroscopy. It is only in the central region, that the ion temperature seems to decrease by ECH overlapping. As to $T_e(r)$, however, the highly focused ECH raised T_e mainly in the central region, as is shown in Fig. 7(b).

As was mentioned in the previous section, the 53 GHz and 106 GHz ECH systems are different as far as the launching conditions are concerned. The power deposition of microwaves in the two cases is estimated from the decay time of $T_{e,ECE}$, the electron temperature measured by an ECE radiometer. Figure 8 shows the evaluated power deposition profiles (note that the diffusion process tends to

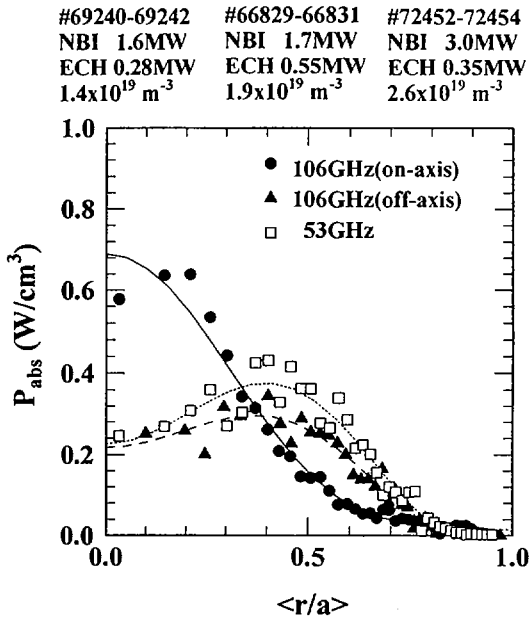

FIG. 8. Experimentally estimated power absorption profiles.

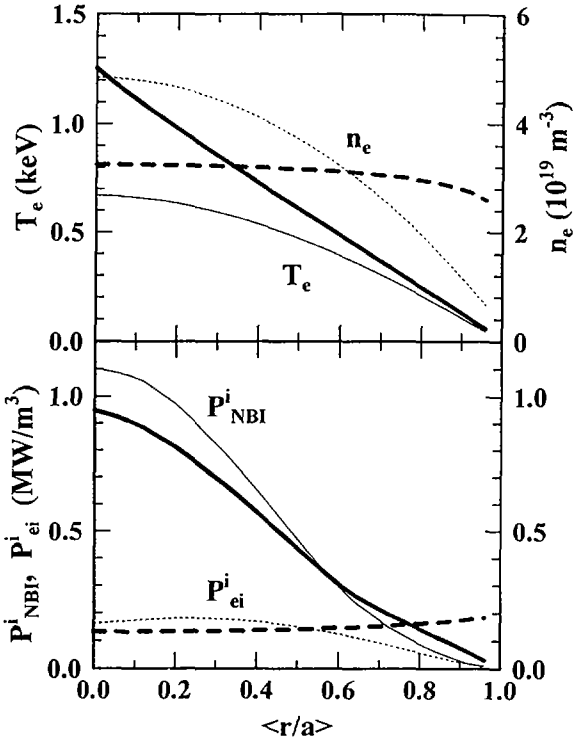

FIG. 9. Model calculation of absorbed power density for peaked n_e profile with rather low T_e (thin lines) and very flat n_e profile with high T_e (thick lines).

broaden the apparent deposition profile). In the 106 GHz second harmonic on-axis ECH case, as is expected, the ECH power is mainly focused in the central region. Although the total launched power is lower than in the 53 GHz case, the absorbed power density in the central region is much higher than in the 53 GHz case. Therefore, we may conclude that the higher local microwave power causes a strong pump-out effect on the NBI plasma although the details of the physical process of this density pump-out are not yet clear.

Both particle pump-out and resulting flat density profile can reduce the NBI ion heating efficiency in the core region. A model calculation shows how the changes in T_e and the density profile affect the power deposited to the ions, as is shown in Fig. 9. In this calculation, the plasma parameters are based on experimental observations, except for n_e, where the flattening effect of the density profile is artificially enhanced under the condition of $n_e\ell \approx$ const. The input power to the ions in the central region becomes small in the model of the ECH overlapping case (high T_e but flat $n_e(r)$). Moreover, as is discussed in Ref. [13], we should bear in mind the degradation of ion heat transport when the peaked profile changes to a broad profile.

Besides these negative effects, the change of the CX flux spectrum in the high energy region is still observed in this case, which suggests an increase in the heating power although the change of the rotation of the fluctuations by ECH overlapping is not clear. The edge E_r was, however, decreased during the ECH pulse in this case [14]. As to the effect of E_r on the orbits of high energy trapped ions, a change of E_r in the peripheral region can modify them more effectively than a change of E_r in the central region.

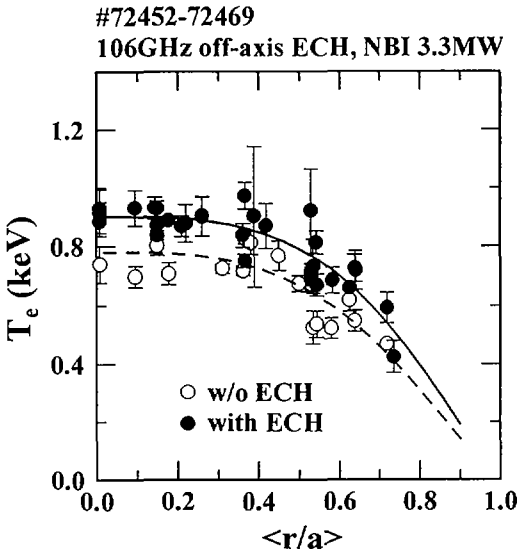

FIG. 10. Comparison of T_e profiles for the off-axis 106 GHz second harmonic ECH overlapping case.

To examine the effect of different power deposition profiles on the density profile in the 53 GHz and 106 GHz cases, the resonance position for the 106 GHz microwaves was moved from the plasma centre to $\langle r/a \rangle \sim 0.2$–$0.3$ by tilting the direction of the microwave beam. Thereby, the power deposition profile changes to almost the same profile as that for the 53 GHz ECH case, as is shown in Fig. 8. In this case, the decrease in $\bar{n}_e$ was mild compared to that in the central heating case. The density profile reconstructed from the seven channel FIR interferometer data shows that the broadening of $n_e(r)$ is also moderate, as is shown in Fig. 6(c). An increase in T_e was observed but not so large as in the central heating case, as is shown in Fig. 10. In this off-centre ECH case, which is characterized by a mild change in the density profile, we observe $\Delta T_i \geq 0$ (black triangles in Fig. 5) although the increase in T_e is not so large.

5. ECH EFFECTS ON FAST IONS

From the viewpoint of the fast ion loss, the effect of ECH on the CX neutral particle flux is analysed [15]. It is observed that the CX neutral particle flux in the high energy region, $E > E_{inj}/2$, for example, is enhanced by ECH superposition. This is observed for both cases of ECH, 53 GHz and 106 GHz. Figure 11 shows the energy spectra for the NBI-only (0.6 MW non-perpendicular (62°) injection) phase (T_e = 300 and 400 eV) and for the NBI + 53 GHz–ECH phase (T_e = 600 eV). Here, the three lines are results from a numerical calculation of the Fokker–Planck equation based on Coulomb collisions. Although the CX spectra during the NBI-only phase are in good agreement with the theoretical prediction, a clear discrepancy is found for the CX spectrum during the NBI + ECH phase. In order to explain this

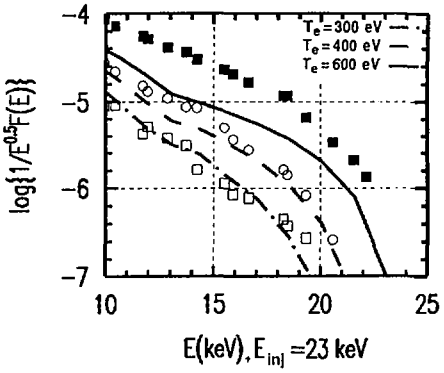

FIG. 11. Change of energy spectrum by 53 GHz ECH overlapping. (□) Initial phase of NBI; (○) just before ECH overlapping; (■) during ECH overlapping. Lines are results of calculations.

discrepancy, it is necessary to introduce some change of the fast ion loss (reduction of loss, in this case). One plausible explanation for the loss reduction is the shrinkage of the loss cone by $\Delta E_r > 0$ [16], which is caused by ECH overlapping. A more direct evidence for the reduction of fast ion loss by the 106 GHz ECH is observed as the fillup of a dip in the CX flux spectrum, which is observed for $E_{inj}/2 < E < E_{inj}$ in the case of perpendicular injection at an extremely inward shifted magnetic configuration (in this case, the resonance position is off-axis). Although a detailed study of this ECH effect remains to be done in future work, especially for the centre focused 106 GHz second harmonic ECH case, the observations discussed here imply a practically useful increase in heating power due to ECH overlapping.

6. CONCLUSIONS

The 106 GHz second harmonic ECH experiments were performed and compared with the 53 GHz ECH results. $T_e(0)$ increased up to 2.8 keV in the low density plasma, and $n_e(0)$ up to the X mode cut-off density was accessible. Owing to the high T_e with peaked profile in the 106 GHz case, a higher stored energy was obtained than in the 53 GHz case, with almost the same level of launched power. The magnetic field window for effective plasma production is narrower in the second harmonic ECH. It was shown that the magnetic shear plays an important role in the wave propagation in heliotron/torsatron devices and that the linearly polarized beam should be launched at a proper angle to the sheared field line to obtain good one pass absorption.

Effects of ECH on NBI plasmas are studied by using two ECH systems with different absorption profiles and resonance conditions. Superposition of ECH on the NBI plasma has shown that $\Delta T_i > 0$ for ECH overlapping with a rather broad power deposition profile, but $\Delta T_i < 0$ for the centrally focused ECH case. The change in ion heating power due to a change in T_e and the density profile caused by ECH overlapping was discussed. An analysis of the CX flux spectra in the higher energy region suggested an increase of effective heating power from NBI for both ECH cases. This increase may be attributed to the shrinkage of the intrinsic loss cone by $\Delta E_r > 0$ induced by ECH. In summary, a key to an explanation of these different effects on T_i is the balance between the gain from $\Delta T_e > 0$ (and, possibly, from $\Delta E_r > 0$) and the loss from the particle 'pump-out' and a resulting flattening of the density profile. This study shows that we can control this balance by changing the absorption profile of ECH.

REFERENCES

[1] YAMAGE, M., et al., J. Nucl. Mater. **220–222** (1995) 743;
KONDO, K., et al., J. Nucl. Mater. **220–222** (1995) 1052.
[2] OBIKI, T., et al., in Plasma Physics and Controlled Nuclear Fusion Research 1994 (Proc. 15th Int. Conf. Seville, 1994), Vol. 1, IAEA, Vienna (1995) 757.
[3] OBIKI, T., et al., in Plasma Physics and Controlled Nuclear Fusion Research 1988 (Proc. 12th Int. Conf. Nice, 1988), Vol. 2, IAEA, Vienna (1989) 337.
[4] UO, K., et al., in Plasma Physics and Controlled Nuclear Fusion Research 1986 (Proc. 11th Int. Conf. Kyoto, 1986), Vol. 2, IAEA, Vienna (1987) 355.
[5] NAGASAKI, K., et al., submitted to Fusion Technol.
[6] SUDO, S., et al., Nucl. Fusion **30** (1990) 11.
[7] NAGASAKI, K., EJIRI, A., Nucl. Fusion **35** (1995) 609.
[8] NAGASAKI, K., et al., Rev. Sci. Instrum. **66** (1995) 3432.
[9] MIZUUCHI, T., et al., paper presented at 10th Stellarator Workshop, IAEA Tech. Comm. Meeting, CIEMAT, Madrid, 1995.
[10] OBIKI, T., et al., ibid.
[11] KADO, S., et al., Fusion Eng. Des. (in preparation).

[12] MIZUUCHI, T., et al., Controlled Fusion and Plasma Physics (Proc. 23rd Eur. Conf. Kiev, 1996), Vol. 20C, European Physical Society, Geneva (1996).
[13] IDA, K., et al., IAEA-CN-64/CP-5, this volume.
[14] MIZUUCHI, T., et al., paper presented at 1996 Int. Conf. on Plasma Physics, Nagoya, 1996.
[15] KURIMOTO, S., in preparation.
[16] HANATANI, K., Doctoral thesis, Kyoto University (1988); SANUKI, H., et al., Phys. Fluids B2 9 (1990) 21552.

DISCUSSION

K. LACKNER: How large is your inferred χ_i^{eff} from the power balance compared with the neoclassical predictions, taking into account your E_r field measurements?

T. OBIKI: χ_i^{eff} is nearly χ_i^{NC} at the centre and about $10\chi_i^{NC}$ in the edge region. We have not calculated χ_i taking into account the effect of E_r.

F. WAGNER: Can you characterize the effect of power degradation, of particle confinement time and of the changes in E_r induced by ECRH on the effectiveness of density pumpout?

T. OBIKI: At present, we consider that density pumpout is a specific phenomenon for ECH. We do have some observations which suggest the buildup of asymmetric potential in ECH plasmas. Such an asymmetric potential structure might enhance the particle transport.

G. GRIEGER: Are there indications that you might have generated B parallel currents by the application of ECRH and that these currents might have invalidated your configuration?

T. OBIKI: In our case the microwave beam path is perpendicular to the magnetic field; thus, the effect of electron cyclotron current drive can be neglected. Also, we have observed no such toroidal current that would affect the iota profile during the ECH overlapping phase.

HIGH ION TEMPERATURES AND HIGH BETA IN W7-AS

M. KICK, J. BALDZUHN, J. GEIGER, O. HEINRICH, R. JAENICKE, A.I. KISLYAKOV[1], G. KÜHNER, H. MAASSBERG, W. OHLENDORF, F.-P. PENNINGSFELD, N. RUST, A. WELLER for W7-AS TEAM[2]
Max-Planck-Institut für Plasmaphysik,
Association Euratom-IPP,
Garching, Germany

Abstract

HIGH ION TEMPERATURES AND HIGH BETA IN W7-AS.

Experimental conditions concerning magnetic configurations, heating scenarios and density control for generating high ion temperatures and high β in W7-AS are described and experimental results are compared with theoretical predictions. Ion temperatures of up to 1.5 keV, the highest in helical systems so far, have been achieved. Energy confinement times about twice as long as predicted by the International Stellarator Scaling are derived for these discharges. This improvement is clearly related to the steep temperature and density gradients in the outer part of the plasma. In the bulk part, the experimental particle and energy fluxes as well as the radial electric field, E_r, are well consistent with neoclassical calculations, but a discrepancy is found for E_r in the gradient region of the profiles, whereas at the outermost part the agreement is good again. The strongly negative E_r in the profile gradient region forms a transport barrier with respect to the ion channel. Both sufficient high ion heating and low anomalous particle fluxes at the outer radii, i.e. low recycling, are mandatory for establishing this strongly negative E_r. The effect of this poloidal plasma rotation on the edge turbulence and confinement may be quite similar as in tokamaks. The availability of 3.0 MW NBI input power gave access to higher β values than in the previous experimental campaigns. Values of up to $\langle\beta\rangle \approx 1.8\%$ have been obtained with maximum heating at magnetic fields between 0.8 and 1.25 T. The achieved β values are in the range of the predicted stability and equilibrium β limit. No hard stability limit has been observed so far.

---

[1] A.F. Ioffe Physico-Technical Institute, St. Petersburg, Russian Federation.

[2] *W7-AS Team:* M. Anton, G. Beikert, E. Bellido, J. Bleuel, R. Brakel, B. Brañas, G. Cattanei, A. Chih Yao Teo, D. Dorst, S. Egorov, M. Ellmauer, A. Elsner, M. Endler, K. Engelhardt, V. Erckmann, Y. Feng, S. Fiedler, C. Fuchs, U. Gasparino, A. Geier, J. Geiger, T. Geist, L. Giannone, C. Görner, P. Grigull, H. Hacker, M. Häse, H.J. Hartfuss, O. Heinrich, G. Herre, M. Hirsch, J. Hofmann, E. Holzhauer, J.K. Hübner, R. Jaenicke, F. Karger, M. Kick, A.I. Kislyakov, G. Kocsis, C. Konrad, J. Koponen, G. Kühner, H. Laqua, L. Ledl, J.F. Lyon, H. Maassberg, C. Mahn, N. Marushchenko, H. Niedermeyer, W. Ohlendorf, W. Ott, F.-P. Penningsfeld, W. Pernreiter, S. Reimbold, H. Ringler, M. Romé, A. Runov, N. Rust, F. Sardei, C. Scheiba, F. Schneider, U. Schneider, U. Siart, E. Simmet, U. Stroth, G. Theimer, E. Unger, F. Wagner, H. Walter, A. Weller, E. Würsching, X. Zhang, S. Zoletnik.

Addresses of external W7-AS Team members:
B. Brañas: CIEMAT, Madrid, Spain; S. Egorov: TUAP, St. Petersburg, Russian Federation; E. Holzhauer: IPF Stuttgart, Germany; J.K. Hübner: IAP, University of Heidelberg, Germany; A.I. Kislyakov: A.F. Ioffe Physico-Technical Institute, St. Petersburg, Russian Federation; G. Kocsis, S. Zoletnik: KFKI Research Institute, Budapest, Hungary; J.F. Lyon: ORNL, Oak Ridge, Tennessee, USA; N. Marushchenko: IPP/NSC, Kharkov, Ukraine; A. Runov: Russian Research Center, Kurchatov Institute, Moscow, Russian Federation.

1. INTRODUCTION

Wendelstein 7-AS (W7-AS) [1] is a modular stellarator with five field periods following the concept of reduced collisional transport by reducing the averaged toroidal curvature in a low shear configuration. Stability is provided at low β by a vacuum magnetic well. W7-AS represents a first step towards an optimized stellarator such as W7-X. The improvement of the equilibrium properties over a classical stellarator (or circular tokamak) as seen in the predicted reduction of the Shafranov shift by a factor of two has been verified experimentally [2] (for W7-X, nearly one order of magnitude is expected). The coil system of W7-AS consists of nine non-planar coils in each period (module) generating the main field configuration. A separate current feed for the corner coils located in the plane of strongest curvature (elliptical plane) may be used to introduce a toroidal field ripple changing the number and toroidal position of trapped particles which are important for neoclassical transport properties in the long mean free path regime (lmfp). It has been shown that this ripple also affects the magnitude of the vacuum magnetic well [3]. A vertical magnetic field serves to centre the plasma column. Shifting the plasma inward, on the one hand, decreases the vacuum magnetic well leading to less stable configurations at low β, and, on the other hand, also influences the number of trapped particles [4]. Two additional toroidal field coils per module are used to change the vacuum rotational transform, ι, in the range from 0.25 to 0.65.

Together with an upgrade of the nearly tangential neutral beam injection (NBI) heating system to 3.0 MW, in combination with electron cyclotron resonance heating (ECRH) at 140 GHz, $P \leq 1$ MW, the operational range concerning ion temperatures and β was extended considerably. Access to higher ion temperatures in the ion lmfp regime of neoclassical transport became available. Another major aim was to test the achievable β values and energy contents and to compare them with theoretical expectations with respect to equilibrium and stability.

2. HIGH ION TEMPERATURES

2.1. Ways to high ion temperatures in W7-AS

Access to ion temperatures higher than 1 keV had been a major problem of W7-AS until recently. Pure ECRH discharges resulted in high electron temperatures up to 3 keV at low densities, whereas ions remained decoupled at temperatures $\leq$400 eV. For high ion temperatures, direct ion heating is needed, but NBI at high densities and low electron temperatures preferably also heats the electrons. Purely NBI heated discharges with an input power of $P_{NBI} \approx 1.2$ MW resulted in very high densities of above 3×10^{20} m^{-3}, because of the increased particle deposition connected with NBI and recycling, but fairly low temperatures of the order of 300–400 eV for both electrons and ions. With reduced heating power of 550 kW and

moderate densities of 0.7 × 10^{20} m^{-3}, stationary conditions could be obtained but ion temperatures did not exceed 500 eV [5].

Higher ion temperatures have been expected in the ion lmfp regime where the electric field derived from the ambipolarity condition of the particle fluxes reduces the otherwise unfavourable $1/\nu$ dependence of the neoclassical ion transport coefficients [6]. In order to access this regime at stationary conditions, experiments with NBI heating and additional ECRH at low densities have been carried out. The power transferred to the ions by NBI is increased with the increased electron temperature due to ECRH. At about 0.5 × 10^{20} m^{-3}, combined heating of counter-NBI, $P_{abs} \leq 550$ kW, and ECRH, $P \leq 700$ kW, resulted in ion temperatures close to 1 keV [7, 8].

In the 1995 experimental campaign the plasma radius was defined by inboard limiters [6]. In order to prevent contact of the plasma with the outer wall, vertical magnetic fields, B_z, were necessary for shifting the plasma inward. The inward shift

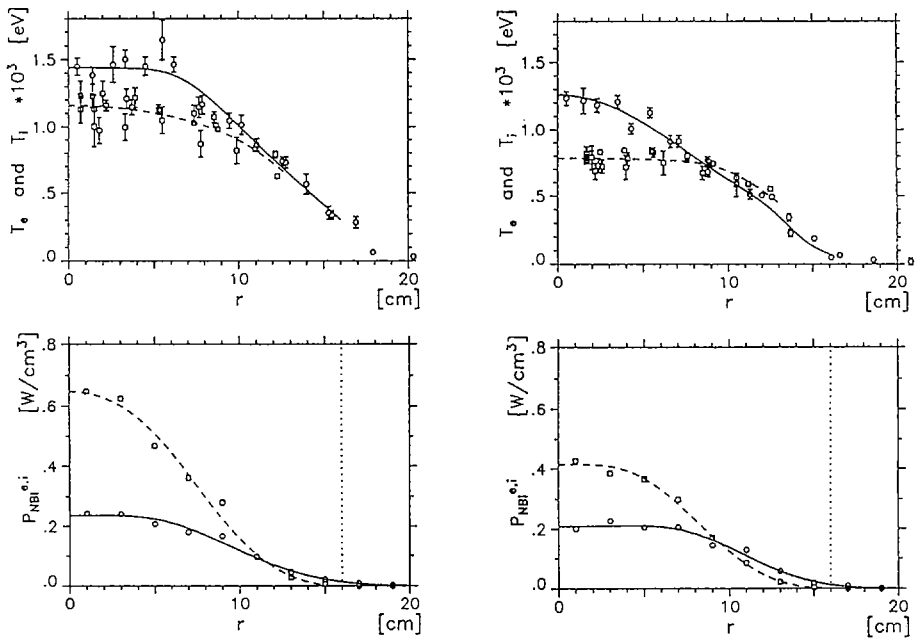

FIG. 1. Calculated absorbed power densities for ions (lower plots, dashed lines) and electrons (solid lines) for co- (left plots) and counter-injection (right plots), together with the measured electron (continuous lines) and ion (dashed lines) temperature profiles (upper plots) for stationary conditions (Nos 31 266 and 31 268, $B_0 = 2.5$ T, $B_z/B_0 = 0.01$, $\iota = 0.34$), each heated by one NBI source, $P_{NBI} \approx 375$ kW leading to 290 or 250 kW absorbed power for co- and counter-injection, respectively, combined with 400 kW of ECRH. In both heating scenarios, the central densities have been kept at 0.6 × 10^{20} m^{-3} with nearly identical profiles.

of the magnetic configuration led to improved neoclassical confinement [4, 6, 8]. First experiments in this configuration at $B_0 = 2.5$ T with $B_z/B_0 \approx 0.005$ with combined ECRH, $P \approx 700$ kW, and NBI heating, balanced injection with 540 kW of heating power, at a central density of 0.5×10^{20} m^{-3}, resulted in central ion temperatures slightly above 1 keV.

For NBI co-injection, Monte Carlo code calculations predict peaked heating profiles with a considerably higher heating efficiency compared to counter-injection with flat heating profiles. Figure 1 shows the calculated absorbed power densities for the ions and electrons for co- (left) and counter-injection (right), together with the measured electron and ion temperature profiles. Because of the rather high electron temperature of about 1.4 keV, more than half of the total NBI heating power is transferred directly to the ions. Whereas comparable electron heating powers lead to fairly similar electron temperatures, the central ion temperature is significantly higher for the co-NBI case than for the counter-NBI case because of the significantly different heating power density profiles for the ions.

As already found in W7-A [9], additional ECRH turned out to be essential for sustaining density control at low and moderate densities in experiments with NBI heating in W7-AS [10]. With ECRH at 140 GHz (X mode), the density range accessible for combined heating is up to 1.2×10^{20} m^{-3} (cut-off density). Experiments at $B_0 = 2.5$ T with $B_z/B_0 \approx 0.01$ at central densities of about 0.5×10^{20} m^{-3} and co-injection at $P_{abs} \approx 580$ kW, combined with 700 kW of ECRH, resulted in central ion temperatures of 1.35 keV [8]. With co-NBI, $P_{abs} \approx 850$ kW, combined with only 350 kW of ECRH at about the same parameters as described above, central ion temperatures up to 1.5 keV have been measured. This experiment has been carried out after a forced conditioning procedure with many high power NBI discharges followed by boronization. Under these conditions, a decrease of the ECRH power to 350 kW has been possible without losing density control. Whereas the central ion temperature after turning off the ECRH remained at about 1.5 keV, the central electron temperature dropped from 1.8 to 1.25 keV because of the decreased direct electron heating. The improved conditioning procedure apparently leads to recycling conditions which, in turn, provide improved density control.

For the above described type of combined NBI and ECR heated discharges, the densities have been varied from 0.5 to 1.2×10^{20} m^{-3}. Both electron and ion temperatures are slightly decreased with increasing density.

2.2. Particle and energy balances

The particle and energy balance analysis is based on the profiles of the electron density measured by Thomson scattering, of the electron temperature by Thomson scattering as well as by ECE (electron cyclotron emission), and of the ion temperature both by charge exchange (CX) neutral particle analysis and by charge exchange recombination spectroscopy (CXRS). By using a pulsed diagnostic neutral beam injector, active CX and CXRS measurements give access to the local T_i profile. The

radial electric field is estimated from the poloidal momentum balance where the poloidal and toroidal velocities are obtained by CXRS from the Doppler shift of impurity lines. For the bulk part of the plasma, gas puffed helium is used for active CXRS and inherent boron for passive CXRS at the outermost radii [11].

For moderate densities, the collisional power transfer, P_{ei}, is sufficiently small, allowing a separation of the ion and the electron energy balances. The P_{ei} term is obtained from the measured profiles. Ion and electron heating by NBI is calculated by the FAFNER Monte Carlo code with fast CX losses taken into account. The ECRH power deposition is modelled corresponding to ray tracing calculations. The radiation losses, P_{rad}, are modelled corresponding to bolometry data. Furthermore, thermal CX losses which contribute to the ion energy balance at outer radii are estimated by the EIRENE code [12]. In this way, the *experimental* ion and electron energy fluxes, Q_i and Q_e, are obtained. The experimental particle fluxes are derived by integrating the NBI particle deposition from the FAFNER code and the particle sources from recycling (and gas puffing) estimated from the EIRENE code.

The neoclassical monoenergetic transport coefficients are calculated by the DKES code [13] (the ripples induced by the discrete coils are neglected in the B-Fourier spectrum) for each magnetic configuration of W7-AS as a function of collisionality, radial electric field and radius. Energy convolution of these monoenergetic transport coefficients is performed either by interpolation in these databases or by a numerical fit algorithm based on traditional analytic theory [14]. With this neoclassical transport matrix, the thermal particle and energy fluxes are obtained from numerical fits, and the radial electric field is estimated from the ambipolarity condition of the neoclassical particle fluxes [15]. With this ambipolar E_r, only the ion transport coefficients are significantly decreased in the 'ion root' solution ($E_r < 0$) expected for $T_e \approx T_i$.

At the outer radii, where recycling results in strong particle sources, an *anomalous* particle flux dominates the neoclassical one which decreases significantly with decreasing temperature. Assuming that this anomalous particle flux, Γ_{an}, is intrinsically ambipolar, E_r is given by the ambipolarity of the neoclassical fluxes alone. In the energy balance, the anomalous transport adds to the neoclassical one at least by $(5/2)T\Gamma_{an}$ (in a purely convective model) and leads to energy exchange between ions and electrons by the $qE_r\Gamma_{an}$ term. This last term may be important at the plasma edge (here, Γ_{an} becomes large) in the case of steep temperature and density gradients which lead to a significant neoclassical $E_r < 0$.

The discharge shown in Fig. 2 is very sensitive with respect to particle confinement and global density control. Corresponding to the diffusive particle transport scaling close to the plasma edge [16] (e.g. $D_{an} \propto P^{0.85}/n^{1.1}$ in the SOL [17]) it was somewhat unexpected that global density control was achieved at this high density with three NBI sources (co-injection; 510 kW and 315 kW power absorbed by ions and electrons, respectively, calculated by the FAFNER code) and a rather low level of ECRH (330 kW at 140 GHz, X mode). Generally, the energy confinement is very good for this type of discharge: $\tau_E \approx 22$ ms (with the thermal energy content

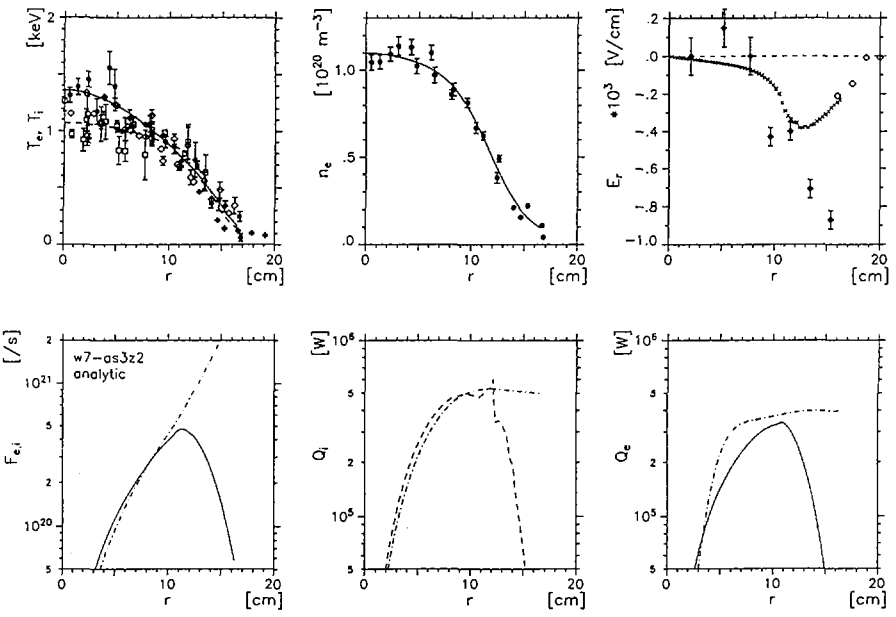

FIG. 2. Profiles, transport analysis and neoclassical predictions for a stationary discharge (No. 34 609, B_0 = 2.5 T, B_z/B_0 = 0.01, ι = 0.34, combined NBI (825 kW) and ECRH (350 kW)). Upper row from left: electron and ion temperatures, T_e (solid line) and T_i (dashed line), electron density, n_e, and radial electric field, E_r, derived from active (helium, full circle) and passive (boron, diamond) CXRS and calculated from the ambipolarity condition (cross). Lower row from left: particle fluxes derived 'experimentally' from EIRENE and FAFNER codes (dash-dotted line) and the neoclassical ambipolar flux (solid line), ion heat fluxes, Q_i, from power balance (dash-dotted line) and calculated (dashed line), and electron heat fluxes, Q_e, from power balance (dash-dotted line) and calculated (solid line).

integrated from density and temperature profiles, $\tau_E \approx$ 16 ms, by using W_{dia}) compared to less than 9 ms from the ISS95 regression analysis [18]. This significant confinement improvement is clearly related to the steep temperature and density gradients at the outer radii (r > 10 cm; compare Fig. 2). In the bulk part of the plasma, the neoclassical particle fluxes are consistent with the NBI particle source (1 MW of NBI corresponds to about 2.5 × 10^{20}/s) and additional recycling sources (see the lower left plot). In this region, also the experimental energy fluxes of ions (in the middle) and electrons (lower right plot) are in reasonable agreement with the neoclassical predictions.

A discrepancy is found between the neoclassical prediction of E_r from the ambipolarity condition and the one estimated from the Doppler shift of the helium line (active CXRS), whereas the passive CXRS with boron at the outermost radii gives good agreement (upper right plot). The neoclassical values of E_r at r > 10 cm

are sufficient to suppress direct losses of ripple trapped particles even at higher energies, i.e. loss cone effects are of minor importance. Furthermore, fast ion orbit losses related to the nearly tangential NBI are also negligible, as estimated by the FAFNER Monte Carlo calculations. In this range, the neoclassical E_r values are very close to the ones determined by the 'toroidal resonance' condition ($B_\Theta v_{th,i}$), where the ion transport coefficients are strongly decreased (the 'helical plateau' in W7-AS configurations is too low to affect the neoclassical fluxes [15]). Non-ambipolar CX driven ion fluxes being proportional to the neutral density gradient are much less than the neoclassical ambipolar particle fluxes. Consequently, the measured strongly negative E_r values are in clear contradiction to neoclassical theory. On the other hand, it seems unlikely that mainly the anomalous ion flux is increased if the assumption of intrinsically ambipolar anomalous particle flux is violated. For example, small scale magnetic field ergodization close to the plasma edge would lead to enhanced electron fluxes, and thus a reduced E_r is needed to satisfy the ambipolarity constraint.

With the purely convective ion energy flux, $(5/2)T_i\Gamma_{an}$, and the additional energy exchange term, $qE_r\Gamma_{an}$ (with E_r from the neoclassical ambipolarity condition), the ion energy balance can be fulfilled also close to the plasma edge where the neoclassical fluxes become small. The energy transferred to the electrons by the neoclassical E_r is about half the ion heating power (the thermal CX losses are less than 20%). Thus the strongly negative E_r at the outer radii forms a transport barrier with respect to the ion channel. Both sufficient high ion heating and low anomalous particle fluxes at the outer radii, i.e. low recycling, are mandatory to establish this region with strongly negative E_r. The effect of the poloidal plasma rotation with strong shear, driven by the neoclassical ion losses, on the edge turbulence (e.g. the reduction of the radial correlation of density and potential fluctuations) and on the edge enhanced confinement may be quite similar as in tokamaks; see, e.g. Ref. [19]. However, toroidal rotation effects are of minor importance since the ripple trapped particles lead to significant toroidal momentum damping in W7-AS. This is confirmed by the CXRS toroidal rotation measurements, in which only small velocities are found in the potential barrier region. The reduction of anomalous transport close to the plasma edge results in a steepening of the temperature gradients, and the strong temperature dependence of the neoclassical transport leads to the 'saturation' of both the ion and the electron temperatures in the bulk part.

3. HIGH BETA

3.1. Equilibrium

In stellarators the confining magnetic field is created by external field coils. At low β the internal equilibrium plasma currents (Pfirsch–Schlüter currents) produce additional magnetic fields which slightly change the magnetic field configuration (flux surface shape, profile of the rotational transform, ι). At higher β values this change is significant. A figure of merit for these changes is given by the equilibrium

β limit [20], where the shift, Δ, of the magnetic axis is half of the minor radius, a. For W7-AS this limit is given by $\langle\beta_{eq}\rangle = 2\iota^2/A$, where A is the aspect ratio and the factor of two which is missing for a classical stellarator comes from the reduction of the Pfirsch–Schlüter currents due to the reduced average toroidal curvature. The values of $\langle\beta_{eq}\rangle$ range from around 2% to 4.5%, depending on ι (e.g. 1/3 to 1/2) and A (≥ 11).

3.2. Experiments

High β discharges at W7-AS are usually performed at reduced field strengths to take advantage of the B scaling of β. For plasma startup at 1.25 T ECRH is used (70 GHz, 200–400 kW). Improvements of the non-resonant RF plasma startup system (900 MHz, 10 kW) additionally gave access to lower field strengths. After startup, the NBI input power was increased stepwise to the full injection power of about 3.0 MW. The increase in plasma energy is usually accompanied by a strong rise in plasma density, leading to rather high values of up to 2.5×10^{20} m^{-3} at $B_0 = 1.25$ T. Often impurity radiation determines the time evolution of the discharges which are usually quenched on an energy confinement time-scale whenever the radiation exceeds about half of the input power.

Electron temperatures measured by Thomson scattering at maximum plasma energy are around 400 eV at half-field. The ion temperatures can be assumed to be equal to the electron temperatures because of the strong thermal coupling at high densities. With equivalent electron and ion contributions, central β values of about 4% can be estimated which lead to $\langle\beta\rangle$ values of about 1.8%, assuming a peaking factor of 2.5. The exact value of $\langle\beta\rangle$ needs numerical equilibrium calculations since the minor plasma radius at startup was defined by inboard limiters. The shift of the plasma column with increasing β leads to a significant increase of the minor radius by a factor of about 1.2–1.5 in the discharges, as shown in Fig. 3.

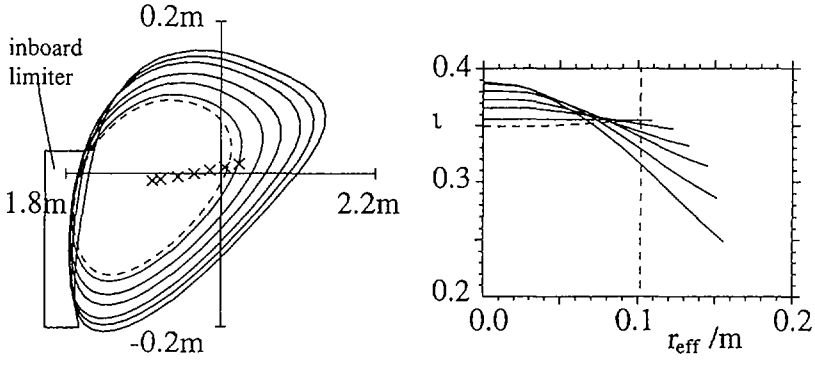

FIG. 3. Evolution of plasma boundary and axis position in the limiter cross-section with increasing β ($\beta_0 = 0$ (dashed line), 0.3, 1.0, 1.7, 2.4, 3.4, 4.0%) for magnetic field configuration of discharge No. 31 114, along with finite β change of rotational transform profile.

The numerical calculations of the equilibrium configurations at high β were done with the free boundary MHD equilibrium code NEMEC [21]. In this context internal toroidal net currents (bootstrap current, ohmic and NBI driven currents) could be neglected owing to the high densities and rather low temperatures at high β. The change of the equilibrium configuration as calculated with NEMEC for an equilibrium sequence from $\beta_0 = 0$ to 4% ($\beta \sim 1 - (r/a)^2$) is shown in Fig. 3, visualizing the increase in volume in the limiter plane as well as the change of the ι profile for shot No. 31 114 at $B_0 = 1.25$ T with a rather high vertical field of 31 mT. The equilibrium at maximum β has been reconstructed in more detail [6] by using the electron density and temperatures as measured by Thomson scattering, resulting in $\langle\beta\rangle \approx 1.8\%$ and $\beta_0 \approx 4\%$. Good agreement was also achieved in a comparison of the calculated flux surfaces with the tomographically reconstructed soft X ray emission which is supposed to be constant on flux surfaces, because of its dominant dependence on the electron temperature [6].

From sequences of equilibrium calculations with different β values the diamagnetic signals were simulated with the DIAGNO package [22] for various discharges with expected high β values. The reconstructed time traces of $\langle\beta\rangle$ for various discharge conditions (B_0, ι, B_z) all showed $\langle\beta\rangle$ values between 1.6 and 1.8%, which is rather close to the predicted equilibrium β limit. The presumably highest $\langle\beta\rangle$ with about 1.8% was achieved at $B_0 = 1.25$ T ($\iota_{vac} = 0.34$). A field scan ($B_0 = 1.25$ T, 1.0 T, 0.8 T) at $\iota_{vac} = 0.4$ shows no increase in β for lower field strengths (see Fig. 4). This is currently being investigated since a net increase in $\langle\beta\rangle$ is expected for lower field strength, although the $1/B^2$ dependence is reduced by the energy confinement time scaling ($\tau_E \sim B^{0.8}$). An additional reduction is due to the degradation of the heating efficiency of the NBI with decreasing field strength [23] and the B dependence of the maximum density.

Figure 5 shows the maximum diamagnetic energy in a ι scan at $B_0 = 1.25$ T with vertical fields of about 20 mT. The observed decrease of the energy content for higher ι values is expected since the ι dependence of the plasma column shift due to finite β ($\sim 1/\iota^2$) leads to a smaller increase in plasma volume at higher ι. The volume decrease is described by the energy confinement time scaling ($\tau_E \sim a^2$ [18]), if one assumes otherwise constant profiles. The last assumption is supported by the electron β profiles from Thomson scattering data at maximum energy which are roughly equivalent. Equilibrium calculations including only the volume effect by keeping the profiles constant reproduce the trend of the energy decrease in the range of the observed one, as has been noted in Ref. [6].

However, the ISS95 scaling [18] also includes a favourable effect according to $\tau_E \sim \iota^{0.4}$ counteracting the volume effect. Although the electron β values around the maximum energy were roughly the same, the discharges are different in some aspects. On the one hand, since the line density evolution has been kept constant the effect of the smaller minor radius at higher ι values leads to higher central densities but lower temperatures. Especially at the boundary, lower temperatures could be further lowered by increased radiation losses as seen in the bolometer signals, leading

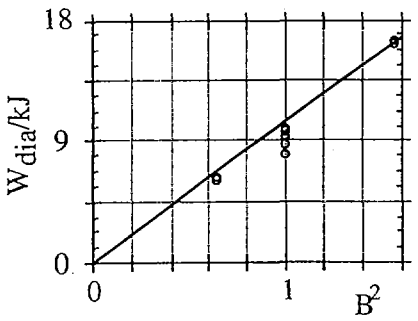

FIG. 4. Diamagnetic energies in a field scan (B_0 = 0.8, 1.0, 1.25 T) at ι = 0.4 with equivalent vertical fields. The almost linear scaling of W_{dia} with B^2 means that β does not increase with decreasing field strength.

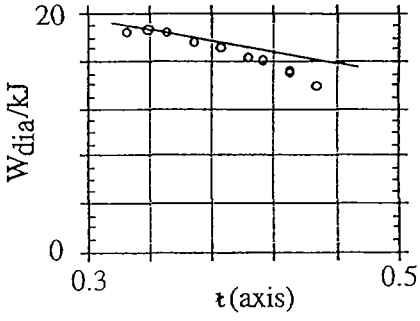

FIG. 5. Diamagnetic energies in a ι scan at B_0 = 1.25 T with vertical fields of about 20 mT. The line is an estimate from free boundary equilibrium calculations using the NEMEC code with constant pressure profiles.

to slightly narrower profiles. This effect of profile deviation shows up much stronger in the energy due to the volume weighting. On the other hand, resonant structures connected with the natural rational ι values (5/m) at the boundary, as known from the vacuum field configurations at high ι values, have been seen by video observations of visible light in the high β phases of the discharges. The corrugated structures cannot be resolved by the equilibrium calculations with NEMEC at present. Thus the NEMEC boundary may be too smooth, leading to an overestimation of the plasma radius especially for higher ι values, i.e. smaller m, where the corrugations are deeper.

3.3. Stability

Particularly in some discharges with very high vertical fields, an increased MHD activity has been observed in the Mirnov and soft X ray signals at the end of the energy rise and the beginning of the stationary phase. There are mainly two phenomena frequently observed during these discharges: First, there are high frequency (50–100 kHz) bursts of MHD activity seen by both the Mirnov and the soft X ray diagnostics. They seem to affect the confinement, which can be seen in profile relaxations in the soft X ray emissivity at the edge and also in small changes of the plasma energy. The second phenomenon is a low frequency (4–8 kHz) coherent mode activity which also may modify the profiles at the edge and affect the plasma energy. Nevertheless, a hard β limiting MHD activity could not yet be observed in the signals. Most of the discharges in the medium vertical field range even displayed rather quiescent Mirnov and soft X ray signals in the high β phase.

The standard configurations of W7-AS (without vertical field) are usually stabilized against resistive interchange and Mercier modes by a vacuum magnetic well for small and moderate β values. Finite β increases the well depth but also the destabilizing terms in the stability criterion. Stability predictions with respect to resistive interchange modes based on calculations with the JMC stability code [24] lead to expected average beta values of 1.5%. With growing β, the analysis indicates that the plasma becomes unstable first at the boundary. Then, the unstable region grows towards the inside with β. The achieved values of $\langle\beta\rangle$ of up to 1.8% are in the range of these stability predictions.

A stability analysis of discharge No. 31 114 with respect to Mercier and resistive interchange modes using the stability code JMC confirms these results. The equilibrium proves to be Mercier stable, but shows a resistive interchange unstable region in the outer third of the plasma (for $r/a > 2/3$). The unstable region extends to the plasma boundary where the resistive interchange criterion is identical with the stability criterion for ideal free boundary modes ('peeling modes') [25]. Actually, a stability analysis with the 3-D code TERPSICHORE shows the appearance of peeling modes at β values slightly above the experimental values [26]. Therefore, resistive interchange and peeling modes might be candidates for the increased high frequency non-coherent MHD activity seen in the Mirnov and soft X ray signals. Similar findings from magnetic fluctuation measurements have been reported in a more detailed study from CHS where saturated magnetic fluctuations at high beta are attributed to saturated resistive interchange turbulence [27]. Also there, no hard stability limits have been observed for $\langle\beta\rangle$ values of up to 2.2% [28].

The activity of the low frequency coherent modes is assumed to be related to the appearance of low order rational ι values in the unstable region of the plasma. Simulations of the soft X ray signals show mode numbers expected from low order rational ι values and changes in the radial mode position according to variations in the ι profile.

4. SUMMARY AND CONCLUSIONS

Very good confinement properties in combined NBI and ECR heated discharges with high ion and electron temperatures were obtained in W7-AS. Strongly negative radial electric fields at outer radii form a potential barrier which acts like a transport barrier for the ion energy loss channel. A fairly high level of direct ion heating by the NBI as well as a sufficiently low particle flux (i.e. low recycling by wall conditioning) seems to be essential in order to establish this transport barrier. In the inner two thirds of the plasma radius, the neoclassical particle fluxes as well as the ion and electron energy fluxes with the ambipolar radial electric field taken into account are in very good agreement with the experimental particle and energy balances.

Rather high values of $\langle\beta\rangle$ up to 1.8% with central β values of about 4% have been reached at W7-AS. Although these values are of the order of the predicted equilibrium and stability limits, a hard stability limit was never found experimentally.

Nevertheless, profile relaxations experimentally observed in some discharges may be driven by resistive interchange instabilities at outer radii. Generally, the accessible β values are limited by radiation losses due to very high densities rather than by MHD instabilities.

On the whole, the good agreement of experimental observations in W7-AS and theoretical predictions in the case of neoclassical theory (high ion temperatures in the lmfp region) as well as for the achieved high β values gives good confidence in the predictions for W7-X, the optimization of which is based on the underlying theories.

REFERENCES

[1] RENNER, H., et al., Plasma Phys. Control. Fusion **31** (1989) 1579.
[2] WELLER, A., et al., Plasma Phys. Control. Fusion **33** (1991) 1559.
[3] GEIGER, J. et al., in Controlled Fusion and Plasma Physics (Proc. 23rd Conf. Kiev, 1996), Vol. 20C, European Physical Society, Geneva (1996).
[4] BEIDLER, C.D., et al., in Stellarators (Proc. 10th Int. Conf. Madrid, 1995), IAEA Tech. Comm. Meeting, Madrid (1995) 326.
[5] AFANASIEV, V., et al., in Controlled Fusion and Plasma Physics (Proc. 18th Eur. Conf. Berlin, 1991), Vol. 15C, Part II, European Physical Society, Geneva (1991) 209.
[6] JAENICKE, R., et al., Plasma Phys. Control. Fusion **37** (1995) A163.
[7] KICK, M., et al., in Controlled Fusion and Plasma Physics (Proc. 20th Eur. Conf. Lisbon, 1993), Vol. 17C, Part I, European Physical Society, Geneva (1993).
[8] KICK, M., et al., in Stellarators (Proc. 10th Int. Conf. Madrid, 1995), IAEA Tech. Comm. Meeting, Madrid (1995) 330.
[9] RINGLER, H., et al., in Plasma Physics and Controlled Nuclear Fusion Research 1986 (Proc. 11th Int. Conf. Kyoto, 1986), Vol. 2, IAEA, Vienna (1987) 603.
[10] RINGLER, H., et al., Plasma Phys. Control. Fusion **32** (1990) 933.
[11] BALDZHUHN, J., OHLENDORF, W., Rev. Sci. Instrum. (in preparation).
[12] REITER, D., THE EIRENE CODE, Version: Jan. 92, Rep. 2599, Users Manual, Institut für Plasmaphysik, Association Euratom-KFA, Jülich, 1992.
[13] VAN RIJ, W.I., HIRSHMAN, S.P., Phys. Fluids B 1 (1989) 563.
[14] BEIDLER, C.D., et al., in Controlled Fusion and Plasma Physics (Proc. 21st Eur. Conf. Montpellier, 1994), Vol. 18B, Part II, European Physical Society, Geneva (1994) 568.
[15] MAASSBERG, H., et al., Phys. Fluids B **5** (1993) 3627.
[16] BRAKEL, R., et al., in Plasma Physics and Controlled Nuclear Fusion Research (Proc. 15th Int. Conf. Würzburg, 1992), Vol. 2, IAEA, Vienna (1993) 501.
[17] GRIGULL, P., et al., in Stellarators (Proc. 10th Int. Conf. Madrid, 1995), IAEA Tech. Comm. Meeting, Madrid (1995) 73.
[18] STROTH, U., et al., Nucl. Fusion **36** (1996) 1063.
[19] WARD, D.J., Plasma Phys. Control. Fusion **38** (1996) 120.
[20] PUSTOVITOV, V.D., Fundamental Stellarator MHD Theory, J. Plasma Fusion Res. **70** (1994) 943 (in Japanese).
[21] HIRSHMAN, S.P., VAN RIJ, W.I., MERKEL, P., Comput. Phys. Commun. **43** (1986) 143.
[22] GARDNER, H., Nucl. Fusion **30** (1990) 1417.
[23] PENNINGSFELD, F.-P., et al., in Controlled Fusion and Plasma Physics (Proc. 23rd Eur. Conf. Kiev, 1996), Vol. 20C, European Physical Society, Geneva (1996).

[24] NÜHRENBERG, J., ZILLE, R., in Theory of Fusion Plasmas, Editrice Compositori, Bologna (1988) 3.
[25] LORTZ, D., Nucl. Fusion **15** (1975) 49.
[26] COOPER, A., Los Alamos National Laboratory, NM, USA, personal communication.
[27] SAKAKIBARA, S., et al., J. Phys. Soc. Jap. **63** (1994) 4406.
[28] YAMADA, H., et al., in Stellarators (Proc. 10th Int. Conf. Madrid, 1975), IAEA Tech. Comm. Meeting, Madrid (1995) 270.

DISCUSSION

R.J. GOLDSTON: Could you tell us about any localized regions of Mercier instability in your high β plasmas? Also, have you evaluated ideal ballooning stability for these plasmas?

R. JAENICKE: The JMC code analyses flux surface averages only, and so the effect of local high pressure gradients cannot be studied. Equally, we do not have a code which could treat the ballooning mode in the fully 3-D geometry.

K. IDA: Do you observe the agreement of measured χ_i with the neoclassical prediction for discharges with low ion temperature ($T_i < 1$ keV) as well as for high T_i discharges?

R. JAENICKE: The ion heat transport is always close to neoclassical in W7-AS.

K. IDA: Is $\mathbf{E} \times \mathbf{B}$ velocity shear stabilization unimportant in W7-AS?

R. JAENICKE: A possible influence of velocity shear stabilization is unknown.

K. TOI: I have a question about the effect of a large radial electric field on electron heat transport. The ion temperature profile has a steep gradient near the negative E_r well, which is consistent with neoclassical transport theory. But I have also found that the electron temperature profile has a steep gradient near the $|E_r|$ maximum ($E_r < 0$). According to neoclassical transport theory, electron transport is not affected by the negative E_r well. How do you interpret this observation in the electron temperature profile? Also, do you observe good correlation of the steep T_e gradient with the $|E_r|$ maximum?

R. JAENICKE: The high ion temperature discharges are the only type of discharges where this observation was made. The relationship between the maximum of $|E_r|$ and the steep electron temperature gradient is not yet understood.

EXPERIMENTAL STUDY OF PLASMA CONFINEMENT AND HEATING EFFICIENCY THROUGH POTENTIAL PROFILE MEASUREMENTS WITH A HEAVY ION BEAM PROBE IN THE COMPACT HELICAL SYSTEM

A. FUJISAWA, S. KUBO, H. IGUCHI, H. IDEI, T. MINAMI,
H. SANUKI, K. ITOH, S. OKAMURA, K. MATSUOKA,
K. TANAKA, S. LEE, M. KOJIMA, T.P. CROWLEY[1],
Y. HAMADA, M. IWASE, H. NAGASAKI, H. SUZUKI, N. INOUE,
R. AKIYAMA, M. OSAKABE, S. MORITA, C. TAKAHASHI,
S. MUTO, A. EJIRI, K. IDA, S. NISHIMURA, K. NARIHARA,
I. YAMADA, K. TOI, S. OHDACHI, T. OZAKI, A. KOMORI,
K. NISHIMURA, S. HIDEKUMA, K. OHKUBO,
D.A. RASMUSSEN[2], J.B. WILGEN[2], M. MURAKAMI[2],
T. WATARI, M. FUJIWARA
National Institute for Fusion Science,
Nagoya, Japan

Abstract

EXPERIMENTAL STUDY OF PLASMA CONFINEMENT AND HEATING EFFICIENCY THROUGH POTENTIAL PROFILE MEASUREMENTS WITH A HEAVY ION BEAM PROBE IN THE COMPACT HELICAL SYSTEM.

In the Compact Helical System, electrostatic potential profiles in the steady states and transient phases of various plasmas have been measured with a 200 keV heavy ion beam probe. Potential profiles in the steady states of ECH and NBI plasmas show electron and ion root characteristics, respectively. A recent extension of the ECH system, in terms of power and controllability of the focus point and polarization direction, produced a plasma with a high central electron temperature of 2 keV with 500 kW EC (53.2 GHz) fundamental heating in operation at 1.7 T. A 300 kW ECH plasma using second harmonic resonance at 0.9 T has a positive profile with $\phi(0) = 400$ V, which exhibits a unique characteristic suggesting an internal momentum transport barrier at $\rho = 0.4$. When NBI is applied to this plasma, a positive potential around the core region is kept for more than 10 ms, which is longer than the energy confinement time of a few milliseconds, although the potential around the edge becomes negative in about 5 ms. During this phase, a dynamic behaviour of the potential, or a transition phenomenon in a few hundred microseconds, is also discovered around the core. A loss cone evaluation based on the measured potential profiles gives an insight into high energy particle behaviours for both positive and negative potential profiles. A periodic change in the potential profile, and internal potential fluctuation, were detected in MHD burst phenomena observed in low density NBI plasmas.

[1] Rensselaer Polytechnic Institute, Troy, New York, USA.
[2] Oak Ridge National Laboratory, Oak Ridge, Tennessee, USA.

1. INTRODUCTION

The Compact Helical System (CHS) [1] is a heliotron/torsatron device which has a small aspect ratio of about 5; the major radius and averaged minor radius are 1.0 m and 0.2 m, respectively. Such a small aspect ratio device has the potential for a higher β limit for MHD stability, and it could be superior from an economic point of view. However, the large toroidicity of such a device gives birth to a large deviation of ripple trapped particles from the magnetic flux surface, resulting in deterioration of confinement properties and heating efficiency in a collisionless regime. The plasma potential is a key physical quantity which affects the confinement property and heating efficiency by inducing an $\mathbf{E} \times \mathbf{B}$ motion in the orbits of helically trapped particles.

The radial electric field of the NBI plasmas in CHS has been deduced from plasma rotation velocity measurements with a charge exchange recombination spectroscopy (CXRS) system [2]. A 200 keV heavy ion beam probe (HIBP) has been put into operation to study the role of the space potential in the CHS plasma [3], and has measured electrostatic potential (or electric field) profiles in both ECH and NBI plasmas over the whole plasma region within a short period (a few milliseconds) of a discharge. The gyrotron system has been recently enhanced to explore the plasma behaviour in a low collisional regime for electrons [4]. In fact, the electron temperature has been observed to be about 2 keV around the core in operation at 1.7 T with fundamental resonance heating of 53.2 GHz.

In this paper we will describe three main experimental topics concerned with potential measurements: (1) potential profiles in the steady states of ECH and NBI plasmas, and a unique potential profile in high power ECH operation; (2) the time evolution of the potential profile and its dynamic behaviour around the core while NBI is applied to a high power ECH plasma; (3) a DC potential oscillation and local potential fluctuation associated with the MHD evolution. The high energy particle behaviour will be discussed by evaluating a loss cone structure from the obtained potential profiles.

2. BRIEF DESCRIPTION OF EXPERIMENTAL SET-UP

2.1. 200 keV HIBP system

According to the principle of potential measurements with HIBPs, singly charged heavy ions (primary beam) are injected into a plasma and doubly charged ions (secondary beam) then emerge from the target plasma with the energy change corresponding to the space potential at the birth point. The HIBP analyser is required to distinguish a change of a few dozen volts (potential) in beams of several hundred kilovolts (primary beam energy).

In the CHS HIBP, a secondary beam sweep system is introduced in addition to the primary sweep system to manage 3-D trajectories in the toroidal helical plasmas. This method, which we call active trajectory control, has the following advantages: (1) it reduces the potential measurement error caused by the uncertainty of the angle of beam injection into the energy analyser; (2) it expands the applicable configurations and the observation regions; (3) it allows the energy analyser to be kept away from locations where the magnetic field would disturb the determination of the beam energy.

2.2. ECH and NBI systems

A 500 kW (106.4 GHz) gyrotron has been installed for high power ECH experiments in a relatively high density regime. With this gyrotron added to the previous two gyrotrons with 700 kW at 53.2 GHz, the total available power becomes 1200 kW. Two outputs of these three gyrotrons are selected to transmit and inject the power to CHS. The combination of the quasi-optical transmission line and launchers provides the following unique functions: (1) a highly focused elliptic Gaussian beam; (2) focal position controllability by means of a steering mirror; (3) arbitrary linear polarization controllability [4]. CHS has been equipped with co- and counter-injected neutral beam systems whose maximum powers are 1.1 and 0.7 MW, respectively.

3. EXPERIMENTAL RESULTS

3.1. Potential profiles in steady states

The experiments presented here were performed on a magnetic field configuration whose axis is located at $R_0 = 92.1$ cm and whose strength is 0.9 T. The necessary energy is 71 keV for 0.9 T operation when a caesium beam is used. The actual observation points are distributed along the toroidal direction, and these points, in Fig. 1(a), are the projections obtained by tracing the magnetic field line from the actual observation points. The toroidal angle ζ_{tor} of the actual observation points is shown in Fig. 1(b), where ζ_{tor} corresponds to the vertically elongated magnetic flux surface in Fig. 1(a). The other configurations can also be accessed with our system, although the observation region is limited for some configurations.

Figure 2(a) shows potential profiles obtained during steady states of ECH and NBI plasmas. The open and closed circles indicate the potential profiles of ECH plasmas with low density ($n_e = 3 \times 10^{12}$ cm^{-3}) and medium density ($n_e = 8 \times 10^{12}$ cm^{-3}), respectively. The central electron temperatures of the low and medium density cases are $T_e(0) = 900$ eV and 400 eV, respectively. The squares indicate the potential profile of a co-injected NBI plasma where the electron density is $n_e = 8 \times 10^{12}$ cm^{-3} and the electron and ion temperatures are $T_e(0) = 300$ eV

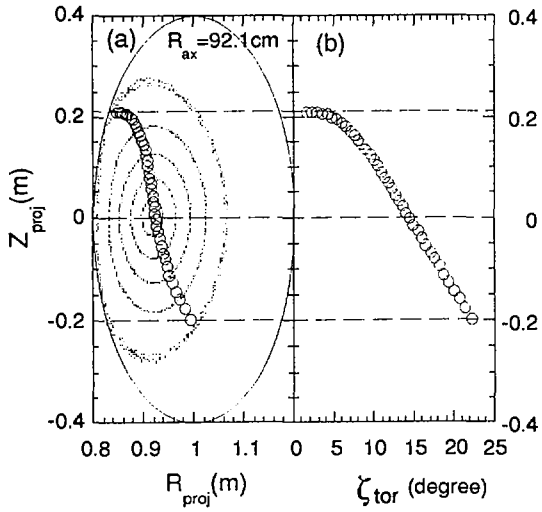

FIG. 1. (a) Projection of observation points with the HIBP; (b) toroidal angle of observation points.

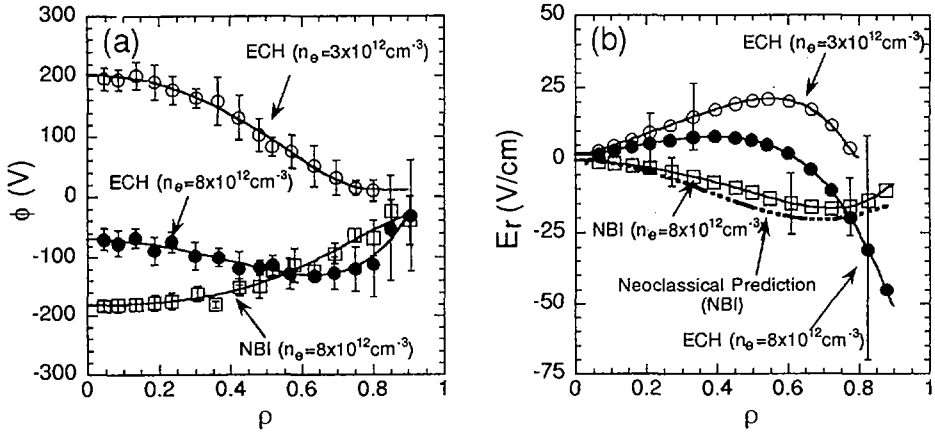

FIG. 2. (a) Potential profiles and (b) electric field profiles in steady states of ECH and NBI plasmas. The expected electric field profile from the neoclassical theory is presented for comparison.

and $T_i(0)$ = 200 eV. The port-through NBI power was 500 kW. These profiles are averages for about 20 ms of steady state, and the error bars represent standard deviations.

The potential is positive with a centre value of about 200 V for a low density ECH plasma with a gyrotron output power of 100 kW, where electrons are almost in a collisionless regime since the electron collisionality is $\nu_e^*(a/2)$ = 1.4. The

definition of collisionality here is $\nu^*(r) = \nu_{eff}(r)/\omega_b(r)$ with $\nu_{eff}(r) = \nu(r)/\epsilon_h$ and $\omega_b = \iota(\epsilon_h T/m)^{1/2}/2\pi R$, where ι is the rotational transform. In the medium density ECH plasma, the potential exhibits an interesting characteristic: the electric field is positive around the core, whereas it has a large negative value (-70 V/cm) near the edge. The electron collisionality is $\nu_e^*(a/2) = 13.1$, and the electrons are in the plateau regime. On the other hand, the potential in the low density NBI plasma is negative, with a centre value of about -200 V. The collisionalities of electrons and ions are $\nu_e^*(a/2) = 6.0$ and $\nu_i^*(a/2) = 8.2$. Both electrons and ions are in the plateau regime.

Figure 2(b) shows radial electric field profiles deduced from polynomial fitting of curves to the obtained potential profiles. In the ECH plasmas, a tendency can be seen for the positive electric field to become more negative as the density increases. In the medium density case, the electric field shows a strong shear around the plasma edge although the statistical error bar is large. In the NBI case, the ion temperature, electron density and temperature profiles are available from the database. Hence, the experimentally obtained electric field can be compared with the electric field predicted with the ambipolarity condition $\Gamma_i^{NC}(E_r) = \Gamma_e^{NC}(E_r)$, where $\Gamma_i^{NC}(E_r)$ and $\Gamma_e^{NC}(E_r)$ represent the ion and electron fluxes in the neoclassical theory, respectively. Figure 2(b) also includes a curve representing a neoclassical prediction for the NBI plasma [5]. The theoretically expected electric field has a similar tendency to the experimental result in this case.

3.2. High power ECH operation and combined heating of ECH and NBI plasmas

The new gyrotron system can produce a plasma with a central electron temperature of 2 keV and a line averaged electron density of 6×10^{12} cm^{-3} when 500 kW fundamental resonance heating is applied to a magnetic field configuration of $R_{ax} = 92.1$ cm and 1.7 T and the microwave beam is focused on the magnetic axis. Figure 3 shows the electron temperature profile measured with a YAG Thomson scattering system whose repetition rate is 10 ms. Here, negative x means that the point is inside the torus.

Potential profile measurements were carried out when 300 kW gyrotron power was input into the magnetic field configuration of $R_{ax} = 92.1$ cm and $B_0 = 0.9$ T. Figure 4 presents the obtained potential profile, represented by open circles, and the deduced electric field profile for a steady state with a line averaged electron density of $n_e = 3 \times 10^{12}$ cm^{-3}. Compared with the potential profile of the 100 kW ECH plasma shown in Fig. 2(a), the potential profile for 300 kW exhibits a sharp peak around the core. Here, negative ρ means that the observation point is located below the magnetic axis. The existence of a sharp change in the gradient of potential (radial electric field) around $\rho = 0.4$ suggests a momentum transport barrier.

Figure 5(a) shows the time evolutions of potential profiles for two sequential shots when NBI is applied to 300 kW ECH target plasmas. The port-through power

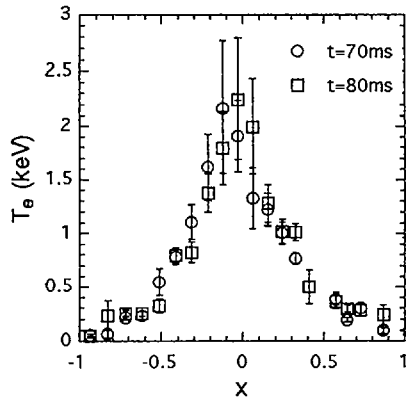

FIG. 3. Electron temperature profiles obtained when 500 kW ECH power is input into a plasma with a magnetic field strength of 1.7 T. The attained central temperature is about 2 keV.

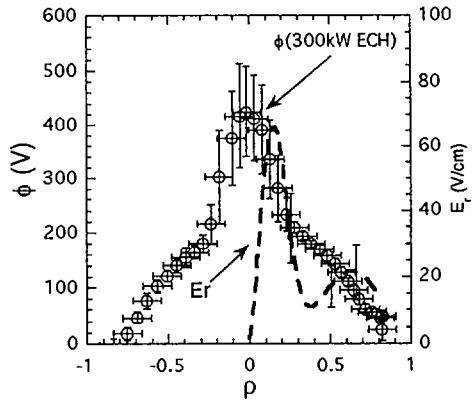

FIG. 4. Potential and electric field profiles in a 300 kW ECH (53.2 GHz) plasma when the magnetic field strength is 0.9 T.

of the NBI was 800 kW. The dashed-dotted line indicates the averaged minor radius of the temporal observation point. Figure 5(b) shows the HIBP observations of time evolutions of potential at several fixed spatial points. Around the plasma core, the potential increases by $\Delta\phi(\rho = 0) = 200$ V for 1 ms just after the NBI is applied. If we estimate the full width at half-maximum in the time derivative of potential $d\phi/dt(\rho = 0, t)$ for these changes, we obtain $\Delta T_{FWHM} = 790$ μs at $t_0 = 50.3$ ms by fitting a function of $(1 + \gamma \exp[-\alpha(t - t_0)])^{-1}$ to the waveform in the transient phase.

The central potential then gradually decreases and a successive abrupt drop and rise, by $\Delta\phi(\rho = 0) = -200$ V with $\Delta T_{FWHM} = 150$ μs and $\Delta\phi(\rho = 0) = 400$ V

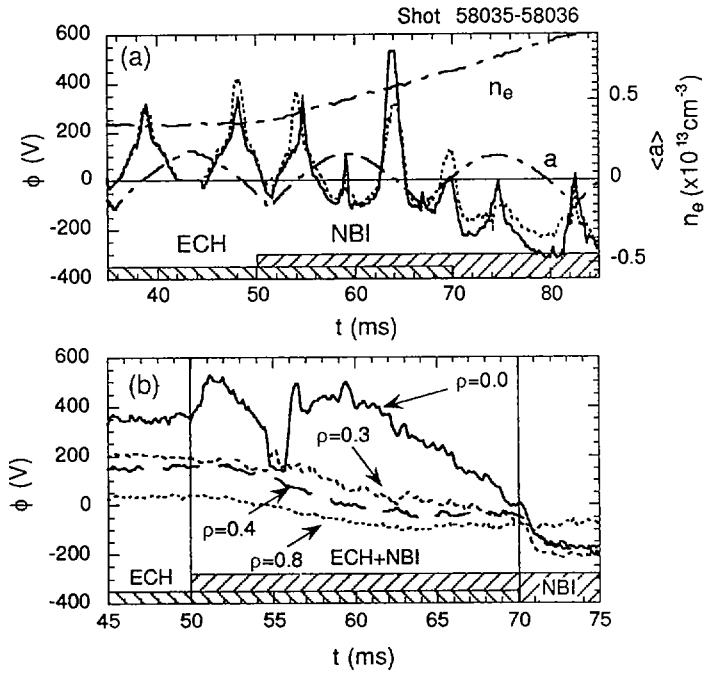

FIG. 5. (a) Potential profile evolution for the case of NBI applied to ECH plasmas, together with line averaged density and the averaged minor radius of the temporal observation point. (b) Time evolutions of potential at several spatially fixed points.

with ΔT_{FWHM} = 450 μs, occur at t_0 = 54.5 and 55.9 ms, respectively. This rapid structural formation around the core suggests a bifurcation of the ambipolar condition $\Gamma_e(E_r) = \Gamma_i(E_r)$ since the time-scale is different in magnitude from the energy confinement time of a few milliseconds.

On the other hand, the potential decreases gradually at points with $\rho > 0.4$. The electric field at the edge of $\rho > 0.8$ becomes negative in about 5 ms from the beginning of the combined heating. In these two shots, the positive potential profiles become flat near zero before the ECH is turned off. After the ECH is turned off, the central potential becomes negative rather rapidly with ΔT_{FWHM} = 800 μs, and the potential profile gradually relaxes into a steady state.

3.3. Dynamic change of potential profiles associated with MHD bursts

Sequential periodic bursts associated with an m = 2 mode have been observed with magnetic probe arrays in a low β NBI heated plasma (β = 0.2%) [6]. Figure 6(a) indicates a typical example of the MHD phenomena detected with a poloidal Mirnov coil at B_0 = 0.9 T, together with the toroidal beam driven current.

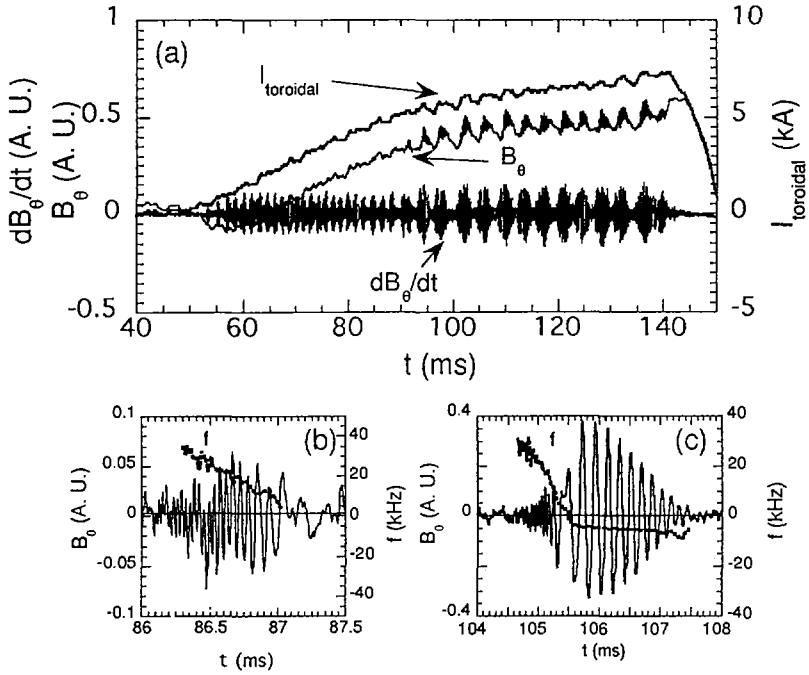

FIG. 6. (a) Overview of raw and integrated signals from a poloidal array of Mirnov pick-up coils and beam driven toroidal current measured with a Rogowski coil. (b) Expanded view of bursts in the early stage of a discharge and change of its oscillation frequency. (c) Expanded view of bursts in the later stage of the discharge and change of its oscillation frequency.

The characteristics of these bursts change according to the evolution of the discharge. The expanded views for early and later stages of the discharges are shown in Figs 6(b) and (c). In the early stage, the bursts are characterized by a high initial oscillation frequency of about 40–50 kHz, which decreases as a function of time. In the later stage, the bursts are divided into two successive phases. The first phase is similar to the early stage of the discharge, after which the bursts develop into the second phase, which is characterized by a low oscillation frequency of about 5–10 kHz and a larger amplitude in the Mirnov signals. Here, we will concentrate on the later stage of the bursts.

A poloidal array of pick-up coils shows that the wave propagation direction changes from the ion to the electron diamagnetic direction as the first phase develops into the second one. The Doppler frequency due to the plasma rotation ($= k_\phi E_r/B$) is estimated to be about 5 kHz if the electric field strength is assumed to be about 30 V/cm around the edge, as is shown in Fig. 2(b). Therefore, the change in the observed frequency should be ascribed to the propagation speed of the mode in the

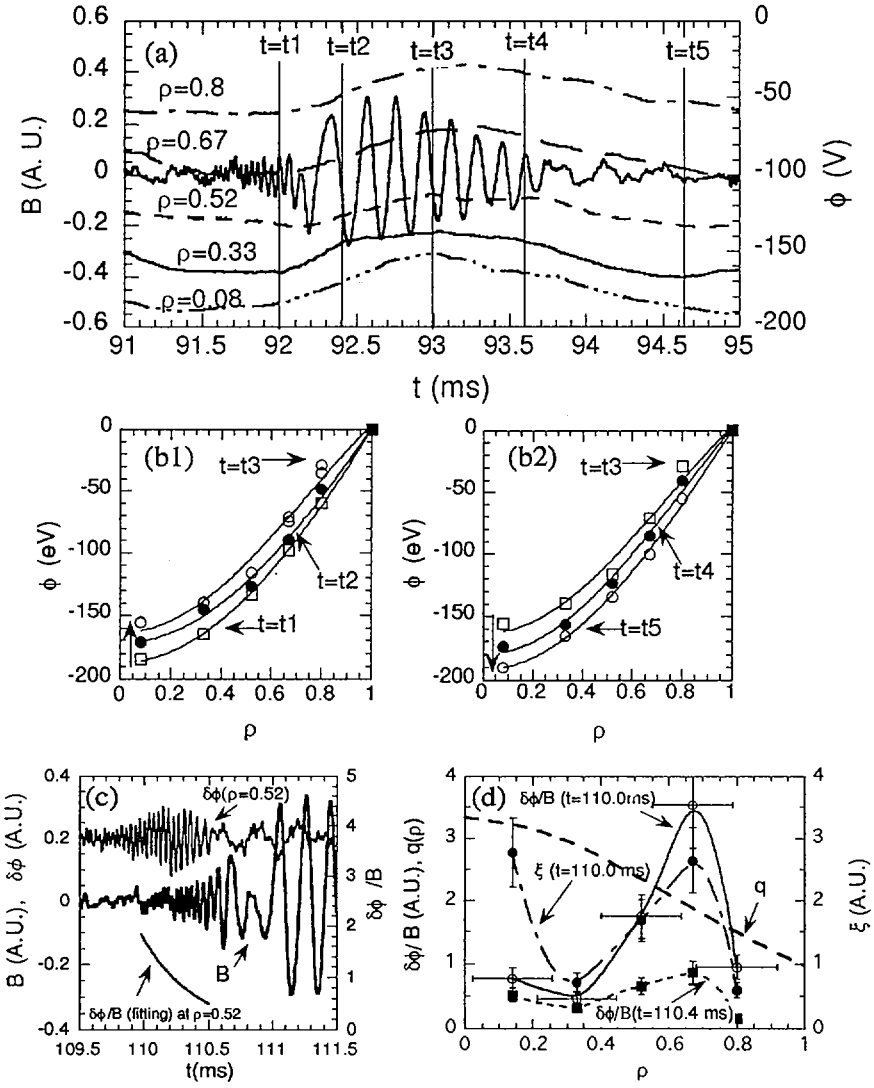

FIG. 7. (a) DC potential changes at several spatial points, accompanied by the growth of magnetic field fluctuation amplitude in the second phase of the bursts in the later stage of discharges. (b1) Change of DC potential profiles in the increasing phase of the magnetic fluctuation amplitude. (b2) Change of DC potential profiles in the decreasing phase of the magnetic fluctuation amplitude. (c) Correlation of potential fluctuation with magnetic field fluctuation. (d) Spatial dependence of the ratio of potential fluctuation amplitude to magnetic field fluctuation amplitude, together with the q profile. A parameter proportional to plasma displacement ξ is also plotted.

plasma frame. The rapid increase in the magnetic field of the second phase is also confirmed not to be caused by the plasma horizontal movement by comparing two signals from poloidal pick-up coils located in horizontally symmetrical positions.

The HIBP detected a periodic oscillation of a DC potential profile accompanied by the evolution of the bursts in the second phase. Here, we divided the measured potential into the following two parts: $\phi = \langle\phi\rangle + \delta\phi$, where $\langle\phi\rangle$ and $\delta\phi$ are, respectively, the time average during 400 μs (DC potential) and the fluctuation part around the DC potential. Figure 7(a) shows the DC potential changes at several spatial points during a cycle of the bursts. The DC potential profile does not change during the first phase of the bursts. On the other hand, Figs 7(b) demonstrate that in the second phase the potential reaches its shallowest value as the magnetic field fluctuation reaches its maximum. That is, the rotation speed of the plasma becomes slower. Then the potential profile becomes deeper again as the mode becomes stabilized. The recovery of the potential at the edge seems to be delayed by a few hundred microseconds with respect to the central potential; however, the detailed spatial and temporal structure of the potential oscillation requires further observations. The relative potential variation seen in this oscillation is about 40 V at the centre. The occurrence of this instability is anticipated to cause deterioration of confinement properties. In fact, the angular momentum change in the plasma accompanied by this potential profile oscillation is roughly estimated to be about 5×10^{-7} N·m·s; in other words, the plasma loses electric charge of about 4×10^{-5} C in a cycle [7].

Moreover, the internal structure of this mode can be inferred from the fluctuation part of the potential. Figure 7(c) shows that the potential fluctuation is well correlated with the magnetic field fluctuation in the first phase. When it comes closer to the second phase, the potential fluctuation becomes smaller and finally disappears in the second phase, and this is valid for the observation point of $\rho < 0.8$. Figure 7(d) indicates the potential fluctuation amplitude normalized by the magnetic field fluctuation amplitude, together with another potential fluctuation normalized by the product of the magnetic field fluctuation amplitude and the electric field strength, which is assumed to be $E_r = -30\rho$ (V/cm). The definition of the latter is explicitly written as $\xi = \delta\phi/BE_r$, and the parameter ξ is proportional to the plasma displacement under the assumption that potential should be constant on the magnetic flux surface. This result implies that the mode in the first phase is dominant in the plasma interior ($\rho < 0.8$).

In contrast, in the second phase we have not observed a coherent potential fluctuation with the Mirnov coil signals at a position of $\rho < 0.8$. Moreover, the total intensity of the secondary beam, which suffers from path integral effects [8], shows a fluctuation synchronized with the magnetic field fluctuation. As is shown in Fig. 7(d), the q value of the vacuum field at the plasma edge is slightly below 1, and the NBI driven current flows in the direction to make q(a) smaller. These facts suggest that the mode in the second phase should be localized in the plasma edge of $\rho > 0.8$, and that the evolution of the first and the second phases should originate from different modes. The switching process between two different modes may occur

at the turning point from the first to the second phase. The information on the plasma interior, as obtained from the HIBP, is essential to identify the instabilities that cause the bursts which will limit plasma performance.

4. BEHAVIOUR OF HIGH ENERGY PARTICLES IN LOSS CONE DIAGRAMS

The loss cone structure can be easily estimated from the obtained potential profiles by use of an analytic formula. According to Ref. [9], the loss cone for deeply trapped particles is expressed as $W_m < W < W_p$, where W is the particle energy, $W_m = -q\phi(0)f(x)/(\epsilon_{ha}(1 - x^2) + \epsilon_{ta}(1 - x))$ and $W_p = -q\phi(0)f(x)/(\epsilon_{ha}(1 - x^2) - \epsilon_{ta}(1 + x))$. Here, ϵ_{ta} and ϵ_{ha} represent toroidal and helical ripple coefficients, respectively, x indicates the horizontal co-ordinate whose origin is on the magnetic axis, and f(x) is a normalized function fitted to the experimental profiles with $f(0) = 1$ and $f(1) = f(-1) = 0$. For the magnetic field configuration with $R_{ax} = 92.1$ cm, we chose $\epsilon_{ta} = 0.16$ and $\epsilon_{ha} = 0.255$.

A loss cone diagram for the NBI plasma is presented in Fig. 8(a). The loss cone plays a role in a collisionless regime when the helically trapped particles can accomplish their one-turn orbits poloidally without a collision. This criterion is roughly expressed as $\omega_{gradB} > \nu/\epsilon_h$. Figure 8(a) plots the critical energy W_{rot} to satisfy the

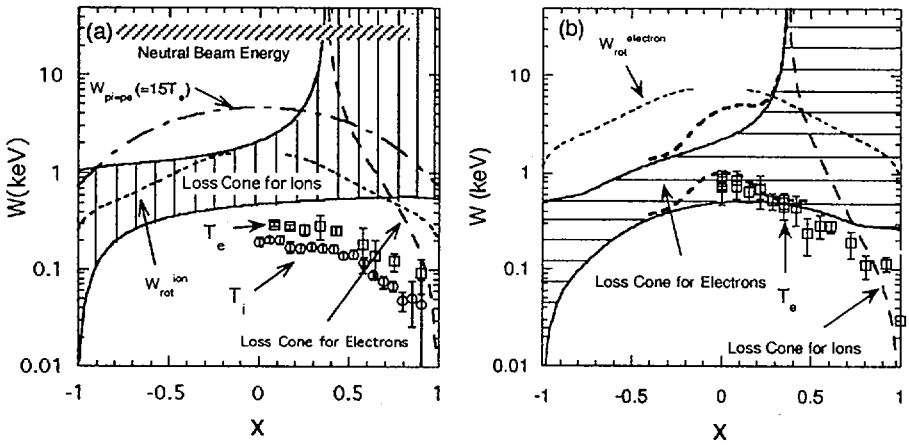

FIG. 8. (a) Loss cone diagram for deeply trapped ions in NBI plasma with $\phi(0) = -200$ V. (b) Loss cone diagram for deeply trapped electrons in ECH plasma with $\phi(0) = 200$ V. Also shown is the loss cone boundary for electrons in 300 kW ECH plasmas. The loss cone plays a role in the region above the line W_{rot}. This line represents the particle (ion or electron) energy at which the particle can accomplish poloidally one-turn orbits.

criterion which is explicitly written as $W_{rot}^{2.5} > 1.4 \times 10^{-2} n_e B r^2 \epsilon_h^{-2}$ (eV, cm^{-3}, T, cm). This criterion is no longer valid around the magnetic axis since there the banana width is larger than the local structure owing to the small poloidal field.

When NBI is applied to this plasma, the energy transfer rates to ions and electrons are a function of electron temperature. The beam energy to heat ions and electrons equally is represented by $W_{pi=pe} = 15 T_e A_b (Z_i^2/A_i)^{2/3}$, where A_b, A_i and Z_i are the atomic mass of the beam particles, and the atomic mass and the charge of the bulk plasma particles, respectively. Above this energy ($15T_e$), the beam particles selectively heat electrons, preserving the pitch angle. On the other hand, the injected beam particles experience pitch angle scattering in the region below this energy, and simultaneously the beam particles transfer their energy to ions. It therefore becomes more probable for the beam particles to enter into the loss cone below this energy.

The neutral beam is tangentially injected into CHS with an energy of about 38 keV (diagonally hatched region in Fig. 8(a)). The effective energy transfer from injected beams to bulk ions occurs in the region between the upper loss cone boundary and the energy of $W_{pi=pe}$ ($= 15T_e$). As for the bulk ions, the temperature is below the lower loss cone boundary. Hence, the bulk ions are confined by the rotation due to $\mathbf{E} \times \mathbf{B}$ motion. If the potential becomes sufficiently negative for the loss cone region to be located above the energy of $W_{pi=pe}$, the ion heating efficiency will be improved since the pitch angle scattering occurs below the loss cone region.

A loss cone diagram for deeply trapped electrons can also be presented for the low density ECH plasma with a positive potential. It is shown in Fig. 8(b) that the loss cone region above the energy of W_{rot} exists only in the plasma exterior ($x > 0$). The critical energy W_{rot} for electrons is higher than that for ions since the collision frequency is higher for the same energy; $W_{rot}^{2.5} > 6.3 \times 10^{-1} n_e B r^2 \epsilon_h^{-2}$ (eV, cm^{-3}, T, cm). Thus, an electron heated by a wave on the outside of the torus will easily enter the loss cone. In the case of the potential profile of the 300 kW ECH plasma, the loss cone boundary around the core region moves towards the high energy side, as is indicated by the long-dashed line. As for ions, the loss cone region in this positive potential is localized only in the periphery of the plasma. The loss cone boundary for ions is shown by the long-dashed line in Fig. 8(b). Therefore, highly effective heating due to high energy ions is expected in the plasmas with positive potential.

As is shown in Fig. 4, a positive potential was observed to be maintained for a time longer than the energy confinement time except in the edge region during a combined heating phase of NBI and ECH, although the positive potential tends to become negative gradually before the ECH is switched off. In the phase of positive potential, it is expected that the deposited high energy particles of NBI may be well confined in the plasma and these high energy particles may heat the bulk plasma effectively. It was observed that in some shots a positive potential was held for about 20 ms until the ECH was turned off. The mechanism of potential generation requires further investigation to realize the high heating efficiency and confinement of toroidal helical plasmas.

5. SUMMARY

We obtained the following results in CHS after a new ECH and 200 keV HIBP system started to operate. (1) A high electron temperature of about 2 keV was achieved for the first time when fundamental 500 kW heating was applied at $B_0 = 1.7$ T. (2) Steady state potential profiles varied widely between NBI and ECH plasmas, which showed negative and positive profiles, respectively, and loss cone diagrams were evaluated using the obtained potential profiles to study the behaviour of high energy particles. (3) A unique potential profile suggesting the existence of a momentum transport barrier was found around the core when 300 kW ECH was applied at $B_0 = 0.9$ T. (4) A transition phenomenon in the electric field, suggesting a bifurcation of solutions in the ambipolar condition, was observed around the plasma core during the combined heating phase of NBI and ECH. (5) The internal structure of the MHD bursts, which may cause deterioration of confinement properties, was investigated by means of measurements of the potential profile and its fluctuation. In conclusion, the HIBP is a powerful tool for studying the physics of toroidal helical plasmas in terms of static and dynamic behaviours in potential, and for giving a better understanding of heating efficiency and confinement.

REFERENCES

[1] MATSUOKA, K., et al., in Plasma Physics and Controlled Nuclear Fusion Research 1988 (Proc. 12th Int. Conf. Nice, 1988), Vol. 2, IAEA, Vienna (1989) 411.
[2] IDA, K., et al., Phys. Fluids B 3 (1991) 5151.
[3] FUJISAWA, A., et al., Rev. Sci. Instrum. 63 (1992) 3694.
[4] KUBO, S., et al., Fusion Eng. Des. 26 (1994) 319.
[5] SANUKI, H., et al., J. Phys. Soc. Jpn. 62 (1993) 123.
[6] SAKAKIBARA, S., et al., J. Phys. Soc. Jpn. 63 (1994) 4406.
[7] ITOH, K., et al., Plasma Phys. Control. Fusion 38 (1996) 1.
[8] ROSS, D.W., et al., Nucl. Fusion 31 (1991) 1355.
[9] ITOH, K., et al., Phys. Fluids B 3 (1991) 1294.

DISCUSSION

R.J. GOLDSTON: In some previous stellarator experiments the beam ion radial current and momentum deposition were considered important in the neoclassical determination of the radial electric field. Have you taken this into account?

A. FUJISAWA: No, I have not. The momentum deposition is not so important in the CHS case because the plasma does not rotate so fast, owing to the parallel viscosity. We have co- and counter-NBI systems, and by using combinations of these beams, it is possible to investigate whether those effects are significant or not.

R. JAENICKE: In the case of W7-AS, hot ion orbit losses are not taken into account in the calculation of E_r. Estimates indicate that their influence is negligible in high ion temperature discharges.

K. HANADA: Dr. Fujisawa, when E_r changes transiently in CHS, does the fluctuation level change at the centre of the plasma?

A. FUJISAWA: The signal level from the plasma centre is not sufficient to estimate the fluctuation at present. I think we will be able to answer your question after the beam current has been enhanced.

K. LACKNER: You mentioned a charge loss associated with the change in rotation. Can you relate this number to any particle reservoir which might be tapped by this process (e.g. slowing down NB ions close to loss orbit regions, or the fraction of these ions whose orbits would be affected by an electrical field change)?

A. FUJISAWA: Yes. In the MHD bursts, slowing down beam ions around the upper loss cone boundary could be related to some part of the current. An analysis will be done to estimate this fraction using a Fokker–Planck code.

ALTERNATIVE SYSTEMS EXPERIMENTS

(Session C2)

Chairperson

E.P. KRUGLYAKOV
Russian Federation

STABILITY AND ADDITIONAL HEATING PROPERTIES OF SPHERICAL TOKAMAK PLASMAS ON START

M.R. O'BRIEN, R.AKERS, R.A. BAMFORD,
M.K. BEVIR, R.J. BUTTERY, A. CALOUTSIS,
P.G. CAROLAN, N.J. CONWAY, M. COX,
G.F. COUNSELL, T. EDLINGTON, C.G. GIMBLETT,
M. GRYAZNEVICH, T.C. HENDER, I. JENKINS,
O.J. KWON[1], R. MARTIN[2], M. MIRONOV[3],
K. MOREL, A.W. MORRIS, M.P.S. NIGHTINGALE,
Y.-K.M. PENG[4], S. PETROV[3], P.D. PHILLIPS,
C. RIBEIRO[5], D.C. ROBINSON, S.E. SHARAPOV[6],
A. SYKES, C.C. TSAI[4], M. TOURNIANSKI[7],
M. VALOVIČ, M.J. WALSH
UKAEA Fusion,
Culham Laboratory,
Euratom–UKAEA Fusion Association,
Abingdon, Oxfordshire,
United Kingdom

Abstract

STABILITY AND ADDITIONAL HEATING PROPERTIES OF SPHERICAL TOKAMAK PLASMAS ON START.

Neutral beam heating has recently been installed on the START tight aspect ratio or 'spherical tokamak' ($R/a \geq 1.2$), using equipment loaned by Oak Ridge National Laboratory, USA. This has led to significant improvements in plasma performance — for example, an increased Murakami parameter, $n_e R/B$. High central (~48%) and volume averaged (~8.5%) β-values have been obtained. Calculations show that Troyon scaling still holds at low aspect ratio (with coefficients ~4 for ballooning modes, ~5 for kink modes), indicating that the START device should reach still higher values of β. It is found that the limiting edge-q rises for aspect ratios less than approximately 1.5, in agreement with theoretical calculations. Energy confinement at low aspect ratio is as good as, or better than, most H-mode scalings from conventional devices (up to twice ITER-93H) — with NBI there is no evidence so far for a power degradation (although $P_{NBI} \leq 1.5P_{OH}$). In both Ohmic and NBI plasmas, the scrape-off layer (SOL) in double null geometry is narrow, providing a valuable test of SOL models. As reported previously, START is resilient against current-terminating disruptions. It does, however, have more benign internal

[1] Taegu University, Republic of Korea.
[2] UMIST, Manchester, UK.
[3] A.F. Ioffe Institute, St. Petersburg, Russian Federation.
[4] Oak Ridge National Laboratory, Oak Ridge, Tennessee, USA.
[5] University of São Paulo, Brazil.
[6] JET Joint Undertaking, Abingdon, Oxfordshire, UK.
[7] Essex University, UK.

reconnection events when approaching density and current limits which show the initial features of a disruption (e.g. transient I_p rise and β_p fall). A model based on helicity conservation shows that, at tight aspect ratio, smaller falls (and sometimes rises) in edge-q result from falls in β_p and l_i, suggesting a possible explanation for the resilience to disruptions of START.

1 INTRODUCTION

Ohmically heated experiments on START [1] have confirmed that as the aspect ratio drops to low values, and the plasma becomes almost spherical, high plasma currents can be supported by a low toroidal field (on START, R~0.2-0.4m, R/a≥1.2, I_p≤300kA, B≤0.5T, limiter and double null configurations, elongation κ typically 1.8 but has been as high as 4 without feedback). These plasmas have improved vertical stability and, so far, no current-terminating disruptions - instead more benign "Internal Reconnection Events" (IREs) are observed. The high I_p/aB ratio means very high β should be possible in spherical tokamaks, and central values ~20% have been observed Ohmically on START. Energy confinement is as good as or better than most H-mode scalings from conventional devices (up to twice ITER-93H), though Edge Localised Modes have not been observed. This paper reports (a) substantial improvement in plasma performance on START with neutral beam injection (NBI), including a much higher value for β, (b) calculations which show how q and β limits change with aspect ratio A=R/a, quantifying the improvements possible by decreasing A, and (c) modelling of IREs, indicating that the behaviour in spherical tokamaks may be qualitatively different from conventional aspect ratio devices, perhaps explaining the resilience of START plasmas to disruptions.

2 NEUTRAL BEAM HEATING ON START

Using equipment loaned by Oak Ridge National Laboratory, USA, hydrogen atoms at power levels ~ 300-600 kW have been injected tangentially into hydrogen plasmas. The beam has a 1/e half-width divergence of 1.2° and is steered to achieve a 1/e half-width of 12cm in the plasma. Energies up to 30keV have been used so far (40keV is possible), and the sub-energy species have significant fractions (typically the power is split 61%, 24%, 15% between the E, E/2 and E/3 components respectively). High plasma current (I_p≥200kA) is employed to minimise orbit losses. As expected from calculations, co-injection is much more effective than counter-injection, with neutral particle measurements showing that fast ions are well confined with a slowing-down type distribution (Fig. 1). The results presented below are for co-injection.

Plasma diagnostics have been greatly improved on START and have aided the interpretation of the NBI experiments. Improvements include the addition of a 30-point Thomson Scattering system, a high speed video camera (up to 40,000 frames per second), enhanced soft X-ray diagnostics, 20 chord spectroscopic ion temperature and toroidal rotation measurements using line

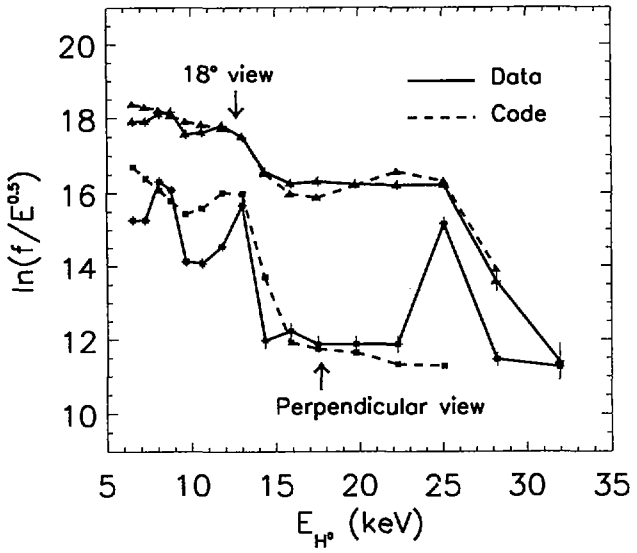

FIG. 1. NPA spectra (solid lines) for viewing perpendicular and 18° towards the beam compared with predictions from the 3D Fokker–Planck code FPP-3D (dashed lines). The classical slowing-down type distribution for the 18° view indicates that charge exchange losses (neglected from the calculation) are not large.

emission from electron impact and charge exchange recombination, extra magnetic diagnostics and a 16-energy-channel neutral particle analyser capable of observing energies up to 50keV. These diagnostics show that the NBI gives significant increases in density and both ion and electron temperature and large Shafranov shift (see Fig. 2) as well as appreciable fast ion energy content. The increased pressure has produced significant improvements in β–values as discussed in the β-limit section below. The NBI-heated plasmas also have a larger operating space than the Ohmic plasmas, with significantly higher Murakami parameter achievable (n_eR/B, see Fig. 3). There is no evidence for a significant degradation of energy confinement with NBI, although the effect of NBI on energy confinement has been difficult to assess due to (i) changing plasma size during NBI, (ii) some uncertainty as to how much power is absorbed, and (iii) the beam power being comparable to the Ohmic power ($P_{NBI} \leq 1.5P_{OH}$). If the beam switches off during a discharge the ensuing Ohmic plasma sustains confinement as good as or better than the best Ohmic discharges without this beam pre-heating. At higher NBI powers, a form of MHD activity not seen in Ohmic plasmas is observed (Fig. 4) with decreasing frequency resembling the "chirping" modes observed on DIII-D [2], suggesting that they may be energetic particle modes arising when the fast ion and thermal pressure gradients are comparable.

Measurements have been made at the strike points in double null mode using an array of domed Langmuir probes in a divertor tile. These have

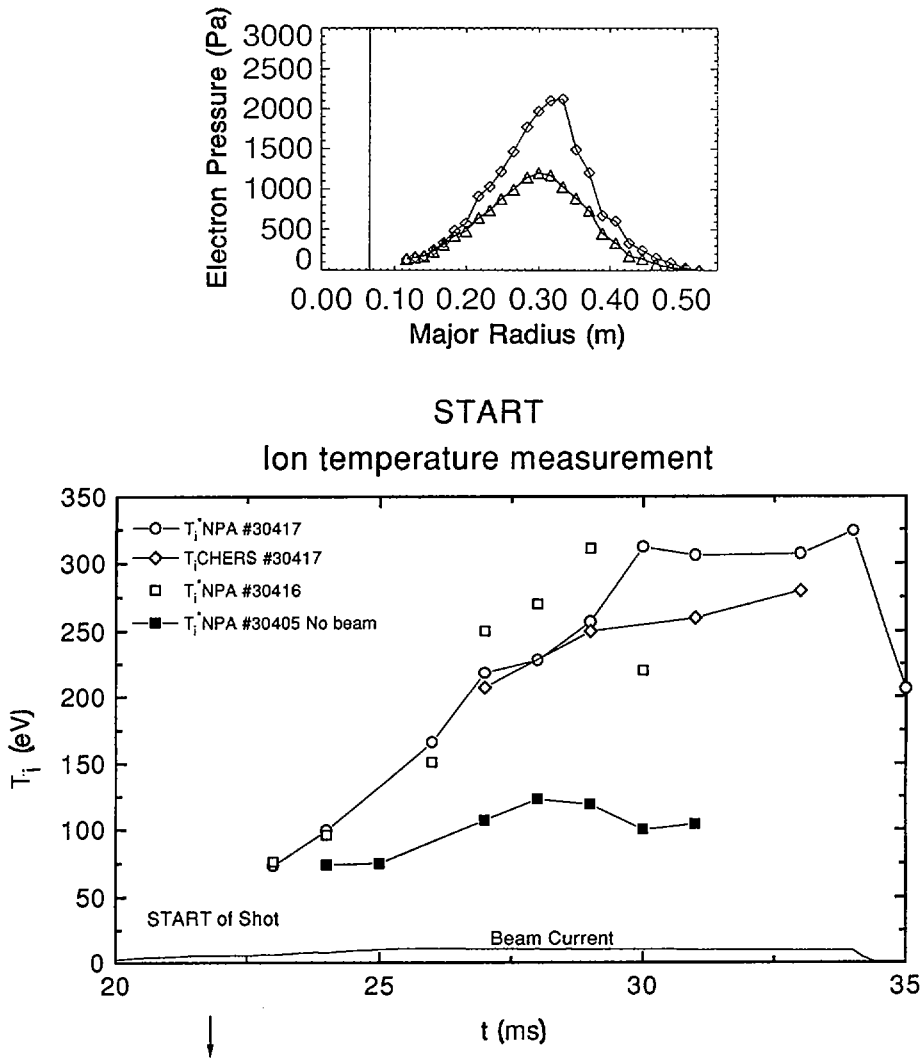

FIG. 2. Typical change in electron pressure profile due to NBI, measured by Thomson scattering (top), and typical rise in ion temperature with NBI (bottom).

shown the existence of a narrow scrape-off layer (SOL) in both Ohmic and NBI plasmas. Despite a spatial resolution with the array of better than 11mm, significant ion saturation currents were typically only observed on a single probe at any time. Thus, estimates of scale lengths for the SOL parameters were derived by analysis of probe data during sweeping of the strike point past the probe, which occurs naturally in START double null mode. Density and temperature profiles across the upper, outboard strike point have been calculated for a typical shot with NBI (see Fig. 5 for density profile). Scale

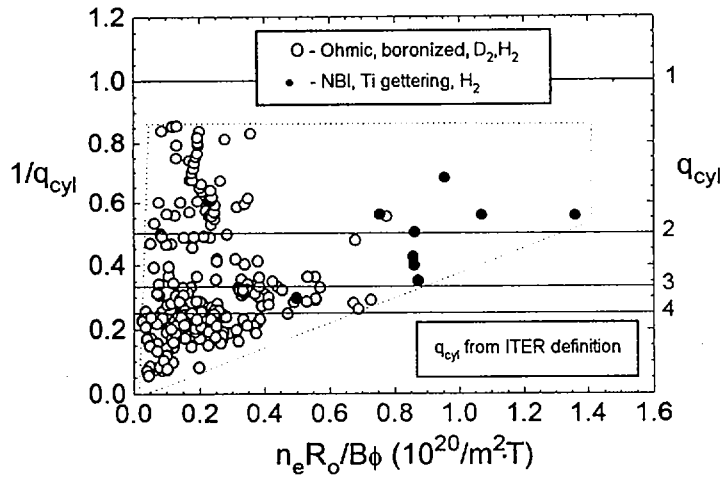

FIG. 3. Increase in achievable Murakami parameter from NBI.

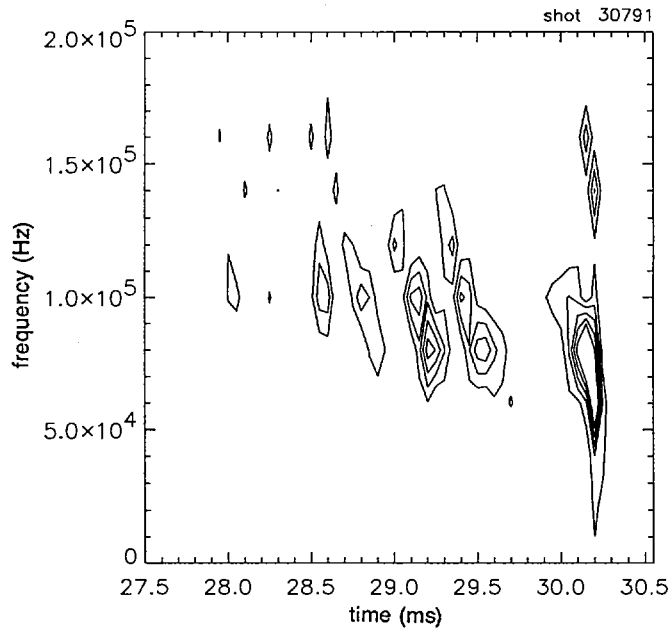

FIG. 4. Evolution of cross-correlation spectrum for two outer midplane Mirnov coils in NBI shot, showing frequency dropping with time ('chirping').

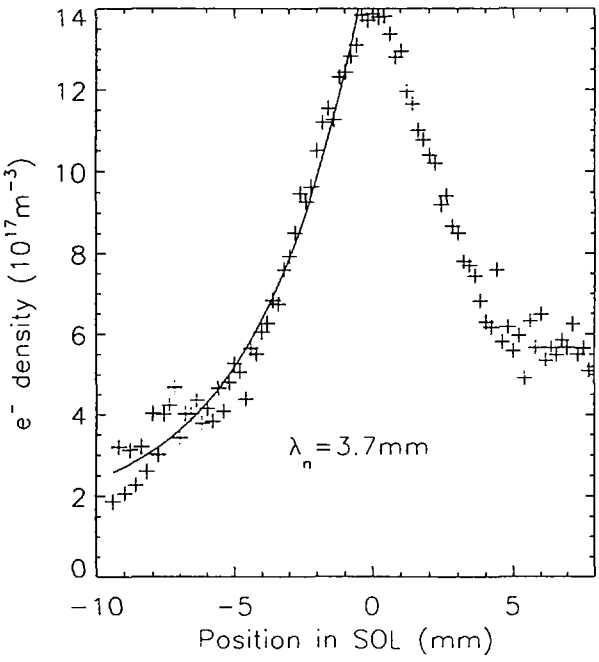

FIG. 5. Variation of density across the upper, outer strike point in an NBI heated double null plasma. Left hand side: scrape-off region; right hand side: private flux region.

lengths in this case are λ_n~3.7 and λ_T~6.8mm. A comparison with scale lengths from conventional aspect ratio tokamaks such as COMPASS-D has been used to evaluate which SOL models work best - the combination of toroidal field and connection length in START geometry provides for an excellent discrimination between competing theories. Preliminary analysis suggests that a simple collisionless convection/diffusion model with constant $\chi_\perp$ gives a good fit to experiment, better than many physics-based models.

3 EDGE-q LIMITS

At conventional aspect ratio there is a limit of q_ψ>2 imposed by the external kink mode. Previous studies have shown this limit becomes more restrictive at tight aspect ratio [3]. Figure 6 shows this is confirmed by experiment; the edge-q limit is explored by ramping up the plasma current and/or ramping down the toroidal field. The limit is manifested as an IRE which after transiently raising the current, lowers it, causing q_ψ to rise. In Fig. 6 the edge-q values for the START experimental points are determined from the ITER formula for q_{95} [4], which has been found to be a reasonably good approximation at low aspect ratio. For discharges with NBI I_p has reached 300kA, and the key ratio of plasma current to toroidal field current, ~0.9,

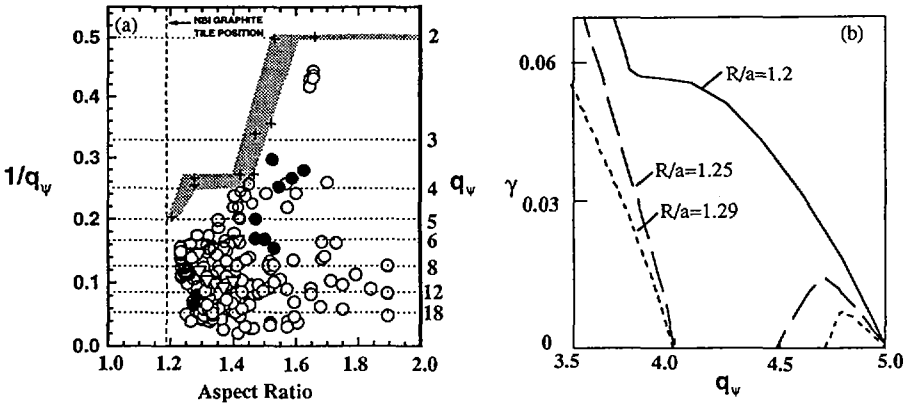

FIG. 6. (a) Experimental operating space ($1/q_\psi$) as a function of aspect ratio and the theoretically calculated limit; the shading indicates the variation in this limit due to the variation in current profile described in the text (the + symbols are calculated limiting cases). The o symbols are Ohmic deuterium pulses, the ▽ symbols are Ohmic hydrogen pulses and the ● symbols are NBI. (b) Calculated growth rate versus q_ψ for R/a = 1.3, q_0 = 1.2 indicating the possibility of a second, weaker band of instability at higher q_ψ.

approaching the value needed in a power plant for acceptable recirculating power. The expected theoretical limit for limiting discharges in Fig. 6 has been calculated using the ERATO ideal MHD code [5] coupled to the CHEASE equilibrium code [6]. A range of current profiles and central-q values ($1.05 \leq q_0 \leq 1.2$) are considered. Since these q_ψ-limit discharges are generally sawtoothing until shortly before the q_ψ-limit IRE (suggesting $q_0 \sim 1$), and then generally make a transition to a continuous mode (probably m=1), the role of varying the central-q is to alter the peripheral current gradient and hence the drive for the external kink. The variation of the q_ψ-limit with β has also been examined and is found to be weak for these discharges which are far from the expected β-limit. From Fig. 6(a) it can be seen that the experimental and computational edge-q limits are qualitatively in agreement, however at aspect ratios less than ~1.4 experiments have not yet reached the predicted q_ψ-limit. There may be other q_ψ-limits related to the existence of narrow bands of instabilities at q_ψ values above the main band. Such secondary bands of instability exist in some cases before merging into the main band of instability as the aspect ratio decreases, as shown in Fig. 6(b). The situation is thus analogous to conventional aspect ratio tokamaks where a secondary band of instability exists for q_ψ<3, introducing some difficulty in passing through q_ψ=3 to the harder limit of q_ψ=2.

4 β LIMITS

The ERATO code has been used to study the aspect ratio dependence of first stability β-limits. Varying the pressure profile to be marginally stable

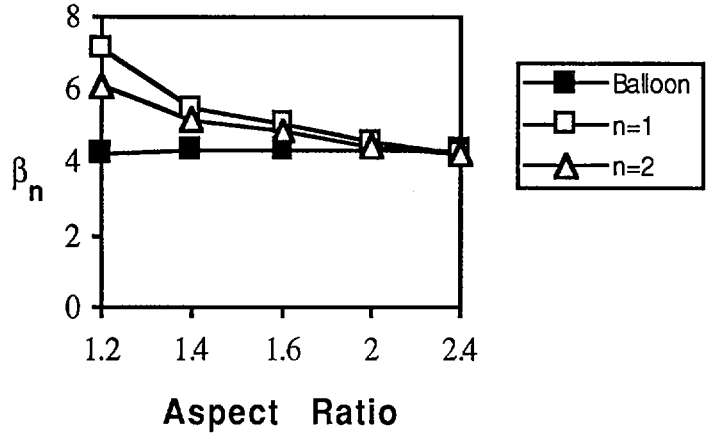

FIG. 7. Variation of normalized β_n with aspect ratio due to ballooning and n = 1, 2 ideal kink modes for $q_0 = 1.05$, $q_\psi = 10$, $\kappa = 1.6$ and $\delta = 0.4$. Here $\langle J \rangle = (1-\Psi) - \lambda \times (1 - \Psi)^2$, where λ is adjusted to fix q_ψ/q_0.

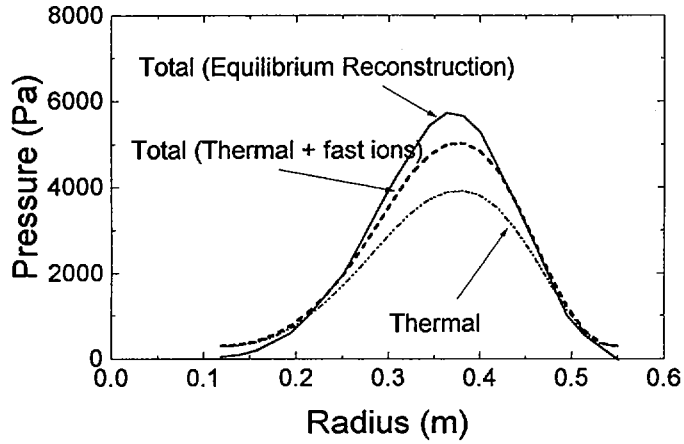

FIG. 8. Pressure profiles deduced by different methods for the maximum central β (~48%), obtained on START.

to ballooning modes shows the Troyon parameter β_{nmax} is almost independent of R/a (β_{nmax} typically ~4 for q_o=1.05, $\beta_n=\beta_T(\%)a(m)B(T)/I_p(MA)$, $\beta_T=2\mu_o\langle p\rangle_{Vol}/B^2$, B is the vacuum toroidal field at the geometric centre of the plasma). At low A=R/a, the limiting β_n due to kink modes for these profiles is higher than for ballooning modes, except for elongations $\kappa > \sim 2.8$ (see, for example, Fig. 7). Despite the more restrictive q_ψ limit, discussed above, as the aspect ratio decreases, the current-carrying capability rises greatly at low A ($I_p \sim A^2(1+\kappa^2)/(q_\psi(A^2-1)^2)$ in the ITER formula [4]), especially since operation

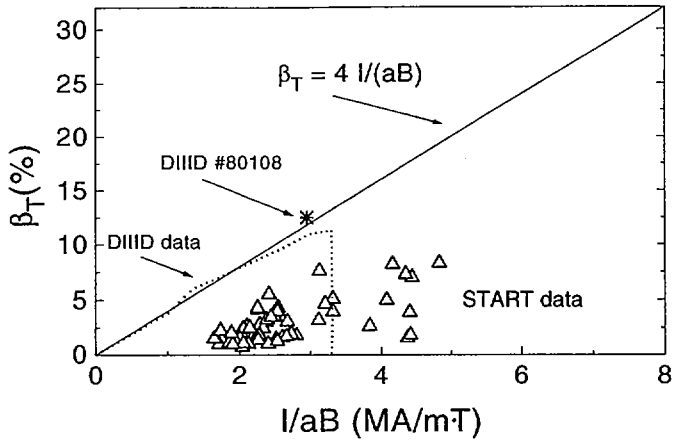

FIG. 9. Beta diagram for START. ERATO calculations indicate that $\beta \approx 4\ I_p/(aB)$ might be possible, showing that START might reach even higher β-values with higher power or improved confinement. The highest β-value from DIII-D [8] and bounds of the DIII-D database from Ref. [10] (dashed line) are shown for comparison.

at higher κ is possible because of the improved vertical stability (as demonstrated on START with and without NBI). The potential for high normalised currents (I_p/aB > 5MA/mT has been achieved in START) means very high β_T should be possible in spherical tokamaks. This makes them suitable near-term candidates as component or divertor test facilities, and means they have the potential for low capital cost electricity generation. Even higher β_T values are possible since a close wall may allow access to second stability [7].

With NBI, independent equilibrium, kinetic and diamagnetic estimates of plasma pressure show that central β values up to ~48% (ratio of pressure to vacuum magnetic field pressure at magnetic axis) have been produced (Fig. 8), more than twice those obtained in Ohmic plasmas and greater than the highest achieved in conventional aspect ratio devices [8]. Volume-averaged β is also very high (8.5%, Fig. 9). The kinetic estimates use thermal electron and ion profile information together with estimates of the fast ion pressure based on Fokker-Planck modelling which gives a close fit to NPA measurements (Fig. 1). The fast ion pressure contributes typically one fifth of β (the electron and ion contributions are comparable). The β achievable appears to be mainly limited by the power available - increased power is planned to make the NBI significantly exceed the Ohmic power. The modelling just described, when applied to the equilibrium of a high β shot, with the profile but not magnitude of the pressure held fixed, gives limiting β_n=4 for ballooning modes and a somewhat higher value for kink modes and so a limiting β ~ 16%. Since higher I/aB (~5.4) has been achieved, β ~ 20% should be possible.

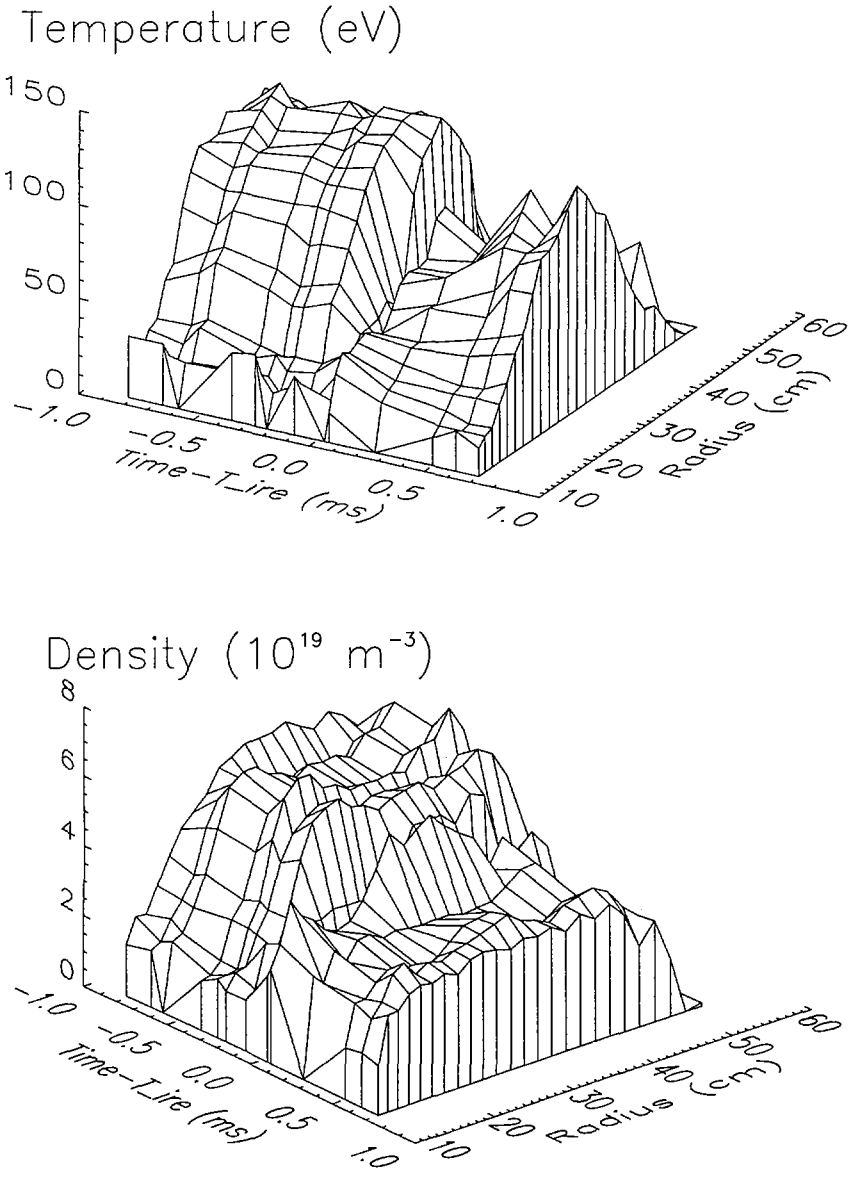

FIG. 10. Variation in electron temperature and density with major radius and time through an IRE (t = 0 at IRE) measured by using Thomson scattering for a series of nominally identical pulses.

5 INTERNAL RECONNECTION EVENTS

At conventional aspect ratio, stresses from current-terminating disruptions, particularly those involving asymmetric vertical displacement events, impose restrictions on design and operation of future large devices like ITER. In over 30000 START discharges at low R/a, IREs and not current-terminating disruptions have been observed to limit the operating space [1]. This is a very promising result for spherical tokamaks which needs further testing under more demanding conditions in devices like MAST ($I_p \leq 2$MA), the successor to START being built at Culham. Although they do not lead to current-termination, IREs on START have many of the properties of disruptions, such as negative V_{loop} spike and increase in κ. Furthermore, IREs have a rapid increase in plasma current ($\delta I_p/I_p \leq 40\%$), are sometimes accompanied by low *m* and *n* modes observed on magnetic, soft X-ray and interferometer diagnostics, and occur for a range of conditions, but predominantly near the density and low q_ψ limits.

START IREs have been the subject of experimental, analytic and numerical study, and the results have been compared with those for conventional aspect ratio tokamaks such as COMPASS-D (A~2.8). Figure 10 shows Thomson scattering data for a series of nominally identical pulses in which reproducible IREs occur late in the discharge (it is necessary to take data for a series of pulses because the present Thomson data can only be obtained once per pulse). This data (and soft X-ray data) show that the central electron density and temperature fall sharply at the IRE ($\beta_e(0)$ falls ~50%), with T_e recovering more quickly than n_e. Reconstructions of plasma changes before and after an IRE have been made using a Grad-Shafranov equilibrium code. In these reconstructions all measured coil currents and the plasma current are matched, as is the measured pressure profile and plasma elongation (which is closely related to the plasma current profile, i.e. l_i). These reconstructions through an IRE form the basis for deciding on likely constraints which can be applied to modelling IREs [9]. It is found that the constraint of no helicity dissipation during the IRE appears to give the best match. Various other constraints such as conservation of toroidal flux, poloidal flux or plasma magnetic energy have been examined but are not found to give such a good match to the reconstructions through an IRE.

The consequences of helicity conservation during an IRE/disruption, for a range of aspect ratios A=R/a, have been examined. The IRE (or disruption) has been simulated by reducing both l_i and β_p by various amounts. The fractional change in minor radius is less at low A and this in turn is related to a significantly smaller change in q_{95} at low A (while q_{95} always drops at conventional A, it can actually rise at low A). This different behaviour at low A gives a possible explanation for the lack of disruptions on START.

6 CONCLUSIONS

The use of NBI heating on the START spherical tokamak has led to increased plasma performance, in particular larger operating space (Murakami parameter) and very high values of β (central $\beta \sim 48\%$, volume-averaged β

~8.5%). There is no evidence so far for confinement degradation, though the NBI power has not yet greatly exceeded the Ohmic power. Calculations of the aspect ratio dependence of q and β limits show (i) consistency with the START operating space, and (ii) an appropriately defined Troyon expression determined by stability to ballooning modes remains good at low aspect ratio indicating that much higher β should be possible on START. The high current-carrying capability of the spherical tokamak together with the Troyon-like behaviour mean that this concept may be a suitable basis for near-term component or divertor test facilities, and has the potential for low capital cost electricity generation. Even higher β values are possible if a close wall allows access to second stability. A model of plasma changes during the Internal Reconnection Events that are observed on START suggests that qualitatively different behaviour can occur at low aspect ratio, perhaps explaining START's resilience to current-terminating disruptions. The results reported in this paper, particularly the performance of START NBI-heated plasmas, augur well for the 2MA MAST experiment. This device, the successor to START, is currently being constructed at Culham and will also use NBI for its main additional heating system.

ACKNOWLEDGEMENTS

We thank the Centre de Recherches en Physique des Plasmas, Switzerland, for providing the ERATO and CHEASE codes. This work was funded by the UK Department of Trade and Industry and by Euratom, and supported by a collaboration with Oak Ridge National Laboratory managed by Lockheed Martin Energy Research Corp. for the US Department of Energy under contract number DE-AC05-96OR22464.

REFERENCES

[1] SYKES, A., in Fusion Engineering (Proc. 16th Symp. Urbana-Champaign, 1995), Vol. 2, IEEE/NPSS (1995) 1442.
[2] HEIDBRINK, W.W., Plasma Phys. Control. Fusion 37 (1995) 937.
[3] BESPOLUDENNOV, S.G., et al., Sov. J. Plasma Phys. 12 (1986) 441.
[4] INTERNATIONAL ATOMIC ENERGY AGENCY, ITER Physics Design Guidelines 1989, IAEA, Vienna (1990).
[5] GRUBER, R., et al., Comput. Phys. Commun. 21 (1981) 323.
[6] LÜTJENS, H., BONDESON, A., ROY, A., Comput. Phys. Commun. 69 (1992) 287.
[7] BUTTERY, R.J., et al., in Plasma Physics and Controlled Nuclear Fusion Research 1994 (Proc. 15th Conf. Seville, 1994), Vol. 2, IAEA, Vienna (1995) 633.
[8] STRAIT, E.J., et al., in Controlled Fusion and Plasma Physics (Proc. 21st Eur. Conf. Montpellier, 1994), Vol. 18B, Part I, European Physical Society, Geneva (1994) 242.
[9] BUTTERY, R.J., et al., in Controlled Fusion and Plasma Physics (Proc. 23rd Eur. Conf. Kiev, 1996), Vol. 20C, European Physical Society, Geneva (1996).
[10] DIII-D TEAM, in Plasma Physics and Controlled Nuclear Fusion Research 1990 (Proc. 13th Int. Conf. Washington, 1990), Vol. 1, IAEA, Vienna (1991) 69.

DISCUSSION

K. TOI: I would like to know whether the plasma energy is expelled owing to the internal reconnection events (IREs), because this energy expulsion towards the wall or divertor plate associated with IREs should be taken into account in a reactor level plasma. This effect may be severe compared with current disruption. Could you tell us about the characteristics of the thermal disruption in ohmic and NBI heated high β plasma?

M.R. O'BRIEN: In the largest IREs the plasma thermal energy can drop by a factor of more than two. We have not yet done a full analysis of IREs in neutral beam heated plasmas. However, a general observation, so far, is that for similar points in the Hugill diagram, IREs are smaller and less frequent in neutral beam heated plasmas than in ohmic plasmas.

INVESTIGATION OF THE EFFECT OF RESISTIVE MHD MODES ON SPHERICAL TORUS PERFORMANCE IN CDX-U

M. ONO, D. STUTMAN, Y.S. HWANG[1], W. CHOE,
J. MENARD, T. JONES, E. LO, R. ARMSTRONG[2],
M. FINKENTHAL[3], V. GUSEV[4], S. JARDIN, R. KAITA,
J. MANICKAM, T. MUNSAT, R. NAZIKIAN, Y. PETROV[4]
Plasma Physics Laboratory,
Princeton University,
Princeton, New Jersey,
United States of America

Abstract

INVESTIGATION OF THE EFFECT OF RESISTIVE MHD MODES ON SPHERICAL TORUS PERFORMANCE IN CDX-U.

Resistive MHD modes and associated effects on spherical torus performance are investigated in the CDX-U device for $I_p \leq 100$ kA. At present, the growth of resistive MHD modes (n = 1/m = 3 or n = 1/m = 2) as the edge q (q(a)) is lowered towards 3.5 appears to limit the maximum current achievable in CDX-U. For low q(a) discharges, a prominent rotating "hot" spot can be seen with the soft x-ray array, indicative of a magnetic island associated with an n = 1/m = 1 mode. The edge mode, which is n = 1/m = 3 or n = 1/m = 2, can be seen by the soft x-ray and edge magnetic pick-up coil array. The growth of those modes in space and amplitude eventually leads to an Internal Reconnection Event (IRE). Prior to the IRE, strong mode-mixing takes place, suggesting magnetic island overlap. The IRE causes a rapid heat loss from the core, causing a strong plasma elongation and current spike due to the plasma inductance drop. With an appropriate discharge control, an MHD quiescent high confinement regime with over twice the central electron temperature relative to the MHD active regime has been found. To assess the halo-induced effects during the MHD events, a pair of segmented Rogowski coils were installed on the center stack. The observed halo-induced current fraction is generally small (less than 5% of the total plasma current) even for the case of forced disruption.

1. INTRODUCTION

The spherical torus (ST) offers a promising possibility for a cost-effective high-performance plasma regime which could lead to a compact volumetric neutron source as well as an attractive economical power reactor [1]. Recent results from ideal MHD calculations are indeed encouraging, as MHD stable plasmas in excess of 45% beta, with ≥ 80% bootstrap (pressure driven)

[1] Korean Advanced Institute of Science and Technology, Seoul, Republic of Korea.
[2] University of Tromsø, Tromsø, Norway.
[3] Johns Hopkins University, Baltimore, Maryland, USA.
[4] A.F. Ioffe Physico-Technical Institute, St. Petersburg, Russian Federation.

fraction and natural elongation of $\kappa \approx 2$, have been predicted[2,3]. With increasing elongation ($\kappa \approx 3$), a regime with 45% beta and nearly 100% bootstrap fraction (fully aligned bootstrap current regime) appears to be possible. On the experimental front, START reported very encouraging results on plasma confinement and the lack of plasma disruptions [4]. Similar observations in CDX-U have been reported [5]. While these experimental and theoretical results are very encouraging thus far, there are important issues regarding resistive MHD which deserve careful investigation. In START, a resistive MHD event, termed the IRE (the internal reconnection event), has been frequently observed. While the IRE does not terminate the plasma (like the hard disruption in a conventional tokamak), it still causes a relatively rapid heat loss from the plasma core. Resistive MHD instabilities, if not controlled, can also limit the ultimate operational parameters of spherical torus plasmas. It is therefore important to clarify the possible effects of resistive MHD modes on spherical torus performance, particularly in view of the next step ST experiments under construction (e.g., NSTX[6]). Recent ST design activity revealed a potential structural problem for high current STs if a significant fraction of plasma current (40%) is induced in the center stack, as is observed in many higher aspect ratio tokamak experiments. To assess the extent of halo-induced current in ST, halo related physics needs to be investigated particularly during strong MHD events such as IRE and disruption.

2. CDX-U EXPERIMENTAL SET-UP

The CDX-U torus is a spherical torus facility with $R \approx 32$ cm, aspect ratio $A \equiv R/a \geq 1.4$, and $B_{TF} \approx 1$ kG. Presently, an OH power supply with 60 m V-S capability is operational on CDX-U. The experiment was conducted up to $I_p \approx 100$ kA and $q(a) \geq 3.5$. Diagnostics include a 2-D scanning microwave interferometer, 30-element poloidal magnetic pick-up coil and toroidal coil arrays, Rogowski coils for plasma and wall eddy currents, a Mach probe, a 2-D scannable magnetic probe, soft x-ray and spectroscopic detectors, a multi-pass Thomson scattering system, and a tangential phase-contrast imaging system. New additions to the CDX-U diagnostics are the 19 channel soft x-ray array for the resistive MHD study and a pair of segmented Rogowski coils around the center-stack to measure the halo-induced currents flowing in the center-stack. The cross sectional view of CDX-U with magnetic and soft x-ray diagnostics is shown in Fig. 1 (a).

SOFT X-RAY DIODE ARRAY FOR MHD STUDY - As shown in Fig. 1, the 16 channel vertical soft x-ray array detects soft x-ray signal for various chordal vertical positions [7]. Instead of the soft X-ray continuum above 1 keV used for MHD monitoring in large fusion devices, the CDX-U diode array uses the line emission of C V (He-like) and C VI (H-like) around 300 and 380 eV, respectively. This is much brighter than continuum emission, and

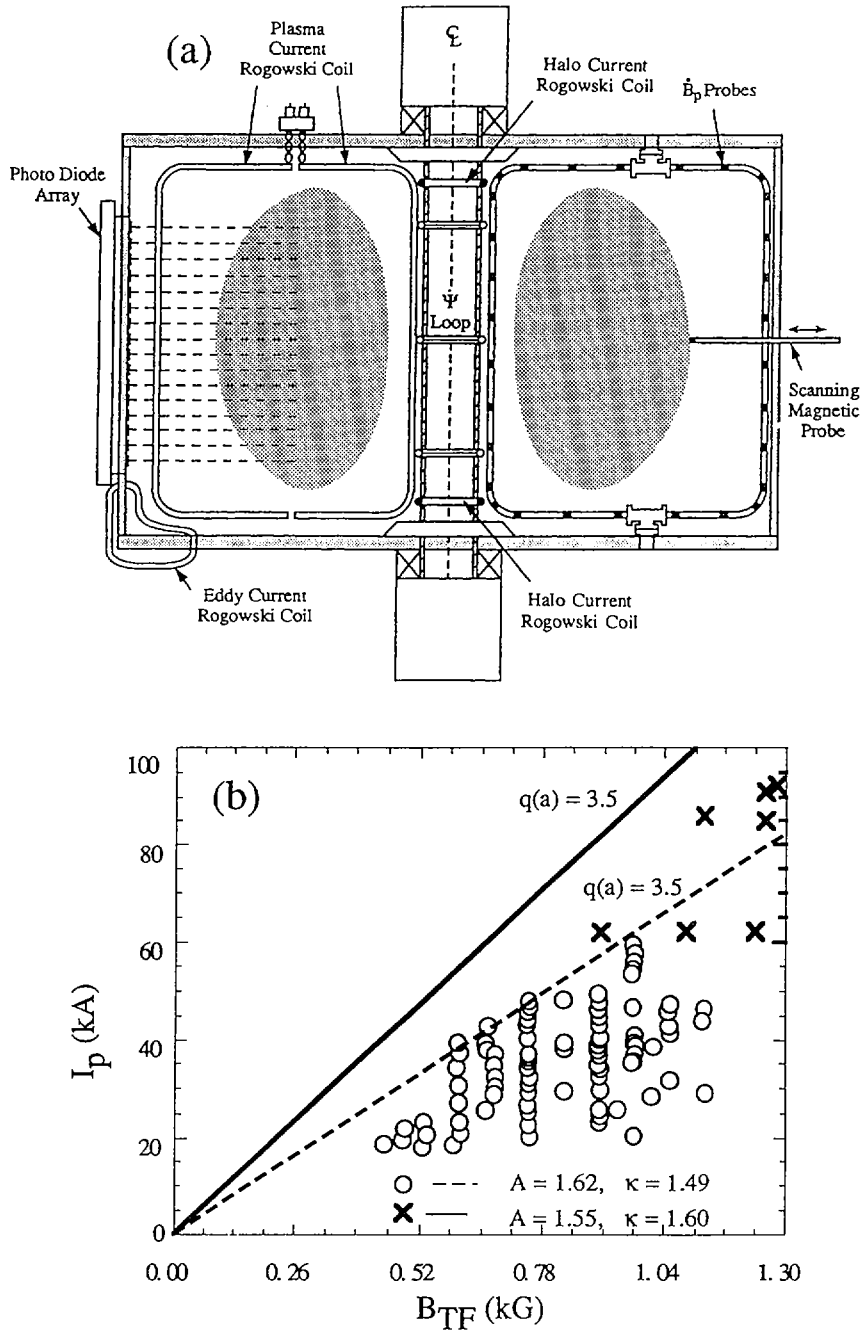

FIG. 1. CDX-U diagnostics and current operational limits. (a) Cross sectional view of CDX-U device with magnetic and soft x-ray diagnostics. (b) Ohmic plasma current versus toroidal magnetic field. The current limit of q(a) is shown for two different values of aspect ratio R/A and elongation κ.

in addition, in the temperature range up to a few hundred eV, these high ionization potential ions sample most of the plasma volume. To separate the high energy (soft X-ray) C line emission from intense emission of lower charge states (e.g. of O V, O VI at about 50-70 eV), we use the M-shell transmission band of very thin (0.2 micron), free standing Ag and Pd foils. The channel separation is 2.54 cm, and the spatial resolution at mid-plane is also ~ 2.5 cm with a total height of ~ 43 cm (Z=± 21.5 cm). An additional channel filtered for low energy (O V, O VI) emission is used at the top (Z= + 24 cm) to monitor emission closer to the edge. Thus, the plasma is sampled on a regularly spaced grid, which is a major simplification in the data interpretation, especially when dealing with a highly shaped plasma as in CDX-U. The detector system has 10 μsec fast time resolution, and therefore, it is a very effective tool for MHD activity observation.

3. PLASMA CURRENT LIMIT AND RESISTIVE MHD MODES

Since ST reactor performance depends strongly on the amount of plasma current which can be supported, it is important to explore this current limit of STs. Experimentally, the current limit in CDX-U is reached when the plasma edge safety factor q reaches about 3.5. Figure 1(b) shows the plasma current values obtained in CDX-U as a function of applied toroidal field strength, and suggests that the plasma current limit is generally proportional to toroidal field. With a modest change (≈ 5%) of plasma aspect ratio and elongation, the allowable current limit for q(a) = 3.5 can be substantially (≈ 40%) increased as shown by the dashed curve. Significantly higher plasma current (≈ 30%) was indeed obtained (crosses versus circles). The minimum q(a) value appears to be limited by resistive MHD instability. Studies of magnetic fluctuations revealed an increasing activity of coherent resistive MHD oscillations as the q(a) is lowered. Temporal and spatial characteristics of the dominant oscillations were measured by poloidal and toroidal magnetic pick-up coil array, soft x-ray array, and phase-contrast diagnostics. Coincident with this current limit, we observe the rapid growth of an n=1, m=3 mode (or the 1/3 mode) [8], and more recently n=1, m=2 (or the 1/2 mode) for higher current cases. While the 1/3 and/or 1/2 modes do not cause a hard disruption, the increased MHD activity makes it difficult to raise the plasma current, imposing a practical limit for the achievable current as shown in Fig. 1(a). In a spherical torus configuration, due to a rapid change in the q value near the edge region, the q=3/q=2 layers are located relatively close to the plasma edge even when q(a) is significantly larger than 3.

4. RESISTIVE MHD MODES AND INTERNAL RECONNECTION EVENTS IN CDX-U

The dominant resistive MHD modes observed thus far are mainly n=1 and m=1, 2, 3. There are several modes of operation which can significantly change the resistive MHD mode behavior. In Fig. 2, we show soft x-ray [(a) and (c)] and magnetic fluctuation signals [(b) and (d)] for two types of discharges, both of which end with an IRE event. The y-axis is diode array position (from top to bottom) and magnetic pick-up coil position covering the whole poloidal angle (top half is low field side and bottom half is high field side). To aid visualization, the signal amplitude for each soft x-ray diode array and magnetic pick up coil array is indicated by shading (i.e., darker for larger amplitude). Figure 2 (a) shows the soft x-ray "hot" spot (n=1/m=1) rotating in time with a frequency of $\approx$ 8-9 kHz. It should be noted that the size of the n=1/m=1 mode (which is also related to the q=1 layer) is quite large, $\Delta Z \approx 25$cm (reflecting the fact $q_{cyl} \approx 1$.). The edge channel shown in the top of Fig. 2(a) also shows an increased activity toward IRE. A similar phenomenon can be seen in the magnetic pick up coil array as shown in Fig. 2 (b). Here, the dominant mode at the edge appears to be n=1 and m=2. It is interesting to note the low field side signals are quite coherent but the high field side signals are complicated with the presence of higher harmonic components. The same frequency for both dominant n=1 modes (m=1 and m=2) indicates that the plasma is rotating toroidally as a rigid body (with a speed of nearly 30 km/sec at the outer plasma edge). As shown in Fig. 2, both internal and external modes grow in size and amplitude while the plasma rotation slows down by 10-20% until the Internal Reconnection Event (IRE) occurs. This observation indicates that the mode-coupling or island overlap is triggering the IRE event. We note here that the phase-contrast-imaging diagnostic also detects similar core MHD fluctuation signals with a radial coherence length consistent with the soft x-ray array result. Figure 2(c) and (d) shows a case which starts with a sawtoothing behavior with relatively quiet edge. However, later in the discharge, coherent modes appear and the discharge evolves into an IRE in a similar manner as the first case. As can be seen in the soft x-ray signal, during the IRE, the heat is transported rapidly from the core to the outer region. When the IRE occurs, due to decreasing core temperature, the current profile relaxes and the plasma inductance drops. This causes a spike-like increase in the plasma current while the plasma naturally elongates due to the decreased plasma internal inductance. It is interesting to note that even with IRE, the plasma is still quite resilient, and we observed that the central core rapidly reheats after the event.

MHD QUIESCENT DISCHARGES - While an IRE does not lead to a hard disruption, it is quite clear that we would like to avoid it if at all possible. Interestingly, we find that if we program our discharge appropriately, we can

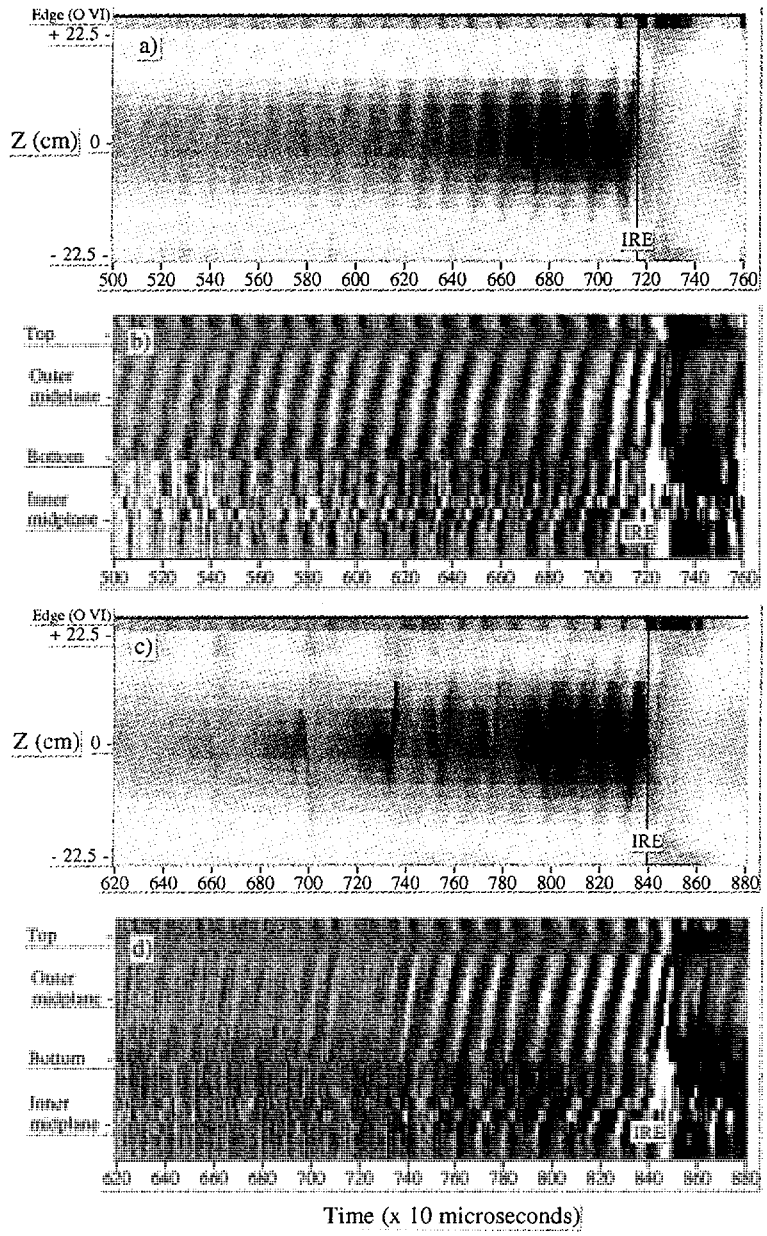

FIG. 2. Temporal behavior of MHD modes leading to IRE. (a) Soft x-ray array and (b) magnetic pick-up coil array signals of an MHD active discharge. Shading indicates MHD amplitude, with darker shading for higher amplitude. (c, d) The same signals for a sawtoothing discharge which later evolves into an MHD active discharge.

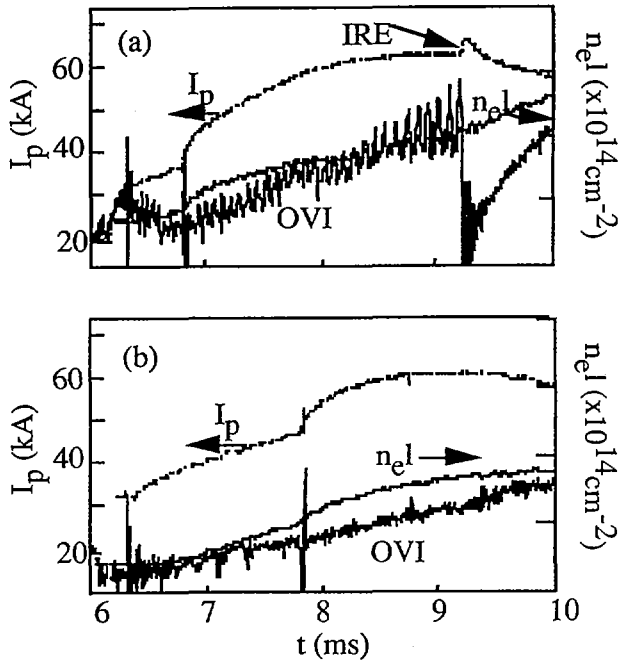

FIG. 3. Temporal evolution of plasma current, line integrated density and soft x-ray signal. (a) Discharge with MHD, (b) discharge with relative MHD quiescence. I_p = 60 kA, B_T = 1 kG.

indeed obtain MHD-quiescent, IRE-free discharges. In Fig. 3(a) and (b), the time evolution of two MHD distinct discharges is shown. The first discharge [Fig. 3(a)] has usual MHD behavior similar to the one shown in Fig. 2. The second discharge, with a slightly different current ramp-up rate [Fig. 3(b)], is relatively free of the MHD activity and IRE. The measured Thomson scattering central temperature for the MHD quiescent discharge is about 140 eV, which is more than twice that of the first case of 65 eV. It is worthwhile to note that the MHD quiescent discharge has a second current ramp up phase, which might give a broader current profile. Since the total plasma current and plasma density are similar for the two cases [i.e., same q(a)], the difference in the MHD behavior can be attributed to differences in the plasma current profiles. It is therefore encouraging that the MHD behavior can be controlled by the discharge programming, yielding a factor of 2 - 3 improvement in plasma confinement. In the higher temperature regime (140 eV), these discharges have very low collisionality, with ν^* below 0.1 in most of the plasma volume.

5. HALO-CURRENT STUDY IN CDX-U

MOTIVATION OF HALO-CURRENT STUDY FOR ST - When a tokamak plasma undergoes a strong MHD event such as a plasma disruption, a variety of currents can be induced on the vacuum vessel wall. The effects of halo-induced current were first observed in PBX-M [9] where it was found that these currents caused significant damage to the plasma facing components (PFC). Subsequent experiments and MHD simulations have shown that when the disrupting plasma touches two poloidal locations on the vacuum vessel, due to the EMF drive of decaying plasma current, a significant poloidal current can flow between the contact points in the vacuum vessel wall [10]. The current path is completed by the so-called halo currents flowing in the plasma edge region. Moreover, since plasmas in the disruption phase often undergo violent non-axisymmetric movements, the observed halo currents are not uniform around the torus. The unbalanced halo-induced currents (observed to be as large as 40% of total current with a peaking factor of 2) in the inner wall (high field side) of large scale tokamaks (with $I_p \approx$ tens of MA, $B_{TF} \approx$ 10T) are of particular concern due to high $I_{halo} \times B_{TF}$ forces on the inner vacuum vessel wall and PFCs ($\approx 10^4$tons/m/10T/10MA). For the future spherical torus device, this halo-induced current in the center-stack (the inner leg of TF) also presents a potentially serious structural problem. It is therefore important to understand the nature of halo currents in the spherical torus plasmas. To facilitate this study, a segmented (4-element) Rogowski coil was placed in the upper and lower areas of the center-stack (as shown in Fig.1), measuring the total poloidal current flowing in the center-stack as well as up-down and toroidal asymmetry. The Rogowski coils are calibrated with the known TF current.

HALO-CURRENTS DURING IRE AND FORCED DISRUPTION IN CDX-U - As mentioned above, during an IRE, the plasma experiences a relatively violent increase in plasma elongation and plasma current, due to decreased plasma inductance. A typical plasma current trace is shown in Fig.4 (a) during the time of the IRE. While the IRE is not a hard disruption, the plasma clearly touches the top and bottom of the vessel due to increased elongation, as seen by a TV camera and limiter currents. The raw halo-induced Rogowski coil voltage is shown in Fig. 4 (b) and (c) for the top and bottom Rogowski coils. As indicated by the figure, the current is obtained by integrating the signal and it is typically less than 1% of the peak plasma current (as indicated by the current fraction "F") for both top and bottom coils. It should be noted that the halo-induced current pulse is very short (50 μsec). During the normal course of CDX-U operation, the IRE is the most serious MHD event in terms of the induced halo current. Otherwise, the ST plasmas in CDX-U are remarkably stable and resilient. It is, however, possible to artificially cause a rapid current termination by deliberately turning down one

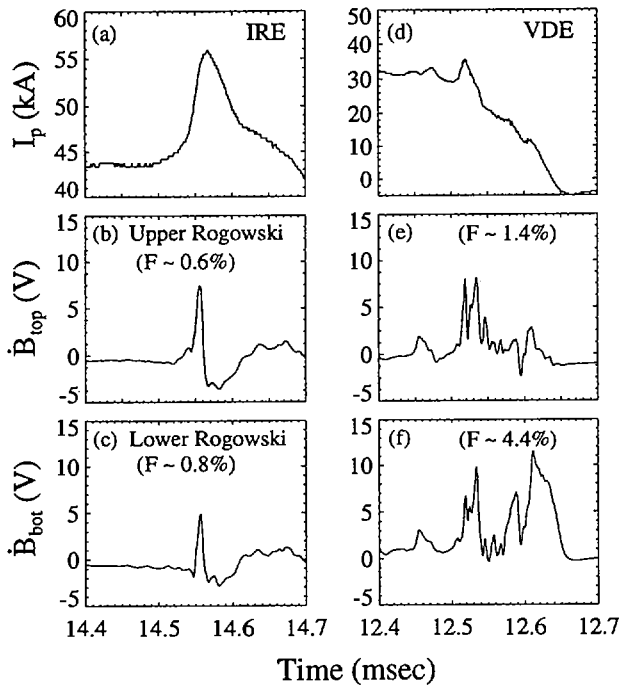

FIG. 4. Halo-induced current in center stack. (a) Plasma current evolution, (b) top Rogowski coil signal trace and (c) bottom Rogowski coil signal trace during IRE and (d-f) during forced disruption.

of the equilibrium coil. This type of situation might be envisioned for some failure mode which may occur during the operational life of a ST reactor. This type of termination is shown in Fig. 4 (d), (e), and (f) where lower poloidal coil was turned off. The integrated Rogowski signal indicates that the rapid termination (or disruption) can induce current in the center-stack of up to $\approx$ 5% of the plasma current value - which is still an order of magnitude lower compared to what has been observed in tokamaks to date. It appears that when the plasma suddenly loses equilibrium, the plasma tends to move up or down, but not inward (due to the strong self-force of ST) which minimizes interactions with the inner wall of the ST. The ST plasma appears to be stable against tilt or shift instability as well. Perhaps largely due to this MHD stability and geometric factor, the halo-induced current in the center-stack may be relatively small during an IRE and/or accidental disruption for STs. While this is an encouraging result for future STs, it is important to understand the physical mechanism of halo current in the ST geometry through further experimentation and theory/modeling.

ACKNOWLEDGMENTS

We thank J. Taylor and J. Robinson for their technical support. We also thank S. Kaye, R. Goldston, and M. Peng for helpful comments. This work is supported by DoE contract Nos. DE-AC02-76-CHO-3073 and DoE grant No. DE-FG02-86ER52314AT.

REFERENCES

[1] PENG, Y.-K.M., et al., in Plasma Physics and Controlled Nuclear Fusion Research 1994 (Proc. 15th Int. Conf. Seville, 1994), Vol. 2, IAEA, Vienna (1995) 643.
[2] MENARD, J., et al., Bull. Am. Phys. Soc. **40** (1995) 1655.
[3] MILLER, R.L., et al., Bull. Am. Phys. Soc. **40** (1995) 1788.
[4] SYKES, A., et al., Plasma Phys. Control. Fusion **35** (1993) 1051.
[5] HWANG, Y.S., et al., Bull. Am. Phys. Soc. **40** (1995) 1654.
[6] ONO, M., et al., Bull. Am. Phys. Soc. **40** (1995) 1655.
[7] STUTMAN, D., et al., Rev. Sci. Instrum. **68** (1997) 1059.
[8] JONES, T.G., PhD Thesis, Princeton Univ., NJ (1995).
[9] KUGEL, H.W., et al., in Controlled Fusion and Plasma Physics (Proc. 16th Eur. Conf. Venice, 1989), Vol. 13B, Part I, European Physical Society, Geneva (1989) 199.
[10] SAYER, R.O., et al., Nucl. Fusion **33** (1993) 969.

DISCUSSION

J.D. CALLEN: You indicated that you could obtain MHD active or quiescent discharges depending on the poloidal field programming in time. What is the key element here, and is the current profile different in the two cases (and in what way)?

M. ONO: In the CDX-U ST experiment, we observe a large variation in the resistive MHD mode behaviour for the same current and density discharges. The main knob which appears to be effective from the operational point of view is the current ramp-up sequence. The second current ramp on top of the already established discharge appears to be responsible for achieving the MHD quiescent discharges. The second current ramp in an already hot discharge would result in a hollow (or less peaked) current profile. We therefore believe that the current profile is a key knob for controlling the restrictive MHD modes in the ST.

M. THUMM: What do you know about the behaviour of the ion temperature during your discharges?

M. ONO: For ST ohmic discharges, there is no experimental evidence of anomalous ion heating as observed in some RFP experiments. In CDX-U, the expected ion temperature is $(0.3–0.5)T_e$, or about 50 eV, on the basis of the START results and the TSC model calculations of our discharges.

I.H. HUTCHINSON: The observation that disruptions in STs do not usually terminate the current is very interesting, but it seems questionable to call these reconnection events 'internal', since you say they involve edge modes. So what fraction of the plasma kinetic energy is lost at the disruption and how much interaction is there with the plasma facing components?

M. ONO: In CDX-U, the IRE is triggered by the simultaneous growth of internal (n = 1/m = 1) and external (n = 1/m = 2, 3) modes as observed by soft X ray and magnetic probe array diagnostics. The soft X ray measurements show a rapid drop of the central electron energy (perhaps as large as 50%) which appears in the edge region in 20–25 μs. These observations suggest that the IRE is caused by mode–mode coupling (or island overlap) of internal and external modes, leading to a very rapid loss of core electron energy. After the core thermal collapse, the plasma elongates vertically (owing to the drop in the plasma inductance) and hits the top and the bottom of the chamber (as viewed by a high speed camera). This is partly due to the relatively closely fitted vacuum vessel configuration of the CDX-U ST experiment.

REDUCING AND MEASURING FLUCTUATIONS IN THE MST RFP: ENHANCEMENT OF ENERGY CONFINEMENT AND MEASUREMENT OF THE MHD DYNAMO

D.J. DEN HARTOG[1], A.F. ALMAGRI[1], M. CEKIC[2], B.E. CHAPMAN[1], J.T. CHAPMAN[1], C.-S. CHIANG[1], D. CRAIG[1], N.C. CROCKER[1], G. FIKSEL[1], P.W. FONTANA[1], A.K. HANSEN[1], C.C. HEGNA[1], H. JI[3], N.E. LANIER[1], K.A. MIRUS[1], S.C. PRAGER[1], J.S. SARFF[1], J.C. SPROTT[1], M.R. STONEKING[1], E. UCHIMOTO[4]

[1]Department of Physics,
University of Wisconsin,
Madison, Wisconsin

[2]Fusion Systems, Inc.,
Rockville, Maryland

[3]Plasma Physics Laboratory,
Princeton University,
Princeton, New Jersey

[4]Department of Physics and Astronomy,
University of Montana,
Missoula, Montana

United States of America

Abstract

REDUCING AND MEASURING FLUCTUATIONS IN THE MST RFP: ENHANCEMENT OF ENERGY CONFINEMENT AND MEASUREMENT OF THE MHD DYNAMO.

A three- to five-fold enhancement of the energy confinement time in a reversed-field pinch (RFP) has been achieved in the Madison Symmetric Torus (MST) by reducing the amplitude of tearing mode fluctuations responsible for anomalous transport in the core of the RFP. By applying a transient poloidal inductive electric field to flatten the current density profile, the fluctuation amplitude $\tilde{b}/B$ decreases from 1.5% to 0.8%, the electron temperature T_{e0} increases from 250 to 370 eV, the ohmic input power decreases from 4.5 to approximately 1.5 MW, the poloidal beta β_θ increases from 6% to 9%, and the energy confinement time τ_E increases from 1 to ~5 ms in I_ϕ = 340 kA plasmas with density $\bar{n} = 1 \times 10^{19}$ m^{-3}. Current profile control methods are being developed for the RFP in a program to eliminate transport associated with these current-gradient-driven fluctuations. In addition to controlling the amplitude of the tearing modes, an understanding of the physics of these fluctuations is being pursued. In particular, plasma flow, both equilibrium and fluctuating, plays a critical role in a diversity of physical phenomena in MST. The key results are: (1) Edge probe measurements show that the MHD

dynamo is active in low collisionality plasmas, while at high collisionality a new mechanism, the "electron diamagnetic dynamo", is observed. (2) Core spectroscopic measurements show that the toroidal velocity fluctuations of the plasma are coherent with the large-scale magnetic tearing modes; the scalar product of these two fluctuating quantities is similar to that expected for the MHD dynamo electromotive force. (3) Toroidal plasma flow in MST exhibits large radial shear and can be actively controlled, including unlocking locked discharges, by modifying E_r with a robust biased probe.

1. INTRODUCTION

A three- to five-fold enhancement of the energy confinement time in a reversed-field pinch (RFP) has been achieved in the Madison Symmetric Torus (MST) by reducing the amplitude of tearing mode fluctuations responsible for anomalous transport in the core of the RFP. By applying a transient poloidal inductive electric field to flatten the current density profile, the fluctuation amplitude $\tilde{b}/B$ halves, the electron temperature T_{e0} increases, the ohmic input power decreases, the poloidal beta β_θ increases from 6% to 9%, and the energy confinement time τ_E increases from 1 ms to ~5 ms in $I_\phi = 340$ kA plasmas. The ion temperature is unchanged, so the ion to electron temperature ratio decreases as might be expected from reduced anomalous ion heating associated with reduced fluctuations. Additionally the radiated power, including bremsstrahlung and H_α, are reduced ~50%, indicating that the plasma is cleaner and that the global particle confinement time is substantially increased. At $I_\phi = 440$ kA, a record high (for MST) electron temperature $T_{e0} = 600$ eV is obtained, although at somewhat lower beta ($\beta_\theta \approx 7.5\%$) but with similar energy confinement ($\tau_E \sim 5$ ms). A robust feature of inductive poloidal current drive is the elimination of sawtooth oscillations. In our first inductive poloidal current drive experiments [1], the magnetic fluctuation amplitude was maintained at the low "between-sawtooth-crash" value when inductive poloidal current drive was present. With improved current drive (longer duration and more uniform amplitude), the fluctuation amplitude in many discharges falls below the between-sawtooth-crash value, and the parameters listed above are achieved. An intriguing and encouraging aspect of these experiments is that only modest inductive poloidal current drive (about 25% of the total poloidal current) was required to produce low fluctuation amplitudes.

In addition to controlling the amplitude of the tearing modes as described above, we are vigorously pursuing an understanding of the physics of these fluctuations. In particular, a series of experiments has been carried out in the the RFP to measure the dynamo electric field parallel to the equilibrium magnetic field. This dynamo arises from the correlation between the fluctuating flow velocity and magnetic field. In the edge plasma, the fluctuating flow velocity is obtained from probe measurement of the fluctuating $\mathbf{E}\times\mathbf{B}$ drift and the electron diamagnetic drift [2]. In low collisionality edge plasmas the pressureless MHD dynamo appears to be active (the fluctuating velocity is dominated by the $\mathbf{E}\times\mathbf{B}$ drift), while at high collisionality, a new "electron diamagnetic dynamo" is observed (the fluctuating velocity is dominated by the diamagnetic drift) [3]. Since probe techniques cannot access the core plasma or measure the plasma velocity directly, we are employing spectroscopic Doppler measurements of impurity ions to achieve these goals. The toroidal velocity fluctuations in the

core plasma and the core tearing mode magnetic fluctuations exhibit coherence below ~15 kHz, indicating that both these quantities are large-scale MHD fluctuations of the order of the plasma size. The velocity fluctuation amplitude and the magnetic fluctuation amplitude grow in magnitude and peak at the sawtooth crash. The scalar product of $|\tilde{v}_\phi|$ and $|\tilde{B}_r|$ exhibits the sawtooth cycle time variation expected for the dynamo electromotive force in MST. In addition to the dynamo, plasma flow also plays a critical role in a diversity of physical phenomena in MST, e.g., magnetic mode rotation and locking, and radial electric field profiles.

2. POLOIDAL INDUCTIVE CURRENT DRIVE FOR FLUCTUATION REDUCTION

In conventional RFP operation, an inductive electric field applied toroidally drives the plasma current. In this experiment, we also apply an inductive poloidal electric field. When this field is applied, the electric field parallel-to-B is increased most in the outer region of the plasma (where the magnetic field is largely poloidal). This facilitates current profile flattening for fluctuation suppression. Inductive poloidal current drive is inherently transient since it produces a changing toroidal flux Φ_ϕ in the plasma volume. The observed improvements last as long as poloidal current drive is present. To distinguish poloidal inductive current drive from conventional RFP operation and as a reminder of the transient nature of this current drive technique, we refer to this experiment as pulsed poloidal current drive (PPCD). With PPCD, the magnetic fluctuation amplitude drops to roughly half its normal value, the electron temperature increases to a record high (for MST) of ~600 eV, and the plasma resistance dramatically decreases. As a result of the decreased plasma resistance and increased stored thermal energy, the global energy confinement time is dramatically increased.

The waveforms of the poloidal and toroidal components of the electric field E_θ and E_ϕ (measured at the plasma surface), the current I_ϕ, the average toroidal magnetic field $\langle B_\phi \rangle = \Phi_\phi / \pi a^2$, and the toroidal field at the surface $B_\phi(a)$ during a PPCD experiment are shown in Fig. 1. The shaded region indicates the time during which the PPCD programming is applied. In the first PPCD experiment [1], the E_θ drive was a single, triangular shaped pulse. Figure 1 illustrates the recently improved PPCD programming that provides a series of four smaller pulses. The improved system drives poloidal current more uniformly throughout the PPCD phase and reduces the plasma-wall interaction, since the E_θ amplitude does not need to be as large. Also, PPCD lasts longer, maintaining the beneficial effects observed in the first experiment for a longer period of time. The sharp negative spikes in E_θ both before and after PPCD are associated with plasma-generated toroidal flux from spontaneous sawtooth (discrete dynamo) events (see Fig. 1c). The E_θ spikes during these events are a result of the passage of toroidal flux through the poloidal break in the conducting shell surrounding the plasma. In contrast, PPCD is a controlled increase in the poloidal current through application of positive E_θ.

A key result of improved PPCD is a greater reduction of the magnetic fluctuation amplitude, resulting in more dramatic improvements in energy confinement and other measures of plasma quality. The spatial rms magnetic

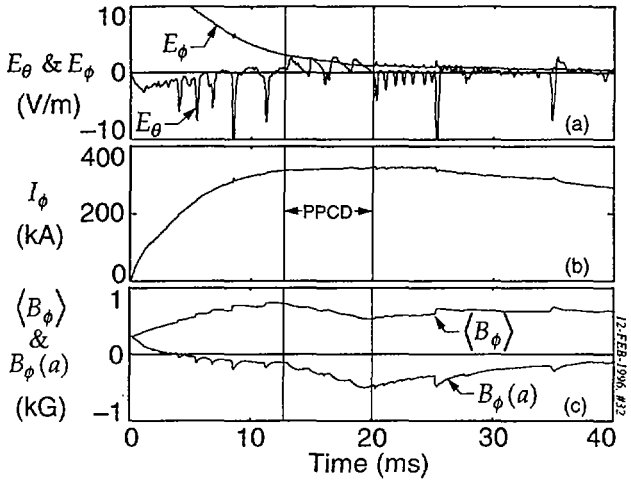

FIG. 1. Waveforms of (a) the surface electric field components, inferred from loop voltages, (b) the toroidal plasma current, and (c) the toroidal magnetic field during PPCD.

field fluctuation measured in an improved PPCD discharge by a toroidal array of 32 pickup coils on the plasma surface is shown in Fig. 2a, normalized to the equilibrium field strength. (The dominant wavelengths that compose this fluctuation are m = 1, n = 6-10 modes.) Before PPCD is applied, the fluctuation amplitude cycles with the sawtooth oscillation. PPCD suppresses sawtoothing, and the fluctuation amplitude first grows slowly and then decreases. Sawteeth are suppressed in virtually all PPCD discharges, but the fluctuation amplitude most often holds at the "between sawtooth crash" value. With improved PPCD programming, the fluctuation amplitude in some discharges (like that of Fig. 2) is reduced below the sawtooth cycle minimum value to record low values. During these periods of very low fluctuation, the improvements in the plasma are most dramatic. The parallel electric field $E_\parallel = \mathbf{E} \cdot \mathbf{B} / B$ measured at the plasma surface is shown in Fig. 2b to emphasize the relationship of reduced magnetic fluctuation and poloidal current drive. While poloidal current is driven by PPCD, the fluctuation amplitude is small.

In a conventional RFP, the tearing fluctuations generate large overlapping magnetic islands that destroy closed magnetic surfaces. The measured fluctuation-induced heat and particle fluxes in MST are large in the plasma core (inside the reversal surface) where the tearing modes resonate [4,5]. During inductive current profile control, the fluctuation amplitudes are reduced and fall near or below estimated island overlap thresholds. It is possible that closed magnetic surfaces form, although the residual fluctuations still produce closely-spaced islands of width w/a ~ 0.05 (about 80% of that required for island overlap).

The global energy confinement time τ_E increases during PPCD as a result of both increased stored thermal energy and decreased plasma resistance, i.e., decreased ohmic input power P_{ohmic}. The shot-averaged line density $\bar{n}_e$, central electron pressure $n_{e0}kT_{e0}$, P_{ohmic}, mean-squared magnetic fluctuation $\tilde{b}^2$, and H_α

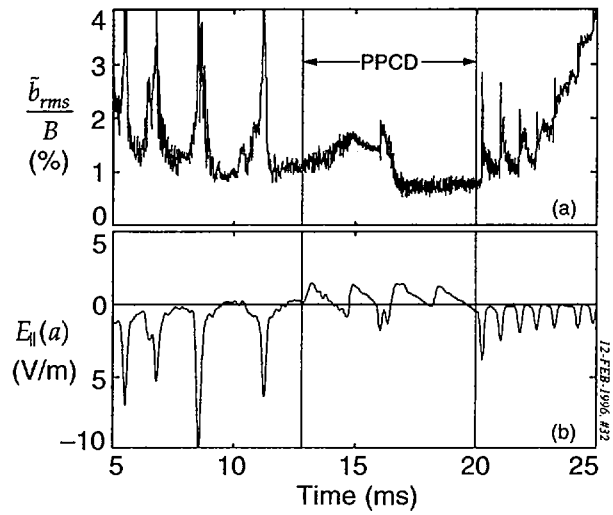

FIG. 2. (a) Spatial rms magnetic fluctuation and (b) the parallel electric field measured at the plasma surface during a PPCD discharge formed with improved poloidal current drive.

radiation for 100 PPCD plasmas are shown in Fig. 3. The same quantities from 80 conventional RFP plasmas are overlayed for comparison. The central electron pressure is measured with a single point (time and space) Thomson scattering diagnostic, varied in time shot-by-shot. In estimating τ_E and β_θ, the $nk(T_e + T_i)$ radial profile is assumed to behave as $[1 - (r/a)^2]$. (An 11-chord interferometer indicates the density profile is centrally peaked, but the temperature profiles are not measured.) The ion temperature measured by charge exchange is $T_i^{cx} \approx 0.5T_{e0}$ in conventional discharges at this density but remains constant while T_{e0} increases by as much as 170% during PPCD. The ohmic input power is derived from the measured total input power (Poynting flux) at the plasma surface by subtracting the rate of change of stored magnetic energy using equilibrium modeling. (The calculation includes power from both E_θ and E_ϕ.) Most of the PPCD plasmas in this ensemble are "ordinary" in that τ_E increases during PPCD from 1.2 ms to ~4 ms and β_θ increases from 6% to ~8%. A subset ensemble of 25 superior PPCD plasmas which exhibit the exceptionally low magnetic fluctuation level features illustrated in Fig. 2a have confinement times $\tau_E \sim 5$ ms and $\beta_\theta \sim 9\%$. Table I summarizes the best PPCD confinement in comparison with conventional RFP confinement at medium current of 340 kA. An MST record $T_{e0} = 615$ eV was measured for similar superior discharges at 440 kA and $\bar{n}_e \approx 1 \times 10^{19}$ m^{-3}, at somewhat lower beta $\beta_\theta \sim 7.5\%$ but similar $\tau_E \sim 5$ ms.

PPCD clearly demonstrates a connection between current profile control, fluctuation suppression, and reduced transport, but it is inherently transient and greater improvement is desirable. Electrostatic and rf current drive can in principle enhance and sustain current profile control. An electrostatic current

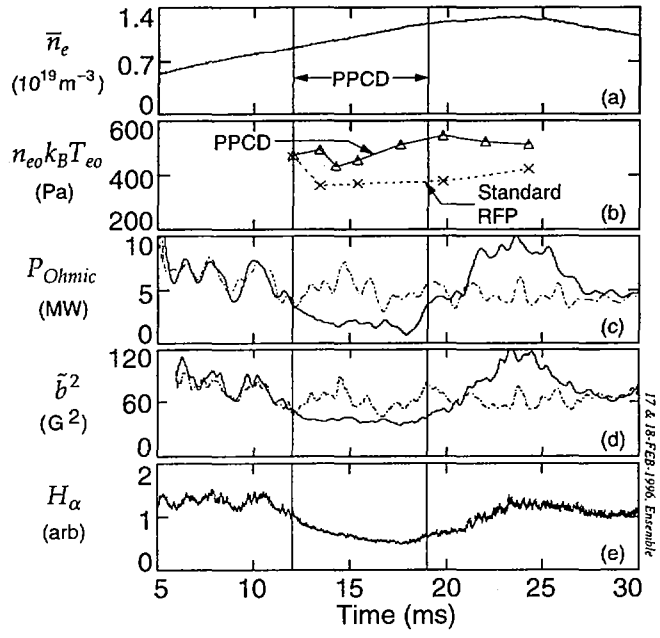

FIG. 3. Shot-averaged waveforms of (a) central chord line average density, (b) central electron pressure from Thomson scattering, (c) ohmic input power, (d) mean-squared fluctuation amplitude, and (e) H_α radiation. The unbroken lines are for 100 PPCD discharges, and the broken lines are for 80 standard RFP discharges.

TABLE I. MST CONFINEMENT PARAMETERS WITH AND WITHOUT PPCD

	PPCD	**Conventional RFP**
Current, I_ϕ	340 kA	340 kA
Density, n_e	1.0×10^{19} m^{-3}	1.0×10^{19} m^{-3}
Temperature, T_{e0}	390 eV	230 eV
Beta, β_θ	9%	6%
Input power, P_Ω	1.45 MW	4.4 MW
Confinement, τ_E	4.8 ms	1.1 ms

injection experiment using plasma-based current sources [6] placed at the edge of the plasma is in progress. The system will provide up to 15 kA of current from 15 localized sources, enough to test tearing stablilization in lower current MST plasmas according to MHD theoretical computation [7]. In the longer term, rf current drive could be the ideal solution, easily targeted to specified locations in the plasma. The lower-hybrid wave has been identified a good candidate for efficient edge poloidal current drive in typical MST plasmas. Initial accessibility and ray tracing calculations [8] are currently being refined.

3. EQUILIBRIUM AND FLUCTUATING PLASMA FLOW

3.1 Edge probe measurements of the dynamo

Spontaneous self-generation of magnetic field in a plasma, the "dynamo effect," is a ubiquitous phenomenon in astrophysical plasmas and occurs in laboratory plasmas such as the RFP and spheromak. In the RFP, the magnetic field, or plasma current parallel to the field, cannot be fully accounted for by the applied toroidal electric field. This is dramatically evident in the outer region of the plasma where the applied parallel electric field is either zero or actually points in the direction opposite to the observed current.

Theoretical study of the RFP dynamo has progressed quite far. The most thoroughly studied mechanism is the MHD dynamo, in which the current is self-generated by the $\langle \tilde{\mathbf{v}} \times \tilde{\mathbf{B}} \rangle$ term in Ohm's law, where $\langle\ \rangle$ denotes an average over a magnetic surface. However, there is a second dynamo term in the parallel Ohm's law that appears to be important [9, 10]:

$$\eta_{\parallel} j_{\parallel 0} - E_{\parallel 0} = \langle \tilde{\mathbf{v}} \times \tilde{\mathbf{B}} \rangle_{\parallel} - \langle \tilde{\mathbf{j}} \times \tilde{\mathbf{B}} \rangle_{\parallel} / en \tag{1}$$

$$= \langle \tilde{\mathbf{E}}_{\perp} \cdot \tilde{\mathbf{b}}_{\perp} \rangle + \langle \nabla_{\perp} \tilde{P}_e \cdot \tilde{\mathbf{b}}_{\perp} \rangle / en \tag{2}$$

where $\mathbf{b} \equiv \mathbf{B}/B$. The first term on the right-hand-side of Eq. (2), $\langle \tilde{\mathbf{E}}_{\perp} \cdot \tilde{\mathbf{b}}_{\perp} \rangle$, represents the contribution to $\tilde{\mathbf{v}}_{e\perp}$ from the fluctuating $\tilde{\mathbf{E}}_{\perp} \times \mathbf{B}_0$ drift, which is a MHD (single fluid) effect. This term, then, represents the MHD dynamo. The second term, $\langle \nabla_{\perp} \tilde{P}_e \cdot \tilde{\mathbf{b}}_{\perp} \rangle / en$, is the contribution from the fluctuating electron diamagnetic drift $\nabla_{\perp} \tilde{P}_e \times \mathbf{B}_0$ which is an electron fluid effect (in a two-fluid framework).

In MST, collisionality (as measured by the ratio of the electron mean free path λ_e to the minor radius a is low, on the order of 2-7. The MHD dynamo dominates in MST plasmas where the coherence at the dominant tearing mode frequencies of the $\langle \tilde{\mathbf{E}}_{\perp} \cdot \tilde{\mathbf{b}}_{\perp} \rangle$ term is much greater than that of the $\langle \nabla_{\perp} \tilde{P}_e \cdot \tilde{\mathbf{b}}_{\perp} \rangle / en$ term. The dynamo term also dominates in low density, low collisionality TPE-1RM20 plasmas. However, in high density TPE-1RM20 plasmas, $\lambda_e / a < 1$, the coherence exhibited by the diamagnetic term $\langle \nabla_{\perp} \tilde{P}_e \cdot \tilde{\mathbf{b}}_{\perp} \rangle / en$ dominates that of the $\langle \tilde{\mathbf{E}}_{\perp} \cdot \tilde{\mathbf{b}}_{\perp} \rangle$ term. In this case, the diamagnetic term is large enough to drive the parallel current required by the dynamo in the edge of the RFP. The physical reason for the transition by collisions from MHD to diamagnetic dynamo is not clear. However, it is interesting to note that the diamagnetic dynamo term can be rewritten as $\langle \nabla_{\perp} \tilde{P}_e \cdot \tilde{\mathbf{b}}_{\perp} \rangle \approx \nabla \cdot \langle \tilde{P}_e \tilde{\mathbf{b}}_{\perp} \rangle$, where the quantity $\langle \tilde{P}_e \tilde{\mathbf{b}}_{\perp} \rangle$ can be regarded as electron momentum (current) flux transported by magnetic fluctuations. This is the idea behind the kinetic dynamo effect [11], although this measurement cannot distinguish whether it is present.

3.2 Spectroscopic measurements of velocity fluctuations

Since the plasma flow velocity $\mathbf{v} = (m_i \mathbf{v}_i + m_e \mathbf{v}_e)/(m_i + m_e) \approx \mathbf{v}_i$, spatially localized measurement of $\tilde{\mathbf{v}}_i$ and its correlation with $\tilde{\mathbf{B}}$ is the most direct way to measure the MHD dynamo term $\langle \tilde{\mathbf{v}} \times \tilde{\mathbf{B}} \rangle$. Our measurement technique on MST [12] approximates the ideal of local measurements of the majority species

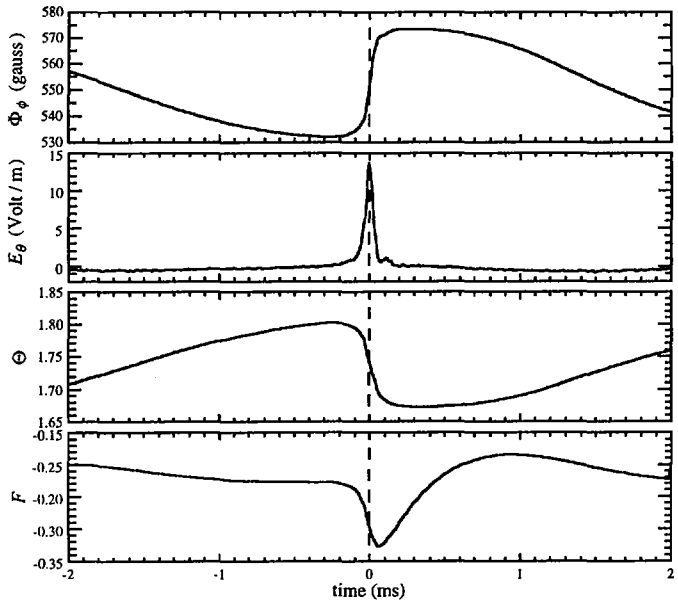

FIG. 4. An ensemble average over 442 sawtooth events illustrating the sawtooth oscillation in toroidal flux Φ_ϕ, surface poloidal electric field E_θ, pinch parameter Θ, and reversal parameter F.

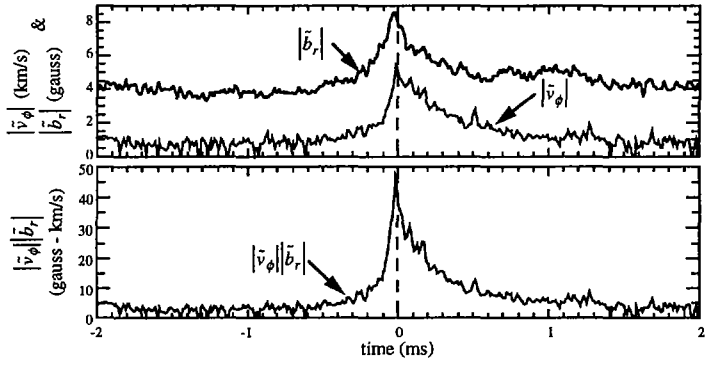

FIG. 5. Sawtooth ensemble-average of (a) $|\tilde{v}_\phi|$ and $|\tilde{B}_r|$, and (b) the scalar quantity $|v_\phi|\ |B_r|$.

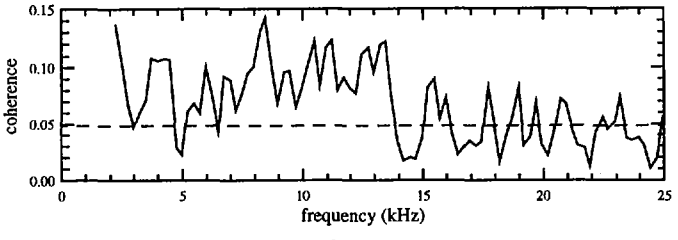

FIG. 6. Coherence amplitude of $\tilde{v}_\phi$ and $\tilde{B}_r$; the dashed line indicates the noise level.

dynamics in two ways. First, our diagnostic records impurity ion dynamics, specifically the Doppler shift and broadening of naturally occurring impurity ion line emission. However, on the time and spatial scales of interest, the impurities should mimic majority species behavior. The second and more problematic approximation to the ideal measurement arises from the fact that our diagnostic passively records a chord-average of the impurity ion emission. Analysis of such data for spatial correlation measurements requires detailed knowledge of the impurity emission profiles in conjunction with careful modeling of the structure of the dominant tearing modes. In spite of these difficulties we have begun to assemble a direct, quantitative measurement of MHD dynamo activity in an RFP.

Dynamo activity in MST is manifested in two distinct ways, a discrete and a continuous dynamo. The discrete dynamo is evident during a sawtooth event [13]. Sawtooth events occur in MST with a period of about 3 ms. Figure 4 illustrates the field generation and relaxation that occurs over a sawtooth oscillation. Strong spontataneous magnetic field generation is evident in the sudden increase of toroidal flux Φ_ϕ during a sawtooth crash (at t = 0 in Fig. 4). The peak of the time derivative of the toroidal flux, measurable as the surface poloidal electric field E_θ, is employed as a time reference for the sawtooth crash. The decreases in the pinch parameter $\Theta \equiv B_\theta(a)/(\Phi_\phi/\pi a^2)$ and the reversal parameter $F \equiv B_\phi(a)/(\Phi_\phi/\pi a^2)$ indicate that, during a crash, the plasma relaxes toward a minimum energy state with a flatter current profile, i.e., current decreases at the core and increases at the edge. Between crashes, flux generation (opposing resistive decay) is present at a low level, indicating operation of a continuous dynamo.

Figure 5(a) illustrates our ensemble-averaged (equivalent to an average over a flux surface) measurement of the MHD dynamo quantities $|\tilde{v}_\phi|$ and $|\tilde{b}_r|$. Note how both the velocity fluctuation amplitude and the magnetic fluctuation amplitude grow in magnitude and peak at the sawtooth crash. These quantities are coherent between 5 - 15 kHz (Fig. 6), indicating that they are representative of the long-wavelength tearing modes expected to be associated with the MHD dynamo in the RFP [14]. The scalar quantity $|\tilde{v}_\phi||\tilde{b}_r|$ is shown in Fig. 5(b). As expected, this quantity is non-zero throughout the sawtooth cycle (indicating the operation of a continuous dynamo) and peaks during the sawtooth crash (indicative of the discrete dynamo). Calculation of the cross product of $\tilde{v}_\phi$ and $\tilde{B}_r$, which is the actual MHD dynamo term, is in process. Determination of the phase between $\tilde{v}_\phi$ and $\tilde{B}_r$ is complicated by the fact that the measured $\tilde{v}_\phi$ is chord-averaged, but initial analysis indicates that the correlation phase provides for a substantial non-zero dynamo electromotive force.

3.3 Equilibrium plasma flow, magnetic mode rotation, and E_r

Plasma flow, magnetic mode rotation, and radial electric field are tightly coupled in MST. The dominant tearing mode fluctuations (which are core resonant) generally phase lock together and co-rotate [15]. The toroidal flow of the core impurity C v ions closely tracks the toroidal phase velocity of the dominant tearing modes. This tracking is especially striking during a sawtooth event when fast changes in toroidal rotation occur [16]. The deceleration time of the magnetic modes and the plasma is about 100 μs, with the modes leading the plasma by about 10 μs. The deceleration of the modes is as expected from a calculation of the electromagnetic torque on a magnetic island, but a simple

calculation of the Braginskii viscous diffusion of the plasma predicts a much longer deceleration time for the toroidal flow velocity. However, this discrepancy can be resolved by accounting for the presence of a number of phase-locked $m = 1$ islands in a diffusive toroidal momentum transport model calculation [17]. The nonlinear interaction of these tearing modes also appears to play a prominant role in momentum degradation and mode locking [18].

Impurity ion states midway between the core and edge (B IV and O V) and in the edge (C III) provide a rough picture of the flow profile; the toroidal plasma flow appears to slow down and even reverse direction near the edge. The oppositely directed flow of the edge plasma may be due to the fact that the radial electric field E_r changes sign at the reversal surface, pointing radially *out* inside the surface and radially *in* outside the surface [19]. E_r can be dramatically altered by the insertion of a biased probe into the plasma; this technique provides control of the rotation of the plasma, including unlocking and spinup of locked discharges [20].

4. SUMMARY

The fluctuation amplitude of the dominant magnetic tearing modes in MST has been halved by application of a transient poloidal inductive electric field to flatten the current density profile. This resulted in an approximate quadrupling of the energy confinement time τ_E to 5 ms and an increase in poloidal beta β_θ from 6% to 9%. The magnetic fluctuations in MST are coherent with fluctuations in the plasma toroidal flow velocity, indicative of MHD dynamo current generation. In higher collisionality RFP plasmas, a new mechanism, the "electron diamagnetic dynamo," is observed.

ACKNOWLEDGEMENT

This work was supported by the U. S. Department of Energy.

REFERENCES

[1] SARFF, J.S., HOKIN, S.A., JI, H., PRAGER, S.C., SOVINEC, C.R., Phys. Rev. Lett. **72** (1994) 3670;
SARFF, J.S., et al., Phys. Plasmas **2** (1995) 2440.

[2] JI, H., ALMAGRI, A.F., PRAGER, S.C., SARFF, J.S., Phys. Rev. Lett. **73** (1994) 668;
JI, H., et al., Phys. Rev. Lett. **74** (1995) 1086.

[3] Work done in collaboration with the TPE-1RM20 group (Y. YAGI, K. HATTORI, Y. HIRANO, T. SHIMADA, Y. MAEJIMA, K. HAYASE).

[4] FIKSEL, G., PRAGER, S.C., SHEN, W., STONEKING, M.R., Phys. Rev. Lett. **72** (1994) 1028.

[5] STONEKING, M.R., et al., Phys. Rev. Lett. **73** (1994) 549.

[6] FIKSEL, G., et al., Plasma Sources Sci. Technol. **5** (1996) 78.

[7] HO, Y.L., Nucl. Fusion **31** (1991) 341.

[8] UCHIMOTO, E., et al., Phys. Plasmas **1** (1994) 3517.

[9] JI, H., et al., Phys. Plasmas **3** (1996) 1935.
[10] LEE, G.S., DIAMOND, P.H., AN, Z.G., Phys. Fluids B **1** (1989) 99.
[11] JACOBSON, A.R., MOSES, R.W., Phys. Rev. A **29** (1984) 3335.
[12] DEN HARTOG, D.J., FONCK, R.J., Rev. Sci. Instrum. **65** (1994) 3238.
[13] HOKIN, S., et al., Phys. Fluids B **3** (1991) 2241.
[14] ORTOLANI, S., SCHNACK, D.D., Magnetohydrodynamics of Plasma Relaxation, World Scientific Publishing, Singapore (1993) 95.
[15] ALMAGRI, A.F., et al., Phys. Fluids B **4** (1992) 4080.
[16] DEN HARTOG, D.J., et al., Phys. Plasmas **2** (1995) 2281.
[17] YOKOYAMA, M., CALLEN, J.D., HEGNA, C.C., Nucl. Fusion **36** (1996) 1307.
[18] HEGNA, C.C., Phys. Plasmas **3** (1996) 4646.
[19] CHIANG, C.-S., et al., Bull. Am. Phys. Soc. **40** (1995) 1753.
[20] ALMAGRI, A.F., et al., Bull. Am. Phys. Soc. **40** (1995) 1753.

DISCUSSION

R.J. GOLDSTON: Could you comment on the electromagnetic power balance? In particular, how does the Poynting flux vary with time, and how do you estimate the ohmic heating power? I notice that the ohmic heating power overshoots after the poloidal current drive is turned off, so one has to be especially careful that the inductive power is accurately calculated.

D.J. DEN HARTOG: The surface Poynting flux during PPCD increases by a small amount owing to the additional poloidal electric field E_θ. Although the toroidal current remains roughly constant, the magnetic energy increases substantially as a result of increased plasma inductance. The increased inductance (not shown in the paper) is independently observed in equilibrium modelling and as an increase in the asymmetry factor $\Lambda = (\ell_i/2) + \beta_\theta - 1$ measured by a poloidal array of magnetic sensors. The ohmic input power is derived from the Poynting flux by subtracting the inductive component using equilibrium modelling. The increase in the ohmic input power (and degradation of confinement with a re-emergence of large fluctuations) results from several extra-large sawteeth that terminate the PPCD phase.

T.R. JARBOE: In your starting fluctuation equation, why is the explicit $\widetilde{\nabla P_e}$ term absent?

D.J. DEN HARTOG: The equation shown is the parallel component of the generalized Ohm's law (which includes the ∇P term). The derivation has been omitted here for brevity but can be found in Refs [2, 9].

IMPROVED HIGH THETA MODE AND DYNAMO ACTIVITY IN A REVERSED FIELD PINCH ON TPE-1RM20

Y. HIRANO, Y. MAEJIMA, T. SHIMADA,
Y. YAGI, S. SEKINE, I. HIROTA, H. SAKAKITA,
T.J. BAIG, G. SERIANNI, H. JI[1]
Electrotechnical Laboratory,
Umezono, Tsukuba-shi, Ibaraki,
Japan

Abstract

IMPROVED HIGH THETA MODE AND DYNAMO ACTIVITY IN A REVERSED FIELD PINCH ON TPE-1RM20.

The conditions for an improved high theta mode (IHTM) are elucidated in TPE-1RM20. The IHTM is an operating mode in a reversed field pinch, where the poloidal beta and the energy confinement time are doubled in the high pinch parameter region ($\Theta \sim 2$). By using the appropriate decay of the plasma current and keeping Θ below 2, the large MHD activity associated with the relaxation of the magnetic field (discrete dynamo event) can be suppressed, and good reproducibility of the IHTM ($\sim 80\%$) is obtained with almost constant reversal and pinch parameters. An analysis of the toroidal magnetic field fluctuation near the plasma edge indicates that the rotation of the $m = 1$ mode is important in suppressing the discrete dynamo event. In addition, two types of mode evolution are observed in the event: one is the growth of a single helical mode ($m/n = 1/7$) and its wall locking, and the other is the rapid growth of toroidally localized magnetic fluctuations. In both cases, a large localized $m = 0$ mode is observed. $m = 0$ modes seem to play a role in the energy loss during the discrete dynamo event. A new dynamo mechanism (diamagnetic dynamo effect) has been found in the analysis of electrostatic and magnetic fluctuations. The dynamo electric field is produced by non-linear interaction between the fluctuations of the magnetic field and the electron diamagnetic drift velocity.

1. INTRODUCTION

In the reversed field pinch (RFP) experiment on TPE-1RM20, a new operation mode was found and termed improved high theta mode (IHTM). In this mode, the values of electron density, poloidal beta and energy confinement time were doubled in the high pinch parameter region ($\Theta \sim 2$) [1–3]. The pinch parameter is the ratio of the poloidal magnetic field at the plasma surface to the volume averaged toroidal magnetic field, $\Theta = B_{pw}/\langle B_t \rangle$. To obtain the IHTM, violent MHD activities should be avoided whose characteristics are rapid growth of the magnetic fluctuations,

[1] Present address: Plasma Physics Laboratory, Princeton University, Princeton, New Jersey, USA.

sudden increase of the toroidal magnetic flux in the plasma (ϕ_t), pulse-like deepening of toroidal magnetic field reversal at the plasma surface (B_{tw}) and a rapid decrease of the soft X ray signal (SX) [4]. This MHD activity is called discrete dynamo event; it had usually beeen observed in the high Θ region of TPE-1RM20.

Even after the IHTM had been found, this event was still difficult to control and the reproducibility of the IHTM was not sufficient ($\sim$40–60%). Moreover, in these IHTM discharges, not only the plasma current (I_p), ϕ_t and B_{tw}, but also Θ and F (F is the reversal parameter, $F = B_{tw}/\langle B_t \rangle$) were time dependent, which means that the relative profile of the magnetic field also changed in time.

As is described in Ref. [2], in many cases the discrete dynamo events were related to a certain type of MHD activity whose characteristics were the growth of a single helical mode resonant near the plasma centre (poloidal mode number $m = 1$ and toroidal mode number $n = 7$) as well as wall locking of this mode. However, different types of MHD activity related to the discrete events have recently been found.

To improve this situation and our understanding of the mechanism of the IHTM, the experimental conditions were surveyed and the magnetic fluctuations were analysed intensively. After optimizing the conditions, the reproducibility of the IHTM is improved up to about 80% with almost constant Θ and F values, except for the initial and final phases of the discharge.

A new dynamo mechanism is found in ordinary operating conditions on TPE-1RM20 (low Θ, $\sim$1.5, not in the IHTM) [5]. Magnetic and electrostatic fluctuations were measured simultaneously by insertable probes. The result indicates that the fluctuation of the electron diamagnetic drift velocity plays a significant role in the dynamo activity (diamagnetic dynamo effect).

2. CONDITIONS FOR IHTM

In oder to find the key experimental conditions for obtaining the IHTM (to avoid the discrete dynamo event), the operating conditions, such as the values of I_p, ϕ_t, B_{tw}, F and Θ, and their wave forms, were surveyed carefully. It was found that one key parameter is the rate of variation of I_p. The result is shown in Fig. 1, where the normalized rate of occurrence of the discrete events is plotted as a function of $(dI_p/dt)/I_p$.

The occurrence of discrete events is counted within each step of the $(dI_p/dt)/I_p$ value. The step width is 0.02 $m \cdot s^{-1}$ in this graph. This counted number is normalized by the summation of the discharge duration times in about 300 shots, where the $(dI_p/dt)/I_p$ value lies within the same step. As is shown in Fig. 1, there is a minimum at $(dI_p/dt)I_p \sim -0.7$ $m \cdot s^{-1}$, i.e. in the decay phase of I_p (the decay time is $\sim$14 ms). In the I_p decay phase, ϕ_t also decays, except at the discrete dynamo event. This optimum $(dI_p/dt)/I_p$ value is almost the same with the L/R time of I_p ($\sim$16 ms for $L \sim 1.6$ μH and $R \sim 100$ $\mu\Omega$). The possibility of obtaining the IHTM

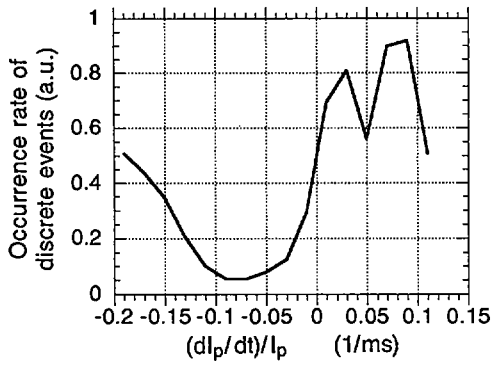

FIG. 1. Normalized rate of occurrence of a discrete dynamo event as a function of the rate of variation of I_p.

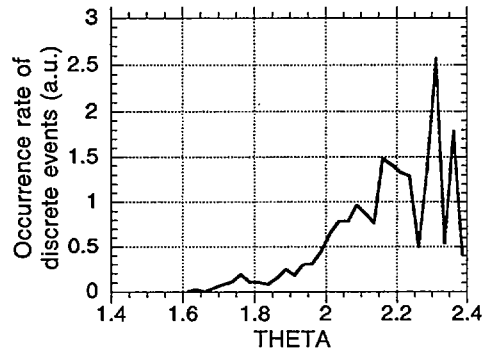

FIG. 2. Normalized rate of occurrence of a discrete dynamo event on Θ.

has its maximum when the experimental decay rate is matched with the decay rate the plasma would have naturally, in other words, when the electromagnetic energy flow across the plasma surface (the surface integral of the Poynting vector) vanishes approximately.

Figure 2 shows the normalized rate of occurrence of discrete events as a function of Θ. The same normalization method is used as before. No discrete events are observed for Θ below 1.6, even in the phase of increasing I_p, where the production of ϕ_t and hence a strong dynamo activity is required. The occurrence of discrete events increases gradually up to $\Theta = 1.95$ and then grows rapidly for $\Theta > 1.95$. The strength of a discrete dynamo event, which may be defined by the variation of Θ during the event, increases with Θ. This suggests that the dynamo activities should be rather continuous for low Θ, while they tend to be discrete for high Θ.

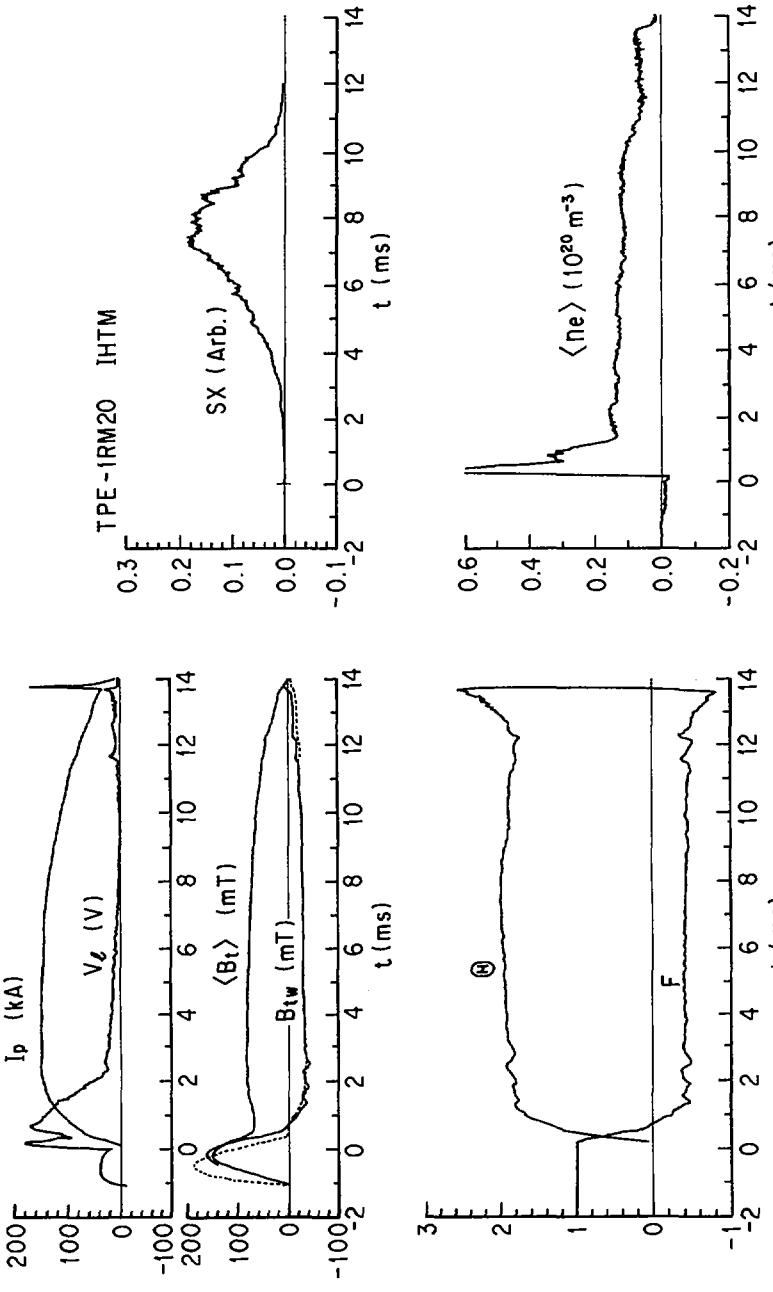

FIG. 3. Time variations of I_p, V_ℓ, $\langle B_t \rangle = \phi_t/\pi a^2$, B_{tw}, F, Θ, SX intensity and $\langle n_e \rangle$ (chord averaged electron density) in a typical IHTM discharge.

Figures 1 and 2 show that the choice of an adequate I_p decay rate, $(I_p/(dI_p/dt) \sim L/R$ of $I_p)$, and keeping Θ below 1.95 are required for obtaining good reproducibility of the IHTM.

Figure 3 shows one of the best IHTM discharges, where both I_p and ϕ_t ($\langle B_t \rangle = \phi_t/\pi a^2$ is shown in the figure) are decaying gradually, with appropriate control of the one turn loop voltage, V_ℓ and B_{tw}. The values of Θ and F are kept almost constant from t = 3 to 11 ms. Neither large discrete events nor a large crash in SX emission is observed, except close to the end of the discharge. The increase in the electron density, $\langle n_e \rangle$, was the most significant feature of the IHTM, which is confirmed by the prolonged IHTM discharges shown here. $\langle n_e \rangle$ is almost constant at relatively high values (1.5×10^{19} m^{-3}). The variations with Θ of other plasma parameters, such as the electron or ion temperatures (T_e and T_i) or V_1, are essentially the same as those reported previously [2, 3], i.e. a small increase in T_e (from 500 to 650 eV), almost constant T_i ($\sim$450 eV) and V_ℓ ($\sim$17 V), when Θ increases from 1.5 to 2.0. Increases in poloidal beta from 0.08 to 0.2 and an energy confinement time from 0.2 to 0.4 ms are also confirmed. The ratio of $\langle n_e \rangle$ to the intensity of the D_α emission, which may correspond to the particle confinement time, shows a variation similar to that of the energy confinement time. The probability of obtaining the IHTM has been improved up to about 80%, and the stable and good confining properties of the IHTM are well demonstrated.

3. MODE ANALYSIS OF MAGNETIC FLUCTUATIONS

To study the mechanism of the IHTM in greater detail, the magnetic fluctuations are analysed intensively. The fluctuations of the toroidal magnetic field on the outer surface of the vacuum vessel are measured at the inner and outer sides of the torus in the equatorial plane of the machine. Thirty-two pairs of coils are equally distributed around the torus. The shielding effect of the vacuum vessel is compensated for numerically [6]. Since only two coils are used in one poloidal cross-section, odd and even poloidal modes can be distinguished. However, in a former measurement it was shown that the odd mode mainly corresponds to m = 1 and the even mode to m = 0 [7]. Therefore, we will denote even modes by m = 0 and odd modes by m = 1.

As is described in Ref. [2], in many cases the occurrence of a discrete event is related to the stop of the rotation of the m = 1 mode. We observe the growth of a single helical m = 1/n = 7 mode, the slowing-down and final stop of the rotation of this mode, a cascading of this mode to several m = 1 modes with higher n, a simultaneous growth of the m = 0 mode in a toroidally localized position and a large SX crash. Then, the m = 1 mode starts rotating again, and the toroidally localized m = 0 mode stays almost at one position. This m = 0 mode decays gradually within 0.5 to 2 ms, and the SX signal increases again after the m = 0 mode has decayed.

In the IHTM discharge, the continuous rotation of a single m = 1 mode (n = 7 or 8) is observed up to close to the end of the discharge. In the phase of increasing SX, the rotation of this mode is very clear, and other modes are very small, as is shown in Fig. 4. Then, a smaller amount of overlap of different modes is expected, and the energy loss caused by the stochastic magnetic field lines may be reduced, which may explain the improved confinement in the IHTM.

Near the end of the IHTM discharge, where the I_p is about 80% of its maximum value, the mode stops rotating, and always a large SX crash takes place. No relaxation of the magnetic field, however, occurs at this time. SX never recovers again after this crash.

The rotation of mode is not so clear in the non-IHTM discharges, where multi m = 1 modes with high n (7–10) are frequently observed as is shown in Fig. 5, even during the period without discrete event.

Roughly speaking, the amount of SX crashes in many cases seems to be related to the degree of slowing-down of the mode rotation. When the rotation stops completely, i.e. wall locking takes place, large SX crash is observed, but when the slowing-down is mild the SX crash is also mild.

It should be noted, however, that in several discharges another type of discrete dynamo event is observed. In this case, no appreciable slowing-down of the mode

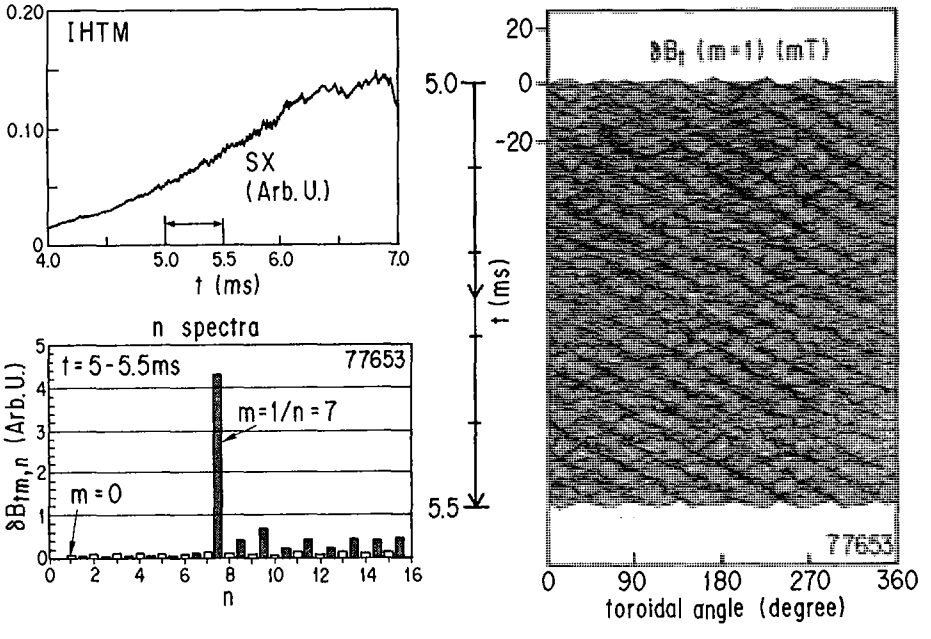

FIG. 4. SX variation, n spectra of m = 0 and m = 1 modes and time evolution of the toroidal variation of the m = 1 fluctuation of the toroidal magnetic field in an IHTM discharge.

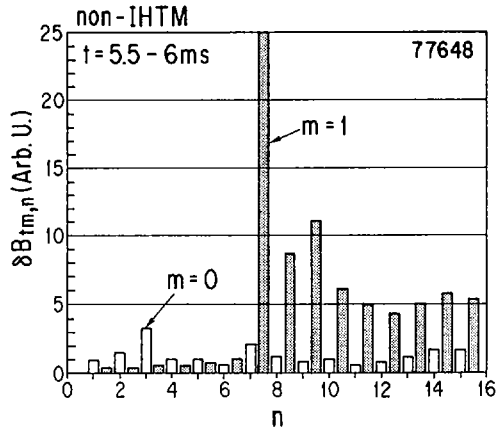

FIG. 5. n spectra of m = 0 and m = 1 modes in the quiet period between two discrete dynamo events in a non-IHTM discharge.

rotation is observed before the discrete event. A sudden growth of m = 1 and m = 0 modes at a toroidally localized place (phase locking of the modes with different n numbers) and a large SX crash take place in a very short time. The modes grow very fast (<0.1 ms).

There is another interesting type of magnetic fluctuation — not frequent, but not negligible either —, where wall locking of a single m = 1/n = 7 mode takes place in the same manner as in the typical case described above; this mode disappears, however, after wall locking. Neither large SX crash nor appreciable changes in Θ and F are observed. No relaxation of magnetic field or plasma thermal energy happens. This case is mainly observed in the strong decay phase of I_p. One difference between this and the SX crash case is that the m = 0 mode does not grow in the former case. The m = 0 mode stays at a low level.

The amplitude of the m = 0 mode is shown to be related to the SX intensity. SX decays rapidly at the time of growth of the m = 0 mode and cannot increase again until the large m = 0 mode has disappeared. When the m = 0 mode is small, the SX can increase, even if the m = 1 mode is not small.

The m = 0 modes are resonant at the reversal surface of the toroidal magnetic field, and the destruction of the magnetic surface in that boundary region may have a significant effect on the electron energy loss.

4. DIAMAGNETIC DYNAMO EFFECT

The dynamo activity is studied in a wide range of the edge electron densities in ordinary operating conditions of TPE-1RM20 (non-IHTM discharges). The electrostatic and magnetic fluctuations are measured by triple probe and pick-up coil

arrays [5, 6, 9]. It is found that the ordinary MHD dynamo term estimated to be given by $\langle E_f \rangle_\parallel = \langle \delta v_s \times \delta B \rangle_\parallel$ is sufficient to balance the resistive term $\langle \eta j \rangle_\parallel$ in the low, but not in the high collision frequency region. Here, δB is the magnetic fluctuation, $\delta v_s = \delta E_s \times B/B^2$, δE_s is the measured electric field, η the resistivity, j the current density, $\langle\rangle$ denotes the time average and $\parallel$ denotes the component parallel to the equilibrium magnetic field. In order to balance $\langle \eta j \rangle_\parallel$, another type of dynamo term should be considered.

Starting from generalized Ohm's equation in a turbulent plasma and considering dominant terms (the usual $v \times B$ and Hall terms), the parallel component of the equation may be reduced to [9]

$$\eta j_{\parallel 0} - E_{\parallel 0} = \langle \delta v_e \times \delta B \rangle_\parallel$$

where δv_e is the fluctuating electron drift velocity and $E_{\parallel 0}$ is the externally applied parallel electric field.

When the ordinary $E \times B$ drift and the electron diamagnetic drift are taken into account, this equation can be written as

$$\eta j_{\parallel 0} - E_{\parallel 0} = \langle \delta E \cdot (\delta B/B) \rangle_\parallel + \langle \mathrm{grad}(\delta p_e) \cdot (\delta B/B) \rangle_\parallel / (en_e)$$

The second term on the right hand side represents the dynamo effect due to the fluctuation of the electron diamagnetic drift (diamagnetic dynamo). By including this term, the balance with $\langle \eta j \rangle$ becomes possible in a wide range of collision frequencies, and a comprehensive understanding of the results of three different RFP machines, TPE, MST and REPUTE, becomes possible [5, 9].

5. SUMMARY

The conditions for obtaining the improved high theta mode (IHTM) are elucidated by an intensive survey of the operating conditions. The IHTM is the operating mode where the poloidal beta and the energy confinement time are doubled in the high pinch parameter region ($\Theta \sim 2$). Strong MHD activity (discrete dynamo event) should be avoided in obtaining the IHTM; the latter can be achieved by using an appropriate I_p decay rate and by keeping Θ below 2. There is an optimum value in the decay time of I_p (~ 14 ms), which is nearly equal to the L/R time of I_p. By choosing the proper operating conditions, the reproducibility of the IHTM is improved to about 80%, and prolonged IHTM discharges are obtained with almost constant G and Θ. The plasma parameters measured in the prolonged IHTM are essentially the same as those reported previously. In the present experiments, the IHTM is otained in the decay phase but demonstrates the possibility of realizing improved confinement in the steady RFP if, by an appropriate method, the dynamo activity is controlled by direct current drive.

In the analysis of the B_{tw} fluctuation, the mechanism of the discrete dynamo event becomes clear. One of the characteristic types is the growth of a single helical mode (m/n = 1/7) and its locking to the wall. Another type is the rapid growth of toroidally localized m = 0 and m = 1 modes. Phase locking of several modes with different n numbers results in this localized mode structure, which may be similar to the slinky mode in OHTE [10].

In both cases, relaxation of the magnetic field (production of ϕ_t and deepening of B_{tw}) and associated energy loss (large SX crash) are observed, and the recovery of the SX intensity takes place after the decay of the large amplitude m = 0 mode.

In the IHTM, a single m = 1/n = 7(n = 8, in some cases) mode rotates almost continuously during the discharge until close to the end of the discharge, where I_p decays to about 80% of its maximum and a large SX crash takes place.

In some discharges with decaying I_p wave form, the evolution of the m = 1 mode is similar to that in the single helical mode case until wall locking takes place, but afterwards the mode decays and again rotates with no relaxation of the magnetic field and no large SX crash. No discrete dynamo event takes place, not even when the rotation stops. In this case, only small m = 0 modes and a small SX crash are observed.

These observations indicate that the m = 0 modes play a significant role in the energy loss during the discrete dynamo event.

In analysing the electrostatic and magnetic fluctuations in the boundary region, a new dynamo mechanism is found. The dynamo electric field is produced by the interaction between the fluctuation of the magnetic field and the electron diamagnetic drift velocity, which is driven by the fluctuation in the electron pressure. This diamagnetic dynamo effect is the first observation that shows the possibility of the pressure gradient playing a role in the dynamo activity.

ACKNOWLEDGEMENTS

The authors are grateful to Dr. K. Sugisaki and the members of the plasma section in the Electrotechnical Laboratory for valuable discussions and support. This research is financially supported by the Japanese Science and Technology Agency.

REFERENCES

[1] YAGI, Y., et al., in Plasma Physics and Controlled Nuclear Fusion Research 1994 (Proc. 15th Int. Conf. Seville, 1994), Vol. 2, IAEA, Vienna (1995) 415.
[2] HIRANO, Y., et al., Nucl. Fusion 36 (1996) 721.
[3] YAGI, Y., et al., Fusion Technol. 27 (1995) 301.
[4] HOKIN, S., et al., Phys. Fluids B 3 (1991) 2241.
[5] JI, H., et al., Phys. Rev. Lett. 75 (1995) 1086.
[6] BRUNSELL, P.R., et al., Phys. Fluids B 3 (1993) 885.

[7] HATTORI, K., et al., Phys. Fluids B 3 (1991) 3111.
[8] JI, H., et al., Phys. Rev. Lett. 69 (1992) 616.
[9] JI, H., et al., Phys. Plasma 3 (1996) 1935.
[10] TAMANO, T., et al., Phys. Rev. Lett. 59 (1987) 1444.

DISCUSSION

R. BARTIROMO: Do you have any information on density and temperature profiles?

Y. HIRANO: We do not have an electron temperature profile measurement, only a rough electron density profile (three chords plus edge).

R. BARTIROMO: Do the profiles change with θ or when internal relaxations are stable?

Y. HIRANO: With approximation by the parabolic profile, there is no appreciable change in the improved high θ mode, although the accuracy may not be sufficient to distinguish the difference.

D.C. ROBINSON: When you go to higher θ, one would expect the $m = 0$ activity to increase as the field reversal surface moves further into the plasma. What do you observe?

Y. HIRANO: Generally speaking, $m = 1$ fluctuations decrease and $m = 0$ fluctuations increase as θ increases. However, if we consider only the improved high θ mode, the increase of the $m = 0$ mode is not clear.

S.A. HOKIN: How does the overall magnetic fluctuation level compare between good low θ and good high θ discharges?

Y. HIRANO: The overall fluctuation level in the improved high θ mode is smaller in than the low θ case.

S.A. HOKIN: Can this account for the improved confinement in high θ discharges?

Y. HIRANO: My answer is partly 'yes'. The reduction of the fluctuations definitely contributes to confinement improvement, but I believe that a single mode structure (less stochastic magnetic field lines) also plays a significant role.

ECRH EXPERIMENTS IN A HOT ION MODE OF THE GAMMA 10 TANDEM MIRROR AND A THEORETICAL STUDY OF PLUG POTENTIAL FORMATION MECHANISMS

T. SAITO, I. KATANUMA, T. AOTA, L.G. BRUSKIN, T. CHO, M. HIRATA, H. HOJO, M. ICHIMURA, K. ISHII, A. ITAKURA, N. KATSURAGAWA, Y. KIWAMOTO, J. KOHAGURA, A. MASE, Y. NAKASHIMA, Y. SAKAMOTO, M. SHOJI[1], T. TAMANO, Y. TATEMATSU, T. TOKUZAWA, K. YATSU, M. YOSHIKAWA, Y. YOSHIMURA
Plasma Research Center,
University of Tsukuba,
Tsukuba, Japan

Abstract

ECRH EXPERIMENTS IN A HOT ION MODE OF THE GAMMA 10 TANDEM MIRROR AND A THEORETICAL STUDY OF PLUG POTENTIAL FORMATION MECHANISMS.

The paper reports on two subjects of tandem mirror studies at the Plasma Research Center, University of Tsukuba. The first concerns ECRH experiments in a hot ion mode. At the 1994 IAEA conference in Seville, the authors reported on a hot ion mode created by ICRH in the GAMMA 10 tandem mirror. In the hot ion mode ($T_i/T_e > (m_i/m_e)^{1/3}$), the main channel of energy drain from core ions in the central cell is drag due to electrons. Therefore, direct electron heating should reduce the electron drag on hot ions, and accordingly more effective ion heating is expected. Recently second harmonic ECRH has been applied to a central cell plasma with an ion temperature of a few kiloelectronvolts. A significant increase in the ion temperature is indeed obtained. The second subject of the paper is a theoretical study of plug potential formation mechanisms. Recent experiments in tandem mirrors indicate that a plug potential is formed without sloshing ions. The study presents a theoretical model in which a plug potential can be formed between the thermal barrier region and the outer mirror throat for plausible ion and electron distribution functions even without high energy sloshing ions.

1. INTRODUCTION

In the hot ion mode of the GAMMA 10 tandem mirror [1], an ion temperature of up to 10 keV has been obtained with an ICRH power of 70 kW radiated from the antennas [2]. However, since the bulk electron temperature T_e is several tens of electronvolts, electron drag is a limiting factor of ion heating efficiency. The electron drag time $\tau_{ie} \approx \tau_{ee}(m_i/m_e)$ is much shorter than the ion collision time $\tau_{ii} \approx \tau_{ee}(m_i/m_e)^{1/2}(T_i/T_e)^{3/2}$, because the relation $T_i/T_e > (m_i/m_e)^{1/3}$ holds in a GAMMA 10

[1] Present address: National Institute of Fusion Science, Toki, Gifu, Japan.

hot ion plasma. Hot ions perpendicularly heated by ICRH lose energy through electron drag before being scattered into the mirror loss cone. Thus electron drag is the largest channel of energy drain from the hot ions. Therefore, direct electron heating should reduce electron drag, and accordingly more effective ion heating is expected. In the present paper, we report a recent experiment in which second harmonic ECRH is applied to a central cell plasma with an ion temperature of a few kiloelectronvolts. The bulk electron temperature increases to a value higher than 100 eV and a significant increase in the ion temperature is indeed obtained. This result reconfirms that the ion temperature is mainly limited by electron drag. Moreover, it presents a prospect for efficient ion heating in a tandem mirror.

Plug potential formation mechanisms in a tandem mirror are also studied. The original proposal for plug potential formation requires high energy sloshing ions as well as ECRH around plug regions [3]. However, only ECRH is required to form an ion confining potential in actual experiments [2, 4]. We present a theoretical model in which a plug potential can be formed between the thermal barrier region and the outer mirror throat for plausible ion and electron distribution functions even without high energy sloshing ions.

2. ECRH EXPERIMENTS IN HOT ION MODE

2.1. GAMMA 10 device and set-up for ECRH

The GAMMA 10 tandem mirror consists of a central solenoid, two anchor cells and two end mirror cells. The anchor cells, with a minimum B configuration, are located in both ends of the central cell and are connected to the end mirror cells. Ions in the central cell are heated by a slow ion cyclotron wave excited by a pair of double half-turn antennas installed near both ends of the central cell. Ions in the anchor cells are heated by other ion cyclotron waves with frequencies different from that in the central cell. The anchor hot ions ensure the MHD stability of a GAMMA 10 plasma. A positive plug potential and a negative barrier potential are formed in the axisymmetric end mirror cells by a combination of fundamental and second harmonic ECRH.

For ECRH in the central cell, a new microwave system has been installed. Microwave power delivered from a 28 GHz gyrotron is launched from a Vlasov antenna onto a second harmonic ECR layer at about 43° from the magnetic axis. The radiated microwave is linearly polarized and about 67% of the radiated power is attributed to the quasi-X mode. The resonance layer is located near the midplane of the central cell. The magnetic field strength B at the ECRH resonance layer is 0.5 T. The ICRH resonance layer in the central cell is located in a position with B slightly higher than 0.5 T.

2.2. Improved ion heating with ECRH

The central cell ECRH is applied to a quasi-steady-state ICRH plasma. Figure 1 shows waveforms pertinent to the present experiment. When ECRH is turned on, the central cell diamagnetic signal Φ_{dc} increases under constant ICRH oscillator power. At the same time, the bulk electron temperature T_e increases, as indicated by the soft X ray signal. The electron density slightly increases. The anchor diamagnetic signal Φ_{da} also increases during ECRH, which suggests an increase in the anchor ion temperature. This indicates an increase in the anchor electron temperature and thus a reduction in electron drag on the hot ions in the anchor cells, since the same bulk electron temperature is expected in the central cell and in the anchor cells.

Radial profiles of the electron temperature evaluated from the soft X ray signal before and during ECRH are plotted in Fig. 2. The on-axis electron temperature was raised from about 60 eV to above 140 eV by the central cell ECRH. The ion temperature T_i in the central cell is measured by using a charge exchange neutral particle analyser. Figure 2 also shows radial profiles of T_i before and during ECRH. The ion temperature on the axis increases from 2.5 to 4.9 keV during ECRH, and a higher temperature component (T_{ih} = 18 keV, about 5% of the total density) is also observed.

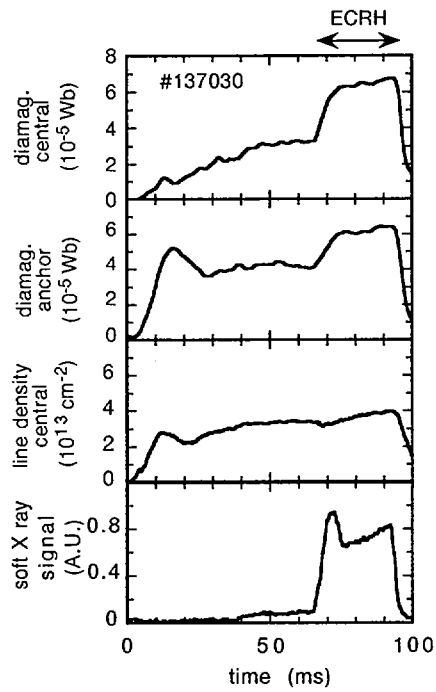

FIG. 1. Waveforms of signals pertinent to the ECRH experiment. The central cell diamagnetism, anchor diamagnetism, central cell line density and soft X ray signals are shown.

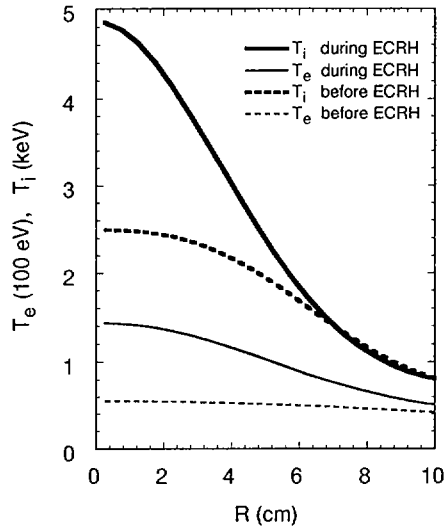

FIG. 2. Radial profiles of ion and electron temperatures before and during ECRH.

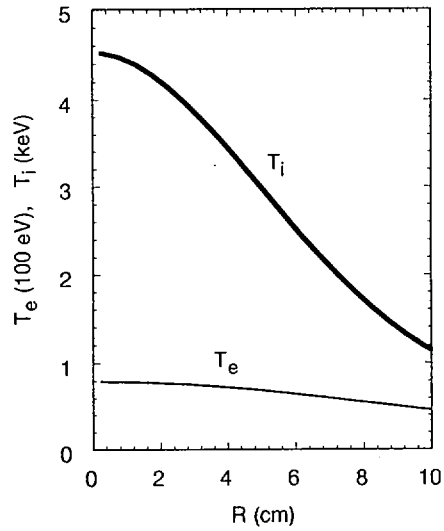

FIG. 3. Radial profiles of ion and electron temperatures during step-up of the ICRH power.

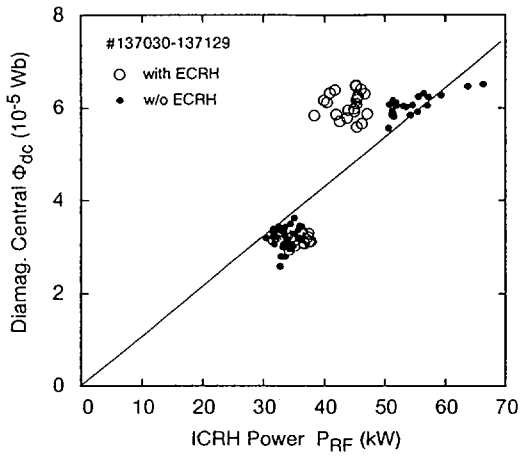

FIG. 4. Central cell diamagnetism plotted as a function of ICRH antenna power.

The ion stored energy evaluated by integrating the ion pressure profile over the cross-section of the central cell plasma accounts for about 80% of the total increase $\Delta\Phi_{dc}$ in the central cell diamagnetic signal.

Experiments with ICRH alone are also carried out. The ICRH oscillator power is increased during a plasma pulse so that Φ_{dc} increases to about the same amount as Φ_{dc} in Fig. 1. Figure 3 shows radial profiles of the same quantities as shown in Fig. 2. The ion temperature on the axis increases to 4.5 keV. The electron temperature also increases because of an increased energy transfer from the ions to the electrons. However, in this experiment with ICRH alone, the on-axis value of T_e is about 80 eV, lower than that in the ECRH experiment. Since the electron drag power is proportional to $T_e^{-3/2}$, the energy drain is evaluated by integrating P_{drag} ($\propto T_i/\tau_{ie}$) over the plasma cross-section. The drag power in the ECRH experiment is about half that in the experiment with ICRH alone.

Figure 4 plots the central cell diamagnetism Φ_{dc} as a function of the ICRH antenna radiated power P_{RF}. Here the increase in the diamagnetism is attributable almost entirely to an increase in the ion energy. Without ECRH, Φ_{dc} is almost proportional to P_{RF}, and 55–60 kW is necessary to obtain a diamagnetic signal corresponding to an ion temperature of about 5 keV. In shots with ECRH, on the other hand, the same Φ_{dc} can be attained with a lower P_{RF} of around 40 kW. Therefore, more effective ion heating is produced by the application of central ECRH.

2.3. Ion power balance

We examine the power balance of the hot ions in the core region ($r < 10$ cm) of the central cell. The following equation is assumed:

$$\frac{dn_iT_i}{dt} = \frac{\eta P_{RF}}{V_{hot\ ion}} - n_iT_i\left(\frac{1}{\tau_{ie}} + \frac{1}{\tau_{CX}}\right) \qquad (1)$$

Here T_i is the perpendicular ion temperature $T_{i\perp}$ and the parallel ion energy is neglected (usually $T_{i\parallel}$ is about one tenth of $T_{i\perp}$). The charge exchange time is denoted by τ_{CX}. The first term of the right hand side is equal to the ICRH power P_a absorbed by the core hot ions per unit volume. The coefficient η stands for the ratio P_a/P_{RF}. Three quasi-steady-state conditions are analysed: (a) before application of the central cell ECRH, (b) during ECRH and (c) the case corresponding to Fig. 3.

The absorbed power P_a is evaluated from a radial integration of Eq. (1) over the core region of the central cell plasma. Finite Larmor radius effects of hot ions are included in this calculation [5]. For case (a), P_a is 11 kW. During ECRH, both T_e and T_i are higher than before ECRH and the electron drag power $P_{drag} \propto T_i/\tau_{ie}$ decreases. Thus a higher ion temperature is attained with a rather low P_a of 10 kW. For case (c), P_{drag} is larger than in case (b) because of the shorter τ_{ie}, which results in a higher P_a of about 17 kW to maintain the same T_i. This is about one and a half times as high as P_a with ECRH. This ratio is consistent with the P_{RF} ratio of 55 to 40 kW. Enhancement of the efficiency of ion heating is most remarkable near the axis, because T_e is highest there, as shown in Fig. 2. With the application of ECRH, the energy confinement time of hot ions increases to about 8 ms, about double that of the other two cases.

The above calculation shows that electron drag is the main channel of energy loss. The calculation also indicates that a nearly constant fraction of about 0.25–0.32 of P_{RF} is coupled to the core hot ions ($r < 10$ cm) for each case, and a non-classical loss channel is not likely to have a role in the present experiment. The charge exchange loss is the second large loss affecting the hot ions. It is comparable to P_{drag} in case (b). Thus the efficiency of ion heating would be much improved by reducing the charge exchange loss. Reduction of neutral gas does indeed seem to lead to a higher ion temperature.

When P_{RF} is set at a higher level and the initial value of Φ_{dc} is higher than a threshold value, little increase of T_i is observed with the application of ECRH. In this case, most of the increase in Φ_{dc} is due to electron energy. We have already reported such saturation of ion temperature [2]. Reflectometer measurements indicate that, when ECRH is applied, the power density of the slow wave decreases near the mid-plane of the central cell. Since hot ions are located in a narrow axial region near the midplane, they no longer interact with the heating wave. A higher Φ_{dc} and/or a higher electron temperature may suppress the power density of the heating wave.

2.4. Electron characteristics during ECRH

Before the application of ECRH, the power source of bulk electron heating is drag energy from hot ions. Direct heating by microwave power is added to electron drag during ECRH and the following equation is used for examining the power balance of the bulk electrons:

$$\frac{3}{2} L_t \frac{dn_e T_e}{dt} = L_i \frac{n_i T_i}{\tau_{ie}} - \frac{3}{2} L_t \frac{n_e T_e}{\tau_E^e} + \frac{\alpha P_{ECRH}}{S_b} \qquad (2)$$

Here L_t is the effective axial length of the plasma and L_i represents the axial extent of the hot ions in the central cell, so that $V_{hot\ ion}$ is equal to L_iS_b, with S_b the cross-section of the core plasma. The ratio L_t/L_i is about 5. Low electron temperature $T_e << T_i$ is also assumed.

Unfortunately, potential measurement at the central cell is not available at the moment and hence we cannot independently evaluate the parallel electron confinement time. We estimate the electron energy confinement time τ_E^e by using Eq. (2) for the three quasi-steady cases. For each case, ECRH in the end mirror cells is turned on and a tandem mirror potential profile is expected to be formed. Experimental values are substituted into each term except the third term of the right hand side. The ECRH power to the bulk electrons is evaluated by a ray tracing calculation. The gyrotron power is about 40 kW. The total efficiency of power transmission of the waveguide and the antenna is estimated to be 0.8. About 67% is radiated in the quasi-X mode and the bulk electron absorption coefficient evaluated from a ray tracing calculation is about 0.35. Thus αP_{ECRH} is about 7.5 kW. The calculated values of τ_E^e are 1.2, 1.3 and 1.1 ms for cases (a), (b) and (c), respectively. These values do not change very much and are consistent with the usual electron confinement time under a tandem mirror potential profile [2].

Hot electrons are also created during ECRH, which is investigated by using hard X ray detectors. Electrons with a mean energy of several kiloelectronvolts are seemingly created during the first few milliseconds and the fraction of electrons with higher energy gradually increases with time. The maximum X ray energy exceeds 200 keV. When both ECRH and ICRH are turned off, the plasma starts to decay and the diamagnetic signal promptly decreases. However, about 10% of the diamagnetism remains as long as a low density plasma remains. Thus it can be considered that about 10% of the increase of the central cell diamagnetism is attributable to hot electrons.

When a higher ECRH power is injected, the diamagnetic signal Φ_{dc} reaches a much higher value. In this case, however, microwave power is consumed not in bulk electron heating but in hot electron production, and the hot electron energy shares a substantial fraction of $\Delta\Phi_{dc}$. Since hot electrons do not take energy from hot ions, the electron drag power is reduced by the fraction of hot electrons. No evidence of a harmful effect on MHD stability has so far been found.

3. THEORETICAL STUDY OF PLUG POTENTIAL FORMATION MECHANISMS

The recent measurements in the GAMMA 10 tandem mirror [2] reveal that a plug potential exists at some point between $z = z_b$ and $z = z_m$, as shown in Fig. 5(a). The ion distribution function measured by the end loss energy component analyser is plotted in Fig. 5(b). It indicates that the distribution has peaks around the loss cones without ECRH, whereas the structure in the distribution disappears with ECRH because of the plug potential formation.

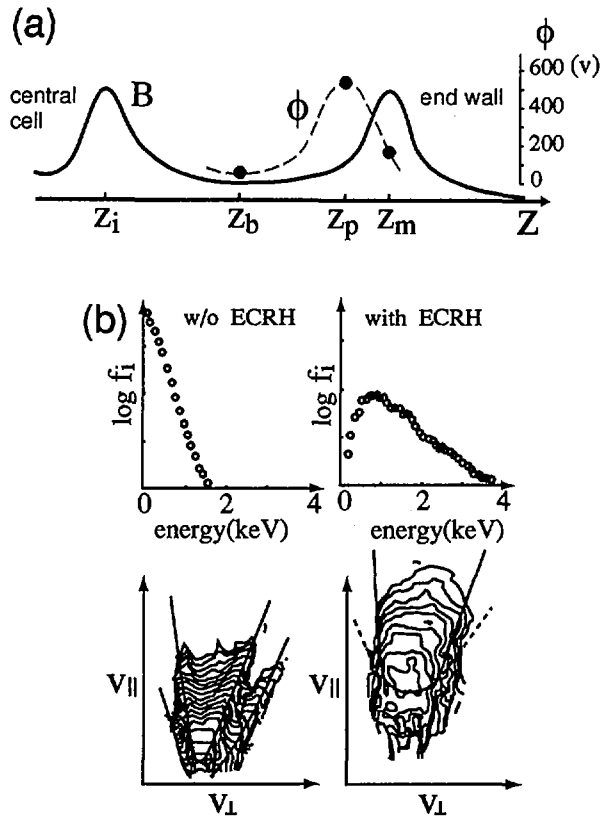

FIG. 5. Experimental results. (a) Potential axial profile. The solid circles are the observed potentials, where the potential at $z = z_b$ is measured by a beam probe and those at $z = z_p$ and $z = z_m$ are measured by Langmuir probes. (b) Contour plot of the ion distribution function.

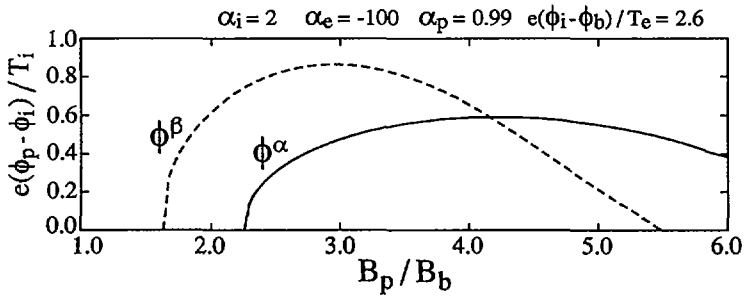

FIG. 6. Solution of ϕ^{α} and ϕ^{β} as a function of B_p/B_b.

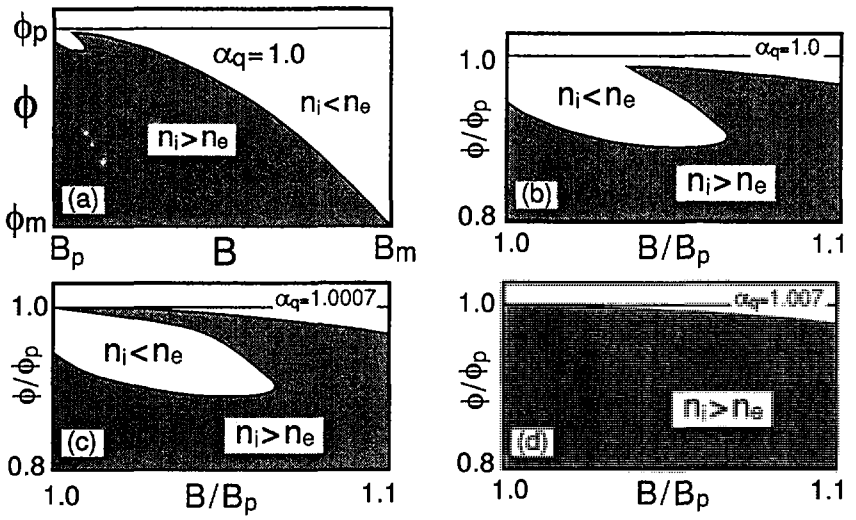

FIG. 7. Contour plots of $n_i - n_e$, where (a) is plotted from plug to outer mirror throat and (b–d) are enlarged around the plug.

In order to model the case with ECRH only, we assume the following distribution functions. Namely, the ion distribution function consists of a passing component (Maxwellian) coming from the central cell and a component (non-Maxwellian) trapped in the thermal barrier region. The electron distribution function consists of a passing component (Maxwellian) coming from the central cell and a component (non-Maxwellian) trapped in the plug potential. Using these distribution functions we determine the potential by the charge neutrality condition $n_i(\phi, B) = n_e(\phi, B)$. Here the non-Maxwellian ion distribution function is $f_i \propto \exp[-(\varepsilon - e\phi_i - \alpha_i\mu B_i)/(1 - \alpha_i)T_i]$ in terms of energy ε and magnetic moment μ. When the constant $\alpha_i < 1$, it becomes bi-Maxwellian at $z = z_b$ with $T_{\parallel} = (1 - \alpha_i)T_i$ and $T_{\perp} = (1 - \alpha_i)T_i/(1 - \alpha_i B_i/B_b)$, while in the case of $\alpha_i \geq 1$ it becomes a pumping type distribution function [6]. The non-Maxwellian electron distribution function is of the same type as that of the ions except that α_e is used instead of α_i.

The plug potential ϕ_p should satisfy the condition that $\phi_p > \phi_i$ (the potential at the inner mirror throat) and $\partial\phi(B_p)/\partial B_p = 0$, which is the condition that the potential is maximum at $z = z_b$. As long as n_e and n_i can be differentiated by ϕ and B, the condition $\partial\phi(B_p)/\partial B_p = 0$ is the same as $\partial n_i(\phi_p, B_p)/\partial B_p = \partial n_e(\phi_p, B_p)/\partial B_p$, because it is written as $d\phi(B_p)/dB_p = -(\partial n_i/\partial B_p - \partial n_e/\partial B_p)/(\partial n_i/\partial\phi_p - \partial n_e/\partial\phi_p)$. Figure 6 shows the solutions $\phi^{\alpha}(B_p)$ and $\phi^{\beta}(B_p)$, where ϕ^{α} satisfies $n_i(\phi^{\alpha}, B_p) = n_e(\phi^{\alpha}, B_p)$ and ϕ^{β} is a solution of $\partial n_i(\phi^{\beta}, B_p)/\partial B_p = \partial n_e(\phi^{\beta}, B_p)/\partial B_p$. There is one intersection of the solutions ϕ^{α} and ϕ^{β} in the region $1 < B_p/B_b < 6$. Here B_b, B_i and B_m are the magnetic field at the thermal barrier, at the inner mirror throat and at the outer mirror throat, respectively, and

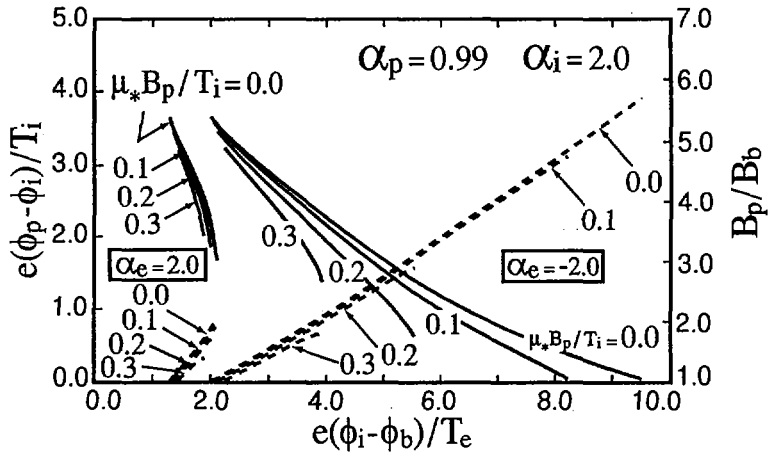

FIG. 8. Magnitude and location of the plug potential as a function of thermal barrier depth. Solid lines represent the magnitude of B_p/B_b and dashed lines are $e(\phi_p - \phi_i)/T$. Here $\mu_* = -e(\phi_p - \phi_m)/(B_p - B_m)$.

$B_i/B_b = B_m/B_b = 6$ is assumed. The potential ϕ and the magnetic field B at the intersection in Fig. 6 are the magnitude of the plug potential and its axial location. It is found that a plug potential can exist between $z = z_b$ and $z = z_m$.

The next problem is whether the charge neutrality condition is satisfied around the plug region. It is known that a sheath potential is generated in the case where half-Maxwellian ions are accelerated by the electrostatic potential from the maximum point of the potential. Figure 7(a) shows an example of the potential calculated by the charge neutrality condition. Here, to display the quasi-neutral profile, we plot the contour surface of the zero level of $n_i - n_e$ as a function of B/B_p and $e(\phi - \phi_p)/T_i$. This procedure ensures that we will find all possible roots of $n_i = n_e$. The location and magnitude of the plug potential are determined by the method mentioned above. A potential jump is observed at $z = z_p$, where a sheath potential is formed. Another remarkable feature in Fig. 7(a) is that $\phi(B)$ has a multivalued solution at a position finitely different than $B/B_p = 1$, so that the full Poisson equation treatment is required to establish the true potential there. The solution of the Poisson equation differs with the boundary conditions, that is, whether starting from $z = z_p$ or from the end wall.

Introducing a population of ions which are produced around the plug and escape to the end wall, we obtain a continuous potential profile, as seen in Figs 7(b–d), where the constant α_q is the parameter characterizing the ion distribution function, i.e. $f_i \propto \exp[-(\varepsilon - e\phi_p - \alpha_q \mu B_p)/(1 - \alpha_q)T_i]$, which is defined in the region $\varepsilon \leq \mu B_p + e\phi_p$, $\varepsilon > \mu B_m + e\phi_m$ and $v_{\parallel} > 0$ in $z > z_p$. When $\alpha_q = 1$ there are no ions produced around the plug. The population of ions produced increases as α_q becomes larger than unity. There is no potential jump when $\alpha_q = 1.0007$ in Fig. 7(c). That is, a continuous potential is obtained, although the potential is multivalued around $z = z_p$. In the case

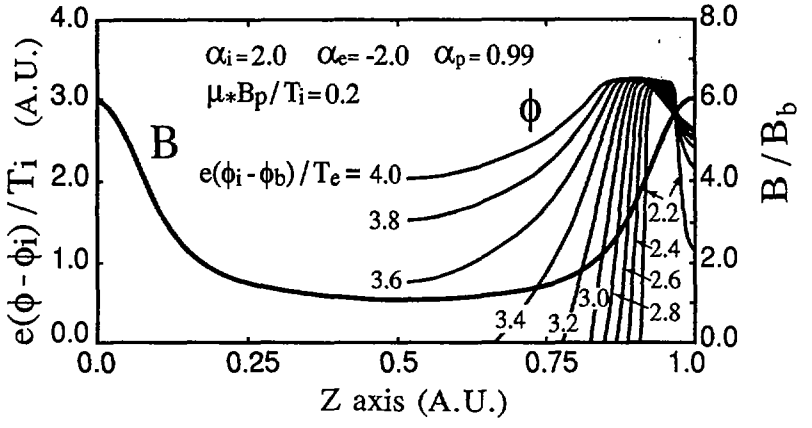

FIG. 9. Potential profiles along z. Here each potential is normalized by the maximum value.

of $\alpha_q \geq 1.007$, the potential has a single-valued solution in Fig. 7(d). The various parameters of α_i, α_e and thermal barrier depth are tried, the results of which are that the continuous potential profile (as in Fig. 7(c)) is obtained as long as α_q is greater than 1.0002–1.0012, depending on the parameters.

Figure 8 shows the magnitude and location of the plug potential as a function of thermal barrier depth. The magnitude of the plug potential becomes larger with greater thermal barrier depth, while the location of the plug moves to the lower magnetic field side with greater thermal barrier depth.

Figure 9 displays the potential profiles for various thermal barrier depths obtained by the charge neutrality condition, as well as the magnetic field profile of the GAMMA 10 end mirror cell. One can see that a plug potential with a continuous axial profile is formed with its peak position midway between the outer mirror throat and the thermal barrier. As the peak position moves towards the lower magnetic field side, the potential profile becomes wider.

The above calculation requires the existence of an ion population born around the plug region and going back to the central cell, the ion distribution function of which is assumed to be $f_i \propto \exp[-(\varepsilon - e\phi_p - \alpha_p\mu B_p)/(1 - \alpha_p)T_i]$ defined in the region $\varepsilon > \mu B_p + e\phi_p$, $\varepsilon > \mu B_m + e\phi_m$ and $v_{\parallel} < 0$ at $z = z_p$. Without that ion population, the plug potential is not formed. These ions are expected to be supplied by an ionization process. The amount of ions supplied is not contradictory to that estimated for GAMMA 10 parameters. This amount has an influence on the location of the plug potential rather than on the magnitude of the potential.

4. SUMMARY

The bulk electrons have been successfully heated by second harmonic ECRH in the central cell of the GAMMA 10 tandem mirror, and the energy drain from the hot

ions due to electron drag has been reduced. As a consequence, direct electron heating has produced more effective ion heating in the hot ion mode and the ion temperature increased from 2.5 to 4.9 keV during 40 kW ECRH.

It is shown theoretically that the plug potential can be formed by using ion and electron distribution functions which are expected to be plausible in the present tandem mirror.

REFERENCES

[1] TAMANO, T., et al., in Plasma Physics and Controlled Nuclear Fusion Research 1994 (Proc. 15th Int. Conf. Seville, 1994), Vol. 2, IAEA, Vienna (1995) 399.
[2] TAMANO, T., Phys. Plasmas **2** (1995) 2321.
[3] BALDWIN, D.E., LOGAN, B.G., Phys. Rev. Lett. **43** (1979) 1318 .
[4] POST, R.S., et al., in Plasma Physics and Controlled Nuclear Fusion Research 1986 (Proc. 11th Int. Conf. Kyoto, 1986), Vol. 2, IAEA, Vienna (1987) 251.
[5] SHOJI, M., et al., J. Phys. Soc. Jpn. **65** (1996) 2846.
[6] COHEN, R.H., Nucl. Fusion **21** (1981) 209.

DISCUSSION

M. THUMM: What is the ion density in the central cell of your GAMMA 10 discharges with combined ICRH and second harmonic ECRH?

T. SAITO: The ion density is about 2×10^{12} cm^{-3}, which is equal to the electron density. Almost all the ions are hot ions.

D. RYUTOV: What was the effect of higher electron temperature on the microstability of the central cell?

T. SAITO: The higher electron temperature itself has no effect on microstability in the central cell. However, the higher ion temperature produced by the higher electron temperature drives the Alfvén ion cyclotron mode.

K. YAMAZAKI: Does the temperature increase from 2.5 to 4.9 keV refer to the perpendicular temperature?

T. SAITO: Yes.

K. YAMAZAKI: How about the temperature parallel to the magnetic field? Did you observe the parallel temperature increase?

T. SAITO: The parallel ion temperature ranges from 0.3 to 0.5 keV and increases slightly during ECRH.

HELICAL SYSTEMS AND ALTERNATIVE SYSTEMS

(Poster Session CP)

HIGH DENSITY ECRH AND SHEAR RELATED CONFINEMENT WITH ECCD IN W7-AS

V. ERCKMANN, H.P. LAQUA, U. GASPARINO,
J. GEIGER, H.-J. HARTFUSS, R. JAENICKE,
G. KÜHNER, H. MAASSBERG, H. NIEDERMEYER,
M. ROMÉ, A. WELLER, W7-AS TEAM
Max-Planck-Institut für Plasmaphysik,
Euratom-IPP Association,
Garching

ECRH GROUP
Institut für Plasmaforschung,
Universität Stuttgart,
Stuttgart,

Germany

Abstract

HIGH DENSITY ECRH AND SHEAR RELATED CONFINEMENT WITH ECCD IN W7-AS.

An overview on physics studies with ECRH and ECCD at W7-AS is presented. Two distinct topics are discussed: In the first section the focus is on ECR heating of high density plasmas beyond the limitations given by the cut-off condition for standard heating scenarios (e.g. X2 mode cut-off for 140 GHz, B_0 = 2.5 T: 1.2 × 10^{20} m^{-3}). The conversion process from the ordinary to extraordinary and finally to the Bernstein mode (O-X-B) provides a possibility to overcome this density limit. Effective plasma heating with this scenario was measured in W7-AS far beyond the X2 cut-off density for resonant and nonresonant conditions. In the second section experimental results on the response of energy confinement on magnetic shear are reported. W7-AS, with its almost shearless vacuum configuration, was operated in a hybrid mode with significant plasma currents. Stationary profiles of the rotational transform with positive or negative magnetic shear are introduced by inductive and/or EC driven currents in the co- and counter-directions with respect to the confining magnetic field. The confinement was investigated in both net current free and current carrying discharges. The electron heat transport is analysed.

1. ECRH VIA THE O-X-B PROCESS AT HIGH PLASMA DENSITY

The commonly used ECRH scenarios provide a good single pass absorption and are 1st harmonic O- or X-mode and 2nd harmonic X-mode launch. These scenarios introduce density limitations by the cut-off condition, which is e.g. for the W7-AS 140 GHz system in X2-mode given by 1.2 × 10^{20} m^{-3}. In view of reactor relevant conditions it may be desirable to have ECRH access to even higher densities. This is provided by O2-mode launch, which has a weak absorption at W7-AS parameters, but is a promising candidate at W7-X [1].

Another candidate is the O-X-B mode conversion process [2] as a possibility to overcome the density limitations. Here O, X, and B are the ordinary, extraordinary and Electron-Bernstein-Mode. The essential part of this scheme is the conversion of the O-wave launched by an antenna from the low field side into an X-wave at the O-wave cut-off layer. This mode conversion requires an oblique O-wave launch near an optimal angle.

As shown in Fig. 1 the transverse refractive indices N_X of the O-wave and X-wave are connected at the optimal launch angle with a corresponding longitudinal (parallel B) index $N_{z,opt} = \sqrt{Y/(Y+1)}$ with $Y = \omega_{ce}/\omega$ (ω is the wave frequency, ω_{ce} is the electron cyclotron frequency) without passing a region of evanescence ($N_X^2 < 0$). For non-optimal launch an evanescent region always exists near the cut-off surface whose geometrical size depends on the density scale length $L = n_e/(dn_e/dx)$. A considerable fraction of the energy flux, however, can be transmitted through this region if L becomes small [3]. Density fluctuations generally lead to a reduced O-X conversion efficiency and are taken into account in the modelling. A significant heating efficiency is obtained only at a very small density scale length (i.e. steep gradients) or a very low fluctuation amplitude. After the O-X-conversion the X-wave propagates back to the upper hybrid resonance (UHR) layer where the refractive index of the X-wave is connected to that of the electron Bernstein waves (EBW) as shown in Fig. 1 and conversion into EBW's may take place. The EBW's propagate then towards the plasma centre where they are absorbed near the electron cyclotron resonance layer or in the nonresonant case by collisional multiple pass damping.

The experiments were performed with two 70 GHz beams launched into a neutral beam (NBI) sustained target plasma at resonant (1.25 T) and nonresonant (1.75 T, 2.0 T) magnetic fields. The launch angle of the incident O-mode polarised wave was varied at fixed heating power (220 kW). An example of the

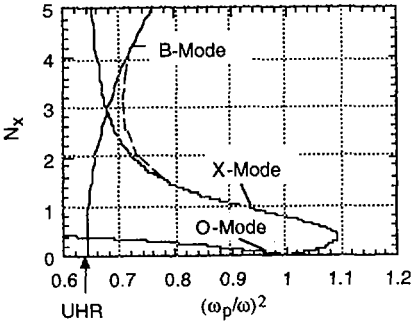

FIG. 1. Refractive index N_x versus $(\omega_p/\omega)^2$ for the O–X–B conversion process at optimum launch angle.

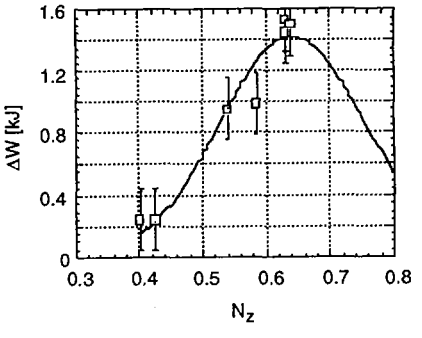

FIG. 2. Measured plasma energy increase by O–X–B heating versus parallel refractive index N_z of the launched O-mode for nonresonant conditions ($B_0 = 1.75$ T).

nonresonant case is shown in Fig. 2. Due to technical limitations of the maximum launch angle, only the left part of the reduced transmission function could be proved experimentally. The increase of the total stored plasma energy (from the diamagnetic signal) depends strongly on the launch angle, which is typical for the O-X-conversion process, and fits well to the calculation. Here the power transmission function was normalised to the maximum energy increase. The central density was 1.5×10^{20} m^{-3}, which is more than twice the cut-off density for 70 GHz, the central electron temperature was 500 eV. Resonant heating at the plasma edge could be excluded since for 1.75 T no electron cyclotron resonance exists inside the plasma.

Parametric instabilities as a fingerprint of the X-B-conversion process near the UHR were measured. Sidebands at $\omega \pm n\omega_{LH}$, where ω_{LH} is the Lower Hybrid Wave and n the harmonic number, were measured with the ECE receiver for a resonant magnetic field of 1.25 T. The LH-wave was detected with a broad band loop antenna.

EBW's experience a cut-off layer at the upper hybrid resonance (UHR) surface (see Fig. 1), which in the nonresonant or higher harmonic ($n > 1$) field totally encloses the inner plasma. The radiation is then trapped inside the plasma and can escape only in the small angular window for O-X- and X-O-conversion, respectively. In the absence of an electron cyclotron resonance in the plasma the EBW's may be absorbed due to finite plasma conductivity after some reflections at the UHR-layer. In both the resonant (1.25 T) and nonresonant cases (2.0 T) efficient heating was observed. Two 70 GHz beams in O-mode polarisation (110 kW power each) were launched with an oblique angle of 40° into an NBI (700 kW) sustained target plasma with a central density of 1.6×10^{20} m^{-3} and temperature of 560 eV. More than 70% of the heating power was found in the plasma taking into account the power scaling of the energy confinement time ($P^{-0.6}$).

2. ELECTRON HEAT TRANSPORT AND MAGNETIC SHEAR

The confining magnetic field in the W7-AS Stellarator has a 'built in' flat profile of the rotational transform, ι. The magnetic shear is weakly positive ($\Delta\iota/\iota$ up to +2%) above $\iota = 0.4$ and weakly negative below (up to -2%). Low order rational values of ι can thus be excluded from the confinement region by a proper choice of ι, which can be varied in a wide range of $0.25 < \iota < 0.65$. The global confinement depends sensitively on ι and exhibits excursions of about 30% with maxima in the close vicinity of the low order rational numbers $\iota = 1/2$, 1/3... [4]. The low shear configuration of the vacuum magnetic field is, however, modified by internal plasma net currents, e.g. the pressure driven bootstrap current. The equilibrium currents (Pfirsch-Schlüter currents) generating the Shafranov shift of finite-ß plasmas play an important role and modify the profile of the rotational transform, too [5]. Experiments with weak and strong, positive and negative shear were performed by running inductive and EC-driven currents in the proper direction. The experiments can be grouped in two categories, i.e. experiments with zero (inductive compensation of the bootstrap current and EC-driven currents) and non-zero net current.

2.1 Low edge shear and the role of rational iota

We compare net-current-free discharges with 0.4 MW ECRH power at 140 GHz (B_0 = 2.5 T, X2) at high (n_{e0} = 0.75 × 10^{20} m^{-3}, T_{e0} = 1.2 keV) and low density (n_{e0} = 0.17 × 10^{20} m^{-3}, T_{e0} = 3.2 keV). For both types of discharges a launch angle scan, i.e. a scan of the EC-driven current, was performed to modify the balance between the contributing internal plasma currents while maintaining zero net current [6]. Figure 3 shows the total stored plasma energy as a function of the launch angle for both types of discharges.

The total stored energy and thus the global confinement changes from 11.5 kJ at full counter current drive to about 8 kJ at full co-current drive in the high density case. Note that the bootstrap current is compensated by the inductive current alone at perpendicular launch (no ECCD). The increase of the stored energy is due to a steepening of both the density and electron temperature gradients. The density profiles are typically flat in the centre and thus the gradient region is localized close to the plasma edge. In the low density case a much smaller (7%) but reproducible dependence of the stored plasma energy on the EC-driven current is observed, which points into the opposite direction, i.e. slightly better confinement at co-CD as compared to counter-CD. In the high density case, the edge value $\iota(a)$ is somewhat below 1/3 due to the finite-ß effect, but was set slightly above 1/3 ($\iota(a)$=0.345) in the low density case. As a consequence, the 1/3-resonance is crossed under counter-CD conditions in the low density case and at co-CD conditions in the high density case, which supports the hypothesis of confinement degradation due to rational values of ι.

Both the bootstrap and EC driven currents are of comparable magnitude and much larger in the low density case (about 6-8 kA) than in the high density case (about 2-3 kA). Thus higher shear is introduced in the low density case, which reduces the degradation due to rational ι (stabilization of resonant modes or

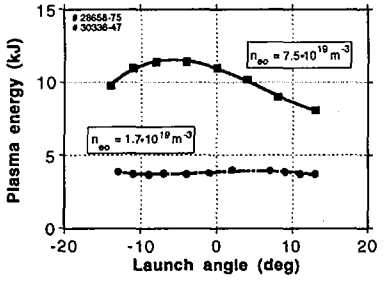

FIG. 3. Total stored plasma energy versus toroidal launch angle of the microwave beam for low and high plasma densities.

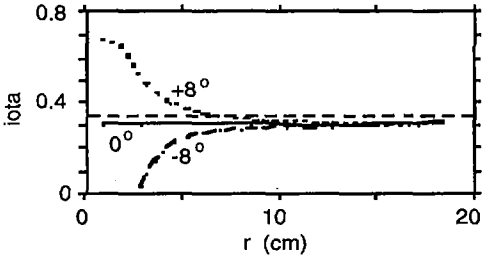

FIG. 4. Radial profiles of ι for the high density case of Fig. 3 at maximum co-CD (launch angle +8°), no CD (launch angle 0°) and maximum counter-CD (launch angle −8°).

reduction of island width). For the high density case the confinement effects are more pronounced, which may be a consequence of the low shear in a wide radial range of the plasma cross section. The calculated ι-profiles for three cases with co, counter and no ECCD are shown in Fig. 4. The resonant $\iota = 1/3$ is met with weak shear in the co-CD case giving rise to a localised flattening of the stationary temperature profile. In the case of no ECCD, ι is almost constant over the minor radius and low order rational values of ι are avoided. In this sense this discharge represents an example for the shearless stellarator. Good confinement is achieved under this condition (see Fig. 3, launch angle 0°); however, the discharge is difficult to control and sensitive to minor changes of the discharge parameters.

2.2 Plasmas with net currents

Although the scenario to operate the same device in net-current free 'Stellarator'-operation and, for comparison, in pure 'Tokamak'-operation cannot be completely verified at W7-AS (the main coils always infer some external rotational transform), hybrid operation with significant net currents is possible. Configurations with positive and negative shear were investigated and may contribute to the understanding of the physics of reversed shear tokamak results, e.g. [7]. Net currents in the range $-30\ \text{kA} \leq I_p \leq +30\ \text{kA}$ were induced by the OH-transformer in ECR-heated target plasmas with on axis deposited heating power of 0.45 MW. The experiments where conducted in long pulse operation > 1 s to obtain steady state conditions on the current-diffusion time scale. The OH-power (typically < 10 kW) can be neglected as compared to the ECRH power. At a feedback controlled density of typically $2 \times 10^{19}\ \text{m}^{-3}$ (typical electron and ion temperatures of 3.5 and 0.4 keV, respectively) the electrons dominate the heat transport and ions play a minor role because they are energetically decoupled from the electrons. By a proper choice of the vacuum ι the discharges were controlled to have an almost constant edge rotational transform of 0.40 ± 0.05. The vacuum ι is 0.55 for -30 kA and 0.25 for +30 kA operation, respectively, indicating that the plasma current contributes significantly to the total rotational transform. The magnetic configurations for the different net currents deviate significantly from the vacuum configuration and the corresponding finite-ß stellarator equilibria with net currents were calculated by the NEMEC code. Radial profiles of the electron temperature from Thomson scattering and ECE are shown in Fig. 5 (left) for three cases with +30, 0, and -30 kA.

Two distinct effects are clearly seen: i) Whereas strong temperature gradients exist within r/a < 0.3 for both the reference case with zero net current and all discharges with positive currents, significantly lower central temperatures are measured in the negative current cases. As seen in Fig. 6, a monotonic decrease of T_{e0} with increasing negative current is observed. ii) Strong temperature gradients exist in the outer plasma region around r/a = 0.8 for all cases with net currents > 5 kA independent of the sign of the current and thus the sign of the shear. The reference case with zero net current and the same edge-ι does not show this steep edge gradients. Net current free discharges at optimum confinement at lower $\iota(a) = 0.34$ also show less pronounced gradients, which are

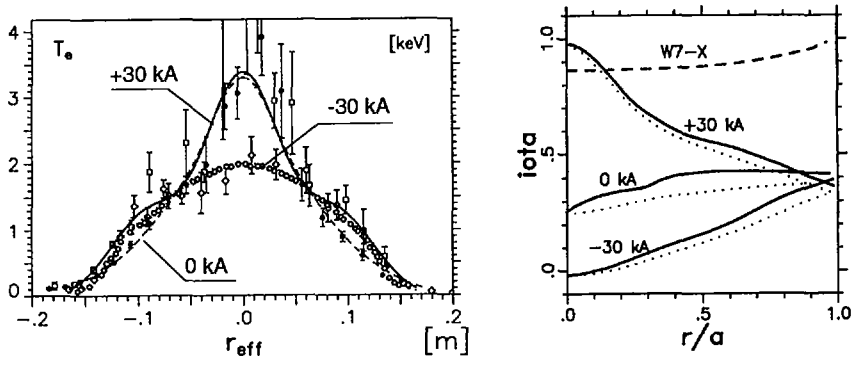

FIG. 5. Radial profiles of the electron temperature (left) with −30 kA (dotted line, diamonds), 0 kA (dashed line, dots) and +30 kA (solid line, squares) and (right) the corresponding profiles of the total rotational transform (solid line). The inductive current contribution without bootstrap current is also indicated (dots). The ι profile of W7-X is shown for reference.

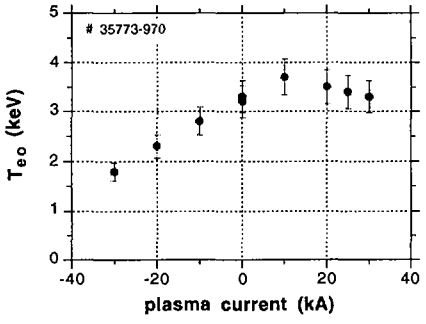

FIG. 6. Central electron temperature for discharges with different plasma current.

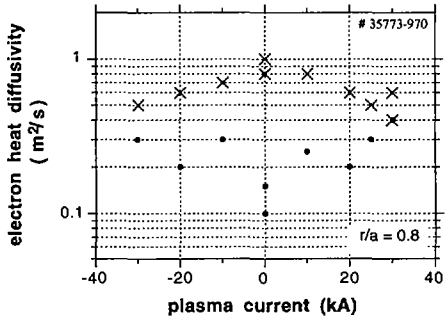

FIG. 7. Comparison of local electron heat diffusivity (crosses) from power balance analysis with neoclassical predictions (dots) at r/a = 0.8 for discharges with different plasma currents.

in between the two cases of Fig. 5. The ι-profiles as seen in Fig. 5 (right) are calculated assuming Z_{eff}=2, the inductive current distribution using the neoclassical resistivity (solid line) and the linear superposition of the bootstrap current contribution is shown (dotted line). The vacuum ι-profile of the W7-X magnetic configuration, which has considerable shear at the edge, is displayed for reference. The current-voltage characteristic gives no evidence for a significant suprathermal electron contribution. Due to the ι-dependence of the bootstrap current (DKES) a self-consistent calculation of the ι-profile is necessary. The iteration is robust at positive currents but turns out to be delicate for the negative currents with low or even zero rotational transform in the centre.

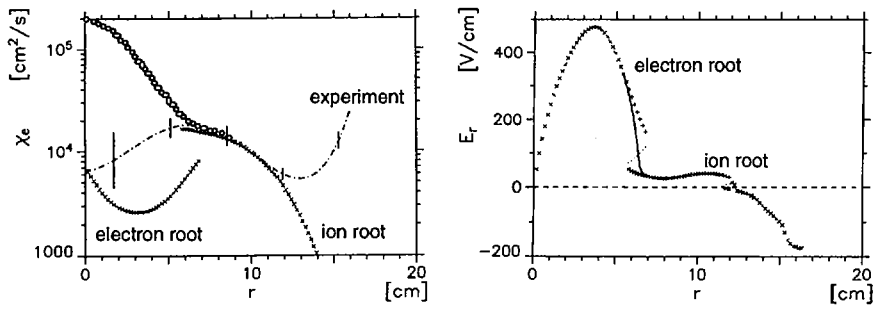

FIG. 8. Electron heat diffusivity (left) and radial ambipolar electric field (right) for the +30 kA case. The neoclassical electron heat diffusivity without (circles) and with (crosses) electric field ('electron root' in the centre) is compared to the experimental values (dashed-dotted line).

The ι-profiles for negative currents indicate low central values approaching zero in the plasma centre, which may explain the central confinement degradation with increasing negative currents. The good confinement in the outer plasma region with both positive and negative net currents may be due to significant shear in this region, which is much smaller in the reference cases with zero net current. The measured local electron heat diffusivity from the steady state power balance approaches the neoclassical values at the high currents even close to the plasma edge up to $r/a < 0.8$ as seen in Fig. 7. This can be interpreted as an expansion of the plasma volume, which is governed by neoclassical transport. Note that the neoclassical transport in the l.m.f.p. is a strong function of the temperature.

From the neoclassical solution of the ambipolarity condition the 'electron-root' for the radial electric field is expected for $r/a < 0.3$. Although no direct measurement is presently available, the existence of the 'electron-root' and of the related improvement of neoclassical confinement is supported by the heat transport analyses. Assuming the usual approach of zero electric field in the plasma centre and of the 'ion root' solution, where existing, the neoclassical predictions fit well in the radial range of $0.3 < r/a < 0.8$, but are more than one order of magnitude higher than the measured values in the plasma centre with $r/a < 0.3$ (see Fig. 8). The 'electron root' solution with strongly positive electric fields has to be assumed in the centre to reduce the neoclassical transport to below the experimental values.

REFERENCES

[1] ERCKMANN, V., KARULIN, N., WOBIG, H., in Controlled Fusion and Plasma Physics (Proc. 21st Eur. Conf. Montpellier, 1994), Vol. 18B, Part II, European Physical Society, Geneva (1994) 1008.

[2] PREINHAELTER, J., KOPECKY, V., J. Plasma Phys. **10** (1973) 1.

[3] MJØLHUS, E., J. Plasma Phys. **31** (1984) 7.

[4] RENNER, H., W7-AS TEAM, NBI GROUP, ICF GROUP, ECRH GROUP, Plasma Phys. Control. Fusion **31** (1989) 1579.

[5] RENNER, H., RINGLER, H., KISSLINGER, J., KÜHNER, G., W7-AS TEAM, NBI GROUP, ECRH GROUP, in Plasma Physics (Proc. Int. Conf. Innsbruck, 1992), Vol. 16C, Part I, European Physical Society, Geneva (1992) 501.

[6] ERCKMANN, V., GASPARINO, U., MAASSBERG, H., Plasma Phys. Control. Fusion **34** (1992) 1917.

[7] STRAIT, E.J., et al., Phys. Rev. Lett. **75** (1995) 442.

COMPARATIVE STUDIES OF STELLARATOR AND TOKAMAK TRANSPORT

U. STROTH, R. BURHENN, J. GEIGER,
L. GIANNONE, H.-J. HARTFUSS, G. KÜHNER,
L. LEDL, E.E. SIMMET, H. WALTER,
ECRH TEAM, W7-AS TEAM
Max-Planck-Institut für Plasmaphysik,
IPP-Euratom Association,
Garching, Germany

Abstract

COMPARATIVE STUDIES OF STELLARATOR AND TOKAMAK TRANSPORT.

Transport properties in the W7-AS stellarator and in tokamaks are compared. The parameter dependences and the absolute values of the energy confinement time are similar. Indications are found that the density dependence, which is usually observed in stellarator confinement, can vanish above a critical density. The density dependence in stellarators seems to be similar to that in the linear ohmic confinement regime, which, in small tokamaks, extends to high density values, too. Because of the similarity in the gross confinement properties, transport in stellarators and tokamaks should not be dominated by the parameters which are very different in the two concepts, i.e. magnetic shear, major rational values of the rotational transform and plasma current. A difference in confinement is that there exists evidence for pinches in the particle and, possibly, energy transport channels in tokamaks whereas in stellarators no pinches have been observed, so far. In order to study the effect of plasma current and toroidal electric fields, stellarator discharges were carried out with an increasing amount of plasma current. From these experiments, no clear evidence of a connection of pinches with these parameters is found. The transient response in W7-AS plasmas can be described in terms of a non-local model. As in tokamaks, also cold pulse experiments in W7-AS indicate the importance of non-local transport.

1 Introduction

The magnetic configurations of stellarators and tokamaks are characterized by different values for parameters which enter sensitively anomalous transport theory. The differences are primarily the amount of toroidal plasma current, the profile of the rotational transform ι and the magnetic shear, the number of low order rational ι values, as well as the trapped particle populations. These parameters enter in various aspects theories for the anomalous transport, and if they are key parameters, transport in the different devices should have very different signatures.

Within the tokamak line, the possibility to vary these parameters is very restricted. Hence, a comparison of the transport properties of stellarators and tokamaks helps to reveal the importance of these elements for anomalous transport. The comparison is done between tokamak results and results from the W7-AS stellarator, which is a low-shear device essentially without net toroidal

current. A previous comparison can be found in Ref. [1]. By the results in this paper, some of the previous conclusions are revised, others substantiated to a greater extent.

2 Global Confinement Time

The global energy confinement time τ_E has to be compared on the basis of empirical scaling expressions. Previously, for such a comparison only tokamak expressions were available. The recently deduced ISS95 scaling [2], which is based on data from heliotron/torsatrons and low-shear stellarators, confirms

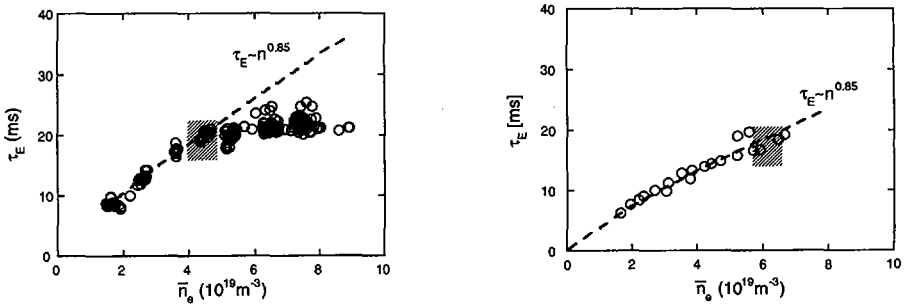

FIG. 1. Evolution of the energy confinement time during density scans in W7-AS. The discharges at B_t = 2.5 T and ι = 1/3 were heated with 0.45 MW (left) and 0.68 MW (right) ECH, respectively. The dashed lines are the result of a regression analysis of the left hand data restricted to $\bar{n}_e \leq 4.5 \times 10^{19}$ m^{-3}. The hatched areas indicate the prediction for the saturation density as deduced from tokamak results.

that stellarator and tokamak confinement times are comparable and do scale in a similar way with plasma parameters [2]:

$$\tau_E^{ISS95} = 0.079 \times a^{2.21} R^{0.65} P^{-0.59} \bar{n}_e^{0.51} B_t^{0.83} \iota_{2/3}^{0.4} \quad (1)$$

(minor radius a and major radius R (m), heating power P (MW), line averaged density $\bar{n}_e$ (10^{19} m^{-3}), toroidal magnetic field B_t (T) and ι at 2/3 of a.)

This expression, which is based on data from small stellarators, describes surprisingly well [2] the tokamak L-mode confinement of devices as large as JET. The good agreement also shows that in tokamak scaling expressions the engineering parameter total plasma current, I_P, can be replaced by magnetic field parameters, which are more relevant for physics considerations. Written in the above form, both stellarator and tokamak confinement can be sketched in the following way: it improves with plasma volume, magnetic field and rotational transform, it decreases with heating power.

3 Density Dependence of Confinement

The density dependence indicated by the ISS95 expression is absent in tokamak scalings. However, the first scalings for tokamaks, like the neo-Alcator scaling, also exhibited an up to linear dependence on density. This was deduced from ohmically heated plasmas and only in larger devices and with additional heating the confinement time turned out to be rather independent of density. At present, the only tokamak regime with a clear density dependence is the linear ohmic confinement (LOC) regime. A study of the critical density $\bar{n}_e^{sat}$ at which the transition to the saturated SOC regime occurs shows [3] that this density decreases with machine size.

In order to anticipate the effect of saturation in a small stellarator device a detailed investigation of ECH heated discharges has been carried out in W7-AS. The energy confinement time as a function of density and for two different heating powers are shown in Fig. 1. For the low power, saturation is indicated at $\bar{n}_e^{sat} \approx 4.5\times10^{19}\,\mathrm{m}^{-3}$. The tokamak expression predicts $\bar{n}_e^{sat}$ for W7-AS reasonably well and also reproduces the experimental observation that saturation occurs at higher densities when the heating power is increased. In the case of the high heating power, no data are available to indicate the saturation but the increase of τ_E with density extends up to a higher value.

Local transport analyses show that the density dependence can be described by a dependence of the electron thermal diffusivity χ_e on local density. In Fig. 2 the variation of χ_e is shown when the density is varied at a fixed radius in a density scan and when it is varied through the radial position. In both cases, the density dependence of χ_e reflects the findings for the global confinement time. In the Tore Supra tokamak very similar trends in τ_E and χ_e are observed [4], although the saturation occurs already at $\bar{n}_e^{sat} \approx 2.5\times10^{19}\,\mathrm{m}^{-3}$. Hence,

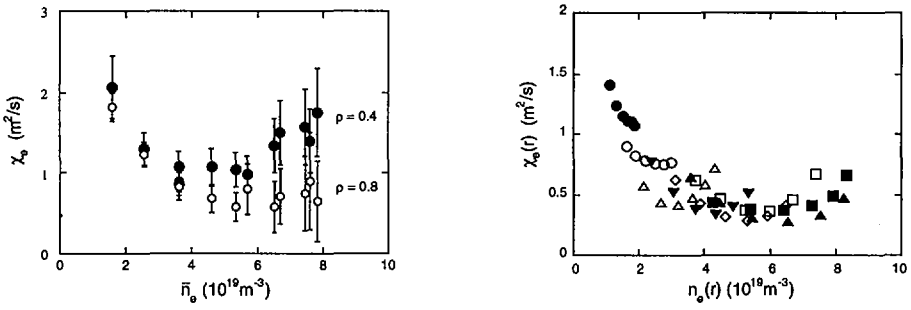

FIG. 2. Left: evolution of the electron thermal diffusivity at two radii during the density scan of Fig. 1. Plotted are radial averages in the core at $\rho = 0.4$ (5 cm $\leq r \leq$ 8.5 cm) and at the edge at $\rho = 0.8$ (12 cm $\leq r \leq$ 15 cm). Right: local electron thermal diffusivity as a function of the local electron density for the discharges of Fig. 1. The different symbols mark the individual discharges, and the region represented extends from the edge to the onset of the flat part of the density.

the observed density dependence in stellarators has close similarity to the one observed in the ohmic tokamaks regimes and, similar as in tokamaks, for larger stellarator devices the density-independent confinement regimes could become more prominent.

4 Stellarator-Tokamak Hybrid Discharges

The similarity of the confinement properties of stellarators and tokamaks has been stressed above. Now we turn to the investigation of the most prominent differences, which might be related to pinches in the particle and electron heat transport. Tokamak density profiles, especially under ohmic heating, show radial gradients also in the source-free plasma core. Since the particle diffusivity is comparable to the heat diffusivity, particle inward pinches have to be considered in order to explain these gradients. Transient particle transport shows the presence of a particle pinch term. In the frame of collisional transport the pinch is related to the toroidal electric field. The flat H-mode density profiles would be consistent with this assumption. In the net-current free W7-AS stellarator, a pinch is not needed in order to describe the density profiles, which are flat in the core.

Similarly, for the heat transport of tokamaks a pinch was postulated in order to describe the electron temperature profile consistency. In W7-AS, electron temperature profile consistency is not observed. Furthermore, a detailed comparison of steady state and transient transport between the RTP tokamak and W7-AS [5] leads to different physical pictures of the heat transport: While the tokamak data are consistent with a heat pinch, the W7-AS results are at variance with local models for the diffusivity.

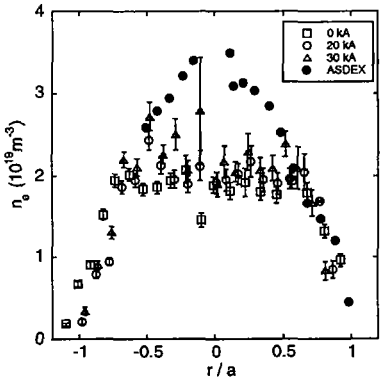

FIG. 3. Electron density profiles for discharges with different contributions of ohmic current in W7-AS, compared with an ohmic profile from the ASDEX tokamak.

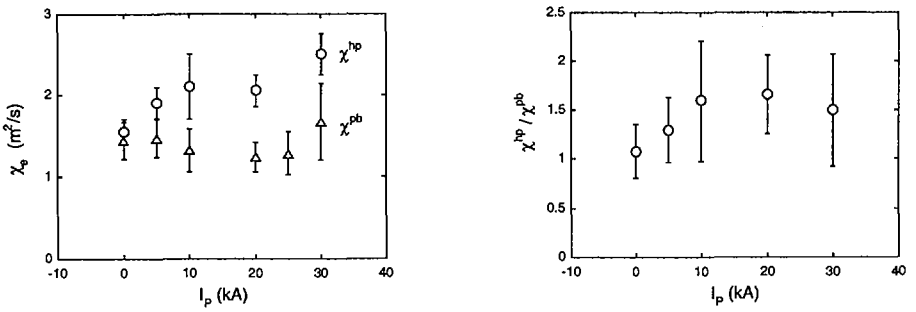

FIG. 4. Absolute values and ratio of the heat diffusivity as determined from heat pulse and power balance analyses as a function of the total plasma current.

In W7-AS, the influence of the toroidal electric field and the plasma current was investigated in discharges where ohmic currents of up to ±30 kA were induced in regular ECH sustained plasmas. At 30 kA, about 40% of the rotational transform comes from the ohmic current and 60% is from the external field. Since the experiments were carried out at low collisionality, the loop voltage was only 0.2 V. The transition in density profile and heat pulse transport from a stellarator to a tokamak-like behavior was studied at various plasma current levels.

In Fig. 3, the density profile of the current discharge is compared with a current-free case and a typical profile from an ohmic tokamak discharge (ASDEX). Up to the current investigated, a peaking of the density profile is not observed. Within the error bars, the density profile remains flat in the source-free region. The value of the Ware pinch, however, is only of the order of 3 cm/s whereas it is 25 cm/s in the ASDEX discharge. In order to study whether higher toroidal electric fields are needed to create a pinch, experiments at higher collisionality will be carried out.

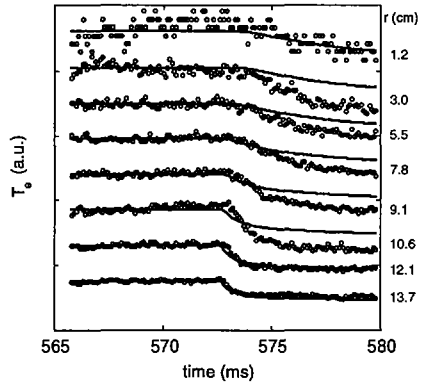

FIG. 5. Electron temperature evolution at different radii (indicated on the right) after carbon impurity injection at the plasma edge of W7-AS.

The onset of a pinch in the energy channel with plasma current would lead to a reduced value of the power balance diffusivity χ^{hp}. The value of the heat pulse diffusivity χ^{pb}, on the other hand, would remain unchanged. In Fig. 4, the evolution of the two estimates for χ with plasma current is depicted. The trend observed is at variance with the expectation from a pinch. Within the error bars, χ^{pb} remains unchanged and χ^{hp} increases slightly. In current-free discharges in W7-AS, both values are approximately equal and the ratio varies between 1 and 1.5 when current is introduced. Hence, these experiments do not provide evidence for a heat pinch related to plasma current or toroidal electric field.

5 Local versus Global Transport

The observation in W7-AS that the heat diffusivity as derived from heat pulse and steady state analyses yields the same value can be reconciled with power degradation in terms of a non-local transport model [6]. A non-local model is also successful in the analysis of the transient phases after changing the heating power by a large amount [6]. In tokamaks, non-local effects have been observed after injecting impurities into the plasma edge of the TEXT tokamak [7]. In TEXT and W7-AS, a fast change in the electron thermal diffusivity at a location distant from the perturbation can describe the data. In the cold pulse experiments at TEXT, the central electron temperature even increases whereas the edge was cooled.

Similar experiments were carried out in W7-AS [8]. Carbon was ablated by a laser and produces a dip in the edge temperature, which propagates inward. From impurity transport simulation with the SITAR code the radiation profile is determined to peak around 13 cm. In a period of 10 ms after ablation, the plasma inside 10 cm should not be affected by the additional carbon radiation. In Fig. 5 the time traces of the electron temperature are depicted at various radii and are compared with results from a time-dependent transport code. In the simulation, a stationary value for the heat diffusivity was used as obtained from a power balance analysis. The diffusivity at the edge had to be artificially enhanced to fit the data outside 12 cm. The observed temperature decay in the core is faster than the one obtained from the simulations. This points to a sudden increase of the diffusivity also further in the plasma core. This preliminary result has to be substantiated by further modeling and experiments.

References

[1] WAGNER, F. and STROTH, U., Plasma Phys. Controlled Fusion **35** (1993) 1321.

[2] STROTH, U., MURAKAMI, M., YAMADA, H., SANO, F., DORY, R. A., OKAMURA, S., and OBIKI, T., Nucl. Fusion **36** (1996) 1063.

[3] SIMMET, E. E. and STROTH, U., Statistical analysis of the density and energy confinement time at the transition from linear to saturated ohmic confinement, to be published.

[4] GARBET, X., PAYAN, J., LAVIRON, C., DEVYNCK, P., SAHA, S. K., et al., Nucl. Fusion **32** (1992) 2147.

[5] PETERS, M., *Electron Heat Transport in Current Carrying and Currentless Thermonuclear Plasmas*, PhD thesis, Technische Universiteit Eindhoven, 1995.

[6] STROTH, U., GIANNONE, L., and HARTFUSS, H. J., Plasma Phys. Controlled Fusion **38** (1996) 1087.

[7] GENTLE, K. W., BRAVENEC, R. V., CIMA, G., GASQUET, H., HALLOCK, G. A., et al., Phys. Fluids (1995).

[8] WALTER, H. et al., Cold pulse experiments in W7-AS, to be published.

A STUDY ON DENSITY PROFILE AND DENSITY LIMIT OF NBI PLASMAS IN THE COMPACT HELICAL SYSTEM

S. MORITA, H. IDEI, H. IGUCHI, S. KUBO, K. MATSUOKA,
T. MINAMI, S. OKAMURA, T. OZAKI, K. TANAKA, K. TOI,
R. AKIYAMA, A. EJIRI, A. FUJISAWA, M. FUJIWARA,
M. GOTO, K. IDA, N. INOUE, A. KOMORI, R. KUMAZAWA,
S. MASUZAKI, T. MORISAKI, S. MUTO, K. NARIHARA,
K. NISHIMURA, I. NOMURA, S. OHDACHI, M. OSAKABE,
A. SAGARA, Y. SHIRAI, H. SUZUKI, C. TAKAHASHI,
K. TSUMORI, T. WATARI, H. YAMADA, I. YAMADA
National Institute for Fusion Science,
Nagoya, Japan

Abstract

A STUDY ON DENSITY PROFILE AND DENSITY LIMIT OF NBI PLASMAS IN THE COMPACT HELICAL SYSTEM.

The mechanism of density profile formation has been studied in the Compact Helical System (CHS). It has generally been known that the profiles become peaked and hollow in limiter and divertor dominated cases, respectively. This tendency does not change for the direction of neutral beam injection (NBI) such as co- and counterinjection, resulting in a difference of the electric field. It is also found that the density profiles are not affected by the magnetic configuration itself. The density profile is, however, affected by limiter insertion. The edge ion temperatures were correlated with the density peaking factor, $n_{e0}/\langle n_e \rangle$. As a result, it was found that a peaked profile ($n_{e0}/\langle n_e \rangle \geq 1.5$) can be obtained with a higher edge ion temperature (≥ 40 eV at $\rho = 0.9$). These results indicate the importance of the energy distribution of the incoming neutral particles. An analysis is done to explain the results. The density limit has also been studied in CHS NBI plasmas. It was found that the density limit was strongly affected by the density profile. The mechanism related to the density limit is discussed.

1. INTRODUCTION

In helical plasmas, density profiles show large variation, in contrast to the tokamak where hollow or flat density profiles cannot be produced easily. In a tokamak, frequently an inward particle velocity is introduced in order to describe the peaked density profile whereas in helical devices the velocity is believed to be very small. The $\mathbf{E} \times \mathbf{B}$ force between the toroidal electric field and the poloidal magnetic field in the tokamak is too weak to explain the inward velocity. At present, our physical understanding of the situation is not sufficient to explain the density profiles so that the mechanism of density profile formation is still an open question.

In the Compact Helical System (CHS), at least, the density profiles seem to change according to a variety of experimental conditions such as R_{ax}, magnetic configuration, n_e, P_{heat}, etc. Furthermore, the density limit and the density profile frequently change according to the method of wall conditioning such as T_i gettering or boronization, which create different conditions between wall recycling and gas puffing rates. Experiments have been carried out to study the mechanism of density profile and density limit formation. In this paper, the results are described of a study on density profile and density limit obtained from neutral beam injection (NBI) plasmas ($n_e \leq 1 \times 10^{14}$ cm^{-3}, $T_e \leq 2$ keV, $T_i \leq 0.6$ keV) of the Compact Helical System (CHS heliotron/torsatron: $\langle a \rangle / R = 0.2/1.0$ m, $B_t \leq 2$ T, $\ell/m = 2/8$. $P_{NBI} = (1.1 + 0.7)$ MW, $P_{ECH} = (0.2 + 0.5)$ MW).

2. MAGNETIC CONFIGURATION OF CHS

In the CHS, the last closed flux surface (LCFS) is defined by the inner wall of the vacuum vessel for $R_{ax} \leq 94.9$ cm since the major radius of the vacuum vessel centre is 100 cm; it is called 'limiter dominated configuration'. On the other hand, for $R_{ax} \geq 97.4$ cm, a small clearance begins to appear between the inner wall and the LCFS, called 'divertor dominated configuration'. The clearance becomes 1 cm for $R_{ax} = 99.5$ cm and 4 cm for $R_{ax} = 101.6$ cm. The magnetic well is performed for almost all configurations, at least in the core region, except for the case of $R_{ax} = 88.8$ cm. The helical ripple ϵ_h is less than 2% at the axis position for $R_{ax} \leq 94.9$ cm and increases when R_{ax} is shifted outward ($\epsilon_h = 8\%$ for $R_{ax} = 101.6$ cm).

3. DENSITY PROFILES OF NBI PLASMAS

Figure 1 shows a typical example of density profiles obtained from NBI plasmas ($B_t = 0.9$ T) [1]. There is a clear tendency for the peaked density profile to be performed in the limiter dominated configuration and for the flat or hollow density profile to be performed in the divertor dominated configuration. In the case of the limiter dominated configuration, the actual limiter area at the inner wall occupies 7–8% of the total plasma surface. The ratio of the hydrogen particle influx from the inner wall limiter, Γ_{lim}, to the total influx, Γ_{tot}, is approximately 40% at $\langle n_e \rangle = 4 \times 10^{13}$ cm^{-3} for the $R_{ax} = 89.9$ cm case. For the $R_{ax} = 101.6$ cm case, Γ_{lim} disappears; instead, the gas puffing rate is increased. The particle influx ratio Γ_{gp}/Γ_{tot} from the location where the gas puffing is carried out reaches 20% for the $R_{ax} = 101.6$ cm case; it is less than 10% for the $R_{ax} = 89.9$ cm case.

A comparison is also made between co- (Fig. 1, left) and counter-NB (Fig. 1, right) injection cases. It is very clear that there is no difference between the two cases. For the counter-injection case, a large amount of NB fast ions is lost by the inward shift of the drift orbit due to the ∇B drift when the inner wall acts as a limiter.

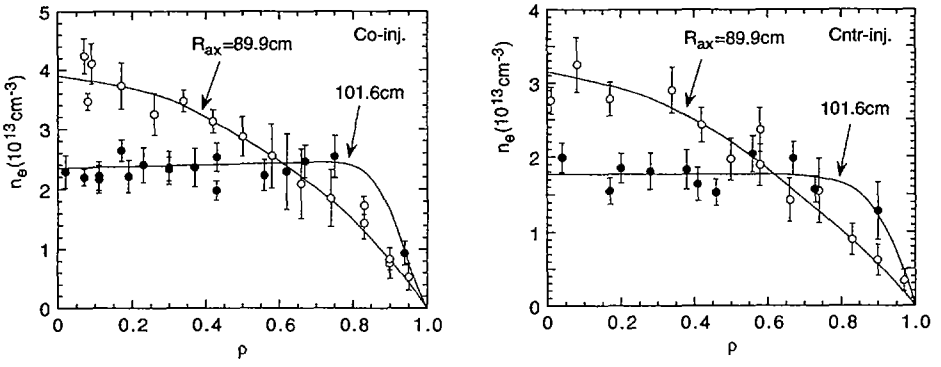

FIG. 1. Radial profiles of n_e as functions of averaged radius ρ for two different cases of magnetic axis (left: co-injection, right: counter-injection).

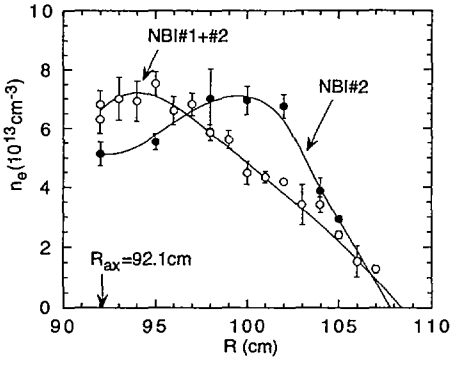

FIG. 2. Two different radial n_e profiles obtained from the same configuration (R_{ax} = 92.1 cm). P_{NBI} is 0.9 MW for #1 (counter-injection) and 0.6 MW for #2 (co-injection).

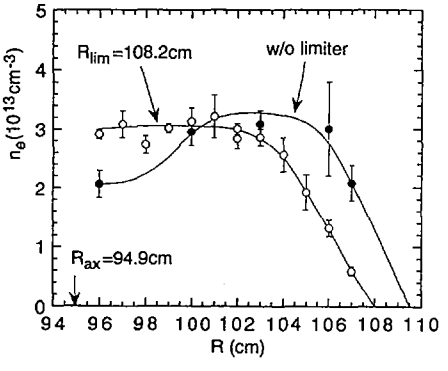

FIG. 3. Radial n_e profiles before and after insertion of carbon head limiter. The limiter was inserted (z = 20 mm) from the bottom of the vertically elongated position.

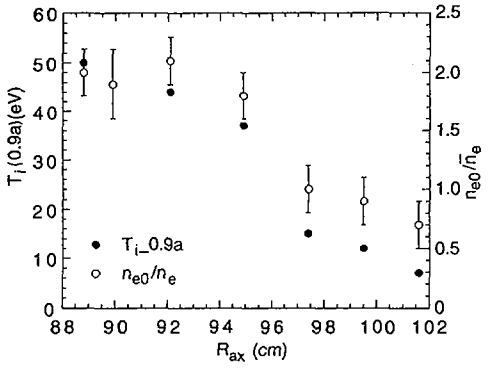

FIG. 4. Comparison between edge T_i (ρ = 0.9) and density peaking factor for different R_{ax} positions.

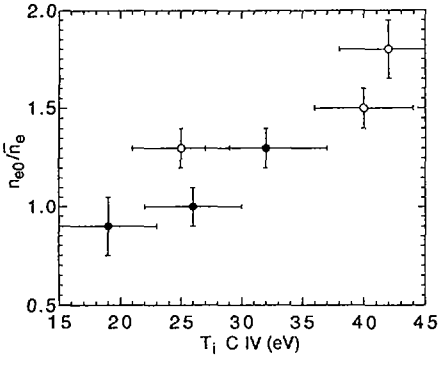

FIG. 5. Density peaking factor as a function of edge T_i obtained from C IV (1548.2Å) broadening for the R_{ax} = 94.9 cm case (solid circles: gas puffing case; open circles: reheat mode case after gas puffing off).

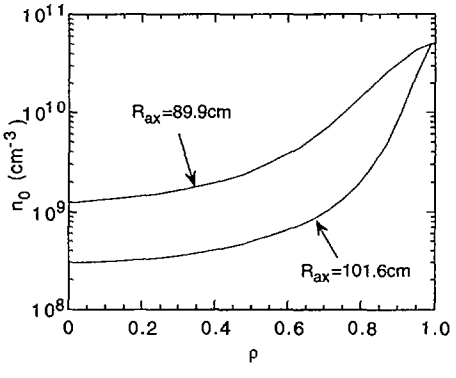

FIG. 6. Calculation of neutral hydrogen profiles for cases with R_{ax} = 89.9 cm and 101.6 cm. The profiles are normalized to a neutral density of 5 × 10^{10} cm^{-3} at ρ = 1.0.

As a result, the electric field and the poloidal rotation are enhanced. The rotation velocity reaches 10 km/s at the plasma edge for the counter-injection case in the limiter dominated configuration (R_{ax} = 92.1 cm) case, whereas it is less than 3 km/s for the co-injection case. This result shows that the electric field does not have any influence on the formation of the density profile.

The experiment was carried out by changing the NBI power for the R_{ax} = 92.1 cm case to study the direct influence of the magnetic configuration on the density profile. In the CHS, the power dependence of the electron temperature is remarkable for the edge region rather than for the central region. The result is shown in Fig. 2. Two different profiles are obtained from the same configuration although it is rare that such a hollow profile is obtained at R_{ax} = 92.1 cm. In the two discharges, the edge T_e was very different from that expected. Here, it should be noted that the input power of NBI #2 is decreased. For the hollow profile, it was 19 eV at ρ = 0.85 (T_{e0} = 233 eV), but for the peaked profile it was 102 eV (T_{e0} = 353 eV). The ion temperature has the same tendency as the electron temperature. From this result, it is understood that the magnetic configuration does not directly affect the density profile.

The limiter was inserted into NBI plasmas with hollow density profile. The result is plotted in Fig. 3. It is understood that the peaked density profile is realized after insertion of the limiter. The T_e profile does not change for the two cases. From this result we understand that the density profile is strongly affected by the existence of the limiter.

The edge T_i (C VI charge exchange line) at ρ = 0.9 is measured with the density peaking factor for different R_{ax} positions (Fig. 4) since the peak position of the radial neutral hydrogen distribution at the outside half along the major radius side normally appears between ρ = 0.90 and 0.95. The peaked density profiles tend to have a high edge T_i and are realized mainly for the limiter dominated configuration. In contrast, the flat density profiles have a low edge T_i for the divertor dominated configuration. We note that the recycling rate R becomes too large for the divertor dominated cases. Especially for the R_{ax} = 101.6 cm case, the value of R is close to 0.98, even for $n_e \leq 2 \times 10^{13}$ cm^{-3} [2].

A similar relation between n_e profiles and edge T_i is obtained for the reheat mode operation in the R_{ax} = 94.9 cm configuration [3]. In the reheat mode, which is observed after switching off the gas puffing in the high density range, density peaking can also be obtained by a large increase in the edge ion temperature. This is shown in Fig. 5. Generally, in the CHS, the density profiles become peaked for the $R_{ax} \leq 92.1$ cases, and flat for the $R_{ax} \geq 99.5$ cm cases. For the R_{ax} = 94.9 cm and 97.4 cm cases, however, the density profiles are extremely sensitive to the conditions of the vacuum–wall surface. In other words, the density profiles change easily every week the experiments are on.

The ionization length λ_i of neutral hydrogen is, typically, 4.7, 6.7 and 10.5 cm for T_i = 10, 20 and 50 eV at $n_e = 3 \times 10^{13}$ cm^{-3}, respectively. These values can easily change the neutral hydrogen profile and the density source term in

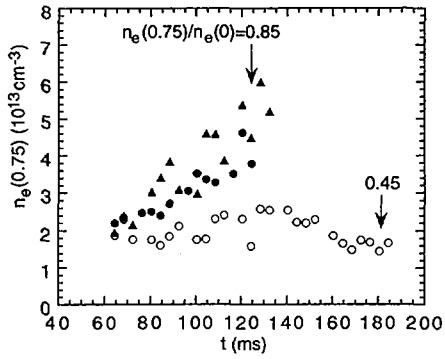

FIG. 7. Time behaviour of edge n_e (ρ = 0.75) from YAG Thomson measurement for three typical NBI discharges with (solid circles and triangles) and without (open circles) plasma collapse.

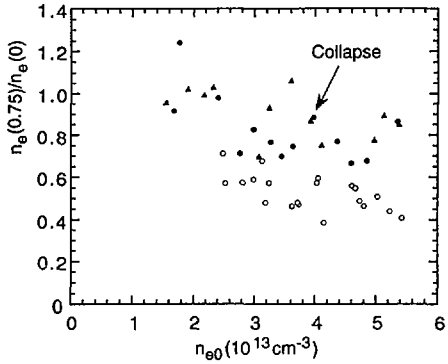

FIG. 8. Density ratio n_e at ρ = 0.75 to n_e at ρ = 0.0 as a function of n_e at ρ = 0.0 (n_{e0}). Solid points indicate collapsed discharges (solid triangles: inner ρ = 0.75, solid circles: outer ρ = 0.75, open circles: both sides ρ = 0.75).

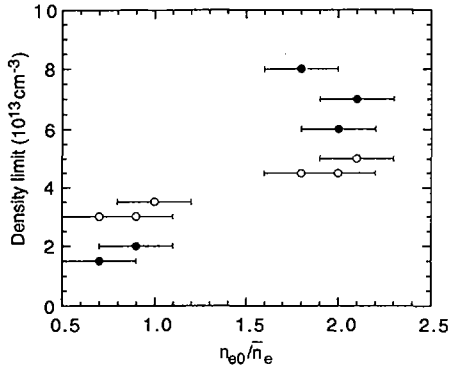

FIG. 9. Density limit in CHS NBI plasmas as a function of density peaking factor obtained at B_t = 1 T and P_{NBI} = 1 MW with T_i gettering (open circles: counter-injection case, solid circles: co-injection case).

the core region. In the limiter dominated configuration, the direct distance, $R_{ax} - R$, between the inner wall surface ($R = 80$ cm) and the magnetic axis (R_{ax}) is very short. Therefore, the distance becomes equal to λ_i when the energy of the neutrals increases. A detailed analysis is being carried out at the moment. A typical example for a neutral hydrogen profile is shown in Fig. 6. The H_α poloidal and toroidal locations are carefully measured in the CHS [2]. The results are included in the calculation. The ion temperature measured from the H_α line profile gives a low value of less than 1–2 eV at the gas puffing position and a relatively high value of 7 eV at the X point. The particle fuelling from the NBI is less than 20% for the total electron density at the plasma centre. Therefore, beam fuelling has no strong influence on the observed density profiles.

4. RELATION BETWEEN DENSITY LIMIT AND DENSITY PROFILES

The time behaviour of the electron densities at $\rho = 0.75$ obtained from the YAG Thomson system is plotted in Fig. 7. The data are taken from three typical discharges with and without plasma collapse. The line averaged density was $(4–5) \times 10^{13}$ cm^{-3} at the end of the pulse for the three cases. It is understood that the edge density rise causes the plasma collapse at $t = 120$ ms. We see that the peaked density profiles are favourable to an increase in the density limit. Figure 8 shows a comparison of the density profile ($n_e(0.75)/n_{e0}$) between collapsed and steady discharges. The results are similar to those shown in Fig. 7.

The density limit obtained is plotted against the peaking factor in Fig. 9. These data are obtained with strong T_i gettering. The highest density achieved in the CHS so far is 9×10^{13} cm^{-3}, as a line averaged density at $B_t = 1$ T. A further effort will be made in the higher B_t range up to 2 T and an NBI power of up to 2 MW (1.1 MW: #1, 0.7 MW: #2). The higher values of the density limit shown in Fig. 9 are obtained from the limiter dominated configuration. In the counter-NBI case, the density limit is lower than in the co-injection case since the fast ions in the counter-NBI case hit the inner wall and impurity buildup becomes serious. The density limit is extremely low for the co-injection case with the divertor dominated plasmas. This combination lowers the net NBI power deposition. Moreover, in the T_i gettering case a large amount of gas puffing is needed to achieve a certain density. This leads to the formation of hollow density profiles and further lowering of the NBI deposition power. Then, the low density limit for the divertor dominated configuration can be improved for a high recycling plasma such as that in the case of boronization [4, 5]. In this case, the density limit reaches the same level as for the limiter dominated plasma although the temperature is relatively low.

When the plasma collapses, the MHD instability is studied. At present, however, no correlation with the collapse has been obtained. Furthermore, the density limit for the $R_{ax} = 88.8$ cm configuration is comparable with other limiter dominated configurations whereas the $m/n = 2/1$ sawtooth oscillation is excited

because of the magnetic hill geometry. Then, these observed values of the density limit are mainly restricted by the radiation and particle losses which are a strong function of the density profile.

5. SUMMARY

The variations of the density profiles of NBI plasmas in the CHS were observed by changing externally controlled plasma parameters such as R_{ax}, the direction of the NBI, the input power of the NBI and limiter insertion. Through these studies it was found that the density profiles were strongly affected by the edge ion temperature. A possible candidate for explaining the density profiles is a change in the neutral hydrogen profile as a source term. The density limit was also correlated with the density profiles. As a result, the peaked density profile is favourable to a rise of the density limit.

ACKNOWLEDGEMENTS

The authors thank all members of the torus group, in particular K. Motoki, S. Hattori and S. Ohtsuka, for their help in carrying out the experiments. The authors are also grateful to Director General Professor A. Iiyoshi for continuous encouragement.

REFERENCES

[1] IGUCHI, H., et al., Plasma Phys. Control. Fusion 36 (1994) 1091.
[2] MORITA, S., et al., Fusion Technol. 27 (1995) 239.
[3] MORITA, S., et al., in Plasma Physics and Controlled Nuclear Fusion Research 1992 (Proc. 14th Int. Conf. Würzburg, 1992), Vol. 2, IAEA, Vienna (1993) 515.
[4] KANEKO, O., et al., in Plasma Physics and Controlled Nuclear Fusion Research 1990 (Proc. 13th Int. Conf. Washington, 1990), Vol. 2, IAEA, Vienna (1991) 473.
[5] YAMADA, H., et al., Jpn. J. Appl. Phys. 33 (1994) L1638.

RESISTIVITY EFFECTS ON THE CRITICAL PRESSURE GRADIENT FOR THE RESISTIVE INTERCHANGE MODES IN HELIOTRON E

H. ZUSHI, Y. SUZUKI[1], M. HOSOTSUBO, Y. NAKAMURA, M. WAKATANI, F. SANO, K. KONDO, T. MIZUUCHI, M. NAKASUGA, S. BESSHOU, H. OKADA, K. NAGASAKI, C. CHRISTOU, Y. KURIMOTO, H. FUNABA, T. HAMADA, T. KINOSITA, T. OBIKI, S. KADO[2], K. MURAOKA[2], S. SUDO[3], K. IDA[3], B.J. PETERSON[3], V.Yu. SERGEEV[4], K.V. KHLOPENKOV[4], V.V. CHECHKIN[5], V.S. VOITSENJA[5]
Plasma Physics Laboratory,
Kyoto University,
Uji, Japan

Abstract

RESISTIVITY EFFECTS ON THE CRITICAL PRESSURE GRADIENT FOR THE RESISTIVE INTERCHANGE MODES IN HELIOTRON E.

Internal disruptions are investigated in currentless heliotron plasmas. An operating boundary above which plasmas become unstable is studied with a beam power versus density diagram. The effects of the resistivity on the critical pressure gradient and stability are studied for the m = 2/n = 1 mode, where m and n are poloidal and toroidal mode numbers. The non-linear dynamics of the m = 2 mode at the crash are investigated as a function of the local gradient near the resonant surface.

1. INTRODUCTION

It has been recognized that a pressure driven instability (m = 1/n = 1), which was first observed in Heliotron E, is destabilized near the q = 1 surface (r/a $\approx$ 2/3) by increased plasma pressure [1], and its non-linear evolution leads to internal disruptions [2] (q is the safety factor). Figure 1 shows an internal disruption which occurs near the q = 2 surface (r/a $\approx$ 0.13). An m = 2 mode with small amplitude grows abruptly near the q = 2 surface and then triggers the internal disruption within about 100–300 μs. In this paper we study: (1) the operating limit (beam power P_{NBI} and density $\bar{n}_e$) at which the m = 2 driven internal disruption occurs; (2) the threshold value of the local electron pressure gradient near the q = 2 surface,

[1] Toshiba Corporation, Japan.
[2] Interdisciplinary Graduate School of Engineering Science, Kyushu University, Kasuga, Japan.
[3] National Institute for Fusion Science, Nagoya, Japan.
[4] State Technical University, St. Petersburg, Russian Federation.
[5] Kharkov Institute of Physics and Technology, Kharkov, Ukraine.

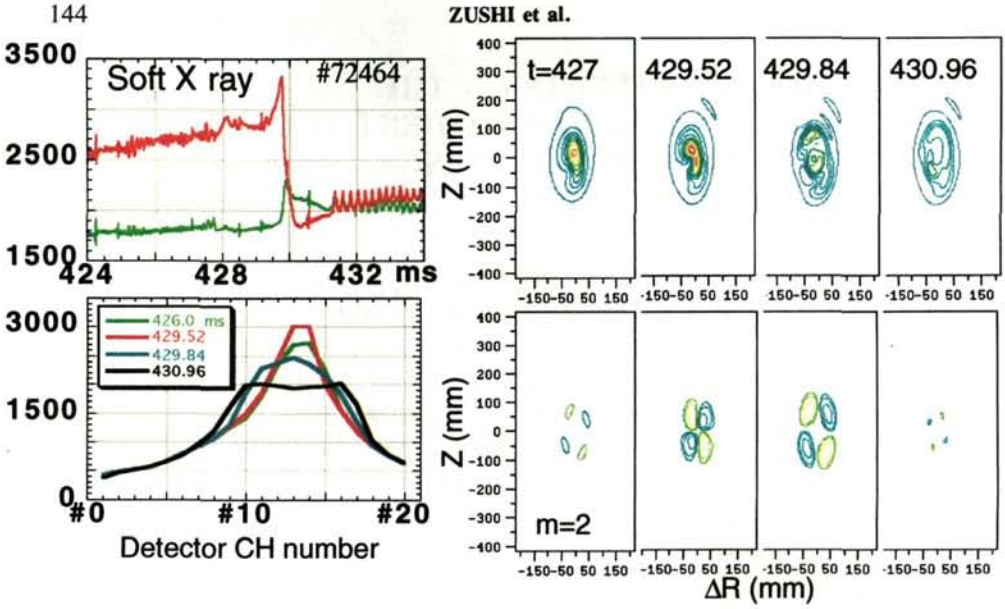

FIG. 1. Typical example of an internal disruption. Integrated soft X ray profiles and tomographically reconstructed emissivity contours are shown during the crash phase. The m = 2 component is also shown. Before the crash it localizes close to the magnetic axis, and then the location departs from the axis, which indicates that the q = 2 surface changes at the crash.

$\nabla P_e|_{q=2}$, above which plasmas become unstable; (3) resistivity effects on the critical $\nabla P_e|_{q=2}$ and m = 2 stability; and (4) the non-linear evolution of the m = 2 mode at the crash. The experimental conditions are as follows: B_0 = 1.9 T, $\bar{n}_e$ = (1–10) × 10^{13} cm^{-3}, $T_e(0)$ = 300–2000 eV and $T_i(0)$ = 200–1000 eV. In the magnetic configuration used there is no magnetic well and weak magnetic shear near the q = 2 surface [3]. Two dimensional structures of the soft X ray emissivity are measured with six soft X ray arrays with 20 detectors each. $P_e(r)$ is measured by Thomson scattering and a FIR interferometer, and $\nabla P_e|_{q=2}$ is determined from a best fit curve of $P_e(r)$. The resistivity η is evaluated at the q = 2 surface with an assumption of Z_{eff} = 1.

2. ONSET OF INTERNAL DISRUPTIONS

In Fig. 2 the onset of internal disruptions is illustrated on a P_{NBI} and $\bar{n}_e$ plane. In general, an abrupt excitation of the high m magnetic fluctuations $\tilde{B}_\theta$ (m = 3–5 and n = 2–5) is observed in the early low density phase of the NBI discharges, and then their amplitude saturates or slightly decreases towards the end phase of the discharge. The high m modes are in the frequency range 30–70 kHz. Internal disruptions, driven mainly by the m = 2 mode, occur usually in the middle to the end phase

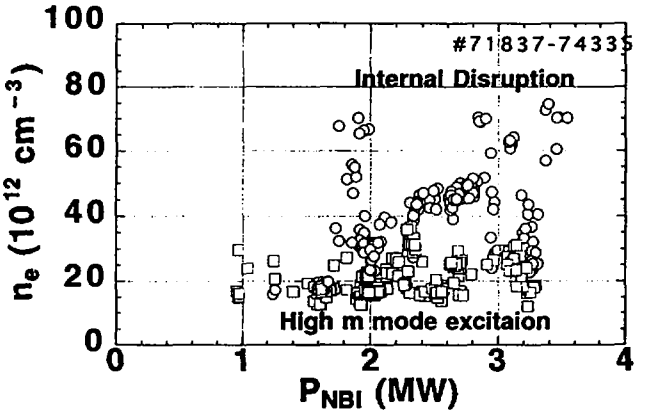

FIG. 2. Onset boundaries for the high m (m = 3-5) magnetic fluctuations (squares) and the m = 2 driven internal disruptions (circles) are shown on a P_{NBI} versus density diagram at B_0 = 1.9 T.

of discharges when $\bar{n}$ increases above a boundary. Pellet injection induces the early occurrence of disruptions because of increased density. A similar operating region is also observed for ECRH plasmas, although plasma β (≡ plasma pressure/magnetic pressure) values are around 0.2%. Strong magnetic bursts and sawtooth oscillations with a short repetition time of 5 ms are characteristic of these ECRH unstable plasmas. This aspect becomes significant when a material limiter is inserted into the plasma. Increased ∇T_e and enhanced η lead to enhanced MHD activity [4].

3. CRITICAL ELECTRON PRESSURE GRADIENT

A critical value of the electron pressure gradient ∇P_e for the m = 2 mode to be destabilized was investigated under constant $T_e(0)$ (~600 eV), i.e. constant η. This was done by varying P_{NBI} from 1.6 to 3.5 MW and $n_e(0)$ from 2×10^{13} to 9×10^{13} cm^{-3}. The central electron pressure $P_e(0)$ could be scanned from 2 to 10 kJ/m^3. In the low pressure case the plasma is stable. No m = 2 or high m mode activities are observed on $\tilde{B}_\theta$, nor is there an indication of MHD activity on the density and soft X ray signals. ∇P_e is 6 kJ/m^4 near the q = 2 surface and ~10 kJ/m^4 near the half-radius, where the q = 3/2, 4/3, 5/4 and 1 surfaces locate. When $\nabla P_e|_{q=2}$ becomes ~20 kJ/m^4, an internal disruption occurs at the end phase of the discharge. As mentioned before, high m $\tilde{B}_\theta$ has already been excited. Therefore a lower threshold ∇P_e (below 20 kJ/m^4) is expected for these modes. At the highest pressure the amplitude of high m $\tilde{B}_\theta$ becomes significant and internal disruptions followed by large amplitude m = 2 post-cursor oscillations occur. ∇P_e is 50 kJ/m^4 at the q = 2 surface and 60 kJ/m^4 at the half-radius. Thus a critical $\nabla P_e|_{q=2}$ is found at about 10 kJ/m^4 for $T_e(0) \approx 600$ eV at B_0 = 1.9 T.

3.1. Resistivity effects

When T_e is decreased, the mode tends to be destabilized even if ∇P_e is reduced. The resistivity effects on ∇P_e were investigated. This was done by varying $T_e(0)$ in NBI plasmas while keeping the electron pressure profile almost constant in the central region. Although $T_e(0)$ is increased from 600 to 1500 eV by additional ECRH, $P_e(0)$ is fixed at about 5 ± 0.5 kJ/m^3 by adjusting $\bar{n}_e$. η varies from 1.5×10^{-8} to 7×10^{-8} Ω·m. Plasmas with the highest $T_e(0)$ and the lowest η are stable, but plasmas with increased η show sawtooth oscillations. Thus it is demonstrated that the critical ∇P_e is reduced when η is enhanced.

Pure ECRH plasmas are also studied from this point of view. For ECRH plasmas $T_e(0)$ is decreased from 1700 to 300 eV with increasing $\bar{n}_e$ from 1×10^{13} to 4.4×10^{13} cm^{-3}, but T_i is unchanged at $\sim$200 eV [5]. Thus $\beta(0)$ could be kept almost constant at $0.2 \pm 0.1\%$, which is much below the ideal β limit β_{lim} [6], and $P_e(0)$ was 3.8 ± 2 kJ/m^3. η could be varied by an order of magnitude from 1×10^{-8} to 2×10^{-7} Ω·m under this condition. Figure 3(a) shows MHD activity

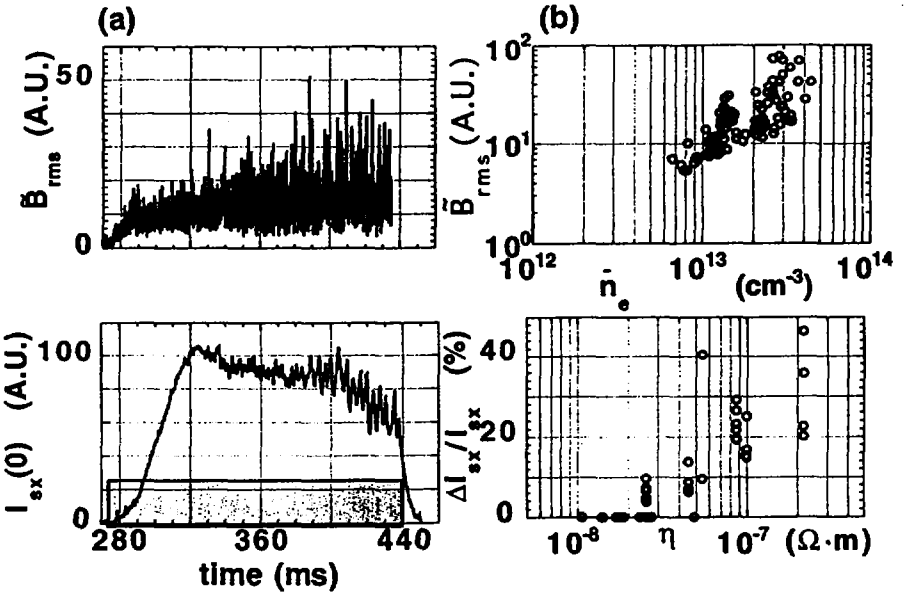

FIG. 3. (a) Typical MHD activity (magnetic bursts and sawtoothing soft X ray signals) for a pure ECRH plasma with a rail limiter. The density increases from 0.5×10^{13} to 2.5×10^{13} cm^{-3} during the ECRH pulse (shaded region). (b) 18 data sets are studied for the case with (3) and without (15) a limiter. The magnetic burst amplitude is plotted as a function of density and the sawtooth amplitude as a function of η ($\Delta I_{SX}/I_{SX} = 0$ means that a high temperature plasma is macroscopically stable).

(magnetic bursts and soft X rays) in a typical plasma with increasing $\bar{n}_e$ from 0.5×10^{13} to 2.5×10^{13} cm^{-3} and decreasing $T_e(0)$ from 1500 to 650 eV. Although ∇P_e near the axis is almost zero (sometimes negative values are also recorded) owing to a hollow $n_e(r)$ profile, and a weak drive term to destabilize the interchange modes is only expected under such conditions, strong MHD activity is clearly observed for the high η condition, as shown in Fig. 3(b). Thus in order to avoid internal disruptions below β_{lim}, it is concluded that electron heating is very important.

3.2. Stabilization by electron heating

The m = 2 mode stabilization has been demonstrated by ECRH in sawtoothing NBI plasmas. The resonance radius for second harmonic ECRH is just outside the q = 2 surface. $T_e(0)$ is increased from 550 to above 2000 eV and $T_e(r)$ becomes broad (NBI) to centrally peaked. $\bar{n}_e$ ((2–4) $\times$ 10^{13} cm^{-3}) is almost unchanged during ECRH, but $n_e(r)$ becomes flat or hollow in the central region owing to the particle pump-out effects [6]. Sawtooth oscillations with a small amplitude ($\sim$10%) appear for $\beta_e(0) \geq 0.4\%$. During ECRH they are stabilized, and then they appear again $\sim$20 ms after ECRH is turned off, as shown in Fig. 4(a). Within this time-scale $T_e(0)$ is reduced to its level before ECRH. It should be noted that $P_e(0)$ and $\nabla P_e|_{q=2}$ could be increased by a factor of 2 without onset of the sawtooth oscillations. One of the possibilities for stabilization is the reduction of η. Figure 4(b) shows a reduction of the MHD activity by decreasing η at the q = 2 surface.

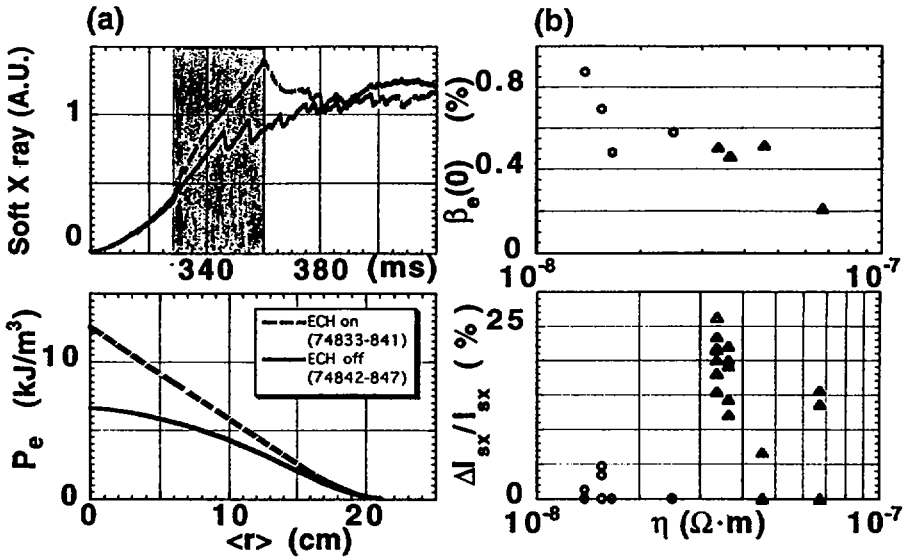

FIG. 4. Sawtooth stabilization by ECRH (shaded area) can be realized with enhanced $\beta_e(0)$ and $\nabla P_e|_{q=2}$, which is ascribed to the strong electron heating (circles), i.e. reduced η. Triangles denote target NBI plasmas.

4. NON-LINEAR EVOLUTION OF THE m = 2 MODE

Two dimensional reconstruction for the soft X ray emissivity ϵ_{SX} is obtained by a Fourier–Bessel expansion technique in which the maximum poloidal mode number of 3 and radial mode number of 8 are used [7]. Figure 1 shows that the m = 2 component $\epsilon_{SX\ m=2}$ grows near the q = 2 surface, which satisfies the characteristics of an interchange mode localized around the q = 2 surface. The time evolution of $\ln(\epsilon_{SX\ m=2}|_{q=2})$ is followed at every 40 μs and the growth rate γ_{obs} of the m = 2 mode is determined as a function of time from a spline fitted curve of $\epsilon_{SX\ m=2}(t)$ with an assumption of $\epsilon \propto \exp(\gamma t)$. The m = 2 mode grows abruptly just before a crash within 0.5–2 ms and the maximum γ_{obs} is found at 10^3–10^4 s^{-1}. These values and plasma parameters (β and the magnetic Reynolds number) suggest that the mode is a resistive interchange mode [8–10]. The time evolution of $\ln(\epsilon_{SX\ m=2}|_{q=2})$ and γ_{obs} is shown in Fig. 5(a). One can see that the mode grows explosively at a particular time and γ_{obs} jumps from ~ 0 to $\sim 1 \times 10^3$ s^{-1}. In order to find an onset condition

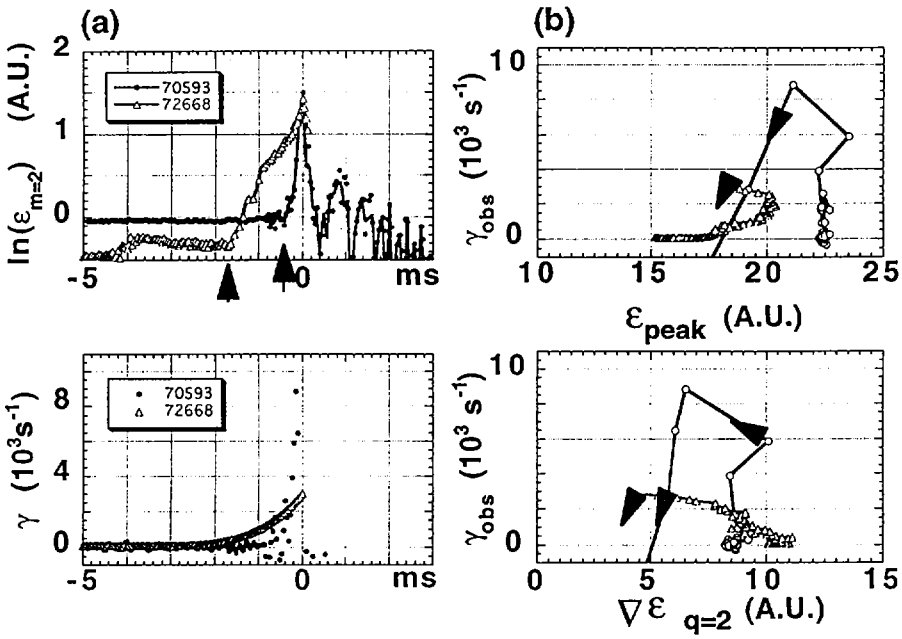

FIG. 5. Time evolution of $\ln(\epsilon_{m=2})$ and γ_{obs} for two typical crash cases with (70593) and without (72668) post-cursor oscillations. t = 0 indicates the crash time. In order to find a critical pressure gradient above which the mode grows explosively, time trajectories of γ_{obs} are traced as a function of the peak emissivity or $\nabla\epsilon|_{q=2}$. γ_{obs} seems to jump from zero to a finite value, although the gradient at the q = 2 surface is unchanged, and it can further increase even when $\nabla\epsilon$ is decreasing.

for the mode to grow, the relation between γ_{obs} and $\nabla\epsilon_{SX}|_{q=2}$ is investigated in detail, as shown in Fig. 5(b). The result shows that there is no critical value for $\nabla\epsilon_{SX}|_{q=2}$ for the mode to grow within the numerical error involved in evaluating $\nabla\epsilon_{SX}|_{q=2}$. γ_{obs} jumps from ~ 0 to $\sim 1 \times 10^3$ s^{-1} under constant $\nabla\epsilon_{SX}|_{q=2}$. During the fast growing phase of the mode, $\nabla\epsilon_{SX}|_{q=2}$ is decreased because of the strong reduction of the emissivity within the q = 2 surface. It should be noted that the mode seems to grow on a resistive time-scale, but there seems to be no critical gradient above which the mode grows on this time-scale. This is also supported by the fact that it is difficult to find a clear change in the density and temperature gradients near the q = 2 surface on this time-scale. Thus γ_{obs} seems to jump from about zero to a finite value on a very fast time-scale which is shorter than the resistive time-scale. The well known $\eta^{1/3}$ dependence of the growth rate does not explain this explosive enhancement of γ_{obs}, because T_e near the q = 2 surface is constant on this time-scale.

5. DISCUSSION AND SUMMARY

The onset conditions are surveyed for the m = 2 mode driven internal disruptions. It is found that there is a clear experimental boundary for the external parameters such as P_{NBI} and $\bar{n}_e$. When these global conditions are fulfilled, the resistivity of the plasma plays an important role in the stability of the m = 2 mode. It is demonstrated that electron heating, i.e. reduction of η, is very effective in stabilizing the m = 2 mode. From these global aspects of the instabilities and the local correspondence of the mode to the rational surface, the unstable mode is identified as a resistive interchange mode. Detailed tomographic analysis is performed to find an onset criterion for particular parameters (for example $\nabla\epsilon_{SX}$ at the q = 2 surface in the present study) above which the mode grows explosively. The growth rate of the mode seems to jump in time from a very low value to a finite value at constant $\nabla\epsilon_{SX}$ within the numerical accuracy, which is different from the theoretical description for the resistive interchange mode based on a critical pressure gradient [11, 12]. The time-scale for the jump is shorter than γ_{obs}^{-1}, where γ_{obs} is obtained as 10^3–10^4 s^{-1}.

ACKNOWLEDGEMENTS

We would like to acknowledge the Heliotron E experimental staff, expecially T. Senju and S. Kobayasi, for their efforts in designing and installing the soft X ray arrays, and K. Yaguchi for his support on detector electronics. We also thank K. Hanada, T. Maekawa and K. Terumichi for their useful comments on tomography technique and analysis methods. One of the authors (H.Z.) acknowledges K. Itoh for his suggestion on the dynamics of the resistive interchange mode.

REFERENCES

[1] HARRIS, J., et al., Phys. Rev. Lett. **53** (1984) 2242.
[2] WAKATANI, M., SHIRAI, H., YAMAGIWA, M., Nucl. Fusion **24** (1984) 1407.
[3] WAKATANI, M., et al., in Plasma Physics and Controlled Nuclear Fusion Research 1990 (Proc. 13th Int. Conf. Washington, DC, 1990), Vol. 2, IAEA, Vienna (1991) 567.
[4] SUZUKI, Y., et al., in Controlled Fusion and Plasma Physics (Proc. 21st Eur. Conf. Montpellier, 1994), Vol. 18B, European Physical Society, Geneva (1994) 424.
[5] OBIKI, T., et al., IAEA-CN-64/C1-3, this volume.
[6] ZUSHI, H., et al., Nucl. Fusion **28** (1988) 1801.
[7] HOSOTSUBO, M., et al., in Proc. Int. Conf. on Plasma Physics, 1996.
[8] FURTH, H.P., KILLEEN, J., ROSENBLUTH, M.N., Phys. Fluids **6** (1963) 459.
[9] ICHIGUCHI, K., NAKAMURA, Y., WAKATANI, M., Nucl. Fusion **31** (1991) 2073.
[10] WAKATANI, M., *et al.*, *Fusion Eng. Des.* **15** (1992) 395.
[11] CARRERAS, B.A., et al., Phys. Fluids **30** (1987) 1388.
[12] ITOH, K., et al., Plasma Phys. Control. Fusion **35** (1993) 723.

DYNAMICS OF ION TEMPERATURE IN HELIOTRON-E

K. IDA, S. HIDEKUMA, K. WATANABE
National Institute for Fusion Science,
Nagoya

K. KONDO, H. ZUSHI, S. BESSHOU
Graduate School of Energy Science,
Kyoto University,
Uji

K. NAGASAKI, F. SANO, J. MIZUUCHI, H. OKADA, T. OBIKI
Institute of Advanced Energy,
Kyoto University,
Uji

T. HAMADA, H. FUNABA, Y. KURIMOTO
Faculty of Engineering,
Kyoto University,
Kyoto

Japan

Abstract

DYNAMICS OF ION TEMPERATURE IN HELIOTRON-E.

The ion temperature dynamics as related to the density profile is studied in the Heliotron-E plasma. The density profiles can be peaked by the H_2/D_2 pellet injection or can be flattened by second harmonic electron cyclotron heating (2nd ECH). Higher ion temperature and better ion transport are observed, associated with the density peaking, and the large density gradient results in radial electric field shear. The improvement of ion transport is related to the radial electric field shear rather than to the bulk velocity shear.

1. INTRODUCTION

The ion temperature dynamics is studied for neutral beam heated plasmas with H_2/D_2 pellet injection and/or second harmonic electron cyclotron heating (2nd ECH) in Heliotron-E, which is an axially asymmetric heliotron/torsatron with $\ell = 2$, $m = 19$, a major radius of $R = 2.2$ m, a magnetic field of $B = 1.9$ T and an NBI power of <3 MW [1]. The time evolution of the ion temperature profiles is measured by multichord charge exchange spectroscopy (TVCXS) with 40 spatial channels and a 16.7 ms time resolution using a charge exchange recombination line of fully stripped carbon [2]. Fast changes in the central ion temperature are measured by a neutral particle analyser (NPA) with a time resolution of 2 ms. The density peakedness is estimated by a seven chord FIR interferometer [3].

2. PELLET INJECTION

As is shown in Fig. 1(a), the central ion temperature keeps increasing after recovering from the H_2/D_2 pellet injection, and the central ion temperature doubles well after the pellet injection (> 50 ms). The electron density profile becomes hollow with pellet injection (t = 332 ms), because the pellet penetrates only up to half the plasma minor radius. The density profile becomes peaked within a few tens of milliseconds after the pellet injection and even more pronounced afterwards (t = 40 ms). Figure 1(b) shows the peaking factor of the ion temperature profiles as a function of the peaking factor of the electron density profiles plotted every 16.7 ms for the pellet injection discharges and also, for reference, for L mode discharges with a similar central electron density. The strong coupling between the peakings of ion temperature and electron density is clearly shown. This strong coupling ($T_i(0)/\langle T_i\rangle$ = 3.1 and $n_e(0)/\langle n_e\rangle$ = 2.6, where $\langle ... \rangle$ stands for the volume average) and an improvement of ion transport due to the density gradient are also observed in high T_i mode discharges [4], where the spontaneous density and temperature peakings occur after the NBI with no gas puff and with low wall recycling due to boron coating.

One of the effects of density peaking is to enhance the radial electric field if the bulk rotation is kept constant. To check this effect, the radial electric field profiles are derived from the impurity poloidal rotation profiles with a radial force balance equation of impurities. From the radial force balance, the force due to the radial

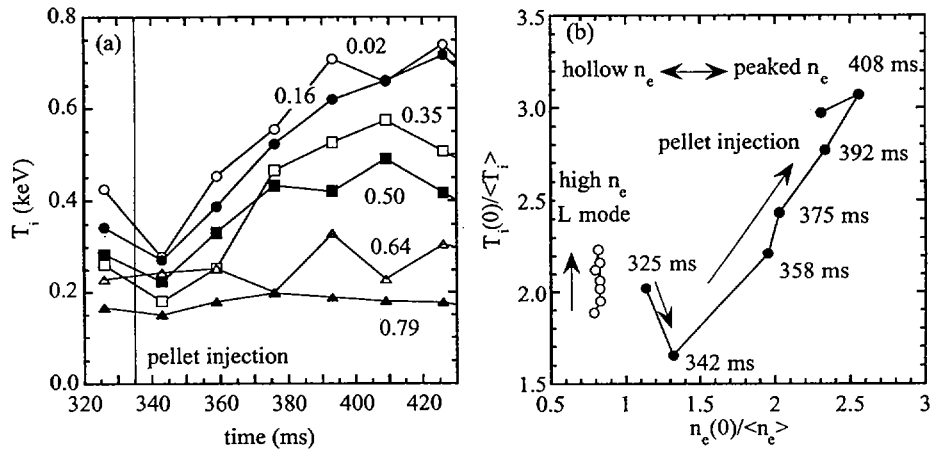

FIG. 1. (a) Time evolution of ion temperature at r = 0.02, 0.16, 0.35, 0.50, 0.64 and 0.79 measured by TVCXS; (b) peaking factor of ion temperature profiles as function of peaking factor of electron density profiles for L mode discharges and discharges with pellet injection in Heliotron-E.

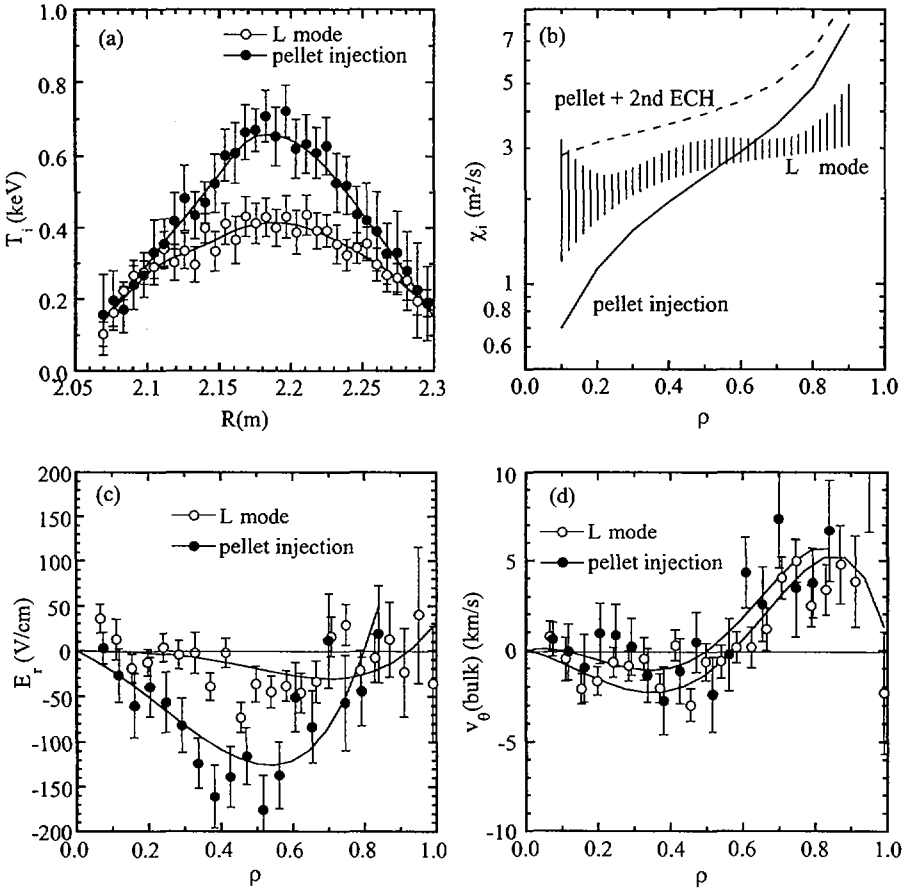

FIG. 2. Radial profiles of: (a) ion temperature; (b) ion thermal diffusivity; (c) radial electric field; (d) bulk poloidal rotation velocity for L mode discharges and discharges with pellet injection ($n_e(0) = 7.3 \times 10^{19}/m^3$) in Heliotron-E.

electric field, E_r, should be balanced by the forces due to the pressure gradient and the Lorentz force due to plasma rotation as $E_r = (1/eZ_in_i)\partial p_i/\partial r + (B_\theta v_\phi - B_\phi v_\theta)$, where p is the pressure, B_θ and B_ϕ are the poloidal and toroidal magnetic fields, and v_θ and v_ϕ are the poloidal and toroidal rotation velocities. The subscript stands for the species: i = H for bulk hydrogen and i = C for the carbon impurity. Z_i is the atomic charge of the bulk ($Z_H = 1$) or carbon impurities ($Z_C = 6$). In the heliotron/torsatron devices, the toroidal rotation is damped by the parallel viscosity, $v_\phi \sim 0$; then, $E_r \sim (1/eZ_in_i)\partial p_i/\partial r - B_\phi v_{\theta i}$. The poloidal rotation profiles of the impurity ions, $v_{\theta C}(R)$, are measured, and the radial electric field, E_r, is calculated as $E_r = (1/eZ_Cn_C)\partial p_C/\partial r - B_\phi v_{\theta C}$. The bulk poloidal rotation velocity is estimated from the radial electric field and the bulk pressure gradient measured as $v_{\theta H} = (1/eB_\phi Z_H n_H)\partial p_H/\partial r - E_r/B_\phi$. Here, it should be noted that the diamagnetic

drift velocity of the bulk ions $(1/eB_\phi Z_H n_H)\partial p_H/\partial r$ is comparable to the E_r/B_ϕ drift velocity. On the other hand, the diamagnetic drift velocity of the carbon impurity, $(1/eB_\phi Z_C n_C)\partial p_C/\partial r$, is much smaller than the E_r/B_ϕ drift velocity.

As is shown in Fig. 2, a more negative radial electric field and greater E_r shear are observed in the pellet injection mode than in the L mode discharges although the bulk poloidal rotation velocity profile in the pellet injection mode is similar to that in the L mode discharge. The peaked ion temperature profiles with pellet injection are due to the improved ion transport (as is seen from the ion thermal diffusivity profiles). The improvement of ion transport can be explained by the radial electric field shear due to the large density gradient (density peaking) triggered by the pellet injection. The greatest improvement of ion transport is observed near the plasma centre, not outside the half plasma minor radius, where the radial electric field has its maximum. Therefore, these results suggest that the E_r shear is more important than the bulk plasma velocity shear in reducing the turbulence and improving the ion transport.

3. SECOND HARMONIC ECH

Second harmonic ECH has particle 'pump-out' in the core region and flattens the density profiles [5]. When the second ECH is applied to a plasma with a peaked density profile, both density peakedness and central ion temperature decrease

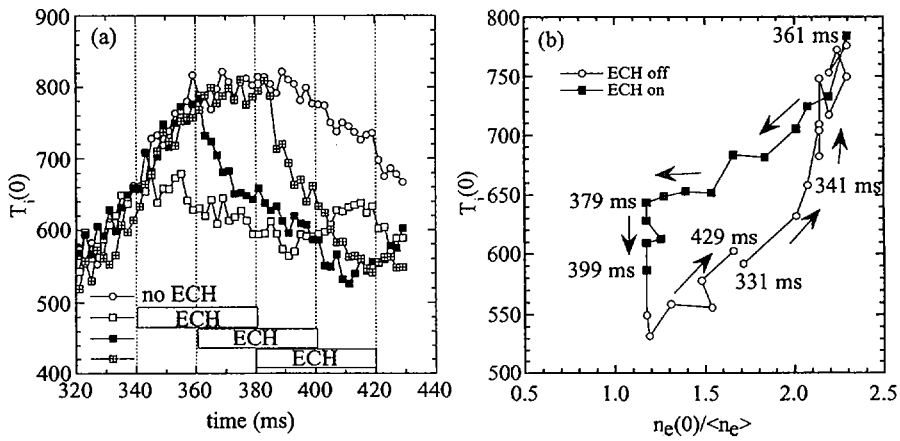

FIG. 3. (a) Time evolution of ion temperature by neutral particle analyser (NPA) for high T_i mode discharge (no ECH pulse) and discharges with second harmonic ECH pulse for t = 340–360 ms, 360–400 ms, and 380–420 ms; (b) central ion temperature profiles as a function of peaking factor of electron density profiles for discharge with second harmonic ECH pulse for t = 360–400 ms in Heliotron-E.

although the total heating power by NBI plus ECH is increased [6]. To study the causal link between the radial electric field shear due to density gradient and the improvement of ion transport, the time evolution of the density peakedness and the central ion temperature is measured at the onset of the second ECH pulse for the high T_i mode discharges, where both the electron density and the ion temperature are peaked. As is seen in Fig. 3(a), the central ion temperature starts to decrease after the second ECH pulse has been turned on and recovers after the ECH pulse has been turned off. These changes in the central ion temperature are associated with the flattening of the density profile.

Figure 3(b) shows the central ion temperature as a function of the density peaking factor. If the density flattening (decrease of the radial electric field shear) and the drop of the central ion temperature take place simultaneously — this is the case where the second harmonic ECH directly deteriorates both particle and heat transports — the time trace should be on one line. When there is causality between these two parameters, the time trace is deformed to become circularly elongated, and the direction of the rotation (clockwise of counterclockwise) shows which change comes first. The measured data clearly show that the change of density peaking factor comes first. These observations support the hypothesis that the density gradient and the radial electric field shear contribute to the improvement of ion transport. The flattening of the density profiles causes the drop in the ion temperature and increases the ion thermal diffusivity. The large ion thermal diffusivity for discharges with second ECH pulse (Fig. 2(b)) is also explained by this mechanism.

4. CONCLUSIONS

The dynamics of the ion temperature for the density peaking phase shows that the increase in the density gradient, which produces a larger radial electric field shear, causes the increase of the ion temperature owing to the reduction of the ion thermal diffusivity. Most L mode discharges in Heliotron-E have a flat electron density and a small E_r shear, which results in a flat ion temperature profile (typically, less peaked than that in a tokamak). However, by controlling the E_r shear (not the bulk poloidal rotation shear) by pellet injection through density peaking, the ion thermal diffusivity, χ_i, can be reduced to 0.7 m^2/s at $\rho = 0.1$, which value lies in between the χ_i values for the L mode and those for the improved modes ($\chi_i(0.1) = 0.5$ m^2/s in the supershot, $\chi_{eff}(0.2) = 0.6$ m^2/s in the PEP mode, $\chi_{eff}(0.2) = 0.4$ m^2/s in the VH mode, and $\chi_i(0.1) = 0.1$ m^2/s in the high β_ρ mode) in tokamaks [7–10]. On the other hand, the second harmonic ECH deteriorates the density peaking and enhances the ion thermal diffusivity (≈ 3 m^2/s) up to as high as, or even higher than, that prevailing in the L mode discharges.

REFERENCES

[1] SANO, F., et al., Nucl. Fusion **30** (1990) 81.
[2] IDA, K., HIDEKUMA, S., Rev. Sci. Instrum. **60** (1989) 867.
[3] ZUSHI, H., et al., Nucl. Fusion **27** (1987) 286.
[4] IDA, K., et al., Phys. Rev. Lett. **76** (1996) 1268.
[5] MIZUUCHI, T., et al., in Controlled Fusion and Plasma Physics (Proc. 23rd Eur. Conf. Kiev, 1996), Vol. 20C, European Physical Society, Geneva (1996).
[6] OBIKI, T., IAEA-CN-64/C1-3, this volume.
[7] HAWRYLUK, R.J., et al., Plasma Phys. Control. Fusion **33** (1991) 1509.
[8] KEILHACKER, M., et al., Plasma Phys. Control. Fusion **33** (1991) 1453.
[9] OSBONE, T.H., et al., Plasma Phys. Control. Fusion **36** (1994) A237.
[10] SHIRAI, H., et al., in Plasma Physics and Controlled Nuclear Fusion Research 1994 (Proc. 15th Int. Conf. Seville, 1994), Vol. 1, IAEA, Vienna (1995) 355.

ORBIT EFFECTS OF ENERGETIC PARTICLES ON THE REACHABLE β VALUE AND THE RADIAL ELECTRIC FIELD IN NBI AND ECR HEATED HELIOTRON PLASMAS

S. MURAKAMI, N. NAKAJIMA, S. OKAMURA, M. OKAMOTO
National Institute for Fusion Science,
Nagoya, Japan

U. GASPARINO
Max-Planck-Institut für Plasmaphysik,
Euratom-IPP Association,
Garching, Germany

Abstract

ORBIT EFFECTS OF ENERGETIC PARTICLES ON THE REACHABLE β VALUE AND THE RADIAL ELECTRIC FIELD IN NBI AND ECR HEATED HELIOTRON PLASMAS.

Effects of energetic particles on the plasma heating process and the radial electric field were studied in NBI and ECR heated heliotrons. The NBI heating efficiency is reduced as the magnetic field becomes weak, even for tangential injection, owing to large orbit deviation, which is changed significantly by finite β effects. It is found that this reduction of heating efficiency due to beam orbit loss plays an important role in determining the reachable β value in high β experiments on the Compact Helical System (CHS). It is also found that the radial flux due to tangentially injected neutral beams can enhance the strong negative radial electric field near the plasma periphery in CHS and that the enhancement of the radial electric field is larger for the high density case, which is consistent with experimental results. Effects of energetic electrons on the heating process and the radial electric field in the case of ECR heating were also studied using a newly developed Monte Carlo simulation code. A large radial broadening of the power deposition profile and a radial flux due to the energetic electrons were obtained. This radial flux can enhance the positive radial electric field with significant heating power, which could explain the transition phenomena of the radial electric field in the CHS experiments.

1. INTRODUCTION

In heliotrons the behaviour of energetic particles created by various heating methods is considerably complicated because of three dimensional magnetic configurations. Further, both changes of the configuration due to the large Shafranov shift (finite β effects) and the generated radial electric field significantly affect the characteristics of the energetic particle orbits, i.e. the drift motions across the magnetic flux surfaces. At the same time, the large drift motions of the energetic particles have an influence on both the plasma heating process, through the deposition profile, and the generation of the radial electric field owing to the enhanced radial flux of

energetic particles. Therefore a self-consistent consideration of magnetic configuration, radial electric field and complex particle motions is necessary to clarify the physics of energetic particles in heliotrons.

In this paper, we examine self-consistent relations between the large drift orbits of energetic particles created by NBI or ECR heating and both the heating process and the generation of the radial electric field. The role of the large drift orbits in the Compact Helical System (CHS, an $\ell = 2$ and $m = 8$ heliotron) [1] is studied and compared with the experimental results. In addition, predictions are made for the Large Helical Device (LHD, an $\ell = 2$ and $m = 10$ heliotron) [2].

2. BEAM ORBIT EFFECTS ON THE REACHABLE β VALUE

High β experiments in CHS (with reduced magnetic field strength) [3, 4] have shown that the obtained β values saturate at $B \approx 0.6$ T and that those values are lower than the one expected from consideration of equilibrium and stability β limit. This suggests that there exist other mechanisms to limit the plasma β, depending on the magnetic field strength. The deviation of drift orbits of tangentially injected neutral beam particles from magnetic surfaces becomes non-negligible in a weak magnetic field. Effects of beam particle orbits on the NBI heated high β plasma have been studied in CHS, including the configuration change due to the Shafranov shift, in a self-consistent way. In this paper we evaluate the energetic particle loss based on the orbital deviation and the birth profile of tangentially injected beams [5], and the orbital aspects of the heating efficiency and the reachable β value are examined.

Figure 1(a) shows the heating efficiency ($1 - N_{loss}/N_{total}$, where N_{total} and N_{loss} are the total deposited particle number and the number of lost particles due to orbit loss) as a function of the magnetic field strength for co-injection NBI heating in CHS. It is found that the heating efficiency is reduced in a weak magnetic field and that the changes in the configuration due to the finite β effect (Shafranov shift) alter the NBI heating efficiency by a large amount. The Shafranov shift changes the magnetic configuration from magnetic hill to well in the heliotron, which is important for MHD stability. This magnetic well or hill condition is also an important factor in determining the heating efficiency in a weak magnetic field.

The achievable plasma β is evaluated by means of β value scaling based on an empirically obtained energy confinement scaling law (LHD scaling, τ_E^{LHD}) [6]:

$$\beta = \frac{2}{3}\frac{P_h \tau_E^{LHD}}{\int (1/2\mu_0) B^2 \, dV} = 0.0144 R^{-0.25} a^2 n^{0.69} B^{-1.16} P_h^{0.42} \qquad (1)$$

The heating efficiency and the reachable β value are non-linear functions of β, and we calculate the configuration change and particle orbits consistently to obtain a reachable β. The comparison of theoretical results with experimental results in CHS [4] at $\bar{n} = 5.0 \times 10^{19}$ m^{-3} is shown in Fig. 1(b). Although the experimental

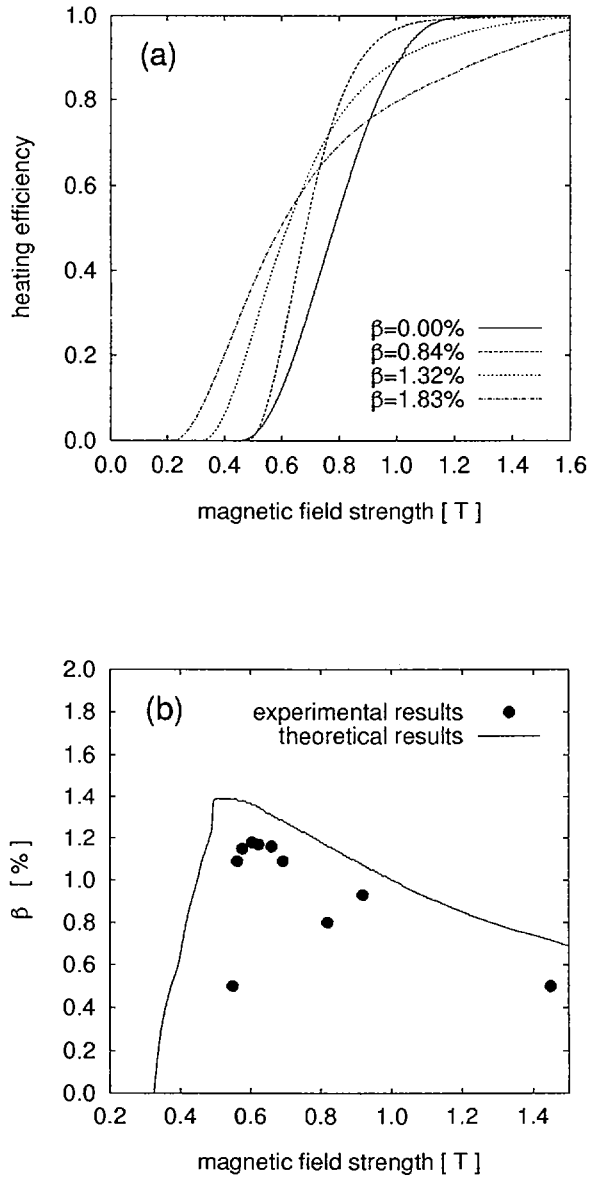

FIG. 1. (a) Heating efficiency of co-injection NBI heating as a function of magnetic field strength with four different β magnetic configurations; (b) comparison of the B dependence of consistently calculated achievable β with experimental values [4] in CHS.

results are slightly lower than the theoretical ones, we can see a good agreement. Saturation of the β value is observed at $B \approx 0.6$ T and a rapid fall is seen at $B < 0.5$ T. This is attributed to the fact that beam orbit losses are significantly enhanced for a weak magnetic field of less than 0.5 T. Thus, beam particle orbits play an important role in determining the achievable β value in CHS high β experiments in a weak magnetic field.

Next we calculate the reachable β value for LHD. We introduce the LHD configuration, called the 'standard configuration', which satisfies the requirements for high plasma performance, i.e. good bulk particle confinement, high plasma beta ($\beta_c \geq 5\%$) and creation of a divertor configuration. A beam energy of 180 keV and a heating power of 20 MW are assumed. Predictions for the LHD plasma show that $\beta = 5\%$ could be achieved at $B = 0.5$ T by assuming an average density of 1.4×10^{20} m^{-3}.

3. BEAM ORBIT EFFECTS ON THE RADIAL ELECTRIC FIELD

A strong radial electric field is expected not only to reduce anomalous transport but also to reduce neoclassical diffusion in heliotrons. Recently a strong negative radial electric field near the plasma periphery was measured in CHS [7]. However, the origin of this negative electric field has been an unsolved problem. In the previous section we showed that the beam loss becomes large even for tangential injection in a weak magnetic field. This loss flux could affect the radial electric field and enhance the negative radial electric field.

We study the effect of beam orbit flux on the radial electric field in heliotrons using Monte Carlo simulations. First, the birth profile of neutral beams is calculated using an NBI deposition code and beam particle orbits are followed, taking into account Coulomb collisions with background plasma particles, until the beam particles are slowed down to thermal energies. Then the radial flux due to beam orbit loss is evaluated using the obtained distribution function of the beam particles. Finally the radial electric field is determined to satisfy the ambipolar condition

$$\Gamma_{beam} + \Gamma_i^{NC} = \Gamma_e^{NC} \tag{2}$$

where Γ_{beam} is the radial flux of the beam particles, and Γ_i^{NC} and Γ_e^{NC} are the radial fluxes of background ions and electrons due to the neoclassical $1/\nu$ ripple diffusion.

Figure 2(a) shows the radial flux due to the beam particles of counter-injection NBI heating at two different densities: $n_0 = 2.0 \times 10^{19}$ and 6.0×10^{19} m^{-3}. We can see the larger radial flux in the high density case because of lower shine-through of the neutral beam and the outwardly shifted deposition profile, which enhance particle loss for counter-injection. The enhanced radial electric field for the two different densities is shown in Fig. 2(b). It is found that a strong negative radial electric field is obtained at the plasma periphery in the higher density case but a small

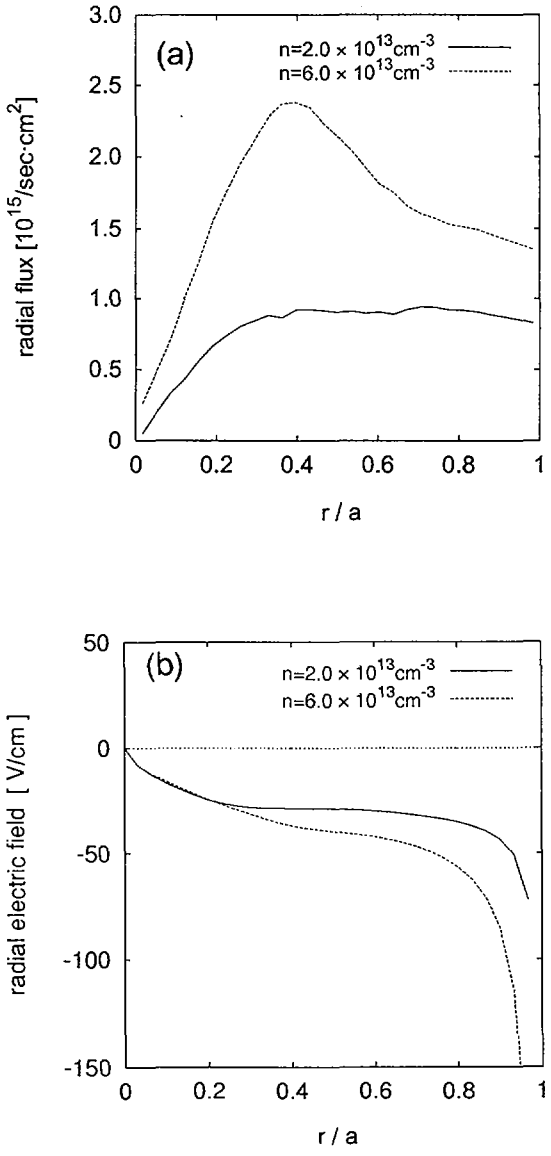

FIG. 2. (a) Radial flux due to energetic beam particles (n_0 = 2.0 × 10^{19} and 6.0 × 10^{19} m^{-3}); (b) buildup of radial electric field due to beam radial flux in CHS.

enhancement is observed in the lower density case. The density dependence of the enhanced radial electric field is consistent with the experimental observation. As a result it is found that the beam enhanced flux plays an important role in generating strong negative radial electric fields as observed in CHS.

Using this enhancement of the radial electric field due to the beam component, we can consider a radial electric field bifurcation scenario in CHS related to the H mode in heliotrons by introducing the non-linear viscosity term. Effects of anomalous and non-linear viscosity are now under investigation.

4. ELECTRON ORBIT EFFECTS IN ECR HEATING

Although linear theory predicts a local absorption of ECR heating power, broader heating profiles are observed in electron cyclotron heating of low density plasmas in both heliotrons and stellarators [8]. It is also observed that the radial electric field can suddenly change when ECR waves are applied to NBI heated plasmas [9]. Ripple trapped energetic particles are created and their drift motions across the magnetic surfaces can play an important role in these phenomena. However, this drift motion effect has not been analysed owing to the difficulty in solving the electron orbits and the radial electric field consistently.

We have developed a Monte Carlo simulation code based on a technique similar to the adjoint equation for dynamic linearized problems [10]. The linearized drift kinetic equation for the deviation from the Maxwellian background $f_l(\underline{x}, \underline{v})$

$$\bar{v}\cdot\nabla f_l + \bar{a}\cdot\nabla_v f_l = C(f_l) + S^0_{ql} \tag{3}$$

is evaluated as

$$f_l(\underline{x}, \underline{v}) = \int_0^\infty dt \int d\underline{x}' \int d\underline{v}'\, S^0_{ql}(\underline{x}', \underline{v}')g(\underline{x}, \underline{v}, t|\underline{x}', \underline{v}') \tag{4}$$

where $C(f_l)$ is the linear Coulomb collision operator and S^0_{ql} is the wave induced flux in velocity space (quasi-linear diffusion term), which is assumed to be a given function. The time dependent Green function $g(\underline{x}, \underline{v}, t|\underline{x}', \underline{v}')$ is the solution of the drift kinetic equation

$$\frac{\partial g}{\partial t} + \bar{v}\cdot\nabla g + \bar{a}\cdot\nabla_v g = C(g) \tag{5}$$

with initial condition $g(\underline{x}, \underline{v}, t = 0|\underline{x}', \underline{v}') = \delta(\underline{x} - \underline{x}')\delta(\underline{v} - \underline{v}')$. The solution of Eq. (5) is obtained using the Monte Carlo simulation, in which the complex magnetic

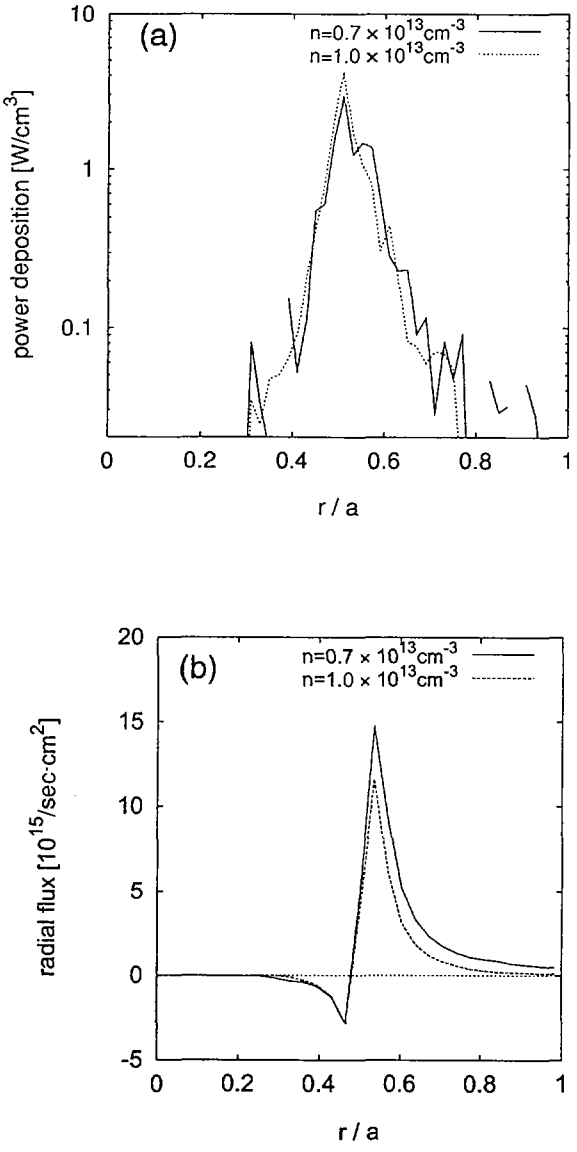

FIG. 3. Radial profiles of (a) power deposition and (b) enhanced radial flux due to energetic electrons in CHS (X mode, second harmonic).

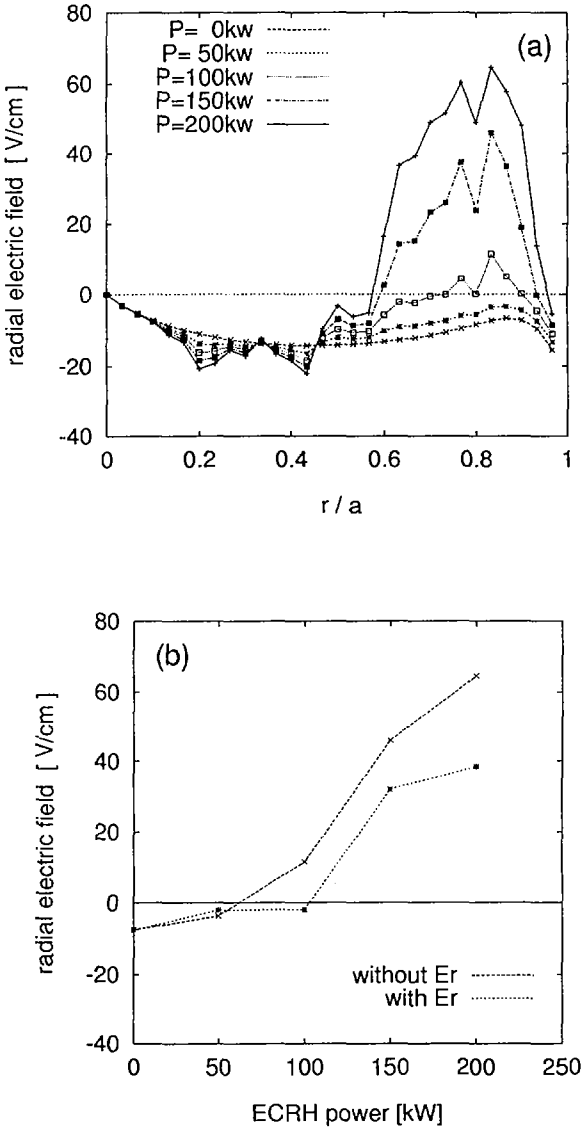

FIG. 4. (a) Buildup of radial electric field due to energetic electrons; (b) radial electric field as a function of ECR heating power in CHS.

field configuration, the finite β effect and the radial electric field can be included [11]. Using this code we investigate the broadening of the heating profile and the orbit effects on the radial electric field.

Figure 3(a) shows the radial profile of the ECR heating power deposition in CHS (X mode, second harmonic) for two different densities: $n_0 = 0.7 \times 10^{19}$ and 1.0×10^{19} m^{-3}. The temperatures are set to 400 eV for electrons and 200 eV for ions (ECR and NBI combined heating). The heating point is the bottom heating case in the CHS experiments [7], which is the bottom of the toroidal field and r/a = 0.5. The quasi-linear diffusion term S^0_{ql} is estimated through an analytical model of ECR heating. We can see the broadening of the power deposition profile due to the large orbit of energetic electrons, and the broadness is larger in the lower density case. Figure 3(b) shows the radial profile of the radial flux due to the electrons, which is enhanced by the ECR heating. The obtained radial flux is comparable with or larger than the neoclassical flux, and it could affect the radial electric field and the density profile.

Next we study the effect of the enhanced radial flux due to the energetic electrons on the radial electric field E_r. Figure 4 shows the change of radial electric field due to the enhanced radial electron flux ($n_0 = 1.0 \times 10^{19}$ m^{-3}) and the radial electric field at $\rho = 0.83$ as a function of ECR heating power for two cases, with and without enhanced E_r, obtained by solving the ambipolarity condition (see Eq. (2)). It is found that the electron radial flux due to ECR heating can enhance the positive radial electric field with significant heating power, which can explain the radial electric field transition phenomena observed in CHS.

ACKNOWLEDGEMENTS

The authors acknowledge the support of the CHS Group and the Heating Group at the National Institute for Fusion Science. They also thank A. Iiyoshi and T. Sato for continuous encouragement.

REFERENCES

[1] NISHIMURA, K., et al., Fusion Technol. **17** (1990) 86.
[2] IIYOSHI, A., et al., Fusion Technol. **17** (1990) 148.
[3] YAMADA, H., et al., in Plasma Physics and Controlled Nuclear Fusion Research 1992 (Proc. 14th Int. Conf. Würzburg, 1992), Vol. 2, IAEA, Vienna (1993) 493.
[4] OKAMURA, S., et al., Nucl. Fusion **35** (1995) 283.
[5] MURAKAMI, S., et al., Nucl. Fusion **36** (1996) 359.
[6] SUDO, S., et al., Nucl. Fusion **30** (1990) 11.
[7] IDA, K., et al., Phys. Fluids B **3** (1991) 515.
[8] ROMÉ, M., et al., Plasma Phys. Control. Fusion (in press).
[9] IDEI, H., et al., Phys. Plasmas **1** (1994) 3400.
[10] FISCH, N.J., Phys. Fluids **29** (1986) 172.
[11] MURAKAMI, S., et al., Nucl. Fusion **34** (1994) 913.

FLUCTUATION AND INTERNAL CURRENT STUDIES IN THE H-1 HELIAC

B.D. BLACKWELL, G.G. BORG, P. CUTHBERT, R.L. DEWAR,
S.A. DETTRICK, H.J. GARDNER, S.M. HAMBERGER,
J. HOWARD, S.R. HUDSON, J.L.V. LEWANDOWSKI,
S.S. LLOYD, M. PERSSON, D.L. RUDAKOV, L.E. SHARP,
D.B. SINGLETON, M.G. SHATS, G.B. WARR
Plasma Research Laboratory,
Australian National University,
Canberra, Australia

W.A. COOPER
Centre de recherches en physique des plasmas,
Ecole polytechnique fédérale de Lausanne,
Lausanne, Switzerland

T. HAYASHI
National Institute for Fusion Studies,
Nagoya, Japan

Abstract

FLUCTUATION AND INTERNAL CURRENT STUDIES IN THE H-1 HELIAC.

Measurements of density fluctuations and internal currents for finite beta conditions ($\langle\beta\rangle \sim 0.05$–$0.3\%$) have been made possible by operating the H-1 device at low DC magnetic fields ($0.05\ \mathrm{T} < B_0 < 0.15\ \mathrm{T}$), using both argon and helium gases. Low order (e.g $m = 1, 2$) global coherent modes are observed at lower magnetic fields. When operating at higher rotational transform, $\iota = 1.43$, one observes the suppression of fluctuations and an increase in the electron density. Under these quiescent conditions, the internal currents (e.g. the Pfirsch–Schlüter currents) have been measured by using Rogowski loops and compared with the theoretical predictions using the HINT code. Improved techniques for modelling the highly non-axisymmetric H-1 equilibrium are being developed by using a new method for defining approximate magnetic surfaces, based on minimizing the 'quadratic flux'.

1. INTRODUCTION

The H-1 [1] heliac is a low shear, three field period helical axis stellarator of medium scale (R/a = 1 m/0.2 m), $B_0 = 0.2$ T (continuous) to 1 T (pulsed), capable of a considerable range ($0.6 < \iota(0) < 1.9$) of 'current-free' configurations. A quasi-continuous operating mode at low fields (<0.2 T DC, 60 ms) provides repetitive plasma pulses in various gases (H_2, He, Ar) by $\leq$ 85 kW RF at 7–23 MHz and allows detailed measurements of mean and fluctuating plasma properties under finite

beta conditions ($\langle\beta\rangle \leq 0.3\%$). Diagnostics include Langmuir, magnetic and Mach probe arrays; internal and external diamagnetic and Rogowski coils; correlation spectroscopy; and a 40 channel, three view FIR ($\lambda = 443\ \mu m$) Michelson interferometer [2]. Typical plasma conditions are $n_e \sim 2 \times 10^{18}\ m^{-3}$, $T_e \sim 10$ eV (Ar); $5 \times 10^{17}\ m^{-3}$, $T_e \sim 50$ eV (H_2).

2. FLUCTUATION MEASUREMENTS

Langmuir probe arrays, FIR interferometer and visible correlation spectroscopic techniques have been used to map the electron density fluctuations. In the

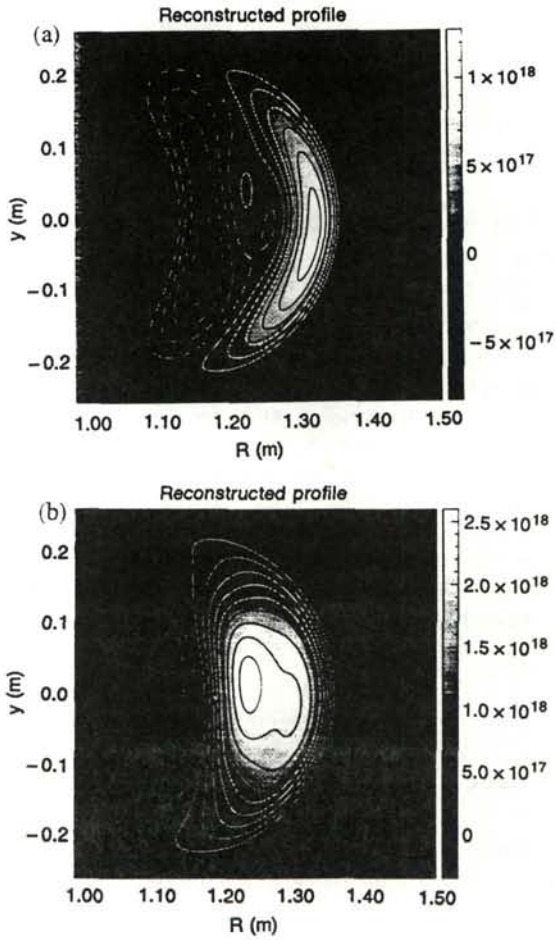

FIG. 1. Tomographic reconstruction of (a) density perturbation associated with global instability and (b) full density profile.

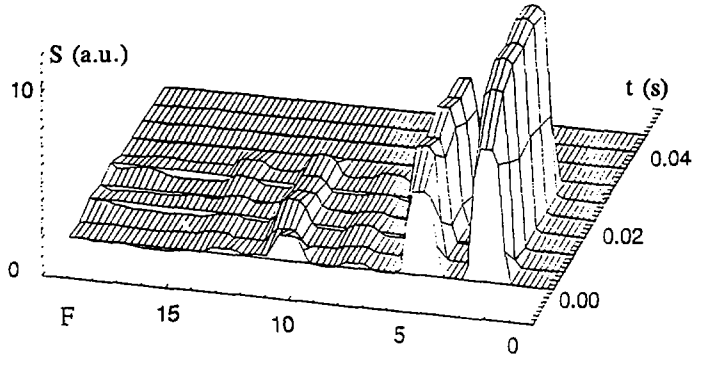

FIG. 2. Frequency spectrum of global m = 1 mode.

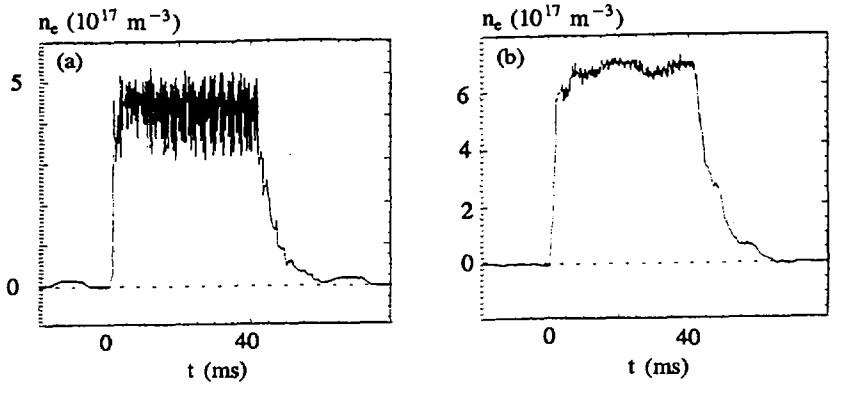

FIG. 3. Time behaviour of electron density for (a) 'fluctuating' and (b) 'quiescent' regimes.

standard configuration, $\iota(0) = 1.1$, $\iota(a) = 1.2$, these fluctuations can have a relative level $(\delta n/\langle n \rangle)_{RMS} \sim 50\%$ and are localized near the region of maximum density gradient. The fluctuation level is observed to decrease with the magnetic field, and the dominant frequency which lies principally within the range of 3 to 30 kHz is also found to depend on the magnetic field as well on the working gas. The correlation probe measurements and FIR interferometer results indicate an m = 1, 2 poloidal mode number. A tomographic reconstruction of the mode obtained from the 40 channel, three view FIR interferometer is shown in Fig. 1.

The DC component of the density is well approximated by a Gaussian distribution with azimuthal symmetry defined in flux co-ordinates.

The evolution of the frequency spectra of the fluctuations in argon is shown in Fig. 2. Typically, up to three to four harmonics of the fundamental f_0 = 2–9 kHz are observed. At higher magnetic fields (and higher ι) the fluctuations can be

suppressed and a dramatic increase in the electron density of up to a factor of two is observed. The enhanced loss of particle flux associated with the presence of the instability (calculated from the correlation between the potential and density fluctuations measured by a triple probe) can account for this observed increase in electron density in its absence. Figure 3 shows the time behaviour of the line averaged density at the higher rotational transform, $\iota(0) = 1.43$, measured with an ($\lambda_0 = 8$ mm) microwave interferometer. Figures 3(a) and (b) correspond to two different magnetic fields, $B_0 = 0.06$ T and $B_0 = 0.1$ T, showing the fluctuation level to decrease by a factor of more than ten while the average density increases by about 70% as the field is increased. We refer to these two regimes as 'fluctuating' and 'quiescent', with the latter characterized by higher electron density and steeper density gradient. Accompanying this transition, the plasma potential changes from being markedly negative (~ -200 V) to slightly positive, and the plasma rotation changes from toroidal to poloidal. The electron temperature in both regimes is, however, similar: $T_e = 7$–9 eV.

3. INTERNAL CURRENTS

Internal moveable Rogowski coils have been used to spatially map the distribution of internal plasma currents to study finite beta ($\langle\beta\rangle \sim 0.05$–$0.2\%$) effects. Two separate glass sheathed Rogowski coils (R = 110/92 mm o.d./i.d. and 100/82 mm o.d./i.d., each 10 turns/mm) were used for these measurements. One was inserted

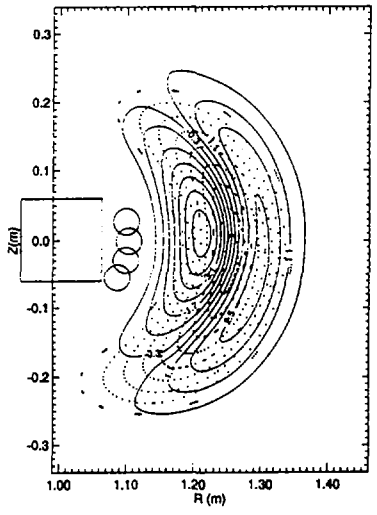

FIG. 4. Contour map of calculated toroidal currents for $\phi = -3°$ plane at $\langle\beta\rangle = 0.13\%$ superimposed on the vacuum magnetic surfaces.

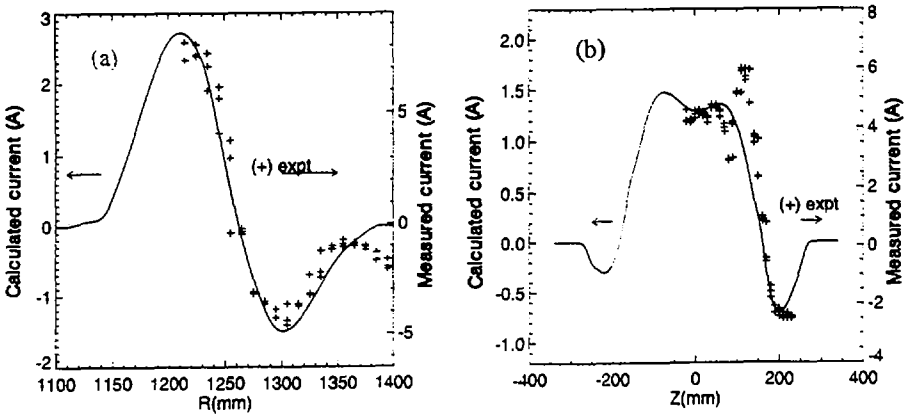

FIG. 5. Comparison of (a) radial profile of calculated and measured toroidal currents at $z = 0$ mm (midplane) and $\phi = -3°$ and (b) vertical profile at $R = 1175$ mm and $\phi = 3°$.

from the outer radius and could scan horizontally, and one was inserted from the top of the vacuum vessel and could scan vertically over the top half of the separatrix. The plasma perturbation produced by these coils was monitored by observing their effects on the mean density, beta and net current, and it was found to be no more than 10–20%.

In the presence of the coherent instability, we observe a total net current of up to 100 A that is not simply related to the plasma pressure. By contrast, in the quiescent regime (i.e. $\iota(0) = 1.4$ at $\bar{a} = 0.15$ m) the net current falls to less than 40 A in argon and a few amperes in helium. The internal toroidal current distribution (the toroidal components of the Pfirsch-Schlüter and diamagnetic currents) that would be measured by the Rogowski coil probe in the vertical plane at the toroidal position $\Phi = -3°$ has been calculated by using the HINT [3] 3-D MHD equilibrium code for the pressure profile $p = p_0(1-\psi^2)$ (ψ being the normalized toroidal flux) at the magnetic field B = 0.93 T. This code includes the effects of magnetic islands. The results are plotted in Fig. 4 as a 2-D contour map superimposed on the vacuum magnetic surfaces for the measurement plane at $\Phi = -3°$ (dots) and show the relative position with respect to the ring and helical control windings. The experimental measurements of the current are compared with the theoretical predictions using a peak beta of 0.3%, in Fig. 5, where the radial distribution of the toroidal currents is plotted along the median plane $z = 0$, at $\Phi = -3°$ (left) and for the vertical distribution of the toroidal currents at the radial position R = 1175 mm, measured in the vertical plane at $\Phi = +3°$ (right). For both cases, the experimental measurements have been corrected for the observed net current of 36 A, possibly associated with the RF plasma production, which is, for simplicity, assumed to be distributed uniformly over the cross-section of the plasma. The average beta measured with a diamagnetic loop for these conditions is 0.14%.

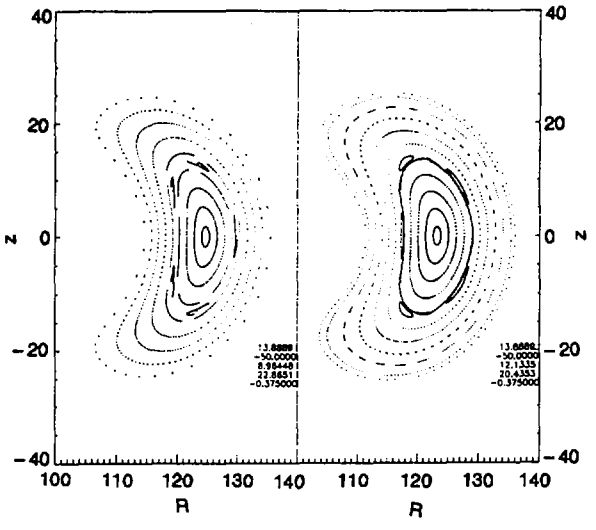

FIG. 6. Poincaré plots showing phase swapping of an (m = 5, n = 9) island chain in H-1.

It should be noted that, although the current profiles compare reasonably, the observed currents are a factor of three larger than those predicted by the HINT code and that Fig. 5(b) shows possible evidence of a sheath current (or an island) in the outer regions of the plasma.

4. THEORETICAL STUDIES

New theoretical techniques for more sophisticated modelling of the highly non-axisymmetric H-1 equilibrium are also being developed. One such area is a new method of defining approximate magnetic surfaces, which do not generically exist in three dimensional geometries, based on minimizing the 'quadratic flux' [4]. One consequence of this method has been a new technique (similar to that in Ref. [5]) for determining magnetic island widths. The application of this technique has led to H-1 configurations in which island widths are minimized, or which have magnetic island phases opposite to those of the standard machine design (Fig. 6).

Finite β equilibria with imperfect surfaces have also been studied by using the HINT code and have revealed that the new configurations exhibit self-healing with plasma pressure [6]. Calculations of collisionless particle orbits in H-1 have been compared with contours of an approximate adiabatic invariant analogous to one used for planar axis stellarators [7, 8]. The extreme non-axisymmetry of the H-1 field and the relatively large value of the rotational transform per field period imply that the approximations leading to the J* invariant of Ref. [7] are not formally valid, but a

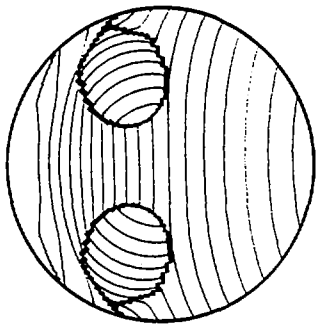

FIG. 7. Contours of the modified approximate invariant in the $\phi = 0$ plane (Boozer space). The 'eyeglasses' mark the boundary between helically and toroidally trapped orbits of near perpendicular particles ($\mu/E = 0.9$).

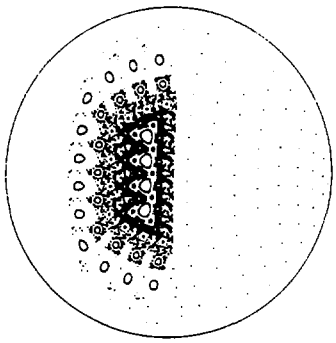

FIG. 8. Poincaré plot of the collisionless drift orbits of 100 eV (H, 1 T) ions in the $\phi = 0$ plane of H-1. The curved loci on the right hand side show unconfined orbits. The confined region on the left hand side corresponds to the bridge between the eyeglasses in Fig. 7. We see that confined orbits do exist at finite temperature and with zero radial electric field.

slight generalization leads to a modified J*, which is of use for helical axis stellarators. Computations show that the collisionless orbit topologies can be given by the surfaces of the modified approximate invariant even at finite particle energies (100 eV), where orbits show a chaotic behaviour about their average surfaces (Figs 7 and 8).

Another area under active development is the WKB ballooning approach to drift wave and ideal MHD ballooning mode stability. This method has been shown to be capable of giving accurate global growth rate eigenvalues in a ten field period torsatron test case [9], but the topology of the ballooning growth rate eigenvalue isosurfaces for the three field period heliac is quite different.

REFERENCES

[1] HAMBERGER, S.M., et al., Fusion Technol. **17** (1990) 123.
[2] WARR, G.B., et al., Trans. Fusion Technol. (in press).
[3] HARAFUJI, K., HAYASHI, T., SATO, T., J. Comput. Phys. **81** (1989) 169.
[4] HUDSON, S.R., DEWAR, R.L., J. Plasma Phys. (in press).
[5] CARY, J.R., HANSON, J.D., Phys. Fluids B **3** (1991) 1006.
[6] HAYASHI, T., SATO, T., GARDNER, H.J., MEISS, J.D., Phys. Plasmas **2** (1995) 752.
[7] CARY, J.R, HEDRICK, C.L., TOLLIVER, J.S., Phys. Fluids **31** (1988) 1586.
[8] ROME, J.A., Nucl. Fusion **35** (1995) 195.
[9] COOPER, W.A., SINGLETON, D.B., DEWAR, R.L., Phys. Plasmas **3** (1996) 276.

IMPROVEMENT OF COLLISIONLESS PARTICLE CONFINEMENT IN $\ell = 1$ HELICAL SYSTEMS

M. YOKOYAMA, Y. NAKAMURA, M. WAKATANI
Graduate School of Energy Science,
Kyoto University,
Uji

M. AIZAWA, K.H. SAITO, K.N. SAITO,
I. KAWAKAMI, S. SHIINA
Atomic Energy Research Institute,
College of Science and Technology,
Nihon University,
Tokyo

Japan

Abstract

IMPROVEMENT OF COLLISIONLESS PARTICLE CONFINEMENT IN $\ell = 1$ HELICAL SYSTEMS.

Two approaches for improving collisionless particle confinement in $\ell = 1$ helical systems are presented. One is to select the optimum bumpy field in a coil system composed of a pitch modulated $\ell = 1$ helical coil, toroidal coils and poloidal coils. When the sign of the bumpy field is opposite to that of the $\ell = 1$ helical field and the magnitudes of the two fields are comparable, the configuration with a toroidal ripple comparable to half the helical ripple seems most effective for suppressing the collisionless particle loss. A four period $\ell = 1$ helical system close to the optimum configuration is discussed. The second approach is to use negative pitch modulation for collisionless particle confinement. In the compact $\ell = 1$ torsatron with 17 periods, negative pitch modulation enhances the fraction of passing particles and simultaneously improves the confinement of trapped particles owing to the significant reduction of the effective toroidal curvature. This also leads to a favourable neoclassical diffusion coefficient.

1. ROLE OF A BUMPY FIELD IN α PARTICLE CONFINEMENT IN AN $\ell = 1$ STELLARATOR COMPATIBLE WITH AN INCREASE OF β

(M. Yokoyama, Y. Nakamura, M. Wakatani)

1.1. Introduction

For the optimization of stellarators the most difficult issue is the compatibility between a high limit of MHD β and good confinement of high energy trapped particles or α particles in a reactor. Several methods have already been proposed to obtain

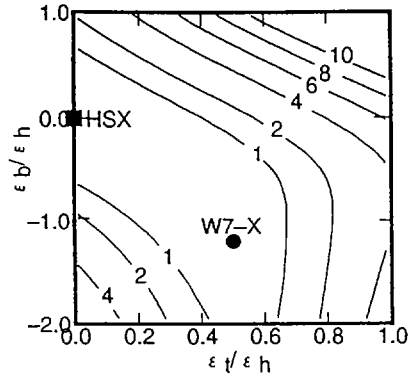

FIG. 1. Contours of the reduction coefficient of neoclassical ripple transport for the $\ell = 1$ stellarator with four periods.

good confinement of trapped particles. One is the inward shift of the magnetic axis in heliotrons [1]. The other is the shift of the helical ripple position to the inner region of the torus, or σ optimization [2]. It has been shown that the shift of the magnetic axis is correlated with the control of sideband helical fields [3]. With respect to the magnetic spectrum, a quasi-helically symmetric (QHS) stellarator is introduced to improve the confinement of α particles [4]. In the QHS stellarator the essential point for α particle confinement improvement is to reduce toroidal effects and to restore helical symmetry.

We discuss the importance of the $\ell = 0$ magnetic field or the bumpy field in the $\ell = 1$ stellarator for improving the α particle confinement. Since the confinement of trapped particles is directly correlated with the neoclassical ripple transport, first we evaluate the particle flux in the simple model field $B/B_0 = 1 + \epsilon_t \cos\theta + \epsilon_b \cos 4\phi + \epsilon_h \cos(\theta - 4\phi)$. Figure 1 shows the reduction coefficient of the neoclassical ripple transport estimated with the expression given by Shaing and Hokin

$$\int [G_1(\partial\epsilon_T/\partial\theta)^2 - 2G_2(\partial\epsilon_T/\partial\theta)(\partial\epsilon_H/\partial\theta) + G_3(\partial\epsilon_H/\partial\theta)^2]d\theta$$

where $G_1 = 16/9$, $G_2 = 16/15$, $G_3 = 0.684$, $\epsilon_T = \epsilon_t \cos\theta$ and $\epsilon_H = (\epsilon_h^2 + 2\epsilon_h\epsilon_b \times \cos\theta + \epsilon_b^2)^{1/2}$ [5]. The vertical co-ordinate is the ratio of the bumpy field (ϵ_b) to the helical ripple (ϵ_h) and the horizontal co-ordinate is the ratio of the toroidal ripple (ϵ_t) to the helical ripple (ϵ_h). In this simple model the QHS stellarator corresponds to $\epsilon_b = \epsilon_t = 0$. The interesting result is that the reduction of ϵ_t is effective when $\epsilon_b/\epsilon_h < 0$, and $\epsilon_b/\epsilon_h \approx -1.0$ and $\epsilon_t/\epsilon_h \approx 0.5$ seem to be optimum. It is noted that W7-X has adopted these parameters [6]. Our optimization method is somewhat different from the case of W7-X using modular coils. We investigated the correlation between the coil system parameters and the magnetic field spectrum.

1.2. An optimized stellarator with an $\ell = 1$ helical coil, toroidal coils and poloidal coils

We will present an optimized $\ell = 1$ stellarator with the winding law $\theta = \pi + 4\phi + 0.45 \sin(4\phi)$, where θ (ϕ) is the poloidal (toroidal) angle [7]. The vacuum magnetic surface is shown in Fig. 2. The rotational transform is almost constant at $\iota = 0.70$, and the average minor radius is $\bar{a} \simeq 19$ cm for major radius $R_0 = 2.2$ m, with the aspect ratio about 11. The overall characteristics are similar to those of W7-X; however, the topological relation between the magnetic surface shape and the $\ell = 1$ coil position is opposite to that of W7-X. The bumpy field with the cos 4ϕ component is controlled to improve the particle confinement. Figure 3(a)

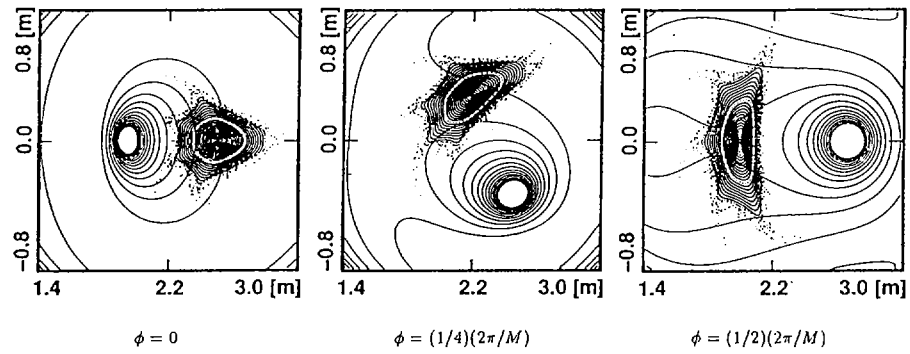

FIG. 2. Cross-sections of vacuum magnetic surfaces for the $\ell = 1$ stellarator with four periods.

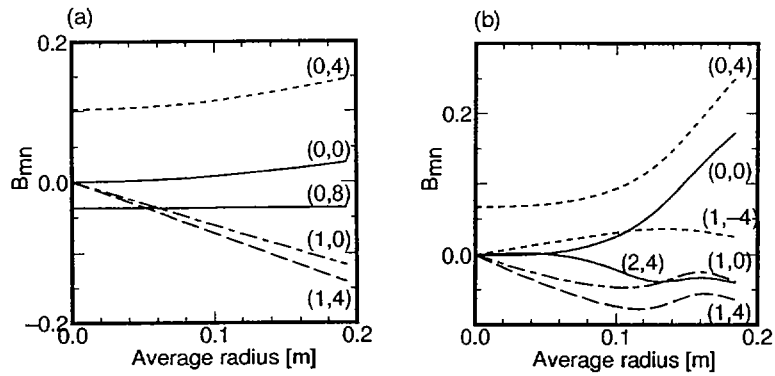

FIG. 3. Magnetic spectrum of the $\ell = 1$ stellarator with four periods in Boozer co-ordinates: (a) $\langle\beta\rangle = 0\%$ and (b) $\langle\beta\rangle = 4.5\%$. The numbers in parentheses are the poloidal (m) and toroidal (n) mode numbers, where the order is opposite to that in Fig. 5.

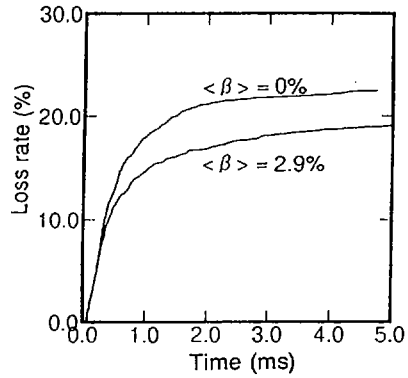

FIG. 4. Time evolution of the loss rate for 1 keV protons started at $\bar{r}/\bar{a} = 0.5$ for $\langle\beta\rangle = 0\%$ and 2.9%.

shows the vacuum magnetic spectrum in the Boozer co-ordinates. This vacuum configuration corresponds to $\epsilon_b/\epsilon_h \approx -1.2$ and $\epsilon_t/\epsilon_h \approx 0.84$ in Fig. 1. The magnetic spectrum for the finite β configuration in Fig. 3(b) is still simple and similar to that in Fig. 3(a). The change of the (0, 0) component is favourable for improving the particle confinement. A magnetic well exists in the whole plasma region even at zero β, and the Mercier criterion is satisfied up to $\langle\beta\rangle \approx 4.5\%$ for a fairly broad pressure profile, where $\langle\beta\rangle$ is volume average β. The Shafranov shift is 43% of the minor radius at this β. The obtained configuration has new characteristics. The magnetic shear is enhanced in finite β plasmas and the magnetic spectrum is controlled by the change of current ratio between the $\ell = 1$ helical coil and the toroidal coils. The bumpy field is also controllable by fixing the average toroidal field. With the flexibility of the magnetic spectrum, magnetic well depth and the efficiency of high energy particle confinement are varied.

For studying confinement of trapped α particles, particle orbits are followed in the Boozer co-ordinates. The loss rates of 1 keV protons uniformly distributed in velocity space and real space (at $\bar{r}/\bar{a} = 0.5$) are shown in Fig. 4. At zero β and $\rho_i/R = 2 \times 10^{-3}$, almost all trapped particles ($\sim$22%) are lost when they are started at the half-radius; however, trapped particle confinement is improved with the increase of β. Here ρ_i is the ion Larmor radius and R is the major radius. Since ignition will start in the phase of sufficiently high β, this property is favourable for α particle confinement. At $\langle\beta\rangle \simeq 2.9\%$ and $\rho_i/R = 2 \times 10^{-3}$ the particle loss becomes about 19% when the particles are started at the half-radius. It is noted that $\rho_i/R = 2 \times 10^{-3}$ corresponds to 53 keV protons in W7-X.

1.3. Summary

It has been shown that the bumpy field in the $\ell = 1$ helical system plays a significant role in improving the particle confinement. The configuration shown in

Fig. 2 may satisfy design requirements for both good high energy particle confinement and high β limit. In order to realize a compact stellarator reactor with a reasonable magnetic field, ρ_i/R about a factor of 2 larger is favourable. Optimization of high energy trapped particle confinement is progressing with control of the bumpy field.

2. COLLISIONLESS PARTICLE CONFINEMENT IN A PITCH MODULATED $\ell = 1$ TORSATRON

(M. Aizawa, K.H. Saito, K.N. Saito, I. Kawakami, S. Shiina)

2.1. Introduction

A large helical excursion of the magnetic axis in a heliac creates a deep magnetic well but a large magnetic island with no external control. The former leads to a high stability β limit (β_{st}) and the latter to an extremely low equilibrium β limit ($\beta_{eq} \ll \beta_{st}$) because of the magnetic surface disruption [8]. Thus it is necessary to suppress the magnetic island associated with the increase of β by external control. The compact $\ell = 1$ torsatron now under consideration has a relatively small helical excursion of the magnetic axis but a high magnetic shear and also a local magnetic well owing to its modifications [9, 10]. It is found that the β limit due to the magnetic island is much higher because of the larger field period number in the compact $\ell = 1$ torsatron [11]. The compact $\ell = 1$ torsatron has some advantages over other stellarators. In addition to the simple coil structure and a local magnetic well keeping a positive magnetic shear, the negative pitch modulation of the coil winding law leads to a nearly complete collisionless particle confinement.

2.2. Collisionless particle confinement in the compact $\ell = 1$ torsatron

We are seeking the best pitch modulation parameter in order to optimize the confinement and to approach a quasi-helically symmetric configuration, which is characterized by $B = B(\psi, \theta - N\phi)$ and in which the helical symmetry leads to complete collisionless particle confinement. Here ψ is the flux and θ, ϕ are the poloidal and toroidal angles, respectively; N (= 17 in our case) is the period number of the magnetic field. The strength of the magnetic field in magnetic co-ordinates (ψ, θ, ϕ) is represented by its Fourier components $A_{n,m}(\psi)$ as follows

$$B(\psi, \theta, \phi) = A_{0,0}(\psi) + 2 \sum_{n,m \neq 0} A_{n,m}(\psi) \cos(n\phi - m\theta)$$

$$\approx A_{0,0}(\phi)[1 - \epsilon_t(\psi) \cos \theta + \epsilon_L(\psi) \cos(17\phi - \theta) + \epsilon_{L-1}(\psi) \cos 17\phi]$$

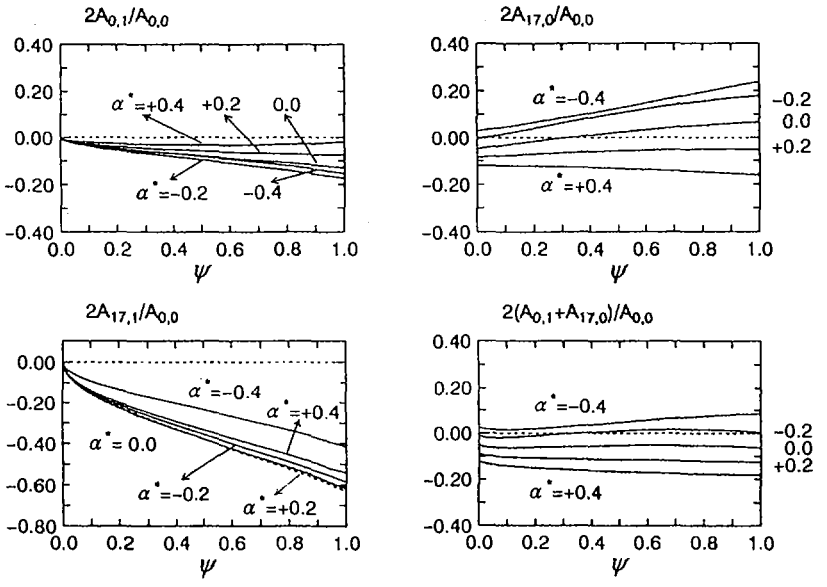

FIG. 5. Fourier components $A_{n,m}$ of the vacuum field B (~4.4 T on the axis) in magnetic co-ordinates for the $\ell = 1$ torsatron with field period number $N = 17$ and plasma aspect ratio $R/a \approx 7.5$, as functions of flux ψ and coil pitch modulation parameter α^*.

where we define $\epsilon_l(\psi) \equiv -2A_{0,1}(\psi)/A_{0,0}(\psi)$, $\epsilon_L(\psi) \equiv 2A_{17,1}(\psi)/A_{0,0}$, and $\epsilon_{L-l}(\psi) \equiv 2A_{17,0}(\psi)/A_{0,0}(\psi)$. Each term $A_{n,m}$ can be determined numerically in an automatic manner by following the field line. Figure 5 shows the three relatively large components normalized by $A_{0,0}$. The $A_{0,1}$ term is the fundamental toroidal harmonic and is due to the toroidal curvature, and the helical curvature term $A_{17,1}$ gives rise to the helical symmetry axis of the system. The satellites of the toroidal harmonic are negligible, except for the satellite of the poloidal harmonic $A_{17,0}$. These Fourier components are compared for different values of the coil pitch modulation parameter α^*; the coil winding law is $\theta = N\phi + \alpha^* \sin N\phi$. The negative pitch modulation ($\alpha^* < 0$) strengthens the good local curvature of the magnetic lines of force and makes a local magnetic well [9, 10]. The absolute value of $A_{17,1}$ is the largest component for any α^* except in the magnetic axis region. The term $A_{0,1}$ has a negative sign and its absolute value $|A_{0,1}|$ becomes larger for $\alpha^* < 0$ and smaller for $\alpha^* > 0$. The term $A_{17,0}$ has a negative sign for $\alpha^* > 0$ and a positive sign for $\alpha^* < 0$, and its absolute value $|A_{17,0}|$ increases with increasing $|\alpha^*|$. This fact suggests an approach to a quasi-helically symmetric configuration, for $\alpha^* = -0.2$, which is associated with the significant reduction of the effective toroidal curvature term ϵ_T defined as $-2(A_{0,1} + A_{17,0})/A_{0,0}$ for trapped particles (see Fig. 5) [12]. To confirm these predictions, the particle orbits are calculated by solving the drift Hamilton's equations in Boozer's magnetic co-ordinates. The confined particle number depends on α^*, so that it is larger in the case of $\alpha^* < 0$ than in the case of

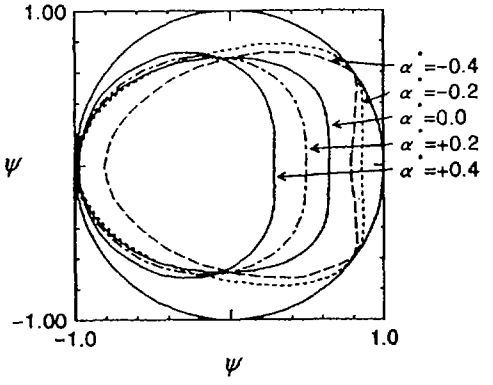

FIG. 6. B_{min} contours in a pitch modulated $\ell = 1$ torsatron, showing the largest area in the case of $\alpha^* = -0.2$.

$\alpha^* > 0$. It is noticed that the deeply trapped particles having $v_{\parallel} \approx 0$ are all confined for $\alpha^* \leq 0$ cases. The confined particle fraction for particles started at aspect ratio A ($\equiv R/r_{start}$) = 15 averaged over starting θ (velocity pitch angle) is 97.5% for particle energy E_k = 100 keV in the case of $\alpha^* = -0.2$. The observed 100 keV proton confinement is comparable to that for an α particle started at A = 40 in W7-X. The nearly complete collisionless particle confinement observed in the case of $\alpha^* = -0.2$ suggests an approach to a quasi-helically symmetric configuration. In order to test the theoretical explanation, the observed orbits are compared with the theory based on the longitudinal adiabatic invariant $J = \int v_{\parallel} d\ell$ [13]. According to the theory, the fraction of particles of a given pitch having transitional orbits as well as the fraction of particles with passing orbits are proportional to the ratio ϵ_t/ϵ_L. Indeed, the observed α^* dependence of the passing particle fraction is qualitatively consistent with the theory. Thus, the $\ell = 1$ torsatron with $\alpha^* < 0$ has advantages over that with $\alpha^* \geq 0$ because of the increased fraction of passing particles. Furthermore, in the case of $\alpha^* = -0.2$ with smaller ϵ_t/ϵ_L than in the case of $\alpha^* = -0.4$, the observed confinement of trapped particles is best in accordance with the smallest ϵ_T, and the area of the closed B_{min} contours which give the locus of the most deeply trapped orbits and the topological 'goodness' criterion is the largest, as seen in Fig. 6.

3. SUMMARY

The negative pitch modulation with $\alpha^* = -0.2$ enhances the fraction of passing particles and simultaneously improves the confinement of trapped particles owing to the reduction of the effective toroidal curvature term ϵ_T. The significant reduction

of ϵ_T also leads to a favourable neoclassical diffusion coefficient. These novel features are encouraging for the development of the stellarator concept as a steady state fusion reactor.

REFERENCES

[1] TODOROKI, J., et al., in Plasma Physics and Controlled Nuclear Fusion Research 1988 (Proc. 12th Int. Conf. Nice, 1988), Vol. 2, IAEA, Vienna (1989) 637.
[2] MYNICK, H.E., CHU, T.K., BOOZER, A.H., Phys. Rev. Lett. **48** (1982) 322.
[3] KATO, A., NAKAMURA, Y., WAKATANI, M., J. Phys. Soc. Jpn. **60** (1991) 494.
[4] NÜHRENBERG, J., ZILLE, R., Phys. Lett. **A129** (1988) 113.
[5] SHAING, K.C., HOKIN, S.A., Phys. Fluids **26** (1983) 2136.
[6] GRIEGER, G., et al., Phys. Fluids B **4** (1992) 2081.
[7] YOKOYAMA, M., NAKAMURA, Y., WAKATANI, M., Nucl. Fusion **34** (1994) 288.
[8] REIMAN, A.H., BOOZER, A.H., Phys. Fluids **27** (1984) 2446.
[9] KIKUCHI, H., et al., J. Phys. Soc. Jpn. **58** (1989) 511.
[10] KIKUCHI, H., et al., J. Phys. Soc. Jpn. **58** (1989) 2779.
[11] AIZAWA, M., et al., in Plasma Physics and Controlled Nuclear Fusion Research 1992 (Proc. 14th Int. Conf. Würzburg, 1992), Vol. 2, IAEA, Vienna (1993) 439.
[12] AIZAWA, M., et al., in Controlled Fusion and Plasma Physics (Proc. 22nd Eur. Conf. Bournemouth, 1995), Vol. 19C, European Physical Society, Geneva (1995) 189.
[13] SMIRNOVA, M.S., SHISHKIN, A.A., Nucl. Fusion **32** (1992) 1147.

MAGNETIC CONFIGURATION SCANS IN THE TJ-I UPGRADE TORSATRON

A. ASCASIBAR, M.A. OCHANDO, C. ALEJALDRE, J. ALONSO,
R. BALBIN, B. BRAÑAS, A. CAPPA, F. CASTEJON, T. ESTRADA,
A. FERNANDEZ, M. FRANCES, C. FUENTES, I. GARCIA-CORTES,
M. GARCIA, J.M. GUASP, J. HERRANZ, C. HIDALGO, J.A. JIMENEZ,
V. KRIVENSKI, M. LINIERS, A. LOPEZ-FRAGUAS, E. DE LA LUNA,
R. MARTIN, K. McCARTHY, F. MEDINA, B. VAN MILLIGEN,
I. PASTOR, M.A. PEDROSA, J. QIN, L. RODRIGUEZ RODRIGO,
A. SALAS, E. SANCHEZ GONZALEZ, J. SANCHEZ-SANZ,
F. TABARES, D. TAFALLA, V. TRIBALDOS, J. VEGA,
V. ZHURAVLEV, B. ZURRO
Asociación Euratom-CIEMAT para Fusión,
Madrid, Spain

D.K. AKULINA, O.I. FEDYANIN, S.E. GREBENSHCHIKOV,
N.K. KHARCHEV, L.V. KOLIK, L.M. KOVRIZHNYKH,
K.M. LIKIN, A.I. MESHCHERYAKOV, Yu.I. NECHAEV,
A.E. PETROV, K.A. SARKSYAN, I.S. SBITNIKOVA
General Physics Institute,
Russian Academy of Sciences,
Moscow, Russian Federation

N.V. MATVEEV, B.M. RASSADIN
Electrotechnical Center,
Istra, Moscow Region, Russian Federation

E.M. TAI
Salut,
Nizhnij Novgorod, Russian Federation

Abstract

MAGNETIC CONFIGURATION SCANS IN THE TJ-I UPGRADE TORSATRON.

ECRH plasmas have been produced over the whole flexibility domain of the TJ-I Upgrade torsatron (ℓ = 1 m, m = 6, R = 0.6 m, $\langle a \rangle$ = 0.1 m, B = 0.5–0.67 T) in order to investigate the effect of magnetic configuration on plasma parameters. The rotational transform ($\iota(0)$ varies from 0.4 to 0.13) and the magnetic ripple were changed by shifting the position of the magnetic axis. As expected, confinement degradation is observed for iota values close to 1/3, but also a decrease in energy content is observed in the lower iota region. The experimental results are discussed in terms of the different fractions of trapped particles present for each configuration and in terms of the different fractions of power absorbed by thermal and superthermal electrons.

1. INTRODUCTION

During the most recent experimental campaign the TJ-I Upgrade torsatron ($\ell = 1$ m, m = 6, R = 0.6 m, $\langle a \rangle = 0.1$ m, B = 0.5–0.67 T) [1] has been operated in modes and regimes that are as close as possible to those expected for the lowest density regime in the ECRH phase in the TJ-II flexible heliac [2]. The relatively wide flexibility domain of the TJ-I Upgrade has been explored to investigate the effect of the magnetic configuration on plasma parameters. Plasmas have been produced and heated by injecting $\approx$200 kW of ECRH power at 37.5 GHz (X mode, second harmonic, pulse length $\approx$20 ms). For the series of discharges analysed here, typical line average electron densities were about (0.2–0.5) $\times$ 10^{19} m^{-3}, and central electron temperatures lay in the range of 100–200 eV. Ray tracing calculations predict single pass absorption of about 20% for standard plasmas; therefore, absorption by superthermal electrons can be expected for high magnetic fields. Although the runaway electrons generated during magnetic field ramp-up and ramp-down were controlled by using appropriate gas puffing rates [3], during ECR plasma production and heating, moderate to high hard X ray fluxes are detected. Correlations have been found between the detailed time evolution of these X ray signals and average density, radiative electron temperature profile and total plasma current, which depend on the magnetic structure, i.e. the rotational transform and the magnetic ripple. In this report, we present the latest results obtained on the TJ-I Upgrade when the magnetic configuration is varied from $\iota(0) \approx 0.4$ to 0.13; this is done by means of magnetic axis displacements of $\pm$3 cm about the centre of the vacuum vessel by controlling the ratios between the helical, external and internal vertical fields. In this range of configurations, the magnetic ripple on the axis decreases when the plasma is shifted inwards (low iota) and increases when the plasma is shifted outwards (high iota).

2. EXPERIMENTAL RESULTS

The specific diagnostic set-up used for the experiments presented here (see Fig. 1) consists of: a Si(Li) detector viewing a plasma radial chord through a beryllium filter of 105 μm at an equivalent toroidal angle $\Phi = 30°$; a NaI(Tl) detector observing the plasma through a glass window, either almost tangential or near perpendicular at $\Phi = 30°$, two NaI(Tl) detectors working in current mode for monitoring the average total hard X ray (HXR) flux; an absolutely calibrated multichannel heterodyne radiometer, covering the 40–45 GHz frequency band and located at $\Phi = 0°$, a five channel charge exchange neutral atom spectrometer viewing the plasma perpendicularly at $\Phi = 30°$; several vertical flux loops encircling an upper port at $\Phi = 10°$, for measuring the magnetic field of the Pfirsch–Schlüter currents; two compensated diamagnetic loops at $\Phi = 20°$ and 30°, for evaluating the perpendicular plasma energy content; and a 1 m monochromator with a fast rotating polygonal mirror, for obtaining line integrated profiles of impurity radiation at $\Phi = 30°$.

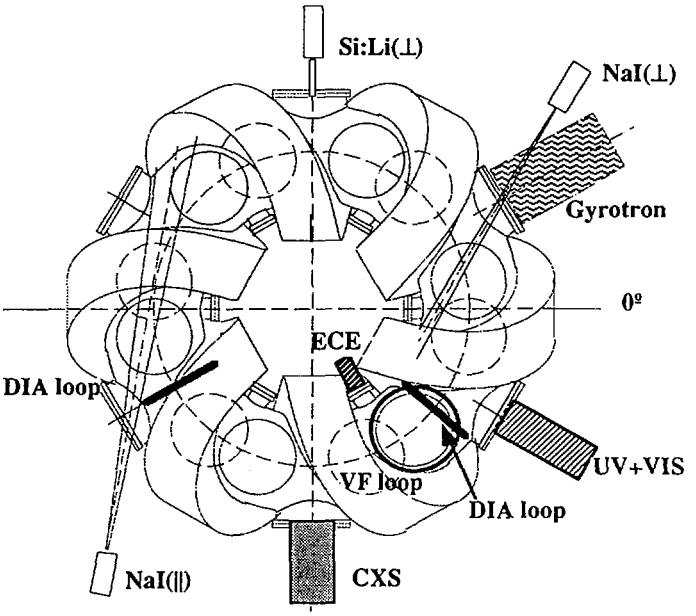

FIG. 1. TJ-I Upgrade experimental set-up. DIA loop: diamagnetic loop; ECE: electron cyclotron emission; VF loop: vertical flux loop; CXS: charge exchange spectroscopy; UV + VIS: ultraviolet and visible spectroscopy.

The time behaviour of the HXR fluxes when compared to the density evolution provides evidence for the two sources of superthermal electron generation in this machine, perpendicular diffusion in momentum space caused by EC waves [4] and enhanced electron acceleration when the collisionality decreases. Figures 2(a) and (b) illustrate this. For a given configuration, the HXR flux increases as the electron density does until the plasma transparency falls to zero. A sudden drop in this signal is then accompanied by drops in all signals from thermal monitors.

This means that the superthermal electron population is built up almost at the same time as the thermal one, by direct absorption on the high field side. When the density cut-off is reached, absorption by either thermal or superthermal electrons no longer takes place. On the other hand, when the density diminishes from a stable condition, an increase in the flux of high energy photons can be detected while the signals of the other monitors fall drastically. This resembles the standard 'tokamak-like' behaviour of high energy electrons associated with a decrease in collisionality. However, in the present case the increase in the HXR flux is highly enhanced because of absorption by fast resonant electrons as the plasma transparency increases. To characterize the fast resonant electron populations for each configuration, soft and hard X ray spectra have been recorded, using Si(Li) (1–30 keV) and NaI(Tl) (over

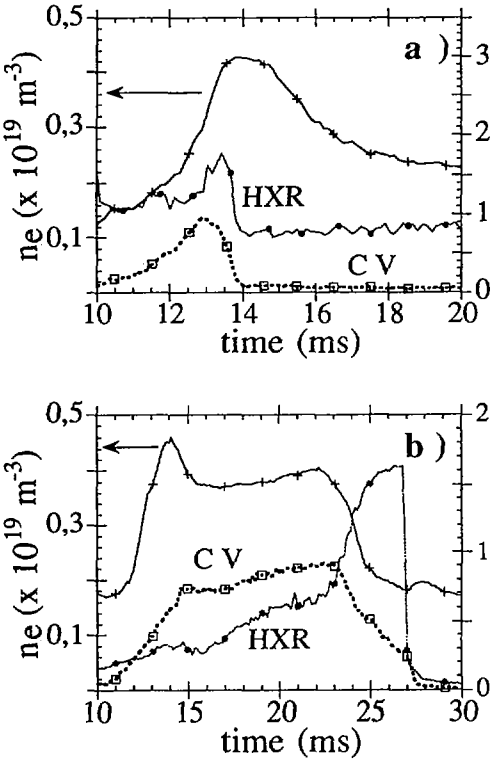

FIG. 2. Time evolution of hard X ray flux signal compared to mean electron density evolution: (a) cut-off density reached at about 13.5 ms; (b) gas puff shut down at 21 ms. For comparison with thermal signals, the 227.1 nm C V line emission is also shown.

20 keV) detectors, for series of repeated discharges (Fig. 3). Evaluation of the energy contained in the high energy tails of the bremsstrahlung intensity spectra allows us to estimate that, for example, the second electron tail of shots with $\iota(0) \approx 0.14$ contains up to 15 times more energy than its equivalent in discharges with $\iota(0) \approx 0.23$.

As was mentioned above, a significant part of microwave power is available for faster resonant electrons on the high field side of the machine. The electron cyclotron emission spectra measured with the multichannel heterodyne radiometer are strongly distorted because of the existence of these fast energy electrons whose EC emission appears downshifted to lower frequencies. From multifilament magnetic field calculations, the thermal plasma emission, for the $\iota \approx 0.23$ magnetic configuration, is expected to cover the range of 42–44.7 GHz, the plasma centre corresponding to 43 GHz. However, as shown in Fig. 4(a), the profile extends to EC frequencies well below 42 GHz. As displayed in Fig. 4(b), the resonant electrons responsible for the

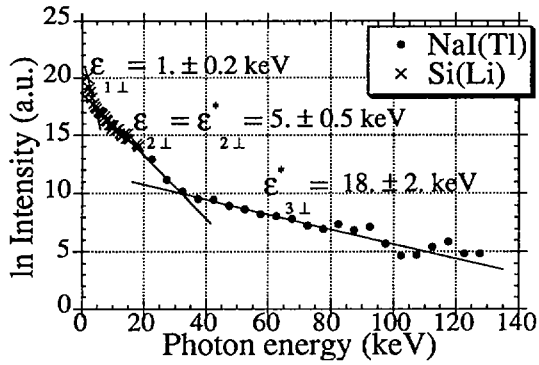

FIG. 3. Full range perpendicular bremsstrahlung from plasmas with ι(0) ≈ 0.23. The characteristic energies for the suprathermal electrons are denoted by ε (obtained from NaI detector) and ε (from Si(Li) detector).*

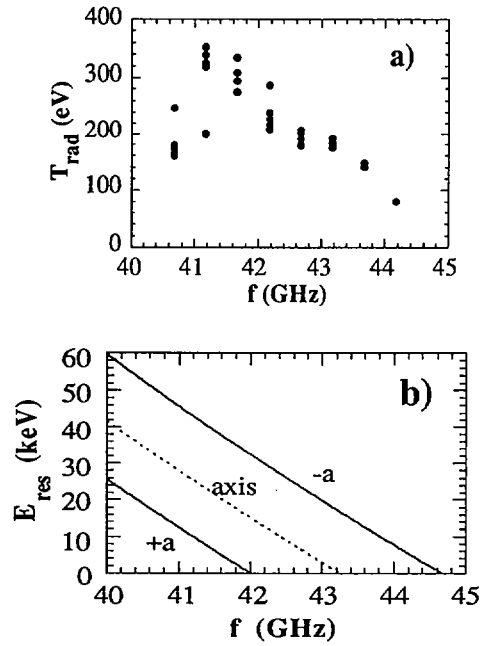

FIG. 4. (a) Emission spectra (radiative electron temperatures) measured on a shot to shot basis, for ι(0) ≈ 0.23 discharges; (b) resonant energies for plasma edges and axis versus frequency.

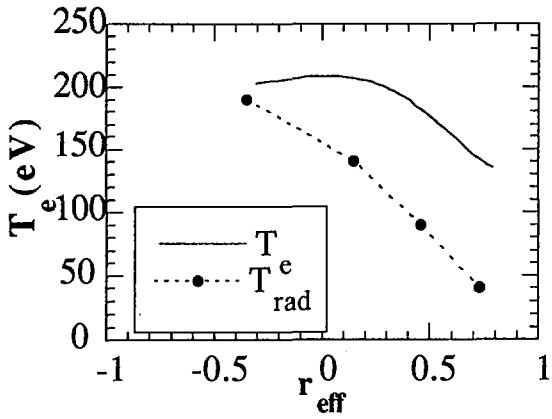

FIG. 5. Reconstruction of electron temperature profile (solid line) with experimental data (dots).

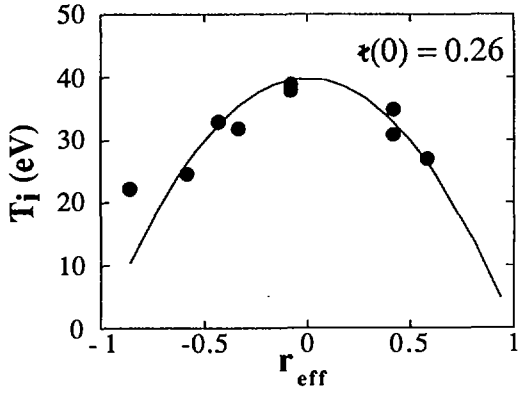

FIG. 6. Radial profile of ion temperature.

emission peak at 41.5 GHz should have energies in the range 5 to 20 keV, which is in full agreement with X ray observations (see Fig. 3). Since the plasma is optically thin for the operating conditions, the radiative temperature is no longer the electron temperature; therefore, we have developed a method to reconstruct the electron temperature profile from the EC emissions [5]. Using this method, we have reconstructed the part of the temperature profile which corresponds to the frequency range not influenced by superthermal electrons (shown in Fig. 5). For lower central iota configurations, the intense downshifted emission from superthermal electrons almost saturates the detectors; thus no reliable electron temperature profile can be reconstructed. On the other hand, in plasmas with a central rotational transform approaching the 1/3 rational value, the thermal electron temperature drops by up to a factor of five.

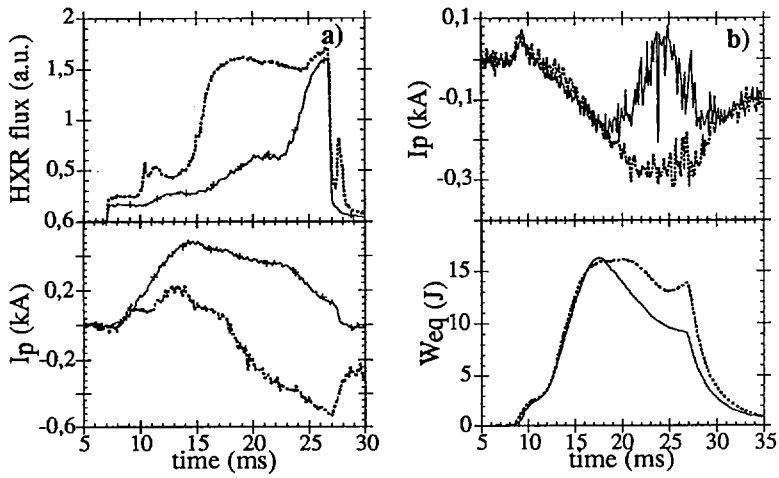

FIG. 7. (a) Hard X ray flux and net plasma current for two shots with $\iota(0) \approx 0.23$ (solid line) and $\iota(0) \approx 0.18$ (dots); (b) effect of changes of plasma current on W_{eq} ($\iota(0) \approx 0.19$).

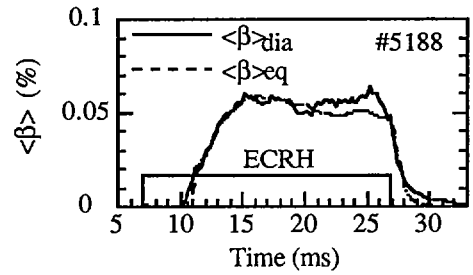

FIG. 8. Measured $\langle\beta\rangle_{dia}$ and $\langle\beta\rangle_{eq}$ in TJ-IU.

In TJ-I Upgrade, the ion temperature radial profile, as deduced from energy spectra produced by charge exchange neutrals, can be described by $T_i(r) \approx T_i(0)$ $[1-(r/a)^2]$. However, depending on the plasma density, non-Maxwellian distributions may also be clearly detected (Fig. 6). $T_i(0)$ ranges from $\approx$70 to 20 eV for magnetic configurations with $\iota(0) \approx 0.32$ to 0.18. When $\iota(0) \leq 0.18$ the profile falls and becomes almost flat. For configurations with the highest ion temperatures, up-down asymmetries have been observed in the spectra for measurements performed at a location in the device where the fraction of trapped particles is maximum. Since this asymmetry reverses when the magnetic field is reversed this fact might be explained in terms of the drift of trapped ions.

Also, the Rogowski coil and all vertical flux loop signals reflect the presence of fast passing electrons. There is a clear correlation between the HXR flux and the

total plasma current, and substantial changes with the magnetic configuration (and electron density) are observed: the lower the iota value (or the lower the electron density for a given magnetic configuration), the higher the HXR flux and the smaller the current, which even changes sign (Fig. 7(a)). In Fig. 7(b), the effect of a sudden change in plasma current on the equilibrium plasma energy (W_{eq}) can be seen, as is deduced from the measurement of the magnetic flux generated by the parallel (Pfirsch-Schlüter) current, $J_{\parallel}$ [6], for a configuration with $\iota(0) \approx 0.16$. For this configuration, W_{eq} does not coincide with the energy content estimated with the diamagnetic loop (W_{dia}). As will be discussed below, this fact may be attributed to non-isotropic pressure profiles to which only W_{dia} measurements are insensitive [7].

For magnetic configurations with $\iota(0) \approx 0.23$, however, both methods yield very similar results, as is shown in Fig. 8. As a general rule, for discharges with the same input power and nearly the same average electron density, the energy content of the thermal plasma is a factor of 2 to 3 lower for $\iota(0) \approx 0.16$ than for $\iota(0) \approx 0.23$. When the central iota is close to 1/3, extremely low quality plasmas are obtained.

3. DISCUSSION

It is well known that in shearless stellarators confinement shows a notable degradation when the rotational transform is close to any low order resonant value. Nevertheless, from the results of the magnetic configuration scan presented here, it can be concluded that there seem to be other causes for the decrease of the energy content in the lower iota plasmas of the explored region ($0.15 \leq \iota(0) \leq 0.18$). A possible explanation for this observation could be related to the fraction of trapped particles present in each magnetic configuration. In our device, the magnetic ripple near the plasma centre decreases as iota decreases and therefore the fraction of trapped particles diminishes. It is also well established that the efficiency of the current generated by the EC waves increases as the number of trapped particles present in a plasma decreases, and that this electron cyclotron current drive (ECCD) could lead to local changes in the net plasma current [8]. Even though iota would remain relatively far from a low resonant value, these eventual changes in amplitude and even in sign of the currents can have either beneficial or detrimental effects on plasma confinement, depending on the magnitude of the local shear they produce, which may enhance or decrease transport. Recently [9] the magnetic turbulence in some tokamaks has been characterized by the shape of HXR spectra. A preliminary analysis applying this method to our experimental data indicates that the average radial extent of the magnetic turbulence is larger for lower iota configurations, and so the transport could be enhanced. Another explanation can simply be expressed in terms of plasma transparency. Although the radial profile of the electron density was not available for these experiments, it was determined that the density peaking factor decreases as the rotational transform decreases. To compare the plasma performance in different configurations we have used discharges with the same average electron

density, which would mean that the central density is lower for the lower iota configuration. Therefore, in the latter case, thermal resonant electrons would be fewer and thermal absorption lower. On the other hand, a higher number of fast resonant electrons would have more power available, giving rise to a more energetic population of superthermal electrons, as is shown by our results. Rough estimates of the absorbed power by thermal electrons point out that there is a notable loss of heating efficiency as iota goes from 0.26 to 0.18.

The present studies in the TJ-I Upgrade torsatron are of relevance for TJ-II when exploring plasma properties in the lowest density region of its operational domain. In this sense, it is worthwhile to study the characteristics of the high energy tails and their dependence on magnetic structure and pressure profile, in order to try to establish whether or not fast electrons can account for a non-negligible amount of absorbed power (part of the missing power?) and the role of magnetic turbulence in stellarator transport. More studies on this subject are in progress.

REFERENCES

[1] ASCASIBAR, E., et al., Trans. Fusion Technol. **27** (1995) 198.
[2] ALEJALDRE, C., et al., Fusion Technol. **17** (1990) 131.
[3] ASCASIBAR, E., et al., in Plasma Physics and Controlled Nuclear Fusion Research 1994 (Proc. 15th Int. Conf. Seville, 1994), Vol. 1, IAEA, Vienna (1995) 749.
[4] FIDONE, I., et al., Phys. Fluids **26** (1983) 3292.
[5] TRIBALDOS, V., et al., Plasma Phys. Control. Fusion (in preparation).
[6] QIN, J., et al., Nucl. Fusion **36** (1996) 381.
[7] QIN, J., et al., in Controlled Fusion and Plasma Physics (Proc. 23rd Eur. Conf. Kiev, 1996), Vol. 20C, European Physical Society, Geneva (1996).
[8] CASTEJON, F., et al., Phys. Fluids **4** (1992) 3689.
[9] RODRIGUEZ-RODRIGO, L., et al., Phys. Rev. Lett. **20** (1995) 3987.

RESISTIVE SHELL OPERATION AND CONFINEMENT IN THE EXTRAP T2 RFP

J.R. DRAKE, H. BERGSÅKER[1], P.R. BRUNSELL,
J.H. BRZOZOWSKI, T. FALL[2], E. GERHARD, G. HEDIN,
A. HEDQVIST[2], G. HELLBLOM, S. HOKIN, P. HÖRLING[2],
D. LARSSON[1], A. MÖLLER, E. RACHLEW-KÄLLNE[2],
J. SALLANDER[2], M. TENDLER, E. TENNFORS,
A. WELANDER
Division of Fusion Plasma Physics,
Alfvén Laboratory,
Euratom-NFR Association,
Royal Institute of Technology,
Stockholm, Sweden

Abstract

RESISTIVE SHELL OPERATION AND CONFINEMENT IN THE EXTRAP T2 RFP.

The effect of resistive shell modes (RSMs) on reversed-field pinch (RFP) operation has been studied on the EXTRAP T2 device. The T2 shell has a magnetic penetration time of 1.5ms and pulses are sustained for about ten shell times. Magnetic diagnostics have been used to measure the mode dynamics. Toroidally localised magnetic perturbations that penetrate the shell are observed. They grow and decay on the shell time-scale but have very small rotation frequencies and are essentially stationary toroidally. Fourier analysis of the mode structure shows that the localised perturbations consist of internally resonant modes with poloidal mode number m=1 and toroidal mode numbers in the range n=10-16. The perturbations can cause a degradation of the pulse primarily through impurity release due to localised plasma wall interaction. In addition to this stationary RSM, m=0 perturbations, associated with the dynamo activity, are observed. These modes rotate in the electron diamagnetic drift direction with velocities of 20-30kms^{-1}. Measurements of the characteristic parameters modelling the parallel current profile indicate that T2 operates close to the marginal linear stability limit for an ideal shell RFP. The operation parameters are in the same range as those measured for conducting shell RFPs, despite the fact that the configuration has a resistive shell and RSMs are observed.

1. INTRODUCTION

The RFP configuration has a conducting-shell boundary to stabilise MHD modes. However the dynamo and relaxation processes which determine the current profile equilibrium are dependent on internal tearing modes, and Taylor RFPs intrinsically operate at the marginal stability limit. According to linear theory, this limit is dependent on the resistivity of the shell and the distance to the shell. Based on large experimental experience, the equilibrium

[1] Department of Physics Frescati, Royal Institute of Technology, Stockholm, Sweden.
[2] Department of Physics I, Royal Institute of Technology, Stockholm, Sweden.

should be centred and the last closed flux surface concentric with the plasma-facing wall and close to the shell for optimal operation. A general observation is that deviations from the ideal configuration result in higher fluctuation levels and degraded confinement. The modes are necessary for relaxation, but the associated fluctuation level increases transport and should therefore be as small as possible.

A resistive shell mode (RSM) is defined as a mode that is stable when an ideal shell is present but becomes unstable when shell resistivity is introduced. The growth rate is determined by the magnetic penetration time, τ_w, of the shell. There is a conflict between the need for radial equilibrium control by an external vertical field (short τ_w) and the need for the best stability properties provided by a conducting shell (long τ_w). Therefore possible stabilising effects on RSMs that may be produced by mode rotation with a resistive shell are vital for the RFP configuration [1,2]. There are two types of resistive shell modes that are regarded as most important for the RFP configuration; internal, resonant, tearing modes and external, nonresonant, ideal kink modes. Linear stability theory indicates that the former can be stabilised by sub-Alfvénic mode rotation where the latter cannot.

Previous experimental work on resistive shell RFPs, HBTX-1C [3] and OHTE [4], resulted in some differences in observations. In HBTX-1C, the magnetic fluctuation levels of the dynamo modes were higher, the non-Spitzer loop voltage associated with driving the dynamo was higher and confinement was degraded as compared to conducting shell operation on the same device. The pulses terminated after a few shell times apparently due to resistive shell mode growth. Preliminary observations on OHTE, with a resistive shell indicated that the negative effects were less evident than in HBTX-1C, and the discharges were sustained for up to ten shell times. The OHTE experiment is now in operation as the T2 experiment in Stockholm [5] and resistive shell effects have been investigated in more detail.

Rotation of non-interacting tearing modes is expected to be in the electron diamagnetic drift direction, but a viscous drag force on the helical perturbation due to plasma flow can alter the propagation velocity. On the other hand, mode propagation is hindered by wall locking due to forces on the perturbations produced by interaction with magnetic field errors. Mode rotation or wall locking is determined by the balance equation between the forces inducing rotation and the electromagnetic force from the field error locking the mode [6, 7]. Flow can thus provide tearing mode rotation and in turn improve stability if the shell is resistive. Any change in the current profile equilibrium can produce a field error, due to shell imperfections, causing wall locking. There can be a secondary negative effect if this locking eliminates potential stabilising effects of rotation on RSMs leading to unstable growth.

The effects of rotation or wall locking on RSMs can also be of importance for tokamak confinement. It is important to relate RFP phenomena to tokamak phenomena in this area in order to exploit the potential for better understanding through cross-configuration studies. Mode-mode interaction and interaction between the mode and externally produced magnetic fields, specifically in connection with wall locking, are important physics areas for both the RFP and tokamak configurations.

2. EXPERIMENTAL RESULTS

EXTRAP T2 is a medium-size reversed-field pinch with high aspect ratio, R/a =1.24/0.183 m = 6.8. The first wall is protected by a full cover of graphite tiles and there are no discrete limiters. It has a resistive shell with τ_w=1.5ms, which is the current ramp-up time scale but much shorter than the pulse length. Radial equilibrium with a positioning sensitivity of 2mm is provided by an external vertical field. For the experiments described here, the plasma current is up to $I_p \approx 250$kA. The density range is $\langle n_e \rangle = 2\text{-}10 \times 10^{19} m^{-3}$ and the electron temperature range is 100-200eV. The toroidal loop voltage shows a large variation, primarily depending on the condition of the graphite first wall and can vary substantially over the pulse as RSMs develop and associated plasma wall interaction causes impurity release. The loop voltages for uncontaminated shots with good wall conditioning have small loop voltage anomaly factors comparable to conducting shell RFPs.

Direct measurements of resistive shell modes have been made using arrays of magnetic field pick-up coils to study the m=0 and m=1 poloidal harmonics of the magnetic perturbations. The arrays are located outside the shell surface and aimed at RSM studies.

Toroidally localised, radial field perturbations (b_r) are seen in the majority of the discharges. They grow and decay on the τ_w time-scale but have very small rotation frequencies and are essentially stationary toroidally. Fourier analysis of the mode structure shows that the localised perturbation consists of internally resonant modes with poloidal mode number m=1, and toroidal mode numbers in the range n=10-16, which are phase locked. This perturbation type can be interpreted as a wall-locked, resistive shell variation of the well known, internally resonant, mode-mode phase locked perturbation.

Variation in vertical field (B_v) equilibrium control affects the wall locking. Discharges that are not at centre, have large perturbation growth at the gap. The locking is reproducible and the phase of the wall locked perturbation is determined by whether the off-centre shift of the discharge axis was inward (perturbed b_r in direction of B_v) or outward (perturbed b_r in opposing direction of B_v). When the equilibrium position is centred, the perturbation locks at different toroidal positions. Perturbations typically start to grow early in the discharge, when shell eddy current-produced field errors are maximum. The perturbation is also seen as a toroidal asymmetry in the toroidal flux measured both inside and outside the shell, which can be as high as 10%. In some discharges there is saturation and decay of the perturbations. Often there is a correlation of the toroidal position of the perturbation and the observed signals on toroidally distributed impurity line radiation monitors. The impurity influx event also affects global parameters, and there can be a significant increase in plasma resistance leading to a decrease in plasma current. In cases where the perturbation decays, the plasma resistance often decreases and a second period of low resistance is observed. This behaviour is similar to that attributed to the "slinky" mode previously observed on OHTE.

These observations are summarised in Fig. 1. Discharge parameters and magnetic pick-up coil measurements are shown for two discharges. For Case I the plasma current, loop resistance, density and a CV impurity line are quite constant over the flat-top part of the pulse. However for Case II, the

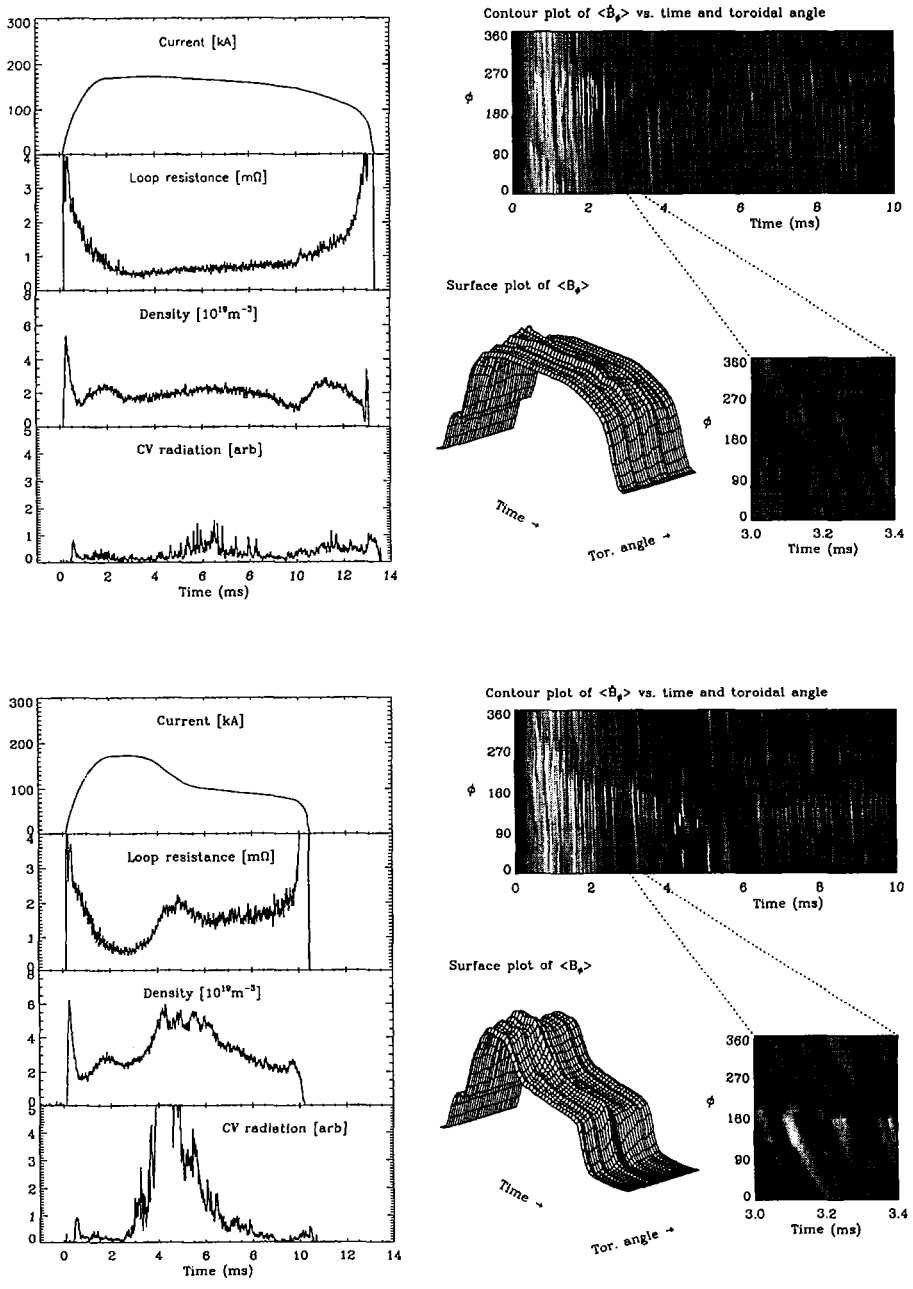

FIG. 1. Discharge parameters (plasma current, loop resistance, density and CV line intensity) and magnetic pick-up coil measurements of $\langle B_\phi \rangle$ and $d\langle B_\phi \rangle/dt$ for two discharges. Case I (top) represents a shot with minimal carbon impurity influx and Case II (bottom) represents a shot with severe influx.

effects of damaging impurity influx are evident in these global parameters. A comparison of the surface plot of the toroidal flux, $<B_\phi>$, for the two cases shows that initially there are toroidal asymmetries for both cases. These measurements are made outside the shell and the asymmetries are the result of RSMs. Initially the difference is small but for Case II the mode grows and an apparent wall load threshold is exceeded leading to major impurity influx. The toroidal flux then decreases substantially as the current decreases.

Surface plots of the (dynamo) poloidal voltage, $d<B_\phi>/dt$, measured with the m=0 loops, versus toroidal position and time are also shown. In experiments, it has been observed that m=0 activity accompanies m=1 tearing mode activity [8]. For example, nonlinear dynamo dynamics can involve three wave coupling of two m=1 modes resulting in a m=0 mode with low toroidal mode number. The plots of $d<B_\phi>/dt$ in Fig. 1 show that m=0 activity coexists with the RSM. It is particularly noteworthy that the m=0 perturbations, which have low n, rotate with phase velocities in the range of 20-30kms^{-1} (~10% of the Alfvén velocity) in the electron diamagnetic drift direction. This rotation occurs despite the presence of the wall locked perturbation.

The surfaces of constant $d<B_\phi>/dt$ versus toroidal position and time are qualitatively quite similar for the two cases although the amplitudes of the perturbations are somewhat larger for Case II. There is also a qualitative observation that the amplitude of the rotating, m=0 perturbation is maximum on the electron diamagnetic drift, down-stream side of the localised RSM perturbation and decreases as it propagates away from the RSM toroidal position. However the general observation is that, although the RSM can affect global performance, particularly if massive impurity release occurs, the underlying dynamo dynamics continues in the presence of the RSM.

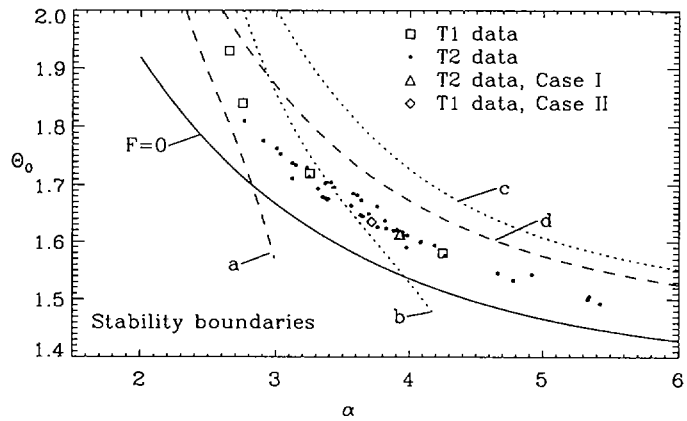

FIG. 2. Stability boundaries for current profile parameters for internal modes based on calculations. Four cases are shown: (a) ideal mode and (b) resistive mode with an ideal shell at the plasma edge, and (c) ideal mode and (d) resistive mode with the shell at infinity [2]. Experimental operation points for EXTRAP T1 (conducting shell [10]) and EXTRAP T2 (resistive shell) are shown.

Further insight into the dynamo and relaxation activity can be gained by examining the characteristic current profile parameters. The global equilibrium profile parameters of T2 have been measured and compared with parameters for conducting shell configurations and with linear stability theory. The results are shown in Fig. 2. In order to discuss stability it is convenient to model the equilibrium by a normalised parallel current profile, $\mu(r) = 2\theta_o/a(1-(r/a)^{\alpha})$ [9]. The instability boundaries in the (α, Θ_o) parameter plane for internal tearing modes have been calculated for an ideal shell at the plasma edge [9] and for a shell at infinity [2]. The latter establish the marginal stability limits for resistive shell modes. For a given Θ_o, the marginally stable current profile is less centrally-peaked (higher α) with a resistive shell. Experimental measurement-based values of (α, Θ_o) for conducting shell experiments have shown that RFPs operate close to the marginal stability boundary with an ideal wall at a given distance outside the plasma edge [10]. Measurements of (α, Θ_o) for T2 discharges are presented in Fig. 2 for a series of discharges with a range of pinch parameter ($1.4<\theta<1.9$) and reversal parameter ($-0.15<F<-0.50$). The two shots presented in Fig. 1 (Case I and Case II) are indicated separately. The values shown are a time average over a 1.5-ms interval around the current peak. For comparison, parameter measurements for EXTRAP T1, a conducting shell experiment, are also shown, calculated using the same routines. The T1 and T2 data overlap, and the operation is close to the ideal-shell stability boundary. These measurements indicate that the T2 equilibria have current profile parameters characteristic for a conducting shell configuration despite the fact that the device has a resistive shell and large RSMs are observed.

3. CONCLUSIONS

The wall locked perturbations and resistive shell perturbations observed on the T2 experiment can lead to intensive local plasma wall interaction which degrades the discharge. However the perturbations can saturate and decay. Although the RSMs are evident, operation of T2 exhibits many similarities in global parameters to conducting shell operation.

- The pulses are sustained for discharges much longer than the shell time.
- The current profile equilibrium parameters (α, Θ_o) lie close to the marginal stability line for an ideal conducting shell RFP.
- The m=0 perturbations associated with nonlinear dynamo activity are observed and rotate apparently coexisting with the RSM.
- The rotation velocity is in the range predicted by theory to have a possible stabilising effect.

ACKNOWLEDGEMENTS

This work was supported by a Contract of Association between EURATOM and the Swedish Natural Sciences Research Board, NFR. The authors wish to acknowledge the vital contributions of the technical staff of the Alfvén laboratory in the construction and operation of the T2 device.

REFERENCES

[1] GIMBLETT, C.G., Nucl. Fusion **26** (1986) 617.
[2] JIANG, Z.X., BONDESON, A., Phys. Plasmas **2** (1995) 442.
[3] ALPER, B., et al., Plasma Phys. Control. Fusion **31** (1989) 205.
[4] GOFORTH, R.R., et al., Nucl. Fusion **26** (1986) 515.
[5] BRUNSELL, P., et al., Europhys. Conf. Abstr. **19C**, Part III (1995) 157.
[6] FITZPATRICK, R., Nucl. Fusion **33** (1993) 1049.
[7] DEN HARTOG, D.J., et al., Phys. Plasmas **2** (1995) 2281.
[8] NORDLUND, P., Phys. Plasmas **1** (1994) 2945.
[9] ANTONI, V., MERLIN, D., ORTOLANI, S., PACCAGNELLA, R., Nucl. Fusion **26** (1986) 1711.
[10] NORDLUND, P., MAZUR, S., Phys. Plasmas **1** (1994) 3936.

INFLUENCE OF EXTERNAL HELICAL PERTURBATIONS ON RFP DYNAMICS

S. MASAMUNE, M. IIDA, N. ODA, K. FUJITSUKA,
M. AWAZU, K. OHTA, H. OSHIYAMA
Department of Electronics and Information Science,
Kyoto Institute of Technology,
Matsugasaki, Sakyo-ku, Kyoto,
Japan

Abstract

INFLUENCE OF EXTERNAL HELICAL PERTURBATIONS ON RFP DYNAMICS.

The plasma response to static external helical perturbations has been investigated in the STE (Separatrix Test Experiment)-2 reversed field pinch (RFP). When perturbations with no resonant surface inside the shell (externally non-resonant) were applied, RFP discharges were improved slightly, with some indication of suppressed mode coupling. On the other hand, RFP discharges resulted in a degradation, with a low level ($\sim 1\%$) of internally resonant perturbations, which have resonant surfaces inside the field reversal. The degradation is shown to be brought about by sufficient overlapping of static and inherent magnetic islands. It has thus been demonstrated that the mode coupling process could be controlled by external helical fields in the RFP.

1. INTRODUCTION

In most of the present reversed field pinches (RFPs), large amplitude MHD fluctuations dominated by core resonant m = 1 tearing modes play a major role both in the sustainment of the RFP (RFP dynamo) and in particle and heat loss mechanisms. Control of the RFP dynamics by MHD stabilization is therefore required for improved confinement in the RFP. It has been demonstrated experimentally that the use of a close fitting shell [1], current profile control [2] and exploration of a new operation regime [3] succeeded in suppressing MHD fluctuations and leading to confinement improvement.

Efforts have been made to study the influence of the boundary conditions on MHD properties in the STE (Separatrix Test Experiment)-2 RFP [4-8]. In this paper, the influence of static helical fields on RFP dynamics (mode coupling process) has been investigated, as a preliminary work to the application of rotating helical fields to the MHD stabilization by plasma rotation [9].

2. EXPERIMENTS

In the STE-2 RFP, we have used a 2 mm thick SS chamber (R/a = 0.4 m/0.1 m) with two insulated poloidal gaps, covered by a 0.5 mm thick (resistive)

shell [4, 6, 7]. Four kinds of helical winding were attached outside the shell, producing quasi-static helical perturbations with m/n $= 1/\pm 8$ and $1/\pm 10$ separately during a discharge, where m and n are the poloidal and toroidal mode numbers of the perturbation field, respectively. Internal field profile measurements [6] showed that the safety factor q was about 0.15 on axis, decreasing to about -0.03 at the edge. The m/n = 1/8 (1/10) field was therefore resonant at r/a ~ 0.4 (~ 0.5) inside the field reversal surface; it will be referred to as internally resonant perturbation. The helical fields with negative n had no resonant surface inside the shell (externally non-resonant).

2.1. Response to externally non-resonant perturbations

Figure 1 shows time evolutions of the plasma current with (m/n = 1/8 perturbation of 1.5% and $1/-8$ of 6.5%) and without helical perturbations. The RFP discharges were slightly improved with the externally non-resonant perturbations applied for a perturbation level $B_{ra}/B_{\theta a}$ of up to 8%, where B_{ra} is the applied radial field and $B_{\theta a}$ the poloidal field at the edge. The improvement mainly resulted from reduced discharge resistance (by 10–20%). The root mean squares edge magnetic fluctuation ($f \geq 8$ kHz) level $|\tilde{B}_{ra}|/B_{\theta a}$ remained almost unchanged around 0.4%.

The edge magnetic fluctuations in the STE-2 were characterized by m = 0 ($f \leq 50$ kHz) and m = 1 ($f \geq 100$ kHz) components [7]. Figure 2 shows the coherence of the edge toroidal fluctuations ($\tilde{B}_\theta$, 100 kHz $\leq f \leq$ 300 kHz), corresponding to the m = 1 component dominant region, as a function of the poloidal length with (m/n = 1/10 perturbation of 3% and $1/-10$ of 8%) and without helical perturbations. The coherence decreases with the poloidal length which, for the edge fluctuations, is regarded approximately as the length along the mean field. Therefore, the e-folding length may provide an estimate of the coherence scale-length $\Lambda_\parallel$, which is determined by the coupling of m = 1 modes and, possibly, also by m = 0 modes [10] and which is a measure of field line stochasticity. $\Lambda_\parallel$ remained almost unchanged or decreased only slightly for the $1/-10$ perturbation. The same tendency was also observed in the m = 0 dominant frequency region.

Phase locking of m = 0 modes, often observed as a localized disturbance of the toroidal magnetic flux near the poloidal gap, was suppressed by externally non-resonant perturbations. Coupling of m = 1 modes might also be suppressed because the observed higher Θ(pinch parameter) tendency is an indication of lower rate conversion from poloidal to toroidal magnetic flux, or of the RFP dynamo, which is caused by m = 1 mode coupling. Although further detailed analysis is required for a consistent explanation of $\Lambda_\parallel$ behaviour, the externally non-resonant perturbations suppressed the mode coupling process, which probably resulted in a slight improvement of the RFP discharges.

External ideal mode (resistive wall mode) stability may also be affected by the helical current; an analysis of this effect is under way.

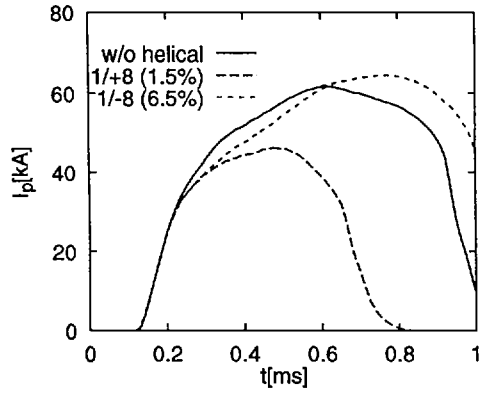

FIG. 1. Time evolution of plasma current with and without helical perturbations.

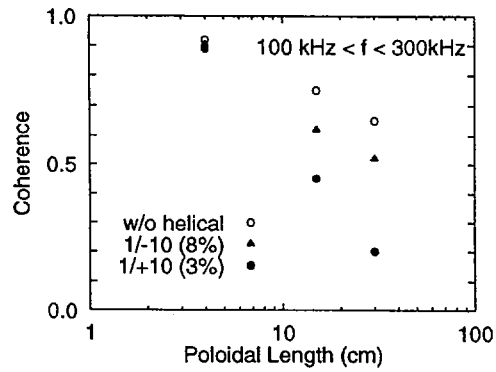

FIG. 2. Coherence of m = 1 dominated edge fluctuations as a function of poloidal length.

2.2. Response to internally resonant perturbations

When an internally resonant perturbation with a level of 1–2% (slightly higher than the inherent fluctuation level associated with m = 1 tearing modes when compared at the edge) was applied, the RFP discharges resulted in a degradation with decreased plasma current, increased loop voltage, and shorter discharge duration, as shown in Fig. 1. The edge magnetic fluctuation level increased by $\lesssim 50\%$, and $\Lambda_\parallel$ decreased, particularly in the frequency region of m = 1 modes, as is shown in Fig. 2. The decreased $\Lambda_\parallel$ is an indication of enhanced m = 1 mode coupling. The enhanced coupling of m = 1 modes is in agreement with the observed lower Θ tendency, which indicates a higher rate conversion of poloidal to toroidal flux. Phase

locking of m = 0 modes was also enhanced in these degraded discharges. The internally resonant perturbations thus enhanced the coupling of both m = 1 and m = 0 modes.

When the m/n = 1/8 perturbation level exceeded ~2%, the RFP configuration could not be sustained for a period longer than 0.2 ms. This critical level for sustained RFP increased up to ~4% for the 1/10 field whose resonant surface was located about 1 cm outside that of the 1/8 field. The difference in the critical levels may be explained by the interaction between static and inherent magnetic islands as will be shown in the following section.

3. MAGNETIC ISLAND IN HELICALLY PERTURBED EQUILIBRIUM

The magnetic island width was calculated in an m = 1 helically perturbed cylindrical RFP equilibrium. In the calculation, free boundary force free equilibrium with uniform $\mu(=j_{\parallel}/B)$ was assumed, and a static m = 1 helical field was taken into account at the plasma-vacuum boundary in the ideal wall with a proximity b/a of 1.05. The magnetic fields were expressed by using the helical flux functions ψ_p in the plasma region and ψ_v in the vacuum region. The ψ_p, ψ_v and $\mathbf{n}\cdot\nabla\psi_p$, $\mathbf{n}\cdot\nabla\psi_v$ were connected, respectively, at the perturbed plasma boundary whose surface normal vector is $\mathbf{n}$. From these matching conditions, we have obtained the relation between magnetic island width and external perturbation amplitude.

Figure 3 shows the calculated island width normalized to a and the perturbation amplitude as a function of Θ. The result shows that the magnetic island width depends weakly upon Θ for a shell proximity of b/a = 1.05 (close fitting shell case). It also shows that an m/n = 1/8 perturbation of 1% amplitude produces an island with a width of 0.1a, which approximately equals the radial distance between neighbouring rational surfaces, while 2% perturbation is required to produce the 1/10 island with the same width. In real RFP plasmas, μ decreases to 0 towards the edge. The radial variation of μ in the core region ($r/a \leq 0.5$), however, is not so large, and, therefore, the present results may apply semi-quantitatively to real RFP plasmas. The critical perturbation level for sustained RFP is thus determined by sufficient overlapping of the static and inherent magnetic islands.

4. DISCUSSION AND SUMMARY

In the STE-2, a field aligned high heat flux (~100 MW/m^2) is carried by superthermal electrons at the edge, the average energy of which is ~400 eV, about ten times the central temperature. Figure 4 summarizes the heat flux measurements with and without helical perturbations. The abscissa denotes the charging voltage of the helical field power supply, positive (negative) values corresponding to internally resonant (externally non-resonant) perturbations. The edge heat flux was almost

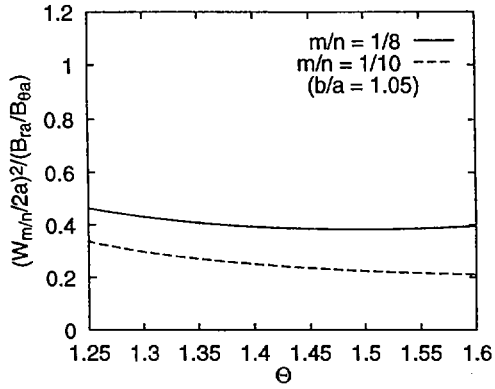

FIG. 3. Normalized magnetic island width versus Θ in m = 1, helically perturbed free boundary RFP equilibria.

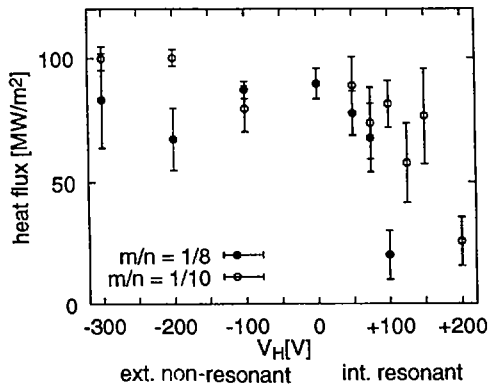

FIG. 4. Summary of edge heat flux measurements with and without helical perturbations. In the abscissa, positive (negative) values denote internally resonant (externally non-resonant) perturbations.

unaffected by the externally non-resonant perturbations for a level of up to ~8%, while it decreased gradually with increasing internally resonant perturbations, up to the critical level for sustained RFP. As noted, the critical level differs for 1/8 and 1/10 perturbations.

In a stochastic system, radial diffusion of the superthermal electrons may be related to the magnetic diffusivity D_M which, in the quasi-linear approximation, is given by the product of $\Lambda_\parallel$ and the radial field fluctuation level squared. If the edge behaviour of $\Lambda_\parallel$ and the radial field fluctuation also holds in the core region, then this quantity decreases mainly by the decrease of $\Lambda_\parallel$ because of the internally

resonant perturbations. This implies that, as the stochasticity increases with internally resonant perturbations, fewer superthermal electrons leak to the edge if both the runaway rate in the core region and the energy of the superthermal electrons at the edge remain unchanged. This dependence is in agreement with the heat flux measurements. Simultaneous application of the m/n = 1/8 and 1/10 perturbations with independent amplitude control will provide a useful means of studying the field line stochasticity in the core region; this experiment is under way.

It has been demonstrated that the mode coupling process could be controlled by means of the static external helical fields in the RFP.

REFERENCES

[1] YAGI, Y., et al., in Plasma Physics and Controlled Nuclear Fusion Research 1992 (Proc. 14th Int. Conf. Würzburg, 1992), Vol. 2, IAEA, Vienna (1993) 611.
[2] SURFF, J.S., et al., Phys. Plasmas **2** (1995) 2440.
[3] HIRANO, Y., et al., Nucl. Fusion **36** (1996) 721.
[4] MASAMUNE, S., et al., Plasma Phys. Control. Fusion **35** (1993) 209.
[5] IIDA, M., et al., Plasma Phys. Control. Fusion **36** (1994) 153.
[6] ISHIJIMA, D., et al., J. Phys. Soc. Jpn. **63** (1994) 3899.
[7] MASAMUNE, S., et al., Trans. Fusion Technol. **27** (1995) 293.
[8] ISHIJIMA, D., et al., Plasma Phys. Control. Fusion **37** (1995) 657.
[9] JIANG, Z.X., et al., Phys. Plasmas **2** (1995) 442.
[10] SATO, K.I., et al., in Plasma Physics and Controlled Nuclear Fusion Research 1988 (Proc. 12th Int. Conf. Nice, 1988), Vol. 2, IAEA, Vienna (1989) 447.
[11] MORI, A., et al., J. Phys. Soc. Jpn. **63** (1994) 3548.

MHD PROCESSES ASSOCIATED WITH SHEAR REVERSAL: AN EXPERIMENTAL APPROACH FROM THE ULTRA-LOW-q REGIME

N. INOUE, T. FUJITA, S. KIDO, S. KONDO,
J. MIYAZAWA, J. MORIKAWA, Y. MURAKAMI,
H. NAKANISHI, Y. OGAWA, K. SASAKI, T. SUZUKI,
S. TAKEJI, M. WATANABE, Z. YOSHIDA
Faculty of Engineering,
University of Tokyo,
Tokyo, Japan

Abstract

MHD PROCESSES ASSOCIATED WITH SHEAR REVERSAL: AN EXPERIMENTAL APPROACH FROM THE ULTRA-LOW-q REGIME.

A tokamak configuration with shear reversal is attracting interest because it may have an advantage in improving the global confinement efficiency. A concern about this class of equilibria stems from double resonant internal kink instabilities. MHD fluctuations and related non-linear processes have been studied in the ultra-low-q (safety factor $q < 1$) regime with direct measurements in the shear reversal region. The MHD relaxation stabilizes kink modes by selecting (self-organizing) appropriate pitches. The self-organized state displays the characteristic of a 'dissipative structure' in that it is accompanied by enhanced energy dissipation; the global resistance of the plasma current is substantially enhanced. The relaxation of the magnetic energy results in heating of the plasma particles.

1. INTRODUCTION

A tokamak configuration with shear reversal is attracting interest because it may have an advantage in improving the global confinement efficiency. However, a concern about this class of equilibria stems from double resonant internal kink instabilities. In this paper, we study MHD fluctuations and related non-linear processes on the basis of direct measurements in the shear reversal region.

We produced a shear reversed tokamak-like configuration in the ultra-low-q (ULQ; safety factor $q < 1$) regime that is intermediate between the tokamak and the reversed field pinch (RFP) (Section 2). The ULQ plasma produces shear reversal as a natural consequence of the interpolation of the tokamak (positive shear) and the RFP (negative shear). The global stability of this system is dominated by the non-linear dynamics of MHD fluctuations (Section 3). We have made direct measurements in the shear reversal region.

Experiments have been done in the REPUTE-1 device: major radius = 0.82 m, minor radius = 0.22 m, toroidal magnetic field $\approx$ 0.3 T, plasma current $\approx$ 0.3 MA, 30 eV $\leq$ electron temperature $\leq$ 350 eV, 100 eV $\leq$ ion temperature $\leq$ 800 eV, 10^{19} m^{-3} $\leq$ electron density $\leq$ 10^{20} m^{-3}. The Lundquist number (the ratio of the magnetic diffusion time to the Alfvén time) is of order 10^6–10^7.

2. SHEAR REVERSAL IN THE ULQ PLASMA

2.1. ULQ configuration

We can classify toroidal discharge plasmas into three different classes in terms of the safety factor q. The tokamak configuration is characterized by the Kruskal–Shafranov limit $q > 1$. The RFP has a very small q, so that the magnetic field lines are tightly twisted. This configuration is close to the force free magnetic field (low β). Therefore it carries a large poloidal current, which has to be generated and sustained by the internal electric field. The RFP configuration is generated through a turbulent phase of startup. The magnetic field distribution has a peculiar structure: the toroidal magnetic field reverses along the radius of the plasma column, and a negative q value occurs in the edge region.

The intermediate range of q between that of the tokamak and that of the RFP is the ULQ regime, where the toroidal and poloidal magnetic fields have comparable magnitudes and a magnetic field line is twisted several times in the plasma column. This type of magnetic field configuration appears most commonly in various space and stellar plasmas. In the ULQ regime, large scale fluctuations behave non-linearly, and many interesting phenomena occur.

The history of research into the ULQ regime goes back to the stabilized pinch experiments in the 1960s [1]. During a later period there were few studies in this area, since the linear theory predicted instabilities of double resonant modes [2]. A renewed interest is arising in this area in connection with MHD relaxation phenomena [3]. When we produce a plasma in the ULQ regime, a 'discrete structure' appears in the parameter space of q, i.e. the plasma takes preferential values of pitch.

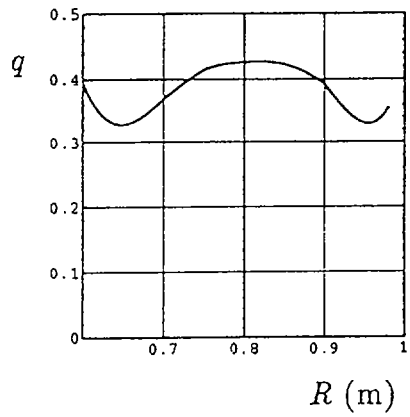

FIG. 1. Direct measurement of the internal magnetic field structure. The distribution of q (R is the major radius) is calculated from the equilibrium solution that fits the measured data.

The discrete nature of the pitch is related to the self-organization process associated with the kink modes (Section 3). After the establishment of the self-organized configuration, the plasma stays stable for a period of time which is much longer than the MHD time-scale.

2.2. Internal magnetic field structure

The distribution of the internal magnetic field of a ULQ plasma was directly measured by insertion of an array of magnetic probes. The array has eight channels each for the toroidal and poloidal directions. The strength of the magnetic field for each position and direction was fitted by a solution of the Grad–Shafranov equation. We measured the poloidal flux at 12 points around the torus to determine the boundary condition. Figure 1 shows the radial profile of q. We observe that q(r) (r is the minor radius) has a minimum within the plasma, and hence the shear is reversed.

The generation of the shear reversed configuration is a consequence of the MHD relaxation (Section 3), as well as the skin current effect. An indication of the improvement in confinement due to the shear reversal can be observed if a pulse of negative toroidal field is applied to enhance the negative shear. After the application of the pulse, the MHD fluctuation becomes small and the loop voltage is reduced.

3. MHD FLUCTUATIONS AND NON-LINEAR EFFECTS

3.1. MHD stability

The ULQ plasma has a larger current than the Kruskal–Shafranov limit ($q > 1$) so that the global kink modes can become unstable. Stepwise MHD relaxation yields a discontinuous change in q. After the relaxation (discontinuous transition of q), q(r) achieves a decreasing profile in the core region, resembling the RFP configuration, while the outer region retains a positive shear (Fig. 1). The resultant shear reversed configuration becomes stable against global kink modes [4]. However, the diffusion of the current changes q(r) and destabilizes the plasma on a longer time-scale. Intermittent MHD relaxation occurs in such a sequence of excitations and stabilizations of global kink modes [5].

The neighbourhood of the shear reversal (the pitch minimum) is unstable against localized double resonant kink modes. Measurement of internal magnetic fluctuation detects localized instabilities (Fig. 2), while the global stability of the discharge is retained for a period of time after the MHD relaxation. This observation is explained by the non-linear self-stabilization effect of the double resonant modes (Section 3.2).

3.2. MHD relaxation

An instability is a spontaneous process of conversion of internal free energy into fluctuations. If the instability has a self-stabilizing mechanism and appropriate energy

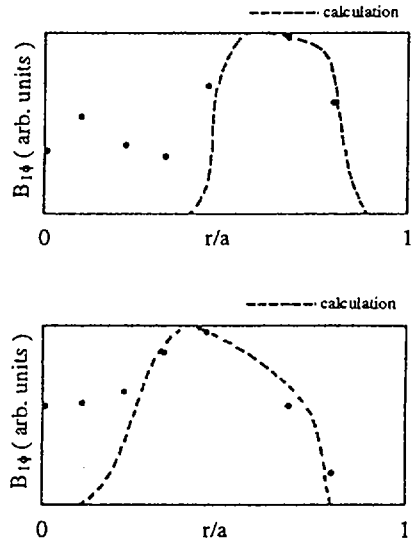

FIG. 2. Measurement of internal structure of magnetic fluctuations. The mode amplitude is localized in the pitch minimum region. The experimentally measured mode structure (dots) is compared with the eigenfunction of the ideal MHD mode.

dissipation processes operate, the system relaxes into a stabilized state with a smaller free energy. This scenario of self-organization applies to MHD relaxation.

Although the decreasing q(r) profile in the core plasma provides global kink mode stability, the pitch minimum in the outer region destabilizes double resonant local modes [2]. The double resonant modes with poloidal mode number m = 1 have large growth rates, while those with m > 1 have relatively small growth rates [4]. Experimental analysis of the internal magnetic fluctuations shows that local modes with m > 1 are destabilized in relatively high β plasmas. The mode structure is in good agreement with the linear normal mode analysis [6]. In the quiescent phase, modes with m = 1 are not observed, because the stabilized ULQ configuration does not have m = 1 rational surfaces (Fig. 1). This observation suggests that the plasma has a self-regulating mechanism to eliminate such resonances.

Numerical simulations of the reconnection process have elucidated the stabilization of the double resonant modes [7]. The non-linear effect of the double resonant tearing mode changes an unstable configuration into a stabilized local Taylor state (constant α force free field) [8]. During the reconnection phase of the double resonant tearing mode, the q profile in the central region remains unchanged, while the pitch minimum region undergoes topological changes. After the reconnection, the resonant surface of the unstable mode disappears, and the q profile becomes locally stable to the mode.

3.3. Non-linear effects

Twisted magnetic field line structures appear commonly in many different space, astrophysical and laboratory plasmas, and they play an essential role in the non-linear dynamics of these systems. A structural change in the magnetic field is accompanied by energy transfer and transformation, and the relaxation of the magnetic energy results in heating of the plasma particles. Stepwise MHD relaxation occurs, resulting in a discontinuous change of the pitch of magnetic field lines. This discrete nature of the pitch stems from the instability of kink (torsional) modes. The MHD relaxation stabilizes kink modes by selecting (self-organizing) appropriate pitches.

The self-organized state displays the characteristic of a 'dissipative structure' in that it is accompanied by enhanced energy dissipation, which appears as two distinct anomalies associated with the magnetic fluctuations. One is the anomalous resistance of the discharge. The voltage required to sustain the discharge is about an order of magnitude larger than that which suffices to compensate for the resistive dissipation of the mean current. The enhanced dissipation of the magnetic energy results in anomalous heating of the plasma. The viscous dissipation heats ions, while the resistive dissipation heats electrons. We observe preferential ion heating in connection with the MHD relaxation process. The viscosity dissipates the fluctuation energy with the helicity conserved [9]. This preferential conservation of the helicity results in the self-organization of the Taylor relaxed magnetic field structure.

4. SUMMARY

A shear reversed configuration has been produced in the ULQ regime. The non-linear dynamics of kink instabilities play an essential role in the determination of the magnetic field structure. In the pitch minimum region, localized internal kink modes are excited. Coinciding with the change of q, local instabilities with different dominant mode numbers appear. However, these modes are self-stabilized, and local Taylor type relaxation occurs. The ion viscosity damps fluctuations, resulting in direct ion heating. Intermittent heating of ions occurs in connection with the excitation of magnetic fluctuations. The ion viscosity dissipation conserves the magnetic helicity. The preferential conservation of the helicity characterizes this relaxation process.

REFERENCES

[1] EVANCE, D.E. (Ed.), Pulsed High Beta Plasmas, Pergamon Press, Oxford and New York (1976).

[2] ROBINSON, D.C., Plasma Phys. **13** (1971) 439.

[3] YOSHIDA, Z., et al., J. Phys. Soc. Jpn. **55** (1986) 450.
[4] MURAKAMI, Y., YOSHIDA, Z., INOUE, N., Nucl. Fusion **28** (1988) 449.
[5] YOSHIDA, Z., KUSANO, K., INOUE, N., Phys. Fluids **30** (1987) 2465.
[6] ITAMI, K., et al., Nucl. Fusion **28** (1988) 1535.
[7] SUZUKI, K., YOSHIDA, Z., KUSANO, K., Nucl. Fusion **31** (1991) 179.
[8] TAYLOR, J.B., Rev. Mod. Phys. **58** (1986) 741.
[9] YOSHIDA, Z., HASEGAWA, A., Phys. Fluids B **4** (1992) 3013.

CHARACTERISTICS OF DIVERTOR RFP PLASMAS IN THE TPE-2M

K. HATTORI, Y. SATO, K. HAYASE, M. WATANABE[1],
T. UMEMOTO[2], M. IRIE[2], K. SUGISAKI
Electrotechnical Laboratory,
Agency of Industrial Science and Technology,
Umezono, Tsukuba, Ibaraki,
Japan

Abstract

CHARACTERISTICS OF DIVERTOR RFP PLASMAS IN THE TPE-2M.

Toroidal and poloidal divertor experiments of reversed field pinch (RFP) plasmas have been performed on the TPE-2M device to control the plasma-wall interaction (PWI), and the dynamics of self-organization and the behaviour of impurity transport in divertor RFP plasmas have been investigated. In toroidal divertor experiments, it is shown that the magnetic field configuration is a toroidally asymmetric Taylor state and its configuration is sustained by an intermittent m = 0 mode fluctuation localized in the vicinity of the toroidal divertor region, generating a poloidal ring current, without the deterioration of m = 1 modes that is usually seen in toroidally symmetric RFPs. In poloidal divertor experiments, impurity buildup is avoided by the installation of a divertor room, accompanied by the reduction of the loop voltage.

1. INTRODUCTION

The application of a divertor field to the reversed field pinch (RFP) plasma represents a promising approach towards helping to control plasma–wall interactions (PWIs). In RFPs, the effects of divertor systems on the configuration characteristics are different from the case of tokamaks because of the predominance of a poloidally aligned edge magnetic field — a situation which is in contrast to that prevailing in tokamaks (Table I). Introducing a poloidal divertor (PD) into RFPs significantly reduces the total magnetic energy, and also the parity of the field line curvature changes its sign, in contrast to tokamaks. On the other hand, a toroidal divertor (TD) configuration in RFPs has the opposite characteristics and favourably results in a longer connection length. In addition, as will be described in this paper, the reversed field of the RFPs shows stronger dissipation, owing to the TD field, i.e. the effect on configuration sustainment (dynamo) is considered to be quite large. From these points of view, an investigation has been performed on TD and PD-RFP plasmas in the TPE-2M device. The issues are focused on the characteristics of the configuration itself as well as on dynamo and impurity transport phenomena.

---

[1] Iwate University, Iwate, Japan.
[2] Waseda University, Tokyo, Japan.

TABLE I. COMPARISON OF TOKAMAK AND RFP DIVERTOR SYSTEMS

		Divertor magnetic energy/Total magnetic energy	
		Small ($\sim 10^{-2}$)	Large ($\sim 10^{-1}$)
		Parity change of separatrix field line curvature	
		No	Yes
Effects on configuration sustainment	Large	TD-RFP	——
	Small	PD tokamak	PD-RFP TD tokamak

2. CONFIGURATION AND DYNAMO OF TOROIDAL DIVERTOR RFP

TPE-2M is a medium sized (a/R = 0.19 m/0.73 m, $I_p < 200$ kA) RFP device equipped with a thick stabilizing shell [1]. Quadra-null TD fields are produced by four sets of toroidally symmetric TD coils that are wound outside the shell. The magnetic field lines of the TD-RFP are plotted schematically in Fig. 1. TD experiments had revealed a reduction in both the resistive loop voltage and the number of impurity lines of light species [2]. Hence, in view of these apparent advantages of the TD-RFP, we must address associated new issues: (1) what magnetic field profile results when we apply an external TD field to a force free magnetic field configuration where, in the latter, a strong vacuum toroidal field — as is characteristic of a tokamak — is absent, and (2) how the dynamo action associated with sustainment (of the magnetic configuration) is affected when the TD field penetrates into the plasma, leading to a loss of field reversal near the separatrix. In order to pursue these lines of research, we present some TD-RFP magnetic field measurements and analyse the results from the point of view of a self-organizing process.

The TD-RFP configuration is obtained by activating the TD coils for approximately 5 ms, so permitting the associated fields to fully diffuse and, then, applying a toroidal voltage. In this case, the resemblance of the F–Θ trajectory (derived from toroidal flux data obtained between TD units) to that of the standard RFP indicates that the two trajectories can be regarded as similar, at least in terms of attractors. Here, Θ denotes the pinch parameter defined as the ratio of edge poloidal to average toroidal field.

The TD-RFP toroidal field profile of a 50 kA discharge was directly measured at the toroidal location of the separatrix by means of a multichannel magnetic field probe. Theoretically, the superposition of the standard RFP measured toroidal field (Fig. 2(a), line 1) and the vacuum TD field (line 2) yields the predicted curve for the TD-RFP (Fig. 2(b), line 3). Clearly, this estimated profile is characterized by a small region of field reversal. However, the experiment demonstrates that, in fact, the

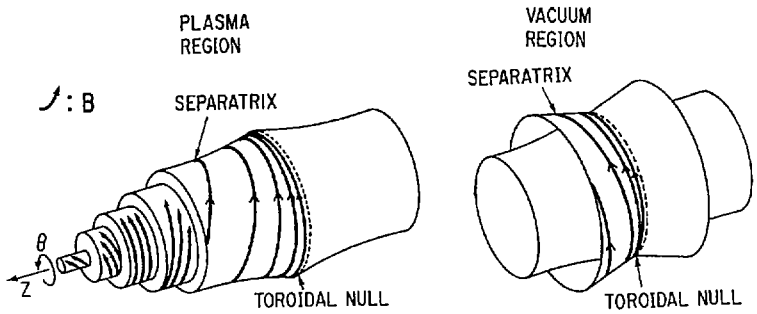

FIG. 1. Schematic drawings of magnetic surfaces of a TD-RFP plasma.

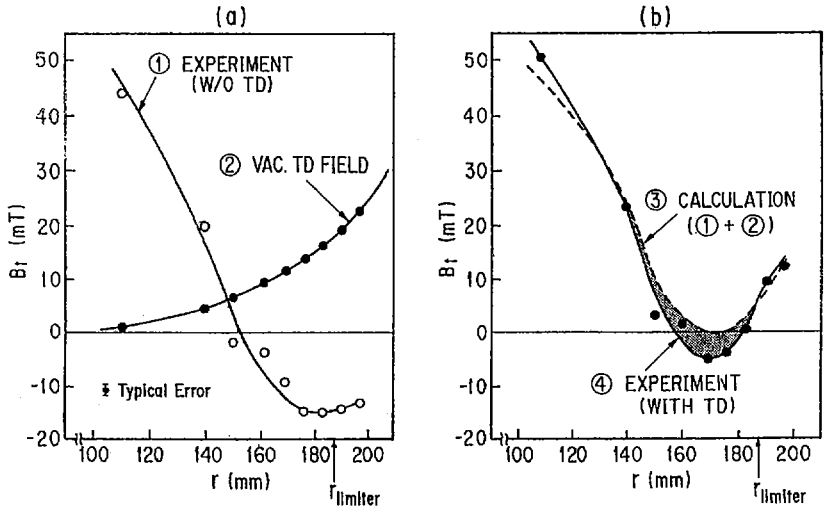

FIG. 2. Edge toroidal field profiles of a TD-RFP plasma.

TD-RFP toroidal field profile at the same location possesses a significant region of field reversal (line 4). The effect of the TD coil currents on the RFP plasma field and, hence, on the current is therefore considerable.

In order to quantify this point analytically, and bearing in mind some of the experimental results that will be presented later, a simple TD profile model is examined [3] that incorporates a Fourier expansion of higher order m = 0 Bessel functions [4] to describe both the TD fields and the plasma response [5]. We begin with the assumption of a force free state, i.e. rot B = λB, where λ is a constant that determines the plasma pinch strength, i.e. λ = 2Θ/a. In terms of a cylindrical co-ordinate system, (r, θ, z), a cylindrically symmetric solution to the above force

free field equation is given by $\mathbf{B}_0 = B_0\,(0, J_1(\lambda r), J_0(\lambda r))$. Subsequently, we shall represent the distortive effects of the TD fields on this configuration by a series of first order, m = 0, perturbations. To do this, we conveniently express the total perturbed magnetic field by using the following flux function representation:

$$\mathbf{B}(r, z) = \nabla\Psi(r, z) \times \nabla\theta + rB_\theta\nabla\theta$$

where B_θ denotes the poloidal magnetic field. Here, the various components of the vacuum magnetic flux, for (a < r < b), are given by

$$\Psi_v(r, z) = c + 1/2r^2B_{te} + \Psi_{resp}(r, z) + \Psi_{div}(r, z)$$

$$\Psi_{resp}(r, z) = \Sigma\,\alpha_n[K_1(k_nr) - K_1^w/I_1^wI_1(k_nr)]r\cos(k_nz)/k_n$$

$$\Psi_{div}(r, z) = \Sigma\,\beta_nI_1(k_nr)r\cos(k_nz)/k_n$$

where $k_n = n/R$, $K_1^w = K_1(k_nb)$, $I_1^w = I_1(k_nb)$ and c, B_{te}, b are, respectively, a constant determined by matching conditions, the zero order toroidal field at the plasma boundary and the minor radius of the shell, and where, finally, K_1, and I_1 are the corresponding modified Bessel functions of the first and second kind. The plasma derived flux function, Ψ_{resp}, is called the scattered field component while that originating from the TD coil, Ψ_{div}, is termed the incoming (or applied) field [5]. The coefficients of the incoming field, b_n, are determined at r = a by a Fourier decomposition of the scalar potential distribution, which is derived from the known TD coil arrangement, i.e. Ψ_{div} (r = a, z). For ease of reference, one of the four toroidally symmetric separatrices is set to be at z = 0. The full details of the analysis entailed are reported in Ref. [3]. So, for brevity, we simply note some of the principal results: The mode with maximum amplitude occurs at n = 8, from which it is possible to estimate the characteristic toroidal decay length of Ψ_{div}. More generally, it is found that the n = 8, 12, 16 and 20 mode amplitudes are effectively determined by the return coil positions. Furthermore, and possibly not surprisingly, the N = 4 amplitude is also large and reflects the quadrupolar symmetry of the TD coil units and, hence, the separatrices.

As to the plasma interior, the flux function in this region, 0 < r < a, is expressed as follows:

$$\Psi_p(r, z) = \Sigma\,\epsilon_nrJ_1(\kappa_nr)\cos(k_nz)/\kappa_n$$

where $\kappa_n = |\lambda^2 - n^2/R^2|^{1/2}$ and $J_1(\kappa_nr)$ is to be replaced by $I_1(\kappa_nr)$ when $\lambda^2 < n^2/R^2$. The unknown parameters α_n and ϵ_n are deduced applying the appropriate boundary conditions [3, 5]. The calculated radial profiles of the total flux function suggest, in analogy to the experimental observation, that the field reversal is deeper in the TD mode than the simple superposition of the vacuum TD fields and the toroidally sym-

metric magnetic profile. Attaining a more detailed profile characterization beyond this point will, in future, require a model that permits λ to vary radially.

Given the TD-RFP toroidal field profile obtained from the above analysis and also the effect of the positive TD coil fields which penetrate into the plasma and destroy the standard RFP configuration, we find that some questions arise on the nature of the new dynamo mechanism required to sustain the TD-RFP against resistive decay. An initial comparison of the relevant time-scales places the inquiry into an appropriate context. The approximate penetration time of the TD coil field into the field reversed region, τ_{Dsep}, is estimated as $\mu_0\delta^2/\eta_{rev}$, where δ denotes the radial distance between the location of the toroidal field minimum (in the TD-RFP configuration) and the plasma edge and η_{rev} represents the averaged electrical resistivity in the field reversed region of the plasma. By contrast, the dissipation time of the toroidal field in a divertorless RFP, τ_D, is estimated as $\mu_0 a^2/\eta_{av}$, where η_{av} is a volume averaged electrical resistivity. On TPE-2M, with the assumptions of $a = 0.19$ m, $\delta = 0.02$ m, T_{eav} (average electron temperature) = 100 eV, T_{erev} (average electron temperature of edge reversal region) = 10 eV and Z_{eff} (effective charge number) = 4, we obtain the following estimates: $\tau_D = 300$ μs and $\tau_{Dsep} = 30$ μs. In view of the latter time-scales, it becomes clear that the toroidal field reversal in the vicinity of the TD coils is lost much faster through TD field penetration than it could be sustained by MHD dynamo processes operating during the characteristic time associated with the axisymmetric plasma configuration. Despite the prior prediction of rapid reversed field loss, the experimentally observed collapse, in the TD-RFP, indicates that, actually, the TD-RFP configuration is sustained for as long as the loop voltage is applied [2].

Utilizing an 18 channel magnetic probe to measure the internal magnetic behaviour, we find that temporal toroidal field behaviour in the TD-RFP near the edge of the separatrix position ($z = 0$) differs significantly from that associated with standard RFP operation, i.e. through the appearance of spiky and intermittent fluctuations. In this region, the fluctuation amplitudes of the TD modes are approximately a factor of three to four larger than those of the divertorless discharge. These pulsed fluctuations are considered to be of the $m = 0$ mode variety since their parity is always negative outside r_s (the reversal radius) and positive inside r_s. Subsequently, and by an application of Ampère's law, the radial profile of the poloidal current density at the separatrix position ($z = 0$) can be deduced (Fig. 3) if we assume that the derivative in the toroidal direction vanishes there.

The profiles of Fig. 3 demonstrate that, in the case of no TD action, the poloidal current increases for a wide range of radial values whereas, by contrast, activating the TD coils results in a sharp increase in the poloidal current distribution near the edge. Really worth noting is the fact that the peak current density value of the TD is almost twice that of the divertorless zero order profile and is localized close to the reversal surface (where the half-width of the maximum perturbative component extends for ~10% of the minor radius). Although the precise toroidal variation of this perturbative profile is not yet known, it is thought likely that this radially peaked

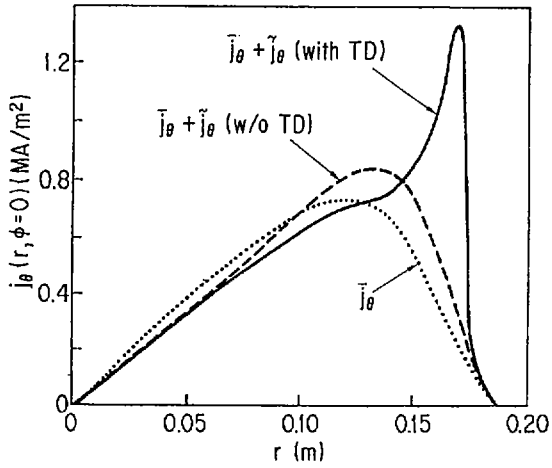

FIG. 3. Deduced poloidal current profile of RFP with and without TD fields.

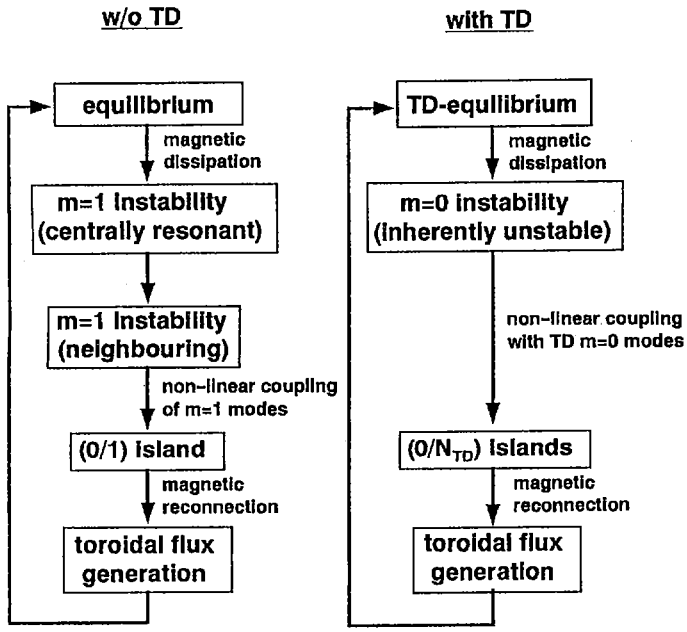

FIG. 4. Scenarios of MHD dynamo processes with and without TD fields.

current distribution exists as a ring of current localized about the separatrix, since the increase of the toroidal flux measured between the TD units is far less than the calculated value from Fig. 3. As far as the growth time for this pulsative m = 0 mode is concerned, it is observed to be 20–40 μs, a time-scale which is consistent with that of a tearing mode, i.e. $(\tau_R\tau_A)^{1/2}$ = 20–30 μs, when T_e = 10–20 eV, Z_{eff} = 4–5 and $n_e = 5 \times 10^{18}$ m^{-3} are the assumed values at the reversal surface, where τ_R and τ_A, respectively, denote the resistive diffusion and the Alfvén times. In addition, no deterioration in the m = 1 modes is apparent during TD operation. It appears, therefore, that the standard RFP (MHD) dynamo sustainment mechanism [6–8], i.e. current driven m = 1 kink instabilities which resonate near the plasma centre and generate the m = 0/n = 1 mode through non-linear coupling, is not considered to play a major role in a TD-RFP. Instead, for this machine, the m = 0 tearing modes, considered to be unstable when n = 4 [3], grow much more rapidly than the m = 1 modes, owing to the reduction in electron temperature near the edge of the plasma. Subsequently, this destablized m = 0 mode is thought to diffuse in the toroidal direction, according to the magnetic diffusion equation: $\partial b_t(r,z)/\partial t = -\eta(r)\mu_0^{-1}(\partial^2 b_r/\partial r\partial z - \partial^2 b_t/\partial r^2)$. At a certain point in this evolution, it seems reasonable to assume that neighbouring m = 0 modes reconnect. Further on in time, the prospect of significant magnetic dissipation in the cool reversal region results in the generation of a net positive contribution to the toroidal field, yielding the conjectured magnetic configuration. Subsequently, this cycle of diffusive, reconnective and then dissipative events repeats itself on a time-scale that is much faster than that of the MHD dynamo mechanism of the standard RFP. A comprison of MHD dynamo processes in the RFP plasma without and with the TD field is shown in Fig. 4.

It should also be noted that the energy confinement properties of the standard RFP configuration appear to be somewhat improved in a TD-RFP, on account of the absence of m = 1 modes in the latter, which act to directly transport energy from the hot plasma core to the cooler outer region. As was observed above, the attendant m = 0 perturbations tend to be localized at the reversal surface and so do not represent as severe a transport loss as the m = 1 mode.

3. CLOSED POLOIDAL DIVERTOR RFP EXPERIMENT

In the previous hardware system which did not have a divertor room, a discharge with an inboard side single null open poloidal divertor configuration is achieved for the duration of a few milliseconds, which is longer than the magnetic diffusion time [2, 9]. The global MHD dynamo activities observed in the PD mode were similar to those of limiter discharges, i.e. an analysis of the magnetic fluctuations revealed that non-linear coupling of m = 1 and m = 0 modes occurs during the flux generation process, in both cases. However, no long pulse discharge with continued PWI control was obtained, because of the impurity bildup in that scheme.

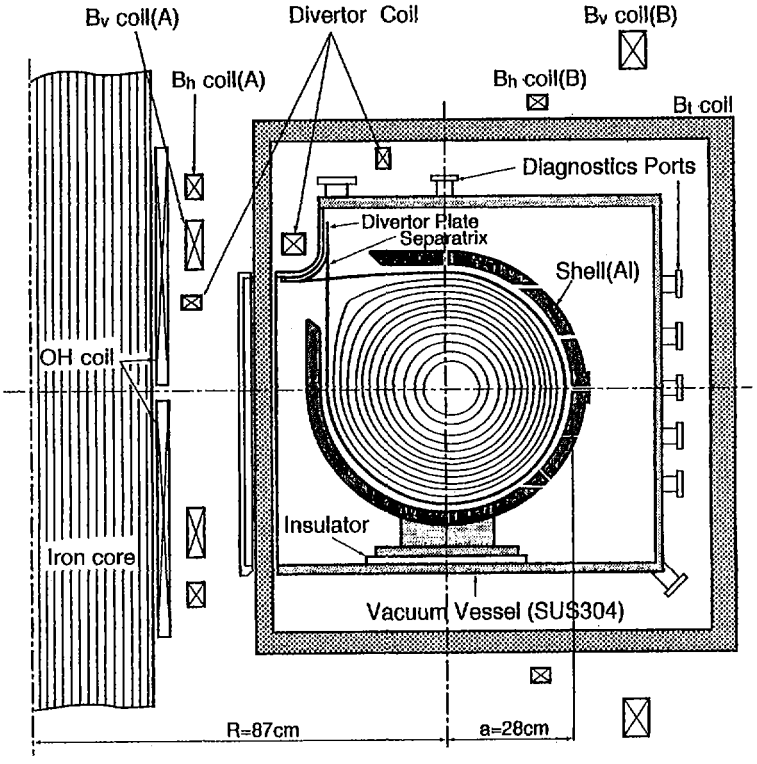

FIG. 5. Cross-sectional view of TPE-2MC.

To overcome these problems, a divertor room is newly installed, and closed poloidal divertor experiments have been performed on TPE-2MC (Fig. 5). An aluminium shell is positioned in an SUS 304 vacuum vessel (R = 87 cm, a = 28 cm, limiter minor radius = 26.8 cm). The skin time of the shell for vertical field penetration is 100 ms. In the poloidal divertor mode, an X point is designed to be located at the upper inboard side of the torus, in contrast to other closed poloidal divertor experiments [10, 11]. The base pressure obtained so far is 8×10^{-7} torr. In the preliminary experiments, a 30 kA limiter discharge lasting 3 ms is obtained. When the PD field is applied (divertor coil current/plasma current = 0.3), the plasma current increases slightly (35 kA, see Fig. 6) with the same loop voltage of the limiter discharge. The F–Θ trajectory of the PD-RFP is similar to that of the limiter discharge, i.e. close to the curve of the polynomial function mode (PFM) [12] (Θ = 1.5–1.7). Detailed measurement of impurity transport of the PD–RFP will be performed in the higher plasma current regime after the wall conditioning is completed. The effects

of the potential change by the ion loss due to the drastic magnetic field reduction near the poloidal null on the MHD characteristics is also an important issue. An experiment on the dynamo control by neutral beam current drive in the poloidal direction [13] is also being prepared.

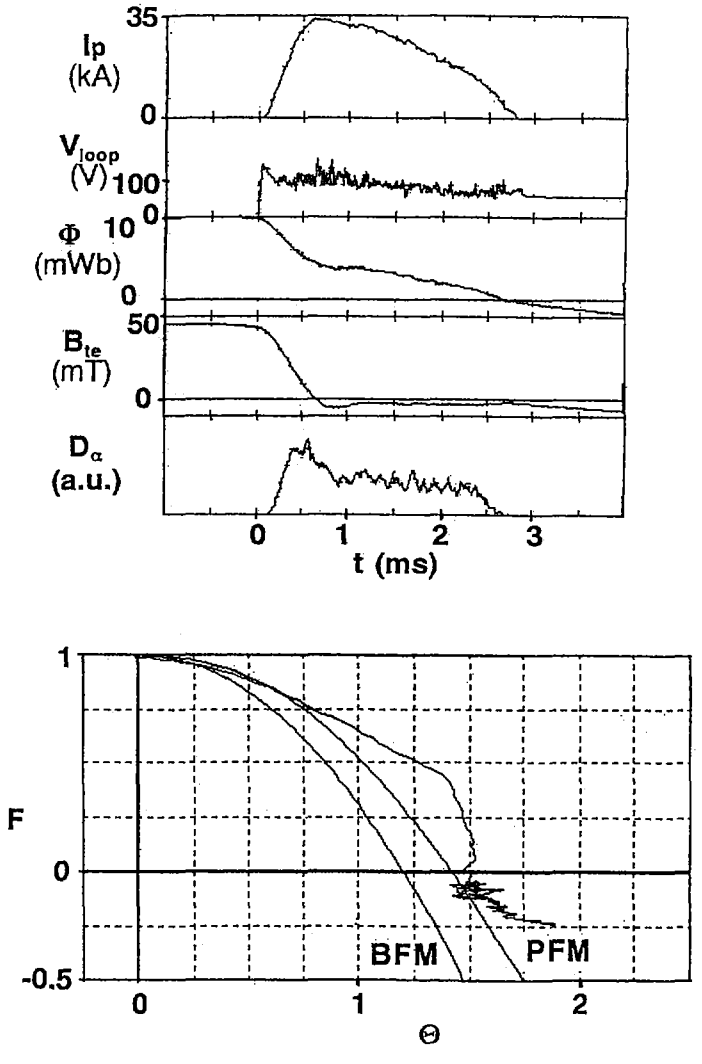

FIG. 6. Waveforms of I_p, V_{loop}, toroidal flux, B_{te}, D_α line and F–Θ trajectory of a PD–RFP discharge.

4. SUMMARY

Summarizing we may state that operating the standard RFP plasma configuration with four toroidally symmetric divertor coils, the TD-RFP is confirmed, by experiment, to be a toroidally asymmetric Taylor (force free) state and to be principally sustained by intermittently generated, m = 0 type perturbations, which are accompanied by the simultaneous production of a poloidal current distribution that is peaked at the outer reversal surface. By installation of a divertor room, sustainment of the PD-RFP plasma is also achieved without impurity buildup.

ACKNOWLEDGEMENTS

The authors are grateful to the Science and Technology Agency for continued support in this research.

REFERENCES

[1] HAYASE, K., SATO, Y., HATTORI, K., paper presented at IEA/RFP Workshop, Stockholm, 1993.
[2] HATTORI, K., SATO, Y., HAYASE, K., in Plasma Physics and Controlled Nuclear Fusion Research 1994 (Proc. 14th Int. Conf. Seville, 1994), Vol. 2, IAEA, Vienna (1995) 363.
[3] HATTORI, K., J. Plasma Fusion Res. 72 (1996) 783.
[4] TAYLOR, J.B., in Pulsed High Beta Plasma (Proc. 3rd Top. Conf., 1975) 59.
[5] PINSKER, R., REIMAN, A., Phys. Fluids 29 (1986) 782.
[6] SCHNACK, D.D., et al., Phys. Fluids 28 (1985) 321.
[7] KUSANO, K., SATO, T., Nucl. Fusion 27 (1987) 821.
[8] HATTORI, K., et al., Phys. Fluids B 3 (1991) 3111.
[9] SATO, Y., et al., J. Nucl. Mater. 220 (1995) 693.
[10] SARFF, J., et al., Nucl. Fusion 29 (1989) 104.
[11] IIDA, M., et al., Plasma Phys. Control. Fusion 36 (1994) 153.
[12] SPROTT, J., Phys. Fluids 31 (1988) 2266.
[13] HATTORI, K., et al., Fusion Technol. 28 (1995) 1619.

HELICITY INJECTION EXPERIMENTS AND TURBULENCE MEASUREMENTS ON THE TOKYO SPHERICAL TOKAMAK

H. TOYAMA, K. HANADA, K. YAMAGISHI, T. OIKAWA[1],
K. SHINOHARA, H. TOTSUKA, E. ISHIYAMA, H. SAITO,
S. SHIRAIWA, M. HASEGAWA, I. NAKAJIMA, M. USHIGOME
Department of Physics,
School of Science,
University of Tokyo,
Tokyo, Japan

Abstract

HELICITY INJECTION EXPERIMENTS AND TURBULENCE MEASUREMENTS ON THE TOKYO SPHERICAL TOKAMAK.

The Tokyo Spherical Tokamak (TST) was constructed to examine areas critical to a new class of 1 MA level ST and to investigate the basic physics of plasma confinement and stability in a low aspect ratio regime. The design parameters of TST are as follows: major radius R = 42 cm, minor radius a = 35 cm, aspect ratio A = 1.2, elongation ratio κ = 2.0 and toroidal field in the centre of the vacuum vessel, $B_{t0} < 0.2$ T. TST experiments successfully produced plasma currents of up to 45 kA with a low toroidal field B_{t0} of 0.08 T and an OH volt-second consumption parameter ψ of 6.2 mV·s. The aspect ratio of 1.2 is obtained very quickly in the early phase of plasma shaping and the elongation ratio increases to 1.8. The relative fluctuation level of the floating potential is ~0.1 in the region from the magnetic axis to R = 22 cm, then increases to ~0.2 and at the edge (R = 33 cm) jumps to ~0.6. Proof of principle experiments of plasma current drive by helicity injection were carried out. An electron emitter of 1.4 kA was operated at low plasma current in a first step towards driving plasma current. The plasma current was multiplied by a factor of 2.7 and the volt-second consumption reduced by a factor of 7. Toroidally symmetrical electrodes of 16 cm width were installed in the TST vacuum chamber at R = 32.5 and 60.5 cm. A voltage of 500 V was applied between the top and bottom electrodes. The duration of the plasma current increased from 0.7 to 1.0 ms.

1. INTRODUCTION

The spherical tokamak (ST) is a candidate for a compact volumetric neutron source (VNS) as well as a high β advanced reactor. The recent results from the Small Tight Aspect Ratio Tokamak (START) are encouraging [1], but START is equivalent to T3 in 1969; the field of spherical tokamaks is quite new and different from conventional tokamaks. The 1 MA level machines, such as the Mega Amp Spherical Tokamak (MAST) and the National Spherical Tokamak Experiment (NSTX), will in the future establish the position of the VNS and the advanced reactor. The Tokyo

[1] Japan Atomic Energy Research Institute, Naka, Ibaraki, Japan.

Spherical Tokamak (TST) has been constructed to examine areas critical to the new class of 1 MA level ST and to investigate the basic physics of plasma confinement and stability in a low aspect ratio regime. Non-inductive current drive is crucial in the ST because of the small flux swing of the OH coil. Results regarding non-inductive current drive from the Helicity Injected Tokamak (HIT) experiment [2] and from CDX-U [3] at Princeton University are encouraging, but HIT uses a type of gun spheromak injection; it is not yet clear whether this is applicable to a normal ST. It is necessary to do more detailed physics experiments to understand the mechanism of helicity injection and to apply it to future 1 MA level machines.

In this paper we report on: (1) the availability of high plasma current using low magnetic field, (2) turbulence characteristics of the ST and (3) proof of principle experiments on plasma current drive by helicity injection.

2. TST DEVICE DESCRIPTION

The design parameters of TST are as follows: major radius R = 42 cm, minor radius a = 35 cm, aspect ratio A = 1.2, elongation ratio $\kappa = 2.0$, toroidal field in the centre of the vacuum vessel, $B_{t0} < 0.2$ T. The device consists of three main parts: (a) a centre post of toroidal field coils (24 magnetically insulated cables of 12 mm diameter), an OH solenoid of 50 turns and an in-board Al shell of 5 mm thickness; (b) a cylindrical vacuum vessel of SUS-310S, 1.6 m high and 1.8 m in diameter, serving as a mechanical support structure; (c) 24 outer toroidal field coils and four poloidal field coils. The design of the TST machine is described in more detail in Ref. [4].

3. PLASMA PROPERTIES OF TST

3.1. Plasma current versus toroidal field

One of the good features of an ST is the possibility of obtaining high plasma current with low magnetic field. The TST experiments have successfully produced plasma currents of up to 45 kA with a low toroidal field B_{t0} of 0.08 T and an OH volt-second consumption parameter ψ of 6.2 mV·s. The plasma current increases linearly with B_{t0} and ψ; the data obtained show that TST can be easily upgraded to the 1 MA class using $B_{t0} = 0.5$ T (6 times higher than at present), $\psi = 100$ mV·s (16 times higher), R = 0.8 m, a = 0.6 m and A = 1.3.

3.2. Aspect ratio and elongation ratio

The characteristic feature of an ST is predicted to appear dramatically when the aspect ratio A is reduced to below 1.5. The time evolutions of A and of the elongation

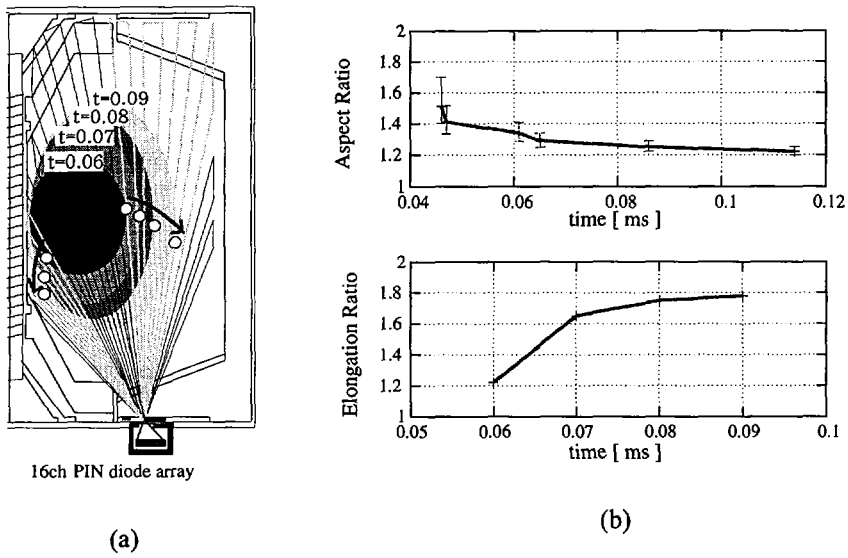

FIG. 1. (a) Cross-sectional view of TST and signals received by PIN diode array; (b) time evolutions of aspect ratio and elongation ratio in the early phase of plasma shaping.

ratio κ for TST in the early phase of plasma shaping are estimated from the time difference of the signals from a 16 channel PIN diode array, as shown in Fig. 1(a). The aspect ratio of 1.2 is obtained very quickly and the elongation ratio increases to 1.8, as shown in Fig. 1(b).

3.3. Measurements of turbulence on TST

The relative fluctuation level of the plasma potential is 0.5–1.0 in the region from $r \approx a/2$ to $r \approx a$ in the REPUTE-1 reversed field pinch plasma [5] and the relative fluctuation level of the electron density is ~ 0.6 in the scrape-off layer of the JFT-2M tokamak OH plasma [6]. To understand plasma confinement comprehensively, the fluctuation of TST is measured by using three triple Langmuir probe arrays. A radial profile of the relative fluctuation levels of the floating potential $e\tilde{\phi}/\kappa T_e$ is shown in Fig. 2. Measurements of the magnetic field made by inserting a probe show that the magnetic field changes sign at R = 18 cm, and the radial profiles of the mean electron density show a peak of 1.2×10^{18} m^{-3} at R = 18 cm; these indicate the magnetic axis to be at $R \approx 18$ cm. The relative fluctuation level of the floating potential is ~ 0.1 in the region from the magnetic axis to R = 22 cm, then increases to ~ 0.2 and at the edge (R = 33 cm) jumps to ~ 0.6.

4. HELICITY INJECTION EXPERIMENTS

The ST sacrifices OH volt-second consumption for a low aspect ratio, so that the role of the current drive is crucial for the ST to be a VNS or an advanced reactor. We report on two proof of principle experiments using a high current electron emitter developed by the Madison Symmetric Torus (MST) group for reversed field pinch current drive [7] and HIT-like helicity injection electrodes.

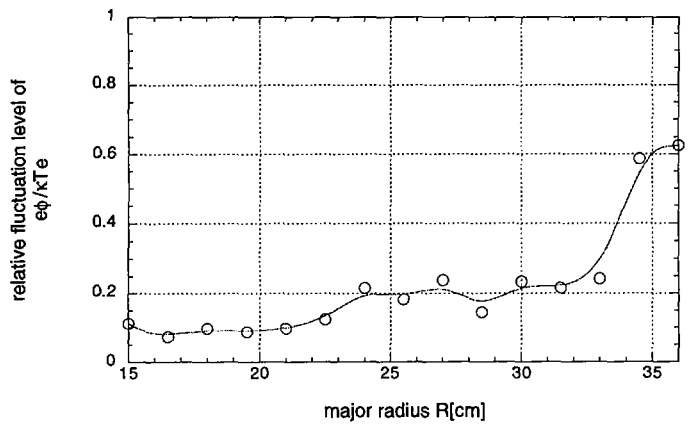

FIG. 2. Radial profile of the relative fluctuation levels of the floating potential.

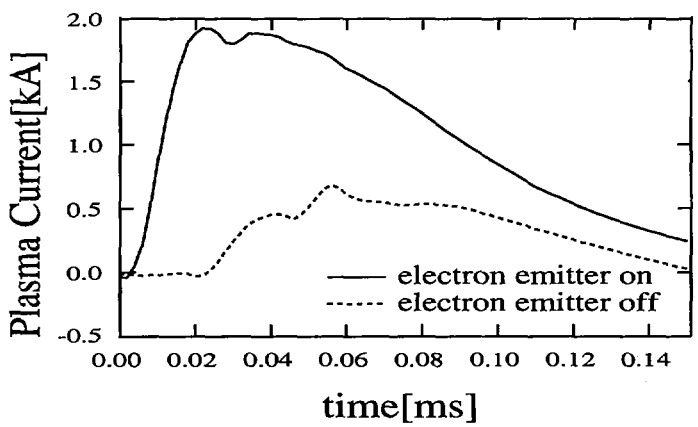

FIG. 3. Time evolution of plasma current with electron emitter on and off.

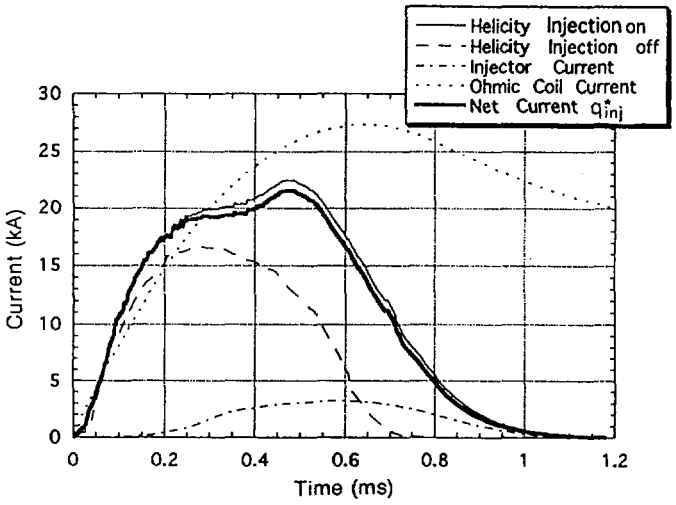

FIG. 4. Helicity injection electrodes experiment. A voltage of 500 V is applied between the top and bottom electrodes (R = 32.5 cm).

4.1. Electron emitter experiment

An electron emitter of 1.4 kA is operated at low plasma current in a first step towards driving plasma current. The value of I_p is multiplied by a factor of 2.7 with an electron emitter, as shown in Fig. 3. The volt-second consumption is reduced by a factor of 7. We will apply 5 to 10 electron emitters to I_p at the 40 kA level after optimizing injection angle and position.

4.2. Helicity injection electrodes experiment

Toroidally symmetrical electrodes of 16 cm width have been installed in the TST vacuum chamber at R = 32.5 and 60.5 cm. A voltage of 500 V is applied between the top and bottom electrodes (R = 32.5 cm) at 0.1 ms after the OH start. The duration of the plasma current increases from 0.7 to 1.0 ms, as shown in Fig. 4.

In the lower current operation, a plasma current of 8 kA is sustained for 2.8 ms. The helicity balance at 2.4 ms is estimated assuming the following:

Electron density $\approx 10^{17}$ m^{-3}

Electron temperature $\approx$ 10 eV

Helicity injection rate, $\dot{K}_{inj} = 2V_{inj}\psi_{inj} \approx 2.1$ Wb^2/s

Helicity injected by ohmic coil, $\dot{K}_{ohmic} = 2V_{loop}\psi_t \approx -0.04$ Wb^2/s, which is negative owing to negative loop voltage at 2.4 ms

Helicity dissipation rate obtained experimentally,
$\dot{K}_{diss} = 2\eta \int \mathbf{j} \cdot \mathbf{B}\, dV \approx 2\eta \langle j \rangle \langle B \rangle V$

Helicity dissipated inside closed magnetic surface, $\dot{K}_{diss\text{-}closed} \approx 1.5\ Wb^2/s$

Helicity dissipated on open magnetic surface, $\dot{K}_{diss\text{-}open} \approx 0.3\ Wb^2/s$, thus
$\dot{K}_{inj} + \dot{K}_{ohmic} \approx \dot{K}_{diss\text{-}closed} + \dot{K}_{diss\text{-}open}$

This work has demonstrated that a current drive scheme like that of HIT can be applicable to an ST.

REFERENCES

[1] SYKES, A., et al., in Plasma Physics and Controlled Nuclear Fusion Research 1994 (Proc. 15th Int. Conf. Seville, 1994), Vol. 1, IAEA, Vienna (1995) 719.
[2] JARBOE, T.R., et al., ibid., p. 725.
[3] HWANG, Y.S., et al., ibid., p. 737.
[4] HANADA, K., et al., Fusion Technol. 27 (1995) 440.
[5] JI, H., et al., Phys. Rev. Lett. 67 (1991) 62.
[6] TOYAMA, H., et al., in Plasma Physics and Controlled Nuclear Fusion Research 1994 (Proc. 15th Int. Conf. Seville, 1994), Vol. 1, IAEA, Vienna (1995) 575.
[7] FIKSEL, G., et al., Rep. UC-426, Univ. of Wisconsin, Madison (1995).

HEATING OF A PLASMA WITH FIELD REVERSED CONFIGURATION BY A FAST RISING MAGNETIC PULSE

S. OKADA, H. TANIGUCHI, H. SAGIMORI,
Y. MIYAWAKI, M. HASE, R. YOSHIDA,
H. HIMURA, M. OKUBO, Y. UEDA,
S. SUGIMOTO, S. OHI, S. GOTO
Plasma Physics Laboratory,
Faculty of Engineering,
Osaka University,
Suita, Osaka,
Japan

Abstract

HEATING OF A PLASMA WITH FIELD REVERSED CONFIGURATION BY A FAST RISING MAGNETIC PULSE.

Field reversed configuration (FRC) plasmas are normally produced in theta pinch machines. Since no material structures link the FRC plasma to its environment, it is moved from the formation region, made of a quartz discharge tube and surrounded by massive high voltage theta pinch coils, to the confinement region. Thus, the heating facilities provide accessibility to the FRC plasmas. Actually, adiabatic compression was applied to such a translated FRC plasma and successful heating was accomplished. The confinement properties, however, degraded. On the FRC injection experiment (FIX) apparatus, a fast rising magnetic pulse, from a pair of half-turn coils, is applied to the translated FRC plasma. By this pulse, the separatrix radius is observed to increase, showing that the plasma is being heated. The increase in radius and temperature is about 15% and 10%, respectively, if assessed at the time when the magnetic pulse has almost completely disappeared. The energy confinement time is also observed to become longer. The tendency that the confinement properties are improved by heating is shown to be consistent with the empirical scaling law $\tau_N \sim \tau_\phi \sim 2\tau_E \propto R^2/\rho_i$. The heating by one pulse is by far weaker than adiabatic compression but can be applied repetitively.

1. INTRODUCTION

Since no material structures link to field reversed configuration (FRC) plasmas [1], these can be moved or translated along the machine axis. Mostly, FRC plasmas are produced in a theta pinch machine and are translated into a metal confinement chamber. By this translation technique the confinement region and the formation region, which is made of a quartz tube and is surrounded by massive high voltage pinch coils, are decoupled. Thus, the FRC plasma becomes accessible to heating and diagnostic facilities.

On the FRX-C/LMS facility in Los Alamos, adiabatic compression heating was used as an 'effective and simple auxiliary heating' for the translated FRC plasma [2].

In this experiment the theta pinch produced FRC plasma was translated into a quartz chamber by a guide field of 0.4 T. An adiabatic compression field which rose up to 1.5 T in 55 μs was applied, and the plasma was heated from a T_{tot} ($= T_i + T_e$) value of 0.6 keV to 2.2 keV. While such effective heating was accomplished by the adiabatic compression, the confinement properties worsened: the energy confinement time τ_E became shorter by a factor of 2 to 3 and amounted to 35 μs. In this experiment, the particle confinement time, τ_N, and the decay time of the trapped reversed magnetic flux, τ_ϕ, scaled, as in many other experiments, like $\tau_N \sim \tau_\phi \sim 2\tau_E \propto R^2/\rho_i$ where R is the radius of the magnetic axis and ρ_i is the gyroradius in the external field.

By some heating, if the plasma radius is increased, contrary to the case of adiabatic compression, the confinement of the FRC plasma may be improved through the scaling law given above. To heat the FRC plasma without impairing its confinement properties, we applied a fast rising magnetic pulse to the plasma in our FRC Injection Experiment (FIX) machine; the result and its interpretation are presented here.

2. APPARATUS

In our FIX machine [3, 4], the FRC plasma is produced in a 0.31 m diameter, 1 m long theta pinch (formation region). Then it is launched into a 0.8 m diameter, 4 m long metal vessel (confinement region) by the unbalanced operation of a pair of mirror coils at both ends of the theta pinch. Both ends of the confinement vessel are tapered, and the magnetic field upstream the confinement region is 0.13 T and downstream it is 0.17 T so as to form a mirror configuration.

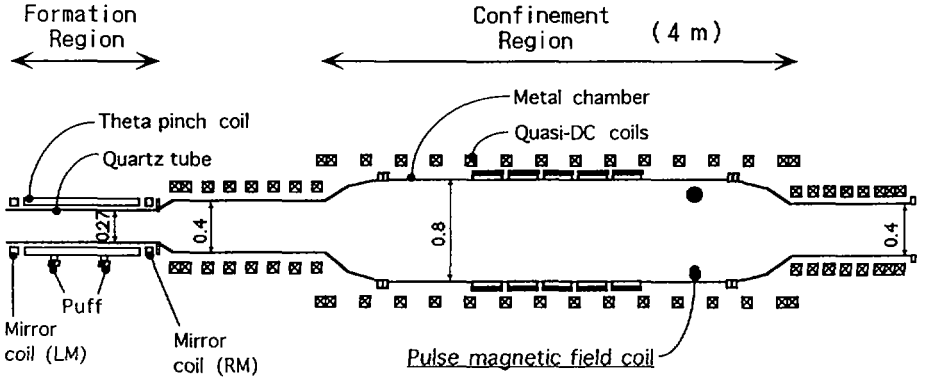

FIG. 1. Schematic drawing of FRC injection experiment (FIX) machine with pulse magnetic field coil.

The pulsed magnetic coil used to heat the FRC plasma is placed near the downstream end of the confinement region, coaxially with the machine axis (Fig. 1). The coil is made of a pair of 19.5 mm diameter copper pipes either of which is shaped into a 0.33 m radius half-turn coil cladded with epoxy resin in order to avoid discharging to the chamber wall through the ambient plasma. Either coil is connected with a crowbar circuit to a 3.3 μF capicator bank through a vacuum gap switch. When the capacitor is charged to 25 kV, a magnetic field, on the axis, of 0.05 T is obtained. The rise-time is 2.5 μs; the crowbarred decay time is 50 μs. From shot to shot, different amplitudes of ringing at around 200 kHz appear.

The shape of the separatrix and its change with time are obtained by an axial array of diamagnetic probes arranged just inside the metal wall. The line integrated plasma density is measured by a CO_2 laser interferometer, the chord of which is arranged across the diameter of the vacuum vessel. The spatially averaged plasma temperature is inferred from the average density, which is obtained from the interferometer and the separatrix radius, through radial pressure balance.

3. EXPERIMENT

The behaviour of the FRC plasma launched into the confinement chamber is seen in Fig. 2. Here the change of the separatrix shape with time is shown. On the horizontal and vertical axes, the axial distance from the centre of the confinement chamber and the radial distance from the machine axis are plotted. In each diagram, the shape of the separatrix at each point of time is shown by a solid line for the case without heating magnetic pulse and by a dashed line for the case with heating pulse. The dotted line refers to the wall of the confinement chamber. The FRC plasma ejected from the formation region is seen in the confinement region at 80 μs. It moves down and is reflected at the downstream mirror at 100 μs. At the upstream mirror, the plasma is again reflected, at 140 μs. At around 200 μs, the average density and the pressure balance temperature were 4×10^{19} m^{-3} and 100 eV, respectively. After 240 μs, the dynamics associated with the translation is hardly seen. In this case, the guide field in the confinement region was about 0.03 T. In the case where the magnetic pulse was applied (solid line) at around 130 μs, the plasma radius is seen to have increased, except for the period from 140 μs, during which the radius is not obtained correctly near the pulse coil ($z = 4.2$ m), for a reason to be stated in the following. As the magnetic flux is conserved inside the confinement chamber, the plasma pressure must have increased with increasing radius. The plasma length, on the other hand, was kept constant, probably by the effect of the mirror fields. It seems that no plasma dynamics was excited by the magnetic pulse.

In Fig. 3, the temporal change of the portion of the plasma volume inside the confinement chamber is shown. The solid line refers to the case with the magnetic pulse applied at around 130 μs, while the dotted line represents the case where no pulse was applied. As the difference in the signals was not large compared to plasma

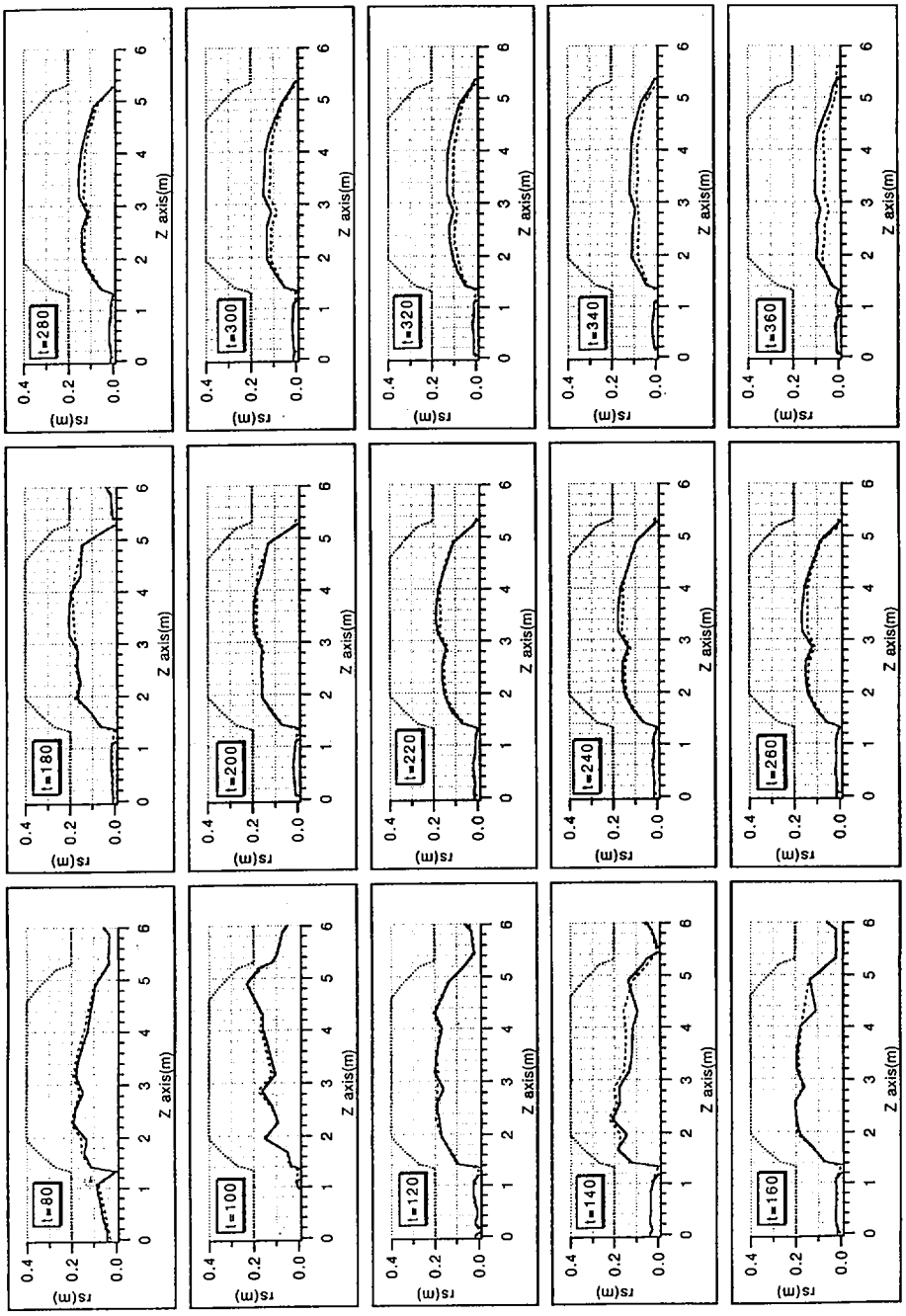
t=80
t=100
t=120
t=140
t=160
t=180
t=200
t=220
t=240
t=260
t=280
t=300
t=320
t=340
t=360
rs(m)
Z axis(m)

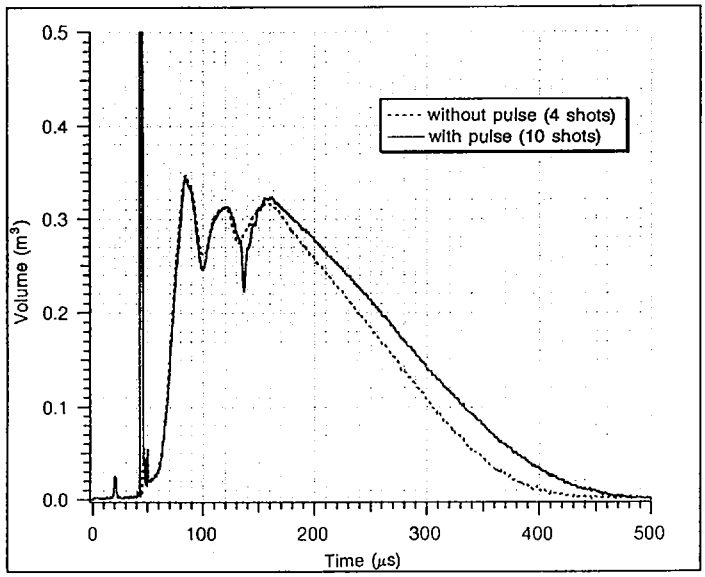

FIG. 3. Change of plasma volume portion inside the confinement region. Solid line: magnetic pulse; dotted line: no magnetic pulse.

reproducibility, either line is the average of four shots (solid line) and ten shots (dotted line). The volume is seen to increase up to 90 μs, by which time the plasma has entirely been translated into the confinement region. When the plasma is reflected at the mirror field at 100 and 150 μs, dips appear in the signals. As the volume was obtained from diamagnetic probes, on the assumption that the magnetic field was uniform outside the separatrix, it is not considered to have been obtained correctly when a rather strong magnetic field is generated by the pulse coil. The sharp dip in the solid line from 134 to 160 μs is such an erroneous signal. After 250 μs, the crowbarred pulse field decayed to less than 15% of the confining field. When no crowbar was applied, the pulsed field vanished completely before 200 μs. Therefore, we studied the effect of the magnetic pulse from the data after 250 μs.

FIG. 2. Behaviour of translated FRC plasma in the confinement region. The temporal change in the separatrix shape with the magnetic pulse applied at 130 μs (solid line) and without pulse (dashed line) is shown. Dotted line: confinement chamber wall.

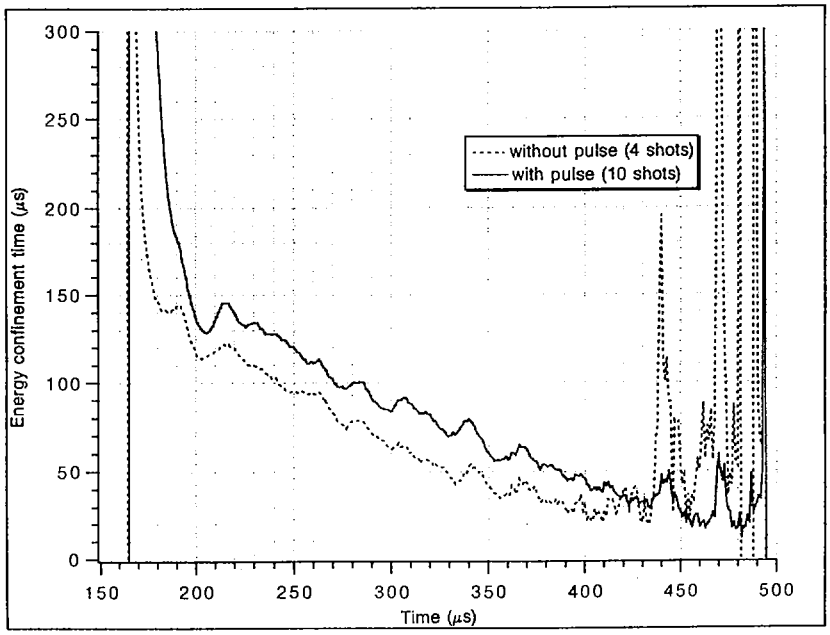

FIG. 4. Change in energy confinement time $\tau_E = ((dE/dt)/E)^{-1}$ with (solid line) and without (dashed line) magnetic pulse.

Since the reproducibility of the interferometer signal was rather poor, that of the temporal change in the total particle inventory was also poor. The reproducibility of the total energy was better, and so the energy confinement time, $\tau_E = ((dE/dt)/E)^{-1}$, plotted in Fig. 4, was used to find the change in the confinement properties due to the magnetic pulse. τ_E is seen to have become longer when a pulse was applied (solid line) compared to the case of no pulse (dashed line). At the present stage, because of the lack of reproducibility the accuracy of the data is not sufficient to allow a conclusion on how the confinement was improved quantitatively.

4. DISCUSSION

If the adiabatic heating of the FRC plasma [5] is assumed to be accomplished in a time shorter than the transport time, we may be able to find the change in the confinement properties from conservation equations and the empirical scaling law,

$\tau_N \propto R^2/\rho_i$, $2\tau_E \sim \tau_\phi \sim \tau_N$ as a function of the compression ratio, $C = B_{w2}/B_{w1}$, where B_{w2} and B_{w1} are the magnetic field strengths just inside the chamber wall after and before the compression. The most appropriate conserved quantity to be chosen may be trapped magnetic flux, $\phi = (\pi/2)r_w^2 B_w (X_s/\sqrt{2})^{3+\epsilon}$, the total particle number, $N = n_{max} \langle\beta\rangle V$ and $\mu = n_{max}^{1-\gamma} T$. Here, instead of the expression $p(2\pi d\ell \int B)^\gamma$ used in Ref. [3], the expression $n_{max}^{1-\gamma} T$ is used. The notations used are as follows: r_w is the chamber wall radius, x_s is the separatrix radius at the midplane normalized by r_w, ϵ takes values between 0 and 1 depending on the radial magnetic field profiles, n_{max} is the plasma density at the magnetic axis, $\langle\beta\rangle$ is the volume average beta value and is written as $1 - x_s^2/2$ for the FRC plasma in a solenoid, and V is the volume of the region surrounded by the separatrix. If the ratio $T_i/(T_e + T_i)$ is denoted by η and charge multiplicity due to impurities is neglected, then the ion gyroradius ρ_i before and after the compression, ρ_1 and ρ_2, changes like $\rho_2/\rho_1 = C^{-1/\gamma}(\eta_2/\eta_1)^{1/2}$. By this compression, the effect of the increased magnetic field prevails over the effect of temperature rise, and ρ_i becomes smaller. The particle confinement time τ_N scales as $(\tau_2/\tau_1) = C^{(1/\gamma - 2/(3+\epsilon))}(\eta_2/\eta_1)^{-1/2}$. When $\gamma = 5/3$, $\epsilon = 0$ and $\eta_2 = \eta_1$, we have $\tau_2/\tau_1 = C^{-1/15}$, implying that the confinement is worsened because the favourable effect of decreased ρ_i is more than cancelled by the unfavourable effect of the decrease in R. In the actual experiment, the confinement time became shorter by a factor of two to three for $C \sim 4$, in spite of its very weak dependence on the compression as predicted above. As the time-scale of the compression was close to the confinement time, a faster decrease in the plasma radius by the energy loss, in addition to the compression, may be responsible for the degradation of confinement.

In the case of heating by a magnetic pulse, the plasma length is limited by the mirror fields, and the trapped magnetic flux may not be written as easily as otherwise. We use the conservation of the magnetic flux outside the separatrix, assuming that the magnetic pulse is short enough. Together with the conservation equation for the particle number and the radial pressure balance equation, a relation between the pressure balance temperature and x_s is obtained. In this relation, the average beta value, $\langle\beta\rangle$, which cannot simply be related to x_s because of the effect of the mirror fields, is included. As the value of $\langle\beta\rangle$ is quite close to 1, no serious error will result, even if $\langle\beta\rangle$ is set equal to 1. When $\langle\beta\rangle$ is assumed to be $1 - x_s^2/2$, the fraction of the ion heating rate η_h defined by $\delta T_i = \eta_h \delta T_{tot}$ is given and the heating rate is small, then the change of the confinement time $\delta\tau/\tau$ with the change of x_s is approximately proportional to $(2(1 - x_s^2/2) - \eta_h/\eta)(\delta x_s/x_s)$. This relation expresses evident facts concerning confinement as improved by the heating; x_s should be smaller, and the heating rate of ions, η_h, should also be smaller. Actually, when x_s is smaller, the increase in the external field strength is smaller and the plasma radius increases more effectively, and when η_h is smaller, then the increase in ρ_i is smaller. Both effects are favourable to an increase in R^2/ρ_i.

5. CONCLUSIONS

It was shown experimentally that the FRC plasma could be heated by the application of a fast rising magnetic pulse. In contrast to adiabatic compression heating where the confinement is degraded, the confinement was improved by this heating. This phenomenon is explained by using the empirical scaling law for the confinement as well as by the fact that the plasma radius has increased as a result of the heating.

REFERENCES

[1] TUSZEWSKI, M., Nucl. Fusion **28** (1988) 2033.

[2] REJ, D.J., TAGGART, D.P., BARON, M.H., CHRIEN, B.E., GRIBBLE, R.J., TUSZEWSKI, M., WAGANAAR, W.J., WRIGHT, B.L., Phys. Fluids B **4** (1992) 1909.

[3] HIMURA, H., OKADA, S., SUGIMOTO, S., GOTO, S., Phys. Plasmas **2** (1995) 191.

[4] OKADA, S., UEKI, S., HIMURA, H., MATUMOTO, K., SADAHIRO, D., SUZUKI, Y., TAKAHASHI, K., ICHINOSE, F., OKUBO, M., UEDA, Y., SUGIMOTO, S., OHI, S., GOTO, S., in Plasma Physics and Controlled Nuclear Fusion Research 1994 (Proc. 15th Int. Conf. Seville, 1994), Vol. 2, IAEA, Vienna (1995) 441.

[5] SPENCER, R.L., TUSZEWSKI, M., LINFORD, K., Phys. Fluids **26** (1983) 1564.

ACCELERATION OF A FIELD REVERSED CONFIGURATION FOR CENTRAL FUELING OF ITER

J.T. SLOUGH, A.L. HOFFMAN
Redmond Plasma Physics Laboratory,
University of Washington,
Seattle, Washington,
United States of America

Abstract

ACCELERATION OF A FIELD REVERSED CONFIGURATION FOR CENTRAL FUELING OF ITER.

Central fueling of tokamaks leads to peaked plasma density profiles which have been shown to increase the average fuel power density and provide for enhanced performance in tokamaks. The Field Reversed Configuration (FRC) is a Compact Toroid with near unity β that is an ideal candidate to provide central fueling for ITER. A new experimental FRC device, LSX/mod, has been constructed to study the formation, translation, acceleration, and penetration of the FRC into a transverse magnetic field. The results from these experiments demonstrate that large mass (0.8 mg) FRCs can be accelerated to high velocity (2×10^5 m/s), and can readily penetrate a transverse field. Little extrapolation is necessary to reach the conditions required to penetrate a large tokamak.

1. Introduction

Present fueling designs for ITER are pellet injection and gas puffing. Since neither scheme can penetrate the fusion plasma beyond the edge, fuel can only reach the plasma core by diffusive processes. A large portion of the fuel will thus be lost before burnup. Present reactor design studies assume only 5% burnup of the fuel injected. Central fueling is essential to reduce the tritium inventory in the pumps and limiters, and could also play a key role in profile control for confinement, as well as reduction in startup ionization losses.

Perkins *et al.* [1] examined the feasibility of accelerated Compact Toroids (CTs), for deep refueling of a large tokamak. A general rule derived for penetration is that the CT directed pressure, $\rho v^2/2$, be comparable to the tokamak central field pressure, $B_{tor}^2/2\mu_0$. Translated CT's have been produced experimentally as low β, oblate spheromaks [2] or high β, highly prolate, Field Reversed Configurations (FRCs) [3]. Both CT configurations have been pursued as possible fuelers. The spheromak CT was the first to be employed for fueling a tokamak [4], and successful non-disruptive fueling has been demonstrated [5]. There are, however, several factors that limit the suitability of the spheromak as a fueler for ITER. The spheromak fuelers employ a magnetized Marshall gun which involves electrodes in the production of the plasma, and constant wall contact in the barrel of the injector. Impurity control

is thus a major problem, and wall drag puts a severe limit on the acceleration efficiency (< 5% for current injectors). The oblate nature of the spheromak combined with a low β formation limit, lead to large port requirements and extremely high rep rates due to the low mass load (10-60 mg in the tokamak fueling experiments). All of the above limitations are avoided if refueling is accomplished using the FRC.

2. LSX/mod FRC Acceleration Experiment

The FRC has been pursued for many years as a fusion plasma in its own right. Since the plasma is confined solely by poloidal fields, the equilibrium plasma β is typically quite high ~ 0.9. The linear, cylindrical geometry allows for easy translation of the FRC from the formation chamber, and the electrodeless inductive formation produces plasmas with near unity Z_{eff}. Recent experiments have been conducted on the LSX/mod facility to evaluate the possibility of producing high mass FRCs and accelerating them at rates suitable to serve as a fueler for a large tokamak such as ITER.

A schematic of the device is shown in Fig. 1. D_2 gas is puffed into the source section (r_c = 0.23 m, l_c = 2 m) where the FRC is generated in a field reversed theta pinch. Employing formation techniques developed in previous experiments [6], it was possible to form FRCs at high mass inventory and reduced coil voltages ($\leq$ 20 kV) from those typically employed in FRC experiments. Barrier magnets at the tube wall were also employed to reduce impurity pickup from the fused silica vacuum wall. The only significant impurity observed in FRC experiments was oxygen and to a lesser extent carbon. These impurities are most likely derived from water radicals and methane adhered to the quartz wall. Since the amount of impurity is fixed by the surface area of the wall, the fraction of impurity becomes quite negligible for the high fill pressure (2.6 Pa) FRC discharges. The estimated oxygen impurity fraction from doping experiments at this fill pressure is < 0.003. By a suitable voltage setting and sequencing of the source coils, the FRC is readily accelerated out of the source section into the smaller radius acceleration section.

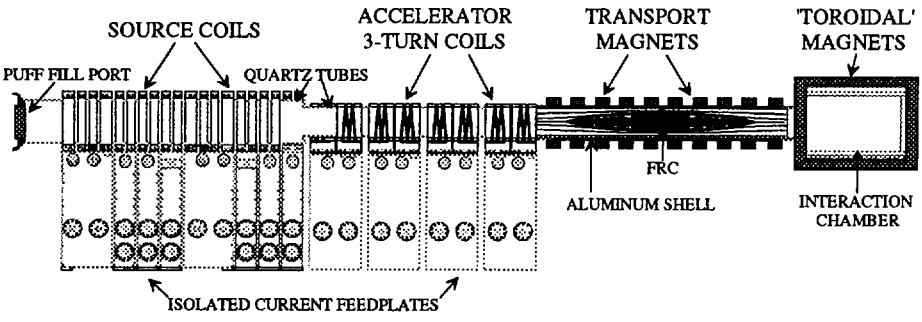

FIG. 1. Schematic of the LSX/mod device.

The acceleration section consists of (4) 0.3 m diameter, 0.42 m long, 3-turn coils. These coils, as in the source section, can be energized individually. For FRC acceleration the coils are energized in a sequential manner. The most efficient acceleration was observed when the largest magnetic field differential was maintained axially between the front and the rear of the FRC. The maximum accelerator field acting on the FRC was limited to ~ 0.8 T in the present experiments due to the relatively slow risetime of the accelerator coil fields (the capacitor bank was constructed for a different load with the consequence that multi-turn coils were required and the applied loop voltage was only 7 kV). Typically the coils are fired in a manner such that the FRC is compressed as it accelerated so that the FRC exits the accelerator with increased density as well as velocity since both are important for penetration. The acceleration section is followed by a 2 m long section where the FRC drifts in a quasi-steady guide field produced by solenoidal coils set around a split aluminum shell which maintains a constant axial flux. This section allows for a more accurate measure of the FRC parameters after acceleration and prior to entering the interaction chamber.

The interaction chamber consists of a cylindrical chamber at a right angle to the accelerator axis. Around the chamber, two rectangular solenoidal coils are each tilted 12° away from the accelerator axis and thus form a wedge with the open end facing the end of the transport section. With this tilt, the coils produce a transverse field with a gradient along the accelerator axis. Within the interaction chamber the measured field gradient is similar to the toroidal field of a tokamak with R = 1.3 m, and a = 0.4 m. Pressure and magnetic probes are located in the chamber to study the penetration of the FRC and the fuel deposition on to this "toroidal" field.

3. Experimental Results

Even with relatively low accelerator fields, it was possible to both accelerate and compress FRC's to velocities of 2×10^5 m/s at peak densities of 1.5×10^{22} m^{-3}. A time sequence for the acceleration of a high mass FRC (m_0 = 0.8 mg) is shown in Fig. 2. It was not possible to maintain a large magnetic field differential across the FRC throughout acceleration (see Fig. 3) due to the high impedance of the 3-turn coils. The average FRC acceleration rate (~5×10^9 m/s^2) through the accelerator coils was roughly half the initial rate. The initial rate could be sustained by employing a low inductance drive for the accelerator coils.

The efficiency of the acceleration process in the accelerator section can be calculated by comparing the increase in FRC kinetic energy: $1/2\ m(v_f^2 - v_i^2) = 10$ kJ, with the increase in magnetic field energy: $10\ \text{kJ} + \pi r_c^2 \ell_c (B_f^2 - B_i^2)/2\mu_0 = 28$ kJ, up to the time the FRC is ejected from each coil. The field at ejection is more characteristic of the true acceleration efficiency since the field increase after that time is due only to the poor match of the coil risetime to FRC velocity in the experiment.

Typically at least 70% of the initial FRC mass of 0.85 mg D_2 is retained through the acceleration process. The acceleration efficiency for the 0.7 mg FRCs was about 35% in these experiments where there was no recovery of the vacuum field

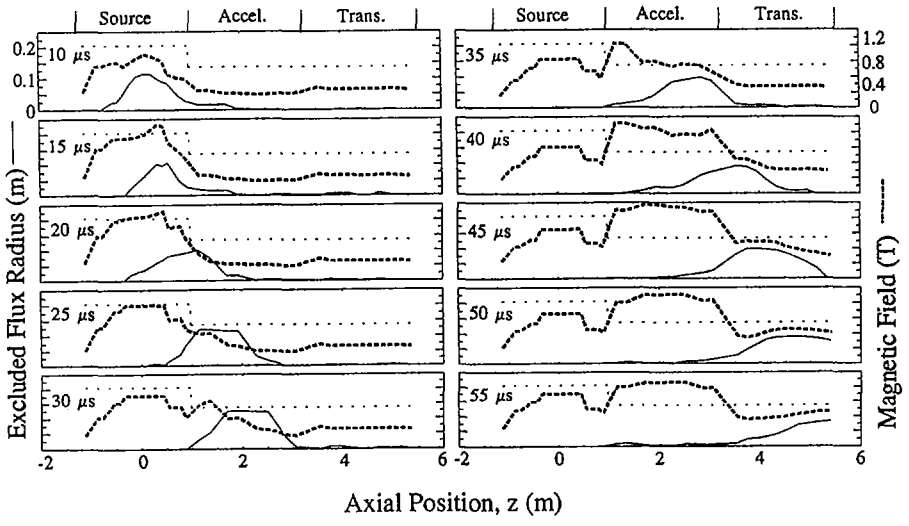

FIG. 2. Acceleration of a high mass FRC in LSX/mod.

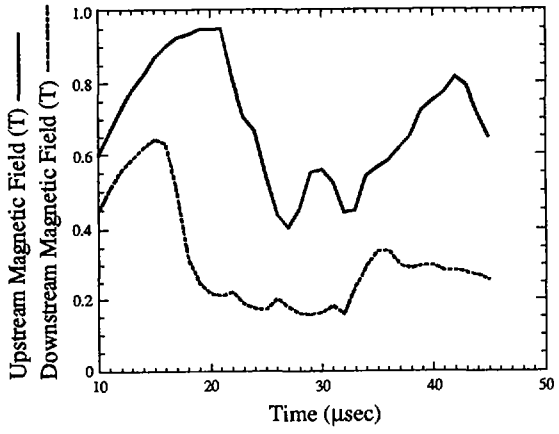

FIG. 3. External axial magnetic field across FRC during acceleration.

energy in the accelerator after FRC ejection. 90% of this field energy however is returned to the capacitors. In a longer accelerator of the type envisioned for ITER, this energy could be switched to much lower inductance accelerator coils downstream of the FRC. This would allow for acceleration efficiencies to approach 80%.

A full, resistive 2D MHD numerical calculation was carried out to match the experimental measurements of the FRC line density, excluded flux, and the external

magnetic field time history (see Fig. 2) during FRC formation and acceleration. The numerical results could then be used to give details of the acceleration process. The velocity and the inferred mass decay for a 2.6 Pa discharge are shown below in Fig. 4.

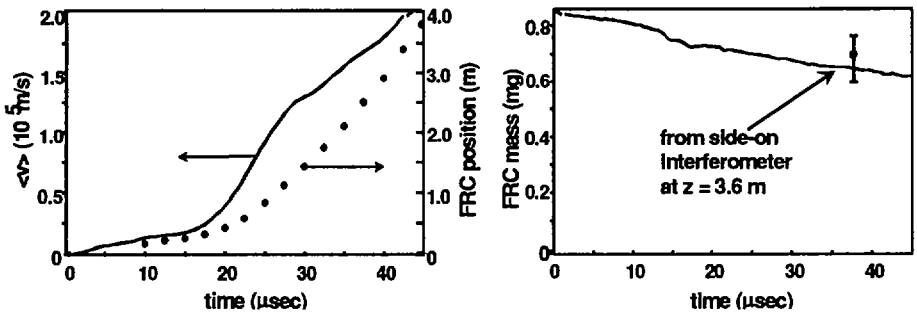

FIG. 4. FRC acceleration based on experimental data and MHD calculations.

4. Discussion and Conclusions

Core penetration in ITER could be achieved by FRCs with directed velocities of 4×10^5 m/s and densities of ~4×10^{22} m^{-3} (see Table I). Assuming that the initial rate of acceleration in LSX/mod is maintained, the accelerator section would need to be extended to 10 m with a peak accelerator field of ~ 2T. The factor of 2-3 density increase over that observed in the LSX/mod experiments could be achieved by employing one additional coil radius reduction, as was done out of the source region on LSX/mod, by roughly a factor of two. The final FRC radius would be less than 0.06 m requiring only a very modest port for injection into the ITER vessel. The highest loop voltage required to maintain the acceleration over the 10 m length would be less than 50 kV. Assuming a 40 s particle confinement and 100% fuel burn-up, a particle injection rate of 10^{21} is required. For the parameters in Table I, a rep rate of 3 Hz would be needed. The kinetic energy acquired by the FRC during acceleration is 80 kJ. Assuming the worst case, 35% efficiency and no magnetic energy recovery, the power required for the fueler is still under 1 MW.

When the same experimental input parameters for the initial fill pressure and magnetic field waveforms were used in the 2D MHD code, the calculations reproduced the observed FRC behavior from formation throughout the entire acceleration process. The same excellent agreement between code and experiment had been found in previous translation experiments [3] as well. The calculations therefore provide a powerful tool by which to evaluate future concept improvements.

A more near term experiment that could act as a proof of concept test would require injecting an FRC into a tokamak such as JET. With a lower central field in JET, only modest changes from the LSX/mod sized FRC fueler would be necessary.

TABLE I. Fueling Parameters

	ITER(95)	JET	LSX/mod results to date	LSX/mod with Variable Voltage Accelerator
$\langle n \rangle$ (m^{-3}) injected FRC	4.0×10^{22}	3.0×10^{22}	1.5×10^{22}	2.7×10^{22}
Toroidal field on axis (T)	5.68	2.8	-	-
injected mass (D)	1 mg	0.55 mg	0.6 mg	0.55 mg
injected particles	3.0×10^{20}	1.6×10^{20}	1.8×10^{20}	1.6×10^{20}
% inventory	0.1%	10%	-	-
penetration velocity (km/s)	405	250	200	280
$\rho v^2/2$ (GJ/m^3)	12.8	3.1	1.0	3.5

Using the same dimensions and length of LSX/mod but allowing for a variable coil voltage, numerical calculations were carried out to optimize the accelerator. It was found that central penetration conditions could be attained while maintaining the loop voltage under 40 kV. The fueling parameters obtained from the calculations are given in Table I.

Based on demonstrated FRC mass loads and acceleration, little extrapolation is needed to design a proof of concept FRC fueler appropriate for ITER that could be demonstrated on JET. There are clear technological challenges in making a rep rated fueler since all previous FRC experiments have been single discharges. With the high fuel load of the FRC though, the required rep rate for either tokamak is in the range of a few Hertz which makes repetitive discharges far more feasible. With very little fuel loss from the FRC during acceleration, combined with the potential high efficiency of the acceleration process, the bank energy as well as the power required can be kept quite modest.

REFERENCES

[1] PERKINS, L.J., HO, S.K., HAMMER, J.H., Nucl. Fusion **28** (1988) 1365.
[2] HARTMAN, C.W., HAMMER, J.H., Phys. Rev. Lett. **48** (1982) 929.
[3] REJ, D.J., et al., Phys. Fluids **29** (1986) 852.
[4] BROWN, M.R., BELLAN, P.M., Phys. Rev. Lett. **64** (1990) 2144.
[5] RAMAN, R., et al., Phys. Rev. Lett. **73** (1994) 3101.
[6] SLOUGH, J.T., HOFFMAN, A.L., MILROY, R.D., Phys. Fluids B **1** (1989) 840.

RECENT RESULTS OF THE HELICITY INJECTED TOKAMAK EXPERIMENT

T.R. JARBOE, M.A. BOHNET, J.P. GALAMBOS,
A.K. MARTIN, B.A. NELSON,
D.J. ORVIS, J. XIE, L. ZHOU
University of Washington,
Seattle, Washington,
United States of America

Abstract

RECENT RESULTS OF THE HELICITY INJECTED TOKAMAK EXPERIMENT.

The helicity injected tokamak experiment produces a small (a = 0.2 m), low aspect ratio (A = 1.5) 200 kA tokamak using only coaxial helicity injection. The experiment has no transformer and has achieved temperatures in the 100 eV range. An n = 1 mode is present during high current operation. The nature of this mode and its possible role in current drive on closed field lines are explored. A very simple model that seems to explain the current distribution on the open field lines is also presented.

1. INTRODUCTION

For the tokamak to make an economicaly attractive reactor, an efficient method of steady state current drive and higher β are needed. When scaled to a reactor, current drive by RF or neutral beams have efficiencies of $\sim 10^{-3}$, requiring a high recirculating power fraction [1, 2]. Coaxial helicity injection current drive has the potential of efficiencies in the tens of per cent for a reactor [3]. This improvement of over a factor of a hundred changes the current drive cost in a reactor from being dominant to being insignificant. The development of an inexpensive and efficient steady state current drive would eliminate the need for the transformer that is at present used to form and sustain tokamaks. The space previously used by the transformer can be used to lower the aspect ratio. Low aspect ratio tokamaks or 'spherical tori' [4] feature natural elongation, high paramagnetism, improved drift surfaces and high predicted β limits [5]. Results from the low aspect ratio tokamak START [6] have shown no disruptions for aspect ratios of less than two.

The helicity injected tokamak (HIT) experiment is designed to study and develop helicity injection current drive and to study the properties of low aspect ratio tokamaks. A description of the experiment and diagnostics (except for the new high speed probe discussed below) is given elsewhere [7, 8]. The HIT experiment has no current drive transformer. This paper reports results where coaxial helicity injection (CHI) is used to produce 200 kA low aspect ratio tokamaks with plasma temperatures reaching 100 eV. These tokamaks are characterized by a rotating n = 1 toroidal distortion, with poloidal distortions occurring only in the outer bad curvature region.

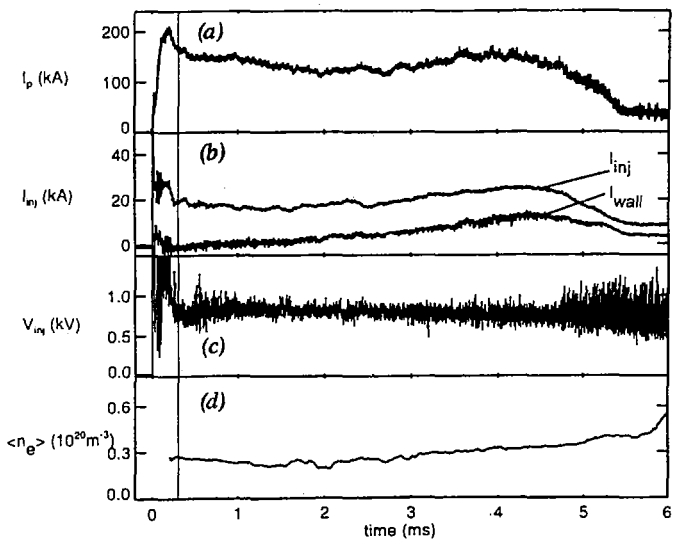

FIG. 1. (a) Toroidal plasma current; (b) injector and wall currents; (c) injector voltage; (d) chord averaged density through magnetic axis. Thomson scattering data were taken at the time marked by the line at about 0.3 ms. The temperature on this discharge was 129 eV.

A simple model addresses the role of the n = 1 mode in the current driven on the closed flux. Another model predicts the current profile on the open field lines produced by the injector.

2. BURNTHROUGH OF LOW Z IMPURITIES

Two operating methods on HIT have produced electron temperatures in the 100 eV range. In the first a low level conditioning discharge is maintained for 3 ms, followed by a high current (I_p > 200 kA) discharge where burnthrough of oxygen is observed and temperatures of over 70 eV are measured around 4–5 ms. This method is reported in Ref. [7]. It has gas puffing at both the inner (cathode) and outer (anode) electrodes in the injector region. In the second method gas is puffed through the cathode only and no conditioning period is used. Figure 1 shows the plasma current, the injector current and voltage, the wall current and the density as a function of time. Between 0.2 and 0.5 ms, Thomson scattering electron temperatures of over 90 eV are routinely obtained.

3. CURRENT DRIVE IN THE CLOSED FLUX REGION AND THE n = 1 MODE

Helicity injection current drive requires plasma relaxation, which causes redistribution of the current throughout the plasma volume. One mode [9] suggests that relaxation occurs through short wavelength phenomena allowing current to smoothly diffuse towards the plasma centre. The result is a monotonically hollow current profile. However, a competing global model is that large wavelength modes directly couple the current of the outer flux surfaces to that of the inner flux surfaces. The current profile will then depend on the structure of the mode and the resistivity profile, allowing profiles that are locally peaked at the magnetic axis [10].

In the generalized Ohm's law, the Hall term is $\omega_{ce}\tau_{ei}$ times larger than the resistive term, where ω_{ce} is the electron cyclotron frequency and τ_{ei} is the electron momentum loss time to ions. For fusion plasmas, $\omega_{ce}\tau_{ei}$ is a very large number ($\omega_{ce}\tau_{ei} \cong 10^8$ for a reactor); therefore, the Hall term is the next correction to ideal MHD. From rotamak theory [11], we know that waves with $\delta\omega_{ci} < \omega < \delta\omega_{ce}$ will lock on to the electrons but not to the ions and directly drive current, where $\delta\omega_{ci}$ and $\delta\omega_{ce}$ are the changes in the electron and ion cyclotron frequencies due to the δB of the wave and ω is the angular frequency of the wave. For a fraction of one to a few per cent of $\delta B/B$, the wave frequencies are comparable to the MHD range. For an intuitive understanding, let us consider the case where ∇p_e is small compared to the Hall term ($\mathbf{j} \times \mathbf{B}$). The Ohm's law including the Hall term can then be written as $\mathbf{E} = \mathbf{v}_e \times \mathbf{B}$, where $\mathbf{v}_e$ is the electron fluid velocity. Thus, the magnetic field is tied to only the electron fluid. This leads to an extremely simple intuitive picture of the current drive mechanism. One frequently observed magnetic phenomenon occurring during high current discharges is a rotating n = 1 mode [8]. If the n = 1 structure is locked on to the electrons and is present on all flux surfaces (open and closed), then driving the electrons on the open field lines causes the mode to rotate and the rotating mode then drags the electrons in the closed flux region driving the closed flux current.

In Fig. 2 the electron drift velocity is compared with the n = 1 mode velocity. The electron drift rotation frequency is the ratio of the toroidal plasma current to the total charge of the electrons. The time evolution of a bridge Rogowski spectrum is constructed by Fourier analysing 1 ms wide data sections. The power spectrum is evaluated for many times, and the results are displayed in a contour plot. The electron drift rotation frequency is plotted over the contour plot. On the assumption that the ions are at rest, Fig. 2 reveals that the mode rotation frequency tracks the electron drift rotation frequency, confirming that the n = 1 is locked to the electron fluid, consistent with the global model.

Existing equilibrium and stability codes are used to study the n = 1 mode. A modified version of the EFIT equilibrium code [12] finds the solution to the Grad–Shafranov equation that best fits the available magnetic measurements. Probe and flux loop data [13] calculated from the resulting equilibrium are compared with the

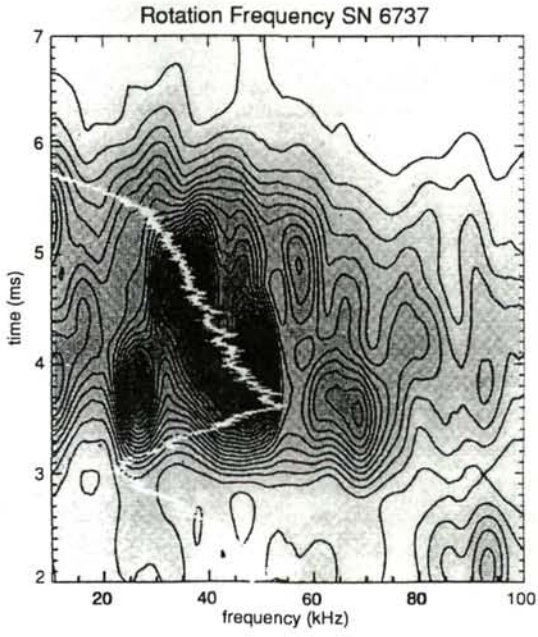

FIG. 2. Time evolution of wall current power spectrum shown as contour plot. Darker areas indicate larger values in the power spectrum. The electron drift rotation frequency versus time is the white line. Note that the white line passes near the peaks in the power spectrum.

measured probe data and the interpolated flux loop values in Fig. 3(a). The resulting equilibrium has a hollow current profile with some locally peaked current at the centre (Fig. 3(b)). Two additional codes, developed at Princeton Plasma Physics Laboratory, can determine the stability of an ideal MHD plasma with closed flux surfaces. The J-Solver code is a fixed boundary equilibrium code which solves for the Grad–Shafranov equation in flux co-ordinates [14]. The code has been modified so that the outer boundary resembles the HIT confinement region. As input, J-Solver uses the current profile calculated by EFIT. Lastly, the PEST MHD stability code finds the most unstable eigenmode for the J-Solver equilibrium (Fig. 3(c)). PEST reveals that HIT equilibria are unstable to $n = 1$ modes. The eigenmode couples the mode resonant flux surfaces (with $q = 11$) on both sides of the peak in q at the separatrix.

The new transient internal probe (TIP) diagnostic has measured the $n = 1$ mode inside the HIT experiment. TIP has been developed to measure the internal magnetic field profile in hot plasmas. The TIP concept involves shooting a magneto-optic probe through the plasma at high velocity (2 km/s), allowing measurement of the local magnetic field before surface boiling occurs [15]. Magnetic field measurements

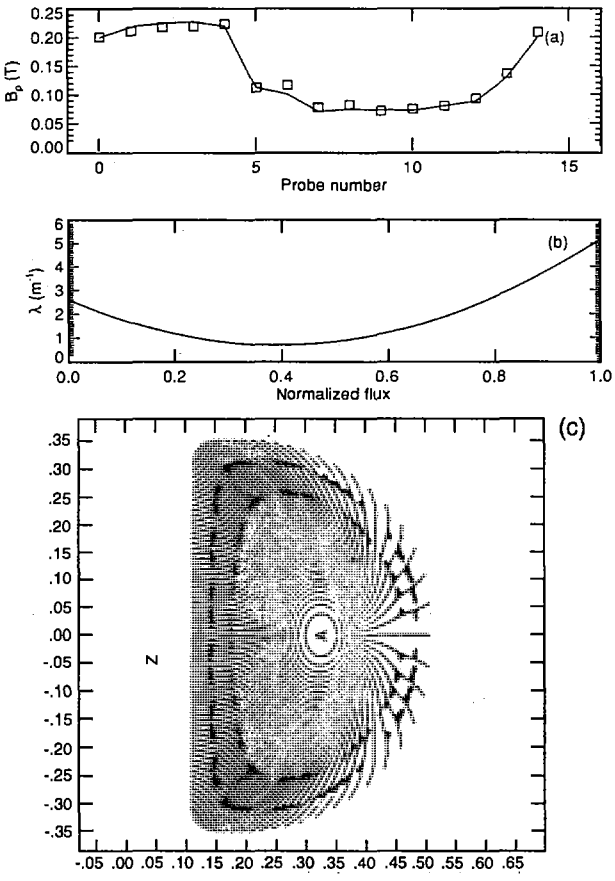

FIG. 3. (a) Comparison of the magnetic fields calculated by EFIT (solid line) with experimental values (squares). (b) Lambda plotted versus normalized flux, with 0 being the magnetic axis and 1.0 being the separatrix. Current profiles calculated by EFIT are hollow with a local peak at the plasma centre. (c) Unstable n = 1 displacement eigenmode as calculated from PEST coupling the outside flux surfaces to the inside.

are obtained by illuminating the probe with an argon laser such that the light passes through the probe material and is retroreflected off the rear surface of the probe to a polarimeter located outside the plasma. Since the probe (10 mm × 4 mm × 4 mm) is made of high verdet constant glass, the local magnetic field is determined by measuring the amount of Faraday rotation in the returned laser light. The magnetic field resolution of ±20 G is independent of field magnitude and the spatial resolution is 1 cm. The bandwidth of TIP is 4 MHz but can easily be increased by using faster detectors in the polarimeter [16].

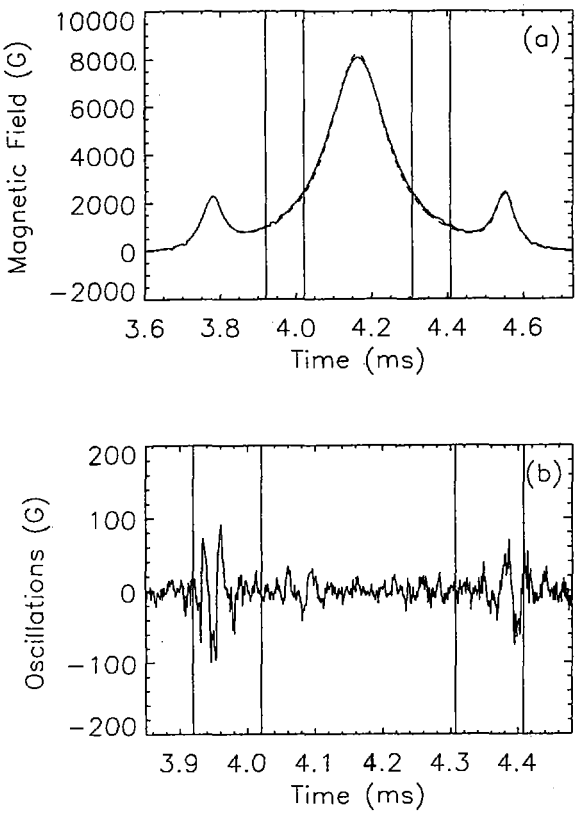

FIG. 4. (a) Toroidal field profile during a HIT discharge. Solid line: TIP measurement at 1.94 km/s along a trajectory with an impact parameter of 0.178 m relative to the machine axis. Dashed line: calculated vacuum field for this trajectory. Outside vertical lines: flux conserving boundary (R = 0.506 m); inside vertical lines: magnetic axis (R = 0.33 m). (b) TIP measurement of HIT toroidal field with high pass filter applied, clearly showing field oscillations. The high pass filter has a 17.5 kHz cutoff frequency.

TIP is used to measure the toroidal field on HIT [17]. the TIP trajectory is in the midplane of the tokamak and passes 0.178 m from the geometric axis. Figure 4(a) shows the measured toroidal magnetic field in the plasma plotted with the calculated toroidal field. Vertical lines mark the location of the flux conserving copper shell and the location of the magnetic axis. A scan from the edge to the magnetic axis is done in 100 μs, and the total time in the plasma is 500 μs. The two smaller peaks in the field outside the plasma occur as the probe travels near to two of the toroidal field coils, and the central peak occurs at the closest point of approach to the geometric axis. Magnetic field oscillations can be seen to occur near the edge of the plasma.

Figure 4(b) shows the same data with a high pass filter applied, eliminating the background toroidal field. The oscillations seen in the figure correspond to the rotating n = 1 oscillations that are present during high current discharges. The amplitude of the n = 1 oscillations is highest near the outer edge and substantially lower near the magnetic axis, which is in agreement with the dominant eigenmode predicted using the PEST stability code.

4. CURRENT PROFILE ON OPEN FIELD LINES

A new model for the injector operation using only a uniform resistivity does surprisingly well in accounting for the edge magnetic fields in cold, low current discharges [18]. This model assumes: (a) a force free equilibrium ($\nabla \times \mathbf{B} = \lambda(\psi)\mathbf{B}$) and (b) a regionwise uniform resistivity. The latter assumption is justified for the following reasons: (a) CTX results show that the saturated plasma dynamic impedance also looks like a resistivity [19], so both the resistive and the dynamic impedances can be modelled as a single η, making the model extremely simple. (b) In low temperature, radiation dominated plasmas, resistivity tends to be uniform because Z_{eff} increases with increasing temperature, offsetting the explicit temperature dependence [19]. (c) On an open field line, heated ohmically and cooled by parallel thermal conduction, the average resistivity along the field line depends only on the applied voltage, independent of the field line length. (This is because the resulting temperature profile is self-similar, and has a peak temperature that is independent of the field line length.) (d) A uniform resistivity is a simple assumption.

There are a number of discharges from early in the operating history of HIT which have little or no closed flux and for which there is an extensive set of B-poloidal measurements both in the injector and in the confinement region. We have

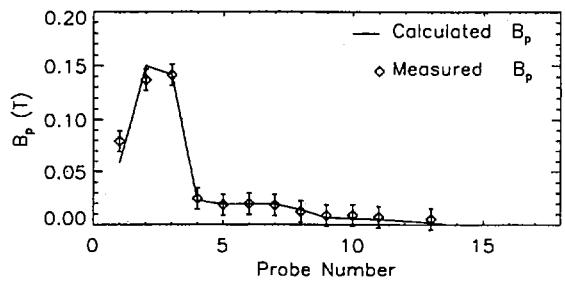

FIG. 5. Comparison of measured surface poloidal magnetic fields with those calculated by using the resistive open field line model at time t = 0.5 ms. A single resistivity of $\eta = 8.0 \times 10^{-5}\ \Omega \cdot m$ is used. Calculated: I_{inj} = 11.3 kA; measured: I_{inj} = 10.9 kA. The goodness of fit parameter for the probes is $\chi^2 = 0.54$.

used these shots initially in developing this model for the following two reasons: (a) The magnetic fields produced by closed flux shorten the field line length and consequently decrease the resistance on these field lines and change the $\lambda(\psi)$ profile. Since knowledge of the closed flux profile is needed to properly include this effect, it is more straightforward to only look at cases with no closed flux; this allows a direct comparison of theory and experiment. (b) Three magnetic field probes were available in the injector region, which allows a stringent test of the applicability of this model. Two of the probes were removed after these early discharges.

The resistive model for $\lambda(\psi)$ is derived by considering the general force free state:

$$\nabla \times \mathbf{B} = \lambda(\psi)\mathbf{B} = \mu_0 \mathbf{J}$$

Integrating this expression along an open field line and using $\mathbf{J} = \mathbf{E}/\eta$ yields the relation:

$$\lambda(\psi) = \frac{\dfrac{\mu_0 V_{inj}}{\eta}}{\int \mathbf{B}\cdot d\mathbf{l}}$$

The equilibrium is solved using a simple non-optimized code; $\lambda(\psi)$ is calculated at every iteration from the $\psi(R, Z)$ of the previous iteration. Two η's are used: one for the short open field lines in the injector region and one for the long open field lines in the confinement region. The η's are varied until a good fit is obtained to the edge magnetic fields and the injector current. Figure 5 shows a comparison of the calculated and measured edge magnetic fields for one such equilibrium, using a single uniform resistivity of $8.0 \times 10^{-5}\ \Omega\cdot m$. The model is now being extended to include closed flux.

5. SUMMARY

The HIT experiment has formed plasmas with over 200 kA and temperatures in the 100 eV range. We are beginning to understand the nature of the observed $n = 1$ mode and are studying its role in driving current in the closed field region. A simple resistive equilibrium model seems to explain the current profile on the open field lines.

REFERENCES

[1] FISCH, N., Rev. Mod. Phys. **59** (1987) 175.
[2] BOOZER, A.H., Phys. Fluids **31** (1988) 591.
[3] JARBOE, T.R., Fusion Technol. **15** (1989) 7.
[4] PENG, Y.-K.M., STRICKLER, D.J., Nucl. Fusion **26** (1986) 769.
[5] HOLMES, J.A., et al., Phys. Fluids B **1** (1989) 358.

[6] COLCHIN, R.J., et al., Phys. Fluids B **5** (1993) 2481.
[7] NELSON, B.A., et al., Phys. Plasmas **2** (1995) 2337.
[8] JARBOE, T.R., et al., in Plasma Physics and Controlled Nuclear Fusion Research 1994 (Proc. 15th Int. Conf. Seville, 1991), Vol. 1, IAEA, Vienna (1995) 705.
[9] BOOZER, A.H., J. Plasma Phys. **72** (1986) 133.
[10] BROWNING, P.K., et al., in Controlled Fusion and Plasma Physics (Proc. 20th Eur. Conf. Lisbon, 1993), Vol. 17C, Part II, European Physical Society, Geneva (1993) 503.
[11] HUGRASS, W.N., GRIMM, R.C., J. Plasma Phys. **26** (1981) 455.
[12] LAO, L.L., et al., Nucl. Fusion **25** (1985) 1611.
[13] ORVIS, D.J., JARBOE, T.R., Rev. Sci. Instrum. **66** (1995) 3263.
[14] DeLUCIA, J., et al., J. Comput. Phys. **37** (1995) 183.
[15] SPANJERS, G., et al., Rev. Sci. Instrum. **63** (1992) 5148.
[16] GALAMBOS, J., et al., Rev. Sci. Instrum. **67** (1996) 469.
[17] GALAMBOS, J., et al., Rev. Sci. Instrum. (in press).
[18] MARTIN, A., JARBOE, T.R., Plasma Phys. Control. Fusion (in press).
[19] BARNES, C.W., et al., Phys. Fluids B **2** (1990) 1871.

COMPARATIVE STUDY OF COMPACT TOROID PLASMAS FORMED BY INDUCTION AND RECONNECTION

M. YAMADA, H. JI, T.A. CARTER, S.C. HSU,
R.M. KULSRUD, N.L. BRETZ, F.C. JOBES
Plasma Physics Laboratory,
Princeton University,
Princeton, New Jersey,
United States of America

Y. ONO, M. KATSURAI
University of Tokyo,
Tokyo, Japan

T.-H. WATANABE, T. SATO, T. HAYASHI
National Institute for Fusion Science,
Nagoya, Japan

Abstract

COMPARATIVE STUDY OF COMPACT TOROID PLASMAS FORMED BY INDUCTION AND RECONNECTION.

By merging inductively formed co-helicity and counter-helicity spheromaks on MRX at PPPL, helicity-amplified spheromaks and FRC's have been successfully generated. This novel formation scheme, which invokes neither conventional fast shock heating nor electrode discharges, has significant advantages in developing a compact reactor core. The paper reports initial results from a comparative study of compact toroid configurations, emphasizing global MHD stability and optimum high beta operation. The helicity-amplified spheromak and FRC formation have been reproduced in numerical simulations.

1. Introduction

In recent years, compact toroids, such as FRC's (field reversed configuration), spheromaks, and spherical tokamaks (or ultra low aspect ratio tokamak, ULART) have been extensively studied in the search for a cost-effective, high-performance plasma regime, which can lead to compact D-T volumetric neutron sources as well as a high power density reactor [1, 2]. They can each confine high beta plasmas with large natural elongation, opening the road to an advanced fuel reactor [2]. The recent results from START [3] showed that the confinement properties of the ULART can be as good as that of conventional tokamaks (aspect ratio ~ 3). FRC and spheromak configurations do not require external toroidal coils, a significant reactor advantage, but they suffer serious

n=1 global tilt/shift instabilities. Furthermore, conventional FRC and spheromak formation relies on fast shock heating or electrode discharges, which are disadvantageous in generating a reactor plasma.

Two spheromak plasmas which have toroidal fields and currents can merge to form a larger (or higher field) plasma, thus allowing plasma formation and subsequent fusion reactions in the merged plasma to occur in separate sections of the chamber [4]. A series of experiments have been carried out to form FRC configurations by merging two spheromaks with opposing toroidal magnetic fields [5]. High ion temperature was obtained during this FRC formation process, and the origin of the observed enhanced ion energy was attributed to the annihilation of toroidal fields during magnetic reconnection [6].

In this paper we demonstrate our novel formation scheme of compact toroids, utilizing induction and merging of co-helicity and counter-helicity spheromaks. Because this formation scheme invokes neither conventional fast shock heating nor electrode discharges, it is significantly advantageous in developing a compact reactor core. Emphasis is given to the formation process and the global MHD characteristics of the compact toroid configurations ($R/a \approx 1.05 - 1.5$).

2. Experimental Setup

The MRX (Magnetic Reconnection Experiment) device [7] has been constructed to investigate the fundamental physics of magnetic reconnection and plasma merging. The device creates an environment to satisfy the criteria for MHD plasmas (Lundquist number $S \gg 1$, ion gyro-radius $\rho_i \ll$ plasma size L), and the boundary conditions can be controlled externally.

Figure 1 shows the experimental setup in MRX, which has two flux cores with 37.5 cm major radii and 10.0 cm minor radii. Inside each core, there is a 4-turn coil (PF coil) that carries a toroidal current and a helical 36-turn toroidal solenoid (TF coil). By pulsing currents in the TF coils after a quadrupole poloidal magnetic field is established by the PF coil currents, plasmas are created around each flux core by induction. At the same time, a common annular plasma

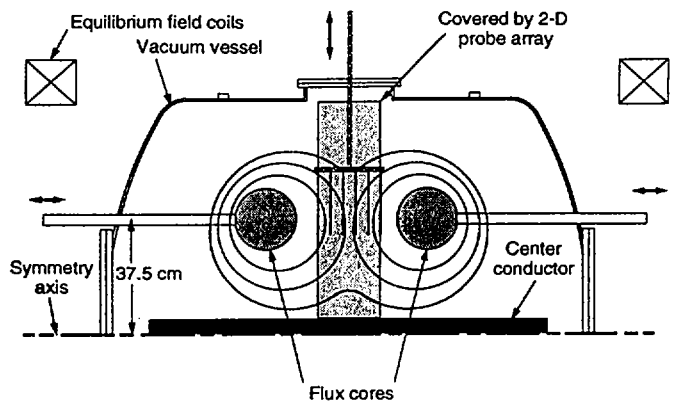

FIG. 1. Cross-sectional view (upper half) of the MRX experimental setup. Here, a thin center conductor (R = 5 cm) ensures axisymmetric formations but no stabilizing effects.

forms outside the two toroidal plasmas surrounding the two flux cores. Thus the magnetic field domain can be divided into two sections, a public domain and private domains of each flux core. Magnetic reconnection is induced when two toroidal plasmas are made to merge by pre-programmed flux core coil currents. These two toroidal plasmas carry identical toroidal currents with the same (co-helicity) or opposite (counter-helicity) toroidal fields. After the annular plasmas are created, the PF coil current is decreased to "pull" the poloidal flux in the common plasma back toward the X point (pull mode) [8]. Counter-helicity reconnection in this case can be regarded as "null-helicity" reconnection, since the incoming poloidal fluxes carry very little toroidal flux.

When the PF coil currents are further reduced to a negative value, the annular plasmas are broken off from the flux cores, forming spheromaks. A larger single spheromak or an FRC, depending on helicity, is formed by merging the two spheromaks. Plasma sizes are 30-100 ion gyro-radii. A Lundquist number $S > 700$ has been attained already in 50-60 kA discharges, and for higher current (100 kA), $S > 1500$ is expected. The start-up diagnostics include magnetic probe arrays, Langmuir probes, interferometer, flux loops and Rogowski coils.

3. Formation of Current Sheet during Magnetic Reconnection

In the initial MRX experiments, the pull modes have been intensively studied in cases with (co-helicity) and without (null-helicity) the third vector component of the magnetic field (B_T). In both cases, toroidal currents of equal magnitude are flowing parallel to each other. While similar 2D pictures of reconnection are expected for both cases, they are quite different in the 3D picture. For co-helicity merging, the transition of the merging angle across the neutral line is gradual and smooth. But in null-helicity merging, the pitch of the field lines changes abruptly at the reconnection point.

Figure 2 shows a comparison of the time evolution of poloidal flux contours derived from internal probe signals for co-helicity and null-helicity plasma merging. Other plasma boundary conditions are the same for each discharge. It has

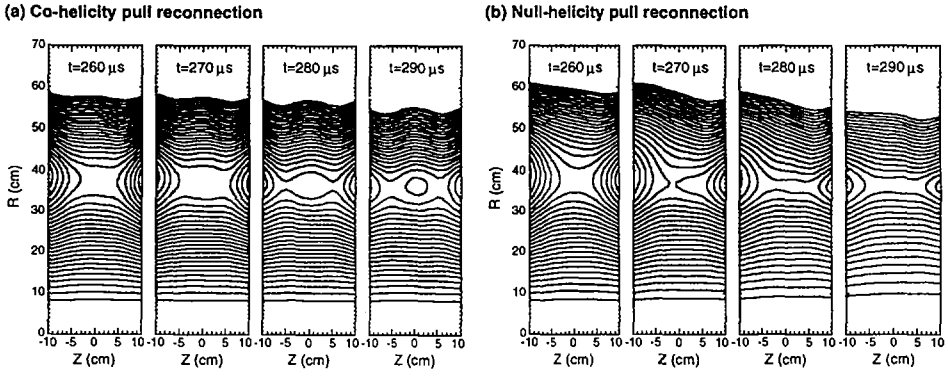

FIG. 2. Time evolution of poloidal flux measured by internal magnetic probes in (a) co-helicity and (b) null-helicity (or counter-helicity) reconnection.

been found that merging of null-helicity plasmas occurs faster than merging of co-helicity plasmas, consistent with the previous results [9]. A cause of the observed slower reconnection rate for co-helicity merging may be due to the toroidal field pressure in the reconnection region.

Generally, a Y-shaped neutral sheet region is identified in null-helicity merging while an O-shaped region is seen in co-helicity merging, as shown in Fig. 2. The neutral current sheet in the null-helicity merging case is much narrower than in the co-helicity merging case. The thickness of the Y-shaped sheet was measured with high resolution of 5 mm and was found to be as thin as 1 cm ($\sim \rho_i$). Toroidal current density contours were deduced for the same sequence of shots, verifying the important 2D feature of neutral sheet currents.

4. Formation and Stability of Spheromaks and FRC's

An inductive formation scheme, which was developed for S-1 spheromak research, generates a spheromak by inducing plasma currents around a flux core [10]. In MRX, we have found that a spheromak can be generated more effectively with two flux cores than with one flux core. As shown in Fig. 3, the seed current developed at the O-shaped diffusion region during co-helicity reconnection grows into a large spheromak when the PF coil current is reduced to a negative value. The stability of the initial seed current seems to be due to an absolute minimum B configuration produced by the initial poloidal plasma current in the outer public region of the quadrupole field. Total plasma current up to 60 kA has been measured.

An FRC can be formed as a result of null-helicity (or counter-helicity) reconnection when the PF coil current is reduced to a negative value. The FRC formation can be divided into two stages; (1) a current sheet forms during null-helicity pull reconnection and serves as the seed of the FRC when the PF coil current is being reduced but still remains positive, and (2) the FRC is formed by merging

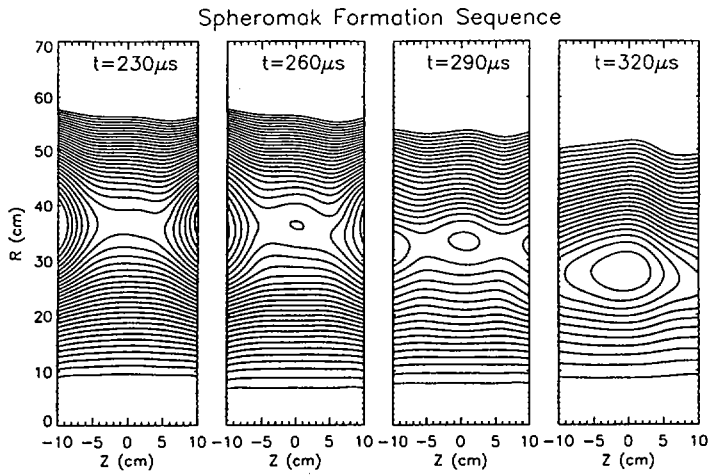

FIG. 3. Spheromak formation as a result of co-helicity reconnection.

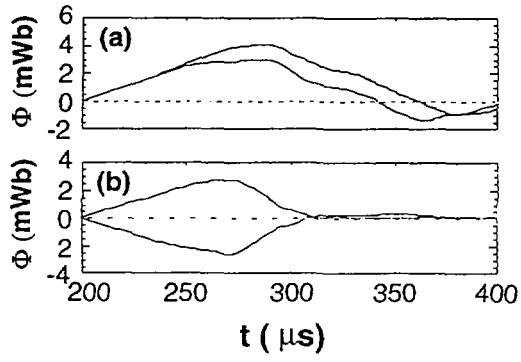

FIG. 4. Waveforms of toroidal flux contained in each plasma during the formation of (a) a spheromak and (b) an FRC.

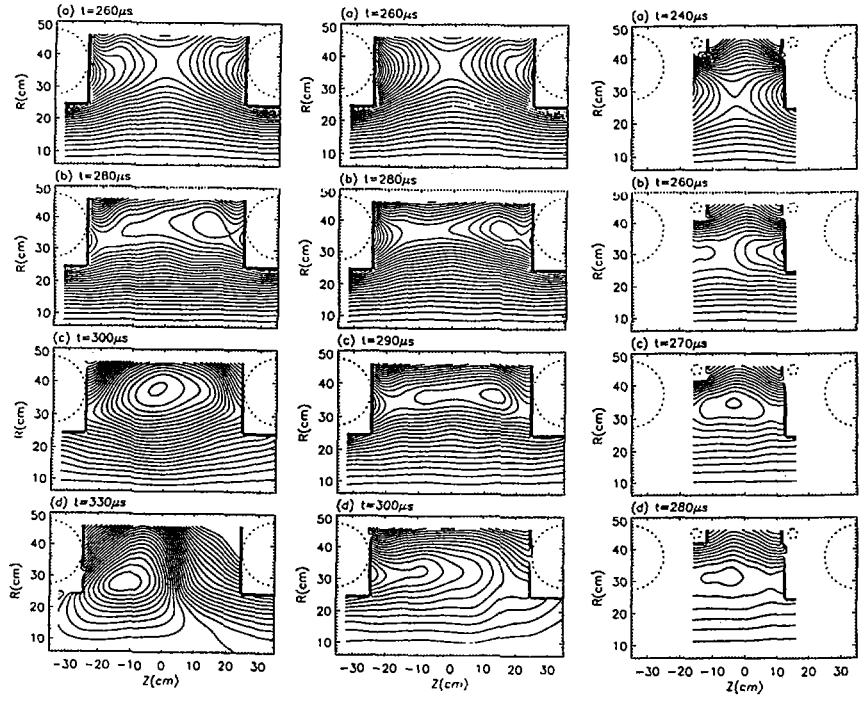

FIG. 5. Each column of pictures shows a formation sequence. From the left: spheromak formation in the initial setup (Fig. 1), FRC formation in the initial setup, FRC formation after two copper rings are added.

the two counter-helicity spheromaks pinched off from the flux cores when the PF coil current is further reduced across zero. Initially, the two spheromaks contain oppositely directed toroidal fluxes, Φ, of the same order as the poloidal fluxes, Ψ. During merging, however, Φ decreases precipitously (Fig. 4(b)) while Ψ remains essentially unchanged, indicating an evolution toward the FRC. The plasma current is up to 40 kA in this case.

Lifetimes of the spheromaks seem to be limited by tilting or axial shifting instabilities. One example is shown in the left column of Fig. 5 where the spheromak starts to tilt slowly 30 μs after formation, leading to a lifetime of 40-50 μs. In order to stabilize the axial shifting mode and improve tilting stability, two copper rings were installed at $Z = \pm 15$ cm and $R = 42$ cm, creating a favorable vertical field. The spheromak lifetime is extended to ~ 70 μs. When a center conductor with a radius of 12 cm is added to further improve tilting and radial shifting stabilities, the spheromaks last more than 100μs.

The FRC's appear to be much more unstable than the spheromaks, presumably due to its large ratio of separatrix radius to ion gyro-radius, s (~ 10). As indicated in the middle column of Fig. 5, the FRC's last $< 10\mu$s in the initial setup shown in Fig. 1. With two passive stabilizing rings added (the right column of Fig. 5), the lifetime is improved to ~ 20 μs, suggesting that FRC's are more sensitive to passive stabilizers. We note two differences between our work and previously successful FRC generation on TS-3 [5]. TS-3 used electrode discharges while we use inductive formation, and MRX plasma size is larger by a factor of two or three.

5. Numerical Simulation of Merging Spheromaks

A 2D MHD simulation [11,12] of both co-helicity and counter-helicity merging of spheromaks has been performed with the aim of studying the formation

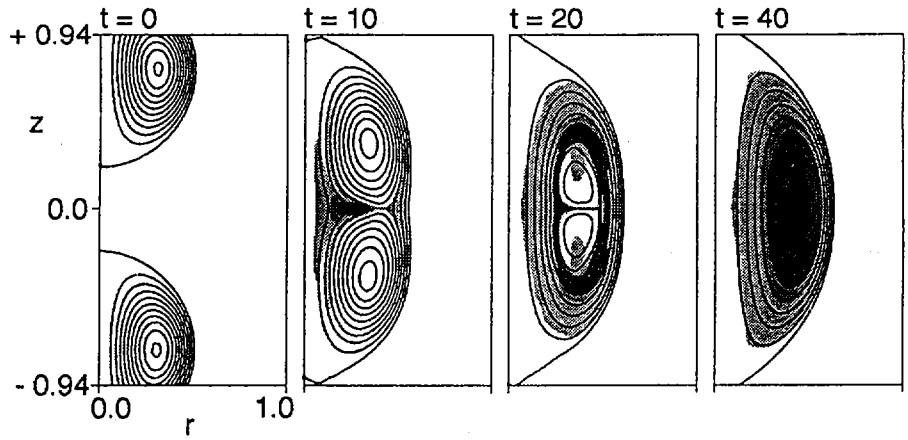

FIG. 6. Contour plots of poloidal flux obtained by MHD simulation of counter-helicity spheromak merging at $t = 0$, $10\tau_A$, $20\tau_A$, and $40\tau_A$. Increased pressure is represented by increased shading of the plot.

processes of spheromaks and FRC's. Computational grids with inhomogeneous spacing in the Z direction are employed so that the very thin current layer formed between reconnecting flux surfaces can be accurately resolved, with $S = 10^4$ and a constant viscosity. The two spheromaks initially located at $Z = \pm 0.75$ with radii of 0.5 attract each other, and the merging process takes place from $t = 5\tau_A$ to $t = 28\tau_A$. We have plotted contour maps of poloidal flux at different time steps in Fig. 6 where the intensity of the pressure is represented by shading. In counter-helicity merging, the anti-parallel toroidal magnetic fields annihilate themselves, converting large amounts of magnetic energy into thermal energy. During the coalescence of spheromaks, the pressure is locally increased in the vicinity of the reconnection point due to Joule and viscous heating. It is found that the local pressure gradient excites a compressive motion of the flux surfaces. Then the pressure profile, whose gradient balances the Lorentz force term, is spontaneously formed. Moreover, the oscillation of the toroidal magnetic field and plasma flows, as was observed in the experiments [5], have been reproduced in the simulation. The Alfvén oscillation was repeated more than four times, relaxing the toroidal magnetic tension. The FRC is obtained in the final state of counter-helicity merging.

6. Summary & Discussion

By effectively utilizing plasma merging, we have demonstrated a new compact toroid formation scheme which has significant reactor relevance. Inductive formation with the double flux cores is superior to electrode discharges because it minimizes plasma-wall interactions. Although the primary goal of this short pulse experiment is not to achieve high electron temperature, we have attained high beta plasmas ($0.1 < \beta \leq 1$), as confirmed experimentally by an interferometer and Langmuir probes. A helicity-amplified spheromak and an FRC have been successfully formed as consequences of co-helicity and null-helicity (or counter-helicity) magnetic reconnection. It is found that an FRC is very unstable against global tilt/shift modes which are attributed to the large value of s. Stability of the spheromaks and FRC's has been improved by adding passive stabilizers, which reduce tilting and axial shifting of the plasma. Numerical studies have been also carried out to simulate both co-helicity and counter-helicity merging.

Table I Outstanding scientific issues which can be addressed by merging compact toroid experiments.

Concept	FRC	Spheromak	RFP	ULART/ST
Issues to be addressed in MRX	• $s = \langle R \rangle / \rho_i >> 1$ • Sustainment • OH • CT merging	• Center-rod stabilization • Flux injection by merging	• Low aspect ratio limit	• Connection to Tokamak / ULART
Common Issues	• Study of transition between configurations • Global confinement & gross MHD stability to low-n modes			

As shown in Table I, the present experiment can address not only many outstanding physics issues of compact toroid plasmas but also important MHD physics of low aspect ratio RFP's (Reversed Field Pinch) and ULART's, which can be formed by driving a current in a thin conductor along the major axis. Primary issues which can be addressed in MRX are (i) formation and sustainment of a large s FRC configuration by merging spheromaks with opposite helicities and by inductive sustainment using an ohmic transformer; (ii) generation of a flux amplified spheromak by merging, and stabilization of low-n MHD modes in this configuration by driving a current in a center rod (connection to ULART); (iii) formation of low aspect ratio RFP's by driving a programmed current in a center rod; (iv) global confinement characteristics of ULART configurations; (v) cross-boundary regimes among these configurations, revealing the highest advantages of each concept for compact reactor design.

The MRX program is jointly supported by the Department of Energy, the National Aeronautics and Space Administration, the National Science Foundation, and the Office of Naval Research of the United States Government.

REFERENCES

[1] Compact Toroids Special Issue, Fusion Technol. **9** (1986).
[2] PENG, Y.M., HICKS, J.B., Fusion Technol. **21** (1992) 1729.
[3] SYKES, A., et al., Plasma Phys. Control. Fusion **35** (1993) 1051.
[4] KATSURAI, M., YAMADA, M., Nucl. Fusion **22** (1982) 1407.
[5] ONO, Y., MORITA, A., ITAGAKI, T., KATSURAI, M., in Plasma Physics and Controlled Nuclear Fusion Research 1992 (Proc. 14th Int. Conf. Würzburg, 1992), Vol. 2, IAEA, Vienna (1993) 619 and references therein.
[6] ONO, Y., et al., Phys. Rev. Lett. **76** (1996) 3328.
[7] YAMADA, M., et al., in Proc. Int. Conf. on Plasma Physics, Nagoya, 1996, p. 558.
[8] JI, H., et al., ibid., p. 554.
[9] YAMADA, M., et al., Phys. Rev. Lett. **65** (1990) 721.
[10] YAMADA, M., et al., Phys. Rev. Lett. **46** (1981) 188.
[11] DASGUPTA, B., et al., Fusion Technol. **27** (1995) 374.
[12] WATANABE, T.-H., et al., Phys. Plasmas **4** (1997) 1297.
[13] YAMADA, M., et al., Nucl. Fusion **36** (1996) 1210.

DISCUSSION

D.D. RYUTOV: My question relates to the merging of two spheromaks with opposite toroidal fields. Why was electron heating so small — about 5% of the ion heating? In other words, did the ohmic dissipation not play a significant role in the annihilation process?

M. YAMADA: In global magnetic reconnection, a significant acceleration of bulk ions is observed (due to slingshot effects) together with compressional heating of ions. The ion motions are thermalized through large ion viscosity. (This can be

interpreted as a viscosity damping of fluctuating ion currents.) The measured electron dissipation is very small.

T.R. JARBOE: What are the Lundquist number and the mean free paths for these experiments?

M. YAMADA: The Lundquist number is 700 on MRX ($a_p \cong 40$ cm) and 300 on TS-3 ($a_p \cong 18$ cm). The mean free path is $\lambda_{mpf} \cong 2$–3 cm for electrons and 1 cm $< \lambda_{mpf} \leq 100$ cm for ions (but T_i is only measured on TS-3).

EXPERIMENTAL OBSERVATION OF DIRECT ION HEATING/ACCELERATION DURING MERGING FORMATION OF AN FRC

Y. ONO, M. KATSURAI, M. INOMOTO, Y. UEDA,
H. YASUDA, T. OKAZAKI, T. AKAO, T. ITAGAKI
Department of Electrical Engineering,
University of Tokyo,
Tokyo, Japan

M. YAMADA
Plasma Physics Laboratory,
Princeton University,
Princeton, New Jersey,
United States of America

Abstract

EXPERIMENTAL OBSERVATION OF DIRECT ION HEATING/ACCELERATION DURING MERGING FORMATION OF AN FRC.

A novel merging formation of a field reversed configuration (FRC) has been developed in the TS-3 merging experiment, leading to a new scenario of FRC slow formation, heating and current amplification. Two force free spheromaks with opposing toroidal fields were merged in the axial direction to form a high β FRC with an ion temperature of up to 200 eV. A central OH coil was used to amplify the FRC by a factor of 2–3. This unique relaxation from the force free ($\beta \approx 0.05$–0.1) spheromaks to the high β ($\beta \approx 0.7$–1) FRC is attributed to direct conversion of toroidal magnetic energy to ion thermal energy through their counter-helicity reconnection.

1. INTRODUCTION

A spheromak and a field reversed configuration (FRC) are both compact toroids whose simply connected topologies allow their axial translations and mergings [1, 2]. The spheromak, with toroidal and poloidal magnetic fields B_t, B_p, is often found to be in the Taylor magnetic energy minimum state, which ensures its global MHD stability. The Taylor state is widely known to be a stable force free state with zero plasma thermal pressure (β = plasma thermal pressure/magnetic pressure = 0) [3]. On the other hand, the FRC, solely with a poloidal magnetic field B_p, has a high β plasma equilibrium which is interpreted not by the low β approximation but possibly by thermal and kinetic effects [2]. Recently, interest has grown in generating FRCs with large values of s (average number of ion gyroradii) to improve their confinement [4], extending the FRC stability into a non-kinetic MHD regime. Slow formation of the FRC is essential to future large scale confinement experiments and also

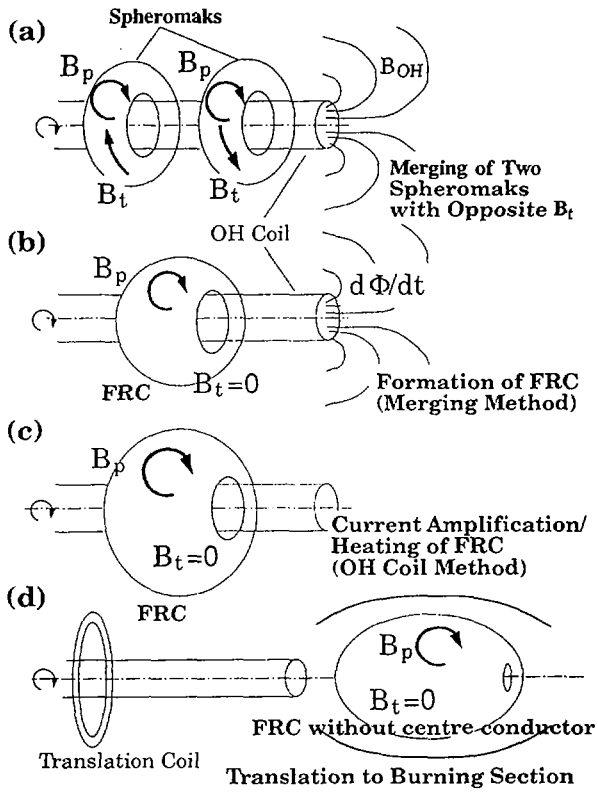

FIG. 1. (a, b) Merging formation of an FRC by use of two spheromaks with opposing B_t; (c) its flux (current) amplification/heating; and (d) its translation to a burning section.

to plasma formation in the large s MHD regime. However, the conventional θ pinch formation was found to have some difficulties in producing large FRCs stably and efficiently on a slow time-scale. New slow formation techniques were developed by use of double coaxial coils at the University of Washington [5] and by use of low β merging spheromaks at the University of Tokyo [6–8]. Though the poloidal fluxes of FRCs were successfully injected on a slow time-scale by the former method, their temperatures tended to be lower than 20 eV, probably owing to lack of the plasma heating source [5]. An important question arises as to whether high temperature FRCs in the high β regime can be produced by use of two merging spheromaks in the low β regime. We have demonstrated the slow formation of an FRC with an ion temperature as high as 200 eV using two merging spheromaks with opposing B_t [6–9].

This paper describes this novel merging formation and the developed scenario of FRC slow formation, heating and flux (current) amplification [6–9]. As shown in Figs 1(a) and (b), two force free spheromaks with opposing toroidal magnetic fields B_t are axially collided. The magnetic reconnection annihilates their opposing B_t, forming an FRC with $B_t \approx 0$ [6–8]. The produced FRC is amplified and heated by use of an OH coil (Fig. 1(c)) [7] and is finally translated to a burning section (Fig. 1(d)) [10]. The cause and mechanism of the equilibrium transition from the low β spheromaks to the high β FRC were made clear by means of selective ion heating properties of magnetic reconnection. The OH current amplification up to a factor of 3 and the high s properties of the produced FRC, such as n = 1 instability, were studied experimentally.

This merging formation has several advantages over the conventional θ pinch formation of an FRC: (1) slow formation (eliminating the need for a fast capacitor bank), (2) a stable formation process with high energy efficiency using minimum energy spheromaks, (3) use of the merging process for initial ion heating, (4) expected large s properties and (5) the applicability of a current transformer for the toroidal current amplification.

2. EXPERIMENTAL SET-UP

Figure 2 shows the experimental set-up in the TS-3 merging device characterized by the Z–θ pinch type formation of the initial two spheromaks [8]. Eight pairs of electrodes and a poloidal field coil are located on each side of the vessel to produce each spheromak. The B_t polarities of the two spheromaks are determined independently by those of the Z discharge currents between the electrodes. A replaceable central OH coil is located along the centre axis to amplify the plasma current of the produced FRC. Its shell is also used to maintain plasma stability against the n = 1 (tilt and/or shift) modes. A 2-D magnetic probe array is placed on the R–Z plane of the vessel to measure 2-D profiles of axial and toroidal magnetic fields B_z and B_t for a single discharge. This 2-D array is composed of 144 pick-up coils covered with thin glass tubes of 5 mm diameter. These data are used to calculate the 2-D contours of poloidal flux (Ψ) and toroidal field amplitudes, and evolution of the magnetic energy W_m within the separatrix, using the following formula:

$$W_m = \int B^2/2\mu_0 \, dv = \int \pi R(B_z^2 + B_r^2 + B_t^2)/\mu_0 \, dR \, dZ$$

Another replaceable 2-D array of magnetic probes is placed on the R–θ plane to measure the toroidal mode (n) amplitudes and phases from n = 1 to n = 3. An electrostatic probe is inserted along the axial line at R = 14 cm to measure the profiles of the electron temperature T_e and the electron density n_e. A CO_2 laser interferometer is used to calibrate the value of n_e. The Doppler shifts and widths of

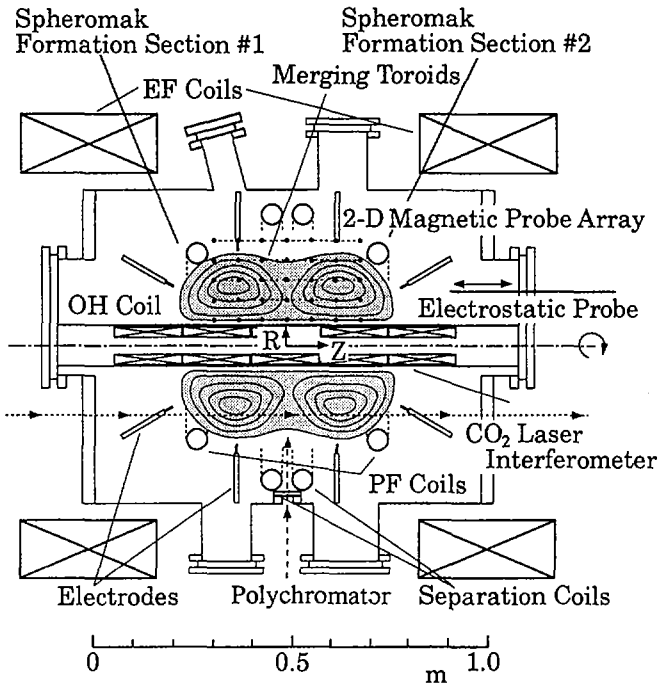

FIG. 2. Experimental set-up of the TS-3 merging device at the University of Tokyo.

C II and H_β spectral lines are measured by a polychromator with an optical multichannel analyser to obtain radial profiles of ion temperature T_i and velocity V on the midplane.

3. EXPERIMENTAL RESULTS

3.1. Direct ion heating during merging formation of an FRC

Recently, a significant increase in ion temperature T_i has been documented during this merging formation of an FRC, revealing a new equilibrium transition mechanism from the low β spheromaks to the high β FRC [6–9]. Figure 3(a) shows the 2-D contours of poloidal flux surface and toroidal field amplitude measured by the 2-D magnetic probe array [8]. The red and blue colours indicate positive and negative toroidal field amplitudes, respectively. Two spheromaks with opposing B_t are produced on a slow time-scale ($\approx$ 40 μs) and merged within 10 μs from t = 10 to 17.5 μs. The opposing B_t fields are annihilated around the reconnection (X) point and the field null region (with no colour) gradually expands as the counter-helicity reconnection proceeds. The reconnected field lines offer an overshoot or an

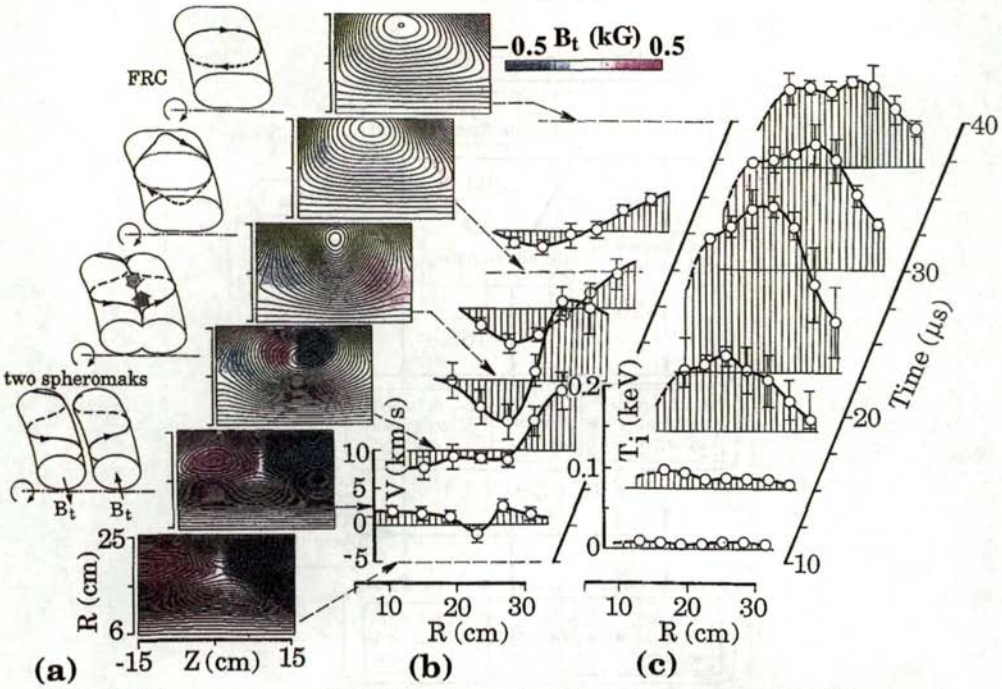

FIG. 3. Time evolutions of (a) 2-D contours of poloidal flux surface and toroidal magnetic field B_t on the R–Z plane, (b) radial profiles of ion toroidal velocity V and (c) radial profiles of ion temperature T_i on the midplane, during the merging of two spheromaks with equal but oppositely directed B_t. The red and blue colours indicate positive and negative amplitudes of B_t, respectively.

oscillation. Initially, the polarity of B_t is positive on the left hand side and negative on the right hand side; then after t = 20 μs it becomes negative on the left hand side and positive on the right hand side. Figures 3(b) and (c) show the radial profiles of ion toroidal velocity V and ion temperature T_i measured on the midplane. From t = 12.5 to 22.5 μs, V is observed to increase in both edge regions. Its polarity is positive for R > 18 cm and negative for R < 18 cm. Both measurements are consistent with the view that the inner halves and the outer halves of the reconnected field lines accelerate plasma ions in opposite senses in the toroidal direction, as illustrated in Fig. 3 [6–9, 11]. The maximum velocity of about 12 km/s (at R = 22 cm) is as large as (0.3–1) times the local Alfvén speed.

Ions are heated significantly and selectively from 10 to 200 eV from t = 15 to 23 μs, as shown in Fig. 3(c). This anomalous ion heating occurs when large velocity shear is formed by the field line acceleration. During this period, the electron temperature T_e stays around 10–20 eV, indicating that the counter-helicity reconnection heats ions selectively. Since the increment in n_e is small, the large increase in T_i is the main cause of the β transition from 0.05–0.1 (spheromak) to 0.7–0.9 (FRC). The produced velocity shear and the B_t field with reversed polarity gradually vanish,

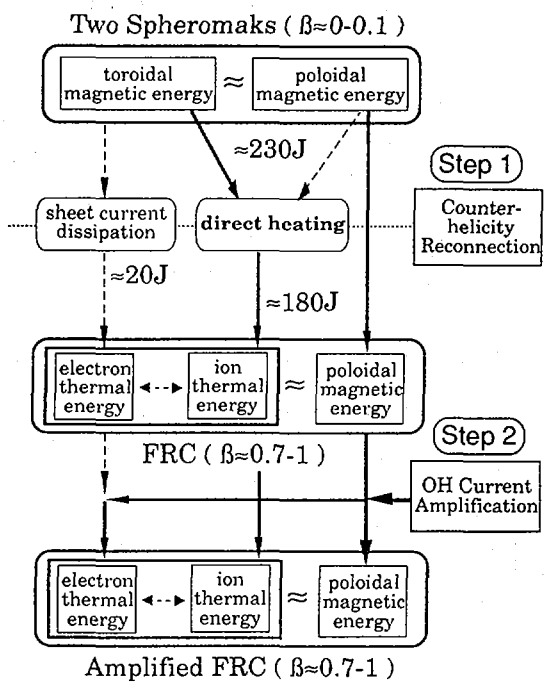

FIG. 4. Energy flows during the merging formation and OH current amplification of an FRC.

relaxing the plasma to an FRC with uniform $B_t \approx 0$ before t = 30–40 μs [6–9]. As shown in Fig. 4, these B, T_i, T_e and n_e measurements indicate that the total increase in the ion thermal energy, $W_{i,th} \approx 180$ J, is as large as 80% of the dissipated magnetic energy, $W_m \approx 230$ J (the whole toroidal magnetic energy and part of the poloidal energy), during the reconnection [9]. Dissipation of the neutral current sheet, $W_{sheet} \approx 2\pi R_X \delta L E_{t,x} j_{t,x}$, is estimated to be as small as 20 J, on the basis of the measured electric field $E_{t,x}$, current density $j_{t,x}$, width δ, length L and radius R_X of the neutral current sheet. These facts indicate that W_m is converted directly to $W_{i,th}$ and that this merging formation is useful not only for the slow formation but also for the initial ion heating of the FRC. Large ion viscosity plays an important role in thermalizing the accelerated ions in the bulk plasma. The viscosity force against the ion acceleration is significantly large, because a wide field null region is produced around the reconnection (X) point, as shown in Fig. 3(a). This viscosity heating of plasma ions is considered to be much larger than that of electrons, because the ions with large gyroradii are unmagnetized much more widely around the X and O points with $B_t \approx 0$ than the electrons with small gyroradii.

3.2. Current amplification using an OH coil

This slow formation method also enables us to install an OH coil along the geometric axis of the produced FRC [6, 7]. After the merging formation is completed, the toroidal electric field is applied to the FRC for its current amplification, as illustrated in Fig. 1. Figure 5 shows the time evolutions of the toroidal plasma currents of the FRCs for five different (vacuum) loop voltages V_{loop} varying from 0 to 540 V. The corresponding evolutions of poloidal flux contours and toroidal field amplitudes are also shown for V_{loop} = 0 and 540 V. Since the total amount of our capacitor bank energy is limited, the energy used for the FRC merging formation

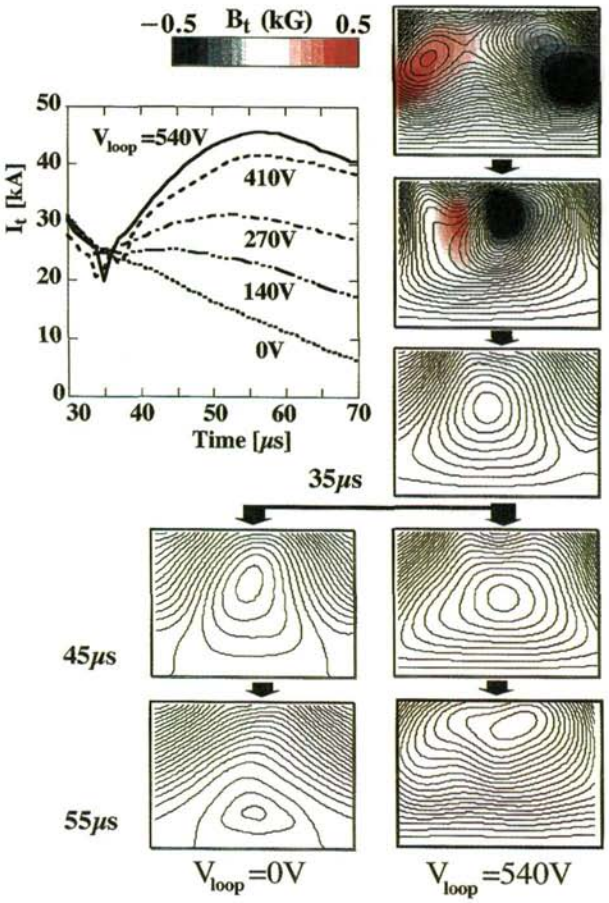

FIG. 5. Time evolutions of toroidal plasma currents when five different (vacuum) loop voltages V_{loop} from 0 to 540 V are applied to the FRCs. The corresponding evolutions of poloidal flux contours and toroidal field amplitudes are also shown for V_{loop} = 0 and 540 V. The red and blue colours indicate positive and negative amplitudes of B_t, respectively.

is about 50% as large as that in Fig. 3. When the applied V_{loop} is as large as 540 V, the toroidal current of the FRC is successfully amplified by a factor of 1.8 from 25 to 45 kA within 20 μs. The poloidal flux of the FRC is also amplified by a factor of 2.5, because the OH coil field also expands the FRC by reducing the external equilibrium field. In the case of $V_{loop} = 0$, the FRC is observed to decay monotonically within 60 μs, in sharp contrast to the cases of $V_{loop} > 0$. It is noted that the current amplification does not cause the FRC to relax to a spheromak with $B_t \approx B_p$ in the minimum magnetic energy state but that B_t of the FRC is kept uniformly zero. It is suggested that the FRC equilibrium has some robust stability against the external flux injection. During the current amplification, T_i stays constant (around 100 eV for $V_{loop} = 540$ V) for 10 μs and then starts decreasing, and T_e increases slowly up to 30 eV. The plasma current increment is found to increase almost linearly with V_{loop}. On the basis of these results, this OH coil method is concluded to be attractive for the current amplification and possible electron heating of the FRC.

3.3. Stability of oblate FRCs in an external magnetic field

Axial translation of the produced oblate FRCs and their stabilities in the future burning section without the centre conductor are being studied in an external magnetic field, on the basis of the scenario in Fig. 1. The external coil current produces

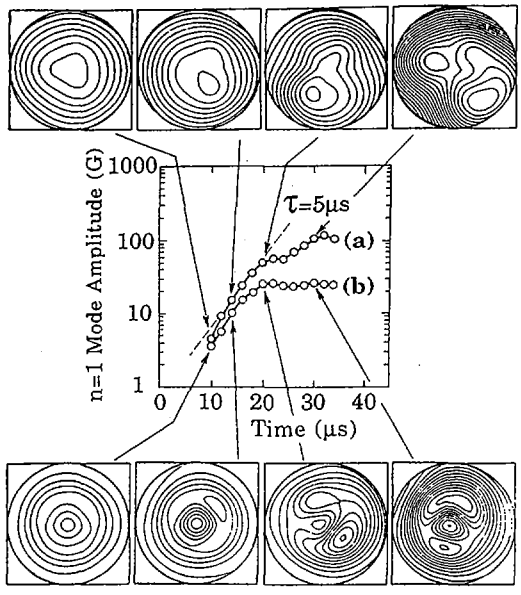

FIG. 6. Axial magnetic field contours on the midplane (R–θ) for two FRCs with different s values of (a) 6.4 and (b) 2.9 (at t = 18 μs). The time evolutions of their n = 1 toroidal mode amplitudes are also calculated at R = 10 cm for these cases.

the field pressure with a rise time of about 10 μs to translate the FRC in the axial direction. With the help of the shells of the centre OH coil, the FRC is observed to move stably with a speed of up to 10 km/s. Once the centre conductor is removed, the n = 1 tilt mode is found to be the most dangerous instability for the oblate high s FRCs in an external magnetic field. In this experiment, the centre OH coil is removed from the set-up in Fig. 2 to let all toroidal modes grow. The produced oblate FRCs have s values varying from 1.5 to 10 and elongation factors e from 0.5 to 2, depending on the filling pressure and the external magnetic field index. Figure 6 shows the 2-D profiles of axial magnetic field amplitudes on the midplane (R–θ) for the two FRCs with different s values of 6.4 and 2.9 (at t = 18 μs). The time evolutions of their n = 1 toroidal mode amplitudes are also calculated at R = 10 cm for these cases. The n = 1 mode amplitude of the high s (6.4) FRC is observed to increase significantly from t = 10 to 30 μs and to destroy the whole FRC equilibrium before t = 40 μs. On the other hand, the FRC with s = 2.9 is observed to rotate in the toroidal direction after the initial growth of the n = 1 mode. As the toroidal rotation evolves, the n = 1 mode amplitude is found to saturate or increase markedly slowly. The n = 1 mode amplitude tends to decrease as the s value is decreased, although the n = 1 mode is not fully suppressed within the experimentally obtained s value of over 1.5. These facts are consistent qualitatively with recent high s experiments on FRCs [12]. A large radius centre conductor (or the OH coil) is found necessary for the high s oblate FRC to fully stabilize its n = 1 tilt mode.

3.4. Close relationship between FRCs and low aspect ratio tokamaks in a diamagnetic regime

One possible method to stabilize the observed n = 1 instability is to apply an external toroidal magnetic field to the high s FRCs. The resulting high β plasma, if maintained, corresponds to the low aspect ratio tokamak in a diamagnetic (high β_p) regime, indicating the close relationship between these two equilibria. Recently, the low aspect ratio tokamak has received increased attention as a future economic reactor, partly because of its possible second stability (high β_p) property. However, the formation of diamagnetic tokamaks requires a hollow current profile, limiting the startup discharges. A question arises as to how we can suppress the paramagnetic component of the toroidal field that tends to prevail in low aspect ratio tokamaks. The merging method, especially its direct ion heating effect, can be used for the current profile control of tokamaks, such as the startup of the diamagnetic tokamak formation. The reconnection with a wide (toroidal) field null region similar to the merging formation of an FRC is obtained by symmetrical merging of two reversed field pinches (RFPs) or possibly by the counter-helicity merging of a tokamak and an RFP. As shown in Fig. 7, the former merging process suppresses the paramagnetic toroidal field by injecting the internal toroidal field in the opposite direction to the external one and by heating plasma ions through reconnection. The toroidal field is observed

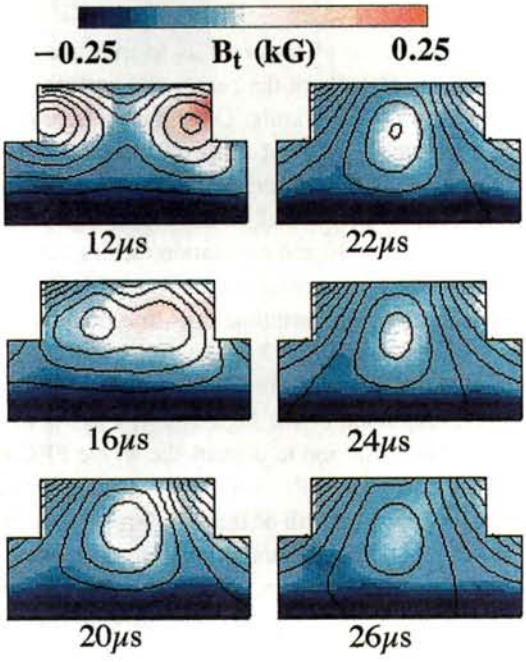

FIG. 7. 2-D (R–Z) contours of poloidal flux surfaces and toroidal field B_t amplitudes during merging of two RFPs. The orange and blue colours indicate positive and negative amplitudes of B_t, respectively.

to vanish during the reconnection, indicating the formation of a diamagnetic tokamak. However, the tokamak is observed to decay quickly (within 5–10 μs). This fact suggests that the produced diamagnetic tokamak is unstable, possibly as a result of some MHD instability related to the current profile. A powerful heating source and control of the instability are needed for the further investigation of this high β tokamak in a diamagnetic regime.

4. SUMMARY AND CONCLUSIONS

A series of experiments has demonstrated a new scenario for the merging formation of an FRC, flux amplification by a centre OH coil and sustainment of the produced and translated FRC in an external magnetic field. The merging formation process for a high β FRC revealed the ion acceleration and direct ion heating effects of the counter-helicity magnetic reconnection with a wide field null region. Contraction of reconnected field lines was observed to accelerate plasma ions toroidally up to a velocity of the same order as the Alfvén velocity and to heat them directly and selectively through the large ion viscosity around the field null (X point) region. This high efficiency direct conversion of toroidal magnetic energy to ion thermal energy

makes possible the novel equilibrium transition from the low β merging spheromaks to the high β FRC. The OH current drive was observed to amplify the FRC successfully by a factor of 2–3 within 20 μs. The merging process is useful for the initial ion heating of the FRC, and the OH current drive for its electron heating. The centre conductor is found necessary to fully stabilize the n = 1 tilt mode of the oblate FRCs with large s numbers up to 10. Without the centre conductor, the oblate FRCs with s > 4 suffer from a large increase in the n = 1 mode, although the n = 1 mode amplitude decreases with decreasing s number. The observed selective ion heating during FRC formation is also consistent with recent macroparticle and MHD simulations [9, 13, 14] and provides a possible explanation for the anomalous ion heating in the RFPs whose X points have a small toroidal magnetic field [15]. The growth and suppression of the n = 1 tilting instability observed in large s and small s regions agree qualitatively with the s scan experiment in FRX-C/LSM [12]. Finally, the close relationship between FRCs and low aspect ratio tokamaks in a high β/diamagnetic regime has been made clear by a new experiment to apply an external toroidal magnetic field to the high β merging toroids.

ACKNOWLEDGEMENTS

The authors are grateful to T. Tajima and R. Matsumoto for their support with the MHD and macroparticle simulations and to R. Kulsrud for useful discussions.

REFERENCES

[1] ROSENBLUTH, M.N., BUSSAC, M.N., Nucl. Fusion **19** (1979) 489.
[2] TUSZEWSKI, M., Nucl. Fusion **28** (1988) 2033.
[3] TAYLOR, J.B., Phys. Rev. Lett. **33** (1974) 1139.
[4] TUSZEWSKI, M., et al., Phys. Rev. Lett. **66** (1991) 711.
[5] PIERCE, W.F., et al., Nucl. Fusion **33** (1993) 117.
[6] ONO, Y., MORITA, A., ITAGAKI, T., KATSURAI, M., in Plasma Physics and Controlled Nuclear Fusion Research 1992 (Proc. 14th Int. Conf. Würzburg, 1992), Vol. 2, IAEA, Vienna (1993) 619;
ONO, Y., YUMOTO, A., KATSURAI, M., in Proc. 13th Int. Conf. on Plasma Science, Saskatoon, 1986, IEEE Service Center, Piscataway, NJ (1986) 77.
[7] ONO, Y., Fusion Technol. **27** (1995) 369.
[8] ONO, Y., et al., Phys. Fluids B **5** (1993) 3691.
[9] ONO, Y., et al., Phys. Rev. Lett. **76** (1996) 3328.
[10] HIMURA, H., et al., Phys. Plasmas **2** (1995) 191.
[11] YAMADA, M., et al., Phys. Rev. Lett. **65** (1991) 721.
[12] TUSZEWSKI, M., et al., Phys. Rev. Lett. **66** (1991) 711.
[13] TAJIMA, T., SAKAI, J.I., Sov. J. Plasma Phys. **15** (1989) 519.
[14] BRAHMANANDA, D., SATO, T., Fusion Technol. **27** (1995) 375.
[15] SCHOENBERG, K.F., et al., in Plasma Physics and Controlled Nuclear Fusion Research 1988 (Proc. 12th Int. Conf. Nice, 1988), Vol. 2, IAEA, Vienna (1989) 419;
SCIME, E., et al., Phys. Fluids B **4** (1992) 4062.

PROGRESS IN DENSE Z-PINCH RESEARCH AT IMPERIAL COLLEGE

M.G. HAINES, R. ALIAGA ROSSEL, T.D. ARBER, J.M. BAYLEY, F.N. BEG, A.R. BELL, J.P. CHITTENDEN, M. COPPINS, A.E. DANGOR, D.F. HOWELL, A. LORENZ, S. LUCEK, I.H. MITCHELL, P.G.F. RUSSELL, M. TATARAKIS, J. WORLEY, G. DECKER[1], H. SCHMIDT[2]
Blackett Laboratory,
Imperial College of Science,
Technology and Medicine,
London, United Kingdom

Abstract

PROGRESS IN DENSE Z-PINCH RESEARCH AT IMPERIAL COLLEGE.

Recent work on Z-pinches at Imperial College is reported. The experimental programme is based around two generators: MAGPIE (2.4 MV, 1.9 MA) and IMP (800 kV, 250 kA). It involves studies of hot spot formation and development, prepulse, disruptions, and Faraday rotation measurements. Simulations of the experiment and theoretical work on stability with large ion Larmor radius effects and sheared flow are also reported.

1. INTRODUCTION

The dense Z-pinch has the potential of being a compact fusion reactor of high power density. For example, it is possible to consider the employment of repetitive pulsed power to drive a Z-pinch in a 200 ns pulse with 100 ns confinement time in a plasma column of 5 cm length, 100 μm diameter and a density of 5×10^{21} cm^{-3} at a current of 1 MA. The return conductor, first wall and breeder would be liquid lithium. The major questions at this stage are physics issues: can a Z-pinch be formed at this high density, and can it be made sufficiently stable to maintain this high density at fusion temperatures? We are considering various possible non-linear stabilizing mechanisms, including large ion Larmor radius effects and sheared flow.

Whilst the main objective of the Imperial College programme (see Ref. [1] and references therein) is to explore the attainment of radiative collapse at a current in excess of the Pease–Braginskii critical value, the above physics issues are relevant to both objectives. The experimental programme is based around the MAGPIE generator (2.4 MV, 1.9 MA, 150 ns rise-time) and a new small generator, IMP (800 kV, 250 kA, 150 ns). The experiments reported here on MAGPIE use 33 μm diameter carbon fibres as well as CD_2 fibres; those on IMP use 7 μm carbon fibres.

[1] Heinrich-Heine-Universität, Düsseldorf, Germany.
[2] Universität Stuttgart, Stuttgart, Germany.

In addition, there is a wide ranging theoretical programme, principally on stability, together with MHD simulations in 1-, 2- and 3-D.

2. HOT SPOTS

A common feature of many Z-pinches and plasma focus experiments has been the occurrence of a series of bright spots of X ray emission along the axis. By means of time resolved optical and X ray streak and framing camera images we have shown that these 'hot spots' are transient in nature; they occur randomly at different times and have the property of bifurcating with supersonic axial velocities ($(1\text{-}3) \times 10^5$ m·s^{-1}). Advection of the magnetic field, which is partially frozen to the plasma, gives rise to gradients of the magnetic field in the axial direction which manifest themselves as radial currents. This produces a $j_r B_\theta$ force which is of opposite sign on either side of the neck of the instability and drives the bifurcation. Figure 1 shows axially aligned streak photographs of both the optical and X ray emission from the plasma. These experiments were conducted on MAGPIE using 33 μm carbon fibres and largely follow the phenomena found in earlier experiments at lower currents (250 kA) and with narrower fibres (7 μm).

By employing an atomic physics package containing ionization and recombination rates and all ionization stages, in our 2-D MHD code we have now modelled the hot spots and shown that they are a coupling of the m = 0 MHD mode to an ionization wave that results in a more rapid conversion of the fibre to a fully ionized state. Figure 2 shows mass density and temperature contours from the 2-D simulation illustrating hot spot bifurcation. Later there is a more quiescent phase.

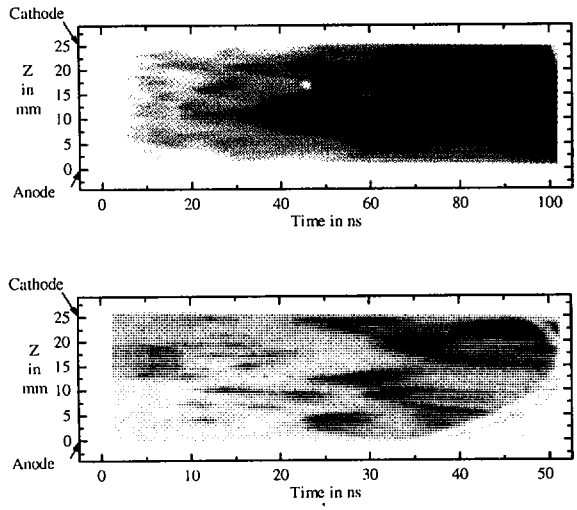

FIG. 1. Optical and X ray axial streak photographs.

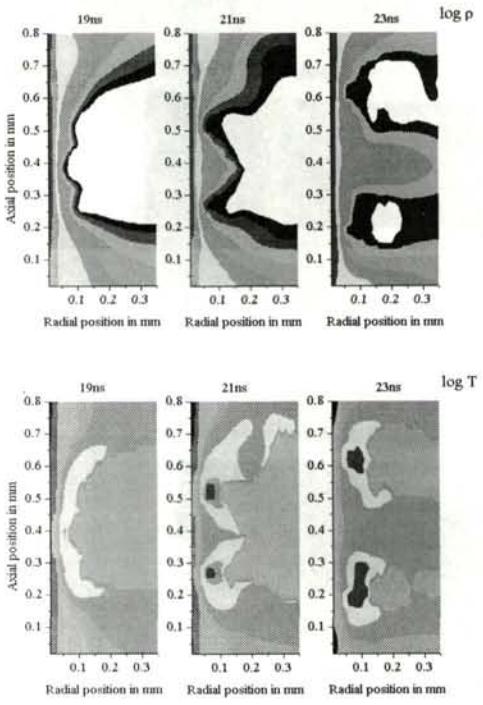

FIG. 2. Mass density and temperature contours from the 2-D simulation.

3. PREPULSE

An 8 kA, 60 ns prepulse has been applied on IMP. When applied between 100–200 ns before the main current, the transient m = 0 hot spots are completely eliminated from the main discharge. Figure 3 shows optical streak photographs with and without prepulse. The development of hot spots at an early time in the latter case can be seen clearly. The prepulse forms a coronal plasma around the fibre, and there is enhanced X ray emission (measured by collimated PIN diodes). The use of a prepulse promises to be a good technique for forming a uniform stable (to m = 0) column although there is some indication of the development of an m = 1 like structure.

4. FARADAY ROTATION MEASUREMENTS

An important experimental question is the current and magnetic field distribution in the discharge. A laser diagnostic system has been developed on the basis of a frequency doubled SLM YAG laser (800 mJ, 5 ns FWHM) which is compressed

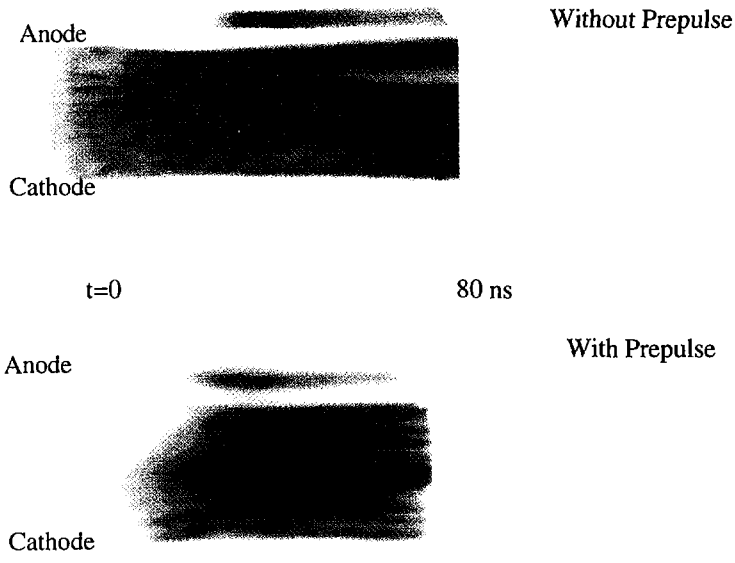

FIG. 3. Streak photographs of discharges without and with prepulse.

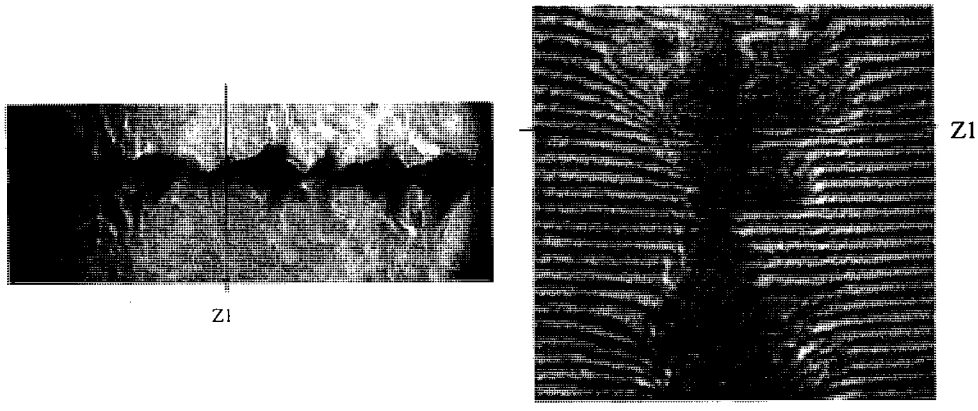

FIG. 4. Simultaneous polarogram and interferogram at 50 ns.

to 200 ps FWHM by using a stimulated Brillouin backscattering technique. This was employed to make simultaneous shadowgrams, interferograms and Faraday rotation polarograms of the coronal plasma. Figure 4 shows a polarogram and an interferogram from the same shot at 50 ns. The polarogram shows the angle by which the plane polarized laser beam is rotated in passing through the plasma ($\theta \propto \int Bn_e d\ell$). Abel inversion of the interferogram gives the electron number density distribution which is necessary to obtain the magnetic field distribution. From this we have shown that a large fraction of the generator current (approximately 90%) flows through the pinch, though much is in the low density corona.

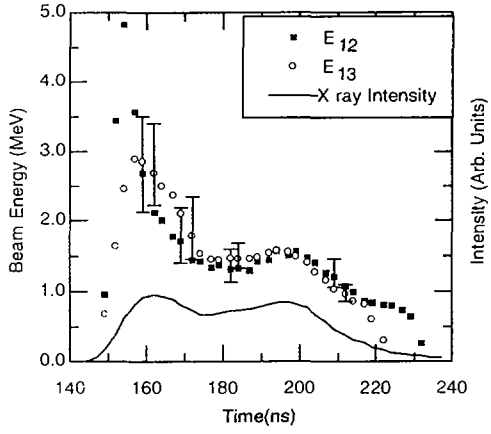

FIG. 5(a). Results from a 33 μm carbon fibre. E_{12} and E_{13} are the electron beam energies obtained from detector pairs 1-2 and 2-3, respectively.

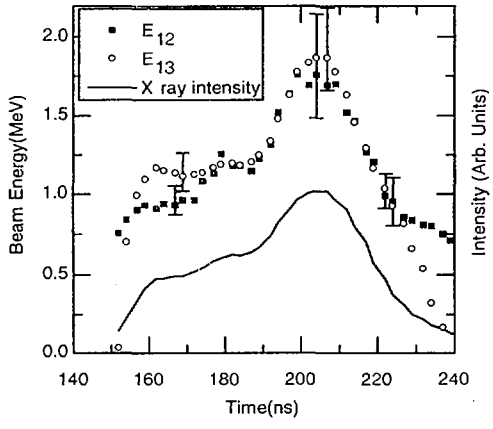

FIG. 5(b). Results from a 25 μm aluminium fibre.

5. DISRUPTIONS

At later times (about 130–160 ns) the m = 0 structures evolve to produce large density islands. Coincident with a dip in dI/dt there is a burst of hard X ray emission from the anode signifying the generation of high energy electron beams. A detailed spectral analysis has been made [2]. The energy is significantly higher than any applied voltage and can be associated with rapid changes of inductance and resistance. Figure 5 shows the electron beam energies obtained from the ratios of differently filtered scintillator/photomultiplier detectors for both a 33 μm carbon fibre load and a 25 μm aluminium fibre.

We speculate that at the m = 0 neck energetic ion and electron beams are produced. Following this the line density drops below a critical value leading to the onset of lower hybrid turbulence with an associated anomalous resistivity. This condition would be characterized by a lack of pressure balance, and an expanding current density in the region between density islands; this expanding current profile or decreasing inductance allows a high voltage to be generated across the islands, and hence electron beams can be produced during this time.

When CD_2 fibres are employed, beam–target neutrons (approximately 10^9 per shot) are produced. Time of flight and anisotropy measurements allow us to infer an ion beam energy of 2–3 MeV. The same energy and degree of anisotropy are found if the polarity of the electrodes is reversed.

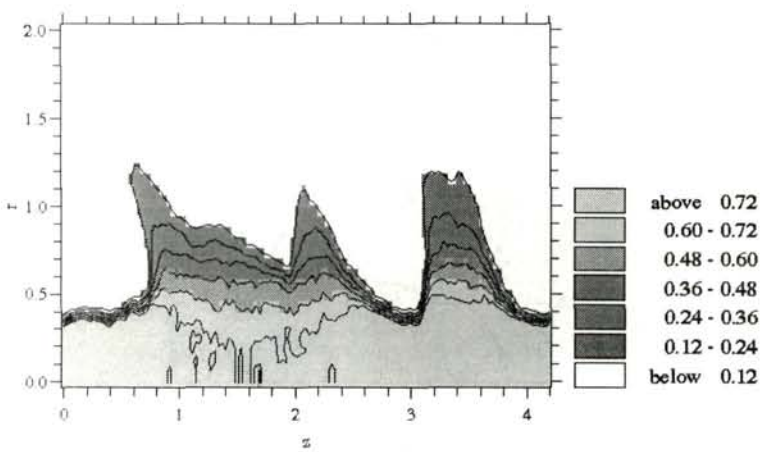

FIG. 6. Density contours for the m = 0 instability in the non-linear, large Larmor radius regime.

6. LARGE LARMOR RADIUS THEORY

Finite and large ion Larmor radius effects should be important in future cryogenic fibre experiments. Our theoretical work [3] has shown that with an optimal value of ϵ (i.e. the ratio of average ion Larmor radius to pinch radius) in the range of 0.1–0.2 the linear growth rate for the uniform current density equilibrium is reduced (from its $\epsilon = 0$ value) by approximately 70% for m = 0 and 80% for m = 1.

A 2-D non-linear hybrid code (kinetic ions/electron fluid) has been developed to explore the possibility of large Larmor radius saturation of the m = 0 instability. Initial results show no saturation in the case of the uniform current density equilibrium at $\epsilon = 0.15$. Figure 6 shows the calculated density profile after 3.5 radial ion thermal transit times. The extreme non-linear behaviour depends sensitively on the treatment of the plasma edge and the coupling to the vacuum. This is where the present model breaks down because of the neglect of anomalous resistivity. Therefore, no definitive conclusions on instability saturation can be drawn until the modelling of the outer part of the plasma has been improved.

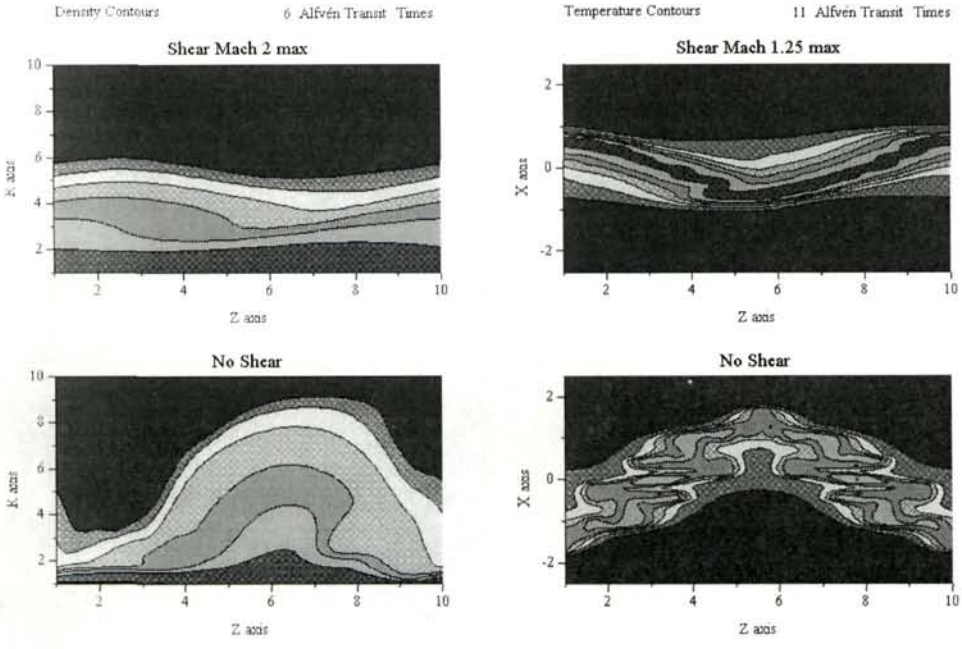

FIG. 7. Effect of sheared axial flow on m = 0 and m = 1 instabilities.

7. SHEARED FLOW

Using linear MHD we find [4] that sheared flow reduces the growth rates of both m = 0 and m = 1 instabilities (Fig. 7). The effect is particularly significant at short wavelengths, for cases in which the maximum flow speed is above about Mach 4. The non-linear regime has been studied by using ideal MHD codes in 2-D (for m = 0) and 3-D (for m = 1). For flow speeds above about Mach 1 to 2, the effect of sheared flow is to smear out the instability structure and prevent it from growing.

ACKNOWLEDGEMENTS

This work was supported by the Engineering and Physical Sciences Research Council and the Ministry of Defence.

REFERENCES

[1] HAINES, M.G., et al., in Plasma Physics and Controlled Nuclear Fusion Research 1994 (Proc. 15th Int. Conf. Seville, 1994), Vol. 2, IAEA, Vienna (1995) 387.
[2] ROBLEDO, A., et al. (in preparation).
[3] ARBER, T.D., et al., Phys. Rev. Lett. **74** (1995) 2698.
[4] ARBER, T.D., HOWELL, D.F., Phys. Plasmas **3** (1996) 554.

PLASMA CONFINEMENT AND STABILITY STUDIES IN THE GAS DYNAMIC TRAP EXPERIMENT

A.V. ANIKEEV, P.A. BAGRYANSKY, P.P. DEICHULI,
A.A. IVANOV, A.N. KARPUSHOV, V.V. MAXIMOV,
I.V. SHIKHOVTSEV, N.V. STUPISHIN, Yu.A. TSIDULKO,
S.G. VOROPAEV, S.V. MURAKHTIN, K. NOACK[1],
H. KUMPF[1], S. KRAHL[1], G. OTTO[1]
Budker Institute of Nuclear Physics,
Novosibirsk, Russian Federation

Abstract

PLASMA CONFINEMENT AND STABILITY STUDIES IN THE GAS DYNAMIC TRAP EXPERIMENT.

Studies on the gas dynamic trap (GDT) are focused on verification of the basic physical ideas underlying the GDT based 14 MeV neutron source to be used in fusion materials tests. Recent experimental results obtained in studies of the relaxation of neutral beam produced fast ions are presented. The parameters of fast ions are compared with those obtained by Monte Carlo simulations in order to reveal possible anomalies in their angular scattering or slowing down which would be caused by instabilities. To within the measurement accuracy (±10%), no anomalies in the relaxation of fast ions were observed. The macroscopically stable confinement of plasma containing fast ions was achieved with a stabilizing cusp end cell. Measurements showed that the stabilizing capacity of the cusp end cell appeared to be high enough to keep the entire plasma within the stability margins in the presence of fast ions whose energy content exceeded 5–10 times that of the bulk plasma. The plasma energy balance was measured in both the stable and unstable regimes. In the stable regimes, axial energy losses through the mirrors dominated the transverse losses as expected.

1. INTRODUCTION

A neutron source plasma consists essentially of two components. The isotropic, relatively cold component is confined in the collisional regime. In addition, the hot anisotropic ions are confined in the kinetic regime. These are produced in the gas dynamic trap (GDT) by neutral beam injection (NBI) at a skew angle at the centre of the device. In order to obtain fast ion density peaks near the mirrors, the angular spread of the ions should be relatively small during slowing down in the plasma. Correspondingly, the macroscopic stability of the plasma contained in the axisymmetric magnetic field and the microstability of anisotropic fast ions produced by NBI are of prime concern in the studies.

[1] Research Center Rossendorf, Inc., P.O. Box 510 119, D-01314 Dresden, Germany.

2. EXPERIMENTAL APPARATUS

The GDT facility is axially symmetrical [1, 2]. As shown in Fig. 1, it consists of a 7 m long central cell bounded at each end by min-B anchor cells of an expander and/or cusp configuration. In the experiments described here, we used the cusp end cell to stabilize curvature driven flute modes. The cusp plasma was fed by central cell plasma losses through the linking mirror. An additional plasma gun was used to vary plasma density in the cusp independently. Typically, the density in the cusp was 3–10% of that in the central cell. The magnetic field at the midplane was 0.22 T and

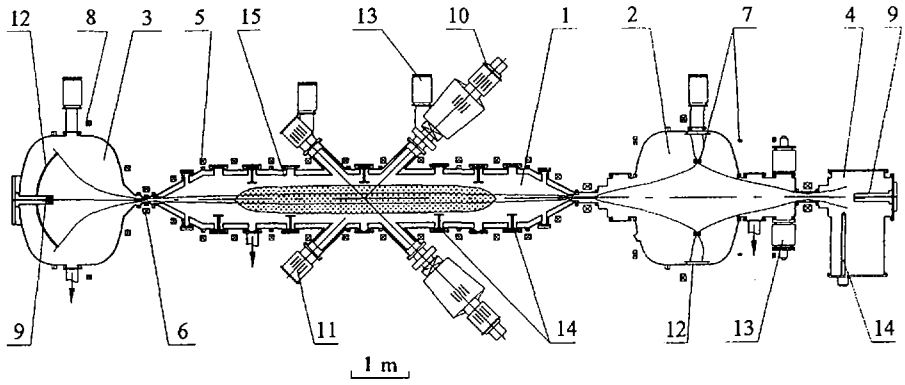

FIG. 1. GDT layout: 1, central cell chamber; 2, cusp tank; 3, expander end tank; 4, end tank; 5, central cell coils; 6, mirrors; 7, cusp coils; 8, expander coil; 9, plasma guns; 10, ion sources; 11, beam dumps; 12, plasma dumps; 13, pumps; 14, Ti evaporators; 15, liner.

the mirror ratio was variable in the range 12.5–75. The inner walls of the central cell vacuum chamber were covered with Ti between shots by making use of arc Ti evaporators. This resulted in significantly reduced outgassing of the first wall, associated in the GDT with access to higher plasma parameters [3]. An initial plasma, whose density varied in the range 10^{19} to 2×10^{20} m^{-3}, was produced by plasma guns located in the end tanks. The plasma was pulsed, with each shot lasting 3–5 ms. In order to heat the gun produced plasma and to provide energetic ions, six neutral beams were injected at the midplane at 45° to the axis. The total injected power of 15–16 keV neutral beams was up to 3.5 MW in 1.2 ms pulses. The injection heated up the target plasma and provided a buildup of fast ions.

3. MACROSCOPIC STABILITY OF A PLASMA WITH FAST IONS

Figure 2 shows the temporal behaviour of plasma energy in a typical plasma shot with NBI. The target plasma density was varied in the range (4–20) $\times 10^{19}$ m^{-3}, whereas the sloshing ion density (mean energy 3–6 keV) reached 5 $\times 10^{18}$ m^{-3}. Central cell electron temperatures approaching $T_e \approx 100$ eV were observed.

With the Ti covered first wall, the charge exchange lifetime of sloshing ions approached 10 ms, so that these losses became negligible in the plasma energy balance. The MHD stability studied involved measuring energy and particle losses from the central cell for various ratios of the plasma pressure of the central cell to that inside the cusp end cell. To quantify the stability property of the plasma, we used the data on radial profiles of the density and the electron temperature in conjunction with measurements of plasma diamagnetism and its profile along the central cell axis. In the central cell, owing to specific features of multicomponent plasma confinement in the GDT, the pressure of the anisotropic ion minority and that of the bulk plasma can be measured separately [3]. The fast ion radial density profile was measured by making use of special microcollectors inserted at the plasma periphery. To characterize the energy and particle confinement, we also used a Thomson scattering system, data from neutral beam attenuation detectors, a pyro-bolometer array and a radially segmented calorimeter which measured transverse energy losses.

To assess the stability of the cusp anchored GDT it was assumed that the pressure in the end cell is determined by the balance of the inward particle flux (entering the cusp from the central cell) and the outward flux (escaping through the ring and point cusps). The plasma temperature was assumed to be constant along the field line and equal to that in the central cell. For the sake of simplicity, we assumed the plasma pressure to be distributed uniformly over the end cell. With these assumptions, the stability of the large scale flute-like modes was evaluated using the sharp boundary plasma model.

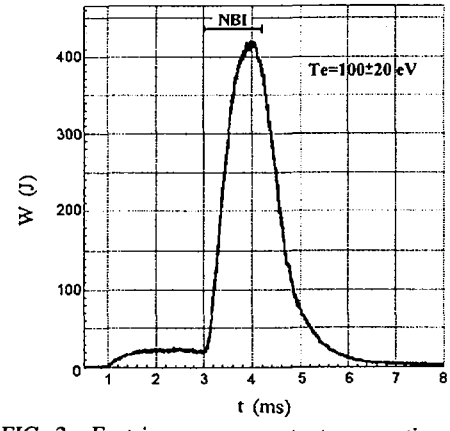

FIG. 2. Fast ion energy content versus time.

TABLE I. PLASMA PARAMETERS MEASURED IN THE STABLE AND UNSTABLE REGIMES FOR MODERATE TRAPPED NEUTRAL BEAM POWER

	Stable	Unstable
Plasma density (10^{19} m^{-3})	~4.5	~1
Trapped neutral beam power (kW)	550	180
Peak electron temperature (eV)	45	15–20
Losses to radial limiter (kW)	30	57
Energy losses through mirrors (kW)	280	45

By varying the plasma pressure inside the cusp, the entire plasma could be made either stable or unstable, so that the transition across the stability boundary could be observed. The plasma parameters in the cusp and in the central cell were measured at the boundary. Their values were found to be in reasonable agreement with those theoretically predicted. The plasma parameters measured in both the stable and unstable regimes for moderate trapped neutral beam power are given in Table I. Besides the significant differences in plasma temperature and density between these regimes, the conclusion can be drawn that in the MHD stable regime plasma is essentially lost longitudinally whereas in the unstable regime transverse losses to the limiter dominate. The stability property of the cusp end cell was measured to be significantly larger than that of the expander end cell [4]. In comparison with the expander stabilized plasma, when the cusp end cell was used the plasma temperature increased from 15 to about 100 eV and the density of fast ions from 10^{17} to 5×10^{18} m^{-3}.

4. LONGITUDINAL ENERGY LOSSES

Generally, from measurements of the plasma energy balance no evidence has been found of an additional cooling of the central cell plasma due to contact with the end walls. In separate experiments, the near axis segment of the end wall was replaced by a plate movable along the axis. When heated, the plate served to deliver into the plasma cold electrons whose current density may have exceeded that of the plasma electrons. It was expected that these electrons would reduce the near wall potential drop, allowing thermal electrons to freely strike the wall, that is, perfect thermal contact with the wall would be thus established. The plasma parameters in the near axis region in the central cell were measured for different positions of the plate in the expander end tank and for different current densities emitted by the plate. It was observed that when the distance between the plate and the mirror exceeded a certain value corresponding to a magnetic field reduction by a factor of 20–40, the

plasma parameters in the central cell were unchanged. Whenever the plate came closer to the mirror, a significant temperature reduction occurred, indicating an increase in the heat conduction to the plate.

Hence, it can be concluded that in accordance with theoretical considerations [5], the electron heat conductivity is suppressed when the magnetic field decreases towards the end wall approximately by a factor of $\sqrt{m_e/M_i}$. The reason is that the large potential drop between the central cell and the wall reflects back most of the hot electrons. In this case, inside the expander there is a population of low temperature trapped electrons. The density of trapped electrons is much smaller than that of transit electrons from the central cell. They are confined in the near end wall region and reduce the potential drop at the wall to a value significantly smaller than the central cell electron temperature. As an illustration, Fig. 3 shows the plasma potential in the central cell for different axial positions of the emitting plate. It can be seen that the potential drop between the central cell and the end wall arises if the

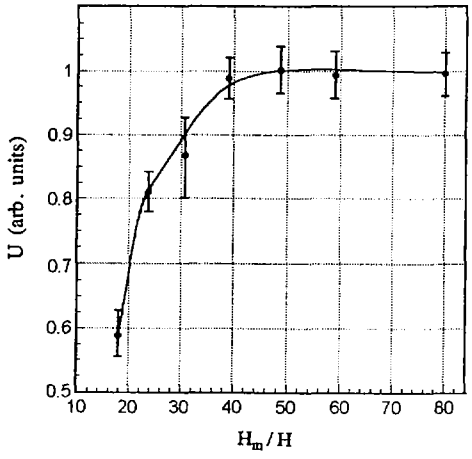

FIG. 3. Plasma potential versus current mirror ratio H_m/H (where H_m is the mirror field).

TABLE II. PLASMA PARAMETERS MEASURED IN THE EXPANDER COMPARED WITH THEORETICALLY PREDICTED VALUES

	Measured	Theoretical
Energy per ion-electron pair carried to end wall	$(8.7 \pm 1.8)T_e$	$7.9T_e$
Mean energy of ions striking wall	$(6.3 \pm 0.1)T_e$	$6.7T_e$
Electron mean energy near wall	$(0.3 \pm 0.15)T_e$	$0.1T_e$
Potential drop in expander	$(4.6 \pm 0.1)T_e$	$5T_e$

magnetic field falls below approximately $\sqrt{m_e/M_i}$ of the mirror field. The plasma parameters in the expander were measured in order to compare the longitudinal energy loss rate with that predicted by the theory of the collisionless regime of plasma flow beyond the mirrors [2]. These parameters are summarized in Table II together with the theoretically predicted values, given in parentheses.

5. CHARACTERIZATION OF FAST IONS

The behaviour of the neutral beam injected fast ions is the issue of primary concern in the studies of plasma containment in the GDT. If these ions scatter or lose their energy faster than they do through Coulomb collisions, the fast ion density in the peaks near the mirrors diminishes and ion energies decrease. This leads to deterioration of the parameters and of the efficiency of neutron production of the GDT based neutron source [2, 6, 7]. To characterize sloshing ions, their experimentally measured parameters were compared with those obtained by simulations. It was presupposed that the relaxation rates of fast ions in a given plasma background are defined solely by Coulomb scattering. The charge exchange losses would contribute an uncertainty to the comparison between the simulation and experimental data. In our case, these were made negligible compared with the others by depositing Ti on the central cell liner. Comparison of the Monte Carlo simulation with the experimentally measured gas pressure in the central cell shows that the recycling coefficient of a chamber wall which has been freshly coated with Ti is close to unity. Owing to strong reduction of the wall recycling, there are just two gas sources controlling the density of neutrals. The first is charge exchange neutrals born from the primary injected beams at the centre of the device. The other is the plasma recombining at the limiters located near the ends. According to simulations, the former contributes

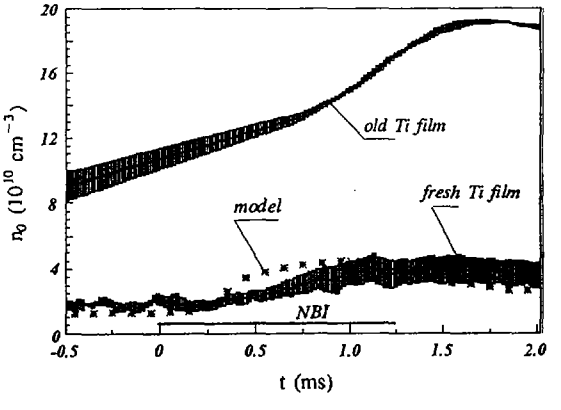

FIG. 4. Temporal variation of gas density.

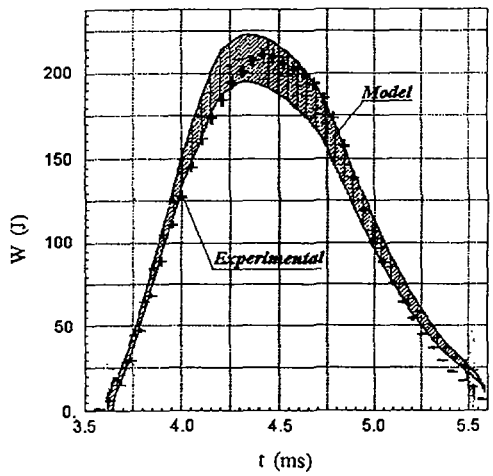

FIG. 5. Fast ion energy content.

merely 10% to the neutral density near the midplane because it is located far from the centre and, additionally, the relatively narrow chamber with the plasma column inside considerably reduces the gas conductance. Therefore, the 'warm' charge exchange neutral source generates about 70% of the total gas density.

The time history of the neutral gas density measured at the midplane is shown in Fig. 4 together with the results of Monte Carlo simulations for two regimes. The first, referred to as 'fresh Ti film', was recorded 5 min after deposition of Ti on the first wall; the other, referred to as 'old Ti film', was recorded 1 h after that. The good agreement between numerical and experimental results allows us to draw three conclusions: firstly, that fresh Ti film may be characterized as a clean Ti wall with a recycling coefficient $\gamma \approx 1$; secondly, that there are actually no other gas sources which could essentially affect the fast ions; thirdly, that after a while the deposited film quality deteriorates, e.g. for the old Ti film the recycling coefficient increases to $\gamma \approx 4$.

Figure 5 shows the temporal behaviour of the sloshing ion energy content. The crosses represent the experimentally measured values and also indicate the data scatter from shot to shot. The shaded area represents Monte Carlo and Fokker–Planck simulations for the given plasma parameters with regard to the scatter in the experimental data and the calculation accuracy. It should be noted that the simulations agree rather well with the experimental observations. Our previous measurements also indicate that the angular spread of the fast ions, averaged over the plasma volume, is quite close to that calculated theoretically [3]. However, the local parameters of the fast ions are expected to be more sensitive to the presence of non-classical mechanisms of plasma–fast ion interaction. The solution for local distribution function measurements of the ions has been to make use of an 'artificial

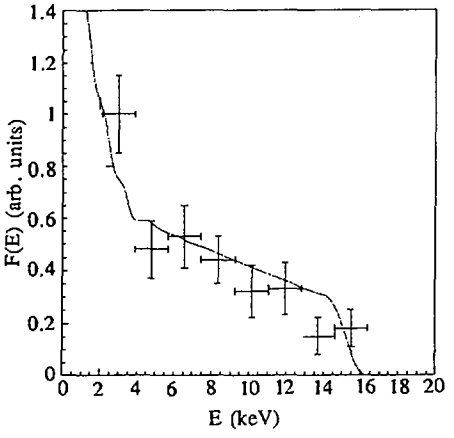

FIG. 6. Energy distribution of fast ions.

charge exchange target' method. This involved the injection of a diagnostic neutral beam at the centre of the device. As a result, fast ions experienced charge exchange collisions with the beam particles, thereby producing secondary neutrals. The spatial resolution of the measurements, which was determined by the beam diameter, was about 4 cm. These measurements were done at the centre of the device, where the injection of the main neutral beam was carried out. Therefore, we were forced to employ a focused diagnostic beam with high current density (equivalent to 0.7–1 A/cm^2 at 15 keV energy) in order to ensure a reasonable signal to background ratio in the presence of neutrals from the main six injectors that totalled 0.2–0.3 A/cm^2 inside the plasma. The injector provided 15–18 A of hydrogen atoms with an energy of 15 keV in 120 μs pulses.

The fast ion distribution at the centre of the device measured at an angle of 45° to the axis is shown in Fig. 6 together with the simulated distribution. These data are in reasonable agreement with the results of calculations taking into account the accuracy of the measurements ($\pm$15%). That is, the conclusion can be drawn that, to within the measurement accuracy, there is no evidence of anomalies in the fast ion relaxation in the plasma.

REFERENCES

[1] MIRNOV, V.V., RYUTOV, D.D., Sov. Tech. Phys. Lett. 5 (1979) 279.
[2] RYUTOV, D.D., Plasma Phys. Control. Fusion 32 (1990) 999.
[3] ANIKEEV, A.V., et al., in Controlled Fusion and Plasma Physics (Proc. 22nd Eur. Conf. Bournemouth, 1995), Vol. 19C, Part IV, European Physical Society, Geneva (1995) 193.

[4] IVANOV, A.A., et al., Phys. Plasmas **1** (1994) 1529.

[5] KONKASHBAEV, I.K., LANDMAN, I.S., ULINICH, F.R., Sov. Phys. — JETP **74** (1978) 956.

[6] IVANOV, A.A., KRUGLYAKOV, E.P., TSIDULKO, Yu.A., KRASNOPEROV, V.G., KORSHAKOV, V.V., in SOFE '95 (Proc. 16th IEEE/NPSS Symp. on Fusion Engineering, Champaign, 1995).

[7] IVANOV, A.A., KOTELNIKOV, I.A., KRUGLYAKOV, E.P., in Fusion Technology 1992 (Proc. 17th Symp. Rome, 1992), Vol. 2, Elsevier, Amsterdam (1993) 1394.

SIX BEAM SPHERICAL COMPRESSION OF PLASMA FOCUS GUNS

A. THEIN
Physics Department,
Dagon University,
Yangon

PE MYINT
Physics Department,
Pathein University,
Pathein

Myanmar

Abstract

SIX BEAM SPHERICAL COMPRESSION OF PLASMA FOCUS GUNS.

A preliminary experiment with a one beam plasma focus is carried out to confirm plasma formation with the lowest input energy of 0.2 kJ for six beam spherical compression of plasma focus guns. The plasma front of this cableless gun can be used for compression and for the coupling of six guns situated along three rectangular axes, providing a good plasma focus pinch instantaneously or many plasma focus pinches continuously. The whole device with the energy bank is mounted on a sphere, and the minimum requirement for the plasma chamber of this sphere is a diameter of ~22 cm.

1. INTRODUCTION

The plasma focus device [1–4] is one of the smallest, but most successful D–D fusion reaction devices; it has been demonstrated experimentally elsewhere as a pulsed neutron source. For the lowest input energy, Michel et al. [1] had reported 10^6 neutrons per shot; they had plotted the scaling law for neutron emission as a function of the input energy as $n \propto E^{2.1}$. Several experiments were carried out up to some hundred kilojoules, but a difficulty arises for higher input energy, because of the geometrical limitations of the device. The two coaxial guns [2] lying on opposite sides had already been studied, and the disk electrode type, high power, hypocycloidal pinch device had also performed well to produce a cylindrical plasma. However, plasma formation was very close to the electrodes.

In our present work, an energy bank with a maximum available energy of 0.192 kJ (8 kV) was constructed with capacitors of the type used for radios and mounted on the circular, grounded header of the outer electrode of a very small plasma focus gun. No cable connection is needed between bank and device. The plasma measurements are taken in order to develop six beam plasma focus guns; the minimum requirement for the size of the device is also studied.

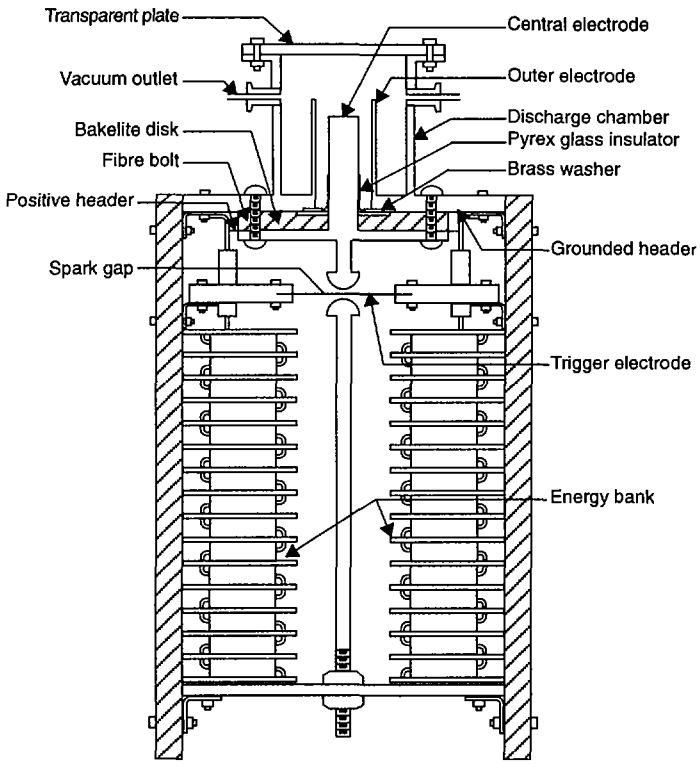

FIG. 1. Plasma gun with energy bank and spark gap.

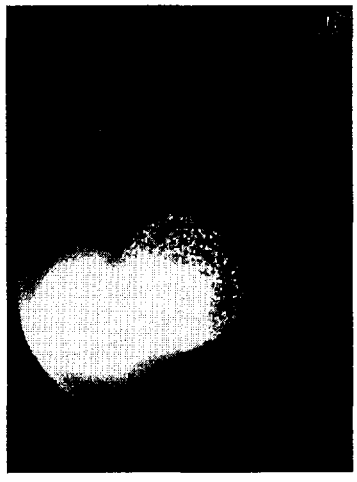

FIG. 2. Plasma formed at the open electrode end.

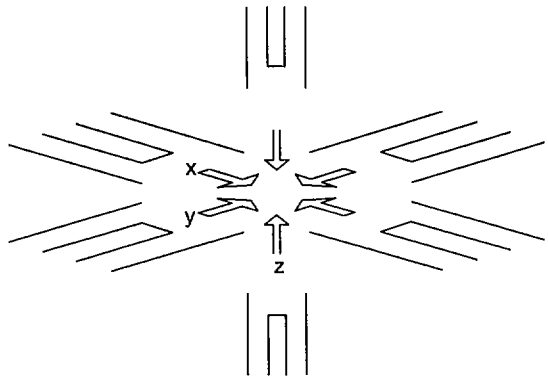

FIG. 3. Six beam spherical compression of plasma focus guns.

2. EXPERIMENTAL ARRANGEMENT AND RESULTS

Figure 1 shows a schematic diagram of the one beam plasma gun, together with the energy bank mounted on the electrodes of the plasma focus device. The bank is directly connected to the gun through a spark gap that is attached to the inner central rod. The gun is of Mather type plasma focus, and the negative outer cylinder extends 1 cm longer than the positive central rod. The diameters are 3 and 1 cm, respectively. The acceleration length is only 5 cm, but the inner rod is 1 cm shorter. A hat-like pyrex glass insulator and a brass washer are also inserted at the gap between the electrodes. Thus, this device is called a small plasma focus gun. The energy bank for the 0.192 kJ, 6 μF, 8 kV system consists of sixteen capacitor modules; each of these modules comprises six 450 V, 16 μF capacitors connected in parallel.

The plasma parameters of the focus plasma such as density, temperature, etc., were measured experimentally by several authors [3, 4]. In the present experiment, the plasma current is measured by a Rogowski coil of 2650 turns wound on a cable of 64 cm length and a cross-sectional area of 0.18 cm^2. The result shows that the current has a maximum at 155.8 A; the circuit inductance is calculated to be 4.2 mH. The plasma formation at the open end of the gun is shown in Fig. 2. This photograph was taken by an ordinary camera with suitable filters. The two electrodes and the plasma production are easily seen in this picture. We also notice that the electrodes are enlarged to twice their size. The plasma is also studied by a light dependent resistor and a photodiode. The results show that the current reaches its peak value at the time when the highest light intensity is emitted. The pulse width of the light is 2 ms; it continues for a rather long time.

Figure 3 is a schematic drawing showing the spherical compression of plasma fronts by six plasma focus guns. The plasma created by the dense plasma focus was about 2 cm away from the end of the central electrode. Here the plasma focus is

utilized as a gun to produce a dense plasma 6 m away from the electrode. Thus, the least separation of oppositely facing central electrodes is ~ 12 cm, and the diameter of the plasma chamber of spherical type is 22 cm. The plasma guns with their energy banks and spark gaps are attached to the six sides of the sphere.

3. DISCUSSION

Plasma was successfully produced by a small plasma focus gun with a very small energy bank of 0.2 kJ. The plasma itself is self-focusing and shows a pinch so that it can be used as a current front for six beam spherical compression. The compact size of the gun with its low energy bank is suitable for forming a six beam device. The bank can also be replaced by ceramic capacitors so as to provide a high and fast energy bank.

The six guns can be fired simultaneously and so represent a focus of six beam spherical compression at a time. The simultaneous arrival of these current sheets at the pinch point is a problem similar to laser beams irradiating a pellet target. Here, a master gap and a delay pulser for six spark gaps can control the arrival of these current fronts. It is also possible to fire two oppositely facing guns at three different times. A sequential operational system may be used to control the spark gaps so as to create a plasma for a considerable continuous time because our bank can also charge continuously. Many optional operations are possible by selecting a trigger pulse system. The advantage of our device is repeated plasma production by charging the bank continuously.

REFERENCES

[1] MICHEL, L., et al., Appl. Phys. Lett. **24** (1974) 57.
[2] MATHER, J.W., Phys. Fluids **8** (1965) 366.
[3] LEE, J.H., et al., Phys. Fluids **20** (1977) 313.
[4] THEIN, A., et al., J. Phys. Soc. Jpn. **42** (1977) 793.

PROFILE CONTROL FOR AN ALTERNATIVE SPHERICAL TOKAMAK

S. SINMAN
Electrical and Electronics Engineering Department,
Middle East Technical University

A. SINMAN
Nuclear Fusion Laboratory,
Turkish Atomic Energy Authority,
Ankara Nuclear Research and Training Center

Ankara, Turkey

Abstract

PROFILE CONTROL FOR AN ALTERNATIVE SPHERICAL TOKAMAK.

Magnetically driven plasma guns that are inserted around a flux conserver at definite angular intervals are considered. The creation and the control of plasma channels are examined. By means of the hybrid model developed, both a system analysis of the Alternative Spherical Tokamak (AST) and relevant computational experiments have been carried out. In addition, by using the results obtained from the numerical scheme, the complex non-inductive current drive mechanisms of bootstrap and helicity injection in the AST system are discussed in detail.

1. INTRODUCTION

In our previous study [1], in which the numerical scheme and the physics basis of this conceptual system were described, the results of a computational experiment were presented in detail. Meanwhile, depending on the plasma parameters and the electrical characteristics of the C gun, a profile analysis including the ohmic heating process of the system has been carried out. It was found that in this Alternative Spherical Tokamak (AST) system there are different current drive mechanisms such as the alternative non-inductive drive mechanism, the bootstrap and the magnetic helicity injection in the relaxed state. In this study, we discuss the bootstrap, the helicity injection current drive mechanisms in the AST system, which affect the configuration of the current channel, and a simple model of the magnetic energy stored on the controlled profiles.

2. MODEL

2.1. Characteristic profile functions

The main profile equations, with the belt function and the transformation equations, read as follows:

$$\rho(\delta, \theta) = \frac{b}{\kappa} [\delta + \cos \theta] \tag{1}$$

$$\begin{aligned} R &= C_1 \cosh u\rho(\delta, \theta) \cos \theta \\ Z &= C_2 \sinh u\rho(\delta, \theta) \sin \theta \end{aligned} \tag{2}$$

2.2. Stored magnetic energy in the profile

We denote by I_{bt} the current in the belt circuit which produces a self-magnetic field and then induces the voltage in the profile circuit. The flux induced in the profile circuit is given by

$$\phi = \frac{\mu_0 I_{bt}}{4\pi} \int_{pf} \int_{bt} \frac{d\ell_{pf}\, d\ell_{bt}}{L_{sr}} \tag{3}$$

where ℓ_{pf} is the profile perimeter, ℓ_{bt} is the belt length and L_{sr} the shear length. On the other hand, the electric field intensity produced in the profile circuit is given by

$$V_{pf} = -\frac{d\phi}{dt} = \frac{d}{dt}\left(\frac{\mu_0 I_{bt}}{4\pi} \int_{pf} \int_{bt} \frac{d\ell_{pf}\, d\ell_{bt}}{L_{sr}}\right) \tag{4}$$

From Eq. (4), we have:

$$\frac{d\phi}{dI_{bt}} = -\left(\frac{\mu_0}{4\pi} \int_{pf} \int_{bt} \frac{d\ell_{pf}\, d\ell_{bt}}{L_{sr}}\right) \tag{5}$$

Remembering, in general,

$$\phi = BA = \mu_0 HA = \frac{\mu_0 NIA}{\ell}$$

we then have

$$\frac{d\phi}{dI} = \frac{\mu_0 NA}{\ell} = L_{si}$$

where L_{si} is the standard inductance. Hence, the right hand side of Eq. (5) defines the self-inductances of profile and belt. In other words, the mutual inductance of this inductive coupling circuit comprises both belt and profile inductances. In this case, $M = \sqrt{L_{pf} L_{bt}}$, and the stored magnetic energy in this frame is given by

$$U_{frame} = \frac{I_{bt}^2 M}{2} \tag{6}$$

2.2.1. *Belt inductance*

Using a binomial series, we can express the characteristic shape function of the belt as

$$z(r)^{-1} = \frac{c^3}{r^2 + c^2} \tag{7}$$

where c is a constant. In general, for a single turn loop inductance, L may be written as

$$L = \frac{d}{dt} [\mu_0 \int_s Hnds] = \frac{\mu_0 S}{d} \tag{8}$$

Here, S and d are the loop area and the total width of the loop, respectively. Using Eqs (7) and (8), we find for the belt inductance, L_{bt}:

$$L_{bt} = \frac{\mu_0}{4\pi} \int_0^{z_b} \frac{a_{bt}^3}{z_{bt}^2 + a_{bt}^2} dz_{bt} \Big/ a_{bt} \tag{9}$$

where z_{bt} is the electrode-gap distance of the C gun and a_{bt} is the belt radius.

2.2.2. *Profile inductance*

The profile perimeter in polar co-ordinates can be expressed as

$$|\ell_{pf}| = \frac{b}{\kappa} \int_0^{\theta} [(\delta + \cos\theta)^2 + \sin^2\theta]^{1/2} d\theta \tag{10}$$

On integrating Eq. (10) over the interval $0 < \psi < 2\pi$, we obtain

$$|\ell_{pf}| = \frac{b}{\kappa} \left[\frac{0.16\delta}{\sqrt{[1 + \delta]^2}} + \left(\frac{2\pi}{\psi}\right)^3 + \sqrt{[1 + \delta]^2} \frac{2\pi}{\psi} \right] \tag{11}$$

Furthermore, the area of the profiles is defined by

$$A_{pf} = \frac{b^2}{2\kappa^2} \int_0^{\theta} [\delta + \cos\theta]^2 \, d\theta \tag{12}$$

Alternatively, this equation can be written as

$$A_{pf} = \left[0.33 \, (1 + \delta) \left(\frac{2\pi}{\psi}\right)^3 + (1 + \delta)^2 \frac{2\pi}{\psi} \right] \tag{13}$$

where δ is the shaping parameter of the profile; it lies in the range of $0 < \delta < 4$. Thus, different profile configurations such as bean shaped, prolate and oblate forms can be obtained. The optimum result has been obtained for $\psi = 8$; hence, the inductance of the profile is easily found as

$$L_{pf} = \frac{\mu_0 A_{pf}}{\ell_{pf}} \tag{14}$$

2.3. Magnetic shear

It is well known that the safety factor is given by

$$q(r) = \frac{R_0 B_t}{2\pi} \int_{\ell} \frac{d\ell}{B_p R^2}$$

Owing to the peculiarity of the current drive mechanisms of the AST system, the toroidal and poloidal magnetic flux densities can be taken as $B_t \cong B_p$. Therefore,

$$\frac{dq(R_0)}{dR_0} = \frac{B_t |\ell|}{2\pi B_p R^2}$$

and

$$\frac{dq(R)}{dR} = -\frac{R_0 B_t B_p |\ell|}{\pi B_p^2 R^3}$$

As a result, for the shear profile,

$$s(r) = \frac{R_0}{R^2} + \frac{2R_0^2}{R^3}$$

is obtained.

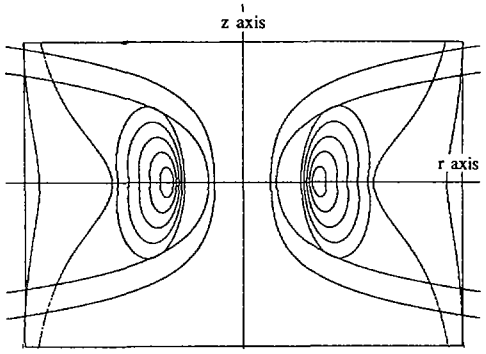

FIG. 1. Controlled prolate profile: inverse aspect ratio: ϵ = 0.67; elongation: κ = 2.5; coupling efficiency: ξ = 0.6. Correlative function parameters: mode constant (a) = 1.5; elongation constant (b) = 2.8; flux density (c) = 2; distance to profile centre (d) = 80; shaping (r) = 3; shaping (z) = 7.

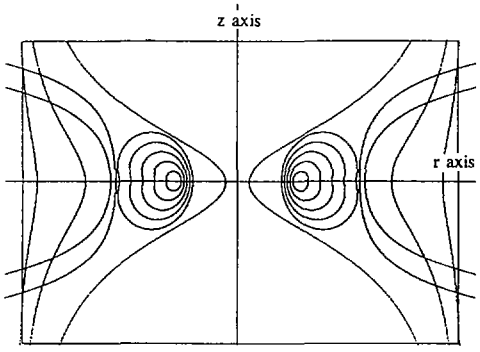

FIG. 2. Controlled bean shaped profile: ϵ = 0.83; κ = 2.14; ξ = 0.6. Correlative function parameters: (a) = 1.5, (b) = 2.8, (c) = 2.4, (d) = 90, (r) = 3.5, (z) = 4.5.

2.4. Bootstrap current

As can be seen in Figs 1 and 2, the profiles are configured by means of the magnetic pressure of the belts. The force on the poloidal current profile is given by

$$d\mathbf{F}_{pf} = I_{pf}\, d\ell_{pf} \times d\mathbf{B}_{bt} \tag{15}$$

where $d\mathbf{B}_{bt}$ is the flux density generated by the belt. It will be seen later that it is given by

$$d\mathbf{B}_{bt} = \frac{\mu_0}{4\pi^2} I_{pt}\, d\ell_{bt} \times \mathbf{r}_0 \tag{16}$$

where $\mathbf{r}_0$ is the vector distance from the belt surface to the profile surface. We now rewrite Eq. (16) as

$$d\mathbf{F}_{pf} = \frac{\mu_0}{4\pi^2} I_{pf} d\ell_{pf} \times [I_{bt} d\ell_{bt} \times \mathbf{r}_0] \tag{17}$$

The perimeter of the profile, $|\ell_{pf}|$, is given by Eqs (10) and (11). On the other hand, the belt length, ℓ_{bt}, can be defined by the line integral of

$$|\ell_{bt}| = \sqrt{P_1^2(r_{bt}) + P_2^2(z_{bt})}$$

where

$$P_1(r_{bt}) = \int_{r_{b1}}^{r_{b2}} \sqrt{1 + \left[\frac{3R_{bt}^2}{Z_{bt}^2 + R_{bt}^2} - \frac{2R_{bt}^4}{(Z_{bt}^2 + R_{bt}^2)^2}\right]^2}\, dR_{bt} \tag{19}$$

and

$$P_2(z_{bt}) = \int_{z_{b1}}^{z_{b2}} \sqrt{1 + \left[\frac{-2R_{bt}^3 Z_{bt}}{(Z_{bt}^2 + R_{bt}^2)^2}\right]^2}\, dZ_{bt} \tag{20}$$

It should be noted that the parametric equations for $P_1(r_{bt})$ and $P_2(z_{bt})$ can be solved for the variable R_{bt} by taking the Z_{bt} constant or for the variable Z_{bt} by taking R_{bt} as a parameter, respectively. Using Eqs (19) and (20), the belt length is calculated from Eq. (18).

The average kinetic pressure of the frame comprising both belt and profile can be defined by $|\langle P_{frame}\rangle| = \langle N_e\rangle U_{frame}$; the state of perfect equilibrium will be determined by the position of the belts interacting with the AST plasma profile. In this case, we obtain $|\mathbf{F}_{pf}|/A_{pf} = \langle N_e\rangle U_{frame}$ for the kinetic pressure depending on the magnetic pressure of the belts. From these considerations, we can express the bootstrap current density as follows:

$$J_{boot} \cong \frac{2\epsilon^{1/2}}{A_{pf}} [(d|\mathbf{F}_{pf}|/dL_{sr})/B_p] \tag{21}$$

2.5. Magnetic helicity injection

The concept of helicity injection can be utilized by applying the magnetically driven plasma gun (C gun). The helicity injection rate [2] of the C gun is given by

$$dK_{cg}/dt = 2V_{cg}\psi_{cg} \tag{22}$$

where V_{cg} is the voltage applied between the electrodes of the C gun and ψ_{cg} is the toroidal flux generated by the C gun itself, penetrating to the belts.

For the ohmic heating helicity in the AST profile inductive coupling circuit, the helicity injection rate is given by $2\phi_{pf}V_t$, where V_t is the toroidal loop voltage. Thus, assuming helicity conservation, an effective toroidal loop voltage from electrostatic helicity injection can be defined as

$$V_{eff} = V_{cg}\psi_{cg}/\phi_{pf} \tag{23}$$

Using Eq. (5) and rewriting Eq. (23), we obtain

$$V_{eff} = - V_{cg}\left(\frac{\mu_0}{4\pi}\int_{pf}\int_{bt}\frac{d\ell_{pf}\,d\ell_{bt}}{L_{sr}}\right) dI_{bt}/\phi_{pf} \tag{24}$$

and, after simplifying Eq. (22), we have

$$J_p = - V_{cg}\sqrt{L_{pf}L_{bt}I_{bt}}/\phi_{pf}\eta\,\ell_{prm} \tag{25}$$

where J_p is the plasma current density, V_{cg} is the voltage on the C gun and L_{pf}, L_{bt} and I_{bt} are the profile inductance, the belt inductance and the belt current, respectively. Furthermore, ϕ_{pf}, η and ℓ_{prm} are the toroidal flux of the profile, the plasma resistivity and the perimeter of the spherical torus, respectively.

3. NUMERICAL SCHEME

It should be noted that the profile analysis has been carried out on the basis of Eqs (2) and (3). The numerical scheme consists of consecutive equations valid in the model. For example, in Figs 1 and 2, with respect to the peculiarity of the profiles (the graphics program developed is interactive with respect to the equations in the model), the main successive equations are Eqs (9), (10), (12) and (14). The basic reference data of the AST system used in the numerical examples are: radius and height of flux conserver: $r_f = 0.25$ m and $h_f = 0.7$ m; bank voltage: $V_{bk} = 25$ kV; belt current of C gun: $I_{bf} = 150$ kA; bank inductance: $L_{bk} = 500$ nH; bank capacitance: $C_{bk} = 96\ \mu$F; bank impedance: $Z_{bk} = 0.16\ \Omega$ ($Z_{bk} = Q_{bk}(L_{bk}/C_{bk})^{1/2}$); logarithmic decrement: $\delta = 1.42(\pi/Q_{bk})$, where $Q_{bk} = 2.2$; discharge period: $\tau = 43.5\ \mu$s; stored bank energy: $U_{bk} = 30$ kJ; belt inductance: $L_{bt} = 12.3\ \mu$H; profile inductances: $L_{pf} = 1.21$ and $0.74\ \mu$H; mutual inductances: $M = 3.86$ and $2.4\ \mu$H for Figs 1 and 2, respectively. By choosing an elongation of $\kappa = 2.5$ and an inverse aspect ratio of $\epsilon = 0.67$ in Figs 1 and 2, profile perimeters of $\ell_{pf} = 2.44$ m and 1.60 m, and profile areas of $A_{pf} = 234 \times 10^{-4}$ m^2 and 94×10^{-4} m^2 have been found.

3.1. Effect of coupling efficiency on plasma parameters

It is well known that in inductively coupled electrical circuits the geometrical coupling coefficient, k, is an important circuit parameter. The coupling profile in the AST system is created and controlled among the belts. The ideal coupling coefficient is normally equal to one. In the following example, as a completely new approach to the AST system we have used a coupling efficiency parameter ξ instead of the mentioned coefficient k. The magnetic helicity injection into the AST system is given by Eq. (25). For a numerical example with an electron density of $n_e = 2 \times 10^{21}$ m^{-3} and two different coupling efficiency values, $\xi = 0.25$ and $\xi = 0.60$, the stored energies in the profile frames of $U_{frame} = 10.9$ kJ and 26.1 kJ are calculated. In these conditions, electron temperatures of $T_e = 236.6$ eV and 575.2 eV and, for a plasma volume of $V_p = 0.14$ m^3, equivalent toroidal magnetic field densities of 0.43 T and 0.67 T were found. In Fig. 1 the profile is given for $\xi = 0.6$. In this condition, a plasma resistivity of $\eta = 9.31 \times 10^{-8}\ \Omega\cdot$m and a toroidal plasma current density of $J_p = 1.97 \times 10^5$ A/m^2 are obtained. Let us now consider the profile in Fig. 1 for a coupling efficiency of $\xi = 0.25$. Using the same reference data as in the the last example, for plasma resistivity and toroidal plasma current density we obtain $\eta = 3.41 \times 10^{-7}\ \Omega\cdot$m and $J_p = 1.27 \times 10^5$ A/m^2, respectively.

3.2. Heating time

The energy needed to heat the plasma in the AST system and the power density can be determined from the relations $U_{ht} = (3/2)nk(T_e + T_i)V_p$ and $W = \eta_1 J_p^2$. To decrease the heating time τ_{ht}, it is necessary to increase the number of C guns up to 12, with identical specifications and the power density of the AST system. For example, in the case of C guns located inside the flux conserver grading at 30° angular intervals for $\xi = 0.25$ and 0.6, heating powers of $W_{ht} = 79.19$ kW and 72.84 kW are estimated; the corresponding heating times are $\tau_{ht} = 0.75$ s and 0.29 s. In Fig. 1 a prolate and in Fig. 2 a bean shaped profile is shown. To compare these two profiles for different specifications, we present the numerical results obtained for the same coupling efficiency of $\xi = 0.6$: plasma resistivity: $\eta = 1.87 \times 10^{-7}\ \Omega\cdot$m; toroidal plasma current density: $J_p = 9.25 \times 10^5$ A/m^2; heating energy: $U_{ht} = 34.32$ kJ; heating power: $W_{ht} = 22.4$ kW. Hence, the calculated total toroidal plasma currents obtained with $\xi = 0.6$ for prolate (P) or bean shaped (B) profiles, by taking into account the 12 belts of the C guns (Bs) and the current drive mechanisms of helicity injection (HI) and bootstrap (BS), are given by

$$16.28\ \text{kA(Bs)} + 55.3\ \text{kA(HI)} + 21.0\ \text{kA(BS)} \cong 92.61\ \text{kA (P)}$$

and

$$11.93\ \text{kA(Bs)} + 8.69\ \text{kA(HI)} + 3.56\ \text{kA(BS)} \cong 24.20\ \text{kA (B)}$$

4. CONCLUSIONS

(a) In accordance with the design of the AST system, the practical data used have been obtained from the results of computational experiments.

(b) As to the current channel in the AST system and its optimization, the electrical characteristics of the C gun and its modes of operation are important factors.

(c) The way the C guns are placed around the flux conserver at definite angular intervals is very important from the viewpoint of the stability of the toroidal plasma current channel.

(d) It has been found that the control belts, acting as a conductive shell, can shape the current profile on the toroidal surface.

(e) By means of a good, simple, multiparameter analytical model it has been possible to analyse the AST system and to carry out computational experiments on it. Thus, the existence of non-inductive current drive mechanisms in the AST system has been verified.

(f) The safety factor q for the AST system has been interpreted once more, and it was observed that the magnetic shear parameter depends only on the major radius of the plasma, R_0, and the major radius of the system, R.

(g) As a result of the non-inductive current drive mechanisms of the AST system, the toroidal and poloidal magnetic field strengths have been determined as lying very close to each other ($H_t \cong H_p$).

(h) As a consequence, it is assumed that, by increasing the number of C guns in the AST, this system can be converted into a small and compact fusion reactor model.

ACKNOWLEDGEMENT

This research was performed under a co-operative agreement between the Turkish Atomic Energy Authority and the International Atomic Energy Agency, Contract No. 7412/R2/RB.

REFERENCES

[1] SINMAN, S., SINMAN, A., in Plasma Physics and Controlled Nuclear Fusion Research 1994 (Proc. 15th Int. Conf. Seville, 1994), Vol. 2, IAEA, Vienna (1995) 303.

[2] TORKIL, H., et al., Phys. Fluids 27 (1984) 2881.

HIGH RECYCLING IN W7-AS ISLAND DIVERTOR CONFIGURATIONS

P. GRIGULL, Y. FENG, D. HILDEBRANDT[1], F. SARDEI, G. HERRE, O HEINRICH, A. ELSNER, S. FIEDLER, J.V. HOFMANN, J. KISSLINGER, G. KÜHNER, H. NIEDERMEYER, R. SCHNEIDER, H. VERBEEK, F. WAGNER, A. WELLER, R. WOLF, W7-AS TEAM
Max-Planck-Institut für Plasmaphysik,
IPP-Euratom Association,
Garching, Germany

Abstract

HIGH RECYCLING IN W7-AS ISLAND DIVERTOR CONFIGURATIONS.

Edge plasma scenarios in W7-AS island divertor configurations ("natural" magnetic boundary islands intersected by targets) are studied by comparing data from moderate to high density NBI discharges with 3D code (EMC3/EIRENE) results. The data strongly indicate that, different from limiter scenarios, stable high recycling with significant particle flux enhancement was achieved in this geometry. However, the open target geometry as well as a relatively strong plasma pressure drop along field lines within the power carrying layer, in particular also at moderate density, restrict high recycling to a narrow density range at $\bar{n}_e \gtrsim 10^{20}$ m^{-3}. The pressure drop is, at low to marginal high recycling, predominantly balanced by cross field transfer of parallel momentum towards the private flux region due to particle diffusion and viscosity; at fully established high recycling CX momentum losses become effective. These scenarios are also in basic agreement with B2/EIRENE code predictions. At $\bar{n}_e \geq 1.5\times10^{20}$ m^{-3} detachment is observed. Improvements are expected from additional coils controlling the field line pitch inside the islands, and from optimized, helically more extended targets with baffles. Both additions are in preparation.

1. INTRODUCTION

In optimized stellarators with low to moderate shear it is planned to utilize the flux diversion properties of inherent magnetic islands at the boundary for plasma exhaust. In the W7-AS stellarator, crucial elements of this island divertor concept can be assessed; the development will be continued at W7-X [1].

Like stellarators in general, W7-AS is strongly non-axisymmetric, and the edge topology is three-dimensional. The device can be operated with magnetic field configurations bounded by inherent, "natural" islands of considerable size. The symmetry of the islands is $5/m$ with five being the number of magnetic field periods and m = 7, 8, 9,... determined by the externally adjustable edge rotational transform $\iota_a = n/m$ [2, 3]. The 5/9 symmetry was chosen as optimum for the present analysis. It provides both sufficient main plasma cross section and

[1] Berlin branch of IPP Garching.

relatively large boundary islands with radial and poloidal dimensions of 5 - 10 cm (Fig. 1). Furthermore, this configuration has proven to be sufficiently stable with respect to equilibrium plasma currents at finite plasma pressure within the relevant range up to $\beta_o \approx 1\%$ [4]. The islands are intersected by ten poloidal graphite targets (toroidally tilted) with toroidal widths of 12 cm, two per magnetic field period (one of them is shown in Fig. 1a, the second, covering the upper half of the inboard side, is at an equivalent, mirror-symmetric position). Field line connection lengths L_c between stagnation points and targets are about 50 to 150 m (depending slightly on β and on the radial distance from the O-point, increasing towards the island separatrix).

The aim of this study was to explore whether high recycling and related divertor scenarios can be established under these conditions. The paper reports first results.

2. MODELLING APPROACHES

The edge plasma was modelled for the 5/9 island topology by a two-dimensional (B2 [5-7]) and a three-dimensional fluid approach (EMC3 [8]), each coupled with the EIRENE neutral transport code [9, 10]. The B2 approach allows to study basic divertor properties with sophisticated physics, but necessarily includes helical averaging of the island configuration and can, in particular, not treat the present target geometry and hence the interaction with neutrals in a fully realistic way. Furthermore, it does not allow direct reference to local experimental data in the actual 3D configuration. The EMC3 code solves the set of fluid equations by a Monte Carlo technique considering the full non-axisymmetric geometry, but suffers, at present, from some simplifications: it treats only single fluid plasma ($T_i = T_e$), neglects heat convection, and treats cross field transport of parallel momentum due to particle diffusion and viscosity by parametrization. A completion of this code is under way. In this study we restrict ourselves to a „complementary" analysis: the EMC3/EIRENE results are directly referred to experimental data by adjusting the free input parameters to match measured densities at certain positions (see below), and the tendencies inferred are briefly compared with B2/EIRENE predictions. Parameters to be adjusted are the upstream density at the inner separatrix n_{es}, the particle diffusion coefficient $D_\perp$ and the above mentioned momentum transport parameter. The electron heat diffusivity $\chi_\perp$ was, in extrapolation of results at $\iota = 0.34$, set to $3\times D_\perp$, and the power P_s crossing the inner separatrix as further input quantity was estimated from the absorbed NBI power corrected for radiation from the core (from bolometer data). Detailed descriptions of the codes and boundary conditions are given in Refs. [5, 8].

3. EXPERIMENTAL

The analysis was made for net current compensated NBI discharges at B = 2.5 T with ECRH start-up and balanced injection. Line-averaged densities $\bar{n}_e$ were varied between 2×10^{19} and 1.5×10^{20} m^{-3}. Heating powers were 0.8 MW for $\bar{n}_e \leq 8\times10^{19}$ m^{-3} and 2 MW for higher densities. Data were taken during flat-top

phases of about 300 ms (low to moderate densities) or 150 - 200 ms (highest densities). In the latter case, density control was lost in general after that time and the discharges were radiatively terminated before switching off the heating power (see below). The edge rotational transform ι_a was 0.564 which corresponds to the configuration with 5/9 boundary islands mentioned. Edge plasma parameters were mainly obtained from two Langmuir probes (CFC tips): a fast reciprocating probe (FRLP) at the position shown in Fig. 1b, and a second probe close to one of the targets (downstream probe, Fig. 1a). The measurements were completed by Thomson scattering, spectroscopic observation (H_α diode arrays viewing at the targets, CCD cameras with filters for H_α or CIII radiation), bolometry, and target thermography.

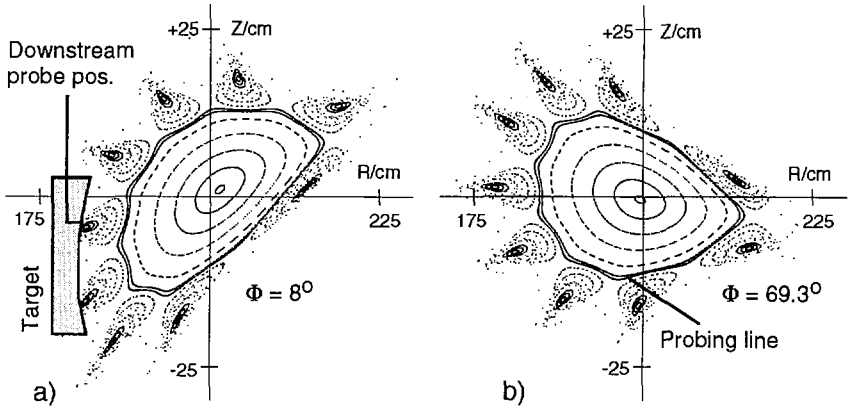

Fig. 1. Cross sections of the W7-AS vacuum magnetic field configuration with 5/9 boundary islands at (a) a target plane and (b) a plane with the FRLP probing line. The downstream probe position is indicated in Fig. a.

4. RESULTS AND DISCUSSION

Radial density profiles across the island (Fig. 2, from FRLP) are, up to $\bar{n}_e = 8\times10^{19}$ m^{-3} ($n_{es} \approx 2\times10^{19}$ m^{-3}), rather flat inside the island but show steep gradients outside the outer island separatrix (private flux region). At $\bar{n}_e = 1.2\times10^{20}$ m^{-3} ($n_{es} \approx 3\times10^{19}$ m^{-3}), a pronounced maximum close to the outer separatrix ("divertor fan") develops, and the downstream density (Fig. 3a) increases to about three times the upstream density. The downstream T_e drops to about 10 eV in this case. H_α intensities from the target vicinity (Fig. 3b) show a similarly strong increase as the downstream density. These are clear experimental signatures for a high recycling scenario as it is known from tokamak divertors [11]. However, the data indicate plasma thermal pressure drops along field lines within the power carrying island layer (PCL) by factors of about four (upstream/downstream ratio) at $\bar{n}_e = 1.2\times10^{20}$ m^{-3} to six at the lowest density, which significantly exceed the factor of two expected only from the sheath acceleration. These drops shift, in effect, the onset of high recycling to higher density and ease the transition to detachment. At $\bar{n}_e = 1.5\times10^{20}$ m^{-3} the above

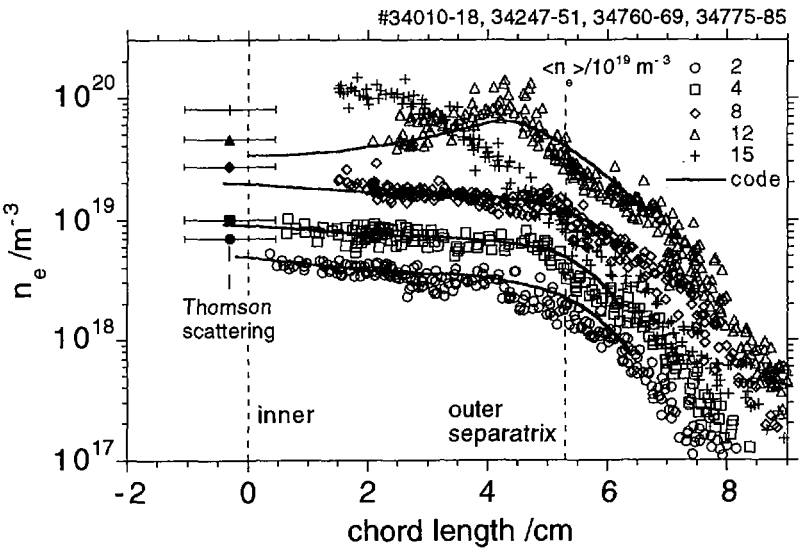

Fig. 2. Electron density profiles measured by the FRLP across an island, Thomson scattering data measured close to the inner separatrix, and EMC3/EIRENE simulations of the probe data. Positions of the island vacuum field separatrix are indicated. Code input data (section 2) were adjusted to match measured densities at the innermost probe positions, at the outermost calculated points, and at the downstream probe position.

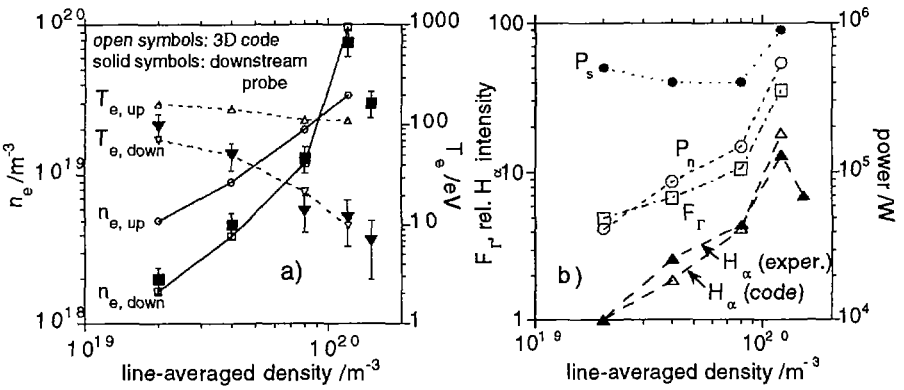

Fig. 3. (a) Upstream and downstream (averaged along the strike line) n_e and T_e values from the EMC3/EIRENE code, and downstream probe data. (b) Powers P_s crossing the inner separatrix, volumetric energy losses P_n due to neutral hydrogen, particle flux enhancement factors F_Γ and H_α intensities from the target. The latter are normalized to unity at the lowest density.

mentioned maximum of the density profile across the island shifts inwards (Fig. 2) and the downstream density decreases („roll over", Fig. 3a) indicating (at least partial) detachment. This latter interpretation is supported by camera observations of H_α and CIII lines from the targets (not shown). The H_α footprints along the strike points (radial observation) disappear, the radiation becomes diffuse and weaker. At the same time the CIII radiation (tangential view) becomes concentrated at the X-point vicinity, and the total power onto the targets is decreased from about 25 to below 10% of the heating power (from thermography). Parallel with the loss of density control, that means on a relatively slow time scale of about 100 ms, the hot plasma cross section shrinks and the discharges become terminated (often via MARFE formation at the inboard side).

For the attached regimes, the EMC3/EIRENE results well reproduce the measured n_e profiles across the island (Fig. 2) as well as downstream T_e values (Fig. 3a) and H_α intensities from the target proximity (Fig. 3b, for the adaption of code input parameters see section 2 and caption of Fig. 2). $D_\perp$ values inferred are 0.6 m^2/s for $\bar{n}_e \leq 8\times10^{19}$ m^{-3} and 0.2 m^2/s for the highest density. Measured T_e profiles (not shown) are satisfactorily reproduced only at low to moderate density; discrepancies at higher density may indicate stronger radiative losses due to impurities (mainly carbon) not considered by the code. Particle flux enhancement factors inferred reach up to 35, volumetric energy losses due to neutral hydrogen correspond to 50% of P_s at $\bar{n}_e = 1.2\times10^{20}$ m^{-3} (Fig. 3b). With the exception of the attached case with highest density, where momentum losses due to CX neutrals become already effective, the excessive, local plasma pressure drops within the PCL mentioned are found to be predominantly balanced by cross field transport of parallel momentum due to particle diffusion and viscosity which cause significant pressure re-distribution in this geometry.

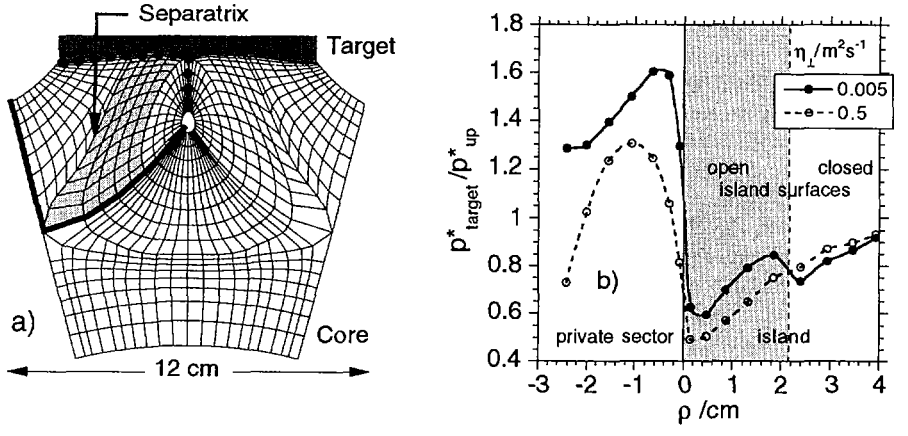

Fig. 4. (a) Geometrical grid used for B2/EIRENE simulation [5]. (b) Calculated downstream/upstream ratios of the total plasma pressure $p^* = p(1+\gamma M^2)$ (with p the thermal pressure, γ the adiabatic coefficient and M the Mach number) versus the mean distance ρ from the island separatrix. Downstream values are taken along the dotted, upstream values along the bold line in (a).

Though not fully comparable, B2/EIRENE simulations [5] predict the same tendency. Figs. 4a, b show the geometrical grid and, as an example (two-fluid run), radial profiles of the downstream/upstream ratio of the total plasma pressure (thermal + dynamic) for two values of the cross field viscosity $\eta_\perp$ at n_{es} = 1.3×10^{19} m^{-3} (marginal high recycling).

In both cases there is net momentum transfer from the PCL to the private flux region, and the PCL downstream total pressure is reduced by a factor of about two. For $\eta_\perp$ = 0.5 m^2s^{-1} ($\hat{=} D_\perp$), CX momentum losses contribute less than 10% to this reduction whereas at $\eta_\perp$ = 0.005 m^2s^{-1} ($\approx$0) convective and CX momentum losses are comparable. The integral losses of the total pressure are, under these conditions, about 10% for $\eta_\perp$ = 0.005 m^2s^{-1} and 20% for $\eta_\perp$ = 0.5 m^2s^{-1}. Besides this, B2/EIRENE two-fluid as well as multi-fluid (with carbon) simulations [5] also predict the establishment of stable high recycling for same transport coefficients and comparable power flow P_s, but the onset is significantly shifted towards lower density ($n_{es} \gtrsim 1\times10^{19}$ m^{-3}). This latter difference to the experiments is primarily attributed to the deviating target geometry and hence neutral density distribution in the 2D approach.

5. SUMMARY AND OUTLOOK

The edge plasma of moderate to high density NBI discharges in a magnetic field configuration with "natural" boundary islands intersected by targets was analyzed with respect to divertor scenarios. Experimental data and 3D edge code (EMC3/EIRENE) results strongly indicate that, different from limiter scenarios, a concentration of the particle sources inside the SOL and significant particle flux enhancement were achieved. However, the open target geometry as well as relatively strong plasma pressure drops along field lines within the PCL shift the onset of high recycling to very high density ($\bar{n}_e \gtrsim 10^{20}$ m^{-3}, $n_{es} \gtrsim 3\times10^{19}$ m^{-3}). The pressure parallel drops are, at low to marginal high recycling, mainly balanced by cross field transfer of parallel momentum (pressure re-distribution) due to particle diffusion and viscosity in this geometry. At fully established high recycling CX momentum losses become effective. These scenarios are in basic agreement with B2/EIRENE predictions. At $\bar{n}_e \geq 1.5\times10^{20}$ m^{-3} the experimental data indicate detachment which, however, could not yet been stably maintained. Further experiments on this issue at improved density control (NBI combined with 140 GHz ECRH) are under way.

Code simulations with varying magnetic field parameters and target geometry predict improved pre-conditions for divertor operation at increased field line pitch inside the islands and with helically more extended targets. The latter will better approximate to 2D conditions and allow, in particular, improved focusing of recycling neutrals into the islands. Respective hardware modifications are under preparation: the installation of additional control coils which will allow to vary the islands' internal rotational transform and thus the field line pitch, and the replacement of the present inboard targets by a set of optimized target/baffle combinations which will also enable active pumping.

REFERENCES

[1] STRUMBERGER, E., Nucl. Fusion **36** (1996) 891
[2] JAENICKE, R. et al., Nucl. Fusion **33** (1993) 687
[3] GRIGULL, P. et al., J. Nucl. Mater. **196-198** (1992) 101
[4] SARDEI, F. et al., in Plasma-Surface Interactions (Proc. 11th Int. Conf. Saint Raphael, France, 1996), to be published in J. Nucl. Mater.
[5] HERRE, G. et al., ibid.
[6] BRAAMS, B. J., A Multi Fluid Code for Simulation of the Edge Plasma in Tokamaks, Rep. (NET) EUR-FU/XII-80/87/68, Comm. of the EC, Brussels 1987
[7] SCHNEIDER, R. et al., J. Nucl. Mater. **196-198** (1992) 810
[8] FENG, Y. et al., in Plasma-Surface Interactions (Proc. 11th Int. Conf. Saint Raphael, France, 1996), to be published in J. Nucl. Mater.
[9] REITER, D., J. Nucl. Mater. **196-198** (1992) 80
[10] REITER, D., J. Nucl. Mater. **220-222** (1995) 987
[11] LOARTE, A., in Plasma-Surface Interactions (Proc. 11th Int. Conf. Saint Raphael, France, 1996), to be published in J. Nucl. Mater.

DISCUSSION

V. PARAIL: Do you see any difference between L mode and ELMy H mode fluctuation spectra?

P. GRIGULL: The ELM is a very short (150–200 μs) event. If you cut out a short time interval during the ELM, fluctuations are broadband, as in the L mode. The quasi-coherent precursor activity preceding the ELM, however, is a different feature.

S.I. ITOH: You observed the magnetic fluctuation before the ELM, whose growth rate shows the fast time-scale. Can you say something about the causal relation between the magnetic fluctuation (trigger) and the ELM?

P. GRIGULL: As far as we can resolve (the resolution is 10 μs), *turbulent* fluctuation and profile changes appear simultaneously. The *coherent* magnetic precursor activity precedes the event, starting about 50 μs before, and the amplitude grows rapidly until turbulence and profile changes occur.

K. IDA: What do the temperature and radiation profiles look like inside the 5/9 island when the peak density profile is observed? Is remote radiative cooling observed in the W7-AS island divertor?

P. GRIGULL: The T_e profile inside the 5/9 island is slightly hollow; the minimum value is about 30 eV. The divertor radiation (mainly from hydrogen and carbon) is peaked at the target vicinity in this case. At the highest density, where the peak of the density profile is shifted inwards, the carbon radiation (C III) becomes concentrated at the upstream separatrix, and the total power onto the targets drops from about 25% to below 10% of the heating power. Experiments with controlled impurity injection have not yet been done in this configuration.

EDGE TRANSPORT BARRIER AND EDGE TURBULENCE DURING H-MODE OPERATION IN THE W7-AS STELLARATOR

M. HIRSCH, E. HOLZHAUER[1], J. BALDZUHN, B. BRAÑAS[2],
S. FIEDLER, J. GEIGER, T. GEIST, P. GRIGULL, H.-J. HARTFUSS,
J. HOFMANN, R. JAENICKE, C. KONRAD, J. KOPONEN[3],
G. KÜHNER, W. PERNREITER, F. WAGNER, A. WELLER,
H. WOBIG, W7-AS TEAM
Max-Planck-Institut für Plasmaphysik,
Euratom–IPP Association,
Garching, Germany

Abstract

EDGE TRANSPORT BARRIER AND EDGE TURBULENCE DURING H-MODE OPERATION IN THE W7-AS STELLARATOR.

H-mode operation in W7-AS is obtained in narrow windows of the edge rotational transform which correspond to minima of the calculated poloidal rotation viscosity. The quiescent H-mode occurs through an ELMy phase in which the time intervals between the ELMs show fluctuation amplitudes and spectra identical to the fully developed quiescent H-mode. The ELMs are used as a spontaneous perturbation to study breakdown and re-establishment of the edge transport barrier. A strong poloidal propagation of density turbulence towards the electron diamagnetic drift direction is found even during the ELM. The changes in fluctuation spectra and macroscopic edge profile gradients associated with an ELM occur on the same timescale of about 100 μs.

1. INTRODUCTION

In the low-shear modular stellarator W7-AS ($R_0 = 2.0$ m, $a \leq 0.18$ m) H-mode operation is achieved in a net currentless plasma [1,2]. The H-mode displays features similar to tokamaks: Confinement improvement is determined by a transport barrier at the plasma edge where turbulence is strongly suppressed. Poloidal impurity rotation measured with spectroscopy increases towards the electron diamagnetic drift direction corresponding to a change of the negative radial electric field by $\Delta E_r \approx -100$ V/cm. ELMs represent an intermittent breakdown of the transport barrier [3]. The improvement of *global* confinement, however, is small ($\Delta W_{dia}/W_{dia} < 30\%$) and achieved only after an ELM-free "quiescent" H-mode of sufficient length ($t > 20$ ms) is established. In contrast to tokamaks the H-mode operational range in W7-AS is governed by the edge rotational transform.

---

[1] Institut für Plasmaforschung, Universität Stuttgart, Stuttgart, Germany.
[2] Asociación Euratom-CIEMAT, Madrid, Spain.
[3] Helsinki University of Technology, Helsinki, Finland.

2. OPERATIONAL RANGE

H-mode operation is achieved with either ECRH or NBI heating at magnetic fields B_{tor} = 2.5 T and 1.25 T. The operational range is characterized by narrow windows of the edge rotational transform ι_a, (ι_a = 0.525±0.005 and $\iota_a \approx 0.48$). These ι-windows are considered to offer a favourable preconditioning for the L-H transition for two reasons : (1) the magnetic edge topology results in a strong radial variation of E_r and thus a velocity shear layer already prior to the transition and (2) magnetic pumping as a damping mechanism for poloidal plasma rotation is minimized :

(1) The magnetic field topology within the operational windows is characterized by a comparatively large plasma minor radius where the plasma boundary is determined by the inner separatrix of a natural island chain (5/10 and 5/9 respectively) with the limiter position right behind it. For this well defined plasma edge the connection lengths decrease to a value of some meters within a radial distance $\Delta r \approx 1$ cm outside the LCFS. A strong radial variation of the radial electric field and a corresponding velocity shear layer are observed already under L-mode conditions [2,4].

(2) In the plateau regime viscosity depends on details of the particle orbits, determined e.g. by the rotational transform. In the case of stellarators the helical magnetic ripple provides an additional mechanism for poloidal rotation damping [5]. For W7-AS the ι-dependence of the calculated poloidal viscosity is shown in Fig.1, taking into account the Fourier coefficients of the islands at $\iota = 5/n$,

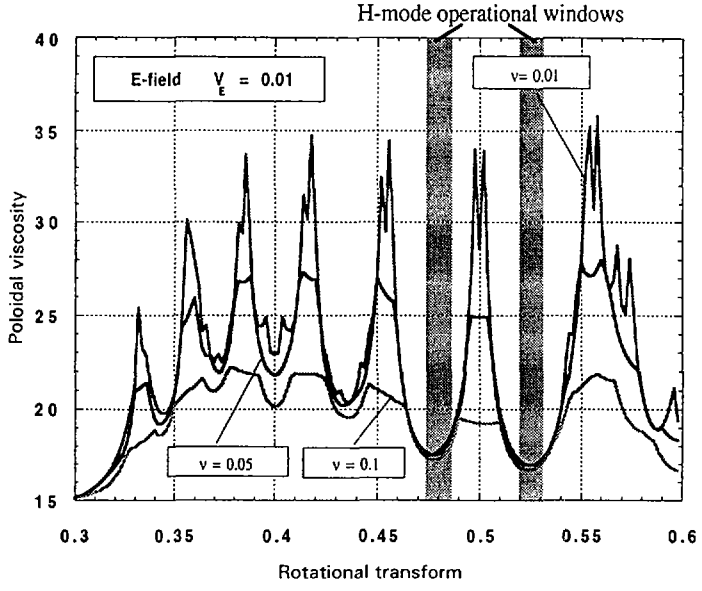

FIG. 1. Calculated poloidal viscosity versus rotational transform. The singularities become less pronounced with increasing collisionality ν.

n=9,10,11 etc. In the vicinity of islands the poloidal rotation is strongly damped by magnetic pumping. At the deepest minima of the calculated poloidal viscosity obtained in between the resonances the H-mode develops spontaneously.

A favourable preconditioning of the plasma edge can explain the easy access to H-mode operation with respect to the heating scenario: as soon as the density exceeds a certain threshold the ELM-free H-mode is achieved already at the lowest available heating power, 200 kW of ECRH (one gyrotron) or 340 kW of NBI (one source) respectively. The actual power threshold might even be lower. At the onset of an ELM-free H-mode the energy flux density across the separatrix is more than a factor of two less than found for the L-H transition in tokamaks [6].

3. TRANSPORT BARRIER AND TURBULENCE IN L- AND H-PHASE

Confinement improvement in the H-phase is characterized by the set-up of a transport barrier for particles and heat in the plasma edge which manifests itself as a steepening of the edge profile gradients on a timescale of about 20 ms : the density gradient around and inside the separatrix ($0.85 < r/a < 1$) increases by 40-60% as measured with Thomson scattering, multichannel microwave interferometry, reflectometry, Li-beam, and Langmuir probes. Electron temperature profiles obtained from ECE show the build-up of an edge pedestal for positions $r/a > 0.7$. This result is confirmed by the SX-camera. The increase of the edge ion temperature is determined spectroscopically from the broadening of impurity lines and from the energy distribution of CX neutrals. The measurements show that the transport barrier evolves around a so-called pivot-point close to the separatrix, inside of which density and temperature increase whereas they decrease outside. However an accurate determination of the relative position of the transport barrier (the pivot-point) with respect to the separatrix is difficult, as the influence of island structures and finite pressure on the topology of the plasma boundary complicates the exact mapping of diagnostic positions.

Edge turbulence in the quiescent H-mode is strongly reduced in comparison to the stationary L-state : the density fluctuations around and inside the separatrix are measured by reflectometry and microwave scattering. For radial positions inside the separatrix the spectral power of broadband density turbulence ($50\text{kHz} < f < 1\text{MHz}$) is reduced by about an order of magnitude. Magnetic fluctuations observed with Mirnov coils ($50\ \text{kHz} < f < 600\ \text{kHz}$) decrease by about the same factor. In some cases coherent mode activity (large scale MHD activity, $f < 50$ kHz) is observed even during the quiescent H-mode. However the influence of these modes on the edge transport barrier seems to be negligible.

4. ELMy H-MODE

In all experiments the quiescent H-phase is reached through an interval which is characterized as an ELMy H-mode (Fig.2): Sequences of periodic and quasi periodic ELMs appear with a typical repetition frequency of 1 to 2 kHz. The concomitant perturbation of T_e- and n_e-profiles is restricted to radial

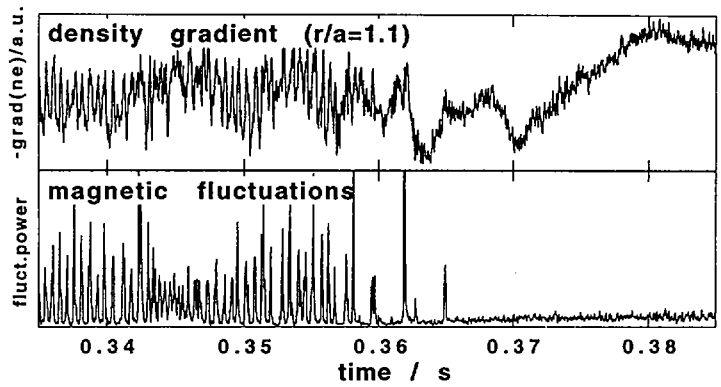

FIG. 2. Transition between ELMy and quiescent H-mode: density gradient at a position slightly outside the separatrix measured with reflectometry and magnetic fluctuations (50 kHz < f < 600 kHz) obtained from a Mirnov coil.

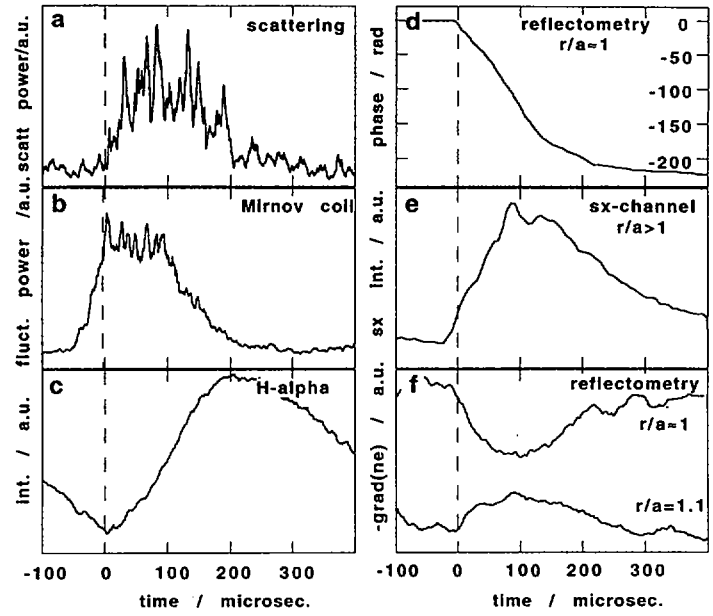

FIG. 3. Fluctuations (a, b) and macroscopic edge profile measurements (e, f) averaged over 15 ELMs. The distinct onset of the density fluctuations has been used as a clock for the averaging process. The Doppler shift of the reflectometry signal (d) displays the poloidal propagation of density structures and the H_α signal (c) the electron transport to the torus wall.

positions r/a > 0.7 and r/a > 0.9 respectively, emphasising the edge localized character of the phenomenon. Global confinement in the ELMy H-mode is close to the L-state. However the short (≥ 200 μs) intervals between the ELMs show magnetic and density fluctuations with frequency spectra *identical* to the quiescent H-mode. No clear "transition" between L-mode and ELMy H-mode is observed within the H-mode operational range as ELMs and quiescent H-phases appear intermittently even in the early phase of the discharge. During the discharge intervals with less periodic ELMs of higher repetition rate and intermittent turbulent phases develop almost continuously towards regular ELM activity.

5. DYNAMICS OF THE TRANSPORT BARRIER

In order to correlate the temporal behaviour of the transport barrier with the changes in fluctuations, a number of diagnostics with temporal resolution of the order of 10 μs are monitored simultaneously during the ELMy H-mode (Fig.3).

5.1. Fluctuations

During an ELM the power of broadband density turbulence (f > 50 kHz) measured with reflectometry and μ-wave scattering increases by an order of magnitude, i.e. to about L-mode level (Fig.3a). Magnetic fluctuations (f> 50kHz, Fig.3b) increase by about the same factor at all available poloidal and toroidal coil positions. At the onset of the ELM in most cases magnetic fluctuations display a quasi coherent activity (f ≈ 400 kHz) which evolves into a short phase of broadband turbulence. Figs. 3a,b show that the start of the magnetic activity precedds the burst of density fluctuations by about 50 μs. Starting simultaneously with the onset of the coherent magnetic activity a small but significant increase of density fluctuations is observed with the reflectometer. After an interval of 150 to 200 μs density and magnetic fluctuations return to the level of the quiescent H-mode. The quasi coherent MHD activity preceding the ELM indicates that the observed ELM phenomenon is not just a switching between equilibrium H- and L-states but is similar to type III ELMs found in tokamaks. In tokamaks a precursor activity f ≤ 150 kHz has been measured [7].

While the fluctuation level is high, the signal from the H_α-monitor (Fig.3c) increases, indicating an increase in radial energy and particle transport associated with the ELM. The radial propagation of the density perturbation is followed with reflectometry on a shot to shot basis using the onset of the H_α-burst as reference. For all positions (spanning a range Δr of 2 to 4 cm) the increase of the density fluctuation level occurs ≤20 μs before the start of the H_α-burst. The perturbation first appears in the layer 0.85 < r/a < 1.0, within 2 cm inside the separatrix.

5.2. Poloidal propagation of turbulence measured via reflectometry

The antenna beams of the reflectometry system are tilted with respect to the normal of the magnetic surfaces. The resulting poloidal wavevector component

k_{pol} allows to measure the poloidal propagation v_{pol} of density turbulence via the Doppler-shift. If the power in the Doppler-shifted component exceeds a certain threshold (power of the unshifted carrier) the phase detector yields a ramped phase output $\Delta\phi/\Delta t$ the so called "phase-runaway" [8]. From the slope of the phase-runaway the Doppler-shift and thus v_{pol} can be calculated. The observed velocity of the turbulence structures v_{pol} is the sum of poloidal plasma rotation and the intrinsic phase velocity of the turbulence itself.

During typical L-mode operation a phase-runaway is observed [8]. In contrast during the quiescent H-phase the amplitude of density turbulence is low, the Doppler-shifted component is below the threshold and the phase-runaway disappears completely. With each ELM the reflectometer detects a strong negative drift of the phase (Fig.3d), i.e. a red-shift of the reflected signal which corresponds to a poloidal propagation in electron diamagnetic drift direction. Because of the threshold character of the phenomenon the phase drift shows a well defined onset at the start of the ELM. During the ELMs short (several μs) intervals with lower fluctuation amplitude intermittently stop the phase drift, a feature which is smeared out by the averaging process used in Fig.3d. An analysis of the individual ELMs shows that the decrease in $\Delta\phi/\Delta t$ towards the end of the averaged ELM in Fig.3d is not caused by a decrease in poloidal propagation velocity but by a decrease of fluctuation level. For positions inside the separatrix region a poloidal velocity of about 20 km/s is estimated even during the ELM using a tilt angle relative to the magnetic surfaces of 2.5°. The exact value of the tilt angles critically depends on the details of the complex edge topology.

5.3. Macroscopic profile gradients

During an ELM the edge electron temperature profile measured with ECE shows an initial flattening around a pivot-point at $r/a \approx 0.85$ to 0.9 followed by a cold-pulse which propagates towards the plasma center. The rapid electron heat transport across the separatrix is displayed in Fig.3d by the increase of T_e measured with the SX-camera along a line of sight which covers positions $r/a \geq 1$.

Changes of the edge density gradient associated with an ELM are obtained from the time delay of the reflectometry signal (Fig.3e, see also Fig.2) using an amplitude modulation technique [9]. This diagnostics for density gradients which is normally used for density profile measurements can be modified by the presence of strong density fluctuations. This effect is currently studied numerically. For different radial positions the change of the density gradient is measured with a temporal resolution of about 10 μs on a shot to shot basis. Fig.3e shows the flattening of grad(n_e) for $r/a = 1$ and an increase at $r/a = 1.1$ indicating a pivot-point position around the separatrix. The density gradient remains unaffected by the ELM for positions $r/a \leq 0.9$. The profile measurements therefore indicate that the layer where the ELM affects n_e is narrower and closer to the separatrix than the layer where T_e is changed.

6. CONCLUSION

In W7-AS the H-mode can be realized in narrow windows of the edge rotational transform which offer possible favourable conditions for the transition in the plasma edge. This model is supported by the easy access to the quiescent H-mode with respect to the heating power. The quiescent H-mode is always reached through an ELMy H-phase where in between the ELMs density and magnetic field fluctuations drop to the level of the fully developed H-mode. Within the operational windows the ELMy H-mode is observed instead of a distinct L-mode even in the early phase of the discharge. The ELMs have a duration of 150 - 200 μs during which turbulence increases and the edge profiles of T_e and n_e are modified. Even during the ELMs the poloidal propagation velocity of density turbulence in the separatrix region is about 20 km/s towards the electron diamagnetic direction. For both start and end of an ELM the changes of turbulence and edge profile gradients occur on the same timescale thus leaving the question of a causal interdependence between both physical quantities open.

REFERENCES

[1] ERCKMANN, V., et al., Phys. Rev. Lett. **70** (1983) 2086.
[2] WAGNER, F., et al., Plasma Phys. Control. Fusion **36** (1994) A61.
[3] HOLZHAUER, E., et al., in Controlled Fusion and Plasma Physics (Proc. 23rd Eur. Conf. Kiev, 1996), Vol. 20C, European Physical Society, Geneva (1996).
[4] WAGNER, F., et al., in Plasma Physics and Controlled Nuclear Fusion Research 1994 (Proc. 15th Int. Conf. Würzburg, 1994), Vol. 1, IAEA, Vienna (1995) 559.
[5] SHAING, K.C., Phys. Fluids B **5** (1993) 3841.
[6] RYTER, F., et al., Plasma Phys. Control. Fusion **36** (1994) A99.
[7] ZOHM, H., Plasma Phys. Control. Fusion **38** (1996) 105.
[8] BRAÑAS, B., et al., in Controlled Fusion and Plasma Physics (Proc. 23rd Eur. Conf. Kiev, 1996), Vol. 20C, European Physical Society, Geneva (1996).
[9] HIRSCH, M., et al., Rev. Sci. Instrum. **67** (1996) 1807.

TRANSPORT THEORY

(Session D1)

Chairperson

M.N. ROSENBLUTH
ITER

ENHANCED REVERSED SHEAR BIFURCATION IN TOKAMAK PLASMAS

A. DAS, S. DASTGEER, P.K. KAW,
K. AVINASH, A. SEN, R. SINGH
Institute for Plasma Research,
Bhat, Gandhinagar, India

Abstract

ENHANCED REVERSED SHEAR BIFURCATION IN TOKAMAK PLASMAS.

The paper presents a transport bifurcation model for transition to the enhanced reversed shear (ERS) mode recently observed in TFTR and DIII-D. The model takes into account effects due to the evolution of magnetic shear and the pressure gradient driven bootstrap current. The zero dimensional version of this model shows that the bootstrap current contributions substantially lower the external power thresholds for ERS transition and enhance the radial extent of the core ERS mode. The one dimensional (r, t dependent) model is also studied and the nature of the front propagation solutions is investigated.

1. INTRODUCTION

Recent tokamak confinement experiments [1, 2] have revealed the existence of the enhanced reversed shear (ERS) mode. The theoretical interpretation of these experiments is based on the general idea that many MHD modes and micro-instabilities (high n ballooning, resistive/electron viscosity driven ballooning, ion temperature gradient, etc.) are linearly stabilized by global negative shear effects [3–5]. It has, however, been pointed out that (a) negative shear is unable to completely suppress many of the linear instabilities (especially because of residual growth due to trapped electron effects [6]), and it is necessary to incorporate non-linear suppression of the fluctuations through velocity shear effects as in the usual theory of L–H transitions [7, 8]; and (b) local negative magnetic shear created by Shafranov shift of magnetic surfaces is as effective as the global negative shear in stabilizing many microinstabilities [9].

In all these models, it has been assumed that the skin time for global shear evolution is long compared with the time-scale of the experiment, so that the global shear profile may be assumed to be frozen in its initial form. We have pointed out previously [10] that in the current experiments, the time-scale separation between the density profile evolution and the global shear evolution is small (only a factor of 2–3) so that it is important to include the global shear evolution in the theories. Furthermore, the global shear evolution equation naturally brings in contributions due to bootstrap currents which also generate hollow current profiles in the central core and hence provide another positive feedback mechanism for the maintenance of reversed

shear profiles. These effects are going to be especially important in future experiments as we move towards steady state advanced tokamak configurations.

In this paper we present detailed results of our investigations of a zero dimensional (0-D) and a one dimensional (1-D) model which incorporate all of the above mentioned physical phenomena. Our 0-D model demonstrates that in the steady state regime the contributions to reversed magnetic shear due to bootstrap current effects formally dominate over the local negative magnetic shear due to Shafranov shift effects. The 1-D model shows the evolution of two distinct fronts. One of them corresponds to the reduction in fluctuation level due to negative shear while the other corresponds to stabilization due to velocity shear. The front propagation speed is found to scale with power deposition.

2. MODEL EQUATIONS

The basic evolution equations of the 1-D model are:

$$\frac{\partial E}{\partial t} = \frac{\gamma_0 N}{1 + \alpha_2 N^4} E - \alpha_1 E^2 + \frac{\partial}{\partial x}\left(D_1 E \frac{\partial}{\partial x} E\right) \tag{1}$$

$$\frac{\partial N}{\partial t} = Q(x) + D_{NC} \frac{\partial^2}{\partial x^2} N + \frac{\partial}{\partial x}\left(D_2 E \frac{\partial}{\partial x} N\right) \tag{2}$$

$$\tau_R \frac{\partial S}{\partial t} = \frac{\partial^2}{\partial x^2} [\eta(x)(S - 2 + \epsilon^{1/2}\beta_p N)] \tag{3}$$

where $N = (a/r)|(dn/dr)|$, E is the fluctuation level $|\delta n/n|$, S is the global shear parameter rq'/q; $Q \equiv \alpha_3 P/WnV$ is proportional to the fuelling rate per unit volume by the neutral beams (P and W represent the neutral beam power and energy and V is the plasma volume); D_{NC} is the neoclassical and D_1E, D_2E are the anomalous transport coefficients; $\gamma_0 = \gamma_0(S_{eff})$ is the linear growth rate, which is a function of the effective shear parameter $S_{eff} = S - \epsilon\beta_p N$ (the $\epsilon\beta_p N$ term being the local shear contribution arising through Shafranov shift of magnetic surfaces [9]); $\alpha_2 N^4$ expresses the reduction of growth rate due to velocity shear effects, where $\partial V_\theta/\partial r \propto N^2$ comes from diamagnetic flow effects [11]; $\alpha_1 E^2$ is the non-linear stabilization term (giving, for $\alpha_2 = 0$, the typical mixing length saturation amplitude $E = \gamma_0 N/\alpha_1$); τ_R is the resistive skin time $4\pi r_s^2/\eta c^2$; $\epsilon^{1/2}\beta_p N$ represents the contribution of bootstrap current to the steady state global shear parameter. Equations (1) and (2) are similar to the ones written by Diamond et al. [8] and Eq. (3) follows from

the neoclassical Ohm's law $E = \eta(j_\parallel - j_b)$. We supplement these equations with a model equation showing suppression of the growth rate by negative shear:

$$\gamma_0 = \gamma_R + \frac{1}{2}(\gamma_1 - \gamma_R)[1 + \tanh(S_{eff}/S_c)] \tag{4}$$

where γ_1 is the usual linear growth rate for the positive shear case and γ_R is the residual growth rate for sufficiently large negative shear. This choice of dependence of γ on S_{eff} is dictated by numerical results of linearized eigenmode calculations [4, 6].

3. ZERO DIMENSIONAL RESULTS

In the 0-D equations, we replace $\partial/\partial x$ by $1/r_s$; these equations may then be treated as local equations describing the dynamics at a point. In the models by Diamond et al. [8] and Drake et al. [9], the shear is frozen; this case can be recovered from the present model by taking the limit $\tau_R \to \infty$. We first consider the case with evolving shear. The stationary points in this case are given by

$$\frac{r_s^2\alpha_1}{D_A}\frac{(1 + \alpha_2 N^4)}{N^2}\left(\frac{\alpha_3 P}{WVn} - \frac{D_{NC}N}{r_s^2}\right) = \psi \tag{5}$$

where we have assumed $D_1 = D_2 = D_A$ and

$$\psi = \gamma_R + \frac{(\gamma_0 - \gamma_R)}{2}\left[1 + \tanh\left(\frac{C - \epsilon^{1/2}\beta_p(1 + \epsilon^{1/2})N}{S_c}\right)\right]$$

In this equation the bootstrap contribution is larger than the contribution due to Shafranov shift. $S = C$ is the initial ohmic shear. In Fig. 1 we plot the two sides of Eq. (5) (for typical TFTR parameters) as a function of P and N. For $P \leq 10$ MW, there are five roots. In the first root, E is large and hence it can be identified with the L mode. This root and, as a result, the third and fifth roots, are stable. At $P \geq P_C^1 = (D_A\gamma_0 WVnr_s^2)/(r_s^2\alpha_1\alpha_3(\epsilon^{1/2} + \epsilon)^2\beta^2)$ the first two roots merge and the plasma makes a transition to the third root, where E and the transport are reduced. This equilibrium can be identified with the reversed shear (RS) mode discussed by Drake et al. [9]. However, the actual reduction will depend on the choice of parameters. If a reduction of transport by a large factor is achieved through negative shear alone, it is in principle possible to make a transition to a state where neoclassical levels are observed. In this case the third root moves towards the fifth root. Only a detailed linear eigenmode calculation can show whether it is realistic to expect a reduction in γ by such a large factor. At $P_C^2 = (D_A\gamma_R WVn)/(2\alpha^{1/2}r_s^2\alpha_1\alpha_3)$ the third and fourth roots merge and the plasma is at $N_5 = (\alpha_3 Pr_s^2)/(WVnD_{NC})$. For TFTR parameters,

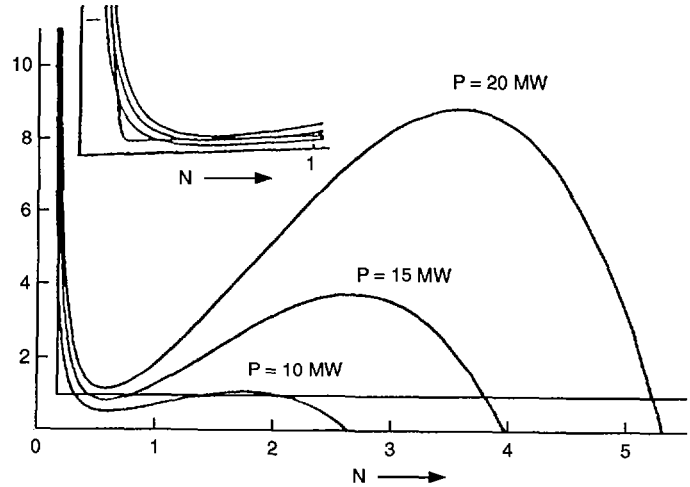

FIG. 1. Plot of the right hand side and the left hand side of Eq. (5) as a function of N for TFTR parameters, $D_A = 5\ m^2/s$, $D_{NC} = 0.04\ m^2/s$, $r_s/a = 0.33$, $W = 80\ keV$, $V = 40\ m^3$, $n = 2 \times 10^{19}\ cm^{-3}$, $\alpha_2 = 10$, $\alpha_1 = 5 \times 10^4$, $\gamma_R = 10^4$, $\gamma_1 = 10^5$, $\tau_R = 3\ s$, and $P = 10$, 15 and 20 MW (r_s is the radius of the negative shear region). The inset shows the details in the range $0 \leq N \leq 1$.

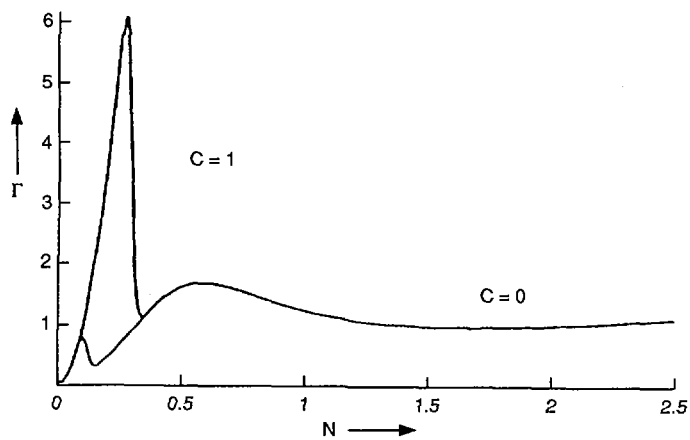

FIG. 2. Plot of particle flux Γ versus N in the core (C = 0) and at the edge (C = 1). Note the higher P and an extra peak in Γ at the edge.

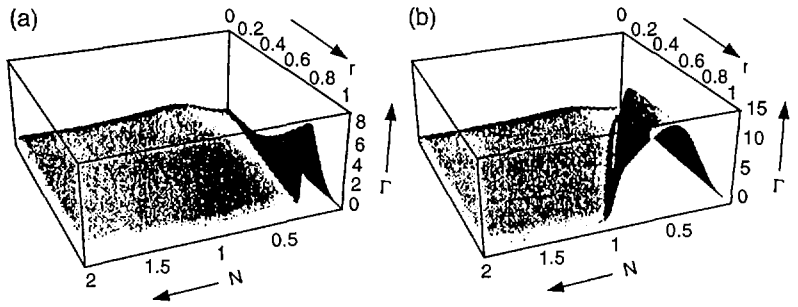

FIG. 3. (a) Flux landscape $\Gamma(x, N)$ with bootstrap current for the parameters of Fig. 1 and $P = 20$ MW. (b) Flux landscape without bootstrap current. Note the larger Γ and the shrunken H mode in the core.

P_c^1 and P_c^2 are about 15–20 MW, which roughly gives the observed threshold. It is instructive to look at plots of particle flux $\Gamma = D_A\gamma N^2/r_s^2(1 + \alpha_2 N^4)\alpha_1 + D_{NC}N/r_s^2$ versus N [12]. The parameter C (which labels the radial co-ordinate) is the ohmic shear, which is about 0 at r = 0 and increases to 1 at r = a. In Fig. 2 we show these plots for C = 0 and C = 1. An extra peak at C = 1 is due to a reduction in γ. In Fig. 3(a) we show the flux landscape, which indicates the extent of ERS confinement. To consider the case of frozen shear we drop unity in the parentheses with $\epsilon^{1/2}$ in Eq. (5). For this case $\tilde{P}_c^1 = (D_A\gamma_0 WVn/r_s^2\alpha_1\alpha_3)S^2/\epsilon^2\beta_p^2$, which is much higher than $\tilde{P}_c^2$ and P_c^1 and thus decides the threshold for the ERS transition. The ratio of the threshold with bootstrap current to that without $\approx \epsilon^2/(\epsilon^2 + \epsilon^{1/2})^2 \approx \epsilon$, which shows that with bootstrap current the threshold is reduced considerably. In Fig. 3(b) we plot the flux landscape without bootstrap current. A smaller region of RS mode and a higher threshold can easily be seen.

4. ONE DIMENSIONAL RESULTS

We next show the numerical solution of our 1-D equations. Figure 4 shows the plots of E and N at two different times for two different power deposition profiles. It should be noted that the fluctuations in the edge region are higher, whereas in the core they are low. The first sharp drop in E (moving towards the core) occurs when γ, the growth rate, switches from a higher value γ_I to γ_R as S_{eff} changes sign. This happens since S, the global shear parameter, is smaller in the core, and the reverse holds for the density gradient N, making $S_{eff} = S - \epsilon\beta_p N$ change sign from a positive to a negative value. The E evolution takes place very rapidly and hence for time-scales of interest (typically the N evolution time-scales) E adjusts very rapidly to the stationary state value $E = \gamma N/\alpha_1(1 + \alpha_2 N^4)$ for the region where $\partial E/\partial x$ is

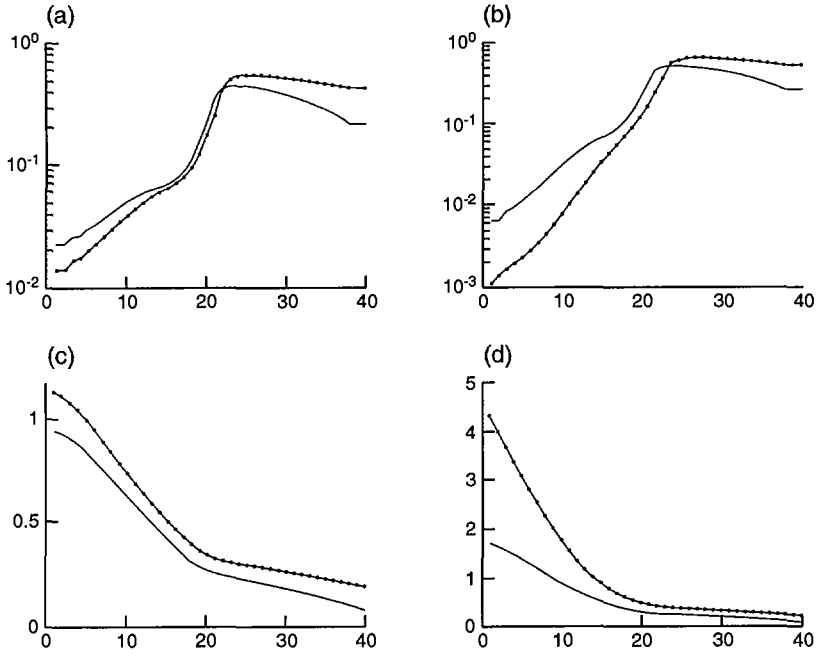

FIG. 4. (a, b) Density fluctuation profiles at different times (solid lines: earlier times; solid lines with dots: later times) (a) for a smaller input power and (b) for a larger input power. (c, d) Density gradient profiles at different times (solid lines: earlier times; solid lines with dots: later times) (c) for a smaller input power and (d) for a larger input power.

small. Hence the sudden drop in γ is echoed in E, giving rise to the front-like structure in the E profile. We call this the RS front. The numerical solution for N indicates that it has a linear profile in x with a discontinuity in the slope at the location of the front. The two states separated by this particular front in E can be identified with the two states described in Ref. [9], as the origins of these two states are governed by similar physics.

As time progresses this front moves towards the edge. The velocity of the front is governed by the power deposition; the larger the power deposition the faster the front propagation towards the edge. The location of the front as well as its dependence on input power deposition can be understood from the following simplified analysis. We distinguish two regions, I and II, which are given by $x > x_f$ and $x < x_f$ (where x_f indicates the location of the front), respectively. The direct input power Q(x) in the two regions separated by the RS front is negligible and hence we drop it from the N equation. Furthermore, we substitute $E = \gamma_R N/\alpha_1$ in the density gradient equation for region II as E equilibrates rapidly and $\alpha_2 N^4 \ll 1$. The

resulting equation can be integrated once to yield the following equation for the density n(x):

$$\frac{\partial n}{\partial t} = -\frac{\partial}{\partial x}\tilde{\gamma}_R N^2$$

where $N = -\partial n/\partial x$ and $\tilde{\gamma}_R = D_2\gamma_R/2\alpha_1$. Thus $\tilde{\gamma}_R N^2$ represents the particle flux. We now use the assumption of stationarity in a frame moving with a velocity U (i.e. choosing $\xi = x - Ut$, $t = t'$), which gives

$$-U\frac{\partial n}{\partial \xi} = -2\tilde{\gamma}_R N\frac{\partial N}{\partial \xi} \tag{6}$$

and shows that in the moving frame $\tilde{\gamma}_R N^2 - Un = \Gamma_0 - Un_0 =$ constant. Here Γ_0 and n_0 are the input particle flux and particle density at the boundary for region II and hence are known. The threshold of input particle flux Γ_M required for the stationary front (i.e. $U = 0$) is given by $\Gamma_M = \tilde{\gamma}_1 N_1^2 = \tilde{\gamma}_R N_2^2$, where N_1 and N_2 represent density gradients in regions I and II, respectively. We integrate across the regions to obtain

$$\Gamma_M(N_2 - N_1) = \int_{N_1}^{\tilde{N}_0} \tilde{\gamma}_1 N^2\, dN + \int_{\tilde{N}_0}^{N_2} \tilde{\gamma}_R N^2\, dN$$

(here $\tilde{N}_0$ is the density gradient required for the transition, i.e. $\tilde{N}_0 = S/\epsilon\beta_p$), and substituting for N_1 and N_2 in terms of Γ_M, $\tilde{\gamma}_1$ and $\tilde{\gamma}_R$ we obtain a relationship between $\tilde{N}_0$ and Γ_M as $\tilde{N}_0 \approx 6^{1/3}\Gamma_M^{1/2}/\tilde{\gamma}_1^{1/3}\tilde{\gamma}_R^{1/6}$. We next use the relationship $N = -\partial n/\partial \xi$ in Eq. (6) to obtain $N = N_0 - U(x - Ut)/2\tilde{\gamma}_R$. This shows that N has a linear profile in space and its slope depends on the velocity of the front. For the special case of $U = 0$, N will be a constant. Thus the faster the motion of the front, the steeper the profile of N, which is indeed what we observe numerically (Fig. 4). The unknowns in the above equation are N_0 and U, and it is of interest to know how U changes as the input flux Γ_0 exceeds Γ_M, the threshold value. The expression for density can be obtained by integrating the equation for N as $n(x) = N_0(x - Ut) - U(x - Ut)^2/2\tilde{\gamma}_R + C$. The unknown constant C can be determined by using the condition of constancy of fluxes which gives $C = n_0 - \Gamma_0/U + \tilde{\gamma}_R N_0^2/U$. Since the front is moving slowly on the relaxation time of region I, we assume N to be a constant having no spatial dependence. This gives $n(x) = B(1 - x)$ for density, where we have used the boundary condition of vanishing density at $x = 1$. The matching of fluxes at the discontinuity yields $B = \sqrt{\tilde{\gamma}_R/\tilde{\gamma}_1}(N_0 - U\xi_f/2\tilde{\gamma}_R)$. In the limit of $\tilde{\gamma}_R \ll \tilde{\gamma}_1$, B is small and hence the value of density is extremely small. The matching of density at ξ_f, using $\tilde{N}_0 = N_0 - U\xi_f/2\tilde{\gamma}_R$ and expressing $\tilde{N}_0$ in terms of Γ_M, yields $U \approx (\Gamma_0 - \Gamma_M)/n_0$, which is the expression of the front velocity in terms of input power. This completes our description of the RS front.

In the core region, with increasing N there appears a second transition which is due to velocity shear suppression of fluctuations (through the $\alpha_2 N^4$ term in the denominator) and can be termed the velocity shear enhanced reversed shear (VSERS) front [13]. However, this front is not as sharp as the RS front. As N increases it further reduces E, resulting in the third region separated by the relatively smooth VSERS front. The reduction in E decreases the anomalous diffusion in the N equation, thereby further enhancing the value of N. The final saturated equilibrium state of this phase is obtained when the neoclassical diffusion takes over. Thus in this phase the transport is entirely governed by the neoclassical values.

5. SUMMARY AND DISCUSSION

We have shown that the inclusion of the temporal evolution of global magnetic shear brings in effects due to bootstrap current which may result in a significant reduction in the power threshold for transition to the ERS mode. The 1-D model calculation shows the evolution of two distinct fronts, one corresponding to stabilization by magnetic shear, the other to stabilization by velocity shear. It is pertinent to ask to what extent the magnetic shear evolution is playing a role in present day experiments such as TFTR and DIII-D. Experimental plots of the time evolution of q(r) (and magnetic shear) in TFTR indicate a time-scale within a factor of 2–3 of that for the evolution of pressure gradients. Furthermore, detailed calculations [1] indicate that the shear evolution can be understood in terms of the neoclassical diffusion of the current coupled to all driven currents, which seems to imply that bootstrap currents are playing a significant role. However, this is only indirect evidence and further careful experimentation is needed to elucidate this point. In any case, these effects are going to be increasingly important as we move towards steady state advanced tokamaks.

REFERENCES

[1] LEVINTON, F.M., et al., Phys. Rev. Lett. **75** (1995) 4417.
[2] STRAIT, E.J., et al., Phys. Rev. Lett. **75** (1995) 4421.
[3] KADOMTSEV, B.B., POGUTSE, O.P., Sov. Phys. — JETP **24** (1967) 1172.
[4] KESSEL, C., et al., Phys. Rev. Lett. **72** (1994) 1212.
[5] KIM, J.Y., WAKATANI, M., Phys. Plasmas **2** (1995) 1012.
[6] BEER, M.A., Plasma Physics Lab., Princeton Univ., NJ, personal communication, 1995.
[7] DIAMOND, P.H., et al., Phys. Rev. Lett. **72** (1994) 2565.
[8] DIAMOND, P.H., et al., in press.
[9] DRAKE, J.F., et al., Phys. Rev. Lett. **77** (1996) 494.
[10] AVINASH, K., KAW, P.K., SINGH, R., paper presented at IAEA Technical Committee Meeting on Research Using Small Tokamaks, Ahmedabad, 1995.
[11] CARRERAS, B.A., NEWMAN, D., DIAMOND, P.H., LIANG, Y.M., Phys. Plasmas **1** (1994) 4014.
[12] STAEBLER, G.M., HINTON, F.L., Phys. Plasmas **1** (1994) 909.
[13] DIAMOND, P.H., LEBEDEV, B., NEWMAN, D.E., CARRERAS, B.A., Phys. Plasmas **2** (1995) 3685.

DISCUSSION

M. YAGI: Can your model predict the location of the appearance of the transport barrier, and do you think that it is correlated with the mode rational surface (q = 2, 3...; q may appear through γ_R)?

P.K. KAW: Yes, the transport barrier is located at the place where the 'effective shear' $S_{eff} = S - \varepsilon\beta_p N$ changes sign. Here $S = (r/q)(dq/dr)$ is the global shear parameter and $N = |(r/n)(dn/dr)|$ is the normalized gradient. Note that because of the second term, the ion temperature barrier may be located in a region of positive global shear parameter S.

M.N. ROSENBLUTH: Do your scaling laws indicate reactor relevant power versus size?

P.K. KAW: Yes, indeed the power requirements are reasonable even when scaled to the reactor regime, especially because there is a significant reduction of the threshold power due to the contributions from bootstrap current effects.

TURBULENCE AND TRANSPORT IN ENHANCED CONFINEMENT REGIMES OF TOKAMAKS: SIMULATION AND THEORY

T.S. HAHM, M. ARTUN, M.A. BEER,
G.W. HAMMETT, W.W. LEE, X. LI,
Z. LIN, H.E. MYNICK, S.E. PARKER,
G. REWOLDT, W.M. TANG
Plasma Physics Laboratory,
Princeton University,
Princeton, New Jersey,
United States of America

Abstract

TURBULENCE AND TRANSPORT IN ENHANCED CONFINEMENT REGIMES OF TOKAMAKS: SIMULATION AND THEORY.

An integrated program of theory and computation has been developed to understand the physics responsible for the favorable confinement trends exhibited by, for example, enhanced reversed shear (ERS) plasmas in TFTR and DIII-D. The paper reports on: (1) the quantitative assessment of $\mathbf{E} \times \mathbf{B}$ shear suppression of turbulence by comparison of the linear growth rate calculated from the gyrofluid/comprehensive kinetic codes and the experimentally measured shearing rate in TFTR ERS plasmas; (2) the first self-consistent nonlinear demonstration of ion temperature gradient turbulence reduction due to ∇P_i driven $\mathbf{E} \times \mathbf{B}$ shear by the global gyrokinetic simulation; (3) a revised neoclassical analysis and gyrokinetic particle simulation results in agreement with trends in ERS plasmas; (4) Shafranov shift induced stabilization of trapped electron mode in ERS plasmas calculated by the gyrofluid code; and (5) new nonlinear gyrokinetic equations for turbulence in core transport barriers.

1. Introduction

Recent significant experimental progress in enhancing plasma confinement[1, 2] presents a new challenge to tokamak confinement theory. Further improvements of simulations and theory are needed to understand and more accurately describe the following plasma properties that are observed in TFTR ERS plasmas[1] and DIII-D negative central shear (NCS) plasmas[2]: (i) The improved confinement is observed throughout the region of reversed shear. The ion thermal transport is reduced to a level below the conventional neoclassical theory prediction. (ii) The pressure gradient scale length in transport barrier regions becomes comparable to the ion poloidal gyroradius. Typically, the density gradient is the sharpest in TFTR ERS plasmas, while DIII-D NCS plasmas exhibit sharp gradients of the ion temperature and toroidal rotation velocity profiles. A common feature of both cases[3–5] is the sharp gradient of the radial electric field. (iii) Density fluctuations drop to an extremely low level throughout most

of the reversed magnetic shear region after the transition to ERS[3] and NCS discharges[5]. Motivated by these observations, the following theoretical issues are addressed using various computational and analytical methods.

2. Nonlinear Gyrokinetic Equations for Core Transport Barriers

We have derived nonlinear gyrokinetic equations which are readily usable for gyrokinetic particle simulation of turbulence in core transport barriers [6]. Without modifying the basic low-frequency gyrokinetic ordering, $\omega/\Omega \sim k_\parallel/k_\perp \sim \epsilon$, and $k_\perp \rho_i \sim 1$, we can describe plasmas with sharp gradients $L_p \sim L_E \sim \rho_{\theta i}$, by introducing an additional small ordering parameter, $\delta_B \equiv B_\theta/B$. The conventional ordering for the fluctuation level, $e\delta\phi/T_e \sim \epsilon$, is not necessarily appropriate for turbulence in a transport barrier. TFTR data show that fluctuation levels are well below the simple mixing-length level, $\delta n/n_0 < \Delta r/L_n$ both before and after the transition to ERS[3]. Therefore, we take $\delta f/F_0 \sim e\delta\phi/T_e \sim \epsilon\delta_B \ll 1/k_\perp L \sim \delta_B$. We also take $u_E/v_{Ti} \sim \delta_B$ consistent with the data from major tokamaks.

From the radial force-balance relation, $E_r/RB_\theta = u_\phi/R - u_\theta B_\phi/RB_\theta + (e_i n_i RB_\theta)^{-1}(\partial P_i/\partial r)$, one can easily find that the ratio between the first term and the third term on the right hand side is $u_\phi L_p/v_{Ti}\rho_{\theta i} \sim 1$. This is indeed a desirable property, since the following nonlinear gyrokinetic equations based on this ordering can be applied to both TFTR ERS plasmas, where the third term is the dominant contributor to E_r[4], and DIII-D VH-mode and NCS plasmas, where the first term is dominant[7, 5]. A universal feature of these enhanced confinement regimes[3–5] is the sharp gradient of the effective toroidal $\mathbf{E}\times\mathbf{B}$ rotation frequency E_r/RB_θ, which is the key parameter for suppression of turbulence[8].

The nonlinear gyrokinetic equation which has been derived via the phase-space Lagrangian Lie perturbation theory can be written in terms of $\delta f \equiv F - F_0$.

$$\frac{\partial \delta f}{\partial t} + \frac{d\mathbf{R}}{dt}\cdot\nabla\delta f + \frac{dv_\parallel}{dt}\frac{\partial \delta f}{\partial v_\parallel} = -\frac{d\mathbf{R}^{(1)}}{dt}\cdot\nabla F_0 - \frac{dv_\parallel^{(1)}}{dt}\frac{\partial F_0}{\partial v_\parallel}. \tag{1}$$

Here, superscript $^{(1)}$ denotes the perturbed parts due to the gyro-averaged perturbed electrostatic potential $\langle\delta\phi\rangle$. $\frac{d\mathbf{R}}{dt}$ and $\frac{dv_\parallel}{dt}$ can be obtained from the following Euler-Lagrange equation,

$$e\mathbf{B}^*\times\frac{d\mathbf{R}}{dt} + M\mathbf{b}\frac{dv_\parallel}{dt} = -\nabla[e\Phi + \mu B + \frac{M}{2}u_E^2 + \frac{\mu B}{2\Omega}(\mathbf{b}\cdot\nabla\times\mathbf{u}_E) + e\langle\delta\phi\rangle], \tag{2}$$

where $\mathbf{B}^* \equiv \mathbf{B} + \frac{M}{e}\nabla\times(\mathbf{u}_E + v_\parallel\mathbf{b})$, $\mathbf{u}_E \equiv \frac{\mathbf{b}\times\nabla\Phi}{B}$, and other notations are standard.

The analytical two point nonlinear theory[9, 8] investigates the competition between the eddy deformation due to the $\mathbf{E}\times\mathbf{B}$ shearing effect and the turbu-

lence induced eddy decay due to the $\delta\mathbf{E} \times \mathbf{B}$ nonlinearity. The ratio between the two terms describing these effects in Eq. (1) is,

$$\omega_E/\Delta\omega_T \sim \Delta r[\frac{\partial}{\partial r}(\mathbf{u}_E \cdot \nabla)]\delta f/\frac{\mathbf{b}}{B_{\|}^*} \times \nabla\langle\delta\phi\rangle \cdot \nabla\delta f \sim \delta_B/\epsilon.$$

Therefore, $\epsilon \sim \delta_B$ is a maximal ordering which allows the study of $\mathbf{E} \times \mathbf{B}$ shear suppression of turbulence in a self-consistent way.

3. Global Nonlinear Gyrokinetic Simulation of ITG Turbulence

Global three-dimensional nonlinear gyrokinetic simulations in realistic tokamak geometry are being used to study the $\mathbf{E} \times \mathbf{B}$ shear effects on ion temperature gradient (ITG)-driven ion heat transport[10]. Global simulation is useful in studying the important effects of profile variation on the structure of the transport barrier.

Focusing on the case where the toroidal flow contribution to E_r is dominant, we have added the toroidal flow shear terms[11] to the standard gyrokinetic equations[12]. Simulation parameters are described in Ref. [10]. We have found moderate $\mathbf{E} \times \mathbf{B}$ shear $\frac{RB_\theta}{B}|\frac{\partial}{\partial r}(\frac{E_r}{RB_\theta})| \simeq \frac{r}{q}\frac{\partial}{\partial r}(\frac{u_\phi}{R}) \simeq 0.01 v_{Ti}/L_T$ has significant effect in reducing the radial mode width of the long wavelength ITG modes ($\sim 50\%$) and the linear growth rate ($\sim 30\%$) to a less extent. However, the reduction in the calculated nonlinear heat transport is much weaker than expected from a naive mixing length estimate γ/k_r^2 based on the linear eigenmode width, as shown in Fig. 1.

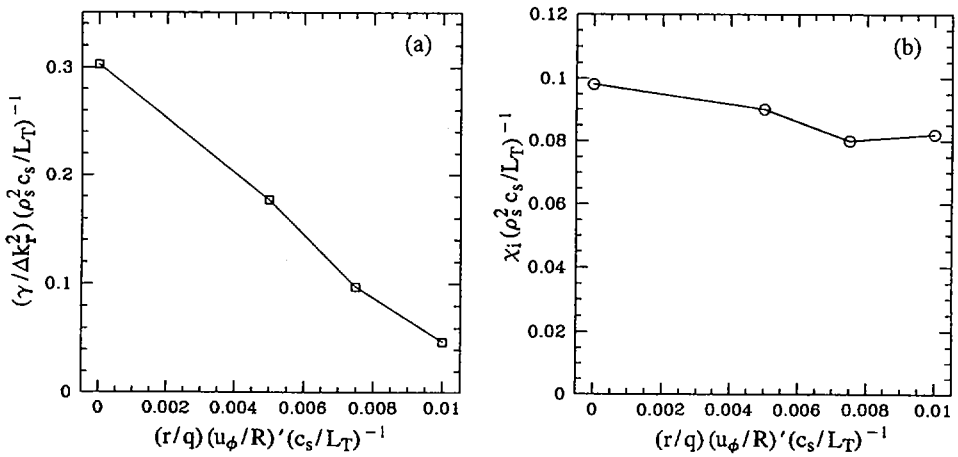

FIG. 1. (a) Simple mixing length estimate of χ_i versus toroidal flow shear. (b) Measured χ_i in the nonlinear quasisteady state versus toroidal flow shear.

This result can be understood from the eddy shape dependence of the $\mathbf{E} \times \mathbf{B}$ shearing rate, ω_E. In general toroidal geometry[8],

$$\omega_E = \frac{k_\theta}{k_\psi} \frac{(RB_\theta)^2}{B} | \frac{\partial}{\partial \psi} (\frac{E_r}{RB_\theta}) |. \tag{3}$$

Here, $\frac{\partial}{\partial \psi}(\frac{E_r}{RB_\theta})$ is function of the poloidal flux (ψ) only in most cases of interest, $(RB_\theta)^2/B$ is the poloidal angle (θ) dependent form factor, and the first factor describes the eddy shape dependence which involves k_ψ and k_θ; the components of the $\mathbf{k}$ vector of fluctuation in the radial ($\mathbf{e}_\psi$) and nonradial perpendicular ($\mathbf{b} \times \mathbf{e}_\psi$) directions. Since toroidal ITG linear eigenmodes are radially elongated with $k_\psi \ll k_\theta$, the shearing effect characterized by ω_E can be significant even for a moderate value of flow shear. However, the fluctuation k-spectrum is observed to be isotropized in the nonlinear regime. Therefore, the shearing effect is reduced in the nonlinearly saturated state in comparison to the linear phase of the instability for the same amount of flow shear.

Our most recent simulation includes the pressure gradient driven $\mathbf{E} \times \mathbf{B}$ shearing effect utilizing new nonlinear gyrokinetic equations[6]. Self-consistency with respect to the radial force balance and profile variations is maintained. We have found that the ion thermal transport at nonlinear saturation is reduced by more than 25% for moderate ω_E from the pressure gradient (with no plasma flow) $\sim 0.5\gamma_{n=4}$, compared to the case without E_r shear.

The radial structure of the fluctuations has important implications for transport barrier formation as well as the transport scalings. In developing an analytic analysis of the global gyrokinetic results, a number of extensions of existing theory have resulted[13]. The high-n ballooning mode formalism can still be applied for moderate values of flow shear and the Weber-like solutions to the radial potential problem have a wider range of validity than that expected from the previous theory. The analytic prediction for the spatial structure of the Weber-like modes is quite similar to that observed in simulations.

4. Gyrofluid and Comprehensive Kinetic Studies of Microinstabilities in ERS Plasmas

The microinstability properties of discharges with reversed magnetic shear in the TFTR and DIII-D experiments with and without confinement transitions have been investigated. A comprehensive kinetic linear eigenmode calculation implementing the ballooning representation[14] was employed with experimentally measured profile data, and using the corresponding numerically computed MHD equilibria. The instability considered was the toroidal drift mode (trapped-electron-η_i mode) where a variety of physical effects change with differing q-profiles. A number of negative magnetic shear discharges at different times in the discharge for TFTR and DIII-D were analyzed. The relative importance of changes in different profiles on the linear growth rates was investigated,

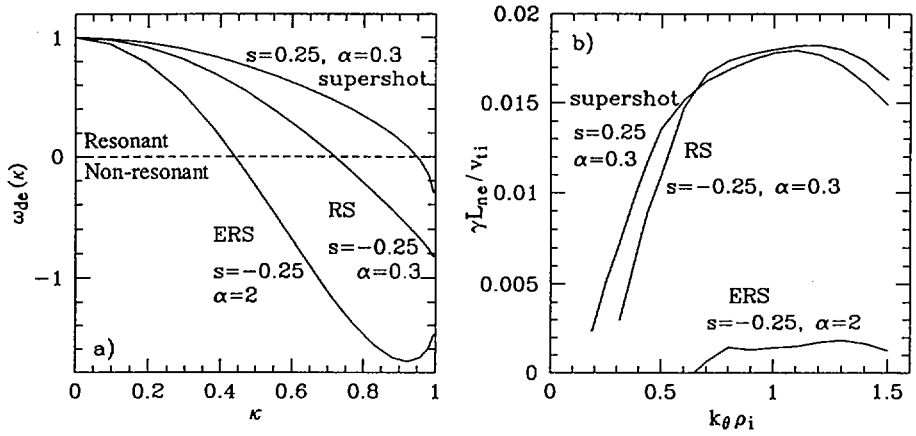

FIG. 2. (a) Trapped electron toroidal precession drift frequency versus pitch angle κ for supershot, RS, and ERS values of ŝ and α. (b) Linear growth rates for the same parameters, showing that the longest wavelengths are stabilized in ERS, but a high-k TEM is still weakly unstable.

and the direct effects of changes with time of the density and temperature profiles were found to be more important than those of changes in the q-profile. The effects of sheared toroidal rotation can be substantially stabilizing.

A gyrofluid code with bounce averaged trapped electron dynamics [15] has been bench-marked with the aforementioned comprehensive kinetic code in the linear regime[14, 16]. The Reversed Shear (RS) regimes begin with peaked density profiles similar to supershots, but with reversed magnetic shear in the core. RS regimes often suddenly transition to ERS regimes characterized by extremely small particle and ion thermal transport and fluctuation levels. We find that the fluctuation character in the core of both RS/ERS regimes is mainly TEM-like. The ITG mode is weaker due to the combination of density peaking (lower η_i) and large T_i/T_e. In the core of RS regime discharges (before the transition to ERS), our simulations predict fluxes in rough agreement with power balance calculations from TRANSP, including the fact that the ion heat transport driven by the TEM is convection dominated.

In the ERS regime, transport is further reduced by stabilization of TEM. Based on the present calculation which includes the pitch angle dependence of the toroidal precession drifts, the dominant stabilizing effect is the reversal of the precession drifts of the barely trapped electrons, so that the resonances which drive the collisionless TEM are eliminated. Two effects are primarily responsible for this drift reversal: 1) the Shafranov shift and 2) negative magnetic shear. The relative importance of these two effects is demonstrated in Fig. 2, which shows the normalized precession frequency and growth rates corresponding to supershot, RS and ERS values of s and α. For typical TFTR ERS parameters, the Shafranov shift is actually more important [17] than negative central

shear, since the core of these plasmas is well into the ballooning second stable regime. Across the transition from the RS regime to the ERS regime, the long wavelength trapped electron modes are stabilized, although a shorter wavelength TEM remains unstable after the transition. Our nonlinear gyrofluid simulations find that the transport after the transition is reduced by a factor of 40. This is in rough agreement with experiment, but underestimates the electron heat transport.

5. Roles of E × B Shear and Shafranov Shift in ERS Transition

Although $\mathbf{E} \times \mathbf{B}$ flow shear has not been included in the gyrofluid calculations yet, its effect is estimated by comparing the shearing rate ω_E in Eq. (3) calculated from the experimentally measured profiles [4], to the maximum linear growth rate γ calculated from the gyrofluid code. While using the decorrelation rate $\Delta\omega_T$ of the nonlinearly saturated turbulence would be more appropriate according to two-point nonlinear theories[9, 8], this quantity is not usually measured in either experiments or nonlinear simulations. Use of the linear growth rate instead has been shown to be an adequate approximation in the gyrofluid simulation of ITG turbulence[18], for example. Fig. 3 shows the time evolution of both ω_E and γ for TFTR ERS plasmas. On the average, the measured ω_E increases while γ decreases with time. After the transition, $\omega_E > \gamma$ demonstrating that both the $\mathbf{E} \times \mathbf{B}$ flow and the linearly stabilizing influence of the Shafranov shift are playing roles in the ERS transition. TFTR ERS data show that fluctuations are small in the region where ω_E exceeds γ[3]. Compared to the values calculated in the RS regime, the increase of ω_E is more visible than the change in γ[14], indicating a more universal role of $\mathbf{E} \times \mathbf{B}$ flow shear.

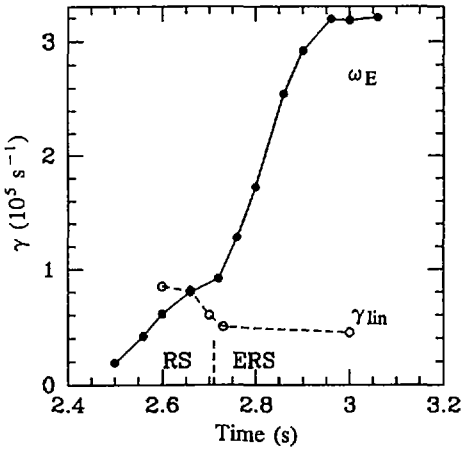

FIG. 3. Measured shearing rate ω_E compared with linear growth rate from gyrofluid calculations for #84011 at $r = 0.25a$. The measured $E \times B$ shearing rate is larger than γ after the transition, demonstrating that $E \times B$ shear is probably playing a role.

Separating these two effects is not easy for plasmas with balanced neutral beam injection, since higher ∇P_i not only increases the Shafranov shift, but is also a main contributor to E_r. Moreover, the Shafranov shift can further increase ω_E at the larger major radius side where the ambient turbulence is stronger before the transition. For a simple circular-shape analytical model equilibrium, the θ-dependent form factor in Eq. (3) can be written as,

$$(RB_\theta)^2/B \propto (1 + (r/R_0)cos\theta)(1 - \Delta' cos\theta)^{-2}, \quad (4)$$

where $\Delta' > 0$ is the Shafranov shift parameter. This in-out asymmetry of ω_E[8] due to Shafranov shift has interesting implications on the scalings of theoretically derived power threshold of ERS transition [19]. Furthermore, higher triangularity and elongation can also enhance ω_E locally, and contribute to the confinement improvements.

Based on the present calculations, a viable explanation for the bifurcation into the ERS regime could come from the following positive feedback mechanism: Steeper pressure gradients lead to larger $\mathbf{E} \times \mathbf{B}$ flow shear[19] and a larger Shafranov shift[17]. Both effects suppress microturbulence and fluctuation induced transport, which in turn lead to even steeper pressure gradients. Reversed (or weak) magnetic shear is beneficial: (i) in reducing the curvature drive of microinstabilities[20]; and (ii) in enhancing ω_E in toroidal geometry and larger Shafranov shift through the small value of B_θ in the core.

The $\mathbf{E} \times \mathbf{B}$ flow shear driven bifurcation scenario as well as the global dynamics of the radial structure of the transport barrier have been estimated in Ref. [19]. This global analysis has been complemented by our simultaneous work which has focused on providing an accurate local calculation of this mechanism. Specifically, we have demonstrated that the measured ω_E is of comparable magnitude to γ calculated from the experimental profiles and exceeds it after the transition to ERS. We note that the transport bifurcation caused by the pressure gradient driven E_r shear at the plasma edge has been proposed as an L to H transition mechanism in Ref. [21].

The TFTR team has also recently studied the relaxation of core transport barriers in ERS plasmas by varying $\mathbf{E} \times \mathbf{B}$ flow shear using NBI at constant power, but for different applied torques. Results indicate that the $\mathbf{E} \times \mathbf{B}$ flow shear plays a more fundamental role in maintaining the enhanced confinement than Shafranov-shift-induced reduction of transport[4].

6. Neoclassical Transport in ERS Plasmas

In the ERS regime, the ion poloidal gyroradius can in fact be larger than the local minor radius and comparable to the pressure gradient scale length, violating the assumption of standard neoclassical theory. Important properties which need to be taken into account in an appropriate theoretical model include: (a) the ion banana width is nearly constant close to the magnetic axis and (b) counter-moving ions have a minimum trapped fraction and all co-moving ions

are poloidally trapped. We present a revised neoclassical analysis and gyrokinetic particle simulation results[22] which show agreement with key confinement trends observed in ERS plasmas. In the usual neoclassical picture, outward ion heat conductivity results from energy flux imbalance between the inward moving slow (lower energy) particles and the outward moving fast (higher energy) particles. When the finite orbit width is taken into account, the outward ion heat conductivity is significantly reduced because this modification is much stronger for the fast particles (i.e., net energy outflow reduced). Therefore, the ion heat conductivity χ_i decreases for smaller minor radii where orbit effects are strongest.

In the limit of small banana width, $\triangle_b \ll r$, standard analysis yields trapped fraction $f_t = \sqrt{2\epsilon}$, and banana width $\triangle_b = \sqrt{8}\rho q/\epsilon^{1/2}$. Now consider the critical region, $\triangle_b \sim r$. For small values of r, it is possible for the guiding center to pass through the magnetic axis at a local minor radius. Then, the banana width is equal to this local minor radius, i.e., it becomes the maximum banana width of the system, $\triangle_{max} = (1+\sqrt{5})(q^2\rho^2 R_0/2)^{1/3}$. Secondly, near the magnetic axis, all co-moving particles ($v_{||} > 0$) are poloidally trapped because the guiding center drift velocity is larger than the poloidal component of the parallel velocity. The counter-moving particle ($v_{||} < 0$) has a minimum velocity space pitch angle at the trapped-passing boundary with the minimum trapped fraction $f_{min} = (2q\rho/R_0)^{1/3}$. It is clear that at minor radius $\triangle_{max}$, the orbit topology begins to deviate from the usual neoclassical picture. For $r < \triangle_{max}$, the banana width and trapped fraction are roughly constant and independent of local ϵ.

The diffusion of trapped particles (banana transport) in the banana regime can be estimated using the standard random walk approximation, i.e., $Q = \alpha \int_0^\infty f_t \frac{\Delta^2}{\tau_{\rm eff}} \frac{\partial f}{\partial r} \frac{mv^2}{2} 4\pi v^2 dv$, where f is the ion guiding center distribution function, $\triangle$ is the random walk step size and $\tau_{eff} = f_t^2/\nu$ is the effective collision time with ν being the ion collision frequency, and α is a constant which normalizes Q to the standard neoclassical banana transport value calculated in the limit of small banana width. Since the temperature gradient scale length (L_T) in ERS plasmas is much larger than the actual ion orbit width, a local Maxwellian distribution can be assumed. The velocity space integral can be separated into two parts. Low energy particles have the conventional step size and trapped fraction, while high energy particles have constant step size, $\triangle = q\rho/\sqrt{\triangle_{max}/R_0}$, and trapped fraction, $f_t = \sqrt{\triangle_{max}/R_0}$. Then the ion conductive thermal transport yields the finite-orbit-modified neoclassical ion heat conductivity,

$$\chi_i^{ba} = \chi_i^{neo}[1 - e^{-x_0}(x_0 + 1)], \tag{5}$$

where $\chi_i^{neo} = 0.66\epsilon^{-3/2}q^2\rho_i^2/\tau_i$ is the standard neoclassical ion heat conductivity[23], $x_0 \equiv (r/r_0)^3$, $r_0 \equiv \triangle_{max}(v = v_{th}) = (1+\sqrt{5})(q^2\rho_i^2 R_0/2)^{1/3}$, and $\rho_i = v_{th}/\Omega$, $v_{th} = \sqrt{2T/m}$. In terms of typical TFTR ERS plasma parameters, $r_0 \sim 20cm$. This result was obtained with a Lorentz collision model of the form, $C = \nu(v)\hat{\mathbf{L}}$, where $\hat{\mathbf{L}}$ is the pitch angle scattering operator, and

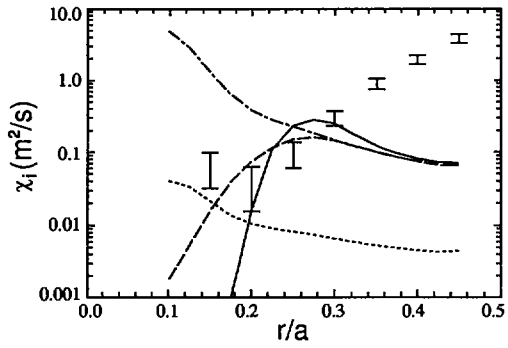

FIG. 4. Comparison of theoretical estimates of χ_i with experimental data. The solid line represents results of numerical solutions to the random walk model, the dashed line represents analytic results, the dotted-dashed line represents the usual neoclassical results, and the dotted line represents the Pfirsch-Schlüter transport. Representative TFTR ERS experimental results are shown with error bars.

$\nu(v) = 3\sqrt{2\pi}/(4\tau_i)(v_{th}/v)^3$. It is also of interest to note here that negative magnetic shear has a favorable effect on the orbit topology. Specifically, if $q \sim r^{-n}$, then $\Delta_{max} \sim \varepsilon^{1/(2n+3)}$. The contribution from the high energy particles to the integral decreases when the dependence of the maximum banana width on energy is weaker. Therefore, the negative magnetic shear helps to reduce the neoclassical ion heat conductivity in the core region.

Comparisons of the theoretical χ_i vs. representative TFTR ERS results are shown in Fig. 4. In contrast to the usual neoclassical values which strongly increase with decreasing minor radius, the finite orbit width analytic results from Eq. (5) indicate a decreasing trend. This is in reasonable agreement with the TFTR ERS results. Note also that the experimental trend begins to track the Pfirsch-Schluter level when χ_i^{ba} properly becomes negligibly small at smaller plasma radii.

In order to validate the results from the random walk analysis, fully toroidal particle simulations using the gyrokinetic neoclassical code (GNC) [24] have been carried out. We use a noise-reduction δf scheme. The nonlinear gyrokinetic delta-f formalism allows a rigorous treatment of both finite ion orbit width dynamics and a Fokker-Planck collision operator conserving momentum and energy. In the simulations, the guiding center distribution function is calculated by integrating the exact marker particle trajectories. The energy flux is calculated by the standard procedure of multiplying each particle energy by its radial drift velocity. The simulation results support the trends from the random walk analysis and indicate that the ion heat conductivity decreases to roughly the Pfirsch-Schluter level in the ERS core regime. Moreover, if the key full ion orbit width dynamics are suppressed, the simulations recover the standard neoclassical results.

Acknowledgments

This paper has benefited from many discussions with our experimental colleagues. We would particularly like to thank Mike Zarnstorff, Ernesto Mazzucato, Ed Synakowski, and the TFTR team, and Keith Burrell and the DIII-D team. This work was supported by the U.S. Department of Energy Contract No. DE–AC02–76–CHO-3073.

REFERENCES

[1] LEVINTON, F.M., et al., Phys. Rev. Lett. **75** (1995) 4417.
[2] STRAIT, E.J., et al., Phys. Rev. Lett. **75** (1995) 4421.
[3] MAZZUCATO, E., et al., Phys. Rev. Lett. **77** (1996) 3145.
[4] SYNAKOWSKI, E.J., et al., The roles of electric field shear and Shafranov shift in sustaining high confinement in enhanced reversed shear plasmas on the TFTR tokamak (in preparation).
[5] LAO, L.L., et al., Phys. Plasmas **3** (1996) 1951.
[6] HAHM, T.S., Phys. Plasmas **3** (1996) 4658.
[7] BURRELL, K.H., et al., in Plasma Physics and Controlled Nuclear Fusion Research 1994 (Proc. 15th Int. Conf. Seville, 1994), Vol. 1, IAEA, Vienna (1995) 221.
[8] HAHM, T.S., BURRELL, K.H., Phys. Plasmas **2** (1995) 1648.
[9] BIGLARI, H., et al., Phys. Fluids B **2** (1990) 1;
SHAING, K.C., et al., Phys. Fluids B **2** (1990) 1492;
HAHM, T.S., Phys. Plasmas **1** (1994) 2940.
[10] PARKER, S.E., et al., Phys. Plasmas **3** (1996) 1959.
[11] ARTUN, M., TANG, W.M., Phys. Plasmas **1** (1994) 2682.
[12] HAHM, T.S., Phys. Fluids **31** (1988) 2670.
[13] MYNICK, H.E., PARKER, S.E., in Proc. Int. Sherwood Fusion Theory Conf. Philadelphia, 1996, paper 2C-24.
[14] REWOLDT, G., TANG, W.M., HASTIE, R.J., Phys. Fluids **30** (1987) 807.
[15] BEER, M.A., HAMMETT, G.W., Phys. Plasmas **3** (1996) 4018.
[16] KOTSCHENREUTHER, M., REWOLDT, G., TANG, W.M., Comput. Phys. Commun. **88** (1995) 128.
[17] BEER, M.A., HAMMETT, G.W., Bull. Am. Phys. Soc. **40** (1995) 1733.
[18] WALTZ, R.E., KERBEL, G.D., MILOVICH, J., Phys. Plasmas **1** (1994) 2229.
[19] DIAMOND, P.H., et al., On the dynamics of transition to enhanced confinement in reversed magnetic shear discharges (in preparation).
[20] KESSEL, C., et al., Phys. Rev. Lett. **72** (1994) 1212.
[21] HINTON, F.L., STAEBLER, G.M., Phys. Fluids B **5** (1993) 1281.
[22] LIN, Z., TANG, W.M., LEE, W.W., Phys. Rev. Lett. **78** (1997) 456.
[23] HINTON, F.L., HAZELTINE, R.D., Rev. Mod. Phys. **48** (1976) 239;
HIRSHMAN, S.P., SIGMAR, D.J., Nucl. Fusion **21** (1981) 1079.
[24] LIN, Z., TANG, W.M., LEE, W.W., Phys. Plasmas **2** (1995) 2975.

DISCUSSION

E.J. DOYLE: Experimental observations on DIII-D show that the transport barrier forms at different radial locations for different quantities such as density and temperature. On TFTR it is observed that the transport bifurcation can occur at different times for different quantities. Are these observations consistent with theory?

T.S. HAHM: Our work as presented in this paper has focused on a local test of the $\mathbf{E} \times \mathbf{B}$ shear suppression mechanism. We will address the question (i) by including electron dynamics in our global non-linear gyrokinetic simulations, and (ii) by including the $\mathbf{E} \times \mathbf{B}$ shear effect in our multifield non-linear gyrofluid simulations. Paper IAEA-CN-64/D1-3 may answer some of your questions.

A. BERS: Do your theory and computations account for bootstrap current, in particular in your comparison with data from TFTR? How does your theory/computation distinguish between bootstrap and Shafranov shift effects on transport barrier formation?

T.S. HAHM: Our $\mathbf{E} \times \mathbf{B}$ shearing rate, which contains an explicit dependence on B_θ (HAHM, T.S., BURRELL, K.H., Phys. Plasmas **2** (1995) 1648), has been evaluated using the experimentally measured profiles. Therefore the effect of bootstrap current is included, although we have concentrated on the effect of the Shafranov shift and have not explicitly analysed the effect of the bootstrap current in detail.

F.W. PERKINS: Most of your comparisons with data involve experiments with a high T_i/T_e ratio. Can one expect $\mathbf{E} \times \mathbf{B}$ shear to improve confinement in plasmas with $T_e = T_i$?

T.S. HAHM: The $\mathbf{E} \times \mathbf{B}$ shear suppression mechanism will still work for $T_e \approx T_i$. However, the hot ion mode ($T_i > T_e$) provides a favourable condition for this mechanism, at least in the ion pressure gradient driven $\mathbf{E} \times \mathbf{B}$ shear case, which we have investigated in collaborative work presented in paper IAEA-CN-64/D1-3. A high temperature ratio ($T_i/T_e > 1$) enhances the ∇P_i driven $\mathbf{E} \times \mathbf{B}$ shearing rate and reduces the fluctuation level driven by the trapped electron η_i mode.

F.X. SÖLDNER: From a synergistic action of magnetic shear reversal and $\mathbf{E} \times \mathbf{B}$ flow shear one would expect a reduction of the threshold power for internal transport barrier formation with increasing negative magnetic shear. Can you make any quantitative prediction with your model?

T.S. HAHM: In our model, the $\mathbf{E} \times \mathbf{B}$ shear plays a more fundamental role in suppressing turbulence and leads to a power threshold prediction which is presented in paper IAEA-CN-64/D1-3. Although reversed magnetic shear is beneficial (i) in enhancing the $\mathbf{E} \times \mathbf{B}$ shearing rate in general geometry and the Shafranov shift through the small value of B_θ in the core, and (ii) in reducing the curvature drive of microinstabilities, the magnetic shear dependence of the power threshold cannot be written in a simple form. Magnetic shear reversal is not sufficient for transition to the enhanced confinement regime.

DEVELOPMENTS IN THE THEORY OF CORE AND EDGE PLASMA TRANSPORT BARRIER DYNAMICS AND CONTROL

V.B. LEBEDEV, P.H. DIAMOND,
M.B. ISICHENKO, P.N. YUSHMANOV
University of California,
San Diego, California,
United States of America

D.E. NEWMAN, B.A. CARRERAS,
V.E. LYNCH
Fusion Energy Division,
Oak Ridge National Laboratory,
Oak Ridge, Tennessee,
United States of America

T.S. HAHM, W.M. TANG, G. REWOLDT
Plasma Physics Laboratory,
Princeton University,
Princeton, New Jersey,
United States of America

K. AVINASH
Institute for Plasma Research,
Bhat, Gandhinagar, India

A. SMOLYAKOV
University of Saskatchewan,
Saskatoon, Saskatchewan,
Canada

Abstract

DEVELOPMENTS IN THE THEORY OF CORE AND EDGE PLASMA TRANSPORT BARRIER DYNAMICS AND CONTROL.

The paper discusses developments in the theory of core and edge transport barrier physics, focusing primarily on reversed shear core barriers (including enhanced reversed shear, negative central shear, weak negative shear and high-β_p internal barrier modes) and the L → H transition leading to the familiar H-mode edge transport barrier.

I. Introduction

Achieving understanding and control of turbulent transport is a necessary prerequisite for the design of an advanced tokamak fusion reactor. Significant progress toward enhanced performance has been made by exploiting the spontaneous transition to high confinement regimes, such as H-mode[1] or VH-mode[2] induced by increased radial electric field shear. Such E_r shear,[3] which is produced by the onset of sheared rotation and the steepening of the ion pressure profile, suppresses turbulence and transport,[4] thus initiating a self-reinforcing feedback[5] which results in a bifurcation to a state with significant local reduction of fluctuations and transport. In H-mode and VH-mode, the transport barrier is initiated at the plasma edge. Recently, core transport barriers discovered in JT-60U[6] and in reversed shear discharges in TFTR and DIII-D[7] have attracted significant attention on account of their remarkable confinement properties. This paper discusses recent progress in the theory of E_r-shear driven transport barriers and how this theory may be applied to the understanding of enhanced confinement modes with reversed shear. We also briefly review recent progress in the theory of edge transport barriers.

II. Enhanced Confinement with Reversed Shear

Recently, a new regime of enhanced core confinement has been discovered in discharges with reversed magnetic shear.[7] In such discharges, formed by intense auxiliary heating of prelude plasmas during current ramp-up, confinement is observed to increase dramatically when a critical power input level (more generally, a critical gradient steepness) is surpassed. Stored energy content builds rapidly, and a transport barrier forms at $r \gtrsim r_{\min}$, where $r_{\min}$ is the location of the minimum of $q(r)$. Typically, particle, ion thermal and momentum transport in the core of such ERS (enhanced reversed shear) and NCS (negative central shear) plasmas is reduced to levels below that of conventional neoclassical theory. This is consistent with the long standing predictions that negative magnetic shear will suppress geodesic curvature driven microinstabilities (such as the toroidal ion temperature gradient (ITG) driven mode, various trapped particle modes and high-n ballooning modes) and that peaked density profiles will quench ITG modes.[8,9] Nevertheless, the theoretical analysis linear stability studies including only magnetic geometry effects[10] *cannot* account for the confinement enhancement. The dual observations of active anomalous transport in (reversed shear) prelude discharges as well as the initiation of a clear bifurcation in particle, energy and momentum content (as evidenced by a discontinuity in the time derivative of local density, ion temperature and toroidal rotation velocity evolution) together suggest that *magnetic shear reversal is not the sole cause of the remarkable confinement improvements observed in ERS/NCS-mode plasmas*. This is consistent with kinetic stability analyses and the observation of internal transport barriers in weakly negative shear discharges, where geodesic curvature drive is not fully eliminated,[11] and in JT-60U, where shear reversal is uncertain. In particular, it appears that a second constituent plays a critical role in ERS/NCS dynamics. Indeed, given that the stabilizing effect of reversed shear is a 29-year old concept, and that the impact of the enhanced Shafranov shift[12] is a simple extension of a familiar concept from MHD stability, it is not too much of an exaggeration to state that the *real* mystery in ERS and NCS plasmas is the identity of this additional mechanism. Moreover, several additional questions then immediately emerge, such as:

i.) what determines transport barrier location, evolution and size?

ii.) what is the optimal prelude plasmas and what sets the transition threshold and the magnitude of the observed hysteresis?

iii.) how fast and how far does the transport bifurcation front propagate?

iv.) how can the high disruptivity of enhanced reversed shear confinement regimes be reduced?

A. Basic Transition Model

Here, we propose a simple model of ERS/NCS transition dynamics. The model consists of an electric field shear driven transport bifurcation[13] which develops in the radially inhomogeneous ambient transport environment characteristic of the prelude phase plasmas. The strong radial inhomogeneity is a consequence of the profiles of $q(r)$ produced by heating and the current ramp. The essential physics intrinsic to the model is a *local* transport bifurcation which occurs when a local profile gradient threshold (entering the determination of E_r') is exceeded. Magnetic shear reversal lowers the local threshold, thus facilitating transition and localizing the region of transport bifurcation and barrier formation to the region of shear reversal. The bifurcation front is predicted to propagate[14] outward in radius until it reaches a radius at which the power, particle or momentum input is insufficient to exceed the local threshold criterion. Note that within the scope of this model, the obvious question of why the *electric* field shear bifurcation is spatially pinned to the region of *magnetic* shear reversal is straightforwardly resolved, since (even weakly) negative shear significantly reduces geodesic curvature drive, thus lowering the *local* (electric field-shear-driven) bifurcation threshold. Thus, magnetic and electric field shear effects are synergistic in our model.

The basic ERS/NCS dynamics are manifested in a very simple two-field model which evolves local fluctuation intensity $\varepsilon(r,t) = \left\langle (\tilde{n}/n)^2 \right\rangle$ and local mean density gradient magnitude $N(r,t) = \left| 1/\langle n \rangle (d\langle n \rangle / dr) \right|$. Density gradient evolution is determined by the evolution of radially integrated mean density $\eta = \int_0^r dr' \langle n \rangle$. Thus, the basic equations are:

$$\frac{\partial \varepsilon}{\partial t} = \frac{\gamma_0((x-x_r)/\Delta_r) N \varepsilon}{1+\alpha_2(r)(V_E'/V_c')^2} - \alpha_1(r)\varepsilon^2, \tag{1a}$$

$$\frac{\partial}{\partial t}\eta = S(x/\Delta_d) - D_0 \varepsilon N - D_n N. \tag{1b}$$

Here $\gamma_0((x-x_r)/\Delta_r)N$ is the spatial profile of microinstability growth in the absence of electric field shear, Δ_r is the scale of variation in γ_0 about the geodesic curvature reversal radius x_r, V_E'/V_c' is the normalized electric field shearing rate, ($V_E'/V_c' \sim N^2$, from radial force balance), $S(x/\Delta_d)$ the integrated particle deposition profile $\left(S(x/\Delta_d) = 1/n \int_0^r dx' S_n(x') \right)$, $D_0\varepsilon$ is the turbulent diffusivity, and D_n is the neoclassical diffusivity. Note $x = r^2$ is understood. Also, $\alpha_1(r), \alpha_2(r)$ are model-dependent proportionality coefficients defined in Ref. (15). The spatial profiles of $\gamma_0((x-x_r)/\Delta_r)$ and $S_n(x/\Delta d)$ are shown in Figs. (1a, b).

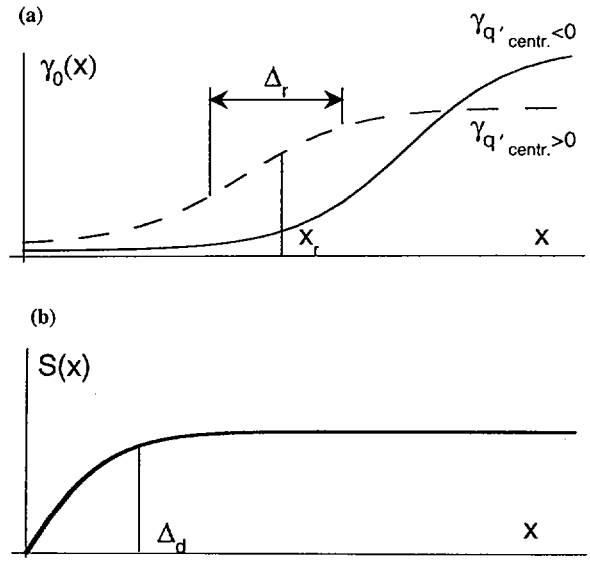

FIG. 1. Spatial profiles of (a) turbulence growth rate and (b) integrated deposition profile.

Note that γ_0 decreases over a scale Δ_r in the neighborhood of x_r, and thus Δ_r corresponds roughly to $(q''/q)^{-1/2}$, namely the characteristic width of shear variation. γ_0 is assumed small for $x < x_r$, corresponding to residual turbulence in the region of reversed shear. The profile of $S(x/\Delta_d)$ corresponds to an assumption of central deposition, with deposition profile width Δ_d.

The stationarity condition for this model is thus simply:

$$\left[1-\frac{D_n N(x)}{S(x/\Delta_d)}\right]=\left[\frac{D_0\gamma_0(x)N(x)^2/\alpha_1}{\left(1+\alpha_2\left(N(x)^2\right)^2\right)S(x/\Delta_d)}\right] \tag{2}$$

The solution of Eqn. (2) determines the stationary profile solution for $N(x)$ in terms of the radially varying integrated deposition profile $S(x/\Delta_d)$ and the magnetic shear variation induced profile of the ambient transport in the prelude phase. Note that $N(x)$ is determined *locally*, and exhibits a distinct prelude (i.e. local L-mode-like) root when $\alpha_2\left(N^2\right)^2 << 1$, namely $N(x) = \left[\alpha_1 S(x)/\left(D_0\gamma_0\right)\right]^{1/2}$, and a steepened gradient (i.e. H-mode-like) root when $\alpha_2\left(N^2\right)^2 >> 1$, namely $N(x) = S(x)/D_n$. In the latter case, the profile is determined by neoclassical transport alone. Here, the neoclassical transport coefficient is treated as constant, for simplicity and convenience. It is apparent from inspection that $N(x)$ will fall into the H-mode-like

state for $x < x_r$, where $\gamma_0((x - x_r)/\Delta_r)$ is small and the *local* "L $\rightarrow$ H" transition threshold is easily exceeded. For $x_r + \Delta_r$, $\gamma_0(x)$ increases rapidly, so the solution for $N(x)$ must revert to an L-mode-like value. Between these regions of asymptotic behavior, a transition region corresponding to the core transport barrier is located.

The non-trivial spatial structure of the stationary state profile is elucidated by considering the surface of constant transport flux Γ (here $\Gamma = D_0 \varepsilon N$) in the position and gradient space (x, N). This *flux landscape* is depicted in Fig. (2). Note that constant N slices of the flux landscape depict the familiar radial profiles of Γ and (implicitly) D, which increase with radius. Correspondingly, a constant - x slice of $\Gamma(x, N)$ traces an S-shaped bifurcation curve which describes the local gradient transition at each radial location. Two prominent features of the flux landscape are a steep ridge at modest values of N, which connects to a "hill" at large-x and modest N. These are hereafter termed the prelude phase ridge and hill, respectively. At large N, a second, topographically simpler slope appears at all values of x. The slope of this inclination, dubbed the H-mode beach, is set by D_{II}, as the large N up-slope corresponds to a neoclassical transport dominated state. The actual solution profile of $N(x)$ is determined by the intersection of the flux landscape with the deposition surface $S(x/\Delta_d)$, which is flat for $x > \Delta_d$, i.e. for radii beyond the deposition region.

The constant flux contours of the landscape illustrate the structure of the solution (intersection) contour. For $x << x_r$ and high input strength, the deposition surface lies above the prelude-ridge, and thus intersects the Γ contour on the high-N H-mode beach, a region of very steep gradient. As x approaches x_r, the deposition surface approaches the steeply sloped prelude phase hill, thus indicating a return to L-mode-like confinement properties. Note that in this model, the location and extent of the "transport barrier" are unambiguously defined and bounded by the positions of the catastrophe transitions between[16] the H-mode beach and the prelude phase ridge and hill. The transition from local H-mode-like to local L-mode-like occurs along the rise of the prelude hill from the prelude ridge. Thus, the spatial extent of the enhanced confinement region is set by the location and width of the deposition region relative to the location and width of the magnetic shear reversal region. In particular, optimum performance follows from "tuning" the deposition profile so that it falls within up-slope of the prelude phase hill, i.e. for $x_d + \Delta_d \leqq x_r - \Delta_r$. This suggestion is easily tested by comparing two cases of equal deposition strength (N, the particle deposition rate, in this simple model) but differing deposition profile

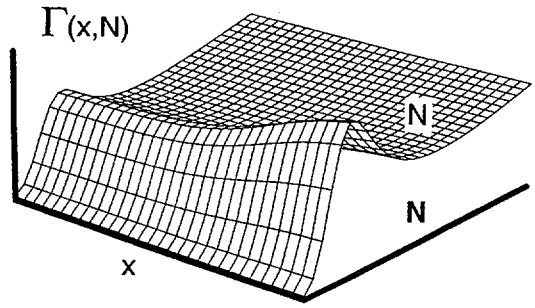

FIG. 2. Transport flux landscape, in position-gradient space.

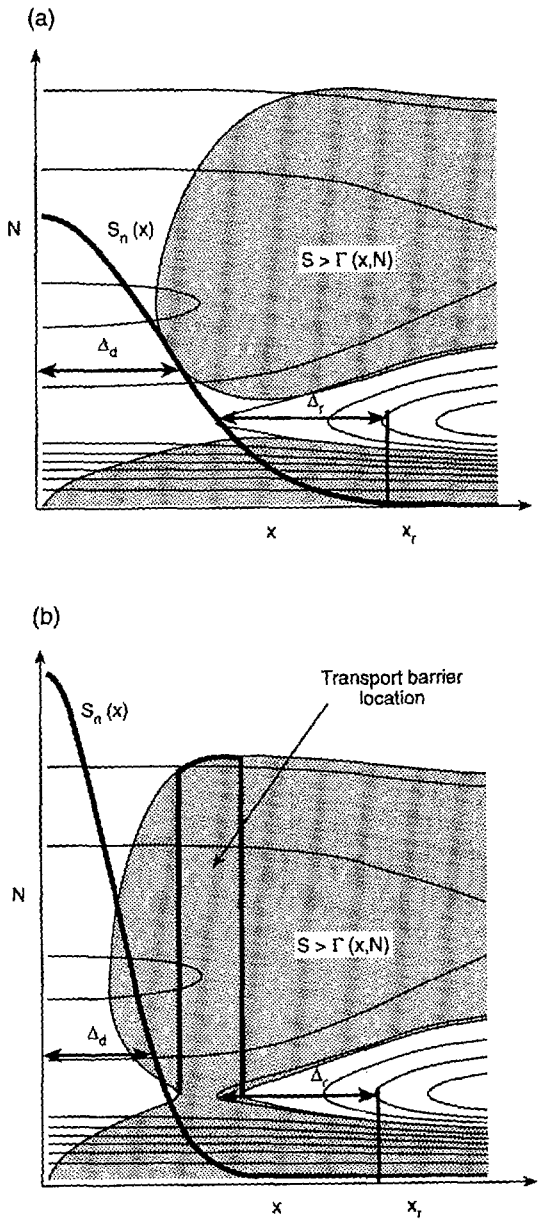

FIG. 3. (a) For broad deposition, the constant flux contours do not intersect, so no barrier forms. (b) For narrow deposition of equal strength, intersection occurs, indicative of barrier formation.

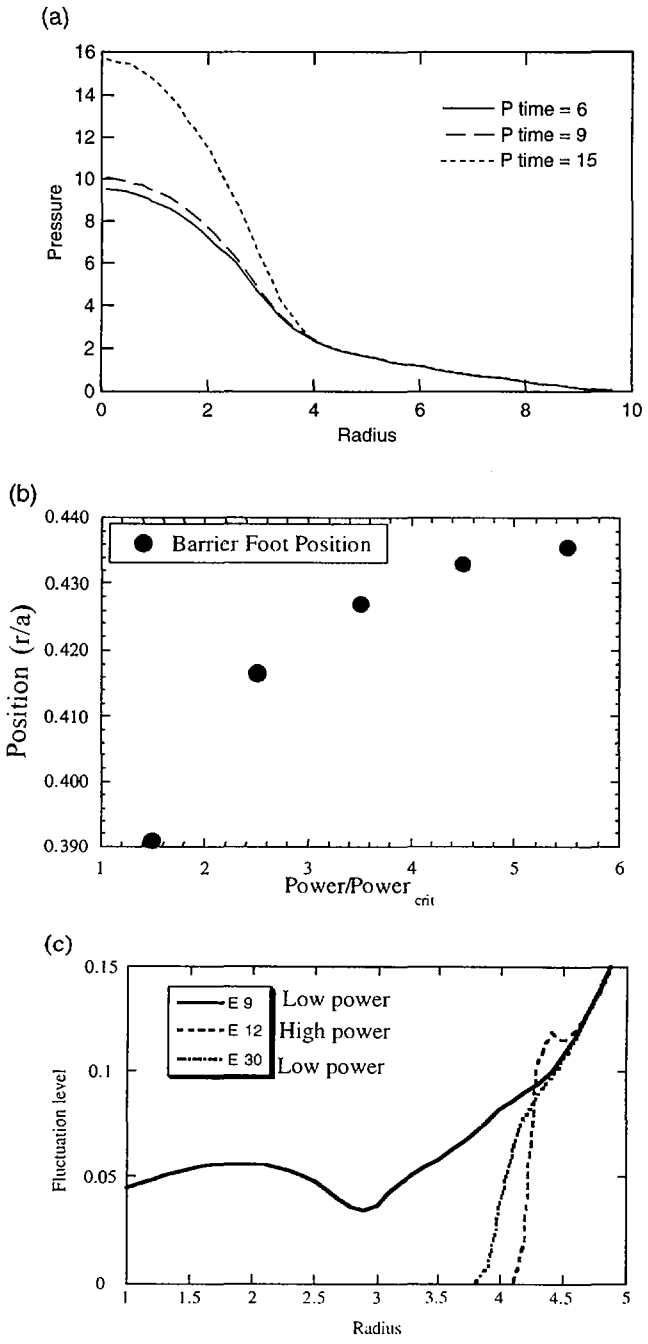

FIG. 4. (a) Pressure profiles during transition, showing profiles growing and moving outwards; (b) barrier foot position moving outwards with power; (c) fluctuation profiles when power is ramped up and then back down, showing hysteresis effect.

width. Relatively broad deposition results in intersection of the deposition surface with only the prelude phase ridge of the $\Gamma(x,N)$ surface, so that no confinement transition occurs (Fig. (3a)). By contrast, narrow deposition allows the solution contour to intersect a $\Gamma(x,N)$ contour which is double-valued in N. As a consequence, a bifurcation to the steep N root occurs for an interval of x, requiring the formation of a transport barrier (Fig. (3b)). These observations suggest that optimal enhanced confinement regimes may be achieved by combining large x_I, (as in weakly negative shear discharges) with peaked central deposition, as obtained with RF.

The dynamics of reversed shear discharge evolution may be studied using a simple extension of the model of Eqs. (1a, b), obtained by retaining radial transport to provide spatial coupling. The extended model equations are:

$$\frac{\partial \varepsilon}{\partial t} = \gamma_0(x) N\varepsilon - \alpha_1 \varepsilon^2 - \alpha_2 V_E'^2 \varepsilon + \frac{\partial}{\partial x}\left(D_0 \varepsilon \frac{\partial \varepsilon}{\partial x} \right), \tag{3a}$$

$$\frac{\partial N}{\partial t} = S - D_n N - \frac{\partial}{\partial x}\left(D_0 \varepsilon \frac{\partial N}{\partial x} \right). \tag{3b}$$

Here, the notation is that of Ref. (14). Straightforward solution of the model equations (3a, b) are shown in Figs. (4a, b, c). In Fig. (4a), density profile evolution in time is shown. Note that both the radially integrated particle content and the radial position of the steep gradient increase with time. The ultimate location of the transport barrier is clearly localized to the vicinity of the magnetic shear reversal region. The temporal evolution of N at various radii during a power ramp is shown in Fig. (4b). A radially local discontinuity in dN/dt clearly occurs at progressively increasing radii, thus indicating a *local* gradient transition which propagates outward in radius as the power input rate is increased. The ultimate location of the transition front is determined by the input strength and the slope of the prelude phase hill of the

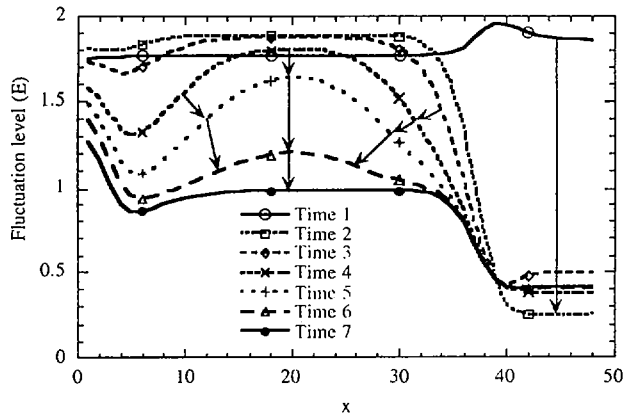

FIG. 5. Fluctuation profiles with V_ϕ in the core adding to the pressure gradient component of the sheared radial electric field and triggering an internal transition as well as the edge transition.

$\Gamma(x,N)$ surface. The precise barrier foot-point location may be obtained from a generalized Maxwell construction, which is discussed in Section (IIc.). Similarly, if the power level is decreased slightly, the profile unpeels like an onion, from the outside in. This is illustrated in Fig. (4c) which shows the time evolution of the fluctuation intensity profile. Fig. (4c) also suggests that the bifurcation manifests a local hysteresis, in that fluctuations reappear locally in a small region at the edge of the good confinement zone when input is abruptly lowered. The magnitude of the predicted local hysteresis ratio (determined for the case of a cubic polynomial S-curve model) is given by $P_{back}/P_{fwd} \cong \left(16 D_{neo}(r)/D_L(r)\right)^{1/2}$ where P_{back} and P_{fwd} refer to the back and forward transition power thresholds and $D_{neo}(r)$, $D_L(r)$ are the local values of the neoclassical and L-mode (prelude) diffusivities).

The one field model presented here is clearly oversimplified, in that it approximates E_r feedback via N only. A more complete model should, of course, evolve *all* fields which enter the $E \times B$ shearing rate, namely $\langle T_i \rangle'$, $\langle \mathrm{V}_\phi \rangle'$, $\langle \mathrm{V}_\theta \rangle'$ and $B_\theta(r)$, and should allow feedback of all of these on V_E'. While the comprehensive model remains incomplete, we have recently extended the simple model of Eqns. (3a, b) to include V_ϕ and T_i. Several interesting phenomena appear in this expanded model, namely:

a.) both inward and outward propagation of the transition front are possible, depending on the orientation of the torque (i.e. V_ϕ drive) relative to ∇P (see Fig. (5)).

b.) just above the transition threshold, quasi-periodic oscillations appear in ion temperature and density. Similar behavior has been observed in TFTR.[17]

c.) the transition may be triggered via increase in heating power (changing T_i'), density peaking, as occurs in pellet injection (for n'), NBI torque (for V_ϕ') or by manipulation of the q profile. The latter process impacts both the shearing rate (via B_θ^{-1}), and the prelude turbulence profile (via γ_0).

It should also be mentioned that ERS-like transitions observed in electron heated plasmas may be explained via:

a.) density peaking, with simultaneous strong electron-ion collisional coupling (i.e. ∇P_i).

b.) strong shear in the electron diamagnetic frequency and precession drift (induced by heating profile control) which can also suppress turbulence via the BDT mechanism.

B. Local Threshold Scaling

The major quantitative question pertinent to describing the ERS/NCS transition is that of the profile threshold required to trigger the bifurcation. In this simple model, the electric field shear is determined primarily by the density gradient, so the relevant threshold parameter is $\dot{N}$, the particle input. In toroidal geometry,[18] the $E \times B$ shear suppression criterion is $\omega_s = \left(\Delta\psi_0/\Delta\phi\right) \partial/\partial\psi \left[\left(cE_r/RB_\theta\right)\right] > \Delta\omega_k^-$, where ψ is the flux coordinate and $\Delta\omega_k^-$ is the turbulent

decorrelation rate. Here, $\Delta\phi$ is the toroidal correlation angle, $\Delta\psi_0 = RB_\theta \Delta r_0$, where Δr_0 is the radial correlation length of the turbulence. Using radial force balance (assuming ∇n controls E_r') and particle balance with the assumption of gyro-Bohm particle diffusion then yields the threshold criterion

$$\frac{\dot{N}(\psi)}{A(\psi)} \geq \langle n \rangle \left(\rho_s^2 c_s / \Delta r_0^2\right) \frac{\left\langle (RB_\theta)^3 f(\theta) \right\rangle}{\langle RB_\theta \rangle \langle RB_\theta \rangle^2} \left(\frac{T_e}{T_i}\right)^2 \left(\frac{\Delta\omega}{\omega_{*_e}}\right)_{\underline{k}}^2 . \tag{4}$$

Here $A(\psi)$ is the surface area defined by ψ. The factor $(RB_\theta)^{-2}$ indicates an in-out asymmetry of the transition threshold which is more strongly favorable with increasing Shafranov shift and the $(T_e/T_i)^2$ factor arises from the presumption of collisionless trapped electron modes (CTEM) as the ambient turbulence of the prelude discharge. $f(\theta)$ is a dimensionless poloidal profile factor of order unity and $\dot{N}$ is understood to correspond to input within ψ for monotonically decreasing particle deposition. The most interesting features of Eqn. (4) are its prediction of favorable dependence of $\dot{N}$ on T_i (via $(T_e/T_i)^2$), and strong in-out asymmetry (i.e. lower threshold for larger Shafranov shift). Taking $\Delta\omega_{\underline{k}} \sim \gamma_{\underline{k}}$ and noting that the growth rate for CTEM scales as $\exp[-R/L_n]$ reveals that $\dot{N}/A(\psi)$ decreases with increasing target density profile peakedness. In particular, transition appears easiest in hot ion, high β_ρ discharges with low B_θ, low current and low density. Thus, hot ion mode plasmas such as super-shots appear to be optimal prelude discharges. Indeed, for parameters typical of TFTR reversed shear discharges (i.e. $B_T = 4.7T$, $R = 250cm$, $a = 82cm$ and $r_d = .2a$), a power threshold of $P_{crit} = 15MW$ is predicted, in good agreement with experimental results. In this case (which assumed drift wave turbulence in the prelude plasma) the shear reversal radius was predicted to fall at $r = .35a$, with $T_i(0) = 24keV$ and $n(0) = 5x10^{14} cm^{-3}$. These values are also in good agreement with experiment. Note also that the transition criterion appears naturally as an input-per-area threshold for local transition, assuming central fueling. We emphasize again that, in general, the threshold condition is not only one of power, but rather one of *whatever* gradient controls V_E' and γ_0'. In particular, transitions may be included by fueling (pellet injection), inducing velocity shear, or manipulating the q and B_θ profiles.

C. Theory of Transport Barrier Dynamics

The goal of core transport barrier control (to minimize disruptivity and facilitate the removal of impurities, ash, etc.) has naturally stimulated interest in transport barrier *dynamics* - namely, the spatio-temporal response function characteristic of the barrier. As this is a new problem, a simple theoretical paradigm is of great utility for gleaning understanding. Here, we briefly summarize progress on such a paradigm.

The simplest possible problem is to consider a one field slab-like system with on axis deposition at $x = 0$ and boundary condition $n(a) = 0$, with neoclassical transport D_{neo} for $n' > n'_{crit}$ (i.e. $x < \ell$) and turbulent transport D_a for $n' < n'_{crit}$ (i.e. $x > \ell$). The problem then reduces to determining $\ell(t)$ for a

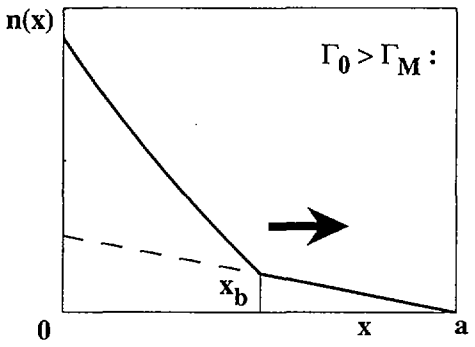

FIG. 6. Composite solution with the front at $x_b(t)$ propagating radially outwards for $\Gamma_0 > \Gamma_{crit}$.

given core flux Γ_0. The solution is described in Ref. (19) and shown in Fig. (6). The stationary barrier position ℓ is determined by the generalized Maxwell construction:

$$\Gamma(n')n' \Big|_{\ell_-}^{\ell_+} = \int_{n'(\ell_-)}^{n'(\ell_+)} \Gamma(n')dn' \tag{5a}$$

where $\Gamma(n')$ is the nonlinear, bi-stable, gradient - driven flux (with S-curve like functional form). Using Eqn. (5a) and straightforwardly obtained matching criteria, it is possible to derive an expression for the time evolution of $\ell(t)$ when $\Gamma_0 \geq \Gamma_{crit}$. Ref. (19) gives the result, which is:

$$\ell(t) \sim \left(\frac{\Gamma_0 - \Gamma_{crit}}{\Gamma_{crit}}\right)^{1/2} (D_{neo}t)^{1/2}. \tag{5b}$$

Here, Γ_{crit} is the critical flux for barrier stationarity at ℓ as given by Eqn. (5a). Note that the barrier-foot moves *diffusively* at the *slow neoclassical* rate. This is a consequence of the fact that information can be "communicated" from the deposition region $(x = 0)$ to the foot-point only at the neoclassical rate, since turbulent transport is suppressed for $x < \ell$! Note also that $\ell(t)$ scales with $\left[(P - P_{crit})/P_{crit}\right]^{1/2}$.

This result, albeit simple, has interesting implications for the control of core transport barriers. In particular, it suggests that significant steepening of the core gradient (to the point where MHD stability constraints are approached or are violated) is unavoidable in core barrier regimes unless the outward propagation of the barrier footpoint can be accelerated! This suggests that an external torque applied in the vicinity of $x = \ell$ for expected power levels, could be very useful in increasing $\ell(t)$, thereby broadening the profile and lowering the pressure gradient. Such a means for profile control is superior to the already familiar tactic of externally

triggering an L→H transition, since the latter method foregoes the virtues of a turbulent edge. Given the past successes with IBW transport control on PBX-M,[20] RF-wave torque[21] is thus suggested as a natural candidate for controlling and broadening core transport barriers and thereby *reducing the disruptivity* of ERS and NCS plasmas.

III. Review of Recent Progress in Edge Transport Barrier Physics

Due to length limitations, discussion of recent developments in edge transport barriers is limited to a survey of recent published literature by the authors, to which the interested reader is directed. The phase transition model of the L→H transition, which was originally presented in Refs. (22) and (23) has been extended to encompass the effects of finite turbulence correlation times,[24] external torque,[25] dynamical magnetic pumping[26] and the effect of neutrals.[27] Finite turbulence correlation time introduces the dynamics of electric field shear effects on the transport phase shift,[24] which is essential to quantitative modeling of the L→H transition evolution. External torques[25] tend to "smooth out" the transition bifurcation, and may totally suppress the turbulence. This topic is of great interest in the context of active transport control. The damping rate of low but finite frequency poloidal flows is calculated in Ref. (26). An interesting feature of this work is the prediction that finite-ω flows may be weakly damped in comparison to $\omega = 0$ flows. Finally, Ref. (27) generalizes the phase transition model to include the effects of neutrals. The quantitative impact of finite neutral density on the predicted power threshold is explored there.

Acknowledgments

We thank Keith Burrell and the DIII-D team, and Mike Zarnstorff, Ed Synakowski and the TFTR team for many useful discussions. This research was supported by the U.S. Department of Energy and by the governments of Canada and India.

REFERENCES

[1] WAGNER, F., et al., Phys. Rev. Lett. **49** (1982) 1408.
[2] JACKSON, G.L., et al., Phys. Rev. Lett. **67** (1991) 3098.
[3] ITOH, S.I., ITOH, K., J. Phys. Soc. Jpn. **59** (1990) 3815.
[4] BIGLARI, H., DIAMOND, P.H., TERRY, P.W., Phys. Fluids B **2** (1989) 1.
[5] DIAMOND, P.H., et al., in Plasma Physics and Controlled Nuclear Fusion Research 1994 (Proc. 15th Int. Conf. Seville, 1994), Vol. 3, IAEA, Vienna (1995) 323.
[6] KOIDE, Y., et al., ibid., Vol. 1, p. 199.
[7] LEVINTON, F.M., et al., Phys. Rev. Lett. **75** (1995) 4417;
STRAIT, E.J., et al., Phys. Rev. Lett. **75** (1995) 4421.
[8] KADOMTSEV, B.B., POGUTSE, O.P., Sov. Phys. — JETP **24** (1967) 1172.
[9] KESSEL, C., et al., Phys. Rev. Lett. **72** (1994) 1212.
[10] LAO, L., et al., Phys. Plasmas **3** (1996) 1951.
[11] STRAIT, E.J., et al., Phys. Rev. Lett. **75** (1995) 4421.
[12] BEER, M.A., in Controlled Fusion and Plasma Physics (Proc. 22nd Eur. Conf. Bournemouth, 1995), Vol. 19C, European Physical Society, Geneva (1995).
[13] STAEBLER, G.M., et al., Phys. Plasmas **1** (1994) 909.
[14] DIAMOND, P.H., et al., Phys. Plasmas **2** (1995) 3685.

[15] DIAMOND, P.H., et al., Phys. Rev. Lett. **72** (1994) 2565.
[16] ARNOL'D, V.I., Catastrophe Theory, Springer-Verlag, Heidelberg (1984).
[17] MAZZUCATO, E., et al., Phys. Rev. Lett. **77** (1996) 3145.
[18] HAHM, T.S., BURRELL, K.H., Phys. Plasmas **3** (1996) 427.
[19] LEBEDEV, V.B., DIAMOND, P.H., Phys. Plasmas **4** (1997) 1087.
[20] ONO, M., et al., in Plasma Physics and Controlled Nuclear Fusion Research 1994 (Proc. 15th Int. Conf. Seville, 1994), Vol. 1, IAEA, Vienna (1995) 469.
[21] CRADDOCK, G.G., DIAMOND, P.H., Phys. Rev. Lett. **67** (1991) 1535.
[22] DIAMOND, P.H., et al., Phys. Rev. Lett. **72** (1994) 2565.
[23] CARRERAS, B.A., et al., Phys. Plasmas **2** (1995) 2744.
[24] ISICHENKO, M.B., DIAMOND, P.H., Phys. Plasmas **2** (1995) 1.
[25] NEWMAN, D.E., et al., Phys. Plasmas **2** (1995) 3044.
[26] LEBEDEV, V.B., et al., Phys. Plasmas **3** (1996) 3023.
[27] CARRERAS, B.A., DIAMOND, P.H., VETOULIS, G., Phys. Plasmas **3** (1996) 4106.

DISCUSSION

E.J. DOYLE: I would like to repeat the question I asked T.S. Hahm in connection with paper IAEA-CN-64/D1-2: Are observations on DIII-D and TFTR of differences in the location and timing of transport barrier formation consistent with theory?

P.H. DIAMOND: Qualitatively, yes. Differences between backtransitions in different channels (in space and time) can appear through the differences in transport phase shifts and hysteresis factors (which depend on neoclassical transport). We have observed such differences in our 2-field model computations but have not yet explored quantitative comparisons with data. This is coming.

S.A. SABBAGH: Many experiments show similar transport barriers and near-neoclassical χ without shear reversal (i.e. 'Li enhanced' supershots (MANSFIELD, D.K., et al., American Physical Society Invited Talk, 1995)). Your model also does not assume a priori that reversed shear is required for transition. However, the dependence of the transition power, etc., on the magnitude of the shear is not clear from your model. Can you give a qualitative discussion of this dependence?

P.H. DIAMOND: The transition dependence on magnetic structure (via both shear reversal and Shafranov shift) enters via $\gamma(x - x_r)/\Delta_r$. In the case of TFTR, the collisionless trapped electron mode (CTEM) is the main player in the pre-transition transport. For the CTEM, $\gamma \approx \omega \exp(-\omega/\omega_D)$, where ω_D is the precession frequency. As $\hat{s}$ drops (but is still greater than zero), $\omega_D \to 0$, so dependence is exponential, i.e. rather like $\exp(-1/\hat{s})$.

Incidentally, your observation is a good argument for the WNS mode, which combines improved microstability with broader profiles and less disruptivity.

TURBULENCE AND THE FORMATION OF TRANSPORT BARRIERS IN FINITE β TOKAMAKS

B.N. ROGERS, J.F. DRAKE, Y.T. LAU, P.N. GUZDAR,
A.B. HASSAM, S.V. NOVAKOVSKI
Institute for Plasma Research,
University of Maryland,
College Park, Maryland,
United States of America

A. ZEILER
Max-Planck-Institut für Plasmaphysik,
Euratom–IPP Association,
Garching, Germany

Abstract

TURBULENCE AND THE FORMATION OF TRANSPORT BARRIERS IN FINITE β TOKAMAKS.

The paper presents the results of 3-D nonlinear simulations of drift-ballooning modes in a torus, including electromagnetic effects, the self-consistent modification of the local magnetic shear due to the finite β shift of the flux surfaces and velocity shear. In the electrostatic limit the simulations reveal that a transport barrier forms spontaneously when the shift of the surfaces reverses the local magnetic shear on the outside midplane. Simulations with electromagnetic effects reveal that in plasmas with circular cross sections a strong increase of the transport occurs well below both the ideal β limit and the point where local shear reversal occurs. This strong enhancement of electromagnetic turbulence prevents the formation of the transport barrier unless the local sheared flow is sufficiently large.

1 Introduction

Energy confinement in tokamaks and other plasma fusion experiments is always lower than can be explained by transport from classical inter-particle collisions. The observation of the formation of transport barriers in tokamaks first in the plasma periphery during the L-H transition [1, 2] and more recently in the core [3–6] has provided strong evidence that transport can be controlled. The development of an understanding of the underlying causes of these barriers is critical if we are to be able to have confidence in our ability to maximize their benefit in improving confinement.

The leading model to explain the L-H transition is based on sheared flow generation and the associated stabilization of turbulence [7, 8]. However, experimental evidence supporting the role of sheared flow in the transition is contradictory [9, 10]. More recently, the formation of internal transport barriers [6, 5] provided evidence that negative magnetic shear can also stabilize fluctuations [11]. A mechanism for the formation

of transport barriers as a result of pressure induced local magnetic shear reversal in a finite β tokamak was proposed [12, 13]: the Shafranov shift causes the local magnetic shear to reverse, stabilizing the turbulence driving transport, and allowing the local pressure gradient to increase. The increased pressure gradient boosts the shift, thereby closing the feedback loop. Three dimensional simulations of drift-resistive ballooning turbulence with a self-consistent Shafranov shift produced a bifurcation consistent with this scenario [13]. An experiment to test the relative roles of velocity shear and pressure induced reversed magnetic shear has provided evidence that in a circular cross section tokamak, the Shafranov shift alone is not sufficient to form the barrier [14].

In this paper we explore the relative role of velocity shear and pressure induced magnetic shear reversal in producing self-consistent transport barriers in finite β toroidal plasma. The calculations are based on $3-D$ simulations of drift-ballooning turbulence using the Braginskii fluid equations and are therefore strictly valid only in the edge region of tokamak plasmas. In the electrostatic limit we present the results of simulations which demonstrate that either velocity shear or the Shafranov shift stabilizes drift-resistive ballooning modes and that the Shafranov shift alone can produce a transport bifurcation when the local magnetic shear on the outside of the torus reverses. With electromagnetic disturbances we demonstrate that in a circular plasma the transport increases dramatically with increasing β well below the ideal MHD stability threshold. This increase is apparently a nonlinear effect and not a consequence of the enhanced linear growth rates of modes as the β limit is approached. A consequence of the enhancement of transport with increasing β is that in a circular cross section tokamak it is not possible for a transport barrier to form due to the Shafranov shift alone.

2 Equations

The calculations are carried out in a flux tube based coordinate system consisting of a poloidally and radially localized domain which winds around the torus [15]. In a simple shifted circle model, the coupled equations for perturbations of the density n, potential ϕ, magnetic flux ψ and parallel flow $v_\parallel$ are given by

$$\frac{dn}{dt} + \frac{\partial \phi}{\partial y} - \epsilon_n C(\phi - \alpha_d n) + (1+\tau)\alpha_d \epsilon_n \nabla_\parallel J + \epsilon_v \nabla_\parallel v_\parallel = 0 \tag{1}$$

$$\nabla_\perp \cdot \frac{d}{dt}\nabla_\perp(\phi + \tau\alpha_d n) + Cn + \nabla_\parallel J = 0 \tag{2}$$

$$(2\pi)^2 \alpha \left(\frac{\partial \psi}{\partial t} + \alpha_d \frac{\partial \psi}{\partial y}\right) + \nabla_\parallel(\phi - \alpha_d n) = J \tag{3}$$

$$\frac{dv_\parallel}{dt} + \epsilon_v \left(\nabla_\parallel n - (2\pi)^2 \alpha \frac{\partial \psi}{\partial y}\right) = 0 \tag{4}$$

where T_i and T_e are assumed to be constant, $J = \nabla_\perp^2 \psi$, C is the curvature operator,

$$C = [\cos(2\pi z + v_0 t) + h(z)\sin(2\pi z + v_0 t) - \epsilon]\frac{\partial}{\partial y} + \sin(2\pi z + v_0 t)\frac{\partial}{\partial x}, \tag{5}$$

$$\frac{d}{dt} = \frac{\partial}{\partial t} - v_0 \frac{\partial}{\partial z} + \hat{z} \times \nabla\phi \cdot \nabla,$$

$$\nabla_{\parallel} = \frac{\partial}{\partial z} - (2\pi)^2 \alpha \hat{z} \times \nabla\psi \cdot \nabla,$$

$$\nabla_{\perp}^2 = \left(\frac{\partial}{\partial x} + h(z)\frac{\partial}{\partial y}\right)^2 + \frac{\partial^2}{\partial y^2}, \tag{6}$$

$$h(z) = 2\pi\hat{s}z - \alpha \sin(2\pi z + v_0 t). \tag{7}$$

The coordinate z lies along the equilibrium magnetic field B_0 and the ambient density gradient is in the x direction. The equations have been normalized using $L_z = 2\pi qR$ as the parallel scale length, $L_0 = 2\pi q(\nu_{ei}R\rho_s/2\Omega_e)^{1/2}(2R/L_n)^{1/4}$ as the transverse scale and the ideal ballooning growth time, $t_0 = (RL_n/2)^{1/2}/c_s$, as the time, where $c_s^2 = T_e(1+\tau)/m_i$, $\rho_s = c_s/\omega_{ci}$ and $\tau = T_i/T_e$. In these normalized units $n/n_0 \sim v_z/c_s \sim L_0/L_n$, $\phi \sim BL_0^2/ct_0$, $\psi \sim 2\pi\alpha B_0 L_0^2/qR$ and the transport scales like

$$D_0 = (2\pi q)^2(1+\tau)\rho_e^2\nu_{ei}R/L_n. \tag{8}$$

Other parameters are the magnetic shear $\hat{s} = r(dq/dr)/q$, $\epsilon_n = 2L_n/R$, the inverse aspect ratio $\epsilon = r/R$, the diamagnetic parameter $\alpha_d = \rho_s c_s t_0/L_n L_0$, $\epsilon_v = c_s t_0/L_z$ with L_n the equilibrium density (or pressure) scale length.

Important new features of these equations include the Shafranov shift which enters through the $\alpha = -Rq^2 d\beta/dr$ term in (7), the magnetic terms which are also proportional to α and the sheared flow which enters through the parameter $v_0 = (dv_{y0}/dr)t_0/(2\pi\hat{s})$ with dv_{y0}/dr the equilibrium velocity shear. The Shafranov shift modulates the local magnetic shear as a function of z. The local magnetic shear on the outside of the torus is given by $\hat{s} - \alpha$ so that the local shear reverses sign when $\alpha = \hat{s}$. The physical basis for the stabilizing influence of reversed shear on curvature-driven fluid instabilities has been previously discussed [16] and is one the factors causing second stability of ideal modes [17, 18]. Electromagnetic portions of the equations can be neglected when α is sufficiently small. The ideal magnetohydrodynamic (MHD) stability boundary from these equations occurs for $\alpha \sim 1$ when $\hat{s} \sim 1$ but the precise value of α where the electromagnetic effects impact the transport must be determined from simulations. The form for the velocity shear follows after two coordinate transformations, the first to a frame which moves with the flow in the y direction and the second to a frame which moves along the magnetic field with a velocity v_0 [19]. Realistic diffusive dissipation terms are added to each equation to model ion viscosity and classical transport. The spatial-differencing and time-stepping schemes used to advance the equations have been described previously [15].

3 Electrostatic Simulations

The results of simulations made with the electrostatic limit of Eqs. (1)–(4) and with $\alpha = 0$ have been discussed in detail earlier [15]. For typical parameters in Ohmic and L-mode plasmas, the turbulence can be characterized as driven by resistive ballooning modes in which drift-wave dynamics play an important but not dominant role.

Negative magnetic shear tends to stabilize curvature driven modes by twisting local disturbances out of alignment with the dominantly radial magnetic curvature in tokamaks [16]. As discussed in Sec. 2 the Shafranov shift drives the local magnetic shear on

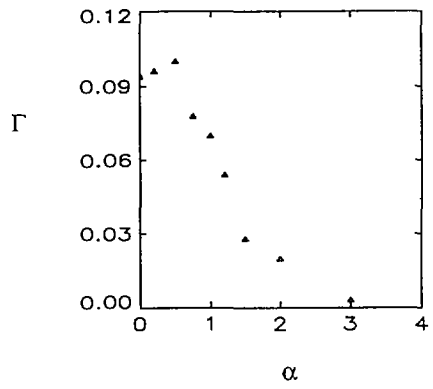

FIG. 1. Average normalized particle flux as a function of α from nonlinear electrostatic simulations with $v_0 = 0$.

the outside midplane negative for sufficiently large values of the ballooning parameter α. Therefore it was expected that increased α would stabilize resistive ballooning modes and therefore reduce transport in the edge region. This effect is shown in Fig. 1 where we plot the particle (or energy) flux $\Gamma = \langle nv_x \rangle$ versus α where $\langle\rangle$ denotes a time average over the entire computational volume. Other parameters are $\alpha_d = 0.25$, $\hat{s} = 1.0$, $\epsilon_n = 0.1$, and $\epsilon_v = 0.02$. The flux drops sharply around $\alpha \sim 1$ where the local magnetic shear on the outside of the torus becomes negative as a result of the Shafranov shift.

Simulations have also been completed to understand the impact of velocity shear on edge turbulence. For the parameters of Fig. 1 the transport drops by a factor of 2 when $v_0 = 0.05$ and a factor of 5 when $v_0 = 0.075$. Thus, in the electrostatic simulations shear in the poloidal velocity as well as local negative shear produced by the Shafranov shift cause stabilization of turbulence. The implications of these results for understanding the formation of the transport barrier during the $L - H$ transition are discussed in Sec. 5.

4 Electromagnetic Simulations

As discussed in Sec. 2 the Shafranov shift and the electromagnetic fluctuations both enter the equations proportional to the ballooning parameter α. There is therefore no rigorous ordering which can justify the electrostatic approximation when α is of order unity, which is required to stabilize the turbulence by reversing the local magnetic shear. The nonlinear electromagnetic simulations are first motivated with a discussion of the dependence of the linear growth rate of unstable modes as a function of the parameter α. The presentation of the results of simulations follows, first without flow shear and then with flow shear.

4.1 Linear Theory

The linear analysis of Eqs. (1)–(4) provides a useful reference point in our study of the full electromagnetic system. In this analysis, we isolate the contribution of the

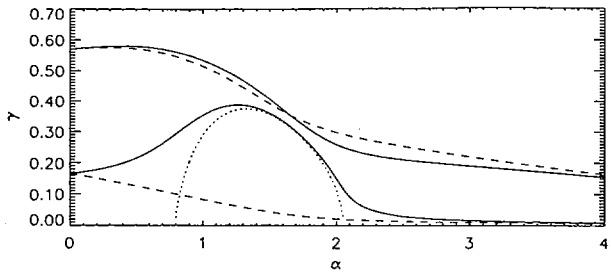

FIG. 2. Growth rate as a function of α for k_y= 7 (upper curves) and k_y= 1 (lower curves). Solid curves: electromagnetic; dashed curves: electrostatic. The dotted curve is the ideal growth rate.

magnetic perturbations by comparing the electromagnetic results with those obtained in the electrostatic approximation.

Linearizing Eqs. (1)–(4) and applying the standard ballooning mode formalism, one obtains a set of ordinary differential equations to be solved for the growth rate and real frequency of the mode. We have carried out a numerical analysis of these equations for a range of parameters that are relevant to the nonlinear simulations which follow. The solid curves shown in Fig. 2 are the growth rate γ as a function of α for two values of the poloidal wave-number: $k_y = 7$ (upper curve), which corresponds to the fastest growing mode at $\alpha \simeq 0$, and a lower value $k_y = 1$ (lower curve). Other parameters are: $\hat{s} = 1$, $\tau = 1$, $\alpha_d = 0.1$, $\epsilon = 0.2$, $\epsilon_n = 0.05$, $\epsilon_v = 0$. The dashed curves in Fig. 2 show the result obtained in the electrostatic approximation, in which all terms containing α in Eqs. (1)–(4) are neglected except those arising from the pressure modulation of the local shear $[\hat{s} - \alpha \cos(2\pi z)]$. The decline of γ seen in the electrostatic curves is due solely to the modulation of the shear. Finally, the dotted curve shows the (k_y-independent) ideal growth rate ($\eta_\parallel \to 0$, $\alpha_d \to 0$, $\epsilon_n \to 0$). This curve defines the first ($\alpha < 0.8$) and second ($\alpha > 2.1$) stability regions obtained in the ideal limit of our model (at $\hat{s} = 1$, $\epsilon = 0.2$).

It is clear from a comparison of the solid and dashed curves in Fig. 2 that electromagnetic effects, while having little impact on shorter wavelengths $\lambda \sim 1$, can be strongly destabilizing at longer wavelengths. As α (or β) is increased from $\alpha \ll 1$ to finite values, this destabilization becomes significant as α approaches the limit of the ideal first stability region, $\alpha \to 0.8$. Therefore, within the first stability region (the region of main concern in this section), electromagnetic effects progressively broaden the smaller-k portion of the unstable k-spectrum as α is increased.

4.2 Nonlinear simulations without velocity shear ($v_0 = 0$)

We turn now to results of nonlinear simulations of Eqs. (1)–(4) in the absence of flow shear. We focus on the α-dependence of the radial particle flux $\langle nv_x \rangle$, averaged over time and poloidal angle. The other parameters, as in the linear study above, are held fixed at values relevant to tokamak-edge discharges: $\hat{s} = 1$, $\tau = 1$, $\alpha_d = 0.1$, $\epsilon = 0.2$, $\epsilon_n = 0.05$, $\epsilon_v = 0.02$. Also as above, we compare simulations of the complete electromagnetic set (1)–(4) to those of the electrostatic system, in which α enters only through its effect on the local shear.

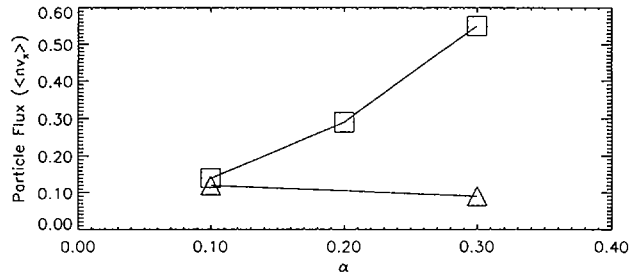

FIG. 3. Average normalized particle flux as a function of α from nonlinear simulations with $v_0 = 0$. Squares: electromagnetic; triangles: electrostatic.

The results are shown in Fig. 3. The upper curve (squares) are data from the electromagnetic simulations, while the lower curve (triangles) shows the electrostatic results. At very small values of α ($\simeq 0.1$, which is a factor of eight below the first ideal stability limit at these parameters), the system is nearly electrostatic, and the two models produce essentially identical results. As α is raised further, however, the particle (and energy) fluxes in the electromagnetic model increase dramatically. At $\alpha = 0.3$, still less than 50% of the ideal mode threshold, the fluxes have increased by more than a factor of six above the electrostatic values. Consistent with the linear results discussed earlier, as α is raised, the dominant modes in the electromagnetic simulations show a progressive shift to longer wavelengths relative to the electrostatic case. (This necessitates an increase in the simulation volume, making higher α studies increasingly computationally intensive.)

The strong enhancement of transport at values of α of order $0.2 - 0.3$ as shown in Fig. 3 is not consistent with the increase in the linear growth rate. In the linear theory the enhancement of γ at $\alpha = 0.3$ relative to $\alpha = 0$ is less than 15% across the entire unstable k spectrum. This does not approach the factor of 6 enhancement of the transport observed in the simulations. This suggests that the increase in transport with α is largely due to an inherently nonlinear mechanism. For example, the turbulence produces regions of locally steep pressure gradient which may become ideally unstable even though the ambient gradient is well below the ideal threshold. At present, however, the explanation of this effect is still under study.

Because the transport levels predicted by the model are sensitive to the proximity of the configuration to the ideal stability boundary, one would also expect these levels to depend strongly on the details of the magnetic geometry under consideration. Because factors such as triangularity, elongation, etc. can boost the ideal ballooning stability threshold and even allow stable access from the first to the second stability regions in the edge region [17, 18, 20] (such access is absent in our model), the transport in the simple shifted circle geometry considered here probably represents an upper limit.

Nevertheless, our results indicate some general trends that seem likely to hold in any geometry. For example, we would expect tokamak confinement (at least in the edge region) to degrade sharply as β approaches some substantial fraction of its ideal ballooning stability limit. Conversely, we expect plasma shaping, other factors being equal, to greatly reduce transport by increasing the margin of ideal ballooning stability.

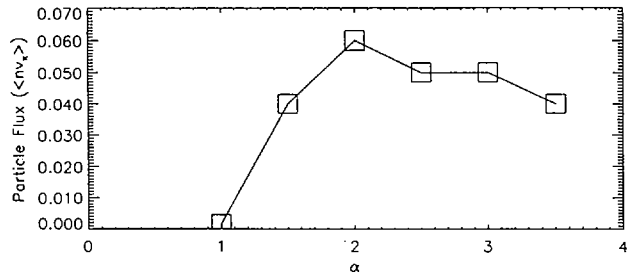

FIG. 4. Average normalized particle flux as a function of α from nonlinear electromagnetic simulations with $v_0 = 0.14$.

4.3 Nonlinear Simulations with Flow Shear ($v_0 \neq 0$)

As in the electrostatic simulations discussed in Sec. 3, the addition of finite flow shear in the electromagnetic model can substantially reduce the particle and energy flux. The stabilizing effect in the electromagnetic case is even more drastic, however, allowing saturated, steady state turbulence to be sustained even in the region of ideal instability.

Figure 4 shows the dependence of the particle flux on α obtained from electromagnetic simulations with $v_0 = 0.14$. The other parameters are the same as those in Fig. 3. Comparing these results to the earlier figure (triangles), note the largest values of the flux with finite v_0 are well below even the smallest values obtained with $v_0 = 0$, despite more than a 10-fold increase in α.

Although a comparison to the electrostatic, finite-v_0 results presented earlier is complicated by differences in the various parameters, it is clear the differences between the electromagnetic and electrostatic models with finite v_0 and α are smaller than those found in Fig. 3 for $v_0 = 0$. One possible explanation is that the flow shear may have a stronger stabilizing effect on longer wavelength modes, leaving behind a shorter wavelength (and thus more electrostatic) unstable k-spectrum which drives the transport.

5 Transport Barrier Formation

Once the anomalous particle or energy flux Γ in the plasma edge as a function of the relevant parameters is known, the onset criterion for the formation of a transport barrier can be formulated. A system in which Γ increases as the local density gradient is increased is stable and will not spontaneously bifurcate into a transport barrier. If, however, the flux decreases as the local gradient increases, a barrier will spontaneously form: the increased gradient reduces the transport, which then allows the gradient to steepen further.

Under normal Ohmic or L-mode conditions where resistive ballooning modes dominate the transport $\Gamma \propto n'^2$ since $\Gamma \sim D_0 n'$ and D_0 in Eqn. (8) is proportional to n'.

Thus, no spontaneous formation of a transport barrier occurs. However, the density gradient enters the transport scaling through several other of the parameters of the equations presented in Sec. 2, including α, α_d and perhaps the shear flow parameter v_0. Thus, the criterion for the barrier formation can be written as

$$\frac{d\Gamma}{dn'} = \frac{\partial \Gamma}{\partial n'} + \frac{\partial \Gamma}{\partial \alpha}\frac{\partial \alpha}{\partial n'} + \frac{\partial \Gamma}{\partial \alpha_d}\frac{\partial \alpha_d}{\partial n'} + \frac{\partial \Gamma}{\partial v_0}\frac{\partial v_0}{\partial n'} < 0. \tag{9}$$

where $\partial\Gamma/\partial n' = 2\Gamma/n'$, $\partial\alpha/\partial n' = \alpha/n'$ and $\partial\alpha_d/\partial n' = \alpha_d/4n'$. The dependence of v_0 on n' is discussed below.

The plot of γ versus α in Fig. 1 from the electrostatic simulations decreases very strongly when $\alpha \geq 1$. Thus, in this region $\partial\Gamma/\partial\alpha < 0$ and the Shafranov shift supports the formation of the barrier. In this electrostatic model it was demonstrated that the formation of a transport barrier could occur even in the absence of sheared flow [13]. The results of electromagnetic simulations presented in Fig. 3, however, dramatically change this conclusion, at least for tokamak discharges with circular cross section. The flux now increases strongly with the ballooning parameter α in the first stability region so that the variation of the flux with α works strongly against the formation of the transport barrier until the plasma can access the second stability region at high α. Without sheared flow or some other mechanism for reducing transport in the ideal unstable region, this does not seem likely. Thus, we conclude that in the absence of sheared flow the transport barrier cannot form in circular cross section tokamaks.

Both in the electrostatic and electromagnetic simulations sheared flow is effective in reducing the fluxes. As noted in Sec. 4 the sheared flow is surprisingly effective in mitigating transport even in the ideal unstable ballooning regime. Given that $\partial\Gamma/\partial\alpha \sim 0$ and the flux decreases rather strongly with v_0 for $v_0 \geq 0.14$, the formation of a transport barrier in a circular machine is possible if the flow shear can reach levels of this order. Converting this criterion back to dimensional units, the sheared flow criterion is given by

$$\frac{dv_{y0}}{dr} \geq \frac{\hat{s}c_s}{(RL_p)^{1/2}}. \tag{10}$$

with L_p the pressure scale length. Several models have been proposed as mechanisms to produce the sheared poloidal rotation. The Stringer mechanism [7] produces poloidal flows which are of the order of the poloidal sound speed $c_s a/qR$. If the scale length of the sheared flow is comparable to that of the pressure, the inequality in Eqn. (10) translates into a condition on the pressure scale length

$$L_p < \frac{a^2}{q^2\hat{s}^2 R}. \tag{11}$$

A second mechanism for producing sheared poloidal rotation is simply that the radial electric field balances the ion pressure gradient [8]. This produces poloidal rotations equal to the ion diamagnetic velocity and again translates into a scale length criterion for the pressure

$$L_p < \left(\frac{R\rho_i^2}{\hat{s}^2}\right)^{1/3}. \tag{12}$$

6 Conclusion

The simulations presented here address the individual and combined impact of three main effects on tokamak edge transport: the modification of the local shear due to the shift of flux surfaces at finite β, the destabilizing role of electromagnetic effects, and the suppression of turbulence by $\vec{E} \times \vec{B}$ flow shear. This analysis is based on a fluid model of the edge region, in which transport arises from the turbulent, nonlinear development of drift-ballooning modes.

The results described here and elsewhere [13] in the electrostatic limit show the effect of pressure gradient modulation of the shear, associated in ideal MHD with the second stability region, to be robustly stabilizing. When the pressure gradient is sufficiently large to reverse the shear on the outside midplane, the particle and energy fluxes are found to drop rapidly and a transport barrier is formed. In a circular machine, the path of the edge configuration to such high β, high confinement states from low β is blocked by the presence of the ideal MHD ballooning mode threshold. Here, we study the behavior of the transport as this threshold is approached with nonlinear electromagnetic simulations. At a β threshold well below the ideal ballooning stability limit, $\beta/\beta_{crit} \sim 0.1$, the contribution of the magnetic perturbations is small, and the simulation results agree with those based on the electrostatic approximation. In the absence of flow shear, however, the transport rises rapidly as β is increased above such values, reaching levels six times higher than the electrostatic case at $\beta/\beta_{crit} \sim 0.4$.

In a non-circular machine in which ideal ballooning instability at high-β may be avoided, this degradation may not arise, and the stabilizing influence of shear reversal found in the electrostatic studies may again become important. In edge configurations without second stability access (e.g. those with circular flux surfaces), however, the formation of a transport barrier by the pressure-induced shear reversal mechanism does not seem possible.

This conclusion does not apply to the effect of flow shear. Even in the circular case at high β, flow shear can cause drastic reductions in the transport in both the electromagnetic and electrostatic models. At sufficiently large values of the flow shear, the simulations demonstrate that steady state fluctuation levels with modest levels of transport can be achieved even in regions of ideal instability.

REFERENCES

[1] WAGNER, F., et al., Phys. Rev. Lett. **49** (1982) 1408.
[2] BURRELL, K., et al. Phys. Fluids B **2** (1990) 1405.
[3] HUGON, M., et al., Nucl. Fusion **32** (1992) 33.
[4] KOIDE, Y., et al., in Plasma Physics and Controlled Nuclear Fusion Research 1994 (Proc. 15th Int. Conf. Seville, 1994), Vol. 1, IAEA, Vienna (1995) 199.
[5] LEVINTON, F.M., et al., Phys. Rev. Lett. **75** (1995) 4417.
[6] STRAIT, E.J., et al., Phys. Rev. Lett. **75** (1995) 4421.
[7] HASSAM, A.B., et al., Phys. Rev. Lett. **66** (1991) 309.
[8] DIAMOND, P.H., et al., in Plasma Physics and Controlled Nuclear Fusion Research 1994 (Proc. 15th Int. Conf. Seville, 1994), Vol. 3, IAEA, Vienna (1996) 323.
[9] BURRELL, K.H., et al., ibid., Vol. 1, p. 221.
[10] HERRMANN, W., ASDEX UPGRADE TEAM, Phys. Rev. Lett. **75** (1995) 4401.

[11] KESSEL, C., et al., Phys. Rev. Lett. **72** (1995) 4420.
[12] BEER, M.A., HAMMETT, G.W., Bull. Am. Phys. Soc. **40** (1995) 1733.
[13] DRAKE, J.F., et al., Phys. Rev. Lett. **77** (1996) 494.
[14] SYNAKOWSKI, E.J., et al., in preparation.
[15] ZEILER, A., et al., Phys. Plasmas **3** (1996) 2951.
[16] ANTONSEN, T.M., et al., Phys. Plasmas **3** (1996) 2221.
[17] LORTZ, D., NÜHRENBERG, J., Phys. Lett. **68A** (1978) 49.
[18] COPPI, B., FERREIRA, A., RAMOS, J.J., Phys. Rev. Lett. **44** (1980) 990.
[19] MILLER, R.L., et al., Phys. Plasmas **2** (1995) 3676.
[20] STRAIT, E.J., Phys. Plasmas **1** (1994) 1415.

FIRST PRINCIPLES CALCULATIONS OF TOKAMAK ENERGY TRANSPORT

M. KOTSCHENREUTHER, W. DORLAND, Q.P. LIU
Institute for Fusion Studies,
University of Texas,
Austin, Texas,
United States of America

G.W. HAMMETT, M.A. BEER, S.A. SMITH
Plasma Physics Laboratory,
Princeton University,
Princeton, New Jersey,
United States of America

A. BONDESON
Institute for Electromagnetic Theory,
Euratom–NFR/Fusion Association,
Chalmers University of Technology,
Göteborg, Sweden

S.C. COWLEY
University of California,
Los Angeles, California,
United States of America

Abstract

FIRST PRINCIPLES CALCULATIONS OF TOKAMAK ENERGY TRANSPORT.

A predictive, physics based model of tokamak energy transport that is based on simulations of the gyrokinetic equation is presented. Calculations of core energy transport are compared with experimental results from JET, TFTR, JT60-U and DIII-D for a variety of discharge conditions. In the region of the plasma predicted to be unstable to ion temperature gradient (ITG) modes (typically between the q = 1.2 surface and r/a = 0.9), the ratio of the model's prediction of the average temperature gradient scale length to the experimental value is 1.08 ± 0.17. Core H-mode temperatures are found to depend strongly on the pedestal temperature. The scaling of H-mode pedestal performance with the gyroradius parameter ρ^* is shown to follow from the underlying scalings of the gyrokinetic equation. An analogy is drawn between H-mode confinement and classic turbulent fluid flow in pipes which highlights the importance of the boundary layer at the edge. Experimental results on fast temperature propagation, wall effects on confinement, ELM scalings, ELM effects on confinement, confinement limits, and VH modes are qualitatively explained as natural consequences of the importance of the boundary layer. Implications of the expected ρ^* scaling of conventional H-mode confinement are unfavorable for ITER. Initial efforts to find a reactor relevant advanced tokamak configuration based on the idea of ITG second stability are described.

1. Introduction

To date, large energy losses have prevented the experimental demonstration of net fusion energy production from a tokamak. Here, we report that calculations based on numerical simulations of the gyrokinetic equation [1] successfully explain energy losses from the core of large tokamaks such as JET, TFTR, JT-60U and DIII-D under many (but not all) conditions. These calculations provide a scientific framework that unifies many seemingly disparate experimental phenomena and allow more realistic predictions of the performance of proposed experiments. The experimental data used to test the theory is taken from the ITER profile database [2]. L-modes, hot-ion modes and ELMy and ELM-free H-modes are included in the dataset. When full numerical equilibria were not available, an approximate magnetic geometry was used that includes the ellipticity, triangularity, axis shift, and their derivatives.

2. Basic Features of the Model

The gyrokinetic equation is the fundamental equation describing drift modes, ion temperature gradient (ITG) modes, ideal and resistive ballooning modes, tearing modes and other microinstabilities with frequencies less than the gyrofrequency. The linear gyrokinetic stability calculations presented here use algorithms that represent the velocity space dynamics of all species numerically, without analytical approximations [3]. Thus, kinetic effects are well described. The main approximations of the codes are that the modes are described by the ballooning transformation, valid for short wavelength modes, and that electromagnetic perturbations proportional to $\delta B_{\parallel}$ are neglected. As previously reported for TFTR L-modes [1], the ITG mode is observed to be the dominant core instability. Trapped particle instabilities are found near the edge of some discharges and in the center of hot-ion discharges. When the trapped particle modes are absent, there is a critical ion temperature gradient below which there is no predicted micro-instability.

Nonlinear toroidal gyrofluid simulations are used to parameterize the transport which results when the ITG instability boundary is crossed [4]. These high-resolution 3D simulations include the **E**x**B** nonlinearities, and linear closure approximations that describe kinetic effects. The gyrofluid simulations are carried out in the radially local, or flux-tube limit, mathematically similar to the ballooning limit. They have been linearly benchmarked with gyrokinetic codes for a wide range of parameters. Limited comparisons with nonlinear gyrokinetic particle simulations have also been carried out.

Results summarizing the performance of the model are shown in Fig. (1). The temperature gradient appears as an instability driving term in the gyrokinetic equation as the inverse scale length $R/L_T = -(R/T)\,dT/dr$. When $R/L_T > R/L_{Tc}$, the ITG mode is unstable. Note that $R/L_{Tc}(r)$ depends on local dimensionless parameters. [Unlike in Ref. [1], here we explicitly calculate R/L_{Tc} using the gyrokinetic codes at each radial point.] In Fig. (1a), the radial average of the experimental gradient to the critical gradient is shown, where the average is taken between the q=1.2 surface and r/a=0.9 for L-modes and H-modes. For non-sawtoothing hot ion modes, the inner boundary extends inward to the region where neoclassical transport becomes comparable to ITG transport. Regions in which there is no critical temperature gradient, because of the appearance of trapped electron modes, are not included in the radial average. The stabilizing effect of velocity shear is estimated using the criterion that the stabilization is linearly proportional to dv_E/dr, and complete stabilization occurs when the linear growth rate $\gamma = dv_E/dr$, as found by nonlinear simulations [5]. As can be seen, ion temperature profiles in H-mode discharges tend to be close to the marginally stable profile, whereas some L-mode discharges are well above it.

The L-mode shots are well above marginal stability toward the edge, as found on TFTR. The departure from marginality in L-modes arises because the turbulent heat flux of the ITG mode scales with temperature as $T^{5/2}$, for fixed deviation from marginal stability, so the ITG mode is not strong enough to force the profile close to marginality in a low-temperature edge. Thus, the ITG

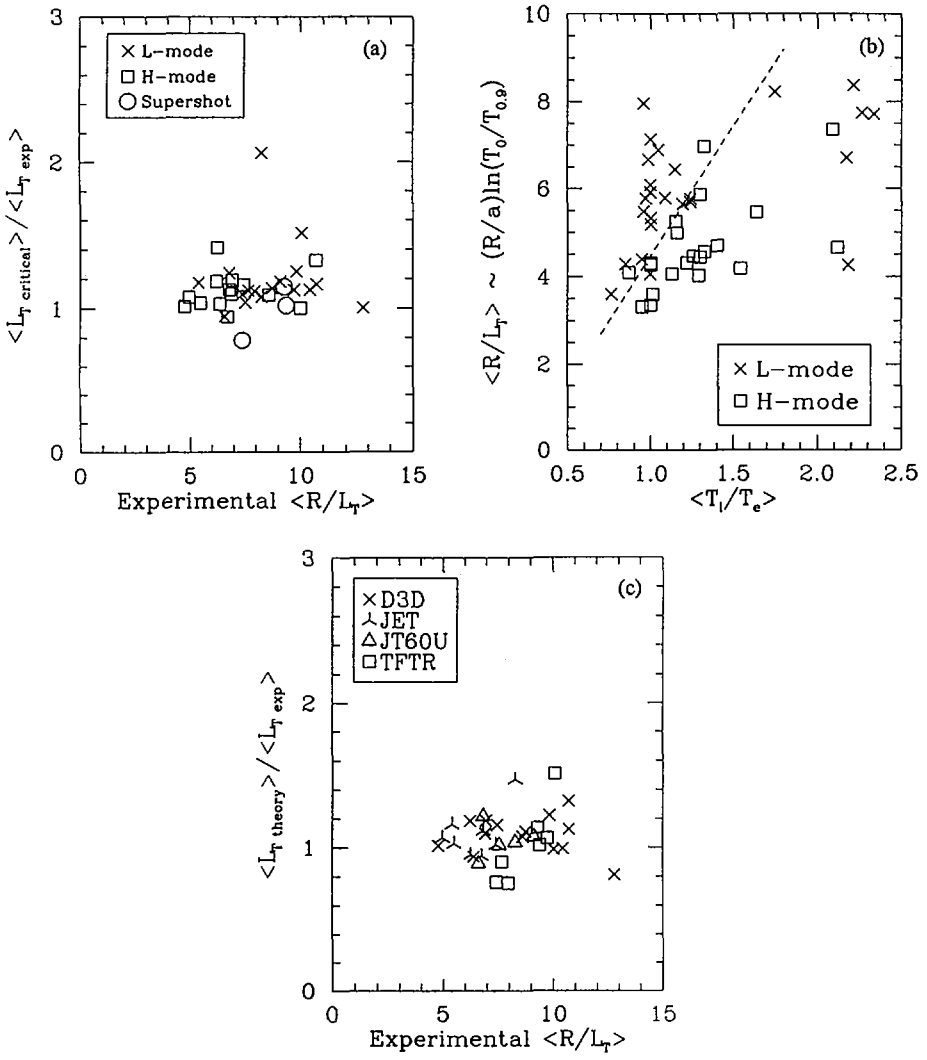

FIG. 1. Radially averaged critical scale lengths, experimental scale lengths, and predicted scale lengths including the gyrofluid χ, in the ITER profile database.

drive (~R/L$_T$) increases to conduct the power at low temperature. Another robust feature of ITG transport is that increasing T_i/T_e weakens the ITG mode, by increasing the critical gradient. Both of these gross features are borne out by the ITER database, in Fig 1. The <R/L$_T$> increases with T_i/T_e, and for fixed T_i/T_e, the L-mode discharges have higher <R/L$_T$>, consistent with a stronger ITG drive and poorer confinement.

Results of nonlinear gyrofluid simulations [4] show that most of the parameter variation in the nonlinear χ from ITG modes can be captured from the linear eigenfunctions. Specifically, it is found that if one defines $W=\chi_{nonlinear}/D_{mixing}$ (where D_{mixing} is the maximum value for all k_θ of

γ/k_{perp}^2)the function W depends strongly only upon the departure from criticality and magnetic shear, and can therefore be parameterized by a modest number of nonlinear simulations [1]. Here, we combine the gyrokinetic code above (which has more complete linear physics) with the gyrofluid results by taking $\chi_{nonlinear} = W D_{mixing}$, where D_{mixing} is computed directly from the gyrokinetic code. The electron heat flux is obtained using the quasilinear ratio of electron to ion heat fluxes from the gyrokinetic code (however, the ion heat flux usually dominates) [1].

When the incremental increase in the temperature gradient beyond R/L_{Tc} is calculated using this algorithm, the average predicted $<R/L_T>$ is 1.08 times the experimental value, and the standard deviation is 0.17 (Fig. 1b). The experimental uncertainty in $<R/L_T>$ is roughly 10%. Errors in the predicted gradient which are from errors in experimental quantitites (such as Z_{eff}, q, *etc.*) are probably at least another 10-20%. Thus, we believe that the agreement in Fig. (1b) is within the error bars.

3. Sensitivity of Global Confinement to Pedestal Performance

The improved core confinement in H-modes follows from the edge transport barrier. For the H-mode discharges in the ITER Profile Database, we find that the predicted ion temperature profiles are within 5% of the marginal stability from the core to the top of the pedestal. In this limit, the core temperature profile is only determined to within a multiplicative constant, since multiplying T(r) by a numerical factor does not change the marginality condition on (R/T) dT/dr. This is a qualitative difference between ITG modes and the RLW model. Specification of the pedestal temperature boundary condition therefore determines the core temperature [1]. The improved confinement in supershots and hot ion modes also arises partly because of improved edge temperatures, but in addition the critical gradient becomes larger for larger Ti/T_e, and modest thermal deuterium dilution[1].

In H-mode experiments, the central temperature rapidly responds to the edge temperature [6,7]. This behavior may be understood from the model: a small deviation from near marginality near the edge leads to a large change in χ, which rapidly propagates to the core by small changes in the temperature profile. Experiments on JET have shown that the central temperature responds in a few milliseconds to edge perturbations from ELMs [6], cold pulses [7], and H to L transitions [6].

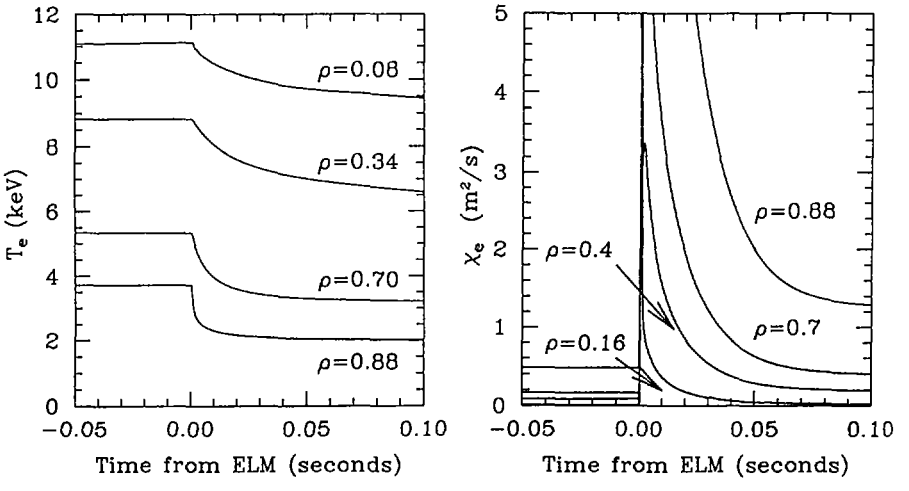

FIG. 2. Time response after a simulated ELM for electron temperature and χ_e from the ITG model.

For example, Ref. [6] reports the electron temperature response to a giant ELM for discharge #30592. Lacking data for this shot, a surrogate was chosen from the ITER database (#26087), and the effect of a giant ELM was simulated by dropping the edge boundary temperatures of all species by a factor comparable to the electron temperature drop found in Ref. [6]. The electron temperature responses in the surrogate ITG simulation [Fig (2)] are as fast as found in Ref. [6]. The electron χ is shown in Fig (2b). It can be seen that there is a rapid increase in χ_e across the discharge. Even though χ is a local function, it seems to behave non-locally. Cold pulse experiments on JET[7] have shown that the experimentally observed response is roughly consistent with a factor of eight increase in χ for roughly 5 milliseconds, similar to Fig (2b). The fact that temperature perturbations from several different sources produce similar results in the core is strong evidence for a close connection between the plasma edge temperature and the core temperature in H-modes.

4. Scaling of Pedestal Performance at Small $\rho*$

Unfortunately, it is not possible to predict the height of the H-mode pedestal due to the complexity of the edge physics. However, useful results can be obtained from the $\rho*$ scalings of terms in the gyrokinetic equation, aided by insight obtained from simulations. The usual arguments for Bohm or gyroBohm global scaling assume that the scaling considerations are uniform across the minor radius. However, there is another class of solutions, in which the turbulence scales as the gyroradius in the core and is strong enough to force the profile close to marginal stability from the core to very near the edge. At the edge there is a boundary layer which scales as the gyroradius (possibly the poloidal gyroradius) where the turbulence is suppressed.

The mode (typically ITG) which is destabilized first as R/L_T is increased above R/L_{Tc} typically has $0.1 < k_\theta \rho_i < 0.6$. If the transport from the ITG mode is robust, R/L_T is forced to be close to R/L_{Tc}, and the unstable fluctuations have $k_\theta \rho_i$ of order 0.3. (Measurements in the core of TFTR show such fluctuations propagating in the ion drift direction [8].) Toward the edge of L-modes, the deviation from criticality increases and long wavelength modes become unstable. Preliminary nonlinear simulations for large values of R/L_T indicate that the ion feature in the predicted fluctuation spectrum becomes dominated by the low $k_\theta \rho$ modes, and is roughly consistent with the large spectral shift observed experimentally [8].

However, H-modes have an edge boundary layer, as does the classic description of high Reynolds number fluid flow and the turbulent flow resistance (i.e., momentum transport) in a pipe [9]. H-mode transport is fundamentally different from pipe flow, since the turbulence scale size is small for the H-mode, but is global for the pipe. However, the more crucial determinants of qualitative transport behavior are very similar: in both cases, the core turbulent dynamics only determine the core profiles to within a constant, which is found by matching to the boundary layer, causing a global sensitivity to edge conditions.

In a pipe [9], the boundary layer arises because there is a turbulence suppressing term (viscosity) in the Navier-Stokes equations which is nominally small, but which enters the equations as a higher derivative than any other term. For pipe flow, the fundamental scaling of the width of the boundary layer is found by balancing of the dominant terms in the governing equations. Gyrokinetic boundary layers form when the scale lengths of equilibrium variations become of order the wavelength of the modes, so that stabilizing terms become important. In the pedestal region, the gradients are very far above marginal stability. Nonlinear gyrofluid simulations with sharp temperature gradients of this magnitude show that an H-mode pedestal would be flattened by the turbulent transport unless the turbulent transport is suppressed by some effect not present in the lowest order of the usual ballooning ordering. We may estimate the required size of such an effect, using some insight from numerical calculations.

For parameters characteristic of H-mode pedestal well after the transition, the linear instabilities with largest growth rates are of the drift type, *e.g.*, ITG modes and TEM (as long as the gradients

are below the MHD stability limit). The modes with the largest growth rates have $k_\theta \rho_i \sim 0.1$-0.5, and they have characteristic frequencies and growth rates of the order of ω^* ($\gamma/\omega^* \sim 1/2$ to 1/5 is common). Within the range of gradients of interest, (*i.e.*, pressure gradients such that $a/L_p \sim 10$-30, but below the ideal MHD ballooning threshold), the growth rates are roughly linear in the gradient until the MHD limit is approached. The characteristic size of terms in the gyrokinetic equation is thus $\gamma_0\, \delta f$, where

$$\gamma_0 = (v_{th}/L)\, k_\theta \rho_i\; G_1(v^*, \beta, q, \varepsilon, Z_{eff}, ...) = (v_{th}/L)\, G(v^*, \beta, q, \varepsilon, Z_{eff}, ...) \qquad (1)$$

Since the most unstable linear modes have $k_\theta \rho_i \sim 0.1$ and $\gamma/\omega_* \sim 1/3$, we anticipate that the typical size of G is roughly 1/30.

In the standard ballooning limit, gradients of the **E** x **B** terms and of the driving terms are small. However, they become important in the pedestal. The widely discussed physical picture of stabilization by the sheared **E** x **B** velocity, dv_E/dr, is that velocity shear tears the perturbations apart on the same time scale as the growth of the perturbation. We note that the gradients in ω_* may have the same physical effect. Formally, the dv_E/dr term enters into the gyrokinetic equation with a size of $(dv_E/dr)k_\theta \Delta x$, where Δx is the radial correlation length. Our flux-tube nonlinear simulations find $k_\theta \Delta x$ is a function of dimensionless parameters, with no indication of an explicit ρ_* scaling. The radial electric field is estimated from the momentum balance equation in the conventional way, and the poloidal and toroidal velocities U_θ and U_ζ are taken to be of order the thermal velocity inside the layer. In the layer,

$$dv_E/dr \sim (\rho_i\, v_{th}\, / L^2)\, S(v^*, \beta, q, \varepsilon, Z_{eff}, ...) \qquad (2)$$

where the leading order scaling in gyroradius is given, and typically $S \sim 1$-2 . Different authors emphasize different mechanisms for the generation of U_θ, and so obtain different functional forms for S consistent with Eq. (2) (*eg.*, Shaing and Crume [10], Carreras, *et al.*, [11], *etc.*). Equation(2) also implies that the dv_E/dr term is of the same order as the term from gradients of ω_*. Note that $(1/v_{th})\, dv_E/dr \sim \rho/L^2$, whereas the other terms in the gyrokinetic equations are of order $(1/v_{th})\, \gamma_0$. As in classical fluid flow, requiring that the stabilizing terms be of order of, or larger than, the other terms in the gyrokinetic equation, we arrive at the necessary scale length of the boundary layer:

$$L < \rho_i\, (G/S). \qquad (3)$$

Since we expect G/S is typically of order 1/40, the actual width could be many gyroradii, or of order the poloidal gyroradius. If the r/R dependence and q dependence of the function G/S were r/(qR) (which is plausible for some instabilities and models for S) the width would actually scale as the poloidal gyroradius. (Similar expressions have been independently derived elsewhere [12].)

5. Experimental Evidence for Pedestal Scaling

In Table I, representative boundary layer widths for seven different tokamaks are presented, using published edge profiles and other data [3,13-18]. The major radius varies from 0.6 m to 3.1 m, the temperature from 30 eV to 1.5 keV, ν_* from 0.05 to 10, and β from 0.1% to 0.7%. Even for such large parameter variation, the layer width normalized to the gyroradius only varies by a factor of 2, and by a factor of 2.6 when normalized to the poloidal gyroradius, consistent with the gyroradius or poloidal gyroradius being the fundamental scaling size.

For fluid pipe flow, wall conditions affect global confinement. Small mechanical projections that disturb the thin boundary layer (so-called "roughened pipes") reduce pipe momentum confinement time (typically by factors of two or more). The classic experimental results for this phenomenon are shown in Fig. (3): the scaling and magnitude of the pipe friction are less favorable when the width of the boundary layer is reduced to the size of the roughness scale. A qualitative analogue in

TABLE I. PEDESTAL WIDTHS FROM VARIOUS TOKAMAKS

	Width (cm)	Width/ρ_i	Width/ρ_p	Width/λ_{mfp}
JET	2.5	16	3.5	6
JT-60U	5.6	27	2.4	8
DIII-D	3.0	16	3.3	3
ASDEX-U	2.0	17	2.3	7
JFT2-M	1.0	12	1.8	8
C-Mod	1.5	30	4.7	1.3
COMPASS-D	2.0	28	4.0	2

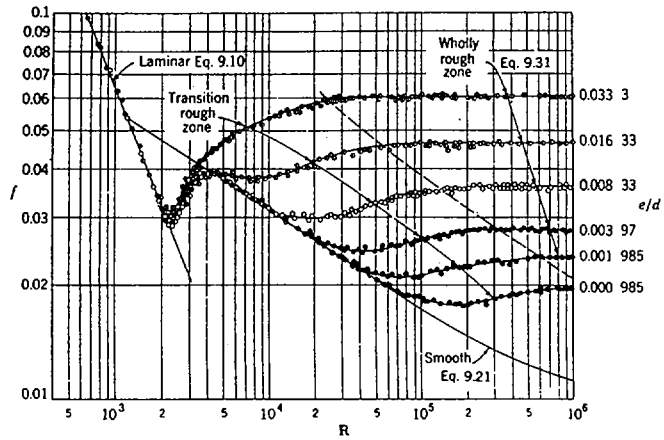

FIG. 3. Flow friction versus Reynolds number for varying wall roughness e/d. Reprinted with permission from VENARD, J.K., Elementary Fluid Mechanics, 6th edn, Wiley, New York (1982).

H-mode physics is the observed sensitivity of confinement to wall conditioning. Atomic processes are necessarily localized to the edge. Table I includes estimates of the mean free path of Frank-Condon deuterium neutrals into the edge. Other neutral processes and impurity penetration lengths are significantly less. Gross effects of neutrals such as convective losses and radiation losses directly affect the pedestal performance. Neutral processes also strongly effect boundary plasma parameters such as Z_{eff}, gradients of Z_{eff}, η, *etc.* Variations in these parameters would be expected to lead to order one changes in the functions G and S, and also in neoclassical and ion orbit heat loss rates, and thereby would be expected to affect global confinement.

The linear stability of the sharp gradient region of the pedestal is considered more quantitatively for an ITER similarity discharge on DIII-D shown in Fig. (4). The linear gyrokinetic code was used with EFIT equilibria. Note that some important parameters, such as Z_{eff} and the ratio of the temperature scale length and the density scale length, η, have considerable uncertainties in this region, so these results are only approximate. As the local pressure gradient is increased (keeping these ratios constant), the ITG/TEM instabilities with $k_\theta \rho_i \sim 0.3$-1.0 become unstable and the

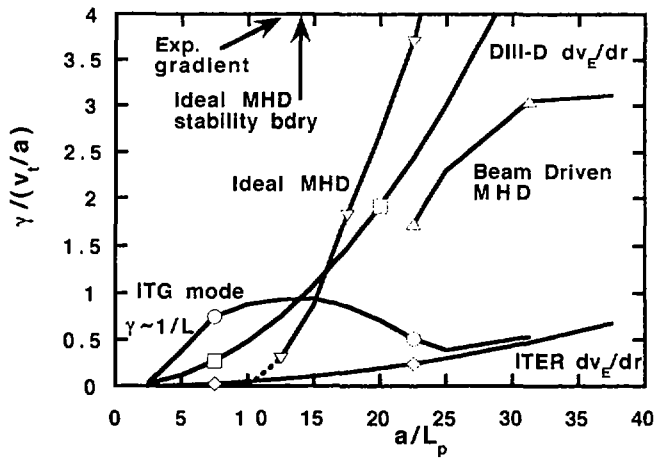

FIG. 4. Growth rates and shearing rates for the steep gradient region of the pedestal of DIII-D ITER-similar discharge 82205 at r/a = 0.97, and for the discharge scaled to ITER.

growth rates increase roughly linearly with $1/L_p$, until the ideal ballooning boundary is approached. The ITG/TEM instability growth rates then decrease, and the MHD mode at low $k\theta\rho_i$ is dominant. Kinetic MHD modes driven by the fast particle pressure gradient also arise at $k\theta\rho_i \sim 0.2$. Figure (4) also shows a rough approximation to the shearing rate, [Eq. (3)] with S estimated to be 1.5. For pressure scale lengths in the experimental range, the stabilizing shearing rate is of the order of the ITG growth rate, and the pressure gradient is close to the ideal MHD ballooning limit.

If the ITG/TEM modes are fully stabilized, and if other energy loss mechanisms are overcome by the heating power, the gradient will increase until the MHD limit is reached. For large dv_E/dr (i.e., large S or large ρ^*), significant penetration into the MHD unstable region is possible. The neoclassical heat flux increases as the distance from the separatrix increases, and eventually this (along with other possible energy loss mechanisms) will pull the gradient down from the MHD limit. Even further from the separatrix, these transport processes reduce $1/L_p$ until the ITG/TEM mode is not stabilized. That is, Eq. (4) is violated, which constitutes the end of the pedestal. Thus, there may be two regions in the pedestal, one forced close to MHD limits, and another where collisional or atomic processes control the profiles.

Figure (4) also shows the estimated velocity shear after scaling this discharge to ITER. As can be seen, the linear ITG/TEM growth rates are now larger than the shearing rate. If MHD effects could be ignored, then by increasing $1/L_p$, the shearing term would eventually stabilize the ITG mode, since without the MHD effects $\gamma \sim 1/L_p$, whereas the velocity shear term increases more strongly, $dv_E/dr \sim (\rho/Lp)^2$. However, the MHD mode prevents this for β values characteristic of DIII-D. Only by decreasing the pedestal β by a factor of order $\rho_*^{ITER} / \rho_*^{DIII\text{-}D}$ can the velocity shear in ITER stabilize the ITG modes without first violating MHD stability.

6. H-Mode Confinement β limits

Due to ITG marginality, any process that limits the pedestal temperature can limit the attainable global confinement. On DIII-D, JT60-U, JET, and other machines, in many types of high β discharges, some fraction of the pedestal is found to be quite close to ideal MHD marginal stability for ballooning modes or kink modes. Predictive simulations with MHD stability and gyrokinetic

transport from the separatrix to the core are beyond our present capabilities. However, some qualitative explanations of physical mechanisms and scalings of important processes are presently possible.

Recent VH-mode experiments [20] provide a comparison of two cases: one where the edge is limited by MHD processes and another where the edge is second stable. When the edge is second stable, VH-modes arise and persist as long as the plasma does not experience ELMs (an indication that MHD edge stability has been lost). After an X event, the discharges revert to ELMing H-modes with half the confinement time of the preceding VH phase. Otherwise similar discharges with less triangularity (which have poorer edge MHD stability) do not enter the high confinement VH phase, but are ELMing H-modes.

Velocity shear driven by neutral beams contributes to VH-mode confinement. This is consistent with boundary effects. As the temperature at the boundary is increased at fixed heating power, the transport power needed to enforce marginality decreases. Thus, local fluctuation levels decrease, leading to a roughly proportional improvement in momentum diffusivity. The resulting increased velocity shear further improves the local effective critical gradient and provides a substantial amplification of the improved confinement from the boundary temperature increase alone. Thus, VH-modes show a correlation between global confinement improvement and improved edge MHD stability which is qualitatively consistent with the ITG model.

The parameter $\alpha = -2\mu_0 (q^2R/B^2)$ dp/dr arises in ballooning stability theory in the well-known s-α model. On JT60-U, this parameter was observed to approach the value for instability before ELM events [21]. Also, the pedestal parameters were found to satisfy an empirical relationship [21], which can be written:

$$\beta (q^2 R) / \rho_{pol} = C (\kappa, \delta, l_i). \quad (4)$$

This is equivalent to the criterion that the ideal ballooning parameter (with the ion β) is at marginal stability if the pressure gradient scale length is replaced by a constant times the poloidal gyroradius [21]. This links the scaling results for the layer width in Eq. (4) to edge MHD stability limits.

The boundary layer nature of confinement in the ITG theory links ELMs to global confinement degradation, both transiently, as in Fig. (2), and also in steady state if the ELMs are frequent. JT-60U found that increased heating power resulted in progressively more frequent ELM events with progressive deterioration in the H factor [21]. Hender *et al.*,[22] found that ELM events frequently signal the end of the good performance phase of JET discharges, by substantially lowering central ion temperatures. Challis, *et al.*, [23] reported transport β limits for low-q discharges similar to ITER, which seemed linked to increased ELM activity (not magnetic islands).

The most direct evidence on JET of a transport limit related to edge ideal MHD instability is reported by Smeulders, *et al.*, [24]. A transport β limit prevented the attainment of large β_N for high magnetic field, but not for low magnetic field. For the high field shots which failed to obtain high β_N, most of the profile was well below the ideal MHD stability limit (by factors of as much as four), so core MHD was not responsible. However the edge was close to computed MHD limits, and the global confinement degradation of high field shots was attributed to observed edge MHD instabilities. According to Eq. (5), a discharge in a large machine at high field would have small ρ^* and thus MHD stability would imply lower pedestal β. For flat density profiles as observed on JET, ITG temperature marginality translate an edge β limit into a core β limit.

Balet, *et al.*, [25] report on a comparison of two ITER similarity discharges with virtually identical core temperature and density profiles, but with differing pedestal density profiles. One discharge had a steeper density profile in the boundary layer, generated by more intense gas puffing. The heating power needed to sustain this discharge was 40% higher. The degraded confinement was attributed to the increase in the frequency of ELMs.

7. Reactor Relevance of H-mode Operation

In light of this, we consider the ρ^* scaling of H-mode confinement for small $\rho*$. Experimental $\rho*$ scans have been described as analogues to the use of wind tunnels, where scale models are tested at Reynolds numbers different than the actual device, and projected performance parameters (*e.g.*, frictional drag) are obtained by scaling in Reynolds number. Consider the Reynolds number scaling of flow drag inside a pipe in Fig. (3). For sufficiently low viscosity, the scale size of the boundary layer shrinks sufficiently so that other physical processes determine the boundary physics, *i.e.*, when the layer shrinks to the size of the mechanical roughness of the pipe wall. The same qualitative process is to be expected for H-mode confinement: the global scaling depends on the boundary layer scaling, which itself may change as the boundary layer width shrinks and MHD effects dominate. Restating this, the assumptions needed to justify conventional $\rho*$ scaling extrapolations are inapplicable, since a crucial dimensionless parameter, the pedestal β, acquires an explicit dependence on $\rho*$ in view of Eq. (4).

The widely used expression ITER93H assumes that confinement depends on all variables in a log-linear way. However, Dorland and Kotschenreuther [26] found that variables containing estimates of $\alpha/\rho*^2$ or $\beta/\rho*^2$ from global quantities consistently show the most evidence of non-log-linear behavior in the dataset. There is a slight non-log-linear degradation of H as the global quantity $\alpha/\rho*^2$ is increased.

The discharges in the H-mode database are limited to $\alpha/\rho* < 45$. Using ITER93-H, $\alpha/\rho* = 160$ for ITER. Let us consider JET discharge #33131, an ITER H-mode demonstration discharge which exhibited an apparent transport β_N limit due to ELMs [25]. This discharge had the highest value of $\alpha/\rho*$ of all the reported JET and DIII-D ITER demonstration discharges, with $\alpha/\rho* = 33.3$. The ELMs in this discharge have been interpreted as being due to proximity to the L-H threshold, since $P_{heat}/P_{thresh} = 2$. However, other ITER similar discharges [25] had $P_{heat}/P_{thresh} = 2$, and did not show degraded degraded confinement. Furthermore, in 33131, the ELM frequency decreased by a factor of two as the heating power was stepped down by a factor of two. This proportionality is consistent with profiles near the $\alpha/\rho*$ limit.

Since the functional form of the confinement degradation with $\alpha/\rho*$ is not known, and there is no statistical data for relevant $\alpha/\rho*$, we use the following reasoning. Analysis by the ITER JCT [27] supports the argument that the edge pressure gradients are limited by MHD ballooning modes over a distance of several ρ_{pol} (and proposes this as a possible physical mechanism for the Greenwald limit, when MARFE's are also included). An expression similar to Eq. (4) is obtained. Since $\rho*$ is about 5--10 times smaller on ITER than on present machines, Eq. (4) implies a severely limited pedestal β. To ameliorate this, we use a larger value of C, which is consistent with strong plasma shaping [21]. To examine ITER, we take the density profile to be flat from the pedestal inward and use Eq. (4) for the boundary temperature. Using the ITG model in a predictive transport code with ITER base case parameters, and depending upon details of the current and density profiles, the energy confinement time is roughly 2.4 seconds, or $\tau \sim \tau_{ITER89\text{-}P}$.

This implication of the limitation of the pedestal pressure on global confinement follows from empirical evidence as well. ITER requires a central temperature of roughly 15 keV. If the boundary temperature is limited to 300 eV, then the required ratio of the central temperature to the pedestal temperature is 50. This ratio is simply related to the radial average of $\langle R/L_T \rangle$ over this region, and this would be 12 for ITER. Experimentally obtained values of $\langle R/L_T \rangle$ (from the ITER profile database) are shown in Fig. (1). Higher values of $\langle R/L_T \rangle$ are found in L-mode plasmas, with higher transport losses, consistent with the ITG model. For $T_i/T_e \sim 1$, ITER would therefore be expected operate deep in the L-mode confinement regime, or in H-mode, with substantially lower central temperatures.

Confinement performance at the L-mode level in ITER would result in Q ~1. This may seem paradoxical, since present machines which are much smaller than ITER are anticipated to achieve Q close to one in high confinement operating modes. This demonstrates that the confinement improvement obtained by taking advantage of favorable parametric dependences of the mechanism causing transport can easily outweigh the confinement advantage of larger size. We thus turn to advanced confinement modes which have been found on TFTR [28], DIII-D [29], and other tokamaks with reversed central shear.

8. Advanced Confinement

Several analyses of TFTR and DIII-D reversed shear discharges have been carried out by ourselves and others in the community. The strong confinement enhancement found in reversed shear discharges is generally found to derive in large part from shear flow stabilization, with assistance from low local magnetic shear to reduce the growth rate. Our further local shear analysis of TFTR discharges shows that typical levels of reversed global shear reduce growth rates only slightly, and that the main contributor to the local shear reversal is from the large Shafranov shift. Because shear flow stabilization has an explicit unfavorable $\rho*$ scaling, one is forced to consider geometries with larger Shafranov shifts to take advantage of "second stability" regimes for ITG/TEM modes.

Maximization of the stabilizing effect of Shafranov shift leads one to consider oblate, reverse triangularity plasmas, with elongation less than unity (inward pointing triangle). There are many potential advantages to this configuration. However, their MHD stability properties are generally regarded to be poor. We have therefore begun a series of profile optimization studies using the MARS and CHEASE codes [30], in conjunction with the gyrokinetic stability codes, to look for self-consistent (transport and MHD) profiles with favorable second stability properties. For κ = 0.6, δ = - 0.5, R/a = 2, and with an ideal wall between r/a = 1.05 and 1.2, we have found profiles stable to MHD ballooning and n=1 kink modes at $<\beta^*>$ = 3.9% and β_N = 4.9. Preliminary microinstability calculations find that pressure profiles with this range of $<\beta^*>$ may be in the second microstability regime for ITG/TEM modes. However, we must upgrade our gyrokinetic codes to describe electromagnetic perturbations proportional to $\delta B_\parallel$ before reaching this conclusion.

In more conventional geometries, VH-mode plasmas find MHD second stability in the plasma edge for strongly shaped, high poloidal β, and appropriate edge current values [Huysmans]. We find that profiles qualitatively consistent with these MHD stability results, which are deeply into the MHD second stable regime, are very close to ITG/TEM second stability, with growth rates so low that velocity shear effects at the stongly reduced levels of a reactor are still sufficient for stabilization. Thus, with edge current profile control, a reactor relevant mode similar to a VH-mode may be possible with sharply reduced velocity shear.

REFERENCES

[1] KOTSCHENREUTHER, M., DORLAND, W., BEER, M.A., HAMMETT, G.W., Phys. Plasmas **2** (1995) 2381;
DORLAND, W., et al., in Plasma Physics and Controlled Nuclear Fusion Research 1994 (Proc. 15th Int. Conf. Seville, 1994), Vol. 3, IAEA, Vienna (1996) 463.

[2] CONNOR, J.W., et al., IAEA-CN-64/FP-21, this volume.

[3] KOTSCHENREUTHER, M., et al., Comput. Phys. Commun. **88** (1995) 128.

[4] BEER, M.A., HAMMETT, G.W., Phys. Plasmas **3** (1996).
BEER, M.A., et al., Phys. Plasmas **2** (1995) 2687;
WALTZ, R.E., et al., Phys. Fluids B **4** (1992) 3138.

[5] WALTZ, R.E., et al., Phys. Plasmas **1** (1994) 2229.

[6] PARAIL, V.V., et al., in Plasma Physics and Controlled Nuclear Fusion Research 1994 (Proc. 15th Int. Conf. Seville, 1994), Vol. 1, IAEA, Vienna (1995) 255.

[7] DE ANGELIS, R., et al., in Controlled Fusion and Plasma Physics (Proc. 22nd Eur. Conf. Bournemouth, 1995), Vol. 19C, European Physical Society, Geneva (1995) I-053.
[8] DURST, R., et al., Phys. Rev. Lett. **71** (1993) 3135.
[9] Introductory fluid mechanics texts usually describe this; see, for example, VENARD, J.K., Elementary Fluid Mechanics, 6th edn, Wiley, New York (1982) 357-387.
[10] SHAING, K.C., CRUME, E.C., Jr., Phys. Rev. Lett. **63** (1989) 2369.
[11] CARRERAS, B.A., et al., Phys. Plasmas **1** (1994) 4014.
[12] CORDEY, J.G., et al., Plasma Phys. Control. Fusion **37** (1995) 773; CHERUBINI, A., et al., in Proc. H-mode Workshop, Plasma Phys. Control. Fusion (1995).
[13] WEISEN, H., et al., Nucl. Fusion **31** (1991) 2247.
[14] HAWKES, N.C., et al., Plasma Phys. Control. Fusion **38** (1996) 1261.
[15] SNIPES, J.A., et al., Plasma Phys. Control. Fusion **38** (1996) 1127.
[16] IDA, K., HIDEKUMA, S., Phys. Rev. Lett. **65** (1990) 1364.
[17] SUTTROP, W., et al., in Controlled Fusion and Plasma Physics (Proc. 22nd Eur. Conf. Bournemouth, 1995), Vol. 19C, European Physical Society, Geneva (1995) III-237.
[18] CAROLAN, P.G., et al., ibid., p. II-133.
[19] HATAE, T., et al., in Rep. 96-018, Japan Atomic Energy Research Inst., Ibaraki (1996) 68.
[20] OSBORNE, T.H., et al., Nucl. Fusion **35** (1995) 23.
[21] KAMADA, Y., et al., Plasma Phys. Control. Fusion **36** (1994) A123.
[22] HENDER, T.C., et al., in Controlled Fusion and Plasma Physics (Proc. 22nd Eur. Conf. Bournemouth, 1995), Vol. 19C, European Physical Society, Geneva (1995) II-029.
[23] CHALLIS, C.D., et al., ibid., p. II-069.
[24] SMEULDERS, P., et al., ibid., p. IV-061.
[25] BALET, B., et al., in Controlled Fusion and Plasma Physics (Proc. 23rd Eur. Conf. Kiev, 1996), Vol. 20C, European Physical Society, Geneva (1996).
[26] DORLAND, W., KOTSCHENREUTHER, M., ITER Expert Group Minutes, Oct. 1995.
[27] PERKINS, F.W., et al., IAEA-CN-64/FP-24, this volume.
[28] LEVINTON, F.M., et al., Phys. Rev. Lett. **75** (1995) 4417.
[29] LAZARUS, E.A., et al., these Proceedings, Vol. 1, p. 199.
[30] LUTJENS, H., BONDESON, A., SAUTER, O., Comput. Phys. Commun. **97** (1996) 219; BONDESON, A., et al., Phys. Fluids B **4** (1992) 1889.
[31] HUYSMANS, G.T.A., et al., in Controlled Fusion and Plasma Physics (Proc. 22nd Eur. Conf. Bournemouth, 1995), Vol. 19C, European Physical Society, Geneva (1995) I-201.

DISCUSSION

K. LACKNER: While I can imagine that your explanation for the fast, 'non-local' response of core transport to edge cooling would hold, through a wave of 'criticality' propagating inwards, I see a difficulty in explaining the fast improvement in the core observed on JET following an L–H transition. If the L mode is indeed substantially in the overcritical regime, the plasma should react as it would to a normal heat wave on a diffusive time-scale.

M. KOTSCHENREUTHER: The L mode plasmas are frequently close to criticality till quite near to the boundary. Thus the temperature pulse has to diffuse only a short distance before criticality propagates the perturbation rapidly to the centre. Therefore the centre still responds much faster than the global confinement time.

P.H. DIAMOND: Since you have opened the Pandora's box of the cold pulse, can you explain the remarkable result of K. Gentle that an edge cold pulse heats the centre? Keep in mind that the time-scale is the easy part — predicting $\Delta T(0)$ is the essence of the problem.

M. KOTSCHENREUTHER: Those experiments are done in ohmic plasmas with $Z_{eff} = 4$. We have not parametrized the transport for such cases. However, since a cold pulse can change T_i/T_e in such a way as to cause stabilization, such a result might be explainable.

V. PARAIL: I wonder if your model can explain the experimentally observed very slow propagation of the sawtooth crash heat pulse.

M. KOTSCHENREUTHER: If the temperature diffusion equation is linearized for a critical gradient χ, the resulting equation for small temperature perturbations has a large diffusivity and also a pinch. The pinch is of the order of the diffusivity for global perturbations. Thus I would expect sawtooth pulse propagation to be significantly slower, but we have not yet simulated this.

L.J. PERKINS: Global scaling relations show that tokamak energy confinement improves with current, elongation, etc. Do these dependences arise principally from the core values of the critical temperature gradient or from values of the pedestal?

M. KOTSCHENREUTHER: The main parameter dependence of the critical gradient is T_i/T_e. To the extent that this is held constant, most of the global confinement variation comes from the edge.

J.D. CALLEN: What would be the key phenomenology that experimentalists should look for in order to see if your ∇T_i based model is relevant to the experimentally observed 'non-local' (rapid inward) transport response from edge cooling or L–H transitions? In particular, would your model imply that the interior local fluctuation level should change rapidly and significantly, and that this causes the rapid change in the transport coefficient in the plasma interior?

M. KOTSCHENREUTHER: Yes, this certainly should happen. In addition, one might try a perturbation experiment where an impurity pellet is injected into the edge. By modifying the Z_{eff} profile, ITG critical gradients can be affected in a way which is unique to the model.

A COMPREHENSIVE GYRO-LANDAU-FLUID TRANSPORT MODEL*

R.E. WALTZ, G.M. STAEBLER,
G.W. HAMMETT[1], J.A. KONINGS[2]
General Atomics,
San Diego, California,
United States of America

Abstract

A COMPREHENSIVE GYRO-LANDAU-FLUID TRANSPORT MODEL.

A physically comprehensive and theoretically based transport model tuned to 3-D ballooning mode gyrokinetic instabilities and gyrofluid nonlinear turbulence simulations is formulated. The model is applied to ITER ignition projections from DIII-D relative gyroradius scaling discharges and a description of enhanced core confinement in negative central shear DIII-D discharges based on rotational shear stabilization.

1. INTRODUCTION

A comprehensive but practically fast dispersion theoretic transport model has been developed which can be tuned to approximate the linear growth rates of a 3–D ballooning mode gyrokinetic stability (GKS) code [1] and the transport coefficients of 3–D nonlinear gyro-Landau-fluid (GLF) simulations [2,3]. As a purely theoretical model, it takes no fitting coefficients from experiments. The model has been tested against the ITER transport profile database with a good degree of correlation. The model contains rotational shear stabilization as well as Shafranov shift stabilization and is used here to illustrate DIII–D ITER H–mode demonstration dimensionally similar ρ^*-scaling discharges which extrapolate to ITER ignition, and to describe enhanced core confinement negative central shear (NCS) regimes in DIII–D in which the rotational stabilization mechanism appears to dominate.

2. FORMULATION OF THE MODEL

It is difficult to accurately and comprehensively capture the parametric dependencies of theoretically based numerical simulations of turbulent transport with simple algebraic formulas. Here we take a dispersion theoretic approach combined with quasilinear theory and a novel mixing rule. The model consists of a linear eigenvalue system obtained from an 8-fold set of reduced GLF perturbed moment equations of motion. The eigenvalue problem is solved at each plasma

* Work supported by the US Department of Energy under grant DE-FG03-95ER54309 and contracts DE-AC02-76CH0307, DE-AC02-89ER53277 and W-7405-ENG-48.

[1] Plasma Physics Laboratory, Princeton University, Princeton, New Jersey, USA.

[2] FOM Instituut voor Plasmaphysica Rijnhuizen, Nieuwegein, Netherlands.

radius for all linear growth rates. Quasilinear electron and ion energy, particle, and toroidal momentum flows, as well as turbulent e-i energy exchange, are then obtained from the phase relation between the perturbed moment eigenvectors and the perturbed E×B velocity. The toroidal ion temperature gradient (ITG) mode, the collisionless to dissipative trapped electron drift modes, and the ideal MHD ballooning modes, as well as the edge resistive modes are included. The model contains finite-β electromagnetic effects and fast ion and impurity stabilization is retained through ion dilution. The 3–D ballooning mode (k_y,k_x,θ) GLF equations of motions given in Ref. [2] are the starting point for the model. We have taken the passing electrons to be massless and isothermal but have retained resistivity.

A key feature of the model is that the dependence on global magnetic shear $\hat{s}$, local shear or Shafranov shift (α), and toroidicity is retained in the reduction of the linear equations. We do this by assuming fixed trial wave functions in the extended ballooning angle θ for the leading $k_y \propto 1/\rho_s$, high-n drift-ballooning mode. With even and odd Gaussian trial functions $\{\Theta_e,\Theta_o\} = \{1,(i\theta/\theta_{rms})\}\ \int \exp(-\theta^2/4\theta_{rms}^2)$ and weighted averages $\langle F\rangle = \int d\theta F\Theta_e^2 / \int d\theta \Theta_e^2$, $\langle F\rangle_{eo} = \int d\theta F\Theta_o\Theta_e / \int d\theta\Theta_o^2$, the along the field line θ dependent quantities become simple numbers: $k_\parallel = \hat{k}\ (1/Rq)$ $\langle i\partial/\partial\theta\rangle_{eo} = \hat{k}\ (1/Rq)/(2\ \theta_{rms})$ for parallel wave number, $\omega_D = k_y\ (2/R)\ \langle[\cos\theta + (\hat{s}\theta - \alpha\sin\theta)\sin\theta]\rangle$ for the curvature drift frequency, $\tilde{k}_x = k_y\ [\langle(\hat{s}\theta - \alpha\sin\theta)^2\rangle]^{1/2}$ the radial wave number, and finally $\sqrt{\varepsilon} = \hat{e}\{(r/R)[1+\langle\cos(\theta)\rangle]/[1+r/R\langle\cos(\theta)\rangle\}^{1/2}$ for the trapping fraction. By making the inverse ballooning mode width $1/\theta_{rms}$ a linearly increasing function of q and of shear $\hat{s}$, as it is physically, we are able to obtain very good fits to a 3–D GKS code with fit factors $\hat{k}$ and $\hat{e}$ near unity. (Physically $1/\theta_{rms}$ is also increasing function of β, but better fits to the GKS code are obtained by an enhancement factor on β.) Since the trapped electron moments include both density and pressure, we are able to retain an energy-dependent collisional detrapping frequency. In all, we have two moments for the trapped electrons and two for the passing electrons, and four (density, parallel velocity, parallel and perpendicular pressure) for the passing ions. The ion gyroradius Bessel functions are evaluated with Pade approximates. Admixture of even/odd trial functions allows treatment of parallel velocity shear.

The drift ballooning mode stability then depends on the $\hat{s}$, α, q, R/a, r/a, β, T_i/T_e, gradient lengths a/L_{n_e}, a/L_{n_i}, a/L_{T_e}, a/L_{T_i} collisionality $\nu_{ei}/(c_s/a)$, and parallel velocity shear rate $\gamma_P = dv_\phi/dr/(c_s/a)$. [In this paper, a is an arbitrary radial norm length, rates are in units of (c_s/a), cross field wave numbers in $1/\rho_s$, and diffusivity in $(c_s/a)\rho_s^2$ with $\rho_s = c_s/\Omega_i$, and $c_s = (T_e/m_i)^{1/2}$.] Figure 1 illustrates some comparative fits for the growth rates for the collisionless ($\nu_{ei} = 0$) electrostatic limit ($\beta = 0$). [Unless stated otherwise, the standard parameters are $\hat{s} = 1$, $\alpha = 0$, $q = 2$. $R/a = 3$, $r/a = 1/2$, $\beta = 0$, $T_i/T_e = 1$, $a/L_{n_e} = 1$, $a/L_{n_i} = 1$, $a/L_{T_e} = 3$, $a/L_{T_i} = 3$, $\nu_{ei} = 0$, and $\gamma_P = 0$, $k_y = 0.3$.] It is apparent that the reduced GLF model captures the q dependence well, the strong negative shear stabilization at high α, and the loss of the critical temperature gradient at peaked electron densities due to the trapped electron branch. We have satisfactorily tested the reduced GLF growth rates against the GKS code varying all parameters around the standard points at low and high trapped electron collisionality. The transition to finite collisionality and onset of the ideal MHD limit is well matched. A more detailed test to verify the accuracy of the critical gradient remains. Conversion of the circular s-α model to real geometry is also left to future work. Here we make the plausible assumption that all gradients should be taken along the average midplane minor axis.

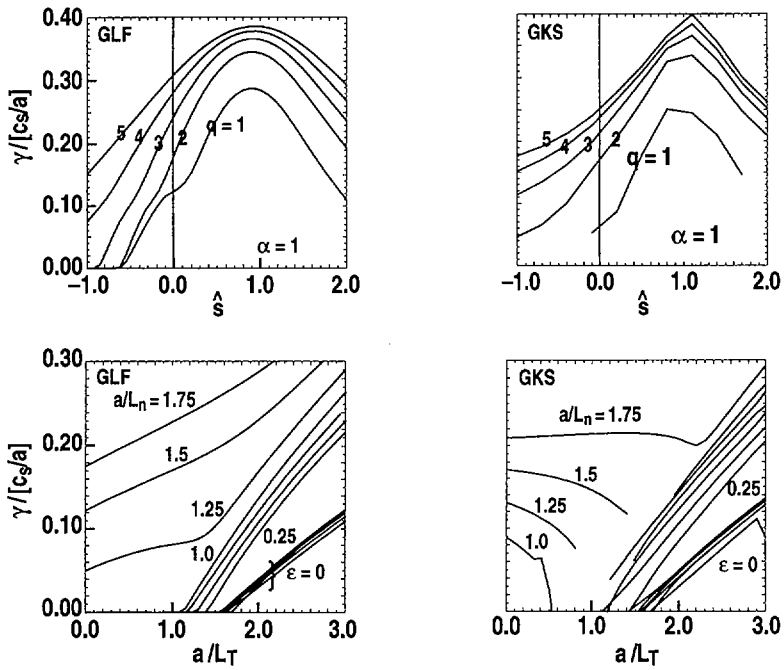

FIG. 1. Example growth rate fits of the reduced GLF model (left) to the GKS code (right).

The model is completed by using a spectrum of 10 k_y drift-ballooning modes to evaluate a mixing length rule for the perturbed E×B velocity used in the quasi-linear flows. The nonlinear saturation (as applied to each k_y and dispersion theory root or branch) is given by the mixing rule rate $\tilde{v}_{E\times B}\cdot k_\perp \approx \gamma_{net}^{1/2}\ \gamma_d^{1/2}$ where γ_{net} is the net growth rate of the leading ballooning modes after accounting for rotational shear stabilization and γ_d is the damping rate of a representative n = 0 radial mode ($k_y = 0$, $k_x \neq 0$) which can be approximated by the ion curvature drift frequency of the corresponding finite-n ballooning mode. In the simple limit of retaining only the E×B motions, it is easily shown that this novel mixing rule results in a quasilinear ion heat diffusivity $\chi \approx 3/2\ \gamma_{net}/k_\perp^2\cdot\gamma_d\gamma/(\gamma^2+\omega^2)$ with the dependence on radial mode damping and saturation with temperature gradient seen in recent adiabatic electron ITG mode simulations [2,3]. (To be more precise, a mixing rule rate $\gamma_{net}^{3/4}\ \gamma_d^{1/4}$ gives a better description of the radial mode dependence and $\gamma_{net}^{1/4}\ \gamma_d^{3/4}$ better describes the extreme temperature gradient saturation. We have taken a compromise which better describes the threshold and the dependence of χ on γ_{net}.) The nonlinear simulations [2] have shown that rotational shear stabilization of transport can be described by setting $\gamma_{net} = \gamma - \gamma_E - \gamma_*$ where γ is the drift-ballooning mode growth rate in the absence of rotational shear, $\gamma_E \approx (r/q)\ d\ (qV_{E\times B}/r)/dr$ is the E×B (or Doppler shift) rotational shear rate, and γ_* is a diamagnetic rotational shear rate associated with other profile variations over the modes. It is likely associated with the drift mode rotation in the absence of E×B, but we shall generally ignore it in applications of the model. (Also, general geometry formulas for γ_E may give significantly larger rates.) Unlike the ballooning mode rate γ which is independent

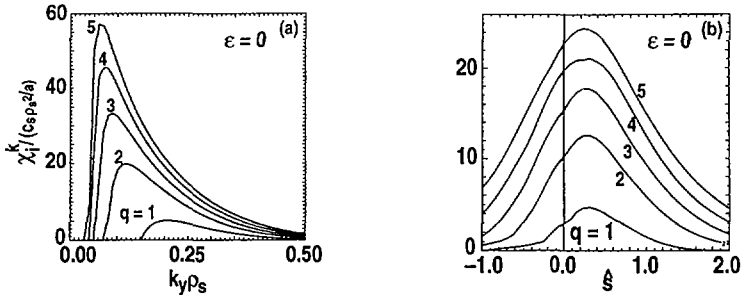

FIG. 2. Diffusivity spectrum (a) and diffusivity (χ_i) versus $\hat{s}$ (b) at several q.

of $\rho^* = (\rho_s/a)$ for $k_y \propto 1/\rho_s$, diamagnetically induced γ_E (and γ_*) increase with ρ^* breaking the otherwise gyroBohm scaling of the transport coefficients. Transport coefficients can decrease going to small ρ^* or decrease to the point of stability at large ρ^* where $\gamma_{net} = 0$. Thus, schematically, in the absence of E×B rotation induced by toroidal rotation v_ϕ, we have $\chi \propto \chi_{Bohm}\cdot\rho_* (1 - \alpha'\rho_*)$ with $\alpha' \propto 1/\gamma$ which has a distinctly non-power law dependence on ρ_*. While this picture was developed from nonlinear ballooning mode simulations (in a local cyclic annulus) with E×B shear linearly coupling the ballooning modes at different k_x [2], the breaking of gyroBohm scaling near threshold by diamagnetic shear stabilization and with correlation lengths continuing to scaled with the local gyroradius ρ_s is fully consistent with recent 2–D full radius toroidal simulations [4].

Figure 2 illustrates some of the parametric dependencies for the ion heat diffusivity in the limit of ITG modes with adiabatic electrons. Figure 2(a) shows how the shift of the diffusion spectrum to lower k_y at higher q results in the nearly linear q dependence of χ_i. χ_i versus $\hat{s}$ at various q is shown in Fig. 2(b). The reduction at reversed shear is more significant at larger α. By construction of the model, increasing γ_E stabilizes the contributions at low-k_y to the point of vanishing χ at $\gamma_E = \gamma_{max}$. The reduction of transport for $\hat{s} < 0$ and stabilization with γ_E has been demonstrated in simulations [2]. Our model has been normed to $\chi_i = 3.7\ (c_s/a)\rho_s^2$, the value from Beer's GLF ITG adiabatic electron turbulence simulations at $R/a = 3$ $a/L_T = 3$, $a/L_n = 1$, $\hat{s} = 1$, $\alpha = 0$, $q = 1.5$, $T_i/T_e = 1$ [3]. All other transport flows follow from quasilinear theory using this norm point. Preliminary checks against χ_e and χ_i simulations with trapped electrons [3] appear satisfactory. However, remaining uncertainties in the grid resolution of the simulations and the model fits could be characterized by as much as a factor 2× larger diffusivity. In most instances, this has no effect on fitting experiments because of forced marginality to the critical gradient. We discuss its effect on ITER projections below.

3. TRANSPORT BIFURCATION MECHANISMS IN THE MODEL

Turbulent transport fluxes typically increase with their corresponding plasma gradients in density, temperature, or rotation at low values; but in some instances, they can decrease at high gradients allowing the transport to bifurcate at a critical flux level jumping to a state of enhanced confinement: a higher gradient supported by the same flux. Our comprehensive model contains transport bifurcation mechanisms based on rotational shear stabilization and possibly on α-stabilization.

In this paper, we discuss only the former which we believe is most relevant to DIII–D NCS core confinement. Figure 3 illustrates some special idealized limits in which the turbulent transport fluxes are plotted against driving gradients and show a maximum in the flow. Figure 3(a) is a heat flow bifurcation and Fig. 3(b) a momentum flow bifurcation. The neoclassical fluxes which increase linearly with gradients have been be added as indicated. In the case where there is no toroidal rotation, the E×B rotation is in balance with the diamagnetic rotation and the neoclassical poloidal rotation. In the banana regime, this is approximately the same as E×B in balance with a density gradient diamagnetic rotation. The E×B rotational shear has a leading term proportional to the temperature gradient that drives the energy flow: $\gamma_E = (\rho_* \cdot a/L_n)\ (a/L_T) + \cdots$. Figure 3(a) shows how quickly the normed power flux ($\hat{Q}$) [normed to $nTc_s\ \rho^{*2}$] threshold (maximum versus gradient) for this bifurcation increases with decreasing density gradient and, more importantly, with decreasing relative gyroradius ρ_*. In this particular instance, the power threshold P_{th} has much worse than Bohm-like $a^2nTc_s\ \rho_*$, or approximately $P_{th}/[a^2nTc_s] \propto (1/\rho_*)^{1/2}$. This type of diamagnetic rotational stabilization heat flow bifurcation has been proposed as a mechanism for the L/H transition [5] and the unfortunate scaling to lower ρ^* may be why the H–mode power threshold has such poor scaling toward reactors at smaller ρ^*. A second rotational shear mechanism can result from E×B rotation arising from beam driven toroidal rotation. Shear in the toroidal rotation γ_P drives instability and transport, but for purely toroidal rotation (ignoring smaller diamagnetic components) $\gamma_E = (r/Rq)\gamma_P$ and the E×B stabilization can win out (particularly at low q/r). Figure 3(b) shows how the normed toroidal momentum flux ($\hat{\Pi}$) can bifurcate to a state of larger rotational shear at fixed temperature gradient. Note that at high values of q/r, the high gradient enhanced rotation state can still be turbulent because of γ_P drive. This type of momentum bifurcation has been proposed as the cause of the VH–mode enhanced confinement in DIII–D [6], and we argue below that it is dominant in the DIII–D NCS core transport barrier. The mechanism has been seen in ITG turbulence simulation of rotationally stabilized viscosity [2]. Since not only the viscosity η_ϕ, but also the heat diffusivity χ will be smaller in the enhanced rotational state, and in steady state the heat and momentum flow maintain a constant ratio, the temperature gradient also will jump to a higher value. In reality, the bifurcations involve transport in density, temperature and rotation, and several

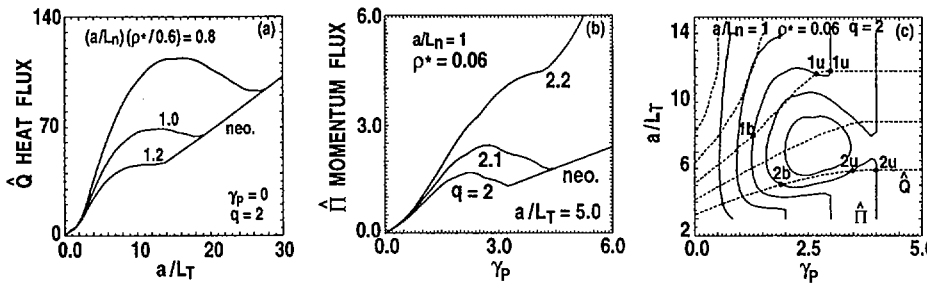

FIG. 3. Bifurcations: diamagnetic heat flow (a), toroidal momentum flow (b), and combined mechanisms (c) showing intersecting contours of $\hat{Q}$ and $\hat{\Pi}$.

mechanisms may contribute simultaneously. The multi-channel nature of L/H mode, VH–mode, and internal transport barrier bifurcation have been treated by Staebler, et al., [6] with rotational stabilization of heuristic models. Our purpose here is to quantify these bifurcations with a comprehensive physical transport model. Figure 3(c) shows a more comprehensive test of a multi-channel bifurcations where we have plotted contours of the momentum flux and the power flux against both the rotational shear γ_P and temperature gradient (a/L_T). Since here $\gamma_E = (r/Rq)\,\gamma_P - (\rho_* \cdot a/L_n)\,(a/L_T)$ both diamagnetic heat flow bifurcations and toroidal momentum bifurcations types are indicated. The three point intersection of $\hat{\Pi}$ and $\hat{Q}$ contours illustrate true bifurcation: b1, u1, n1 are respectively the bifurcation, unstable, and neoclassical points for the diamagnetic type and b2, u2, n2 are the corresponding points for the toroidal rotation type bifurcations.

4. L– AND H–MODE DATA SETS, DIII–D-ITER DEMO SHOTS, AND DIII–D NCS DISCHARGES

Using a fast "shooting" transport code, the model has been tested against data sets of L– and H–modes from the ITER transport database of more than 50 discharges from DIII–D, JET, TFTR, and JT–60. Using experimental boundary conditions at the 90% minor radius, and taking density profiles from the experiment, correlation with confinement times or stored energy is within an rms of 20% (or about 40% in the $n_0T_0\tau$ values). One might hope for 10% (or 20%) correlation in the range of experimental error bars, but uniform testing of several currently popular empirical and theory based models on this data set has not found higher correlation [7]. The rms deviation of "incremental stored energy" (above the boundary temperature) ratios is 30%. This deviation is comparable to global empirical scaling results applied to the small data set. A persistent problem with the present model which includes trapped electron modes is that it often cannot support peaked experimental density profiles with the limited core plasma flow supplied by the beam fueling.

Figure 4 illustrates transport code simulations of the DIII–D ITER H–mode demonstration dimensionally similar ρ^*-scaling discharges: a (Shot 82788) high-ρ^* shot in Fig. 4(a) and a (Shot 82205) low-ρ^* shot (1.6× lower ρ^*) in Fig. 4(b). This pair was found experimentally to have gyroBohm global confinement time or power scaling [8]. Rotational stabilization is an important consideration for these discharges. In fact, it is almost impossible to keep the same Mach number fixed as it should be for dimensionally similar discharges with the same beta, collisionality, safety factor, shape, and allowing only ρ^* to change. However, rotational effects are counteracting: diamagnetic against toroidal co-rotation in determining γ_E, and destabilization by γ_P against stabilization by γ_E. Ignoring rotational effects (setting $\gamma_E = 0$ and $\gamma_P = 0$, and turning our model into a gyroBohm scaling model), drops the peak temperatures by about 20% in <u>both</u> the high-ρ^* and low-ρ^* discharges. We believe that neither rotational effects nor differences in ρ^*-scaling account for the relatively poorer fit of our model to the high-ρ^* shot in Fig. 4(a); the difference can be traced to dissimilarity in the density profiles. The temperature profiles are close to marginal with a 2× increase in model diffusivity giving the same result.

Figure 4(c) shows the model ignition simulation of the low-ρ^* discharge scaled up by 3.2× in the B-field and 4.6× in the radii to ITER at a 7.8× smaller ρ^*. The dimensionally similar peaked density profiles with 10% ion deficit is scaled by 2.9×

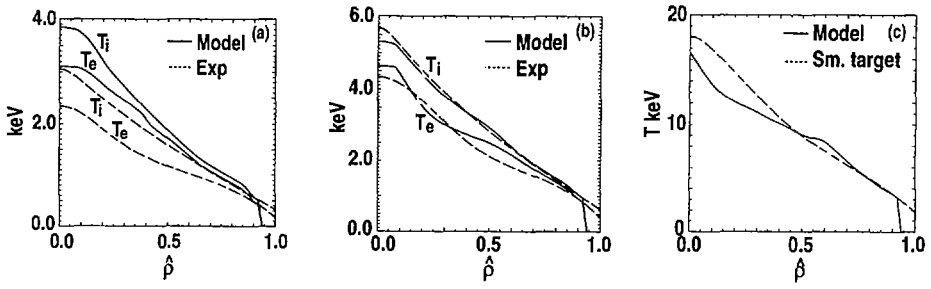

FIG. 4. Model comparison with DIII-D high ρ (a) and low ρ* (b) ITER demonstration discharges, and (c) near dimensionally similar ignition projection to ITER.*

from $\bar{n}_e = 5$ to 15×10^{13} cm^{-3} and the H–mode pedestal e-i average temperature at 90% is scaled by 3.6× from 0.95 to 3.5 keV. This keeps all dimensionless parameters fixed except ρ*. The temperature equilibrated ignited state has no auxiliary power or rotation ($\gamma_E = 0$, and $\gamma_P = 0$) and only alpha-power heating and bremsstrahlung (as well as synchrotron) loss. The model temperature self-consistent with the net alpha heating is coincidentally close to the dimensionally similar target temperature profile with 3.6× larger e-i average temperature shown as a dashed line. At 1× (and 2×) the model diffusivity strength, the alpha power production is 324 (235) MW (close to the ITER design point) and the transport loss (alpha power less radiation) through the boundary is 242 (162) MW. This is close to a 53× Bohm-like scaling of the 4.8 MW of transport power from the DIII–D discharge to 255 MW even though the gyroBohm scaling of the DIII–D shots at perfect similarity would require only 6.8 × 4.8 MW or 33 MW of transport power. This loss of gyroBohm scaling is due to forced equilibration which removes any hot ion stabilization and, more importantly, loss of rotational stabilization at lower ρ* and negligible toroidal rotation. (If we had retained the rotational shear rates fixed at DIII–D experimental values, turning our model into a purely gyroBohm model, the peak temperatures would have been 30% higher and the alpha power driven up to 700 MW.) A key uncertainty in projection of the H–modes to ignition is whether the pedestal temperatures can be maintained at the rather high similarity values used. At 70%, the assumed pedestal temperature H–mode ignition becomes marginal as T(0) drops from 16.8 (14.5) to 14.2 (11.5) keV and the alpha power to 177 (105) MW, and the transport power to 110 (44) MW which may be insufficient to support the H–mode threshold. The projection results at 2× the model diffusivity are virtually identical to those for the IFS–PPPL model [9] in this peaked density profile case.

A distinguishing feature of the present model is its ability to describe many aspects of enhanced core confinement as in the NCS DIII–D discharges without further modification. (Again, a 2× increase in model diffusivity makes no difference.) Taking the rotational shear rates from the experiment, we find that γ_E can become so large as to shut off transport from low-k drift ballooning modes in all channels allowing only neoclassical transport over a large core plasma. Neoclassical electron transport is exceedingly small and there is no evidence that it is obtained experimentally. A residual electron heat transport may be caused by high-k η_e-modes with (nearly) adiabatic ions. We include these in our model by

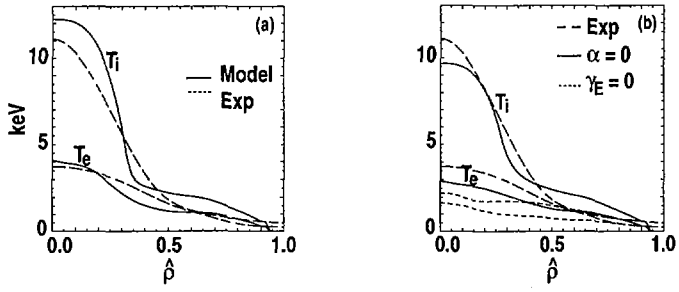

FIG. 5. Model comparison to NCS DIII-D discharge (a) and $\alpha = 0$ and $\gamma_E = 0$ (b).

assuming a simple isomorphism (or e-i reversal of labels) with adiabatic electron η_i-mode (or ITG) turbulence. Their $(m_i/m_e)^{1/2}$ larger growth rates prevent η_e-modes from being stabilized by γ_E. Normally, their transport is so small as to be ignorable, but inside the ion neoclassical transport barrier they prevent the electron temperature from running away with neoclassical electrons. Figure 5(a) shows a DIII–D NCS discharge (Shot 84736 at 1300 ms) [10]. A 25% decrease in the experimental γ_E profile results in a peak ion temperature drop of more than 50%. Although for numerical reasons we have not yet succeeded in reproducing the formation of this core transport barrier with a full-time dependent simulation of the heat and toroidal momentum channels, and determining the scaling of power thresholds with ρ^*, there seems little doubt that it must be dominated by a momentum channel bifurcation. γ_E is about 150% co-toroidal rotation with a compensating 50% diamagnetic component at the barrier ($\hat{\rho} = 0.3$). The maximum negative shear is $\hat{s} = -0.25$ and shear reversal point is near $\hat{\rho} = 0.4$. The maximum α is 0.7 in the barrier and α-stabilization adds to the good confinement. Figure 5(b) shows the effect of setting $\alpha = 0$ and the effect of setting $\gamma_E = 0$. No barrier is evident without γ_E. In this particular NCS discharge, there is experimentally no significant improvement in the core plasma transport (no large density peaking) and although core toroidal momentum diffusivity (viscosity) is significantly reduced, it may not reach neoclassical levels (as does the ion heat transport). This is in contradiction to our model as formulated. We can only speculate that had we allowed high-k η_e-modes to have some non-adiabatic ion response; or, more likely, allowed some of the high-k η_e-mode turbulence to cascade to lower k_y where the ions could respond, then some level of turbulent plasma diffusion and viscosity might survive. In fact, a general weakness of our model is that it counts no transport for stable k_y-modes.

ACKNOWLEDGMENTS

We wish to acknowledge numerous conversations with Dr. W. Dorland, and Dr. M. Kotschenreuther (Institute for Fusion Studies, University of Texas) and Dr. M.A. Beer (Princeton Plasma Physics Laboratory). This is a report of work sponsored by the U.S. Department of Energy under Grant No. DE-FG03-95ER54309 and Contract Nos. DE-AC02-76CHO0307, DE-AC02-89ER53277, and W-4705-ENG-48. J.A.K supported by Niels Stensen Stickting and National Organization for Scientific Research, and Euratom-FOM.

REFERENCES

[1] KOTSCHENREUTHER, M., Bull. Am. Phys. Soc. 37 (1992) 1432.
[2] WALTZ, R.E., KERBEL, G.D., MILOVICH, J., HAMMETT, G.W., Phys. Plasmas 2 (1995) 2408; Phys. Plasmas 1 (1994) 2229.
[3] HAMMETT, G.W., et al., in Plasma Physics and Controlled Nuclear Fusion Research 1994 (Proc. 15th Int. Conf. Seville, 1994), Vol. 3, IAEA, Vienna (1996) 273;
BEER, M., PhD Thesis, Princeton Univ., NJ (1994).
[4] GARBET, X., WALTZ, R.E., Phys. Plasmas 3 (1996) 1898.
[5] HINTON, F.L., STAEBLER, G.M., Phys. Fluids B 3 (1991) 696.
[6] STAEBLER, G.M., et al., Phys. Plasmas 1 (1994) 909;
STAEBLER, G.M., WALTZ, R.E., WILEY, J.C., Nucl. Fusion 37 (1997) 287.
[7] KONINGS, J.A., WALTZ, R.E., Nucl. Fusion 37 (1997) 863.
[8] PETTY, C.C., et al., Phys. Plasmas 2 (1995) 2342.
[9] KOTSCHENREUTHER, M., DORLAND, W., BEER, M.A., HAMMETT, G.W., Phys. Plasmas 2 (1995) 2381.
[10] LAO, L.L., et al., Phys. Plasmas 3 (1996) 1951.

DISCUSSION

V. PARAIL: It was shown in a JT-60U experiment that χ_e is reduced in the reversed shear discharges together with χ_i. Your model seems to have difficulty explaining the χ_e reduction because of the large γ for η_e instability. Can you comment on this discrepancy between model and experiment?

R.E. WALTZ: In the model, the low k (low γ) contributions to all transport coefficients vanish completely through $\mathbf{E} \times \mathbf{B}$ shear stabilization. Only the high k contributions from η_e modes to χ_e remain to prevent the electron channel having extremely low neoclassical χ_e (60 times less than neoclassical χ_i). Hence the total χ_e can be reduced. It is possible that the model fits the JT-60 internal barrier in the electron channel, but this has not yet been checked with an actual simulation. The paper discusses known difficulties for the model and speculates on how they may be repaired.

K. LACKNER: You state that the ∇p driven $\mathbf{E} \times \mathbf{B}$ shear stabilization effects would break the gyro-Bohm scaling in extrapolation to ITER, in spite of the observed gyro-Bohm behaviour within the DIII-D data alone (in H mode). Would this not also imply that you should not have observed gyro-Bohm scaling between DIII-D and JET?

R.E. WALTZ: The combined diamagnetic and toroidal rotational stabilization effects on both the low and high ρ^* DIII-D similarity H mode pair amount to about 20% in the peak temperature. The diamagnetic effect on JET will be smaller but the toroidal effect may remain. Toroidal rotation data from the JET ρ^* experiment have only recently become available to me and I hope to check this point. However, I would note that from consideration of many transport models, it has proven difficult to relate the intrinsic ρ^* of χ with the scaling of power versus global confinement time because of imperfect similarity conditions. A case in point is the recent work of Kinsey and

Bateman, which shows gyro-Bohm χ fitting worse than Bohm confinement in DIII-D L mode similarity pairs.

M. YAGI: My question is about the non-linear simulation of the GLF model. In the non-linear simulations, you may specify the boundary condition. For example, in the local simulation the condition of the fixed pressure gradient without local pressure flattening ($m = 0$ mode) may be used as a boundary condition, and in the global simulation you may put the source into the system allowing the local pressure flattening and so on. There may be another choice of the boundary condition. Do you have any criterion to judge which boundary condition is more relevant for experimental situations?

R.E. WALTZ: The non-linear GLF simulations, on which the transport model is based, are done in a non-linear ballooning mode representation equivalent to a local radial annulus with cyclic boundary conditions with a fixed time average local pressure gradient. They do include the $n = 0$ ($m \approx 0$) or radial modes which can allow the local instantaneous pressure gradients to fluctuate to zero. In fact this is the crucial saturation mechanism, as I have noted. The paper discusses the dependence of the model on the damping rate for the $n = 0$ modes γ_d.

B. SCOTT: You've had a lot of experience in the past with magnetic fluctuations in non-linear simulations; what would be their effect in your present model?

R.E. WALTZ: The model includes finite β effects on growth rates and $\mathbf{E} \times \mathbf{B}$ transport. I believe magnetic flutter transport is completely negligible. Below the MHD β limit, increasing β leads to a small improvement in confinement. The model reproduces the circular MHD β limit, but this is inadequate for the shaped plasmas we treat, which have much higher limits. Until the model has been generalized to real geometry, I have turned off the finite β effects to avoid a false β limit.

B. SCOTT: Is the model for transport dependent on linear instabilities?

R.E. WALTZ: The model transport thresholds are completely linear. If recent simulation evidence for subcritical (non-linear) thresholds can be confirmed for core plasmas, the model will need to be modified.

MHD AND ENERGETIC PARTICLE THEORY

(Session D2)

Chairperson

T. SATO
Japan

EVOLUTION OF GLOBAL MODES AND MAGNETIC RECONNECTION IN FUSION BURNING PLASMAS*

B. COPPI, S. MIGLIUOLO, L.E. SUGIYAMA
Massachusetts Institute of Technology,
Cambridge, Massachusetts,
United States of America

F. BOMBARDA, P. DETRAGIACHE
ENEA,
Italy

Abstract

EVOLUTION OF GLOBAL MODES AND MAGNETIC RECONNECTION IN FUSION BURNING PLASMAS.

Plasmas under ignition conditions have relatively high peak pressures that can make them vulnerable to the effects of large scale pressure gradient driven modes of both ideal MHD and reconnecting types. These modes can manifest themselves as large sawtooth oscillations or as triggers of more extensive instabilities. The electron collision frequencies are higher than the diamagnetic frequencies so that the reconnecting modes are collisional. Given the very low thresholds that are found, numerically for ideal MHD, $n = 1$ modes in realistic configurations, the limits of the relevant linear stability analysis are investigated. For toroidal geometry the excitation of an $n = 2$ component of the toroidal current density is seen to mark the transition from the linear to the nonlinear stage at very low amplitudes. This and the fact that the relevent layers whose reconnection can take place are extremely narrow lead to identify a range of parameters corresponding to low values of $\gamma_{MHD}\,\tau_A$ (here, γ_{MHD} is the ideal MHD growth rate), where existing analyses have to be replaced by others including, e.g. the effects of an underlying state of microscopic turbulence that can affect the electron momentum transport and involve broader reconnection layers. A second approach is the analysis of sawtooth oscillations that are observed in most of the plasma regimes produced by the Alcator C-Mod machine which cover the range of collisionalities relevant to ignition experiments but are below the threshold for ideal MHD $n = 1$ instabilities. The main trends of the relevant observations are found to be consistent with the existing theoretical framework for reconnecting modes. The indications of existing theory and experimental analysis are that high magnetic field ignition experiments at present offer the most secure route to achieve their main objectives.

1. Introduction

Ignition regimes in Deuterium-Tritium plasmas can be reached under a multiplicity of conditions that restrict considerably the feasibility of experiments that can be realistically conceived for their attainment. The excitation of global plasma modes involving the central part of the plasma column is a primary example [1]. These modes can hinder ignition by mixing the particle

* Work supported in part by the US Department of Energy, USA, and ENEA, Italy.

thermal energy and density of the central region with that of the colder surrounding region, decreasing the fusion reaction rate, spoil the confinement of the fusion products in the region where the plasma confinement characteristics are superior and, in the worst cases, result in instabilities that involve the entire plasma column. Relevant macroscopic modes can be found within the ideal MHD approximation, or under less restrictive conditions when magnetic reconnection is involved. In existing experiments, modes of the latter type are most common and their excitation is associated with periodic sawtooth oscillations of the central plasma pressure.

The understanding of magnetic reconnection in high temperature regimes and its role in determining global stability remains one of the fundamental problems of plasma theory. In magnetically confined plasmas, the toroidicity, the global scope of the driving energy, and the particle/kinetic nature of plasmas at high temperature combine to form a complex picture. In addition, the nonlinear phase of these modes involves processes that are not usually considered and need be taken into account.

D-T ignition regimes have two relevant characteristics:

i) the central plasma pressure is relatively high, typically $p_0 \simeq 1.4 - 3.8$ MPa in the two reference regimes of operation considered for the Ignitor [2] and the proposed ITER [3] devices.

ii) The electron collision frequency ν_e is larger than the diamagnetic frequencies $\omega_{de,i}$, that are characteristic of reconnecting modes when the relevant growth rates do not exceed them [4].

Thus modes driven by the plasma pressure gradient are of primary importance, as the series of experiments carried out on D-T burning plasma by the TFTR machine has proven. In addition, characteristic ii) means that weak collisionless reconnecting modes (i.e. easy to stabilize and involving very small transitional layers) can be ruled out from consideration, while the effects of electron collisions are important in the reconnection processes. We note therefore that experiments carried out by the Alcator C-Mod machine that we analyze and that have, typically, T_e not too different from T_i and $\nu_e > \omega_{de}$, are of special interest in order to anticipate the situation of fusion burning plasmas.

In assessing the seriousness of an instability that may be found theoretically, a number of factors are taken into account. For $n = 1$ modes, where n is the toroidal mode number, it is important to evaluate the relative volumes enclosed by the $q(\psi) = 1$ and 2 surfaces, as the two main poloidal harmonics $m = 1$ and $m = 2$ of these modes have finite amplitudes within these surfaces, respectively. The analytical form of the unwinding function $q(\psi)$ that we have considered for our estimates is

$$q(\psi_N) = q_0 + (q_\psi - q_0)\psi_N^{\alpha_q} \tag{1}$$

where $\psi_N = (\psi - \psi_{axis})/(\psi_{edge} - \psi_{axis})$ is the normalized poloidal flux ($0 \leq \psi_N \leq 1$) and $q_\psi \equiv q(\psi_N = 1)$ is the so-called safety factor. We note that the value of the shear parameter $\hat{s} \equiv 2(\psi/q)dq/d\psi$ at the $q = 1$ surface is

$\hat{s} = (1 - q_0)\alpha_q$ and for the range of values of α_q that we consider ($2 \leq \alpha_q \leq 3$), $\hat{s}$ is finite on this surface. We note also that for a plasma with $q_\psi \simeq 3$, typically $r_1/a \simeq 0.5$ and $r_2/a \simeq 0.75$ where a is the horizontal minor radius and r_1 and r_2 are the radii of the $q = 1$ and $q = 2$ surfaces respectively.

Since r_1/a and r_2/a are related to q_ψ we consider the following parameter of merit against the excitation of significant internal modes:

$$M_Q = \frac{q_\psi}{\beta_{p0}} \tag{2}$$

where $\beta_{p0} = 2\mu_0 p_0/\bar{B}_p^2$ and $\bar{B}_p$ is the mean poloidal magnetic field at the plasma boundary.

When, in high temperature regimes, the modes that are excited depend on the decoupling of the plasma motion from that of the magnetic field lines and the associated electric fields have a large electrostatic component, the central plasma pressure can be transported outward without modifying the magnetic configuration. This has been predicted by one of us in the mid-seventies [5] and has been well verified by the experiments [6] showing that the $q(\psi)$ profile does not vary as a consequence of a sawtooth event. Therefore the rate of recurrence of the relevant instability depends on the rate of local heating and the rate of thermal energy transport due to underlying microscopic turbulence away from the central part of the plasma column.

The class of pressure profiles that we consider for our analysis is of the form

$$p(\psi_N) = p_0(1 - \psi_N^{\alpha_F})^{\alpha_p} \tag{3}$$

where α_p and α_F are two parameters introduced to characterize the considered profiles. A flattened pressure profile that does not allow the excitation of ideal MHD modes even for $q_\psi \simeq 3$ and relatively high values of β_{p0} corresponds typically to $\alpha_F \gtrsim 5$. We note that the equilibrium configurations found using a particular form of the PEST code [7] and assuming the forms (1) and (3) have an unrealistic current density gradient at the edge of the plasma column and we have made provisions to avoid their (spurious) effects, e.g. by placing a perfectly conducting shell at a radius $r_{sh} \simeq 1.1a$.

Since the internal modes that we consider are driven by the plasma pressure gradient and are strongly dependent on the $q(\psi)$ profile, we note that there are early experimental indications of low q_ψ regimes, besides the one we analyze primarily in this paper, that are compatible with higher values of $\beta_p = \beta_{p0}\langle p \rangle/p_0$ [8], where $\langle p \rangle$ is the volume average pressure, which have elements of the so called Second Stability Region and, clearly, deserve future attention.

2. The Case of Ignitor

The Ignitor experiment is designed to reach ignition with low values of β_p, such as $\beta_p \approx 0.25 - 0.3$, and $q_0 > 1$ by properly programming the current

evolution and then "settling down" at a total plasma current $I_p \approx 11$ MA corresponding to $q_\psi \simeq 3.6$. A scenario where the plasma current rises to 12 MA and is then decreased to 10 MA ($q_\psi \simeq 4$) is also considered. The toroidal field is 13 T, while the plasma column dimensions are $R_0 \simeq 1.32$ m, $a \simeq 0.47$ m, $b \simeq 0.87$ m with triangularity $\delta_G \simeq 0.4$. The reference ignition scenario involves peak plasma densities $n_0 \simeq 10^{21}\mathrm{m}^{-3}$ and temperatures $T_0 \simeq 12$ keV corresponding to a pressure $p_0 \approx 3.84$ MPa. For $I_p \simeq 11$ MA, $\bar{B}_p \simeq I_p/(5\sqrt{ab}) \simeq 3.45$ T we estimate $M_Q \simeq 4.5$. Thus Ignitor is designed to prevent the $q = 1$ surface from becoming excessively large even in the "relaxing" phase of the current pulse and avoiding the onset of large scale ideal MHD modes, thanks to the high field technology adopted.

High q_ψ regimes of operation are of special interest for high field devices as, even though the enhancement factor of the energy confinement time that is found in these regimes may be considerable, the total plasma current cannot be excessively decreased in an experiment aimed at ignition. Reversed shear regimes, where $q(\psi) > 1$ everywhere, fall in this class. Then ballooning modes associated with the steep pressure gradients that form in these regimes, and modes involving magnetic reconnection become a concern.

3. The Case of ITER

As presently proposed, the ITER machine would have a field $B_T \simeq 5.7$ T on axis, corresponding to $B_c \simeq 12.5 - 13$ T at the coils, plasma column dimensions $R_o \simeq 8.14$ m, $a \simeq 2.84$ m, $b \simeq 4.5$ m, $\delta_G \simeq 0.24$ and would operate with a maximum plasma current $I_p \simeq 21$ MA. This corresponds to $q_\psi \simeq 3.0$ and, since the considered peak pressure is $p_0 \simeq 8.5 \times 10^{21}\mathrm{keV}/m^3(1.4\mathrm{MPa})$, $\beta_{p0} \simeq 2.6$ and $M_Q \simeq 1.1$. We have carried out a numerical stability analysis of ideal MHD, $n = 1$ modes for this configuration using the PEST-1 code and adopting the profiles (1) and (3) with $q_0 = 0.85, q_\psi = 3, \alpha_p = 3/2$ and $\alpha_F = 1$. This implies that $p_0/ < p > \simeq 3.3$.

The main results are shown in Fig. 1: the mode growth rates, normalized to the poloidal Alfvén time, $\tau_A = r_1/v_{A\theta}$, are high (of the order of a few percent of the inverse poloidal Alfvén time), and considerably larger than the relevant diamagnetic (or drift wave) frequency. We estimate that fusion α-particles carry a substantial pressure in the reference ITER regime and may contribute unfavorably to the instability of internal $n = 1$ modes. In fact [9], there is a maximum value of β_{p0} beyond which the contribution from energetic particles changes from stabilizing to destabilizing.

As shown in Fig.2, the perturbation has a significant amplitude up to the $q = 2$ surface given the importance of the $m = 2$ harmonic for the considered equilibrium configuration. In this manner, a large portion of the plasma is directly affected by this "internal" mode. After a few e-folding times the plasma pressure in the neighborhood of the $q = 1$ surface can increase as a result of the excitation of $n = 1$ modes and, in turn, this may lead to instability of ballooning modes, as has been shown [10] to occur in TFTR just prior a major disruption.

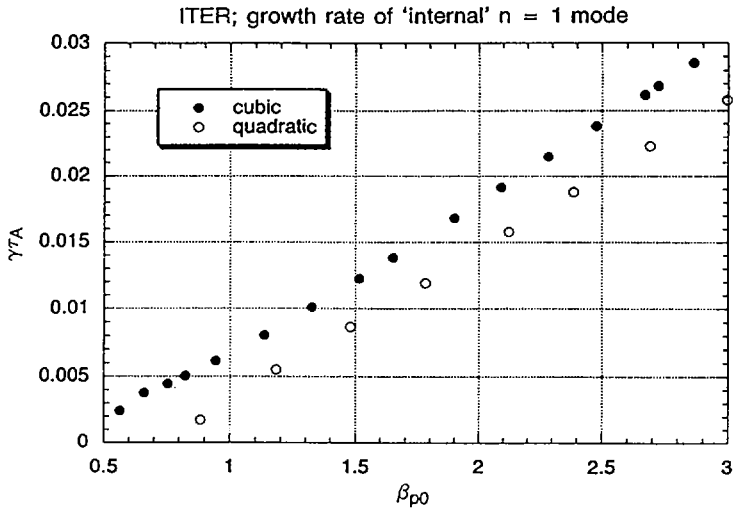

Fig. 1. Ideal MHD growth rates for the profiles presented by Eqs (1) and (3) as a function of $\beta_{p0} = 2\mu_0 p_0/\overline{B}_p^2$. *Two profiles for* $q(\psi)$ *are considered:* $\alpha_q = 2$ *and* $\alpha_q = 3$, *while only one profile for* $p(\psi)$ *with* $\alpha_F = 1$, $\alpha_p = 3/2$ *is considered. The other parameters correspond to those typical of the proposed ITER experiment for which* $\beta_{p0} \cong 2.6$ *is the reference value and* $\gamma\tau_A \cong (2.2\text{–}2.5) \times 10^{-2}$.

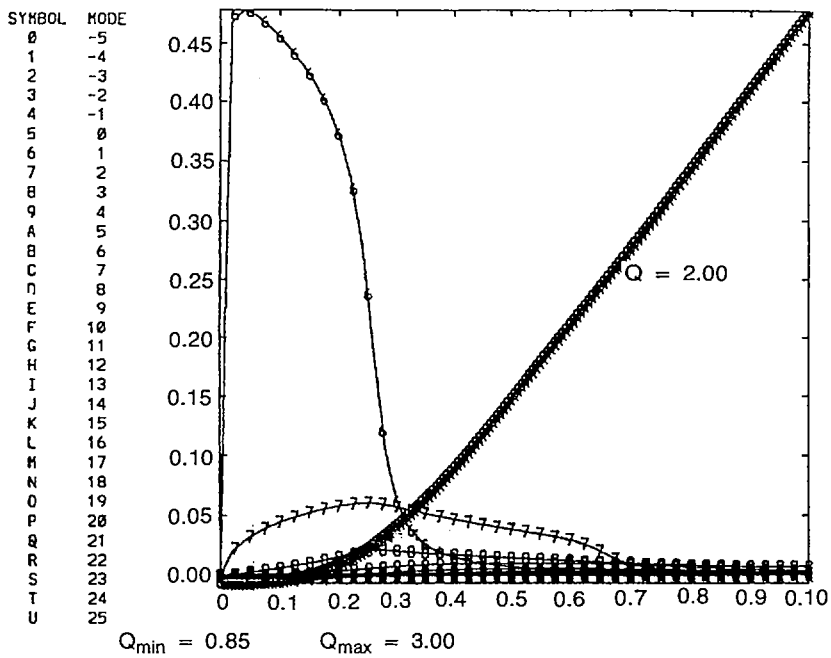

FIG. 2. Poloidal harmonics of radial displacement, represented by $\vec{\xi} \cdot \nabla\psi_N$, *versus normalized poloidal flux* ψ_N *for* $\alpha_q = 3$, $\alpha_F = 1$, $\alpha_P = 3/2$.

We note that $\psi_{N1} = [(1 - q_o)/(q_\psi - q_o)]^{1/\alpha_q}$. Therefore, decreasing the volume enclosed by the $q = 1$ surface, by taking $\alpha_q = 2$ instead of 3, reduces the growth rate of the mode. Since the principal agent for instability is the pressure gradient within the central region [11], moving the location of the maximum pressure gradient outward, e.g. by increasing α_F in Eq.(3), will result in stabilization of these modes. However, it is unrealistic to assume that, for the ITER reference regime of operation, the pressure profile is flattened in the central region to the extent that $\alpha_F \gtrsim 5$.

4. Limits of the Ideal MHD Theory

The ideal MHD analysis indicates that marginal stability conditions for $n = 1$ modes correspond to very low values of β. The question then arises whether the transition from large scale, fast instabilities associated with ideal MHD modes to instabilities which involve magnetic reconnection at their onset can be related to the ideal MHD linearized growth rate. The ideal MHD linear approximation itself may break down at small perturbation size. Nonlinearly, the ideal mode saturates to a neighboring MHD equilibrium state with a singular current sheet, in cylinder [12,13] and torus [14]. When the layer becomes sufficiently narrow, magnetic reconnection can become important in determining the ultimate state of the instability. Toroidal effects strongly influence these processes, in ways that are not yet included in analytic models. The toroidal effects are discussed with the help of the two-fluid and MHD initial value code MH3D-T [15].

Under realistic conditions, the ideal MHD linearized approximation becomes unphysical early in the evolution of the mode. The linear $m = 1$ harmonic varies sharply within a layer centered at surface $r = r_1$, whose width is $\delta \sim (\gamma\tau_A)r_1$. One way in which the linearized approximation breaks down is when the perturbed pressure gradient in the δ region becomes comparable to the equilibrium pressure gradient there, $|\partial\hat{p}/\partial r| \sim |dp/dr|$. Since $\hat{p} \simeq -\hat{\xi}_r(dp/dr)$, where $\hat{\xi}_r$ is the radial plasma displacement, breakdown occurs when $|\hat{\xi}_r| \gtrsim \delta \sim (\gamma\tau_A)r_1$. Therefore we introduce a practical criterion, $\gamma\tau_A < c_m$, where, e.g. $c_m \simeq 0.1\%$, below which the ideal linearized theory should not apply.

In a realistic torus, however, numerical simulation shows that the mode layer width for a given growth rate is much broader than for the cylindrical case. For a case with large ideal growth rate, $\gamma\tau_A = 0.016$, nonlinear effects first enter through the development of a toroidal $n = 2$ component in the toroidal current density J_ϕ while the displacement is still small, $\hat{\xi}_r < \delta \simeq \delta_{LIN}$. At this stage, $\hat{\xi}_r$ is approaching its saturation value and the mode growth rate γ has begun to decrease from its linear value. The relative magnitude of the perturbed pressure gradient and current density is still small.

One problem in ignition and other high temperature regimes is that the linearized theory, derived in the thin-layer limit, predicts that the characteristic thickness of the layer where reconnection associated with collisional resistivity or electron inertia can take place is very small. (It is represented by $\epsilon_\eta^{1/3}$

Table 1
Characteristic Parameters for Reference Regimes of Operation

	Ignitor	ITER	Alcator (Ohmic)	Alcator (RF)
$q_\psi \approx$	3.6	3.0	3.5	4.3
q_0	$\gtrsim 0.85$	≈ 0.85	< 1	< 1
$B_T \simeq$	13T	5.7T	5.4T	5.4T
$\beta_0 \simeq$	5.7%	10.6%	1.1%	1.4%
$\beta_{p0} \simeq$	0.8	2.6	0.6	1.1
$r_1 \approx$	0.2m	1.4m	0.08m	0.06m
$\nu_e/\omega_{de} \simeq$	2.9	1.5	34.8	1.1
$\epsilon_\eta \simeq$	8.6×10^{-9}	4.7×10^{-10}	2.5×10^{-6}	1.3×10^{-6}
$\rho_s/r_1 \simeq$	4.6×10^{-3}	2.4×10^{-3}	1.0×10^{-2}	2.3×10^{-2}
$d_e/r_1 \simeq$	8.3×10^{-4}	3.4×10^{-4}	3.5×10^{-2}	6.7×10^{-3}
$T_{e0} \simeq$	12keV	25keV	1.1keV	3.6keV
$T_{i0}/T_{e0} \simeq$	1	1	0.9	0.8
$n_0\,(\mathrm{m}^{-3}) \simeq$	10^{21}	1.5×10^{20}	3.9×10^{20}	1.6×10^{20}
$I_p \simeq$	11MA	21MA	976kA	823kA

for modes near ideal MHD marginal stability, where $\epsilon_\eta \equiv \mathcal{D}_m/(v_A r_1^2/R_o)$, $\mathcal{D}_m = \eta_\parallel/\mu_0$, and r_1 is the radius at which $q = 1$. Typical values are shown in Table 1.) In a torus, the width of the negative current sheet is as large, or even broader, than in a cylinder with the same global parameters, although the cylindrical mode has a much faster growth rate. An example is shown in Fig. 3, where $\gamma\tau_A = 0.039$ compared to 0.0017 in the torus. In the torus, the mode is weak enough that the current density has oscillations extending away from the layer. The thin-layer growth rate criterion, $\gamma\tau_A \sim \epsilon_\eta^{1/3}$, still roughly determines the influence of resistivity on the mode [16]. Table 2 compares the effect of resistivity on strongly and weakly ideally unstable toroidal modes. Other mechanisms may lead to a broader characteristic reconnection layer [17]. Toroidal modes are thus sensitive to resistivity at much larger layer widths than their cylindrical counterparts.

Two stabilizing effects are found numerically for the toroidal mode. First, the mode has an important $m = 2$ component at the $q = 1$ surface, in the current density $\hat{J}_\phi$, with magnitude comparable to that of the $m = 1$ component for strongly ideal-unstable modes. (For weakly ideal-unstable modes, the current density structure is more complex, as discussed below.) This effect occurs in addition to the expected coupling of the main $m^o = 1$ mode to $m = m^o \pm 1$, which extends the perturbation to the $q = 2$ surface, and it is strong even at large aspect ratios, e.g. $R/a = 10$. The perturbed $\hat{p}$ and the velocities v_ψ, v_θ remain predominantly $m = 1$.

The negative current sheet at the resonant surface exists primarily on the inboard half of the torus, as shown in Fig. 3a for a weakly ideal-unstable mode.

Table 2
Growth Rates for the $m^o = 1$, $n = 1$ MHD Mode*

ϵ_η	Sound Wave	$\gamma\tau_A$	δ_I/r_1	δ_O/r_1
Torus, Weakly Ideal MHD Unstable: $\beta_o = 0.032$				
0	OFF	0.0017	0.39	0.16
1.5×10^{-3}	OFF	0.035	0.47	0
1.5×10^{-4}	OFF	0.020	0.40	0
1.5×10^{-5}	OFF	0.014	0.39	0.18
1.5×10^{-3}	ON	0.019	0.62	0
1.5×10^{-4}	ON	0.012	0.55	0
1.5×10^{-5}	ON	0.006	0.39	0.23
Torus, Strongly Ideal MHD Unstable: $\beta_o = 0.048$				
0	OFF	0.016	0.55	0
1.5×10^{-3}	OFF	0.048	0.74	0
1.5×10^{-4}	OFF	0.037	0.62	0
1.5×10^{-5}	OFF	0.034	0.61	0
1.5×10^{-3}	ON	0.035	0.76	0
1.5×10^{-4}	ON	0.020	0.56	0
1.5×10^{-5}	ON	0.018	0.64†	0
Cylinder, $\beta_o = 0.032$				
0	OFF	0.039	0.34	0
1.5×10^{-3}	OFF	0.056	0.49	0
1.5×10^{-3}	ON	0.054	0.49	0

*Parameters as for Fig. 3, except β_o increased for strongly unstable case. Full widths δ_I, δ_O of the inboard and outboard current sheets at $q = 1$ are shown (at $\hat{J}_\phi \simeq 0$, when kink motion is inboard). $\eta = 0$ cases have $\kappa_\parallel$ due to sound wave only, $\eta \neq 0$ have strong $\kappa_\parallel$ equivalent to $8\times$ the shear Alfvén wave velocity.
†Base wide; half-height width similar to $\epsilon_\eta = 0$ and 1.5×10^{-4} cases.

At intermediate ϕ angles, both a negative and a positive current sheet exist at the $q = 1$ surface, but they are displaced poloidally towards the inboard half of the cross-section. For weakly unstable modes, there are also oscillations in $\hat{J}_\phi$ that extend outward into $q > 1$ and, associated with them, a smaller, narrower negative current sheet at $q = 1$ on the outboard side where the plasma kink motion is directed outboard. (The inverse of this sheet, with positive sign, can be seen on the outboard (right) side in Fig. 3a, opposite the direction of the

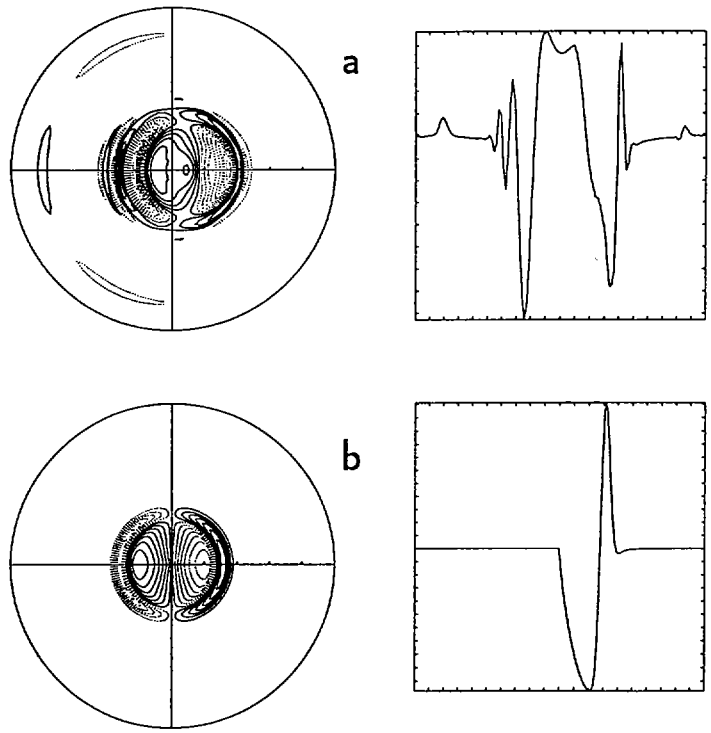

FIG. 3. Perturbed toroidal current density $\hat{J}_\phi$ or ideal MHD $m^0 = 1$, $n = 1$ mode in (a) torus and (b) a cylinder at the same global parameters, showing the importance of the $m > 1$ components in the torus. Contours of constant $\hat{J}_\phi$ in a cross-section and corresponding profile across midplane (arbitrary units) are shown. The plasma kink moves to the left (inboard). The TFTR supershot-like equilibrium has $R/a = 3$, $q_o = 0.8$, $q_a = 2.9$, $\beta_o = 0.032$ and a steeply peaked pressure profile. The $q = 1$ surface intersects the torus midplane at $r/a = -0.23$ (main negative current sheet) and $+0.41$ (narrow positive sheet) and the cylinder midplane at $r/a = \pm 0.32$ (only half the midplane profile is shown). The narrow outboard sheet in the torus vanishes together with the inboard oscillations at higher beta. The torus is weakly unstable with $\gamma\tau_A = 1.7 \times 10^{-3}$, the cylinder strongly so, with $\gamma\tau_A = 3.9 \times 10^{-2}$.

kink motion.) At strong ideal instability or large resistivity, the oscillations in $\hat{J}_\phi$ are damped and the negative current sheet on the outboard kink side of the torus also disappears, or leaves only a vestigial remnant. In the cylinder, in contrast, the linear mode always has perfect helical symmetry, $m/n = 1/1$, as shown in Fig. 3b.

The second stabilizing effect that is strong in toroidal geometry is the coupling of the linear resistive mode to sound waves, which transport energy out of the layer. The waves can broaden the layer and also damp the growth rate significantly. The effect increases with resistivity. It is important nonlinearly.

A similar phenomenon has been observed for modes with $m > 1$, for resistive MHD ballooning modes [18] and for two species plasmas (electrons and ions), first for collisionless reconnecting modes [19]. Examples of the effect on the linear mode growth rates are shown in Table 2. These new stabilizing effects may help explain why analytic estimates of the ideal MHD growth rates always predict much greater instability than do fully toroidal calculations such as PEST.

5. The Alcator C-Mod experiments

In spite of a broad variety of plasma regimes produced by the Alcator C-Mod machine [20] ($R_0 \simeq 0.67$ m, $a \simeq 0.21$ m, elongation $\kappa \lesssim 1.7$, $B_T \lesssim 8$ T, $I_p \lesssim 1.5$ MA), sawtooth oscillations are present in nearly all cases. The sawtooth period, as well as the amplitude, is observed to be independent of density for ohmic heated plasmas [see Fig. 4]. We elaborate on this referring to the nonlinear model equation for sawteeth that was introduced first in Ref.[21], which involves the three representative terms in the electron thermal energy balance:

$$\frac{3}{2}n\frac{\partial T_e}{\partial t} = E_\parallel^2\sigma_\parallel - n\nu_L T_0^0\left(\frac{T_e - T^0}{T_0^0}\right)^4 H\left(\frac{T_e - \alpha_T T^0}{T_0^0}\right) \tag{4}$$

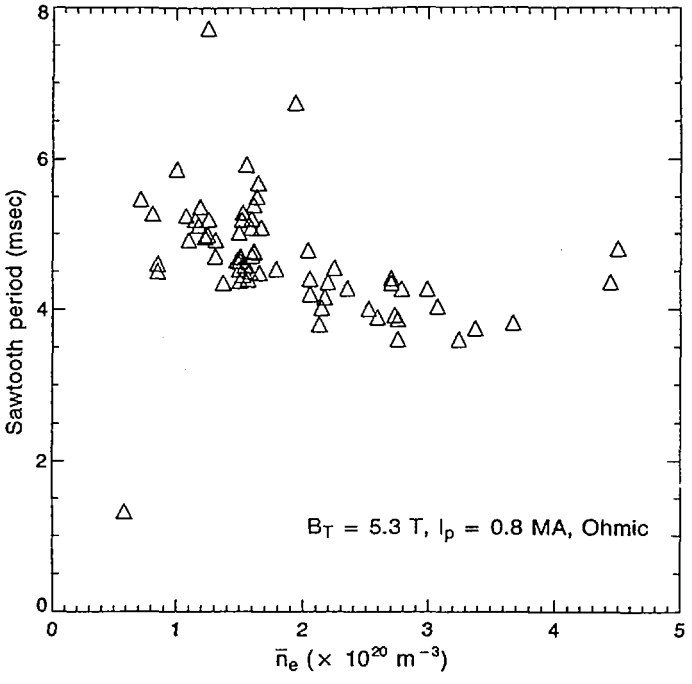

FIG. 4. Sawtooth repetition time in plasmas produced by the Alcator C-Mod machine, as a function of density.

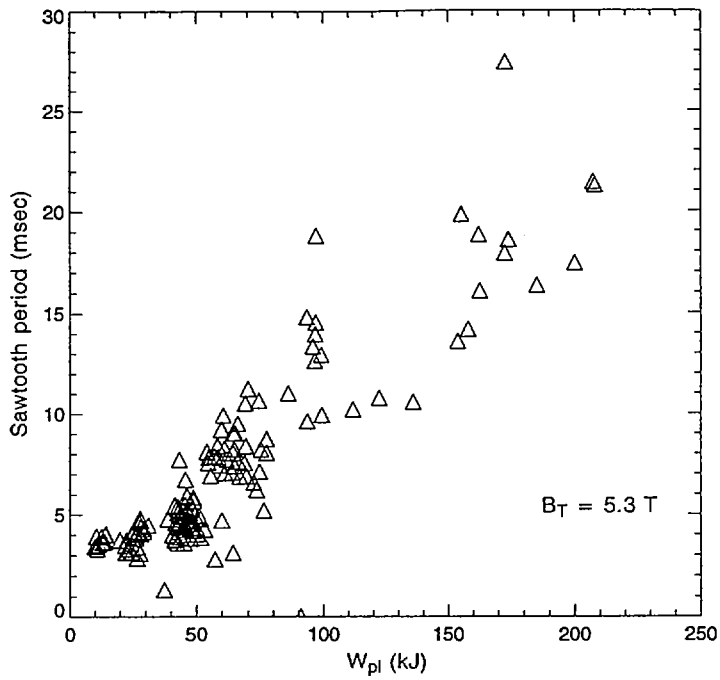

FIG. 5. Sawtooth repetition time in plasmas produced by the Alcator C-Mod machine, as a function of stored energy.

where $E_{\|}$ is the applied (constant) electric field and $\sigma_{\|} \propto T_e^{3/2}$ is the longitudinal electrical conductivity. The last term models the effect of the excitation of $m^0 = 1$ modes. The relevant threshold temperature is indicated by T^0, H is the Heaviside function and $\alpha_T = sgn(\partial T_e/\partial t)$. Thus we argue that, since the applied electric field is observed to increase with density, the rate of temperature increase should not increase by changing n. The independence of n of the sawtooth period indicates that the strength coefficient $\nu_L T_0^0$ as well as the threshold temperature T^0 are density independent. In the case where RF heating is added the sawtooth period is found to increase. To discuss this case a temperature and density independent source term S_{RF} should be added to the r.h.s. of Eq. (4).

Among the important factors not included in the model Eq.(4) we mention the loss of thermal energy, due to collisions and microscopic turbulence, and the influence of the plasma column surrounding the $q = 1$ surface. To gain insight into the nature of these factors we note that a good correlation is found also between the sawtooth period and the plasma stored energy for both Ohmic and RF heated plasmas, within the L and H confinement modes [Fig. 5]. The relevant range is $4 - 25$ msec and $W \simeq 10 - 250$ kJ at $B_T \simeq 5.3$ T. Finally we note that when the plasma current increases at constant B field, and the radius of the $q = 1$ surface increases, the sawtooth period is observed to increase also.

A systematic analysis of over twenty discharges where $q_\psi^{95} \simeq 3-4$ has been carried out, for the first time, and the typical collisionalities are in the range $\nu_{ei}/\omega_{de} \simeq 1.4 \rightarrow 35$ with Ohmic discharges being typically more collisional than RF heated discharges, where $\omega_{de} = -(c/enBr_1)(dp_e/dr)_1$ is the electron diamagnetic frequency. For comparison, the collisionality in the reference Ignitor machine is estimated as $\nu_{ei}/\omega_{de} \simeq 3$. This analysis has involved:

i) An investigation of ideal–MHD stability for representative profiles and parameters, using the PEST-1 code. The results indicate that most discharges are stable against pressure–driven ideal modes.

ii) Estimating analytically the approximate values of the ideal–MHD stability parameter λ_H (which turns out to be negative).

iii) A comparison of the behavior of the discharges to the predictions of the two–fluid resistive linear stability theory [4]. The location in parameter space of the inferred normalized quantitites $\lambda_H/\epsilon_\eta^{1/3}$ and $\omega_{de}\tau_A/\epsilon_\eta^{1/3}$ is estimated and related to the predicted [22] marginal stability curve. The Alcator C-Mod parameters have been found to correspond to the domain of predicted instability for resistive modes.

These calculations have been carried out using q–profiles obtained from reconstruction of the equilibrium by the EFIT code [23] that is used as a free-boundary equilibrium solver in the present case. Hence there is considerable uncertainty in the value of the magnetic shear parameter, $\hat{s}_1 = r_1(dq/dr)_1$. We have evaluated the ideal MHD stability parameter λ_H using the analytical formula

$$\lambda_H = \pi \left(\frac{r_1}{R_0}\right)^2 \frac{1}{\hat{s}_1^2} \left[-\delta\bar{W}_C\left(\beta_{p1}\right) - \delta\bar{W}_{shape}\right]$$

where $\delta\bar{W}_C = k_0 + k_1\beta_{p1} + k_2\beta_{p1}^2$ is the normalized perturbed potential energy in a toroidal configuration with circular cross sections, derived in [11], and $\delta\bar{W}_{shape}$ is a correction arising from the shaping of the plasma cross section [24]. Here $\beta_{p1} = \left(-8\pi/B_{p1}^2\right)\int_0^{r_1} dr\ \left(r/r_1\right)^2 (dp/dr)$, and the k–coefficients depend on the q–profile. We have computed these terms for a q–profile relevant to Alcator C-Mod with $q_0 = 0.9$, $q_\psi = 4.1$ and $r_1/a \approx 0.33$, finding that the ideal–MHD $n = 1$ mode becomes unstable at $\beta_{p1} \approx 0.16 \rightarrow 0.26$ (the critical value is rather sensitive to details in the q-profile that is chosen) and that shaping effects are weak, $\left|\delta\bar{W}_{shape}/k_0\right| \approx 7\%$. For a typical discharge with $T_{e0} \simeq 2$ keV and $n_{e0} \simeq 1.3 \times 10^{20}$ m^{-3}, we find that β_{p1} is below the critical value, concluding that Alcator C-Mod is stable against these ideal modes. A numerical analysis, using the PEST-1 code and that considers a configuration that more closely matches Alcator C–Mod, agrees qualitatively with this.

Five discharges, that is a very small minority of all those produced by Alcator C-Mod, exhibited no regular sawteeth but instead showed evidence of irregular, low–amplitude fluctuations in the ECE polychromator diagnostic. Of these all but one are predicted to be either stable or near marginal stability by the two-fluid theory, as shown by the data, indicated by crosses, in Fig. 6 (the quantity λ_H shown in this figure has been estimated via a simplified

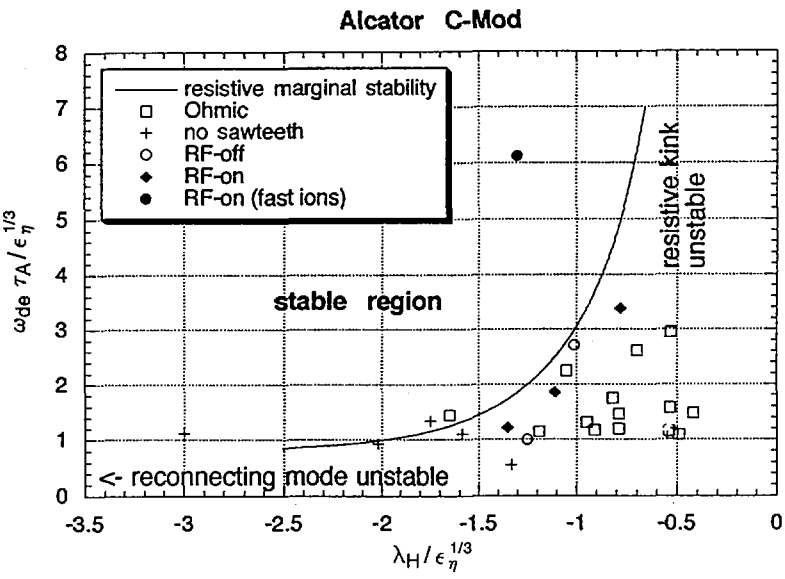

FIG. 6. Location of selected Alcator C-Mod plasmas in relevant parameter space, characterized by electron diamagnetic frequency ω_{de} and the ideal MHD stability parameter, λ_H (note that $\lambda_H < 0$ corresponds to ideal linear stability). Here, $\tau_A \equiv \sqrt{3}R_0/v_A$. All points have been verified to have $\lambda_H < 0$ by the PEST code. Given the uncertainty involved in the evaluation of $|\lambda_H|$, this figure has only indicative value.

expression, obtained from Ref. [11], which will give qualitatively significant answers).

Special attention has been given to an H-mode discharge involving high power radiofrequency minority heating and a long sawtooth period, $\tau_{saw} \approx 25$ msec. A numerical simulation of the RF power deposition, coupled with a kinetic stability analysis [25], indicates that the stabilizing contribution from energetic minority ions is sufficient to change an otherwise ideal mode ($\lambda_H > 0$) to one of the reconnecting type ($\lambda_H + \lambda_K < 0$).

Among the many discharges produced by Alcator C-Mod none has been found to have all the relevant dimensionless parameters close to those envisioned for the reference Ignitor plasmas. In Table 1 we quote two, with different degrees of collisionality one of which has a lower q_ψ and the other a larger value of β_{p0} than that quoted for the Ignitor case. Both of these discharges have $\lambda_H < 0$.

We conclude by noting that our estimate for the classical diffusion time for the plasma current within the $q \leq 1$ volume, $\tau_J = (2/\nu_{ei})(\nu_1/d_e)^2$, is more than an order of magnitude larger than the sawtooth repetition time ($\tau_J \sim 80 - 400$msec for ohmic regimes and $\tau_J \sim 300$msec $-$ 1 sec for RF heated plasmas). Since the sawtooth repetition time is between one and two orders

of magnitude smaller than τ_J it is clear that in predicting the sawtooth period of plasmas under ignition conditions the current redistribution time cannot be considered as a plausible estimate.

REFERENCES

[1] COPPI, A.C., COPPI, B., Nucl. Fusion **32** (1992) 205.
[2] COPPI, B., et al., Phys. Scr. **45** (1992) 112.
[3] ROSENBLUTH, M.N., et al., in Plasma Physics and Controlled Nuclear Fusion Research 1994 (Proc. 15th Int. Conf. Seville, 1994), Vol. 2, IAEA, Vienna (1995) 517.
[4] ARA, G., et al., Ann Phys. (N.Y.) **113** (1978) 441.
[5] COPPI, B., et al., invited paper presented at the International Conference for Plasma Physics (ICPP), Nagoya, 1980.
[6] YAMADA, Y., et al., Phys. Plasmas **1** (1994) 10.
[7] GRIMM, R.C., et al., J. Comput. Phys. 4 (1983) 94.
[8] LAZARUS, E.A., et al., IAEA-CN-64/A1-2, these Proceedings, Vol. 1, p.199.
[9] COPPI, B., Phys. Fluids B **2** (1990) 927.
[10] ZAKHAROV, L.E., et al., "Non-ideal effects in MHD", Beta Limits in Long Pulse Discharges (Proc. MHD Workshop, General Atomics, 1995).
[11] BUSSAC, M.N., Phys. Rev. Lett. **35** (1975) 1638.
[12] ROSENBLUTH, M.N., et al., Phys. Fluids **16** (1973) 1894.
[13] PARK, W., et al., Nucl. Fusion **20** (1980) 1181.
[14] PARK, W., Phys. Rev. Lett. **75** (1996) 1763
[15] SUGIYAMA, L.E., PARK, W., Growth of Magnetic Islands in a Two-fluid Torus, Rep. MIT-PTP-96/2, Massachusetts Inst. of Technol., Cambridge, MA, USA (1996).
[16] COPPI, B., et al., Fiz. Plazmy **6** (1976) 961.
[17] COPPI, B., et al., in Plasma Physics and Controlled Nuclear Fusion Research 1994 (Proc. 15th Int. Conf. Seville, 1994), Vol. 2, IAEA, Vienna (1995) 785.
[18] COPPI, B., ROSENBLUTH, M.N., in Plasma Physics and Controlled Nuclear Fusion Research 1965 (Proc. 2nd Int. Conf. Culham, 1965), Vol. 1, IAEA, Vienna (1966) 617.
[19] COPPI, B., et al., Ann. Phys. **119** (1980) 370.
[20] PORKOLAB, M., et al., in Plasma Physics and Controlled Nuclear Fusion Research 1994 (Proc. 15th Int. Conf. Seville, 1994), Vol. 1, IAEA, Vienna (1995) 123.
[21] COPPI, B., et al., in Plasma Physics and Controlled Nuclear Fusion Research 1978 (Proc. 7th Int. Conf. Innsbruck, 1978), Vol. 1, IAEA, Vienna (1979) 487.
[22] MIGLUOLO, S., et al., Phys. Fluids B **3** (1991) 1338.
[23] LAO, L.L., et al., Nucl. Fusion **25** (1985) 1611.
[24] CONNOR, J.W., HASTIE, R.J., The Effect of Shaped Cross-Sections on the Ideal Internal Kink Mode in a Tokamak, Rep. CLM-M106, Culham Lab., UK (1985).
[25] COPPI, B., et al., Phys. Rev. Lett. **63** (1989) 2733.

3D SIMULATION STUDIES OF TOKAMAK PLASMAS USING MHD AND EXTENDED-MHD MODELS

W. PARK, Z. CHANG, E.D. FREDRICKSON,
G.Y. FU, N. POMPHREY
Plasma Physics Laboratory,
Princeton University,
Princeton, New Jersey

H.R. STRAUSS
New York University,
New York, N.Y.

L.E. SUGIYAMA
Massachusetts Institute of Technology,
Cambridge, Massachusetts

United States of America

Abstract

3D SIMULATION STUDIES OF TOKAMAK PLASMAS USING MHD AND EXTENDED-MHD MODELS.

The M3D (Multi-level 3D) tokamak simulation project aims at the simulation of tokamak plasmas using a multi-level tokamak code package. Several current applications using MHD and Extended-MHD models are presented: high-β disruption studies in reversed shear plasmas using the MHD level *MH3D* code; ω_{*i} stabilization and nonlinear island rotation studies using the two-fluid level *MH3D-T* code; studies of nonlinear saturation of TAE modes using the hybrid particle/MHD level *MH3D-K* code; and unstructured mesh *MH3D*$^{++}$ code studies. In particular, three internal mode disruption mechanisms are identified from simulation results which agree well with experimental data.

1. Introduction

Recent nonlinear MHD simulation results for high-β disruptions[1] and double tearing sawteeth[2] have reaffirmed that many global behaviors of tokamak plasmas can be successfully explained using MHD simulation. However, as tokamak experiments reach higher performance regimes, more sophisticated experimental diagnostics coupled with ever expanding computer capabilities have increased both the need for and the feasibility of 3D nonlinear global simulations using models more realistic than MHD. We currently use various "Extended-MHD" models as well as the MHD model to study the global behavior of tokamak plasmas. These include a two-fluid model which is used to study finite

gyroradius drift-MHD modes, and a Particle/MHD hybrid model which is used to study the nonlinear evolution of kinetic-MHD modes. These and the unstructured mesh capability represent the present status of our M3D(Multi-level 3D) tokamak simulation project.

The M3D project aims at the simulation of tokamak plasmas using a multi-level tokamak code package. A multi-level code is necessary for the study of tokamaks, where complex phenomena can be modeled with various levels of realism. By comparing results from different levels, one can delineate the physics involved and ensure that particular approximations are relevant. This is also a step by step path which leads toward a comprehensive tokamak simulation code which would include most of the relevant physics and also allow various option levels in complexity of physics and geometry. A higher level M3D code contains the lower level codes, such that lower level benchmarks are still useful and the simulation can change to a different level at any point in the calculation. (A simulation code with complete physics, but without intermediate option levels, would produce results too complex for the user to delineate the physics involved and would be very difficult to benchmark completely.)

In the following sections, we present 3D simulation studies using various option levels of the M3D project; high-β disruption studies in reversed shear plasmas using the MHD level *MH3D* code, ω_{*i} stabilization and nonlinear island rotation studies using the two-fluid level *MH3D-T* code, studies of nonlinear saturation of TAE modes using the hybrid particle/MHD level *MH3D-K* code, and unstructured mesh $MH3D^{++}$ code studies.

2. MHD simulation

The MH3D code is used to study the mechanisms of internal mode disruption in reversed shear plasmas. Previous studies of normal shear plasmas have shown that toroidally localized high-n ballooning modes can be driven unstable by local pressure steepening in the bad curvature region, which arises from the evolution of low-n modes.[1] Nonlinearly, the high-n mode becomes even more localized and produces a strong local pressure bulge which destroys the flux surfaces resulting in a thermal quench.

A similar behavior is also seen in simulations of reversed shear plasmas. The Fig. 1(a) shows pressure contours of a 3D equilibrium which results from the nonlinear evolution of an n=1 linear instability using a TFTR initial profile with 3.8% peak β. (The aspect ratio used is 2.9, but a smaller aspect ratio is depicted in the figure only to save space.) This 3D equilibrium has two local pressure steepenings both on the outboard side as indicated with arrows; the stronger one inside the reversed shear core region at toroidal angle $\phi = 0$, and the other in the normal shear region at $\phi = \pi$. A toroidally localized high-n ballooning mode grows out of the local steep pressure region in the normal shear region and eventually destroys the flux surfaces resulting in a thermal quench, as shown in

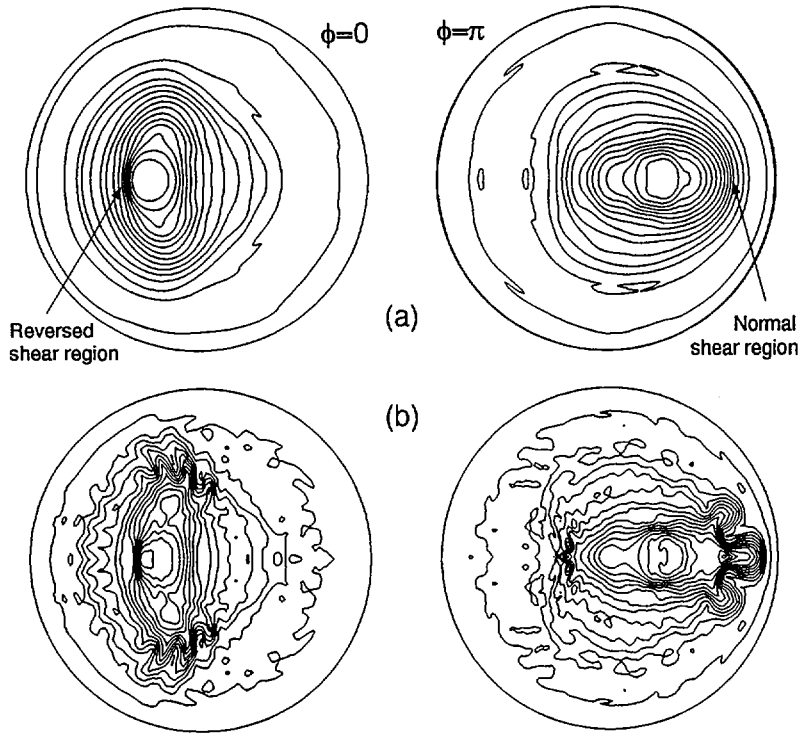

FIG. 1. (a) Pressure contours of the 3D equilibrium. Two local pressure steepenings occur, the stronger one inside the reversed shear core region at $\phi = 0$, and the other in the normal shear region at $\phi = \pi$. (b) The later nonlinear development of the pressure. The localized high-n ballooning mode develops only from the pressure steepening in the normal shear region.

Fig. 1(b). The toroidally localized steep pressure gradient inside the reversed shear core, although much stronger than the one outside, remains stable, showing that the advantage of the reversed shear profile regarding pressure driven modes extends far into the 3D configuration.

For reversed shear cases, disruptions can also be caused by low-n modes alone without a toroidally localized high-n ballooning mode, when the q_{min} is close enough or lower than 2. (This will probably also apply to q_{min} close to other rational numbers like 3.) Fig. 2 shows the nonlinear deformation of pressure evolving from an m=2 dominant n=1 mode. In this case, a toroidally localized high-n ballooning mode is not destabilized, probably because the q profile used has a smaller flat region around q_{min} compared to the previous case. The pressure bulge shown on the right figure pushes the plasma into the plasma boundary and drives magnetic reconnection until the outer region becomes stochastic.

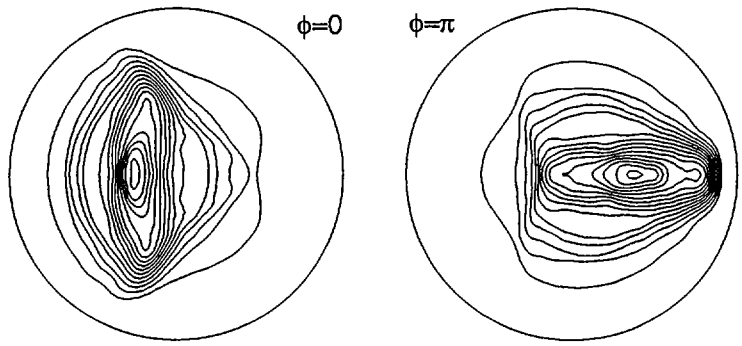

FIG. 2. Nonlinear deformation of pressure contours evolving from an m = 2 dominant n = 1 mode, when toroidally localized high-n modes are stable.

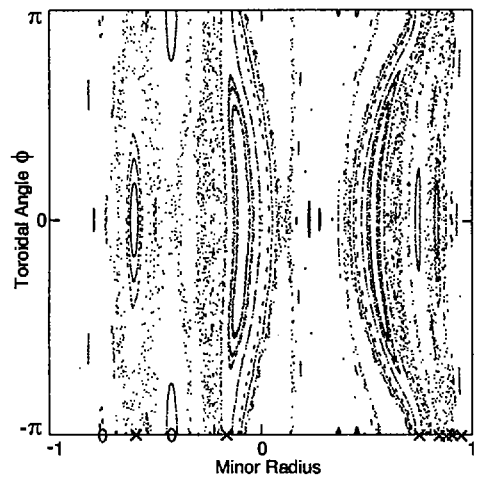

FIG. 3. Puncture plot of field lines on the toroidal mid-plane of the torus.

This is seen in Fig. 3 which shows the puncture plot of field lines on the toroidal mid-plane of the torus. The pressure bulge shown on the right figure of Fig. 2 corresponds to the bulge on the right side of the $\phi = -\pi$ line(which is the same line as $\phi = \pi$). This bulge drives reconnection producing aligned X-points of various island chains as indicated by $X's$ on the figure, and causes stochasticity. On the inboard side, mixed X-points and O-points occur as shown by $X's$ and $O's$ on the left side of the $\phi = -\pi$ line. (This mechanism is similar to the pressure bulge in m=1 reconnection cases.[3])

The above two mechanisms of internal mode disruption are due to high-β effects. Another mechanism which can cause disruption for a reversed shear

plasma is when a double-tearing reconnection occurs with a large mixing radius.[2] This can happen for both high-β and low-β plasmas. In summary, three mechanisms are identified that can cause an internal mode disruption in high temperature reversed shear plasmas: (1)toroidally localized high-n modes driven unstable by local pressure steepening in the bad curvature region that arises from the evolution of low-n modes, (2)a large pressure bulge caused by the nonlinear development of a low-n mode, (3)a double-tearing reconnection with a large mixing radius. The mechanism (3) can occur only when q_{min} is lower than 2(or other low mode number rational surfaces), while mechanisms (1) and (2) do not have such a restriction. All three mechanisms are seen in the experiment and the experimental data agrees well with the scenarios presented here. In addition, the mechanism (3) can be mixed with either of the other two mechanisms to produce a disruption.

3. Two-fluid simulation

The *MH3D-T* code[4] is the two-fluid extension of the *MH3D* code. The two-fluid equations are obtained by generalizing the perturbative drift ordering[5] to arbitrary perturbation size. They are closely related, although not identical, to the collisional Braginskii equations [6]. The model was chosen, in part, to transform smoothly into the resistive MHD equations in the limit of vanishing gyroradii.

The drift ordering [5] assumes fluid velocities and growth rates small compared to the thermal velocity scales of the MHD ordering, $v/v_{th} \sim \delta$, $\partial/\partial t \sim \delta v_{th}/L$, and $\omega/\Omega_{ci} \sim \rho_i/L \sim \delta$, where δ is a characteristic small parameter, v_{th} is the ion thermal speed, L a characteristic equilibrium scale length, ω a typical frequency, Ω_{ci} the ion cyclotron frequency, and ρ_i the ion gyroradius. The ordering introduces the diamagnetic velocities

$$\mathbf{v}_{*j} = \mathbf{B} \times \nabla p_j/(q_j n_j B^2) \quad (1)$$

$$\mathbf{v}_{*Tj} = \mathbf{B} \times \nabla T_j/(q_j B^2), \quad (2)$$

for $j = e$, i, where q_j is the particle charge.

The fluid velocities can be written exactly as

$$\mathbf{v}_i = \mathbf{v} + \mathbf{v}_{di} \quad (3)$$

$$\mathbf{v}_e = \mathbf{v} + \mathbf{v}_{*e} - \mathbf{J}_{||}/en_e \quad (4)$$

$$\mathbf{v} = \mathbf{v}_\perp + \mathbf{v}_{i||}, \quad (5)$$

where $\mathbf{v}_\perp$ is the perpendicular guiding center velocity of the electrons and ions, neglecting magnetic drifts. The generalized "diamagnetic" part $\mathbf{v}_{di}$ of the ion fluid velocity perpendicular to the magnetic field is defined to be

$$\mathbf{v}_{di} \equiv \frac{\mathbf{J}_\perp}{en_e} + \mathbf{v}_{*e}, \quad (6)$$

where $\mathbf{v}_{*e}$ is given by Eq. (1) with $j = e$.

In rationalized emu units, the essential features of our two-fluid model can be summarized as

$$\frac{\partial \mathbf{v}}{\partial t} + (\mathbf{v}\cdot\nabla)\mathbf{v} = -(\mathbf{v}_{di}\cdot\nabla)\,\mathbf{v}_\perp + \frac{\mathbf{J}\times\mathbf{B}}{nm_i} - \frac{\nabla p}{nm_i} + \mu\nabla^2\mathbf{v}_i \tag{7}$$

$$\frac{\partial \mathbf{B}}{\partial t} = -\nabla\times\mathbf{E} \tag{8}$$

$$\mathbf{E} + \mathbf{v}\times\mathbf{B} = \eta\mathbf{J} - \frac{\nabla_\parallel p_e}{en} \tag{9}$$

$$\frac{\partial p_i}{\partial t} + \mathbf{v}_i\cdot\nabla p_i = -\Gamma_i p_i\nabla\cdot\mathbf{v}_i + \nabla\cdot n\kappa_{\perp i}\nabla_\perp(\frac{p_i}{n}) + \nabla\cdot n\kappa_{\parallel i}\nabla_\parallel(\frac{p_i}{n}) - \Gamma_i\nabla\cdot(p_i\mathbf{v}_{*Ti}) \tag{10}$$

$$\frac{\partial p_e}{\partial t} + \mathbf{v}_e\cdot\nabla p_e = -\Gamma_e p_e\nabla\cdot\mathbf{v}_e + \nabla\cdot n\kappa_{\perp e}\nabla_\perp(\frac{p_e}{n}) + \nabla\cdot n\kappa_{\parallel e}\nabla_\parallel(\frac{p_e}{n}) - \Gamma_e\nabla\cdot(p_e\mathbf{v}_{*Te}) \tag{11}$$

$$\frac{\partial n_e}{\partial t} + \mathbf{v}_e\cdot\nabla n = -n\nabla\cdot\mathbf{v}_e \tag{12}$$

$$\mathbf{J} = \nabla\times\mathbf{B} \tag{13}$$

$$0 = \nabla\cdot\mathbf{B}. \tag{14}$$

The electron mass is neglected and quasineutrality, $n_e = n_i = n$, is assumed. Here $p_j = nT_j$, p is the total pressure. The Γ_j's are the ratios of the specific heats. The large $\kappa_{\parallel j}$ is accurately modeled using the artificial sound method.[7]

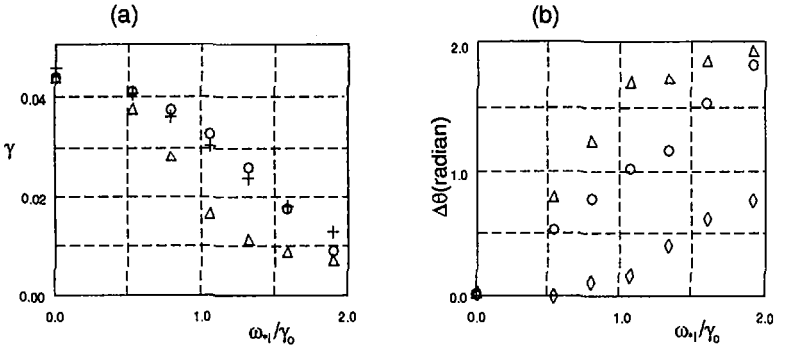

FIG. 4. (a) Stabilization of the m = 1, n = 1 resistive mode compared with the analytic dispersion relation. Crosses represent the analytic growth rates, circles the MH3D-T results for equilibrium profiles $p_e = p_i$. Triangles show the MH3D-T case with $p_e = 0$, illustrating the destabilizing effect of ω_{*e}. (b) Direction of the m = 1, n = 1 plasma kink flow relative to the reconnection X-point in a poloidal cross section. Circles represent the ion fluid flow $\mathbf{v}_i$ and diamonds the guiding center velocity $\mathbf{v}$ for equilibrium $p_e = p_i$. Triangles represent $\mathbf{v}_i$ for $p_e = 0$.

The code has been benchmarked against analytic theory for the diamagnetic stabilization of the $m = 1$, $n = 1$ mode in a cylinder. The analytic dispersion relation was solved numerically [8] for a narrow reconnection layer. A uniform resistivity $\eta = S^{-1} = 3.24 \times 10^{-5}$ and toroidal plasma beta $\beta_o = 0.067$ at the center of the plasma was used. Viscosity and thermal and particle diffusion were small compared to the resistivity. q varied from $q_o = 1.1$ to $q_a = 5$, with $q = 2$ at $r/a = 0.63$. In the first case, it was assumed that $p_e = p_i$ in equilibrium. The results are shown in Fig. 4(a), where the growth rate γ is plotted against the diamagnetic parameter ω_{*i}/γ_o. Crosses represent the analytic results, and circles the numerical results. Good agreement is found over a wide range of growth rate. The destabilizing effect of the electron diamagnetic frequency ω_{*e} at fixed total β is seen by comparing the case $p_e \equiv 0$ (triangles).

The ion diamagnetic stabilization has a simple physical interpretation.[4] The direction of the outward kink motion of the plasma inside the $q = 1$ surface rotates poloidally away from the reconnection X-point as ω_{*i}/γ_o increases, up to approximately $\pi/2$. This reduces the efficiency of the mode drive, and slows the rate of reconnection. The relative angle $\Delta\theta$ versus ω_{*i}/γ_o is plotted in Fig. 4(b). For the case $p_e = p_i$ the angle of the radial ion fluid flow v_{ir} is given by circles and the particle flow v_r by diamonds. The electron diamagnetic drift ω_{*e} exerts its destabilizing effect by resisting the rotation of the kink. When $p_e \equiv 0$, flow rotation and mode stabilization develop much faster (triangles show v_{ir}).

The *MH3D-T* code has been used to study the rotation of linear and nonlinear resistive modes in a torus. The linear mode rotates in the ω_{*e} direction if p_e is comparable to p_i, and in the ω_{*i} direction if p_e is small (in the electron guiding center frame). Nonlinearly however, the magnetic island rotation is quite different. From Eq. 9, one can see that finite size islands have to be stationary (except for a slow speed proportional to η) in the electron guiding center frame, if $\nabla_{||} p_e$ is small. This is because the X-point has to move with $\mathbf{v}_\perp$ from the frozen-in flux condition for $\eta = 0$. Any rotation speed on the order of a fractional power of η would require a fast reconnection process. This requires a large free energy which is absent near the saturation of the mode. Simulation results agree with this reasoning. For $\nabla_{||} p_e \neq 0$, islands rotate with ω_{*e}. However, $\nabla_{||} p_e \propto n\nabla_{||} T_e + T_e \nabla_{||} n$ and $\nabla_{||} T_e$ becomes negligibly small in the electron transit time scale, while $\nabla_{||} n$ becomes small in the sound wave time scale(as also seen in Ref. 9 and 10 using reduced equations). If the plasma rotation is very fast, $\nabla_{||} n$ can remain significant due to centrifugal force, but for a realistic rotation speed it can be neglected. In the simulation with TFTR parameters, it takes about 100 to 1000 sound wave transit times for $\nabla_{||} n$ to become small for islands of a few cm, because of the proximity of low mode number rational surfaces. This gives 0.1 to 1 $msec$ for $\nabla_{||} n$ flattening. ($\nabla_{||} T_e$ flattening is much faster.) Since magnetic islands in tokamaks can form as fast as ~ 0.1 $msec$ through a fast reconnection precess, an experimental measurement of the slowing down of the magnetic island rotation(in the electron guiding center frame) due to the flattening of $\nabla_{||} n$ may be feasible.

4. Particle/MHD hybrid simulation

To model the nonlinear interaction of energetic particles with MHD waves, a hybrid particle/MHD model had been developed.[11] The plasma is divided into two parts: the bulk plasma, which contains the thermal electrons and ions, and the energetic hot ions. The bulk plasma is described by the ideal MHD equations, whereas the hot ions are described by the gyrokinetic equations[12]. The particle part can be coupled to the bulk plasma part through one of two almost equivalent, accurate coupling schemes, the pressure coupling and current coupling. In the pressure coupling scheme, the hot particle pressure tensor P_h is coupled to the bulk plasma momentum equation:

$$\rho_b \frac{d\mathbf{v}_b}{dt} = -\nabla P_b - (\nabla \cdot \mathsf{P}_h)_\perp + \mathbf{J} \times \mathbf{B}, \tag{15}$$

In the current coupling scheme, the hot particle current density $\mathbf{J}_h$ and charge density q_h are coupled to the bulk plasma momentum equation:

$$\rho_b \frac{d\mathbf{v}_b}{dt} = -\nabla p_b + (\nabla \times \mathbf{B} - \mathbf{J}_h) \times \mathbf{B} + q_h \mathbf{v}_b \times \mathbf{B}, \tag{16}$$

where the subscript b denotes the bulk part and the subscript h denotes the hot ion component. The last term of Eq. 16 can be thought of as the subtraction of the $\mathbf{J} \times \mathbf{B}$ force on the electrons whose density is the same as the hot particles. This term cannot be neglected because the $\mathbf{E} \times \mathbf{B}$ drift can be comparable to the perturbation of the magnetic drift of the hot particles.

Equation 15 or Eq. 16, together with the other MHD equations form the MHD part which is advanced in time using particle quantities given by the particle part. The new $\mathbf{E}$ and $\mathbf{B}$ are in turn used by the particle part to advance the particle quantities in time. The model is fully self-consistent, including nonlinear Landau damping and other hot particle interactions with MHD waves, and the nonlinear MHD mode coupling.

Using the particle/MHD hybrid *MH3D-K* code we have found that wave particle trapping is the dominant mechanism for the nonlinear TAE saturation.[13] In this work, the pressure coupling scheme was employed. The "double trajectory method" was used to reduce the simulation noise in the linear regime. In this method, two sets of particles are used, one following the equilibrium field and the other the total electromagnetic field. The hot particle pressure tensor $\mathsf{P}_h(t)$ is replaced by $(\mathsf{P}_h(t) - \mathsf{P}_{h,0}(t)) + \mathsf{P}_{h,0}(0)$ where $\mathsf{P}_{h,0}$ is evaluated from the equilibrium orbits. The advantage of the double trajectory method is that it can be applied self-consistently to any 3D equilibrium with an arbitrary distribution of particles including a delta function in velocity space. The disadvantage is that it is only valid for the linear regime.

The δf method of noise reduction[15], on the other hand, also applies in the nonlinear regime. However, because of difficulties, it has not been applied in a

self-consistent manner to a 3D electromagnetic problem with a self-consistent equilibrium. We have devised a scheme for a self-consistent δf method for such cases, and implemented it in the MH3D-K code. The new linear results agree closely with the double trajectory method results, while improved nonlinear saturation results have been obtained which still give the same conclusion as obtained before in Ref. 13. The self-consistent δf method and MH3D-K simulation results of TAE saturation will be described at this conference by Fu et al. in a TAE mode paper (IAEA-CN-64/D2-6, this volume).

5. Unstructured mesh code

As demonstrated in fluid dynamics research, the most efficient way to represent general geometric effects is to use an unstructured numerical mesh. Finite element, unstructured mesh methods are now just beginning to be used in MHD computations. Unstructured meshes offer two important advantages. They may be fitted to complicated geometries. This is necessary for simulations of divertor tokamaks.[16, 17] The second advantage is the ability to introduce localized mesh refinement. For example, extra vertices may be added at a magnetic X-point.

The meshpoints of the unstructured mesh are the vertices of triangles (see Fig. 5(a)), located at points $\vec{r}_i$. The most convenient basis functions are piecewise linear "tent" functions, $\lambda_i(\vec{r})$, which are nonzero at a vertex common to several triangles, and which vanish at all other vertices.

The variables in the MHD equations are represented as a sum over poloidal finite element basis functions and toroidal Fourier harmonics. We use a mixed

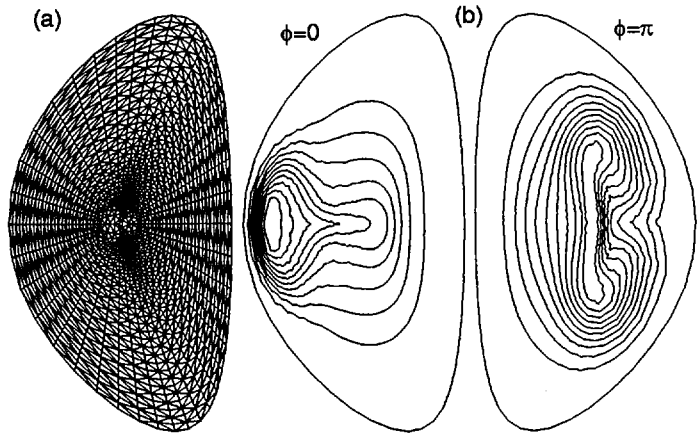

FIG. 5. (a) An unstructured mesh for an ITER-like geometry. Note that the mesh has no origin. (b) Pressure contours resulting from nonlinear development of a pressure driven mode after a pellet injection.

method in which the variables to be expanded in basis functions include the electrostatic potential ϕ, magnetic flux ψ, toroidal vorticity W and toroidal current C. The MHD equations are discretized with a zero residual Galerkin approach, in which the equations are multiplied by a basis function λ_j and integrated over the domain. This gives a set of sparse matrix equations, in which the differential operators become sparse matrices involving integrals of the basis functions and their derivatives. These can be done analytically. In the Laplacian, integration by parts is used to avoid having to take second derivatives. The primary matrices appearing in the discrete equations are the mass matrix $\mathbf{M}$, the stiffness matrix $\mathbf{S}$, and the Poisson bracket tensor $\mathbf{P}$, defined by

$$M_{ij} = \int \lambda_i \lambda_j d^2x \tag{17}$$

$$S_{ij} = -\int \nabla\lambda_i \cdot \nabla\lambda_j d^2x \tag{18}$$

$$P_{ijk} = \int \lambda_i \nabla\lambda_j \times \nabla\lambda_k \cdot \hat{z} d^2x \tag{19}$$

Both the stiffness and mass matrices are symmetric. The Poisson bracket is anti-symmetric under the exchange of any two indices. This assures that some of the most important integral relations satisfied by the differential equations are preserved by the finite element discretization. This includes conservation of energy and magnetic flux in the absence of dissipation. The matrices are very sparse, having nonzero elements only between those vertices connected by the side of a triangle.

Although the use of the stiffness matrix causes no problems when the electrostatic potential ϕ is calculated from the toroidal vorticity W, there is a loss of accuracy and even convergence when the toroidal current C is calculated from the poloidal flux ψ using the stiffness matrix. Convergence is restored by calculating the current in two steps: first calculating the poloidal magnetic field components from ψ, and expanding the result in basis functions; then taking the toroidal component of the curl and again expanding in basis functions. This is equivalent to using a larger stencil for the current calculation, which preserves the necessary symmetries for energy conservation [18].

The finite element unstructured mesh discretization has been incorporated into *MH3D*$^{++}$ with an object oriented approach. A benefit of object oriented programming is that the objects are like black boxes whose inner workings are hidden from and protected from the user. They can be linked with other code in a simple way, without having to be concerned with details of their inner workings. The unstructured mesh objects, called MeshObject, generate an unstructured mesh, create all necessary auxiliary arrays, and produce the sparse matrices which implement differential operators including gradient, curl, and divergence, as well as various Poisson solvers based on the Incomplete Cholesky Conjugate Gradient method.

An important feature of this approach is that most of the *MH3D* code is retained. The user has the option of linking the code in the standard way, to produce a code that runs as a finite difference/Fourier code; or linking with MeshObject, to give an unstructured mesh. This allows direct benchmarking of the two versions against each other. Equilibrium and stability calculations using the two versions have been compared, and there is good agreement.

As a nontrivial example of the use of the $MH3D^{++}$ code, we consider pellet injection into an ITER like tokamak. The pellet is assumed to rapidly heat and form a large pressure perturbation, which is poloidally and toroidally localized. The peak pressure of the perturbation is 0.25 of the peak pressure in the tokamak, which has 4% peak β. The initial state consists of an equilibrium, on which the pellet perturbation is superposed. A pressure driven instability develops and undergoes a large distortion as shown in Fig. 5(b). The implication of this result is currently under study.

6. Conclusion

The M3D(Multi-level 3D) tokamak simulation project aims at the simulation of tokamak plasmas using a multi-level tokamak code package. Several current applications are presented: high-β disruption studies in reversed shear plasmas using the MHD level *MH3D* code, ω_{*i} stabilization and nonlinear island rotation studies using the two-fluid level *MH3D-T* code, studies of nonlinear saturation of TAE modes using the hybrid particle/MHD level *MH3D-K* code, and unstructured mesh $MH3D^{++}$ code studies. In particular, three internal mode disruption mechanisms are identified from simulation results which agree well with experimental data.

The successful applications of these MHD and Extended-MHD codes support the premise of the M3D project that a multi-level simulation code is necessary for the study of tokamaks, where the complex phenomena can be modeled with various levels of realism. It is also a hopeful sign that this step by step path could eventually lead to a comprehensive tokamak simulation code which would include most of the relevant physics and also allow various option levels in complexity of physics and geometry.

Acknowledgements

This work was supported by the United States Department of Energy under Contract DE–AC02–76–CHO–3073, Contract DE-FG02-91ER54109, and Grant DE-FG02-86ER53223.

REFERENCES

[1] PARK, W., et al., Phys. Rev. Lett. 75 (1995) 1763.
[2] CHANG, Z., et al., Phys. Rev. Lett. 77 (1996) 3553.

[3] PARK, W., MONTICELLO, D.A., FREDRICKSON, E., McGUIRE, K., Phys. Fluids B **3** (1991) 507.
[4] SUGIYAMA, L.E., PARK, W., Rep. PTP-96/1, Massachusetts Inst. of Technology, Cambridge (1996).
[5] HAZELTINE, R.D., MEISS, J.D., Phys. Rep. **121** (1985) 1;
Plasma Confinement, Addison-Wesley, Redwood City, CA (1992).
[6] BRAGINSKII, S.I., in Reviews of Plasma Physics (LEONTOVICH, M.A., Ed.), Vol. 1, Consultants Bureau, New York (1965) 205.
[7] PARK, W., MONTICELLO, D.A., STRAUSS, H., MANICKAM, J., Phys. Fluids **29** (1986) 1171.
[8] MIGLIUOLO, S.M., Massachusetts Inst. of Technology, Cambridge, personal communication.
[9] BISKAMP, D., Nucl. Fusion **19** (1979) 777.
[10] SCOTT, B.D., HASSAM, A.B., DRAKE, J.F., Phys. Fluids **28** (1985) 275.
[11] PARK, W., et al., Phys. Fluids B **4** (1992) 2033.
[12] LEE, W.W., J. Comput. Phys. **72** (1987) 243.
[13] FU, G.Y., PARK, W., Phys. Rev. Lett. **74** (1995) 1594.
[14] BERK, H.L., BREIZMAN, B.N., YE, H., Phys. Rev. Lett. **68** (1992) 3563.
[15] PARKER, S.E., LEE, W.W., Phys. Fluids B **5** (1993) 77.
[16] STRAUSS, H.R., LONGCOPE, D.W., in preparation.
[17] STRAUSS, H.R., Phys. Plasmas **2** (1995) 1229.
[18] STRAUSS, H.R., Phys. Plasmas **3** (1996) 4095.

DISCUSSION

H.L. BERK: Does your code for TAE include dissipation of plasma, besides α drive? Do you have a source to replenish energetic particles?

W. PARK: Yes, the MH3D-K code includes viscosity, resistivity and thermal conductivity. We could include an energetic particle source rather easily, but for the cases studied we did not do so because we were not studying long time steady state behaviour.

R.J. TAYLOR: Are you planning to compute flow stabilization effects, and when would these be available? What are the main issues?

W. PARK: The MH3D code includes shear flow effects. From previous simulations, it has been found that shear flow generally stabilizes internal ballooning modes but destabilizes external modes. We are also currently studying self-generated flow effects using the two fluid MH3D-T code.

F. ROMANELLI: Are electron diamagnetic effects important in the non-linear evolution of the island?

W. PARK: They are important in the early phase of the non-linear evolution of the island, modifying the growth rate and giving rotation in the ω_{*e} direction. However, as $\nabla_{\|}p_e$ goes to zero, the ω_{*e} effects become small, giving essentially the same saturation width and non-rotation in the electron guiding centre frame as in the $\omega_{*e} = 0$ case.

VLASOV-MHD AND PARTICLE-MHD SIMULATIONS OF THE TOROIDAL ALFVÉN EIGENMODE

Y. TODO, T. SATO,
COMPLEXITY SIMULATION GROUP[1]
National Institute for Fusion Science,
Nagoya, Japan

Abstract

VLASOV-MHD AND PARTICLE-MHD SIMULATIONS OF THE TOROIDAL ALFVÉN EIGENMODE.

Two simulation codes, the Vlasov-MHD code and the particle-MHD code, are developed to elucidate the nonlinear behavior of hybrid kinetic-MHD modes and energetic particles. Simulations of the toroidal Alfvén eigenmode (TAE mode) destabilized by energetic alpha particles are carried out. Vlasov-MHD simulation reveals that particle-trapping by a finite-amplitude wave causes the saturation. After saturation, amplitude oscillation takes place with a frequency corresponding to the bounce frequency of the alpha particles trapped by the TAE mode. Particle-MHD simulations are performed with conditions more relevant to fusion plasmas. Saturation level is found to be amplified with multiple modes.

1. Introduction

In fusion reactors, successful confinement of alpha particles is required for self-sustained operation. The alpha particles born from D-T reactions are supposed to destabilize the macroscopic modes such as the toroidal Alfvén eigenmode (TAE mode) [1] and the fishbone mode. Nonlinear behaviors of such hybrid kinetic-MHD modes and alpha particles are one of the major physics uncertainties for fusion reactors. We have developed two simulation codes, Vlasov-MHD code [2] and particle-MHD code, to analyze hybrid kinetic-MHD modes. In both simulation codes the background plasma is described by an MHD fluid model, and the fully nonlinear MHD equations are solved by a finite difference method. In the Vlasov-MHD code the kinetic evolution of alpha particles is followed by the drift kinetic equation which is solved by a finite difference method, while the particle simulation method is used for the alpha particle component in the particle-MHD code. Alpha particle current except for $\mathbf{E}\times\mathbf{B}$ current is extracted from the total current in the MHD momentum equation to take into account the effects of alpha particles on the background plasma in a self-consistent way. Nonlinear kinetic effects such as the particle trapping by a finite-amplitude wave which suppresses the Landau damping can be followed by these codes. The Vlasov-MHD code has an advantage that it is free from numerical noise of particle discreteness, though it demands larger computer power than the particle-MHD code. On the other hand, the δf method [3-5] has been developed to reduce the numerical noise in particle simulations. We employ it in the particle-MHD code.

[1] T. Hayashi, K. Watanabe, R. Horiuchi, H. Takamaru, T.-H. Watanabe, A. Kageyama.

In the remainder of this paper, the plasma model is described in section 2. Vlasov-MHD simulations are carried out with a simplified alpha particle distribution and results are presented in section 3. Results of particle-MHD simulations with more realistic alpha particle distribution are given in section 4, and summary is given in section 5.

2. Plasma model

In the model employed here, the background plasma is described by the ideal MHD equations and the electric field is given by the MHD description. This is a reasonable approximation under the condition that the alpha density is much less than the background plasma density. The MHD equations are given by

$$\frac{\partial \rho}{\partial t} = -\nabla\cdot\rho\mathbf{v}\,, \tag{1}$$

$$\rho\frac{\partial \mathbf{v}}{\partial t} + \rho\mathbf{v}\cdot\nabla\,\mathbf{v} = -\nabla p + \frac{1}{\mu_0}\nabla\times\mathbf{B}\times\mathbf{B}\,, \tag{2}$$

$$\frac{\partial \mathbf{B}}{\partial t} = -\nabla\times\mathbf{E}\,, \tag{3}$$

$$\frac{\partial p}{\partial t} = -\nabla\cdot p\mathbf{v} - (\gamma-1)p\nabla\cdot\mathbf{v}\,, \tag{4}$$

$$\mathbf{E} = -\mathbf{v}\times\mathbf{B}\,, \tag{5}$$

where μ_0 is the vacuum magnetic permeability and γ is the adiabatic constant, and all other quantities are conventional.

The drift kinetic description is used for the alpha particles. The guiding-center velocity $\boldsymbol{v}_D$ is

$$\mathbf{v}_D = \mathbf{v}^*_{//} + \mathbf{v}_E + \mathbf{v}_B\,, \tag{6}$$

$$\mathbf{v}^*_{//} = \frac{v_{//}}{B}(\mathbf{B} + \rho_{//}B\nabla\times\mathbf{b})\,, \tag{7}$$

$$\mathbf{v}_E = \frac{1}{B}(\mathbf{E}\times\mathbf{b})\,, \tag{8}$$

$$\mathbf{v}_B = \frac{1}{q_\alpha B}(-\mu\nabla B\times\mathbf{b})\,, \tag{9}$$

$$\rho_{//} = \frac{m_\alpha v_{//}}{q_\alpha B}\,, \tag{10}$$

$$\epsilon = \frac{1}{2}m_\alpha v_{//}^2 + \mu B\,, \tag{11}$$

$$m v_{//}\frac{dv_{//}}{dt} = \mathbf{v}^*_{//}\cdot(q_\alpha\mathbf{E} - \mu\nabla B)\,, \tag{12}$$

$$\frac{d}{dt}\mu B = \mu(\mathbf{v}^*_{//}\cdot\nabla B + \frac{\partial B}{\partial t}) + q_\alpha\mathbf{v}_B\cdot\mathbf{E}\,, \tag{13}$$

where μ is the magnetic moment which is the adiabatic invariant.

To complete the equation system in a self-contained way, we take account of the effects of the alpha particles on the bulk plasma in the MHD momentum equation

$$\rho\frac{\partial \mathbf{v}}{\partial t} + \rho\mathbf{v}\cdot\nabla\mathbf{v} = (Q - Q_\alpha)\mathbf{E} + (\frac{1}{\mu_0}\nabla\times\mathbf{B} - \mathbf{j}_\alpha)\times\mathbf{B} - \nabla p\,, \tag{14}$$

$$\mathbf{j}_\alpha = \int \mathbf{v}_D f d^3v + \nabla\times\mathbf{M}\,, \tag{15}$$

$$\mathbf{M} = -\int \mu\mathbf{b} f d^3v\,, \tag{16}$$

where Q and Q_α are the total charge density and alpha particle charge density, and $\mathbf{j}_\alpha$ is the alpha particle current density. The total charge density Q is negligible in the MHD context where the quasi-neutrality is satisfied. Equation (14) is rewritten into the following form paying attention to that $-Q_\alpha\mathbf{E}$ cancels out with the Lorentz force of $\mathbf{E}\times\mathbf{B}$ currrent of alpha particles

$$\rho\frac{\partial \mathbf{v}}{\partial t} + \rho\mathbf{v}\cdot\nabla\mathbf{v} = -\nabla p + (\frac{1}{\mu_0}\nabla\times\mathbf{B} - \mathbf{j}_\alpha')\times\mathbf{B}\,, \tag{17}$$

$$\mathbf{j}_\alpha' = \int (\mathbf{v}_{//}^* + \mathbf{v}_B) f d^3v + \nabla\times\mathbf{M}$$
$$= \mathbf{j}_{\alpha//} + \frac{1}{B}(P_{\alpha//}\nabla\times\mathbf{b} - P_{\alpha\perp}\nabla\ln B\times\mathbf{b}) + \nabla\times(-\frac{P_{\alpha\perp}}{B}\mathbf{b})\,. \tag{18}$$

This model is the same as that of Parker et al. [6] and the conservation of total energy is proved in Ref. 2.

3. Vlasov-MHD simulation

From Eqs. (6)-(13) we can obtain the drift kinetic equation which describes the time evolution of the alpha distribution function in the phase space (x, $v_{\|}$, μ)

$$\frac{\partial}{\partial t}f(\mathbf{x}, v_{//}, \mu) = -\frac{1}{B}\nabla\cdot(B\mathbf{v}_D f) - \frac{\partial}{\partial v_{//}}(\frac{dv_{//}}{dt}f) - f\frac{\partial}{\partial t}\ln B\,. \tag{19}$$

The Vlasov-MHD simulations have been carried out to elucidate the basic physics of the TAE mode saturation [2]. Due to the restriction of the present computer power, the magnetic moments of the alpha particles are set to be zero, namely, the phase space is reduced to 4-dimension (x, $v_{\|}$) and the drift kinetic equation is given by

$$\frac{\partial}{\partial t}f(\mathbf{x}, v_{//}) = -\nabla\cdot(\mathbf{v}_D f) - \frac{\partial}{\partial v_{//}}(\frac{dv_{//}}{dt}f)\,. \tag{20}$$

The aspect ratio of the system is 3 and the poloidal cross section is rectangular. The cylindrical coordinate system (R, ϕ, z) is used. An axisymmetric equilibrium solution is obtained by an iterative method both for the MHD force balance and the distribution function of the alpha particles. The volume-averaged beta value of alpha particles $<\beta_\alpha>$ is 0.44%. We focus on the n=2 TAE mode and its nonlinear evolution including generation of n=0 modes. The most unstable n=2 TAE mode is excited, and the growth rate is agreeable with that of the linear theory [7].

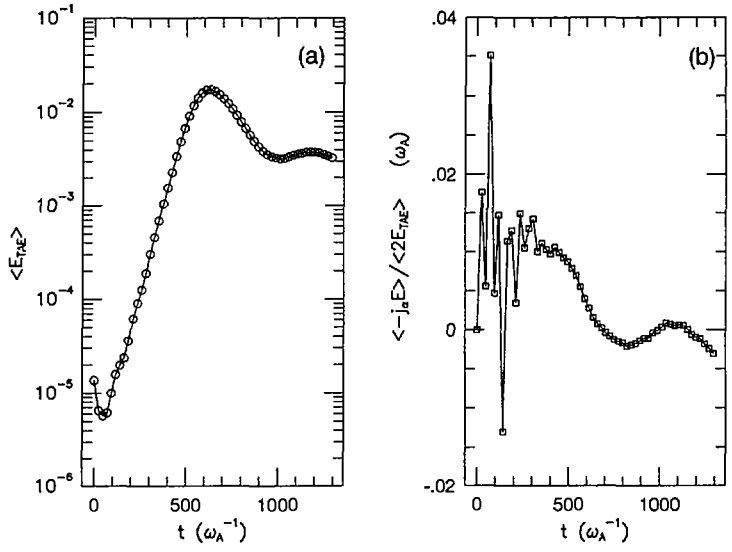

FIG. 1. Time evolutions of (a) TAE mode energy and (b) ratio of the power transfer rate $\langle -\mathbf{j}_\alpha \cdot \mathbf{E} \rangle$ *to the TAE mode energy, which is divided by a factor of 2 to relate directly to the growth rate. The decrease of this ratio leads to the saturation of the TAE instability.*

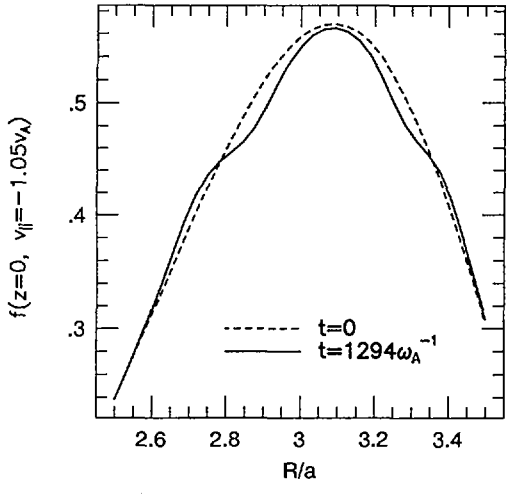

FIG. 2. Alpha particle distribution functions f(R) at $v_\parallel = -1.05 v_A$ *and* $z = 0$ *which are averaged in the* ϕ*-direction and normalized by* $f(v_\parallel = 0, t = 0)$ *at the magnetic axis.*

In order to identify the saturation mechanism we analyze the time evolution of the power transfer rate from alpha particles to the MHD component, namely, $<-\mathbf{j}_\alpha \cdot \mathbf{E}>$ (< > means volume integration). We show the temporal evolution of the TAE mode energy in Fig. 1a and the ratio of the power transfer rate to the TAE mode energy (divided by a factor of 2 to relate directly to the growth rate) in Fig. 1b. At t=470 ω_A^{-1} the ratio begins to decrease, thus leading to saturation of the instability. It is evident that the decrease of the power transfer rate is the cause of the saturation. After saturation an amplitude oscillation occurs, of which frequency is 3 times larger than the linear growth rate. The frequency of the amplitude oscillation is consistent with the theory of the bounce frequency of particles trapped by the TAE mode [8].

Fig. 2 shows distributions of alpha particles at $v_{\|} = -1.05\ v_A$ and $z = 0$ (midplane) as a function of R which are averaged in ϕ-direction at $t=0$ and $t=1294\omega_A^{-1}$, respectively. The spatial gradient of the distribution function is reduced to half near $R=2.8a$ and $3.3a$. The $m=0$, $n=0$ quasi-linear mode of the alpha particle distribution is generated through the nonlinear coupling between the $n=2$ TAE mode and the $n=2$ mode of alpha particle distribution. This quasi-linear mode spatially flattens the distribution function, removing the free energy source of the instability. Thus, we conclude that the saturation is caused by the particle trapping by the wave.

4. Particle-MHD simulation

Saturation by **ExB** trapping was theoretically predicted in Ref. 9 and recently confirmed by computer simulations [2, 10, 11]. Nevertheless, no simulation took account of both realistic distribution of alpha particles and MHD nonlinearity. Realistic alpha particle distribution is indispensable to investigate alpha particle loss induced by TAE mode. In this section, we present the results of particle-MHD simulations which are carried out with more relevant condition to ignited plasmas. The initial alpha particle distribution is the slowing-down distribution which is isotropic in the velocity space with the maximum energy of 3.5 MeV. The magnetic field strength at the magnetic axis is 5T, the number density of the background plasma is 10^{20} m^{-3}, the minor radius is 0.9m, and the aspect ratio is 3.

For the alpha particle component, δf method is employed, which reduces the numerical noise in particle simulations. Using this method, $\mathbf{j}_\alpha'$ in equation (18) is evaluated through

$$P_{\alpha//} = P_{\alpha//0} + \sum_i w m_\alpha v_{//}^2 S(\mathbf{x}-\mathbf{X}_i)\,, \tag{21}$$

$$P_{\alpha\perp} = P_{\alpha\perp 0} + B\sum_i w \mu S(\mathbf{x}-\mathbf{X}_i)\,, \tag{22}$$

where w is the weight and $S(\mathrm{x}-\mathrm{X}_i)$ is the shape function of each particle. The time evolution of w is described by [5]

$$\frac{d}{dt}w = -(1-w)\frac{d}{dt}\ln f_0\,, \tag{23}$$

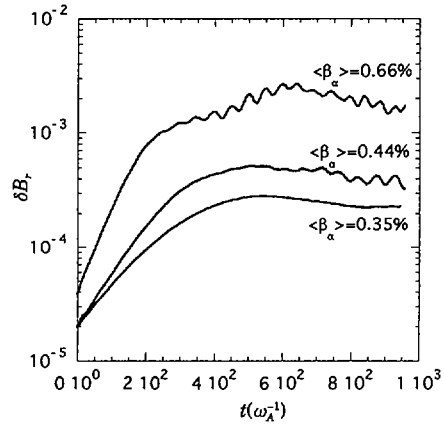

FIG. 3. Time evolution of the (m = 2, n = 2) component of δB_r on the r = 0.23a magnetic surface for $\langle\beta_\alpha\rangle$ = 0.35%, 0.44% and 0.66%.

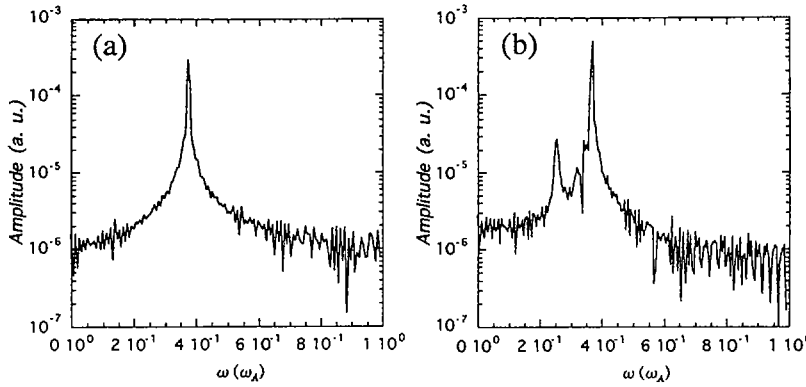

FIG. 4. Fourier spectrum of the (m = 2, n = 2) component of δB_r on the r = 0.23a magnetic surface for (a) $\langle\beta_\alpha\rangle$ = 0.35% and (b) $\langle\beta_\alpha\rangle$ = 0.44%.

where f_0 is the initial distribution. The initial distribution is taken to be a function of magnetic surface and energy.

A new linear δf simulation code is developed to obtain a kinetic eigenmode which is used as an initial perturbation of nonlinear simulation. This linear simulation technique has an advantage against the standard nonlinear one in that it requires much less computer power. This technique utilizes Fourier mode in the symmetric direction of the equilibrium. All MHD variables are linearized and assumed to have a form of $exp(in\phi)$. The particle weight is also assumed to have a

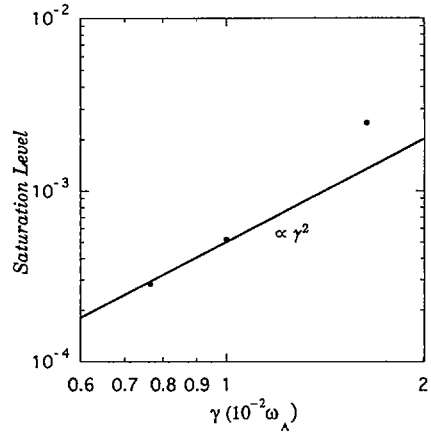

FIG. 5. Saturation amplitude of the (m = 2, n = 2) component of δB_r on the r = 0.23a magnetic surface versus linear growth rate. The saturation amplitude for $\langle\beta_\alpha\rangle$ = 0.66% is larger than the extrapolated value from the low-beta cases.

form of *exp(inφ)* and particles are followed in *(R, z, $v_{||}$, μ)* space along their equilibrium orbits. Equation (23) is transformed into

$$\frac{d}{dt}w = -(\frac{d}{dt})_1 \ln f_0 - in\frac{v_\phi}{R}w, \tag{24}$$

$$(\frac{d}{dt})_1 = (v_{//}\delta\mathbf{b} + \mathbf{v}_E)\cdot\nabla + \frac{d\epsilon}{dt}\frac{\partial}{\partial\epsilon}. \tag{25}$$

For investigation of nonlinear saturation with the slowing-down distribution, we focus on the *n*=2 mode as well as in the Vlasov-MHD simulation. Time evolution of amplitude of (m=2, n=2) component of B_r at *r=0.23a* for three different initial $<\beta_\alpha>$ (0.35%, 0.44%, and 0.66%, respectively) is shown in Fig. 3. While only the (m=2, 3, n=2) TAE mode is excited for $<\beta_\alpha>$=0.35% case, (m=3, 4, n=2) TAE mode is additionally destabilized in the other cases. Fourier analysis of frequency is shown in Fig. 4 and the frequencies of these two modes are 0.04-0.05ω_A lower than the center of the gap. Appearance of this additional mode is also known from the oscillation of the amplitude in Fig. 3 of which frequency is consistent with the difference between the frequencies of two TAE modes. Saturation level is plotted against linear growth rate for three cases in Fig. 5. Saturation level is in proportion to the square of the linear growth rate between the two lower $<\beta_\alpha>$ cases. This relation supports the conclusion of Vlasov-MHD simulation that particle-trapping causes saturation.

For $<\beta_\alpha>$=0.66% case, however, the saturation level is not on the extrapolation from the other two cases. The theory of overlapping of multiple TAE modes [9, 12] will nicely explain the amplification of saturation level. Detailed analysis is required to confirm this hypothesis.

The ratio of lost particles to total alpha particles for $<\beta_\alpha>$=0.35%, 0.44%, and 0.66% is 3×10^{-5}, 5×10^{-4}, and 5×10^{-3}, respectively.

5. Summary

Vlasov-MHD and Particle-MHD simulations of the toroidal Alfvén eigenmode are carried out. These simulations demonstrate that saturation of a single mode is caused by **ExB** trapping. For multiple modes, amplification of saturation level is observed. More detailed analysis is required to elucidate the amplification mechanism. Simulations with multiple toroidal modes are under way and will be presented elsewhere [13].

Acknowledgment

Numerical computations are performed at the Advanced Computing System for Complexity Simulation of National Institute for Fusion Science. This work is partially supported by Grants-in-Aid of the Ministry of Education, Science and Culture (No. 07832024 and No. 07858057).

REFERENCES

[1] CHENG, C.Z., CHANCE, M.S., Phys. Fluids **29** (1986) 3659.
[2] TODO, Y., SATO, T., WATANABE, K., WATANABE, T.-H., HORIUCHI, R., Phys. Plasmas **2** (1995) 2711.
[3] KOTSCHENREUTHER, M., Bull. Am. Phys. Soc. **34** (1988) 2107.
[4] DIMITS, A.M., LEE, W.W., J. Comput. Phys. **107** (1993) 309.
[5] PARKER, S.E., LEE, W.W., Phys. Fluids B **5** (1993) 77.
[6] PARK, W., et al., Phys. Fluids B **4** (1992) 2033.
[7] FU, G.Y., VAN DAM, J.W., Phys. Fluids B **1** (1989) 1949.
[8] BERK, H.L., BREIZMAN, B.N., YE, H., Phys. Fluids B **5** (1993) 1506.
[9] BREIZMAN, B.N., BERK, H.L., YE, H., Phys. Fluids B **5** (1993) 3217.
[10] FU, G.Y., PARK, W., Phys. Rev. Lett. **74** (1995) 1594.
[11] WU, Y., WHITE, R.B., CHEN, Y., ROSENBLUTH, M.N., Phys. Plasmas **2** (1995) 4555.
[12] BERK, H.L., BREIZMAN, B.N., PEKKER, M., Phys. Plasmas **2** (1995) 3007.
[13] TODO, Y., SATO, T., COMPLEXITY SIMULATION GROUP, Particle-MHD Simulation Study of the Toroidal Alfvén Eigenmode (in preparation).

DISCUSSION

F. ROMANELLI: Is the conclusion that TAE saturation is due to wave–particle trapping correct, and does this also apply in the case of kinetic TAE?

Y. TODO: Yes, I think so.

KINETIC INERTIA AND ION LANDAU DAMPING FOR BAE AND RESISTIVE WALL MODES IN TOKAMAKS

A. BONDESON
Institute for Electromagnetic Field Theory,
Euratom–NFR Association,
Chalmers University of Technology,
Göteborg,
Sweden

M.S. CHU
General Atomics,
San Diego, California,
United States of America

Abstract

KINETIC INERTIA AND ION LANDAU DAMPING FOR BAE AND RESISTIVE WALL MODES IN TOKAMAKS.

Drift-kinetic theory is applied to calculate inertia and ion Landau damping for MHD modes at finite frequency and arbitrary q. Toroidal trapping decreases the Landau damping and increases the inertia for frequencies below $(r/R)^{1/2}v_{thi}/qR$. The theory is applied to the beta-induced Alfvén eigenmode (BAE) and resistive wall mode (RWM) in rotating plasma. It is proposed that the BAE has a similar magnetic perturbation as the TAE but the frequency is lower because of toroidal inertia enhancement when the parallel phase velocity is subsonic. The inertia enhancement also reduces the plasma rotation required for the stabilization of RWM.

1. INTRODUCTION

Inertia and ion Landau damping influence the behavior of finite frequency modes such as Alfvén eigenmodes and resistive wall modes in rotating plasmas. When the phase velocity along the magnetic field lines is comparable to or below the ion thermal speed, the parallel dynamics contributes to inertia and damping. MHD describes these effects rather crudely. Damping occurs in radially localized resonances with the sound continuum, and the inertia of the parallel motion is accounted for by the Pfirsch-Schlüter factor in toroidal geometry. Kinetic theory gives significantly different results for finite frequency modes. Here we calculate the inertia and ion Landau damping for MHD modes using the drift kinetic energy principle [1–3]. The results are applied to BAE and RWM in tokamaks.

2. KINETIC FORMULATION

In drift kinetic theory, the parallel dynamics is solved for in terms of the displacement perpendicular to the magnetic field lines $\vec{\xi} \equiv \vec{\xi}_\perp$. If we ignore parallel electric fields, the kinetic energy principle implies that $\Delta W \equiv \Delta W_F(\vec{\xi}) + \Delta W_K(\vec{\xi}) - \omega^2 I_\perp/2 = 0$, where $\Delta W_F(\vec{\xi})$ is the MHD potential energy without the fluid compression term, and $I_\perp = \frac{1}{2}\int \rho|\xi_\perp|^2 d^3x$ is the inertia of the perpendicular displacement.

For simplicity, we ignore the gyrocentre and diamagnetic drift frequencies so that the contribution from the circulating particles to ΔW_K is:

$$\Delta W_C = \frac{1}{2}\sum_{m'}\int d^3x \int_{circ} d^3v \frac{\omega(-\partial f/\partial E)}{\omega - (nq - m')\omega_t}|\langle \exp(i\chi_{m'})H\rangle|^2 \qquad (1)$$

where ω_t the transit frequency and $H = \mu Q_L + m v_{||}^2 \vec{\xi}\cdot\vec{\kappa}$. The averages are made along the unperturbed orbits with respect to time. The trapped particle contribution is similar, except that $(nq - m')\omega_t$ is replaced by $-m'\omega_b$, where ω_b is the bounce frequency. We assume an isotropic Maxwellian particle distribution.

In the limit of large aspect ratio $\epsilon_r = r/R << 1$ and circular flux surfaces, ΔW_C can be calculated as follows. Using $B \approx B_0(1 - \epsilon_r \cos\theta)$ and the conservation of the magnetic moment μ and energy E, the transit frequency becomes $\omega_t = \pm\omega_s(E/T)^{1/2}\tau^{-1}$, where we introduced the sound frequency

$$\omega_s \equiv \frac{(2T/M)^{1/2}}{qR} \qquad (2)$$

the normalized transit time $\tau = \hat{K}(k)(\kappa_C/2\epsilon_r)^{1/2}$, and where $k^2 = 2\lambda\epsilon_r/[1 - \lambda(1 - \epsilon_r)]$, $\lambda = \mu B_0/E$, $\hat{K}(k) \equiv 2K(k)/\pi$ and $\kappa_C \equiv k^2(1 - \epsilon_r) + 2\epsilon_r$.

For low frequency MHD modes, $H \approx -(E/R)(2 - \lambda)\xi_R$, so that

$$|\langle \exp(i\chi_{m'})H\rangle| = (E/R)(2 - \lambda)c_{m'}(r, \lambda),\ c_{m'} \equiv |\langle \exp(i\chi_{m'})\xi_R\rangle| \qquad (3)$$

For well-passing particles, $\chi_{m'} \approx -m'\theta$ so that $c_{m'}$ equals the $m = m'$ poloidal harmonic of ξ_R. For simplicity, we use this approximation for all the particles.

The contribution to ΔW_K from the circulating particles can be written

$$\Delta W_C = 2\pi^2 R \sum_{m'}\int c_{m'}^2 r dr q^2 \rho \omega_s^2 \hat{\Delta}_{Cm'} \qquad (4)$$

where

$$\hat{\Delta}_{Cm'} = \int_0^\infty x^6 \exp(-x^2)\frac{dx}{\sqrt{\pi}}\int_0^{1/(1+\epsilon_r)} \frac{\omega^2}{\omega^2 - (nq - m')^2\omega_t^2}\,\tau(2 - \lambda)^2 d\lambda \qquad (5)$$

is a normalized potential energy. After integration with respect to energy $\hat{\Delta}_C$ can be expressed in terms of the plasma dispersion function as

$$\hat{\Delta}_C = -\frac{\Omega_C^2}{2}\int_0^{1/(1+\epsilon_r)} \left[\frac{3}{4} + \frac{1}{2}\Omega_C^2\tau^2 + \Omega_C^4\tau^4 + \Omega_C^5\tau^5 Z(\Omega_C\tau)\right]\tau^3(2-\lambda)^2 d\lambda \qquad (6)$$

where we introduced the normalized frequency

$$\Omega_C = \frac{\omega}{|nq - m'|\omega_s} \tag{7}$$

At low frequency, the ratio $-\hat{\Delta}_C/\Omega_C^2$ represents a normalized inertia.

In the "high-frequency" or "cylindrical" limit, $|\Omega_C| > \epsilon_r^{1/2}$, where the trapping effects on the parallel dynamics are small, the damping is

$$-\mathrm{Im}(\hat{\Delta}_C) = D_C = \sqrt{\pi}\,\Omega_C(1 + 2\Omega_C^2 + 2\Omega_C^4)\exp(-\Omega_C^2) \tag{8}$$

3. LOW FREQUENCY, TOROIDAL CALCULATION

At low frequency, $|\Omega_C| < O(\sqrt{\epsilon_r})$, the damping is decreased by toroidal trapping. The number of particles with large normalized transit time $\tau > \epsilon_r^{-1/2}$ decreases exponentially with τ. Therefore, when $|\Omega_C| < \sqrt{\epsilon_r}$, the damping comes mainly from the low energy particles. The damping term can be written as $D_C = \Omega_C \Omega_{C\epsilon}^6 F_C$, where

$$F_C(\Omega_{C\epsilon}, \epsilon_r) = \frac{\sqrt{\pi}}{16}\int_0^1 \hat{K}^8(k)\exp(-\frac{1}{2}\hat{K}^2\Omega_{C\epsilon}^2\kappa_C)(2\kappa_C - k^2)^2 dk^2 \tag{9}$$

and $\Omega_{C\epsilon} \equiv \Omega_C/\epsilon_r^{1/2}$. The dominance of the low energy particles in the damping at low frequency together with the strong weighting of the high energy particles in $\hat{\Delta}_C$ reduces the cylindrical damping (8) by six powers of $\Omega_{C\epsilon}$ [4].

Toroidal effects also influence the inertia when $|\Omega_{C\epsilon}| < 1$. Power series expansion of the Z-function in (6) gives a power series for $\hat{\Delta}_C$ in $\Omega_{C\epsilon}$:

$$\hat{\Delta}_C = -\frac{\Omega_C^2}{\sqrt{2\epsilon_r}}\left\{\sum_{l=0}^{\infty} a_l(\epsilon_r)\Omega_{C\epsilon}^{2l} + i[b(\epsilon_r)\Omega_{C\epsilon}^5 + ...]\right\} \tag{10}$$

The coefficients are given by $a_l = \left\{\frac{3}{8}, \frac{1}{8}, \frac{1}{8}, -\frac{1}{8}, ...\right\} C_l(\epsilon_r)$, where $C_l(\epsilon_r) = \int_0^1 \hat{K}^{2l+3}(k)\kappa_C^{l-5/2}(2\kappa_C - k^2)^2 dk^2$ and $b = (\pi/128)^{1/2} C_{5/2}(\epsilon_r)$. Numerically,

$$a_0 = 1.370 + (2\epsilon_r)^{1/2} + O(\epsilon_r)\ .\ b = 10.37\,(1 + 4.21\epsilon_r + 4.63\epsilon_r^2) \tag{11}$$

Higher order terms in ϵ_r have been included here, because they significantly change the result for aspect ratios of practical interest.

The calculation for the trapped particles closely parallels that for the circulating particles. We introduce the normalized frequency

$$\Omega_T \equiv 2\omega/m'\omega_s \tag{12}$$

The power series for the normalized contribution to the potential energy $\hat{\Delta}_T$ takes the same form as for circulating particles,

$$\hat{\Delta}_T = -\frac{\Omega_T^2}{\sqrt{2\epsilon_r}}\left\{\sum_{l=0}^{\infty} a_l(\epsilon_r)\Omega_{T\epsilon}^{2l} + i[b(\epsilon_r)\Omega_{T\epsilon}^5 + ...]\right\} \tag{13}$$

Here, $a_l = \left\{\frac{3}{8}, \frac{1}{8}, \frac{1}{8}, -\frac{1}{8}, ...\right\} T_l(\epsilon_r)$, $b = (\pi/128)^{1/2} T_{5/2}(\epsilon_r)$ and $T_l(\epsilon_r) = \int_0^1 \hat{K}^{2l+3}(k) \kappa_T^{l-5/2} (2\kappa_T - 1)^2 dk^2$ with $\kappa_T = 1 - \epsilon_r + 2\epsilon_r k^2$; numerically

$$a_0 = 0.915 + 0.517\epsilon_r + O(\epsilon_r^2)\ , b = 11.04(1 + 3.71\epsilon_r + 3.60\epsilon_r^2) \tag{14}$$

3.1 Comparison with MHD. Numerical results

$\Delta W_K = \Delta W_C + \Delta W_T$ corresponds, in MHD language, to the fluid compressional energy minus the kinetic energy associated with the parallel motion. The kinetic result for ΔW_K at low frequency resembles the Pfirsch-Schlüter inertia enhancement in MHD. To see this, we note that at large aspect ratio $\xi_R = \xi_r \cos\theta - \xi_\theta \sin\theta$. In the "inertial layers", where $|\xi_\theta| >> |\xi_r|$, this gives $\xi_{R,m} \approx \frac{i}{2}(\xi_{\theta,m+1} - \xi_{\theta,m-1})$. Thus, for the well-passing particles $c_m = \frac{1}{2}|\xi_{\theta,m+1} - \xi_{\theta,m-1}|$. If ξ_θ is dominated by one single poloidal harmonic m, (10) and (13) show that to lowest order in $\epsilon_r^{1/2}$ and $\Omega/\epsilon_r^{1/2}$

$$-\mathrm{Re}(\Delta W_K) = \frac{q^2}{\sqrt{2\epsilon_r}} \left[\frac{0.34}{(m-1-nq)^2} + \frac{0.34}{(m+1-nq)^2} + 0.92 \right] \frac{\omega^2}{2} I_\perp \tag{15}$$

For incompressible MHD modes at low frequency and *arbitrary* q, the MHD enhancement is given by [5]

$$F_{PS} = 1 + \frac{q^2}{(m-1-nq)^2} + \frac{q^2}{(m+1-nq)^2} \tag{16}$$

which reduces to $1 + 2q^2$ at the zero-frequency resonances $q = m/n$.

Thus, in the low frequency limit, $\Omega_C << \sqrt{\epsilon_r}$, the perpendicular inertia is enhanced by a factor of order $q^2 \epsilon_r^{-1/2}$. The $O(\epsilon_r^{-1/2})$ enhancement comes from particles near the trapping boundary. (5) shows that the particles going faster than the wave decrease ΔW_C, i.e., add to the inertia, while the slower particles subtract from the inertia. The toroidal reduction of the number of particles with low average parallel velocity in a torus therefore *increases* the inertia.

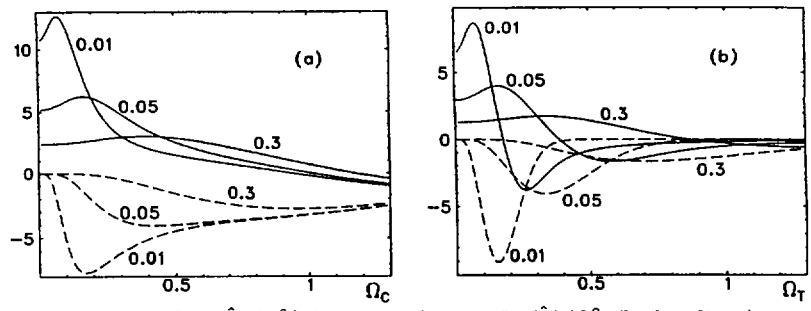

Figure 1. Inertia [-Re($\hat{\Delta}$)/Ω^2] (solid lines) and +Im($\hat{\Delta}$)/Ω^2 (broken lines) versus normalized frequency for inverse aspect ratios ϵ_r = 0.01, 0.05 and 0.3. (a) circulating and (b) trapped particle contributions.

The damping is strongly reduced by toroidicity at low frequency, $|\Omega_C| < \epsilon_r^{1/2}$. Figure 1 shows the real and imaginary parts of the normalized inertia $-\hat{\Delta}/\Omega_C^2$ for passing and trapped particles versus the normalized frequency at different aspect ratios from numerical integration of (6). The low-frequency MHD result corresponds to $-\hat{\Delta}/\Omega_C^2 = 4$.

4. TOROIDAL AND BETA-INDUCED ALFVEN EIGENMODES

Beta-induced toroidal eigenmodes (BAE) are observed in DIII-D discharges at high β_N. The BAE has a significantly lower frequency than the TAE [6]. The present theory explains several properties of the BAE. In the experiment reported by Heidbrink *et al*, [6], the sound frequency in the central region was $\omega_s/2\pi = 45/q$ kHz. The frequencies of the BAE and TAE were found to be $f_{TAE} \approx 58$ kHz, $f_{BAE} \approx 22$ kHz after subtraction of the "Doppler shift" (which also eliminates the effects of the diamagnetic frequency to the lowest order in ω_{*i}/ω_{BAE}).

First consider the MHD approximation. The phase velocity of the TAE is supersonic. Therefore, the parallel motion is small and the associated inertia is negligible. However, for the BAE, which has low frequency and occurs for high beta, the phase velocity may be subsonic. In this case, parallel displacements attempt to make the motion incompressible. At the TAE resonance, $m = nq \pm \frac{1}{2}$, and the low frequency inertia enhancement factor (16) for MHD is $F_{PS} = 1 + \frac{40}{9}q^2$. Therefore, if the perpendicular displacements for the TAE and BAE are similar, the ratio of their frequencies should be $\omega_{TAE}/\omega_{BAE} = (1 + \frac{40}{9}q^2)^{1/2}$. As shown by Fu and Cheng [7], the TAE frequency is decreased by finite beta. If we introduce a factor $f = \omega_{TAE}/\omega_{TAE}(\beta = 0)$ (in the range of 0.5 to 1) to account for this, the BAE frequency for $40q^2/9 >> 1$ is

$$\omega_{BAE} \approx f\omega_A/4q^2 \tag{17}$$

In order for the BAE to be approximately incompressible, its phase velocity must be subsonic. Roughly, this means that $\Omega = 2\omega_{BAE}/\omega_s < 1.5$. Using (17) for the BAE frequency, the incompressibility condition becomes

$$\beta_i q^2 > 0.1 f^2 \tag{18}$$

This implies that the BAE can only occur close to or beyond the first stability limit for ballooning. The MHD prediction for the ratio of frequencies coincides with experimental result $\omega_{TAE}/\omega_{BAE} \approx 2.6$ if $q \approx 1.2$. At this value of q, the TAE mode is clearly supersonic, while the BAE mode is slightly subsonic. This of course means that kinetic theory is required.

In kinetic theory, the frequency is determined from $K(\omega) \equiv \omega^2 I_\perp/2 - \Delta W_K = \Delta W_F(\vec{\xi}_\perp)$. We estimate $\Delta W_F \approx f^2 2\pi^2 R\rho \int |\xi_\theta|^2 r dr$, which gives the correct frequency for the TAE. We now assume $nq - m = \frac{1}{2}$ and $c_{m\pm1} = \frac{1}{2}|\xi_m|$.

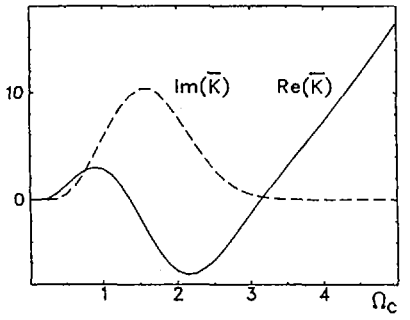

Figure 2. Real and imaginary parts of $\bar{K}(\Omega_C)$ for $\epsilon_r = 0.2$, $q = 1.1$.

Then the frequency of the Alfvén eigenmodes can be determined from

$$\bar{K}(\Omega) \equiv \Omega^2 - 2q^2\hat{\Delta}_{m\pm1} = \frac{f^2}{4\beta_i} \tag{19}$$

For q large enough, $\mathrm{Re}(\bar{K})$ is a non-monotone function of frequency. Figure 2 shows the real and imaginary parts of $\bar{K}(\Omega)$ for $q = 1.1$ and $\epsilon_r = 0.2$.

When the pressure increases, the required value for $\bar{K}$ decreases, because the TAE frequency decreases when measured in terms of the sound frequency. When $f^2/4\beta_i$ falls below the low frequency maximum of $\mathrm{Re}(\bar{K})$, there are three solutions to (19). The highest frequency is the TAE solution and the lowest frequency gives the BAE. For the intermediate frequency, the damping is strong and this mode should be harder to excite.

According to Fig. 2, the BAE should first appear with Ω slightly above unity. The experimental result $\Omega = 2\omega_{BAE}/\omega_s \approx q$ therefore indicates that the BEA is centered at q somewhat above 1. Figure 2 also shows that $\omega_{TAE}/\omega_{BAE} \approx 3$, when the BAE first comes into play, which is reasonably close to the experimental value of 2.6. We point out that if the mode occurred for $q > 1.2$, it would be rather strongly damped. Consideration of the damping thus makes it plausible that the mode localized to $q \leq 1.2$.

The low-frequency maximum of $\mathrm{Re}(\bar{K})$ in Fig. 2 is about 3. Therefore, according to (19), the condition for a BAE to occur at $q = 1.1$ becomes $\beta_i > f^2/12$ [which coincides with the MHD condition (18)]. The central ion beta in DIII-D discharge 71524 is about 0.06 at the time the BAE mode is observed. This agrees with the kinetic theory if $f \leq 0.9$.

4. RESISTIVE WALL MODES

The stability of the RWM is important for "advanced tokamaks", where the central part of the plasma has reverse shear and is in the second stability regime for ballooning. Wall stabilization of low-n modes is required in order for such equilibria to reach reasonable beta [8]. When the finite conductivity of the wall is taken into account, the wall stabilized low-n modes turn into

resistive wall modes which can be stabilized by plasma rotation at a few percent of the Alfvén speed [9,10]. It is known that dissipation, such as ion Landau damping, can stabilize the RWM in a rotating plasma [9,10]. The kinetic results on damping and inertia are therefore relevant for understanding the stability of the RWM [11].

Experimental results from DIII-D, e.g. shot 80111 [12,13], show that significant wall stabilization occurs for toroidal rotation speeds as low as 1% of the Alfvén speed, which is clearly subsonic. Numerical stability computations [13] indicated that the Landau damping has to be a significant fraction of its cylindrical value in order for the RWM to be stable for such slow rotation. The strong reduction of the ion Landau damping at low rotation frequency by the toroidal trapping therefore raises difficulties in understanding the wall stabilization of this discharge. The most likely resolution is an enhanced effect of the flow because of the toroidal inertia enhancement at high q.

To estimate the required rotation frequency including the inertia enhancement, we note that in the MHD approximation (16), the lowest branch of the Alfvén continuum is limited to frequencies below $\omega_A/4q^2$. Therefore, a drastic change of the mode structure is to be expected when

$$\omega_{rot} > \omega_A/4q^2 \tag{20}$$

If $\omega_{rot}/\omega_A = 0.01$, this change of the mode structure occurs for $q > 5$. It should be noted that the decreased rotation speed needed for strong modification of the mode structure (20) applies only *below* the sound frequency v_{thi}/qR so that the motion is incompressible. This is similar the condition for an incompressible BAE to exist (18). Because of the toroidal inertia enhancement, kinetic theory gives a less stringent condition than MHD at large aspect ratio. For DIII-D discharge 80111 the incompressibility condition (18) is satisfied in the entire region where $q \leq 5$. Furthermore, the condition for the frequency to exceed the lowest Alfvén continuum band (20) is satisfied for $q > 5$. Therefore, the MHD mode structure is significantly modified by rotation around the $q = 5$ surface in DIII-D discharge 80111. To show conclusively that this is responsible for the observed wall stabilization, numerical solution of the full drift kinetic stability equation is required.

Acknowledgement. This work was funded in part by the European Communities under an association contract between EURATOM and the Swedish Natural Science Research Council (A. B.) and by U. S. Department of Energy under grant DE-FG03-95ER54309 (M. S. C.).

REFERENCES

[1] ANTONSEN, T.M., LEE, Y.C., Phys. Fluids **25** (1982) 132.
[2] van DAM, J.W., ROSENBLUTH, M.N., LEE, Y.C., Phys. Fluids **25** (1982) 1349.
[3] CHENG, C.Z., Phys. Reports **211** (1992) 1.

[4] MIKHAILOVSKII, A.B., SURAMLISHVILI, G.I., Sov. J. Plasma Phys. **5** (1979) 523.
[5] WAHLBERG, C., BONDESON, A., J. Plasma Phys. (1996).
[6] HEIDBRINK, W.W., et al, Phys. Rev. Lett. **71** (1993) 855.
[7] FU, G.Y., CHENG, C.Z., Phys. Fluids **B2** (1989) 985.
[8] KESSEL, C., et al, Phys. Rev. Lett. **72** (1994) 1212.
[9] BONDESON, A. WARD, D.J., Phys. Rev. Lett. **72** (1994) 2709.
[10] WARD, D.J., BONDESON, A., Phys. Plasmas **2** (1995) 1570.
[11] MIKHAILOVSKII, A.B., KUVSHINOV, B.N., Plasma Phys. Rep. **21** (1995) 802.
[12] STRAIT, E.J., et al, Phys. Rev. Lett. **74** (1995) 2483.
[13] CHU, M.S., et al, Phys. Plasmas **2** (1995) 2236.

DISCUSSION

F. ZONCA: You assume that diamagnetic effects are negligible. Thus you look at low frequency to minimize ion Landau damping. One could consider ω_{*pi} to play a role, thus giving inverse ion Landau damping. In fact, experimental results on BAE show that $\omega \cong \omega_{*pi}$. Can you comment on this point?

A. BONDESON: A agree that ω_{*pi} should be included, which will modify the results. A reasonably complete theory would probably have to include both the toroidal effects on the particle orbits and ω_* effects. However, the experimental results from DIII-D indicate that ω_* effects give only minor corrections for $n = 1$ and 2.

R.J. GOLDSTON: Do you have a quantitative estimate of how much the toroidal rotation requirement is reduced by your effect?

A. BONDESON: This has not been analysed yet. The present theory indicates that the observed wall stabilization at $v_{rot}/v_A = 0.01$ in DIII-D discharge 80 111 can be explained by a pronounced change in the mode structure for $q \gtrsim 5$ (this applies to the outer 10% of the poloidal flux). At higher q, i.e. lower plasma current, the required rotation velocity should decrease proportionally to $1/q^2 \propto I_p^2$.

ALPHA PARTICLE TRANSPORT DUE TO ALFVÉN WAVE EXCITATION*

H.L. BERK, B.N. BREIZMAN, J. CANDY, B. DEMSKY, J. FITZPATRICK, M.S. PEKKER, J.W. VAN DAM, H.V. WONG, D. BORBA[1], A. FASOLI[2], H. HOLTIES[3], G.T.A. HUYSMANS[1], W. KERNER[1], S. SHARAPOV[1], L.C. APPEL[4], T.C. HENDER[4], S.D. PINCHES[4], K.L. WONG[5], F. PORCELLI[6], T. OZEKI[7]
Institute for Fusion Studies,
University of Texas at Austin,
Austin, Texas,
United States of America

Abstract

ALPHA PARTICLE TRANSPORT DUE TO ALFVÉN WAVE EXCITATION.

An overview of progress in linear and nonlinear theory of Alvén wave instabilities driven by energetic particles (such as alpha particles in fusion plasma experiments) is presented. Linear analysis shows that a rich spectrum of Alfvén waves can be excited in usual tokamaks during low-shear discharges, or in low-aspect-ratio spherical tokamaks. These waves do not readily disappear with increasing plasma β as previously expected. A nonlinear theory of resonant wave–particle interaction is also described, where collisional effects are included. An interpretation of TFTR experimental data is suggested on the basis of this analysis. This interaction is studied in the case where there is no resonance overlap (single-mode theory), as well as in the regime of mode overlap. Mode-amplitude bursting scenarios are described in both cases, and a surprisingly large saturation level is found near the instability threshold. The theory also describes unstable waves that do not exist in the absence of energetic particles. A frequency 'chirping' explosive solution is found for such waves (including fish-bone oscillations). It is also shown that mode frequency sweeping is a possible method for the conversion of fast-ion free energy to wave energy even in linearly stable systems.

* This is a report of work supported by US DOE Contract Nos DE-FG03-96ER-54346 and DE-AC-AC02-76-CH0-3073.

[1] JET Joint Undertaking, Abingdon, Oxfordshire, UK.

[2] CRPP/Ecole polytechnique fédérale de Lausanne, Lausanne, Switzerland.

[3] FOM Institute for Plasma Physics "Rijnhuizen", Nieuwegein, Netherlands.

[4] UKAEA Fusion, Abingdon, Oxfordshire, UK.

[5] Plasma Physics Laboratory, Princeton, New Jersey, USA.

[6] Dipartimento di Energetica, Politecnico di Torino, Turin, Italy.

[7] Japan Atomic Energy Research Institute, Naka-machi, Naka-gun, Ibaraki-ken, Japan.

1 Introduction

The transport of fusion-product alpha particles [1] that drive kinetic instabilities is a key issue for a tokamak reactor, as indicated by the anomalous loss of fast ions in NBI- and ICRH-heated discharges [2]. It is essential to understand the structure of linear modes that are subject to these instabilities, as well as the mechanisms that cause these instabilities to saturate, in order to determine whether significant alpha particle losses will occur. In this paper, we describe recent developments in the linear theory of low-shear toroidal Alfvén eigenmodes (LSTAE) [3-5] and report on numerical tools which have been developed to study geometry-dependent aspects of the linear and nonlinear problems [6-9]. Further, we summarize the cogent results from a nonlinear theory of the kinetic instabilities [10]. The understanding of the critical issues that determine saturation and transport is not strongly dependent on the precise geometry, but rather emphasizes the effect of discrete modes and finite collisionality. We outline how experimental data can be interpreted within this theoretical perspective [11].

2 Low-Shear TAE Modes

Early analytic studies [12] showed that finite-β effects stabilized the ideal TAE mode by causing a frequency shift downwards into the Alfvén continuum. Numerical work [13], however, indicated that ideal modes persisted in the weak-shear plasma core region at higher than expected values of β. An analytic explanation [3] indicated that previously neglected finite-aspect-ratio effects were responsible for the persistence of the *lower core-localized mode* well into the finite-β regime. It was also realized that an ideal *upper core-localized mode* exists [4,14], and that these modes smoothly evolve into kinetic Alfvén waves as shear increases.

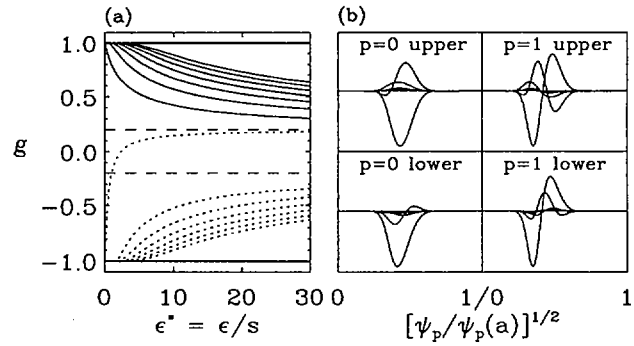

FIG. 1 *(a) The spectrum of values of the relative eigenfrequency shift g calculated using the local theory of Ref. [5] ($g = \pm 1$ define the top and bottom of the gap, respectively). (b) The first two upper and lower radial LSTAE eigenmodes ($p = 0, 1$), calculated using* MISHKA-1, *in a low-aspect-ratio geometry, with $a/R_0 = 0.75$. Note, in general, the symmetric polarization of the lower modes, and anti-symmetric polarization of the upper modes.*

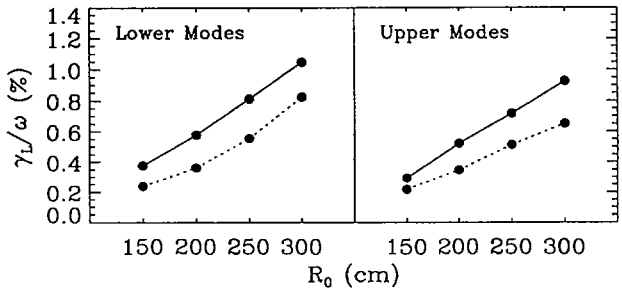

FIG. 2 *Linear alpha particle drive for $p=0$ (solid lines) and $p=1$ (dotted lines) upper and lower LSTAE modes of Fig. 1 with $B_0=2.5$ T and $\langle\beta_\alpha\rangle=7.4\times10^{-5}$.*

More recently, a rich spectrum of multiple upper and lower modes – which we will refer to as low-shear TAE modes (LSTAE) – has been shown to unfold in a single gap as the aspect ratio increases at fixed shear so as to make $\epsilon^* \equiv \epsilon/s > 1$ (see Fig 1a) [5]. These mode are especially appropriate for the low-shear central region of so-called spherical tokamaks, and also in enhanced confinement regime tokamak operation where the low- and reversed-shear regions are typically radially extended. Indeed, LSTAE activity during reversed shear operation, in both TFTR (alpha particles) and JT-60U (ICRH tail ions), has been observed [15].

In general, we expect that modes of the core-localized type will exist for a wide range of operating parameters as either ideal or nonideal modes. Observe that as ϵ^* decreases the ideal LSTAE spatial width ($\Delta w \sim \epsilon^*$) decreases while the nonideal parameter $\lambda \sim n\rho/(\epsilon^*\sqrt{\epsilon})$ increases. Thus, the LSTAE-type mode is expected to convert to a core-localized KTAE-type mode, for which $\Delta w \sim \lambda^{2/3}$. Here, ρ is the ratio of ion Larmor radius to minor radius and n is the toroidal mode number.

Numerical simulations with the ideal MHD code MISHKA-1 [6] were performed for a weak/reversed-shear equilibrium in a tight-aspect-ratio low-β tokamak with $a/R_0=0.75$. For this equilibrium, the computed spectrum of $n=20$ ideal LSTAE was found to consist of at least 36 discrete eigenmodes associated with the gap at $q=(n+3/2)/n=1.075$. The first two upper and lower modes are shown in Fig. 1b. It is also observed that as plasma pressure is increased the lower branch, which is subject to radiation damping, is increasingly suppressed, while the upper branch is less strongly affected. This property is also indicated by numerical studies with the antenna version of CASTOR-CR [14], which detects only up-shifted modes for moderate β [16]. The FAC code [7,8] has been used to calculate the linear growth rates of LSTAE driven by a realistic distribution of thermonuclear alphas. Numerical results show, for example, that γ_L increases with the major radius R_0, and decreases with radial quantum number, as shown in Fig. 2.

3 Relevance to ITER

In an ITER-type ignited plasma, the population of fusion alpha particles will be strongly peaked near the magnetic axis, where core-localized TAE are expected

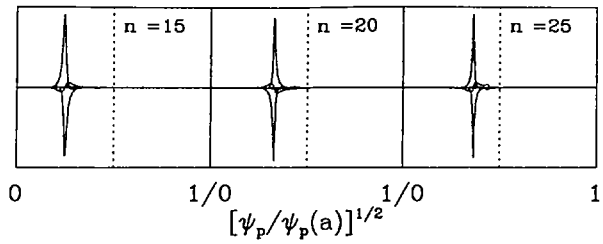

FIG. 3 *Eigenmode structure for three selected core-localized modes in the* $m = (n-1, n-2)$ *series, calculated using an ITER-type equilibrium.*

to exist for a wide range of toroidal mode numbers ($10 \lesssim n \lesssim 40$). Thus, the possible excitation by alpha particles of LSTAE modes is particularly relevant. Presently, work is in progress to establish a catalogue of these core-localized eigenmodes, to investigate the most unstable but more conventional TAE modes that exist at larger shear values, and to perform an accurate calculation of the alpha particle destabilization together with the dominant damping mechanisms. High-n modes are a computational challenge. CASTOR-CR and MISHKA-1 have so far been used to obtain various families of core-localized modes/KTAE that can exist inside the $q = 1$ surface for ITER-type equilibria. Core-localized KTAE in the range $7 \leq n \leq 14$ have been found in the $q = (n - 1/2)/n$ gap – that is, where the dominant coupling is for the harmonics $m = (n-1, n)$ – by CASTOR-CR. Further, core-localized-modes for $13 < n < 26$ (see Fig. 3) have been found in the $q = (n - 3/2)/n$ gap with MISHKA-1. Preliminary calculations of the ion Landau damping (expected to be the dominant damping mechanism) with the CASTOR-K code [7] indicate that for core-localized KTAE at relatively low temperature ($T_i = 10$ keV), the damping exhibits a strong increase with n not predicted by the local passing-particle theory. This result is shown in Fig. 4.

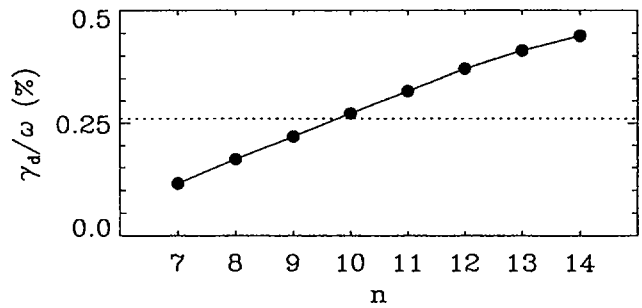

FIG. 4 *Ion Landau damping of core localized modes in the* $q = (n - 1/2)/n$ *gap as a function of* n *for* $T_i = 10\,keV$. *The dotted line is the local estimate obtained from an analytic, passing particle model.*

4 Nonlinear Particle-Wave Dynamics

The nonlinear theory focuses on the dynamics of particles nearly resonant with a wave. In a tokamak, this resonance condition is $\Omega_\ell \equiv \omega - n\omega_\varphi - \ell\omega_\theta = 0$, where ω is the mode frequency, ω_θ and ω_φ are the frequencies of poloidal and toroidal motion in the unperturbed fields, and n and ℓ are integers with n the toroidal mode number. Since the wave frequency is much less than the ion cyclotron frequency, the particle magnetic moment, μ, is conserved. Also, the particle energy in the wave frame, $\mathrm{E}' = \mathrm{E} - (\omega/n)\mathrm{P}_\varphi$, is conserved. The toroidal canonical momentum, P_φ, or equivalently $\Omega_\ell(\mathrm{P}_\varphi, \mathrm{E}', \mu)$, exhibits a universal behavior [17] that reduces to a pendulum equation, $d^2\chi/dt^2 + \omega_{\mathrm{b}\ell}^2 \sin\chi = 0$, such that $\Omega_\ell = d\chi/dt$. The trapping frequency, $\omega_{\mathrm{b}\ell}$, which generally scales as the square root of the mode amplitude, is given by

$$\omega_{\mathrm{b}\ell}^2 = \left| \frac{n\omega_\theta e_\alpha}{2\pi\omega} \left[\frac{\partial \Omega_l}{\partial \mathrm{P}_\varphi} \right]_{\mathrm{E}',\mu} \int_0^{2\pi/\omega_\theta} d\tau\, \vec{\mathcal{E}}(\vec{r}(\tau), \tau) \cdot \vec{v}(\tau) \right| \qquad (1)$$

where $\vec{\mathcal{E}}$ is the mode electric field, $\vec{v}$ the energetic particle velocity, and e_α the particle charge. The integration is to be performed along the unperturbed resonant particle orbit, with the initial point on the trajectory chosen to maximize $\vec{\mathcal{E}}\cdot\vec{v}$. The first integral of the pendulum equation gives $\Omega_\ell^2/2 - \omega_{\mathrm{b}\ell}^2 \cos\chi = C$, with C a constant. For $-\omega_{\mathrm{b}\ell}^2 \lesssim C \lesssim \omega_{\mathrm{b}\ell}^2$, particles mix in the trapping region so that the width of the resonance is $\Delta\Omega \sim \omega_{\mathrm{b}\ell}$. The width $\omega_{\mathrm{b}\ell}$ generally varies along the resonant surface, $\Omega_\ell(\mathrm{P}_\varphi(\mathrm{E}', \mu), \mathrm{E}', \mu) = 0$. Its magnitude is determined by the field amplitude, the eigenmode structure, and the unperturbed particle orbits. A schematic view of the width for several resonances in $(\mathrm{E}, \mathrm{P}_\varphi)$-space at fixed μ is shown in Fig. 5. If the widths of the resonances are separated, a single mode nonlinear theory applies; if they overlap appreciably, a quasilinear theory is applicable. A method which describes the transition between these regimes is given in Sec. 8.

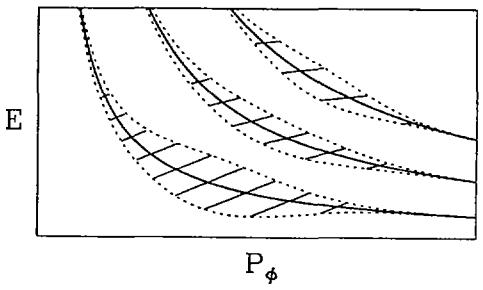

FIG. 5 *Illustration of resonances* $\Omega_\ell(\mathrm{E}, \mathrm{P}_\varphi) = 0$ *(solid curves). Dotted curves indicate the resonance widths* $\Delta\Omega_\ell$*. Tilted lines show the direction of constant* E'.

Collisional effects, together with sources and sinks, are often important [10]. With a Fokker-Planck collision operator, the distribution function, $f(\Omega_\ell, \mathrm{E}', \mu)$, near resonance is found to satisfy a reduced kinetic equation

$$\frac{\partial f}{\partial t} - \omega_{\mathrm{b}\ell}^2 \sin\chi \frac{\partial f}{\partial \Omega_\ell} + \Omega_\ell \frac{\partial f}{\partial \chi} + \nu_{\mathrm{eff}}^3 \frac{\partial^2 f}{\partial \Omega_\ell^2} = 0 \tag{2}$$

where ν_{eff} is the rate (when $\omega_{\mathrm{b}\ell} \to 0$) at which particles pass through the resonance region via velocity space diffusion caused by stochastic processes such as collisions and RF heating. The boundary condition for Eq. 2 requires that, far from resonance, $\partial f/\partial \Omega_\ell$ asymptote to its value determined by sources and sinks when there is no wave perturbation. Together with Eq. 2, we need to solve the evolution equation for the wave amplitude which takes into account the wave damping at a rate, γ_{d}, due to the power dissipated by the background plasma, as well as the wave excitation by the resonant particles – which in linear theory is γ_{L} in the absence of dissipation. In the limit near instability threshold (*i.e.*, $\gamma_{\mathrm{L}} - \gamma_{\mathrm{d}} \ll \gamma_{\mathrm{L}}$), the problem can be reduced to a dynamical equation for the mode amplitude A [10] (with $|A| \simeq \omega_{\mathrm{br}}^2$, and ω_{br} the bounce frequency at a conveniently selected point Γ_{r} on the resonant surface in phase space):

$$e^{-i\phi} \frac{dA}{dt} - (\gamma_{\mathrm{L}} - \gamma_{\mathrm{d}})A + \tag{3}$$
$$\frac{\gamma_{\mathrm{L}}}{2} \int_0^{t/2} z^2\, dz \int_0^{t-2z} dx\, e^{-\nu_{\mathrm{eff}}^3 z^2 (2z/3+x)} A(t-z)\, A(t-z-x)\, A^*(t-2z-x) = 0$$

In Eq. 3, φ is a constant that depends on the linear wave properties. When the wave evolution is treated perturbatively, $\phi = 0$ and A is real. In this case, Eq. 3 has a steady-state solution $A = 1.40(1 - \gamma_{\mathrm{d}}/\gamma_{\mathrm{L}})^{1/2} \nu_{\mathrm{eff}}^2$, which is stable if $\nu_{\mathrm{eff}}/(\gamma_{\mathrm{L}} - \gamma_{\mathrm{d}}) > 2.15$.

The saturated amplitude can also be calculated [10] for $\gamma_{\mathrm{d}}/\gamma_{\mathrm{L}} \ll 1$, and an interpolation formula may be used to obtain an estimate of the steady saturation level for arbitrary $\gamma_{\mathrm{d}}/\gamma_{\mathrm{L}}$. The resulting relation is

$$\gamma_{\mathrm{d}}/\gamma_{\mathrm{L}} = \frac{\sum_\ell \int d\Gamma\, \omega_{\mathrm{b}\ell}^4\, G(\Gamma)/H(\Gamma)}{\sum_\ell \int d\Gamma\, \omega_{\mathrm{b}\ell}^4\, G(\Gamma)} \to \begin{cases} 1 - \alpha(\omega_{\mathrm{br}}/\nu_{\mathrm{eff,r}})^4 & ; \quad 1 - \gamma_{\mathrm{d}}/\gamma_{\mathrm{L}} \ll 1 \\ \beta(\nu_{\mathrm{eff,r}}/\omega_{\mathrm{br}})^3 & ; \quad \gamma_{\mathrm{d}}/\gamma_{\mathrm{L}} \ll 1 \end{cases} \tag{4}$$

where $G(\Gamma) = \delta(\Omega_\ell)[\partial F/\partial \mathrm{P}_\varphi]_{\mathrm{E}',\mu}([\partial \Omega_\ell/\partial \mathrm{P}_\varphi]_{\mathrm{E}',\mu})^{-2}$ (with F the equilibrium fast-particle distribution), $H(\Gamma) = 1 + au/(1 + b/u)^{1/3}$, $u = \omega_{\mathrm{b}\ell}^3/\nu_{\mathrm{eff}}^3$, $a = 0.57$ and $b = 1.45$. Also, α and β are dimensional numerical coefficients that depend on the phase space position Γ_{r}.

5 Interpretation of Experimental Data

Quasi-steady TAE signals have been observed in TFTR when hot particles are produced by ICRH minority-ion heating, augmented in DT discharges by alpha

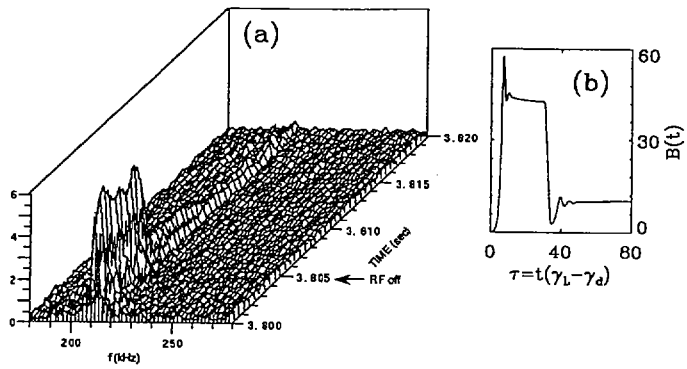

FIG. 6 *(a) Decrease and persistence of Alfvén signal in TFTR after turnoff of ICRH, and (b) replication of this effect achieved with the nonlinear mode equation, Eq. 3.*

particles [11]. A feature that illustrates the role of velocity-space diffusion in the quasi-steady Mirnov fluctuations can be deduced from the data shown in Fig. 6a. Prior to $t = 3.805s$, the ICRH is on, and fast ions are produced at a heating rate $\nu_h \propto \nu_{eff}^3$. The experimental mode saturation levels are also shown. When the heating is turned off, the principal collisional mechanism that persists is pitch angle scattering of resonant ions, with $\nu_s < 0.1\nu_h$, so that ν_{eff}, which is proportional to $\nu_h^{1/3}$, decreases to roughly half of the ICRH-on value. This leads to a lower level of quasi-stationary oscillations, as seen after $t = 3.805s$. Only after a relatively long time (15ms) do the oscillations cease.

We interpret the two quasi-stationary levels seen in the experiment as single-mode solutions with different values of ν_{eff}. A numerical solution of Eq. 3 for which ν_{eff} is abruptly reduced by 1/2 shows a similar decrease in saturation level. This is illustrated in Fig. 6b. The Alfvén fluctuations are finally quenched after RF turn-off because the fast-ion population is reduced by ion drag. This is seen to occur on a time-scale about 1/10th the slowing-down time, presumably because the fast-ion distribution was only slightly above marginal stability.

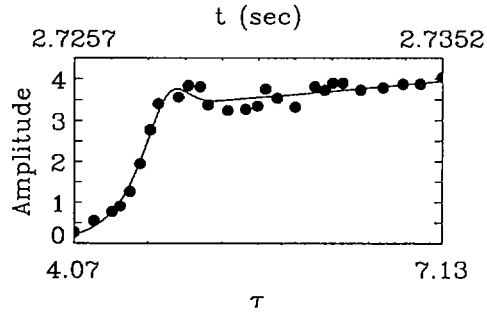

FIG. 7 *Comparison of theory (solid curve) and TFTR data (dots).*

A fit of the solution to the experimental data is shown in Fig. 7, where an unstable mode first emerges. In the simulation, the growth rate, $\gamma \equiv \gamma_L - \gamma_d$, is taken to vary linearly in time from $0 < \gamma < 0.1\gamma_L$, and the response is fitted to experimental data. From the fitting, we infer that the ratio of perturbed to equilibrium magnetic field is roughly 10^{-5}, and the RF heating time is 0.2s – results that are consistent with the experiment. Thus, there is experimental evidence that saturated modes can be explained by a single-mode theory that requires the inclusion of sources and sinks.

6 Nonlinear Mode Evolution in ITER

Two similar codes, FAC [8] and HAGIS [9], have been developed to compute the nonlinear evolution of TAE of modes in general tokamak geometry. Preliminary studies of the self-consistent transport of alphas due to TAE excitation have been performed with FAC. Fig. 8 shows the nonlinear evolution of 8 core-localized TAEs ($7 \leq n \leq 14$ in the $m = (n, n-1)$ series) collectively interacting with a realistic alpha population in an ITER-like plasma. Although $\langle \beta_\alpha \rangle = 1.75\%$ is higher than expected for ITER, and the saturated amplitudes for some modes exceed $\delta B/B = 10^{-3}$, there is no significant anomalous redistribution, even locally. This result indicates that ITER alpha profiles are highly resilient to instability of isolated modes, and even to localized clusters of unstable modes. However, this sort of simulation must be extended to include many more modes (global and core-localized) before the anomalous transport issue can be adequately resolved.

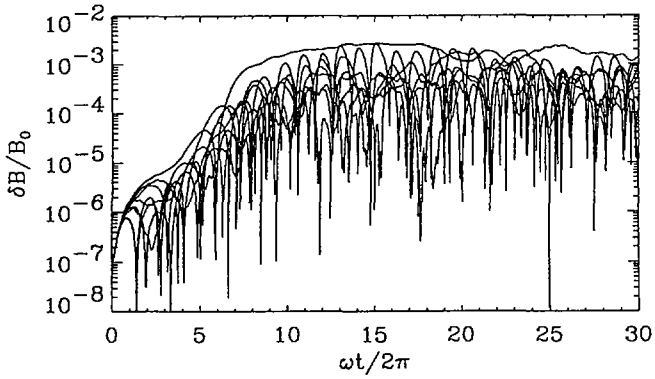

FIG. 8 *Nonlinear evolution of 8 upper-core-localized modes in ITER-like geometry for* $\langle \beta_\alpha \rangle = 1.75\%$ *and background damping. The modes saturate at a relatively large amplitude but do not cause appreciable anomalous redistribution.*

7 Resonance Widths and Mode Overlap

The single-mode oscillations discussed in Secs. 4 and 5 assume no mode overlap. Their effect on particle loss is typically benign since resonant particles, which mix rapidly within a separatrix width, cannot readily cross the regions between

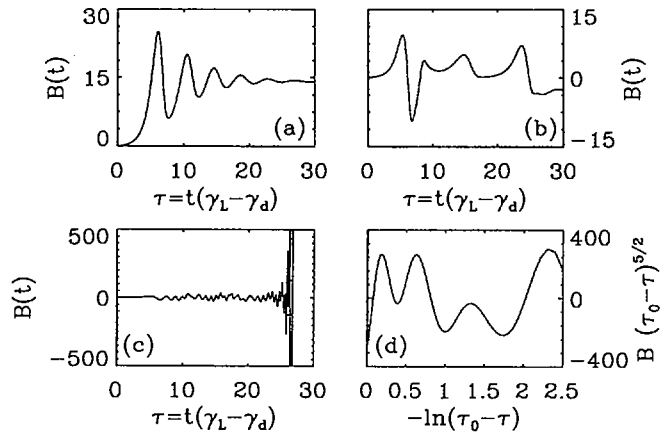

FIG. 9 *Solution of Eq. 3 for* $\nu_{\rm eff}/(\gamma_{\rm L}-\gamma_{\rm d}) = 3.11$ *(a), 1.72 (b), and 1.274 (c). Here,* $B(t) \equiv A(t)\gamma_{\rm L}^{1/2}/(\gamma_{\rm L}-\gamma_{\rm d})^{5/2}$. *In cell (d), an expanded view of cell (c) is shown for the interval* $25.9 < \tau < 26.7$.

the separatrices. Thus, there is no rapid global diffusion. Further, there will not be a significant amount of direct ion loss if the separatrices are far from the particle loss regions.

The results of the previous section allow an estimate for the resonance width, including collisions, of the form $\Delta\Omega \sim \omega_{\rm b} + \nu_{\rm eff} \sim \nu_{\rm eff}(\gamma_{\rm L}/\gamma_{\rm d})^{1/3}$. This estimate is applicable if $\nu_{\rm eff} > (1-\gamma_{\rm d}/\gamma_{\rm L})\gamma_{\rm L}^{2/3}\gamma_{\rm d}^{1/3}$. When this inequality is violated, bursting of individual modes will occur [10]. Saturation levels in this regime are $\omega_{\rm b} \sim \gamma_{\rm L}$ (*i.e.*, the level for the *initial-value problem*: $\nu_{\rm eff} = \gamma_{\rm d} = 0$). Bursts occur with a rate $\nu_{\rm eff}^3/\gamma_{\rm L}^2$, with $\omega_{\rm b}/\gamma_{\rm L}$ about half the initial-value result. Perhaps a surprising result is that if $\gamma_{\rm L}-\gamma_{\rm d} \ll \gamma_{\rm L}$ and $\nu_{\rm eff}/(\gamma_{\rm L}-\gamma_{\rm d}) < 1$, the saturation level still scales as $\omega_{\rm b}/\gamma_{\rm L} \sim 1$. This follows from Eq. 3. Fig. 9 shows numerical solutions of Eq. 3 for various values of $\nu_{\rm eff}$. If $\nu_{\rm eff}$ is not too small, the mode either reaches a steady state, or pulsates at a level $\omega_{\rm b}/\gamma_{\rm L} \sim (1-\gamma_{\rm d}/\gamma_{\rm L})^{5/4}$ with increasingly complex behavior as $\nu_{\rm eff}$ decreases.

Finally, for sufficiently small $\nu_{\rm eff}$, the solution diverges in a finite time; that is, as t approaches t_0. A self-similar "explosive" solution to Eq. 3 of the form $g[\alpha\ln(t_0-t)]/(t_0-t)^{5/2}$ exists, with $g(x)$ a periodic function of x and α an eigenvalue. In the explosive phase, the assumptions leading to Eq. 3 break down, but one can show by dimensional analysis that the breakdown only occurs as $\omega_{\rm b} \to \gamma_{\rm L}$.

As the energetic particle drive builds up, the modes first go unstable and saturate at a low level related to the increment above marginal stability (*viz.*, $\omega_{\rm b}/\nu_{\rm eff} \to [1-\gamma_{\rm d}/\gamma_{\rm L}]^{1/4}$). As $\gamma_{\rm L}$ increases slowly in time, the mode amplitude follows this scaling unless a condition where $\gamma_{\rm L}-\gamma_{\rm d} \geq \nu_{\rm eff}$ is reached. In this case, there is a transition in the saturation level and it rapidly increases to $\omega_{\rm b} \sim \gamma_{\rm L}$ in what can be described as a "mini-explosion". With increasing $\gamma_{\rm L}$, mode overlap

will ultimately be achieved with either the quasi-stationary or mini-explosive scenario. Then, conditions are established for rapid global diffusion, not only because KAM surfaces disappear, but also because in the global mixing process the unstable energetic particle distribution releases much more free energy than will occur with isolated modes [10]. There is then a global "phase-space explosion" for which the resulting diffusion coefficient, proportional to the wave energy, causes a rapid loss of particles. It is conceivable that observed NBI-induced losses in some experiments are a manifestation of the overlap of several unstable modes.

The experiments have not reported a persistent low-level precursor prior to a large burst. Perhaps this is because the overlap is being triggered through the mini-explosion route, where the steady oscillations can be at a very low level until the conditions occur for mini-explosions of several modes, which then rapidly lead to overlap and detectable signals.

8 Line-Broadened Quasilinear Theory

We now examine the system evolution when saturation levels permit mode overlap. We have developed a model that is applicable to this transition case. The quasilinear equation, including a particle source and sink, is

$$\frac{\partial f}{\partial t} - 2\pi \sum_{\ell} \left(\frac{\omega}{n} \frac{\partial}{\partial \mathrm{E}} + \frac{\partial}{\partial \mathrm{P}_\varphi} \right) \left[\frac{\omega_{\mathrm{b}\ell}^4 \mathcal{T}}{[\partial \Omega_l / \partial \mathrm{P}_\varphi]^2_{\mathrm{E}',\mu}} \right] \left(\frac{\omega}{n} \frac{\partial}{\partial \mathrm{E}} + \frac{\partial}{\partial \mathrm{P}_\varphi} \right) f = S + \mathcal{C}(f) \quad (4)$$

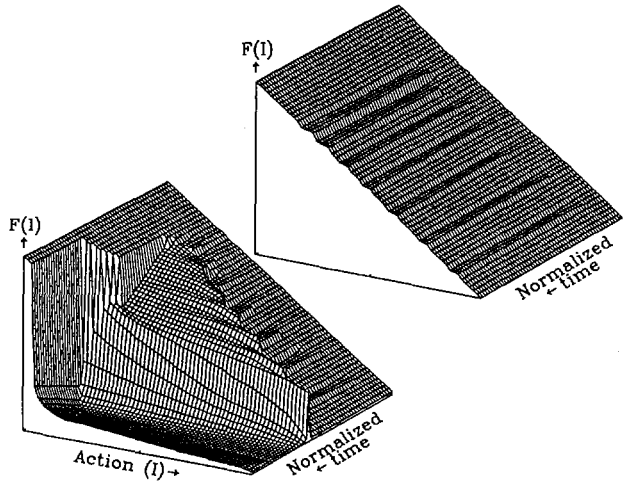

FIG. 10 *Line-broadened quasilinear simulation of the evolution of a generic distribution of hot particles in the case of nonoverlapping modes (right) and overlapping modes (left). The nonoverlaping modes show only benign pulsations, while overlapping modes cause an explosive particle-to-wave energy transfer.*

where C is a Fokker-Planck collision operator, and $\mathcal{T}$ – which in standard quasilinear theory is the delta function $\delta(\Omega_\ell)$ – is a broadened function with width $\Delta\Omega_\ell = c_1 \nu_{\text{eff}} + c_2 \omega_{b\ell} + c_3 |\gamma|$. Here, γ is the instantaneous linear growth rate, and the c_i are chosen so that steady and single-mode pulsed solutions to Eq. 4 fit particle simulation and analytic results. The time evolution of $\omega_{b\ell}^2$ satisfies the linear wave equation where the resonant particle drive is calculated with the same broadening function $\mathcal{T}$ as in Eq. 4. As the wave grows, mode overlap can occur and, as discussed, leads to a much larger conversion of particle energy into wave energy than in the nonoverlapped case. In the extreme, a "domino-effect" [10] is possible. In this case, large gradients arise at the interface between flattened and unperturbed regions of phase space, which increase the saturated amplitude. Overlap even occurs between modes whose resonant frequencies are spread more widely than the linear growth rate γ_L. This case is illustrated in Fig. 10, which shows a generic particle distribution as a function of one action variable, for two cases with linear growth rates 10% apart. In the former case with no overlap there are benign pulsations; in the latter, modes overlap and trigger a domino-effect, giving rise to a complete sweeping-out of particles in the explosive quasilinear pulse.

9 Frequency Chirping of Energetic-Particle-Induced Modes

The theories discussed thus far apply to modes that exist in the absence of an energetic particle population, and for which the effects of this population are perturbative. Alternatively, hot particles can cause a nonperturbative wave response, and the very existence of a mode may depend on the presence of a hot particle population. Examples include fishbones [18], energetic beam TAE modes [19] and energetic electron interchange modes [20]. A common experimental phenomenon observed during such excitations is frequency shifting, or "chirping". We note that a frequency shift can arise from either an external change of parameters determining the system's state, or by a self-consistent effect on the system's nonlinearity. In the former case, an externally induced alteration of the resonance conditions can be brought about by the changing of the background density by means of gas puffing, sawtooth crashes, or application of a modulated frequency to an antenna-driven mode. Previously, we noted that when collisions are negligible the saturation level is $\omega_b \sim \gamma_L$ (where it was assumed that the resonance condition is constant in time). However, when there is resonance "sweeping" – that is, when the resonance condition changes in time – the saturation level scales as either $\omega_b \sim (\omega\gamma_L)^{1/2}$ (fast sweeping: $d\omega/dt > \omega^2/\omega_b$), or $\omega_b \sim \omega^{2/3}\gamma_L^{1/3}$ (adiabatic sweeping: $d\omega/dt < \omega^2/\omega_b$). Further, one can show that with adiabatic sweeping the power transfer of waves to particles can be faster than linear. This observation allows an energy conversion mechanism where the kinetic energy of energetic particles can be directly extracted to electric energy, even though the energetic particle distribution is stable to linear excitations. Hence this mechanism is an alternative to energy "channeling" [21].

The self-consistent chirping mechanism occurs in modes like fishbones where fast particles are essential for the existence of a mode that emerges at marginal stability. The mode can be described by Eq. 3, but with A complex and φ nonzero.

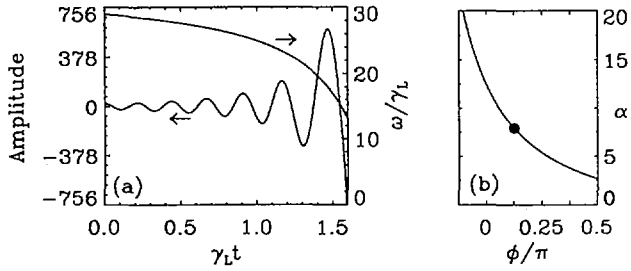

FIG. 11 *(a) Self-similar solution of Eq. 3 for $\phi = \pi/8$, showing a normalized amplitude proportional to $Re[A(t)\exp(-i\omega t)]$, (oscillatory curve) and the chirped frequency (monotonic curve), and (b) the eigenvalue α as a function of ϕ. The dot in (b) corresponds to the solution in (a).*

A self-similar chirping solution proportional to $\cos[\omega t + \alpha \ln(t_0 - t)]/(t_0 - t)^{5/2}$ (see Fig. 11a) can be shown to exist, with $\alpha(\varphi)$ an eigenvalue (Fig. 11b). If ν_{eff} is sufficiently small, the mode exhibits explosive behavior, with a shifting frequency (downward, as observed experimentally for the fishbone mode). The frequency shift is in the direction that allows the particle-to-wave power transfer to increase.

REFERENCES

[1] PUTVINSKI, S., et al., in Plasma Physics and Controlled Nuclear Fusion Research 1994 (Proc. 15th Int. Conf. Seville, 1994), Vol. 2, IAEA, Vienna (1996) 535.

[2] WONG, K.L., et al., Phys. Rev. Lett. **66** (1991) 1874; also HEIDBRINK, W.W., et al., Nucl. Fusion **31** (1991) 1635.

[3] FU, G.Y., Phys. Plasmas **2** (1995) 1029.

[4] BERK, H.L., VAN DAM, J.W., BORBA, D., CANDY, J., HUYSMANS, G.T.A., SHARAPOV, S., Phys. Plasmas **2** (1995) 3401.

[5] CANDY, J., BREIZMAN, B.N., VAN DAM, J.W., OZEKI, T., Phys. Lett. A **215** (1996) 299.

[6] MIKHAILOVSKII, A.B., HUYSMANS, G.T.A., KERNER, W., SHARAPOV, S., Rep. JET-P(96) 25, 1996.

[7] BORBA, D., CANDY, J., FASOLI, A., KERNER, W., MUIR, D., SHARAPOV, S., Rep. JET-P(96) 30, 1996.

[8] CANDY, J., J. Comput. Phys. (in press).

[9] JET TEAM (presented by D. START), IAEA-CN-64/A2-6, these Proceedings, Vol. 1, p. 303.

[10] BERK, H.L., et al., Phys. Plasmas **3** (1996) 1827; also BERK, H.L., BREIZMAN, B.N., PEKKER, M., Phys. Rev. Lett. **76** (1996) 1256.

[11] WONG, K.L., et al., IFS Report IFSR No. 753, July 1996, submitted to Phys. Plasmas.

[12] CHEN, L., in Theory of Fusion Plasmas, Società Italiana di Fisica, Editrice Compositori Bologna (1989) 327; also FU, G.Y., CHENG, C.Z., Phys. Fluids B **2** (1990) 985; ZONCA, F., CHEN, L., Phys. Fluids B **5** (1993) 3688.

[13] CHENG, C.Z., et al., in Plasma Physics and Controlled Nuclear Fusion Research 1994 (Proc. 15th Int. Conf. Seville, 1994), Vol. 3, IAEA, Vienna (1996) 373.

[14] POEDTS, S., KERNER, W., GOEDBLOED, J.P., KEEGAN, B., HUYSMANS, G.T.A., SCHWARZ, E., Plasma Phys. Control. Fusion **34** (1992) 1397; also BORBA, D., CANDY, J., HOLTIES, H., HUYSMANS, G.T.A., KERNER, W., SHARAPOV, S., in Controlled Fusion and Plasma Physics (Proc. 22nd Eur. Conf. Bournemouth, 1995), Vol. 19C, Part II, European Physical Society, Geneva (1995) 237.

[15] NAZIKIAN, R., et al., IAEA-CN-64/A2-4, these Proceedings, Vol. 1, p. 281; also KIMURA, H., et al., IAEA-CN-64/E-6, these Proceedings, Vol. 3.

[16] HOLTIES, H., PhD thesis (1996).

[17] CHIRIKOV, B.V., Phys. Reports **51** (1970) 253.

[18] McGUIRE, K., et al., Phys. Rev. Lett. **50** (1983) 891; also CHEN, L., WHITE, R.B., ROSENBLUTH, M.N., Phys. Rev. Lett. **52** (1984) 1122.

[19] ZONCA, F., CHEN, L., Phys. Plasmas **3** (1996) 323.

[20] WARREN, H.P., MAUEL, M.E., BRENNAN, D., TAROMINA, S., Phys. Plasmas **3** (1996) 2143.

[21] FISCH, N.J., RAX, J.R., Phys. Rev. Lett. **69** (1002) 612.

RECENT PROGRESS IN LINEAR AND NONLINEAR STUDIES OF TOROIDAL ALFVÉN EIGENMODES

G.Y. FU, Y. CHEN, R.V. BUDNY, Z. CHANG,
C.Z. CHENG, D.S. DARROW, E.D. FREDRICKSON,
E. MAZZUCATO, R. NAZIKIAN, W. PARK,
R.B. WHITE, K.L. WONG, Y. WU, S.J. ZWEBEN
Plasma Physics Laboratory,
Princeton University,
Princeton, New Jersey,
United States of America

D.A. SPONG
Oak Ridge National Laboratory,
Oak Ridge, Tennessee,
United States of America

H. KIMURA, T. OZEKI, M. SAIGUSA
Japan Atomic Energy Research Institute,
Naka-machi, Naka-gun, Ibaraki-ken,
Japan

M.S. CHU, W.W. HEIDBRINK, E.J. STRAIT
General Atomics,
San Diego, California,
United States of America

Abstract

RECENT PROGRESS IN LINEAR AND NONLINEAR STUDIES OF TOROIDAL ALFVÉN EIGENMODES.

Toroidal Alfvén eigenmodes (TAEs) are studied in linear and nonlinear regimes using several kinetic/MHD hybrid models. It is shown that the stability of the TAE is largely determined by its radial mode structure. The calculated stability thresholds are correlated well with observations, including the recently observed alpha-driven TAEs in the TFTR DT experiments. In the nonlinear regime, quasilinear simulations with multiple modes show that the saturation level is enhanced by nonlinear wave–particle resonance overlapping when the linear growth rate exceeds a critical value. A fully self-consistent δf noise reduction method for the 3D particle/MHD hybrid model is developed.

1. Introduction

An important issue for tokamak fusion reactors is whether the Toroidal Alfvén Eigenmode[1] (TAE) can become unstable[2] and affect alpha particle confinement. This issue has been assessed in the past experiments where the TAEs were strongly destabilized by energetic beam ions in the NBI-heated plasmas or by fast minority tail ions in the ICRF-heated plasmas[3–6]. Recently, alpha-driven TAE instability has been observed in the TFTR DT experiments[7] with reduced central magnetic shear and elevated central safety factor, although alpha particle loss has not yet been seen. In ITER, high-n TAEs are predicted to be unstable. This gives new impetus to benchmark codes with experimental results and to study alpha particle loss induced by TAEs. In this paper, recent results of linear and nonlinear studies of TAEs are presented.

2. Linear Stability

The linear stability of TAEs is studied using a kinetic MHD stability code NOVA-K[8, 9]. The NOVA-K code is applied to several recent experiments, including the TFTR DT experiments, the JT-60U ICRF experiments and the DIII-D NBI experiments. The NOVA-K code calculates perturbatively the fast ion drive, the electron/ion/beam Landau damping, the collisional damping due to trapped electrons, and the "radiative" damping due to the coupling to the radially propagating kinetic Alfvén waves. The important physics of finite orbit width of fast ions is included. The continuum damping is neglected. All the calculations are valid for realistic equilibria with experimental parameters and profiles as obtained from the TRANSP code[10].

The TAEs are calculated to be stable[11, 12] in the initial TFTR DT experiments in supershot regime with up to 10MW of fusion power, consistent with the observations[13]. The main damping mechanisms are beam ion Landau damping and the "radiative" damping. The stability is sensitive to the mode structure which depends on the details of plasma parameters and profiles, especially the q profiles. There are two types of TAEs as shown in Fig. 1: (a) the global modes and (b) the core-localized modes (CLMs). The CLMs[14, 15] peak near the center of the plasma where the magnetic shear is weak, and tend to be less stable than the global modes since the alpha pressure profile is sharply peaked at the center. The stability of CLMs is sensitive to the central magnetic shear. Since the radial mode width is inversely proportional to the magnetic shear, a weaker shear results in larger alpha drive and smaller "radiative" damping. This led to the prediction[12] that the CLMs can be destabilized by alpha particles with a weakly negative central magnetic shear and small beam ion Landau damping in the TFTR DT experiments. Figure 2 show the ratio of alpha drive to the total damping as a function of the magnetic shear at $r/a = 0.15$ for an $n = 5$ CLM in a high fusion power TFTR DT discharge (#76770). We see that the mode

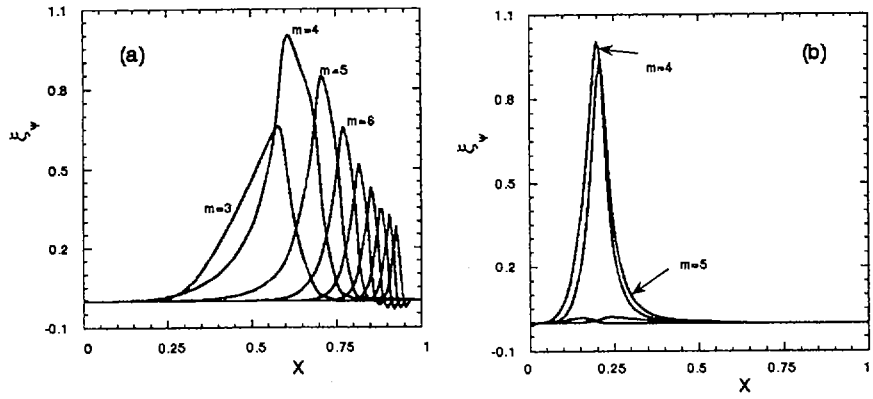

FIG. 1. Radial mode structure of (a) a global mode and (b) a CLM.

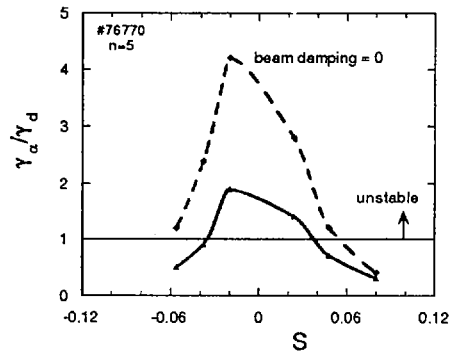

FIG. 2. Ratio of alpha drive to total damping versus the central magnetic shear with (dashed line) and without (solid line) beam damping.

becomes unstable as the shear becomes smaller. It should also be pointed out that the beam damping has an important effect on the stability. This implies that the mode tends to become more unstable when the beam ions slow down after the beam power is turned off. These results are confirmed qualitatively by the recent observation of alpha-driven TAE activity after NBI in the TFTR DT experiments[7].

In these new DT experiments, the plasmas have a higher central safety factor ($q(0) > 1$), lower central magnetic shear and lower beta values. Figure 3 shows the calculated ratio of alpha drive to the damping of an $n = 3$ mode versus $q(0)$ for such a plasma (TFTR shot #93404) where the central alpha beta value is 0.014% (at $t = 3.2$sec, when the instability appeared). The corresponding alpha

beta threshold is very low, on order of $\beta_\alpha(0) = 0.01\%$ for the likely range of $2.3 < q(0) < 2.5$. This is in qualitative agreement with the experimental results. Physically, such a low stability threshold is caused by several factors. First, the beam damping is significantly reduced due to slowing down of beam ions. Second, the plasma beta is reduced after NBI, which leads to smaller radiative damping, especially for the CLMs. Finally, the alpha drive is relatively larger for higher $q(0)$ (when plasma beta is sufficiently low) and weaker magnetic shear. It can be shown analytically that the alpha drive is approximately proportional to q/s, where s is the magnetic shear. From Fig. 3, we also see that the stability is a sensitive function of $q(0)$. The instability is maximized at about $q(0) = 2.45$ at which the CLM is located in the region of large alpha pressure gradient. As $q(0)$ varies from 2.5 to a smaller value, the mode location shifts from the center of the plasma toward the edge. This change in the mode location results in large variation of alpha particle drive. Work is in progress to analyze the alpha-driven TAE experiments in TFTR for a wider parameter range and results will be reported elsewhere.

The stability of TAEs in the TFTR DT plasmas has also been analyzed using a gyrofluid model[16]. The model calculates excitation of the TAE using a set of fluid moment equations which have been constructed to include Landau resonance effects. The model also includes continuum damping, ion/electron Landau damping and the radiative damping. The fast ion distribution is currently constrained to be a Maxwellian. The calculations are performed with realistic equilibria and are non-perturbative. We find that the conventional global TAE and the CLMs can be present for different parameter regimes. The parameter which determines which mode dominates is the ratio of the averaged alpha velocity to the Alfvén velocity (v_α/v_A). Figure 4 shows the linear growth

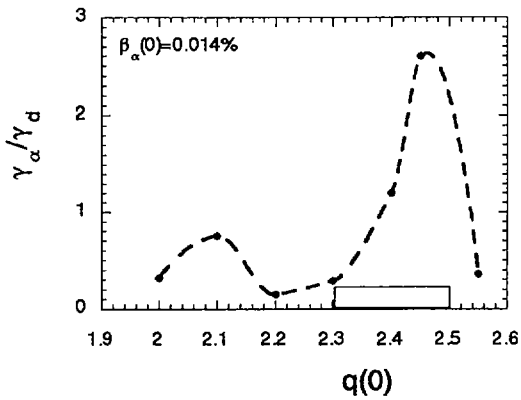

FIG. 3. Ratio of drive to damping versus q(0) for an n = 3 mode in a TFTR DT discharge (#93404).

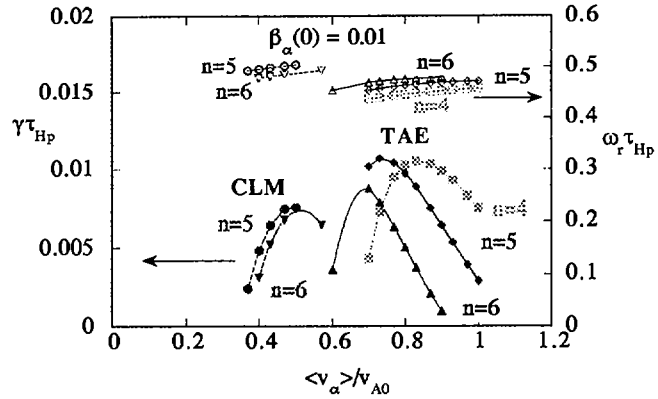

FIG. 4. Growth rates and the real frequencies of the CLM and the global modes as a function of v_α/v_A for several toroidal mode numbers.

rates as a function of v_α/v_A for the global mode and the CLM and several toroidal mode numbers. As indicated, the CLM resonates at somewhat lower values of v_α/v_A ($0.3 < v_\alpha/v_A < 0.6$) than the global TAE ($0.6 < v_\alpha/v_A < 1$). Realistically, the alpha energy distribution and v_A are constantly evolving in time so making a scan in v_α/v_A can be viewed as encompassing the dynamic behavior of the actual experiment.

The stability of TAEs in JT60U and DIII-D plasmas has also been analyzed using the NOVA-K code. In the recent JT-60U ICRF experiments, the high-n TAEs were excited sequentially during the sawteeth stabilizing phases. The instability was induced by the fast minority ions powered by the ICRF heating. The results of the NOVA-K code indicated that the stability of the TAE is a strong function of mode location[17]. This dependence results in sequential mode excitation as $q(0)$ drops in time. More recently, high-n TAE instability was observed in the JT-60U ICRF experiments with reversed shear profiles[18]. The mode activity only appeared after the second mini-collapse. Our calculations show that the stability is mainly determined by mode structure. It is found that that the mode is unstable only when it peaks in the region of weakly negative shear just inside the q_{min} radius since the fast ion drive of such a mode is much larger than that of the mode which peaks outside the q_{min} radius. Furthermore, the existence of the mode just inside q_{min} depends on the density gradient in this region. The mode exists only when the density gradient is small or the continuum gaps are well aligned near the q_{min} radius. This result is in good agreement with the experimental observations since the mini-collapses reduce the density gradient significantly. Details of these results are reported by Kimura et al.[18] at this conference. Finally, for the DIII-D NBI experiments, the calculated critical beam ion beta is $\beta_{beam}(0) \approx 10\%$ for the TAE instability.

This is in approximate agreement with the observations. Compared to the TFTR NBI and the JT-60U ICRF experiments, the critical fast ion beta in the DIII-D NBI-heated plasmas is much higher due to the edge localized mode structure.

3. Nonlinear Particle/MHD Hybrid Simulations

Here, we study nonlinear evolution of the TAEs using Particle/MHD hybrid simulations. Two models are used: a quasilinear model developed by Chen and White[19] and the fully nonlinear model by Park et al.[20]. First, the quasilinear model is used to study the saturation of TAEs. The model is valid when the mode amplitudes are low enough such that the mode-mode coupling effects can be neglected in the nonlinear stage. In this limit, each mode is described by a slowly varying amplitude and phase with fixed mode structure. Given the linear mode structure $\eta_n(x)$, we can represent the solution as

$$\xi(\mathbf{x},t) = \sum A_n(t)\eta_n(\mathbf{x})sin(\omega_n t + \alpha_n(t)) \tag{1}$$

where ω_n is the mode frequency. The equations for the amplitude $A_n(t)$ and the phase $\alpha_n(t)$ can be derived from the momentum equation with the current-coupling scheme and are given by

$$\gamma_n = -<\int \mathbf{J}_h \cdot \mathbf{E}_n d^3\mathbf{r}> /(\omega_n^2 A_n^2) \tag{2}$$

$$\dot{\alpha}_n(t) = -<\int \mathbf{J}_h \cdot \frac{1}{\omega_n}\frac{\partial \mathbf{E}_n}{\partial t} d^3\mathbf{r}> /\omega_n^2 A_n^2 \tag{3}$$

where the growth rate $\gamma_n = \dot{A}_n/A_n$ and $<>$ represents averaging over a wave period, and J_h is the fast ion current density. The J_h is calculated from the fast ion distribution which is obtained by solving the drift-kinetic equation using the δf method. A Hamiltonian guiding center code [21] *ORBIT* is used to follow the particle trajectories in the presence of TAEs. Notice that Eq. 2 just expresses the energy conservation of the system. Previously, the energy conservation was used to advance the wave amplitude for a single mode with fixed phase. It was observed[22] that resonant particles, which lose energy to the mode through inverse Landau damping, shift outwards, thus the density gradient which gives the free energy to the wave is flattened at the resonant surface as time evolves, eventually leading to mode saturation. These observations are confirmed by using Eq. (2) and (3)directly. We also found that using Eq. (2) and (3) instead of explicit energy conservation can lower the noise significantly. We now consider the simultaneous evolution of multiple modes. Of particular concern in the multiple modes case is whether the TAE amplitudes become large enough to cause resonance overlap, which can lead to global particle diffusion and energy loss. As shown previously[23], resonance overlap is greatly facilitated

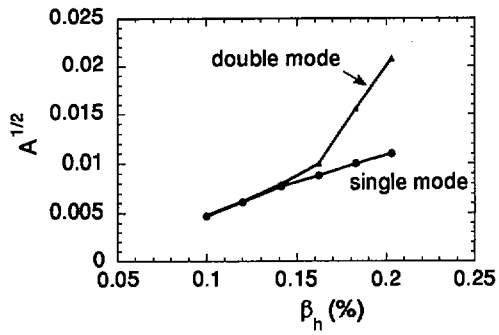

FIG. 5. Saturation level as a function of β_h for a single mode case (broken line) and a double mode case (solid line).

by the simultaneous excitation of multiple modes. In the following simulation we use ITER-like parameters: $R = 800cm$, $a = 300cm$, $B = 6T$, $\delta r = a/3$. Only $n = 2$ and $n = 3$ are considered and mode frequencies are $\omega_{n=3}/\Omega_c = 1.34 \times 10^{-3}$, $\omega_{n=2}/\Omega_c = 1.12 \times 10^{-3}$ where Ω_c is the on-axis gyro-frequency. The equilibrium particle distribution is assumed to be $f_0(r,\varepsilon) = e^{-r^2/\delta r^2}\varepsilon^{-\frac{3}{2}}$. The mode structures are obtained from the NOVA-K code. Figure 5 shows the saturated amplitude of an $n = 3$ mode as a function of β_h from a single mode case and a two mode simulation ($n = 2, 3$). We see that for the single mode case the saturation level $A^{1/2}$ is approximately linear in β_h, which gives the expected trapping scaling of $A \propto \gamma_h$ since the linear growth rate γ_h is proportional to β_h. Apparent deviation between the saturation levels starts at about $\beta_h = 0.16\%$, when resonance overlap occurs. This result shows that the saturation level is enhanced by resonance overlap.

In the fully nonlinear hybrid model, the MHD equations are coupled with gyrokinetic energetic particles through the pressure tensor.[20, 24] The plasma is divided into two parts: the bulk plasma, which contains the thermal electrons and ions, and the energetic hot ions. The bulk plasma is described by the ideal MHD equations, whereas the hot ions are described by the gyrokinetic equations[25]. The effects of hot ions couple to the bulk plasma motion through the pressure tensor term in the momentum equation as follows:

$$\rho_b \frac{d\mathbf{v}_b}{dt} = -\nabla P_b - (\nabla \cdot \mathsf{P}_h)_\perp + \mathbf{J} \times \mathbf{B}, \tag{4}$$

where the subscript b denotes the bulk part, the subscript h denotes the hot ion component, P_b is the isotropic pressure of the bulk plasma, and the P_h is the pressure tensor of the hot ions. The P_h is calculated from the hot ion distribution function f represented by an ensemble of particles which follow the gyrokinetic equations with the self-consistent electromagnetic field. Equation 4 and the other MHD equations are advanced in time using P_h given by the particles. The new $\mathbf{E}$ and $\mathbf{B}$ are in turn used to advance the particle quantities in

time. The model is fully self-consistent, including self-consistent effects of hot particles on the MHD dynamics and the nonlinear MHD mode coupling.

Using the particle/MHD hybrid *MH3D-K* code, we had found that wave particle trapping is the dominant mechanism for the TAE saturation[24]. In that work, the "double trajectory method" was used to reduce the simulation noise in the linear regime. Two sets of particles are used, one following the equilibrium field and the other the total electromagnetic field. The hot particle pressure tensor $\mathsf{P}_h(t)$ is replaced by $(\mathsf{P}_h(t) - \mathsf{P}_{h,0}(t)) + \mathsf{P}_{h,0}(0)$ where $\mathsf{P}_{h,0}$ is evaluated from the equilibrium orbits. The advantage of the double trajectory method is that it can be applied to any 3D equilibrium with an arbitrary distribution of particles including a delta function in velocity space. The disadvantage is that it is only valid for the linear regime. In this work, we adopt another noise reduction scheme, namely, the δf method[26], which is valid in both linear and nonlinear regimes. However, it is difficult to apply the scheme in a self-consistent manner to a 3D electromagnetic problem with a self-consistent equilibrium. For the first time, a scheme for the δf method is developed for such cases, and implemented in the MH3D-K code. The new linear results agree closely with the double trajectory method results, while improved nonlinear saturation results have been obtained for realistic parameters and profiles. The two main components for the self-consistent treatment of the δf method are the loading of particles and finding a self-consistent equilibrium. The particles are loaded according to an analytic function $f(P_\phi, E, \mu)$. (The equilibrium distribution f is written in terms of the constants of motion in the equilibrium fields, namely, the toroidal angular momentum P_ϕ, the kinetic energy E, and the magnetic moment μ.) Specifically, the distribution function is integrated in velocity space to get the particle density, $\rho_p(r, \theta)$. Then, the particles are loaded in real space according to $\rho_p(r, \theta)$ and in velocity space according to f_0. Note that the real space variables and the velocity variables are coupled together due to P_ϕ so that the loading in velocity space cannot be separated from that in real space.

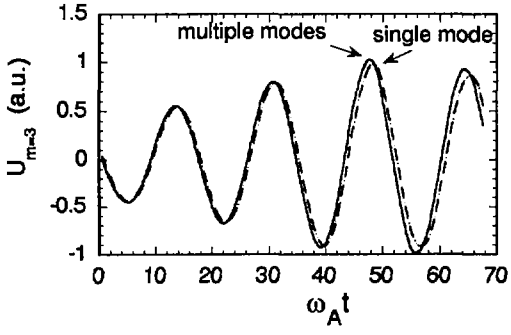

FIG. 6. Mode amplitude versus time obtained with a simple mode (dashed line) and multiple modes (solid line).

An equilibrium solution consistent with the analytic distribution $f_0(P_\phi, E, \mu)$ is obtained by an iterative method. The particles are first loaded according to an analytic distribution for the initial equilibrium field, and the equilibrium is allowed to relax with the self-consistent pressure. Then, the particles are re-loaded for the new equilibrium field and the equilibrium relaxes again. This process is repeated until the converged equilibrium is consistent with the particle distribution.

In the fully nonlinear simulations, we considered parameters and profiles similar to those of the TFTR NBI experiments[3] where the TAEs were destabilized by energetic beam ions: the aspect ratio $R/a = 3.0$, $q(0) = 1.0$, $q(a) = 3.5$, the plasma density profile $\rho = \rho_0(1-0.8(r/a)^2)$, and the hot ion beta $\beta_h(0) = 2.5\%$. Figure 6 shows the evolution of the $n = 2$ TAE for a single mode simulation and a multiple mode simulation with $n = 0, 1, 2$ and 3. We find that the saturation level obtained from a single mode is nearly the same as that from a multiple mode simulation. Thus, the nonlinear mode-mode coupling is not important for the mode saturation, as least for the case considered. Further work is in progress to assess the importance of mode-mode coupling in a wider parameter range.

4. Conclusions

The linear stability analysis of TAEs has been carried out for the parameters and profiles of several tokamak experiments, including the most recent TFTR DT experiments where alpha-driven TAEs were observed for the first time. The predicted stability trend by the NOVA-K code is well correlated with the observations. However, more work is needed in order to have accurate quantitative comparisons with the experimental thresholds for the instability, especially at levels of individual drive and damping mechanisms. This can be done in two ways. First, the theoretical model can still be improved in order to have all the important damping mechanisms and fast ion drive more self-consistently. Second, future experiments should be designed to investigate more systematically the dependence of stability on parameter and profiles. Our analysis has shown that the stability is sensitive to plasma profiles, especially the q profile. In the nonlinear regime, hybrid simulations using a quasilinear model as well as a fully nonlinear model have been carried out to assess the nonlinear saturation mechanisms for realistic parameters and profiles. The nonlinear resonance overlapping which enhances the saturation level is demonstrated for ITER parameters. A fully self-consistent δf method for the global electromagnetic Particle/MHD model is developed for the first time and is used in the MH3D-K code simulations for realistic parameters. More work is needed to compare the calculated saturated mode amplitudes and related fast ion transport with the experimental observations.

Acknowledgements

This work was supported by the United States Department of Energy under Contract DE–AC02–76–CHO–3073 and Grant DE-FG02-86ER53223.

REFERENCES

[1] CHENG, C.Z., CHEN, L., CHANCE, M.S., Ann. Phys. (N.Y.) **161** (1985) 21.
[2] FU, G.Y., VAN DAM, J.W., Phys. Fluids B **1** (1989) 1949.
[3] WONG, K.L., et al., Phys. Fluids B **4** (1992) 2122.
[4] HEIDBRINK, W.W., et al., Nucl. Fusion **31** (1991) 1635.
[5] WILSON, J.R., et al., in Plasma Physics and Controlled Nuclear Fusion Research 1992 (Proc. 14th Int. Conf. Würzburg, 1992), Vol. 1, IAEA, Vienna (1993) 661.
[6] SAIGUSA, M., et al., Plasma Phys. Control. Fusion **37** (1995) 295.
[7] NAZIKIAN, R., et al., these Proceedings, Vol. 1, p. 281.
[8] CHENG, C.Z., Phys. Rep. **211** (1992) 1.
[9] FU, G.Y., CHENG, C.Z., WONG, K.L., Phys. Fluids B **5** (1993) 4040.
[10] BUDNY, R.V., et al., Nucl. Fusion **34** (1994) 1247.
[11] FU, G.Y., et al., Phys. Rev. Lett. **75** (1995) 2336.
[12] FU, G.Y., et al., Phys. Plasmas **3** (1996) 4036.
[13] STRACHAN, J.D., et al., Phys. Rev. Lett. **72** (1994) 3526.
[14] FU, G.Y., Phys. Plasmas **2** (1995) 1029.
[15] BERK, H.L., et al., Phys. Plasmas **2** (1995) 3401.
[16] SPONG, D.A., et al., in Plasma Physics and Controlled Nuclear Fusion Research 1994 (Proc. 15th Int. Conf. Seville, 1994), Vol. 3, IAEA, Vienna (1996) 567.
[17] FU, G.Y., et al., Nucl. Fusion **36** (1996) 1759.
[18] KIMURA, H., et al., IAEA-CN-64/E-6, these Proceedings, Vol. 3.
[19] CHEN, Y., WHITE, R., Rep. PPPL-3182, Plasma Physics Lab., Princeton Univ., NJ (in press).
[20] PARK, W., et al., Phys. Fluids B **4** (1992) 2033.
[21] WHITE, R., CHANCE, M., Phys. Fluids **27** (1984) 2455.
[22] WU, Y., WHITE, R.B., CHEN, Y., ROSENBLUTH, M.N., Phys. Plasmas **2** (1995) 4555.
[23] BERK, H.L., BREIZMAN, B.N., YE, H., Phys. Rev. Lett. **68** (1992) 3563.
[24] FU, G.Y., PARK, W., Phys. Rev. Lett. **74** (1995) 1594.
[25] LEE, W.W., J. Comput. Phys. **72** (1987) 243.
[26] PARKER, S.E., LEE, W.W., Phys. Fluids B **5** (1993) 77.

DISCUSSION

A. JAUN: To calculate radiative damping in a perturbative manner you have to make assumptions on the mode conversion to the kinetic Alfvén wave. How sensitive are your stability analyses to these assumptions?

G.Y. FU: In this work, the radiative damping is one of the main damping mechanisms. Our model is valid when the kinetic Alfvén wave damps before reaching the neighbouring continuum gap.

DIVERTOR EDGE PHYSICS AND ALTERNATIVES

(Session D3)

Chairperson

D. BALDWIN
United States of America

MODELLING OF RADIATION DISTRIBUTION AND IMPURITY DIVERTOR COMPRESSION IN ASDEX UPGRADE

R. SCHNEIDER, D.P. COSTER, K. BORRASS, H.-S. BOSCH,
J. NEUHAUSER, K. LACKNER, M. KAUFMANN,
A. KALLENBACH, K. BEHRINGER, K. BÜCHL, R. DUX,
C. FUCHS, G. HAAS, A. HERRMANN, F. MAST,
J. SCHWEINZER, N. TSOIS, B.J. BRAAMS[1], D. REITER[2],
ASDEX UPGRADE TEAM
Max-Planck-Institut für Plasmaphysik,
Euratom–IPP Association,
Garching and Berlin,
Germany

Abstract

MODELLING OF RADIATION DISTRIBUTION AND IMPURITY DIVERTOR COMPRESSION IN ASDEX UPGRADE.

Coupled B2-Eirene time dependent multifluid calculations are presented, using a simplified ELM model (periodically enhanced radial transport during the ELM). The experimental signatures of various diagnostics of the effect of type I ELMs on the divertor and the SOL are successfully reproduced. From the results of type I ELM modelling the CDH mode with smaller type III ELMs is modelled, especially by checking the radiation distribution as measured by bolometers. Buffering of type III ELMs in the SOL and divertor is achieved by a rise in radiation loss during the ELM. On the basis of the validated transport model the compression of neon and helium as a function of neutral gas flux density is reproduced. A simple model explains the difference between neon and helium based on the impurity recycling cycle in the outer SOL up to the pumping baffle. Modelling of L mode density limit scenarios for ASDEX Upgrade is used for the discussion of a SOL based density limit. ASDEX Upgrade modelling reproduces the experimentally observed power dependence of the separatrix density at the density limit. The scenarios indicate the existence of a power independent regime (as for JET) for higher net input power. The density limit is characterized by complete detachment driven by the onset of volume recombination and marfe formation in the main chamber. The appearance of a shoulder in the H_α emission in the divertor close to detachment is well reproduced by the modelling due to the contributions from the high density marfe region.

1. INTRODUCTION

Analysis of impurity transport in the scrape-off layer is one of the most challenging topics, both for experiments and for modelling, because of the complexity of the problem, since the motion of neutrals and ions is, at least, two dimensional.

---

[1] Courant Institute, New York University, New York, N.Y., USA.

[2] IPP, Forschungszentrum Jülich GmbH, Euratom Association, Jülich, Germany.

Also, an understanding of the important aspects of impurity transport requires a validated model accounting for the impurity generation at the plates and sidewalls, proper description of the transport process (including atomic and/or molecular processes), especially adequately describing the delicate balance of thermal force (trying to push away the impurities from the divertor) and parallel electric field and friction forces (entraining the impurities towards the plate close to it), determining the transport along the field line plus the anomalous diffusion across the flux surfaces.

We report 2-D multifluid simulations, using the coupled B2-Eirene code package in a fully time dependent mode [1] applied to modelling of type I ELMs for pure hydrogenic plasmas and the completely detached H mode (CDH) with type III ELMs for a deuterium plasma with carbon as intrinsic impurity plus neon and helium, experimentally obtained in ASDEX Upgrade [2] by combined puffing of hydrogen and neon. Lowering the midplane density (without changing any of the validated transport parameters in the code) we vary the neutral gas flux density in the divertor by one order of magnitude (going from CDH to more attached conditions). This allows an analysis of neon and helium compression at the position of the pump duct relative to the midplane density. Another critical issue is the understanding of the density limit, at least with respect to divertor and SOL properties. Modelling of L mode density limit scenarios for ASDEX Upgrade is used for the discussion of a SOL based density limit and specific features of the H_α emission in the divertor.

2. TYPE I ELM MODELLING

ELMs (edge localized modes) appear in the H mode and periodically expel particles and energy from a region inside the separatrix (in ASDEX Upgrade about 5 cm). Type I ELMs are experimentally observed as large, regular, isolated H_α spikes. Their frequency increases with the heating power, and they are probably associated with an ideal ballooning instability (critical pressure gradient). In the following, the effect of ELMs on the SOL and divertor properties will be simulated. For this, the different time-scales have to be considered.

The time-scales involved in ELMs are the characteristic ELM time-scales for enhanced transport (0.1 to 1 ms) and for repetition (from 1 up to some 10 ms). These have to be compared with parallel plasma transport times of electron heat conduction by tail electrons (0.001 to 0.01 ms) and for ions (0.1 to 1 ms). In addition, the flight times of neutrals have to be considered: typically, atoms are flying 10 m per ms. For a divertor dimension of about 1 m, this defines a time of 0.1 ms. Molecules are about a factor of ten slower than atoms, which gives typical flight times of some milliseconds. Comparing these different time-scales we see that time dependent modelling (not only for the plasma, but also for the neutrals) is necessary.

In B2-Eirene an ELM is modelled by enhanced radial transport in the edge region. The transport coefficients are increased from their equilibrium values (about

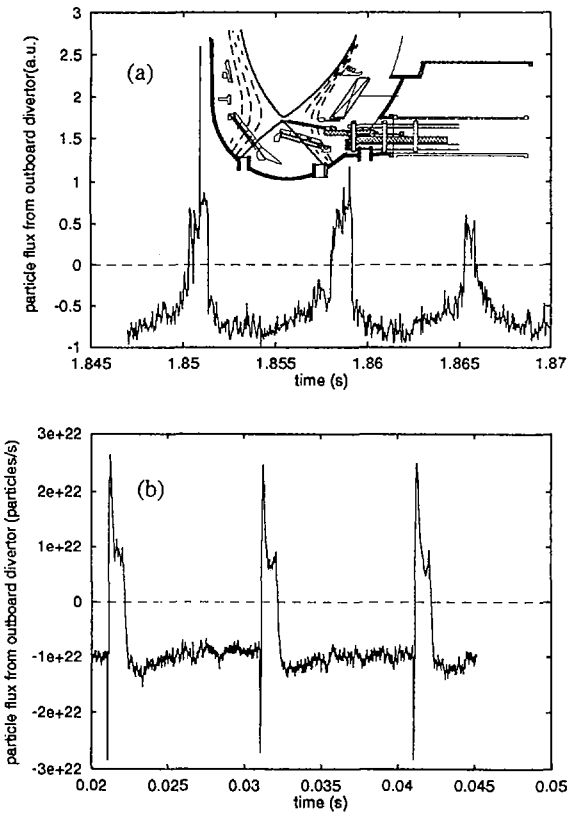

FIG. 1. Particle fluxes at the outer divertor entrance as (a) measured with a movable Langmuir probe and (b) modelled. Positive fluxes are fluxes going from the divertor into the main chamber.

0.1 m^2/s) to large values (5 m^2/s), repeated according to the measured ELM repetition time. The best agreement of modelling with experimental thermography profiles on divertor profiles is obtained if radial particle diffusion coefficients as well as radial heat conduction coefficients are enhanced during the ELM [3]. The modelling results also indicate that the ELM effect of enhanced transport extends over the core region into the region of open field lines in the SOL. A problem still exists with the in–out asymmetry of the target plate power load during the ELM, which is much stronger in the experiment than in modelling. This problem can be solved by applying, instead of our standard model of radial diffusion, according to the radial distance during the ELM, a diffusion law based on the magnetic flux space. As a consequence of this description, the turbulent transport during the ELM is no longer larger on the outer than on the inner side (effect of the Shafranov shift), but is equal.

The experimental signatures of H_α, Langmuir probe and spectroscopy ELM resolved measurements are reproduced very well [4]. The global features are characterized by a fast response due to the fast change of the target particle flux. This is driven by the electron heat conduction which changes the pressure in front of the plate and thus the recycling. The second feature is an asymmetric and slower decay, which is due to the ion particle and neutral transports. 2-D divertor Langmuir probe measurements in ASDEX Upgrade at the entrance of the outer divertor show deuterium backflow from the divertor into the main chamber during ELMs (Fig. 1). The same signature shows up in the simulation. The enhanced pressure in front of the plate drives flow reversal as the system tries to achieve pressure equilibration. In addition, the neutral reservoir was ionized by the fast response of the target particle flux, which is also driving this backflow.

As was shown before, type I ELMs produce additional power loading problems of the divertor, owing to the ELM bursts. These burn through any cold divertor necessary for safe divertor operation. Therefore, scenarios have to be studied with tolerable ELMs. This will be done in the next chapter.

3. CDH (TYPE III ELM) MODELLING

Because of the combination of high neutral gas pressure in the divertor and additional (feedback controlled) impurity radiation losses by neon, stable operation close to the H–L backtransition threshold is established. The plasma shows H mode confinement, but no longer burns through the divertor during strong type I ELMs; instead, it remains detached with much smaller type III ELMs.

Carbon is produced at the target plates and side walls by physical and chemical sputtering (although physical sputtering is unimportant because of the low plasma temperatures). A chemical sputtering coefficient of 0.02 is used, except at the target plates, where a ten times smaller value has to be used as otherwise the high carbon influx would result in radiation collapse (this reflects the experimentally observed strong flux dependence of chemical sputtering). Neon is introduced by a gas puff and is feedback controlled to a separatrix neon density of 3×10^{17} m^{-3}. Helium is included as a trace impurity (density of about 10^{16} m^{-3}) to analyse the pumping. An input power into the computational domain of 7 MW, equally into electrons and ions, was chosen. The best overall agreement for the CDH scenario with midplane density and temperature profiles, target plate thermography, pressure gauges, bolometer and spectroscopy measurements was obtained for a hydrogen core density of 8×10^{19} m^{-3} (at the separatrix, 5×10^{19} m^{-3}) and the following anomalous transport coefficients: a particle diffusion coefficient of 0.2 m^2/s was used for all species (no pinch velocity), and electron and ion heat diffusivities of 1.0 m^2/s in the core up to about 2 cm inside the separatrix and from there up to the SOL with a value of 0.5 m^2/s.

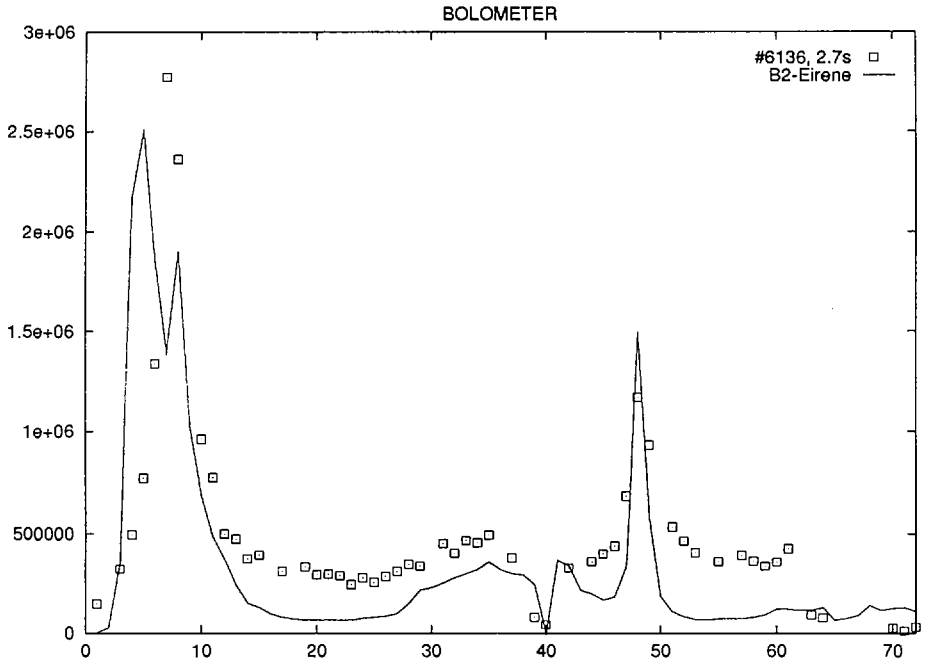

FIG. 2. Experimental (open symbols) and B2-Eirene (full line) bolometer signals.

To obtain a reasonable fit of the bolometer signals for the radiation distribution (Fig. 2), we have to include a model for the type III ELMs (following the results of type I modelling [4]) by increasing the radial transport for a period of 0.1 ms to 5 m^2/s in the whole domain, repeated every 0.7 ms (these times are chosen according to experimental C II and C III measurements). The missing background is due to radiation in the core not covered by the B2 grid.

The type III ELMs stabilize the system because (owing to the enhanced power flow into the divertor during the ELM) they push the detachment zone closer to the plate, moving to the X point again after the ELM. We see a kind of dynamic jittering of the C II, C III and H_α signals. This pushback effect allows a larger radiation loss than without ELMs, where the radiation loss zone would have a tendency to form an X point marfe and move into closed flux surfaces. During the ELM, because of the increased temperature at the midplane (rise of about 10 eV) and the widened density profile, energy losses from impurities increase strongly, partially buffering the ELM effect.

4. COMPRESSION ANALYSIS

On the basis of the validated model presented in the last chapter, the neutral gas flux density in the divertor was varied by one order of magnitude (going from CDH

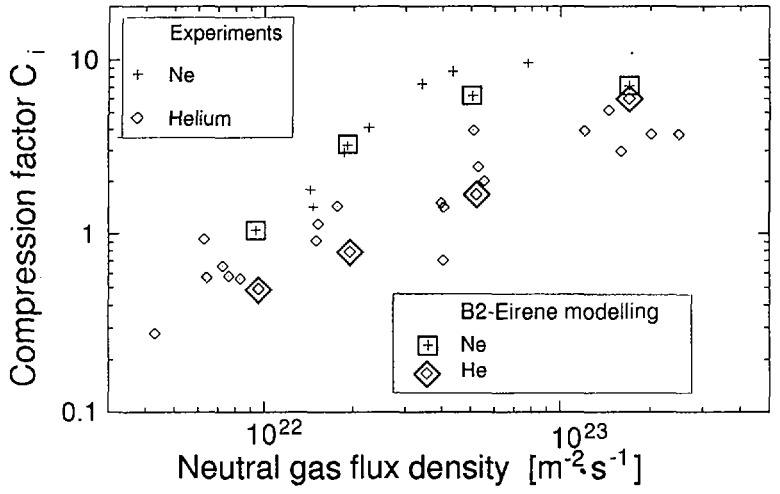

FIG. 3. Experimental and modelling results for the compression of neon and helium as a function of divertor neutral gas flux density.

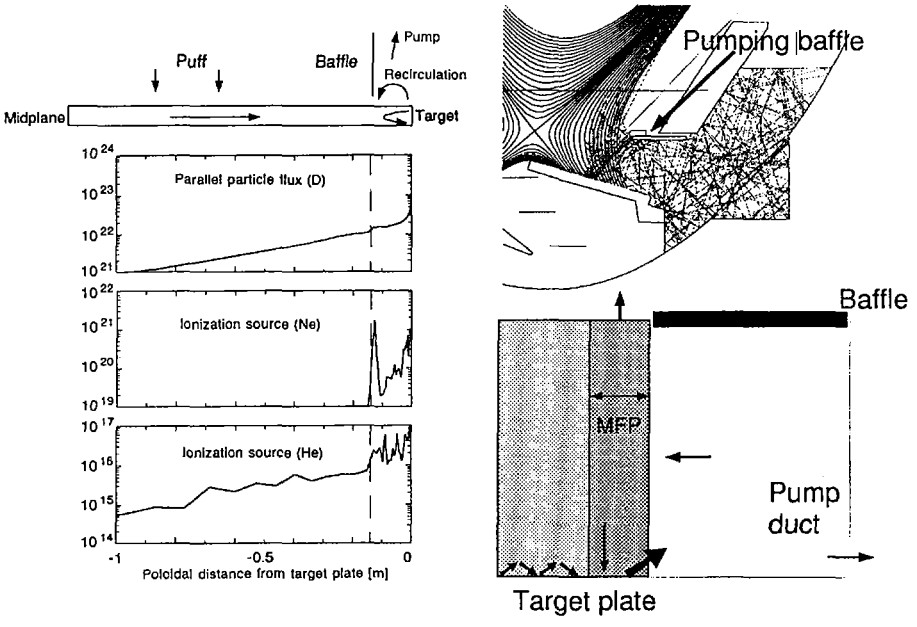

FIG. 4. Radially integrated parallel particle flux (D) and ionization sources (Ne and He) for the outer divertor (left hand side). Trajectories of 100 neon neutrals from the outer target plate (right hand side, top) and schematic model (right hand side, bottom).

to more attached conditions) by carrying out a midplane density scan (without changing any of the validated transport parameters in the code) to lower densities [5]. Analysing for this scan the compression of neon and helium at the position of the pump duct relative to the midplane density (in the model, this quantity is not sensitive to the existence of ELMs because of the long time-scales of the neutral feeding of the large duct volume) and comparing with the experimental results, we find that the model calculations can obviously describe the observed experimental behaviour qualitatively and quantitatively: compression of neon and helium (neon is better compressed than helium) increases with higher neutral gas flux density in the divertor (Fig. 3).

The basic compression mechanism is the recycling cycle in the outer SOL. For ASDEX Upgrade the existence of a pumping baffle in the outer divertor is quite important for the observed compression (Fig. 4). Integrating the modelling result over the SOL, we see that this baffle affects the parallel particle flux of the deuterium background, owing to the effect of recirculation of neutrals in the pumping duct (limited leakage by the baffle) back to the SOL. The difference between neon and helium can be seen from the different distributions of the radially integrated ionization sources, where neon neutrals are kept more efficiently in the divertor than helium, because of their shorter mean free paths.

The physics of the compression can be reduced to a rather simple model (see Fig. 4), characterized by a layer of the width of the mean free path of the impurity neutrals, from where they are able to feed the pump duct below the baffle, establishing a second particle flux maximum in the outer SOL at the plate. A simple flux balance at the entrance of the box [5] shows that the compression is determined by the instreaming flow velocity of the impurity. In this outer SOL region, there are no strong temperature gradients, and the deuterium background has a relatiely strong forward flow. Therefore, the impurity flow velocity is due to the dominant friction force of the deuterium background and is practically identical (at least for higher densities) with this background velocity. Increasing the midplane separatrix density and therefore the neutral gas flux density in the divertor results in larger deuterium flows in this outer part, because of the stronger friction with charge exchange neutrals. As a consequence, a higher deuterium neutral gas flux density in the divertor yields a greater compression. The difference of neon and helium is just a consequence of the mass difference (which is the dominant factor in the difference of the mean free paths of the neutrals). From these considerations, the difference of deuterium and the other impurities is also clear: deuterium neutral transport is dominated by charge exchange, in contrast to the impurity neutrals. Deuterium recycling is well confined in this baffle region under conditions where the impurity neutrals are leaking out, because charge exchange in this outer part of the SOL with low densities and low temperatures very effectively traps the deuterium neutrals. Therefore, the effect of the baffle is less pronounced for deuterium than for impurities. The compression of deuterium therefore varies by a factor of two to three only, in agreement with the experiment.

This kind of concept offers a very attractive potential for separation of power and particle exhausts: particle exhaust can be performed just in the outer part of the SOL (allowing geometry optimization), whereas power exhaust is related to the region close to the separatrix.

5. L MODE DENSITY LIMIT

In this section, results of L mode density limit studies for ASDEX Upgrade are discussed with respect to a recently proposed SOL based density limit [6] and specific features of the H_α emission in the divertor.

For ASDEX Upgrade, B2-Eirene runs were done for different input powers simulating the density ramp experiments. A central element of the SOL based density limit is the observation that maximum separatrix densities are reached at complete detachment [6, 7]. Typically, detachment is characterized by a large drop in the integral of the ion saturation current (at least by one order of magnitude), an increase of the D_α signal in the divertor and an increase of the divertor neutral fluxes. In the modelling this is explained by the onset of volume recombination [8], which was also spectroscopically observed in ASDEX Upgrade L mode high density discharges [7, 9]. In contrast, the CDH mode does not show this strong volume recombination emission, again consistent with modelling predictions, because the CDH mode is characterized by a much smaller integral drop of the ion saturation current by only a factor of three to four and is more detached in the sense of layer detachment (or partial detachment, preferentially close to the separatrix), driven by upstream main chamber losses and not so much by divertor losses.

Experimentally, it was proven on ASDEX Upgrade that complete detachment and density limit are correlated [7]. In L mode density limit studies in ASDEX Upgrade, a power dependence of the maximum separatrix density on the net input power is found ($P^{0.6}$ for D and $P^{0.6}$ for H, where P is the net input power defined as the difference of heating power and total radiation losses). The net input power is the power into the gas target and the adequate parameter to characterize a SOL with a well developed gas target. As was shown in Ref. [6], the actual splitting of radiation losses into main chamber core and SOL/divertor radiation has a virtually negligible effect on the upstream separatrix density. In addition, the splitting of radiation is usually difficult to determine experimentally. As soon as a marfe is formed, the dominant emission is close to the X point. B2-Eirene runs give (as long as only the data in the experimental range of net input power less than 2.5 MW are considered) a power scaling ($P^{0.4}$ for H) for this kind of SOL detachment limit (Fig. 5). The difference might be due to the fact that, in the modelling, the radial heat conduction coefficients were chosen to be constant, resulting in radial heat fluxes increasing with increasing densities. Experimental results indicate a more constant SOL power width; therefore an 'Alcator–INTOR' type of scaling of the radial heat conduction coefficients inverse with the density will be tested and should result (because of smaller

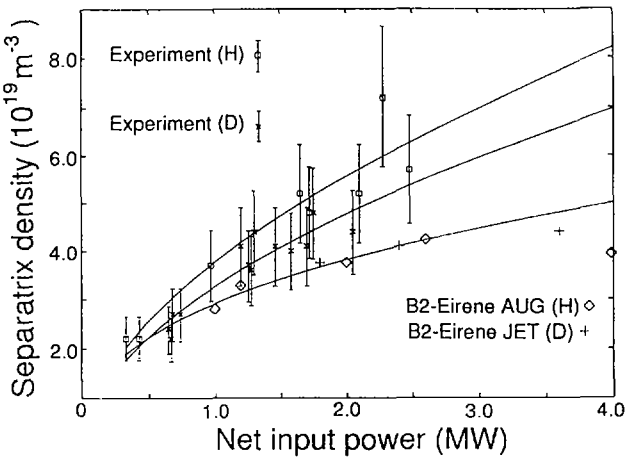

FIG. 5. Maximum separatrix density versus net input power for ASDEX Upgrade. Included are also B2-Eirene modelling results for ASDEX Upgrade and JET.

SOL widths for higher separatrix densities) in slightly higher detachment densities [10, 11]. In contrast, B2-Eirene studies for JET gave a power independent, 1/q type scaling (Hugill–Greenwald type scaling, $P^{0.1}$) [6]. The condition for the existence of such a power independent scaling is an intermediate transverse neutral collisionality in the divertor. At the gas target entrance, which is formed at complete detachment, this results in a sufficiently strong variation of the Mach number with transverse neutral collisionality, limiting the maximum separatrix density [6]. B2-Eirene modelling results for ASDEX Upgrade also indicate a transition into this kind of intermediate transverse neutral collisionality for net input powers of above 2.5 MW.

A detailed comparison of modelling and experimental results was done for shot No. 7888 (4.0 MW power into the SOL for hydrogen), focussing, in particular, on the comparison of the H_α values in the divertor. From low recycling to detachment, the H_α profile at the target plate (viewed from the top; see Fig. 6) changes in intensity and shape. In the phase from low to high recycling, the intensity becomes higher. As soon as a marfe appears an additional shoulder develops. This behaviour is well reproduced by the code. The shoulder is related to H_α radiation from the high density marfe region.

Finally, some possible shortcomings of the modelling concerning radiation from deuterium should be discussed. The divertor conditions in these density limit discharges with high volume recombination and, therefore, high neutral densities may result in a very low degree of ionization. Under these conditions, it is very likely that the hydrogen Lyman lines are starting to become optically thick. This opacity effect changes the population of the excited states and also the integral collisional–radiative ionization rate coefficients used in the simulation. These changes should be evaluated

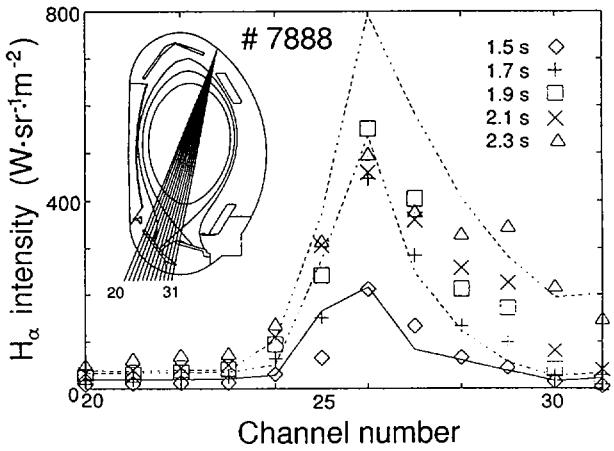

FIG. 6. Measured (symbols) and modelled (lines) H_α intensity profiles in the inner divertor for density limit shot No. 7888.

for the detached regime, resulting in additional complexity of the modelling (radiation transport calculations might be necessary). The influence of vibrationally excited molecules has also to be studied, because they can enhance the volume recombination rates by up to a factor of three [12] and give an additional contribution to H_α in the divertor. The most critical experimental input is the vibrational state of the molecules coming from the wall, because this probably determines whether this process becomes important or not.

6. CONCLUSIONS

2-D multifluid B2-Eirene simulations in a fully time dependent mode were done for modelling the effect of type I ELMs on SOL and divertor properties for pure hydrogenic plasmas and the CDH mode with type III ELMs for a deuterium plasma with intrinsic impurity carbon plus neon and helium. By using a simplified ELM model (periodically enhanced radial transport in the core and in the SOL during the ELM), many experimental signatures were reproduced.

In carrying out a midplane density scan (without changing any of the validated transport parameters in the code) to lower densities, the neutral gas flux density in the divertor was varied by one order of magnitude (going from CDH to more attached conditions). An analysis of the neon and helium compression at the position of the pump duct relative to the midplane density was performed in agreement with the experiment. The existence of an outer pumping baffle and the set-up of a pump duct recycling in the outer part of the SOL are the important ingredients for understanding the compression.

Modelling of L mode density limit scenarios for ASDEX Upgrade was used for the discussion of a SOL based density limit. ASDEX Upgrade modelling reproduces the experimentally observed power dependence of the separatrix density at the density limit. The modelling results indicate the existence of a power independent regime (as for JET) for higher net input power.

The density limit is characterized by complete detachment driven by the onset of volume recombination and marfe formation in the main chamber. The appearance of a shoulder in the H_α emission in the divertor close to detachment is well reproduced by the modelling because of the contributions from the high density marfe region.

REFERENCES

[1] REITER, D., et al., J. Nucl. Mater. **220–222** (1995) 987.

[2] GRUBER, O., et al., Phys. Rev. Lett. 74 (1995) 4217.

[3] COSTER, D., et al., "Theory and modelling of time dependent phenomena in the plasma edge", Plasma Edge Theory (Proc. 5th Workshop Asilomar, USA, 1996), Vol. 36 (1996) 150.

[4] COSTER, D., et al., in Controlled Fusion and Plasma Physics (Proc. 21st Eur. Conf. Montpellier, 1994), Vol. 18B, Part II, European Physical Society, Geneva (1994) 846.

[5] COSTER, D.P., et al., "B2-Eirene modelling of ASDEX Upgrade", Plasma-Surface Interactions in Controlled Fusion Devices (PSI96) (Proc. 12th Int. Conf. Saint-Raphaël, 1996), to be published in J. Nucl. Mater.

[6] BORRASS, K., et al., A Scrape-Off Layer Based Model for Hugill–Greenwald Type Density Limits, Rep. IPP-5/70, Max-Planck-Institut für Plasmaphysik, Garching (1996).

[7] MERTENS, V., et al., IAEA-CN-64/A4-4, these Proceedings, Vol. 1, p. 413.

[8] BORRASS, K., et al., "Study of recombining gas targets", Plasma-Surface Interactions in Controlled Fusion Devices (PSI96) (Proc. 12th Int. Conf. Saint-Raphaël, 1996), to be published in J. Nucl. Mater.

[9] NAPIONTEK, B., et al. (in preparation).

[10] SCHNEIDER, R., et al., J. Nucl. Mater. **220–222** (1995) 1076.

[11] BOSCH, H.-S., et al., Extension of the ASDEX Upgrade Programme: Divertor II and Tungsten Target Plate Experiment; Application for Preferential Support, Phase I and II, Rep. IPP-1/281a, Max-Planck-Institut für Plasmaphysik, Garching (1994).

[12] KRASHENINNIKOV, S., et al., "Plasma–neutral gas interaction in a tokamak divertor: effects of hydrogen molecules and plasma recombination", Plasma-Surface Interactions in Controlled Fusion Devices (PSI96) (Proc. 12th Int. Conf. Saint-Raphaël, 1996), to be published in J. Nucl. Mater.

DISCUSSION

M.R. WADE: You focused on impurity compression in the pumping plenum region, which is important for particle exhaust. Have you looked at the code output to determine the impurity compression in the upper SOL of the divertor, which is important for obtaining high radiation in the divertor without contaminating the core plasma?

R. SCHNEIDER: In ASDEX Upgrade, the pumping plasma as defined by the pumping baffle extends nearly up to the X point. Therefore we analysed the compression in the whole outer divertor. In the private flux region the compression is very poor, because for attached conditions the impurities have to move through the whole divertor plasma fan.

L.J. PERKINS: Divertor modelling can generate important detailed information regarding divertor physics. Can you say whether the radiation per unit volume is enhanced over coronal equilibrium values?

R. SCHNEIDER: The typical enhancement factor for high radiation but non-MARFEing solutions is 1.2 (20% enhancement over equilibrium rates). However, the density distributions show strong deviations from the equilibrium, because of transport effects.

ENERGY AND PARTICLE TRANSPORT MODELLING WITH A TIME DEPENDENT COMBINED CORE AND EDGE TRANSPORT CODE

JET TEAM[1]
(Presented by A. Taroni)

JET Joint Undertaking,
Abingdon, Oxfordshire,
United Kingdom

Abstract

ENERGY AND PARTICLE TRANSPORT MODELLING WITH A TIME DEPENDENT COMBINED CORE AND EDGE TRANSPORT CODE.

A new time dependent code has been developed by linking the $1\frac{1}{2}$ D core plasma transport code JETTO to the 2D edge plasma transport code EDGE2D/NIMBUS. The code includes a combined Bohm-gyro-Bohm type transport model for energy transport in the plasma core, and this has been extended to include particle transport and a neoclassical transport barrier at the plasma edge for the simulation of JET hot ion H modes. Outside the separatrix the transport coefficients extrapolated from the model are assumed to be constant. It is shown that the code gives a completely consistent time dependent simulation of the measured plasma profiles across the entire cross section of hot-ion ELM free discharges, including the scrape-off layer and divertor regions. The code also predicts that the ballooning stability limit is reached when a giant type I ELM appears in experiments.

1. INTRODUCTION

The importance of a global approach to transport studies modelling simultaneously the entire plasma from the centre to the scrape-off layer (SOL) and divertor regions has been stressed recently by the development of transport models [1-2], relating the overall plasma performance to the behaviour of plasma in the boundary region.

As an example a model developed for the simulation of hot-ion H mode plasmas in JET is considered. The model is based on the formation of a neoclassical transport barrier just inside the separatrix. The strength of the barrier depends on recycling. In the absence of accurate measurements of all the quantities relevant for an accurate evaluation of particle and energy sources and sinks just inside the separatrix, the assumptions made require to be validated by the proper modelling of experimental observations outside the separatrix.

At JET such a global approach to transport studies is now possible [3] thanks to the combination in a single code of the $1^1/_2$ D core plasma transport code JETTO and the 2D edge plasma transport code EDGE2D/NIMBUS, as described in section 2. The transport model presently used in the code is given in section 3, while in section 4 results of the simulation of a typical JET hot-ion H-mode are presented.

---

[1] See Appendix to IAEA-CN-64/O1-4, these Proceedings, Vol. 1.

2. THE COMBINED CODE

The stand alone versions of the codes that have been combined into a global time dependent code are among the most advanced of their kind and are extensively used for the analysis and prediction of JET results. A link between JETTO and the impurity transport code SANCO, allowing a full multi-species treatment of impurities in the plasma core, has recently been completed. Coupling between SANCO and the multi-species impurity package in EDGE2D/NIMBUS is in progress.

EDGE2D has been upgraded to include all components of the classical particle drifts in the equations and boundary conditions for all plasma species. Another recent upgrade of EDGE2D is the implementation of a 21 moment description of parallel transport. The transport coefficients are calculated using the reduced charge state (RCS) method [4], with no assumption on impurity density or atomic mass.

In linking the codes at a prescribed interface inside the separatrix continuity of densities and temperatures and of the corresponding total particle and energy fluxes at a chosen interface is enforced. This is achieved by imposing proper boundary conditions into each code at each time step. Poloidal averages of the quantities in EDGE2D/NIMBUS are used at the interface. Continuity of neutral profiles and fluxes is also enforced in order to have a consistent evaluation of particle sources.

An important point is that at the interface one code receives a variable or flux from the other and returns the corresponding flux or variable. This procedure ensures continuity of all relevant quantities with sufficient accuracy, even for fast transients, by simply running both codes with time steps typical of EDGE2D/NIMBUS, avoiding extra iterations at each time step. As a result the coupled code is very robust and requires less than 10% additional computer time with respect to the stand alone EDGE2D/NIMBUS code [3].

3. ENERGY AND PARTICLE TRANSPORT MODELS

The transport models used in the code are mainly empirical. Their derivation and justification can be found in [5].

The transport model for energy is a combination of Bohm and gyro-Bohm-like terms. The corresponding thermal conductivities are:

$$\chi_e = \chi_B + \chi_{gB}$$
$$\chi_i = 2\chi_B + \chi_{gB} + \chi_{neo,i} \qquad \text{for} \quad 0<r<r_1$$

The model includes a region of finite width at the plasma edge from a radius r_1 to the plasma boundary $r=a$ ($\rho_1<\rho<1$ in a normalised radial flux surface co-ordinate) where transport is close to neoclassical. A neoclassical barrier for impurity transport in JET ELM free H mode discharges was previously considered in the SANCO code [6] and taken into account as a boundary condition of the energy equations in JETTO [1].

The Bohm and gyro-Bohm parts of the model, used for $\rho < \rho_1$, are given by:

$$\chi_{gB} = c_{gB}\sqrt{T_e}\,\frac{\nabla T_e}{B_T^2}$$

$$\chi_B = c_B\,\frac{\nabla P_e}{nB_T}\,q^2 a^2 L_{T1}^{-1}$$

where to compute the average of the inverse of the characteristic length of the temperature variation:

$$L_{T1}^{-1} \equiv < \nabla T_e / T_e >_{0.8<\rho<\rho_1}$$

the first order approximation is taken: $L_{T1}^{-1} \sim \left(T_{e,\rho=0.8} - T_{e,\rho=\rho_1}\right) / T_{e,\rho=\rho_1}$. c_{gB} and c_B have been chosen by calibrating the model in a number of JET L mode discharges and are kept constant [1].

The Bohm-like term is non local, via its dependence upon L_{T1}^{-1}. This dependence allows the use of the model in both H and L mode, by reducing the Bohm-like term in H mode. In L mode the transport barrier is switched off.

In the same region particle transport is given by an effective diffusion coefficient:

$$D_{eff} = \alpha_D(r) \frac{\overline{\chi}}{\langle n_e \rangle} \text{ with: } \overline{\chi} = \frac{\chi_e \chi_i}{\chi_e + \chi_i}$$

where $<n_e>$ is the volume average density and $\alpha_D(r)$ is a shape factor (including a normalising constant density) that reduces D_{eff} with respect to χ as ρ increases (Fig.1). Such an empirical dependence of D_{eff} seems to be required to match at the same time:

a) the experimental density profiles;
b) the neutral fluxes computed by EDGE2D (which match experimental values of D_α emission); and
c) the lack of strong variation with time of the ion saturation current density at the divertor targets in low recycling ohmic and hot ion H mode discharges.

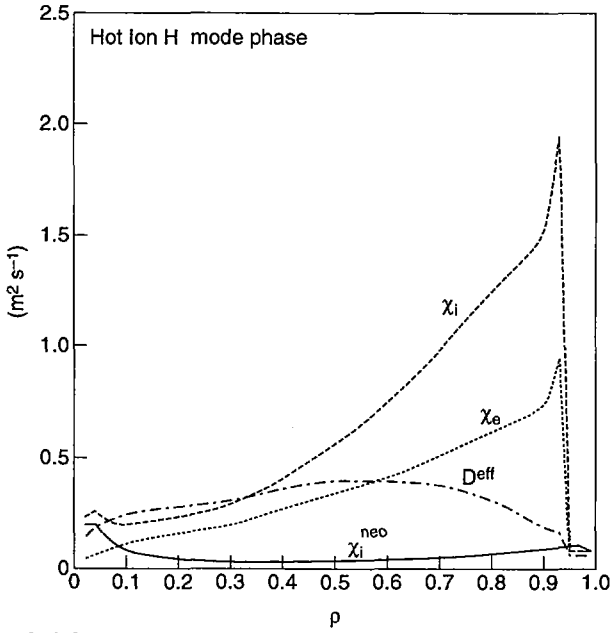

Fig.1 Radial dependence of the transport coefficients in the hot ion H mode.

The shaping factor $\alpha_D(r)$ and the inverse dependence upon $<n>$ are to be considered as an indication of the existence of an inward particle pinch velocity term increasing strongly towards the boundary and increasing with density. Work is in progress to include explicitly such a term in the model.

In the present version of the code the width of the neoclassical boundary transport barrier $\Delta=a- r_1$ is imposed and kept constant in time. Typically $\Delta\approx 5$ *cm*, which for the JET hot ion H modes with plasma current $I\approx 3$ *MA* simulated so far corresponds to a few ion banana orbit radii ρ_b. The main effect of the barrier is to act as a 'plug' which at low collisionality provides thermal fluxes essentially independent of temperature but directly proportional to $n^2 Z_{eff}$ [1]. Such plugging is obtained by assuming within the barrier region:

$$\chi_i = \chi_e = D \propto \frac{\Delta}{\rho_b} \chi_i^{neo}$$

where χ_i^{neo} is the neoclassical ion thermal diffusivity. This corresponds in first approximation to assuming $\chi_i=\chi_e=D_{eff}\approx\chi_i^{neo}$ and $\Delta\propto\rho_b$.

For the simulations shown in the next section, the transport coefficients in the SOL region are assumed to be the same as the transport coefficients computed at the JETTO/EDGE2D interface (≈ 2 *mm* inside the separatrix) from the core transport model. However better agreement with measurements in the divertor region is obtained by including an explicit inward pinch velocity term $V\approx 15\ D/a$ in the SOL particle flux (even if the particle diffusion coefficient is rather small as shown in Fig.1).

4. SIMULATION OF HOT ION H MODES

The hot ion H mode is a very interesting plasma regime in JET, and has provided record values of energy confinement and fusion reaction rate. This regime is usually entered directly from a low recycling ohmic regime following the formation of the separatrix X-point, soon after ($\approx 100\text{-}150$ *ms*) the application of vigorous neutral beam injection (NBI) heating. The good, ELM-free, confinement phase is characterised by an almost linear increase of the energy content lasting for about one second, and usually terminates as a result of some MHD activity (sawtooth, giant type I ELM, "outer" mode) [7]. These pulses have been extensively studied by means of the JET transport codes. In the following results will be presented of the simulation of a typical representative of these pulses, the *3MA*, *3.4T* Pulse Number 32919 obtained with the Mark I divertor configuration.

The simulation has been carried out assuming a pure plasma but including Z_{eff} and impurity radiation from the experimental data base. NBI power deposition profiles computed by the TRANSP code as a function of time have been used, assuming that the injected particles (and corresponding energy) lost via shine-through and direct charge exchange losses at the plasma periphery are promptly lost at the vessel wall. This assumption might have to be reviewed, if necessary,when an accurate experimental evaluation of the SOL power balance will become available.

The results presented here refer mainly to the time evolution of the discharge from the ohmic phase ($11.6s\text{-}12s$) into the ELM-free high performance phase ($t<13s$). Some results for the so called roll-over phase preceding a giant ELM at $t\approx 13.3s$ will also be briefly referred to. The transition to H mode is simulated by switching on the neoclassical boundary barrier $0.125s$ after NBI is switched on at $t\approx 12.0s$. The benign ELMs at the beginning of the H mode are ignored (Fig.2).

The density decrease during the ohmic phase is simulated by assuming that the target recycling coefficient R_t is less than unity during this phase (see Table I, showing typical values of the quantities that characterise particle recycling during the ohmic and H mode phases). The rate of increase of the total plasma particle content dN/dt during the NBI phase exceeds the NBI fuelling source S_n^{NBI}. The extra influx of neutrals Φ_0^{ex} necessary to simulate the plasma density increase, without any external puff being activated, has been assumed to be released from the divertor or from different regions along the vessel walls without significant variations of the computed core plasma performance. The numerical results shown in this paper refer to divertor release. Table I shows for comparison also values, computed by the code, of the influx of neutrals into the core Φ_0^c, the outflux of ions from the core Φ_i^c, the total flux of ions to the target Φ_i^t, the pumped flux of neutrals Φ_0^{pump} and the flux of neutrals through the bypass leaks [8] in the sub-divertor region Φ_0^{leak}. Units are 10^{21} s^{-1}.

The temporal evolution of the computed and experimental averaged and peak core plasma density in the ohmic and H regime is shown in Fig.2. The same figure compares the evolution of the D_α emission integrated along lines of view looking at the inner (D_α^I) and outer (D_α^O) divertor plates, and of the thermal energy content.

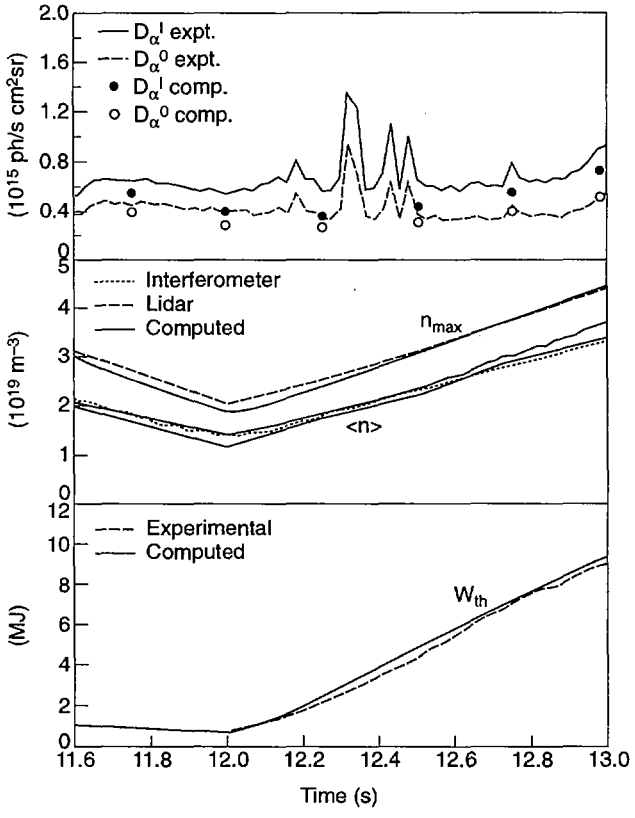

Fig.2 Experimental and computed time evolution of D_α emissivities (see text), averaged and peak core plasma densities, and thermal energy content.

TABLE I. RECYCLING QUANTITIES IN OHMIC AND H MODE PHASES

	dN/dt	S_n^{NBI}	F_0^{ex}	F_0^c	F_i^c	F_i^t	F_0^{pump}	F_0^{leak}	R_t
OH	*-1.35*	*0.0*	*0.0*	*3.3*	*4.65*	*30*	*0.14*	*0.4*	*0.96*
H	*1.75*	*1.4*	*0.5*	*3.2*	*2.85*	*30*	*0.15*	*0.5*	*1.0*

Figure 2 indicates, in particular, that the distribution of neutrals in the SOL and divertor regions, their influx into the plasma core, and the particle transport in both regions are all consistent with experimental observations. The resulting charge exchange loss terms computed by the code reach a maximum in excess of *2.5 MW* at *t≈13 s*. Their profiles are strongly peaked at the separatrix being negligible at the plasma centre.

Figure 3 compares experimental and computed profiles of the ion saturation current density in the ohmic and H mode phases, showing little variation of this quantity, consistent with recycling being very low in both phases.

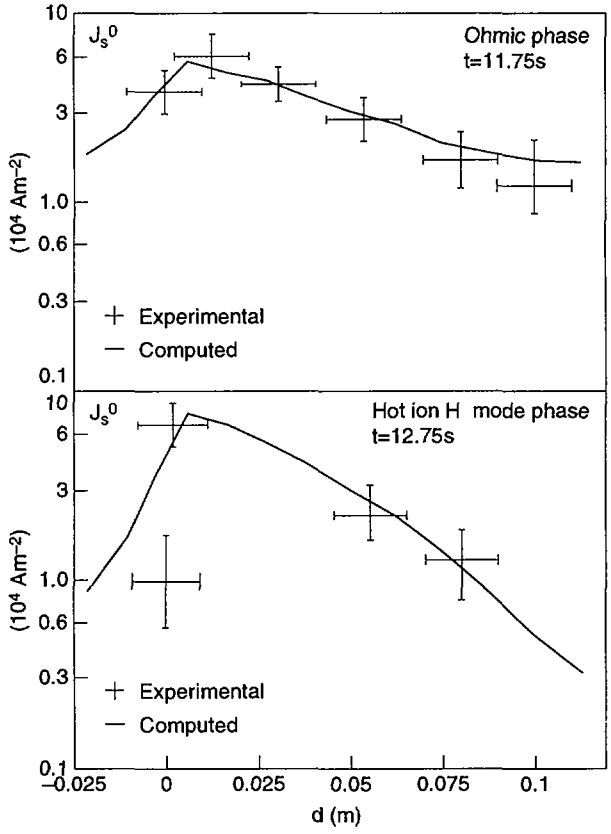

Fig.3 Computed and experimental spatial variation of the ion saturation current density at the outer target as a function of distance from the separatrix.

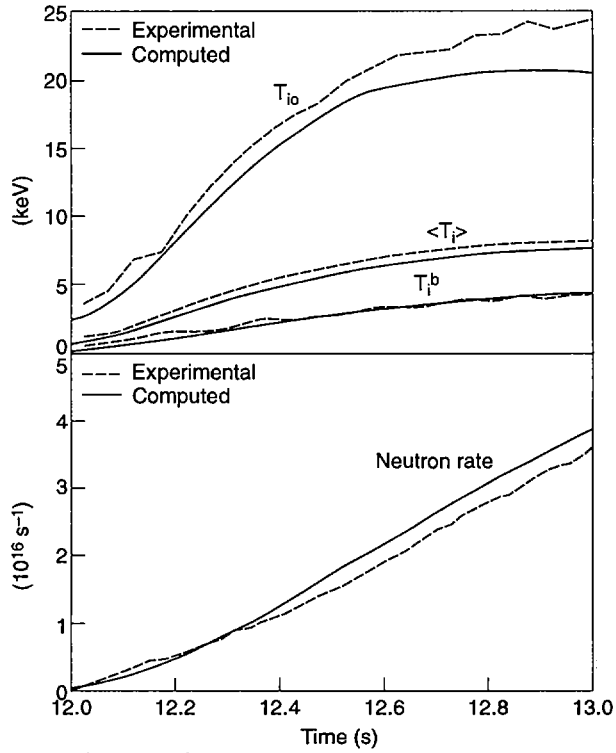

Fig.4 Experimental and computed time evolution of the ion temperature at the plasma centre and at the top of the transport barrier. The average ion temperature and the neutron rate are also shown.

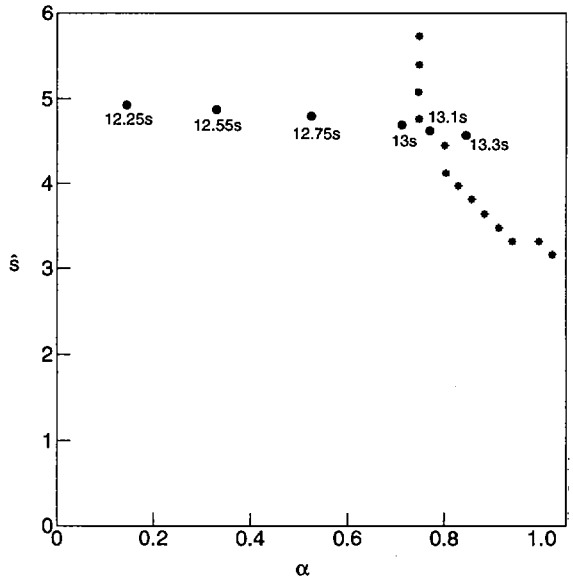

Fig.5 Trajectory of the discharge in the ballooning stability diagram of s (the normalised shear) versus α (the normalised pressure gradient).

The simulated and predicted evolution of the ion temperature and of the total neutron rate is given in Fig.4. It can be seen that a natural saturation of the ion temperature is predicted by the model as a consequence of the density increase. It can also be seen that the model somewhat underestimates the central ion temperature towards the end of the good performance phase, while the neutron rate is slightly overestimated. This seems to indicate a small inconsistency in the experimental data, which is confirmed by TRANSP analysis of this kind of pulse.

A number of code runs have been dedicated to the simulation of the roll-over phase by increasing the core fuelling from the SOL and Z_{eff} before the roll-over takes place. While some features of the roll-over, such as the saturation of the energy content, are correctly represented in these simulations, others are not. For example, the predicted decrease of the central ion temperature is generally underestimated while the increase in the ion saturation current is overestimated. Clearly more work is required for a complete modelling of the roll-over phase.

An interesting result is found by computing at the core plasma boundary the trajectory of the discharge in the ballooning stability diagram. This is done using the simulated plasma profiles in the IDBALL package [9] linked to the combined code. This trajectory approaches and hits the stability limit at approximately the time when first a roll-over that practically does not modify the neoclassical transport barrier ($t \approx 13.1$), and then a giant ELM that strongly reduces it ($t \approx 13.3$) take place (Fig.5).

5. CONCLUSION

The combined code for core and edge transport studies developed at JET together with the availability of measurements in the two regions is a powerful tool to simulate tokamak discharges in a time dependent way.

By eliminating ad hoc (and sometimes convenient) assumptions at the interface between core and boundary region this code provides a very tough and complete test for transport models, including the effect on the SOL of transport assumptions in the core and vice versa. Results from the combined code can be used to improve modelling in the stand alone core and edge transport codes.

The transport model used in the code, although not fully predictive and essentially empirical, has proven to be useful to clarify some important aspects of the evolution of hot ion H modes. In particular it supports the hypothesis that type I giant ELMs might be caused by ballooning instability in the edge transport barrier region.

ACKNOWLEDGEMENTS

Particularly grateful acknowledgement is due to the following for their contribution in developing the code and the transport models, for discussion of the results, and for providing experimental information:

B.Balet, A.V.Chankin, A.Cherubini, G.Corrigan, M.Erba, M.Fichtmueller, H.Guo, L.Lauro-Taroni, G.K.McCormick, V.V.Parail, G.Radford, R.Simonini, J.Spence, E.Springmann.

REFERENCES

[1] CHERUBINI, A., et al., Plasma Phys. Control. Fusion **38** (1996) 1421.

[2] KOTSCHENREUTHER, M., et al., Phys. Plasmas **2** (1995) 2381.

[3] TARONI, A., et al., in Controlled Fusion and Plasma Physics (Proc. 23rd Eur. Conf. Kiev, 1996), Vol. 20C, European Physical Society, Geneva (1996).

[4] BOLEY, C.D., et al., Phys. Fluids **22** (1979) 1280.
[5] ERBA, M., et al., Plasma Phys. Control. Fusion **39** (1997) 322.
[6] LAURO-TARONI, L., et al., in Controlled Fusion and Plasma Physics (Proc. 17th Eur. Conf. Amsterdam, 1990), Vol. 14B, Part I, European Physical Society, Geneva (1990) 247.
[7] JET TEAM (presented by P.J. LOMAS), IAEA-CN-64/A1-5, these Proceedings, Vol. 1, p. 239.
[8] JET TEAM (presented by G.C. VLASES), IAEA-CN-64/A4-1, ibid., p. 371.
[9] HENDER, T., personal communication, 1996.

DISCUSSION

D.D. RYUTOV: What boundary condition do you impose on the electrostatic potential and the parallel velocity on the separatrix? For example, $v_{\parallel}$ experiences a strong poloidal variation (even changes its sign) on the open field lines. How do you match this to $v_{\parallel}$ inside the separatrix?

A. TARONI: The interface between the 1½-D code JETTO and the 2-D code EDGE2D is not at the separatrix but somewhat inside. At this interface, the parallel velocity and the electric field are assumed to be zero. Parallel velocity and electric field then develop in the 2-D region (including the separatrix), where the full set of equations, including parallel momentum, is solved by EDGE2D.

NOVEL MECHANISM OF ION CYCLOTRON EMISSION IN TOKAMAKS

Ya.I. KOLESNICHENKO
Institute for Nuclear Research,
Kiev, Ukraine

D. ANDERSON, T. FÜLÖP, M. LISAK
Institute for Electromagnetic Field Theory,
Chalmers University of Technology,
Göteborg, Sweden

Abstract

NOVEL MECHANISM OF ION CYCLOTRON EMISSION IN TOKAMAKS.

It is shown that the key mechanism at the origin of superthermal ion cyclotron emission (ICE) appearing in tokamak fusion experiments is the instability of fast magnetoacoustic waves with very small longitudinal wavenumbers excited through toroidicity affected cyclotron resonance with an energetic ion population. This type of cyclotron resonance leads to an instability growth rate well exceeding the inverse bounce/transit period of fast ions, even for a very small number of high energy ions. The proposed theory explains the main features of the ICE spectrum observed in JET.

1. INTRODUCTION

Superthermal ion cyclotron emission (ICE) is a phenomenon that has been observed in both fusion and space experiments. The most probable source of ICE in experiments on tokamaks [1–4] is a plasma instability localized near the outer circumference of the torus, where $\beta \ll 10^{-2}$ ($\beta = 8\pi p/B^2$; p denotes the plasma pressure and B the magnetic field). The instability is driven by a very small number of superthermal ions ($n_\alpha/n \ll 10^{-3}$, where n_α and n denote the densities of the superthermal particles and the plasma background particles, respectively) with a characteristic velocity (v_α) of the order of the Alfvén velocity (v_A). Theory indicates that such an instability is associated with fast magnetoacoustic waves having frequencies close to the cyclotron harmonics of the superthermal ions, and the first theoretical work was carried out well before any experimental observations of ICE (see overview [5]). During recent years, several mechanisms for wave destabilization have been suggested [6–10], predicting features that are at least in partial agreement with the experimental results. However, in our opinion, a satisfactory understanding of the origin of ICE has not been reached, and, moreover, a number of essential features of the observed spectra remain unexplained.

The purpose of the present work is to elucidate the general physical picture of the origin of ICE as well as to explain the mean features of the ICE spectrum observed in experiments on JET with deuterium and deuterium–tritium plasmas.

2. RAPID RESONANT DESTABILIZATION OF CYCLOTRON MAGNETOACOUSTIC WAVES BY FAST IONS IN THE PRESENCE OF TOROIDAL DRIFT

We consider waves with exponentially small damping due to thermal plasma particles by assuming

$$\eta \equiv \left|\frac{\Delta\omega}{k_\parallel v_{Ti}}\right| \gg 1, \ \eta_e \equiv \frac{\omega}{|k_\parallel| v_{Te}} \gg 1 \tag{1}$$

where $\Delta\omega = \omega - \ell\omega_B$, ℓ is an integer, v_T is the thermal velocity, and the subscripts e and i denote electrons and thermal ions, respectively. Assuming also that $1 \ll \omega/\omega_B \ll \sqrt{M_i/M_e}$ (M is the particle mass), the dispersion relation for the fast magnetoacoustic waves can be written as

$$1 - \frac{\omega^2}{k^2 v_A^2} = \frac{\omega^2}{\omega_{pi}^2}(\epsilon_{11}^T + \epsilon_{11}^\alpha) \tag{2}$$

Here, according to the eigenmode analyses, e.g. in Ref. [6], it is assumed that $k \simeq |m|/r$, where m is the poloidal wavenumber, ω_{pi} is the plasma frequency of the background ions, and ϵ_{11}^T and ϵ_{11}^α are contributions to the component of the dielectric permeability tensor due to plasma thermal effects and fast ions, respectively. ϵ_{11}^T is given by

$$\epsilon_{11}^T = -\frac{\omega_{pi}^2}{\omega} \sum_{s\neq 1} \frac{s^2 I_s(a_i)\exp(-a_i)}{a_i(\omega - s\omega_B)} \tag{3}$$

where $I_s(a_i)$ is the modified Bessel function, s is an integer and $a_i = k_\perp^2 v_{Ti}^2/(2\omega_B^2)$.

In order to study wave destabilization due to wave–particle resonant interaction, we only take into account the imaginary part of ϵ_{11}^α. In this case, the real part of the wave frequency is completely determined by the bulk plasma properties. In the location region of the ICE source, β is very small, $10^{-3} < \beta \ll 10^{-2}$. This implies that the expression $I_s(a_i)\exp(-a_i)$ in Eq. (3) is also small since $a_i \sim \ell^2\beta_i/2 \ll 1$ for $kv_A \sim \ell\omega_B$. Hence, ϵ_{11}^T can be neglected when ω is not too close to the cyclotron harmonics, and, in the absence of the fast ion contribution, Eq. (2) yields $\omega = kv_A$. However, near the cyclotron harmonics, ϵ_{11}^T essentially contributes to the dispersion relation, and the solution of Eq. (2) describes two wave branches in the vicinity of

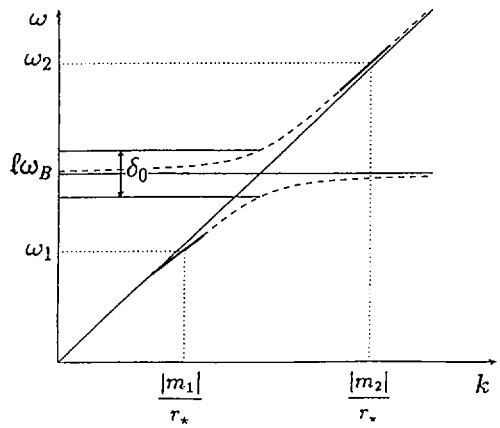

FIG. 1. Qualitative plot of wave branches near the intersection point of lines $\omega = \ell\omega_B$ and $\omega = kv_A$. Only the parts of the dispersion curves shown by solid lines can be destabilized. $\omega_{1,2} \simeq |m_{1,2}|v_{A*}/r_*$ are the frequencies corresponding to the expected peaks of the doublet ICE spectral lines, $\delta_0 \ll (\omega_1 - \omega_2)$, where δ_0 is the distance between the wave branches for $k = \ell\omega_B/v_A$.

$\omega = kv_A$ (see Fig. 1), which can be approximated as $\omega = \omega_0(1 + y_{1,2})$ with $\omega_0 = kv_A$ and

$$y_{1,2} = -\frac{\Delta\omega}{2\omega_0} \pm \left(\left(\frac{\Delta\omega}{2\omega_0}\right)^2 + \sigma_i\right)^{1/2} \tag{4}$$

where $|\Delta\omega| = |\omega_0 - \ell\omega_B| \ll \omega_0$ and $\sigma_i = \ell^2 I_\ell(a_i) \exp(-a_i)/(2a_i)$.

We find that in the limit $|\Delta\omega| \ll 2\omega_0\sqrt{\sigma_i}$, the minimum distance between the two wave branches is of the order of $2\omega_0\sqrt{\sigma_i}$, which is much less than the experimentally observed distance between the two peaks of the ICE spectral doublet lines (in fact, this is true even if the contribution of the real part of ϵ^a_{11} is taken into account).

Proceeding now to the stability analysis, we assume that the waves are localized in a small region near the outer midplane of the torus. This assumption is supported by the eigenmode studies of Refs [6, 10]. Let us take $|\Delta\omega|/\omega_0 \gg 2\sqrt{\sigma_i}$, which according to Eq. (4) implies that we are considering wavenumbers for which one of the wave branches is very close to kv_A, whereas the other one is close to $l\omega_B$. Equation (2) then yields the following result for the imaginary part of the frequency, γ:

$$\frac{\gamma}{\omega_0} = -\frac{\omega_0^2}{2\omega_{pi}^2} \operatorname{Im} \epsilon^a_{11}(\omega_0) \tag{5}$$

For fast instabilities, $\gamma > \tau_b^{-1}$, where τ_b is the particle bounce/transit period, only a time interval $\Delta t \ll \tau_b$ contributes significantly to the expression for Im ϵ_{l1}^{α}, and consequently no bounce resonances appear in the resonance condition (contrary to the case of slow instabilities with $\gamma < \tau_b^{-1}$ considered in Refs [9, 10]). Nevertheless, the resonance condition differs from that in a straight magnetic field because of the presence of the toroidal drift of the fast ions which, as will be shown, plays a crucial role for instabilities which are localized near the midplane of the torus (but which is negligible in the vicinity of the vertical plane crossing the plasma centre for the considered waves with $k_r \ll k$). Taking into account the effect of the toroidal drift of fast ions, the expression for Im ϵ_{l1}^{α} can be written as

$$\text{Im } \epsilon_{l1}^{\alpha} = - \sum_{s,\chi_r} 2\pi^2 \frac{\omega_{p\alpha}^2}{\omega^2} \frac{s^2\omega_B^2}{k_\perp^2}$$

$$\times \int_0^\infty dvv \left\{ \frac{J_s^2(\xi)}{|\partial\Omega/\partial\chi|} \left[\omega \frac{\partial f_\alpha}{\partial v} + \left(\frac{\omega - s\omega_B}{\chi} - \omega\chi \right) \frac{1}{v} \frac{\partial f_\alpha}{\partial \chi} \right] \right\}_{\chi_r} \tag{6}$$

where $J_s(\xi)$ is the Bessel function, $\xi = (k_\perp v/\omega_B)\sqrt{1 - \chi^2}$, $\chi = v_\parallel/v$ is the pitch angle, and χ_r is the resonance pitch angle determined by the resonance condition ($s = \ell$),

$$\Omega \equiv \omega - \ell\omega_B - k_\parallel v_\parallel - \omega_D = 0 \tag{7}$$

Here, $\omega_D = -v_D m/r$ is the toroidal drift frequency, $v_D = v^2(1 + \chi^2)/(2\omega_B R)$ is the toroidal drift velocity, and R is the major radius of the torus. We note that the importance of including the inhomogeneity of the magnetic field into the cyclotron resonance condition has been mentioned in Ref. [11]. Furthermore, the resonance condition (7) in the limit $|\Delta\omega| \ll \omega_0$ (i.e. $k_\parallel v_\parallel = \omega_D$) has been used in Ref. [6] to calculate the growth rate of an instability relevant to ICE, based on a general expression of Ref. [12].

Because of the appearance of the toroidal drift frequency in the resonance condition $\Omega = 0$ and the dependence of Im ϵ_{l1}^{α} on $|\partial\Omega/\partial\chi|$, the growth rate, γ, depends strongly on the ratio $\Delta\omega/\omega_D$. The growth rate has a maximum when $\Delta\omega \approx \omega_D$ and $k_\parallel v_\parallel \ll \omega_D$ (for estimates of γ, characteristic values of v and χ_r can be used). In this case it is easy to show that the growth rate exceeds that corresponding to the usual resonance $\Delta\omega = k_\parallel v_\parallel$ (the case of, e.g., Refs [4, 8]) by a factor $\chi_r^{-2}\nu \gg 1$, where $\nu \equiv |\Delta\omega|/\omega_D$. Note that $\nu \gg 1$ is the condition for the applicability of the resonance $\Delta\omega = k_\parallel v_\parallel$. When $\nu \ll 1$, the resonance condition reduces to $k_\parallel v_\parallel = \omega_D$ (the case of Ref. [6]), and the corresponding growth rate has an intermediate magnitude, being less than γ_{max} by a factor of χ_r^2. Note also that ν cannot be arbitrarily small since the resonance condition $k_\parallel v_\parallel = \omega_D$ must be consistent with the condition of weak wave damping ensured by Eq. (1) ($\eta \gg 1$). The

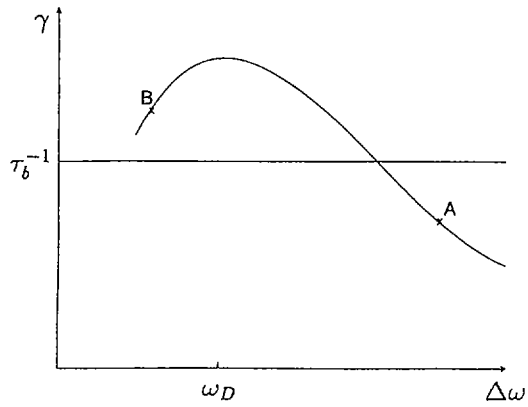

FIG. 2. Qualitative plot of γ *versus* $\Delta\omega = \omega - \ell\omega_B$. γ *has a maximum for* $\Delta\omega = \pm|\omega_D|$, *and therefore* $|\Delta\omega| = |\omega_D|$ *(taken as characteristic values of fast ion energy and pitch angle) represents the half-width of the doublet ICE spectral line. Around the point denoted by A the growth rate is due to the usual resonance* $\Delta\omega = k_\parallel v_\parallel$, *which dominates in the region* $|\Delta\omega| \gg |\omega_D|$, *and around point B (in the region* $|\Delta\omega| \ll |\omega_D|$*) the growth rate is determined by the resonance* $k_\parallel v_\parallel = \omega_D$. *Waves are destabilized in the frequency region where* $\gamma\tau_b > 1$, *with* $\gamma\tau_b$ *depending on* n_α/n.

restriction $|\Delta\omega|/\omega_0 \gg \sqrt{\sigma_i}$ is less important and, in fact, the instability will persist even when this condition is not satisfied.

A qualitative picture of the instability growth rate is shown in Fig. 2. The growth rate γ has two maxima which are symmetric with respect to $\omega = \ell\omega_B$ and the distance between the maxima is $2\omega_D$. This means that destabilization of waves with $\omega = \ell\omega_B \pm |\omega_D|$ is the most probable outcome of the wave–particle interaction and should result in a splitting of the ICE spectral lines into doublets with a width which can be estimated as $\delta_D = 2\omega_D$. The ratio δ_D/ω can be written as $\delta_D/\omega = (\rho/R)(v/v_A) \times (1 + \chi_r^2)$, where $\rho = v/\omega_B$, and for $R/\rho = 30$, $v/v_A = 1.6$, $\chi_r^2 = 0.3$ (for trapped particle driven instability), we obtain $\delta_D/\omega = 0.07$, in agreement with the experimental data of Ref. [2]. The only important characteristic of the fast ions which affects δ_D/ω is their energy. This explains why the doublet width in experiments with deuterium plasmas producing 3 MeV protons is approximately the same as in the case of DT plasmas with 3.5 MeV α particles (assuming v_A to be approximately the same) [2].

We emphasize that the usual resonance, $\Delta\omega = k_\parallel v_\parallel$, leads to a doublet structure only when $f_\alpha(v)$ is strongly anisotropic [8]. For the beam-like distribution, $f_\alpha = f_1(v_\parallel) f_2(v_\perp)$, where $f_1(v_\parallel)$ is strongly peaked at $v_\parallel = v_1$, the resonance yields $\Delta\omega = |k_\parallel| v_1$, i.e. the width of the doublet is $2|k_\parallel| v_1$. For the parameters used in Ref. [8], we find that $|k_\parallel| v_1 \simeq \omega_D$, and therefore the value of the doublet width obtained in Ref. [8] is close to the experimental value. However, this result is beyond

the applicability of the straight magnetic field approximation, which requires that the condition $k_\parallel v_\parallel \gg \omega_D$ be satisfied.

Although $\gamma(\Delta\omega = +|\omega_D|) = \gamma(\Delta\omega = -|\omega_D|)$, it does not necessarily follow that the intensity of the ICE at the two peaks of a doublet line will be equal. In fact, the discrete character of the allowable wavenumbers may exclude the frequencies at which $\gamma = \gamma_{max}$, if the minimum frequency 'step' $\delta_\omega = \omega_{m+1} - \omega_m \simeq v_A/r$ (where $\omega_m \approx (m/r)v_A$) is not too small in comparison with δ_D. A simple estimate shows that δ_ω/δ_D is very small only in the high frequency region (for JET parameters, $\delta_\omega/\delta_D \sim 1/\ell$), and thus we expect the intensity peaks to be asymmetric, as is indeed observed in experiments. Furthermore, the discrete character of the wavenumbers makes an excitation of doublet lines impossible in the region of low cyclotron harmonics where $\delta_\omega \simeq \delta_D$, thus explaining the observed fact that the spectral lines corresponding to $\ell = 1$ and $\ell = 2$ in the ICE spectrum are single. In order to discuss this point in some more detail, we analyse the resonance condition assuming $k_\parallel = 0$ in Eq. (7). The discrete wavenumbers corresponding to $\omega > \ell\omega_B$ and $\omega < \ell\omega_B$ are m_1 and m_2, respectively; they are determined by the resonance condition as $g_{1,2}$:

$$|m_{1,2}| = g_{1,2}(v, \chi) \simeq \ell \frac{r\omega_B}{v_A}\left[1 \pm \frac{\rho}{2R}\frac{v}{v_A}(1 + \chi_r^2)\right]\left(1 - \frac{\alpha v_A}{\ell r \omega_B}\right) \tag{8}$$

where $m_1 < 0$, $m_2 > 0$, $\alpha = |m|k_r^2/(2k^2) = O(1)$. Since $|m_1| - |m_2| \geq 1$, we conclude that

$$\ell \geq \frac{R}{r}\frac{v_A^2}{v^2}\frac{1}{1 + \chi_r^2} + \frac{\alpha v_A}{r\omega_B} \tag{9}$$

For experimentally relevant parameters, the right hand side of Eq. (9) slightly exceeds unity, and thus the resonance condition cannot be fulfilled for both m_1 and m_2 simultaneously when $\ell = 1$. Furthermore, we can show that the probability of $g_{1,2}(v, \chi)$ being an integer in a narrow region δv decreases with decreasing ℓ. This provides a further indication that the spectral lines should be single for $\ell = 1$ and even for $\ell = 2$, and finally the difference between ω_m and the frequency where $\gamma = \gamma_{max}$ explains why the intensities of the two spectral peaks in a doublet line are different.

The longitudinal wavenumbers of the excited waves can be estimated from the condition $k_\parallel v_\parallel < \omega_D$, which yields

$$k_\parallel < \frac{(1 + \chi_r^2)v\ell_{max}}{2\chi_r R v_A} \tag{10}$$

Taking as appropriate JET experimental parameters $\ell_{max} = 10$, $\chi_r^2 = 0.25$, $v/v_A = 1.6$ and $R = 3$ m, we obtain $k_\parallel < 7\ m^{-1}$, which qualitatively agrees with an analysis of the power spectrum on JET ($0 \leq k_\parallel \leq 7\ m^{-1}$) [2], the agreement being improved with the decrease of χ_r.

The above conclusions on the mode properties are based on general assumptions about the distribution function, the only restriction on f_α being that Im $\epsilon_{\ell}^{\alpha} < 0$, i.e. that the waves are destabilized. From Eq. (6), we infer that both the terms proportional to $\partial f_\alpha/\partial v$ and $\partial f_\alpha/\partial \chi$ in the expression for Im ϵ_{ℓ}^{α} may lead to wave destabilization, but their roles are different. The first term leads to an instability when $f_\alpha(v)$ is non-monotonic with a half-width $\Delta v < v_A/\ell$ around v_α, where the distribution function has a maximum (then the function $J_s^2(\xi)$ can be considered as a slowly varying function in the integral) and when v_α is larger than v_A. This term may in fact lead to a simultaneous destabilization of several cyclotron harmonics for which the condition $\partial J_s^2(\xi)/\partial \xi < 0$ is satisfied. The second term describes wave destabilization due to an anisotropy of $f_\alpha(v)$ and may lead to instability even when $v_\alpha < v_A$, and may furthermore destabilize many cyclotron harmonics simultaneously (however, when v_α/v_A is small, the damping due to the first term dominates). When sharp velocity gradients occur at sufficiently small values of χ_r, the instability arises independently of the signs of $\partial f_\alpha/\partial \chi$ and $\Delta\omega = \omega - \ell\omega_B$, destabilization depending only on the sign of $\Delta\omega\ \partial f_\alpha/\partial \chi$. Thus if $f_\alpha(\chi)$ has a sharp gradient at one pitch angle only, the second term leads to a single ICE spectral line.

In the special case when $f_\alpha(v) = f_1(v_\parallel)f_2(v_\perp)$, where $f_1(v_\parallel)$ is a shifted Maxwellian with a strong gradient around $v_1 \ll v_2$ and $f_2(v_\perp) \sim \delta(v_\perp - v_2)$, (see Ref. [8]), the resonance condition (7) leads to an additional strong enhancement, by a factor of $\omega/|\Delta\omega|$, of the instability growth rate caused by the gradient of $f_1(v_\parallel)$. This can be seen after rewriting the integral of Eq. (6) as

$$\int_0^\infty dv_\perp \frac{J_\ell^2}{|\partial\Omega/\partial v_\parallel|}\left(\Delta\omega \frac{v_\perp}{v_\parallel} f_2 \frac{\partial f_1}{\partial v_\parallel} + \ell\omega_B f_1 \frac{\partial f_2}{\partial v_\perp}\right)_{v_\parallel = v_r} \tag{11}$$

and integrating the second term by parts. The new expression will involve the derivative $\partial f_1(v_r)/\partial v_\perp$ since $\omega_D \neq 0$.

Our theory requires that $\gamma > \tau_b^{-1}$. For consistency, we also a posteriori estimate γ. Taking $f_\alpha = \delta(v - v_\alpha)/(4\pi v_\alpha^2)$, we obtain for the $\Delta\omega = \omega_D$ case:

$$\gamma \simeq \frac{n_\alpha}{n} \frac{\ell v_A R}{|\chi_r|\rho_\alpha^2} \tag{12}$$

where $|\chi_r| > v_A/(v_\alpha\sqrt{2\ell})$ and $\rho_\alpha = v_\alpha/\omega_B$. This estimate indicates that γ is much larger than τ_b^{-1} for $n_\alpha/n \simeq 10^{-4}$. The anisotropy driven growth rate can exceed that given by Eq. (12), resulting in an instability even for $n_\alpha/n \simeq 10^{-4}$ with all harmonics being excited simultaneously. However, when $|\Delta\omega| \gg |\omega_D|$ (the case of the $\omega - \ell\omega_B = k_\parallel v_\parallel$ resonance), the condition $\gamma > \tau_b^{-1}$ can hardly be fulfilled. We note that for small $k_\parallel$ the resonance of Eq. (7) leads to a large growth rate and thus provides significant broadening of the spectral lines. As $\delta_\omega/\omega_B \simeq v_A/(r\omega_B) < 0.1$, the growth rate $\gamma \simeq 10^{-2}\omega$ is sufficient to make the spectral lines merge into a continuum at $\ell \simeq 10$.

3. CONCLUSIONS

The toroidal drift of fast ions is shown to be a factor which strongly enhances the growth rate of the resonance cyclotron magnetoacoustic instability localized near the outer circumference of the torus ($r \simeq a$, $|\theta| \ll 1$). The growth rate has a maximum when the resonance condition $\omega - \ell\omega_B = \omega_D$ dominates.

The rapid instability excited through the toroidicity affected cyclotron resonance interaction between superthermal and fast magnetoacoustic waves with very small $k_\parallel$ is the most probable source of the ICE in tokamaks. This statement is based on the agreement of the instability considered with the main features of the ICE spectrum observed in experiments on JET, in particular such as: (i) the sharp maxima of the ICE intensity at the frequencies $\omega \cong \ell\omega_B$, where ω_B is the ion gyrofrequency at the outer midplane of the torus; (ii) the single peaked spectral lines for $\ell = 1, 2$; (iii) the doublet lines for $2 < \ell < 8$ with peaks of different intensities and with widths that are approximately the same in deuterium and deuterium–tritium plasmas; (iv) the continuous spectrum for $\ell \geq 8$; (v) the presence of waves with the longitudinal wavenumber $k_\parallel$ in the range of $0 \leq k_\parallel \leq 7\ m^{-1}$ [2]. Furthermore, the instability growth rate exceeds the inverse bounce period of fast ions for small magnitudes of n_α relevant to experimental conditions.

ACKNOWLEDGEMENTS

This work has been supported by the European Communities under an association contract between Euratom and Sweden, and by the State Committee on Science, Technology and Industrial Policy of Ukraine. One of the authors (Ya.I. Kolesnichenko) would like to acknowledge the hospitality of Chalmers University of Technology, Sweden, as well as research support by the International Science Foundation during 1995.

REFERENCES

[1] COTTRELL, G.A., DENDY, R.O., Phys. Rev. Lett. **60** (1988) 33.
[2] COTTRELL, G.A., et al., Nucl. Fusion **33** (1993) 1365.
[3] GREENE, G.J., et al., in Controlled Fusion and Plasma Physics (Proc. 17th Eur. Conf. Amsterdam, 1990), Vol. 14B, Part IV, European Physical Society, Geneva (1990) 1540.
[4] CAUFFMAN, S., et al., Nucl. Fusion **35** (1995) 1597.
[5] KOLESNICHENKO, Ya.I., Nucl. Fusion **20** (1980) 727.
[6] COPPI, B., Phys. Lett. A **172** (1933) 439.
[7] BELIKOV, V.S., KOLESNICHENKO, Ya.I., Fusion Technol. **25** (1994) 258.
[8] DENDY, R.O., et al., Phys. Plasmas **1** (1994) 1918.
[9] BELIKOV, V.S., KOLESNICHENKO, Ya.I., SILIVRA, O.A., Nucl. Fusion **35** (1995) 1603.
[10] GORELENKOV, N.N., CHENG, C.Z., Nucl. Fusion **35** (1995) 1743.
[11] MIKHAILOVSKAYA, L.V., Sov. Phys.-JETP Lett. **5** (1967) 279.
[12] COPPI, B., et al., Phys. Fluids **29** (1986) 4060.

DISCUSSION

R.O. DENDY: You concentrated mainly on JET ICE observations. TFTR DT operations have generated a much larger alpha particle ICE database; the two most exciting experimental results have been the time evolution of the ICE intensity, and the critical dependence on the Alfvén velocity at the edge. A quantitative theoretical account of these observations has been published (see the paper by R.O. DENDY et al., these Proceedings, Vol. 1, p. 699). What does your theory say about these two key experimental results?

Ya.I. KOLESNICHENKO: I think that the primary question in the ICE problem is what mechanism of wave–particle interaction is responsible for the ICE, and the present work suggests an answer. In the new theory, as well as in your theory, the instability is sensitive to the Alfvén velocity, which can explain the time evolution of the ICE intensity observed on TFTR. An additional factor which seems to be important for TFTR is the contribution of Re ϵ_{11}^{α} affecting the dependence of γ on n_{α}.

BALLOONING MODES IN HELIOTRONS/TORSATRONS

N. NAKAJIMA, K. ICHIGUCHI, M. OKAMOTO
National Institute for Fusion Science,
Nagoya, Japan

R.L. DEWAR
Plasma Research Laboratory,
Australian National University,
Canberra, Australia

Abstract

BALLOONING MODES IN HELIOTRONS/TORSATRONS.

The characteristics of the high-n ballooning modes and the corresponding β (= kinetic pressure/magnetic pressure) limit are discussed in a planar-axis $L = 2/M = 10$ heliotron/torsatron with a large Shafranov shift (L and M are the polarity and toroidal pitch number of helical coils). The exact incompressible high-n ballooning mode equation for three-dimensional equilibria is solved in the covering space (ψ, η, α) where ψ and α are the labels of the flux surface and the magnetic field line and η is the coordinate along the magnetic field line ($-\infty < \eta < \infty$). In three-dimensional equilibria, the eigenvalue generally depends on α: $\omega^2 = \omega^2(\psi, \theta_k, \alpha)$ with θ_k the radial wave number. From the analyses of the local magnetic shear associated with the toroidal force balance, the physical mechanism is clarified for the fact that high-n ballooning modes can be unstable even in the region with stellarator-like global magnetic shear. Such high-n modes have strong α-dependence of ω^2 for a peaked pressure profile giving Mercier stable equilibria. In contrast, a broad pressure profile allows high-n modes with weak α-dependence of ω^2. The relationship between the high-n and low-n ballooning modes and the related β limit are also considered through the α-dependence of ω^2.

1. INTRODUCTION

In currentless helical systems with a planar-axis, such as heliotron/torsatron devices, the global rotational transform ι of the vacuum magnetic field increases in the minor radius direction. Using a low-β approximation, Shafranov[1] speculated that if the global shear is stellarator-like, then high-n ballooning modes would not become unstable when the Mercier modes are stable. Using three-dimensional equilibria, Cooper *et al.*[2] found high-n ballooning modes in the stellarator-like global magnetic shear region of the ATF[3]; however, they did not give the physical mechanism. The spectrum of ballooning modes in general toroidal systems has been investigated by Dewar *et al.*[4] using a model tokamak with toroidal field ripples in order to study the effects of symmetry breaking on the ballooning spectrum. Recently, an examination similar to that in Ref. [4]

was carried out for high-n ballooning modes in an LHD[5] equilibrium with a broad pressure profile, thus strongly Mercier-unstable[6]. In that work, a modified high-n ballooning equation is used, so that it was not clear how the kinetic energy norm affected the eigenvalues so obtained.

In this paper, we will investigate the stability properties of ballooning modes, both in strongly Mercier-unstable and completely Mercier-stable equilibria, for an $L = 2/M = 10$ heliotron/torsatron system with a large Shafranov shift, with the use of the exact incompressible three-dimensional high-n ballooning mode equation[7].

2. GLOBAL EQUILIBRIUM CHARACTERISTICS

For the vacuum configuration, we will use the planar-axis $L = 2/M = 10$ heliotron/torsatron configuration. Only currentless equilibria will be calculated with the use of the VMEC code[8] for fixed boundary conditions, with the boundary determined as the outermost flux surface of the vacuum field. Two types of pressure profiles will be used in order to examine the relationship of Mercier stability to that of high-n ballooing modes: a peaked profile[9] given by $P(\psi_N) = P_0(1-\psi_N)^2$, and a broad profile[6] given by $P(\psi_N) = P_0(1-\psi_N^2)^2$. Here $\psi_N = \psi/\psi_{edge}$ is the normalized toroidal flux, with $r_N = \sqrt{\psi_N}$ the normalized minor radius. Note that the peaked pressure profile is the profile that is

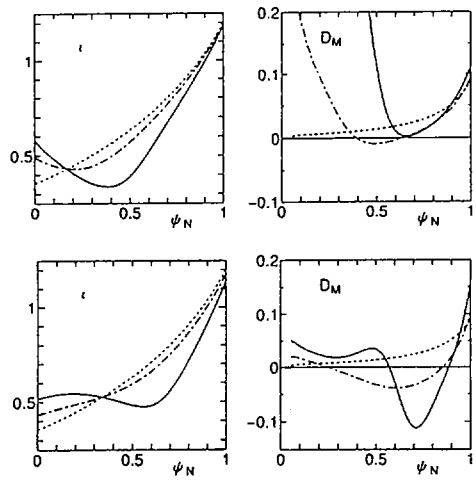

FIG. 1. ι and D_M versus ψ_N. The upper (lower) graphs are for the peaked (broad) pressure profile. The dotted, dotted-dashed and solid curves correspond to $\beta_0 = 0\%$, 4% and 8%, respectively. $D_M > 0$ implies Mercier stability.

normally used in stability calculations for the LHD[9], and that peaked pressure profiles similar to above one are observed in ordinary experiments in CHS[10].

Figure 1 shows the global rotational transform ι and the Mercier criterion parameter D_M as functions of ψ_N for both the peaked and broad pressure profiles with three different central β values. For the vacuum configuration considered here, the Shafranov shift is quite large, i.e., there is a substantial Pfirsch-Schlüter current. Consequently, ι and so the global magnetic shear s become highly deformed as β increases for both types of pressure profile. In particular, ι increases near the magnetic axis, but decreases near the periphery. Because a region of tokamak-like global magnetic shear appears near the magnetic axis and the stellarator-like magnetic shear is increased near the periphery, a shearless region occurs between them. As β increases, the global magnetic shear becomes very strong in the stellarator-like region near the plasma periphery.

3. LOCAL EQUILIBRIUM CHARACTERISTICS

A. Local magnetic shear

Equally spaced (ψ, θ) meshes in the Boozer coordinate system (ψ, θ, ζ) for the peaked pressure profiles with three different central β values are shown in Fig. 2 on horizontally and vertically elongated poloidal cross sections.

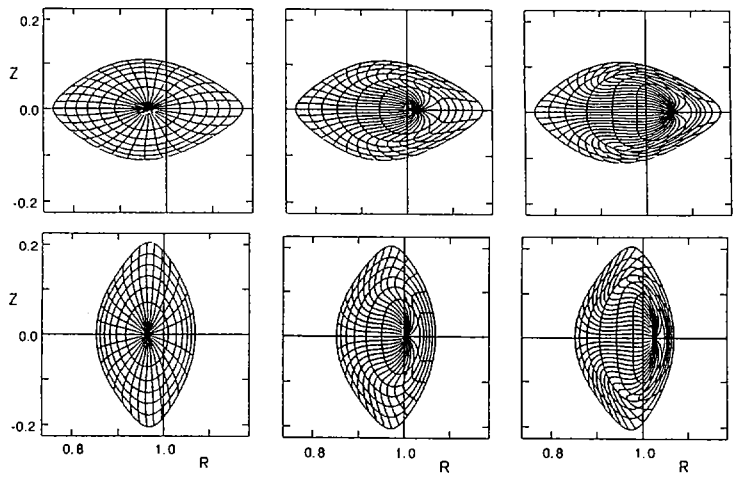

FIG. 2. Equally spaced (ψ, θ) mesh in the Boozer coordinate system for $\beta_0 = 0\%$, 4% and 8% for the left, middle and right graphs, respectively.

In the field line coordinate system or covering space (ψ, η, α), which is related to the Boozer coordinate system (ψ, θ, ζ) as $\eta = \theta, \quad \alpha = \zeta - \theta/\iota$ with α the label for the magnetic field lines, the local magnetic shear $\hat{s}$ can be expressed in terms of the global magnetic shear s and its oscillatory component $\tilde{s}$, as follows:

$$\hat{s} = s + \tilde{s}, \quad s = \frac{2\psi}{\iota}\frac{d\iota}{d\psi}, \quad \tilde{s} = \frac{\partial}{\partial\eta}\left\{\frac{2\psi g_{\psi\theta}}{g_{\theta\theta}}\right\}, \quad \int^{\eta} \hat{s} d\eta = s(\eta - \theta_k) + \frac{2\psi g_{\psi\theta}}{g_{\theta\theta}}, \quad (1)$$

where $g_{ij} = \partial_i \vec{r} \cdot \partial_j \vec{r}$, $(i, j = \psi, \theta, \zeta)$ and θ_k is the radial wave number. In the coordinate system used here, $\theta = 0$ or $\eta = 0$ corresponds to the outer side of the torus. Almost all the information about the local compression of the poloidal field appears in the behavior of the poloidal angle θ, as can be seen in Fig. 2. As the value of β_0 increases, there appears a *turning surface* (i.e., where $g_{\psi\theta} = 0$), which reflects the properties of the local magnetic shear through $\tilde{s}$. Near the magnetic axis, the global magnetic shear s is tokamak-like ($s < 0$) for the peaked pressure profile or very small ($s \sim 0$) for the broad pressure profile; this property can be seen in Fig. 1. Therefore, the local compression of the poloidal field increases

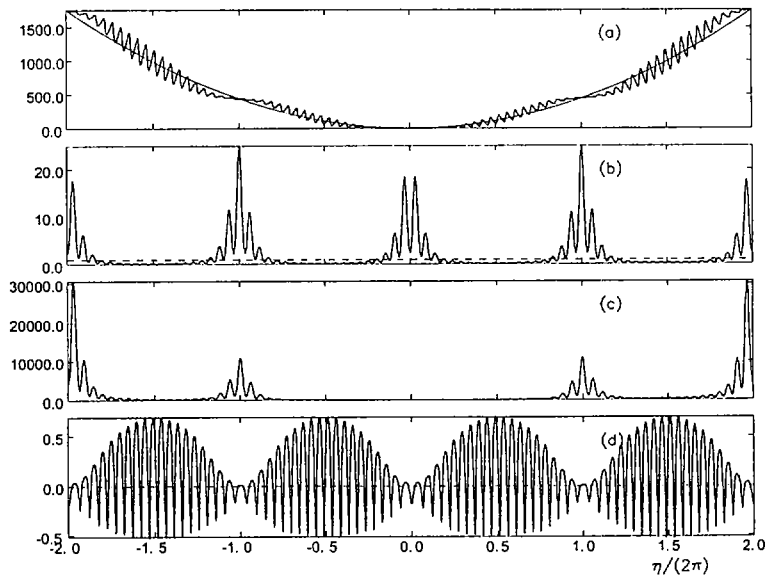

FIG. 3. Variation along a magnetic field line of (a) $[\int^{\eta}\hat{s}d\eta]^2$, with the reference $(s\eta)^2$ (thin curve); (b) $|\nabla\psi|^2/(2\psi B_0)$, with the reference $|\nabla\psi|^2/(2\psi B_0) = I$ (thin dotted curve); (c) $|\vec{k}_\perp|^2$; and (d) κ^n. These quantities are shown at $\psi_N = 0.56$, $\theta_k = 0$ and $\alpha = 0$ for an equilibrium with a peaked pressure profile with $\beta_0 = 8\%$.

radially outward in order to maintain toroidal force balance: $g_{\psi\theta} \sim c\sin\theta$ with $c > 0$, which leads to the situation with $s \lesssim 0$ and $\tilde{s} > 0$. In contrast, near the plasma periphery, ι exceeds unity and s is strongly stellarator-like ($s > 0$). The local compression of the poloidal field decreases radially outward, due to the large poloidal field on average: $g_{\psi\theta} \sim c\sin\theta$ with $c < 0$, which leads to the situation with $s > 0$ and $\tilde{s} < 0$. In both regions, $\hat{s}$ is reduced.

The reduction of the stabilizing effect of the local magnetic shear in the region with stellarator-like global shear ($\psi_N = 0.56$) is exhibited in Fig. 3(a) for the peaked pressure profile with $\beta_0 = 8\%$, where the integrated local shear, $\left[\int^{\eta} \hat{s} d\eta\right]^2$, for $\theta_k = 0$, is plotted along a field line with $\alpha = 0$; on a horizontally elongated cross section, this field line passes through the outer midplane of the torus. For reference, the average integrated local shear $(s\eta)^2$ is also plotted in Fig. 3(a). We can understand that as β increases, the stabilizing effect of the local magnetic shear near $\eta = 0$ is significantly reduced. The vanishing of the (integrated) local magnetic shear at the outer side of the torus does not strongly depend on either the type of pressure profile or the magnetic field line label α, except that the critical β value at which the local magnetic shear vanishes does depend on the pressure profile.

B. Local shape of flux surfaces

At the outer side of the torus, the flux surfaces are locally compressed, because this is where the compression of the poloidal field varies radially. This situation is reflected in the local shape of the flux surfaces at the outer side of the torus, as expressed by $|\nabla\psi| = B\sqrt{g_{\theta\theta}}$. As shown in the poloidal cross sections with $\beta_0 = 8\%$ in Fig. 2, the variation of $|\nabla\psi|$ in the minor radius direction significantly changes across the *turning surface* on the outer side of the torus. At the outer side of the torus, adjacent flux surfaces become progressively nearer to each other in radius as the *turning surface* is approached. In other words, the flux surfaces become more and more compressed. Once the *turning surface* is crossed, however, the flux surfaces become less compressed radially. The local compression of the flux surfaces at the outer side of the torus causes the flux surfaces to be locally uncompressed at the inner side of the torus due to toroidal flux conservation. Thus, the change of the local shape of a flux surface $|\nabla\psi|$ along a field line is quite noticeable as is shown in Fig. 3(b). Since it is caused by toroidal force balance (i.e., the Shafranov shift), the local compression or decompression of the flux surfaces becomes most noticeable as the value of β increases; however, it is independent of α, the magnetic field line label.

The variation of the local shape of the flux surfaces $|\nabla\psi|$ plays an important role in the stabilization of high-n ballooning modes for equilibria with large Shafranov shifts. The reason for this can be seen from the expression for the perpendicular wave number $|\vec{k}_\perp|$,

$$|\vec{k}_\perp|^2 = \frac{2\psi B^2}{B_0|\nabla\psi|^2} + \frac{|\nabla\psi|^2}{2\psi B_0}\left[\int^\eta \hat{s}d\eta\right]^2. \tag{2}$$

The secular stabilizing term $s(\eta - \theta_k)|\nabla\psi|$ is amplified through $|\nabla\psi|$ each time the field line transits the outer side of the torus, near $\eta = 2p\pi$ with p an integer, leading to an enhancement of its stabilizing effect. On the other hand, each time the field line transits the inner side of the torus, near $\eta = (2p+1)\pi$, the secular stabilizing term is diminished through $|\nabla\psi|$, leading to the reduction of its stabilizing effect. The characteristics of the local shape of the flux surfaces as expressed by $|\nabla\psi|$ are universal, at least for $L = 2$ heliotron/torsatron systems.

In Fig. 3(c), $|\vec{k}_\perp|^2$ is plotted along the same field line as that for Fig. 3(a). This graph shows that the field line bending stabilization effect on high-n ballooning modes is strongly modified as β is increased. Within one poloidal period along the field line ($|\eta| < \pi$), this stabilizing effect is significantly suppressed, both because the local shear associated with the poloidal field which is compressed at the outer side of the torus vanishes (Fig. 3(a)) and because the flux surfaces on the inner side of the torus are decompressed (Fig. 3(b)). On the other hand, this stabilizing effect is significantly enhanced farther out along the field line ($|\eta| \sim 2\pi$) due to the local compression of the flux surfaces at the outer side of the torus (Fig. 3(b)). This sort of modification is universal in $L = 2$ heliotron/torsatron systems with a large Shafranov shift and is almost independent of both the magnetic field line label and the pressure profile, except for the β value at which the modification becomes significant.

C. Local magnetic curvature

The local magnetic curvature in heliotron/torsatron systems consists of two components. One component is due to toroidicity, just as in a tokamak plasma. This mainly comes from the vacuum toroidal field and hence has no dependence on α. The other component is due to helicity (i.e., of the helical coils), which mainly arises from the saddle-like profile for the magnetic field strength, reflecting that in a straight helix. On every poloidal cross section, the outside of the torus corresponds to locally "bad" magnetic curvature, and the inside to "good" curvature, in terms of the toroidicity contribution. In terms of the helicity contribution, however, the regions between the helical coils correspond to the locally bad magnetic curvature in each poloidal cross section, and the regions

under the helical coils to locally good curvature. The variation of the magnetic field strength due to the helicity is comparable with that due to the toroidicity. Therefore, the local magnetic curvature is worst at the outer side of the torus in a horizontally elongated poloidal cross section (cf. upper graphs in Fig. 2). At the outer side of the torus in a vertically elongated poloidal cross section (cf. lower graphs in Fig. 2), the locally bad magnetic curvature due to the toroidicity is canceled by the locally good magnetic curvature due to the helicity. Thus, the local magnetic curvature at the outer side of the torus strongly depends on α, the label of the magnetic field line in the covering space (ψ, η, α). This situation is completely different from that in a tokamak plasma. In a tokamak plasma, the local magnetic curvature is independent of the field line label α because of the toroidal symmetry.

In Fig. 3(d), the contravariant normal magnetic curvature $\kappa^n = 2\psi\vec{\kappa}\cdot\nabla\psi/|\nabla\psi|^2$ is plotted along the magnetic field line. The phase due to the toroidicity and that due to the helicity are both quite evident. At the outer side of the torus, where $\eta = 2p\pi$ with p an integer, locally unfavorable magnetic curvature occurs near $\eta = 0$ and $\pm 4\pi$, but locally favorable curvature at $\eta = \pm 2\pi$. Because of such behavior, the local magnetic curvature is expected to have a strong dependence on the magnetic field line (i.e., on α). This sort of strong magnetic field line dependence (α-dependence) of the local magnetic curvature is a universal feature in heliotron/torsatron systems with appreciable helical ripple.

4. STABILITY PROPERTIES

Pressure profiles have a strong influence on high-n ballooning modes through the Mercier criterion. The broad pressure profiles create the highly Mercier unstable equilibria with the maximum pressure gradient within the Mercier unstable region. In such equilibria, the high-n ballooning modes are easily destabilized at a relatively low-β value, which leads to the situation that high-n ballooning modes become unstable before the stabilizing effects within (near) one poloidal period along the field line are suppressed (enhanced) enough by the Shafranov shift. Thus, high-n modes have a tendency to have an extended interchange-like structure along the magnetic field line. The high-n modes occurring near a flux surface giving the marginal stability have the extended interchange-like structure as is shown in Fig. 4(a). The extended structure so relaxes the α-dependence of the destabilizing term that near the marginal stability high-n modes become tokamak-like modes with the eigenvalue $\omega^2 \sim \omega^2(\psi, \theta_k)$. Away from the flux surface giving the marginal stability, high-n modes have fairly localized structure so that α-dependence of ω^2 becomes strong. Thus, in (ψ, θ_k, α) space, the spheroidal level surfaces of ω^2 of localized modes are surrounded with the cylin-

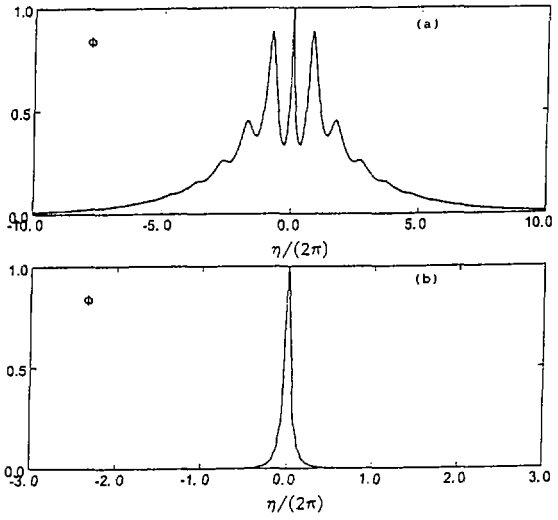

FIG. 4. High-n ballooning mode eigenfunction (a) $\Phi(\psi_N = 0.39, \theta_k = 0, \alpha = 0)$ for a strongly Mercier-unstable equilibrium with the broad pressure profile with $\beta_0 = 4\%$; and (b) $\Phi(\psi_N = 0.56, \theta_k = 0, \alpha = 0)$ for a completely Mercier-stable equilibrium with the peaked pressure profile with $\beta_0 = 8\%$.

drical level surfaces of ω^2 of extended modes. Although the growth rates of these tokamak-like extended modes are small, they are dangerous since they may lead to low-n modes.[6]

In contrast, in the slightly Mercier unstable or completely Mercier stable equilibria, created by the peaked pressure profiles usually used in standard stability analyses[9] and obtained in ordinal CHS experiments[10], the high-n ballooning modes are destabilized after the stabilizing effects within (near) one poloidal period along the magnetic field line are suppressed (enhanced) enough by the Shafranov shift. Thus, these modes are highly localized within one poloidal period as is shown in Fig. 4(b), which leads to such a strong α-dependence of the eigenvalues that the level surfaces of $\omega^2(\psi, \theta_k, \alpha)$ (≤ 0) become topologically spheroid in (ψ, θ_k, α) space as shown in Fig. 5. The area indicated by the thick closed curves corresponds to the contours for the negative eigenvalues of high-n ballooning modes, and the area indicated by the thin unclosed curves to the contours for the positive eigenvalues of high-n TAE modes. Note that the unstable region in θ_k is very narrow. Those highly localized modes with the spheroidal level surfaces of ω^2 never lead to the low-n modes and are inherent to three-dimensional equlibria. Note that the tokamak-like modes leading to low-n modes appear only near the marginal stability in highly Mercier unstable equilibria. Although those inherent high-n modes with the spheroidal level surfaces of ω^2 may be considered to give β-limit to completely Mercier

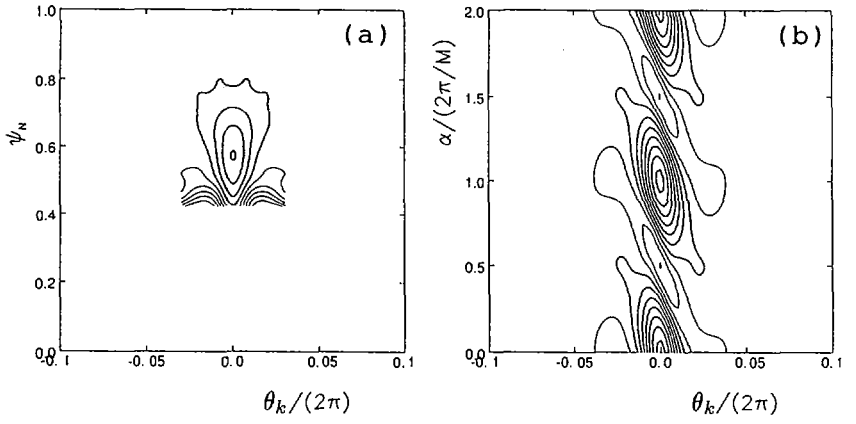

FIG. 5. (a) θ_k and ψ-dependence of Ω^2, with $\alpha = 0$; and (b) θ_k and α-dependence of the most unstable Ω^2, with $\psi_N = 0.56$, both for the peaked pressure profile with $\beta_0 = 8\%$.

stable equilibria, we should notice that those modes are considered to be so highly localized in each toroidal pitch of the helical coils in the configuration space that the expected toroidal mode numbers n would be quite large, i.e., $n \sim n_{min}, n_{min}+M, n_{min}+2M, n_{min}+3M, \cdots$, where n_{min} is at least the order of M. Therefore, in order to evaluate the β-limit due to these high-n modes inherent to three-dimensional equilibria, kinetic effects due to an ion diamagnetic frequency and Finite Larmor Radius stabilizing effects must be evaluated along with them. Such kinetic effects on these high-n modes inherent to three-dimensional equilibria and the relation to ones in other devices will be addressed.

ACKNOWLEDGMENTS

The authors acknowledge to Prof. A. Iiyoshi and Prof. T. Sato for continuous encouragement.

REFERENCES

[1] SHAFRANOV, V.D., Phys. Fluids **26** (1983) 357.
[2] COOPER, W.A., HIRSHMAN, S.P., LEE, D.K., Nucl. Fusion **29** (1989) 617.
[3] LYON, J.F., et al., Fusion Technol. **10** (1986) 179.
[4] DEWAR, R.L., GLASSER, A.H., Phys. Fluids **26** (1983) 3038.
[5] IIYOSHI, A., et al., Fusion Technol. **17** (1990) 148.
[6] COOPER, W.A., et al., Phys. Plasmas **3** (1996) 275.
[7] HAZELTINE, R.D., MEISS, J.D., Phys. Rep. **121** (1985) 1.
[8] HIRSHMAN, S.P., Phys. Fluids **26** (1983) 3553.
[9] ICHIGUCHI, K., et al., Nucl. Fusion **33** (1993) 481.
[10] OKAMURA, S., et al., Nucl. Fusion **35** (1995) 283.

DISCUSSION

R.J. GOLDSTON: On the basis of your studies, do you see a route to second stability for high n modes in a stellarator configuration?

N. NAKAJIMA: At present it is an open question whether a route to second stability exists or not. By using a model equation for high n ballooning modes in heliotron/torsatron systems, this question will be clarified in the near future.

J.D. CALLEN: What is the possible role and importance of the geodesic curvature in the types of ballooning modes you are considering for stellarators and heliotrons?

N. NAKAJIMA: The role of the geodesic curvature becomes quite important when second stability is considered.

THEORY

(Poster Session DP)

OPTIMIZATION OF NEGATIVE CENTRAL SHEAR DISCHARGES IN SHAPED CROSS-SECTIONS

A.D. TURNBULL, M.S. CHU, T.S. TAYLOR,
T.A. CASPER[1], J.M. GREENE, C.M. GREENFIELD,
R.J. LA HAYE, L.L. LAO, B.J. LEE[2], R.L. MILLER,
C. REN[3], C.L. RETTIG[4], T.L. RHODES[4], B.W. RICE[1],
O. SAUTER[5], E.J. STRAIT, K. TRITZ[3]
General Atomics,
San Diego, California,
United States of America

Abstract

OPTIMIZATION OF NEGATIVE CENTRAL SHEAR DISCHARGES IN SHAPED CROSS-SECTIONS.

Magnetohydrodynamic (MHD) stability analyses of Negative Central Shear (NCS) equilibria have revealed a new understanding of the limiting MHD instabilities in NCS experiments. Ideal stability calculations show a synergistic effect between cross-section shape and pressure profile optimization; strong shaping and a broader pressure profile independently lead to moderately higher β limits, but broadening of the pressure profile in a strongly dee-shaped cross-section leads to a dramatic increase in the ideal β limit. Localized resistive interchange (RI) modes can be unstable in the negative shear region and are most restrictive for peaked pressure profiles. Resistive global modes can also be destabilized significantly below the ideal β limit. Experiments largely confirm the general trends, and diagnostic measurements and numerical stability calculations are found to be in good qualitative agreement. Observed disruptions in NCS discharges with L mode edge and strongly peaked pressure appear to be initiated by interactions between the RI and the global ideal and resistive modes.

1. INTRODUCTION

The aim of research in tokamak concept development has been the identification and achievement of configurations with significantly improved β limits, enhanced confinement, and sustained non-inductive current-drive. Each has been achieved, with varying degrees of success, in separate regimes in DIII-D [1–3], and other major tokamaks [4–7], but meaningful gains in *fusion performance* with substantially reduced size and cost [8] will require that all three features be achieved simultaneously with adequate fusion power and particle exhaust — this is the concept of the Advanced Tokamak (AT) [9,10].

---

[1] Lawrence Livermore National Laboratory, Livermore, California, USA.
[2] University of California, San Diego, California, USA.
[3] University of Wisconsin, Madison, Wisconsin, USA.
[4] University of California, Los Angeles, California, USA.
[5] CRPP-EPFL, Lausanne, Switzerland.

Reversal of the central shear is one possible route to the AT goal [11]. Negative Central Shear (NCS) experiments in DIII–D [1,12–14], and TFTR [15] show some of the desired features, most notably, the expected [11,16] core transport improvements [1,12–14,17], to a lesser extent, the high bootstrap fraction [12–14] necessary for practical steady-state operation [11,16], and in some instances [1,12,14], high β limits as well. However, these configurations are so far transient, and are ultimately limited by a variety of magnetohydrodynamic (MHD) instabilities. Further progress requires a more thorough understanding of these MHD limits.

This work presents the results from systematic numerical calculations of the MHD stability limits in NCS configurations and correlates the limiting instabilities with the MHD activity observed in the experiments. The following section presents the ideal MHD stability picture, showing the dependence on the safety factor q and pressure p profiles, and on the cross-section shape. In particular, the effects of optimizing the pressure profile and shape are synergistic; moderate increases in the β limit are obtained by either broadening the pressure profile or increasing the triangularity, but a dramatic increase in the β limit results with strong shaping and broadened pressure together, in the presence of a nearby conducting wall. In Section 3 resistive interchange modes are shown to be destabilized by a pressure gradient in a region of negative shear. Global resistive modes can also be unstable significantly below the ideal β limit. Both are most restrictive for peaked pressure profiles. In Section 4, the observed β limits and MHD activity are in good agreement with the predicted ideal and resistive β limits over the range of parameters considered. The conclusions are summarized in Section 5.

2. IDEAL MHD STABILITY

2.1. Dependence on q_{min}

A systematic study of the maximum stable wall position was performed for sequences of equilibria with varying minimum q value (q_{min}) at fixed total current and fixed β_N, and with the axis value q_0 fixed. Here, $\beta_N = \beta/(I_N)$, where $I_N \equiv I/aB$, I is the total plasma current in MA, a is the minor plasma radius in meters, and B is the toroidal magnetic field in T. The parameters describing the equilibrium were those of Ref. [11], with $q_0 = 3.9$, q_{95} (q at the 95% flux surface) = 5.1, $\beta_N = 5.0$ (% mT/MA) and the radius of q_{min}, $r_{min} = 0.65$, measured as a fraction of the square root of the normalized poloidal flux ψ. The pressure gradient was given by $p'(\psi) = p_0(1 - 5/8\psi)$, which closely matches that in Ref. [11]. The wall was taken to have the DIII–D wall shape, but expanded uniformly to vary the plasma-wall separation, with expansion parameter $\lambda = 1$ corresponding to the real wall in DIII–D. Stability to toroidal mode numbers $n = 1$ and $n = 2$ was computed using the ideal MHD code GATO [18].

The results are summarized in Fig. 1. The optimum q_{min} in Fig. 1 is at $q_{min} = 2.05$ for both $n = 1$ and $n = 2$ ideal kink modes. This is not surprising since taking $q_{min} = 2.05$ with $q_0 = 3.9$ provides the largest stabilizing shear without the destabilizing effect of having $q = 2$ surfaces present (q_{min} values lower than 1.8 were not considered). Two features in Fig. 1, however, are significant. First, there is a secondary optimum at $q_{min} = 2.85$. This can be explained by large coupling of poloidal harmonics from the finite aspect ratio $R/a \sim 2.7$ and strong cross-section shaping — the usual intuition from straight cylindrical models with no coupling would lead one to anticipate degraded stability for $2.5 \lesssim q_{min} \lesssim 3$ for both $n = 1$ and $n = 2$ modes.

Second, the optima for $n = 1$ and $n = 2$ modes coincide. In particular, there is no significant degradation in the stability of the $n = 2$ modes just below $q_{min} = 2.5$, as

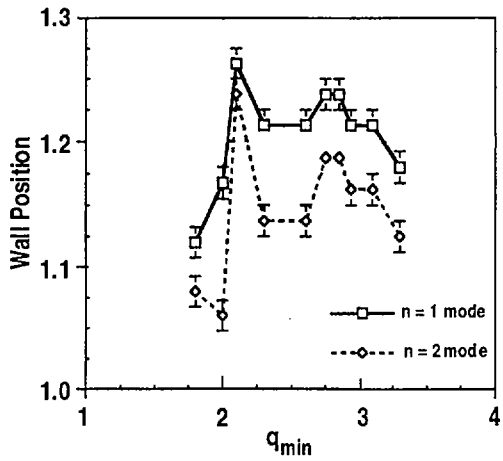

FIG. 1. Maximum stable wall position versus q_{min} for n = 1 and n = 2 ideal kink modes for free boundary DIII-D-like NCS equilibria with q_0 = 3.9, q_{min} = 2.1, $\beta_N \simeq 5$, and a DIII-D-shaped wall.

might again be anticipated from the usual intuitive pictures. The fact that the optima for n=1 and n=2 modes occur at the same $q_{\min}$ makes operation of NCS much simpler than it otherwise would be since there is no compromise necessary between the stability of the two most dangerous modes.

The effect of varying q_0 was also studied. Varying q_0 from 3.9 to 3.1 had a small effect on the stability so this was not pursued further. The effect of $q_{\min}$ on the stability is significant. In terms of placement in the wall position for the $\beta_N = 5$ case studied, the difference between the optimum $q_{\min}$ and the least stable $q_{\min}$ translates into roughly an extra 10 cm in the separation of the plasma from the wall for a DIII–D sized machine. This could have important consequences in the engineering design of an AT power plant.

2.2. Dependence on Cross-section and Pressure Profile

The pressure profile can have a dramatic effect on the stability. A systematic study was performed to investigate this dependence in a variety of cross-section shapes. The pressure profiles were given by $p'(\psi) = p_0(1-\psi)^{\nu}$, where ν was used to specify the peaking factor $p_0/\langle p\rangle$, and p_0 specifies the pressure on axis. $\langle p\rangle$ is a volume average over the cross-section. Note that p' vanishes at the edge for $\nu > 1$. The cross-sections were parameterized by varying elongation and triangularity, and the q profiles were fixed near the optimum from Section 2.1, with $q_0 = 3.9$, $q_{\min} = 2.1$; $r_{\min} = 0.65$, and $q_{95} = 5.1$. In contrast to the study in Section 2.1, the wall position was fixed here to be a conformal (i.e. constant normal distance) wall at 1.5 times the mid-axis minor plasma radius. The β limits were computed by considering sequences of similar equilibria with increasing pressure. Note that I is not held fixed and varies with cross-section shape. Also, the current density was forced to vanish at the plasma edge by allowing slight modifications to the edge q profile so as to avoid β ravines as the pressure was increased [19]. The β limits for each peaking factor were computed by increasing p_0 keeping ν fixed, and computing the n=1 stability using the GATO code [18].

The results are summarized in Fig. 2 in terms of the β limit versus peaking factor for each of the cross-sections. The two curves correspond to the circular $(\kappa, \delta) = (1.0, 0.0)$ and highly triangular elongated case with $(\kappa, \delta) = (1.8, 0.7)$, for which complete scans over peaking factor were performed. For the intermediate cross-sections, β limits for the two extreme peaking factors were computed.

Several important conclusions can be drawn from these results. First, for a circular cross-section, the variation of the β limit with peaking factor is quite weak. Broad pressure is marginally better in terms of β, but in terms of the Root Mean Square (RMS) β, $\beta^* = (\int p^2 dV)^{1/2}/B^2$, which is perhaps more relevant to fusion performance [20], the strongly peaked profiles are marginally better. For an elongated cross-section, however, the dependence on pressure peaking is stronger and increases considerably with higher triangularity. For the most strongly shaped cross section $(\kappa, \delta) = (1.8, 0.7)$ an increase in the β limit of a factor 3 is achievable by broadening the pressure profile, with a similar gain in β^* as well.

Second, comparing the circular and highly shaped cross-sections, the β limits for the latter are above those in the circular case for all peaking factors, and the optimum β is a factor 5 above the optimum achievable in a circular cross-section. The same holds for β^* as well as β. The increase from shaping is due partly to the increased current-carrying capacity of a highly elongated, highly triangular cross-section at the same q, but is also due to a significant increase in the normalized β_N limit. For the most peaked profiles, this increase in β_N from shaping is relatively weak. However, for the broad pressure profiles it is a factor of 2.

The factor of 5 increase in β^* from optimizing both shaping and pressure profile translates into a factor 25 gain in the expected fusion reactivity since $P_{fus} \sim (\beta^*)^2 B^4 V$ (V is the plasma volume). The fusion yield Q_{dd} is increased by a factor of 5, since, with given field and major radius RB, Q_{dd} can be represented as [20]

$$Q_{dd} \sim (RB)^2 (\beta^*) [F(q, \kappa, \delta)] \tag{1}$$

This large increase can be viewed as a route to increasing Q_{dd}. Alternatively, if one requires a certain Q_{dd}, the product BR can be reduced by a factor of $\sqrt{5}$ with a roughly proportional reduction in the system capital cost.

2.3. Dependence on Wall Position

Wall stabilization is necessary for achieving large β_N values in NCS discharges. A study was undertaken, in which the β limits for the circular and highly shaped cross-sections of Section 2.2 were computed with several conformal wall positions, as well as with no wall. This was done for the two extreme peaking factors with $\nu = 1.5$ and 5.0. The results are summarized in Fig. 3, showing the four β limits as a function of wall position.

Much of the gain in β_N from shaping results from the presence of a nearby stabilizing wall. If a closer wall is allowed, the gains are even more dramatic than in Fig. 2; the n=1 β_N limit for the strongly shaped equilibria increases extremely fast as the wall is brought closer to the plasma. This is true for both extreme pressure profiles, but is especially so for the optimum broad profile. In this case, $\beta_N > 10$ for a wall at 1.2 times the plasma minor radius, which is still within present engineering limits. The circular cross-section β limits are largely unaffected by the wall until the wall is brought within 1.1 times the minor radius. Note that the comparison here is with conformal walls — the plasma wall distances around the poloidal cross-section are fixed

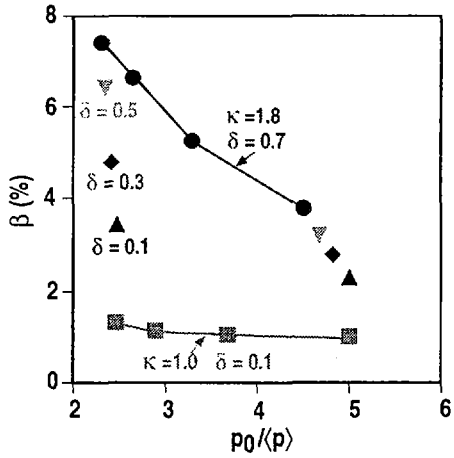

FIG. 2. β limit versus peaking factor for circular and highly shaped (κ = 1.8, δ = 0.7) cross-sections. Shown also are the β limits for cross-sections with κ = 1.8 and δ = 0.1 (Δ), δ = 0.3 (◇), and δ = 0.5 (▽), with broad (ν ~ 1.5) and peaked (ν ~ 5) pressure profiles. For the circular case, I_N = 0.47, and for the highly shaped dee, I_N = 1.4.

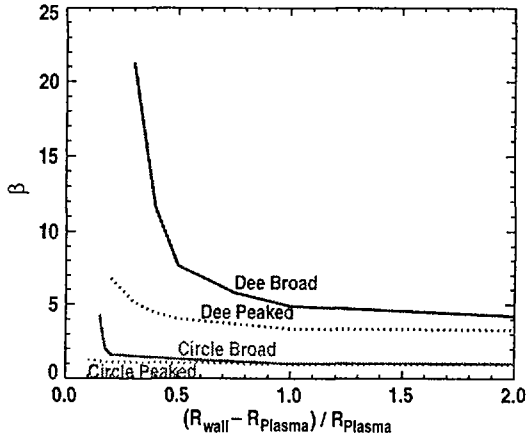

FIG. 3. β limit versus conformal wall position $(R_{wall} - R_{plasma})/R_{plasma}$ for a cross-section with ν = 1.5 and ν = 5 and a highly shaped dee cross-section, also with ν = 1.5 and ν = 5.

and are the same for the two different shapes. Note also that only n=1 modes were considered here. From the results in Section 2.1, the $n \geq 2$ modes are expected to have similar trends but would be more limiting at the large β values shown in Fig. 3.

3. RESISTIVE STABILITY

Two distinct resistive modes are of concern in the case of negative shear. Double tearing modes [21] have been predicted to be virulently unstable and global in nature as a result of coupling between the two rational surfaces with the same helicity. Second, although *ideal* interchange stability tends to be easily satisfied in the negative shear region, negative shear destabilizes the *resistive* interchange (RI) mode. This can be demonstrated by analysis and numerical evaluation of the analytic RI criterion [22], as well as by stability calculations for $n \approx 1$ modes using the MARS resistive MHD code [23]. The latter calculations used model equilibria having $q_{min} = 1.5$, $q_0 = q_{min} + 1$, $q_{95} = 5.1$, $r_{min} = 0.5$, and a self-similar, rather than conformal, wall; that is, at each point on the plasma surface, the wall was extended along a ray subtended from the geometric center of the plasma by a constant factor, so that the plasma and wall shapes are similar but the plasma-wall separation varies with poloidal angle. The wall factor was taken to be at 1.3 times the minor radius ,

3.1. Localized Interchange Stability

For an axisymmetric tokamak, the condition for RI instability is [22]

$$D_R \equiv D_I + \frac{1}{4}(1-2H)^2 > 0 \tag{2}$$

where the Mercier criterion [24] $D_I > 0$ implies instability to ideal interchanges, and H is given in Ref. [22]. Numerical evaluation of D_R across the plasma for the NCS equilibria in Section 2 invariably shows $D_R > 0$ in the negative shear region when β is above a critical value that is below the ideal $n = 1$ kink limit. However, like the ideal β_N limit, the RI β_N limit depends strongly on the pressure profile peakedness, and for a given cross-section roughly follows the ideal limit at some fraction below it. For the highly triangular dee shapes, this fraction is in the range 65% to 80%, whereas for a circular cross-section it is generally closer to 85% to 90%, reflecting the fact that the dependence of the RI β_N limit is less sensitive to cross-section shape than the ideal kink limit. Nevertheless, the dependence on shape is still considerable. This dependence can be seen from the following analysis. D_R can be written

$$D_R \equiv \left[\frac{p'}{(q')^2}\right]\left[V\dagger\dagger + p'\hat{H}2 - q'\hat{H}\right] \tag{3}$$

where

$$H \equiv \left(\frac{p'}{q'}\right)\hat{H} \tag{4}$$

and

$$D_I \equiv \left[\frac{p'}{(q')^2}\right] V\dagger\dagger - \frac{1}{4} \tag{5}$$

with $V\dagger\dagger$ given in Ref. [24]. The primes here refer to derivatives with respect to ψ. For typical NCS equilibria, $V\dagger\dagger > 0$, when $q > 1$, so Mercier stability is usually satisfied ($p' < 0$). Also, from Eq. (3), the term proportional to p' is always destabilizing for any p'. The last term, however, flips sign when q' is reversed. Taking $\hat{H} < 0$, as is usually the case with a large Shafranov shift, the last term in Eq. (3) is stabilizing for normal shear, *but destabilizing for negative shear.*

Negative shear, coupled with a large Shafranov shift and large negative p' can therefore lead to positive D_R and RI instability, even when the system is Mercier stable with $V\dagger\dagger > 0$. This can also be seen pictorially as follows. The condition for localized RI instability can be evaluated simply in a space spanned by varying p' and q', in the same way as the so-called (s, α) diagram is constructed for ideal ballooning and interchange stability in Ref. [24]. The generic stability diagram for the case $V\dagger\dagger > 0$ and $\hat{H} < 0$ is shown in Fig. 4(a), showing the Mercier unstable region as in Ref. [24] and the two RI regions. The physically relevant half plane is $p' < 0$. For negative shear, there is a *critical negative pressure gradient* $p'_{crit} \equiv -V\dagger\dagger / |\hat{H}|^2$, beyond which the RI mode is always unstable. Also, there is a *critical negative shear* $q'_{crit} \equiv -V\dagger\dagger / |\hat{H}|$, beyond which any negative pressure is unstable. For $q'_{crit} < q' < 0$, there is a local limit to the stable pressure gradient $p'_{crit} < p' < 0$. For positive shear, the p' limit is much larger and arises only when $H < -1/2$ so that the term proportional to p' dominates both $V\dagger\dagger$ and the, now stabilizing, shear term.

Both $V\dagger\dagger$ and $\hat{H}$ depend quite strongly on the shape and the external shape tends to penetrate well into the internal negative shear region of NCS equilibria [25]. The

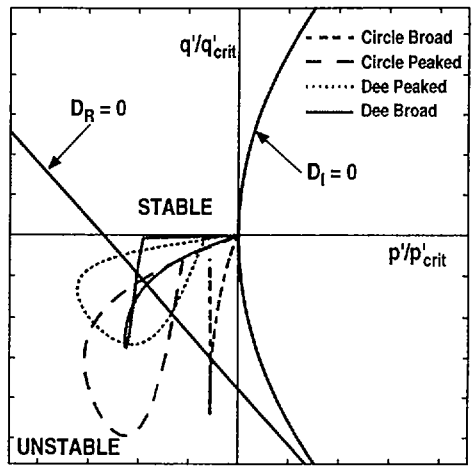

FIG. 4. Normalized RI stability limits versus $p'/|V\dagger\dagger/\hat{H}^2|$ and $q'/|V\dagger\dagger/\hat{H}|$ for circular and dee shaped cross-sections with peaked and broad pressure profiles.

dependence on shape is shown in comparing the extreme shapes and extreme pressure profiles from the series of model equilibria with $q_0 = q_{\min} + 1$. This comparison can be shown as a series of rescaled local RI stability diagrams, whereby the (p', q') plane for each flux surface is rescaled such that the axis intersections of the RI stability boundary are scaled to unity. This is possible over the region where the diagram topology is unchanged. All quantitative information is lost in the rescaling, but the trajectory of the actual equilibrium profile can then be plotted with respect to the stability boundaries. This is done in Fig. 4, where the diagrams for the four extreme cases are overlayed. For comparison, the four cases were chosen at their respective ideal β limits. From this pictorial representation, it is clearly seen that the unstable RI region covers most of the internal region of the plasma for the peaked pressure cases.

Numerical calculations using the MARS code [23] for NCS equilibria have identified unstable RI modes on the innermost low order rational surfaces. These have been found to be unstable in systematic investigations using the model equilibria with $q_0 = q_{\min} + 1$, as well as in reconstructions of DIII–D NCS equilibria. The β limit for their onset is typically close to the value at which $D_R > 0$ on the respective rational surface. Figure 5 shows the computed unstable mode for a reconstructed DIII–D L–mode NCS discharge #87009 at 1620 ms. The features shown are quite typical of the most unstable modes in strongly shaped NCS equilibria. Figure 5(a) displays the Lagrangian displacement v_r Fourier analyzed in the straight field line poloidal angle. The mode is localized entirely around the inner $q = 3$ surface ($q_{\min} = 2.05$), and $D_R > 0$ over most of the negative shear region. The perturbed radial magnetic field b_r is shown in Fig. 5(b). This is also highly localized around $q = 3$.

The structure is that of an interchange mode, with v_r having dominant poloidal mode number $m = nq$, and b_r having dominant $m = nq + 1$ and $nq + 2$ components. Numerical grid sensitivity and convergence tests for several cases, including that shown in Fig. 5, have verified that the computed modes are properly resolved and are unstable. Scaling studies with varying resistivity [26] also confirm the expected $\eta^{1/3}$ scaling of the RI growth rate [22]. The growth rate is found to be insensitive to plasma boundary conditions and sheared plasma rotation, as expected from the localized nature of the mode, and the real mode frequency scales with the local fluid rotation. Systematic studies of the critical β_N for the onset of the RI mode with respect to various equilibrium parameters reveal a strong decreasing dependence of $\beta_{N\,crit}$ on increased pressure peaking, in line with the similar dependence of the D_R criterion. However, $\beta_{N\,crit}$ is found to be relatively insensitive to $q_{\min}$; although the surface at which the computed mode appears varies with $q_{\min}$, $\beta_{N\,crit}$ does not. This is consistent with the instability criterion $D_R > 0$ indicating instability over most of the NCS region in each case — while there is at least one rational surface in this region, there will be a corresponding RI instability. The RI diagram for this discharge is essentially that shown in Fig. 4 for the peaked pressure dee shape.

3.2. Global Resistive Modes

NCS equilibria with multiple low order rational surfaces of the same helicity are known to be susceptible to double tearing mode instabilities, with a global mode structure straddling the two rational surfaces, and significantly higher growth rates ($\gamma \sim \eta^{1/3}$) than the usual single pitch tearing modes [21]. Numerical calculations with the MARS code [23] have identified these instabilities routinely in NCS equilibria.

However, in many cases, the global mode structure is modified from the simple double tearing structure by external conditions, most notably, the plasma shape and associated

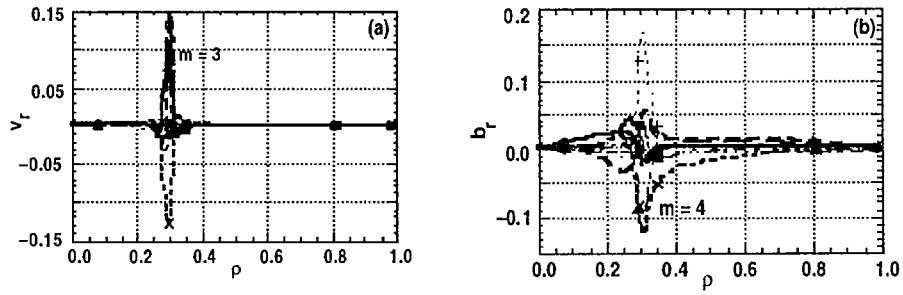

FIG. 5. Unstable RI mode computed for DIII-D discharge No. 87 009 at 1620 ms: (a) perturbed radial displacement v_r; (b) perturbed radial field b_r.

boundary conditions, plasma rotation, and finite β effects. In general, the resulting mode has some double tearing-like structure, some RI component at the inner rational surface, plus an ideal kink-like component. The dependence on external conditions can be summarized as follows. For circular cross-sections, in the absence of plasma rotation, the mode has a critical β_N below the ideal and RI limits. On the other hand, in dee shaped cross-sections it is invariably more stable than the RI mode, having higher critical β_N and a lower growth rate. In either case, near the critical β_N, the global mode is still predominantly double tearing, with growth rate scaling like $\gamma \sim \eta^{\alpha}$, where $\alpha \sim 1/3$. Plasma rotation can, however, greatly affect the mode structure, and rotation speeds of the order of those measured experimentally in DIII–D can stabilize the mode near the critical β_N by decoupling the two rational surfaces to produce a mode with characteristics of the more stable single pitch tearing mode.

Increasing β, however, increases the coupling between the global resistive mode and the external boundary. The unstable mode then takes on increasing ideal characteristics. The resonant structures at the rational surfaces are broadened and dominated by the global structure across the plasma and out to the edge. In addition, there is increased coupling to the RI with increasing β. The resistivity scaling $\gamma \sim \eta^{\alpha}$ becomes more ideal, as α decreases; at the ideal β limit, $\alpha \rightarrow 0$ and the mode becomes a global ideal mode such as was discussed in Section 2.

These trends appear to be quite robust, although the details depend quantitatively on the external boundary conditions, such as the presence of a nearby wall, or a nearby divertor. In particular, the higher growth rate of the global mode in circular cross-section, and of the RI in the dee shaped cross-sections is a significant observation, as will be discussed in Section 4. A typical unstable resistive global mode, displaying most of the features, is shown in Fig. 6. This is for the same DIII–D discharge as in Fig. 5, but at a later time (1675 ms), and corresponds to the most unstable $n = 1$ mode at this time: The double tearing structure can be seen in the two peaks in v_r [Fig. 6(a)]. The coupling with the edge of the plasma is also clearly seen and contributes ideal characteristics to the mode. Also clear is the relative dominance of the innermost peak in v_r due to mixing with the RI mode. However, the global character of this mode is most obvious in the plot of b_r in Fig. 6(b). The perturbation in b_r extends from the core of the plasma to the plasma boundary, with no obvious resonant structures at the rational q surfaces, characteristic of an ideal instability.

Systematic stability studies for the dependence of the global mode on the equilibrium parameters have not been performed since the RI mode is the more unstable in

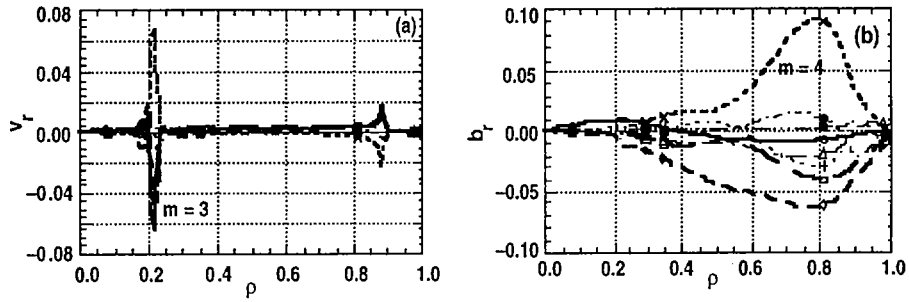

FIG. 6. Unstable resistive global mode computed for DIII-D discharge No. 87 009 at 1675 ms: (a) perturbed radial displacement v_r; (b) perturbed radial field b_r.

dee shaped plasmas, and since the global mode stability is sensitive to external boundary conditions and plasma rotation. Nevertheless, since the stability limit for these modes lies between the more unstable RI mode and the more stable ideal modes, it is a strongly decreasing function of the pressure peaking. The dependence on q_0 and $q_{\min}$ is less clear and merits further investigation. It is notable, however, that unstable resistive global modes have been identified when $q_{\min} > 2$, as well as when $q_{\min} < 2$.

4. EXPERIMENTAL CONFIRMATION

In DIII–D and TFTR, NCS discharges with L–mode type edge conditions are sometimes observed to form an internal barrier near the minimum q position [12–15]. With continued neutral beam fueling, this results in a dramatic peaking of the density profile and ultimately the discharges undergo a fast $n=1$ disruption at low β_N values near 2.0. In strongly shaped DIII–D discharges the β_N limit is typically a little above 2.0, and in circular cross-section TFTR, β_N is usually a little below 2.0. Also, bursts of $n=1$ MHD activity are commonly observed in DIII–D during the discharge evolution. In TFTR, these bursts have not been observed.

Broadening the pressure profile greatly increases the achievable β limit. In DIII–D this is achieved by forcing a transition to H–mode prior to reaching the disruption β limit [13]. In that case, β_N continues to increase with continued neutral beam fueling, reaching values in excess of $\beta_N \sim 4$ — double the L–mode limit. This limit is generally not disruptive and corresponds to the onset of ELMs, though the NCS region usually then collapses.

These general observations are in good agreement with the overall stability picture found in Sections 2 and 3. Figure 7 shows the ideal and resistive β limits as functions of the pressure profile peakedness, for the model equilibria with $q_0 = q_{\min} + 1$ overlaid with the experimental data obtained from the DIII–D NCS experiments. For strongly peaked pressure profiles with $p_0/\langle p \rangle \sim 5$ to 7, as observed in the experiments near the disruption times, the ideal β limits are typically $\beta_N \gtrsim 2$ for strongly dee shaped equilibria. The global resistive β limits are generally around 10% to 20% lower than this.

Moreover, in the noncircular cases, the localized resistive interchange limit is the most stringent. Thus, the prior MHD bursts in DIII–D can be identified with the resistive interchange mode [26]. In addition, the mode structures as identified from soft x–ray (SXR) and other fluctuation diagnostics on DIII–D show a structure localized very close to the inner rational surfaces as predicted for a resistive interchange mode.

One can therefore hypothesize that in the noncircular DIII–D L–mode discharges, the equilibria evolve with increasing β and increasing peakedness, reaching first the resistive interchange limit in Fig. 7 at $\beta_N \sim 1.5$ to 2.0 and consequently suffering the observed localized MHD bursts. These bursts cause some changes in both the magnetic and rotational shear profiles [14], which have a significant destabilizing effect.

However, the modes stabilize and the discharges recover since the perturbations are quite localized in both v_r and b_r. The trajectory of discharge #87009 is shown in Fig. 7. This was an L mode discharge with an early MHD burst and final disruption as shown. The computed resistive interchange mode for this discharge is shown in Fig. 5 using an equilibrium reconstructed from motional Stark effect (MSE), pressure profile, and magnetic data, at the time of one of the early MHD bursts (1620 ms). Of particular note is the high degree of localization of b_r around the $q = 3$ surface. In contrast, the fastest growing mode computed just prior to the time of the fast $n > 1$ disruption (Fig. 6), shows structure in the fluid displacement at both $q = 3$ surfaces. More important, however, is the global nature of b_r in Fig. 6(b), especially the large relative amplitude near the edge. This seems likely to cause a gross disturbance over the whole plasma, which could be identified with the observed disruption.

Another general observation is consistent with the calculations in Section 3. Both the calculations and experiments show no discernible dependence of either the disruption limit or the prior bursts in DIII–D on the value of q_{min}, particularly near $q_{min} = 2$. For the resistive interchange modes, when $q_{min} < 2$, unstable modes can be found on either of the $q = 2$ or $q = 3$ surfaces, though the experimental data has not been analyzed in sufficient detail to determine if and when the bursts are predominantly $m = 2$ or $m = 3$, in such cases. SXR analysis has shown an $m = 3$ structure at the $q = 3$ surface in the one instance where complete analysis was done. For the disruption, the gross characteristics also appear to be independent of whether $q_{min} < 2$ or $q_{min} > 2$. The calculations show global modes generally associated with the lowest double rational surface in the plasma but they are otherwise similar, as are the ideal modes in Section 2.

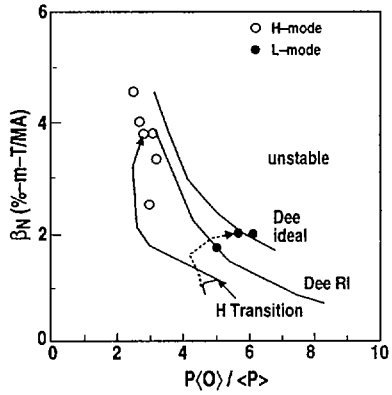

FIG. 7. Comparison of computed ideal and RI β limits for model equilibria with $q_0 = 2.5$, $q_{min} = 1.5$, and $q_{95} = 5.1$ as a function of $p_0/\langle p \rangle$, with DIII-D NCS discharges (solid points: L mode, open points: H mode). Discharge trajectories for No. 87 009 (L mode) and No. 84 736 (H mode) are shown overlayed, the latter with the H transition identified.

The trajectory of an NCS discharge, #84736, in which a transition to H–mode was triggered during the density peaking, is also shown in Fig. 7. Following the transition, $p_0/\langle p \rangle$ suddenly decreases, and β_N is then able to increase to $\beta_N \sim 4$ while remaining in the stable region. This discharge does not reach any of the computed β limits (ideal or resistive) shown in Fig. 7. Instead, the discharge was ultimately limited by the onset of ELMs, at which point the inverted q profile collapsed — the discharge continued ELMing at lower β with a monotonic q profile. The first ELM which resulted in the profile collapse appears to be associated with an ideal or resistive instability not considered in the present calculations since the edge pressure gradient was taken to vanish; this first ELM bears many of the characteristics of the VH–mode termination event [27] which has been identified as a low n, edge-localized ideal kink mode driven unstable by the finite edge pressure gradient. With this proviso, the development of this discharge is also consistent with the stability limits in Fig. 7.

Finally, the TFTR β limits are also consistent with the limits for circular cross-section, being limited to $\beta_N \lesssim 2$. The fact that the resistive interchange-like MHD bursts are not observed is in accordance with the calculation result that, for circular cross-section, the resistive global mode is found to be more unstable than the RI.

5. SUMMARY

Investigation of the ideal and resistive MHD stability of NCS equilibria reveals a new understanding of the effects of profiles and cross-section shape on the MHD instabilities that presently limit the performance of NCS discharges. For global, low n, ideal modes, stability is optimized when q_{min} is just above a rational value as expected. However, local, sub-optimum values also exist between the rational values that are not intuitively predicted. Cross-section shape and the pressure profile, together, have a synergistic effect on the ideal stability. For a circular cross-section, β_N is limited, for any reasonable pressure profile, to values of $\beta_N \sim 1.5$ to 2.5. Optimization of the pressure profile in a strongly dee shaped cross-section, however, leads to qualitatively different optimum profiles and dramatically higher ideal β limits, up to factors of five above those obtainable in a circular cross-section. If a closer wall is allowed, the quantitative gains in β from pressure and cross-section optimization are even more dramatic. These general trends are robustly insensitive to the details of the q profile and the shape of the stabilizing wall.

Localized RI modes can be unstable in the negative shear region due to destabilization of the magnetic well by profile effects. For the most strongly peaked pressure profiles, these modes are the most restrictive on β_N. They depend sensitively on the pressure peakedness and the degree of inner shear reversal, $q_0 - q_{min}$, but are relatively insensitive to q_{min}, *per se*. The dependence on the cross-section shape is less than that for the ideal kink modes, but is nonetheless still significant. Resistive global modes can also be easily destabilized below the ideal β limits if the plasma rotation is low. Sheared plasma rotation, however, can decouple multiple rational surfaces with the same or different helicity if the equilibrium is sufficiently far from the ideal limit, and this can stabilize the modes.

Experiments in the DIII–D tokamak largely confirm the general trends. In cases where the detailed comparisons have been done, diagnostic measurements and numerical stability calculations are found to be in excellent agreement. Observed disruptions in NCS L mode discharges with strongly peaked pressure appear to be initiated by interactions between the RI, and the global ideal and resistive modes, directly, and indirectly through the current density, pressure, and rotation profiles.

A clear and consistent picture has therefore emerged which goes a long way to explaining the observed MHD behavior of NCS discharges, but some challenges still remain. First, identification of the disruption event, as a near-ideal resistive global mode, from direct observation of the mode structure during the disruption is needed. The large ELMs in the H mode phase also need to be unambiguously identified. As for the MHD bursts, though the internal fluctuation diagnostic measurements are in good agreement with the localized nature of the computed RI modes, the observed linear growth rates of the fluctuations are typically up to an order of magnitude faster than the computed growth rates for the experimental Lundquist values. This needs to be resolved. Also, linear MHD calculations find $n = 2$ and higher n modes with faster growth rate than the $n = 1$ modes ($\gamma \sim n^{1/2}$). Yet $n = 2$ bursts are rarely observed and $n > 2$ bursts have not been identified. The resolution of this is probably to be found in kinetic or neoclassical corrections to the linear MHD theory.

6. ACKNOWLEDGMENTS

This is a report of work sponsored by the U.S. Department of Energy under Contract Nos. DE-AC03-89ER51114 and W-7405-ENG-48, Grant Nos. DE-AC03-95ER54299 and DE-FG03-86ER53266, and in part by the Swiss National Science Foundation.

REFERENCES

[1] LAZARUS, E.A., et al., Phys. Fluids B **4** (1992) 3644.
[2] JACKSON, G.L., et al., Phys. Rev. Lett. **67** (1991) 3098.
[3] POLITZER, P.A., et al., Phys. Plasmas **1** (1994) 1545.
[4] HUGON, M., et al., Nucl. Fusion **32** (1992) 33.
[5] KOIDE, Y., et al., Phys. Rev. Lett. **72** (1994) 3662.
[6] HOANG, G.T., et al., Nucl. Fusion **34** (1994) 75.
[7] STRACHAN, J.D., et al., Phys. Rev. Lett. **58** (1987) 1004.
[8] GALAMBOS, J.D., et al., Nucl. Fusion **35** (1995) 551.
[9] TAYLOR, T.S., Plasma Phys. Control. Fusion **36** (1994) B229.
[10] GOLDSTON, R., Plasma Phys. Control. Fusion **36** (1994) B213.
[11] TURNBULL, A.D., et al., Phys. Rev. Lett. **74** (1995) 718.
[12] STRAIT, E.J., et al., Phys. Rev. Lett. **75** (1995) 4421.
[13] RICE, B.W., et al., Phys. Plasmas **3** (1996) 1983.
[14] LAO, L.L., et al., Phys. Plasmas **3** (1996) 1951.
[15] LEVINTON, F., et al., Phys. Rev. Lett. **75** (1995) 4417.
[16] KESSEL, C., et al., Phys. Rev. Lett. **74** (1994) 1212; MANICKAM, J., et al., Phys. Plasmas **1** (1994) 1601.
[17] ZARNSTORFF, M., PPPL, personal communication, 1996.
[18] BERNARD, L.C., et al., Comput. Phys. Commun. **24** (1981) 377.
[19] PHILLIPS, M., et al., Nucl. Fusion **28** (1988) 1499.
[20] LAZARUS, E.A., et al., Nucl. Fusion **37** (1997) 7;
LAZARUS, E.A., et al., Phys. Rev. Lett. **77** (1996) 2714.
[21] DEWAR, R.L., PERSSON, M., Phys. Fluids B **5** (1993) 4373.
[22] GLASSER, A.M., et al., Phys. Fluids **19** (1985) 567.
[23] BONDESON, A., et al., Phys. Fluids B **4** (1992) 1889.
[24] GREENE, J.M., CHANCE, M.S., Nucl. Fusion **21** (1981) 453.

[25] LEE, B.J., et al., submitted to Nucl. Fusion.
[26] CHU, M.S., et al., Phys. Rev. Lett. 77 (1996) 2710.
[27] STRAIT, E.J., et al., in Controlled Fusion and Plasma Physics (Proc. 20th Eur. Conf. Lisbon, 1993), Vol. 17C, Part I, European Physical Society, Geneva (1993) 211.

RESISTIVE WALL STABILIZATION BY TOROIDAL ROTATION EFFECTS OF PARTIAL WALL CONFIGURATIONS AND ASPECT RATIO

D.J. WARD
Centre de recherches en physique des plasmas,
Association Euratom-Confédération Suisse,
Ecole polytechnique fédérale de Lausanne,
Lausanne, Switzerland

Abstract

RESISTIVE WALL STABILIZATION BY TOROIDAL ROTATION EFFECTS OF PARTIAL WALL CONFIGURATIONS AND ASPECT RATIO.

Toroidal rotation of the plasma coupled with resistive walls can fully stabilize pressure-driven kink modes and allow the beta value to be extended beyond the Troyon limit. It is well understood that for a rotating resistive wall mode (RWM), the mode is more stable when the wall is moved farther away, as long as the wall is close enough to stabilize the ideal plasma mode. By introducing gaps in the resistive wall — an effect similar to moving the wall away — the RWM can be stabilized at a lower rotation frequency. This effect is greatly enhanced by gaps near the outboard midplane, where the pressure-driven kink couples most strongly to the wall. This improvement in stabilization comes at the cost of requiring a closer wall to stabilize the ideal plasma mode, but this trade-off can be quite desirable: it will be shown that an advanced tokamak equilibrium can be stabilized by a pair of close-fitting plates at a rotation frequency reduced by a factor of 3.6 compared with a fully surrounding wall while maintaining ideal stability. Increasing the number of rational surfaces residing in the plasma is also seen to lower the rotation frequency needed to stabilize the RWM. By lowering the aspect ratio, and thereby increasing the toroidal coupling and the number of rational surfaces inside the plasma, the necessary rotation frequency can be greatly reduced. An optimized low-aspect-ratio equilibrium with 55% beta can be fully stabilized against the $n = 1$ pressure-driven kink with $\omega_r/\omega_A = 0.005$.

I. Introduction

Numerical calculations [1,2] have shown that it is possible to stabilize pressure-driven kink modes, where the value for β (the ratio of the plasma particle pressure to the magnetic field pressure) is above the Troyon limit, in a tokamak plasma surrounded by a resistive wall, given sufficient toroidal rotation. Experimental results [3,4] have confirmed this stabilizing effect.

There are, in fact, two modes which must be stabilized simultaneously [1,2]: (1) the ideal "plasma mode", and (2) the "resistive wall mode" (RWM). The plasma mode is stable when the wall separation is less than the marginal position for stability with an ideally conducting wall. The resistive wall mode is stable for a given (sufficient) rotation when the wall separation is larger than some marginal value. This results in a region of stability, in terms of wall position, for a given rotation speed. Increasing the rotation speed moves the marginal position for stability of the resistive wall mode closer to the plasma, thus widening the stability region. Conversely, by moving the resistive wall farther from the plasma (but remaining always within the marginal ideal wall threshold), the resistive wall mode can be stabilized at a lower rotation speed.

Introducing gaps in the wall has much the same effect as moving the wall farther away, in that it is easier to stabilize the resistive wall mode (i.e., the resistive wall mode can be stabilized at a lower rotation speed). For pressure-driven, external kink modes, the instability couples most strongly to the wall at the outboard midplane. Therefore, toroidally continuous gaps near the outboard midplane can have a very strong effect. This effect moves the region of stability, in terms of wall position, closer to the plasma and reduces it in extent, but allows stabilization to be reached at a lower rotation speed. This effectively makes wall stabilization more accessible.

Toroidal coupling between different poloidal harmonics and between the Alfvén and sound waves complicates the effect of rotation on pressure-driven modes. Rotation modifies the eigenfunction at resonances near the rational surfaces, and calculations indicate [2,4] that additional rational surfaces, particularly those in regions of relatively high pressure, make the stabilization more effective. The effect of lower aspect ratio, which increases toroidal coupling and the number of rational surfaces residing in the plasma, on resistive wall stabilization will be examined in Section III.

II. Partial Wall Configurations

Because of the importance of wall stabilization for advanced tokamak equilibria [5] (that is, equilibria with reverse-shear, high-β, high bootstrap fraction) we will focus on such equilibria in this section. The equilibrium considered here is a reverse-shear equilibrium used in calculations presented in Ref. [2]. This particular equilibrium is identical to that in Fig. 9 of Ref. [2] at $\beta^* = 5.2\%$ (β^* is the rms value of β, i.e., $\beta^* \equiv 2\mu_0\langle p^2\rangle^{1/2}/\langle B^2\rangle$). This equilibrium is very similar to the equilibria described in Ref. [5]. It has $q_0 = 2.5$, $q_{min} \approx 2.2$, $q_S = 4.1$, high β^*, and a bootstrap fraction of nearly unity with the bootstrap current well aligned with the total plasma current. It is stable everywhere to ballooning modes and has good stability properties with respect to various microinstabilities [5], but is unstable to the low-n pressure-driven, external kink. In the absence of a conducting wall, the limit in β^* is 2.49%.

Figure 1 shows the results with a wall separation of $d/a = 1.04$ and with gaps in the wall centered at the *outboard* midplane with half-widths of $\theta_g = 0.2\pi$, $\theta_g = 0.27\pi$, and a slightly larger gap of $\theta_g = 0.3\pi$. as well as for $\theta_g = 0$ (full wall). For $\theta_g = 0.2\pi$, the threshold rotation frequency above which the resistive wall mode is stabilized is $\omega_T/\omega_A \approx 0.103$ — a reduction of 13% from the case with a full wall. For a somewhat larger outboard gap of half-width $\theta_g = 0.27\pi$, the threshold rotation frequency is $\omega_T/\omega_A \approx 0.092$ — a 22% reduction from the case with a full wall.

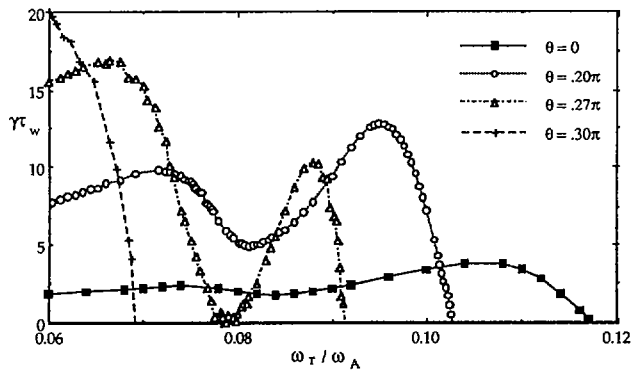

FIG. 1. Stabilization of high-pressure kink with outboard gaps.

Figure 1 shows that the threshold stability value of ω_r for the case with an outboard gap of $\theta_g = 0.3\pi$ is $\omega_r/\omega_A \approx 0.069$. This is a reduction of 41% of the necessary rotation frequency to stabilize compared to the case with a full wall. The necessary wall separation needed to stabilize the ideal plasma mode is $d/a = 1.06$ for the case with an outboard gap of $\theta_g = 0.3\pi$, compared to $d/a = 1.36$ for the full wall. This results in the need to have the wall somewhat closer in order to stabilize the ideal plasma mode when there is such a gap, but there is a significant reduction in the necessary rotation to stabilize the resistive wall mode.

II.A. Wall Stabilization with Discrete Conducting Plates

In the Tokamak Physics Experiment (TPX) design [6] passive stabilization against the axisymmetric, vertical instability and against the ideal external kink is provided by conducting plates on the inboard and outboard sides. In fact, the passive structure is not quite axisymmetric and actually takes the form of a three-dimensional "cage". But it can be approximated as two pairs of axisymmetric plates. A resistive wall on the inboard side has very little effect on the pressure-driven kink mode in high-β equilibria; therefore the inboard plates will be ignored in the following calculations. The calculations use a pair of conformal wall sections on the outboard side with the same poloidal angular extent as the outboard TPX plates (from $|\theta| = 0.18\pi$ to $|\theta| = 0.48\pi$).

The results are shown in Fig. 2. The growth rates are normalized to the same wall time (calculated for a complete resistive wall) as in Fig. 1. Here we see that the growth rates are considerably higher than for the cases in Fig. 1, particularly in the peak just short of the critical rotation frequency for stabilization. But we see that stabilization occurs at a much lower rotation frequency. In fact, the necessary critical frequency for stabilization is reduced by a factor of approximately 3.6 compared to the case with a complete wall with the same plasma–wall separation (with a full wall at $d/a = 1.04$ there is stabilization at $\omega_r/\omega_A \approx 0.12$).

Therefore we see that a large outboard gap, or even limiting the nearby conducting structure to a pair of discrete plates, can have a beneficial effect on the stabilization of the resistive wall mode by lowering the necessary rotation speed by a significant factor. There is, of course, a trade-off in that in order to also stabilize the ideal plasma mode (and both modes *must* be stabilized at the same time), the maximum plasma wall separation is reduced. However, it is well understood that any configuration must be stable with an *ideal* wall. These results show that for a configuration with close-fitting plates, or a wall with a large outboard gap, the necessary rotation speed for stabilization of the resistive wall mode is greatly reduced compared to that which would be necessary with a continuous, completely surrounding resistive wall.

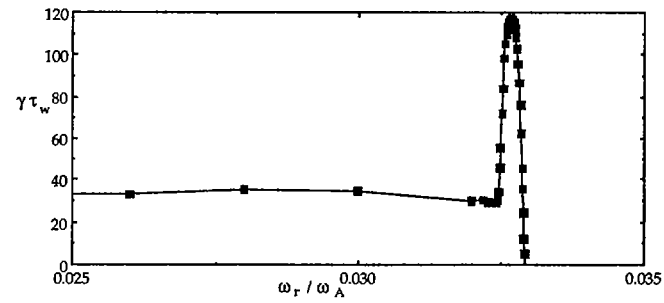

FIG. 2. TPX-like equilibrium with close-fitting, discrete conducting plates.

III. Resistive Wall Stabilization of Low-Aspect-Ratio Tokamaks

The stabilization of resistive wall modes by toroidal rotation requires resonant surfaces inside the plasma [1,2], and toroidicity plays an important role in this stabilizing effect. Previous results [2] have indicated that the presence of a larger number of rational surfaces in the plasma enhances this stabilizing effect. It seems likely, therefore, that resistive wall stabilization may be more effective for low-aspect-ratio equilibria, in which toroidal effects are enhanced, and in which a large number of rational surfaces naturally reside in the plasma.

Table I shows the results of resistive wall calculations for various aspect ratios. The table lists characteristics of the equilibria, such as inverse aspect ratio ε, values of β and β^*, the normalized values of beta (g and g^*), the ratio of the normalized beta for the equilibrium to that for the corresponding equilibrium which is marginally stable to the free-boundary kink mode ($g/g_{\rm lim}$), q at the surface, the growth rate (without rotation) normalized to the wall time (for a wall at $d/a = 1.05$), the ideal wall position for marginal stability, and finally the value of rotation that stabilizes the resistive wall mode (for a wall at $d/a = 1.05$). A scan was made of the aspect ratios $\varepsilon = 0.3$, 0.6, and 0.7; the definition for the profiles was kept the same, and the magnitude of the pressure was varied to make equilibria that are unstable to the pressure-driven kink. The characteristic values for the marginally stable ($g/g_{\rm lim} = 1.00$) equilibria are also shown for those three aspect ratios.

We see that the magnitude of $\gamma\tau_W$ (without rotation) and the value of d/a(ideal) are both good measures of the strength of the instability, and are inversely correlated. As the instability becomes stronger (higher growth rate) it takes a larger rotation speed to stabilize it. Therefore it is quite striking that at the higher values of ε (0.6 and 0.7) the equilibria listed here are very unstable (by a factor of over thirty, in one case, over the $\varepsilon = 0.3$ unstable equilibrium), and yet the necessary rotation speed is quite comparable to that required to stabilize the $\varepsilon = 0.3$ case. A useful measure of how difficult it is to stabilize the RWM is the ratio of the rotation speed needed to stabilize the RWM divided by the passive growth rate with no stabilization. Note that the equilibria in the aspect-ratio scan (with the exception of the last equilibrium) are not optimized in any way, and consequently the equilbria at low aspect ratio are considerably more unstable than for the higher aspect ratio cases.

The final equilibrium listed in Table I ($\varepsilon = 0.714$) is a highly optimized (to give high beta, ballooning stability, and near unity bootstrap fraction) low-aspect-ratio equilibrium developed by R. L. Miller et al. [7]. In this case very high values of beta are achieved ($\beta_X = 55\%$, where $\beta_X \equiv 2\mu_0\langle p\rangle/B_0^2$ — here, B_0 is the magnetic field at the axis, following the convention commonly used for defining beta at low aspect ratio), and yet the passive growth rate is only $\gamma\tau_W = 2.735$, and the equilibrium is completely stabilized (with a wall separation of

Table I: Aspect-ratio scan

ε=1/A	β	β^*	g	g^*	$g/g_{\rm lim}$	q_s	$\gamma\tau_W$	d/a(ideal)	ω_s/ω_A
0.3	5.153	5.848	2.67	3.03	1.00	4.12	0.00	∞	0.00
0.3	6.026	6.841	3.165	3.593	1.185	4.279	1.33	1.44	0.0236
0.6	14.05	15.98	4.17	4.74	1.00	9.05	0.00	∞	0.00
0.6	15.28	17.35	4.638	5.267	1.112	9.493	2.78	1.275	0.0182
0.6	17.26	19.61	5.49	6.237	1.316	10.41	12.44	1.112	0.035
0.7	18.13	20.60	5.285	6.003	1.00	15.99	0.00	∞	0.00
0.7	18.72	21.27	5.557	6.314	1.052	16.67	42.75	1.07	0.0312
0.7	19.78	22.48	6.083	6.915	1.151	18.18	24.17	1.092	0.0144
0.714	40.59	43.59	6.313	6.780	N/A	14.83	2.735	1.26	0.0047

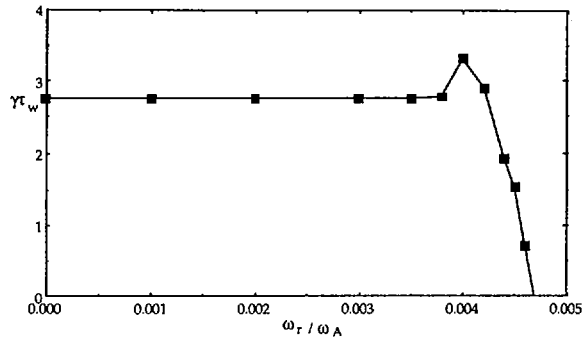

FIG. 3. Optimized low-aspect-ratio equilibrium.

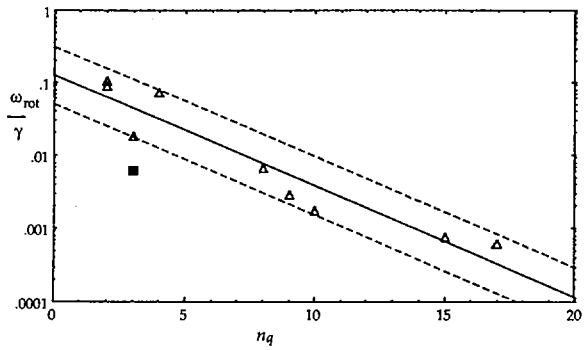

FIG. 4. Ratio of stabilizing ω to passive growth rate versus number of rational surfaces.

$d/a = 1.05$) at a normalized rotation speed of less than 0.005. Figure 3 shows the normalized growth rate for this case with respect to normalized rotation speed. Therefore, we see that this highly optimized, high-β equilibrium is stabilized at quite modest values of rotation speed.

Figure 4 shows the ratio of the rotation speed necessary to stabilize the RWM (normalized to the Alfvén time) divided by the growth rate (normalized to the wall time) at zero rotation. The denominator measures the strength of the instability, and the numerator measures how much rotation is needed for stabilization. This ratio is plotted versus the number of rational surfaces inside the plasma. The points plotted are for 10 different equilibria with varying profiles, shape, aspect ratio, etc. The solid line is a fit to the results (resulting in an exponential, since this is a log–linear plot), and the dotted lines are parallel to and differ by a magnitude of 2.5 higher or lower than the fit. One can see that all 9 triangular points lie within the factor of 2.5 from the line. Only the solid square falls outside the region, and this is a somewhat special case: the PBX-M experimental equilibrium analyzed in Ref. [4]. It is the only equilibrium tested here which has a q=1 surface, and it was seen that the eigenfunction was strongly modified at the q=1 surface, which lies well within the high-pressure region of the equilibrium and was noticeably more affected by the rotation and damping than the other surfaces.

We learn from Fig. 4 that there is a strong reduction in the necessary rotation speed necessary to stabilize a RWM with a given passive growth rate as the number of rational surfaces inside the plasma is increased. Therefore, the stabilizing effect is greatly enhanced by

increasing the number of q surfaces inside the plasma, and thus low-aspect-ratio equilibria benefit, since by their nature they have high q at the edge and many rational surfaces. This agrees qualitatively with the work of Bondeson and Chu [8], which shows that there is a toroidal inertia enhancement with increasing edge-q so that the mode structure is drastically changed (thus enhancing the stabilizing effect of rotation) when the rotation exceeds a crititcal value that is approximately $\omega_r > \omega_A/4q^2$.

The result of enhanced stabilization with increasing number of rational surfaces is general, and if the equilibrium is also optimized to minimize the instability (i.e., the growth rate in the absence of rotation) while maximizing beta and other favorable quantities, such as in the last entry of Table I, the optimized low-aspect-ratio equilibrium of Ref. [7] (the point in Fig. 4 at n_q=10), it can be fully stabilized at a reasonably low rotation speed, as seen in Fig. 3.

Summary

Results have been presented which demonstrate that gaps in the resistive wall, particularly at the outboard midplane, can significantly reduce the necessary rotation speed to stabilize the RWM at the cost of requiring a somewhat closer wall for ideal stability. In particular, it was shown that with a pair of close-fitting conducting plates (which leave a large gap at the outboard midplane) a high-β equilibrium at conventional aspect ratio can be stabilized at a rotation speed reduced by a factor of over 3.5 compared to a fully surrounding, continuous and complete wall at the same separation, while maintaining stability to the ideal plasma mode.

The results also show that low-aspect-ratio equilibria can be stabilized at significantly lower rotation speeds than those for equilibria at conventional aspect ratio. There is a definite reduction in the necessary rotation speed needed to stabilize an instability with a given growth rate as the number of rational surfaces inside the plasma increases. These two effects can perhaps be combined to enhance even further the effect of resistive wall stabilization at low aspect ratio.

Acknowledgments

I would like to thank R. L. Miller and O. Sauter for helpful discussions and for providing the optimized low-aspect-ratio equilibrium used in Section III. This work was supported by the Fonds National Suisse pour la Recherche Scientifique.

REFERENCES

[1] BONDESON, A., WARD, D.J., Phys. Rev. Lett. **72** (1994) 2709.

[2] WARD, D.J., BONDESON, A., Phys. Plasmas **2** (1995) 1570.

[3] STRAIT, E.J., et al., Phys. Rev. Lett. **74** (1995) 2483.

[4] OKABAYASHI, M., et al., Nucl. Fusion **36** (1996) 1167.

[5] KESSEL, C., MANICKAM, J., REWOLDT, G., TANG, W.M., Phys. Rev. Lett. **72** (1994) 1212.

[6] GOLDSTON, R.J., et al., in Controlled Fusion and Plasma Physics (Proc. 20th Eur. Conf. Lisbon, 1993), Vol. 17C, Part I, European Physical Society, Geneva (1993) 319.

[7] MILLER, R.L., et al., Rep. GA-A22321, General Atomics, San Diego (1996).

[8] BONDESON, A., CHU, M.S., Phys. Plasmas **3** (1996) 3013.

OPERATIONAL LIMITS FOR ADVANCED TOKAMAKS

J.W. CONNOR, R.O. DENDY, C.G. GIMBLETT,
R.J. HASTIE, P. HELANDER, T.C. HENDER,
K.G. McCLEMENTS, J.B. TAYLOR, H.R. WILSON
UKAEA Fusion,
UKAEA–Euratom Fusion Association,
Culham, Abingdon, Oxfordshire,
United Kingdom

C.C. HEGNA
University of Wisconsin,
Madison, Wisconsin,
United States of America

Abstract

OPERATIONAL LIMITS FOR ADVANCED TOKAMAKS.

Advanced tokamaks aim to operate at high poloidal β_θ, thus maximising the bootstrap current and reducing the current drive requirements; the goal is an economic, steady state tokamak power plant. High β_θ requires operation at relatively low current, I_p, and the resulting loss of confinement is compensated by operation in an enhanced confinement mode, such as the reverse shear mode. High normalised $\beta_N(\equiv\beta(\%)a(m)B(T)/I_p(MA))$ avoids the need for a high field B, which motivates strong shaping. Here, a number of theoretical advances obtained by using MHD and hybrid kinetic/MHD models with implications for such advanced tokamaks are presented.

1. β-limitations

Ideal MHD sets a limit to the maximum achievable β in a tokamak, which can be expressed in terms of the quantity β_N proposed by Troyon [1]. While collisional, short pulse discharges appear to obey the Troyon limit, there is increasing experimental evidence which suggests that a reduced β limit is experienced in low collisionality, long pulse discharges that may be typical of a tokamak power plant. This clearly has serious implications for advanced tokamaks, which plan to operate at high β_N. In this section we discuss recent advances which have been made in tearing mode and edge MHD stability theory, both of which are plausible candidates to explain the reduced β limit, and consider the implications for advanced tokamaks.

Neoclassical MHD. Recent experimental evidence suggests an increase in low m/n tearing mode activity in low collisionality discharges (m and n are respectively the poloidal and toroidal mode numbers). Reference [2] demonstrated good agreement with theories for the magnetic island drive based on the

self-consistent perturbation of the 'bootstrap' current caused by the flattening of the pressure profile across the island [3]. However, a threshold island size of $\sim$1.5 cm was observed on TFTR, below which no islands were detected; such a threshold is not predicted by the basic theory of these bootstrap driven islands. We report here on a calculation of the island evolution which takes the ion polarisation current into account; in the collisionless regime relevant to TFTR (defined by $\nu_i/\epsilon\omega \ll 1$, where ν_i is the ion collision frequency, ϵ the inverse aspect ratio of the rational surface and ω is the island propagation frequency in the frame where $E_\tau = 0$) this results in a threshold width which is of order the trapped ion banana width [4] and is consistent with the size observed experimentally. A feature of the neoclassical ion polarisation current is that it is larger in a more collisional plasma which satisfies $\epsilon\omega < \nu_i < \epsilon\omega_{bi}$, where ω_{bi} is the bounce frequency of trapped ions. This results in a larger threshold island width and provides an attractive interpretation of the collisionality dependence of the β limit. A semi-phenomenological model for the island evolution which can be derived from the theory and reproduces many of the experimental trends [5] is

$$\frac{\mu_0}{1.22\eta_{nc}}\frac{dW}{dt} = \Delta' + a_1\epsilon^{1/2}\frac{\beta_\theta}{W}\frac{L_q}{L_p} - a_2 g(\epsilon, \nu_i)\left(\frac{\rho_{\theta i}}{W}\right)^2\left(\frac{L_q}{L_p}\right)^2\frac{\beta_\theta}{W} \qquad (1)$$

where $g(\epsilon, \nu_i) = \epsilon^{3/2}$ if $\nu_i/\epsilon\omega_{*pe} < C$, and 1 otherwise. The first term on the RHS of eq.(1) is the standard Rutherford current profile term, the second is the bootstrap current drive and the third is due to the ion polarisation current. All parameters are local: η_{nc} is the neoclassical resistivity, L_p and L_q scale lengths associated with the pressure and safety factor profiles, $\rho_{\theta i}$ the ion poloidal Larmor radius, W the island width and ω_{*pe} the electron diamagnetic frequency based on L_p. Choosing $a_1 = a_2 = 7$ (for $L_p \sim L_q$) and $C = 0.3$ gives good agreement with experiment [5] and is consistent with theoretical predictions; these choices will be used below.

Assuming $\Delta' < 0$, eq.(1) predicts that the evolution of large islands with $W > W_{\rm sat}$, where $W_{\rm sat}$ is given by a balance between the bootstrap drive and the Δ' damping, is dominated by the Rutherford term and these will decay. For smaller islands $W < W_{\rm sat}$ the bootstrap term becomes important and the island will grow provided $W > W_{\rm crit}$ ($W_{\rm crit}$ is given by a balance of the bootstrap and polarisation current terms). For $W < W_{\rm crit}$ the ion polarisation current is important and results in island decay. So, provided a 'seed' island of width $W > W_{\rm crit}$ can be produced (from any ambient MHD activity) it will be amplified to the large saturated width $W_{\rm sat}$. Equilibria with large $W_{\rm crit}$ are therefore likely to be stable to neoclassical tearing modes; comparisons with ASDEX Upgrade and DIII-D indicate that these machines are stable for $W_{\rm crit} \gtrsim 2$cm [5].

To assess the role of neoclassical tearing modes in advanced tokamaks we calculate a series of discharges with decreasing plasma current corresponding to conventional (ITER-like) tokamaks at high current and advanced (high β_θ) tokamaks at low current. The current profile is assumed to be given by the

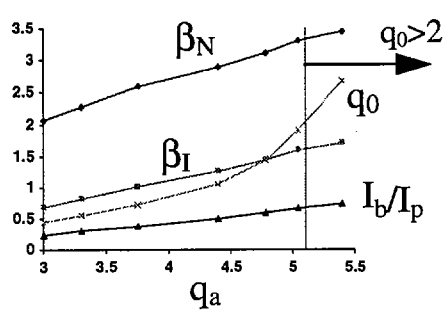

Fig.1(a)

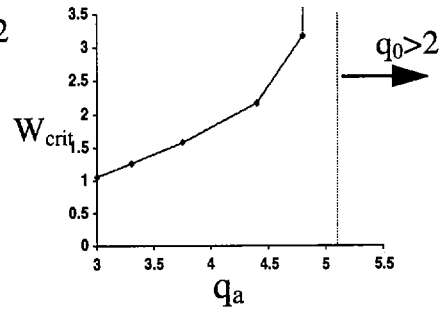

Fig.1(b)

Equilibrium and stability features of a sequence of ITER – like equilibria

sum of Ohmic, bootstrap, diamagnetic and Pfirsch-Schlüter currents which are calculated self-consistently with the equilibria. We assume the same stored thermal energy $W_{\rm th}$ can be achieved at each current, and hold the magnetic field constant; thus β_N rises with edge q_a in the manner shown in Fig. 1(a). For ITER–like parameters ($W_{\rm th}$ = 1.1GJ, B = 5.7T, R = 8.14m, I_p = 21MA, $T_e(0) = T_i(0)$ = 21keV) $q_a = 3$, $\beta_\theta = 0.68$ and the bootstrap current fraction is relatively low ($I_b/I_p = 0.24$); this results in a peaked current profile, with $q_0 < 1$. As the current is reduced β_θ increases and there is a corresponding increase in the bootstrap current fraction. q_0 increases with q_a until $I_b/I_p \gtrsim 50\%$, when the bootstrap current begins to broaden the current profile and results in a more rapid rise in q_0 with q_a; for $q_a \gtrsim 5.5$ the q–profile becomes non-monotonic for $W_{\rm th}$ = 1.1GJ.

We now consider the properties of the most dangerous $m/n = 2/1$ tearing mode. Figure 1(b) shows that $W_{\rm crit}$ increases with q_a, demonstrating increased stability to tearing modes in advanced tokamaks. In calculating the threshold, eq.(1) was solved for the series of equilibria calculated for Fig 1(a). The increase in $W_{\rm crit}$ arises because the $q = 2$ surface moves towards the plasma centre, where $\rho_{\theta i}$ becomes large; at sufficiently high $q_a \gtrsim 5.1$ this surface moves out of the plasma and there is no $m/n = 2/1$ mode. We have taken L_q/L_p to be independent of q_a; for flat pressure profiles this ratio may decrease as q_a increases (ie as the $q = 2$ surface moves towards the plasma centre) though the trend that $W_{\rm crit}$ increases with q_a remains.

It is interesting to note that one proposed method of achieving the high confinement necessary for advanced tokamak operation is to operate in the reverse shear mode, where the magnetic shear s is negative over a region around the magnetic axis. The bootstrap current term is actually stabilising there, and no neoclassical tearing modes are predicted in the negative shear region. Further, the outer region of the plasma, where the shear is positive, will be more collisional so that $W_{\rm crit}$ may be larger as a consequence of its dependence on $g(\epsilon, \nu_i)$.

Edge MHD. Edge MHD events can also limit the effective β limit, either because of the substantial deterioration in confinement caused by ELMs, or through the so-called 'outer mode' which has a dramatic effect in reducing the performance of JET discharges [6]. Understanding the mechanism for localised edge MHD events has been hampered by the lack of a rigorous formalism for calculating the stability of high-n localised ballooning modes toroidally coupled to the current-driven external kink (peeling) modes. This becomes computationally difficult with global MHD codes, and the ballooning mode formalism is not valid at the plasma edge where the local growth rate, $\gamma(r)$, does not exhibit a maximum γ_{max}. We find that high-n ballooning modes at the edge of a limited plasma *can* be approximated by conventional ballooning theory when the coupling to peeling instabilities can be neglected. The difference between an edge ballooning mode (where $\gamma(r)$ is essentially linear in r) and a conventional ballooning mode (localised around the position of γ_{max} if it exists) is in the radial structure: the conventional mode couples $\sim n^{1/2}$ rational surfaces with a Gaussian envelope, while the edge mode couples $\sim n^{1/3}$ surfaces and has an envelope related to the Airy function.

Thus the ballooning stability criterion provides a necessary condition; when the role of the peeling mode is considered, instability can occur below the threshold for ballooning instability [7]. Stability to the peeling mode depends on a balance between the Mercier index, D_M (stabilising), and edge current density (destabilising) [8], so that by exploiting the effect of plasma shaping on D_M it may be possible to stabilise the peeling mode in advanced tokamaks. In particular, using the large aspect ratio expression for D_M [9] together with a quadratic q–profile, $q = 1 + 4(r/a)^2$, we find at the plasma edge

$$D_M = (\alpha\epsilon/s^2)[0.96 + 1.7(\beta_\theta - 2.1)(E_a/a) + 15.8E_aT_a(R_0/a^3)] \qquad (2)$$

where $\alpha = -(2\mu_0 R_0 q^2 p')/B_0^2, E_a/a = (\kappa - 1)/(\kappa + 1)$ is the ellipticity of the magnetic surfaces (κ is the elongation) and T_a the triangularity. Thus, triangularity is highly stabilising when combined with ellipticity, while the role of pure ellipticity depends on β_θ but is typically destabilising. Note that advanced tokamaks have higher β_θ which enhances the beneficial effects of shaping. Thus, the peeling mode may be less important in advanced tokamaks, and the stability of the plasma edge to localised modes is expected to be determined by the local ballooning stability criterion.

2. Global MHD stability of reverse shear profiles

Tokamak current density profiles with a minimum at the magnetic axis produce non-monotonic $q(r)$ profiles, with a region of negative magnetic shear inside the surface where $q = q_{min}$ is a minimum. Theory suggests and experiment confirms [10] that plasma stability is locally improved within this region. We consider global MHD stability of reverse shear equilibria in which q_{min} lies just below a rational value, m/n, so that a mode has two close rational surfaces at r_1, r_2. In a

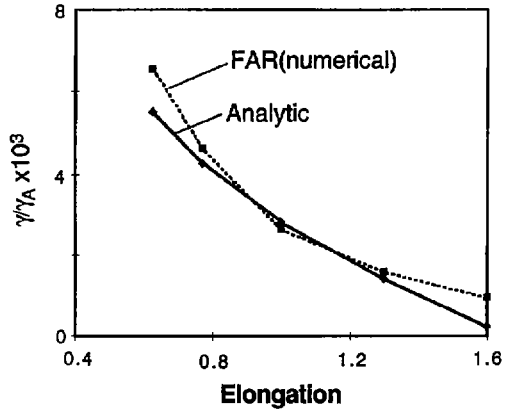

Fig.2

Dependence of growth rates on ellipticity : FAR and analytic results

cylindrical model it has been demonstrated [11] that such an equilibrium is ideal MHD unstable as $\Delta \equiv (1 - nq_{min}/m) \rightarrow 0$. Negative dp/dr and unfavourable curvature are responsible for the instability. We have addressed this stability problem in toroidal geometry employing a large aspect ratio, $\beta < \epsilon$, tokamak expansion. We find four ingredients in the potential energy δW available to drive instability:

$$\delta W \propto (8/15)(m^2 - 1)\Delta^2 + \epsilon\alpha(1 - q_{min}^{-2}) - \Lambda\alpha^2\Delta^{1/2} + \alpha^2 E' \qquad (3)$$

Here Λ is a number which encapsulates information regarding the poloidal sideband harmonics ($m \pm 1$) which play a crucial role in the stability calculation. In eq.(3) the first term is due to field line bending, the second to the favourable average curvature in a torus, the third represents the effect of ballooning which arises because of the sideband coupling, while the last term is a shaping modification to the field line bending. Ellipticity is also responsible for coupling to ($m \pm 2$) harmonics, but this effect is weaker. From δW we obtain a most unfavourable value of $\Delta = [15\alpha^2\Lambda/32(m^2 - 1)]^{2/3}$, and a marginal value of $\beta \propto \epsilon^{8/5}$, validating the use of the low β expansion. Comparison of the analytic growth rates with values obtained from the FAR toroidal stability code at small $\epsilon \sim 10^{-2}$ shows good agreement. The dependence of growth rates on ellipticity from FAR and the analytic results are shown in Fig. 2.

We see that vertical elongation is stabilising (in contrast to its effect on Mercier modes). We conclude that avoidance of equilibria with small positive values of Δ is important if reverse shear equilibria are to remain stable to the 'double-kink' mode at high β. Taking a specific equilibrium with $q = q_0\left\{(1 + 31.4\rho^8)^{1/4} - 3.2\rho^2 \exp\left[-15(\rho - 1/4)^2\right]\right\}$ and pressure profile $p(r) = p_0(1 - \rho^2)^{4.5}$, where $\rho = r/a$, the critical β_N values for the most unfavourable values of Δ are (circular case): $\beta_N = 3.86(a/R_0)^{3/5} = 2.0$ (at $R_0/a = 3$) for $m/n = 2/1$; and $\beta_N = 5.23(a/R_0)^{3/5} = 2.7$ (at $R_0/a = 3$) for $m/n = 3/2$.

3. The double kink mode and fast particles

The stability of double kink modes is influenced by the presence of fast ions. Indeed, fast ions play a similar role as in the internal kink mode in conventional equilibria with $q_0 < 1$. A suitable expression for the kinetic part of the work done on a population of energetic particles by a displacement $\vec{\xi}$ is [12]

$$\delta W_{\rm k} = -\frac{2\pi^2}{ZeM^2}\sum_{\sigma}\int dp_\varphi \int d\mathcal{E}\int d\mu\, \tau_b \frac{\partial f}{\partial \mathcal{E}}$$

$$\times \sum_{p=-\infty}^{\infty} \frac{\omega - n\omega_*}{\omega - p\omega_b + n\langle\dot{\varphi}\rangle}\left|\left\langle\left(\frac{v_\perp^2}{2}+v_\parallel^2\right)\vec{\xi}_\perp\cdot\vec{\kappa}\, e^{i(\omega - p\omega_b + n\langle\dot{\varphi}\rangle)t}\right\rangle\right|^2 \qquad (4)$$

where $f(\mathcal{E},\mu,p_\varphi)$ is the unperturbed distribution function, $\mathcal{E} = Mv^2/2$, $\mu = Mv_\perp^2/2B$, $p_\varphi = MR_0v_\varphi - Ze\psi$, $\sigma = v_\parallel/|v_\parallel|$, $\omega_* = (\partial f/\partial p_\varphi)/(\partial f/\partial\mathcal{E})$, $\langle\cdots\rangle$ the orbit average, $\vec{\kappa}$ the magnetic field curvature, and $\tau_b = 2\pi/\omega_b$ the bounce time.

If the mode frequency is small, $\omega \ll \langle\dot{\varphi}\rangle$, the trapped ions make the dominant contribution to $\delta W_{\rm k}$. In the limit when the banana width Δ_b is small in comparison with the mode width $\Delta_m = r_2 - r_1$, the integral (4) becomes

$$\delta W_{\rm k} = -2^{3/2}\pi R_0^{-1/2}\int_0^a \xi_{0r}^2 p_\alpha' r^{3/2} dr$$

for an isotropic fast-ion distribution with pressure p_α. When written in this form, $\delta W_{\rm k}$ is identical to the fast-ion response to the internal kink mode. In the opposite limit, $\Delta_m \ll \Delta_b \ll r$, δW_k becomes

$$\delta W_{\rm k} = -32.6\,\epsilon ZeB_\theta R_0 X^2 \ln\vartheta \int_0^\infty \frac{\partial f}{\partial r} v^3 dv$$

where $X = \int_0^a \xi_{0r} dr$, $\vartheta^2 \sim \Delta_b/\max(\rho,\Delta_m) \gg 1$, and B_θ is the poloidal field strength. In this case, the dominant contribution to $\delta W_{\rm k}$ comes from trapped particles whose orbits intersect the mode at the outer midplane. In both cases the fast-ion action is stabilizing, and a phenomenon analogous to sawtooth stabilisation thus appears possible for double kink modes. For a slowing-down distribution $f \sim v^{-3}$, the ratio between the two limits is

$$\frac{\delta W_{\rm k}(\Delta_b \ll \Delta_m)}{\delta W_{\rm k}(\Delta_m \ll \Delta_b)} \sim \frac{\Delta_b}{\Delta_m \ln\vartheta}$$

When the mode frequency is finite, the fast-ion response is, again, similar to that in the case of internal kinks. In particular, the same precessional drift resonance is present in (4), and a fishbone-type instability [13] is possible.

4. Sawtooth and tearing mode suppression

The presence of sawteeth degrades core confinement and provides a 'seed' for neoclassical tearing modes, so it may be necessary to suppress them in Advanced Tokamaks and ITER. In JET they have been temporarily stabilised by ICRF heating, but reappear before the ICRH is switched off [14]. This correlates with a change in sign of the total potential energy δW of the ideal $m = 1$ internal kink. The calculation of δW [15] uses a model for the heated minority ions that is consistent with Fokker-Planck calculations and incorporates new JET measurements [16] obtained with a neutral particle analyser; it also includes

the minority ion contribution to the Shafranov shift and the effects of shaping, as well as kinetic stabilising effects. Calculation of δW for isotropic α-particle populations shows that the combined kinetic and Shafranov effects give a net stabilising contribution when $q_0 = 0.9$, but not when $q_0 = 0.75$ for typical profiles. Furthermore, toroidal coupling of $m = 1$ and $m = 2$ modes changes the $m/n = 2/1$ tearing mode parameter Δ'; hence α-particle effects on the $m = 1$ mode can affect the 2/1 tearing mode stability. Stabilisation of the $m = 1$ mode also removes the source of the 'seed island' required for neoclassical tearing mode growth, and may increase the β-limit in low collisionality tokamaks.

Acknowledgments

This work was funded jointly by the U.K. Department of Trade and Industry and Euratom.

REFERENCES

[1] TROYON, F., et al., Plasma Phys. Control. Fusion **26** (1984) 209.
[2] CHANG, Z., et al., Phys. Rev. Lett. **74** (1995) 4663.
[3] CARRERA, R., et al., Phys. Fluids **29** (1986) 899; QU, W.X., CALLEN, J.D., Rep. UWPR 85-5, Wisconsin Univ., Madison, WI (1985).
[4] WILSON, H.R., et al., Phys. Plasmas **3** (1996) 248.
[5] WILSON, H.R., et al., Rep. UKAEA-FUS 336, to appear in Plasma Phys. Control. Fusion.
[6] JONES, T., et al., Plasma Phys. Control. Fusion **37** (1995) A359.
[7] HEGNA, C.C., et al., Phys. Plasmas **3** (1996) 584.
[8] WESSON, J.A., Nucl. Fusion **18** (1978) 87.
[9] LÜTJENS, H., et al., Nucl. Fusion **32** (1992) 1625.
[10] LEVINTON, F.M., et al., Phys. Rev. Lett. **75** (1995) 4417; LA HAYE, R.J., et al., Phys. Rev. Lett. **75** (1995) 4421.
[11] FURTH, H.P., RUTHERFORD, P.H., SELBERG, H., Phys. Fluids **16** (1973) 1054.
[12] PORCELLI, F., et al., Phys. Plasmas **1** (1994) 470.
[13] CHEN, L., WHITE, R.B., ROSENBLUTH, M.N., Phys. Rev. Lett. **52** (1984) 1122.
[14] CAMPBELL, D.J., et al., Phys. Rev. Lett. **60** (1988) 2148.
[15] McCLEMENTS, K.G., DENDY, R.O., HASTIE, R.J., MARTIN, T.J., Phys. Plasmas **3** (1996) 2994.
[16] KOROTKOV, A.A., GONDALEKAR, A., in Controlled Fusion and Plasma Physics (Proc. 21st Eur. Conf. Montpellier, 1994), Vol. 18B, Part I, European Physical Society, Geneva (1994) 266.

KINETIC ALFVÉN EIGENMODES IN A HOT TOKAMAK PLASMA

A. JAUN[1], K. APPERT[2], A. FASOLI[2,3], T. HELLSTEN[1], J. LISTER[2], J. VACLAVIK[2], L. VILLARD[2]

[1] Alfvén Laboratory,
Royal Institute of Technology,
Stockholm, Sweden

[2] Centre de recherches en physique des plasmas,
Ecole polytechnique fédérale de Lausanne,
Lausanne, Switzerland

[3] JET Joint Undertaking,
Abingdon, Oxfordshire, United Kingdom

Abstract

KINETIC ALFVÉN EIGENMODES IN A HOT TOKAMAK PLASMA.

Global Alfvén eigenmodes are studied using fluid and kinetic plasma models to determine how the finite Larmor excursions of the bulk species and the resonant Landau interactions modify the spectrum in the toroidicity Alfvén eigenmode (TAE) range of frequencies. A new kinetic Alfvén mode conversion mechanism is described taking place away from the resonances through toroidal coupling, when the spatial scales of the fast and the kinetic Alfvén waves become comparable. If the Landau damping of the mode converted wave is sufficiently small, groups of kinetic Alfvén eigenmodes (KAE) appear inside and above the fluid gap; those induced in the neighborhood of a global fluid mode have a broad radial extension that could lead to substantial α-particle losses. Using an experimental equilibrium, the theoretical Alfvén spectrum is directly compared with saddle-coil antenna measurements from the JET tokamak, showing that the multiple peaks observed on the response are KAE induced in the neighborhood of an elongation induced Alfvén eigenmode.

1 Introduction

Resonant destabilization of Alfvén waves by fusion produced $\alpha-$particles is an important issue for thermonuclear reactors [1]. It may occur for phase velocities lower than the birth velocity of the particles, when the drive from the pressure gradients in configuration space exceeds the damping from resonant interactions in velocity space. Saturation is expected to generate substantial transport [2], particularly when unstable modes have a broad radial extension and reach the plasma core where the $\alpha-$particle density is large.

In this paper, groups of global and weakly damped kinetic Alfvén eigenmodes (KAE) are described, which appear inside and above fluid gaps when the spatial scale of the global wavefield meets the kinetic Alfvén wavelength. Such mode conversion induced spectra with groups of weakly damped modes have recently been observed in JET [3].

2 Models

To determine the kinetic effects in the entire TAE spectrum, the toroidal wave equations have to be solved non-perturbatively using a model that takes into account the dispersion and the damping of the fast magnetosonic and the kinetic Alfvén wave. Here, the equations are solved with the toroidal PENN code [4] featuring a fluid-resistive [5] and a kinetic-FLR [6] plasma model.

The fluid approximation is valid at low temperatures, for the modeling of fast and shear Alfvén waves, with a power absorption occurring through resistive dissipation.

The kinetic model is appropriate for higher temperatures, when the dispersion from the finite Larmor radius (FLR) excursions of the particles in an inhomogeneous plasma and the resonant interactions such as Landau damping become important. To avoid solving an integral equation to evaluate the wave-particle resonance $\omega - k_{||} v_{||} = 0$, only passing particles have been retained and a functional dependence $k_{||} = n/R$ has been assumed, keeping the exact operator $k_{||} = -iB^{-1}\vec{B} \cdot \nabla$ only in the Maxwell equations. In this form, the kinetic model properly describes the fast, the kinetic Alfvén wave (KAW), and to some extent also the ion-acoustic and the drift waves [7].

3 Fluid plasma - TAE mode

A simple force-free toroidal equilibrium (major radius $R_0 = 2.7$ m, magnetic field $B_0 = 2$ T, aspect ratio $R_0/a = 4$) of circular cross-section and relatively flat safety factor profile ($q_0 = 1.10$, $q_a = 1.97$) is obtained numerically [8]. For a constant density ($n_e = n_D = 2.2 \times 10^{19}\mathrm{m}^{-3}$), a toroidicity gap appears at a normalized radius $s = \sqrt{\psi/\psi_a} = 0.75$ with a toroidal mode number $n = 1$ and coupled poloidal harmonics $m = -1, -2$. To excite bulk modes which may be driven by fast particles, an oscillating helical source current (ω, $n = 1$, $m = -1$) is distributed around the gap, coupling energy into the fixed boundary plasma. The global response is defined in terms of the absorbed power P, the stored energy W, and the ratio $P/(\omega W)$ measures the damping.

With the fluid model, the gap $\omega_N \in [0.44; 0.74]$ and a TAE mode [9] $\omega_N = 0.517$ appear on the response $P(\omega_N)$ as illustrated in fig.1a, where $\omega_N = \omega R_0/c_A$ stands for the frequency normalized to the major radius and the Alfvén velocity at the magnetic axis. For realistic values of the resistivity, the damping inside the gap is very low, much lower than observed in experiments [3],[10]. An unphysically high resistivity has been used in fig.1.

The TAE mode wavefield illustrated in fig.1d has a global character independent of the resistivity and the current excitation. It reflects the coupling between the poloidal Fourier harmonics $m = -1, -2$ which is strongest in the gap region around $s = 0.75$.

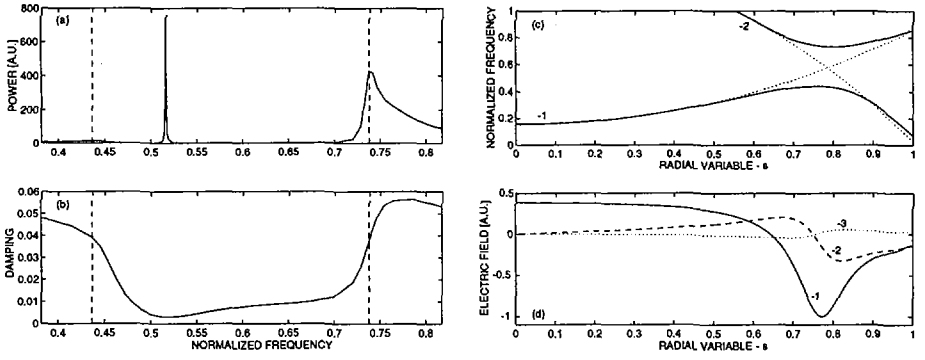

FIG. 1. On the left, the response (a) and the damping (b) using the fluid plasma model with an unphysically high resistivity. On the right, a sketch of the Alfvén gap structure (c) based on a cylindrical model (dotted lines), and the Fourier components of the radial electric field $\Re e(E_n)$ for the TAE mode at $\omega_N = 0.517$ (d).

Because of their global extension and extremely weak resistive damping, such TAE gap modes have been identified as a serious threat for tokamak reactors such as ITER. Fluid models are however not sufficient to describe thermonuclear plasmas, in which FLR effects and Landau damping are both expected to be important.

4 Kinetic plasma - groups of kinetic Alfvén eigenmodes (KAE)

To study how the spectrum is modified when kinetic effects are included, the same equilibrium is used as in the previous section, varying the species temperatures with profiles of the form $T_\alpha(s) = T_{\alpha,0}(1 - 0.8s^2)^2$.

Raising the deuterium temperature and keeping that of the electrons fixed at $T_{e,0} = 3$ keV, fig.2 shows how standing KAW create groups of kinetic modes in the neighborhood of the fluid TAE and the lower/upper frequency ends of the gap.

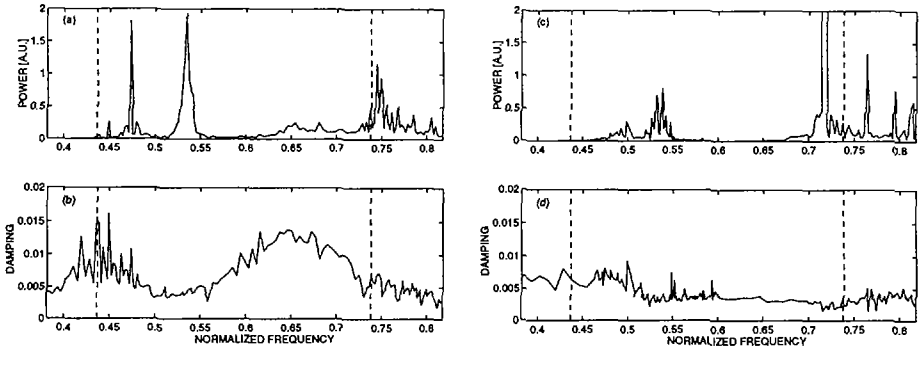

FIG. 2. Response (top) and damping (bottom) using the kinetic plasma model with a low $T_{D,0}$ = 1 keV (left) and a higher bulk ion temperature $T_{D,0}$ = 3 keV (right).

Just above the lower gap edge, the toroidal coupling to the fluid $m = -1$ continuum induces a group of KAE near $\omega_N \simeq 0.5$ as radial standing waves are formed between the gap position and the plasma axis (fig.3a). The enhanced electric field component parallel to the magnetic field $E_{||}$ associated with this mode conversion gives rise to an electron Landau damping decreasing from about 0.7% at the former continuum edge to 0.4% inside the gap (fig.3d). This Landau damping has the same physical origin as the one which has been modeled as "radiative damping" in ref.[13]. The TAE peak at $\omega_N \simeq 0.53$ consists of several overlapping KAE modes that split apart when the FLR effects become important and the damping rate $P/(\omega W) \simeq (\delta\omega/\omega)^{FWHM} \simeq 0.004$ is sufficiently low. They have global $m = -1, -2$ wavefield components with characteristic KAW oscillations around the gap position (fig.3b). Since the mode conversion takes place here purely inside the fluid gap, it has to be of different nature than the process occurring at resonant surfaces [11] where the wavelength of the fast and the KAW gets comparable as $k^{fast} \to \infty$ and $k^{KAW} \to 0$. It is the toroidal coupling which induces here the mode conversion as the spatial scale of the gap mode is similar to the KAW wavelength $k^{fast} \simeq k^{KAW}$. This new KAW mode conversion mechanism forms standing waves between such toroidal mode conversion regions, generating a group of KAE in the neighborhood of the fluid TAE. At the upper frequency end of the gap, a group of KAE appears through toroidal coupling with the fluid $m = -2$ continuum above the gap, with strong KAW oscillations between the gap position and the edge of the plasma. In fig.3c, they appear around $\omega_N = 0.72$ and almost overlap with the series of modes at $\omega_N = 0.773, 0.793, 0.812$ formed by mode conversion at the $m = -1, -2$ resonances in the former fluid continuum above the TAE gap (fig.3d) [12].

If the eigenmode damping exceeds the frequency spacing between consecutive KAE modes, each KAE group will appear on the response as a single broad peak with a full width at half maximum (FWHM) that may not anymore be related to the physical damping. This occurs here as well around $\omega_N = 0.53$ in fig.2a as when $T_{e,0} = 2T_{D,0} = 6$ keV, showing that high temperatures do not necessarily create multiple response peaks.

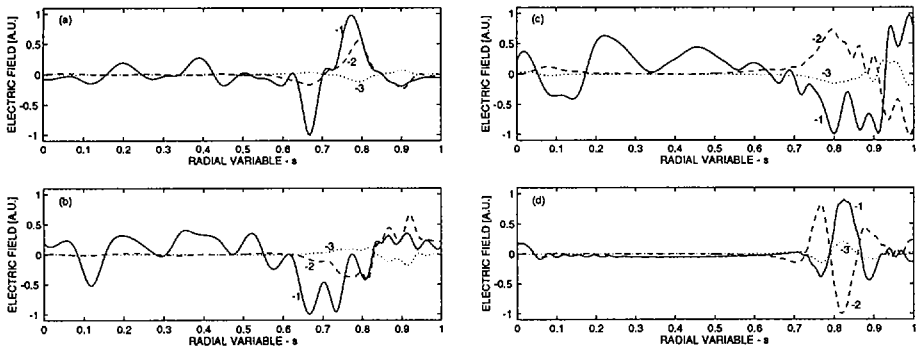

FIG. 3. Fourier components of the radial electric field $\Re e(E_n)$ for different sorts of KAE modes around $\omega_N^a = 0.499$, $\omega_N^b = 0.538$, $\omega_N^c = 0.716$ and $\omega_N^d = 0.793$ using the kinetic plasma model at $T_{e,0} = T_{D,0} = 3$ keV.

5 Comparison with experiments

In antenna driven experiments [3],[10], the response is determined by the coupling; global modes with a broad radial extension out to the plasma edge will dominate in amplitude over modes localized in the core.

Using an experimental equilibrium for the JET discharge #33157 at 19 s, the linear plasma response is modeled using the fluid LION [14] and the kinetic PENN codes for a bottom saddle coil excitation $n = 2$ similar to the experiment. Fig.4a shows that two groups of peaks appear around 200 and 250 kHz. The first is associated with a perturbation dominant in the TAE gap ($s < 0.8$), with a global kinetic wavefield at 205.5 kHz similar to the fluid counterpart and at 209.6 kHz a weakly coupled core-localized KAE in the upper $m = -2, -3$ continuum well. The second group has stronger wavefields in the elongation gap ($s > 0.8$), and characteristic standing KAWs formed between the toroidal mode conversion region $s \in [0.2; 0.4]$ and the plasma axis: they are responsible for the fine structure in the response, which can therefore be identified as a group of weakly damped KAE modes $P/(\omega W) \simeq 0.001$. Note that the same damping is obtained independently from $(\delta\omega/\omega)^{FWHM}$; together with the agreement between the power emitted by the antenna and the total plasma absorption, this is a good self-consistency check of the numerical solution.

The comparison with the response in fig.2 of ref.[3] shows that the first group of modes is in the experiment strongly damped, but that reasonable agreement is achieved for the second, with a theoretical electron Landau damping in the same range. An analysis of the sensitivity of the theoretical prediction to the uncertainties in the equilibrium reconstruction shows that the damping of the first group is dramatically affected by small changes in the gap structure, while the second is much more robust with KAE spacings in frequency that change according to the resonator length where standing KAWs are

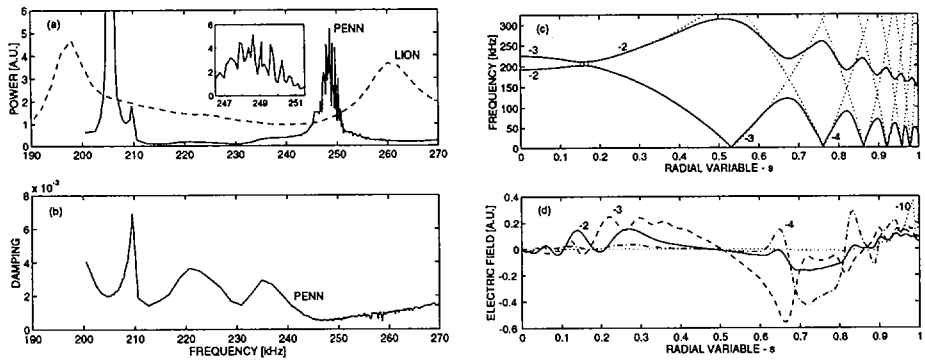

FIG. 4. Response (a) and damping (b) obtained using the fluid LION and kinetic PENN codes, sketch of the Alfvén gap structure (c) and the Fourier components of the radial electric field $\Re e(E_n)$ for the KAE mode at 249.75 kHz (d). The parameters of the reconstructed JET experiment #33157 at 19 s are $I_p \cong 3$ MA, $B_0 = 3.37$ T, $q_0 = 1.23$, $q_a = 4.78$, $n_e = n_D = 3 \times 10^{19}(1 - 0.9s^2)^{0.5}$ m^{-3}, $T_e = 2T_D = 6(1 - 0.995s^2)^{0.7}$ keV.

formed. This makes the experimental observation of multiple peaks in the Alfvén spectrum compatible with the theoretical prediction of series of KAE modes induced in the neighborhood of global Alfvén modes, but cannot account for the series of peaks extending over a factor two in frequency (Pulse No 33272 15.5s in fig.3 of ref.[3]).

ACKNOWLEDGEMENTS

One of the authors (A.J.) would like to thank S. Sharapov and D. Borba for discussions. This work was supported in part by the Swedish and the Swiss National Science Foundations and by the supercomputer centers in Lausanne and Linköping.

REFERENCES

[1] FU, G.Y., VAN DAM, J.W., Phys. Fluids B **1** (1989) 1949.
[2] BREIZMAN, B.N., BERK, H.L., YE, H., Phys. Fluids B **5** (1993) 3217.
[3] FASOLI, A., et al., Phys. Rev. Lett. **76** (1996) 1067.
[4] JAUN, A., APPERT, K., VACLAVIK, J., VILLARD, L., Comput. Phys. Commun. **92** (1995) 153.
[5] VACLAVIK, J., APPERT, K., Nucl. Fusion **31** (1991) 1945;
JAUN, A., PhD Thesis, Rep. LRP-513/95, Centre de recherches en physique des plasmas, Lausanne (1995).
[6] BRUNNER, S., VACLAVIK, J., Phys. Fluids B **5** (1993) 1695.
[7] HEIDBRINK, W.W., JAUN, A., HOLTIES, H., CAROLIPIO, E., VILLARD, L., Nucl. Fusion (in press).
[8] LÜTJENS, H., BONDESON, A., ROY, A., Comput. Phys. Commun. **69** (1992) 287.
[9] CHENG, C.Z., CHANCE, M.S., Phys. Fluids **29** (1986) 3695.
[10] FASOLI, A., et al., Phys. Rev. Lett. **75** (1995) 645.
[11] HASEGAWA, A., CHEN, L., Phys. Rev. Lett. **35** (1975) 370.
[12] METT, R.R., MAHAJAN, S.M., Phys. Fluids B **4** (1992) 2885.
[13] FU, G.Y., CHENG, C.Z., WONG, K.L., Phys. Fluids B **5** (1993) 4040.
[14] VILLARD, L., APPERT, K., GRUBER, R., VACLAVIK, J., Comput. Phys. Rep. **4** (1986) 137.

RESONANT EXCITATION OF ALFVÉN MODES BY ENERGETIC PARTICLES IN TOKAMAKS

S. BRIGUGLIO, L. CHEN[1], F. ROMANELLI, R.A. SANTORO[1],
G. VLAD, F. ZONCA
Associazione Euratom-ENEA sulla Fusione,
Centro Ricerche Frascati,
Frascati, Rome,
Italy

Abstract

RESONANT EXCITATION OF ALFVÉN MODES BY ENERGETIC PARTICLES IN TOKAMAKS.

The stability properties of both high ($\omega \approx \omega_A$) and low ($\omega \approx \omega_{*pi} \approx \omega_{ti}$) frequency Alfvén modes are discussed, and it is shown that a transition between the two branches occurs as either the core plasma or the energetic particle pressure is increased. Results from nonlinear numerical simulations indicate that, above the excitation threshold for the Energetic Particle Modes (EPM), a strong redistribution in the energetic particle source can take place, possibly leading to large particle losses.

1. Existence of tokamak operation regimes free of Toroidal Alfvén Modes

It has been demonstrated [1] that the most dangerous Alfvén modes which can seriously affect the confinement properties of fusion alpha particles are *ideal* instabilities, in the sense that their dynamics can be modeled as those of a *core* plasma component, described via ideal MHD, in which *energetic particles* (E) - that need a fully kinetic description - provide the free energy source to drive the instabilities.

Kinetic Toroidal Alfvén Eigenmodes (KTAE) are usually stable or moderately unstable, since they merge into the ideal Energetic Particle Mode (EPM) branch when they are strongly driven [1]. The EPM branch, however, has an instability threshold in the energetic particle density, n_E.

It has been also demonstrated that, under certain plasma conditions, the ideal Toroidal Alfvén Eigenmodes (TAE) can be shifted downward in frequency and out of the toroidal frequency gap in the Alfvén continuum. For high toroidal mode numbers (n) and for an (s, α) model equilibrium (s being the magnetic shear and $\alpha = -q^2 R\beta'$), this has been shown to occur for $\alpha_{core} > \alpha_c(s)$ [2–4], i.e., above a critical threshold in the core plasma pressure gradient. In the case of realistic ITER-relevant plasma equilibria, the local threshold $\alpha_c(s)$ of the (s, α) model corresponds to a threshold, β_{oc}, in the core plasma β on axis. The

[1] Department of Physics and Astronomy, University of California, Irvine, California, USA.

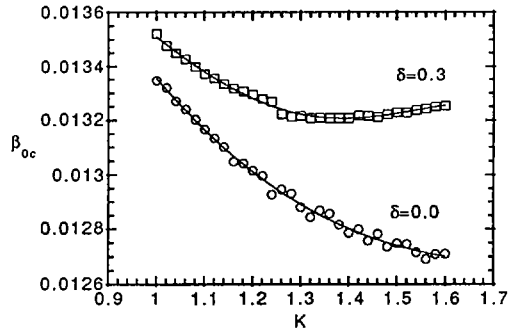

FIG. 1. Value of β_{oc} above which the TAE mode is shifted into the lower continuum versus plasma elongation K, at different values of plasma triangularity, δ = 0.0 (○), 0.3 (□).

existence of such a threshold has a practical relevance, since it demonstrates that there exist tokamak operation regimes free of *ideal* instabilities for $\beta_o > \beta_{oc}$ and below the excitation threshold of the EPM branch. Such regimes are the most desirable in a reactor relevant plasma since they are affected, at most, by moderately unstable KTAE's.

Previous global studies of TAE stability, using a 2D-WKB code [5] applied to analyses of an (s, α) model of ITER, have shown that $\beta_{oc} \simeq 1.8\%$. This value was computed using aspect ratio, minor radius and toroidal magnetic field $A = R_o/a = 2.63$, $a = 2.3$m and $B_o = 5.7$T, respectively, and a parabolic q profile with $q_o = 1.0$ and $q_a = 3.0$. Physically, β_{oc} was shown to be a consequence of the merging of the TAE mode structure into the lower continuum at $(r/a) \simeq 0.4$. Figure 1 shows the values of β_{oc} for a realistic ITER equilibrium vs. the plasma elongation, K, and for two values of the triangularity, $\delta = 0.0$ and $\delta = 0.3$. These results are "local" in the sense they are obtained by "imposing" that, at threshold, the TAE mode structure merges into the lower continuum at $(r/a) = 0.5$. Thus, the self-consistent calculation of the TAE mode structure with the 2D-WKB code has not been done. The present choice is justified by previous global analyses [5] based on the (s, α) model, which suggest that the results of Fig. 1 are representative of the "true" global threshold β_{oc}.

In general, Fig. 1 indicates that the effect of the elongation is beneficial (since it lowers β_{oc}) whereas that of triangularity is detrimental. Nevertheless, plasma shaping seems to generally have a small effect on the value of β_{oc}. The most remarkable difference with respect to previous (s, α) model results is that β_{oc} for a realistic equilibrium is appreciably smaller. This is a consequence of the asymptotic expansion in the inverse aspect ratio used in the (s, α) model. More comprehensive studies of TAE stability in realistic ITER equilibria using the 2D-WKB code [5] are in progress.

2. Transition from Toroidal Alfvén Modes to Energetic Particle Modes

We examine the dependence of the Toroidal Alfvén Eigenmode (TAE) instability on α_{core} using a recently developed high-n gyrokinetic - magnetohydrodynamic simulation code [6] in which the energetic particle dynamics are treated nonperturbatively. The results are shown in Fig. 2, where we have fixed all parameters ($\epsilon = r/R = 0.1$, $s = 0.32$, $v_E/v_A = 1.0$, $\alpha_E = 0.121$,...) except α_{core} and maximized the growth rate as a function of k_θ. Consistent with theoretical predictions for the TAE [2,4], ω_r decreases as α_{core} increases. In fact, ω_r for the TAE lies inside the lower continuum for $\alpha_{core} \geq 0.10$ as predicted theoretically [4]. The key difference between our new results and past theoretical predictions based on perturbative treatments of the energetic ion dynamics [3] is that we consider several possible modes (such as Energetic Particle Modes (EPM)) instead of focusing solely on the TAE. This is important because once the TAE approaches the lower continuum it is no longer the dominant mode. There is a transition to the Energetic Particle Mode branch of the Kinetic Ballooning Mode (KBM/EPM). In contrast to the TAE, the growth rate of the KBM/EPM increases with α_{core} as ω_r moves further into the lower shear Alfvén

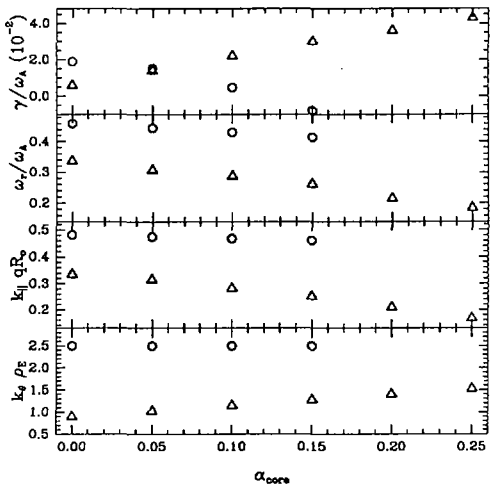

FIG. 2. A transition from the TAE to the KBM occurs as α_{core} increases. The circles correspond to the TAE while the triangles represent an EPM branch of the KBM. Top plot: growth rate, γ, of the instability as a function of α_{core}. Second plot from top: real frequency of the mode, ω_r, as a function of α_{core}. Third plot: peak in the $k_\parallel$ spectrum as a function of α_{core}. $k_\parallel$ is given in units of $1/qR$. Bottom plot: $k_{\theta\rho E}$ for which γ is maximized for each mode. $k_{\theta\rho E}$ values corresponding to the two most unstable modes are shown here. See text for parameters.

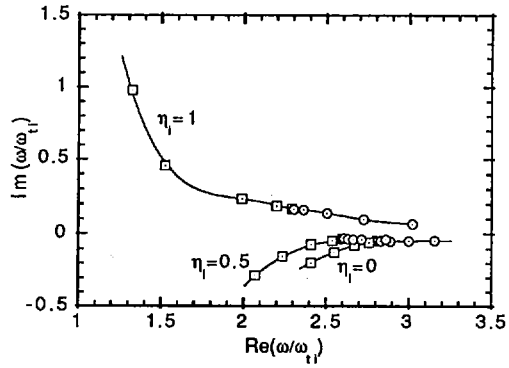

FIG. 3. BAE branch for $\beta_i = 0.01$, $\tau = 1$, $q = 1.5$ and $\omega_{*ni}/\omega_{ti} = 0.5$. The BAE spectrum is reported for the three values of $\eta_i = 0, 0.5, 1$. Open squares: gap mode, for which $\delta W_{MHD} \in (-0.2, 0)$; open circles: continuum $q(r)R_o k_\parallel(r) \in (0, 0.2)$.

continuum. As shown in Fig. 2, it is possible to observe both the TAE and KBM simultaneously near the transition point where their growth rates are comparable. In addition, it should also be noted that in order to achieve this type of transition there must be sufficient energetic particle $\alpha_E \geq \alpha_{E0}$ where $\alpha_{E0} \simeq 0.05$. We emphasize here that these low frequency unstable continuum modes are EPM, *not ideal* ballooning instabilities. The transition from TAE to KBM/EPM occurs below the *ideal* ballooning limit and for this reason we have chosen to set $\omega_{*pi} = 0$ for simplicity and focus on the EPM rather than the KBM gap mode. The inclusion of ω_{*pi} and finite ion compressibility will be discussed shortly. The transition is also indicated by the change in the $k_\parallel$ spectrum. As shown in Fig. 2, $k_\parallel$ decreases significantly as α_{core} increases. This type of transition from TAE to KBM is consistent with the transition from the TAE to the β-induced Alfvén eigenmode (BAE) observed in DIII-D [7].

We next consider diamagnetic effects and finite core plasma ion compressibility on the same footing [8] and focus on high-n low frequency ($\omega \sim \omega_{*pi} \sim \omega_{ti} < \omega_A$) Alfvén waves in a high-β tokamak equilibrium. In this part of our study, energetic-particle contributions are ignored in order to concentrate on Alfvén waves due to the core plasma. The β-induced Alfvén eigenmode (BAE) and KBM are found to be two separate branches of the low frequency shear Alfvén spectrum, which are independent only for $\eta_i \equiv L_n/L_T = 0$. In the general case, $\eta_i \neq 0$, the two branches are coupled. Specifically, it is found that, for $\omega_{*pi}/\omega_{ti} \gg \sqrt{7/4 + \tau}q$, the KBM are the most unstable modes of those considered in ref. [8]. Here, $\tau = T_e/T_i$. More importantly, it has been demonstrated [c.f. Fig. 3] that for $\omega_{*pi}/\omega_{ti} < \sqrt{7/4 + \tau}q$, a critical value η_{ic} exists above which the BAE is the most unstable branch. In Fig. 3, it has also been shown [8] that for $\eta_i > \eta_{ic}$, part of the continuous Alfvén spectrum may be unstable, thus

implying that non-collective modes may be present in the plasma, formed as a superposition of local oscillations which are growing quasi-exponentially in time. This new feature is entirely due to the inclusion of finite core plasma ion compressibility in the theoretical analysis. Finally, it is found that the most unstable low frequency Alfvén modes occur for $\omega_{*pi}/\omega_{ti} \geq \sqrt{7/4 + \tau q}$, corresponding to a parameter range in which BAE and KBM are strongly coupled.

3. Hybrid MHD-particle simulation

In this section the results of hybrid MHD-gyrokinetic simulations [9] of low-toroidal-mode-number Alfvén modes are presented.

In Fig. 4 the results of linear simulations are reported. The linear growth rate and the real frequency of the most unstable mode are shown at different values of the ratio between the energetic-particle on-axis density n_E and the bulk-ion one n_i. Only modes with toroidal mode number $n = 4$ and poloidal mode numbers ranging from $m = 4$ to $m = 8$ are retained. The initial energetic particle population is Maxwellian, with thermal speed equal to the Alfvén velocity. At low values of energetic-particle density, a regime characterized by weakly unstable TAE with growth rate increasing linearly with n_E, is observed. The real frequency, in this regime, is well inside the gap. At intermediate values of n_E/n_i, the real frequency decreases, merging into the lower continuum. Correspondingly, the KTAE turns out to be the most unstable mode. Its growth rate exhibits a weak dependence on n_E/n_i, because increasing n_E tends to enhance both drive and radiative damping [10]. Above a certain threshold in n_E/n_i, the Energetic ParticleContinuum Mode appears, with growth rate sharply increasing with n_E. The real frequency is deeply inside the lower continuum. Note that this result is analogous to that of Fig. 2, where a similar transition from TAE to EPM is observed as the core plasma pressure gradient increases.

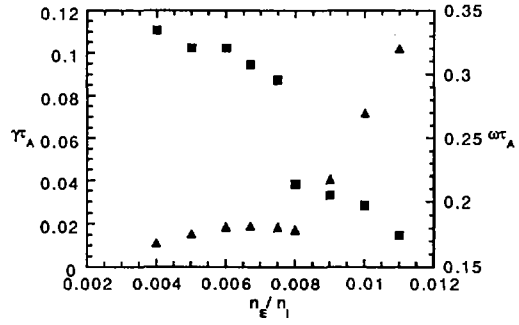

FIG. 4. Linear growth rate (triangles) and real frequency (squares) at different values of n_E/n_i. Only modes with toroidal mode number $n = 4$ have been retained.

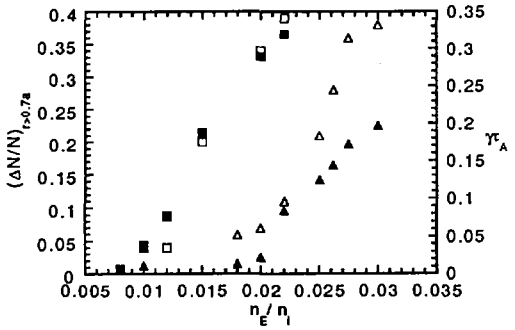

FIG. 5. Fraction of energetic particle population displaced out of $r = 0.7a$, at different values of n_E/n_i, for cases $n = 1$ and $n = 4$ (open triangles and squares, respectively). The corresponding linear growth rates are also shown (full triangles and squares).

Concerning the nonlinear saturation, our attention is focused on the mechanisms related to energetic-particle dynamics. Above the threshold for the EPM destabilization the wave-particle interaction induces a secular radial drift of the particle, instead of a small oscillation around the unperturbed orbit. Saturation is then reached because the source of the instability is macroscopically displaced, rather than because of trapping of resonant particles in the potential well of the wave [11].

As a consequence the effect of this mechanism on the energetic-particle confinement can be dramatic. In Fig. 5, the fraction of energetic-particle population displaced out of a given radial position ($r = 0.7a$, in this case) is shown, at different values of n_E/n_i, for the cases $n = 1$ and $n = 4$ (open triangles and squares, respectively). The corresponding linear growth rates are also shown (full triangles and squares). It is evident that the destabilization of EPM's corresponds to a sharp increase of the fraction of displaced particles and then, eventually, of the fraction of lost particles. Moreover, Fig. 5 demonstrates that the effects of the instability on the energetic particle population become more relevant as the mode number increases, or, conversely, that at higher n the threshold for the onset of EPMs is lower.

Although the threshold for strong redistribution in the energetic-particle source shown in Fig. 5 corresponds to unrealistically high values of energetic-particle density, the more unstable high-n cases [1,2,5,12] may cause the same phenomenology for realistic values of n_E/n_i.

REFERENCES

[1] ZONCA, F., CHEN, L., Phys. Plasmas **3** (1996) 323.

[2] CHEN, L., in *Theory of Fusion Plasmas*, edited by J. Vaclavik, F. Troyon and E. Sindoni, Editrice Compositori, Bologna (1989) 327.

[3] FU, G.Y., CHENG, C.Z., Phys. Fluids B **4** (1992) 3722.

[4] ZONCA, F., CHEN, L., Phys. Fluids B **5** (1993) 3668.

[5] VLAD, G., ZONCA, F., ROMANELLI, F., Nucl. Fusion **35** (1995) 1651.

[6] SANTORO, R.A., CHEN, L., Phys. Plasmas **3** (1996) 2349.

[7] HEIDBRINK, W.W., STRAIT, E.J., CHU, M.S., TURNBULL, A.D., Phys. Rev. Lett. **71** (1993) 855.

[8] ZONCA, F., CHEN, L., SANTORO, R.A., *Kinetic theory of low frequency Alfvén modes in tokamaks*, Plasma Phys. Controlled Fusion (in press).

[9] BRIGUGLIO, S., VLAD, G., ZONCA, F., KAR, C., Phys. Plasmas **2** (1995) 3711.

[10] METT, R.R., MAHAJAN, S.M., Phys. Fluids B **4** (1992) 2885.

[11] BERK, H.L., BREIZMAN, B.N., Phys. Fluids B **2** (1990) 2246.

[12] BRIGUGLIO, S., KAR, C., ROMANELLI, F., VLAD, G., ZONCA, F., Plasma Phys. and Controlled Fusion **37** (1995) A279.

FORMATION OF TRANSPORT BARRIERS

V. ROZHANSKY[1], M. TENDLER[2], S. VOSKOBOYNIKOV[1]

[1] St. Petersburg State Technical University,
St. Petersburg, Russian Federation

[2] Alfvén Laboratory,
Royal Institute of Technology,
Stockholm, Sweden

Abstract

FORMATION OF TRANSPORT BARRIERS.

The formation of transport barriers in a tokamak is addressed. A particle continuity equation with a diffusion coefficient that depends on the shear of the poloidal $\mathbf{E} \times \mathbf{B}$ drift is solved numerically. Therefore the paradigm of $\mathbf{E} \times \mathbf{B}$ shear suppression is employed in the context of the dynamics of the formation of transport barriers in tokamaks. It is asserted that the crucial element determining the evolution of the barrier is the density profile. The impact of this is governed by subtle details of the density profiles. Various methods of triggering transitions, such as pellet injection and adiabatic compression, are considered. Special emphasis is given to the detailed dynamics of L–H and H–L transitions, including that of the pellet induced H mode. Hysteresis is demonstrated to be a robust feature of the transitions. The basic features of transport barrier formation are corroborated by numerical simulations. It is shown that the barrier front propagates rapidly compared with the confinement times.

1. MODEL

The transport barrier resulting from the paradigm of $\mathbf{E} \times \mathbf{B}$ shear suppression [1–3] is modelled by the diffusion equation

$$\frac{\partial n}{\partial t} - \frac{\partial}{\partial x}\left(D(\alpha)\frac{\partial n}{\partial x}\right) = 0 \qquad (1)$$

where $x = (r - a)\Theta/\rho_{ci}$ is the dimensionless distance from the separatrix, ρ_{ci}/Θ is the poloidal gyroradius and t is in units of $(\rho_{ci}/\Theta)^2/D^{min}$. The parameter α is proportional to the shear of the radial electric field, $\alpha \sim |dE_r/dr|$ [2–5]. The electric field is supposed to be neoclassical with the toroidal rotation damped by the anomalous inertia and viscosity [6]

$$E_r^{neo} = \frac{T_i}{e}\left(\frac{d\ln n}{dr} + (1 - k)\frac{d\ln T_i}{dr}\right) \qquad (2)$$

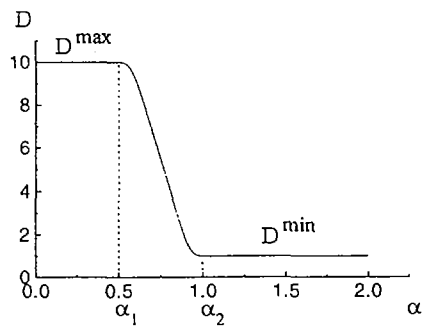

FIG. 1. Diffusion coefficient as a function of α.

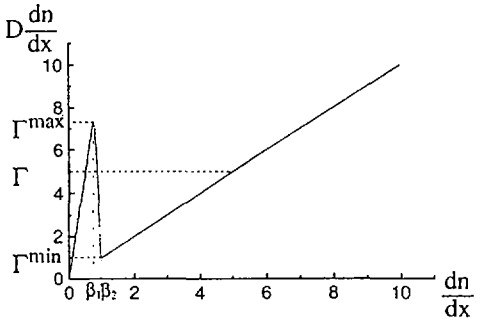

FIG. 2. D dn/dx as a function of dn/dx.

where k is a numerical coefficient which depends on collisionality. This field is typical of the L regime, while for the steep density profiles typical of the H mode an additional equation for the electric field has to be solved [4–8]. Leaving this for a future publication, we focus on the initial stage of the barrier formation when Eq. (2) is satisfied. Assuming that the density gradient is steeper at the edge than the temperature gradient, the diffusion coefficient is governed by

$$\alpha = \frac{\rho_{ci}^2}{\Theta^2}\left|\frac{d^2 \ln n}{dr^2}\right| = \left|\frac{d^2 \ln n}{dx^2}\right| \tag{3}$$

The arbitrary diffusion coefficient $D(\alpha)$ is shown in Fig. 1. The values α_1 and α_2 can be estimated by comparing the decorrelation frequency associated with the shear of the rotation with the turbulent diffusion decay [1]. We choose $\alpha_1 = 0.5$, $\alpha_2 = 1$ and $D^{max}/D^{min} = 10$. Equation (1) has been solved within the region $0 \leq x \leq 1$ with the boundary conditions $n(x = 0) = 1$, $D\, dn/dx(x = 1) = \Gamma$. The point $x = 0$ defines the separatrix, $x = 1$ is the location of the interface between the transport barrier and the hot core, and Γ is a given particle flux from the core. The case that includes the SOL dynamics is also investigated. The influence of the SOL is taken into account by employing instead of $n(x = 0) = 1$ the following boundary condition:

$$k\frac{\partial n}{\partial t}(x = 0) = \Gamma(x = 0) - \frac{n(x = 0)}{\tau}$$

Here, the density variation in the SOL is proportional to the difference between the flux from the core and the flux to the plates, modelled by $n(x = 0)/\tau$, and k is a numerical coefficient dependent on the volume of the SOL. The adiabatic compression was simulated by incorporating the constant convective velocity V into Eq. (1):

$$\frac{\partial n}{\partial t} - \frac{\partial}{\partial x}\left(D(\alpha)\frac{\partial n}{\partial x} + Vn\right) = 0 \qquad (4)$$

which was switched on at t = 0 and off at a given time.

2. QUALITATIVE ANALYSIS

For small Γ, the stationary profile is determined by D^{max} and depends linearly on x with a gradual slope

$$n(x) = 1 + \Gamma x/D^{max} \qquad (5)$$

In Fig. 2 the local flux $D(\alpha)\, dn/dx$ is shown as a function of dn/dx for the linear profile $n(x) = 1 + \beta x$ at the separatrix x = 0, where $\alpha = \beta^2/(1 + \beta x)^2$. Here, for x = 0 the turning points are $\beta_1 = \alpha_1^{1/2}$ and $\beta_2 = \alpha_2^{1/2}$ (Figs 1 and 2). The steady state solution is governed by the relation $\Gamma < \Gamma^{max}$ or $\Gamma > \Gamma^{max}$. If $\Gamma < \Gamma^{max}$ the steady state solution is yielded by the linear function given by Eq. (5). In contrast, for $\Gamma > \Gamma^{max}$ the steady state solution is yielded by a non-linear function with a steep gradient, thereby resulting in the H mode. The ion temperature and density at the separatrix affect the relation between Γ and Γ^{max}. From Eq. (3) it follows that for higher temperatures and/or lower densities the value of Γ^{max} drops because the shear suppression becomes more effective. Therefore the L–H transition is more easily accessible for a given particle flux. For the linear profile given by Eq. (5), if the temperature rises and/or the density decreases, Γ may become larger than Γ^{max}. Hence the transition occurs. Furthermore, in order to trigger the reverse, H–L transition the particle flux must drop to a very low value, below Γ^{min}. Thus the fundamental phenomenon of the hysteresis, which is well documented for the transition, emerges.

3. RESULTS OF THE SIMULATION

First the solution of Eq. (1) employing the boundary condition n(x = 0) = 1 and the initial profile given by Eq. (5) is shown in Figs 3 to 6 evolving in time: curve 1, t = 0 (initial profile); curve 2, t = 0.0005; curve 3, t = 0.001; curve 4, t = 0.005; curve 5, t = 0.01; curve 6, t = 0.05; curve 7, t = 0.1; curve 8, t = 0.5; curve 9, t = 1; curve 10, t = 4. To solve Eq. (1) numerically, a small artificial viscosity was added. Note that the initial density gradient was $\beta = \Gamma/D^{max}$ with $\Gamma = 7.5 > \Gamma^{max}$. Simultaneously, the density deviation from the linear profile Δn rises, whereas the diffusion coefficient, shown in Fig. 5, and the particle flux into the SOL, Γ(0), shown in Fig. 6, drop. The diffusion coefficient is dramatically reduced within the entire barrier on the fast time-scale $t_f = x^2/D^{max}$ (this is 0.1 in our units at x = 1). Yet, briefly and close to the separatrix, the barrier front propagates even faster than t_f (Fig. 7).

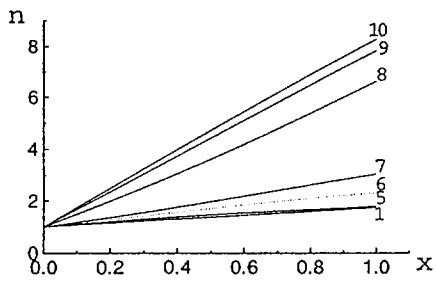

FIG. 3. Evolution of density during L–H transition for $\Gamma = 7.5 > \Gamma^{max}$.

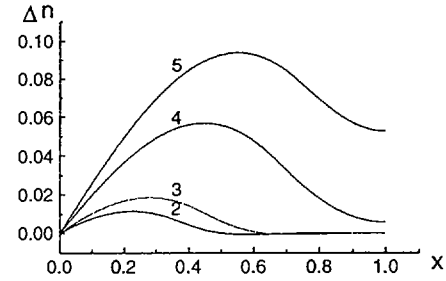

FIG. 4. Evolution of the deviation from the linear profile given by Eq. (5) during L–H transition for $\Gamma = 7.5 > \Gamma^{max}$.

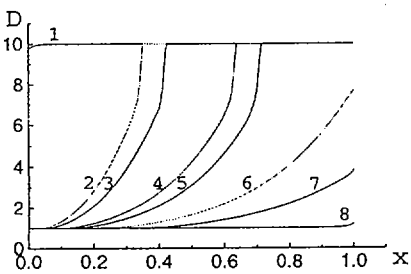

FIG. 5. Evolution of the diffusion coefficient during L–H transition for $\Gamma = 7.5 > \Gamma^{max}$.

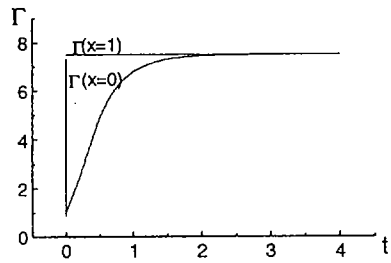

FIG. 6. Evolution of particle fluxes during L–H transition for $\Gamma = 7.5 > \Gamma^{max}$.

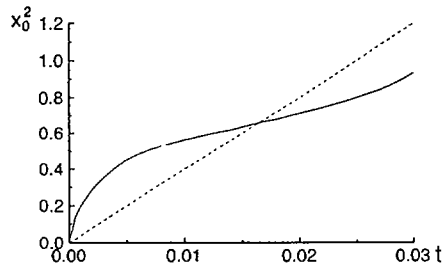

FIG. 7. Propagation of the front of the transport barrier where the diffusion coefficient is suppressed. The broken line shows the diffusion law $x_0^2 = 4D^{max}t$.

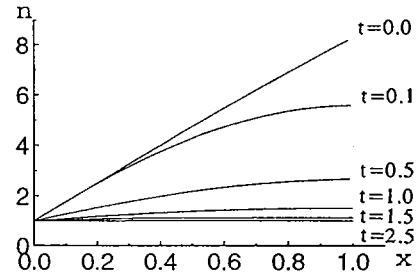

FIG. 8. Evolution of density during H–L transition.

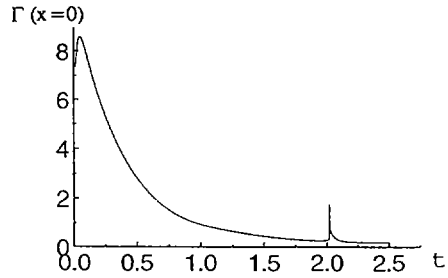

FIG. 9. Particle flux during H–L transition.

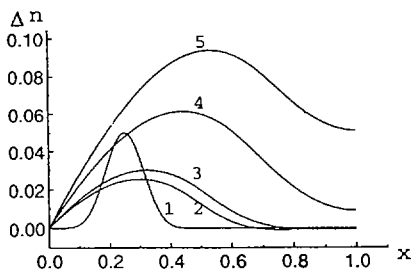

FIG. 10. Pellet induced transition for $\Gamma < \Gamma^{max}$ (Γ = 6.75, small pellet).

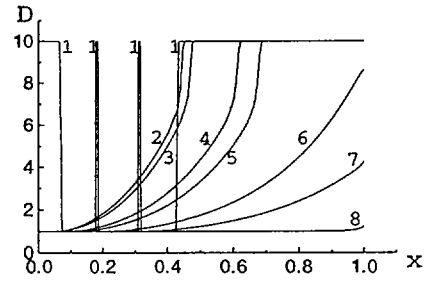

FIG. 11. Diffusion coefficient during pellet induced transition for $\Gamma < \Gamma^{max}$ (Γ = 6.75, small pellet).

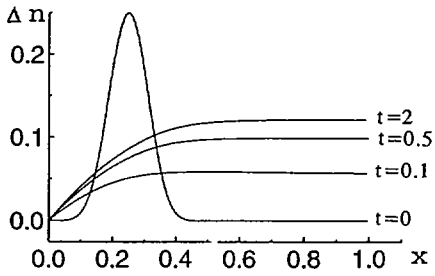

FIG. 12. Pellet induced transition for $\Gamma < \Gamma^{min}$ (Γ = 0.25, large pellet).

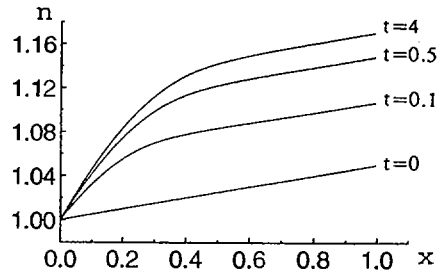

FIG. 13. Formation of the barrier during pellet injection for $\Gamma < \Gamma^{min}$ (Γ = 0.25, large pellet).

Focusing now on the H–L transition, a novel effect arises. Indeed, in order to bring the plasma back to the L state, the flux from the core must decrease to an extremely low value, below Γ^{min}. This effect implies hysteresis, which is inherent to the physics of the phenomena. Note that it is described by the model in Figs 8 and 9. The H–L transition results only for very small flux, $\Gamma \leq 0.25$. Although the flux from the core is now strongly reduced, the final profile is still described by Eq. (5) with $D = D^{max}$.

The triggering of the L–H transition by small and slow pellet injection has been addressed both theoretically and experimentally [4, 5, 7] (Figs 10 and 11). Here, the model is extended to the case of large pellet injection, shown in Figs 12 and 13. The L–H transition already results for the much smaller flux (both fluxes are subcritical for the direct L–H transition; $\Gamma = 6.75$ for small pellets and $\Gamma = 0.25$ for large pellets), owing to the large size of the pellet. For the large pellet the transition always occurs when the flux is kept subcritical, $\Gamma < \Gamma^{max}$. Yet, for very small flux, $\Gamma < \Gamma^{min}$, the transition differs from the L–H type. Indeed, the profile has steep and gradual parts, and the impermeability is greatest within the outer part of the barrier.

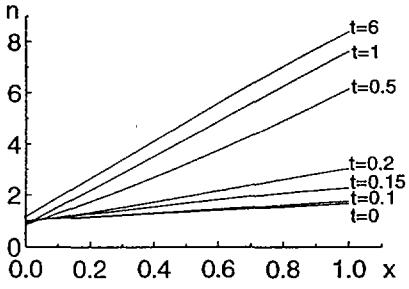

FIG. 14. L–H transition after the rise of flux from the core from $\Gamma < \Gamma^{max}$ to $\Gamma > \Gamma^{max}$.

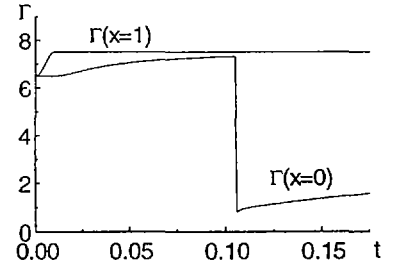

FIG. 15. Flux for L–H transition after the rise of flux from the core from $\Gamma < \Gamma^{max}$ to $\Gamma > \Gamma^{max}$.

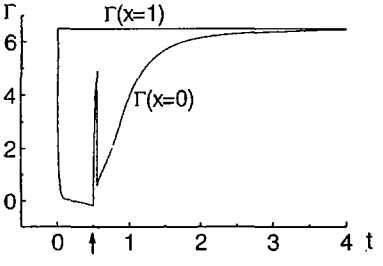

FIG. 16. Diffusion fluxes for adiabatic compression with $V = 0.75$. The moment when the compression is switched off is shown by an arrow.

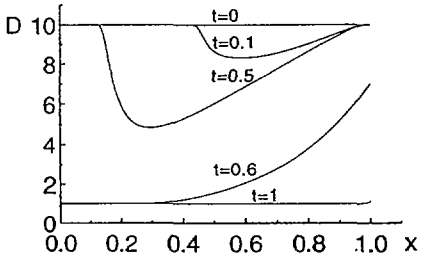

FIG. 17. Evolution of the diffusion coefficient in the case of adiabatic compression with $V = 0.75$.

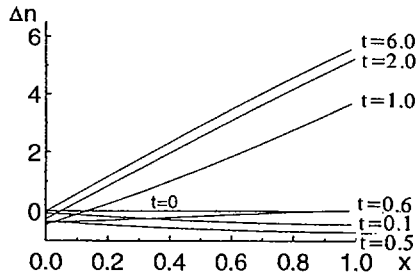

FIG. 18. Evolution of density in the case of adiabatic compression with V = 0.75.

A different scenario of barrier formation is modelled by changing the inner and outer boundary conditions (Figs 14 and 15). If the flux from the core at t = 0 is increased from 6.5 to 7.5 and the boundary condition is at x = 0,

$$k\frac{\partial n}{\partial t}(x = 0) = \Gamma(x = 0) - \frac{n(x = 0)}{\tau} \tag{6}$$

where k = 7.5 and $\tau = 0.15$, then the transition is delayed until the density perturbation reaches the outer boundary (here, the separatrix) on the time-scale $t_f = x^2/D^{max}$ ($t_f = 0.1$). Note that the transition occurs, provided the density perturbation is carried down towards the outer boundary.

An important method of triggering the transition (for example, adiabatic compression) is addressed by employing a convective term in the fundamental Eq. (5). The convection is switched on at t = 0 and off at t = 0.5 (Figs 15–18). Importantly, the flux from the core is intentionally kept subcritical. Although the density profile flattens, the transition occurs owing to the reduced density at the separatrix. This effect results because of the sensitivity of the shear suppression mechanism to subtle yet crucial details of the density profiles.

4. CONCLUSIONS

It is proposed that the density gradient, via the impact of electric field shear suppression, is the crucial parameter for triggering a transport barrier in a tokamak. The formation of the transport barrier is governed by subtle yet crucial details of the density profiles. It is shown that the front of the transport barrier can propagate on a very short time-scale, shorter than the confinement time of the transport barrier. A wide range of different methods of triggering the transition, such as the injection of both small and large pellets, adiabatic compression and time changes in the SOL dynamics, result from the model.

ACKNOWLEDGEMENTS

The work of V.R. and S.V. was supported by RFFI grant 95-01-00524.

REFERENCES

[1] BIGLARI, H., DIAMOND, P.H., TERRY, P.W., Phys. Fluids B 2 (1990) 11.
[2] GROEBNER, R.J., Phys. Fluids B 5 (1993) 2343.
[3] MOYER, R.A., et al., Phys. Plasmas 2 (1995) 2397.
[4] ASKINASI, L.G., et al., Phys. Fluids B 5 (1993) 2420.
[5] KAPRALOV, V.G., ROZHANSKY, V.A., KHLOPENKOV, K.V., in Controlled Fusion and Plasma Physics (Proc. 22nd Eur. Conf. Bournemouth, 1995), Vol. 19C, European Physical Society, Geneva (1995) 117.
[6] ROZHANSKY, V., TENDLER, M., Phys. Fluids B 4 (1992) 1877.
[7] ROZHANSKY, V., TENDLER, M., VOSKOBOYNIKOV, S., in Controlled Fusion and Plasma Physics (Proc. 23rd Eur. Conf. Kiev, 1996), Vol. 20C, European Physical Society, Geneva (1996) a163.
[8] TENDLER, M., DAYBELGE, U., ROZHANSKY, V., in Plasma Physics and Controlled Nuclear Fusion Research 1992 (Proc. 14th Int. Conf. Würzburg, 1992), Vol. 2, IAEA, Vienna (1993) 243.

THEORY BASED TRANSPORT MODELLING OF TOKAMAK TEMPERATURE AND DENSITY PROFILES

G. BATEMAN, J.E. KINSEY, A.H. KRITZ,
A.J. REDD, J. WEILAND[1]
Physics Department,
Lehigh University,
Bethlehem, Pennsylvania,
United States of America

Abstract

THEORY BASED TRANSPORT MODELLING OF TOKAMAK TEMPERATURE AND DENSITY PROFILES.

A fixed combination of theoretically derived transport models is used to predict the time evolution of temperature and density profiles in tokamaks. The average deviation between simulated and experimentally measured profiles is less than 15% for more than 40 L-mode and H-mode discharges from TFTR, DIII-D, JET and other tokamaks. It is found that the authors' purely gyro-Bohm transport model produces the experimentally observed non-gyro-Bohm behavior in gyro-radius (ρ_*) scans because edge neutrals change the shape of the density and temperature profiles from one end of each scan to the other. The simulations also reproduce the observed transport scaling with plasma current, density, heating power, and dimensionless parameter scans. The transport model used in these simulations combines contributions from the Weiland model for drift modes together with the Guzdar-Drake model for resistive ballooning modes, along with smaller contributions from kinetic ballooning modes and neoclassical transport.

We use a fixed combination of theoretically derived transport models in time dependent simulations to predict the evolution of temperature and density profiles in tokamaks [1]–[9]. We find that simulated profiles agree remarkably well with experimental data for more than 40 discharges from TFTR, DIII-D, JET, as well as from other tokamaks. These discharges include L-mode scans in current, heating power, density, normalized gyro-radius (ρ_*), collisionality (ν_*) and β, as well as TFTR supershot current scans and twenty five discharges from the ITER Profile Database including H-mode discharges. A global measure of this agreement is seen in Fig. 1 where the total stored energy predicted by each simulation is compared with the experimentally determined stored energy at the diagnostic time for 41 different L-mode and H-mode discharges. (The solid line indicates a perfect fit.) We find that the relative root mean square deviation, defined by $\sigma = \sqrt{\frac{1}{N}\sum_{i=1}^{N}\left[\frac{W_{\mathrm{sim}_i}-W_{\mathrm{exp}_i}}{W_{\mathrm{exp}_i}}\right]^2}$, is approximately 9%.

[1] Chalmers University of Technology, Göteborg, Sweden.

1. Transport Model

The transport model used in all of our studies combines the Weiland Ion Temperature Gradient (ITG) and Trapped Electron Mode (TEM) model with the Guzdar-Drake resistive ballooning mode model, along with smaller contributions from kinetic ballooning modes and neoclassical transport. Figure 2 shows the typical radial profile of the effective diffusivity from an L-mode simulation (at the high end of a TFTR ρ_* scan) [1]. It can be seen that the ITG mode dominates over most of the plasma core, while the resistive ballooning mode transport rises near the relatively cold plasma edge. We showed in 1992 [8] that transport from ITG modes increases with radius because the mode is marginally stable near the magnetic axis and increasingly deviates from marginal stability with increasing radius. This effect overwhelms the $T_e^{3/2}$ dependence of ITG transport.

The basic Weiland model [10, 5], which included effects from the impurity profile, fast ions and $T_e \neq T_i$, has been extended to include parallel ion motion[11] and electromagnetic effects [12]. Furthermore, we found that the nominal Guzdar-Drake resistive ballooning model[13] yields a better match with current scan data than does the nominal Carreras-Diamond model (*i.e.*, with multiplicative factor of 1.0) while maintaining agreement with density and power scan data [3].

The time-dependent boundary conditions (at $r/a > 0.95$) and the time evolution of the line-average density, current, Z_{eff}, and plasma shape are taken from experimental data. In the H-mode simulations, our boundary conditions

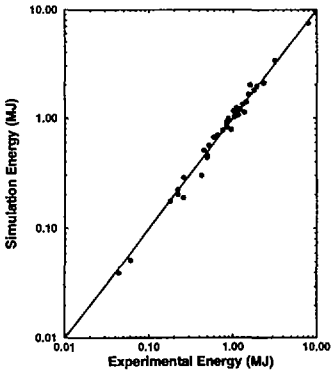

FIG. 1. Total stored plasma energy from 41 simulations compared with corresponding experimental data for L-mode and H-mode scans in TFTR, DIII-D and JET. The root mean squares deviation is about 9%.

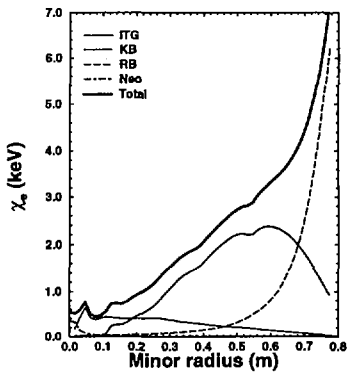

FIG. 2. Radial form of effective electron thermal diffusivity from simulation of TFTR L-mode 50 921. The total diffusivity and contributions are shown from ITG, kinetic ballooning (KB), resistive ballooning modes (RB) and neoclassical transport.

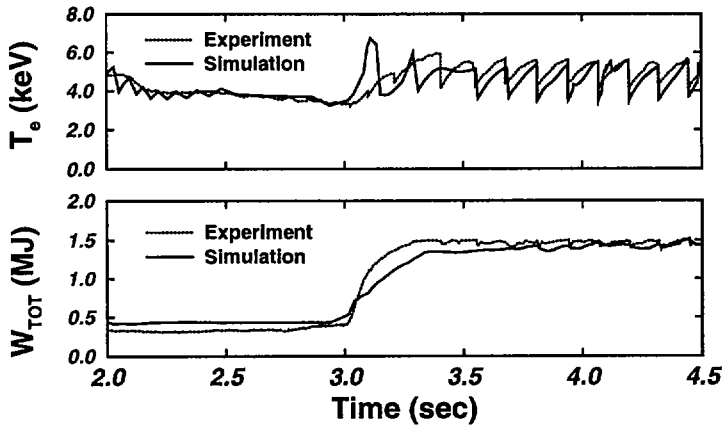

FIG. 3. Time traces of central electron temperature (above) and total plasma energy content (below) from simulation (solid) compared with experiment (dashed) for TFTR L-mode 45 950 with P_{NBI} = 11.4 MW, $\bar{n}_{e19}$ = 3.45 m^{-3}, I_p = 2 MA, Z_{eff} = 2.7.

are normally taken at the top of the pedestal. When comparing the simulations with experimental data, we find that it is important to match profiles at the same relative phase of the sawtooth oscillations. As shown in Fig. 3, our simulations are run for several confinement times during the Ohmic stage, and then through the auxiliary heating stage until the time of interest. We have carried out sensitivity studies on the input data used in the simulations and we find that our L-mode simulations are relatively insensitive to variations in the boundary conditions [4].

2. Gyro-Radius Scans

The simulations of the ρ_* scans from DIII-D, TFTR and JET are particularly interesting because we find that our fundamentally gyro-Bohm transport models reproduce the non gyro-Bohm behavior of the experimental data[1]. Since edge neutrals penetrate less deeply into into the higher density (lower ρ_*) plasmas, they change the shape of the density and collisionality profiles near the plasma edge which, in turn, changes the scaling of the transport. This effect cascades into the core of the plasma, where small changes in profile shape have a relatively large effect on the transport (where the ITG mode is closer to its marginal stability point). Hence, we understand the physics of gyro-radius scaling in our simulations. These simulations agree with the experimentally measured temperature and density profiles in both RF and neutral beam heated L-mode ρ_* scans in DIII-D, TFTR and JET, spanning $\rho_*^{\max}/\rho_*^{\min} = 3.5$.

If the observed non gyro-Bohm confinement is due to edge effects, as we find in our simulations, then the global energy confinement (τ_E) scalings may

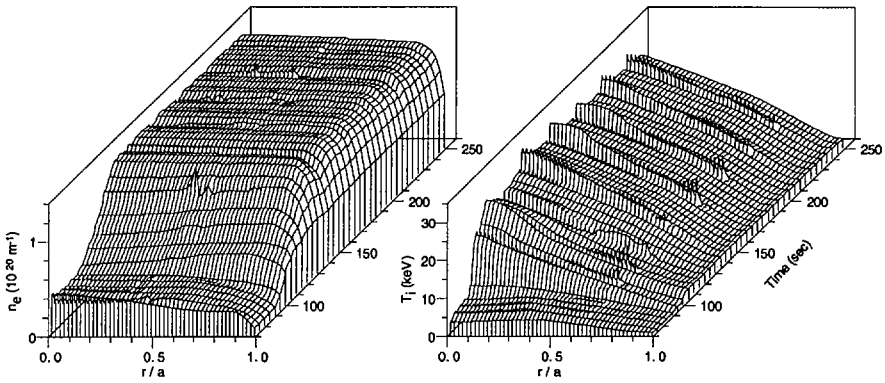

FIG. 4. T_i and n_e as a function of radius and time for ITER simulation with I_p = 21 MA, B = 5.7 T, R = 8.14 m, a = 2.8 m, κ = 1.6, δ = 0.24, P_{NBI} = 50 MW from 90 to 150 sec with 1 MeV injection energy, $\bar{n}_{e20}$ = 1.15, and Z_{eff} = 1.5. At 250 sec, P_α = 338 MW and P_{rad} = 165 MW.

be misleading when they are extrapolated to large or high-field tokamak reactors. At constant β and collisionality, the $nT\tau_E$ product scales like $a^{5/2}B^3$ for gyro-Bohm transport[1] compared with $a^{5/4}B^2$ for Goldston scaling[14] (with similar results for the other L-mode and H-mode empirical energy confinement scalings). Hence, the fundamentally gyro-Bohm scaling of our transport model produces much more optimistic results for large tokamak reactor designs (such as ITER), where the edge effects are less important than in present-day experiments. Because of this effect, our simulations of ITER (shown in Fig. 4) generally indicate approximately twice the L-mode energy confinement time, even with low temperature boundary conditions. Our simulations of this large ITER design ignite easily and we find that the fusion power production can be controlled by varying the fuel density.

3. H-mode Simulations

Seven H-mode discharges from DIII-D have been simulated, including density, power, and elongation scans, as well as five H-mode discharges from JET, including two pair of ρ_* scans, using data stored in the ITER Profile Database. We find that the average deviation between simulated and experimental stored energy is 9.1%. In general, the electron temperatures at the top of the edge pedestal are higher than the edge temperatures in most L-modes, which greatly reduces the edge collisionality (ν_*) and thus reduces the resistive ballooning contribution to transport in these simulations. Note, we use the same transport model in our H-mode simulations as we use in our L-mode simulations. The only difference is the boundary conditions, which we take from the experimental data in all these simulations. The improved confinement results from the

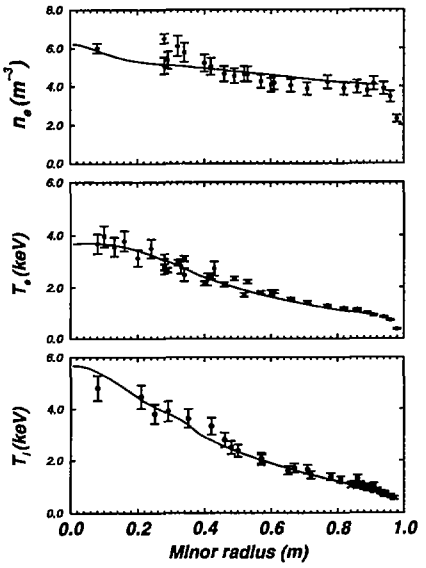

FIG. 5. Radial profiles of electron density, electron temperature and ion temperature for DIII-D H-mode discharge 81 499.

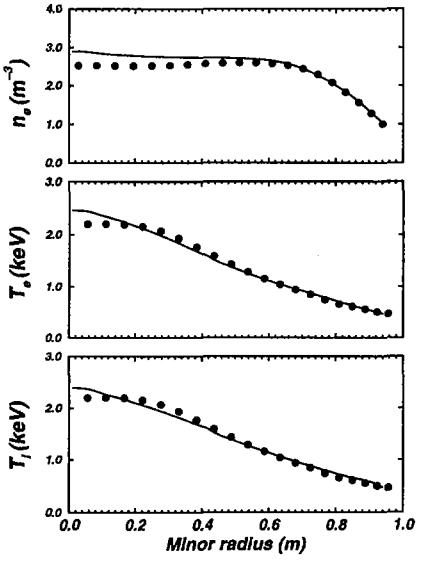

FIG. 6. Radial profiles of electron density, electron temperature and ion temperature for JET H-mode discharge 35 171.

elevated boundary conditions and the generally flatter profiles in the core of these H-mode plasmas.

Figures 5 and 6 show the radial profiles of electron density, electron temperature, and ion temperature for two of these H-mode simulations. For the DIII-D shot 81499 shown in Fig. 5, the parameters are $R = 1.69$ m, $a = 0.63$ m, $\kappa = 1.68$, $\delta = 0.32$, $B_T = 1.91$ T, $I_p = 1.35$ MA, $\bar{n}_{e19} = 4.81$, $Z_{\text{eff}} = 2.33$, and $P_{\text{NBI}} = 5.92$ MW. For the JET shot 35171 shown in Fig. 6, the parameters are $R = 2.86$ m, $a = 0.93$ m, $\kappa = 1.56$, $\delta = 0.18$, $B_T = 1.10$ T, $I_p = 1.01$ MA, $\bar{n}_{e19} = 2.33$, $Z_{\text{eff}} = 1.10$, and $P_{\text{NBI}} = 2.91$ MW.

4. Supershot Simulations

In supershot simulations, it is found that the influx of edge neutrals with energy comparable to the edge ion temperature has a strong effect on the ion temperature and less of an effect on the electron temperature and density profiles. With a hydrogenic recycling rate of about 80%, our simulations match experimental data for several TFTR supershots with different plasma currents and heating power levels. These simulations predict the strongly hollow Z_{eff} profile observed in experiments.

All the transport model coefficients are held fixed in all the L-mode and H-mode simulations. However, for supershot simulations, a strongly reduced

coefficient in front of the kinetic ballooning mode model yields the best fit with experimental data. (Note that transport from the kinetic ballooning mode is usually small in L-mode, H-mode and Ohmic discharges.) After making this one change, our simulations match the power and current scaling of TFTR supershots. We are currently investigating the possibility that sheared flows might reduce the transport in the deep core of supershots as well as in some DIII-D H-modes.

5. Objective Testing of a Predictive Transport Code

In order to test both the modelling capability and the systematic simulation methodology, a blind test was devised in which the modellers were told only the data necessary for running a simulation of a TFTR discharge, but not the profiles or shot number. In particular, all the boundary conditions were given as a function of time, together with the line-averaged density, volume-averaged Z_{eff}, beam power (the orientation of the beam boxes was already prescribed), plasma geometry, toroidal field and plasma current. The predicted density and temperature profiles were then subsequently compared against experimental data. We are grateful to Drs. Stanley M. Kaye and Wayne Houlberg for preparing the data needed for this simulation.

In this first blind test, we found that our previous methodology for preparing an input dataset for the BALDUR code was inadequate. The protocol had to be modified to be less sensitive to the edge Z_{eff} relative to the volume-averaged Z_{eff}. It was found that it was important to influx impurity neutrals at low energy ($\sim$ 40 eV) while the hydrogenic neutrals are influxed at the edge ion temperature for the best results in our simulations. It was also found to be essential to accurately prescribe the time evolution of the line-averaged density.

After revisions to the simulation methodology, the resulting density and temperature profiles agreed with the experimental profiles to within 10%. There was no indication from this study that any recalibration of the multi-mode transport model employed in BALDUR is required. The combination of theoretically derived models used in our time dependent transport simulations is able to predict both the shapes and the systematic scalings of the density and temperature profiles in a wide variety of tokamak plasmas.

Acknowledgments

We would particularly like to thank Dr. Clifford Singer for his early contributions to our theory-based transport modelling research.

This work was supported by the U.S. Department of Energy, under Contract No. DE-FG02-92-ER-54141.

REFERENCES

[1] KINSEY, J., BATEMAN, G., Phys. Plasmas 3 (1996) 3344.
[2] KRITZ, A.H., et al., in Controlled Fusion and Plasma Physics (Proc. 23rd Eur. Conf. Kiev, 1996), Vol. 20C, European Physical Society, Geneva (1996).
[3] KINSEY, J., et al., Phys. Plasmas 3 (1996) 561.
[4] REDD, A.J., et al., Sensitivity of predictive tokamak plasma transport simulations, Phys. Plasmas (in press).
[5] BATEMAN, G., et al., Phys. Scr. 51 (1995) 591.
[6] KINSEY, J., et al., Phys. Plasmas 2 (1995) 811; Phys. Scr. 52 (1995) 428.
[7] BATEMAN, G., et al., Theory-Based Transport Modelling of TFTR Supershots, Rep. CTH-IEFT/PP-1994-28, Chalmers Univ. of Technology, Göteborg, Sweden (1994).
[8] BATEMAN, G., Phys. Fluids B 4 (1992) 634.
[9] BATEMAN, G., et al., in Controlled Fusion and Plasma Physics (Proc. 18th Eur. Conf. Berlin, 1991), Vol. 15C, Part I, European Physical Society, Geneva (1991) 237.
[10] NORDMAN, H., WEILAND, J., Nucl. Fusion 29 (1989) 251.
[11] FRÖJDH, M., et al., Nucl. Fusion 32 (1992) 419.
[12] WEILAND, J., HIROSE, A., Nucl. Fusion 32 (1992) 151.
[13] GUZDAR, P.N., et al., Phys. Fluids B 5 (1993) 3712.
[14] GOLDSTON, R.J., Plasma Phys. Control. Fusion 26 (1984) 87.

DRIFT WAVE TRANSPORT SIMULATIONS OF JET GYRO-RADIUS SCALING EXPERIMENTS

H. NORDMAN, P. STRAND, J. WEILAND, A. JARMÉN
Chalmers University of Technology
and
Euratom-NFR Association,
Göteborg, Sweden

J.P. CHRISTIANSEN
JET Joint Undertaking,
Abingdon, Oxfordshire,
United Kingdom

Abstract

DRIFT WAVE TRANSPORT SIMULATIONS OF JET GYRO-RADIUS SCALING EXPERIMENTS.

Predictive transport code simulations of gyro-radius scaling experiments have been performed using experimental data from JET profile databases. Two pulses taken from the L-mode similarity scans are considered. Self-consistently derived steady state profiles of density, temperatures and heat diffusivities are compared with the experiments. The simulations are based on a gyro-Bohm transport model for ion-temperature-gradient (ITG) modes and collisionless trapped electron (CTE) modes. The experimental profiles are well reproduced by the simulations. In particular, apparent Bohm- and Goldston-like scalings of the local diffusivities are obtained as the gyro-radius is varied. The electron diffusivity scales close to Bohm-like whereas the ion diffusivity scales slightly worse than Goldston-like. The results are due to small systematic variations in the other dimensionless parameters (assumed to be constant) between the low field and the high field discharges. Although the deviations from self-similarity are generally small, they have a large effect on the resulting transport scaling owing to the sensitivity of the drift wave (ITG- and CTE-mode) stability properties close to marginal stability.

1. INTRODUCTION

A critical issue for estimating the performance of a future fusion reactor is the scaling of transport with normalized gyro-radius [1]. Experimentally, this scaling has recently been investigated in a series of dimensionally similar tokamak discharges [2-4]. In these experiments the normalized gyro-radius $\rho_* = \rho_s/a$ is varied while the other dimensionless parameters characterizing the discharge are kept almost constant, at values projected for an ignition device. In the JET [2] and TFTR [3] L-mode similarity scans, the local effective diffusivity was found to satisfy a Bohm-scaling. In DIII-D on the other hand, the scaling of the effective diffusivity varied from Goldston-like to gyro-Bohm-like depending upon whether the ions or electrons dominated the heat flux [4]. Theoretically, drift wave models of anomalous transport are generally gyro-Bohm-like

corresponding to a diffusive stepsize that scales with the gyro-radius. A Bohm scaling is expected if the stepsize scales with the machine size.

In the present paper, a gyro-Bohm transport model is used in predictive transport code simulations of JET L-mode gyro-radius scaling experiments. The model [5-7] is based on a first-principle 2-fluid model for ion-temperature gradient (ITG) modes and collisionless trapped electron (CTE) modes. Steady state profiles of density, temperatures and heat diffusivities are self-consistently derived and compared with experiments.

2. PREDICTIVE TRANSPORT SIMULATIONS

The discharges simulated are taken from the ion cyclotron rf heated L-mode similarity scans at JET [2]. The two pulses considered are the high field discharge #27654 (B=3.4T, I=4MA) and the low field discharge #27658 (B=1.7T, I=2MA). The normalized gyro-radius varied by a factor 1.6 between the two discharges while the other dimensionless parameters were held almost constant. The rf-power increased from 3.1 MW for the low field pulse to 10.3 MW for the high field pulse in order to satisfy the similarity scalings $T \propto B^{2/3}$ and $n \propto B^{4/3}$ and keep the collisionality and β constant in the experiments. A detailed local transport analysis showed that the confinement, both locally and globally, was Bohm-like [2].

The discharges are simulated self-consistently by a predictive transport code [8]. The evolution of ion pressure p_i, electron pressure p_e and density n ($n=n_i=n_e$) are followed in the region $0 \leq r/a \leq 0.8$ with the outer boundary conditions taken from TRANSP profile data and with zero derivatives imposed on the axis for each profile. Boundary values are updated from JET profile databases at each timestep, together with source terms and geometrical quantities. The transport model used is based on a higher order fluid model for ITG- and CTE-modes [5-7]. The effective diffusion coefficients, derived from quasi-linear theory and nonlinear numerical simulations, are given in [7].

Close to the axis (for $r/a \leq 0.3$), the transport coefficients of the ITG/CTE modes tend to zero. In this region, artificial diffusivities are added to represent the effects of inner core transport. In the present simulations, we used $\chi_i^{art} = 2\chi_e^{art} = 4D^{art} = \chi^{art}$ where χ^{art} was changed from 0.5 m^2/s to 0.25 m^2/s between the pulses #27658 and #27654 to ensure that all diffusivities used satisfy a gyro-Bohm scaling. However, the results in the relevant region (for $r/a \geq 0.3$) are rather unsensitive to this choice.

The transport equations are solved with a standard finite difference technique using a predictor-corrector approach for the non-linearities.

3. RESULTS AND DISCUSSION

In Figures 1-2, the predicted density and temperature profiles for shots #27654 and #27658 are compared with experimental data (as functions of

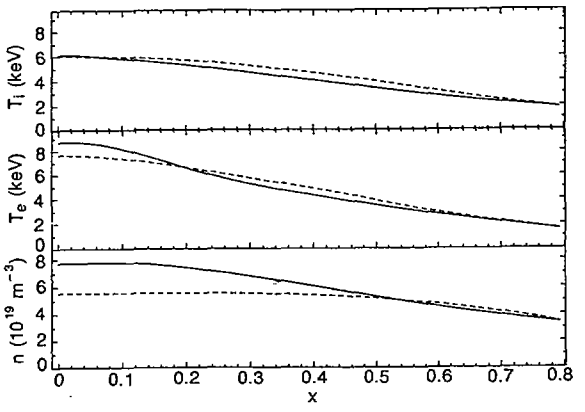

FIG. 1. Comparison between simulated profiles (solid lines) and TRANSP profiles (broken lines) as a function of normalized minor radius for ion temperature (top), electron temperature (middle) and density (botton) for discharge #27654 at 51.5 s.

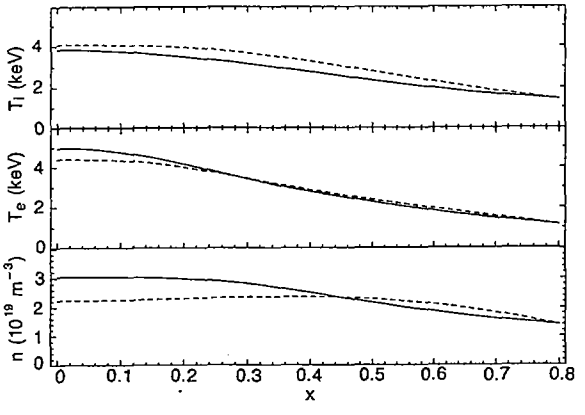

FIG. 2. Comparison between simulated profiles (solid lines) and TRANSP profiles (broken lines) as a function of normalized minor radius for ion temperature (top), electron temperature (middle) and density (bottom) for discharge #27658 at 55 s.

normalized minor radius), after 3s of simulation time. The experimental profile data were obtained from the interpretative code TRANSP. For the ion temperature, however, only measurements of $T_i(0)$ are available. The ion temperature profile data were calculated by the use of a neoclassical multiplier method [2]. The agreement between the predicted and experimental profiles is good, in particular for $r/a \geq 0.3$. In order to quantify the performance of the simulations, a root mean square deviation, σ, between the predicted and the experimental profiles was calculated. For pulse #27654, the rms deviations $\sigma_{Te}=0.09$ and $\sigma_n=0.21$ were obtained. The corresponding results for #27658 were

σ_{Te} =0.06 and σ_n =0.19. Hence, no systematic trend was found in the deviations between the weak field (high ρ_*) and the strong field (low ρ_*) cases (see Figs. 1-2), although only gyro-Bohm transport coefficients were used in the simulations whereas a Bohm-scaling was inferred from the experiments.

In Fig. 3, the ratios (3.4T to 1.7T) of the ion and the electron heat diffusivities as obtained in the simulations are shown as functions of the normalized minor radius. As observed, only close to the magnetic axis is a gyro-Bohm scaling observed ($\chi \sim B_T^{-1}$). In this region, however, the scaling is a result of the artificial diffusivities used in the simulations. Outside the inner core region,

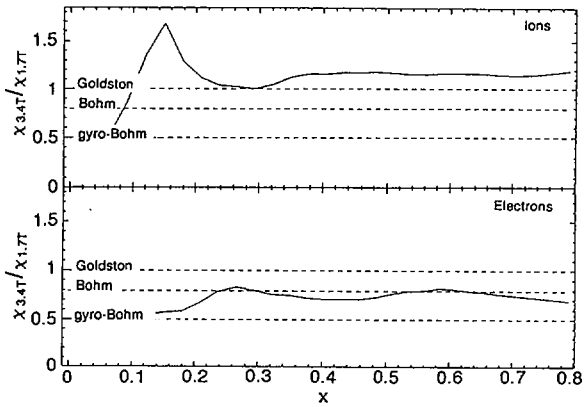

FIG. 3. High field (B = 3.4T) to low field (B = 1.7T) ratios of ion and electron thermal diffusivities as obtained in simulations. Ratios corresponding to gyro-Bohm, Bohm and Goldston scalings are indicated.

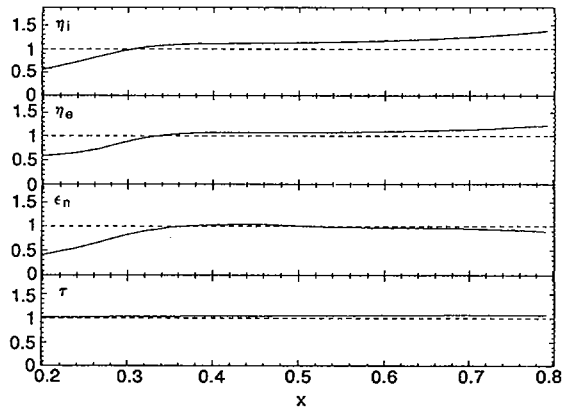

FIG. 4. High field (B = 3.4T) to low field (B = 1.7T) ratios of profile parameters $\eta_j = L_n/L_{Tj}$, $\epsilon_n = 2L_n/L_B$ and $\tau = T_e/T_i$ as obtained in the predictive simulations.

the electron diffusivity scales close to Bohm-like ($\chi \sim B_T^{-1/3}$) whereas the ion diffusivity scales slightly worse than Goldston-like ($\chi \sim B_T^{0}$).

The scalings observed in the simulations are due to small systematic variations in the other dimensionless parameters, assumed to be constant, between the low ρ_* and the high ρ_* pulses. This is displayed in Fig. 4 where the ratios (3.4T to 1.7T) of the relevant dimensionless profile parameters are given. Although the profiles of the two pulses are generally well matched, the ratios of the temperature gradient parameters $\eta_{i,e}$ show small but systematic departures from unity. This trend was also observed in the experimental data [2, Fig.5]. Although the imperfections in the dimensionless parameters are rather small, they have a large effect on the transport scalings due to marginal stability effects. For example, at the typical normalized radius r/a=0.4, the low field discharge have η_i=1.13 and η_e=1.51 in steady state (Fig. 2). The corresponding stability thresholds are given by $\eta_{i,th}$=1.04 and $\eta_{e,th}$=1.37 respectively, i.e. the profiles resides only approximately 10% above marginal stability. Hence, the reduction in transport expected with increasing magnetic field in the simulations is partly compensated by an increase in $\eta_{i,e}$ and a corresponding increase in the ITG- and CTE-mode transport in the high field discharge. We also note that the ion diffusivity is more strongly affected than the electron diffusivity in the simulations. This is likely to be the case also in the experiments since the electron temperature can be measured (and therefore matched) with better accuracy than the ion temperature profile.

The increase in $\eta_{i,e}$ in the high field discharge is due to edge effects which enter the simulations through the boundary conditions. The high field discharge has a lower edge temperature than expected from the similarity scaling $T \propto B^{2/3}$ and this leads to larger values of $\eta_{i,e}$ over the whole cross-section. While the profile effects are larger close to the edge, the deviation from marginal stability is smaller close to the axis thus causing a higher sensitivity in this region. Since the present simulations exclude the edge region, the reason for this deviation from self-similarity is not studied here. We note, however, that a degradation of edge confinement with increasing field has been observed in simulations of gyro-radius scaling experiments including edge transport from resistive modes [9]. Although the resistive modes scale gyro-Bohm-like, it was found that the edge transport appeared to scale worse than Bohm-like due to imperfections in edge parameters in the similarity scans. It seems that this result is related to the change in magnetic field in the similarity experiments. Hence, a change in ρ_* by increasing the system size may lead to a different result.

Work performed under JET Task Agreement NFR/TA4

REFERENCES

[1] WALTZ, R.E., DEBOO, J.E., ROSENBLUTH, M.N., Magnetic-field scaling of dimensionally similar tokamak discharges, Phys. Rev. Lett. **65** (1990) 2390.

[2] CHRISTIANSEN, J.P., et al., The scaling of transport with normalized Larmor radius in JET, Nucl. Fusion **33** (1993) 863.

[3] PERKINS, F.W., et al., Nondimensional transport scaling in the Tokamak Fusion Test Reactor: Is tokamak transport Bohm or gyro-Bohm? Phys. Fluids B **5** (1993) 477.

[4] PETTY, C.C., et al., Gyroradius scaling of electron and ion transport, Phys. Rev. Lett. **74** (1995) 1763.

[5] JARMÉN, A., ANDERSSON, R., WEILAND, J., Fully toroidal ion temperature gradient driven drift modes, Nucl. Fusion **27** (1987) 941.

[6] WEILAND, J., JARMÉN, A., NORDMAN, H., Diffusive particle and heat pinch effects in toroidal plasmas, Nucl. Fusion **29** (1989) 1810.

[7] NORDMAN, H., WEILAND, J., JARMÉN, A., Simulation of toroidal drift mode turbulence driven by temperature gradients and electron trapping, Nucl. Fusion **30** (1990) 983.

[8] FRÖJDH, M., et al., Comparison between JET profile data and the predictions of a transport model based on ITG and trapped electron modes: Interpretative comparison of heat fluxes and predictive comparison of profiles, Plasma Phys. Control. Fusion **38** (1996) 325.

[9] KINSEY, J.E., BATEMAN, G., Theory-based transport modeling of the gyro-radius experiments, Phys. Plasmas **3** (1996) 3344.

NONLINEAR ASPECTS OF THE NEOCLASSICAL THEORY OF PLASMA ROTATION AND EQUILIBRIUM BIFURCATIONS

A.L. ROGISTER
Institut für Plasmaphysik,
Forschungszentrum Jülich GmbH,
Association Euratom-KFA,
Jülich, Germany

Abstract

NONLINEAR ASPECTS OF THE NEOCLASSICAL THEORY OF PLASMA ROTATION AND EQUILIBRIUM BIFURCATIONS.

It is shown that large velocities and electric fields occurring in a thin layer are consistent with the revised neoclassical theory of the plasma edge. The latter includes finite Larmor radius effects and nonlinear drive of the poloidal rotation, as well as a momentum source term and momentum losses by charge exchange collisions. The description of the space and time evolution of the parallel flow velocity and the radial electric field is given by a nonlinear first order partial differential equation away from the singular layer, but by a nonlinear second order differential equation near to it. The occurrence of large local velocities and velocity shears may be identified with the trigger of the transport barriers and bifurcations from the low (L) to the high (H) energy confinement mode observed in tokamaks and stellarators. Most of the results which are presented are independent from the particular choice of boundary condition imposed on the last closed magnetic surface. A particular type of boundary condition is thoroughly discussed which leads: (i) to negative local values of the large radial electric field; (ii) to either aperiodic or periodic solutions according to the values of the various parameters here kept fixed (i.e. those describing the temperature, the density and the Z_{eff} profiles, as well as the charge exchange neutrals and the momentum injection rate). The results suggest that, under these conditions, steepening of the temperature profile after the transition from L to H confinement may ultimately lead to ELMy behaviour (type III ELMs) with ELM frequencies of the order of 10–20 s^{-1}.

1. DESCRIPTION OF THE THEORETICAL CONCEPTS

In view of the impact of improved confinement modes on economic fusion reactor designs, a large theoretical effort has been directed to clarifying the mechanisms which govern the transition from low (L) to high (H) confinement since the experimental discovery of the H mode in 1982 on the ASDEX tokamak [1]. At the heart of the scenarios which have been proposed however often lie unproven conjectures invoking anomalous processes or the questionable assumption of direct orbit losses.

We make use here of an in depth revision of neoclassical theory to prove that the ambipolar electric field and the parallel flow velocity must bifurcate from

smooth to strongly peaked edge profiles when a certain criterion – which will be explicitly given – is met; both the recycling properties (via charge exchange collisions) and the local temperature gradient (hence also the input power) are involved, as well as the density and Z_{eff} profiles. These results, which agree qualitatively with experiment [2] – the formation of a potential barrier being linked to an increased heat flow and/or to a reduced friction via charge exchange – are straightforward consequences of a generalized theory including finite Larmor radius (FLR) effects *in a systematic fashion* [3]; these remove the automaticity of the flow ambipolarity. Hence they contribute to the radial electric field and, opposing magnetic pumping, drive the poloidal rotation, mostly when and where the large electric field peak sets in. The sharp edge gradient and the associated large drift and parallel velocities also lead to nonlinear terms in the neoclassical ambipolarity constraint. These are precisely those nonlinearities that may lead to large peaks within the calculated profiles, the solutions being kept finite only by the FLR terms driving the poloidal rotation. Terms describing the role of an external momentum source as well as the plasma momentum lost to the walls via charge exchange are finally included in the equations, which have so far been obtained for the high collisionality (Pfirsch-Schlüter) regime only; although extension to the low collisionality (banana) regime is a great challenge, the results should not be qualitatively different.

The theory assumes, in its present form, that the evolution of the ambipolar electric field and of the parallel momentum can be dissociated from heat and ambipolar particle transport – the temperature, density and Z_{eff} profiles are actually frozen – with the understanding that a highly localized velocity shear will reduce or suppress anomalous transport. As a result of this assumption, the parallel flow velocity and the radial electric field are found to obey first order nonlinear partial differential equations in the absence of or away from the transport barrier. Near the latter, a multiple length-scale analysis leads to a second order nonlinear ordinary differential equation, of which the solution has to be matched.

The nonlinear first order differential equation admits two equilibrium solutions, of which one is unstable and violates causality. The radial electric field and the parallel flow velocity become proportional to the ion temperature gradient at a depth of a few gradient length-scales; the stable asymptotic electric field corresponds to the most positive of the two equilibrium solutions (the positive direction pointing outwards).

The most general solution of the nonlinear first order partial differential equation contains an arbitrary function $H[\tau - f(r)]$ in relation to which an *inward* propagation velocity can be identified. This feature – as well as the fact that the solution is independent from time at a depth of a few temperature gradient length-scales – suggests that the boundary condition has to be imposed at the LCMS, as intuition would also dictate. The boundary condition should encompass and reflect all the phenomena which occur at the transition between the scrape off layer (SOL) and the confined plasma; its physical content, which may depend on the geometry –

diverted or limited – is therefore not a trivial matter. We accordingly stress that all results mentioned so far are independent from the nature of the boundary condition.

To proceed further with theory, we now adopt a boundary condition, namely

$$U_{\|,i}^{-1}\frac{\partial U_{\|,i}}{\partial r}\bigg|_{LCMS} \equiv \left[\frac{\partial}{\partial r}\left(V+\frac{1+\eta_i}{e}T_i\right)\right]^{-1}\frac{\partial^2}{\partial r^2}\left(V+\frac{1+\eta_i}{e}T_i\right)\Big|_{LCMS} = C\,, \qquad (1)$$

which allows for two types of solutions, aperiodic and periodic, as determined by the form of the function $H\left[\tau - f(x)\right]$, according to the values of the parameters entering the problem; here $U_{\|,i}$ is the parallel flow velocity, V is the electric potential and $\eta_i \equiv (d\ell nT_i / dr):(d\ell nN / dr)$ is considered as being constant. If, for example, we let $C=0$, the assumption would be that the parallel velocity has an extremum at the LCMS, as well as the sum of the $\vec{E}\times\vec{B}$ and diamagnetic velocities. In the absence of any other compelling prescription, our choice has been motivated by the intuition that some of the edge localized modes – most likely type III ELMs [4] – which may occur in high confinement discharges are actually brief periodic H-L-H transitions, linked to a periodic character of the potential well responsible for the transport barrier. In our theoretical model, this periodic character is a consequence of the ambipolarity constraint for certain values of the fixed parameters (including those characterizing the temperature, density and Z_{eff} profiles); there are even conditions for which the equations admit no real solution, as discussed elsewhere [5]. In relation to type III ELMs, it is suggestive to note that the multi-dimensional parameter range in which periodic solutions obtain is contiguous to that in which large peaks are predicted within the profiles of the aperiodic solutions; large peaks occur recursively within the electric field and parallel velocity profiles of the periodic solutions themselves. When the conditions are fulfilled for the formation of a stationary potential barrier, the large radial electric field facing the LCMS is predicted to be *negative*; hence the negative potential well; the electric field is fairly small otherwise. These conclusions agree with the "numerous studies in DIII-D with co-injected neutral beams show(ing) that the only place in the plasma with a negative E_r is the transport barrier" [2]. Increasing the power and/or decreasing the charge exchange rate are found to favour the L to H transition, also as observed.

2. GOVERNING EQUATIONS

The validity of the generalized neoclassical equations obtained in [3] includes situations where the dimensionless parameters $\Lambda_1 \equiv \nu_i q^2 R^2 / \Omega_i r L_\psi$ and $\Lambda_2 \equiv \left(m_e / m_i\right)^{1/2}\left(qR\nu_i / c_i\right)^2$ are of order unity [qR is the connection length, L_ψ a relevant equilibrium radial length-scale, ν_i and Ω_i are the ion collision and gyro-frequencies, $c_i = \left(T_i / m_i\right)^{1/2}$ is their thermal velocity]. Λ_2 – which can be identi-

fied with the ratio of the energy equipartition and parallel heat conduction times – is generally smaller than unity; we let $\Lambda_2 \to 0$ hereafter.

$\Lambda_1 \sim \left[(cT_i / eB)/ rL_\psi\right]\left[\left(\chi_{\|,i} / N\right)/ q^2 R^2\right]$ – where $\chi_{\|,i}$ is the parallel heat conduction coefficient – is also mostly small, except near the transition barrier where the radial electric field E_r, the parallel velocity $U_{\|,i}$, and the poloidal and toroidal rotation speeds $U_{\theta,i}$ and $U_{\phi,i}$, vary rapidly. We shall accordingly also let $\Lambda_1 \to 0$ *at first.* We reintroduce $\Lambda_1 \neq 0$ when and where the solution of the resulting nonlinear first order partial differential equation is found to diverge and the radial length scales $L_\psi \equiv L_{U_{\|,i}}$ and $L_\psi \equiv L_{E_r}$ are sharply reduced; we then obtain *locally* a nonlinear second order ordinary differential equation.

As a consequence of the large parallel viscosity (note that $\eta_{0,i} = m_i \chi_{\|,i} / 4$), the parallel momentum equation of Ref. [3] leads – with $\Lambda_2 = \Lambda_1 = 0$ – to the well known high collisionality result (valid up to order $\varepsilon = r / R$):

$$U_{\theta,i} = \frac{B_\theta}{B} U_{\|,i} + \frac{B_\phi}{B} \frac{cT_i}{eB}\left(\frac{e}{T_i}\frac{\partial V}{\partial x} + \frac{\partial \ell n P_i}{\partial x}\right) = 0 \tag{2}$$

where P_i is the ion pressure and x measures the radial distance from the LCMS. The ambipolarity constraint – resulting from the action of FLR (i.e. gyroviscosity and inertia), charge exchange neutrals and a momentum source $\left(\dot{m}_{\|,i}\right)$ – reads

$$D^{-1}\left[\left(\frac{\partial}{\partial t} + \nu_{cx}\right)\frac{B_\theta}{B_\phi} U_{\|,i} - \frac{B_\theta}{B_\phi}\dot{m}_{\|,i}\right] = -\frac{4}{r}\frac{cT_i}{eB}\frac{\partial}{\partial x}\left(\frac{B_\theta}{B_\phi} U_{\|,i}\right) + \frac{1}{r}\left(\frac{B_\theta}{B_\phi} U_{\|,i}\right)^2$$

$$-\frac{2}{r}\left(3\frac{\partial \ell n N}{\partial x} + 2\frac{\partial \ell n T_i}{\partial x} - \frac{e\partial V}{T_i \partial x} + 2\frac{\partial \ell n D}{\partial x}\right)\frac{cT_i}{eB}\frac{B_\theta}{B_\phi} U_{\|,i}$$

$$+ D^{-1}\frac{1}{r}\frac{cT_i}{eB}\frac{1}{P_i}\frac{\partial}{\partial x}\left\{DP_i\frac{cT_i}{eB}\left[(1-2\eta_i)\frac{\partial \ell n N}{\partial x} - 5\frac{e\partial V}{T_i \partial x}\right]\right\} \tag{3}$$

where $$D(x) \equiv -1.25 q^2 N \chi_{\|,i}^{-1} \frac{cT_i}{eB} r \frac{\partial \ell n T_i}{\partial x} \tag{3'}$$

Introducing the dimensionless velocity and electric field

$$\hat{u}_{\|,s} f(x,t) = \left[(cT_i / eB)\partial \ell n T_i / \partial x\right]^{-1} B_\theta U_{\|,i} / B_o , \tag{4}$$

$$\hat{e}_{r,s} g(x,t) = -\left(\partial \ell n T_i / \partial x\right)^{-1} e\partial V / T_i \partial x , \tag{4'}$$

and assuming (for simplicity) temperature, density and Z_{eff} profiles of the form

$$T_i = T_{i,s}(\kappa x+1)^p, \quad N = N_s(\kappa x+1)^{p/\eta}, \quad Z_{eff} = Z_{eff,s}(\kappa x+1)^z \tag{5}$$

(the effective charge enters via the ion collision frequency), the *most general solutions* of Eqs. (2) and (3) can be cast in the form $\hat{u}_{\|,s} f(x,t) = \hat{u}_{1(2)} f_{1(2)}$ where $\hat{u}_{1(2)}$ are the two solutions of the algebraic equation

$$\hat{u}_{\|,s}^2 - \left(F\nu_{cx} - \frac{2}{\eta} - \frac{3}{2} + \frac{z-2}{p}\right)\hat{u}_{\|,s} - 3\left(\frac{2}{\eta}+1\right)\left(\frac{2}{\eta}+\frac{1}{2}+\frac{z-2}{p}\right) - \tilde{m} = 0 \tag{6}$$

and

$$f_{1(2)} = \left[c_{1(2)} - \hat{u}_{2(1)}(\kappa x+1)^{pc_{1(2)}} H_{1(2)}\right]\left[c_{1(2)} - \hat{u}_{1(2)}(\kappa x+1)^{pc_{1(2)}} H_{1(2)}\right]^{-1}. \tag{7}$$

Here, $c_{1(2)} = \hat{u}_{1(2)} - \hat{u}_{2(1)}$; $H_{1(2)}$ is an arbitrary function of $t^+ = t - \kappa p \int_0^x (\kappa x'+1) F(x') dx'$ which will be determined from the boundary condition; $F = -\tau D^{-1}$, with $\tau = \left[(cT_i / eB)\partial \ell n T_i / \partial x\right]^{-1} r$; $\tilde{m}_{\|,i} = \tau^2 D^{-1} B_\theta \dot{m}_{\|,i} / r B_o$. $F\nu_{cx}$ and $\tilde{m}_{\|,i}$ are assumed to be x–independent for commodity; the charge exchange rate coefficient $\langle \sigma v \rangle_{cx}$ varying slowly with T_i, the first assumption requires, strictly speaking, $N_0 \propto F^{-1} \propto (\kappa x+1)^{-\alpha}$ with $\alpha = p(0.5 - \eta^{-1}) + (2-z)$: that condition is compatible with the neutral density increasing outwards; the second assumption is not critical: $\tilde{m}_{\|,i}$ can be regarded as an average over the edge layer. Note also that the time-scale $F \equiv 3.2\left[\nu_i q^2 a_i^2 \left(\partial \ell n T_i / \partial x\right)^2\right]^{-1}$ would be about ten times longer than the local neoclassical energy conduction time $\left(1+1.6q^2\right) 2\nu_i a_i^2 T_i^{-1} \partial^2 T_i / \partial x^2$, if it were not that the divergence of the heat flow vanishes in leading order at the plasma edge.

The two solutions $f_1 \hat{u}_1$ and $f_2 \hat{u}_2$ are not independent: they go one into the other upon $H_1 H_2 = -\left(\hat{u}_1 - \hat{u}_2\right)^2 / \hat{u}_1 \hat{u}_2$. We shall thus only consider $f_1 \hat{u}_1$ hereafter and assume – without loss of generality – that $c_1 = \hat{u}_1 - \hat{u}_2 < 0$. We further note that

i) $\lim\left(x \to -\infty\right) f_1 = 1$; we conclude – cf. Eqs. (4) and (4') – that the toroidal velocity $U_{\phi,i} \cong B_\phi U_{\|,i} / B$ and the radial electric field E_r are proportional to $\partial T_i / \partial x$ far from the LCMS and converge to the most positive of the two equilibrium solutions compatible with the gradient, charge exchange and momentum injection forces; the other equilibrium solution violates causality;

ii) information propagates from the LCMS towards the interior since the equation $df[x(t),t]/dt = 0$ leads to $dx/dt = (\kappa x + 1)/F\kappa p < 0$ ($\kappa < 0$, $F > 0$);

iii) the solutions diverge when and where the denominator of Eq. (7) vanishes.

Assuming now Eq. (1) as boundary condition, i.e. $f^{-1}(\partial f/\partial x)_{x=0} = C - \kappa(p-1) = \zeta$, it is easy to show that $H_1(t^+) = H_0 + G(t^+)$, with

$$H_0 = \frac{\hat{u}_1 - \hat{u}_2}{2\hat{u}_1\hat{u}_2}\left[(\hat{u}_1 + \hat{u}_2) + \frac{\kappa p}{\zeta}(\hat{u}_1 - \hat{u}_2)^2\right] \tag{8}$$

and, either

$$G(t^+) = \frac{(\hat{u}_1 - \hat{u}_2)^2}{2\hat{u}_1\hat{u}_2}\Delta^{1/2}(co)\tanh\left(\frac{\zeta}{2\kappa p}\Delta^{1/2}\frac{t^+ - t_0}{F_s}\right), \tag{9a}$$

if $$\Delta \equiv 1 + 2\frac{\kappa p}{\zeta}(\hat{u}_1 + \hat{u}_2) + \frac{\kappa^2 p^2}{\zeta^2}(\hat{u}_1 - \hat{u}_2)^2 \tag{10}$$

is positive, or

$$G(t^+) = -\frac{(\hat{u}_1 - \hat{u}_2)^2}{2\hat{u}_1\hat{u}_2}(-\Delta)^{1/2}(co)\tan\left[\frac{\zeta}{2\kappa p}(-\Delta)^{1/2}\frac{t^+ - t_0}{F_s}\right] \tag{9b}$$

if Δ is negative; here $F_s = F(x=0)$ and t_0 is an arbitrary integration constant. Thus the solution $\hat{u}_1 f_1$ is aperiodic or periodic according to the sign of Δ.

3. TRANSPORT BARRIER

Equation (7) shows that a transport barrier may occur with any boundary condition. We shall here discuss the requirements for an aperiodic transport barrier corresponding to the boundary condition Eq. (1). As $t \to \infty$, f_1 goes into

$$\lim_{t\to\infty} f_1 = \left[X - \frac{c_1}{2\hat{u}_1}\left(-1 + \frac{\kappa p}{\zeta}c_1 + \sigma\Delta^{1/2}\right)\right]\left[X - \frac{c_1}{2\hat{u}_2}\left(1 + \frac{\kappa p}{\zeta}c_1 + \sigma\Delta^{1/2}\right)\right]^{-1} \tag{11}$$

where $\sigma = sign(\zeta/\kappa p)$ and $X = (1+\kappa x)^{-pc_1} - 1 \geq 0$. This expression diverges for some $x \in [0, -\infty]$ if the three conditions

$$\hat{u}_2 < 0 \quad , \quad \kappa p/\zeta > 0 \quad , \quad 1 + \kappa p(\hat{u}_1 - \hat{u}_2)/\zeta > 0 \tag{12}$$

are fulfilled simultaneously; we identify the occurrence of this divergence with the formation of the transport barrier. Returning to the general equations of Ref. [3], it can be shown that Eq. (2) actually breaks down in this zone, where a local two

length-scales analysis leads in fine to a nonlinear second order ordinary differential equation for either $U_{\parallel,i}$ or E_r.

For $\hat{u}_2$ to change sign, passing from a slightly positive to a slightly negative value as required by condition (12), the product

$$\hat{u}_1\hat{u}_2 = -3\left(\frac{2}{\eta}+1\right)\left(\frac{2}{\eta}+\frac{1}{2}+\frac{z-2}{p}\right)-\tilde{m}$$

must pass from 0^- to 0^+. This might be achieved either by increasing η or, for $z<2$, by decreasing the profile index p. Both trends might result from an increase of the heating power if κ simultaneously increases (N.B.: $L_{T,s}^{-1}=\kappa p$). The sum

$$\hat{u}_1+\hat{u}_2 = F\nu_{cx}-\frac{2}{\eta}-\frac{3}{2}+\frac{z-2}{p}$$

must further be negative, requiring that ν_{cx} be smaller than a certain critical value.

We assume here, for order magnitude estimates, the following values: $T_{i,s}$ = 64 eV, $(NZ_{eff})_s = 0.66 \times 10^{13}$ cm^{-3}, B = 2 Tesla, q = 4, $\eta = 2$, (2-z)/p = 2, and, at first $L_{T,s}$ = 3 cm; thus F = 0.090 s. Equilibrium bifurcation $\left(\hat{u}_1+\hat{u}_2 \le 0\right)$ is forbidden – even if the second and third conditions under (12) are fulfilled – if the flux surface averaged neutral density at the LCMS, $N_{0,s}$, is larger than 1.15×10^9 cm^{-3}. $L_{T,s}$ and $F \propto L_T^2$ decrease after the transition has occurred; $\hat{u}_1\hat{u}_2$ then becomes more positive and $\hat{u}_1+\hat{u}_2$ more negative: the plasma remains in the H mode of confinement. Simultaneously, however, Δ [Eq. (10)] decreases and eventually changes sign. The solution then becomes periodic – perhaps a type III ELMy H-mode–. The ELMs frequency may be estimated by assuming now $L_{T,s}$ = 1 cm, $\Delta = -1$, $2\kappa p/\zeta = 1$: thus $f = (2\pi)^{-1}\,(\zeta/2\kappa p)\,(-\Delta)^{1/2}\,F_s^{-1}$ = 16 hz, which is comparable to the lowest ELM frequencies mentioned by Burrell et al. [6].

ACKNOWLEDGEMENTS

N. Antonov has participated in the early stages of this research.

REFERENCES

[1] WAGNER, F., et al., Phys. Rev. Lett. **49** (1982) 1408.
[2] BURRELL, K.H., et al., Plasma Phys. Control. Fusion **34** (1992) 1859 and references therein.
[3] ROGISTER, A., Phys. Plasmas **1** (1994) 619.
[4] COSTER, D.P., et al., Contrib. Plasma Phys. **36** (1996) 150.
[5] ROGISTER, A., ANTONOV, N., Contrib. Plasma Phys. **36** (1996) 182.
[6] BURRELL, K.H., et al., Plasma Phys. Control. Fusion **31** (1989) 1649.

EFFECT OF WEAK/NEGATIVE MAGNETIC SHEAR AND PLASMA SHEAR ROTATION ON SELF-ORGANIZED CRITICAL GRADIENT TRANSPORT IN TOROIDAL PLASMAS — FORMATION OF INTERNAL TRANSPORT BARRIER

Y. KISHIMOTO, J.-Y. KIM, T. FUKUDA,
S. ISHIDA, T. FUJITA
Naka Fusion Research Establishment,
Japan Atomic Energy Research Institute,
Naka-machi, Naka-gun, Ibaraki-ken, Japan

T. TAJIMA, W. HORTON, G. FURNISH,
M.J. LeBRUN
Institute for Fusion Studies,
University of Texas at Austin,
Austin, Texas,
United States of America

Abstract

EFFECT OF WEAK/NEGATIVE MAGNETIC SHEAR AND PLASMA SHEAR ROTATION ON SELF-ORGANIZED CRITICAL GRADIENT TRANSPORT IN TOROIDAL PLASMAS — FORMATION OF INTERNAL TRANSPORT BARRIER.

It is becoming increasingly clear that anomalous transport in an L mode tokamak plasma is dominated by radially extended non-local modes in a toroidal geometry. This indicates that various improved modes such as the internal transport barrier (ITB) being formed in a recent JT-60U negative shear experiment can be achieved by suppressing such a global structure of the toroidal mode. The role of plasma shear rotation and negative/weak magnetic shear on these non-local modes is studied by employing the authors' toroidal simulation code, together with a non-local theory. From simulations, in addition to the overall reduction of the wave excitation in the entire negative magnetic shear region, it is found that the weak or zero magnetic shear which appears near the q-minimum surface breaks up the toroidal coupling. This leads to a discontinuity (or gap) in the global mode at the q minimum surface, leading to the emergence of the ITB. The plasma shear rotation which is observed in the experiment enhances the discontinuity so that the performance of the ITB is increased.

1. INTRODUCTION

The turbulent structure of drift waves in a toroidal geometry is becoming clearer because of recently developed toroidal simulation [1–3] and theory [4, 5]. According to these studies, the drift modes in a toroidal geometry form a radially extended non-local structure whose correlation length Δr is given by

$$\Delta r \simeq (\rho_i L)^{\alpha} \quad \text{with } \alpha \simeq 0.5 \tag{1}$$

i.e. the geometrical mean between the ion Larmor radius ρ_i and the equilibrium scale length L (such as $L \sim a$, the plasma minor radius or $L \sim L_T \equiv -(\partial \ln T_i/\partial r)^{-1}$, the ion temperature scale length). Such a non-local mode shows a twisted thin eddy structure with up-down asymmetry characterized by a finite tilted poloidal angle θ_0 from the midplane ($\theta_0 = 0$) (θ_0 is the Bloch shift parameter, which represents the most unstable poloidal angle as we shall discuss later). The basic characteristics in a typical L mode such as (i) Bohm-like diffusion, (ii) radially increasing fluctuation and heat diffusivity, (iii) near marginal properties and (iv) profile resilience are found to belong to one physical category which originates from the non-local mode [2]. This understanding leads to the strategy that improved modes can be achieved by suppressing such a mode structure. In this paper, in order to obtain improved modes, we investigate the role of plasma shear rotation and negative/weak magnetic shear in these non-local modes using toroidal numerical simulation and also theory. Specifically, we present a model of the internal transport barrier (ITB) as formed in recent JT-60U reversed shear experiments [5, 6] and perform a toroidal particle simulation. Negative magnetic shear actually has a stabilizing effect on the toroidal drift mode, but not enough to form an ITB that is sharply localized in space. We have found that the weak and/or zero magnetic shear breaks up the toroidal coupling and the associated global mode structure characterized by Eq. (1), leading to a *discontinuity* (or *gap*) in the mode excitation inside and outside the q minimum (q_{min}) surface. Specifically, the weak and/or zero magnetic shear plays a crucial role in forming the ITB.

2. SCALING STUDY OF THE RADIALLY EXTENDED NON-LOCAL MODE BY A GLOBAL TOROIDAL PARTICLE SIMULATOR

As was discussed in Section 1, our model of the improved mode is based on Eq. (1) in an L mode plasma where the transport is anomalous. The scaling given by Eq. (1) was investigated for a rather small scale tokamak of a size around $a/\langle\rho_i\rangle \sim 50$–$150$, where $\langle\rho_i\rangle$ is the Larmor radius averaged over the system. In order to computationally confirm the scaling for a realistic tokamak size, we investigate the dependence of the radial correlation length Δr on the size $a/\langle\rho_i\rangle$ by using the GTS (generalized tokamak simulator) code [7] with $a/\langle\rho_i\rangle$ as large as 500. In the GTS, we employ gyrokinetic ions, but electrons are treated adiabatically. We assume a circular cross-section with a normal q profile and shear as is used in Ref. [1], although the GTS supports an arbitrary shape for the tokamak cross-section. The density and temperature profiles are chosen so that $\eta_i \simeq L_n/L_T = 4$ is satisfied over the minor radius; we measure the correlation length of the excited waves both from the instantaneous radial mode width and also from the radial power spectrum distribution, $S(\omega, r)$, which is calculated by the time average. The results of these measurements are presented in Fig. 1. We note the very clearly increasing tendency of $\Delta r/\langle\rho_i\rangle$ over the entire $a/\langle\rho_i\rangle$ range, indicating that the correlation length

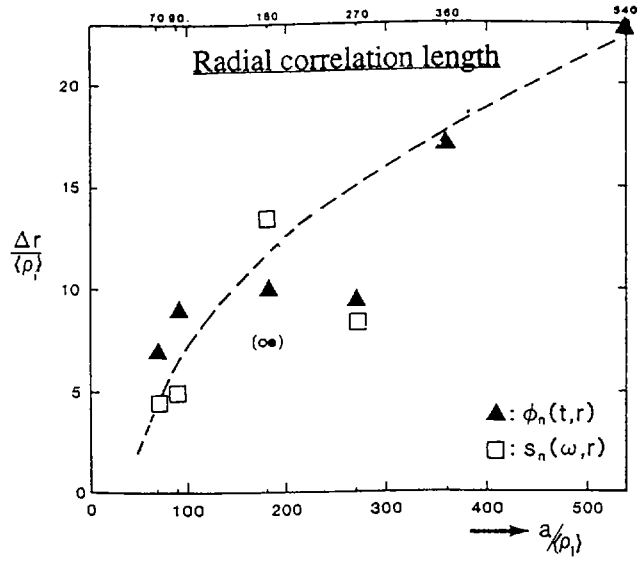

FIG. 1. Scaling of $\Delta r/\langle\rho_i\rangle$ with $a/\langle\rho_i\rangle$ for η_i. The q profile is a monotonic function with q(0) = 0 and q(a) = 3.3.

roughly scales by $\alpha \simeq 0.5$ in Eq. (1). On the other hand, $\Delta r/\langle\rho_i\rangle \simeq$ const should have been observed if Δr were related to the local gyroradius as $\Delta r \simeq \langle\rho_i\rangle$. Thus, it is confirmed that the radially extended non-local toroidal mode described by Eq. (1) is actually excited at a high toroidal mode number around n $\simeq$ 50–60 and is responsible for the basic characteristics of the anomalous tokamak transport.

3. EFFECT OF TOROIDAL SHEAR FLOW ON NON-LOCAL TOROIDAL MODE

In JT-60U discharges it is observed that, before and during ITB formation, typically, a large toroidal flow of the order of $V_\phi \sim 10^5$ m/s exists. This flow is considered to result from the external momentum input in the parallel direction or from the $\mathbf{E} \times \mathbf{B}$ drift with a radial electric field generated by the ripple loss of fast particles. The effect of the plasma shear flow on the non-local ITG mode with the correlation length given by Eq. (1) was first investigated by using toroidal particle simulation. The shear flow was found not only to reduce the mode growth rate, but also to shrink the mode width, changing the transport characteristics from $\alpha \simeq 0.5$ (Bohm) to $\alpha \simeq 0$ (gyro-Bohm) [1, 2]. To check the possibility of the ITB being triggered by the flow shear, we here present an estimate of the effect of flow shear on the toroidal ITG mode.

For this estimate we utilize the formula developed from our recent work which takes into account the first order envelope effect of the background plasma profile [8]. It is shown there that in linearly varying equilibrium profile plasmas such as the shear flow plasma, the maximum growth rate mode has an angle of poloidal asymmetry:

$$\pm(\theta_0)_{max} \simeq \pm|\delta|^{1/3} = \pm\left|\frac{\omega_r'}{2nq'\hat{\gamma}_0}\right|^{1/3} = \pm\left|\frac{\omega_r'/\hat{s}}{2k_\theta\hat{\gamma}_0}\right|^{1/3} \tag{2}$$

with a corresponding growth rate of $\gamma \sim \hat{\gamma}_0 \cos\theta_0$, where $\omega_r' = \partial\omega_r(r)/\partial r$ with real frequency ω_r in non-shear flow plasma. The $\pm$ sign in Eq. (2) corresponds to the cases $\omega_r'/\hat{s} > 0$ and $\omega_r'/\hat{s} < 0$, respectively. Note that for a given ω_r', the tilted poloidal angle θ_0 changes its sign, depending on the sign of the magnetic shear $\hat{s}$. The effect of plasma flow comes through the Doppler shift of ω_r to $\omega_r + \omega_f$ with $\omega_f(x) = k_\theta V_\phi - k_\theta V_\theta$, where V_ϕ and V_θ are the toroidal and poloidal flow velocities, respectively. The angle of poloidal asymmetry given by Eq. (2) then rotates to

$$(\theta_0)_f \simeq \pm\left|\frac{\omega_r' + \omega_f'}{2nq'\hat{\gamma}_0}\right|^{1/3} = (\theta_0)_{max}\left|1 + \frac{\omega_f'}{\omega_r'}\right|^{1/3} \tag{3}$$

with a growth rate of $\gamma \sim \hat{\gamma}_0 \cos(\theta_0)_f$. It is found from Eq. (3) that the growth rate is effectively reduced when ω_f' has the same sign as ω_r'. The toroidal mode is significantly stabilized when the flow shear makes $|\theta_0| \geq \pi/2$ or roughly $\delta = \omega_f'/2nq'\hat{\gamma}_0 \sim 1$, assuming $|\omega_f'| \gg |\omega_r'|$. Here, we note that δ is inversely proportional to the magnetic shear $\hat{s}$; so the flow shear effect is enhanced in the weak magnetic shear regime.

Using the above formula, we now present an estimate of the shear flow effect for a JT-60U negative shear discharge [5, 6]. With the approximate values of $V_\phi \sim 1 \times 10^5\ m \cdot s^{-1}$, $L_{V_\phi} \sim 30$ cm, $k_y\rho_i \sim 0.3$, $R \sim 3$ m, and $n \sim 50$ for the mode with $k_y\rho_i \sim 0.3$, the toroidal flow shear is estimated to be $\omega_f' = (n/R) \times (V_\phi/L_{V_\phi}) \sim 5 \times 10^4\ s^{-1} \cdot cm^{-1}$, while the growth rate $\hat{\gamma}_0$ is roughly $\hat{\gamma}_0 \sim \omega_{Di} \simeq 2k_y\rho_i v_i/R \sim 1 \times 10^5\ s^{-1}$. We then have $\delta \sim 0.25/\hat{s}$, which indicates that δ becomes of the order of one when the magnetic shear $\hat{s}$ is smaller than 0.25. We thus see that strong stabilization can occur from the toroidal flow shear effect in the weak shear region. This result suggests that the toroidal flow shear can be a trigger for ITB formation, even though a more careful study is necessary for a really thorough conclusion.

4. EFFECT OF NEGATIVE/WEAK MAGNETIC SHEAR ON THE NON-LOCAL TOROIDAL MODE

It had been well known that negative shear has a strong stabilizing effect on the ideal MHD ballooning mode. It was indeed this fact which made the negative shear

regime attractive for the high β plasma. Meanwhile, it was not so clear whether negative shear could have a similar strongly stabilizing effect on microinstabilities such as the toroidal ITG mode and/or the trapped electron mode, which are widely believed to be responsible for anomalous transport. In order to investigate the effect of negative/weak magnetic shear on the non-local toroidal ITG mode, with some theoretical considerations, we here perform a toroidal particle simulation by employing the TPC to two topologically different magnetic configurations, i.e. (a) the linear q profile and (b) the parabolic (reversed) q profile, which has a minimum q (q_{min}) and then a zero shear region. In this paper, we concentrate on the linear stage where the toroidal modes have well separated quantum numbers.

4.1. Linear q profile case

Figure 2 shows the linear growth rate of the electrostatic potential as a function of magnetic shear at r = a/2. The potential contour in the (r, θ) poloidal cross-section is also shown for different values of $\hat{s}$, i.e. (a) the normal shear case of $\hat{s} \simeq 1.3$, (b, c) the weak positive and negative cases with $\hat{s} = \pm 0.15$ and $\hat{s} = -0.15$, respectively. For the normal shear case, a typical non-local toroidal mode which has a pronounced ballooning structure with up–down asymmetry as determined by Eq. (2) is excited. The maximum growth rate occurs at around $\hat{s} = 0.5$–1.0, and, with a decrease in the magnetic shear, the growth rate decreases and the radial mode width shrinks. In the negative shear region ($\hat{s} < 0$), the mode is more weakly excited than in the positive case, indicating a stabilizing effect from negative shear. The reduction of the growth rate at $|\hat{s}| > 1$ is predicted from a local analysis of the dispersion, which assumes ballooning asymmetry in the mode equation and essentially comes

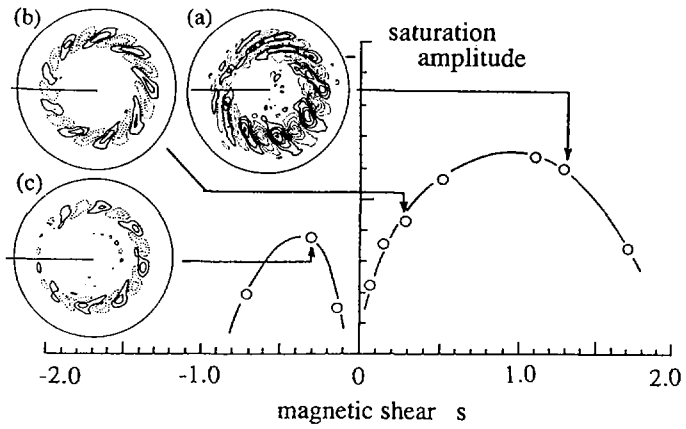

FIG. 2. Saturation amplitude of electrostatic potential obtained by TPC as a function of global magnetic shear on the assumption of a linear q profile. Diagrams (a) to (c) represent the potential contours in the poloidal cross-section for different values of magnetic shear.

from the $\hat{s}$ dependence on the magnetic drift term, i.e. $\omega_d \simeq \hat{\omega}_d'[\cos\theta + \hat{s}(\theta - \theta_0) \times \sin\theta]$. However, this effect is continuous around the zero shear region, and no drastic change happens if we rely on local analysis.

On the other hand, in the global simulation (Fig. 2), the mode is strongly stabilized around the weak shear region ($|\hat{s}| < 0.2$), and this qualitatively suggests the existence of a transport barrier around $\hat{s} \simeq 0$. This strongly stabilizing effect comes from the weakening of the toroidal coupling around $\hat{s} \simeq 0$. Specifically, in the local calculation of the microinstability utilizing a zeroth order ballooning representation, the mode localized at a rational surface is assumed to be tightly coupled to the adjacent sidebands, satisfying the condition

$$(\Delta r)_{s.m.} > (\Delta r)_{r.s.} \tag{4}$$

where $(\Delta r)_{r.s.} = 1/sk_\theta$ and $(\Delta r)_{s.m.}$ represent the interval of adjacent rational surfaces and the typical mode width of slab harmonics, respectively. In the incompressible limit, for example, we can calculate from the ITG mode equation that $(\Delta r)_{s.m.} \simeq \alpha\rho_i/\sqrt{s}$, where $\alpha \simeq \sqrt{q/\omega_d\gamma\omega}$ is typically O(1). Note that the formation of a well defined non-local toroidal mode with $\Delta r \sim (\rho_i L)^{1/2}$ is only possible when Eq. (4) is satisfied. The breakdown of the toroidal coupling then occurs for a weak magnetic shear of $|\hat{s}| < 1/(\alpha k_\theta \rho_i)^2$.

A milder but more explicit criterion for the breakdown of toroidal coupling may be obtained if we replace the mode width by the global width of the toroidal mode in the above condition. Note the global width of a toroidal mode will always be larger than the radial width of the Fourier harmonics of which it consists. Then, since the global width of toroidal ITG modes is typically given by $(\Delta r)_{g.m.} \sim (L\rho_i/\hat{s})^{1/2}$, adding the magnetic shear effect to Eq. (1), the breakdown condition of the toroidal coupling, $(\Delta r)_{g.w.} \leq (\Delta r)_{r.s.}$, then yields

$$s \leq \frac{\rho_i}{L} \frac{1}{(k_y\rho_i)^2} \tag{5}$$

From the simulation shown in Fig. 2, breaking of the toroidal coupling is expected for $|s| \leq 0.25$. For the JT-60U negative magnetic shear discharge in Ref. [5], $L \simeq L_{Ti} \sim 15$ cm, and $\rho_i \simeq 0.3$ (deuterium with $T_i \simeq 5$ keV) in the ITB region, we then obtain the breaking condition $\hat{s} \leq 0.22$, assuming $k_\theta\rho_i \simeq 0.3$. The radial extent δr, which covers the condition $\hat{s} \leq 0.22$ in the experiment, is estimated to be $\delta r \simeq 6$ cm, which is of the same order as the barrier width. Thus, it is expected that the excitation of the non-local toroidal mode is suppressed in the ITB region.

4.2. Parabolic q profile case

Here, we model the reversed shear experiment by choosing a parabolic q profile as shown Fig. 3(a), which has a minimum q [i.e. $q(r_{min}) = q_{min}$] inside the plasma

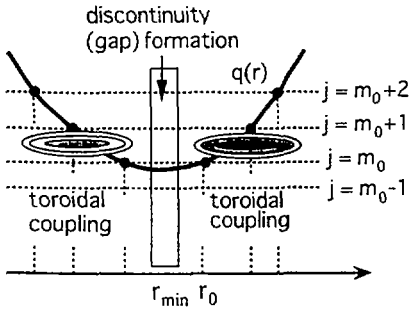

FIG. 3. Relation between reversed q profile and mode rational surface. The existence of a discontinuity/gap for mode excitation at the q minimum surface is shown schematically.

column. Note that for the toroidal mode number n, the poloidal harmonic given by $j = m_0$ has two rational surfaces around $r = r_{min}$, but no rational surface for the harmonics with $j \leq m_0 - 1$. In the simulation, we change the location of q_{min} under the fixed temperature profile which provides an unstable ITG mode as observed in Fig. 2(a) [$\hat{s} = 1.3$ case]. Before we show the simulation results, let us consider how the usual ballooning symmetry property breaks up in a situation such as that shown in Fig. 3(a). The basic equation describing the above toroidal coupling of the harmonics is given by

$$\frac{\partial^2 \phi_m}{\partial x^2} + [\beta_1 (x - 1 - \ell)^2 + \beta_2]\phi_m + \lambda(\phi_{m+1} + \phi_{m-1}) = 0 \qquad (6)$$

where $m = m_0 + \ell$ with $m_0 = nq(r_0)$ and $x = nq'(r_0)(r - r_{min})$ with $nq'(r_0)(r_0 - r_{min}) = 1$ are used. The second term on the left hand side of Eq. (6) represents the magnetic shear which determines the radial structure of the slab harmonics, while the last term gives the toroidal coupling of these slab harmonics. In a typical plasma region with finite shear, owing to the second term, the slab harmonics have the structure $\phi_m(x) \sim \Phi(x - m)$, with their local eigenvalues being almost identical. This similarity of slab harmonics, i.e. the *ballooning symmetry*, enables the existence of a toroidal coupling.

Let us now consider how the above property is changed near the local minimum of the q profile. As is shown in Fig. 3(a), it is first observed that there is no rational surface for the harmonics with $j \leq m_0 - 1$. This means that it is no longer possible to have the form $\phi_j = \Phi(x - j)$ for the mode $j \leq m - 1$ and the ballooning symmetry is thus broken for $j \leq m - 1$. Therefore, toroidal coupling becomes difficult below $m - 1$ and will result in the rapid decay of the amplitude of the corresponding poloidal harmonics. As is shown in Fig. 3(b), it is then expected that a discontinuity and/or a gap at the q minimum surface in the global mode structure occur.

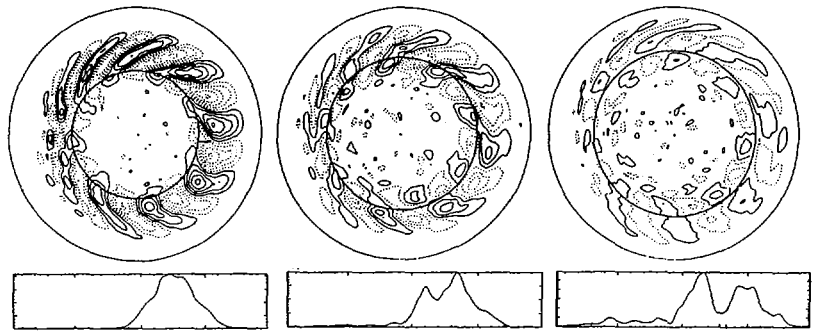

FIG. 4. Potential structure in poloidal cross-section and corresponding radial profile for reversed (parabolic) q profile for three different q minimum locations (solid lines in the figure): (a) $\bar{r}_{min} = 0.5$; (b) $\bar{r}_{min} = 0.6$; (c) $\bar{r}_{min} = 0.65$. The parameters except for q profile and shear are the same as in Fig. 2. The location of the maximum pressure gradient r_* is around $r_* \simeq 0.6$ and $r_* \simeq r_{min}$ in case (b).

(a) Simulation result (without shear flow): In the toroidal simulation, the q profile is chosen as $q(r) = q_{min} + c_1(\bar{r} - \bar{r}_{min})^2$, where $\bar{r} = r/a$ and $q_{min} = 0.888$ and $c_1 = 6.45$, so that $m = 8$ has two rational surfaces around the 9 mm surface, but no rational surface for $m = 7$. In Fig. 4, we show the potential contours of the linear ITG mode together with its radial profile for different locations of q_{min}, i.e. $\bar{r}_{min} = 0.5$ (a), $\bar{r}_{min} = 0.6$ (b), and $\bar{r}_{min} = 0.65$ (c), respectively, and the corresponding q_{min} surfaces are also shown. We here define the location of the maximum amplitude of the electrostatic potential for the normal shear case by $r = r_*$, which approximately corresponds to the location of the 'maximum pressure gradient' for the ITG mode and is roughly estimated from Fig. 2(a) as $\bar{r}_* \simeq 0.6$. As is seen in Fig. 4(a), when the q minimum point is located inside $r = r_*$ (i.e. $r_{min} < r_*$), non-local toroidal modes are clearly excited outside the q minimum surface, but are almost stabilized inside. When r_{min} begins to coincide with the 'maximum pressure gradient' point as is shown in Fig. 4(b), the overall wave excitation (growth rate and saturation amplitude) is weakened compared with the case of Fig. 4(a), which is interpreted as the result of the stability effect of the negative/weak shear as shown in Fig. 2. Furthermore, as is seen in Fig. 4(b), mode excitation is found to be separated inside and outside the plasma column across the q minimum surface. This indicates the existence of a *discontinuity* and/or a *gap* in toroidal coupling, and, as a result, the formation of the global mode is prevented. It is also found that, since $\omega_r' \simeq \omega_d' < 0$, and then $\omega_r'/\hat{s} > 0$ and $\omega_r'/\hat{s} < 0$ inside and outside the q minimum surface, respectively, the poloidal tilt angle providing the maximum growth rate $(\theta_0)_{max}$ changes the sign from (+) to (-) across the q minimum surface, according to the discussion following Eq. (2); this is actually confirmed by Fig. 4(b). We note that weak coupling connecting the inside and the outside across the q minimum surface

is also shown, constructing a twisted, but radially extended mode around $|\theta| \simeq \pi/2$. Such a weak mode coupling across the q minimum surface is a result of the excitation of the non-resonant mode $\phi_j = m_0 - 1$ (in this case, $j = 7$) as is shown in Fig. 4(a). Specifically, $\phi_{j=m_0-1}$ is dominated by the equation

$$\frac{\partial^2 \phi_{m_0-1}}{\partial x^2} + [\beta_1(\bar{c}_1 x^2 + \bar{c}_2)^2 + \beta_2]\phi_{m_0-1} + \lambda[\phi^{(L)}_{m_0}(x) + \phi^{(R)}_{m_0}(x)] = 0 \qquad (7)$$

where $\bar{c}_1 = c_1/(nq')^2$ and $\bar{c}_2 = nq_{min} - (m_0 - 1)$. Here, $\phi^{(L)}_{m_0}(x)$ and $\phi^{(R)}_{m_0}(x)$ in Eq. (7) are the wave functions of $j = m_0$ with a rational surface on the left and right hand sides of the q minimum surface, respectively. The mode $\phi_{m_0-1}(x)$ actually suffers damping from the second term of the left hand side in Eq. (7), owing to the non-vanishing nature of the parallel wavenumber, but it can still be excited by coupling with $\phi^{(L)}_{m_0}$ and $\phi^{(R)}_{m_0}$ through the third term on the right hand side of Eq. (7). In other words, this implies that the wave functions $\phi^{(L)}_{m_0}$ and $\phi^{(R)}_{m_0}$ which have a rational surface on both sides of the q minimum surface can be coupled with each other through the non-resonant mode ϕ_{m_0-1}. In the simulation, we have actually observed the excitation of the $m = 7$ mode. Since such a coupling is expected to be weak, the plasma shear rotation (both toroidal and poloidal) as observed in JT-60U is expected to severely affect the coupling between ϕ_{m_0-1}, $\phi^{(R)}_{m_0}(x)$ and $\phi^{(L)}_{m_0}(x)$.

When the q minimum surface moves outside the 'maximum pressure gradient' (i.e. $r_{min} > r_*$), it is not only the wave excitation that is further suppressed, but also the discontinuity (or the gap) becomes much clearer as is seen in Fig. 4(c). This results from the fact that the non-resonant mode $\phi_{m_0-1}(x)$ described by Eq. (7) is strongly damped. Since the toroidal mode is independently excited inside and outside the q minimum surface, each mode has a different eigenfrequency determined by the local plasma parameter. Since $\omega \sim \omega_d \propto T_i/r$, assuming $q(r) \sim q_{min}$, the angular velocity of the mode rotation in the inside region (positive poloidal direction) is faster than that outside.

(b) Simulation result (with shear flow): Figure 5 shows the result when the radial electric field $E_r(r) = (\langle T_i \rangle/ea)\beta(\bar{r} - 0.5)$ [$\beta = -3.125$(a) and $\beta = +3.125$(b)] and then the poloidal shear flow $V_\theta(r) = cE_r(r)/B$ are applied to the case of Fig. 4(b). It is found that in the case of (a), as discussed in Eq. (3), $\omega_r'/\omega_i' > 0$ is satisfied and then the tilt angle is enhanced inside ($\theta_0 > 0$) and outside ($\theta_0 < 0$) the q minimum surface so that the discontinuity is emphasized. On the other hand, in case (b), since $\omega_r'/\omega_i' < 0$, the tilt angle is reduced on both sides across the q minimum surface. Then, as is seen in Fig. 5(b), the discontinuity is weakened (or even disappears) so that the mode is excited across the q minimum surface although the amplitude is much reduced with respect to the case without flow. Thus, the direction of flow shear is essential for sustaining the discontinuity. Let us note that the shear flow observed in the JT-60U experiment corresponds to the case of Fig. 5(a), so that the discontinuity is sustained.

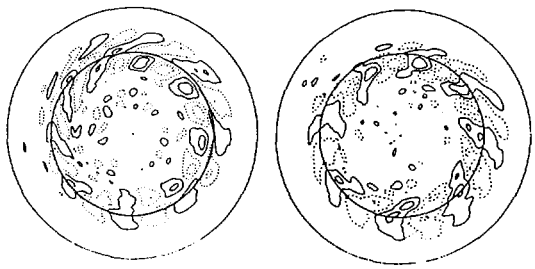

FIG. 5. Potential structure in poloidal cross-section in the presence of a poloidal shear flow induced by the radial electric field for (a) $\beta = -3.125(\omega_*'/\omega_f' > 0)$; (b) $\beta = +3.125(\omega_*'/\omega_f' < 0)$.

The gap width will depend on the toroidal mode number n or the rational surface interval, becoming smaller with increasing n. When we approximate the gap width by an interval between rational surfaces, we have $(\Delta r)_{gap} \sim (\Delta r)_{r.s.} \simeq 1/sk_y$. For a JT-60U discharge with $\rho_i \sim 0.3$ cm near the ITB, $(\Delta r)_{gap}$ provides almost the same value for the radial extent where the condition $|\hat{s}| \leq 0.22$ is satisfied. Thus, the observed discontinuity (or gap) plays a crucial role in forming the ITB near the q minimum region, together with the general tendency of reduction in growth rate associated with weak/negative magnetic shear.

5. CONCLUSIONS

The radially extended non-local modes are confirmed to be actually excited in an L mode plasma via the gyrokinetic GTS, in which realistic plasma parameters are chosen. Various improved confinement modes can be achieved by suppressing this non-local (global) mode character by changing from $\alpha \simeq 0.5$ (Bohm like) to $\alpha \simeq 0$ (gyro-Bohm like) in a mode width of $\Delta r = \rho_i^{1-\alpha} L^{\alpha}$. Negative shear plays a role in reducing the mode activity through a change in the toroidal magnetic drift, which is, however, not sufficient to explain the sharply changing nature of the internal transport barrier (ITB). The weak or zero magnetic shear which appears near the q minimum surface breaks up the toroidal coupling, leading to a discontinuity (and/or a gap) in the radially extended non-local mode. The q minimum surface thus behaves as a singular surface so that the mode activities between inside and outside the q minimum surface are separated. This is considered to be basically the origin of ITB formation. It is also found that the discontinuity (or gap) efficiently works as a thermal barrier when the q minimum surface is located just outside the maximum pressure gradient, which is consistent with the experimental results [5, 6]. The shear flow structure is found to enhance the character of the discontinuity when the flow shear is in the same direction as the mode rotation as in the case of the experiment [5, 6] and to significantly suppress the mode activity in the gap region. As a result, strong stabilization near the q_{min} surface is achieved.

ACKNOWLEDGEMENTS

The authors acknowledge M. Kawanobe for supporting the simulation work. This work was supported by JAERI and USDOE.

REFERENCES

[1] KISHIMOTO, Y., et al., in Plasma Physics and Controlled Nuclear Fusion Research 1994 (Proc. 15th Int. Conf. Seville, 1994), Vol. 3, IAEA, Vienna (1995) 299.
[2] KISHIMOTO, Y., TAJIMA, T., HORTON, W., LeBRUN, M.J., KIM, J.-Y., Phys. Plasmas **3** (1996) 1289.
[3] PARKER, S.E., LEE, W.W., SANTORO, R.A., Phys. Rev. Lett. **71** (1993) 2042.
[4] CONNOR, J.W., TAYLOR, J.B., WILSON, H.R., Phys. Rev. Lett. **70** (1993) 1803; KIM, J.Y., WAKATANI, M., Phys. Rev. Lett. **73** (1994) 2200.
[5] KIMURA, H., JT-60 TEAM, Phys. Plasmas **3** (1996) 1943.
[6] FUJITA, T., et al., IAEA-CN-64/A1-4, these Proceedings, Vol. 1, p. 227.
[7] FURNISH, G., Gyrokinetic Simulation of Tokamak Turbulence and Transport in Realistic Geometry, Rep. IFSR-740, Univ. Texas, Austin (1996).
[8] KIM, J.-Y., KISHIMOTO, Y., WAKATANI, M., TAJIMA, T., Phys. Plasmas **3** (1996) 1712.

CONTROL OF TRANSPORT BARRIERS AND THE PHYSICS OF THE TRANSPORT β LIMIT

A. FUKUYAMA
Faculty of Engineering,
Okayama University,
Okayama

M. YAGI, S.I. ITOH
Research Institute for Applied Mechanics,
Kyushu University,
Kasuga, Fukuoka

K. ITOH
National Institute for Fusion Science,
Nagoya

Japan

Abstract

CONTROL OF TRANSPORT BARRIERS AND THE PHYSICS OF THE TRANSPORT β LIMIT.

Improved confinement modes associated with transport barriers, which are caused by the modification of the magnetic shear (current profile), are investigated by means of transport simulation. The transport coefficients are based on the theory of the self-sustained turbulence of current diffusive pressure driven modes. The buildup of internal transport barriers with low or negative shear is demonstrated. The formation and sustainment of the barriers are found to require careful control from the outside. The combination of central and off-axis current drive is shown to sustain stationary improved confinement with reduced shear. A new limit cycle in the dynamic evolution of the plasma profile is predicted to appear. In order to obtain a perspective on burning plasmas, the paper also examines the ignition condition in the case of improved confinement. For high β plasmas, a theory of electromagnetic (EM) self-sustained turbulence is developed. It is found that the EM non-linearity drives a new instability in high β plasmas. This EM turbulence has a higher saturation level and causes a stronger power degradation ('M mode') than in the L mode. The transport β limit is attributed to this degradation. A direct non-linear simulation is performed, which confirms the strong non-linear instability with high fluctuation amplitude. Stronger normal and inverse cascade processes are also observed.

1. INTRODUCTION

Transport barriers have been observed in various improved confinement modes in toroidal confinement devices. For instance, H mode with an edge transport barrier is an important requirement to ignite the ITER plasma. Internal barriers may strongly

affect the fusion power in burning plasmas. It is indispensable to understand the physics of transport barriers, develop control methods and estimate the impact on burning plasmas. Problems associated with the β limit can occur owing to the steep pressure gradient near the barriers. We present an integrated theoretical analysis in the following.

2. TRANSPORT MODEL

The L mode transport and the improvement of core plasma confinement in tokamaks are described well by the transport model based on the self-sustained turbulence of the current diffusive ballooning mode [1, 2]. The transport coefficient was derived as

$$\chi_i \approx \chi_e \approx F(s, \alpha)\alpha^{3/2}\delta_e^2 \frac{v_A}{qR} \tag{1}$$

The skin depth $\delta_e = c/\omega_{pe}$, the Alfvén velocity $v_A^2 = B^2/(\mu_0 n_0 m_i)$, the shear $s = r\,d\ln q/dr$, the pressure gradient $\alpha = \alpha_e + \alpha_i$, $\alpha_{e,i} = -q^2R\,d\beta_{e,i}/dr$, $\beta_{e,i} = 2\mu_0 p_{e,i0}/B_0^2$.

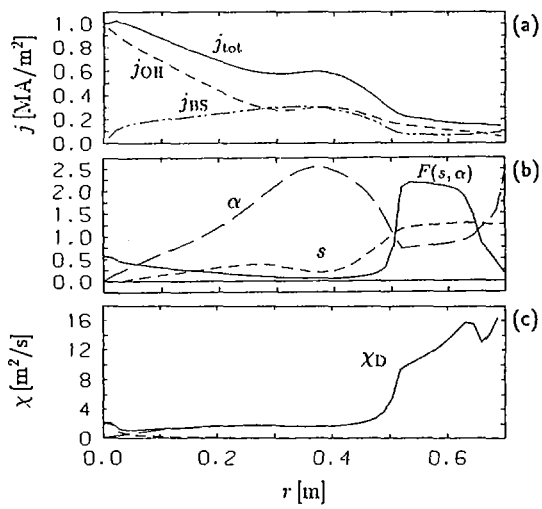

FIG. 1. Internal transport barrier in the JT-60U type of plasma. The current profile is given in (a). The magnetic shear, α and form factor F(s, α) are shown in (b). The thermal transport coefficient is shown in (c). R = 3.05 m, a = 0.7 m, B = 4.4 T, I_p = 1 MA, $n_e(0) = 5 \times 10^{19}$ m^{-3}, P_{in} = 40 MW.

The function F(s, α) represents the effect of the magnetic shear and the Shafranov shift [2]. The thermal component of the energy confinement time is derived for the L mode plasma as

$$\tau_E^L \propto aR^{6/5} n_{e0}^{3/5} I_p^{4/5} P_T^{-3/5} A_i^{1/5} \quad (2)$$

The favourable dependences of τ_E^L on I_p and on ion mass and the power degradation are recovered. The profile resiliency is explained as well.

In this model, the coefficient F(s, α) is reduced in the negative (or weak) magnetic shear cases. The reduced magnetic shear ($s < 0.3$), combined with the Shafranov shift of the magnetic axis, strongly reduces the transport to the level of the neoclassical theory. The transport simulation reproduced the formation of the internal transport barrier in the high β_p mode and indicated quantitative agreement with experimental results on confinement improvement [2]. The fitting formula of the simulation results is obtained as

$$\tau_E = \tau_E^L (1 + \beta_p^4)^{0.2} \quad (3)$$

Figure 1 shows the formation of the internal transport barrier with the low magnetic shear. It should be noticed that the formation of the internal barrier is very sensitive to the heating profile; central heating with a steep gradient of the absorption profile is found to be necessary.

3. CONTROL OF THE MAGNETIC SHEAR PROFILE

A negative magnetic shear configuration is usually established by starting additional heating during the current ramp-up phase. The formation and sustainment of the configuration are studied through transport simulation. Figure 2 shows typical results for 23 MW heating with current ramp-up from 1 to 3 MA in 1 s. The plasma parameters are those of a present day tokamak. The energy confinement time τ_E is enhanced by a factor of 2 compared with that of the fixed current case with 3 MA (Fig. 2(b)). Penetration of the plasma current reverses the gradient of the q profile (Fig. 2(c)) and intense heating delays the relaxation of the current profile. The negative magnetic shear and also the shift of the magnetic axis due to the steep pressure gradient reduce the thermal diffusivity in the core region of the plasma column (Fig. 2(d)) in the same way as the high β_p mode. The enhancement factor of τ_E and the duration of the improved state strongly depend on the operation conditions (e.g. current ramp rate, sequence, timing and shape of heating).

To sustain the improved confinement with the negative shear configuration, off-axis current drive is effective. By replacing about half of the heating power by the current drive ($r/a \approx 2/3$) and applying a small amount of on-axis current drive power (~5%), the hollow current profile can be sustained in a steady state with an enhanced

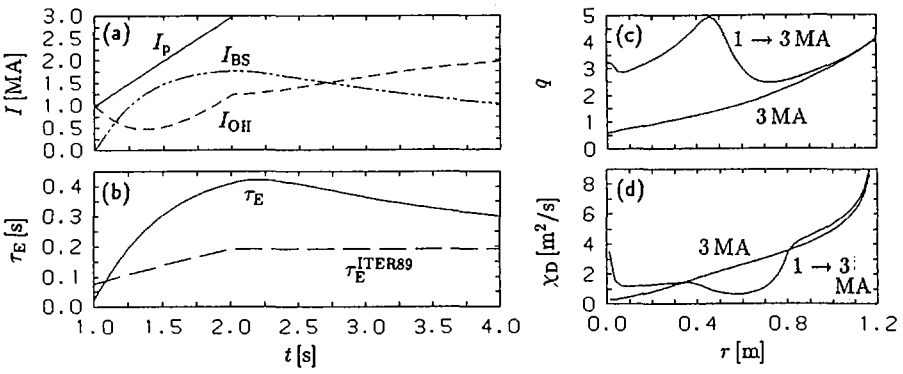

FIG. 2. Time traces of (a) plasma current and (b) energy confinement time. Radial profiles of (c) safety factor and (d) thermal conductivity. $R = 3$ m, $a = 1$ m, $B = 3$ T, $n_e(0) = 5 \times 10^{19}$ m^{-3}, $P_{in} = 23$ MW.

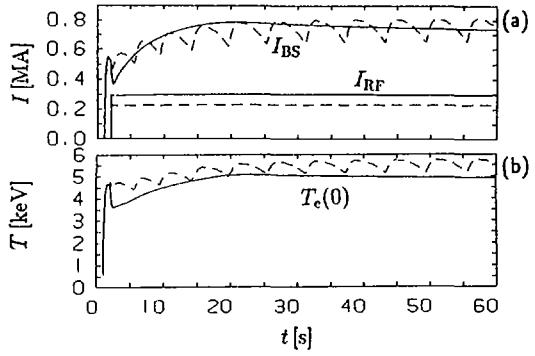

FIG. 3. Time evolution of (a) current and (b) central temperature. With off-axis current drive of 1.5 MW and 0.5 MW on-axis the improved state with an internal transport barrier is sustained ($P_{heat} = 10$ MW (solid lines)). The case of weak current drive (1 MW off-axis, 0.5 MW on-axis and $P_{heat} = 13.5$ MW (dashed lines)) shows self-generated oscillation. $I_p = 1$ MA and other parameters are the same as in Fig. 2.

confinement factor of 1.6. Figure 3 shows the long time evolution of the temperature and the current. It should be noted that the coupling of the current profile and the transport coefficient causes a new dynamic evolution of the plasma structure. If the off-axis current drive is reduced, then the shear is more easily modified by the plasma pressure profile. Self-generated oscillation may occur, as is shown by the dashed lines. This limits the operation region for the steady improved confinement with an internal transport barrier.

4. PERFORMANCE IN BURNING PLASMAS

The confinement improvement in the core region strongly affects the fusion reactivity and the ignition condition. From Eq. (3) the existence of a low plasma current branch of the ignition condition is predicted [3]. The simulation result for the ITER-grade tokamak is shown in Fig. 4. The fusion output power is depicted as a function of the plasma current I_p for various values of central electron density n_{20}. The fusion output power is very sensitive to the plasma density for the low I_p region (16 MA < I_p < 25 MA) because a small increment of β_p leads to better confinement. In the lower I_p region (I_p < 16 MA), a reasonable amount of power is enough to sustain full current drive with Q > 5, but that amount of power may easily lead to a thermal instability.

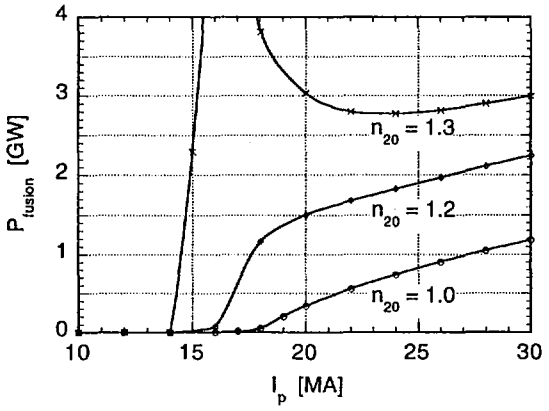

FIG. 4. Fusion power of the ITER-grade plasma as a function of plasma current. Density is varied for three cases.

5. TRANSPORT β LIMIT

The electromagnetic (EM) effects on the self-sustained turbulence can be essential as the pressure gradient becomes steeper. When the pressure gradient α exceeds a critical value α_c, stronger turbulence due to the magnetic perturbation enhances the transport considerably. The L mode transport is a saturated state of the electrostatic (ES) turbulence. The ES turbulence model is extended to the EM model.

We start from the following model equations for the EM interchange mode:

$$\partial_t \nabla_\perp^2 \phi + [\phi, \nabla_\perp^2 \phi] - [A, \nabla_\perp^2 A] = -ik_\parallel \nabla_\perp^2 A - ik_y \alpha_e p_e - ik_y \alpha_i p_i$$

$$\partial_t \nabla_\perp^2 A + [\phi, \nabla_\perp^2 A] - \xi_e [A, \nabla_\perp^2 A] = ik_\parallel \phi$$

$$\partial_t p_e + [\phi, p_e] - \xi_e [A, p_e] = -ik_y \phi$$

$$\partial_t p_i + [\phi, p_i] = ik_y \phi$$

where the normalization $t/\tau_{A\theta} \to t$, $r/\delta_e \to r$, $(\tau_{A\theta}/\delta_e^2)\phi/B_0 \to \phi$, $(r/B_\theta\delta_e^2)A \to A$, $(\tau_{A\theta}/\delta_e)\sqrt{m_e/m_i}v_{\parallel e} \to v_{\parallel e}$, $(L_{pe}/\delta_e p_{e0})p_e \to p_e$, $(L_{pi}/\delta_e p_{i0})p_i \to p_i$ is used with the poloidal Alfvén time $\tau_{A\theta}^2 = \mu_0 n_0 m_i r^2/B_\theta^2$, $k_\parallel = sk_y x$ and $\xi_e = v_{\parallel e0}/v_A$. If we set $\xi_e = 0$, then this model reduces to the previous ES model [4].

The transport coefficients $\chi_{e,i}$ are estimated as

I. ES turbulence regime ($\alpha < \alpha_c$): Eq. (1) with $F(s, \alpha) = 1/s^2$

II. EM turbulence (M mode) regime ($\alpha > \alpha_c$):

$$\chi_i \approx \frac{\alpha_i^2}{s^3}\delta_e^2\frac{v_{eth}}{qR}, \qquad \chi_e \approx \frac{\alpha_i^{5/2}}{s^4}\sqrt{\beta_e\frac{m_i}{m_e}}\delta_e^2\frac{v_{eth}}{qR} \tag{4}$$

In regime II, the transport coefficients show strong power dependences on the pressure gradient, such as $\alpha_i^{5/2}$ (electron) and α_i^2 (ion). The electron transport coefficient increases much more than the ion transport coefficient. The electron

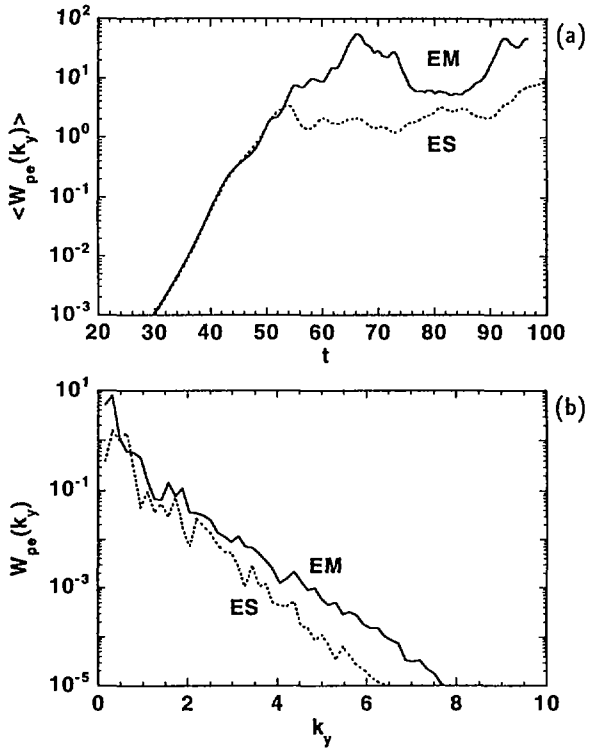

FIG. 5. (a) Fluctuating energy of electron pressure $\langle W_{pe}\rangle$ versus time, showing a further nonlinear growth due to the EM effect compared with the ES case. (b) Power spectra of W_{pe} depicted at $t = 90$ are shown for corresponding cases. $\alpha_e = \alpha_i = 0.25$, $s = 0.5$, $\mu_c = \chi_{ce,i} = 0.2$, $\lambda_c = 0.01$.

viscosity further enhances the non-linear instability, while the electron pressure gradient is decreased strongly. As a result, the ion pressure gradient plays a key role in driving the instability. The critical pressure gradient for the transition from regime I to regime II, or the collapse of the transport barrier, is given by $\alpha_c \approx s^2 m_e/(m_i \beta_e)$. The transition to the M mode is possible, which provides the model of giant ELMs [5].

Using the relations $\tau_E^e \approx a^2/\chi_e$, $\tau_E^i \approx a^2/\chi_i$, we obtain the scaling laws of the energy confinement time as

$$\tau_E^e \approx a^{12/19} R^{47/19} n_{e0}^{3/19} B^{14/19} I_p^{18/19} P_T^{-17/19} A_i^{-6/19} \tag{5}$$

$$\tau_E^i \approx a^{17/19} R^{8/19} n_{e0}^{9/19} B^{4/19} I_p^{16/19} P_T^{-13/19} A_i^{1/19} \tag{6}$$

Comparing Eqs (2), (5) and (6), we find the following: (1) Power degradation stronger than that of the L mode is expected for both electron and ion confinement times, which may lead to the transport β limit. (2) Distinct parameter dependences of τ_E^e and τ_E^i are seen on R, n_{e0}, B and A_i; for example, a strong B dependence appears for electron confinement, and the dependence of density on ion confinement time is stronger than on electron confinement time.

In order to estimate the EM effects on the turbulence quantitatively, non-linear simulation has been carried out in regime II. Figure 5(a) shows the time evolution of electron pressure energy $\langle W_{pe} \rangle$. Here the energy is defined by $\langle W_{pe} \rangle = \Sigma_{k_y} W_{pe}(k_y)$, $W_{pe}(k_y) = \int_{-L/2}^{L/2} dx |p_e(x, k_y)|^2/2$. The cases with and without the EM non-linearity term $[A, \nabla_\perp^2 A]$ proportional to ξ_e in Ohm's law are calculated with parameters $\xi_e = 1$, $s = 0.5$, $\alpha_e = \alpha_i = 0.25$, $k_{ymin} = 10/64$, $k_{ymax} = 10$, $L = 80$. The solid curve shows the case with the non-linearity ($\xi_e = 1$) and the dotted curve the case without it ($\xi_e = 0$). In the case with the non-linearity, a higher saturation level is predicted than for the case without it. Figure 5(b) shows the power spectrum of the electron pressure at the time $t = 90$ with and without the non-linearity. This non-linearity leads to strong normal and inverse cascades.

REFERENCES

[1] ITOH, K., et al., Plasma Phys. Control. Fusion **35** (1993) 543.
[2] FUKUYAMA, A., et al., Plasma Phys. Control. Fusion **37** (1995) 611.
[3] FUKUYAMA, A., et al., Nucl. Fusion **35** (1995) 1669.
[4] YAGI, M., et al., Phys. Plasmas **2** (1995) 4140.
[5] ITOH, S.I., et al., Plasma Phys. Control. Fusion **38** (1996) 527.

ENERGY AND PARTICLE TRANSPORT MODELING FOR THE TOKAMAK EDGE/SOL REGION*

T.D. ROGNLIEN, G.D. PORTER, F. WISING[1,2],
H.L. BERK[3], R.H. COHEN, J.A. CROTINGER,
M.E. FENSTERMACHER, S.P. HIRSHMAN[4], D.A. KNOLL[5,6],
A.E. KONIGES, S.I. KRASHENINNIKOV[1,7], N. MATTOR,
M.E. RENSINK, D.D. RYUTOV, D.J. SIGMAR[1], G.R. SMITH,
A.G. TARDITI, Yu.A. TSIDULKO[3,8], H. WÜRZ[9], X.Q. XU,
DIII-D[10] and ALCATOR C-MOD[1] TEAMS
Lawrence Livermore National Laboratory,
Livermore, California,
United States of America

Abstract

ENERGY AND PARTICLE TRANSPORT MODELING FOR THE TOKAMAK EDGE/SOL REGION.

The paper reports recent results from modeling detached divertor operation in the DIII-D and Alcator C-Mod tokamaks using the integrated 2-D transport code UEDGE and from a more detailed analysis of specific aspects of the scrape-off layer (SOL) transport problem. Topics include attached/detached divertor operation with impurities, origin of SOL turbulence, electrostatic potential description across the separatrix, and plate sheath current-voltage characteristics that lead to a method for broadening the SOL. The transport modeling prediction of electron temperatures in the 1-2 eV range for detached divertor plasmas is confirmed by Langmuir probe and Thomson scattering measurements.

* Work performed for USDOE under Contract Nos W-7405-ENG-48 at LLNL, DE-FG02-91-ER-54109 at MIT, DE-FG03-96ER-54346 at IFS, DE-AC05-96OR22464 at ORNL, AC07-76ID01570 at INEL, W-7405-ENG-36 at LANL, DE-AC03-89ER51114 at GA, and the Swedish Nat. Sci. Res. Council.

[1] Plasma Fusion Center, MIT, Cambridge, Massachusetts, USA.
[2] Institute of Electromagnetic Field Theory, Chalmers University of Technology, Göteborg, Sweden.
[3] Institute for Fusion Studies, University of Texas at Austin, Austin, Texas, USA.
[4] Oak Ridge National Laboratory, Oak Ridge, Tennessee, USA.
[5] Idaho National Engineering Laboratory, Idaho Falls, Idaho, USA.
[6] Los Alamos National Laboratory, Los Alamos, New Mexico, USA.
[7] Kurchatov Institute, Moscow, Russian Federation.
[8] Budker Institute of Nuclear Physics, Novosibirsk, Russian Federation.
[9] Forschungszentrum Karlsruhe, Karlsruhe, Germany.
[10] General Atomics, San Diego, California, USA.

1. Model Validation for DIII-D and Alcator C-Mod

Understanding and developing validated models of energy and particle transport through the SOL of tokamak devices is central to the design of larger machines. The DIII-D and Alcator C-Mod tokamaks provide diverse conditions for such model validation. DIII-D has an open divertor with numerous diagnostics, highlighted by the new divertor Thomson scattering measurements of the electron density, n_e, and temperature, T_e, giving 2-D divertor-leg profiles. In addition, we compare Thomson n_e and T_e profiles near the midplane, IRTV divertor heat flux, H_α line emission, and impurity emissions in the VUV. Alcator C-Mod has a more closed divertor with a highly inclined divertor plate and operates at higher plasma densities. Here we compare with plate values of ion flux and T_e from Langmuir probe arrays and the integrated radiated power from bolometer arrays.

We present two types of UEDGE simulations of these devices: qualitative with fixed anomalous diffusion coefficients (D for n and $\chi_{e,i}$ for energies), and quantitative where D and $\chi_{e,i}$ are changed to fit individual discharges. UEDGE includes classical transport along **B** and anomalous in the radial direction on a nonorthogonal mesh with a parallel Navier-Stokes fluid neutral model which couples to the ion parallel flow via charge exchange. Cross-field neutral transport is diffusive, arising from charge-exchange and neutral-neutral collisions which effectively transport momentum and energy radially. We include volume recombination which is very important for detachment. Experimentally, detached plasmas (low energy and particle fluxes) often occur at the inner divertor plate and can be induced at the outer plate by injection of deuterium or impurity gas; excessive injection leads to a MARFE on the closed flux surfaces and deterioration of confinement. We find this same behavior from UEDGE simulations for the DIII-D geometry [1]. For pure deuterium plasmas, scans from high-to-low input power show progressively that the inner plate plasma becomes detached first, then the outer leg detaches, leading to a broad $T_e \sim 1$ eV region below the x-point, and finally a cold, high density MARFE forms within the separatrix. The effect of intrinsic carbon impurity radiation, described with either a fixed-fraction model or multispecies model, is similar to input power reduction.

With the tilted plate, Alcator C-Mod simulations also show the progression just described. An added complexity of these systems is illustrated by two different solutions for the same parameters with 0.5% carbon fraction [2]. This bifurcation has one solution with the 240 kW of carbon radiation peaking about 6 cm above the outer divertor plate, while the second is a MARFE solution with 330 kW of carbon radiation peaking inside the separatrix above the x-point. The existence of these two detached solutions is qualitatively in agreement with the rapid manner in which detached plasma can develop and the potential difficulty is controlling the location of the radiating regions. Although precise comparisons have not been completed, the location and magnitude of the carbon radiation is roughly consistent with the bolometer data.

Detailed simulations of 10 DIII-D discharges that include comparison with the divertor Thomson scattering have been done by adjusting the D and $\chi_{e,i}$ to fit the midplane profiles, yielding $\chi's$ in the range of 0.1 to 1.4 m^2/s for a range of parameters with D being 1/2 to 1/3 smaller. No particle pinch is used. In general, the $\chi's$ increase with heating power. The measured divertor power

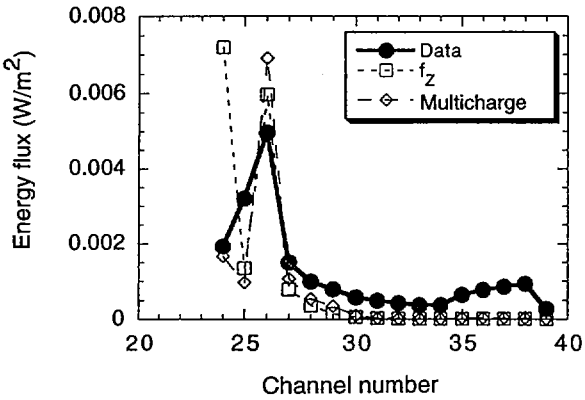

FIG. 1. Comparison of DIII-D bolometer measurements from the side-viewing array (channel 24 just inside outer strike point, 26 at the inner strike point) and UEDGE modeling from the fixed-fraction model (f_z) and the multicharge state model with chemical sputtering (force balance).

profile is fit well with these simulations with the in/out asymmetry arising from parallel current and radiation effects. The H_α signals are fit well except for chords through the private flux region, a discrepancy presently under studied with the DEGAS neutral Monte Carlo code. Simulations of detached plasmas show a broad region of relatively constant T_e (~1-2 eV) near the divertor plates with the ionization layer located part way to the x-point near where $T_e \sim 5$ eV; these profiles are similar to the 2-D data obtained from the divertor Thomson scattering system on the outer divertor leg. Reduction of plate ion flux is caused by volume recombination which can be large between the ionization layer and the plate, especially on the inner leg, and is enhanced by the very subsonic parallel ion velocity there. Molecular processes are ignored which can further enhance recombination [3]. The role of carbon impurity radiation is to enhance the degree of detachment, especially in the outer leg, and the position of the ionization layer. While we have used both a fixed fraction impurity model and a multispecies model with physical sputtering, the best fit comes from adding chemical sputtering to the multispecies model as found by the ASDEX-U and JT-60 groups. Comparison of bolometer measurements from DIII-D discharge 87506 in Fig. 1 show the results for a self-consistent multispecies model using a 0.5% chemical sputtering rate in the private flux region. Here ~80% of the radiation comes from the carbon. Also plotted is the result for $0.002n_e$ fixed-fraction of carbon showing differences in the detailed location of the radiation near the x-point. Larger chemical sputtering source from the private flux or wall regions is needed to explain the level outside the divertor/x-point region which also have core contributions neglected here.

Detailed Alcator C-Mod simulations have been done for an Ohmic discharge with separatrix power and density of 600 kW and 10^{20} m^{-3}, respectively. The radial diffusion coefficients are $D = \chi_{e,i} = 0.25$ m^2/s. The comparison between the measured and simulated ion parallel currents is shown in Fig. 2 for fixed-fraction carbon levels of 0% and 0.5%. The medium density experimental curve

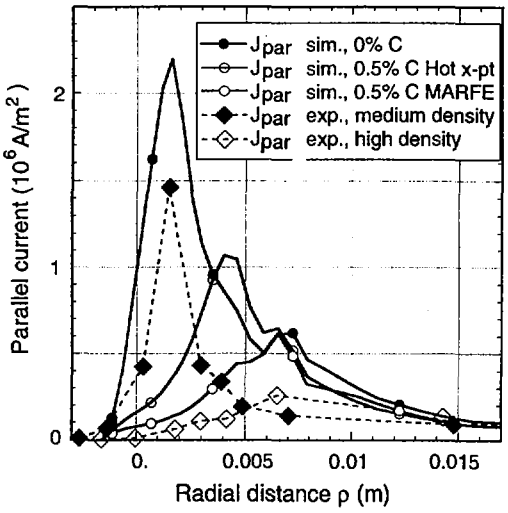

FIG. 2. Comparison of Alcator C-Mod parallel current density on the outer divertor plate (dashed lines) with UEDGE simulations at different carbon levels.

from Langmuir probes shows an attached plasma which then becomes detached at high density. The detachment is induced in the simulation by increasing the carbon fraction, showing the large drop in the current close to the strike point ($\rho = 0$). As with DIII-D simulations, the volume recombination is important in explaining the decrease in ion flux. The two cases with 0.5% carbon correspond to the two bifurcated solutions referred to earlier in the text. A similar reduction near the strike point is found in the divertor power and T_e in both the experiment and the simulation, and the quantitative comparison for T_e typically within a factor of two across the profile and better near the strike point with both yielding $\sim$1 eV there (experimental high density case). Simulations have also been done with 0.3% neon which shows less detachment than the carbon cases and gives the substantially broader distribution of radiated power.

On different aspects of the modeling, we obtain reasonable agreement for heat load profiles on the divertor plates during a disruption in DIII-D. We find that abruptly raising the diffusion coefficients in UEDGE to $D = \chi_{e,i} = 20$ m^2/s produces the observed poloidal heat flux of $\sim$100 MW/m^2 while maintaining moderate midplane T_e of $\sim$150 eV. We have also improved a 2-D model for radiation transport during disruptions that includes calculating the radiation power flux to the divertor side walls.

2. Coupling Edge and Core

Coupling between the SOL and core is modeled using the Corsica-2 code. Here the 1-D core transport and the 2-D UEDGE SOL transport are self-consistently coupled through the density and temperature variables at a boundary inside the separatrix [4]. The coupling is achieved at each timestep by a

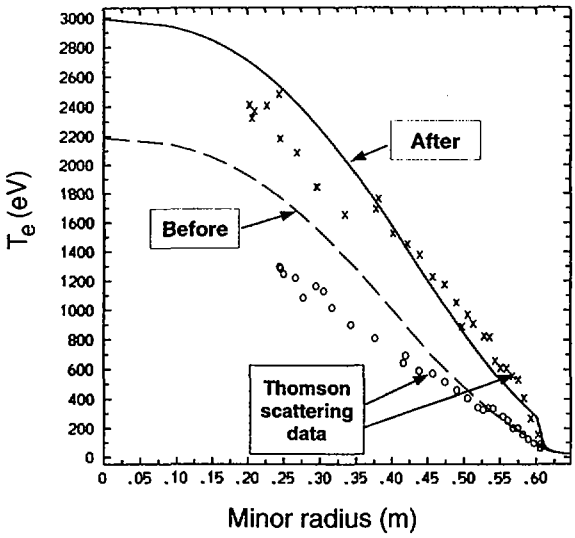

FIG. 3. Comparison of T_e profiles for an L–H transition in DIII-D with the Corsica-2 code evolving the core and SOL regions together.

Newton predictor-corrector method that requires the particle and energy fluxes from each region to match to a specified tolerance. We compare the density and temperature profiles for DIII-D discharge 86586 before and after an L-H transition. The transition is induced in the simulation by decreasing the edge/SOL energy diffusion coefficients ($\chi_{e,i}$) from 4.5 to 1.5 m^2/s while the corresponding D is dropped from 0.4 to 0.3 m^2/s; these values come from stand-alone UEDGE modeling of the edge/SOL. The results for the T_e profiles are shown in Fig. 3. The simulation fits the data well, especially after the transition; some adjustments to the pre-transition diffusion coefficients in the core would improve that fit. The formation of a characteristic H-mode temperature pedestal near the edge is evident. We are developing a dynamical self-consistent description of the diffusion coefficients based on additions of toroidal flow and a K-epsilon turbulence model.

3. Edge/SOL Turbulence

Studies of SOL turbulence are performed by 3-D electrostatic fluid simulations that include edge, SOL and private-flux regions with a quasi-ballooning coordinate representation. Instability drives include rotation relative to conducting end walls, radial and axial (parallel) shear in $\mathbf{E} \times \mathbf{B}$ velocity, field-line curvature, and radial gradients in $v_\parallel$. For attached, low-recycling divertor plasmas with n_e and T_e uniform, the fluctuations are roughly constant along $\mathbf{B}$, and for typical DIII-D parameters, give diffusivities of ~ 2 m^2/s. We model detached plasmas via a fixed background with T_e dropping a factor of 50 to the plate and n_e increasing a factor of 5 [5]. For simulations with no magnetic

shear, the fluctuation levels are about 50% larger than the attached case at the midplane, but are strongly reduced at the plate. The larger amplitude at the midplane and a bigger phase shift between potential and density fluctuations gives a midplane diffusivity an order of magnitude larger, while the plate diffusivity is much smaller than in the attached case. We expect inclusion of magnetic shear to reduce the midplane diffusivity.

We present results of instability analysis including the divertor presheath region under detached plasma conditions. For the parameters DIII-D, we find that a new dissipative axial-velocity shear instability due to the strong variation of electron resistivity between the x-point and the divertor plates. The resistive dissipation is large only in a narrow region of the presheath termed the resistive layer. Thus, the dissipative instability consists of a collisionless electromagnetic mode in the midplane connected to the layer by a resistive electrostatic mode in the presheath. The key parameter for dissipative instabilities is the resistivity of the presheath, which is proportional to integral of the difference of the electron collision rate between the plate and midplane, $R_p \propto \int_0^s [\nu_e(s) - \nu_e(\infty)]\, ds$. For a single-end problem with outgoing-wave boundary conditions to model modes near the separatrix, we find two major effects: (1) the axial shear mode growth rate is enhanced by the added resistivity from the narrow resistive layer, and (2) a new dissipative instability arises from the presheath resistive layer with a growth rate $\gamma \propto R_p$. When the sheath dissipation rate is much larger than the layer dissipation rate, the new instability growth rate can be estimated as following: $\gamma/\omega_E \propto (k_\perp \rho_i)^3 (m_e/m_i)^{1/2} l^2/(\lambda_{mfp} L_{Te})$, where $\omega_E = k_\perp v_E$, v_E is the $\mathbf{E} \times \mathbf{B}$ velocity, l is the parallel length of presheath, λ_{mfp} is the presheath electron mean-free path length, and L_{Te} is the radial gradient scale-length of T_e. For a double-end problem with two bounding divertor plates, the conducting-wall mode is modified in two respects: (1) the growth rate, γ, is strongly enhanced by the presheath potential [$\gamma \propto \Lambda^{2/3}$ and $\chi_e \propto \gamma/k_\perp^2 \propto \Lambda^{4/3}$ with $\Lambda = e\Phi_{sheath}/T_{esheath} + 0.71(T_{emid} L_{Tesheath})/(T_{esheath} L_{Temid})$], and (2) the destabilizing effect of the sheath is partially offset by the resistive layer. For typical DIII-D parameters, effect (1) dominates over (2).

4. Electric Field and Current Effects

To properly close the set of equations describing plasma behavior in the SOL, one has to formulate the current-voltage characteristics (CVC) of the plate sheath including effects of electric drifts and diamagnetic currents. When the angle α between the magnetic field line and divertor plate is small, this boundary condition reads [6]:

$$j_n = \alpha j_0(\phi) + (cen/B)(\partial\phi/\partial x_\perp) + (c/B)(\partial p_i/\partial x_\perp) \qquad (1)$$

where ϕ is a plasma potential with respect to a conducting plate a few ion gyroradii from the plate, $j_0(\phi)$ is the CVC for the case of $\alpha = \pi/2$, and $x_\perp$ is a coordinate normal to the magnetic surface in the vicinity of the plate. Here we have specialized to the case where the poloidal component of the magnetic field is perpendicular to the plate. This boundary condition is now used in UEDGE simulations.

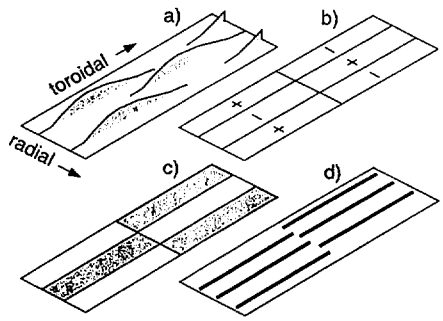

FIG. 4. Schemes of radial and toroidal variations in divertor plates to enhance convective SOL transport: (a) wavy plates; (b) biased segments; (c) varying secondary emission coefficients; (d) gas puffing through alternating slots.

Another application of Eq. (1) is related to the enhancement of cross-field transport in the SOL, thereby decreasing heat loads on the divertor plates. Equation (1) shows that, in the presence of electric drifts and diamagnetic currents in the SOL plasma, the floating potential should strongly depend on the intersection angle α. Thus, by making the divertor plate slightly wavy in the toroidal direction (so that α varies by $\sim 50 - 100\%$), one can create toroidally varying potential perturbations of SOL which cause convective cross-field transport.

To optimize the convective transport, one has to select the toroidal and radial wavelengths of the "waves" or patterns on the divertor plate (see Fig. 4a). The main factor determining the optimum toroidal wavelength is the stretching of the magnetic flux tube as it passes near the x-point; if the toroidal period is too small, this stretching results in the radial thickness of the flux-tube becoming less than the ion gyro-radius. For a tokamak with a major radius of 2 m, the optimum toroidal wavelength is $\sim$1.5 m. The number of waves across the "wetted" surface of the plate should be 2-3 [7], as shown in Fig. 4a. This transport can lead to diffusion coefficients comparable to, or somewhat exceeding, the Bohm coefficient.

Toroidal variations of the SOL potential can also be produced by alternate biasing sections of the divertor plate or by applying plate coatings with a varying secondary emission coefficient (Fig. 4b,c). In detached regimes, one can produce toroidal potential variations by gas-puffing at alternating toroidal locations in the vicinity of the x-point (as through plate slots in Fig. 4d). The attractive feature of all these methods is that they can substantially increase the transport on the open field-lines, thereby reducing the power density on the divertor plate, without any significant increase of transport inside the separatrix.

We have derived, and implemented in UEDGE, a model of the equilibrium electrostatic potential, ϕ, that applies to both closed and open B-field regions. The key change to UEDGE is obtaining the radial current from an angular momentum transport equation, instead of the previous mobility model. Parallel transport is classical, and radial transport is anomalous, having diffusive and Reynolds stress contributions. The model correctly gives the change from positive to negative electric field in moving from the SOL to the core edge and affects $\mathbf{E} \times \mathbf{B}$ flows near the plates.

REFERENCES

[1] PORTER, G.D., et al., Plasma Phys. 3 (1996) 1967.
[2] WISING, F., et al., Simulation of plasma flux detachment in Alcator C-Mod and ITER, J. Nucl. Mater. (in press).
[3] CATTO, P.J., IAEA-CN-64/DP-13, this volume.
[4] TARDITI, A., Contrib. Plasma Phys. 36 (1996) 132.
[5] XU, X.Q., COHEN, R.H., Contrib. Plasma Phys. 36 (1996) 202.
[6] COHEN, R.H., RYUTOV, D.D., Plasma Phys. 2 (1995) 2011.
[7] COHEN, R.H., RYUTOV, D.D., in Fusion Engineering (Proc. 16th IEEE-NPSS Symp. Urbana-Champaign, 1995), Vol. 1 (1996) 696.

DISCUSSION

R.J. GOLDSTON: With the data you now have from DIII-D and C-Mod, perhaps you can comment on $\chi_\perp$ and its scaling. This is, of course, very important for the future of divertor tokamaks.

T.D. ROGNLIEN: We have done some scaling of $\chi_\perp$ for DIII-D H modes with input power, showing $\chi_\perp$ increasing roughly linearly from 0.1 to 0.8 m^2/s for input powers of 1 to 10 MW. For low power L mode operation, $\chi_\perp$ is about four times larger than for the H mode. A 0.6 MW ohmic discharge in Alcator C-Mod fits with a $\chi_\perp$ of 0.25 m^2/s. A systematic study of $\chi_\perp$ scaling for these various operating modes in different machines is possible by using a SOL transport code such as UEDGE. A theoretical understanding of SOL turbulence is probably needed to have strong confidence in extrapolations of $\chi_\perp$ to larger machines.

TOKAMAK EDGE PHYSICS AND MODELING

P.J. CATTO[1, 2], S.I. KRASHENINNIKOV[1, 3], D.J. SIGMAR[1],
R.D. HAZELTINE[4], P. HELANDER[1, 5], D.A. KNOLL[6],
A.Yu. PIGAROV[3, 7], O.V. BATISHCHEV[1, 2, 8], X.Q. XU[9],
J.A. BYERS[9], R.H. COHEN[9], T.D. ROGNLIEN[9],
T.K. SOBOLEVA[10, 3], A.A. BATISHCHEVA[1]

[1] Plasma Fusion Center,
Massachusetts Institute of Technology,
Cambridge, Massachusetts,
United States of America

[2] Lodestar Research Corporation,
Boulder, Colorado,
United States of America

[3] Russian Research Center,
Kurchatov Institute,
Moscow, Russian Federation

[4] Institute for Fusion Studies,
University of Texas,
Austin, Texas,
United States of America

[5] UKAEA Government Division, Fusion,
Euratom–UKAEA Fusion Association,
Abingdon, Oxfordshire,
United Kingdom

[6] Idaho National Engineering Laboratory,
Idaho Falls, Idaho,
United States of America

[7] Plasma Physics Laboratory,
Princeton University,
Princeton, New Jersey,
United States of America

[8] Keldysh Institute for Applied Mathematics,
Moscow, Russian Federation

[9] Lawrence Livermore National Laboratory,
Livermore, California,
United States of America

[10] Instituto de Ciencias Nucleares,
Universidad Nacional Autónoma de México,
Mexico City, Mexico

Abstract

TOKAMAK EDGE PHYSICS AND MODELING.

Results have been obtained that relate to six areas of tokamak SOL behavior: (1) obstruction of impurity core penetration by radial gradients; (2) divertor similarity studies using advanced 2D fluid codes; (3) molecular effects on recombination; (4) the effects of transport on impurity radiation; (5) kinetic modeling of detachment; and (6) kinetic modifications to probe temperature measurements.

1. Impurity core penetration obstruction by radial gradients and transport

The edge plasma in the SOL is not confined by the magnetic field. Indeed, the plasma flows predominantly along the magnetic field lines towards the limiter or the divertor collector plates, and the loss is balanced by cross-field transport. Consider, for example, the ion continuity equation,

$$\nabla_{\|}(N_i V_{i\|}) = \partial / \partial r(D \partial N_i / \partial r) \qquad (1)$$

where N_i is the density, $V_{i\|}$ the parallel ion flow velocity, r the radius, and D the radial diffusion coefficient. Conventional kinetic equations do not allow a balance such as Eq. (1) and are thus inappropriate in the plasma edge. Therefore, we have derived and solved novel kinetic equations, allowing such a balance, and constructed distinctive transport laws for impure, collisional, edge plasmas. It is found that the friction force acting between different ion species is different from that found in the literature [1-2]. In highly sheared flows the new terms can obstruct impurity penetration into the core plasma. In a plasma with a main hydrogenic ion species and a heavy impurity, the force on the former is $R_i = R_i^{Brag} + R_i^{edge}$, where the first term is conventional:

$$R_i^{Brag} = -\alpha M N_i \nu_{iz} (V_{i\|} - V_{z\|}) - \beta N_i \nabla_{\|} T$$

with $\nu_{iz} = 4(2\pi)^{1/2} N_z e_z^2 e_i^2 \ell n\Lambda / 3M^{1/2} T^{3/2}$, T the ion temperature, M the ion mass, N_z the impurity density, $V_{z\|}$ the parallel impurity velocity, and α and β friction coefficients depending upon the impurity strength $N_z e_z^2 / N_i e_i^2$. The precise form of the correction R_i^{edge} depends on the underlying mechanism.

If the radial ion transport is classical, arising from Coulomb collisions with a heavy impurity species, then in the Lorentz limit ($\alpha = 3\pi/32$ and $\beta = 3/2$)

$$R_i^{edge} = M N_i D_c \frac{\partial V_{i\|}}{\partial r}\left(-\frac{0.53}{N_i}\frac{\partial N_i}{\partial r} + \frac{2.3}{T}\frac{\partial T}{\partial r}\right) - 0.32\frac{\partial}{\partial r}\left(M N_i D_c \frac{\partial V_{i\|}}{\partial r}\right)$$

where $D_c = \nu_{iz}\rho_i^2$ is the classical diffusion coefficient with $\rho_i^2 = T / M\Omega_i^2$.

If the diffusion is anomalous with a diffusion coefficient D due to electrostatic turbulence, the corresponding expression for the ion-impurity force for arbitrary $N_z e_z^2 / N_i e_i^2$ is

$$R_i^{edge} = 2\beta M N_i D(\partial V_{i\|}/\partial r)(\partial \ell nT/\partial r)$$

Thus, in the presence of anomalous radial diffusion, parallel ion transport cannot be entirely classical, as is usually assumed.

The new thermal forces, which are not found with conventional orderings, can oppose the tendency of the usual thermal force to drive impurities toward hotter regions, and may therefore be beneficial for impurity retention in the tokamak divertor. The usual thermal force occurs because ions moving in the direction of $\nabla_{\|}T$ originate in a colder, more collisional region than the ones moving in the opposite direction, and thereby exert a net force on the impurities in the $\nabla_{\|}T$ direction. The new thermal forces arise in a similar way. In the anomalous case, for example, if $\partial V_{i\|}/\partial r < 0$ and $\partial T/\partial r < 0$ then diffusion transports hot ions with large $V_{i\|}$ radially outwards in the SOL to replace cooler, slower moving ones, thereby resulting in a net force on the impurities that opposes the conventional thermal force.

2. Divertor similarity

A rectangular version of UEDGE with a fully recycling target, thermally equilibrated neutrals and plasma, anomalous plasma transport, and only two-body processes in an optically transparent plasma is used to verify two-body similarity [3] by quadrupling the geometry (including the grid spacing) and anomalous transport coefficients, and reducing the upstream pressure and parallel heat fluxes by a factor of four, to obtain the same normalized solution. To demonstrate the risks of relying on two-body scaling laws we then investigated departures from two-body similarity by retaining the full ionization, radiation, and recombination rates including multi-step atomic processes involving the population dynamics of the excited states of the neutrals [4-5] and three-body recombination [5].

In Ref. [4] we pointed out the crucial role that multi-step atomic interactions involving the excited states of atomic hydrogen play in altering the ionization and radiation rates via the one body process of spontaneous decay even during attached operation. By studying detached cases as well we have found that two body scaling interpretations of experimental data fail due to multi-step processes when a significant region exceeds a plasma density of 10^{19} m^{-3}. The violation of two body scaling due to multi-step transitions occurs when electron impact ionization and excitation of a significant population of excited atoms takes place before they are able to spontaneously decay to the ground state [6].

Recently, the important role that three body recombination plays in strongly detached operation has been recognized [7]. Our investigations of detached plasmas have found that three body recombination alters two body scalings whenever there is a significant region in which the temperature is < 1 eV while the plasma density is $> 10^{20}$ m^{-3}.

When the scaling law studies are repeated by considering both the higher density base case and the lower density, four times larger scaled case we find that for the base (scaled) case multi-step processes result in a higher (lower) pressure normalized target heat load until the plasma becomes deeply detached at low

values of the pressure normalized entering heat load [5]. The higher (lower) normalized heat flux to the target occurs because at higher (lower) densities fewer (more) excitations and decays occur prior to ionization, so the energy cost per ionization decreases (increases) while the ionization rate increases (decreases) because the plasma is warmer (cooler). Recent work has found that this behavior is insensitive to plasma collisionality over a wide range (±50%). The sensitivity of these results to the sidewall boundary conditions is still under investigation.

Recombination is found to be negligible in the base case runs because the density is $< 10^{20}$ m^{-3} in regions where the temperature is below 1 eV. However, for the scaled curves recombination reduces the target heat load substantially because there is a large region with the temperature below 1 eV due to multi-step processes while the density is $> 10^{20}$ m^{-3}. Not surprisingly, the threshold for detachment is lower and the ionization front distance from the target larger when energy and momentum are lost to recycling sidewalls. Moreover, the location of the ionization front becomes a very sensitive function of the normalized entering heat load once it becomes low enough for the plasma to be strongly detached.

These studies demonstrate that two body scaling arguments are often inappropriate in the divertor but that detailed scaling law information can be obtained from numerical simulations to aid in the design of a dissipative divertor for ITER. For example, a plot of the power to the plate P_{plate} normalized by the major radius R vs. the power P entering the divertor normalized by R results in the curves shown in Fig. 1 (which would be identical for two body scaling). For the constant anomalous diffusivity over R and constant collisionality scalings considered, Fig. 1 implies that larger machines have lower P_{plate}/R, and can obtain detachment at higher upstream P/R.

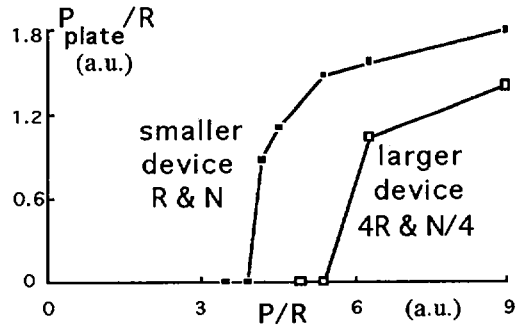

FIG. 1. Power to the plate P_{plate} normalized by R versus power P entering the divertor over R for the base (upper) and scaled (lower) cases.

3. Molecular effects on plasma recombination

Plasma recombination [8] in the divertor region seems the most probable explanation of the decrease in the plasma particle flux in detached divertor regimes. References 6 and 9 found that apart from conventional electron-ion two- and three- body plasma recombination (EIR), molecular activated recombination (MAR) involving vibrationally excited molecular hydrogen, $H_2(v)$, can be a very

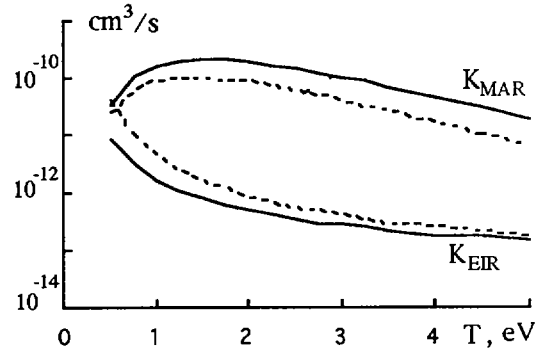

FIG. 2. Molecular activated (K_{MAR}) and electron–ion (K_{EIR}) recombination rate constants versus temperature T. Plasma density n = 10^{14} cm^{-3} (solid curves) and 10^{15} cm^{-3} (dashed curves).

important mechanism to extinguish plasma in a tokamak divertor. There are two chains of reactions leading to the MAR: a) $H_2(v)+e \rightarrow H+H^-$ followed by $H^+ + H^- \rightarrow 2H$ [6], and b) $H_2(v)+H^+ \rightarrow H_2^+ + H$ followed by $H_2^+ + e \rightarrow 2H$ [9]. We investigate MAR with the code CRAMD [10] based on a collisional-radiative (CR) model involving the ground, vibrationally and electronically excited states of hydrogen molecules and molecular ions, the ground and excited states of hydrogen atoms, and positive and negative atomic hydrogen ions. We find that chain b) dominates and the effective recombination rate constant of MAR, K_{MAR}, can be as high as 2×10^{-10} cm^3/s, confirming our previous estimate [9]. The dependencies of K_{MAR} and the EIR rate constant, K_{EIR}, on the gas-plasma temperature, T, as found from our CR model are shown in Fig. 2 for two plasma densities, $n=10^{14}$ and 10^{15} cm^{-3} (solid and dashed curves, respectively). From Fig. 2 we see that the plasma sink due to MAR, $S_{MAR}=n[H_2]K_{MAR}$, exceeds the EIR sink, $S_{EIR}=n^2K_{EIR}$, for molecular densities $[H_2]>3\times10^{-2}n$, which are rather typical for detached divertor regimes.

We incorporate MAR into a 1D self-consistent model of plasma-neutral interaction in the long mean free path regime of neutral gas transport [11]. This model assumes that the neutral gas (with fixed temperature $T_N \sim 1$ eV) is homogeneously distributed in a "gas box" within a poloidal distance L_N=5 cm of the divertor plate. We take the plasma pressure $P_u=10^{16}$ cm^{-3} eV, the heat flux, and zero plasma particle flux as the boundary conditions at the upstream entrance into the "gas box" and assume complete plasma recycling at the plate. We find the neutral gas density, the plasma temperature, T_d, and pressure, P_d near the plate, and plasma flux onto the plate, j_d, self-consistently from the continuity and energy balance equations. As a result of the modeling we conclude: i) the strong decrease of j_d and P_d (which are typically observed detached divertor regime characteristics) at reasonably high plasma temperatures ($T_d > T_N$) can only be obtained when recombination is included; and ii) for the model of plasma-neutral interactions we employ, MAR is the dominant channel of divertor plasma recombination as shown in Fig. 3, where S_{ion} is the ionization source.

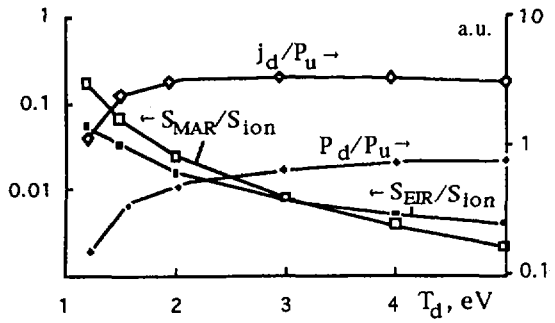

FIG. 3. Plasma flux j_d and pressure P_d near the divertor plate, and MAR and EIR sinks as functions of plasma temperature T_d.

4. Effect of plasma and neutral gas transport on impurity radiation loss

Experimentally it is observed that in the presence of MARFE's or for a radiative divertor, a significant amount of radiation comes from a relatively small volume of rather cold plasma. However, simple 1D models of the impurity radiation loss, based on the balance of parallel heat conduction of the plasma and radiation loss, predict that the main radiation should come from a high temperature region of the SOL (e. g. [6]). This is due to a very small plasma parallel heat conductivity at low temperatures which results in an insignificant volume being occupied by the low temperature plasma. In [12] it was found that perpendicular energy transport enlarges the low temperature, high plasma density volume and causes a substantial increase in the impurity radiation loss from this region. Plasma convection and neutral energy transport can also influence the radiation loss from the low temperature region. These analytic estimates were supported by 2D UEDGE runs for Alcator C-Mod like SOL plasma parameters showing that almost 100% of the Carbon radiation emanates from the low temperature (<10 eV), high plasma density divertor region.

To quantify this we investigate the effects of perpendicular plasma energy transport on impurity radiation loss with a 2D nonlinear heat conduction equation with the energy sink modeling plasma temperature distribution and energy loss due to impurity radiation in the SOL:

$$\partial_x(\kappa_\perp \partial_x T) + \partial_y(\kappa_\parallel (B_p/B)^2 \partial_y T) = R(T) \qquad (2)$$

where x and y are the "radial" and "poloidal" coordinates; R(T) is the sink function describing impurity radiation loss; $\kappa_\perp = \hat{\kappa}_\perp T^{\alpha_\perp} |\partial_x T|^\beta$ and $\kappa_\parallel (B_p/B)^2 = \hat{\kappa}_\parallel T^{\alpha_\parallel}$ are the perpendicular and parallel heat conduction coefficients, $\hat{\kappa}_\perp$ and $\hat{\kappa}_\parallel$ are their normalization constant counterparts, and $\alpha_\perp$, $\alpha_\parallel$, and β (where $\beta > -1$) are constants determining the scalings for $\kappa_\perp$ and $\kappa_\parallel$ with plasma temperature and its radial derivative; and B/B_p is the ratio of total to poloidal magnetic field strength. We find that the character of the solution of Eq. (2) is determined by the values of the characteristic "poloidal" heat flux, q_L, and "radial" width, Δ_L, of the heat flux profile at a distance $y = L$ from the target. For

the case which is more relevant to the solution of Eq. (2) in the divertor region, the domain of interest can be split into a set of weakly coupled poloidal layers. In this case for an R(T) peaked at $T = T_R$ the radiative front is V-shaped and perpendicular energy transport determines the radiation loss if

$$(2L_x/\Delta)^2 \kappa_\perp(T_R) \geq (B_p/B)^2 \kappa_\parallel(T_R) \qquad (3)$$

with L_x the poloidal target to X-point distance, and Δ the SOL width. For $L_x/\Delta \approx 10$, $B/B_p \approx 10$, and $\kappa_\parallel(T_R)/\kappa_\perp(T_R) \approx 10 \times (T_R[eV])^{5/2}$, we find from Eq. (3) that perpendicular energy transport determines the radiation loss for $T_R < 28$ eV.

We solve Eq. (2) numerically for Alcator C-Mod like geometry with $\alpha_\perp = \beta = 0$, and $\alpha_\parallel = 2.5$ for $R(T) \propto H(T - T_{min})(T_{mid}/T)^2$, where H(T) is the Heaviside step function, $T_{mid} = T(x, L)$ is the temperature at the midplane $y = L$, and $T_{min} = 10$ eV. Notice that this model for R(T) corresponds to constant impurity fraction, constant plasma pressure along the y coordinate, and no peaking of the radiative function at low temperature. The results of the numerical solution of Eq. (2) (for rectangular SOL divertor geometry) show (see Fig. 4) that even in this case the variation of $\kappa_\perp$ in the divertor strongly alters the divertor radiation loss giving results consistent with experimental observations and 2D UEDGE modeling.

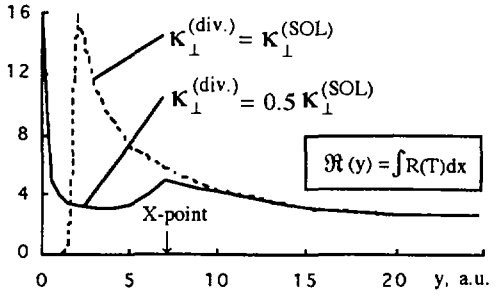

FIG. 4. Decrease of $\kappa_\perp$ in the divertor region causes reduction of radiation $\Re$ from divertor and plasma reattachment.

5. Kinetic modeling of divertor detachment

We simulate a transition from attached to detached SOL plasma flow with C-Mod parameters using the fully kinetic particle-in-cell code W1 [13]. Our kinetic model is free from the short mean free path expansion [1] of fluid plasma codes, which can fail because of sharp plasma gradients. We include Coulomb collisions among all plasma species, the self-consistent ambipolar electric field, a logical sheath potential, neutral transport, plasma-neutral interactions via charge exchange, and electron-impact ionization and excitation. To study SOL bifurcation, we vary only the heat flux q_{mid} entering the SOL from the midplane. In Fig. 5 we show the ratios of the upstream, P_{mid}, to divertor plasma pressure, P_d, and of q_{mid} to the divertor heat flux, q_d, as well as the particle flux onto the divertor, j_d, as functions of q_{mid}/P_{mid} (in units of 10^{-20} MW-m/eV) a key

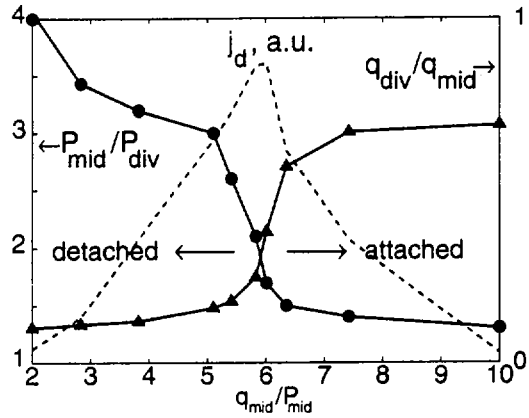

FIG. 5. Evolution of midplane to plate pressure drop, fraction of divertor heat flux to incoming heat flux, and particle flux onto divertor.

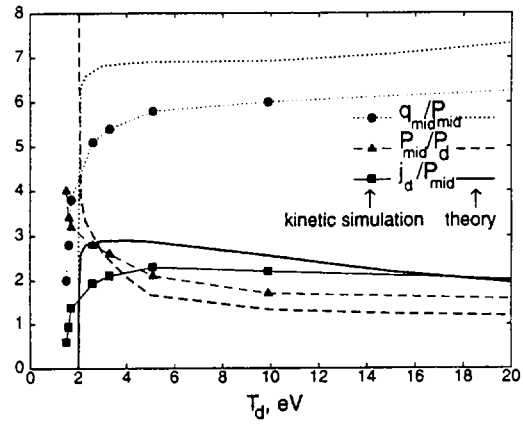

FIG. 6. Comparison between present simulation and theory [14] results.

parameter determining the transition to the detached divertor regime [14]. We use a mass ratio of 100. The plasma behaviour with q_{mid}/P_{mid} exhibits the main features of the transition into detachment observed experimentally [15]. The agreement with theory shown in Fig. 6 remains good to within about 30% until we reach the extremely detached regime, characterized by low divertor temperature ($T_d \leq 2$eV). We also find that reasonable quantitative agreement between kinetic and fluid simulations can only be obtained by using corrections in the fluid codes that go beyond the simple thermal flux limit (see also [16]). These include corrections in the boundary conditions and spatially dependent energy transport coefficients that contain non-local information.

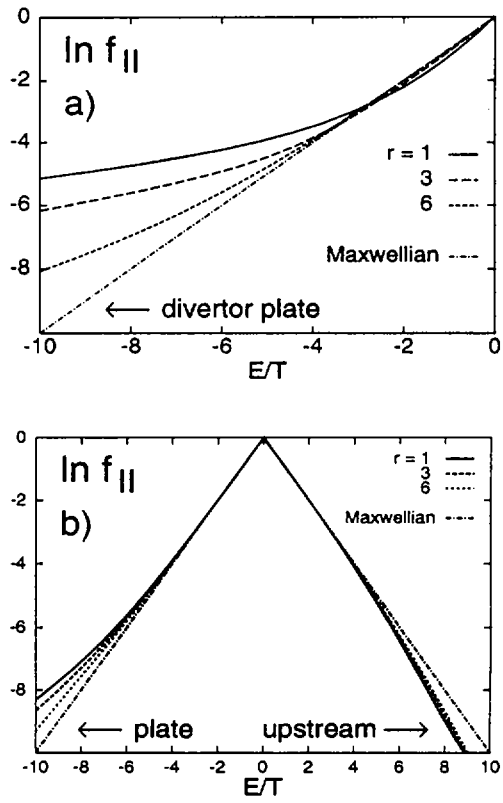

FIG. 7. Normalized electron distribution function at Alcator C-Mod divertor (a), and reciprocating probes (b) for different flux surfaces, which are at distance r (mm) from the separatrix at the equatorial plane.

6. Kinetic modifications to probe temperature measurements

The suprathermal electrons are responsible for the inferred electron "temperature", T, measured by Langmuir probes. The floating potential for a deuterium plasma is ≈ 3T. The high heat flux onto the probe makes it impossible to measure electron temperature below 2T. The preceding means that the electron current is measured in the energy interval 2T to infinity. Because the number of electrons absorbed by the probe rapidly decreases as the positive biasing of the probe increases, the slope of the probe Volt-Ampere characteristic measured within the narrow interval of 2-5T about the floating potential value is routinely interpreted as the actual temperature. However, the effective temperature T_{eff} of the electron distribution function f(ε) as evaluated from $T_{eff}(\varepsilon) =$

$-[d\ell nf(\varepsilon)/ d\varepsilon]^{-1}$, where ε is the parallel energy, can be significantly different from T for a non-thermal tail. We employ our 1D2V Fokker-Planck code ALLA [17] to study the equilibration of the electron distribution function for the experimentally measured plasma profiles from Alcator C-Mod shot #950308013 [18]. The parallel distribution function found at the divertor is shown in Fig. 7a. It has an elevated tail resulting in factor of two higher temperature being measured by the divertor probes. Due to non-local effects the parallel electron distribution function is asymmetric around the reciprocating probes, with different upstream (against the flow) and downstream (towards the plate) tails as shown in Fig. 7b. If a reciprocating probe is shielded to collect only electrons from one side, it can measure different temperatures in the upstream and downstream directions. The 30% variation of the upstream and downstream temperatures found is in agreement with C-Mod measurements [18].

REFERENCES

[1] BRAGINSKII, S.I., Reviews of Plasma Physics, Vol. 1 (LEONTOVICH, M.A., Ed.), Consultants Bureau, New York (1965) 205.

[2] HINTON, F.L., Handbook of Plasma Physics, Vol. 1 (GALEEV, A.A., SUDAN, R.N., Eds), North-Holland, Amsterdam (1983) 187.

[3] LACKNER, K., Comments Plasma Phys. Control. Fusion **15** (1994) 359.

[4] CATTO, P.J., et al., Phys. Plasmas **3** (1996) 3191.

[5] CATTO, P.J., et al., J. Nucl. Mater. (in press).

[6] POST, D.E., J. Nucl. Mater. **220–222** (1995) 143.

[7] WISING, F., et al., Contrib. Plasma Phys. **36** (1996) 136;
PORTER, G., et al., Phys. Plasmas **3** (1996) 1967.

[8] KRASHENINNIKOV, S.I., Contrib. Plasma Phys. **36** (1996) 293.

[9] KRASHENINNIKOV, S.I., et al., Phys. Lett. A **214** (1996) 285.

[10] PIGAROV, A.Yu., et al., Bull. Am. Phys. Soc. **40** (1995) 1884.

[11] KRASHENINNIKOV, S.I., SOBOLEVA, T.K., Phys. Plasmas **3** (1996) 2280.

[12] KRASHENINNIKOV, S.I., KNOLL, D., Contrib. Plasma Phys. **36** (1996) 266.

[13] BATISHCHEV, O.V., et al., Contrib. Plasma Phys. **34** (1994) 436.

[14] KRASHENINNIKOV, S.I., et al., Phys. Plasmas **2** (1995) 2717.

[15] HUTCHINSON, I.H., et al., Phys. Plasmas **1** (1994) 1511.

[16] BATISHCHEV, O.V., et al., Phys. Plasmas **3** (1996) 3386.

[17] BATISHCHEVA, A.A., et al., Phys. Plasmas **3** (1996) 1634.

[18] BATISHCHEV, O.V., et al., J. Nucl. Mater. (in press).

EFFECT OF HIGH Z IMPURITIES ON H-L TRANSITION IN ITER

V.A. ABRAMOV, A.R. POLEVOJ
Russian Research Center,
Kurchatov Institute,
Moscow, Russian Federation

Abstract

EFFECT OF HIGH Z IMPURITIES ON H-L TRANSITION IN ITER.

The effect of high Z impurities on the radiative losses in thermonuclear plasmas is considered. It is shown that for the Li, Be (etc.) like ions a substantial part of the losses is caused by ion excitation of transitions with $\Delta n = 0$, where n is the principal quantum number of the state. The impact of such ions on alpha particle energy losses due to the excitation of transitions with $\Delta n = 0$ is analysed. It is shown that taking into account this additional channel of losses for deuterons (tritons) and alpha particles dramatically decreases the permissible level of the impurity fraction in ITER caused by the H-L transition threshold. The loss mechanisms under consideration should be taken into account in the energy balance analysis of fusion plasmas for both magnetic and inertial confinement systems.

In the ITER basic concept it is assumed that the ITER nominal mode of operation is the ELMy H mode with a small percentage of light impurities (He 15%, Be 2%). The possibility of H mode operation depends crucially on the radiative losses from the core plasma. The models used for the radiative loss calculations usually take into account impurity ion excitation by electron impact only. This holds for the case of plasma contamination by low Z impurities. However, high Z impurities may be present in ITER. This could be associated with using high Z materials in the divertor construction such as Mo and W as well as with the particular plasma seeding by heavy ion gases (Ne, Ar, etc.) in order to reduce the heat load onto the divertor plates due to increased radiative losses. Alcator-C Mod experiments show that rather good operation regimes are possible with molybdenum divertor plates. ASDEX-Upgrade and DIII-D experiments with neon puffing reveal an increase in radiation.

The possibility to use tungsten as a divertor construction material in ITER is being discussed because of the small tungsten sputtering coefficient for low energies. The possibility of the presence of high Z impurities in ITER high temperature plasmas ($T \sim 10$–20 keV) led to the consideration of additional energy losses due to the excitation of multicharged ions by deuterons (tritons) and alpha particles. The importance of these effects was first mentioned in Ref. [1]. It was shown there that the role of heavy particles is most important in plasma regions where non-fully stripped impurities having transitions with $\Delta n = 0$ exist (n is a principal quantum number of state). Obviously, it is necessary to solve the complete set of balance equations for the ion species in all charge states of the plasma with prescribed temperature

and density distributions. To calculate the total radiative losses in the plasmas with tungsten impurity, we use here the model assumption that, for a given electron temperature T_e, there is only single ion with $Z = \langle Z \rangle$ determined from the standard coronal model [2]. The calculations of the excitation cross-sections by deuterons (tritons) and alpha particles are carried out by using the results obtained in Refs [1, 3]. We modify the expression for the excitation cross-section of the 2s-2p transition in the Li like ion, σ, and obtain the following expression:

$$\sigma = 1.26 \times 10^{-19}\, J(528/E)/Z^2E \tag{1}$$

where σ is in cm^2, E in eV and Z is an ion charge. The function J(x) is given by

$$J(x) = \ln(1 + x^{-1}) - \sum_{k=1}^{3} \frac{1}{k(1 + x)^k} - \frac{4}{7(1 + x)^7} \tag{2}$$

The asymptotic behaviour of J(x) is as follows:

$$J(x) = \ln x^{-1} \quad \text{for} \quad x \to 0$$

$$J(x) = 1/(6x) \quad \text{for} \quad x \to \infty \tag{3}$$

For transitions with $\delta n = 0$ in the other ions, we use the formulas from Ref. [3].

Using the well known expressions for the power losses due to Coulomb collisions, P^{Coul}, we obtain the following expression for the alpha particles [1]:

$$Q = \left\{ \frac{2}{3} \frac{R}{\ln[\frac{2}{3}R + 1]} - 1 \right\}^{2/3} \tag{4}$$

where Q is the ratio of the energy lost by Coulomb friction to energy loss due to the excitation of the transition with $\Delta n = 0$; $R \equiv P^{Coul}/P^{excit}$ is the ratio of the power loss due to Coulomb friction to the power loss due to the excitation of the transition with $\Delta n = 0$ at $E_\alpha = 3.5$ MeV.

To obtain expression (4), we have only taken the Coulomb collisions with electrons into account.

The analysis of the ion structure of W^{+q} ions with q = 20–65 (typical for T_e = 1–30 keV) shows that the main contribution is due to the transitions with $\Delta n = 0$ (the contribution of the transitions with $\Delta n = 1$ has been evaluated approximately).

The reduction of the power flux through the separatrix below the threshold of the H–L transition ($P_{H\text{-}L} > P_s$) caused by additional radiative losses leads to a termination of burning. The dependence of the heat flux across the separatrix on the

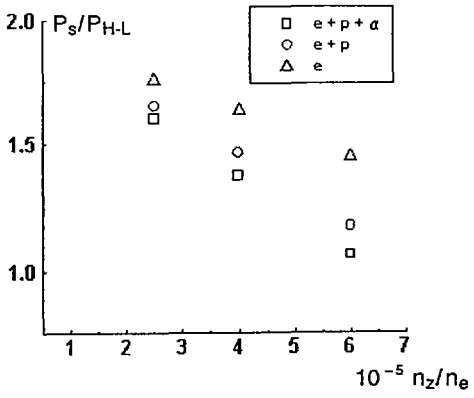

FIG. 1. P_s/P_{H-L} *versus* n_z/n_e *for* $\langle n \rangle = 6 \times 10^{19}\ m^{-3}$.

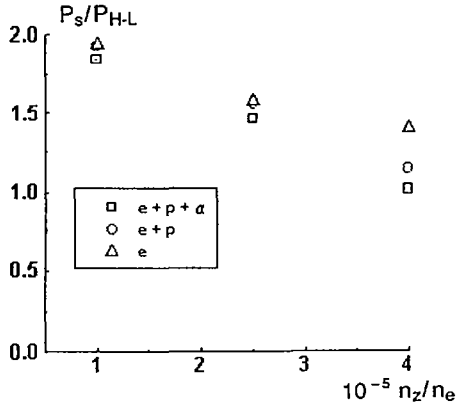

FIG. 2. P_s/P_{H-L} *versus* n_z/n_e *for* $\langle n \rangle = 8 \times 10^{19}\ m^{-3}$.

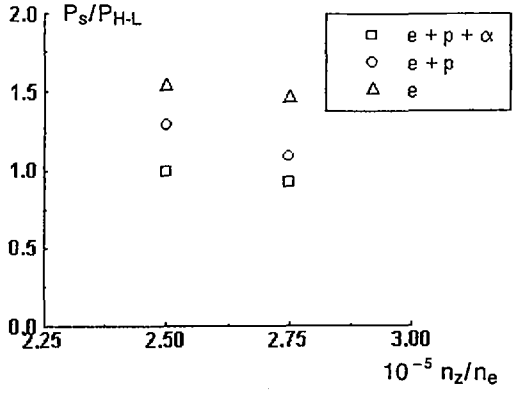

FIG. 3. P_s/P_{H-L} *versus* n_z/n_e *for* $\langle n \rangle = 10^{20}\ m^{-3}$.

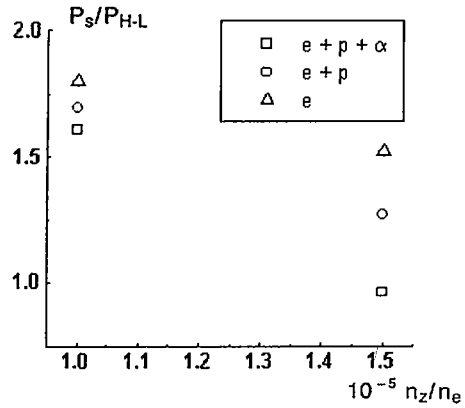

FIG. 4. P_s/P_{H-L} versus n_z/n_e for $\langle n \rangle = 1.3 \times 10^{20}\ m^{-3}$.

plasma density and the impurity fraction is analysed for different approximations for the radiative losses.

It is more convenient to estimate the influence of the additional channels of energy loss for the main plasma species by using the fixed plasma density and temperature profiles in order to exclude uncertainties caused by transport model specification. For the total tungsten ion density distribution we use the approximation $n_z/n_e(r)$ = const confirmed by calculations of ITER discharges in different regimes [4]. All calculations are carried out for plasma profiles with an energy confinement time corresponding to the ELMy H mode scaling law and helium confinement with $\tau^*_{He}/\tau_E = 10$.

The model described above is used for calculating the critical level of tungsten concentration corresponding to the threshold for the H–L transition for different types of processes taken into account (ordinary coronal model, coronal model + additional losses due to the excitation by fuel ions (deuterons/tritons), coronal model + additional losses due to the excitation by fuel ions and fast alphas). The results of the calculations for some regimes are presented in Figs 1 to 4.

CONCLUSIONS

Our results show that the additional losses caused by W ion excitation by deuterons/tritons and fast alpha particles dramatically decrease the H–L power threshold (and the permissible level of the impurity fraction). The model using only the standard coronal model losses overestimates the value of the H–L transition threshold (about 1.5 times for the regimes considered).

It should be emphasized that the additional channels of the energy losses due to the excitation of high Z impurity ions by fuel ions and fast alpha particles must be taken into account for both types of fusion systems, i.e. with magnetic and with inertial confinement.

REFERENCES

[1] ABRAMOV, V.A., GONTIS, V.G., LISITSA, V.S., Fiz. Plazmy **10** (1984) 400.
[2] POST, D.E., et al., At. Data Nucl. Data Tables **20** (1977) 397.
[3] SHEVELKO, V.P., SCOBELEV, I.Yu., VINOGRADOV, A.V., Phys. Scr. **16** (1977) 123.
[4] BECKER, G., Nucl. Fusion **35** (1995) 39; **35** (1995) 969.

INTEGRATED IMPURITY MODEL FOR ACTIVELY COOLED PLASMA FACING COMPONENTS

J. HOGAN, C.C. KLEPPER, J. HARRIS,
P.K. MIODUSZEWSKI, R.C. ISLER
Fusion Energy Division,
Oak Ridge National Laboratory,
Oak Ridge, Tennessee,
United States of America

D. GUILHELM, M. CHATELIER, C. DeMICHELIS,
M. GONICHE, W. HESS, M. MATTIOLI, W. MANDL,
R. MITTEAU, P. MONIER-GARBET, J. SCHLOSSER,
EQUIPE TORE SUPRA
Département de recherches sur la fusion contrôlée,
Centre d'études de Cadarache,
Saint-Paul-lez-Durance,
France

S. TOBIN
Northern Kentucky University,
Highland Heights, Kentucky,
United States of America

V. PHILIPPS, U. KOEGLER, J. WINTER
Institut für Plasmaphysik,
Forschungsanlage Jülich,
Jülich,
Germany

Abstract

INTEGRATED MODEL OF ACTIVELY COOLED PLASMA FACING COMPONENTS.

A model has been developed to describe impurity production from the actively cooled graphite plasma facing components in Tore Supra, as well as the resulting transport in the scrape-off layer (SOL), penetration through the SOL and transport into the plasma core. The system consists of a 3-D Monte Carlo SOL impurity transport code (BBQ), a 3-D, time dependent thermal code (CASTEM-2000) and a radial core plasma impurity transport code. Such a code system is required to determine the limits due to intrinsic impurity generation in long duration operation under conditions of high heat flux (e.g. in ITER and large scale helical devices), and the characteristics of long term erosion processes. This Tore Supra system is the first of its kind. Production by chemical and physical sputtering (due to D^+ and C^{n+}), RES and ablation processes are included. Comparisons have been made with Tore Supra ohmic discharges with an inertially cooled outboard limiter, and TEXTOR experiments using an inertial test limiter which serves as a standard for studies of impurity generation from graphite surfaces in tokamaks. Limiting processes have been studied for steady peak heat fluxes up to 15 MW/m^2 in the actively cooled lower vertical limiter and LH grills of Tore Supra.

1. BACKGROUND

The fusion relevance either of advanced toroidal concepts (e.g., helical systems) or of advanced operating regimes (e.g., enhanced shear modes) depends critically upon the feasibility of their sustainment in long pulses leading to steady state. Sustainment, in turn, requires the ability to handle long pulse heat fluxes and (in the case of the tokamak) to deal with the conditions of low edge density and high T_e which favor active current drive. Uniquely, Tore Supra is an actively cooled graphite machine equipped to explore these issues. Further, as a limiter machine, the detailed study of limiting impurity generation processes is easier to make than with high recycling divertors. The efflux power in Tore Supra is shared among several plasma facing components: a large area (~12 m^2) inner wall, six lower and one outboard limiter, the lateral protection armor of the RF antennae and LH grills, and the neutraliser plates of an Ergodic Divertor. In order to understand the limiting processes, a code system has been developed to permit detailed comparison with experiment. Since impurity generation rates for graphite (chemical sputtering and RES) depend strongly on the surface temperature distribution, and this is detemined by the active cooling system, calculation of the surface thermal conditions is an important facet of the model.

2. MODEL ELEMENTS

The code elements of the integrated model are CASTEM-2000, BBQ and the Tore Supra group radial impurity transport code. CASTEM-2000 is a 3-D, time-dependent finite elements thermal and mechanical transport code (1). The Tore Supra version incorporates validated thermal hydraulics models for conditions near to critical boiling (2). Engineering applications of CASTEM employ a prescribed heat flux, while the 'physics variant' used here calculates the sheath-transmitted heat flux self-consistently and includes secondary electron emission, thermionic emission, evaporation, and SOL transport and redeposition. The condition of zero net electron current to the surface defines the sheath potential: $n_e v_e e e^{-e\phi/T} \beta / 4 - J_T = \Gamma_i e$, where v_e is the electron thermal speed, Γ_i is the incident ion flux, $\beta \equiv (1-\sigma_e) / (1+\sigma_i)$, ($\sigma_e$: secondary electron emission - SEE) ; and J_T is the thermionic current density. The heat flux then is: $q_{ps} = \gamma \Gamma_i T$, where $\gamma = 1 + \Phi + z_T$, $\Phi = e\phi/T = \ln [(m_i / \pi m_e)^{1/2} / z_T]$, $z_T = 2 (1+y_T)/\beta$, and $y_T = J_T / e \Gamma_i$. As described in (3), the value of the SEE coefficient for a-C:H surfaces can vary from 0.5 to ~0.85. Thermionic emission plays a strong role at high surface temperature, and our model for the thermionic current effect on heat flux is based on (4). Ablation cooling is limiting at very high temperatures (> 3000K). The ablation model used in CASTEM-2000 was developed by the ITER team (5). The additional heat flux due to sheath-accelerated, redeposited multiply charged impurities is found from the BBQ code.

The BBQ scrape-off layer impurity transport code is described in (6). It incorporates a particle transport model patterned after that of the LIM code (7), including parallel streaming along field lines, anomalous perpendicular diffusion, parallel friction and electrostatic drifts. For chemically sputtered impurities, the Langer-Erhardt database (8) for CD_4 break-up reactions is incorporated, as described in (9). The detailed 3-D plasma-facing geometry of each component is treated. The magnetic field geometry is given (for cases discussed here) by analytic shifted, oblate or

elongated circles (depending on β_{pol}). Core impurity transport is calculated with the Tore Supra group's radial impurity transport code (10). The radial code matches calibrated visible bremsstrahlung emission (at 523.8 nm), core soft X-ray emission and XUV spectroscopy of H-like and He-like C ions (see p 15 of (11) and (12)).

3. INERTIAL LIMITER CASES

3.1 Tore Supra Phase I limiter

Comparisons of local impurity generation with core accumulation have been made for a Tore Supra inertially cooled graphite limiter (5890PT, Carbon Lorraine). Ohmic discharges (13) produced a surface temperature range from 500-2300K. For T_{surf}~800-1000K substantial impurity generation due to chemical sputtering is calculated, but the low penetration efficiency for this case results in a dominant core source due to physical sputtering. Generated impurites enter the plasma inside the last closed flux surface with both a toroidal and poloidal distribution. BBQ-calculated impurity fluxes are used as boundary conditions for the Tore Supra group's radial transport code. The usual radial transport assumption that all impurities enter as neutrals at a fixed radius was replaced and the BBQ flux surface averaged influx was used instead. The comparison of BBQ and measured core impurity content is shown in the Table. V_A is the inward convection velocity at the limiter radius and $n_C(r=0)$ is the measured core carbon concentration. The match parameters are $G \equiv I_R/I_I$, where $I_{I,(R)}$ are the intensities of the intercombination, (resonance) lines of He-like C; Lyα/R: ratio of CVI Lyα to resonance line intensity of CV; CVI: Lyα brightness (ph/cm^2/s/sr). Agreement is attained when the BBQ impurity flux is sufficient to match the observed core content (C_{imp} = 1.0 in the Table). It is found for a range of cases with varying density. The ratio (Y_f) of the required physical sputter yield to the TRIM code recommended fit (14) is Y_f = 4.0. Given the remaining geometric uncertainties involved in the 3-D to 1-D joining procedure, C_{imp}~2 is a reasonable match criterion, in which case values with Y_f~2 (more representative of the measured basic sputtering data) also match.

TABLE: BBQ - experiment comparison

Shot	$T_e(a)$	$n_e(a)$	C_{imp}	SOL	Radial		CVI	Lyα/R	G	$n_C(r=0)$
	eV	10^{18}		D_{SOL}	D_{core}	V_A	10^{13}			10^{17}
		m^{-3}		m^2/s	m^2/s	m/s				m^{-3}
13814	75	4.0	1.10	2.5	0.9	1.90	7.5	2.00	0.40	2.50
13820	75	6.0	1.05	2.5	1.0	2.50	8.0	1.60	0.40	3.00
13806	125	2.2	1.15	5.0	0.7	3.20	6.0	1.70	0.35	6.50

3.2 TEXTOR test limiter

Detailed experiments in TEXTOR and TEXTOR-94 have characterized graphite impurity generation processses from an inertially cooled test-limiter (15, 16). Experiments on this test-limiter represent a standard for comparison of calculated and observed impurity generation rates under conditions of finite incident plasma flux. Modeling of impurity generation in the 3-D geometry has been carried out for this standard case. The material is EK98 graphite (density 1.85 g/cm^3, specific heat 1.8×10^3 Ws / kg·K, conductivity σ = 33.3 W / mK). The assumed plasma parameters are: q(a)=4.0, $n_e(a)=5\times10^{12}$ cm^{-3}, $T_e(a)=T_i(a)$=50 eV, ion/electron side D^+ flux asymmetry 1.3/0.7, σ_e=0.8, Y_f=2.5, the ratio of perpendicular / parallel incident heat flux

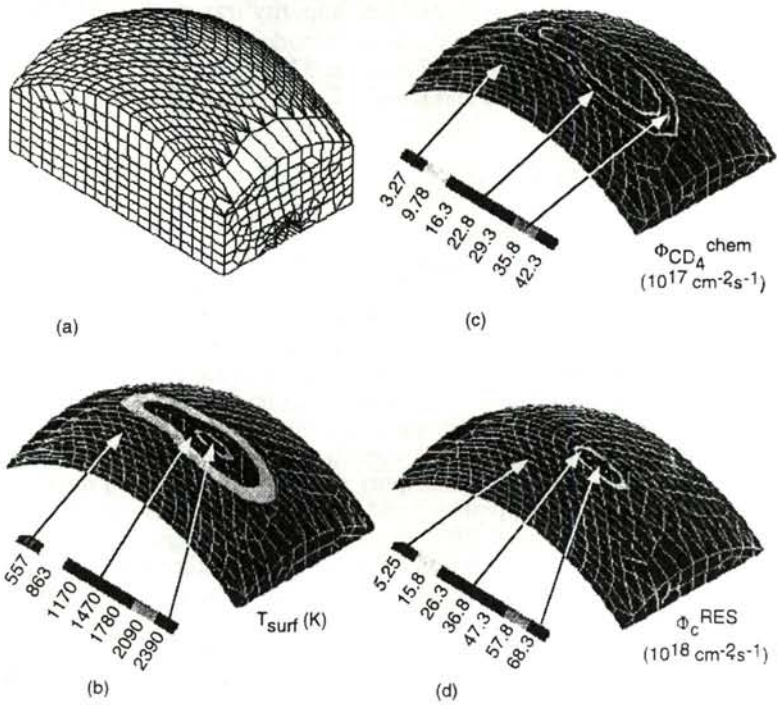

FIG. 1. CASTEM-2000 results for inertially cooled graphite test-limiter in TEXTOR. (a) Test-limiter computational mesh; (b) T_{surf} distribution; (c) distribution of emitted flux of chemically sputtered CD_4; (d) flux of C_0 from RES.

$q_\perp/q_{//}$=0.3, the SOL radial decay length for the heat flux λ_q=8 mm. Figure 1 shows (a) the geometry, (b) the calculated surface temperature distribution and (c, d) the distribution of chemical sputtered fluxes and RES carbon emission for the test-limiter case. The local temperature dependence of chemical sputtering and RES produces a significant spatial variation in impurity emission for the standard test-limiter. More detailed comparisons will be discussed elsewhere.

4. ACTIVE COOLING CASES

4.1 Lower vertical limiter

The limiting steady state heat flux has been examined experimentally in series of experiments using the Lower Vertical Limiter (17, 18). Calculations with the model show that the highly localized heat flux due to redeposited impurities can be important in determining the limiting behavior, when this limiter is operated in the regime 4 MW/m^2<P_{lim}<7 MW/m^2. As described in (18), superbrilliance events occur near the heat flux limit, in which a sudden rise in temperature occurs, leading to a new equilibrium. Since both the external plasma conditions and the thermal hydraulic conditions (water at 40 bar, 7 m/s, 150C) are unchanged, such behavior is difficult to reproduce without assuming a material-related defect, such as local (and perhaps

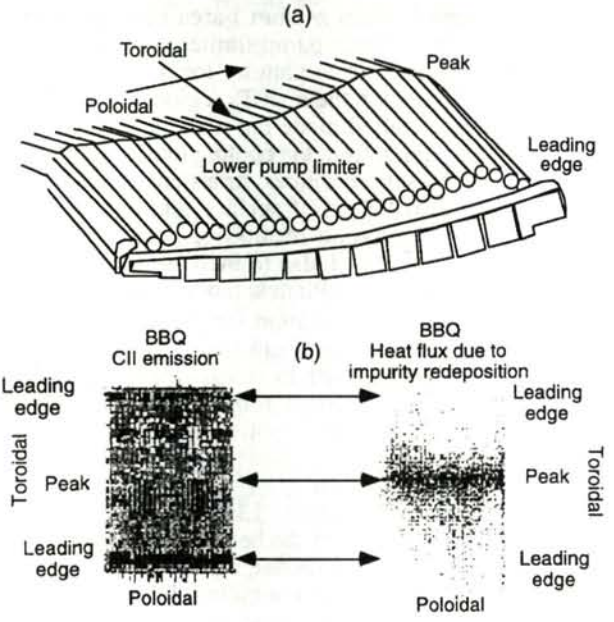

FIG. 2. (a) Schematic of geometry of lower pump limiter; (b) BBQ results for C II emission (left) and heat flux from redeposited carbon (right).

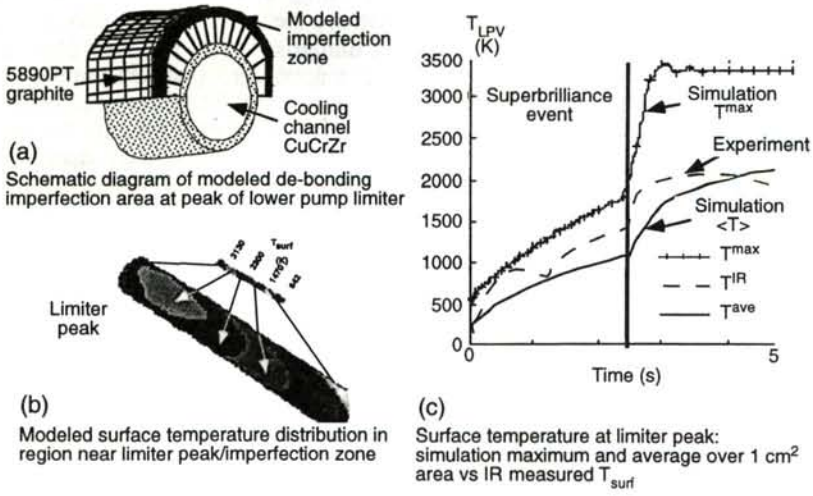

FIG. 3. (a) Detail of imperfection zone model on the Tore Supra lower pump limiter used in CASTEM-2000; (b) calculated T_{surf} near the limiter peak; (c) comparison of measured maximum T_{surf} and CASTEM-2000 results with an assumed debonding event at $t = 2.5$ s.

transient) debonding of a small (1mm x 1mm) area near the limiter peak. Figure 2 shows a schematic view of the bottom pump limiter (a) and the calculated impurity emission and the impurity re-deposition pattern, localized on the limiter crown (b). Such a redeposition source, located in the high T_e region, can produce the high thermal stresses resulting in a defect. Detailed modeling with an assumed defect zone (Figure 3a) due to debonding of the graphite from the cooling tube (modeled as reduced thermal conductivity) can reproduce the superbrilliance transient effect. Figure 3b (simulation) shows the highly localized distribution of surface temperature in the region of the defect. Figure 3c shows the simulation results for peak surface temperature. This increases rapidly, due to the defect and also to increased heat flux due to thermionic emission, reaching 3500K where the Planck radiation is as strong as the plasma heating. Fig. 3c also compares the simulation temperature averaged over the 1 cm^2 spatial sensitivity of the infrared system, and the temperature measured by the IR system. Additional sensivitity studies with modeled defects ranging from 0.5 -1.5 mm in radial extent, and 0.5-2 mm in axial extent produce the same maximum temperature, and lead to a 20% variation in the simulated spot-averaged temperature.

4.2 Lower hybrid lateral protection

Local acceleration of electrons near the LH grilles can generate fast electron tails and this can lead to local enhancement of the heat flux transmitted through the sheath (19). Using the self-consistent heat flux model, the local impurity generation rate for the Tore Supra lateral protection has been computed. A model has been developed, in which a chemical rather than RES source appears to be involved for hot spot generation on the LH lateral protection.

5. DISCUSSION

An integrated model for surface temperature-dependent impurity generation, SOL transport, core penetration and core diffusion has been developed to evaluate long pulse limits due to impurity generation and accumulation. Reasonable agreement is found between measured core impurity content and the edge impurity fluxes calculated by the model, for Tore Supra ohmic cases. Comparison with the TEXTOR standard test limiter case for high heat fluxes shows characteristics (surface temperature and pattern of emission) which are in reasonable agreement. Impurity-related processes have been identified as playing a role in heat flux limit experiments for the lower vertical limiter in Tore Supra. Local sheath-accelerated impurity deposition can contribute, along with imperfections in limiter bonding, to superbrilliance events. A model for local hot spots on the LH grills generated by fast electrons has been developed. Thus, comparison with Tore Supra experiments exploring heat flux limits gives encouragement that the code system is a useful tool for the interpretation of these experiments.

REFERENCES

[1] BOHAR, L. (Département des études mécaniques et thermiques), CASTEM-2000 Notice (1994).
[2] SCHLOSSER, J., et al., CASTEM Transfer Models (1996) (internal report).
[3] PEDGELY, J.M., McCRACKEN, G., Plasma Phys. Control. Fusion **35** (1993) 397.
[4] TOKAR', M.Z., et al., Nucl. Fusion **32** (1992) 15.
[5] IGITKHANOV, Yu., et al., in Controlled Fusion and Plasma Physics (Proc. 22nd Eur. Conf. Bournemouth, 1995), Vol. 19C, Part IV, European Physical Society, Geneva (1995) 333.
[6] HOGAN, J., BBQ: Impurity Scrape-off Layer Transport Code, Rep. ORNL-TM-13 312, Oak Ridge National Lab., Oak Ridge, Tennessee, USA (1996).

[7] STANGEBY, P., Contrib. Plasma Phys. **28** (1988) 507.
[8] LANGER, W.D., ERHARDT, A.B., J. Nucl. Mater. **162–164** (1989) 329.
[9] HOGAN, J., POSPIESZCZYK, A., Modelling of Hydrocarbon Fueling, ORNL-TM-11 542, Oak Ridge National Lab., Oak Ridge, Tennessee, USA (1990).
[10] TFR GROUP, Nucl. Fusion **25** (1985) 981.
[11] CARRARO, L., et al., Collisional-Radiative Models for Hydrogen-like and Helium-like Carbon and Oxygen Ions and Applications to Experimental Data from the TS Tokamak and the Reversed Field Pinch RFX, Rep. EUR-CEA-FC-1541, Association Euratom–CEA, Centre d'études de Cadarache, France (1996).
[12] GUIRLET, R., DeMICHELIS, C., MATTIOLI, M., HESS, W., MONIER-GARBET, P., in Controlled Fusion and Plasma Physics (Proc. 21st Eur. Conf. Montpellier, 1994), Vol. 18B, Part III, European Physical Society, Geneva (1994) 1280.
[13] TOBIN, S.J., et al., Plasma Phys. Control. Fusion **38** (1996) 251.
[14] ECKSTEIN, W., GARCIA-ROSALES, C., ROTH, J., OTTENBERGER, W., Sputtering Data, Rep. IPP/9/82, Max-Planck-Institut für Plasmaphysik, Garching, Germany.
[15] PHILIPPS, V., et al., J. Nucl. Mater. **220–222** (1995) 467.
[16] PHILIPPS, V., et al., Nucl. Fusion **33** (1993) 953.
[17] EQUIPE TORE SUPRA, in Plasma Physics and Controlled Nuclear Fusion Research 1994 (Proc. 15th Int. Conf. Seville, 1994), Vol. 2, IAEA, Vienna (1995) 133.
[18] GUILHELM, D., et al., J. Nucl. Mater. (in press).
[19] GONICHE, M., et al., in Controlled Fusion and Plasma Physics (Proc. 23th Eur. Conf. Kiev, 1996), Vol. 20C, European Physical Society, Geneva (1996).

DEGAS 2 NEUTRAL TRANSPORT MODELING OF HIGH DENSITY, LOW TEMPERATURE PLASMAS

D.P. STOTLER, A.Yu. PIGAROV[1,2], C.F.F. KARNEY,
S.I. KRASHENINNIKOV[1,2], B. LaBOMBARD[1], B. LIPSCHULTZ[1],
G.M. McCRACKEN[1], A. NIEMCZEWSKI[1,3], J.A. SNIPES[1],
J.L. TERRY[1], R.A. VESEY[4]
Plasma Physics Laboratory,
Princeton University,
Princeton, New Jersey,
United States of America

Abstract

DEGAS 2 NEUTRAL TRANSPORT MODELING OF HIGH DENSITY, LOW TEMPERATURE PLASMAS.

Neutral transport in the high density, low temperature plasma regime is examined using the DEGAS 2 Monte Carlo neutral transport code. DEGAS 2 is shown to agree with an analytic fluid neutral model valid in this regime as long as the grid cell spacing is less than twice the neutral mean free path. Using new atomic physics data provided by the collisional radiative code CRAMD, DEGAS 2 is applied to a detached Alcator C-Mod discharge. A model plasma with electron temperature ~ 1 eV along detached flux tubes, between the target and the ionization front, is used to demonstrate that recombination is essential to matching the experimental data. With the CRAMD data, ~20% of the total recombination is due to molecular activated recombination.

1. INTRODUCTION

Detaching the plasma from the divertor target has been proposed as a method of power dispersal in the ITER[1] divertor. Typical plasma conditions in the detached state are electron temperatures ~ 1 eV, electron densities $\sim 10^{21}$ m^{-3}, and neutral densities $\sim 10^{20}$ m^{-3}. Under these conditions, the chemical reactions involving hydrogen atoms, molecules, and ions are tightly coupled.

The short mean free path neutral transport and atomic physics reactions used in DEGAS 2[2] must be accurately represented if the detached plasma sources, sinks and radiation are to be computed reliably. To this end, we benchmark the neutral transport in DEGAS 2 against an analytic model of a partially

---

[1] Plasma Fusion Center, Massachusetts Institute of Technology, Cambridge, Massachusetts, United States of America.

[2] Russian Research Center, Kurchatov Institute, Moscow, Russian Federation.

[3] Presently at McKinsey & Company, Inc., London, United Kingdom.

[4] Presently at Sandia National Laboratories, Albuquerque, New Mexico, United States of America.

ionized fluid plasma[3]. In addition, the collisional-radiative atomic physics code CRAMD[4] has been developed in parallel with DEGAS 2 for the purpose of computing the effective ionization, recombination, dissociation, and radiation rates for these high density, low temperature plasmas. Initial applications to a partially detached Alcator C-Mod[5] discharge will be described.

2. COMPARISON WITH FLUID MODEL

The fluid equations in Ref. [3], derived under the assumption of a constant charge exchange cross section, contain terms representing the thermal force and diffusion thermoeffect. Neglecting viscosity, ionization, and recombination, the resulting fluid neutral momentum balance in a slab geometry is

$$\frac{d}{dx}\left(mnv^2 + nT\right) = \alpha_T n \frac{dT}{dx} - m\nu_{cx} nv, \tag{1}$$

where n is the neutral density, v its flow velocity, T is its temperature (assumed equal to the ion temperature T_i), and m is the ion and neutral mass. The thermal force coefficient, $\alpha_T = 0.24$, and the charge exchange frequency, $\nu_{cx} = 2.93\sigma_{cx} n (T/m)^{1/2}$.

With a neutral source on one end of the slab ($x = 0$) and an exit at the other ($x = L$), an approximate analytic solution to Eq. (1) can be obtained by writing the exiting flux as $j = \gamma n(L)[T(L)/m]^{1/2}$, where $\gamma \sim 1$ is an undetermined numerical factor. The results are insensitive to the precise value of γ. Equation (1) can be written in terms of the relative density $\eta \equiv n(x)/n(L)$,

$$\frac{d\eta}{dx} = -\left[\frac{\frac{(1-\alpha_T)}{T(L)}\frac{dT(x)}{dx}\eta + \frac{\gamma\nu_{cx}}{[T(L)/m]^{1/2}}}{\frac{T(x)}{T(L)} - \frac{\gamma^2}{\eta^2}}\right], \tag{2}$$

and numerically integrated from $x = L$ to $x = 0$ using specified plasma temperature profiles.

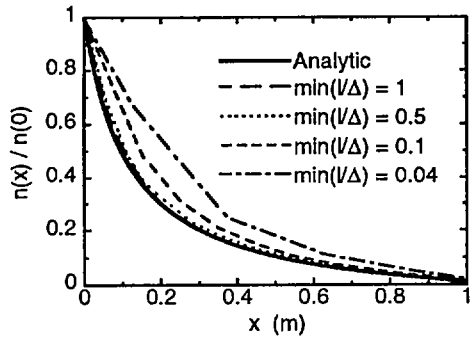

FIG. 1. Comparison between four DEGAS 2 simulations at different mean free path to grid spacing ratios and an analytic solution [Eq. (2)] of the normalized neutral density variation with distance in a slab geometry.

The critical parameters in the comparison between Eq. (1) and DEGAS 2 are the mean free path to system size ratio $l/L = [T(L)/m]^{1/2}/(L\nu_{cx})$ and the mean free path to grid spacing ratio l/Δ, where Δ is the width of the individual DEGAS 2 grid cells. If l/L is too big, the neutrals and ions are not well coupled, and Eq. (1) is not valid. If l/Δ is too small, the DEGAS 2 neutrals do not experience enough temperature variation to resolve the thermal force.

Simulations exploring the parameter space indicate agreement between DEGAS 2 and Eq. (2) when $\max(l/L) \leq 0.1$ (i.e., maximum value of l/L in the plasma) and $\min(l/\Delta) \geq 0.5$. Figure 1 demonstrates the latter inequality with four runs, all with $\max(l/L) = 0.1$, and $\min(l/\Delta) = 0.04$, 0.1, 0.5, and 1.

3. ATOMIC PHYSICS MODELS

Ions striking the divertor targets in DEGAS 2 are assumed to reenter the plasma either as reflected atoms or desorbed molecules[6]. The fraction reflected and their energies are taken from experimental data and surface physics simulations[6].

For temperatures in excess of a few eV, molecules predominantly undergo dissociation and ionization. The original version of DEGAS[6] explicitly incorporated these reactions using rates taken from the literature. Atomic H ionization and H^+ recombination were treated with a collisional-radiative calculation. This atomic physics model ("model I") is available in DEGAS 2 as well.

At temperatures below a few eV, the rates of dissociation and ionization decrease, and vibrational excitation, dissociative attachment [$H_2(v) + e \rightarrow H^- + H$], and ion conversion [$H_2(v) + H^+ \rightarrow H_2^+ + H$] become dominant[4]. Product ions of the last two reactions rapidly recombine into two neutral atoms via $H^- + H^+ \rightarrow 2H$ and $H_2^+ + e \rightarrow 2H$. Through this "molecular activated recombination" (MAR), the break-up of a single molecule effectively results in a source of *three* atoms and a sink of one ion.

The CRAMD package[4] aims to incorporate all relevant processes involving the ground and excited states of atoms, molecules, and their ions into a self-consistent, multispecies, collisional-radiative calculation. The resulting effective rates for hydrogen molecule break-up, atom ionization, and radiative and three-body recombination can be used directly by DEGAS 2 to compute the neutral transport of hydrogen atoms and molecules ("model II").

Model II incorporates newer cross sections for transitions between the various hydrogen atomic excited states, as well as a more careful treatment of near continuum states. For $T_e = 5$ eV, the effective ionization rates in model II are a factor of 1.6 smaller than those in model I. At 1 eV, the recombination rate in model II is a factor of 1.4 smaller.

4. DIVERTOR PLASMA MODELS

As in Ref. [7], radial plasma density and temperature profiles in Alcator C-Mod are taken from a fast scanning probe in the main scrape-off layer and domed probes in the divertor targets. The ion fluxes to the targets are obtained from the measured parallel ion fluxes using the magnetic field line angle of incidence[7] as computed from the equilibrium. A pure deuterium plasma is assumed with $n_i = n_e \equiv n$ and $T_i = T_e \equiv T$.

In the baseline plasma model, "model A", an analytic procedure[8] is used to interpolate the plasma parameters onto the computational mesh cells[7] between the probe locations. In this model[8], the temperature profile along each flux tube is the solution of the parallel heat conduction equation with a delta-function radiation sink at $T = T_{\rm rad} = 8$ eV and uniform heat source from the core plasma. Parallel ion momentum loss due to charge-exchange is assumed to occur at a constant rate for $T < T_{\rm cx} = 5$ eV.

Plasma "model B" is a limiting case in which we set the T gradient to zero[9] along detached flux tubes between the target and the point where $T = T_{\rm rad}$; otherwise it the same as model A. Detached flux tubes are identified as having a factor of four or more drop in the measured isotropic pressure P from upstream to the plate. In this model, a factor of four decrease in pressure is assumed to occur at $T = T_{\rm rad}$. Any further reduction is spread linearly between there and the plate. The density is determined from $n = P/(2T)$.

Recent work[10] has suggested that the bulk electron temperatures in divertor plasmas may be lower than are indicated by the probe data. We consider a variant of model B, plasma "model C", in which the plate temperatures are multiplied by 0.5 before the profiles are defined. The plate densities are modified to maintain the same particle fluxes as the other two cases.

5. DEGAS 2 SIMULATIONS

The results of the six runs obtained with the two physics models and three plasma models of Alcator C-Mod shot 950308012 are summarized in Table I. At the simulated timeslice, $t = 0.96$ s, the plasma is partially detached along the outer target with measured temperatures there of 1–2 eV.

The experimentally observed volume-integrated Balmer-α emission rate D_α and divertor neutral gas pressure[9] P_g are included in Table I for comparison with the DEGAS 2 results. Since the "gas box" containing the neutral pressure gauge is not simulated, we use the D and D_2 densities ($n_{\rm D,div}$, $n_{\rm D_2,div}$) and pressures at the bottom of the divertor, where the entrance to the gas box would be, to compute the total neutral flux. P_g is found by then assuming that the same flux of room temperature molecular gas reaches the gauge[9]. The effective atom temperature at the bottom of the divertor $T_{\rm D,div}$ varies with the

Table I. RESULTS FROM DEGAS 2 RUNS WITH THREE PLASMA MODELS (A, B, C) AND TWO ATOMIC PHYSICS MODELS (I, II)

	A.I	A.II	B.I	B.II	C.I	C.II	Meas.
D_α (10^{21} s^{-1})	1.73	1.17	2.63	2.01	33.6	26.4	8.87
P_g (mTorr)	0.57	0.57	1.4	1.6	26.	23.	32.2
$n_{D,div}$ (10^{19} m^{-3})	0.18	0.18	0.46	0.59	8.2	7.7	-
$n_{D_2,div}$ (10^{19} m^{-3})	0.36	0.39	1.3	1.3	32.	26.	-
$T_{D,div}$ (eV)	3.2	3.2	2.6	2.4	2.0	2.0	-
Γ_{recyc} (10^{22} s^{-1})	5.40	5.40	5.36	5.36	5.29	5.29	-
Γ_{recom} (10^{22} s^{-1})	0.054	0.053	0.50	0.38	40.	18.	-
$\Gamma_{D,ion}$ (10^{22} s^{-1})	5.0	4.7	5.4	5.1	44.	24.	-
$\Gamma_{D_2,ion}$ (10^{22} s^{-1})	0.44	0.74	0.50	0.68	1.9	-0.84	-
Γ_{MAR} (10^{22} s^{-1})	-	0.066	-	0.10	-	2.7	-

background plasma and not with atomic physics model. It is, thus, governed more by charge exchange and wall reflection processes than molecular dissociation.

By particle conservation, $\Gamma_{recyc} + \Gamma_{recom} = \Gamma_{D,ion} + \Gamma_{D_2,ion}$, where Γ_{recyc} is the recycling rate (ion flux to targets), Γ_{recom} is the recombination rate (both are input to DEGAS 2), $\Gamma_{D,ion}$ is the ionization rate of atoms, and $\Gamma_{D_2,ion}$ is the rate of ion generation from molecular dissociation. In the model II runs, the rate of atoms generated by MAR, Γ_{MAR}, enters implicitly as a negative contribution to $\Gamma_{D_2,ion}$ and is balanced by an equal positive contribution to $\Gamma_{D,ion}$.

In plasma model A, the electron temperature is greater than 5 eV throughout the divertor plasma. Neither recombination nor MAR are important. The lower D_α in A.II is the result of a smaller number of Balmer-α photons per ionization in model II for $T > 3$ eV. In both A.I and A.II, molecules are predominantly broken up in regions with $T \simeq 5$–10 eV. Over this range, model II yields more ions per molecule, leading to the larger $\Gamma_{D_2,ion}$ in A.II.

With the detached 1–2 eV region, plasma model B yields significant recombination and MAR. Recombination is in fact observed experimentally; it has been found that the number of ions lost to recombination can be comparable to the number striking the divertor plates[11]. However, in B.I and B.II, recycling is still dominant, and the results are qualitatively similar to A.I and A.II.

In plasma model C, the factor of two reduction in temperature relative to model B leads to recombination rates which are more than three times the recycling source. In C.II, MAR contributes another 15% to the source of recombined atoms. The sink of ions due to MAR exceeds the rate at which they are created from D_2 dissociation; hence, $\Gamma_{D_2,ion} < 0$. Again, the drop in the D_α rate between C.I and C.II results from the lower conventional recombination rate and the higher number of the photons / ionization in model II. The other

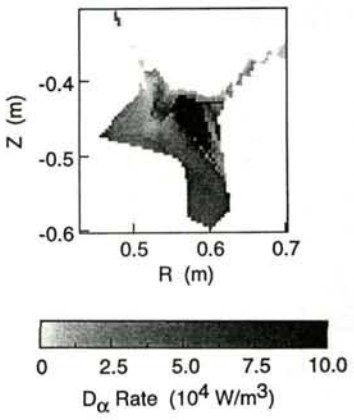

FIG. 2. D_α emission in model C.II. The scale maximum has been reduced from 3×10^6 W/m^3 to enhance contrast.

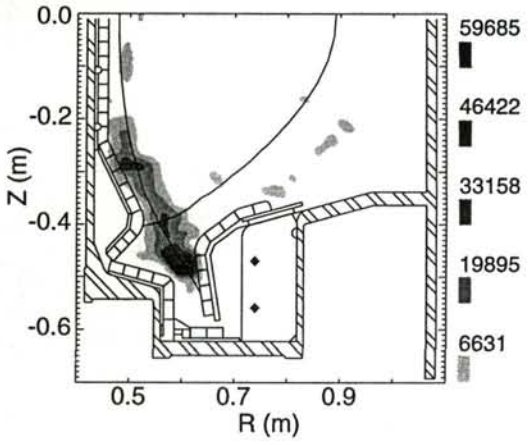

FIG. 3. Tomographic reconstruction of the experimental D_α emission in W/m^3 from Alcator C-Mod shot 950308012 at $t = 0.96$ s.

differences between the C.I and C.II results arise predominantly from the lower rate of recombination predicted by model II. The spatial distribution of the D_α emission is shown in Fig. 2; Fig. 3 presents a tomographic reconstruction of the measured D_α emission for comparison. Both show peaks in the detached region near the outer target where recombination is suspected to occur.

For C.I and C.II, the divertor pressures are comparable to the measured values. The global Balmer-α emission rates exceed the measured rate, however. Obtaining better agreement will require improvements to both the plasma and atomic physics models. The present approach to modeling the plasma would benefit from the addition of more experimental data regarding the private flux region plasma. But, given the strong dependence of recombination on plasma temperature and density, a self-consistent coupling of DEGAS 2 and CRAMD with a 2-D edge plasma code may be needed to match the data. The next steps in refining the DEGAS 2 atomic physics would be the inclusion of ion-neutral and neutral-neutral elastic scattering.

ACKNOWLEDGMENTS

This work was supported by U.S. Department of Energy Contracts No. DE-AC02-76-CHO-3073 and DE-FG02-91-ER-54109. The authors wish to acknowledge useful discussions with J. Kesner.

REFERENCES

[1] JANESCHITZ, G., et al., J. Nucl. Mater. **220–222** (1995) 73.
[2] STOTLER, D.P., KARNEY, C.F.F., Contrib. Plasma Phys. **34** (1994) 392.
[3] HELANDER, P., et al., Phys. Plasmas **1** (1994) 3174.
[4] PIGAROV, A.Yu., KRASHENINNIKOV, S.I., Phys. Lett. A **222** (1996) 251.
[5] HUTCHINSON, I.H., et al., Phys. Plasmas **1** (1994) 1511.
[6] HEIFETZ, D.B., "Neutral particle transport", Physics of Plasma-Wall Interactions in Controlled Fusion (POST, D.E., BEHRISCH, R., Eds), Plenum Press, New York (1986) 595–771.
[7] STOTLER, D.P., et al., in Plasma Physics and Controlled Nuclear Fusion Research 1994 (Proc. 15th Int. Conf. Seville, 1994), Vol. 3, IAEA, Vienna (1996) 363.
[8] KESNER, J., Phys. Plasmas **2** (1995) 1982.
[9] NIEMCZEWSKI, A., Neutral Particle Dynamics in the Alcator C-Mod Tokamak, PhD Thesis, Massachusetts Inst. of Technology, Cambridge (1995).
[10] STANGEBY, P.C., Plasma Phys. Control. Fusion **37** (1995) 1031.
[11] LUMMA, D., et al., Radiative and 3-Body Recombination in the Alcator C-Mod Divertor (in preparation).

SPECIAL ASPECTS OF MHD EQUILIBRIUM AND STABILITY CALCULATIONS FOR A DIVERTOR TOKAMAK CONFIGURATION*

C.V. ATANASIU
Institute of Atomic Physics,
Bucharest, Romania

A.A. SUBBOTIN
Russian Research Center,
Kurchatov Institute,
Moscow, Russian Federation

Abstract

SPECIAL ASPECTS OF MHD EQUILIBRIUM AND STABILITY CALCULATIONS FOR A DIVERTOR TOKAMAK CONFIGURATION.

A method is presented to calculate MHD equilibrium and stability in an axisymmetric divertor tokamak configuration. For equilibrium calculations, a 'classical' flux co-ordinate system, refined by a 'cast function', is used. Thus, the unknown moments — the solution of the equilibrium equation — are determined by the difference between the real flux surface contours and those described by the cast function only. As boundary conditions for the second order differential equation governing the tearing mode stability, 'natural' boundary conditions for the plasma boundary have been found by calculating the surface charge distribution (from potential theory), where the normal component of the perturbation is known. As an example for this approach, the metric coefficients for a particular equilibrium configuration and boundary conditions for the flux function perturbations, of different mode numbers, have been computed for the ASDEX Upgrade tokamak.

1. INTRODUCTION

X points occur in a wide variety of plasma confinement devices. In order to control impurities, diverted toroidal configurations use solid conductors to draw off field lines from the outside of the plasma and to lead them to a neutralizer divertor plate.

Most toroidal flux co-ordinate systems implicitly assume a nested flux surface structure. However, in a diverted torus the presence of a separatrix breaks this structure, and the usual toroidal flux co-ordinates cannot be used directly.

The separatrix problem was treated in several papers. In Refs [1, 2], a method of determining the region of ergodic field lines about the separatrix magnetic surface with a two wire divertor model is presented. Specifying the shape of a flux surface

* Part of this work was performed during a stay of one of the authors (C.V.A.) at the Max-Planck-Institut für Plasmaphysik, Garching, Germany.

and the poloidal magnetic field on that surface [3], by using the information from a linear filamentary multipole magnetic field, the equilibrium equation is solved locally by expansion in the neighbourhood of a single flux surface. An investigation of the plasma–vacuum separatrix in MHD equilibria with plane symmetry is presented in Refs [4, 5]. More recently, accurate and efficient calculations of the axisymmetric equilibrium up to the separatrix have been performed in Ref. [6] by using a combination of the boundary layer expansion near the separatrix and a spectral method in the core with matching at a virtual boundary.

If the plasma boundary is described by a smooth function, the determination of the moments on the boundary (to be used as boundary values by a fixed boundary equilibrium moment solver) is no longer a problem. The presence of an X point implies difficulties: because of the discontinuity of the first derivative, the description of a separatrix by means of Fourier series needs a very high number of moments, which causes numerical difficulties. Our approach consists of introducing a 'cast function' exhibiting exactly the same singularity in the X point, in order to describe the separatrix contour either approximately or 'exactly', and to represent the internal flux surface contours in an approximate way.

It is obvious that, owing to the same separatrix, the boundary conditions for the second order differential equation governing the tearing mode stability can no longer be taken, as is usual, at the magnetic axis and at infinity axis (practically, at two plasma radii). Therefore, we consider a 'natural' boundary condition at the plasma boundary (the separatrix).

2. EQUILIBRIUM CALCULATION

Within the system of co-ordinates (a, ω, ζ) it is possible to represent the co-ordinate transformation through Fourier series in ω:

$$\rho^2(\alpha, \omega) = a^2 + \mathrm{Re}\left[\sum_{\substack{m=1\infty \\ m\neq 0}}^{\infty} \delta_m e^{im\omega}\right]; \; a^2 = \frac{\Phi(a)}{\pi B_0} \tag{1}$$

where $\delta_m(a)$ are the complex moments, Φ is the toroidal flux and B_0 is the toroidal magnetic field on the magnetic axis ($a = 0$).

Starting from the pressure equilibrium equation and the Maxwell equations, as written for an axisymmetric configuration, and using this representation of magnetic surfaces we obtain the following system of differential equations for complex moments [7]:

$$\eta_m'' + \left(3+2\frac{\mu' a}{\mu}\right)\frac{\eta_m'}{a} - (m^2 - 1)\frac{\eta_m}{a^2} = -2\frac{W_m}{\mu a^2} \tag{2}$$

where $\eta_m = \delta_m/a$, $\mu = 1/q$ is the rotational transform, $W_m = W_m(a, \mu(a), g_{ik}(a, \omega), p'(a), B_0, R, \delta_{\ell, \ell \neq m})$ is a non-linear functional, p is the scalar plasma pressure and g_{ik} are the metric coefficients; the prime denotes a derivative with respect to a.

By solving Eq. (1) with the boundary conditions $\delta_m(0) = 0$ and given $\delta_{m, m \neq 1}(1)$, we obtain the $\delta_m(a)$ dependence over the full plasma region and thus the full equilibrium description of the plasma considered. An accurate description of the separatrix corner would require a large number of harmonics, i.e. 40 to 60.

Using a 'classical' flux co-ordinate system, refined by a 'cast function' [8], the unknown moments — the solution of the equilibrium equation — are determined by the difference between the real flux surface contours and those described by the cast function only.

Introducing now a cast function f, which, to a desired accuracy, describes the given separatrix curve, we write:

$$f^2 = f_0^2 + \tilde{f}^2 = f_0^2 + \mathrm{Re}\left[\sum_m \hat{\delta}_m e^{im\omega}\right] \tag{3}$$

where $f_0^2 = \langle f^2 \rangle_\omega$ is the averaged part of f^2, while $\tilde{f}^2 = f^2 - f_0^2$ is the periodic part of f^2. Thus, Eq. (1) reads:

$$\rho^2(a, \omega) = a^2 + \mathrm{Re}\left[\sum_m \bar{\delta}_m e^{im\omega}\right] + \tilde{f}^2 \tag{4}$$

where the moments $\bar{\delta}_m = \delta_m - \hat{\delta}_m$ describe functions of class C^1 or higher. The moments $\bar{\delta}_m$ to be determined, in order to describe the MHD plasma equilibrium, are now related to the difference between the real flux surface contours and the contours described by the cast function only.

Two models of cast function have been considered: the first one approximately describes the plasma boundary, while the second one reproduces this boundary 'exactly' (i.e. to a given accuracy, depending on some free parameters). For example, to describe the mentioned separatrix with the help of the second model of the cast function, only up to 12 moments with a maximum relative error of 0.05% in ρ are necessary. Whatever the model of cast functions adopted, this function remains invariant during the fixed boundary equilibrium iterative calculation. Constant surface contours using only a cast function, which describes exactly a particular ASDEX Upgrade separatrix configuration [9], are presented in Fig. 1(a).

3. STABILITY CALCULATION

Writing, in a co-ordinate system (a, θ, ζ) with straight field lines, the general expression for the potential energy W in terms of the flux function perturbation

(instead of the plasma displacement), $\psi = \sum_m Y(a) \cos(m\theta - n\zeta)$ [10], and performing an Euler minimization, we obtain the following system of equations [11]:

$$\mathbf{Y}'' = \mathbf{f}^{-1}(\mathbf{GY} + \mathbf{VY}') + S\vec{\delta}_m(a - a_{m/n}) \tag{5}$$

where **f**, **V** and **G** are matrices whose elements depend on the metric coefficients, and **Y** is the vector of the flux function perturbations; S is a constant, while the Dirac operator $\vec{\delta}_m$ has to be considered as a vector with a single non-zero element corresponding to the resonant harmonic m/n (m and n are the poloidal and toroidal mode numbers). The boundary conditions for the system (5) are: $\mathbf{Y} = \mathbf{0}$ for $a = 0$ and $a = \infty$. It is obvious that for a divertor configuration, as well as for the case when a separatrix outside of the plasma boundary is close to the plasma boundary, a 'natural' boundary condition for **Y** at $a = 1$ has to be considered.

In view of the fact that for an axisymmetric toroidal geometry the individual poloidal harmonics are coupled together, while the toroidal harmonics remain independent, the normal $\tilde{B}_{Nn}$ and the tangential magnetic field component $\tilde{B}_{\tau n}$ to the plasma boundary, corresponding to the perturbation of the flux function, ψ, can be written as

$$\begin{aligned} \tilde{B}_{Nn} &= 1/\sqrt{g_{22}g_{33}} \sum_m mY_{mn} \sin(m\theta - n\zeta) \\ \tilde{B}_{\tau n} &= 1/\sqrt{g_{11}g_{33}} \sum_m Y'_{mn} \cos(m\theta - n\zeta) \end{aligned} \tag{6}$$

where **N** is the outer normal to the plasma boundary.

From potential theory [12], knowing the $\tilde{B}_{Nmn}$ normal component (for given poloidal and toroidal mode numbers and for an arbitrarily chosen $Y_{mn}(1)$), the surface (magnetic) charge distribution can be found using a Fredholm's integral equation of the second kind:

$$2\pi\sigma_{mn}(\ell) + \oint \sigma_{mn}(\ell')b_{Nmn}(\ell, \ell')d\ell' = \tilde{B}_{Nmn(\ell)} \tag{7}$$

where $b_{Nmn}(\ell, \ell')$ is the normal magnetic field at ℓ produced by a unit surface charge located at ℓ', with ℓ being a contour co-ordinate. Let us assume, for each mode, a surface charge distribution on the $a = 1$ surface of the form: $\sigma_{mn} = C_{mn}\sin(m\theta - n\zeta)$. Each of these surface charge distributions will produce the field components $\tilde{B}_{Nmn}(\theta, \zeta)$ and $\tilde{B}_{\tau mn}(\theta, \zeta)$. The resulting field components produced by all these charges are:

$$\tilde{B}_{Nn} = \sum_m C_{mn}\tilde{B}_{Nmn} = 1/\sqrt{g_{22}g_{33}} \sum_m mY_{mn}\sin(m\theta - \zeta)$$
$$\tilde{B}_{rn} = \sum_m C_m\tilde{B}_{rmn} = 1/\sqrt{g_{11}g_{33}} \sum_m Y'_{mn}\cos(m\theta - n\zeta) \quad (8)$$

or, in vector form,

$$\mathbf{DC} = \mathbf{Y}; \quad \mathbf{FC} = \mathbf{Y}' \quad (9)$$

where

$$d_{i,j} = \frac{2}{i}\langle\sqrt{g_{22}g_{33}}\, B_{Njn}\sin(i\theta - n\zeta)\rangle_{\theta,\zeta}$$
$$f_{i,j} = 2\,\langle\sqrt{g_{11}g_{33}}\, B_{rjn}\cos(i\theta - n\zeta)\rangle_{\theta,\zeta} \quad (10)$$

Using for the numerical integration of Eq. (5) as sweep method of the form [11],

$$\mathbf{Y}_k = \vec{\alpha}_k\mathbf{Y}_{k+1} + \vec{\beta}_k \quad (11)$$

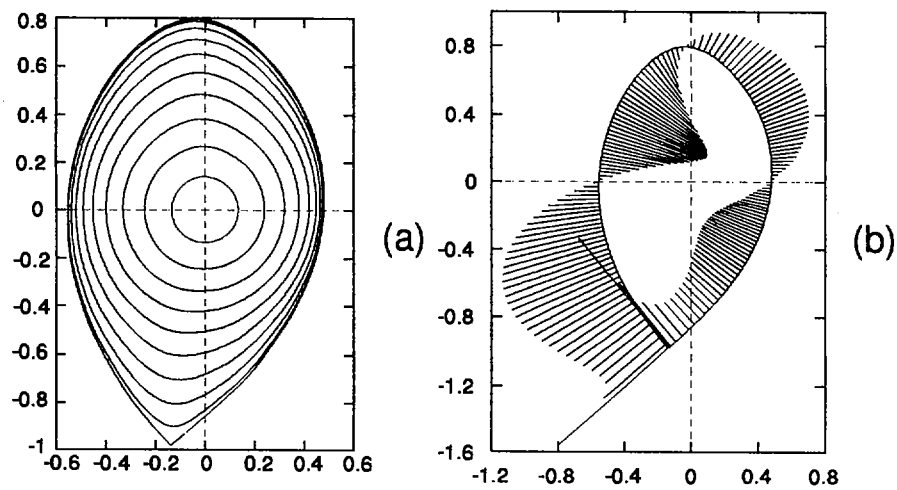

FIG. 1. (a) Constant flux surface contours given by the cast function only (parameters are corresponding to the ASDEX Upgrade separatrix [9]); (b) surface charge distribution for m = 2 and n = 1, as a single harmonic.

with $\vec{\alpha}_k$ an [m × m] known coefficient matrix and $\vec{\beta}_k$ an [m] known coefficient vector, we obtain the following boundary condition at the plasma boundary:

$$\mathbf{Y}_{k+1} = (\mathbf{I} - \mathbf{hFD}^{-1} - \vec{\alpha}_k)^{-1} \vec{\beta}_k \tag{12}$$

with I the unit matrix and h the size of the 'radial' integration mesh.

As an illustration of our approach, the surface charge distribution for m = 2 and n = 1, corresponding to a single harmonic, is given in Fig. 1(b).

Note that, for our axisymmetric toroidal geometry, the individual poloidal harmonics being coupled together, the boundary conditions for Y are the result of a toroidal coupling of each surface charge distribution.

4. CONCLUSIONS

In this paper, an improved moments method for calculating the fixed boundary equilibrium in diverted toroidal configurations is presented. Because of the presence of the separatrix, no direct use of a flux co-ordinate system can be made. To overcome this difficulty, the cast functions method has been introduced: the cast functions, exhibiting the same type of singularity at the X point, describe the separatrix contour to a prescribed accuracy and, approximately, the internal constant flux surface contours. Thus, the moments to be determined are related to the difference between the real flux surface contours and the surface contours described by the cast function only. Such an approach permits the use of a reasonable number of moments to accurately describe a quite complicated separatrix configuration, and ensures the time efficiency of our computations.

Two models of cast function have been considered: for the first model, deduced from physical considerations, the constant flux surface contours near the magnetic axis are closer to the real a^2 surface dependence, while for the second model, a better modelling of the separatrix and the constant flux surface contours near the separatrix is obtained.

A third model of cast functions, which describes 'exactly' the separatrix contour and approximates, as well as possible, the internal equilibrium constant flux surface contours derived just from equilibrium considerations, is now being developed.

Because of the same separatrix, the determination of the flux function perturbation (necessary for stability calculations) can no longer make use of the boundary conditions of this perturbation at infinity. Starting from the potential theory, a 'natural' boundary condition for the flux function perturbation, just at the plasma boundary, has been deduced.

As an application of our approach, a particular equilibrium configuration of the ASDEX Upgrade tokamak has been considered for both equilibrium and stability calculations.

ACKNOWLEDGEMENTS

Stimulating discussions with Professor K. Lackner are greatly appreciated. Parts of this work were supported by the Max-Planck-Institut für Plasmaphysik under the auspices of BMBF Project No. X052.8 and the Russian Foundation of Fundamental Research Grant No. 95-02-05519a.

REFERENCES

[1] BOOZER, A.H., RECHESTER, A.B., Phys. Fluids 21 (1978) 682.
[2] AUERBACH, S.P., BOOZER, A.H., Phys. Fluids 23 (1980) 2396.
[3] BISHOP, C.M., et al., Idcal MHD Ballooning Stability in the Vicinity of a Separatrix, Rep. CLM-P724, UKAEA, Culham Lab., Abingdon, UK (1984).
[4] KAISER, R., et al., Phys. Fluids B 4 (1992) 529.
[5] SPIES, G.O., Phys. Fluids B 4 (1992) 535.
[6] ZAKHAROV, L.E., GLASSER, A.H., in Numerical Simulation of Plasmas (Proc. 15th Int. Conf. Valley Forge, Pennsylvania, USA, 1994) 41.
[7] ATANASIU, C.V., SUBBOTIN, A.A. (in preparation).
[8] ATANASIU, C.V., et al., Calculation of Metric Coefficients for a Divertor Tokamak Configuration, Rep. IPP 5/63, Max-Planck Institut für Plasmaphysik, Garching, Germany (1995).
[9] ZEHRFELD, H.P. (Garching) personal communication, 1996.
[10] ZAKHAROV, L.E., in Plasma Physics and Controlled Nuclear Fusion Research 1978 (Proc. 7th Int. Conf. Innsbruck, 1978), Vol. 1, IAEA, Vienna (1979) 689.
[11] ATANASIU, C.V., et al., in Controlled Fusion and Plasma Physics (Proc. Eur. Conf. Innsbruck, 1992), Vol. 16C, Part I, European Physical Society, Geneva (1992) 367.
[12] MARTENSEN, E., Acta Math. 109 (1963) 76 (in German).

SELF-CONSISTENT COMPUTATION OF TRANSPORT BY FLUID DRIFT TURBULENCE IN TOKAMAK GEOMETRY

B. SCOTT, S. CAMARGO, F. JENKO
Max-Planck-Institut für Plasmaphysik,
IPP–Euratom Association,
Garching, Germany

Abstract

SELF-CONSISTENT COMPUTATION OF TRANSPORT BY FLUID DRIFT TURBULENCE IN TOKAMAK GEOMETRY.

In tokamak geometry, poloidal variation of the local drift scale, ρ_s, is found to be as important as, or more important than, magnetic curvature in determining the level of drift wave turbulence. Coupling to weakly damped Alfvén waves renders tokamak edge turbulence intrinsically electromagnetic for all parameters down to those of cold edges such as in TEXT. The transport is, however, still due to fluctuating $\mathbf{E} \times \mathbf{B}$ flows. As the plasma pressure is increased with the scale lengths kept fixed, a maximum in the normalised transport is seen directly at pre-transition L-mode parameters. This indicates a prominent role in the L–H transition for the regime boundary between weakly electromagnetic drift wave and drift Alfvén wave turbulence.

1. Introduction and Summary

It has been widely assumed that collisional electrostatic turbulence should play a central role in the L-H transition in fusion experiments. This is because the turbulence depends on a strong collisionality, which decreases strongly with rising temperature, such that when the plasma edge temperature reaches a certain level, the zone of importance for collisional drift wave turbulence is pushed out of the plasma [1,2]. Recent three dimensional (3-D) computations have confirmed the expected parameter dependence: the turbulence in a model with electrostatic, collisional electron dynamics weakens sharply with decreasing collisionality [3,4,5]. The basic mechanism in both 2-D sheared-slab and 3-D cases is the nonlinear drift wave instability [6,7].

It has become clear, however, that the edge temperature and density at the transition obey a scaling which is incompatible with any model based primarily on collisionality: the transition temperature falls with the density, while a collisionality-based scenario would require it to rise with the density [8]. This motivates scenarios with a role for the local plasma beta ($\beta = 4\pi nT/B^2$); if a boundary occurs at a particular value of β, then the local temperature and density would follow a relation which is consistent with the data.

One such scenario is presented here – based on the finite-beta universal mode model of Molvig *et al* [9], also studied by Waltz [10]. Considering large enough computational grids for the first time, we have found that electromagnetic effects internal to the turbulence dynamics are important enough to give a qualitative change in the turbulence morphology, such that the long-perpendicular-wavelength energy sink in electrostatic turbulence is removed. A transition occurs roughly at $\beta \sim m_e/M_i$, at which the collisionless skin depth ($\sigma_0 = c/\omega_{pe}$) is pushed out of the spectrum towards high $k_\perp$ (perpendicular wavenumber). Here, the normalised transport has a maximum, which should facilitate the

bifurcation phenomenon, such that the L-H transition may be triggered by the transition from partially electrostatic drift wave turbulence to wholly electromagnetic drift Alfvén turbulence.

This electromagnetic transition also happens in our 2-D computations [11], but it is more important in three dimensions because of the broad range of parallel wavelengths to which the ExB turbulence is coupled. The new result is that turbulence on closed field lines is electromagnetic all the way down (in β) to TEXT-edge parameters.

The computations so far are in the context of a fluid model. Since collisionality is found to be a weak effect, a parallel effort is underway to check the model with a companion, 3-D simulation with drift kinetic electrons.

Geometric Effects on Electrostatic Turbulence

Drift wave turbulence under the electrostatic, collisional model has been studied over the last two years in sheared-slab [3] and in tokamak geometry [4]. Here, tokamak geometry refers to the coordinate system being built around a realistic model of the flux surfaces under Hamada coordinates. The importance is that toroidicity involves other effects additional to magnetic curvature, including variation of the local drift scale (given by $\rho_s^2 = c^2 M_i T_e / e^2 B^2$) around the flux surfaces, contribution of the magnetic unit vector to parallel divergences, *etc.*. The Hamada coordinates are modified to follow the local flux surface geometry, such that θ is a parallel coordinate (see [12]).

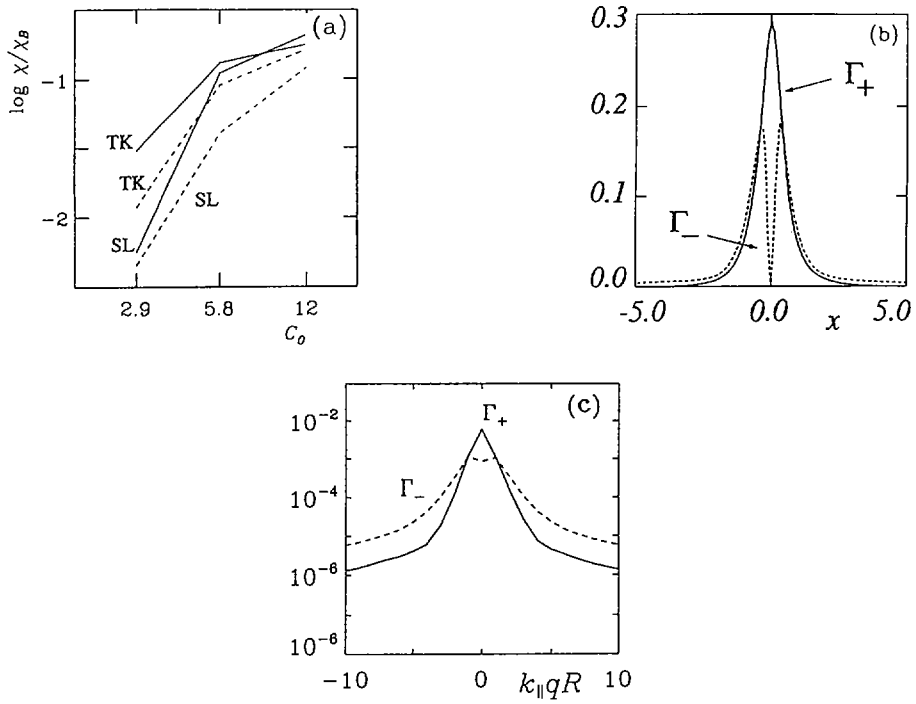

FIG. 1. (a) C_0 dependence of electrostatic turbulence, with (solid) and without (dashed) curvature; (b) source/sink profiles in x in the slab model; (c) source/sink spectra in $k_\parallel$ in tokamak geometry, showing qualitative similarity of parallel dynamics.

The equations used in [4] are those of collisional drift wave turbulence including temperature gradient and fluctuations. These electrostatic studies were done in tokamak geometry and compared to companion results from cylindrical models in which magnetic curvature terms were inserted as the sole toroidal effects. Fig. 1 shows a summary of these comparisons for cases of varying drift wave collisionality: $C_0 = (\nu_e L_\perp/c_s)(m_e/M_i)(qR/L_\perp)^2$, where $L_\perp$ is the profile scale length and R is the major radius. The solid (dashed) lines refer to runs with (without) the curvature terms, and tokamak and cylindrical geometry are labelled by 'TK' and 'SL' respectively (note cylindrical and slab geometry are physically similar). Further study has shown the poloidal variation of the local ρ_s to be at least as important as curvature, sometimes more so. Moreover, curvature was never found to alter the qualitative state of the turbulence (spectrum, free energy transfer, which regions are source and sink, *etc.*), even when it had a dominant quantitative effect. Thus, we speak of curvature driven drift wave turbulence as the proper paradigm.

The source and sink spectra of the turbulence in the 3-D tokamak [4] and 2-D slab [6] models are qualitatively similar (Fig. 1), for $k_\parallel$ as well as $k_\perp$. This shows that both models exhibit transfer of free energy among differing $k_\parallel$, which is the essential physics of the nonlinear instability behind collisional drift wave turbulence [7]. Indeed, the phenomenon of "convection back to the resonant surface" seen in the 2-D slab [13] can be re-interpreted in terms of inverse $k_\parallel$-transfer for fluctuations in the electrostatic potential ($\widetilde{\phi}$).

Drift Alfvén Turbulence and the L-H Transition in Tokamaks

The role of magnetic fluctuations in drift wave turbulence is to transform it into drift Alfvén turbulence. Generally, this fluid-drift turbulence, in which the simplifications in reduced MHD [14] hold, is a competition between nearly 2-D ExB turbulence and dissipative parallel electron dynamics at somewhat higher $k_\parallel$ [6,7]. A finite β turns the damped nonadiabatic transients of drift wave turbulence into near-ideal shear Alfvén waves, especially at large scale (low $k_\perp \rho_s$) [11].

The equations used to study this phenomenon are:

$$\left(\frac{\partial}{\partial t} + \mathbf{v}_E \cdot \nabla\right) \nabla_\perp^2 \phi = \nabla_\parallel J_\parallel - \kappa\,(T+n) \tag{1}$$

$$\hat{\beta}\frac{\partial}{\partial t}\psi + \hat{\mu}\left(\frac{\partial}{\partial t} + \mathbf{v}_E \cdot \nabla\right) J_\parallel = \nabla_\parallel\,(T+n-\phi) - \hat{\mu}\nu\left[J_\parallel + \frac{0.71}{1.6}\,(q_\parallel + 0.71 J_\parallel)\right] \tag{2}$$

$$\left(\frac{\partial}{\partial t} + \mathbf{v}_E \cdot \nabla\right) n = -\omega_n \frac{\partial \phi}{\partial y} + \nabla_\parallel\,(J_\parallel - u_\parallel) - \kappa\,(T+n-\phi) \tag{3}$$

$$\frac{3}{2}\left(\frac{\partial}{\partial t} + \mathbf{v}_E \cdot \nabla\right) T = -\frac{3}{2}\omega_t \frac{\partial \phi}{\partial y} + \nabla_\parallel\,(J_\parallel - u_\parallel - q_\parallel) - \kappa\,(3.5T+n-\phi) \tag{4}$$

$$\hat{\mu}\left(\frac{\partial}{\partial t} + \mathbf{v}_E \cdot \nabla\right) q_\parallel = -\frac{5}{2}\nabla_\parallel T_e - a_L q_\parallel - \hat{\mu}\nu\frac{5/2}{1.6}\,(q_\parallel + 0.71 J_\parallel) \tag{5}$$

$$\epsilon_s\left(\frac{\partial}{\partial t} + \mathbf{v}_E \cdot \nabla\right) u_\parallel = -\nabla_\parallel\,(n+T) - \mu_\parallel \nabla_\parallel^2 u_\parallel \tag{6}$$

where the current is given by $J_\parallel = -\nabla_\perp^2 \psi$ and $\mathbf{v}_E \cdot \nabla$ represents ExB advection in terms of $\mathbf{v}_E = \nabla s \times \nabla \phi$. Normalisation is in terms of ρ_s and c_s, as usual, except that $\nabla_\parallel$ is normalised to $1/qR$.

The differential operators are $\nabla_\perp^2 = (\partial/\partial x - Ss\partial/\partial y)^2 + (\partial/\partial y)^2$ for the perpendicular Laplacian, and $\nabla_\parallel = (\partial/\partial s) - \hat{\beta}\nabla s \times \nabla \psi \cdot \nabla$ for the parallel gradient. Magnetic curvature is modelled with $\kappa = \omega_B[\cos s(\partial)/\partial y + \sin s(\partial)/\partial x]$, with $s \in [-\pi, \pi]$.

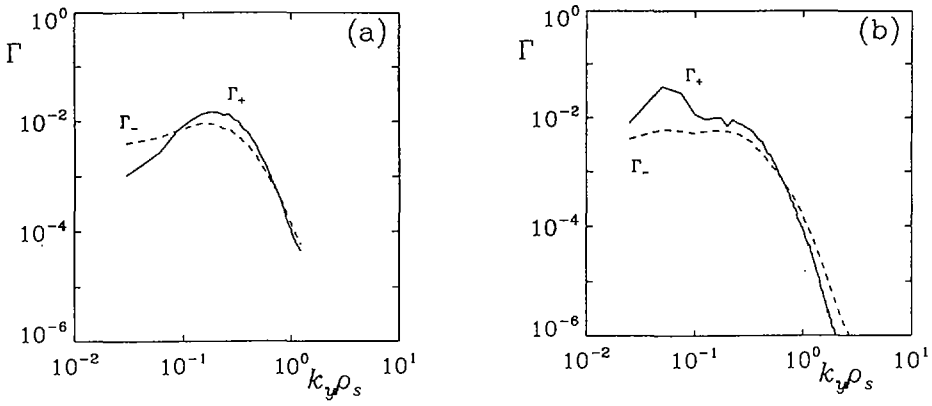

FIG. 2. Fluctuation free energy source (solid) and sink (dashed) spectra, for the (a) drift wave and (b) drift Alfvén models, for $\hat{\beta} = 0.3$. The qualitative difference at low $k_\perp$ is clear.

The parameters $\hat{\beta} = (4\pi n T_e/B^2)(qR/L_\perp)^2$, $\hat{\mu} = (m_e/M_i)(qR/L_\perp)^2$, $\nu = \nu_e L_\perp/c_s$, $\omega_n = L_\perp/L_n$, $\omega_t = L_\perp/L_T$, $\omega_B = 2L_\perp/R$, and ϵ_s, a_L (Landau damping, see [15]), and S (magnetic shear) are all constants. In keeping with the ASDEX-Upgrade edge situation ($L_\perp = 2.5\,\mathrm{cm}$, $R = 165\,\mathrm{cm}$, $B = 2\,\mathrm{T}$), these were set to $\hat{\mu} = 10$, $\nu = 0.5$, $\omega_n = \omega_t = 1$, $\omega_B = 0.03$, $\epsilon_s = 3000$, $a_L = \hat{\mu}(V_e L_\perp/c_s qR)$, and $S = 1$. Varying $\hat{\beta}$ was used according to the varying background n_0 and T_0. The range of runs was $\hat{\beta} = 0.3$ (TEXT edge), 1.0 (OH edge), 3.0 (low L-mode), 10.0 (L-H transition), and 30.0 (H-mode), corresponding to varying ASDEX-Upgrade conditions, except for the one TEXT case which corresponds to the nominal case ($C_0 = 5.5$) from the electrostatic study. Grid sizes were $64 \times 64 \times 16$ and $64 \times 256 \times 16$ for (x, y, s) respectively. The range of $k_\perp$ was 0.1 to 3.0 for 64 y-nodes and 0.025 to 3.0 for 256 y-nodes.

The resulting spectrum shows activity at lower $k_\perp \rho_s$ than does its counterpart from the electrostatic model. The source and sink spectra are shown in Fig. 2. The electrostatic model (a) has a sink region at low $k_\perp$, while the electromagnetic model (b) the same parameters ($\hat{\beta} = 0.3$) shows this to be a source region – the drift Alfvén waves have time to excite n and T fluctuations from ∇n and ∇T before they are dissipated through resistivity and Landau damping. This range of $\beta M_i/m_e$ is important: when $\beta M_i/m_e < 1$ the collisionless skin depth, σ_0, is larger than ρ_s and so the electron inertia renders the transients electrostatic at $k_\perp \rho_s \lesssim 1$. As $\hat{\beta}$ is then increased, the Alfvén transients become slower, reducing the constraints on the ExB turbulence as it taps free energy. When $\hat{\beta} = \hat{\mu}$ (*i. e.*, $\beta M_i/m_e = 1$), the entire spectrum becomes electromagnetic, so that for higher $\hat{\beta}$ the main effect is to reduce the coherence between $\tilde{\phi}$ and $\tilde{n}$ or $\tilde{T}$ and hence the efficiency of free energy access. This combination of effects produces a maximum in the normalised transport, as shown in Fig. 3 (a).

Test cases in which first magnetic curvature and then the collision terms were removed indicate that these are weak effects, since the low-$k_\perp$ drift Alfvén portion is not an energy sink (curvature mostly affects the low-$k_\perp$ portion [16]). It follows that the electrostatic, collisional models, based on collisional drift waves or on resistive ballooning modes, are outside their realm of applicability at tokamak edge parameters, for almost any edge plasma of interest.

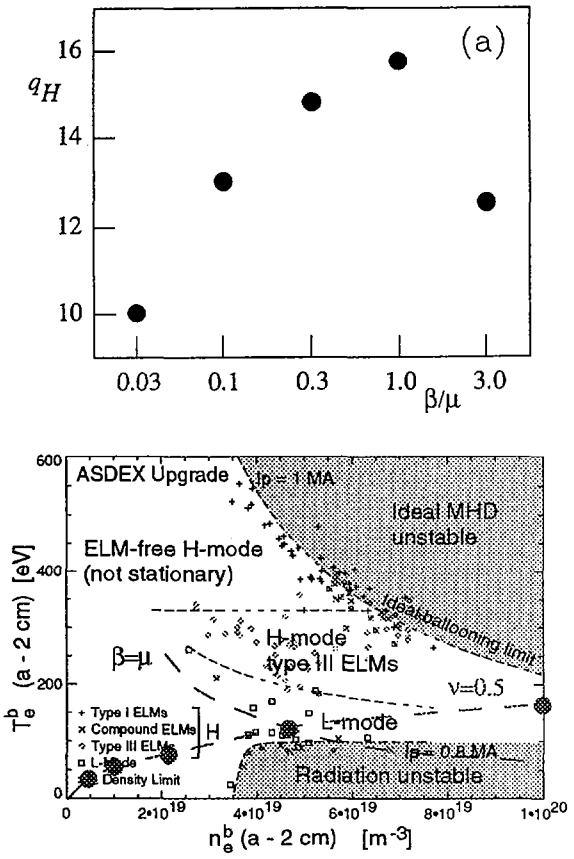

FIG. 3. (a) Maximum in normalised heat transport as a function of $\beta M_i/m_e$. (b) ASDEX Upgrade L-H transition diagram in terms of local n and T, with the $\beta = m_e/M_i$ line drawn, and the five runs shown as large dots (along the $\nu = 0.5$ line).

Our 2-D computations, in a simplified model with electron inertia and temperature fluctuations absent [11], showed a simple drop in the transport for $\hat{\beta} > 1$, as linear theory expected [17]. In three dimensions, however, the ability to exchange among differing $k_\parallel$ makes the electromagnetic component stronger. In both systems, the principal effect is the slowing of the Alfvén wave transients, with the nonlinear dynamics still controlled mostly by the ExB velocity.

It is most noteworthy that the regime boundary between partially electromagnetic drift wave turbulence and completely electromagnetic drift Alfvén turbulence occurs right at the L-H transition in ASDEX-Upgrade. The experimental situation is shown in Fig. 3 (b) [18]. The temperature and density measured 2 cm inward of the separatrix are related at the transition (either L-to-H or H-to-L) through the dotted line. The dashed lines show where $\hat{\beta} = \hat{\mu}$, *i. e.*, where $\beta M_i/m_e = 1$, and the path of increasing β at constant $\nu = 0.5$, which was the run series (indicated by the large dots). Not only is the correct parameter region (finite-m_e, $10^{-6} < \beta < 10^{-4}$) being studied, the regime boundary corresponds

closely to the observed transition. This result indicates that drift Alfvén turbulence has at least an equal role to other effects (such as ion gyroviscosity, ExB shear, *etc.*) in that transition.

Drift Kinetic Computation

The transcollisional fluid model shows clearly that the salient regime is that of very weak collisionality; removing collisions altogether causes no great change in the results. We are therefore building a complete drift kinetic electron simulation to provide a benchmark. The model will be solved numerically on a Cray T3E parallel computer in both slab and toroidal geometries. Up to now, running within the electrostatic simplification, we have confirmed a result from the drift kinetic, 2-D slab model, which is that the linear modes are unstable for $k_y\rho_s \sim 1$ if the resolution is moderate [19]: up to about 10 x-nodes per ρ_s in our case. Additionally, we have confirmed the Hirshman-Molvig scenario [20] by applying a cross-field diffusion to the electrons within the 2-D slab model. Since the turbulence does not effectively excite x-direction scales below ρ_s, the fact that the linear modes are formally stable [19] is not of practical interest.

REFERENCES

[1] WAKATANI, M., HASEGAWA, A., Phys. Fluids **27** (1984) 611.
[2] SCOTT, B., Phys. Fluids B **4** (1992) 2468.
[3] ZEILER, A., BISKAMP, D., DRAKE, J.F., GUZDAR, P.N., Phys. Plasmas **3** (1996) 2951.
[4] SCOTT, B., in Controlled Fusion and Plasma Physics (Proc. 22nd Eur. Conf. Bournemouth, 1995), Vol. 19C, Part I, European Physical Society, Geneva (1995) 229.
[5] ZEILER, A., et al., IAEA-CN-64/DP-19, this volume.
[6] SCOTT, B., Phys. Rev. Lett. **65** (1990) 3289.
[7] BISKAMP, D., ZEILER, A., Phys. Rev. Lett. **74** (1995) 706.
[8] ZOHM, H., et al., IAEA-CN-64/A5-1, these Proceedings, Vol. 1, p. 439.
[9] MOLVIG, K., HIRSHMAN, S.P., WHITSON, J.C., Phys. Rev. Lett. **43** (1979) 582.
[10] WALTZ, R.E., Phys. Fluids **28** (1985) 577.
[11] CAMARGO, S., SCOTT, B., BISKAMP, D., Phys. Plasmas **3** (1996) 343.
[12] DEWAR, R.L., GLASSER, A.H., Phys. Fluids **26** (1983) 3038.
[13] BISKAMP, D., WALTER, M., Phys. Lett. A **109** (1985) 34.
[14] STRAUSS, H., Phys. Fluids **19** (1976) 134.
[15] HAMMET, G., PERKINS, F.W., Phys. Rev. Lett. **64** (1990) 3019.
[16] SCOTT, B., in Plasma Physics and Controlled Nuclear Fusion Research 1992 (Proc. 14th Int. Conf. Würzburg, 1992), Vol. 2, IAEA, Vienna (1993) 203.
[17] DRAKE, J.F., HASSAM, A.B., Phys. Fluids **24** (1981) 1262.
[18] KAUFMANN, M., et al., IAEA-CN-64/O1-5, these Proceedings, Vol. 1, p. 79.
[19] ROSS, D.W., MAHAJAN, S.M., Phys. Rev. Lett. **40** (1978) 324; TSANG, K.T., CATTO, P.J., WHITSON, J.C., SMITH, J., Phys. Rev. Lett. **40** (1978) 327.
[20] HIRSHMAN, S.P., MOLVIG, K., Phys. Rev. Lett. **42** (1979) 648.

DISCUSSION

J.D. CALLEN: Recently, C.C. Hegna and I have been developing a pseudo-MHD model for ballooning type modes taking account of electromagnetic effects and

adiabatic electron response on short ($\sim R_0 q$) parallel length scales. A critical element in these new modes is that the effective $k_\parallel$ is of the order of $(1/10)(1/R_0 q)$ for small $k_\theta \rho_s$. Are these characteristics present in the low $k_\theta \rho_s$ electromagnetic modes you find in your simulations?

B. SCOTT: This depends greatly on how $k_\parallel$ is defined: on unperturbed field lines or as the total nonlinear parallel gradient. The fluctuations show a dramatic change in parallel structure as $\hat{\beta}$ is increased — the correlation length along unperturbed field lines becomes very short. However, the relative amplitude levels of the perturbed parallel heat flux, $q_\parallel$ and the temperature fluctuations show that the parallel gradient itself is not strongly changed. In fact, the very long parallel correlation seen at low $\hat{\beta}$ — and consistent with the results of probe experiments summarized by M. ENDLER et al. (Nucl. Fusion **35** (1995) 1307) — is maintained at increased $\hat{\beta}$, on perturbed field lines, as indicated by the low $k_\parallel$. This is a feature of collisional drift wave turbulence in three dimensions in general (D. BISKAMP, A. ZEILER, Phys. Rev. Lett. **74** (1995) 706).

R.E. WALTZ: We expect to see strong radial variations in the gradients and plasma parameters near the edge, particularly in transition to the H mode. Do either of the papers you presented treat the effect of shear in the equilibrium $\mathbf{E} \times \mathbf{B}$ or diamagnetic rotations?

B. SCOTT: Both papers (IAEA-CN-64/DP-18 and DP-19) do so in principle since the variation in the profiles of both the potential, φ, and the density and temperature is self-consistently followed. In the paper by Scott et al., the radial boundaries are fixed rather than periodic. This allows an anchor for the φ profile, essentially a way of exchanging $\mathbf{E} \times \mathbf{B}$ momentum with the boundary. The result is that $\mathbf{E} \times \mathbf{B}$ spin-up is very severe, perhaps accelerated by flux surface averaged Reynolds stresses driven by the magnetic fluctuations. Realistic computations have to contain a model for rotation damping, and the one we use is based on magnetic pumping, as is the work by the Maryland group on shear layer formation.

THREE DIMENSIONAL PLASMA EDGE TURBULENCE INCLUDING ELECTRON AND ION TEMPERATURE FLUCTUATIONS

A. ZEILER, D. BISKAMP
Max-Planck-Institut für Plasmaphysik,
Euratom-IPP Association,
Garching, Germany

J.F. DRAKE, B.N. ROGERS
Institute for Plasma Research,
University of Maryland,
College Park, Maryland,
United States of America

Abstract

THREE DIMENSIONAL PLASMA EDGE TURBULENCE INCLUDING ELECTRON AND ION TEMPERATURE FLUCTUATIONS.

Three dimensional nonlinear simulations of collisional plasma turbulence are presented to model the edge region of plasmas in toroidal confinement devices. Previous work is extended by including electron and ion temperature dynamics. The electron temperature dynamics leads to no qualitative changes of the nature of the turbulence: for realistic values of η_e the temperature gradient does not drive the fluctuations because T_e fluctuations are strongly damped by parallel heat conduction. Ion temperature fluctuations, in contrast, strongly affect the turbulence if $\eta_i \geq 2$. At low temperature, ∇T_i enhances the ballooning drive. In contrast to the density gradient driven resistive ballooning mode, it is only weakly affected by electron diamagnetic effects. At high temperature, the resistive ballooning mode converts into a toroidal η_e mode.

1 Introduction

Plasma edge turbulence is a key issue in understanding the anomalous transport observed in toroidal confinement devices such as tokamaks and stellarators. The suppression of the fluctuations in the edge region is generally believed to be the origin of the confinement improvement in the H-mode, where, however, the detailed mechanism of the L/H transition and the formation of the transport barrier still remains unclear [1]. Whereas earlier experimental results support models based on sheared flow stabilization [2], in recent measurements no change in the radial electric field is observed preceding the suppression of turbulence [3]. These results emphasize the need for a better understanding of the intrinsic properties of edge turbulence, in particular the sensitivity to changes in the local parameters.

In previous work neglecting temperature fluctuations and assuming ions to be cold the resistive ballooning instability was identified as the likely source of L-mode transport [4, 5], and a nonlinear instability was discovered which provides the dominant drive for H-mode parameters [5, 6, 7]. In the present paper we include the complete electron and ion temperature dynamics not captured in the previous model. The electron temperature dynamics is known to nonlinearly destabilize the two dimensional sheared slab [8]. The ion temperature part of our equations connects the resistive drift-ballooning turbulence to η_i mode driven turbulence investigated by many authors [9, 10, 11].

In contrast to the usual approach we do not assume an adiabatic electron response, which is only valid in the hot core plasma but not at the plasma edge, where nonadiabatic effects are the source of the resistive ballooning and the nonlinear instability.

2 Equations

In our investigations we use the complete two-fluid reduced Braginskii equations [4, 5, 12]

$$\frac{d}{dt}\nabla_\perp^2\phi - \alpha\tau\nabla_\perp\cdot\left[(1+\eta_i)\frac{\partial}{\partial y} + \nabla p_i\times\vec{z}\cdot\nabla_\perp\right]\nabla_\perp\phi + \hat{C}\frac{p_e+\tau p_i}{1+\tau} + \frac{\partial^2 h}{\partial z^2} = 0 \tag{1}$$

$$\frac{dn}{dt} + \frac{\partial\phi}{\partial y} - \epsilon_n\hat{C}(\phi-\alpha p_e) + \alpha\epsilon_n(1+\tau)\frac{\partial^2 h}{\partial z^2} + \gamma\frac{\partial v_\parallel}{\partial z} = 0 \tag{2}$$

$$\frac{dv_\parallel}{dt} + \gamma\frac{\partial}{\partial z}\frac{p_e+\tau p_i}{1+\tau} = 0 \tag{3}$$

$$\frac{dT_e}{dt} + \eta_e\frac{\partial\phi}{\partial y} - \frac{2}{3}\left[\epsilon_n\hat{C}(\phi-\alpha p_e) - 1.71\epsilon_n\alpha(1+\tau)\frac{\partial^2 h}{\partial z^2} - \gamma\frac{\partial v_\parallel}{\partial z}\right] + \frac{5}{3}\epsilon_n\alpha\hat{C}T_e - \frac{2}{3}\kappa\frac{\partial^2 T_e}{\partial z^2} = 0 \tag{4}$$

$$\frac{dp_i}{dt} + (1+\eta_i)\frac{\partial\phi}{\partial y} - \frac{5}{3}\left[\epsilon_n\hat{C}(\phi+\tau p_i) - \gamma\frac{\partial v_\parallel}{\partial z}\right] = 0 \tag{5}$$

for the fluctuating quantities n, ϕ, $v_\parallel$, T_e, p_i with $h = \phi - \alpha(p_e + 0.71T_e)$, $p_e = n + T_e$, $d/dt = \partial/\partial t - \nabla_\perp\phi\times\vec{z}\cdot\nabla_\perp$, the curvature operator $\hat{C} = [\cos(2\pi z) + 2\pi\hat{s}(z-z_0)\sin(2\pi z) - (a/R)]\partial/\partial y + \sin(2\pi z)\partial/\partial x$, and the parameters $\alpha = c_s^2 t_0/[(1+\tau)\omega_{ci}L_nL_0]$, $\epsilon_n = 2L_n/R$, $\tau = T_{i0}/T_{e0}$, $\gamma = c_s t_0/L_z$, $\kappa = \kappa_\parallel t_0/(n_0 L_z^2) = 1.6\alpha^2\epsilon_n(1+\tau)$ using $c_s^2 = (1+\tau)T_{e,0}/m_i$. Space and time units are the ideal ballooning growth time $t_0 = (RL_n/2)^{1/2}/c_s$, the perpendicular wavelength of the most unstable modes $L_0 = [n_0\eta_\parallel/(m_i t_0)]^{1/2}L_z e/\omega_{ci}$ and the connection length $L_z = 2\pi q_a R$. The anomalous transport is related to the dimensionless fluxes through

$$D = \langle nv_r\rangle D_0,\ \chi_e = \langle T_e v_r\rangle D_0/\eta_e,\ \chi_i = \langle T_i v_r\rangle D_0/\eta_i,\ D_0 = L_0^2/t_0 \tag{6}$$

The basic structure of the turbulence is controlled by three key parameters: α, $\alpha^2\epsilon_n(1+\tau)$, and η_i. The parameter α is a measure of the strength of diamagnetic drift [4, 5]. For α very small, diamagnetic drifts are relatively unimportant while for α large, they dominate. The parameter $\alpha^2\epsilon_n(1+\tau)$ controls the adiabaticity [6, 5]. For $\alpha^2\epsilon_n(1+\tau) \ll 0.1$, the turbulence is hydrodynamic while in the opposite limit it becomes adiabatic ($\phi \simeq \alpha n$). Both of these parameters are typically small in the cold edge plasma and increase rapidly as one moves into the hotter core plasma. The parameter η_i controls strength of the drive due to the ion pressure gradient both in the resistive ballooning regime and in the η_i mode regime.

For further details about the normalization and the numerical approach we refer to Refs [4, 5, 13].

3 Cold ion limit

In the cold ion limit $\tau = 0$ the turbulence is comprised of fluctuations in the density of electrons and ions, the potential and the electron temperature with the electron pressure gradient as a source for turbulent energy. As pointed out in previous work neglecting electron temperature fluctuations [5], the system is characterized by two regimes. For low values of the diamagnetic parameter α (~ 0.5), the resistive ballooning mode is the dominant driver of the system. As α increases and approaches 1.5 curvature plays essentially no role, consistent with linear theory [14], and the drift wave dynamics dominates. In this regime the turbulence is driven by a nonlinear instability [6, 7]. Based on these results with constant electron temperature we investigate the impact of electron temperature dynamics in the two regimes separately. Since the details are presented elsewhere [13] we discuss the key issues only.

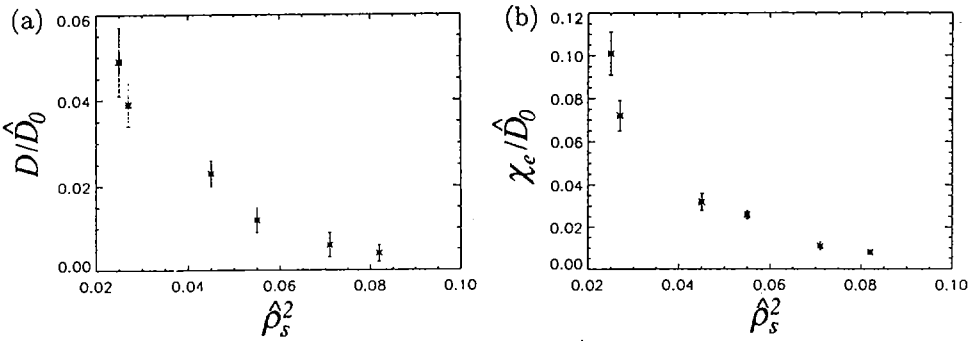

FIG. 1. (a) Anomalous particle diffusion coefficient $D/\hat{D}_0$ and (b) anomalous heat conductivity $\chi_e/\hat{D}_0$ versus $\hat{\rho}_s^2$ at different values of η_e. In the simulations with $\hat{\rho}_s^2$ = 0.025/0.07, we have η_e = 2; with $\hat{\rho}_s^2$ = 0.045, η_e = 0.5, and for the remaining runs, η_e = 1.

The resistive ballooning mode, which dominates for low α, is in principle driven by the electron pressure gradient. Our simulations, however, show that already for moderate $\alpha \simeq 0.5$ the parallel heat conduction (which is proportional $\alpha^2\epsilon_n$ with $\epsilon_n \simeq 0.04$) becomes large enough to completely suppress the electron temperature gradient contribution. We performed runs [13] at $\alpha = 0.4$, $\epsilon_n = 0.04$, $\hat{s} = 1$, $\epsilon = 0.25$, $\gamma = 0.03$ and η_e varying between 0.5 and 2. The particle flux remains unchanged as the electron temperature gradient is varied at fixed density gradient and assumes the same level as for a run with constant electron temperature, whereas the anomalous electron heat flux is proportional to the temperature gradient. These results imply that T_e is convected as a passive scalar by the turbulence, which is driven by the electron density gradient but which is unaffected by the electron temperature gradient. As a consequence the anomalous diffusion coefficients D and χ_e are both independent of the electron temperature gradient.

As α becomes large (~ 1.5) the ballooning instability becomes very weak [14], and the turbulence is sustained by a nonlinear instability mechanism [5, 6, 7]. In this regime the curvature can be neglected and transport is controlled by two parameters, η_e and $\hat{\rho_s}^2 \equiv \epsilon_n \hat{s}^{4/3}\alpha^{4/3}(1+\tau)$. The transport scaling is given by [5]

$$D = \hat{D}_0 \cdot f_1(\hat{\rho_s}^2, \eta_e), \quad \chi_e = \hat{D}_0 \cdot f_2(\hat{\rho_s}^2, \eta_e), \quad \hat{D}_0 = D_0\alpha^{4/3} \tag{7}$$

In simulations without electron temperature fluctuations [5, 7] the particle transport is a strongly decreasing function of $\hat{\rho_s}$. The transport results plotted in Figure 1 show that this trend persists. Furthermore we observe that all of the data for both D and χ_e fall on a single curve regardless of η_e. This implies that the transport rates (functions f_1, f_2) do not depend strongly on η_e. Only for very large values of η_e (above 4) does the electron temperature gradient impact the transport rates. As in the ballooning regime, the electron temperature gradient is therefore only a weak driver of the turbulence.

4 Finite ion temperature

Dropping the cold ion approximation $\tau = 0$ introduces three significant new features. The ion pressure gradient is now a potential source of energy to drive the turbulence. However, it is known from linear theory [14] that the ion diamagnetic convection in the vorticity Equation (1) has a stabilizing influence on the resistive ballooning instability, particulary in the high α regime. Finally, the ion temperature gradient introduces η_i modes as a third instability mechanism [9, 10, 11] besides ballooning and the nonlinear drive. Since previous work almost exclusively treats η_i modes in the adiabatic electron limit, an important question is how these modes modify the turbulence in the resistivity dominated plasma edge.

4.1 Linear properties of η_i and resistive ballooning modes

The linear properties of the curvature driven η_i and resistive ballooning modes can be understood from the following simplified subset of equations for ϕ, n and p_i (normalized, respectively, to T_{e0}/e, n_0, and $n_0 T_{e0}$),

$$-k_\perp^2 \rho_s^2(\gamma - i\omega_{*i})\phi + i\omega_c(n + p_i) + D_{\|e}\frac{\partial^2}{\partial z^2}(\phi - n) = 0 \tag{8}$$

$$\gamma n + i\omega_{*n}\phi + D_{\|e}\frac{\partial^2}{\partial z^2}(\phi - n) = 0 \tag{9}$$

$$\gamma p_i + i\omega_{*i}\phi = 0 \tag{10}$$

where for clarity we have written the independent parameters in dimensional units: γ the growthrate of the mode, $\rho_s^2 = T_e/m_i\omega_{ci}^2$, $\omega_{*n} = k_y cT_e/eBL_n$, $\omega_{*i} = k_y cT_i(1+\eta_i)/eBL_n$, $\omega_c = 2k_y(cT_e/eBR)$ $[\cos(z/qR) + \hat{s}(z/qR)\sin(z/qR) - a/R]$, and $D_{\|e} = T_e/\eta_\| n_0 e^2$. The relationship between resistive ballooning and toroidal η_i modes can most easily be seen by examining a local dispersion relation with $\partial/\partial z = ik_\|$ and neglecting the ambient density gradient ω_{*n},

$$k_\perp^2\rho_s^2(\gamma - i\omega_{*i}) - \frac{\omega_c\omega_{*i}}{\gamma} + \frac{\gamma k_\|^2 D_{\|e}}{\gamma + k_\|^2 D_{\|e}} = 0 \tag{11}$$

The parallel diffusion rate $D_{\|e}$ is the control parameter which governs whether the instability is in the resistive ballooning or toroidal η_i regime. For small $D_{\|e}$, the last term in Eqn. (11) can be neglected and we obtain the resistive ballooning dispersion relation [14],

$$\gamma(\gamma - i\omega_{*i}) = \frac{\omega_c\omega_{*i}}{k_\perp^2\rho_s^2} \tag{12}$$

which in this simple limit is the same as that of the ideal interchange mode. In the opposite limit when $D_{\|e}$ is large, we obtain the dispersion relation of the toroidal η_i mode,

$$\gamma^2 = \omega_c\omega_{*i} \tag{13}$$

Since the ambient density gradient has been discarded, for simplicity, there is no η_i threshold for instability in Eqn. (13). Thus, the resistive ballooning and toroidal η_i modes are simply limiting cases of a more general dispersion relation, which describes the evolution of the instability from resistive ballooning at large resistivity to the η_i mode at low resistivity.

To test these ideas without the simplifying assumptions made to obtain Eqns. (8)-(10), we solve for the eigenmodes of Eqs. (1-5) using the ballooning mode respresentation. Shown in Fig. 2(a) is a plot of the growth rate versus ϵ_n (or equivalently the adiabaticity parameter $\hat{\rho}_s$) for $\eta_i = 0$ and 5 with $\alpha = 0.25$, $k_y = 1$, $\tau = 1$, $\hat{s} = 1$, and $\eta_e = 0.0$. For $\eta_i = 0$ the growth rate drops rapidly with

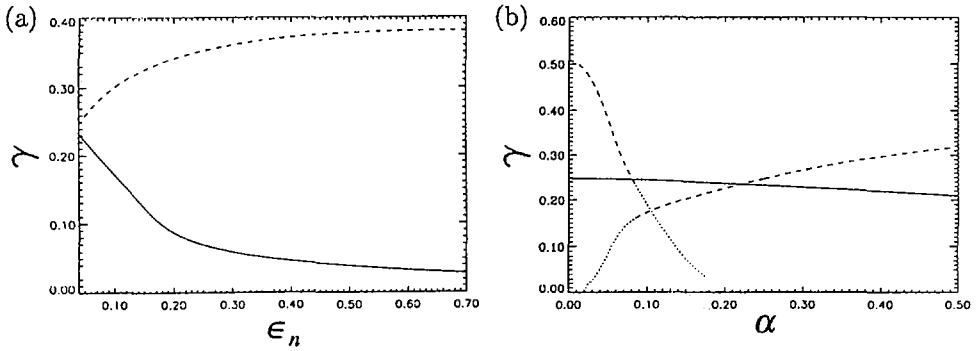

FIG. 2. Growth rate versus (a) ϵ_n and (b) α for $\eta_i = 0$ (solid) and $\eta_i = 5$ (dashed).

increasing ϵ_n as the resistive ballooning mode at small ϵ_n evolves into the adiabatic, drift wave regime. In contrast, for $\eta_i = 5$ the growth rate actually increases slightly as the resistive ballooning mode makes a transition to the toroidal η_i mode. Thus, ion thermal dynamics allow the spectrum of unstable fluid modes to extend into higher temperature regimes.

It is clear from Fig. 2(a) that the resistive ballooning and toroidal η_i modes are members of the same unstable branch, at least for the parameters of this figure. This conclusion is not true for all parameters. This is illustrated in Fig. 2(b). Shown is a plot of the growth rate versus α for $\eta_i = 0$ (solid) and $\eta_i = 5$ (dotted/dashed) with $\epsilon_n = 0.04$. Other parameters are as in Fig. 2(a). For $\eta_i = 0$ the growth rate decreases weakly with α. With $\eta_i = 5$, there are two branches which can be unstable. The first starts as a resistive ballooning mode at low α, with a growth rate which is enhanced by η_i. This mode is stabilized by ion diamagnetic effects at relatively low α. Another root appears at a finite value of α and has a growth rate which increases with α. This is the η_i mode. The adiabaticity parameter $\hat{\rho}_s$ increases with α. Thus, as in Fig. 2(a) moving to the right in Fig. 2(b) moves to the more adiabatic electron regime where the η_i mode can grow. The dashed portions of the two $\eta_i = 5$ curves in Fig. 2(b) correspond to the regions where these modes are on the same branch as the resistive ballooning mode with $\eta_i = 0$. That is, for $\alpha > 0.08$ the resistive ballooning mode with $\eta_i = 0$ maps to the η_i mode as η_i increases from 0 to 5 while for $\alpha < 0.08$ the η_i mode is on a different branch. In the parameter range most relevant to tokamak edge plasma $\alpha > 0.08$ the resistive ballooning and η_i modes are simply different limits of the same general dispersion relation. Whether the η_i mode in Fig. 2(b) at high α is interpreted as an η_i mode or a resistive ballooning mode depends on the level of adiabaticity of the electrons.

4.2 Nonlinear simulations

The nonlinear simulations with finite T_i address two primary issues: the impact of the ion pressure gradient on the turbulence and transport drive by the resistive ballooning and nonlinear drive mechanisms studied previously in the cold ion limit; and the role of the η_i mode in driving turbulence in the plasma edge. Generally, the conclusions are that for typical edge parameters η_i significantly enhances the strength of resistive ballooning turbulence. The usual η_i mode does not appear because the edge resistivity is too large for the electrons to become sufficiently adiabatic.

To study the impact of finite T_i on resistive ballooning turbulence, we performed several runs at $\alpha = 0.4$, $\tau = 1$, and small ϵ_n with the electron dynamics well within the resistivity dominated regime. The transport rates are summarized in Table 1. At small η_i ($\simeq 0.5$) the ion temperature gradient is weak and the turbulence is driven by the density gradient. Due to the ion diamagnetic stabilization proportional to ω_{*i}, the transport level is smaller than for $T_i = 0$ (compare Ref. [13]). If η_i is increased, boosting the ion temperature gradient, we observe a strong increase of the transport, which is caused by the increased ion pressure gradient and by the reduced influence of the stabilization by electron drift effects. The adiabatic condition, $\phi \sim \alpha n$, is not well satisfied. Thus, the turbulence should be characterized as resistive ballooning mode turbulence enhanced by η_i rather than η_i mode turbulence.

As expected, large values of η_i significantly broaden the parameter regime in which resistive ballooning dominates the nonlinear drive mechanism. When α is large and the ions are cold, the turbulence is typically driven by the nonlinear mechanism [5, 6]. With $\tau = 1$ and $\eta_i < 2$ the turbulence remains in the nonlinear drive regime and the turbulence is primarily driven by the density gradient. For $\eta_i = 4$, however, the particle flux develops a strong inside/outside asymmetry, indicating that the turbulence is again curvature driven. The electrons are again not strongly adiabatic ($\hat{\rho}_s$ is small) so at high η_i the resistive ballooning mode again dominates the nonlinear drive mechanism. Thus, the drive due to the ion pressure gradient strongly inhibits the electron diamagnetic stabilization of the resistive ballooning mode.

As discussed in the previous section on linear stability, the toroidal η_i mode is only unstable when the electrons are sufficiently adiabatic. For $\eta_i = 1$, $\alpha = 1.25$ and low ϵ_n (corresponding to low $\hat{\rho}_s$) the turbulence is driven by the nonlinear instability. If $\hat{\rho}_s$ is increased by increasing ϵ_n, the nonlinear drive is suppressed as in Fig. 1. However, if $\hat{\rho}_s$ is increased further, we observe the onset of a curvature driven η_i mode. The anomalous transport is dominated by ion thermal heat flux, and it is strongly peaked on the outside of the torus. Table 2 shows the transport rates, indicating that the transport grows further if the adiabatic parameter $\hat{\rho}_s$ is increased. In these simulations the

TABLE 1. TRANSPORT RATE AT $\alpha = 0.4$, $\tau = 1$, ϵ_n OF ORDER 0.1 AND DIFFERENT VALUES OF η_i.

η_i	$\langle nv_r \rangle$		$\langle T_e v_r \rangle$		$\langle T_i v_r \rangle$	
	outside	inside	outside	inside	outside	inside
0.0	0.020	0.008	0.036	0.021	0	0
0.5	0.031	0.011	0.051	0.025	0.009	0.009
1.0	0.044	0.012	0.064	0.028	0.030	0.014
2.0	0.10	0.009	0.075	0.025	0.38	0.025
3.0	0.40	0.009	0.28	0.027	5.4	0.09

TABLE 2. η_i MODE TURBULENCE: TRANSPORT RATE AT $\alpha = 0.25$, $\tau = 1$, $\eta_i = 1$ AND DIFFERENT $\hat{\rho}_s^2$.

$\hat{\rho}_s^2$	$\langle nv_r \rangle$		$\langle T_e v_r \rangle$		$\langle T_i v_r \rangle$	
	outside	inside	outside	inside	outside	inside
0.11	0.008	0.001	0.004	0.001	0.12	0
0.22	0.052	0.002	0.026	0.004	0.92	0
0.33	0.083	0.002	0.037	0.004	1.52	0

electrons are quite adiabatic since $\hat{\rho}_s$ is large. A sweep of $\hat{\rho}_s$ for low α analogous to that shown in Table 2 demonstrates the transition of the curvature driven modes. For low η_i ($\simeq 1$) the resistive ballooning turbulence is stabilized by increasing $\hat{\rho}_s$ consistent with the solid curve in Fig. 2(a). At large η_i and low $\hat{\rho}_s$ the transport is high due to the ion pressure gradient driven ballooning mode and remains high at larger $\hat{\rho}_s$ since the instability makes the transition to the toroidal η_i mode as shown in the dashed curve in Fig. 2(a).

5 Conclusion

The results presented show that electron temperature dynamics does not qualitatively alter the properties of the tokamak edge turbulence. Ion temperature, by contrast, has a much larger impact. Our results demonstrate that the usually studied toroidal η_i mode requires a sufficient level of adiabaticity to compete with resistive ballooning. The typical tokamak edge plasma is too collisional for the η_i mode to be important. However, the ion temperature gradient typically enhances resistive ballooning driven turbulence. Therefore, any realistic simulation of plasma edge turbulence must include ion temperature dynamics.

REFERENCES

[1] WAGNER, F., Phys. Rev. Lett. **49** (1982) 1408.

[2] BURRELL, K.H., et al., in Plasma Physics and Controlled Nuclear Fusion Research 1994 (Proc. 15th Int. Conf. Seville, 1994), Vol. 1, IAEA, Vienna (1995) 221.

[3] HERRMANN, W., Phys. Rev. Lett. **75** (1995) 4401.

[4] GUZDAR, P.N., et al., Phys. Fluids B **5** (1993) 3712.
[5] ZEILER, A., et al., Phys. Plasmas **3** (1996) 2951.
[6] DRAKE, J.F., et al., Phys. Ref. Lett. **75** (1995) 4222.
[7] ZEILER, A., et al., Phys. Plasmas **3** (1996) 3201.
[8] SCOTT, B.D., Phys. Rev. Lett. **65** (1990) 3289.
[9] HAMAGUCHI, S., et al., Phys. Fluids B **2** (1990) 1833.
[10] WALTZ, R.E., Phys. Fluids **31** (1988) 1962.
[11] OTTAVIANI, M., et al., Phys. Fluids B **2** (1990) 67.
[12] BRAGINSKII, S.I., Transport Processes in a Plasma, Reviews of Plasma Physics, Vol. 1, Consultants Bureau, New York (1965) 205.
[13] ZEILER, A., et al., Electron-temperature fluctuations in drift resistive ballooning turbulence, submitted to Phys. Plasmas.
[14] NOVAKOVSKII, S.V., et al., Phys. Plasmas **2** (1995) 781.

ANOMALOUS TRANSPORT THEORY FOR THE REVERSED FIELD PINCH

P.W. TERRY[1], C.C. HEGNA[2], C.R. SOVINEC[3], N. MATTOR[4], S.C. PRAGER[1], B.A. CARRERAS[5], P.H. DIAMOND[6], C.G. GIMBLETT[7], D.D. SCHNACK[8], A. THYAGARAJA[7], A.S. WARE[5]

[1] Department of Physics,
University of Wisconsin,
Madison, Wisconsin,
United States of America

[2] Department of Nuclear Engineering
and Engineering Physics,
University of Wisconsin,
Madison, Wisconsin,
United States of America

[3] Los Alamos National Laboratory,
Los Alamos, New Mexico,
United States of America

[4] Lawrence Livermore National Laboratory,
Livermore, California,
United States of America

[5] Oak Ridge National Laboratory,
Oak Ridge, Tennessee,
United States of America

[6] University of California,
San Diego, California,
United States of America

[7] UKAEA Government Division, Fusion,
Culham Laboratory,
Abingdon, Oxfordshire,
United Kingdom

[8] Science Applications International Corporation,
San Diego, California,
United States of America

Abstract

ANOMALOUS TRANSPORT THEORY FOR THE REVERSED FIELD PINCH.

Physically motivated transport models with predictive capabilities and significance beyond the reversed field pinch (RFP) are presented. It is shown that the ambipolar constrained electron heat loss observed in the Madison Symmetric Torus (MST) can be quantitatively modeled by taking account of the clumping in parallel streaming electrons and the resultant self-consistent interaction with collective modes; that the discrete dynamo process is a relaxation oscillation whose dependence on the tearing instability and profile relaxation physics leads to amplitude and period scaling predictions consistent with experiment; that the Lundquist number scaling in relaxed plasmas driven by magnetic turbulence has a weak $S^{-1/4}$ scaling; and that radial E×B shear flow can lead to large reductions in the edge particle flux with little change in the heat flux, as observed in the RFP and tokamak.

1. INTRODUCTION

Recent measurements in the reversed field pinch (RFP) have provided new information crucial to the development of predictive models of anomalous transport for both core and edge plasmas with significance beyond the RFP. Measurements in the Madison Symmetric Torus (MST) have demonstrated that anomalous heat loss inside the reversal layer is caused by the low frequency global tearing modes resonant at the few lowest order rational surfaces in the core [1]. The heat loss just inside the reversal layer is convective (despite the presence of a temperature gradient). Its magnitude is well matched by a Rechester-Rosenbluth diffusivity, *but with the ion thermal velocity for the streaming factor.* Deep in the core, the magnitude of the heat loss appears to be consistent with a standard Rechester-Rosenbluth diffusivity with the electron thermal velocity for the streaming factor [2]. This observation poses a challenge to theoretical modeling because magnetic fluctuation-induced heat transport is not conventionally subject to ambipolar constraints [3]. The established importance of tearing mode fluctuations to core confinement also points to the need for a reconsideration of the Lundquist number scaling issue [4] and the desirability of modeling the nonstationary tearing mode activity known as the discrete dynamo process [5-7]. In the edge, application of an externally driven shear flow is observed to reduce particle transport with little or no change in the heat loss [8]. Noting that heat and particle losses are sensitive to phase angles between different fluctuations, this observation indicates the need for a theoretical portrayal of the effect of shear flow on transport phase angles.

This paper presents theoretical work that models the plasma behavior underlying these and related observations. Specifically, this paper: 1) describes a theory for ambipolar constrained magnetic fluctuation-induced electron heat transport that accounts for resonant energy and momentum exchanges between aggregated electrons moving along the stochastic magnetic field and the Landau damped plasma shielding response; 2) models the discrete dynamo process as a relaxation oscillation and predicts amplitude and period scalings consistent with experiment; 3) incorporates dynamo physics to predict that magnetic turbulence has a weak Lundquist number scaling with an

exponent of less than 1/4; and 4) demonstrates quantitatively how radial electric field shear can suppress the particle flux with little change in the heat flux, as observed in the edge of the RFP and tokamak.

2. AMBIPOLAR CONSTRAINTS

The magnetic fluctuation-induced electron thermal heat flux in the edge of MST is convective [1] and ambipolar constrained [2], despite the presence of a temperature gradient. The ambipolar constraint is evidenced in the magnitude of the thermal diffusivity, which requires the ion thermal velocity to enter the product with the magnetic diffusivity. (The standard Rechester-Rosenbluth flux estimate with electron thermal diffusivity overestimates the edge flux by more than an order of magnitude.) This measurement is constructed from the correlated product of the field aligned heat flux with the radial component of the perturbed field. The cross power spectrum for this quantity peaks at 10 kHz and is zero above 20 kHz, indicating that core resonant tearing modes are driving the transport, even near the inside of the reversal layer.

Ambipolar constraints in the transport fluxes derived from higher order moments of the electron distribution (such as the heat flux) are a signature of the dissipative electron-ion coupling process associated with the ballistic motion of electron clumps [9]. Clumps are aggregates of parallel streaming electrons. Under the exponential separation of stochastic magnetic field lines, electrons on closely neighboring field lines remain correlated far longer than those on more remotely spaced field lines. Sufficiently close electrons remain correlated for a time that exceeds collective plasma responses. As such correlated electrons move through the plasma, they generate a wake by emitting into the collective modes of the plasma shielding response. Damping of the wake on the ion distribution regulates the rate of turbulent energy exchanges between fluctuations and thereby introduces the ambipolar constraint [2].

The radial electron heat flux is an energy moment of the transport correlation associated with E×B motion (electrostatic component) and the radial component of electron motion along the perturbed field $\delta\mathbf{b} = \nabla A_{\|}\times\mathbf{b}_o$. Thus, the heat flux is given by

$$Q_e = \mathrm{Re}\int d^3v\ (m_e v^2/2)\ \Sigma_k\ (ic/B_o)\mathbf{k}\times\mathbf{b}_o\cdot\mathbf{r}\langle(\phi - v_{\|}A_{\|}/c)\ h_e\rangle. \qquad (1)$$

The perturbed electron distribution function h_e has a coherent response, representing the electron contribution to the collective normal mode response, and an incoherent response, representing the correlated electrons that move along the field. These two components of the electron distribution are linked through quasineutrality and Ampere's Law, which together describe the shielding of the correlated electrons by the collective mode response. Including both components of h_e in Eq. (1) and imposing quasineutrality and Ampere's Law constraints leads to an electron heat flux expression given by

$$Q_e = v_i(\delta b/B_o)^2 k_o^{-1}\ L_n^{-1}[\omega/k_o v_i]^2(4\pi)^{-1/2}(1-\Delta k_{\|}^2/4k_o^2)^{-2}, \qquad (2)$$

where δb is the spectrum averaged magnetic fluctuation level, k_o is the value of

parallel wavenumber at which the spectrum of transport causing fluctuations peaks, and $\Delta k_{||}$ is the width of the spectrum in parallel wavenumber. This result is appropriate for adiabatic ions ($\omega/k_{||} \leq v_i = \sqrt{T_i/m_i}$), and for a spectrum in which transport-causing fluctuations are resonant at a distant rational surface, while locally resonant fluctuations make no contribution to transport (k_o-$\Delta k_{||} > 0$). Both conditions apply to the MST edge. There, the frequency spectrum of the heat flux unambiguously identifies the transport producing fluctuations as tearing modes resonant at interior surfaces corresponding to m=1 and n=5-8. Furthermore, $\omega/k_o \approx v_i$, and the above expression becomes a Rechester-Rosenbluth flux, but with ion thermal velocity in place of the electron thermal velocity. Its magnitude is consistent with the measured flux.

In regions where transport is caused by locally resonant fluctuations, such as the core of the RFP, the parallel wavenumber spectrum peaks at zero and Eq. (2) is no longer valid. The correct expression in this regime is given by

$$Q_e = v_e(\delta b/B_o)^2 \Delta k_{||}^{-1} L_T^{-1} (4\pi)^{-1/2}. \quad (3)$$

The core heat flux has no ambipolar constraint, but follows the standard Rechester-Rosenbluth form with electron thermal velocity as the streaming factor. Equations (2) and (3) are consistent with experimental observations. As noted, the measured edge heat flux is consistent in its magnitude with an ambipolar constraint in the form of an ion thermal velocity streaming factor. In contrast, the transient response of the central temperature through a sawtooth cycle indicates that core heat transport requires an electron thermal velocity streaming factor. The above model is also consistent with observations in the CCT tokamak, where magnetic transport at low order surfaces satisfies a Rechester-Rosenbluth diffusivity, but falls to much lower values away from the surface.

The ambipolar constrained edge flux of heat represented in Eq. (2), and a related flux of field-aligned momentum [10] have important implications. The exchange of momentum and energy from electrons to ions means there is an anomalous ion heating process and an anomalous ion current in the direction of bulk electron motion. Both of these features are observed in MST and warrant further investigation.

3. NONSTATIONARY RFP DYNAMO

Reversed field pinch experiments exhibit relaxation phenomena which sustain the magnetic configuration longer than should be allowed by electrical resisitvity. This effect is usually attributed to the MHD dynamo. A novel feature of the dynamo is that the relaxations often occur as a discrete and nearly periodic set of sawtoothy bursts [4-6].

A simple analytic model for the RFP sawtooth has been developed [11]. The sawtooth cycle is viewed as a relaxation oscillation describing the competition between the dynamo producing tearing instabilities which try to keep the RFP in a relaxed state and the diffusion properties of the equilibrium which reacts to a driving toroidal electric field which peaks the current profile.

As such, the RFP is described as a dynamical system with two reduced degrees of freedom. The basic model used in the calculation is resistive MHD, where all physical quantities are written as the sum of an initial time independent equilibrium, a slowly evolving "equilibrium" quantity and a fluctuation associated with tearing instabilities. The two degrees of freedom are the average value of the current gradient $\Delta\lambda$, which measures how close to a relaxed state the system becomes ($\Delta\lambda = 0$ represents the Taylor state), and the tearing mode induced MHD dynamo W. Coupled dynamical equations for $\Delta\lambda$ and W are derived and given by

$$\frac{d\Delta\lambda}{dt} = 1 - W - \varepsilon_1 \Delta\lambda \ , \tag{4}$$

$$\frac{dW}{dt} = \Lambda(\Delta\lambda - 1)W\,\Phi(W) + \varepsilon_2\, W(W-1)(1-\sigma W) \, , \tag{5}$$

where time is normalized to a fraction of the resisitive diffusion time associated with how long the initial equilibrium takes to diffuse to a tearing unstable current profile. The first equation describes the evolution of the average current gradient where the terms on the right side are the driving electric field, the dynamo and resisitive diffusion. The second equation describes the evolution of the dynamo. The first term indicates the excitation of tearing instabilities when a critical current gradient is reached and $\Phi(W)$ describes the quasilinear and nonlinear modifications to the tearing modes. The last term is associated with an inductive back reaction associated with the fact the equilibrium is evolving as described in Eq. (4) [12]. Formally, the last terms in each equation are small.

We seek solutions of Eqs. (4) and (5) by assuming $\varepsilon_1, \varepsilon_2 << 1$. To lowest order, the system has an integral of motion which parameterizes a family of solutions. The solution, $\Delta\lambda = 1$, $W = 1$ is an elliptic fixed point under the modest assumption $\Phi(1) > 0$. Typically, the cyclic solutions are characterized by two phases. In the slow ramp phase, W remains smaller than unity and $\Delta\lambda$ grows in time indicating a peaking of the normalized current profile. In the sawtooth crash phase, W grows rapidly when $\Delta\lambda$ gets sufficiently larger than unity. The rapid rise in the dynamo term then causes a flattening of the current profile which removes the free energy source for the tearing fluctuations.

By including the small order ε terms, the integral of motion is broken. The solution then asymptotes to a stable limit cycle solution. The model predicts that the sawtooth cycle and amplitude increase with plasma current and Lundquist number, both of which appear to be qualitatively consistent with MST observations.

4. LUNDQUIST NUMBER SCALING

The link between thermal transport and tearing mode fluctuations calls for a reconsideration of the Lundquist number scaling of magnetic turbulence in the RFP. This scaling quantifies how turbulence in the RFP, and other relaxed plasmas such as the spheromak, is affected by plasma resistivity (the Lundquist number is the ratio of resistive diffusion time to an Alfvén time). Because the linear growth rate of tearing modes decreases with decreasing resistivity

according to the familiar fractional power [13], it has long been assumed that the magnitude of turbulence in the RFP should also decrease as the plasma becomes less resistive. While experiments of OHTE indicated a Lundquist number scaling of $\delta b \propto S^{-1/2}$, where δb is the root-mean-square magnetic fluctuation level and S is the Lundquist number, recent numerical and experimental work has suggested a weaker scaling [4, 14-15].

To investigate this issue, three-dimensional, nonlinear MHD simulations with Lundquist number ranging from 2.5×10^3 to 4×10^4 have been completed. These simulations were carried out with a pseudo-spectral algorithm, and hyper-dissipation terms were utilized in the pressureless MHD equations to suppress numerical aliasing [16]. The results indicate a weak Lundquist number scaling: $\delta b \propto S^{-0.18}$. It is important to understand mode interactions that contribute to this result. In particular, m=0 modes, whose fluctuation level increases with S in this range, have a significant impact on the scaling. This behavior is attributed in part to enhanced nonlinear coupling as dissipation is reduced and in part to changes in the parallel current profile. The parallel current gradient at the m=0 resonance surface increases with S due to an increasingly more effective MHD dynamo. This effect is expected to eventually saturate at larger S, leading to a decreasing m=0 fluctuation level and a stronger overall scaling.

The temporal behavior of the simulations also changes as S is increased. Oscillations in the reversal parameter become more regular, acquiring a sawtooth character at the largest values of S studied. Similar but less dramatic observations have been reported earlier [17]. Here, the nonlinear coupling between internally resonant m=1 modes and m=0 modes plays an important role. The events leading to a sawtooth crash are consistent with a three phase description of quasiperiodic oscillations at modest S [18]. The three phases (1. interior m=1 modes gain energy, 2. nonlinear transfer of energy to m=1 modes that are resonant near the reversal surface, and 3. mean poloidal current drive) produce enhanced current inside the reversal surface. However, at large S, there is an added phase of mean current redistribution from m=0 modes, which subsequently suppresses these modes. When they are small, the second phase of the dynamo is impeded until the m=1 modes are large enough to nonlinearly drive the m=0 modes back to a significant level.

The scaling of magnetic turbulence with S has also been examined analytically from a theoretical framework that links the fluctuation spectrum to the dynamo through the cascade properties of three dimensional MHD and also accounts for the role of discrete dynamo events [19]. For a discrete (sawtoothing) dynamo, the time averaged root-mean-square magnetic fluctuation level scales as $\delta b \propto S^0$, but it can be argued that the averaged flux surface destroying magnetic fluctuations scale as $\delta b_{br} \propto S^{-1/2}$. For a continuous dynamo, with a steady state saturated turbulence spectrum, the magnetic field perturbations scale as $\delta b \propto S^{-1/4}$.

5. RADIAL ELECTRIC FIELD SHEAR AND EDGE TRANSPORT

Suppression of turbulent fluctuations by sheared E×B flow [20] has emerged as a robust paradigm that is thought to explain key features of

confinement improvements in H and VH modes and in the enhanced reversed shear or negative central shear discharges. A challenge for this paradigm is to explain detailed transport measurements and measurements of phase angles, whose dependence on the shear flow can be puzzling or counterintuitive. One such set of experiments involves the creation of a sheared radial electric field in the CCT tokamak and in MST by an emitting probe [21] or by electron current injectors [8]. In these experiments there is a marked decrease in particle transport with little or no change in the heat flux. These results are difficult to explain with the standard treatments of shear suppression, which only account for amplitude reductions by shear flow, but do not address the effect of shear flow on the phase angles that contribute to the transport fluxes.

We present a calculation of heat and particle fluxes that accounts for shear flow effects on both phase angle and amplitudes [22]. This calculation is relevant to edge fluctuations in machines such as CCT and MST where the observations were made, and utilizes an edge turbulence model based on resistive interchange turbulence. An important feature of this model is the effect of parallel thermal conductivity on temperature fluctuations. Though the instability in the present calculation is the resistive interchange mode, the results are generally representative of classes of instabilities driven by density and vorticity dynamics with temperature playing a secondary role.

The model consists of evolution equations for vorticity, density, and temperature, with E×B advection of each field the dominant nonlinear process. An equilibrium poloidal flow with radial shear is also included in the advective term. Field line bending provides localization of fluctuations in the neighborhood of the rational surface, i.e., the linear mode width is set primarily by the balance of the field line bending term and the time derivative of vorticity. Shear induces a shift of the eigenmode structure away from the rational surface and generally enhances the effect of field line bending. The instability is driven by curvature and the pressure gradient. Due to the magnitude of parallel thermal conduction in the edge of Ohmic discharges, the density gradient is assumed to provide the free energy and temperature fluctuations are treated as a passive scalar. The nonlinearities are renormalized in the usual fashion, yielding three equations, each of which has an amplitude dependent turbulent diffusivity. A nonlinear eigenmode calculation solves the renormalized equations, yielding the magnitude of the diffusivity (and hence the magnitude of the saturated turbulence), the mode width at finite amplitude, and the magnitude of the shift of the eigenmode structure induced by the flow shear [23].

From this solution, particle and heat transport fluxes are constructed from the correlations of density and temperature fluctuations with the electrostatic potential. These correlations depend on amplitude and phase angle, both of which in turn depend on the flow shear, dissipation, and the nonlinear diffusivity. The latter quantity itself depends on shear flow through the shift of the eigenmode structure. The particle and heat fluxes are given respectively by $\Gamma = \sum_k |v_k||n_k|\cos\delta_n$ and $Q = \sum_k |v_k||T_k|\cos\delta_T$ where v_k, n_k, and T_k are Fourier amplitudes for fluctuations in the flow, density and temperature, and δ_n and δ_T are the phases for the particle and heat fluxes. The phase angle factors $\cos\delta_n$ and $\cos\delta_T$ are given by

$$\cos\delta_n = 1 - \frac{[0.2k_y^2 V_E'^2 W^2/\gamma^2]}{[1\text{-}0.9k_y^2 V_E'^2 W^2/\gamma^2]^2} \quad (6)$$

$$\cos\delta_T = 1 - \frac{[2k_y V_E' W]^2}{[\chi_{\|e} k_y^2 W^2/n_o L_s^2]^2} \quad (7)$$

where V_E' is the shear in the E×B flow, W and γ are the mode width and growth rate of the resistive interchange mode for zero shear, $\chi_{\|e}$ is the parallel electron thermal conductivity, and the phase angle cosines are normalized to their values in the absence of a shear flow. From these expressions, it is evident that for strong parallel thermal conduction, shear flow has a weak effect on the phase angle factor for the heat flux. In contrast, the phase angle factor for the particle flux is highly sensitive to the turbulent diffusivity, which in turn is sensitive to the shear flow. For parameters consistent with the edge of CCT and MST, a level of shear flow sufficient to make $\cos\delta_n$ equal to zero, produces a change in $\cos\delta_T$ of only a few percent. When combined with the amplitude factors, both fluxes decrease with flow shear, but the variation in the particle flux is much stronger due to the variation of its phase factor. This demonstrates that the dependence of the phase angle on flow shear is an important aspect of shear flow suppression. Moreover, it is apparent that with phase angle effects, different transport fluxes need not respond identically to a sheared E×B flow. In particular, a dissipative process with a shorter time scale than the shear decorrelation time can make a flux whose phase angle depends on that dissipative process relatively impervious to the effect of shear flow.

This work is supported by USDOE.

REFERENCES

[1] FIKSEL, G., et al., Phys. Rev. Lett. **72** (1994) 1028.
[2] TERRY, P.W., et al., Phys. Plasmas **3** (1996) 1999.
[3] THOUL, A.A., SIMILON, P.L., SUDAN, R.N., Phys. Plasmas **1** (1994) 601.
[4] LA HAYE, R.J., et al., Phys. Fluids **27** (1984) 2576.
[5] WATT, R.G., NEBEL, R.A., Phys. Fluids **26** (1983) 1168.
[6] HOKIN, S., et al., Phys. Fluids B **3** (1991) 2241.
[7] DEN HARTOG, D.J., et al., Phys. Plasmas **2** (1995) 2281.
[8] CRAIG, D., et al., Bull. Am. Phys. Soc. **41** (1996) 1407.
[9] TERRY, P.W., DIAMOND, P.H., HAHM, T.S., Phys. Rev. Lett. **57** (1986) 1899.
[10] TERRY, P.W., DIAMOND, P.H., Phys. Fluids B **2** (1990) 1128.
[11] HEGNA, C.C., et al., "Theory of discrete dynamo activity in laboratory plasmas: RFP saw-teeth", paper presented at Int. Sherwood Theory Conf. Philadelphia, 1996.
[12] THYAGARAJA, A., HAAS, F.A., Plasma Phys. Control. Fusion **37** (1995) 415.
[13] FURTH, H.P., KILLEEN, J., ROSENBLUTH, M.N., Phys. Fluids **6** (1963) 459.
[14] SARFF, J.S., et al., Bull. Am. Phys. Soc. **41** (1996) 1409.
[15] CAPPELLO, S., BISKAMP, D., Nucl. Fusion **36** (1996) 571.
[16] SOVINEC, C.R., SCHNACK, D.D., paper presented at Int. Sherwood Fusion Theory Conf. Dallas, 1994.

[17] CAPPELLO, S., BISKAMP, D., in Proc. Int. Conf. on Plasma Physics, Foz do Iguacu, Brazil, 1994.
[18] HO, Y.L., CRADDOCK, G.G., Phys. Fluids B **3** (1991) 721.
[19] MATTOR, N., Phys. Plasmas **3** (1996) 1578.
[20] BIGLARI, H., DIAMOND, P.H., TERRY, P.W., Phys. Fluids B **2** (1990) 1.
[21] TYNAN, G., et al., Plasma Phys. Control. Fusion **38** (1996) 1301.
[22] TERRY, P.W., et al., paper presented at 9th Transport Task Force Workshop, Philadelphia, 1996.
[23] WARE, A.S., et al., Plasma Phys. Control. Fusion **38** (1996) 1343.

HIGH-HARMONIC ION CYCLOTRON HEATING AND CURRENT DRIVE IN ULTRA-SMALL ASPECT RATIO TOKAMAKS*

D.B. BATCHELOR, E.F. JAEGER,
M.D. CARTER, L.A. BERRY
Oak Ridge National Laboratory,
Oak Ridge, Tennessee

J.R. WILSON, R. MAJESKI, M. ONO,
J. MENARD, S.M. KAYE
Plasma Physics Laboratory,
Princeton University,
Princeton, New Jersey

United States of America

Abstract

HIGH-HARMONIC ION CYCLOTRON HEATING AND CURRENT DRIVE IN ULTRA-SMALL ASPECT RATIO TOKAMAKS.

Ultra-small aspect ratio tokamaks present a totally new plasma environment for heating and current drive experiments and involve a number of physics issues that have not been explored previously. These devices operate at low magnetic field and relatively high density so that the effective dielectric constant of the plasma to high harmonic fast waves (HHFWs) is quite high and the perpendicular wavelength of the fast waves is very short, $\lambda \sim 2.0$ cm, compared with $\lambda \sim 10$–20 cm. This allows strong electron absorption at high harmonics of the ion cyclotron frequency, Ω_i, and at fairly high phase velocity in relation to the electron thermal velocity. If the antenna system can control the parallel wave spectrum, this offers the promise of high efficiency off-axis current drive and the possibility of current drive radial profile control. Antenna phasing is ineffective for profile control in conventional tokamaks because of central absorption. There are also challenges for antenna design in this regime because of the high dielectric constant and the large angle of the magnetic field with respect to the equatorial plane (~45°), which varies greatly during current ramp. Preliminary experiments in this HHFW regime are being carried out in CDX-U.

* The Oak Ridge research was performed by ORNL, managed by Lockheed Martin Energy Research Corporation, for the US Department of Energy under Contract No. DE-AC05-96OR22464. — The Princeton research was supported by the US Department of Energy under Contract No. DE-AC02-76CHO3073.

1. NATIONAL SPHERICAL TOKAMAK EXPERIMENT

We have carried out studies for the proposed National Spherical Tokamak Experiment (NSTX) [1,2], a low aspect ratio (A = 1.25), major radius R = 0.8 m tokamak with toroidal magnetic field B = 0.32 T and I_p up to 1MA. The high harmonic fast waves (HHFW) system envisioned for NSTX will consist of two six-strap antennas located on opposite sides of the torus (Fig. 1). The single-ended current straps will be tilted at 30° to the vertical. Since the field line tilt at the outer midplane of the plasma is expected to evolve from ~15–45° during HHFW-assisted startup, this choice of angle ensures that the current straps will be within 15° of perpendicular to the local magnetic field line throughout the discharge history. The center-to-center separation between straps will be 28 cm, so the peak in the vacuum antenna spectrum can be varied over a range in n_ϕ of ~5–10, by varying the phasing from 60–120°. Each current strap will be Faraday shielded and fitted with insulating boron nitride side limiters to reduce radio frequency (rf)-induced scrape-off layer self-bias effects [3]. Six transmitters will feed the two antenna sets, and each transmitter will drive one current strap in each antenna set. The initial operating frequency has not been determined but will be in the range of 30–40 MHz. The phase between adjacent current straps may therefore be electronically modified at the low-power rf source level, to change n_ϕ during the discharge. Decoupling will be incorporated in the antenna matching circuitry to allow arbitrary phase operation between straps.

2. ANTENNA ANALYSIS

The major questions for antenna design are these: how does the strap angle relative to the static field affect the loading scenarios, what is the launched power spectrum from the antenna, how does the spectrum change during a shot as the poloidal magnetic field at the antenna changes from zero to values that are roughly equal to the toroidal magnetic field, and what is the effect of heating by the antenna near-fields.

We have addressed the issues with the RANT3D code [4] combined with the GLOSI plasma surface impedance code [5] to generate the toroidal and poloidal antenna

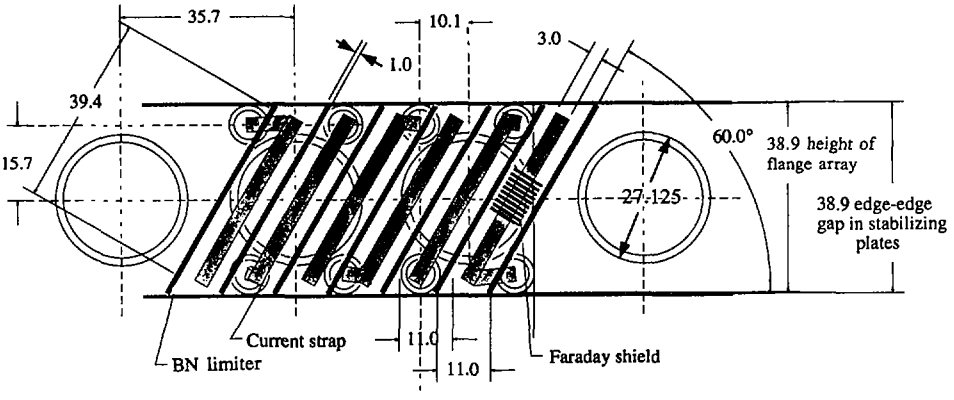

FIG. 1. Layout of the NSTX six-strap ICRF antenna. The dimensions are given in centimeters.

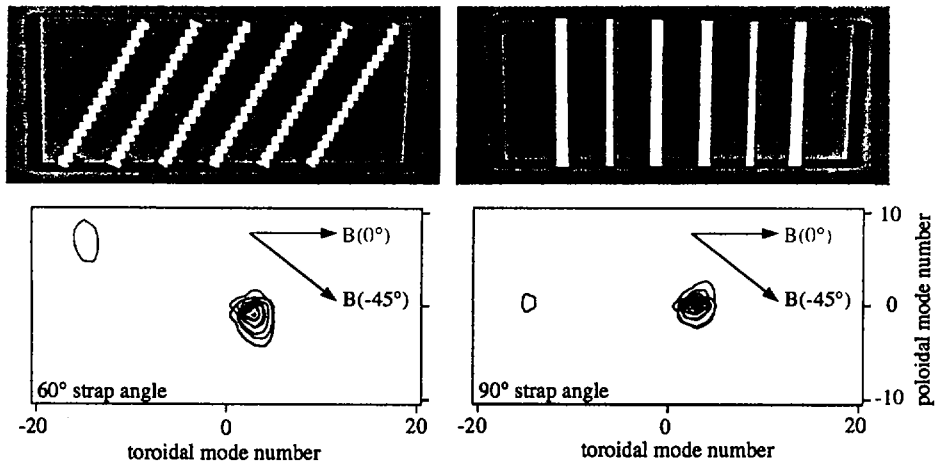

FIG. 2. Power spectra from the RANT3D model. Top pictures: current strap configuration and antenna sidewall structure in the model. Below: corresponding pair of overlaid antenna spectra. Light contours: power for the startup case. Dark contours: power for full current operation. Contour levels: 0.5, 1.5, 2.5, 3.5, and 4.5 W.

spectrum and loading information. The RANT3D code allows for arbitrary orientation of the current straps, which were oriented with a 60° angle relative to the toroidal direction to match the design. For comparison, calculations were also done with the straps at 90° (vertical). The Gaussian electron temperature profile had a peak value of 2 keV. The electron density profile was parabolic with an exponential scrape-off layer. To model full-current operation, the equilibrium magnetic field profiles included a sheared poloidal field, increasing to $B_P = B_T$ (i.e., $\theta_B = 45°$) at the plasma edge. To model $I_P = 0$ startup conditions, calculations were also done with $B_P = 0$ (i.e., $\theta_B = 0°$).

These results are summarized in Fig. 2, which shows the RANT3D antenna model geometry (60° strap angle and 90° strap angle) and contours of the radiated power spectrum (n = toroidal mode number, m = poloidal mode number) for the full current and startup. For current drive scenarios, the straps were progressively phased by $\Delta\phi = 60°$ to drive current in the co (parallel to plasma current) direction. Figure 2 also shows that the waves tend to follow the magnetic field lines even if the current straps are not rotated because the peak in the spectrum moves to $m < 0$ for the full current cases. Even a toroidally symmetric antenna phasing ($\Delta\phi = 180°$) can result in a nonsymmetric launched power spectrum, which may result in a significant driven current even for a heating antenna phasing. The average loading per strap was as follows:

60° strap angle: R_L(full current) = 14Ω R_L(startup) = 14Ω
90° strap angle: R_L(full current) = 11Ω R_L(startup) = 15Ω

The strap-to-strap variation in loading is ~50%, necessitating the use of decoupling circuitry.

3. FULL WAVE HEATING AND CURRENT DRIVE ANALYSIS

The PICES global wave code [6] has been extended to include the needed harmonics, 20–40, and the small $k_\perp \rho_i$ expansion has been replaced with the full modified bessel function form for the ion conductivity. A problem common to all full-wave calculations is the appearance of short-wave-length ion Bernstein waves (IBW) with spatial scale lengths too small to resolve numerically in two dimensions. One method of dealing with these waves (and the method used in PICES) is to prevent their formation by artificially reducing the order of the differential wave equation [6, 7]. This approach, called the "reduced order" method, replaces differential operators acting on the electric field in the plasma conductivity with the local wave number $k_\perp$ obtained from a second-order expansion of the warm plasma dispersion relation. Because the dispersion relation used is expanded to second-order in the Larmor radius, a question arises in regard to the validity of the reduced-order method for NSTX parameters. For low ion temperature, the expansion is clearly valid. Furthermore, results show that wave propagation and absorption are relatively insensitive to ion dynamics for temperatures below ~1 keV. In addition, more detailed solutions of the full plasma dispersion relation including unexpanded Bessel functions up to 40 ion harmonics show that the second-order expansion gives a reasonable approximation for $k_\perp$ as long as the ion temperature remains below 1 keV. In these cases, the reduced-order method seems justified. However, for ion temperatures above a few keV, significant differences can exist between solutions of the expanded and full dispersion relation, and the validity of the reduced-order method comes into question.

For simplicity, a Solovev magnetic equilibrium has been used. Figure 3 shows the locations of ion resonances. Harmonic numbers lie between 1 and 10 for hydrogen and between 4 and 20 for deuterium. Twenty ion harmonics are included in the ion conductivity and absorption calculation. Results in Fig. 4 show power deposition as

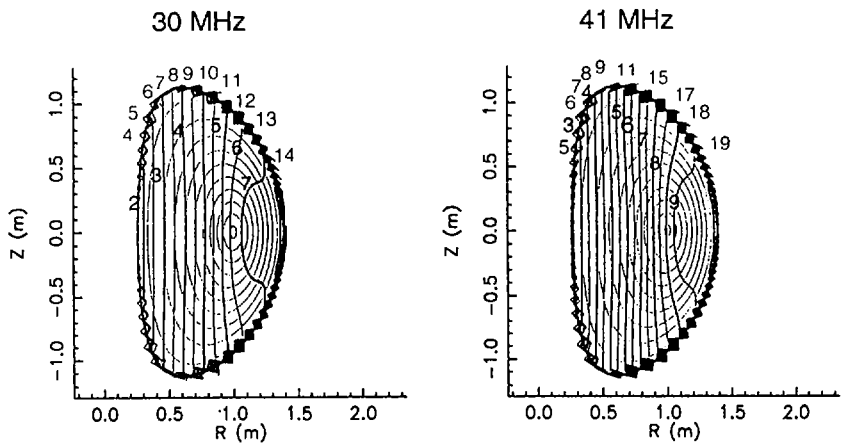

FIG. 3. Ion resonances in NSTX at high cyclotron harmonics. Light lines: majority deuterium resonances; heavy lines: minority hydrogen resonances.

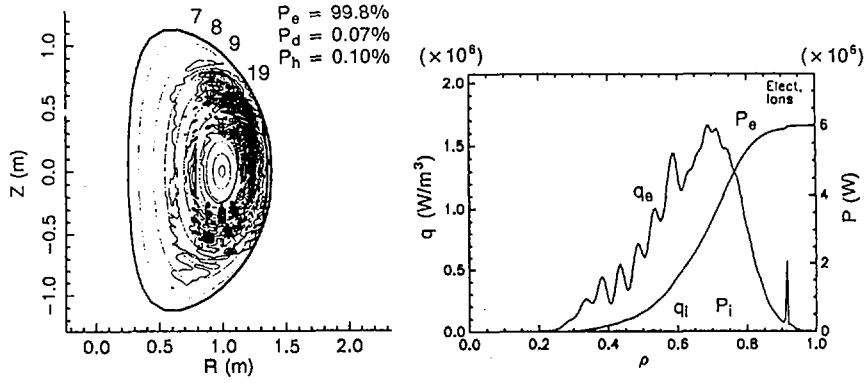

FIG. 4. Power deposition in NSTX using full modified Bessel functions with 20 ion harmonics. Light contours: electron power absorption; dark contours: ion absorption. T_e = 5 keV, n_ϕ = 8, f = 41 MHz.

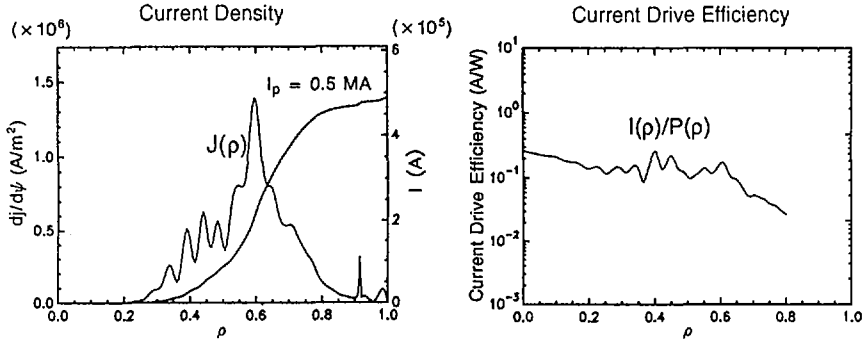

FIG. 5. Noninductive current drive in NSTX for 6 MW of RF power; T_e = 5 keV, n_ϕ = 8, f = 41 MHz, Z_{eff} = 2.0.

calculated by PICES for the expected plasma parameters in NSTX (i.e., $n_e(0) \sim 5 \times 10^{19}$ m^{-3}; $T_e(0) \sim 5$ keV and $T_i(0) \sim 1$ keV; and a single toroidal harmonic, $n_\phi = 8$). Because of the high plasma β, Landau damping and magnetic pumping are strong, and waves launched from the low field side are completely absorbed before reaching the plasma center. The result is a noninductive current that is driven well off-axis, as shown in Fig. 5. Current drive efficiency is reasonably high in this case, with ~0.5 MA driven for 6 MW of rf power, or ~0.08 A/W. If the ion temperature is reduced to 0.01 keV, the results are essentially unchanged, indicating that the overall wave propagation and absorption are insensitive to the ion dynamics. This is in agreement with solutions to the complete dispersion relation for $T_i < 1$ keV. Results similar to those in Figs 4 and 5 have also been found with a somewhat lower frequency, f = 30 MHz .

To model the rf antenna structure more accurately, the PICES code has been interfaced with the RANT3D antenna model previously described. Tangential electric fields, as calculated by RANT3D, are applied as boundary conditions in the PICES code without the use of external currents to model the antenna. If, for example, the antenna spectrum calculated by RANT for 60° current straps in a 45° magnetic field is used and 50 toroidal harmonics are kept in PICES, a reduction in current drive of about a factor of two results. If a lower electron temperature, T_e, is assumed, the current drive efficiency decreases approximately in proportion to T_e.

The strong electron absorption by Landau damping and magnetic pumping observed in Figs 4 and 5 depends on the upshift in $k_{||}$ afforded by the large poloidal field in NSTX. If the poloidal field is set to zero (as in startup scenarios, for example), PICES shows as much as a 50% reduction in the power absorbed by the electrons, and the remaining 50% goes to ions at the high-cyclotron harmonics in front of the antenna. In addition, if hot ions are present, as might be expected during neutral beam injection, additional amounts of power can be absorbed in the hot ion component. A 10% fraction of hot ions with $T_{hot}(0)$ = 25 keV and T_{hot}(edge) = 16 keV absorbs ~40% of the rf power, which reduces the power absorbed by electrons to ~60% of that in Fig. 4, and current drive efficiency is reduced by a corresponding amount.

Strong differences are observed in the plasma response to co-current and counter-current drive phasings in NSTX. Similar differences are now being seen experimentally in DIII-D fast wave current drive experiments [8]. At first, such differences are puzzling because at the core of nearly all rf heating models is the homogeneous dielectric tensor which does not exhibit any obvious asymmetries in toroidal propagation. However, coupling is also a critical part of the problem, and it is here that the asymmetries become apparent.

Even for the homogeneous plasma case, up-down asymmetries exist in the electric field structure, caused by the sign dependence of the Hall currents with respect to the magnetic field and most clearly manifest in the m (poloidal mode number) dependence of waves in a magnetized plasma column with straight field lines [9]. Symmetry still exists in the toroidal mode number n_ϕ, but this symmetry is broken when a poloidal field is added. This effect was seen in ST experiments [10] in which split eigenmodes were seen for each n_ϕ value. The net effect for NSTX is that for the same equilibrium plasma parameters the rf fields tend to be more focused toward the axis for counter phasing, giving narrower, more highly peaked current drive profiles. For the same parameters as in Figs 4–5 (except T_e = 2 keV rather than 5 keV), ~40% more current is driven with counter current drive phasing as with cophasing.

4. PRELIMINARY RESULTS FROM CDX-U

Experiments in progress on the CDX-U device at the Princeton Plasma Physics Laboratory will provide an early test of HHFW on a low aspect ratio tokamak. CDX-U has a major radius of 34 cm, minor radius of 22 cm (aspect ratio of 1.5), and a toroidal field on axis of 1 kG. The plasma current is typically 60–100 kA, so that the magnetic field line pitch is typically 20–40° at the outer midplane of the plasma. The field line pitch is therefore in the range expected for NSTX, which will permit detailed studies of antenna coupling issues. However, the plasma beta is expected to be limited to ~5%,

with $n_e(0) \sim 5 \times 10^{12}$ cm^{-3} and $T_e(0) \sim 200$ eV. The duration of the discharge flat top is 5–10 msec.

The CDX-U rf system delivers as much as 100 kW of power to the plasma with up to a 20-msec pulse length at a frequency of 10–20 MHz. This frequency corresponds to 7–14 Ω_i for discharges in hydrogen, which is the working gas at present, and to ~20 Ω_i (typical of NSTX) for future operation in deuterium. The antenna consists of two 25-cm-long straps driven in π phasing. The separation between the current straps is 22 cm (center to center). The vacuum antenna spectrum peaks at 14 m^{-1}, with $n_{||}$ in the range of 30–70 and $v_\phi / v_{Te} \sim 1$. Each strap is separately Faraday shielded and fitted with surrounding limiters of insulating boron nitride to reduce rf-induced modifications to the scrape-off layer [3]. In order to investigate the effect of the extreme field line pitch, which is characteristic of low aspect ratio tokamaks on fast wave coupling, the CDX-U antenna is designed to be manually rotatable (between discharges) in order to vary the relative angle between the current straps and the magnetic field line. The antenna is also inductively decoupled [3] so that in principle a toroidally asymmetric wave spectrum may be produced, although the directivity with a two-strap antenna will, of course, be poor. At present, only initial loading measurements with a single current strap excited at low power have been made. These measurements indicate that the single-strap loading is in the range of one to a few ohms, sufficient to couple 50–100 kW of rf power.

REFERENCES

[1] MENARD, J., MAJESKI, R., ONO, M., WILSON, J.R., in Radio Frequency Power in Plasmas (Proc. 11th Top. Conf. Palm Springs, 1996), American Institute of Physics, New York (1996) 59.

[2] ONO, M., Phys. Plasmas **2** (1995) 4075.

[3] MAJESKI, R., et al., Fusion Eng. Des. **24** (1994) 159.

[4] CARTER, M.D., et al., Nucl. Fusion **36** (1996) 209.

[5] WANG, C.-Y., et al., Phys. Plasmas **2** (1995) 2760.

[6] JAEGER, E.F., BATCHELOR, D.B., STALLINGS, D.C., Nucl. Fusion **33** (1993) 179.

[7] SMITHE, D.N., COLESTOCK, P.L., KASHUBA, R.J., KAMMASH, T., Nucl. Fusion **27** (1987) 1319.

[8] FOREST, C.B., personal communication, May 1996; see also PRATER, R., et al., IAEA-CN-64/E-1, these Proceedings, Vol. 3.

[9] MESSIAEN, A.M., et al., Nucl. Fusion **15** (1975) 75.

[10] ADAM, J., et al., in Plasma Physics and Controlled Nuclear Fusion Research 1974 (Proc. 5th Int. Conf. Tokyo, 1974), Vol. 1, IAEA, Vienna (1975) 65.

REMOVAL OF HELIUM ASH AND IMPURITIES BY USING ICRH DRIVEN RIPPLE TRANSPORT

K. HAMAMATSU, C.S. CHANG[1], T. TAKIZUKA, M. AZUMI,
T. HIRAYAMA, S. COHEN[2], K. TANI
Naka Fusion Research Establishment,
Japan Atomic Energy Research Institute,
Naka-machi, Naka-gun, Ibaraki-ken,
Japan

Abstract

REMOVAL OF HELIUM ASH AND IMPURITIES BY USING ICRH DRIVEN RIPPLE TRANSPORT.

A new method of helium ash removal is numerically confirmed by the orbit following Monte Carlo simulation. Ion cyclotron resonance heating (ICRH) is applied to drive He^+ ions, which are produced by charge exchange recombination with fuel neutrals near the peripheral region, into the ripple trapped regime of the velocity space. These ions escape from the edge region by ripple transport. Simulation results show that the ICRF power necessary to reduce the edge helium ash density by half, for a fusion output power of 1.5 GW in an ITER grade reactor, is about 10–15 MW. This method is also applied to the removal of impurity ions.

1. INTRODUCTION

Removal of helium ash is an important factor in sustaining a stationary burning plasma in a magnetically confined fusion reactor. Since the radial density profile of helium ash is determined by the spatial transport properties as a diffusion problem, the helium ash density in a burning core can be directly related to that at the plasma periphery. If the helium ash in the peripheral region is effectively exhausted, the helium ash in a central region can easily be removed.

In this paper, on the basis of an idea set forth in Ref. [1], a numerical study is performed to investigate the application of ion cyclotron resonance heating (ICRH) to driving helium ions into the ripple trapped regime and to estimate the efficiency of ash removal. It is difficult to have a preferential coupling of an electromagnetic wave in the ion cyclotron range of frequencies (ICRF) with He^{2+} ions, because the cyclotron frequencies of D^+ and He^{2+} are identical. However, we can couple an ICRF wave energy selectively with He^{2+} ions near the peripheral plasma on the low field side (LFS). After an He^{2+} ion has been trapped into the ripple well with high energy, the

[1] Courant Institute of Mathematical Sciences, New York University, New York, N.Y., USA.
[2] Plasma Physics Laboratory, Princeton University, Princeton, New Jersey, USA.

helium ion is spontaneously lost by ∇B drift motion. A numerical simulation is performed by using an orbit following Monte Carlo (OFMC) code, which includes the ICRH effect and the ripple trapped effect in a realistic tokamak geometry. This scheme is also applied to the removal of impurity ions.

2. BASIC IDEA AND SIMULATION METHOD

Helium ions are usually fully ionized when the electron temperature is higher than about 100 eV. However, He^{2+} ions can exchange their charges with neutral deuterium, D^0, or tritium, T^0, atoms ($He^{2+} + D^0/T^0 \leftrightarrow He^2 + D^+/T^+$). The density ratio of $n_{He^\cdot}$ to $n_{He^{2+}}$ is in proportion to the density ratio of n_{DT° to the electron density, n_e:

$$\frac{n_{He^\cdot}}{n_{He^{2+}}} = \eta \frac{n_{DT^\circ}}{n_e} \tag{1}$$

where $\eta = \langle\sigma v\rangle_{cx}/\langle\sigma v\rangle_{ion}$, $\langle\sigma v\rangle_{cx}$ is the charge exchange rate and $\langle\sigma v\rangle_{ion}$ is the ionization rate. The value of η varies in the range of 1 to10 as a function of the temperatures of He^{2+}, $T_{He^{2+}}$, and of D^0/T^0, T_{DT°, (Fig. 1). The lifetime of He^+ is evaluated to be several microseconds for reionization back to He^{2+}, when

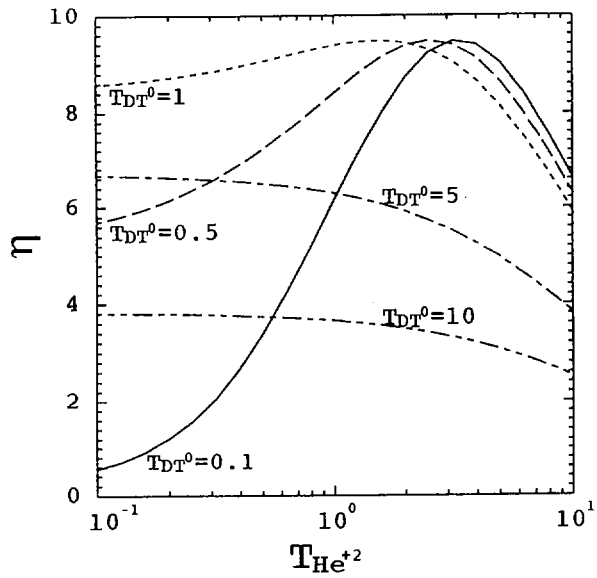

FIG. 1. Temperature dependence of coefficient η. Temperatures are given in keV.

$n_e \sim 5 \times 10^{19}$ m^{-3}. This lifetime is enough to accelerate He^+ ions perpendicularly to the magnetic field by the ICRF wave and to drive them into the ripple trapped regime of the velocity space.

In order to simulate the physical processes described in this scenario, we use the OFMC cord. We briefly explain the numerical procedure to be followed in evaluating an amount of removed helium ash. (1) We stipulate a uniform birth profile of He^+ ions on many magnetic surfaces, where the particle density is normalized on each magnetic surface. The velocity distribution of the He^+ ions is assumed to be Maxwellian with $T_{He^{2+}}$, which is equal to the bulk plasma temperature. (2) The orbit of a He^+ ion is followed up to its ionization to He^{2+}. The effects of ICRF heating are taken into account by the Monte Carlo technique. When the particle passes through the cyclotron resonance point, the electric field changes the perpendicular velocity of the particle. The change of the perpendicular velocity is calculated from the quasi-linear theory. (3) The orbit of a particle interacting with the ICRF wave is followed until it hits the first wall or is slowed down by the Coulomb collisions. The loss rates for particle and absorbed ICRF power are obtained on all magnetic surfaces. (4) We evaluate the density profile of He^+ by assuming the density and temperature profiles of D^0/T^0. The loss rates of particle and absorbed ICRF power for the whole plasma column are obtained as a convolution of the He^+ density and the results obtained in the previous step (3).

3. HELIUM REMOVAL

The simulation results presented here are for an ITER grade machine with 20 TF coils, where the toroidal magnetic field is 5.7 T at the plasma centre. The toroidal field ripple is about 1% at the plasma edge for the ITER. To achieve effective ash removal, we install a local ripple coil in order to increase the ripple field to 3%. We assume the following plasma parameters on the separatrix: $n_e = 5 \times 10^{19}$ m^{-3}, $n_{He} = 5 \times 10^{18}$ m^{-3}, $n_{D^+} = n_{T^+}$, $T_e = T_{He} = T_{D^+} = T_{T^+} = 2$ keV. The scrape-off layer is placed outside the separatrix, where the e folding lengths of plasma density and temperature are denoted by Δ_n and Δ_T. We assume that the density profile of D^0/T^0 is expressed in terms of the density on the separatrix, n_{DT^0}, and the e folding length, Δ_{DT^0}.

3.1. Wave propagation

In order to analyse the ICRF wave propagation and power absorption due to He^+ ions in the peripheral region, we use a one dimensional ICRF wave code in a slab geometry [2]. This code solves the kinetic wave equation along the direction of the major radius (x direction) with periodic boundary conditions in the toroidal direction (z direction) within the linear theory. Here, the plasma is assumed to be homogeneous in the z and y directions, where y denotes the poloidal direction. The frequency of the ICRF wave is chosen to be 16.8 MHz, which is the fundamental cyclotron resonance

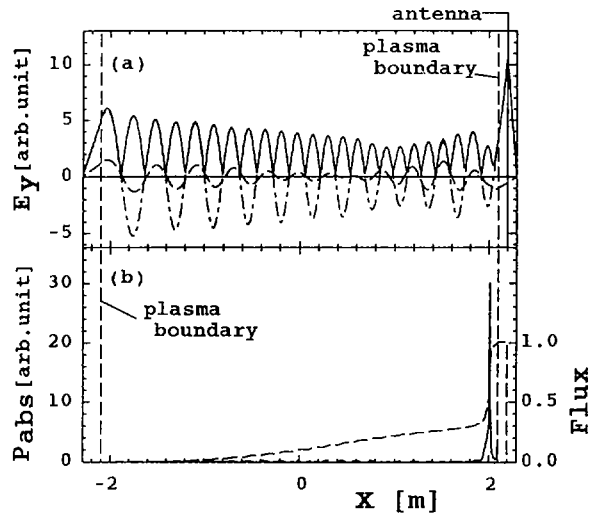

FIG. 2. Radial profile of ICRF wave field and absorbed power density. (a) Electric field E_y; dashed curve: real part; dash-dotted curve: imaginary part; solid curve: absolute value. (b) Solid curve: power density absorbed by He^+; dashed curve: power flux.

frequency of He^+ near the plasma periphery on the LFS. To remove the helium ash, we use only one ICRF antenna array set between a pair of toroidal coils on the LFS. In this work, the antenna array consists of seven antennas, which carry the sheet currents in the poloidal direction, with controlled phase, and are arranged in the toroidal direction, at distances of about 0.33 m. The antenna array size along the poloidal and toroidal directions is (2 m × 2 m). In order to avoid power absorption due to electron Landau damping, we must excite a wave with small wavenumber along the magnetic field, $k_{\|}$. If these seven antennas carry the sheet currents with the same phase, the condition of wave excitation in the range of $-2\ m^{-1} \lesssim k_{\|} \lesssim 2\ m^{-1}$ is easily satisfied. Figure 2 shows the radial profiles of the electric field, E_y, the absorbed power and the power flux, where the density of the He^+ ions is $2.5 \times 10^{15}\ m^{-3}$ at the separatrix. We see strong damping due to the cyclotron resonance of He^+ in Fig. 2(b). The power absorbed by He^+ is about 70% of the total input power, and the rest of the power is absorbed by electrons. By scanning the plasma parameters it is found that the power absorbed by He^+ is not so much affected by n_{He^+} if T_{He^+} is kept higher than 2 keV at the separatrix.

3.2. Orbit following Monte Carlo simulation

In the OFMC simulation, $k_{\|}$ and the profile of the ICRF electric field, E_{rf}, must be given as parameters. In the following analysis, $k_{\|}$ is chosen to be zero. The electric

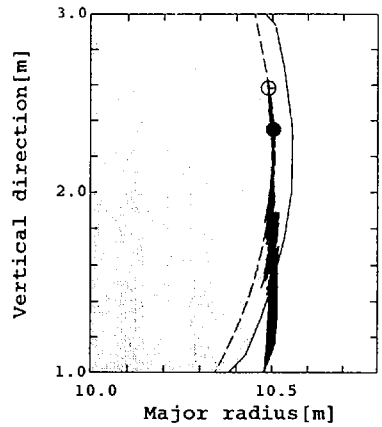

FIG. 3. Trajectory of lost particle projected on poloidal plane.

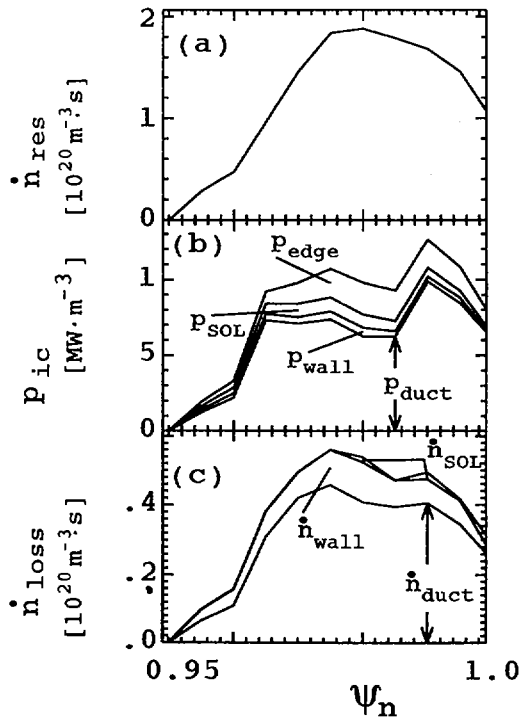

FIG. 4. Simulation results starting from each magnetic surface. Resonance particle number rate, absorbed ICRF power and particle loss rate are shown in (a), (b) and (c), respectively.

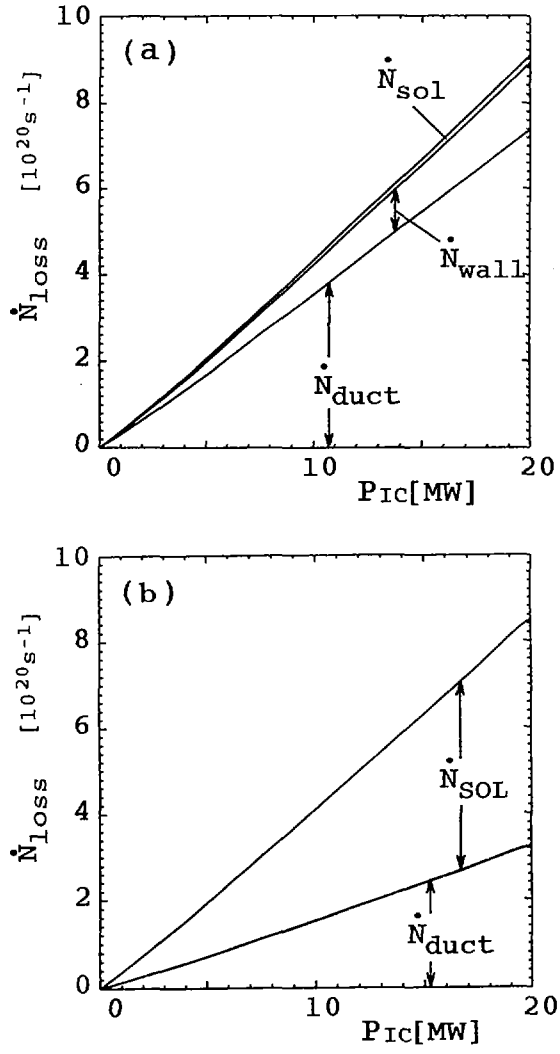

FIG. 5. Absorbed power dependence of particle loss rate. (a) Δ_n = 2 cm and Δ_T = 4 cm; (b) Δ_n = 2 cm and Δ_T = 1 cm.

field amplitude is assumed to be constant in front of the antenna array. First, we show the behaviour of a single particle in Fig. 3. A particle is accelerated by an ICRF wave and trapped in the toroidal ripple field. Then it is expelled from the plasma and the SOL region by ∇B drift motion. Most of these lost particles hit spatially localized positions on the first wall under the ICRF antenna. These helium particles can easily be guided into the pump duct. Henceforth, we shall call these particles 'ducted particles'. However, we can also find two other types of lost particle. One type hits the

wall well away from the duct, because of detrapping from the ripple well. The other type has slowed down in the SOL, because these helium ions remain in the SOL for about several milliseconds longer than the Coulomb collision time. We show two simulation results under different SOL conditions, since the efficiency of helium ash exhaust is affected by the slowing down processes in the SOL.

We examine weak slowing down, where Δ_n = 2 cm and Δ_T = 4 cm. Figure 4 shows a simulation result obtained by using a group of He^+ ions born on each of the magnetic surfaces, labelled by a normalized magnetic flux, ψ_n. This result corresponds to the numerical procedure (3) explained in the previous section. The density of He^+ is normalized to 10^{18} m^{-3} on each magnetic surface. The lifetime of He^+ can be estimated from the ionization time, ~2.5×10^{-6} s. The He^+ yield, Y_{He^+}, is inversely proportional to the ionization time, i.e. $Y_{He^+} \approx 4 \times 10^{23}$ $m^{-3} \cdot s^{-1}$. The number of particles in resonance with the ICRF wave per second, $\dot{n}_{res}$, is plotted in Fig. 4(a), where ψ_n = 0 and ψ_n = 1 refer to the magnetic axis and the separatrix, respectively. As to the numerical conditions, 1000 test particles are used as ICRF resonant particles. The absorbed ICRF power density, p_{IC}, and the lost power density are shown in Fig. 4(b). The lost power density consists of p_{duct} and p_{wall}, which denote the densities of the power loaded on the duct and on the wall, respectively. Figure 4(c) shows the loss rate of the particle density, $\dot{n}_{loss}$ which is divided into three parts, namely, $\dot{n}_{duct}$, $\dot{n}_{wall}$ and $\dot{n}_{SOL}$. The part of $\dot{n}_{SOL}$, is due to the particles slowed down in the SOL.

According to the numerical procedure (4) set forth in Section 2, we obtain the total absorbed ICRF power, P_{IC}, and the total particle loss rate, $\dot{N}_{loss}$. Figure 5(a) shows the absorbed ICRF power dependence of the particle loss rate, which is divided into $\dot{N}_{duct}$, $\dot{N}_{wall}$ and $\dot{N}_{SOL}$. In this calculation, Δ_{DT^0} is scanned with $n_{DT^0} = 3 \times 10^{17}$ m^{-3} and $E_{rf} = 2 \times 10^4$ $V \cdot m^{-1}$. The absorbed ICRF power is determined by the relationship of Δ_{DT^0}, n_{DT^0} and E_{rf}. We have checked some other cases and found that the ambiguity of the obtained results is about 10% unless n_{DT^0} is less than about 10^{17} m^{-3}. We show the case of strong slowing down, where Δ_n = 2 cm and Δ_T = 1 cm, in Fig. 5(b). Half of the lost particles are slowed down in the SOL. To keep the same removal rate as in the previous case, the power necessary is increased twice. A detailed analysis taking into account the plasma profiles of the SOL is left to future studies.

3.3. Estimation of ash density

We apply a zero dimensional analysis in the ICRF resonant region, which is enclosed by two magnetic surfaces, ψ_N = 0.95 and ψ_N = 1. This region will henceforth be called 'working region'. The volume of this working region, V, is 128 m^3. The equations of particle number conservation in the working region can be written as

$$\frac{dn_0}{dt} = -\nu_{I_0} n_0 - \frac{n_0}{\tau_p} + R \frac{n_0 + n_1 + n_2}{\tau_p} \tag{2}$$

$$\frac{dn_1}{dt} = \nu_{I_0} n_0 - \nu_{I_1} n_1 + \nu_{R_2} n_2 - \frac{n_1}{\tau_p} - \frac{n_1}{\tau_{ic}} \tag{3}$$

$$\frac{dn_2}{dt} = \nu_{I_1} n_1 - \nu_{R_2} n_2 - \frac{n_2}{\tau_p} + s_\alpha \tag{4}$$

where n_0, n_1, n_2 denote the densities of He^0, He^+, He^{2+} and ν_{R_n} and ν_{I_n} are the charge exchange and ionization frequencies in the nth state. The particle source, s_α, is caused by the particle flow into the working region from the core region, where the He^{2+} ions are generated by fusion reactions with a rate of $S_\alpha = 3.55 \times 10^{20}$ P_f[GW], i.e., $s_\alpha = S_\alpha/V$. The loss flux due to the ICRF wave, n_1/τ_{ic}, is evaluated by $\dot{N}_{duct}/V$. If the duct wall is formed as a honeycomb wall [3], we assume that the recycling rate for L_{duct} is negligibly small. The plasma densities, $n_1 = 2.5 \times 10^{17}$ m^{-3} and $n_2 = 4.7 \times 10^{18}$ m^{-3}, are sustained for $P_f = 1.5$ GW and $\tau_p = 0.12$ s and the recycling rate of $R = 0.9$. Figure 6 shows the absorbed power dependence of the He^+ density in the working region. In order to reduce the helium density to 50% in the peripheral region, the necessary absorbed ICRF powers are about 8 MW for $\Delta_T = 4$ cm and about 11 MW for $\Delta_T = 1$ cm.

4. IMPURITY REMOVAL

Another important issue is how to keep the impurity ions in the peripheral region away from the core plasma. Recently, neon ions have been used to enhance radiation cooling in the divertor region [4]. Injected neon ions can be quite beneficial if they are

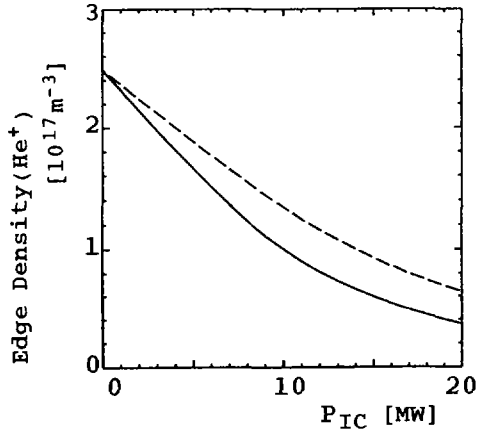

FIG. 6. Absorbed ICRF power dependence of He^+. Solid and dashed curves correspond to Figs 5(a) and (b), respectively.

confined to the divertor region only. However, many experimental observations show that impurity ions invade the core region. We examine the impurity removal for two species, i.e. argon and neon.

The charge state of fully ionized argon is +18, and its mass number is 40. In argon removal, there is no competition with D^+ and T^+, i.e. $\Omega_{Ar} \neq \Omega_{D^+}, \Omega_{T^+}$. In the corona equilibrium, the population ratio of ionization states is $Ar^{18+}:Ar^{17+}:Ar^{16+}$ = 14:16:40 for T_e = 2 keV and $Ar^{16+}:Ar^{15+}$ = 72:18 for T_e = 0.5 keV. By changing the wave frequency, argon impurities can be removed from the core plasma region independently of T_e. The loss time, τ_{ic}, is about 0.25 s for P_{IC} = 16 MW with a wave frequency of $\Omega_{Ar^{17+}}$ = 28.45 MHz.

As to neon removal, we couple the ICRF wave with Ne^{9+} since the cyclotron frequencies of Ne^{10+} and D^+ are identical. The population rate is evaluated as $Ne^{10+}:Ne^{9+}$ = 98:2 for T_e = 2 keV and 55:37 for T_e = 0.5 keV. Unless the edge electron temperature is lower than 0.5 keV, the efficiency of the Ne^{9+} removal is not good enough. If the edge temperature is lower than 0.5 keV, neon puffing for the radiative divertor can also be controlled by this method. The loss time, τ_{ic}, is evaluated to be about 0.13 s for P_{IC} = 18 MW with a wave frequency of 30.1 MHz.

5. SUMMARY

We have presented a possible method of helium ash and impurity ion removal by utilizing ripple enhanced transport driven by ICRF heating. The key issue is to couple the ICRF wave energy selectively with He^+ ions without resonance with D^+. The necessary ICRF input power is about 10 to15 MW for reducing 50% of the helium ash for a fusion power of 1.5 GW.

ACKNOWLEDGEMENTS

The authors would like to thank Drs H. Kubo and A. Sakasai for useful discussions and advice.

REFERENCES

[1] CHANG, C.S., et al., Comments Plasma Phys. Control. Fusion (in press).
[2] FUKUYAMA, A., et al., Nucl. Fusion **23** (1983) 1005.
[3] CRAMER, S.N., et al., Nucl. Fusion **15** (1975) 339.
[4] ITAMI, K., et al., Plasma Phys. Control. Fusion **37** (1995) A255.

ELECTROMAGNETIC RESONANCES IN TOROIDAL CAVITIES

D.C. GIRALDEZ, I.C. NASCIMENTO,
R.M.O. GALVÃO, J.K.C. PINTO
Laboratório de Física de Plasmas,
Instituto de Física,
Universidade de São Paulo,
São Paulo, Brazil

M. BRUSATI
European Commission,
Brussels

Abstract

ELECTROMAGNETIC RESONANCES IN TOROIDAL CAVITIES.

Electromagnetic resonances in a toroidal cavity are studied both theoretically and experimentally. In the theory the dispersion relation is obtained solving Maxwell's equations in the cavity using perturbation theory, as in the literature, but with a different expansion which keeps the singularity for unit aspect ratio. The results are obtained in zeroth order, including toroidal effects, in terms of hypergeometric functions for which the values of the eigenfrequencies can be calculated. In the experiment the eigenfrequencies are measured in a toroidal cavity with aspect ratio 1.25 ($R_0 = 0.125$ m and $r_0 = 0.100$ m). The results, although they do not consider a detailed comparison of modes, show an overall disagreement with theoretically calculated values of the paper and of the literature, varying from a few per cent to 100%.

1.Introduction

The study of electromagnetic resonances in toroidal cavities has attracted interest due to its application not only in plasma physics and controlled fusion but also in microwave theory and physics of accelerators, as has been mentioned by several authors. In plasma physics, resonant electromagnetic waves were used, as early as in 1973, by Ivanov, Kovan and Los [1] for optimization of the breakdown of the gas in a tokamak chamber. For RF heating the importance of resonant modes is mentioned in most of the papers on the problem. Since the useful frequencies depend on plasma properties their compatibility with the resonant modes of the torus requires a good knowledge of them for a correct choice. Another point is that, with the recent interest in low aspect ratio tokamaks, the study of RF resonances in toroidal cavities becomes more important because in this geometry the

eigenfrequencies are more separated. In general, RF modes in toroidal cavities have a complex structure; however, this may be advantageous for applications and therefore a detailed knowledge of them is necessary. These potentialities and the lack of experimental data on resonances in toroidal chambers motivated us to start this research on electromagnetic resonances in toroidal cavities.

It is well known that although the theoretical problem of determining the eigenmodes of a toroidal cavity can be straightforwardly formulated, its solution is rather involved and has not yet been obtained in a closed analytical form. This is essentially due to the wave equation not being separable in toroidal coordinates. Many different approximate solutions to the problem have been presented by several authors.

Brambilla and Finzi [2] in one of the first papers on the problem, using quasi-toroidal coordinates r, θ, ϕ, obtained from Maxwell equations a system of coupled differential equations for the E_ϕ and H_ϕ components of the field and solved them up to first order using as expansion parameter the inverse aspect ratio. The solutions resemble the ones of the cylinder and they classify the modes as quasi-TE (Transverse Electric) and quasi-TM (Transverse Magnetic) according to their cylindrical limit. Mishustin and Shcherbakov [3] use a method similar to the one used by Brambilla and Finzi but introduce scalar potentials for the description of the fields. The system of equations is solved using the perturbation method, developing the potentials in series, with taking the inverse aspect ratio as the expansion parameter. The results are given in second order approximation for low quasi-TM mode. Cap and Deutsch [4, 5] present two different solutions in two papers. In the first, introducing the Hertz vector to describe the electromagnetic field, they write a scalar Helmholtz equation for each component of the Hertz vector. Separating the toroidal part and using the perturbation method with expansion in the inverse aspect ratio up to terms of fourth order they obtain the solution for low poloidal and arbitrary toroidal numbers. In the second paper [5], like Mishustin and Shcherbakov [3], they introduce two potentials to describe the fields. Dispersion relations are obtained for arbitrary toroidal m values. Lileg, Schnizer and Keil [6] calculated toroidal uniform modes in empty tori with high accuracy. Taking the toroidal number equal to zero in the equations obtained in [5], the problem is simplified and, using perturbation theory, approximate solutions are obtained by expanding the solution of the equations in terms of those of the cylinder. In another paper, Keil [7] treats the case of nonuniform toroidal modes by numerical methods and obtains a full set of E and H modes with an expected accuracy of 10^{-4} up to inverse aspect ratio of the order of ~ 0.8. Han-Ming Wu et al [8] analyze the resonant modes in elliptical cross section cavities using a direct variational method; the results show frequency shifts of

11-29% for m=0 toroidal mode when the elongation changes from 1 to 2. Janaki and Dasgupta [9], instead of the usual quasi-toroidal (r, θ, ϕ) system of coordinates, used a toroidal system (s, ψ, ϕ), ψ and ϕ being angle variables, and s the aspect ratio. Although the wave equation remains not separable, this system could have some advantage because Laplace's equation, which corresponds to the static limit, is separable and has solutions in toroidal harmonics. As in [4], the Helmholtz vector equation is transformed to a scalar equation in the components of the Hertz vector. The solutions are obtained in terms of hypergeometric functions and the eigenvalues are given for any value of the toroidal and poloidal numbers.

On the experimental side, as far as we know, the only paper published is the one by Ivanov et al [1] referred to above.

This paper contains two parts. In the first, a theoretical development is presented following the main lines of the previous works already cited, especially the one by Janaki and Dasgupta [9], but using different expansions for the propagating factor with the advantage of keeping the singularities around s=1. The perturbation method is used to solve the equations. The second part is the experimental measurement of the eigenfrequencies of a low aspect ratio cavity.

2. Theoretical Development

The determination of the eigenmodes of a toroidal cavity can be quite conveniently formulated by representing the electromagnetic fields in terms of the Hertz vector $\vec{\Pi}$ [4][9]. The relation between $\vec{E}, \vec{B}$ and $\vec{\Pi}$ is:

$$\vec{E} = \vec{\nabla}(\vec{\nabla}.\vec{\Pi}) - \mu_0\varepsilon_0 \frac{\partial^2 \vec{\Pi}}{\partial t^2} \quad \text{and} \quad \vec{B} = \mu_0\varepsilon_0 \vec{\nabla} x \frac{\partial \vec{\Pi}}{\partial t} \tag{1}$$

The eigenvalues and eigenfunctions are then given by solutions of the wave equation:

$$\nabla^2 \vec{\Pi} + \mu_0\varepsilon_0\omega^2 \vec{\Pi} = 0 \tag{2}$$

subjected to the proper boundary conditions.

To solve this equation we used, as in [4][9], the toroidal coordinate system (σ, ψ, ϕ), given by the transformation laws:

$$x = \frac{a \sinh\sigma}{\cosh\sigma - \cos\psi}\cos\phi, \quad y = \frac{a \sinh\sigma}{\cosh\sigma - \cos\psi}\sin\phi, \quad z = \frac{a \sin\psi}{\cosh\sigma - \cos\psi} \tag{3}$$

where $a^2 = R_0^2 - r_0^2$, R_0 is the major radius and r_0 is the minor radius of the torus. In this system the aspect ratio $R_0/r_0 = \cosh\sigma_0 \equiv s_0$. As shown in [4] and [9], the vector wave equation (Eq.(2)) can be reduced to a scalar equation:

$$\nabla^2 \Pi_j + \kappa^2 \Pi_j = 0 \tag{4}$$

where $j = x, y, z$ and $\kappa^2 = \mu_0 \varepsilon_0 \omega^2$. Π_x, Π_y and Π_z are all functions of σ, ψ, ϕ.

The toroidal components Π_σ, Π_ψ and Π_ϕ are obtained from Cartesian components using a proper transformation given in [9].

Now, introducing the variables $P_j = \Pi_j/(s - \cos\psi)^{1/2}$ and $s = \cosh\sigma$ and decomposing P_j in Fourier components in the separable ϕ coordinate, it can be shown that the scalar wave equation reduces to:

$$\frac{\partial}{\partial s}[(s^2-1)\frac{\partial P_j}{\partial s}] + \frac{\partial^2 P_j}{\partial \psi^2} + (\frac{1}{4} - \frac{m^2}{s^2-1} + \frac{\kappa^2 a^2}{(s-\cos\psi)^2})P_j = 0 \qquad (5)$$

where m (the separation constant) is any integer, including zero.

This equation is not separable, but an approximate solution can be found expanding the propagation term and applying the perturbative method. It is important to keep the singular behavior at $s = 1$ (the lower value of the aspect ratio), and for this we use expansion [10]:

$$\frac{1}{(s-\cos\psi)^2} = \frac{2}{\sqrt{s^2-1}} \sum_{n=1}^{\infty} \frac{n}{(s+\sqrt{s^2-1})^n} \frac{\sin(n\psi)}{\sin\psi} \qquad (6)$$

We remark that the expansion used by Janaki and Dasgupta [9] keeps the singularity in $s = 0$ which has no physical meaning.

Substituting Eq.(6) into Eq.(5), considering $u = e^\sigma$, and attempting a series solution for P_j, i.e., $P_j = P_{j0} + \varepsilon^1 P_{j1} + \ldots$, where $\varepsilon \sim s^{-1}$, the zeroth order solution becomes separable, keeping the contribution of the singularity at $s = 1$ associated with the propagation factor $\kappa^2 a^2$. This equation for the zeroth order solution is:

$$\frac{u^2}{u^2-1}\frac{d}{du}[(u^2-1)\frac{dF}{du}] + [\frac{1}{4} - \ell^2 - \frac{4m^2u^2}{(u^2-1)^2}]F + \frac{4\kappa^2 a^2}{u^2-1}F = 0 \qquad (7)$$

where $P_{j0}(u, \psi) = e^{i\ell\psi} F(u)$. Eq.(7) can be put in hypergeometric form by making the transformations: $v = 1/u^2$ and $F(v) = v^{\frac{1}{4}+\frac{\ell}{2}}(1-v)^m G(v)$. After some algebraic manipulations, we get:

$$v(1-v)\frac{d^2G}{dv^2} + [\gamma - (1+\alpha+\beta)v]\frac{dG}{dv} - \alpha\beta G = 0 \qquad (8)$$

where $\alpha = \frac{\ell+1}{2} + m + \sqrt{\frac{\ell^2}{4} + \kappa^2 a^2}$, $\beta = \frac{\ell+1}{2} + m - \sqrt{\frac{\ell^2}{4} + \kappa^2 a^2}$, $\gamma = 1 + \ell$.

The solution of Eq.(7) for any Cartesian component Π_{j0} is given by:

$$\Pi_{j0} = \sqrt{s-\cos\psi}\, P_{j0}(s) e^{il\psi} e^{im\phi} \qquad (9)$$

where

$$P_{j0}(s) = [s+\sqrt{s^2-1}]^{-(\ell+1/2+2m)}[(s+\sqrt{s^2-1})^2 - 1]^m \times$$

$$\times\, {}_2F_1(\alpha, \beta, \gamma; 1/(s+\sqrt{s^2-1})^2)$$

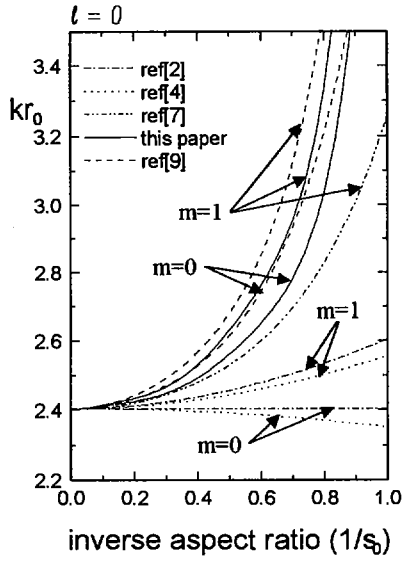

FIG. 1. Theoretical eigenvalues as a function of the inverse aspect ratio for TM modes (cylindrical limit). Poloidal mode number $\ell = 0$; toroidal mode numbers $m = 0, 1$.

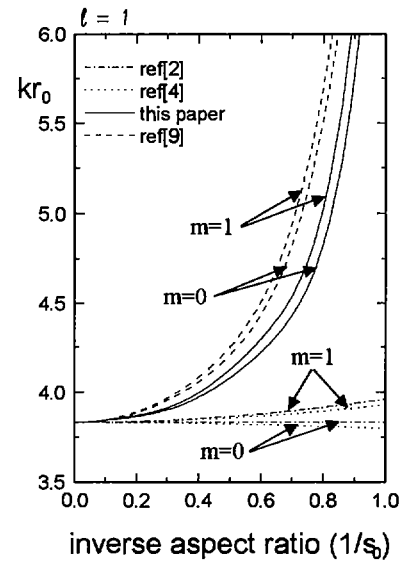

FIG. 2. Theoretical eigenvalues as a function of the inverse aspect ratio for TM modes (cylindrical limit). Poloidal mode number $\ell = 1$; toroidal mode numbers $m = 0, 1$.

In order to obtain the eigenfrequencies and a dispersion relation we have to impose the electromagnetic boundary conditions. These conditions are: $B_\sigma = E_\psi = E_\phi = 0$, where the field components are in toroidal coordinates. However, the conditions cannot be satisfied integrally, because Π_{j0} is an approximate solution of the problem. Actually, in the expression for B_σ derived from Π_{j0}, only zeroth order terms appear, whereas in the expressions for E_ψ and E_ϕ terms of first order also occur. These first order terms are incomplete, because the equation was not solved up to P_{j1}. In this way, we lose the contributions of higher order terms in 1/s (which should be small). Nevertheless, we are able to satisfy the boundary conditions in zeroth order using the expression for B_σ and obtain the dispersion relation:

$$P_{j0}(s_0) \mid \ell, m = 0 \,. \tag{10}$$

The zeros of this equation lead to the eigenfrequencies of the toroidal cavity. If a zero κa occurs at $p_{\ell m}$, then the eigenfrequency is obtained from:

$$\kappa r_0 = \frac{p_{\ell m}}{\sqrt{s_0^2 - 1}} \tag{11}$$

Figures 1 and 2 show the behavior of the eigenvalues (κr_0) with respect to the inverse aspect ratio $1/s_0$ for different values of toroidal m and poloidal ℓ mode numbers. Our results were computed using the Mathematica program and are presented together with the results of other authors. In Section 4 our results are discussed and compared to the ones of the other approaches.

3. Experiment

The experiment has been designed to check the theoretical results. The experimental set up consists of a toroidal cavity, antenna and a microwave power generator. The cavity has been chosen in order to have frequency separation as large as possible.

From the theory we know that the degeneracy of the eigenfrequencies tends to be removed when the aspect ratio of the cavity decreases. Then, we have decided to construct a cavity with aspect ratio 1.25 which should allow a severe test of the theory, and with the advantage of being in the region of aspect ratios proposed for spherical tokamaks.

The cavity has been chosen as small as possible, considering the losses and the detection accuracy of the main parameters to be measured, i.e., resonant frequencies and Q values. The construction was made by molding the cavity in two toroidal shells. These halves were carefully adapted one against the other for good electrical contact. The measured values for the

major and minor radius are respectively $R_0 = 12.56 \times 10^{-2}$m and $r_0 = 10.00 \times 10^{-2}$m, giving the aspect ratio, $s_0 = 1.256$. Holes of 4 mm in diameter were made, located on the equator and on the top of the cavity. Microwave connectors of the SMA series were used because of their small dimensions and the frequency range. The excitation and detection could be made from the top or from the equator of the chamber, $\theta = 0, \pi/2$.

An HP Network Analyzer and a dipole electric antenna have been used for the excitation of the cavity and detection of resonances.

The procedure for the excitation of the cavity was to sweep the generator up to 4 GHz. The resonances were detected as absorption spectra of the cavity, and the first peaks obtained with the value in GHz are:

0.913	0.953	1.084	1.182	1.206	1.265	1.340
1.429	1.438	1.449	1.468	1.517	1.529	1.569

For the first 4 peaks the Q values are: $\sim 5 \times 10^3$ for the first and above 10^4 for the other 3. The excitation was at the equator and at the top of the torus ($\theta = 0°$ and $\theta = \pi/2$). The first 3 peaks could be excited only at the equator and the fourth only at the top. Above the frequency of 1.6 GHz the apparatus can still separate the peaks, but their concentration per frequency interval becomes very high. In this work it has not been possible to determine the values of the mode numbers. Nevertheless, it is possible to guess that the poloidal number ℓ is ≥ 1 due to the results obtained for excitation at $\theta = 0$ and $\theta = \pi/2$. Modes with $\ell = 0$ could not be detected.

4. Discussion and Conclusions

The results of the theoretical calculation of the eigenvalues as a function of the inverse aspect ratio are presented in Figs. 1 and 2 for this work and for references [2, 4, 7, 9]. Fig. 1 shows the results for $\ell = 0$ and Fig. 2 for $\ell = 1$. We see that all the curves in the two figures in the limit of high aspect ratio converge to the values 2.40 and 3.83, which are the cylindrical eigenvalues for modes TM with $\ell = 0$ and 1. As can be seen the values of the eigenvalues increase and the splitting becomes more pronounced for decreasing aspect ratios and higher toroidal number.

The eigenvalues calculated theoretically in the present work are lower than the ones obtained in Janaki and Dasgupta's [9] paper but are higher than the values predicted using the other theoretical developments shown in Figs. 1 and 2. These data were taken from plots or dispersion relations presented in these papers.

TABLE I - RESONANT FREQUENCIES - THEORY AND EXPERIMENT
(R_0 = 0.125m; r_0 = 0.100m)

Experiment	Theory			
GHz	Brambilla and Finzi [2]	Cap and Deutsch [4]	Keil [7] a=antisymmetric s=symmetric	This work
0.913	0.879 TE_{110}	1.132 TM_{101}	0.940 TE^{s}_{111}	1.450 TM_{100}
0.953	0.958 TE_{111}		0.953 TE^{a}_{111}	1.592 TM_{101}
1.084	1.148 TM_{100}		1.347 TM^{s}_{101}	1.956 TM_{102}
1.182	1.165 TE_{112}		1.518 TE^{s}_{121}	2.307 TM_{111}
1.206			1.528 TE^{a}_{121}	2.402 TM_{111}
1.265			1.977 TM^{s}_{111}	2.445 TM_{103}

The experimental values of the eigenfrequency are shown in Table I together with the theoretical predictions. We can see that, except for the antisymmetric mode TE^{a}_{111} predicted by Keil [7] and by Brambilla and Finzi [2], all the others are not in agreement with the experimental values, with discrepancies varying from 3% to 100%. Considering only the values of the first four eigenfrequencies from the experiment and comparing with the theoretical values, we see that the better agreement is with the ones from Brambilla and Finzi [2] and, taking the first two, there is also agreement with Keil [7]. However, a better comparison cannot be made because we do not have yet sufficient experimental data for determining the ℓ, m numbers of the mode and their cylindrical limit characteristic viz., TE or TM.

In conclusion, we can say that the calculation of eigenmodes in toroidal cavities needs to be improved and, on the other hand, more experimental data is also needed.

Acknowledgments

We express our special thanks to Dr. A. Ferreira for his contribution and discussions.

This work was partially supported by FINEP - Financiadora de Estudos e Projetos and CNPq - Conselho Nacional de Desenvolvimento Científico e Tecnológico.

REFERENCES

[1] IVANOV, I.A., KOVAN, I.A., LOS, E.V., Sov. Phys. — Tech. Phys. **18** (1975) 326–327.
[2] BRAMBILLA, M., FINZI, U., IEEE Trans. Plasma Sci. **PS2** (1974) 112–114.
[3] MISHUSTIN, B.A., SHCHERBAKOV, V.I., Sov. Phys. — Tech. Phys. **22** (1977) 298–300.
[4] CAP, F., DEUTSCH, R., IEEE Trans. Microwave Theory Tech. **MIT26** (1978) 478–486.
[5] CAP, F., DEUTSCH, R., IEEE Trans. Microwave Theory Tech. **MIT28** (1980) 700–703.
[6] LILEG, J., SCHNIZER, B., KEIL, R., AEU **37** (1983) 359–365.
[7] KEIL, R., AEU **38** (1984) 30–36.
[8] WU, Hanming, CARRERA, R., DONG, J., OAKES, E., IEEE Trans. Plasma Sci. **20** (1992) 19–23.
[9] JANAKI, M.S., DASGUPTA, B., IEEE Trans. Plasma Sci. **18** (1990) 78–85.
[10] FERREIRA, A., Instituto de Física, Universidade de São Paulo, personal communication.

STABILITY OF KINETIC BALLOONING AND DRIFT TYPE MODES IN TOKAMAKS WITH NEGATIVE SHEAR

A. HIROSE, M. ELIA
Plasma Physics Laboratory,
University of Saskatchewan,
Saskatoon, Saskatchewan,
Canada

M. YAMAGIWA
Naka Fusion Research Establishment,
Japan Atomic Energy Research Institute,
Naka-machi, Naka-gun, Ibaraki-ken,
Japan

Abstract

STABILITY OF KINETIC BALLOONING AND DRIFT TYPE MODES IN TOKAMAKS WITH NEGATIVE SHEAR.

Stability analysis carried out for a tokamak discharge with negative shear indicates that a kinetic ballooning mode driven by ion magnetic drift resonance persists in a shear window, $-0.4 \lesssim s \lesssim -0.1$, provided α (ballooning parameter) $\gtrsim 0.1$. In negative shear, the toroidal ion temperature gradient mode is stabilized by finite β and nonequilibrium ion temperature, $T_i \gtrsim 2.5\ T_e$. The trapped electron drift mode appears to be most persistent, particularly in the long wavelength regime where coupling to the ion acoustic transit mode is predominant without suffering ion Landau damping. Stabilization of the mode requires a strong negative shear, $s < -0.6$.

1. Introduction

Recent experimental observations clearly suggest that negative magnetic shear in tokamaks is beneficial to achieving higher plasma β [1]. While shear reversal in these experiments has been induced by various means, a higher plasma energy content (often accompanied by a peaked pressure profile) in the central region is a common feature indicative of improved plasma confinement and reduced transport due to shear reversal.

The absence of the ideal MHD (magnetohydrodynamic) ballooning mode in negative shear regime is well known [2] and it is a signature of greater macroscopic stability associated with negative shear. However, the kinetic ballooning mode identified in the MHD second stability regime with positive shear [3] may still persist when shear is negative, for the mode is driven largely by the ion magnetic drift resonance which remains active regardless of the sign of shear. A finite ion temperature gradient, albeit modest, is required for the mode and the

growth rate is not necessarily small compared with the MHD counterpart. For negative shear, a similar kinetic ballooning instability persists even though the growth rate is small (of the order of the diamagnetic frequency). As for positive shear, a finite ion temperature gradient is essential to the instability, $\eta_i \gtrsim 0.5$. The mode is unstable in the region $-0.4 \lesssim s \lesssim -0.1$ and the critical ballooning parameter is rather small, $\alpha \gtrsim 0.1$ (when $s = -0.2$).

In general, short wavelength electrostatic drift type modes are further destabilized when the magnitude of shear is reduced. An exception is the long wavelength ion acoustic drift mode recently put forward [4] which exhibits significant reduction in the growth rate at small $|s|$. When electromagnetic (finite β) effects are included, the growth rates of short wavelength drift type modes (η_i and trapped electron drift modes) are also reduced at small $|s|$ through enhanced coupling to magnetic perturbation. Stabilizing influence of nonequilibrium temperatures ($T_i > T_e$) on the η_i mode known in electrostatic limit [5] also persists when finite β correction is made.

Both kinetic ballooning and short wavelength drift type modes corrected for finite β can be described by a common mode equation provided the ion transit frequency remains small. Effects of the ion transit frequency can then be implemented perturbatively in stability analysis. In analyzing stability of the long wavelength ion acoustic drift mode, electrostatic approximation will be used, for destabilization by finite β is a relatively weak effect.

2. Kinetic Ballooning Mode

It has recently been shown that the MHD second stability regime in positive shear region ($s > 0$) is subject to a higher order kinetic ballooning mode provided the ion temperature gradient exceeds a critical value, $\eta_i \gtrsim 0.6$ [3]. The instability is driven by the ion magnetic drift resonance which is further enhanced by the ion temperature gradient. Eigenfunctions are highly extended in the ballooning space and the ion finite Larmor radius (FLR) parameter $(k_\perp \rho)^2$ tends to exceed unity. However, two-fluid and gyro-fluid approximations are able to reveal the mode qualitatively [6]. Since the ion magnetic drift resonance continues to be active in negative shear region, it is expected that the kinetic ballooning mode persists in tokamaks with reversed magnetic shear.

The present stability analysis is based on the following ballooning mode equation derived from the charge neutrality condition and parallel Ampere's law for circular magnetic surfaces with the Shafranov shift:

$$\frac{d}{d\theta}\left\{[1+(s\theta-\alpha\sin\theta)^2]\frac{d\phi}{d\theta}\right\}+V(\theta)\phi=0 \tag{1}$$

where

$$V(\theta)=\frac{q^2\beta_e}{2\varepsilon_n^2}\left\{(\hat{\omega}-F)(\hat{\omega}-1)+\eta_e F-\tau\delta^2 M_{i2}-\frac{(\hat{\omega}-1-\tau\delta M_{i1})^2}{1+\tau(1-M_{i0})}\right\}$$

$\widehat{\omega} = \omega/\omega_{*e}, \tau = T_e/T_i, \varepsilon_n = L_n/R, \delta = \langle k_\parallel \rangle_\theta v_{Ti}/\omega_{*e}, F = \omega_{De}/\omega_{*e} = 2\varepsilon_n[\cos\theta + (s\theta - \alpha\sin\theta)\sin\theta]$,

$$M_{in} = \left\langle \left(\frac{v_\parallel}{v_{Ti}}\right)^n \frac{\omega + \widehat{\omega}_{*i}(v^2, \eta_i)}{\omega + \widehat{\omega}_{Di}(\mathbf{v}, \theta) - \langle k_\parallel \rangle_\theta v_\parallel} J_0^2\left(\frac{k_\perp v_\perp}{\Omega_i}\right) \right\rangle_{\mathbf{v}}$$

$\widehat{\omega}_{*i,e}(v^2, \eta_i)$ and $\widehat{\omega}_{Di,e}(\mathbf{v}, \theta)$ are the energy and velocity dependent ion diamagnetic and magnetic drift frequencies, and $\langle \cdots \rangle_{\mathbf{v}}$ indicates velocity averaging with Maxwellian weighting for the ions. The quantity δ perturbatively implements effects of the finite ion transit frequency with $\langle k_\parallel \rangle_\theta$ the effective norm of the parallel gradient of the scalar potential $\phi(\theta)$. For the ballooning mode with $|\omega| \simeq \omega_A = V_A/qR$ (the Alfven frequency), δ may be ignored. Effects of weakly stabilizing trapped electrons are also ignored in this study.

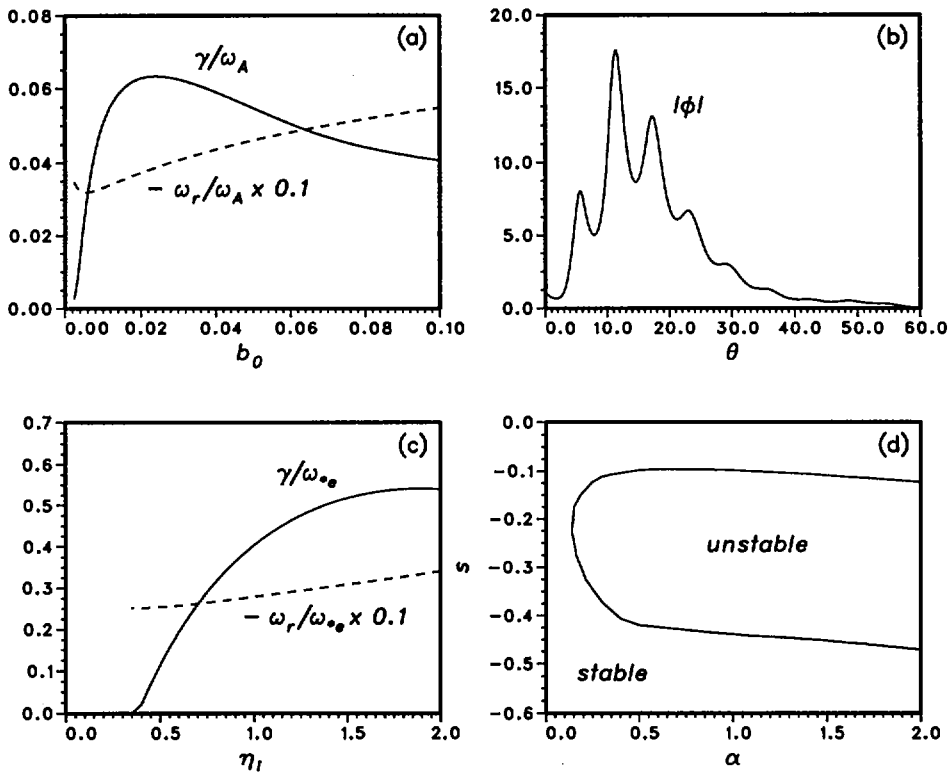

FIG. 1. (a) γ/ω_A (solid) and $-\omega_r/\omega_A$ (dashed) versus b_0 when $s = -0.2$, $\alpha = 1.2$, $\epsilon_n = 0.2$, $\eta_i = 2$; (b) eigenfunction $|\phi(\theta)|$ when $b_0 = 0.01$, $\alpha = 1$, $\eta_i = 1$. (c) γ/ω_{*e} and $-\omega_r/\omega_{*e}$ versus η_i. $b_0 = 0.01$, $\eta_e = 1$, $\alpha = 1.2$, $\epsilon_n = 0.1$; (d) stable-unstable boundary in (s, α) plane when $\epsilon_n = 0.1$, $\eta_i = 1$ and $b_0 = 0.01$. $\tau = 1$ is assumed in all cases.

Results of shooting code analysis for the mode equation in negative shear regime are summarized in Fig. 1. Fig 1 (a) shows the dispersion relation (ω vs. $b_0 = (k_\theta \rho)^2$) when $s = -0.2, \alpha = 1.2$. The growth rate peaks at relatively long wavelength $b_0 \simeq 0.02$ and the maximum growth rate is approximately ω_*. The mode frequency varies between $-0.3\omega_A$ and $-0.6\omega_A$, or hovers at around $\omega_r \simeq -V_A/2qR$. The magnitude of the eigenfunction $|\phi(\theta)|$ is depicted in Fig. 1 (b). As in the case of kinetic ballooning mode in the MHD second stability regime ($s > 0$), the eigenfunction extends to large value of θ. The ion FLR parameter $(k_\perp \rho)^2 = (k_\theta \rho)^2[1 + (s\theta - \alpha \sin\theta)^2]$ exceeds unity because of the extended eigenfunction which necessitates employing kinetic analysis for satisfactory assessment of the eigenvalue although both two-fluid and gyro-fluid approximations are able to reveal the instability qualitatively [6]. Fig. 1 (c) demonstrates the existence of a threshold in the ion temperature gradient for the kinetic ballooning mode. The critical η_i is modest, $\eta_i \gtrsim 0.5$, which is satisfied in most tokamaks. Finally, instability boundary in the (s, α) plane is shown in Fig. 1 (d) for the case $\eta_i = \eta_e = 1, \varepsilon_n = 0.1, b_0 = 0.01$. The critical α for $s = -0.2$ is 0.1. For $\alpha > 0.3$, the unstable window in s resides in the region $-0.4 < s < -0.1$. Stabilization at sufficiently negative shear is due to effective deactivation of the ballooning drive $\omega_* \langle \omega_D \rangle$ where $\langle \omega_D \rangle = 2\varepsilon_n \omega_* \langle \cos\theta + (s\theta - \alpha \sin\theta) \sin\theta \rangle_\theta$ is the norm of the magnetic drift frequency. Stabilization at small shear $|s| \lesssim 0.1$ is caused by the Shafranov shift.

3. Toroidal Ion Temperature Gradient Mode with Finite β Correction

Extensive studies have been made in the past of the toroidal ion temperature gradient (η_i) mode because of its plausible relevance to the anomalous transport in tokamaks [7]. Its persistence in negative shear regime has been predicted in electrostatic approximation [8]. Stabilizing influence of finite β and nonequilibrium ion temperature ($T_i > T_e$) on the instability has been put forward in

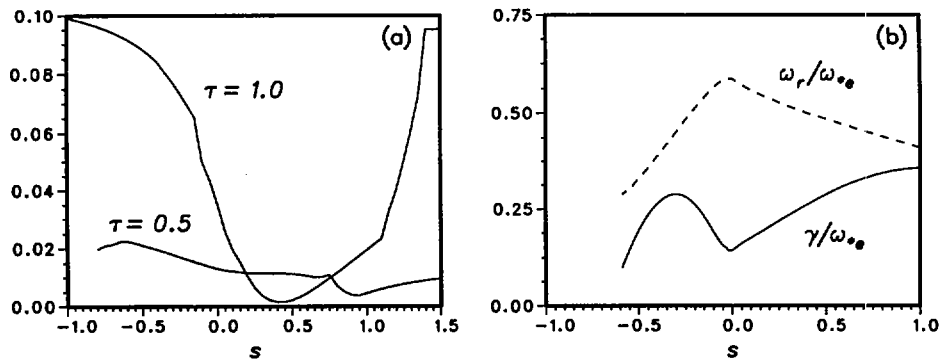

FIG. 2. (a) γ/ω_A of the electromagnetic η_i mode versus s for $\tau = 1$ and 0.5. $\alpha = 0.4$, $\epsilon_n = 0.2$, $\eta_i = \eta_e = 2$, $b_0 = 0.2$. (b) ω_r/ω_{*e} (dashed) and γ/ω_{*e} (solid) of the electrostatic drift mode versus s when $b_0 = 0.03$, $\epsilon_n = \epsilon = 0.1$, $\eta_e = 1$, $\tau = 1$.

several investigations [9, 5]. Stabilization due to finite β becomes effective only at ballooning parameters α comparable with the threshold of the MHD ballooning mode.

The mode equation (1) is equally applicable to the η_i mode corrected for finite β. When β (or α) is small, shear is stabilizing and, in general, the growth rate decreases with $|s|$. As β increases, a threshold in s (> 0) appears and shear dependence of the growth rate becomes strongly asymmetric with respect to the shear. This is shown in Fig. 2 (a) for the cases $\tau = T_e/T_i = 1$ and 0.5. Strong stabilizing influence of nonequilibrium ion temperature ($T_i > T_e$) is also seen and complete stabilization is observed for $\tau \lesssim 0.43$ for the parameters chosen. In some tokamaks, τ as small as 0.3 has been observed in reversed shear operation and the results of the present investigation tend to suggest that the η_i mode should be much less active (if not stabilized) in the region of reversed shear.

4. Electrostatic Drift Mode

In toroidal geometry, the ion resonance is suppressed for modes propagating in the electron diamagnetic direction since the ion velocity space that can satisfy the resonance condition

$$\omega + \frac{Mck_\theta}{eBR}\left(\frac{1}{2}v_\perp^2 + v_\parallel^2\right)\left[\cos\theta + (s\theta - \alpha\sin\theta)\sin\theta\right] - k_\parallel v_\parallel = 0$$

is severely restricted when $\omega > 0$. Consequently, the unstable wavenumber spectrum is extended to small FLR parameter where the diamagnetic drift frequency becomes comparable with the ion transit frequency, $b_0 = (k_\theta\rho)^2 \gtrsim 1/128q^2 = \mathcal{O}(10^{-2})$. Coupling to the ion acoustic transit mode is predominant in such long wavelength regime and unstable mode frequency may exceed the electron diamagnetic frequency, $\omega > \omega_{*e}$. Finite β correction to the ion acoustic drift mode is further *destabilizing* albeit weakly [5]. However, the ion temperature gradient, if varied independently of the electron temperature gradient, is stabilizing.

Within electrostatic fluid approximation, the ion density perturbation valid for arbitrary magnitude of the ion transit frequency is

$$\left(\omega + \omega_{Di} - k_\parallel \frac{T_i/M}{\omega + \omega_{Di}} k_\parallel\right)\frac{n_i}{n_0} = \left(\omega_{*e} - \omega_{De} - (\omega + \omega_{*i})(k_\perp\rho_s)^2 + k_\parallel \frac{T_e/M}{\omega + \omega_{Di}} k_\parallel\right)\frac{e\phi}{T_e}$$

Destabilization is provided by resonant trapped electrons and the electron density perturbation is

$$n_e = \left(1 - \left\langle \frac{\omega - \widehat{\omega}_{*e}(v^2, \eta_e)}{\omega - \widehat{\omega}_{De}(\mathbf{v}, \theta)} \right\rangle_{\epsilon v_\perp^2 > v_\parallel^2}\right)\frac{e\phi}{T_e} n_0 = (1 - M_{et})\frac{e\phi}{T_e} n_0$$

Imposing charge neutrality leads to the following mode equation:

$$\left(\frac{c_s}{qR}\right)^2 \frac{d}{d\theta}\left(\frac{1}{\omega+\omega_{Di}}\frac{d\phi}{d\theta}\right) + (\omega+\omega_{Di})V(\theta)\phi = 0 \tag{2}$$

where $V(\theta)$ here is

$$V(\theta) = \frac{1}{1-M_{et}+\tau}\left(1 - M_{et} - \frac{\omega_{*e}-\omega_{De}-(\omega+\omega_{*i})b(\theta)}{\omega+\omega_{Di}}\right)$$

with $b(\theta) = (k_\theta \rho_s)^2(1+s^2\theta^2)$ and $\omega_{De,i}(\theta) = 2\varepsilon_n \omega_{*e.i}(\cos\theta + s\theta\sin\theta)$.

Shear dependence of the eigenvalue ω/ω_{*e} is shown in Fig. 2 (b) for a long wavelength mode with $b_0 = 0.01$. The growth rate has a local minimum at zero shear. This is due to the coupling to the ion acoustic transit mode $\omega = k_\parallel c_s$ which increases with shear $|s|$. Complete stabilization of the instability requires a relatively strong negative shear, $s < -0.6$.

5. Conclusions

It has been shown that an ion temperature gradient driven kinetic ballooning mode, similar to the one identified in the MHD second stability regime, persists in negative shear. The threshold of the plasma pressure gradient for the instability is small ($\alpha \gtrsim 0.1$ when $s = -0.2$) and the required ion temperature gradient is also modest, $\eta_i \gtrsim 0.5$. The growth rate of the toroidal η_i mode with finite β correction exhibits sensitive dependence on the shear parameter s and temperature ratio T_i/T_e. As in positive shear, both finite β and nonisothermal temperatures ($T_i > T_e$) have stabilizing effects on the η_i mode. The long wavelength ion acoustic drift mode appears to be most persistent in negative shear and stabilization of the mode requires relatively strong negative shear, $s \lesssim -0.6$.

Acknowledgments

This research has been sponsored in part by the Natural Sciences and Engineering Research Council and National Fusion Program of Canada.

References

[1] LAZARUS, E. A. *et al.*, Phys. Fluids B **4** (1992) 3644; LEVINGTON, F. M. *et al.*, Phys. Rev. Lett. **75** (1955) 4417; STRAIT, E. J. *et al.*, ibid. 4421; KIMURA, H. and JT-60 Team, Phys. Plasmas **3** (1996) 1943.

[2] GUO, S. C., Acta Phys. Sin. **31** (1982) 17.

[3] SYKES, A., TURNER, M. F., in *Proc. 9th Europ. Conf. on Controlled Fusion and Plasma Physics*, (EPS, Petit-Lancy, Switzerland, 1979), vol. 1, p. 161; CHANCE, M. S., GREENE, J. M., Nucl. Fusion **21** (1981) 453.

[4] HIROSE, A., ZHANG, L., ELIA, M., Phys. Rev Lett. **72** (1994) 3993.

[5] HIROSE, A. *et al.*, Phys. Scripta **52** (1995) 421.

[6] NORDMAN, H. *et al.*, Phys. Plasmas **2** (1995) 3440.

[7] KIM, J. Y., HORTON, W., DONG, J. Q., Phys. Fluids B **5** (1993) 4030 and references therein.
[8] KIM, J. Y., WAKATANI, M., Phys. Plasmas **2** (1995) 1012.
[9] HONG, B. G., HORTON, W., CHOI, D. I., Plasma Phys. Controlled Fusion **31** (1989) 1291; WEILAND, J., HIROSE, A., Nucl. Fusion **32** (1992) 151; HIROSE, A., ELIA, M., Comm. Plasma Phys. Controlled Fusion **17** (1996) 69.

STATUS OF THE RFX EXPERIMENT

V. ANTONI, L. APOLLONI, M. BAGATIN, W. BAKER, R. BARTIROMO, M. BASSAN, F. BELLINA, P. BETTINI, R. BILATO, T. BOLZONELLA, A. BUFFA, P. CAMPOSTRINI, S. CAPPELLO, L. CARRARO, E. CASAROTTO, R. CAVAZZANA, F. CHINO, G. CHITARIN, S. COSTA, A. DE LORENZI, D. DESIDERI, P. FIORENTIN, E. GAIO, L. GARZOTTI, L. GIUDICOTTI, F. GNESOTTO, M. GUARNIERI, S. GUO, O. HEMMING, P. INNOCENTE , A. LUCHETTA, G. MALESANI, G. MANDUCHI, G. MARCHIORI, L. MARRELLI, P. MARTIN, E. MARTINES, S. MARTINI, A. MASCHIO, A. MASIELLO, M. MORESCO, A. MURARI, P. O'LEARY, R. PACCAGNELLA, R. PASQUALOTTO, S. PERUZZO, R. PIOVAN, N. POMARO, R. PUGNO, M.E. PUIATTI, G. ROSTAGNI, A. SARDELLA, F. SATTIN, P. SCARIN, G. SERIANNI, P. SONATO, E. SPADA, A. STELLA, C. TALIERCIO, V. TOIGO, L. TRAMONTIN, F. TREVISAN, M. VALISA, S. VITTURI, Y. YAGI[1], P. ZACCARIA, E. ZILLI, G. ZOLLINO

Group for Fusion Research,
Euratom–ENEA–CNR–Università di Padova Association,
Padua, Italy

Abstract

STATUS OF THE RFX EXPERIMENT.

The first results obtained in the RFX reversed field pinch experiment after the 1995 machine modifications are reported. The confinement, for fully stationary discharges at 0.6 MA, has now reached the expected values, even in the presence of MHD wall locked modes. Studies on locked mode effects have evidenced currents flowing from the plasma into the vessel in the region of locking. Measurements on plasma rotation and radial electric field have shown a perpendicular velocity shear at the edge similar to what is found in tokamaks and stellarators. New measurements on edge superthermal electrons and some evidence of their correlation with plasma core characteristics are included.

1. INTRODUCTION

The RFX reversed field pinch (major and minor radii 2.0 and 0.46 m, respectively; maximum design current 2 MA) [1] began experiments in 1992 [2]. With one short break, it operated successfully up to 1995, establishing a detailed database

[1] Electrotechnical Laboratory, Tsukuba, Japan.

at a plasma current of about 500 kA, with different set-up modes and a certain range of densities [3]. The plasma parameters were broadly in agreement with the expectations, and the maximum obtained value of the energy confinement time, $\tau_E \sim 1.5$ ms, agreed with RFP scaling [4]. Some studies at were carried out 0.8 MA. The loop voltage contained an anomalous (non-Spitzer) component [5] attributed in part to field errors, as is often the case; locked modes were always observed and proved difficult to control [6].

In 1995, RFX was shut down for machine improvements, including field error reduction by closing the outer equatorial gap and partially closing one poloidal gap, installation of an eight pellet injector, and a new boronization system with diborane, in order to fit new diagnostics.

This paper describes the obtained plasma improvements, including increased τ_E and β, a 10% reduction in the loop voltage accompanied by much better pulse reproducibility and insensitivity to small residual field errors. We also present new results on locked modes, plasma–vessel currents, particle confinement using pellet injection, plasma rotation (globally from spectroscopy and close to the edge by Langmuir probes) and new edge measurements of superthermal electrons.

2. EFFECT OF MACHINE MODIFICATIONS ON PLASMA PERFORMANCE

As a consequence of the equatorial gap short-circuit, the fluctuating radial field at the gap has been reduced by a factor of two to three; during flat-top it remains below 1% of the main poloidal field $B_\theta(a)$. The closure of one poloidal gap, together with an improvement of the equilibrium feedback control system, reduced the maximum radial field through the vertical gaps to less than 4% of the main poloidal field and to

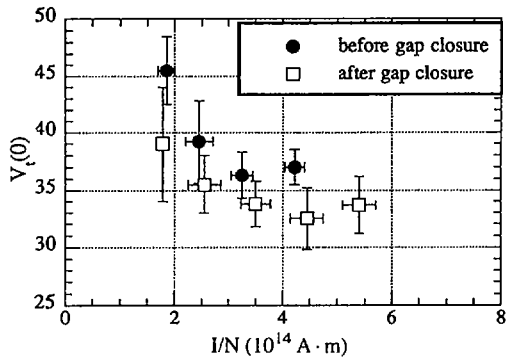

FIG. 1. Loop voltage during the current flat-top versus I/N, the ratio between the toroidal plasma current, I, and the average line density, N.

~1% in the optimized pulses [7]. The effect of shell gap closure resulted, at 0.6 MA, in better pulse reproducibility, with reduced scatter of data and a more reliable density behaviour under the same experimental conditions. A global decrease of ~10% (Fig. 1) in loop voltage and a corresponding increase in the energy confinement time were obtained. β_θ remained essentially unchanged. The voltage reduction corresponds to a decrease in the anomalous voltage from ~15 to ~12 V [8].

Gap field errors and shift are now kept within a range where their influence on the loop voltage is negligible [7]. The remaining portion of anomalous voltage can probably be attributed to the magnetic field distortion due to the MHD locked modes.

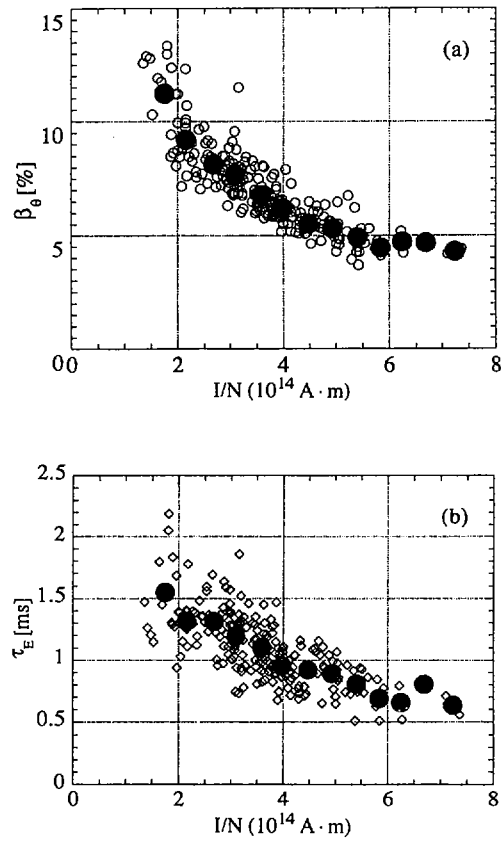

FIG. 2. (a) Poloidal β ($\beta_\theta = 2\beta_{\theta e}$) and (b) energy confinement time versus I/N. Solid circles: ensemble averages of data.

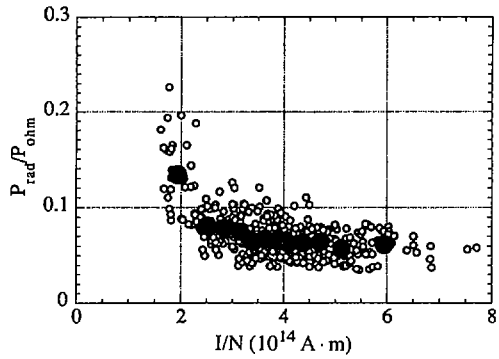

FIG. 3. Ratio of radiated power over ohmic input power versus I/N.

3. GLOBAL PERFORMANCE AT 0.6 MA

After a graphite boronization by diborane (which allowed the achievement of $Z_{eff} \sim 1.2$), an extensive exploration of the dependence of plasma performance on the density for fully sustained discharges at 0.6 MA has been carried out. As shown in Fig. 2, both β_θ and τ_E increase monotonically as the density is raised up to the maximum value compatible with sustained discharges in the present conditions of operation, obtained at $I/N > 1 \times 10^{-14}$ A·m.

The average β_θ reaches ~11% and τ_E ~1.5 ms, with maximum τ_E values exceeding 2 ms. The total radiated power, measured by absolutely calibrated bolometric tomography (Fig. 3), is normally between 5 and 10% of the input power for I/N above 3×10^{-14} A·m. At lower I/N the radiation increases, reaching 20% of the input power at the minimum I/N value ($> 1 \times 10^{-14}$ A·m), where it has been possible to sustain a stationary discharge. At I/N lower than 1×10^{-14} A·m, the loop voltage is so high that no steady state can be obtained and the plasma current decays. In any case, even in these conditions, there is no evidence of plasma disruptions. The radiation emission is always concentrated at $r/a > 0.75$.

4. LOCKED MODES AND PLASMA CURRENT FLOWING INTO THE VESSEL

Despite the improvements in the overall confinement, in RFX an anomalous loss effect remains, related to stationary magnetic disturbances still present in all pulses, because of MHD locked modes. These locked modes cause a local helical deformation of the magnetic surfaces extending for about 30–40° toroidally, driving large local dissipation of power and helicity.

Parallel power fluxes of the order of 100 MW/m^2 were measured in the 1994 campaigns [9], mostly caused by superthermal electrons flowing along the field lines, which heated the tiles up to 2000°C in the region where the graphite wall was intersected by the distorted magnetic surfaces. Tile heating led to an enhancement of the influx of carbon by a factor of ~100, of oxygen by a factor of ~40 and of hydrogen by a factor of ~30. In high current discharges (0.8–1 MA), the carbon tile temperature might reach values close to that of carbon sublimation (3350°C), resulting in frequent carbon blooming phenomena, with a consequent increase in Z_{eff} (from ~1.2–1.5 up to ~2) and in density, which caused a decrease in temperature and an increase in loop voltage [9]. Damages observed during the 1995 shutdown on the contact surface between the graphite tiles and the vacuum vessel have been ascribed to the effect of currents flowing poloidally from the plasma into the stiffening rings of the vacuum vessel. These currents have a dominant m = 1 mode; moreover, a strong toroidal asymmetry has been observed. Approximately 3 kA of current flowing through one graphite tile of the first wall and the vessel stiffening ring are necessary, on the basis of numerical and experimental evaluations, to obtain the damages observed in RFX [10]. On the assumption that the magnetic deformation has a toroidal extension of 30°, the total current flowing into the vessel for each shot was estimated to be of the order of 10% of the toroidal plasma current [9, 10].

A preliminary measurement of the poloidal voltage on the vacuum vessel has confirmed the presence of these currents in the region dominated by the helical perturbation with strong toroidal asymmetry. The measured voltage also shows a poloidal asymmetry and a resistive distribution of the current in the vessel. These currents are stationary during the shots, with the presence of a significantly high frequency oscillation. The maximum currents estimated from the voltage measurements amount to an average value between 1 and 2 kA for each vessel stiffening ring. This value is lower, by a factor of five to ten, than the value estimated on the basis of the observed damages. The difference can be ascribed to the strong toroidal asymmetry and the experimental operating conditions. Much work remains to be done to clarify these phenomena.

5. PLASMA ROTATION AND RADIAL ELECTRIC FIELD

Plasma flow and radial electric field have been measured both by spectroscopy and Langmuir probes (Fig. 4).

The poloidal and toroidal rotation velocities of the impurities have been deduced from Doppler shift measurements on the lines of C V (2271 Å, fifth order), C III (2296 Å, fifth order), B IV (2823 Å, fourth order), O V (2781 Å, fourth order), C VI (5290 Å, second order). As shown in Table I, the toroidal velocity changes sign close to the toroidal field reversal surface (r/a ~ 0.9). The plasma flow measurements by Langmuir probes (Fig. 5) at the extreme edge detect the presence of parallel (nearly poloidal) and perpendicular (nearly toroidal) drifts with a velocity of ~10^4 m/s and a

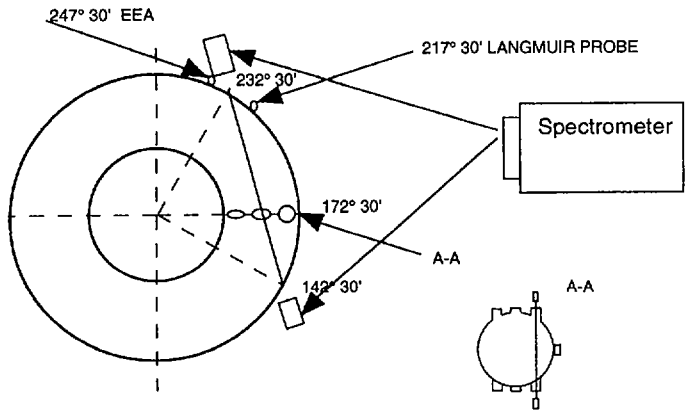

FIG. 4. Layout of spectroscopic and EEA diagnostics.

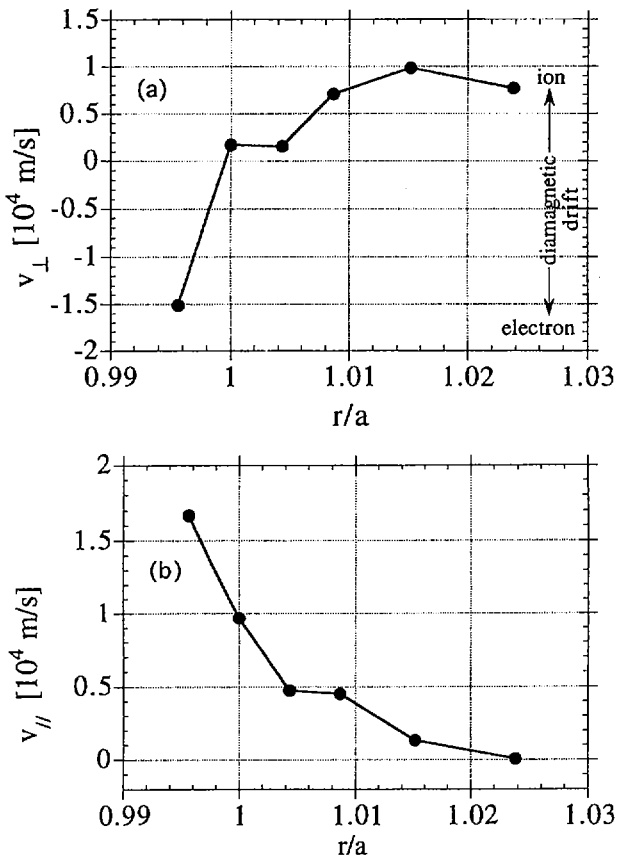

FIG. 5. Plasma flow velocity (a) perpendicular and (b) parallel to the magnetic field as functions of normalized radius.

TABLE I. TOROIDAL AND POLOIDAL ROTATION VELOCITIES OF IMPURITIES

Ion	r/a	V_{tor} (10^3 m/s)	V_{pol} (10^3 m/s)
C III	0.95	(–5)–(–10)	0–2
O V	0.9	(–2)–1	1–4
B IV	0.8	2–4	0–5
C V	0.7	5–10	0–3
C VI	0.4	2–5	—

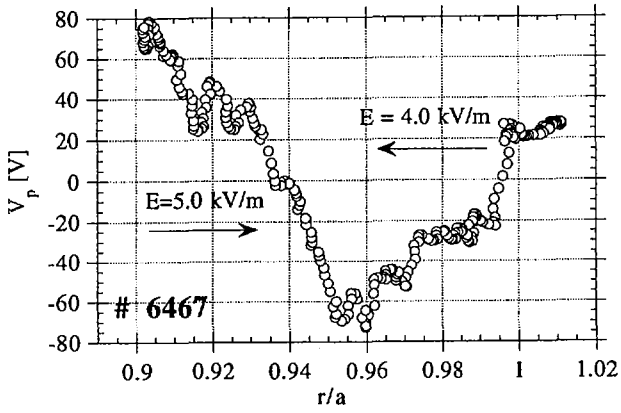

FIG. 6. Plasma potential as a function of normalized radius, showing inversion of the radial electric field.

perpendicular velocity shear, $dv/dr \sim 10^6\ s^{-1}$, comparable to what is found in tokamaks and stellarators.

The perpendicular drift velocity of the impurities has the same direction of the majority ions. The plasma potential in the edge region measured by a fast insertion Langmuir probe (Fig. 6) shows that the radial electric field is directed inwards and changes sign when going deeper into the plasma, where it is in agreement with what is established in a stochastic magnetic field in order to restrain the electron flow.

The perpendicular drift is consistent with a drift velocity of $v_E \approx E_r/B_\theta$ due to the radial electric field. The perpendicular drift is in the ion diamagnetic drift direction at the extreme edge and changes sign when going deeper into the plasma. Langmuir probe measurements indicate that this change in sign is located between the first wall and the toroidal field reversal surface.

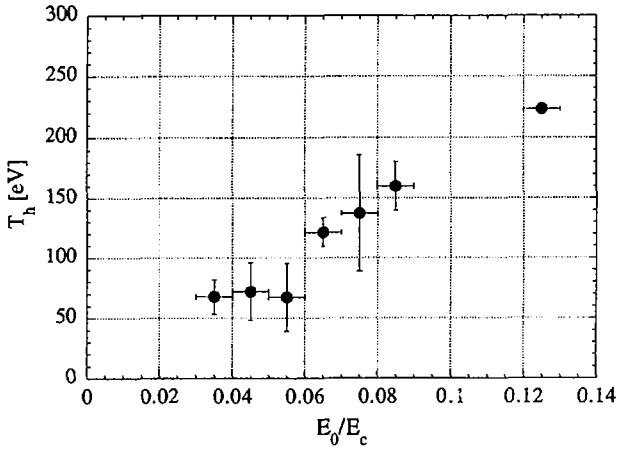

FIG. 7. Superthermal electron temperature as a function of the ratio between on-axis induced electric field and on-axis critical fields.

6. SUPERTHERMAL ELECTRONS AT THE EDGE

Superthermal electrons have been measured by an electrostatic electron energy analyser (EEA) developed at the Electrotechnical Laboratory of Tsukuba (Japan) and jointly operated in RFX [11].

An unidirectional flow of superthermal electrons along the magnetic field is observed with a backflow less than 10%. The energy distribution function is well approximated by a half-Maxwellian of temperature T_h. A relationship between T_h and the ratio between the on-axis applied electric field E_0 and the on-axis critical Dreicer field E_c is found (Fig. 7). This result suggests that superthermal electrons are produced are the centre of the plasma (as confirmed by pellet trajectories) and then are transported to the edge. Superthermal electrons are found to carry a large parallel current density at the edge, in the range of 200–600 kA/m^2.

To account for the maximum parallel energy flux at the edge (~100 MW/m^2) measured by calorimeter probes and CCD cameras, equal parallel and perpendicular temperatures must be assumed.

7. PELLET INJECTION

A first programme of pellet experiments has been performed at currents of $\approx$ 0.6 MA: one or two pellets of small (1.5×10^{20} atoms) or intermediate (3×10^{20} atoms) size have been launched during the current flat-top phase with a speed of 500–900 m/s. The small pellets fired at low velocity (500–600 m/s) are completely

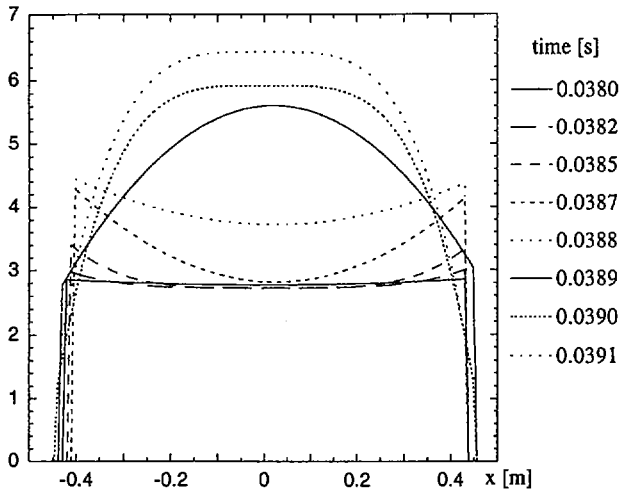

FIG. 8. Shot 6185 showing inverted n_e profiles (10^{19} m^{-3}).

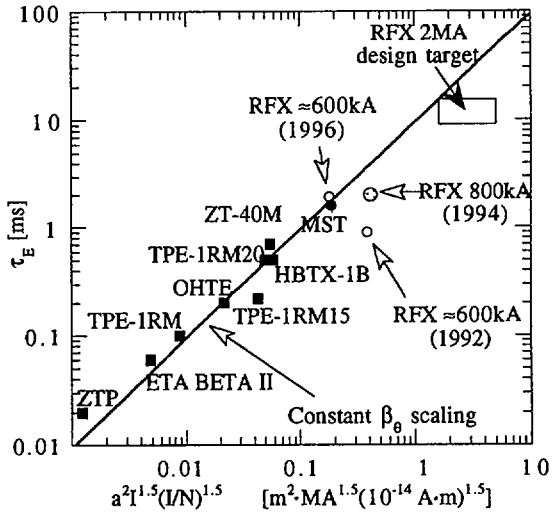

FIG. 9. Comparison of RFX data with optimum experimental confinement fit to Connor–Taylor scaling [13].

ablated in the plasma, and large global density increases (typically, $\Delta n/n \approx 1$) are obtained, causing relatively small effects on plasma current and loop voltage. Even in the most perturbing cases, when $\Delta n/n \approx 2$ and the after-pellet plasma is in a high radiation regime, no disruptive process is excited. With optimized parameters, the pellets are ablated in the plasma core, and the after-pellet density is well fitted by a parabolic profile on top of a constant pedestal (Fig. 8). A peaking factor of $n_e(0)/\langle n_e \rangle \leq 2$ is achieved, which decays in a few milliseconds.

The time behaviour of the density profiles indicates that the particle diffusion coefficient is $\approx$20–40 $m^2 \cdot s^{-1}$ in the plasma core. Pellet trajectory deflections of 10–15 cm are measured, both toroidally and poloidally, which has been simulated by an NGPS ablation code [12] considering an asymmetric ablation by superthermal electrons flowing unidirectionally along field lines not only at the plasma edge but also in the plasma core. Estimates of T_e after injection indicate a T_e drop of 70–100 eV. The toroidal loop voltage increases by 2–3 V. Assuming that the T_e profile is unchanged, the value of β_θ and τ_E should be higher by 30–50% after injection, which is consistent with the empirical RFX scaling of β_θ with I/N (Fig. 2(a)).

8. CONCLUSIONS

After the recent machine modifications, which allowed a more accurate field error correction and a better control of plasma shift and shape, and by wall conditioning and boronization, which permitted operation at low Z_{eff} (~ 1.2–1.5) and a better density control, RFX has, at 0.6 MA, achieved the expected performance (Fig. 9) in completely stationary discharges lasting up to 100 ms.

In order to achieve a similar control of the magnetic surfaces at higher currents, a more effective preionization system is required (in preparation).

The impact of locked modes on the discharge performance remains to be clarified. It has been observed that the helical deformation causes an increase in the impurity influx and the generation of currents flowing from the plasma to the first wall and the vessel. On the other hand, plasma rotation up to 10 km/s has been observed, even in the presence of locked modes.

Special attention has been paid to the study of edge physics, in order to clarify to which extent it may affect global confinement. Radial electric field and velocity shear comparable to those in tokamaks and stellarators have been identified.

Pellet experiments have permitted a first evaluation of the particle diffusion coefficient. Pellet trajectory deflection has proved the presence of superthermal electrons, also in the plasma core.

ACKNOWLEDGEMENTS

It is a pleasure to acknowledge Dr. H.A.B. Bodin's valuable suggestions. The authors wish to express their appreciation to the RFX technical staff.

REFERENCES

[1] RFX TEAM, Fus. Eng. Des. (special issue) **25** 4 (1995).
[2] RFX TEAM, in Plasma Physics and Controlled Nuclear Fusion Research 1992 (Proc. 14th Int. Conf. Würzburg, 1992), Vol. 2, IAEA, Vienna (1993) 583.
[3] ANTONI, V., et al., in Plasma Physics and Controlled Nuclear Fusion Research 1994 (Proc. 15th Int. Conf. Seville, 1994), Vol. 2, IAEA, Vienna (1994) 405.
[4] BUFFA, A., GNESOTTO, F., in Fusion Engineering (Proc. 16th IEEE Symp. Urbana-Champaign 1995), Urbana-Champaign (1995) 1395.
[5] CARRARO, L., et al, in Controlled Fusion and Plasma Physics (Proc. 22nd Eur. Conf. Bournemouth, 1995), Vol. 19C, Part III, European Physical Society, Geneva, (1995) 161.
[6] BUFFA, A., et al., in Controlled Fusion and Plasma Physics (Proc. 21st Eur. Conf. Montpellier, 1994), Vol. 18B, Part I, European Physical Society, Geneva (1994) 458.
[7] BOLZONELLA, T., et al., in Controlled Fusion and Plasma Physics (Proc. 23rd Eur. Conf. Kiev, 1996), Vol. 20C, European Physical Society, Geneva (1996) c002.
[8] BUFFA, A., RFX TEAM, ibid., c001.
[9] VALISA, M., et al., in Plasma–Surface Interactions (Proc. 12th PSI Conf. Saint-Raphaël, 1996).
[10] SONATO, P., et al., ibid.
[11] YAGI, Y., et al., in Controlled Fusion and Plasma Physics (Proc. 23rd Eur. Conf. Kiev, 1996), Vol. 20C, European Physical Society, Geneva (1996) d001.
[12] GARZOTTI, L., et al., ibid., c003.
[13] CONNOR, J.W., TAYLOR, J.B., Phys. Fluids **27** (1984) 2676.

MAGNETIC-COMPRESSION/ MAGNETIZED-TARGET FUSION (MAGO/MTF): A MARRIAGE OF INERTIAL AND MAGNETIC CONFINEMENT

I.R. LINDEMUTH, C.A. EKDAHL, R.C. KIRKPATRICK,
R.E. REINOVSKY, P.T. SHEEHEY, R.E. SIEMON, F.J. WYSOCKI
Los Alamos National Laboratory,
Los Alamos, New Mexico,
United States of America

V.K. CHERNYSHEV, V.N. MOKHOV, A.N. DEMIN, S.F. GARANIN,
V.P. KORCHAGIN, I.V. MOROZOV, V.A. YAKUBOV
All-Russian Scientific Research Institute
of Experimental Physics,
Sarov, Arzamas-16, Russian Federation

J.L. EDDLEMAN, J.H. HAMMER, D.D. RYUTOV, A. TOOR
Lawrence Livermore National Laboratory,
Livermore, California,
United States of America

D.H. McDANIEL, C. DEENEY
Sandia National Laboratories,
Albuquerque, New Mexico,
United States of America

J.H. DEGNAN, G.F. KIUTTU, R.E. PETERKIN, Jr.
Phillips Laboratory,
Albuquerque, New Mexico,
United States of America

Abstract

MAGNETIC-COMPRESSION/MAGNETIZED-TARGET FUSION (MAGO/MTF): A MARRIAGE OF INERTIAL AND MAGNETIC CONFINEMENT.

Recent advances in high-energy pulsed power capabilities, plasma formation techniques, plasma diagnostics, and multidimensional plasma computer codes make possible the evaluation of an unexplored approach to controlled thermonuclear fusion that is intermediate between magnetic confinement (MFE) and inertial confinement (ICF) in time and density scales. Existing capabilities appear adequate to explore the major physics issues in this area, perhaps up to and including fusion ignition, with relatively low operating costs and essentially no major capital investment.

I. Introduction

Intermediate between magnetic confinement (MFE) and inertial confinement (ICF) in time and density scales is an area of research now known in the US as magnetized target fusion (MTF) and in Russia as MAGO (MAGnitnoye Obzhatiye--magnetic compression). MAGO/MTF uses a closed magnetic field embedded in a preheated, wall-confined plasma fusion fuel within an implodable fusion target. The magnetic field suppresses thermal conduction losses in the fuel during the target implosion and hydrodynamic compression heating process.

In contrast to direct, hydrodynamic compression of initially ambient-temperature fuel (i.e., ICF), MAGO/MTF involves two steps: (a) formation of a warm (e.g., 100 eV or higher), magnetized (e.g., 100 kG) plasma within a fusion target prior to implosion; (b) subsequent quasi-adiabatic compression by an imploding pusher, of which a magnetically driven imploding liner is one example. A number of computational models have been used previously to explore the potential parameter space of MAGO/MTF. A simple survey model enabled an extensive exploration by permitting thousands of target computations [1]. As summarized in Fig. 1, the survey computations identified new islands in parameter space where substantial fusion energy release could be obtained.

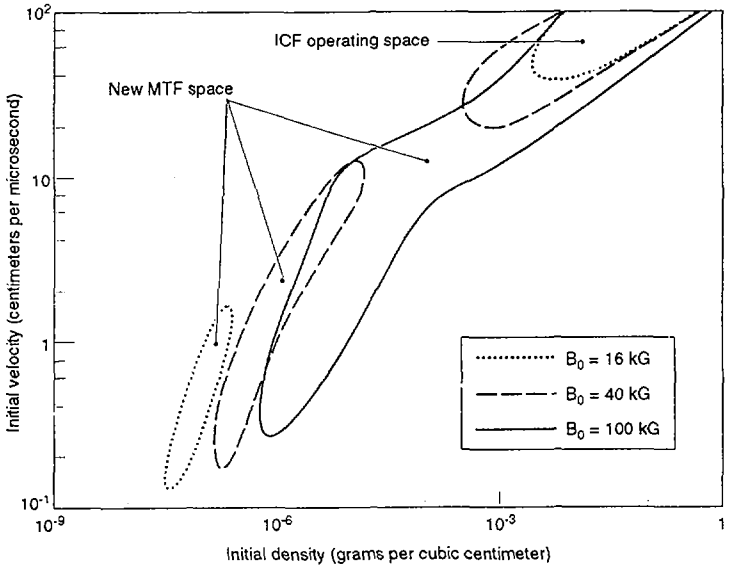

FIG. 1. Parameter space for MAGO/MTF. The actual extent of the parameter space depends on many parameters, including the pusher kinetic energy, the fuel mass, and the initial fuel temperature [1].

As shown in Fig. 1, the magneto-thermal insulation of the fuel permits lower implosion velocities and lower initial densities than are required for unmagnetized fuel. In gas target implosions, the rate, in watts, at which the implosion driver must deliver energy to the target is proportional to $\rho_0^{1/2}v_0$ and the intensity, in watts/cm^2, to which the energy must be focused is proportional to $\rho_0 v_0$, where ρ_0 is the initial density of the gas (plasma) fill and v_0 is the implosion velocity. Hence, in the new MAGO/MTF space, the lower velocity and density mean that the difficult-to-achieve power and intensity requirements can potentially be reduced by orders of magnitude.

Furthermore, because the implosion process is quasi-adiabatic, the radial convergence ratio of a MAGO/MTF target may be lower than 10:1, depending upon the temperature achieved in the formation stage. Also, because of the adiabaticity of the process, precisely timed shocks, such as required for unmagnetized fuel, are not necessary. Because the magnetic field is amplified under implosion conditions, it may become large enough to trap charged fusion products and enhance fuel self-heating. Therefore, the areal density required to achieve fusion ignition potentially is substantially reduced. Because the implosion process substantially reduces the fuel burn time, when compared to non-imploded configurations, simple plasma formation and magnetization schemes can be considered.

Many of the basic principles of MAGO/MTF have been demonstrated previously. Experiments at Columbia University demonstrated classical reduction of thermal conduction in a wall-confined, magnetized plasma [2]. Experiments at Los Alamos demonstrated good symmetry in a liner driven magnetically to a velocity of 1 cm/μs and a radial convergence of ten [3]. The 3-mm-diameter "phi" target experiments at Sandia National Laboratory produced 10^6 neutrons at an implosion velocity of 4 cm/μs and provide a "soft proof of principle" of MAGO/MTF [4]; two-dimensional magnetohydrodynamic computations predicted that essentially no neutrons would have been produced at such low implosion velocity without the preheating and magnetization of the fuel [5].

Although the possible benefit of a magnetic field in a fusion target was recognized in the 40's by Fermi at Los Alamos and at approximately the same time by Sakharov in the former Soviet Union, it is only in light of recent advancements in plasma formation techniques, implosion system drivers, plasma diagnostics, and large-scale numerical simulation capabilities that the prospects for fusion ignition using this approach can be evaluated. In this paper, we present ongoing activities and potential future activities in this relatively unexplored area of controlled thermonuclear fusion.

II. Plasma Formation Schemes

Any potential candidate for forming the pre-implosion plasma must be readily able to be integrated with a target implosion driver. Although liner compression of magnetically confined plasmas, e.g., plasma separated from the imploding pusher by a vacuum magnetic field, can be considered (see, for example, [6]), plasmas in contact with the pusher appear to be more readily attainable and more readily mated with an implosion system and appear to put less stringent requirements on the symmetry and stability of the imploding pusher. Note, however, that the local plasma β, defined as the ratio of local plasma pressure to magnetic pressure, does

not necessarily have to be greater than unity, although $\beta>1$ is advantageous from an efficiency-of-compression perspective. The actual plasma parameters, e.g., density, temperature, and magnetic field, depend in part upon the implosion parameters, such as velocity, radial convergence, and geometry (i.e., cylindrical vs. spherical), and there are tradeoffs between formation system and implosion system requirements. For example, high volumetric compression reduces the temperature required in the formation phase. Conversely, a high temperature achieved in the formation process can substantially reduce the compression needed in the second phase.

Although some theoretical [7] and computational [8] studies of the interaction of a magnetized plasma with a cold wall have been performed, the behavior of wall-confined plasmas is not well understood. Computational work by Dawson [9] suggests that the thermal conduction of energy from the plasma should be "classical," but experimental verification is needed. Impurities in the plasma can potentially lead to radiative quenching of the adiabatic heating during implosion, so the plasma formation scheme must form a plasma of sufficient purity. As suggested by Fig. 1, the densities of interest in MAGO/MTF are sufficiently high that magnetohydrodynamic models of the plasma should describe many of the basic features.

Perhaps the simplest plasma formation candidate is a cryogenic fiber z-pinch, as illustrated in Fig. 2. The cryogenic fiber z-pinch has, in the past, been of interest as a fusion energy source when early experiments appeared to show "anomalous stability" [10]. With such anomalous stability, it appeared possible to directly heat a fiber-formed z-pinch to fusion temperatures through an electrical discharge using modest energy readily available from modern pulsed power facilities. Unfortunately, subsequent second generation experiments and detailed two-dimensional computations [11] showed that m=0 instabilities prevented such a z-pinch from reaching fusion conditions directly. However, more recent computations using the same computational methodology suggest that the m=0 instabilities actually provide a mechanism for the pinch to fill an implosion vessel by forming a Kadomtsev-stable, wall-confined plasma suitable for subsequent implosion. Fiber-formed z-pinch experiments are underway on the Colt capacitor bank (100 kV, 2 MA, 200 kJ) at the Los Alamos National Laboratory (LANL) to confirm these predictions [12].

Building on ideas originally proposed by Nobel Peace Prize laureate A. D. Sakharov, the All-Russian Scientific Research Institute of Experimental Physics (VNIIEF) has made major progress in forming a plasma suitable for subsequent implosion [13]. Several variants of plasma formation chambers and pulsed power drivers have been used. Up to 4×10^{13} fusion reactions have been observed [14] as an "accidental" by-product of the formation process. The plasma formation chamber shown in Fig. 3 has been tested in three joint LANL/VNIIEF experiments. Because explosively driven electrical generators have matured more rapidly than stationary, capacitor bank technology in the former Soviet Union, the VNIIEF chamber is powered by a helical flux compression generator and explosively operated opening and closing switches, although there is no fundamental reason why the chamber could not be powered by a suitable capacitor bank (e.g., the Shiva-Star facility at Phillips Laboratory).

The current waveforms from the three joint experiments are shown in Fig. 4. Data from one experiment have been previously reported [15]. VNIIEF variable-width duct flow computations [13] and two-dimensional magnetohydrodynamic

(MHD) computations performed at LANL [15], Lawrence Livermore National Laboratory (LLNL) [16], and the Phillips Laboratory [17] are consistent with many of the experimental observations. The computations suggest that the small variation in chamber current shown in Fig. 4 can make significant changes in event timing and plasma parameters. For example, computations using the waveform of Fig. 4a predict an average late-time average temperature of approximately 260 eV, more than 60% higher than the 160 eV predicted for the waveform of Fig. 4b [18].

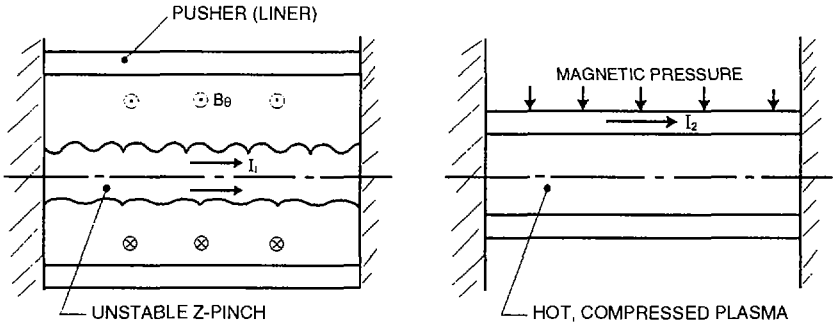

FIG. 2. Cryogenic fiber z-pinch. Left: plasma formation; right: implosion of a cylindrical liner.

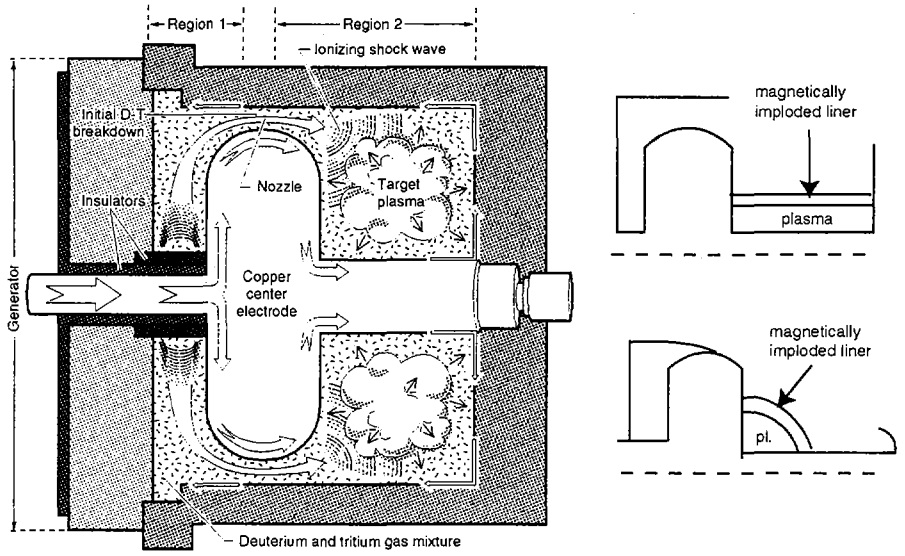

FIG. 3. Left: artist's conception of the operation of the VNIIEF plasma formation chamber. Chamber diameter is 20 cm. Right: possible implosion scenarios.

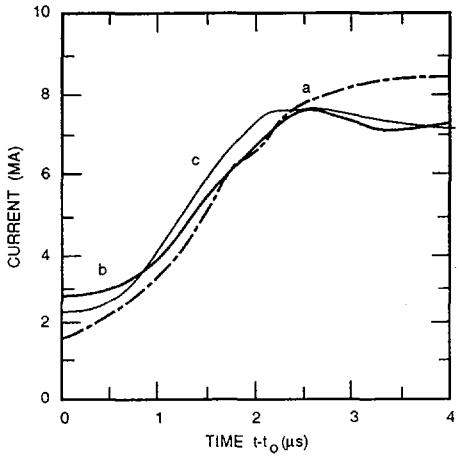

FIG. 4. Electrical current delivered to the VNIIEF plasma formation chamber in three different experiments: (a) t_0 = 351 μs; (b) t_0 = 347 μs; (c) t_0 = 349 μs.

The combination of experimental observations and detailed computations provide a reasonably complete understanding of the chamber operation. An initial slowly rising bias current magnetizes the gas volume but, because of its low voltage, does not cause an electrical breakdown of the initially neutral, room-temperature gas. The operation of the opening switch, however, generates a voltage large enough to lead to an electrical breakdown of the gas.

Breakdown occurs initially in the nozzle region (Fig. 3), and the Lorentz J x B force drives an ionizing shock wave into the right hand side of the chamber (region 2). A weaker breakdown following about 1 μs later at or near the insulator (region 1) carries a small fraction of the current, resulting in an inverse z-pinch directed radially outward. The inverse z-pinch drives plasma that was formed in the left-hand chamber through the nozzle. The plasma that exits the nozzle has high velocity and low density. When the fast moving plasma collides with the shock-wave-formed bulk plasma already in the right-hand chamber, the kinetic energy is converted to thermal energy, a small fraction (<10%) of the total plasma mass reaches a temperature of several keV, and a burst of neutrons is produced.

After a 3-4 μs dynamic phase, the computations indicate that a "warm" (100-300 eV) target plasma remains in the right hand chamber (region 2). The plasma is in contact with the chamber walls, but heat losses to the wall are substantially reduced because of the magneto-thermal insulation due to the embedded magnetic field. It is this relatively quiescent, late-time plasma that is of interest in an MTF context as a plasma suitable for subsequent compression. The computations based upon an assumption of a purely hydrogenic plasma predict that the late-time plasma indeed has the proper density, temperature, and magnetization for proceeding to the subsequent compression stage and could give a fusion yield of 1 GJ at an implosion velocity of 2 cm/μs [15]. However, some observations are not yet satisfactorily explained by the computations, and definitive measurements of plasma purity and late-time density and temperature have not yet been made.

Other plasma formation schemes, e.g., plasma guns (either gas filled or gas "puff") , field-reversed configurations (FRC), spheromaks and other compact tori, are potential candidates for the pre-implosion plasma required in MAGO/MTF. At this point in time, only the chamber of Fig. 3 has both experimental data and detailed computational modeling to suggest that the plasma formed is suitable for subsequent compression. With the exception of the fiber z-pinch discussed above, essentially all other configurations have traditionally operated at much lower densities than the optimum in Fig. 1 and research has focused on magnetically confined configurations, not wall-confined configurations as desired for MAGO/MTF. To our knowledge, no reasonably credible computations have yet been performed to suggest that these other configurations can reach suitable plasma parameters. Furthermore, the various configurations may have topological constraints that substantially reduce the available parameter space and possible gain. For example, Armstrong found that excessive length excursions and liner/plasma contact limited the fusion gain and operating space in liner compression of magnetically-confined, FRC plasmas [19].

III. Liner Implosion Drivers

Although a variety of target implosion drivers such as lasers and particle beams can be considered as candidates for powering MAGO/MTF's second stage, a major attraction of MAGO/MTF is the fact that the lower velocity required according to Fig. 1 for MAGO/MTF is readily achievable by magnetically driven liners powered by existing pulsed power facilities. Furthermore, the kinetic energy that can be imparted to an imploding liner by existing pulsed power facilities is orders of magnitude higher than possible with other existing target drivers. The energy available with existing magnetic flux compression generators appears to be more than adequate to achieve fusion ignition via MAGO/MTF.

Since magnetically driven liners can be solid, liquid, or plasma, some consideration must be given to determining the most appropriate liner state based upon stability concerns and velocity requirements.

Magnetically driven imploding liner experimental campaigns are already in progress on LANL's Pegasus capacitor bank facility (4 MJ, 12 MA) [20]. These experiments are aimed primarily at investigation of the stability properties of imploding liners. Use of imploding liners as impactors to develop strong shocks for material studies is also under investigation. A typical Pegasus aluminum cylindrical liner has a diameter of 4.8 cm, a length of 2 cm, and a thickness of 0.4 mm.

A new "slow mode" of operation for the Saturn accelerator at Sandia National Laboratories/Albuquerque (SNLA) has made solid liner implosions a possibility. In the slow mode of operation presently being implemented, the current will rise to 11 MA in 200 ns, followed by a flat top period lasting about 1 μs. One-dimensional MHD calculations of cylindrical implosions indicate that a composite aluminum-tantalum (or tungsten) liner with a total mass of 3.5 g, length of 2 cm, and an inner (outer) diameter of 0.8 cm (1.12 cm) should reach 10-fold radial compressions with the tantalum inner liner unmelted. The peak liner velocity is 1.45 cm/μs and there is no evidence of spallation during the initial pressure pulse. The inner liner kinetic energy is 60 kJ at 10-fold compression. Interestingly, one advantage of comparatively small liners such as this example is the high energy

density achieved at reasonable compression ratios. The stagnation of the liner in the one-dimensional calculations leads to pressures in excess of 100 MB. Slightly after stagnation, with the inner liner within a radius of 1/10 the initial radius, the pressure in the tantalum liner is a fairly uniform 60 MB. These conditions are more than adequate to produce substantial adiabatic heating of a magnetized plasma. Empty liner experiments and further calculations would optimize the liner design for MTF applications.

The Shiva-Star facility at the Phillips Laboratory has been used to drive solid and quasi-spherical liners. The quasi-spherical liner experiments have shown reasonable symmetry and stability at a radial convergence of 6:1 [21].

Other existing pulsed power facilities such as the PBFA-Z (14 MJ, 25 MA) facility at SNLA are, in principle, useful tools for studying the physics of liner implosions. The Atlas facility under design at Los Alamos should prove a very powerful tool for MAGO/MTF studies, as illustrated in Table I.

TABLE I. PROJECTED ATLAS PERFORMANCE FOR ALUMINUM CYLINDRICAL LINERS

Radius (cm)	10	6	3
Length (cm)	8	5.6	2.9
Thickness (mm)	1	1.5	3
Velocity (cm/μs)	1	1.6	1.8
Energy (MJ)	6.7	10.4	7.4
Current (MA)	60	45	39

The Los Alamos Procyon system couples a helical magnetic flux compression generator with an explosively operated opening switch to develop approximately 20 MJ of inductively stored energy [22]. Procyon has been used to deliver a 16 MA, 3-μs-rise pulse to a 2-cm-long, 8-cm-diameter, 1-mm-thick cylindrical aluminum liner, which reached a velocity greater than 1 cm/μs.

VNIIEF-developed magnetic flux compression generators provide a means for driving target implosions at energy levels more than an order of magnitude higher than any other existing or near-term target driver and appear to provide sufficient energy for tests of the MAGO/MTF concept at the scale required for significant fusion gain. Generators delivering over 200 MJ of electrical energy have been demonstrated [23]. A recent VNIIEF/LANL experiment used a VNIIEF 5-module, 1-m-diameter disk explosive magnetic generator (DEMG) to drive a massive, cylindrical aluminum liner that had an initial radius of 24 cm, a thickness of 4 mm, and an initial length of 10 cm. Because the z-pinch electrodes had a 6 degree slope, the length of the liner was somewhat less than 6 cm when it contacted a central measuring unit located at a radius of 5.5 cm. The DEMG delivered a current pulse in excess of 100 MA to the liner. Preliminary post-shot computations suggest that the liner had a velocity of 0.65 cm/μs and a kinetic energy greater than 20 MJ when it contacted the measuring unit. The large body of experimental data obtained will provide an important basis for projecting the utility of such ultrahigh energy liners in a MAGO/MTF context.

IV. Integrated Liner-on-Plasma Implosions

If MAGO/MTF is to achieve the goal of controlled fusion ignition, a suitable plasma formation system must be mated with an implosion driver. All of the pulsed power facilities discussed in the previous sections can be considered drivers for integrated experiments, although some modification may be necessary to incorporate the chosen plasma formation scheme. The survey model [1] suggests that the pulsed power driver must provide 5-20 MJ for each mg of plasma fuel. Hence, for a given facility, the energy available limits the mass of the plasma, and correspondingly, the size of the target. During the compression stage, the liner must retain adequate symmetry and stability.

Effects such as the liner material strength and Ohmic heating of the liner must be taken into consideration. Contaminants introduced into the fuel during the liner acceleration and implosion process are of concern, although most contaminants "burn through" at relatively low temperatures. Even without volume mixing, impurity-induced radiation at an edge layer may cause accretion of plasma at the liner/plasma interface and limit adiabatic heating.

Three major goals can provide the focus of research in this area. First would be a "proof-of-principle" demonstration of quasi-adiabatic heating of magnetized plasma by a magnetically driven pusher with the goal, for example, of doubling the plasma temperature under implosion conditions. The second goal would be to reach and measure the achievement of a fusion temperature (e.g., 4 keV). Third would be to actually demonstrate thermonuclear fusion ignition and large fuel burn-up.

Possible implosion scenarios for the cryogenic fiber z-pinch and the VNIIEF plasma formation schemes are illustrated in Figures 2 and 3, respectively. For the same initial temperature and the same radial convergence, the cylindrical schemes will not reach as high temperature as the corresponding spherical convergence, as noted in Table II. However, cylindrical systems provide greater diagnostic access and would appear preferable for initial confirmation of the implosion heating principle of MAGO/MTF.

The fiber z-pinch and the VNIIEF chamber are sufficiently different as to place differing demands on the implosion system. Each must address the closing and sealing of a gap in the system, for the fiber pinch the power flow entrance and for the VNIIEF chamber the plasma injection gap. Under implosion conditions, the fiber z-pinch plasma must carry all magnetization current, whereas, in the VNIIEF chamber, the central conductor may carry substantial current, if, for example,

TABLE II. IDEAL GAS LAW CONVERGENCE REQUIRED TO REACH FUSION TEMPERATURES

Initial temperature (eV)	0.025	10	50	300
Final temperature (keV)	5	5	5	5
Spherical convergence (r_0/r_f)	447	22.3	10	4.1
Cylindrical convergence (r_0/r_f)	946	106	31.6	8.3

instabilities increase the resistance of the plasma. Although the chamber central conductor is clearly necessary for the magnetization that takes place before electrical breakdown, the conductor may be disadvantageous from an implosion perspective.

In a MAGO/MTF context, the "phi" targets [4] provide the only presently available integrated liner-on-plasma data. The phi-targets were powered by an electron beam, and the beam's low-energy precursor provided the voltage that drove a diffuse z-pinch that provided preheat and magnetization. Hence, the phi-targets do not necessarily demonstrate that modern pulsed-power driven formation systems can be satisfactorily mated with an imploding liner system.

However, in another context, the Phillips Laboratory has recently mated a plasma formation system with the quasi-spherical liner implosion system discussed in the previous section. A coaxial plasma gun was used to form a magnetized plasma, and magnetic acceleration of the plasma provided the means for injecting the plasma into a quasi-spherical liner. Since the goal was to use the plasma as a "working fluid," radial vanes at the injection port "stripped" the magnetic field from the plasma, and the liner was filled with essentially unmagnetized plasma. The imploding liner then compressed the working fluid, which in turn compressed an inner metallic rod [24]. Radiographs suggest that the liner moved across the injection ports without the introduction of substantial perturbations and sealed the working fluid volume. The working fluid density at injection was approximately $10^{20}/cm^3$ and the temperature was approximately 1.3 eV, so the density was substantially higher than required for MAGO/MTF, and the plasma temperature was lower than required. A lower density, higher temperature plasma with the magnetic field not stripped away appears feasible in this system. With a suitable plasma gun, the injected plasma could have a spheromak configuration. The Phillips experience provides confidence that plasma formation systems can be mated with an imploding liner driver.

V. Concluding Remarks

A number of advanced plasma diagnostic capabilities developed in other contexts, e.g., time- and space- resolved x-ray spectroscopy, x-radiography, etc., can be used to characterize the plasma and the liner behavior for MAGO/MTF. These diagnostics provide a means of validating the several large-scale computer codes already being used to simulate liner implosions and magnetized plasmas. The potential for a very strong synergism between experimentation and time-dependent, multidimensional computer modeling enhances the prospect for understanding in this area.

Existing and near-term modern pulsed power capabilities, plasma formation techniques, diagnostics, and computer codes provide the necessary tools for an evaluation of MAGO/MTF without a major capital investment and with relatively low operating costs. Near-term experiments with laboratory pulsed power devices and magnetic flux compression generators will validate calculations and test critical issues such as the mix of wall/insulator material with the fuel. These experiments would be at the appropriate plasma conditions to allow proof-of-principle tests of MAGO/MTF as a path to fusion.

For fusion reactor scenarios based on MAGO/MTF, major engineering design and major capital expenditures to replace the one-shot electrical sources with a fixed, repetitive pulsed power facility would occur only after ignition and substantial fuel burn-up have been demonstrated. Magnetized targets may prove to

be ideal for reactors using heavy ion beams as target implosion drivers. At least two reactor approaches come to mind: (a) ICF-like pulsed reactor system; (b) maximized energy output per shot, with lower repetition rate. If relatively inexpensive electrical pulsed power could be used as the implosion driver, smaller, more economically viable reactors than for conventional fusion approaches might be possible. Because MAGO/MTF is qualitatively different from inertial or magnetic confinement fusion--different time, length, and density scales--MAGO/MTF reactors will have different characteristics and trade-offs, increasing the chances that a practical fusion power scheme can be found.

Acknowledgments

The US/Russian collaboration represented by the work reported here would not have been possible without the support and encouragement of many officials of the governments of Russia and the United States and many administrators and colleagues at the All-Russian Scientific Research Institute of Experimental Physics and the home institutions of the US authors [25].

The remaining authors regret the loss of their colleague, Jim Eddleman, who died in October, 1996. His technical expertise and his never-ending sense of humor are deeply missed.

REFERENCES

[1] LINDEMUTH, I.R., KIRKPATRICK, R.C., Nucl. Fusion **23** (1983) 263.
[2] FEINBERG, B., Plasma Phys. **18** (1978) 265.
[3] SHERWOOD, A., et al., in Megagauss Physics and Technology (TURCHI, P., Ed.), Plenum Press, New York (1980).
[4] CHANG, J., et al., in High Power Electron and Ion Beam Research and Technology (Proc. 2nd Int. Conf. Ithaca, NY, 1977) (NATION, J.A., SUDAN, R.N., Eds), Cornell Univ., Ithaca (1977) 195.
[5] LINDEMUTH, I.R., WIDNER, M.M., Phys. Fluids **24** (1981) 746.
[6] RAHMAN, H., WESSEL, F., ROSTOKER, N., Phys. Rev. Lett. **74** (1995) 714.
[7] VEKSHTEIN, G., RYUTOV, D., CHEBOTAEV, P., Sov. J. Plasma Phys. **1** (1975) 220.
[8] LINDEMUTH, I., et al., Phys. Fluids **21** (1978) 1723.
[9] DAWSON, J., Methods Comput. Phys. **16** (1976) 281.
[10] SETHIAN, J., et al., Phys. Rev. Lett. **59** (1987) 892; **59** (1987) 1970(E).
[11] SHEEHEY, P., et al., Phys. Fluids B **4** (1992) 3698.
[12] KIRKPATRICK, R., et al., in Proc. 10th IEEE Conf. on Pulsed Power, Albuquerque, 1995.
[13] BUYKO, A.M., et al., in Proc. 9th IEEE Conf. on Pulsed Power, Albuquerque, 1993 (PRESTWICH, K.R., BAKER, W.L., Eds), Inst. of Electrical and Electronics Engineers, Piscataway, NJ (1993).
[14] CHERNYSHEV, V.K., et al., in Megagauss Magnetic Field Generation and Pulsed Power Applications (COWAN, M., SPIELMAN, R., Eds), Nova Science Publishers, Commack, NY (1994).
[15] LINDEMUTH, I., et al., Phys. Rev. Lett. **75** (1995) 1953.
[16] EDDLEMAN, J., HARTMAN, C., Rep. UCRL-JC-114685, Lawrence Livermore Natl Lab., CA (1993).

[17] PETERKIN, R.E., Jr., et al., in Proc. 31st Joint AIAA–ASME–SAE–ASEE Propulsion Conf., Publ. AIAA-95-2899, American Inst. of Aeronautics and Astronautics, Washington, DC (1995).
[18] SHEEHEY, P., et al., in Proc. 7th Int. Conf. on Megagauss Magnetic Fields and Related Topics, Sarov, Russian Federation, 1996.
[19] ARMSTRONG, T., et al., in Megagauss Technology and Pulsed Power Applications (FOWLER, C., CAIRD, R., ERICKSON, D., Eds), Plenum Press, New York (1987).
[20] HOCKADAY, M., et al., in Proc. 10th IEEE Conf. on Pulsed Power, Albuquerque, 1995.
[21] DEGNAN, J.H., et al., Phys. Rev. Lett. 74 (1995) 98.
[22] GOFORTH, J., et al., in Proc. 7th Int. Conf. on Megagauss Magnetic Fields and Related Topics, Sarov, Russian Federation, 1996.
[23] ANDREEV, V., et al., ibid.
[24] DEGNAN, J.H., et al., ibid.
[25] Los Alamos Science, Vol. 24 (COOPER, N., Ed.), Los Alamos Natl Lab., NM (1996).

ITER

(Session F)

Chairperson

K. LACKNER
Germany

ITER PHYSICS*

S. PUTVINSKI[1], R. AYMAR[1], D. BOUCHER[1], C.Z. CHENG[2], J.W. CONNOR[3], J.G. CORDEY[4], A.E. COSTLEY[1], F. ENGELMANN[5], N. FUJISAWA[1], M. FUJIWARA[6], J. JACQUINOT[4], R. KHAYRUTDINOV[7], H. KISHIMOTO[8], S.V. KONOVALOV[7], A. KUKUSHKIN[1], B. KUTEEV[9], V. LUKASH[7], S. MIRNOV[7], D. MOREAU[10], V. MUKHOVATOV[1], W.M. NEVINS[11], F.W. PERKINS[1], A.R. POLEVOJ[7], D. POST[1], N. PUTVINSKAYA[12], M.N. ROSENBLUTH[1], O. SAUTER[1], N. SAUTHOFF[2], M. SHIMADA[8], Y. SHIMOMURA[1], Yu.A. SOKOLOV[7], R.D. STAMBAUGH[13], T. TAKIZUKA[8], N. UCKAN[14], M. WAKATANI[15], J. WESLEY[1], J. WILLIS[16], R. YOSHINO[8], K. YOUNG[2]

[1] ITER Joint Central Team

[2] Plasma Physics Laboratory,
Princeton University,
Princeton, New Jersey,
United States of America

[3] UKAEA Government Division, Fusion,
Culham Laboratory,
Abingdon, Oxfordshire,
United Kingdom

[4] JET Joint Undertaking,
Abingdon, Oxfordshire,
United Kingdom

[5] NET Team,
Max-Planck Institut für Plasmaphysik,
Garching, Germany

[6] National Institute for Fusion Science,
Nagoya, Japan

[7] Russian Research Center,
Kurchatov Institute,
Moscow, Russian Federation

[8] Japan Atomic Energy Research Institute,
Ibaraki, Japan

[9] State Technical University,
St. Petersburg, Russian Federation

[10] Centre d'études de Cadarache,
Saint-Paul-lez-Durance, France

[11] Lawrence Livermore National Laboratory,
Livermore, California,
United States of America

[12] Science Applications International,
San Diego, California,
United States of America

[13] General Atomics,
San Diego, California,
United States of America

[14] Oak Ridge National Laboratory,
Oak Ridge, Tennessee,
United States of America

[15] Kyoto University,
Kyoto, Japan

[16] United States Department of Energy,
Washington, D.C.,
United States of America

Abstract

ITER PHYSICS.

The ITER physics specifications provide the basis for the engineering design requirements. They are based on experimental results obtained on present day tokamaks, plasma theory and extrapolation to the ITER parameters. The present paper summarizes recent results obtained from the ITER physics R&D programme conducted by the four ITER Parties and presents projections for ITER plasma performance, operational scenarios and plasma control obtained by the ITER Joint Central Team and Home Teams.

1. INTRODUCTION

The goal for the ITER physics programme is the demonstration of controlled ignition and sustained burn in DT plasmas and the development of long pulse/steady state operational scenarios for fusion power production and experimental demonstration of their feasibility. As a first reactor scale machine, ITER will encounter problems which are typical for a tokamak reactor. The most important plasma physics issues are: energy and particle confinement of the core plasma in the ignited regime, power handling and divertor operation consistent with an ignited plasma, advancing to high β regimes and plasma operation near or above the Greenwald density limit. It is also very important to develop reliable plasma scenarios and control systems to avoid or mitigate plasma disruptions.

In the area of physics R&D, the ITER Joint Central Team (JCT) works in close contact with the Home Teams and the Four Parties Physics Programme. The ITER design work highlights important physics issues which are addressed through the physics programmes. Recent examples include: the study of the threshold power of the L to H mode transition, the development of a reliable 1-D transport model, the study of a closed radiative divertor and plasma detachment, halo current asymmetry and the plasma density limit. A new area of experimental work is fast plasma termination by killer pellets, which is needed in ITER for mitigation of disruptions and vertical displacement events (VDEs). The JCT together with the ITER Physics Expert Groups have been working on improvement of our understanding of the experimental results obtained in present day tokamaks.

Physics R&D programme results provide the basis for the rules and understanding applied in the ITER physics design work aimed at developing physics specifications and design requirements. In the present paper, we summarize the latest developments and critical points of the ITER physics and review the major directions of the physics design work since the Interim Design Report [1]. The paper does not include physics and design efforts in the area of the ITER divertor, which are presented elsewhere [2].

2. OPERATIONAL LIMITS

New results have been obtained in the analysis of the ideal and resistive MHD stability and β limit in ITER. Simulations have confirmed that ITER profiles are stable for ideal MHD modes up to a high value of normalized β (β_N = 3.5–4). At this β the fusion power in ITER could be as high as 2.2–2.5 GW, which is far above the ITER goal of 1.5 GW. A normalized β of 3.5 or even higher (the record value is $\beta_N > 5$) has been achieved on many present day tokamaks [3]. However, most of these high β regimes were obtained only transiently or during short pulses. Experimental study of ITER demonstration discharges and attempts to reproduce ITER discharges by matching ITER dimensionless parameters such as plasma collisionality ν^* have shown the existence of a soft β limit. A degradation of plasma energy confinement was observed in several tokamaks (ASDEX Upgrade [4], DIII-D [5], JT-60U [6], COMPASS) at $\beta_N \approx$ 1.8–2.5 and at low (ITER type) collisionality. The saturation of β is accompanied by development of low m, n islands and degradation of the plasma confinement. A study of β saturation is just beginning and the emerging theoretical model ([7] and references therein) suggests that confinement degradation is connected with neoclassical tearing modes excited by flattening of the pressure profiles and reduction of the bootstrap current within the island. The theory predicts that these modes can exist in a reactor type plasma and that they could be present in ITER. The expected threshold of the soft β limit in ITER, β_N = 2–2.5, is about that which is needed for the achievement of 1.5 GW of fusion power in ITER (β_N = 2.2 in the ignited regime or even less in the case of driven burn). However, it does not leave much margin, and advances to high β regimes which will be a part of the ITER physics programme will require study of the soft β limit and of means to increase β above this limit. One of the ways [7] is current drive within the island which will compensate reduction of the bootstrap current and stabilize modes. The first estimations are encouraging [7]. It could also happen that ITER flat density profiles will be less susceptible to the neoclassical tearing modes than the peaked profiles in the present experiments. Clearly this is an important issue which requires more experimental and theoretical study to clarify possible effects on the ITER scenarios and operational limits.

The density limit which is observed on present tokamaks usually satisfies the empirical Greenwald scaling, $\bar{n}_e = I/\pi a^2$ (10^{20} m^{-3}, MA, m). The scaling of the density limit to a reactor size machine is still under discussion. The Greenwald scaling, $\bar{n}_e \propto B/R$, is very unfavourable for tokamak reactors and ITER because of their larger size at the limited magnetic field which can be produced by superconducting coils. The reference ITER operational scenarios require a density of 1.1–1.5 times the Greenwald limit, which is more restrictive than the β limit in ITER.

There are several cases in which this limit was overcome without serious degradation of the plasma confinement. ASDEX Upgrade used a combination of deep pellet injection and gas puffing to achieve, in a quasi-steady state, an H mode with a density 1.5 times the Greenwald limit. Similar results were obtained in DIII-D. This

demonstrates that there is no fundamental density limit in tokamaks but that the observed limit is probably connected to the limitations caused by fuelling or plasma edge radiation. It is clear that the Greenwald limit, which has a natural explanation in ohmic discharges as a power balance limit, is too simplified in the case of auxiliary heated plasmas and probably contains a number of hidden parameters of the edge plasma. Several attempts have been made to explain the Greenwald density limit by edge plasma ballooning stability [7] or edge power balance [8], but so far there is no widely accepted explanation of the Greenwald scaling. In these circumstances the extrapolation to ITER by the Greenwald formula should be done with caution. For example, the presence of even a weak power dependence $P^{1/4}$ in the density limit scaling would increase the prediction of the density limit by a factor of about 2, which is sufficient to remove a density limit in ITER above the β limit. Below we shall discuss the limitations imposed on ITER operational scenarios by the density limit.

3. PLASMA DISRUPTIONS

Plasma disruption and loss of plasma vertical position control will produce large heat loads on the plasma facing components. A major disruption with a large β drop cannot be controlled by the poloidal field system and will be followed by a VDE which will produce large mechanical loads on the in-vessel elements. Plasma disruption is a challenge to the design of the plasma facing components, and the development and refinement of the plasma specifications in this area constitute one of the most important tasks for the ITER physics designers.

A major new development over the last two years is the discovery of toroidal asymmetry of the halo current which is observed now on many tokamaks during VDEs (Alcator C-Mod, ASDEX Upgrade, COMPASS-D, DIII-D, JET, JT-60U).

TABLE I. SUMMARY OF HALO CURRENT DATABASE

Experiment	Number of sets N_{total}	Plasma elongation κ_x	Safety factor q_{95}	Plasma current I_{p0} (MA)	$I_{h,max}/I_{p0}$ at $q_{95} = 3$, $\kappa_x \geq 1.6$
Alcator C-Mod	1477	0.95–1.96	2.2–10.1	0.18–1.16	0.20 ± 0.03
ASDEX Upgrade	78	1.01–1.78	3.1–6.5	0.37–1.18	0.33 ± 0.05
COMPASS-D	53	1.6	2.9–7.2	0.10–0.19	0.20 ± 0.05
DIII-D	18	1.62–1.92	2.7–5.6	0.96–1.49	0.15 ± 0.07
JET	708	1.02–1.92	2.4–12.5	1.00–6.96	0.10 ± 0.05
JT-60U	48	1.25–1.52	2.0–11.0	0.44–1.53	0.15 ± 0.05

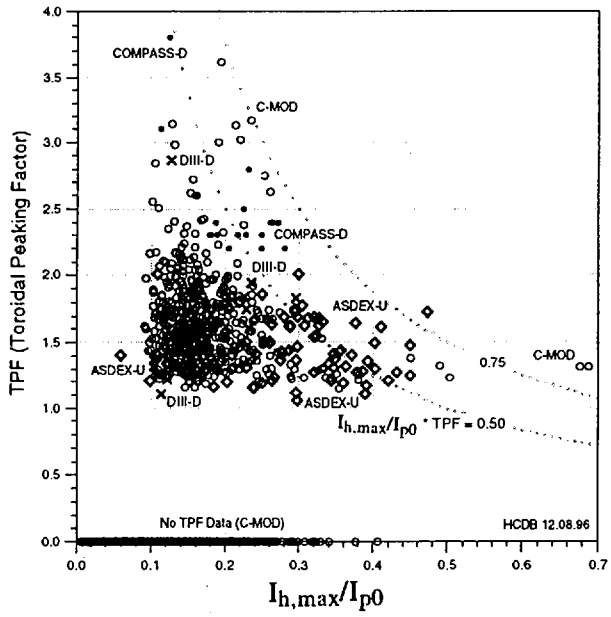

FIG. 1. Halo current database: TPF versus normalized halo current magnitude.

The toroidal asymmetry creates a large net horizontal force and increases local mechanical loads on the ITER shield and vacuum vessel.

Substantial progress has been made in collecting and analysing the ITER halo current/disruption database. Table I summarizes the overall parameters of the database, which comprises 2382 data sets from six tokamaks [9]. The last column contains mean values and standard deviations of the normalized magnitude of the halo current derived from the database for ITER type conditions.

Figure 1 shows the toroidal peaking factor (TPF) of the halo current as a function of its magnitude. One can see a general inverse correlation between the quantities. Most of the data fall within a domain bounded by $TPF(I_{h,max}/I_{p0}) = 0.75$, $I_{h,max}/I_{p0} \leq 0.50$ and $TPF \leq 4$.

The empirical data are not yet supported by the solid theoretical or interpretative work that is required for development of a reliable extrapolation and specifications of halo current magnitude and asymmetries in ITER. Most of the asymmetry develops when the safety factor becomes as low as $q = 1$, when the development of strong MHD instabilities can be expected. The inverse correlation between peaking factor and magnitude of the halo current could indicate a limit of the current density of the halo current. Non-linear 3-D MHD analysis will be very helpful for interpretation of the observed phenomena.

4. PLASMA CONFINEMENT AND PREDICTIONS OF ITER PERFORMANCE

ELMy H mode is considered as a prototype regime for achieving sustained ignition in ITER. Projections for ITER energy confinement time mainly rely on the global confinement time scaling which was derived from ITER confinement databases containing a large number of well documented discharges from the tokamaks Alcator C-Mod, ASDEX, ASDEX Upgrade, COMPASS, DIII-D, JET, JFT-2M, JT-60U, PDX and PBX-M. The main efforts in the ITER related experimental programme were concentrated on study of ITER type discharges, i.e. long pulse discharges with dimensionless parameters similar to or close to ITER's.

The plasma core confinement study includes development of a reliable scaling for the H mode power threshold. ITER is expected to be able to sustain ELMy H mode, but the H–L transition may limit access to the full operation domain (e.g. high density and low temperature or low fusion power). However, there are still uncertainties in the scaling for extrapolation of the power threshold in ITER and significant efforts in the physics programme are being devoted to better understanding the physics of L–H (and H–L) transitions.

In the area of 1.5-D transport modelling, work is in progress on creating a reliable transport model. An international working group has begun systematic work on collecting a profile database, with the aim of creating a suitable experimental test bed for validation of transport models and codes. The profile database contains fully documented discharges from ASDEX Upgrade, DIII-D, JET, JT-60U, TEXTOR, TFTR, Tore Supra, T-10 and RTP. More than ten of the existing transport codes based on different transport models were used in an attempt to reproduce selected discharges. The results show that a few models achieved better than 30% error (almost none better than 20%) in fitting experimental results [10]. This is still no better than fitting the H mode database by 0-D energy confinement scaling (RMS error of about 15%). Further benchmark work and theoretical analysis are needed, but it seems clear that only experiment with a reactor size plasma such as ITER's will provide the answer. So far the 1-D models predict a wide range of plasma performance from very large ignition margins (T-11) to poor plasma confinement (ion temperature gradient models) at which only driven burn is possible.

In the area of the design work, a substantial effort has been made to develop a simplified SOL/divertor model which makes it possible to provide self-consistent boundary conditions and to connect central He impurity concentration with fuelling and pumping rates [11]. The transport codes (PRETOR, ASTRA, TRANSP) have been used to develop and refine the ITER operational scenarios, including the reference ignited scenario, and long pulse non-inductively driven and steady state scenarios based on the reversed shear plasma configuration. The main emphasis was on the following issues: (a) self-consistent simulations of the core and divertor; (b) modelling of the effect of impurity seeding on the ignited plasma performance;

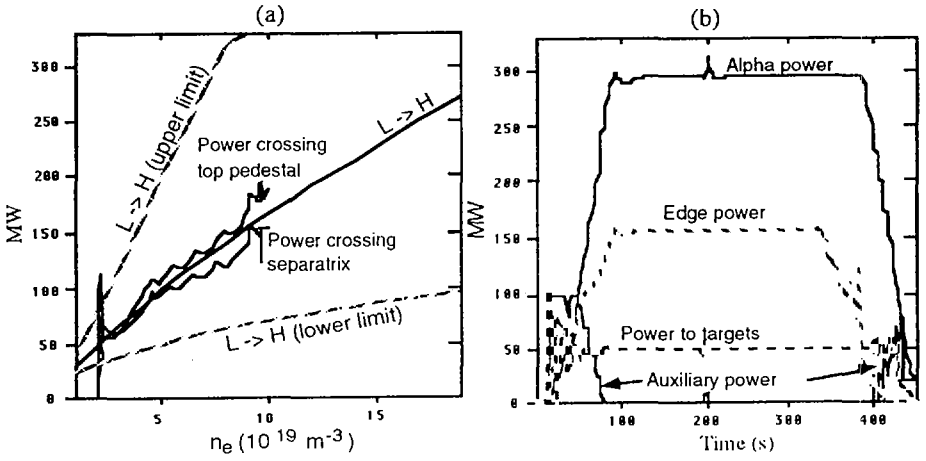

FIG. 2. (a) Plasma trajectory in edge power versus plasma density, and (b) time traces of plasma core and edge powers.

(c) ITER operation below the Greenwald density limit; and (d) steady state and driven scenarios under the constraints of ITER auxiliary systems.

A new divertor model has been added to the code PRETOR to predict self-consistently He and Ar levels in the plasma [11]. Argon is considered as a candidate for impurity seeding, which is an element of the present ITER divertor concept. The model predicts that an Ar level of 0.2% is needed to reduce the power reaching the divertor target plates to 50 MW. At the same time the self-consistent He levels correspond to $\tau^*_{He}/\tau_E = 3.5$–7, which is lower than was assumed previously. Modelling has shown that ignition at constant power can be sustained if impurity fuelling, DT fuelling and auxiliary heating have feedback control loops which keep fusion power, divertor heat loads and plasma density at the required level. Figure 2(b) shows time traces of the key plasma parameters. It can be seen that the power at the divertor target plates is sustained at the level of 50 MW with a total fusion power of about 1.5 GW. This is achieved by Ar radiation (~100 MW) from the SOL/divertor plasma. The Ar concentration is about 0.2% at the flat-top. The auxiliary power of 100 MW causes the transition to the H mode at a plasma density of 2×10^{19} m^{-3}, and the H mode is maintained successfully through the whole pulse even without the assumption of hysteresis in the reverse, H–L transition. The dashed lines in Fig. 2(a) show the uncertainty in the predictions from the present day database.

The example presented in Fig. 2 shows that impurity seeding allows ITER to operate in the ignited mode with a fusion power of 1.5 GW and simultaneously with low divertor heat loads. The other impurities can also be seeded without loss of plasma ignition. The modelling shows that in the case of Ne the required concentration is about 0.75%, whereas in the case of Kr it is 0.013%.

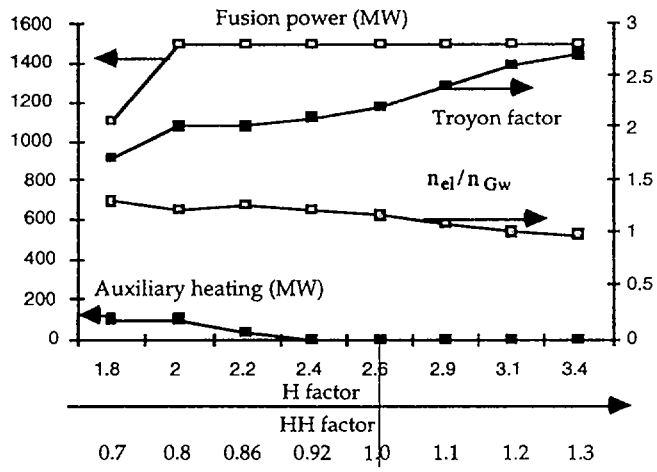

FIG. 3. Fusion power, auxiliary heating power, normalized density relative to the Greenwald limit, and β_N for a range of confinement from −30% to +30% of the reference value. Reference plasma parameters.

The effect of the plasma confinement on ITER performance is illustrated in Fig. 3, where the main plasma parameters are presented as functions of the enhancement factor H_H for ELMy H mode confinement scaling (0.85ITER93H) [7]. At the lowest limit, which corresponds to a 30% reduction in the energy confinement (enhancement factor of H = 1.8 for the Bohm type L mode scaling), the maximum fusion power decreases to about 1 GW at 100 MW of auxiliary power. For the reference assumptions on plasma confinement, H_H = 1, ITER has about a 10% margin in the energy confinement, β limit and H mode power threshold. However, at 1.5 GW of fusion power ITER has to operate above the Greenwald density limit unless the energy confinement is 20% better than predicted by the ITER reference energy confinement scaling.

TABLE II. LOWEST LIMITS OF PLASMA PERFORMANCE

I_p (MA)	H_H factor	n/n_{GW}	P_{aux} (MW)	P_{fus} (MW)	P_{scp}/P_{H-L}	β_N
21 (reference)	1	1.13	0	1500	1.05	2.2
21	0.7	1	100	850	1.3	1.5
21	0.7	1.3	100	1100	1.3	1.5
24	0.7	1	100	1300	1.5	1.7
24	0.7	1.05	100	1500	1.5	1.8

To ensure achievement of ITER goals, the impacts of possible shortfalls in the plasma energy confinement and operational limits have been analysed. Among the shortfalls are the Greenwald scaling for the density limit and a possible reduction in the energy confinement due to uncertainty in the extrapolation to ITER conditions. The lowest limits of plasma performance based on these shortfalls are summarized in Table II. All cases except the reference case correspond to driven burn with 100 MW of auxiliary power. At the maximum plasma current of 24 MA the reduction in fusion power is not very large even with the worst combination of the unfavourable factors. The ITER poloidal field system allows the plasma current to be increased to 24 MA ($q_{0.95} = 2.6$) at the expense of the pulse length, which is about 700–800 s at this current. At 24 MA, ignition (or $Q > 50$) is also possible but at a reduced fusion power of ≤ 800 MW.

The previous study of steady state plasma scenarios outlined the possible range of plasma parameters in ITER: plasma current 12–14 MA, fusion power 1–1.5 GW and bootstrap fraction $\geq 70\%$. The recent work was aimed at the optimization of these regimes for each of the ITER auxiliary systems. The modelling of neutral beam driven steady state scenarios has shown that at a beam power of less than 150 MW the fully steady state regimes (plasma current of 12 MA) can be achieved only if plasma confinement and the β limit are improved to be above the reference ITER values (to $H_H \geq 1.2$ and $\beta_N > 2.5$). The greater the improvement in confinement and β the less auxiliary power is needed for steady state operation. It appears that the demanding requirements for steady state operation mode can be met by a reversed shear scenario which requires off-axis current drive. The neutral beam can provide the off-axis current drive necessary for a reversed shear configuration in a smaller

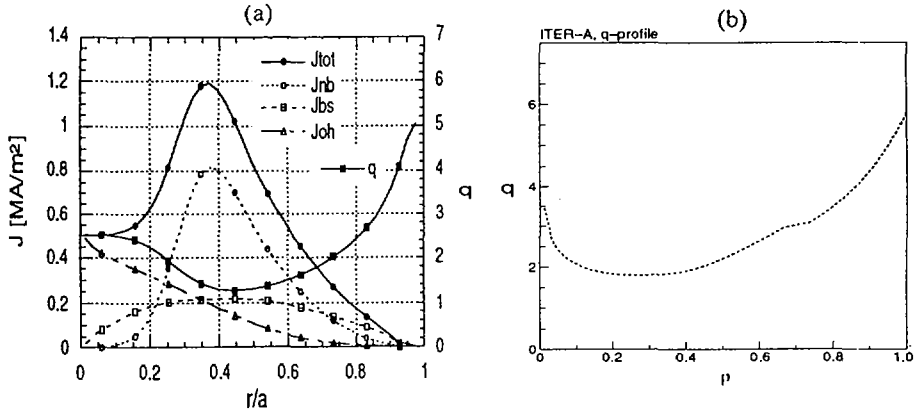

FIG. 4. Self-consistent reversed shear q profiles produced by ITER current drive systems. (a) Off-axis NBCD in a plasma displaced downwards; a = 2 m, I_p = 12 MA, n_e = 6 × 10^{19} m^{-3}, P_{NB} = 100 MW. (b) LHCD and FWCD driven scenario in the reference ITER configuration; I_p = 13 MA, n_e = 1.15 × 10^{19} m^{-3}, P_{LH} = 60 MW, P_{FWCD} = 40 MW.

plasma displaced downwards by about 1–1.5 m (the X point remains in the divertor throat). An example of the q profile produced by NBI is shown in Fig. 4(a). In this particular example the seed current is produced by the ohmic current but it could be replaced by non-inductive current (driven by ICRH, for example).

Modelling has shown that similar current profiles can also be driven by a combination of lower hybrid and ICRH (see Fig. 4(b)) and ECRH current drive systems. The optimal range of the plasma current for the pure steady state scenarios is 12–14 MA. It was found that because of a strong coupling between the current profile, transport, plasma heating and bootstrap current, maintaining the steady state regime would probably require an appropriate feedback scheme with a real time estimate of the current density profile.

While the pure steady state scenarios require enhanced plasma confinement, auxiliary heating power of 100 MW allows the pulse length to be extended and a high neutron wall load to be maintained even in the ELMy H mode regime. These high fluence driven scenarios are envisioned as candidates for neutron testing. Study of the ECRH driven scenarios has shown that the pulse length can be extended to 8000–9000 s at a fusion power of about 1 GW. The longest pulse length corresponds to a plasma current of 16–18 MA.

Therefore at the nominal parameters ITER will achieve sustained, ignited burn with 1.5 GW fusion power. The simulations show that, with 100 MW of auxiliary heating and driven burn operation, pulse lengths in excess of 1000 s can be attained with more than 1000 MW of fusion power under the following restrictions: (1) the density is restricted to the Greenwald limit; (2) there is no hysteresis in the H–L transition; and (3) the confinement time is reduced by a factor of 0.7.

5. CONFINEMENT OF ENERGETIC PARTICLES

The main efforts in fast α particle physics in ITER physics design and the physics R&D programme were concentrated on analysis of α particle ripple loss and development of numerical tools capable of analysing high n TAEs in ITER.

Experimental study of fast particle ripple loss has been continued in JET, JT-60U and TFTR. JET has performed experiments with the ITER type plasma shape and variable ripple profile [12] with the aim of studying the effect of the ripple on plasma performance and fast particle confinement. Comparison of the experimental results with the results of the modelling of the fast particle loss shows a good quantitative agreement, which allows us to conclude that the classical models [13] well describe the fast particle ripple loss. The same conclusion was reached in the analysis of JT-60U results [14].

Monte Carlo simulations of ripple loss in ITER confirm a low loss fraction for the reference ignited mode. However, the low current, reversed shear configurations have been found to be unfavourable for the α particle ripple loss, placing constraints on plasma position and current. The results for α particle loss are summarized in Table III.

TABLE III. RESULTS OF MONTE CARLO MODELLING OF α PARTICLE RIPPLE LOSS

	Plasma current					
	21 MA (reference)		12 MA (slim plasma)		12 MA (short plasma)	
Drift direction	Up	Down	Up	Down	Up	Down
Ripple trapped loss/banana loss	2.15	0.016	5.41	0.01	2.28	0.023
Particle loss fraction (%)	2.82	5.57	40	32	18.8	9.0
Power loss fraction (%)	1.09	2.2	19.4	16.4	5.03	3.2
Peak heat load (MW/m^2)	1.2	0.3	4.8	1.3	2.5	0.5

The two low current plasmas in Table III correspond to candidates for plasma equilibrium in steady state plasma scenarios. They are different in respect of plasma position — the slim plasma has maximum radial displacement in the region with the large ripple (worst case) while the short plasma is removed from the high ripple. These results demonstrate that even with the present ripple profile we can have a low current, high fusion power regime, but the ripple loss restricts configurational flexibility. The heat load for the reference downward drift direction is within the design specifications for the first wall. Moreover, in this case the heat load occurs on the high heat flux components — limiter and baffle. For the opposite drift direction, the peak heat load is above the specifications (0.5 MW/m^2). One of the possible ways to ameliorate the effect of toroidal field ripple is to replace the stainless steel shield plates located between the walls of the vacuum vessel by ferritic plates in the sectors under the outer toroidal field coil legs. Previous estimations [15] have shown that the ripple amplitude can be reduced by a factor of 2.5. In this case the restrictions on the low current plasma configurations and/or fusion power imposed by the α particle ripple loss will be removed.

The first modelling results on the ripple loss of the 1 MeV particles produced by NBI show a significant loss of beam particles and appreciable first wall heat loads. The effect is due to the flat density profile in ITER and the relatively large source of neutral beam particles at the plasma edge where toroidal field ripple is large. The power loss fraction in a high density plasma ($n = 10^{20}\ m^{-3}$) is about 5% in the case of co-injection and 17% with counter-injection. In the case of upward toroidal drift, the peak heat load is larger than 1 MW/m^2 at a total neutral beam power of 50 MW. This can also be reduced significantly by the ferritic inserts. The study of the ripple loss of the high energy tails produced by ICRH is in progress. However, because of the central heating we can expect much less ripple effect than in the case of NBI.

Tritium experiments on TFTR have demonstrated α particle driven TAEs in rough agreement with theory, but have not shown large fusion α particle loss. The high n TAEs remain a threat for collective loss of α particles in ITER. Progress has been achieved in linear stability analysis of the TAEs as well as in the understanding of non-linear saturation and loss of α particles. A review of collective α particle effects in ITER can be found in Ref. [16].

6. FAST PLASMA TERMINATION

Development of fast plasma shutdown scenarios for ITER is an important aspect of ITER physics design and operation planning. The reasons why a fast shutdown capability is needed include: (1) to limit the consequences of loss of first wall/divertor cooling; (2) to limit the thermal consequences of poloidal field control failures that result in plasma mispositioning relative to the first wall or divertor channel/targets; (3) to mitigate disruption erosion of the divertor target surfaces; and (4) to mitigate the severity of the thermal and electromagnetic loading consequences of VDEs. To avoid damage to the plasma facing component surfaces, the fast shutdown system must be able to terminate the fusion power and remove the plasma thermal energy in a time shorter than 3 s [1]. Minimum and maximum shutdown requirements for ITER are summarized in Table IV.

TABLE IV. MINIMUM AND MAXIMUM THERMAL AND CURRENT QUENCH TIMES

	Minimum	Maximum
Thermal quench time t_{th} (s)	0.01 (melting of the surface layer of the first wall)	3 (to avoid local melting of the plasma facing components in the case of loss of cooling or of plasma position control)
Current quench time t_c (s)	0.02 (large local mechanical loads on blanket modules)	3 (upper estimation for VDE time)

Injection of impurities (killer pellets) was proposed as a candidate for producing fast plasma shutdown in ITER [1, 17]. Impurity radiation can provide the required termination time and distribute the plasma thermal and magnetic energy over the large first wall surface area. Impurity pellet injection has been tested in the present experiments, and initial experimental results are encouraging.

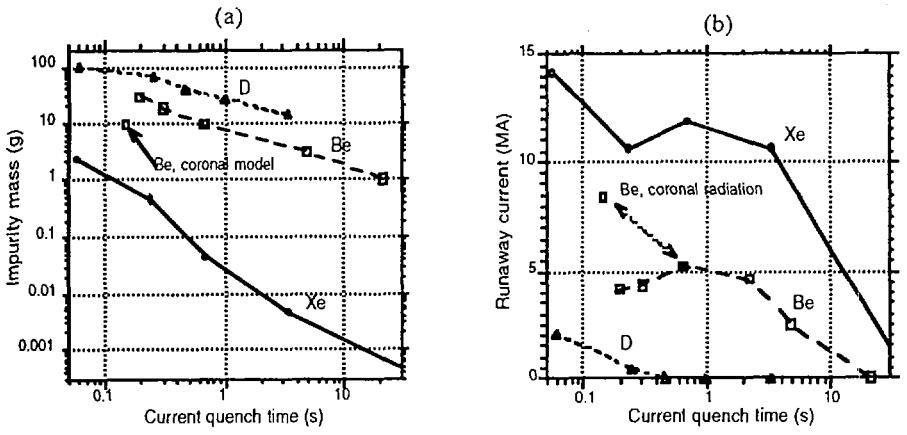

FIG. 5. (a) Mass of impurity needed to provide the required resistive current quench time, and (b) magnitude of the runaway current.

Significant progress has been achieved in the modelling of fast plasma termination and development of the concept of the fast plasma shutdown system in ITER [18]. The modelling includes different aspects such as 1-D modelling of plasma radiative collapse (specifications for the kind and amount of impurities), modelling a plasma VDE followed by impurity injection (plasma control, forces on the passive structures), modelling runaway electrons (discrimination of impurities) and modelling the delivery of impurities into the plasma core (specification for the injection system).

Fast termination of the plasma thermal and magnetic energy in ITER can be achieved by injection of a variety of impurities. We discuss below the results for Xe, deuterium and Be, which represent respectively a high Z impurity, the lowest Z 'impurity' and an impurity that is easy to inject and that is the most compatible with the ITER Be first wall. The impurity radiates the stored plasma thermal energy during the first phase of the plasma radiative collapse (thermal quench). After the end of the thermal quench, $t = t_{th}$, the magnetic plasma energy is converted to thermal energy by ohmic heating and then is also radiated by the impurity. During this phase (current quench) the plasma current decays. The amount of impurity (Xe, deuterium, Be) needed to provide the required resistive current decay time is shown in Fig. 5. In the case of deuterium injection the main radiation channels are bremsstrahlung and recombination radiation. At the required densities of deuterium the plasma becomes opaque to the line radiation. Analysis has shown that the corona radiation model is adequate for high Z impurities. An adequate and simple radiation model for Be is still lacking and we used upper (coronal equilibrium) and lower (bremsstrahlung + recombination radiation) limits to evaluate results. The thermal quench time for a

given current quench time is not very sensitive to the type of impurity. For example, for a current quench time of 1 s the thermal quench time can vary from 100 to 300 ms, depending on the kind of impurity.

Modelling of the evolution of the plasma equilibrium following the thermal quench (the DINA code [19]) has shown that the perturbations (β drop, current decay) caused by impurity radiation are large and that plasma poloidal field control will be lost. Impurity pellet injection will be followed by an upward VDE. However, the mechanical loads on the plasma facing components can be reduced if the current quench time is fast enough. To reduce the net vertical force on the passive structures (by a factor of ~ 2), the current quench time should be less than 1 s. For a current quench time of 1–2 s we can expect only a moderate reduction of the net force ($<30\%$).

We have found that for current quench times $t_c < 10$ s ($t_{th} < 1$ s), almost all impurities cause production of runaway electrons which carry a substantial part of the plasma current. The main mechanism responsible for the runaway production is an avalanche of high energy electrons from close electron–electron collisions. The large amount of volt-seconds available in ITER makes ITER significantly different from the present day tokamaks [18]. ITER also has, in addition to Dreicer acceleration, sources of high energy electrons such as γ radiation from the activated first wall and tritium decay. The magnitude of the runaway current as a function of the current quench time is shown in Fig. 5(b). Only deuterium (or possibly He) injection does not produce runaway electrons in the required range of the current quench time.

The runaway current in the case of high Z impurity injection has a decay time of several tens of seconds and persists in the plasma until the end of the VDE. Modelling of the plasma poloidal field control has shown that the runaway current at the level of 10 MA produced by high Z impurity injection cannot be controlled by the poloidal field control system and eventually will be lost on the wall in less than 1 s.

The amount of the high Z impurity needed to terminate the ITER discharge is relatively small, and pellets of this mass cannot penetrate deeply into the plasma, which makes the use of high Z materials questionable. Injection of Be can be done using the present pellet injector.

As can be seen from the above results, the injection of deuterium would be the best solution for the fast plasma termination in ITER. However, the required mass of deuterium (about 50 g) and the subsequent increase of the plasma density are very large. Modelling shows that 50 pellets of 1 g each would penetrate gradually up to the plasma centre in ITER at a pellet velocity of less than 1 km/s and would provide the required density profile. An interesting solution could be a liquid cryogenic jet instead of a solid pellet. Analysis of ablation of a cylindrical jet in the plasma predicts the following parameters of the required jet: diameter 8 mm and velocity 600 m/s, which appears feasible [18]. There are still many uncertainties in the propagation of the jets in vacuum and plasma and in the plasma response to such a large increase of the plasma density. Clearly, R&D and physics studies are needed.

Modelling of the fast plasma shutdown in ITER showed that runaway electrons could be a serious problem in ITER. Study of the runaway formation in ITER has shown that they will almost certainly be produced during the current quench of 'normal disruptions' if the plasma is contaminated by Be or other impurities during the thermal quench of the disruption. Runaway electrons could possibly impose a low density limit during plasma startup and current ramp-up phases. Study of the effect of the runaway electrons on the first wall should be carried out and, if necessary, additional protection should be provided for in the design of the first wall.

7. CONCLUSIONS

In conclusion, the ITER physics design analysis has made significant progress. The main emphasis during the last two years has been on an integration of the different aspects of ITER performance and operational scenarios. Experiments with 'ITER demonstration discharges' have been performed on all major tokamaks. These experimental studies have strengthened the basis for ITER performance predictions, but have also raised new issues, such as the soft β limit at low plasma collisionality, which are being addressed by the physics R&D programme. However, no basic limitations which could preclude achieving the projected ITER performance have surfaced. ITER has the capability to achieve more than 1000 MW of fusion power for a long duration and to explore ignited plasmas, even with cautious assumptions on the plasma confinement and operational limits.

ACKNOWLEDGEMENTS

Much of the work presented in this paper was carried out during the 1994–1996 meetings of the ITER Expert Groups. The authors are grateful to the Expert Group members and other participants of the meetings for their collaboration.

REFERENCES

[1] ITER Interim Design Report Package and Relevant Documents, ITER EDA Documentation Series No. 9, IAEA, Vienna (1996).
[2] JANESCHITZ, G., et al., IAEA-CN-64/F-2, this volume;
KUKUSHKIN, A., et al., IAEA-CN-64/FP-27, ibid.
[3] STRAIT, E.J., Phys. Plasmas 1 (1994) 1415.
[4] ZOHM, H., et al., in Controlled Fusion and Plasma Physics (Proc. 23rd Eur. Conf. Kiev, 1996), Vol. 20C, European Physical Society, Geneva (1996).
[5] LA HAYE, R.J., LAO, L.L., STRAIT, E.J., TAYLOR, T.S., Nucl. Fusion 37 (1997) 397.
[6] KAMADA, Y., et al., these Proceedings, Vol. 1, p. 247.
[7] PERKINS, F.W., et al., IAEA-CN-64/FP-24, this volume.

[8] BORRASS, K., et al., A Scrape-off Layer Based Model for Hugill-Greenwald Type Density Limit, Rep. IPP-5/70, Max-Planck-Inst. für Plasmaphysik, Garching (1996).
[9] WESLEY, J., et al., IAEA-CN-64/FP-25, this volume.
[10] CONNOR, J.W., et al., IAEA-CN-64/FP-21, ibid.
[11] BOUCHER, D., et al., IAEA-CN-64/FP-22, ibid.
[12] TUBBING, B.J.D., JET TEAM, in Controlled Fusion and Plasma Physics (Proc. 22nd Eur. Conf. Bournemouth, 1995), Vol. 19C, Part IV, European Physical Society, Geneva (1995) 1.
[13] YUSHMANOV, P.N., Reviews of Plasma Physics, Vol. 16 (KADOMTSEV, B.B., Ed.), Consultants Bureau, New York (1987) 103.
[14] TOBITA, K., et al., Nucl. Fusion **35** (1995) 1585.
[15] PUTVINSKI, S., et al., in Plasma Physics and Controlled Nuclear Fusion Research 1994 (Proc. 15th Int. Conf. Seville, 1994), Vol. 2, IAEA, Vienna (1995) 535.
[16] CHENG, C.Z., et al., IAEA-CN-64/FP-23, this volume.
[17] KUTEEV, B.V., SERGEEV, V.Yu., SUDO, S., Nucl. Fusion **35** (1995) 1167.
[18] ROSENBLUTH, M.N., et al., IAEA-CN-64/FP-26, this volume.
[19] KHAYRUTDINOV, R.R., LUKASH, V.E., J. Comput. Phys. **109** (1993) 193.

DISCUSSION

K.M. McGUIRE: Since ITER has a strong physics mission, I would like to know what percentage of the programme is being used for diagnostics?

S. PUTVINSKI: The cost of the diagnostics necessary to meet the ITER requirements for control and evaluation measurements has been estimated as amounting to about 5% of the total construction cost. The proportion is roughly the same for the ITER EDA diagnostic design and R&D programmes. According to present plans, approximately half the diagnostics — the diagnostic 'startup set' — will be completed and available for first plasma operation.

K.M. McGUIRE: We have heard about the toroidal field dependence of the β limit from our JET colleagues and also from TFTR. How are these results being incorporated into the ITER design? What R&D work needs to be done to clarify this situation?

S. PUTVINSKI: The design specification for ITER, $\beta_N = 2.5$, is based on the observed β limit in the ELMy H mode plasmas, including quasi-steady-state discharges with close to ITER collisionality and q (ASDEX-Upgrade, DIII-D, JT-60U, JET).

It is not clear what MHD phenomena are responsible for the mentioned degradation of β with magnetic field and how to extrapolate these results from hot ion mode regimes to ITER scenarios.

ITER DIVERTOR, AND PUMPING AND FUELLING SYSTEM DESIGNS*

G. JANESCHITZ, H.D. PACHER[1], G. FEDERICI, Yu. IGITKHANOV, A. KUKUSHKIN, E. MARTIN, D. POST[2], M. SUGIHARA, R. TIVEY, T. ANDO, A. ANTIPENKOV, S. CHIOCCHIO, S. HIROKI, P. LADD, H. NAKAMURA, R. PARKER, K. SCHAUBEL, Divertor Expert Groups for ITER JOINT CENTRAL TEAM and HOME TEAMS

ITER Joint Central Team,
Garching Joint Worksite,
Garching, Germany

Abstract

ITER DIVERTOR, AND PUMPING AND FUELLING SYSTEM DESIGNS.

Design requirements for the ITER divertor are presented. The experimental background and the resulting modelling considerations for the ITER divertor are reviewed. Operational limtis of divertor operation are discussed, and the choice of plasma facing materials is presented. The adopted design solutions (cassette design, remote handling, pumping and fuelling) are described.

1 INTRODUCTION

The ITER divertor must exhaust the major part of the alpha particle power (300 MW) at acceptable power loads on the divertor targets and exhaust the He ash, keeping the core He concentration below 10%. The goal for the component lifetime is 3000 full power discharges, including up to ~ 10% full power disruptions and 10% transient power excursions (~ 20 MW/m^2, up to 10 s of "attached" operation). The divertor must withstand thermal and electromagnetic loads during disruptions and must be exchangeable by remote handling within 6 months. For good energy confinement, the neutral (DT, He,...) leakage from the divertor should be below ~30

---

[1] NET Team, Garching, Germany.

[2] ITER JCT, San Diego, California, USA.

Pa-m^3/s (neutral pressure difference of ~ 10^4). To meet these requirements, it is necessary to operate in the semi-detached or fully detached divertor regime found in experiments (Sec. 2). The basic physics picture of this operation in ITER is described in [1], [2], the relevant atomic processes are given in [3] the modelling prediction for the ITER divertor is discussed in detail in [1], [4], [5]l, and the Divertor experiments as they apply to ITER have been reviewed in [6] and more recently in [7].

2 EXPERIMENTAL EVIDENCE FOR ITER DIVERTOR OPERATION

Detached divertor regimes have now been observed on most divertor tokamaks ([7] and references therein) with a reduction of the peak heat flux onto the divertor plates by a factor of five or more even for the maximum available heating power. In all these cases detachment is achieved by either strong gas puffing (H, D) or by a combination of impurity seeding (N, Ne, Ar) and gas puffing. Strong gas puffing increases radiation of intrinsic impurities, whereas impurity seeding often increases both edge and divertor radiation (depending on the radiator chosen) and permits detachment at lower densities.

Whereas many early experiments showed a rapid transition from attached operation to X-point Marfe recent experiments in both vertical target and flat plate divertors indicate a more gradual transition and radiation within the divertor when feedback control on gas and impurity fuelling is used. These discharges are often detached near the separatrix but remain attached in the outer SOL, i.e. are "semi-detached". Vertical target configurations which have good baffling for neutrals have the lowest density threshold for detachment [8]. Completely detached plasmas often have strongly degraded energy confinement, close to L-mode, possibly due to a high neutral pressure in the main chamber (reduced plasma plugging) [9] and low plasma edge temperatures (X-point marfe). Semi-detached discharges or those with medium Z impurity injection tend to have lower densities and neutral pressures and better confinement but often have high Z_{eff} (>2.5). A detached discharge that simultaneously has good confinement and a low Z_{eff} has not yet been observed experimentally. However, present experiments are much more open to neutrals (looser baffling or bypass leaks) than ITER, so that better results may be expected from planned divertor experiments with tighter baffling and ITER.

The retention of intrinsic as well as seeded impurities tends to decrease even in semi-detached regimes when compared to fully attached divertor operation. Both flow reversal and the reduction of baffling might be responsible for this observation.

It therefore appears likely from these experiments and modelling based on them that detached and semi-detached divertor operation can be achieved also in ITER at reasonable upstream densities ($5.10^{19}m^{-3}$) and powers (~ 200 MW)in a vertical target configuration, reducing the peak power load by a factor > 5. A combination of gas puffing and impurity seeding with two different impurities in ITER (mantle (Ar, Kr), and divertor (N, Ne)) should permit detachment and simultaneous control of the ELM regime (type I vs type III) and the target power [10]. However, both core contamination and H-mode power threshold limit the allowable impurity concentration in ITER.

3 PHYSICS OPERATIONS SCENARIO AND MODELLING RESULTS

In the modelling studies, described in detail in [5], scenarios are described to distribute the power between the various regions (table 1) using controlled impurity seeding, reducing the power to the divertor plate to ~ 50 MW while maintaining impurity ($Z_{eff} < 1.8$) and H-mode threshold limits.

TABLE I. ITER POWER BALANCE SUMMARY

Process	Power (MW)	Range
Alpha heating (plus auxiliary heating)	300	300–400
Bremsstrahlung from plasma core	100	60–120
Mantle (Ne, Ar or Kr)	50	50–150
Divertor/SOL losses (CX, H, He, Be/C, Ne/Ar/Kr)	100	50–200
Divertor plate	50	50–100

Radiation by Bremsstrahlung in the core is important for ITER because of its low heating power density (0.13 MW/m^3) and its high density and temperature. At Z_{eff} of 1.6 (n_{He}/n_e ~ 10%, n_{Be}/n_e ~ 1%, n_{Ne}/n_e 0.3%.),100 MW are typically radiated by Bremsstrahlung . Edge radiation when seeding impurities (Ne or Ar assuming $\Delta Z_{eff} \sim 0.3$) has been estimated to be 40 to 100 MW with a simple model [11] and up to 110 MW with a 1-1/2 D model with multi-species impurity transport [12] (0.1% Ar). The remaining SOL power must remain above the H-mode power threshold, predicted to be between 50 and 200 MW in ITER. The nominal remaining power is 150 MW, whereas 200 MW are assumed for the modelling studies.

The predicted target power load depends strongly on the cross field transport (D, χ_i, χ_e) determined from model fits to experimental decay lengths, which in turn depend strongly on the accuracy of the separatrix location. Model validation has yielded a range of values for the transport coefficients; present modelling uses values in the high part of the range following recent experiments such as the consistency checks of separatrix position on JET [13]. Relative to JET, the power decay length for ITER is larger by a factor 1.5 for both Bohm transport and constant transport coefficients, smaller by a factor 1.1 for Gyro-Bohm and larger by a factor 3 for stochastic transport.

A set of calculations with B2-Eirene in ITER geometry with full multispecies transport assuming cross field transport as discussed above have been performed [4], [5] using Ne seeding to control the power onto the divertor targets. Because of the thermal force, the impurities peak near the edge of the SOL, where they do not radiate optimally. For values of impurity concentration and upstream density (0.5% Ne at the core-edge interface, n_s 4.5 10^{19} m^{-3}) typical for a burning ITER plasma, the divertor is in a semi-detached regime. Of the 200 MW flowing across the separatrix about 80 MW are radiated, with Ne ions, He ions, and neutrals contributing about equally. The strongly recombining fully detached state (Fig. 1c) found at higher Ne levels in [4] is transient; the transition to detachment and the operating window is being investigated in [5]. However, even the semi-detached operation characterised by the point at 0.7% Ne is found to yield peak power levels of 5 MW/m^2 (Fig. 1b), i.e. falls within the acceptable range similar to the value of 7 MW/m^2 found in [14] using EDGE2D/NIMBUS.

The divertor and pumping system must remove the He ash produced (2 $Pa\text{-}m^3s^{-1}$) to keep the core helium concentration below 10%. Most present experiments show similar confinement of He and background plasma in the core, with a He "enrichment" in the divertor of > 0.2 (divertor relative to separatrix) [15]. Attached operation on a vertical target would require that the He atoms traverse a relatively hot plasma toward the private flux region, yielding poor pumping. In a semi-detached or detached regime at low temperatures near the separatrix (below 5 eV), He pumping is improved. Modelling shows [4,5] that reasonable He partial

pressures are achieved in the private flux region only for a Ne concentration of 0.5% and above, for which the divertor plasma starts to detach. A He "enrichment" of 0.04 is found for strongly attached conditions, rising to 0.15 for semi-attached conditions (0.5% Ne point). The latter value yields a He partial pressure of 0.03 Pa above the 0.01 Pa that would be required at the designed net pumping speed of 200 m^3/s.

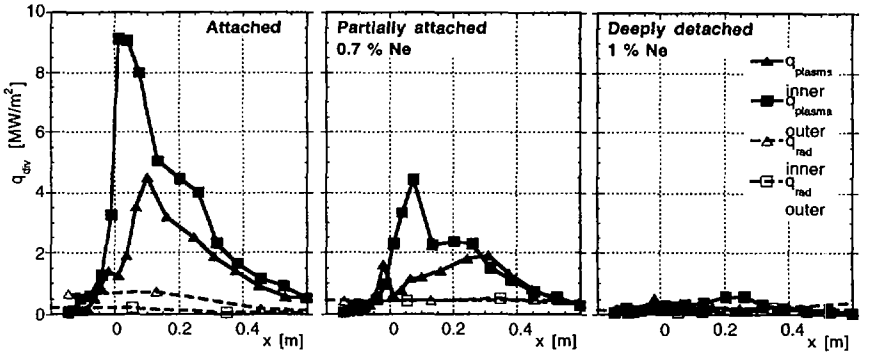

Fig. 1. Profiles of power load onto the divertor targets for the three cases: attached, partially attached and deeply detached [5].

These results together with similar results from EDGE2D/NIMBUS and UEDGE indicate that semi-attached operation on ITER is likely to provide an acceptable operating point in upstream density (4.5 10^{19} m^{-3}), impurity concentration (e.g. 0.5% Ne) , divertor power load (7-10 MW/m^2) and He partial pressure (0.03 Pa) for the vertical target divertor. The geometry and impurity mix must be optimised and the transport coefficients varied to optimise the operating window and scenarios.

4 OPERATIONAL LIMITS FOR DETACHED DIVERTOR REGIMES

Divertor operation is constrained by burn control and the edge density limit. Burn control requires control of the central plasma density, which is much less sensitive to edge fuelling variations than the divertor density, while the latter one determines the divertor state (detachment threshold). Two control loops are therefore required: one on deuterium fuelling to adjust the central density and another on impurity seeding to modify the impurity level and thus to maintain the divertor state. These control loops are best investigated by simpler models. Present results available for ITER stem from the PRETOR code coupled to a simple analytic divertor model [16]. The divertor model calculates the radiation losses in the divertor using Ar impurity seeding, the target power, the upstream temperature and the neutral density in the divertor (pumping). The edge density and impurity concentration are coupled to the core code, which also assumes a given He enrichment in the divertor of 0.2. The results [17] show that combined divertor and burn control is feasible in ITER (0.2% Ar needed to keep the target power < 50 MW) and that the core He concentration remains < 10%, allowing burn at 9.0 10^{19} m^{-3} line average density (n_S ~ 4.0 10^{19} m^{-3}). A more sophisticated 1.5-D edge model presently under development will be coupled to the ASTRA core plasma code in collaboration with the Canadian / EU Home Team. Both models must be calibrated against the more complete 2D models.

The second limitation is the edge density limit which is found experimentally (Greenwald limit) but for which there is no accepted physics based scaling. More

than one limit may be involved: a cold edge density limit (SOL collapse followed by marfe formation) and a hot edge limit (high density H-mode limit, ballooning modes triggering ELMS). Present machines find it difficult to exceed the Greenwald limit with H-mode confinement except at low current / low field together with high heating power or with deep pellet fuelling [18]. However, in the latter case the density profile peaks strongly and the edge density may remain below the Greenwald density.

Explanations for the cold edge density limit [19] require the SOL plasma to be fully detached, i.e. collapsed toward the X-point. Subsequently a marfe develops, cooling the X-point region, increase the density there (pressure balance) and finally might trigger instabilities causing a disruption. The power radiated from the marfe scales as n_{marfe}^2 (Prad α $n_m^2 czL(T)$) while n_{marfe} α n_s^3 (i.e. the upstream density varies only weakly with the power (as $P_{SOL}^{1/6}$)). However, the upstream density for onset of detachment and thus onset of this marfe varies as the square root of power, and depends also on the impurity concentration (and its radiation characteristic). The onset of detachment calculated by the model described in [16] is shown in Fig. 2 for typical ITER parameters and Ar as radiator. For ITER, therefore, a density limit based on this effect could lie well above the Greenwald density.

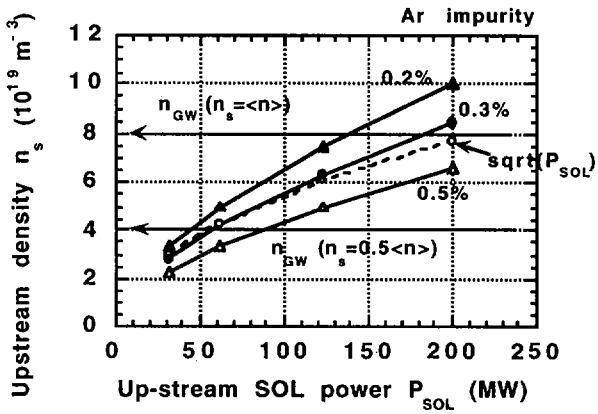

Fig. 2. Onset of detachment vs.upstream density and power with the Ar concentration as a parameter as calculated by the model of [16]. n_{GW} is the Greenwald limit.

A hot edge density limit could be inferred from recent observations on JET [20] where the frequency of type I ELMs increases when approaching the Greenwald density in H-mode, clamping the density and degrading particle confinement. This limit may be due to ballooning modes, as proposed in [21]. Since the edge temperature is essentially determined by SOL power (~ 150 eV for JET, ~300 eV for ITER), the pressure gradient limit for ballooning mode onset can be interpreted as an edge density limit.

ITER performance and divertor control probably will not be limited by the "cold edge density limit" since it is intended to operate far from full detachment. The "hot edge density limit" might pose a problem for ITER, but its value and the exact scaling with plasma parameters (e.g. pressure gradient scale length) has not yet been determined . However, it is expected [21] that its value can be influenced by plasma shaping. For both limits, the average core density can be increased by deeper fuelling.

5 CHOICE OF PLASMA FACING MATERIALS

The plasma facing materials (Be, CFC, W alloy) are chosen on the basis of erosion lifetime, tritium retention, potential contribution to radiation losses and Z_{eff} in the main plasma as well as mechanical considerations.

An assessment of the erosion lifetime of the divertor plates near the strike point due to sputtering, disruption thermal quench and slow high power transients has been carried out [22]. Physical sputtering for Be, CFC and W alloy and chemical sputtering for CFC (with a magnitude in accord with tokamak experiments) is considered. Erosion by disruption thermal quench assumes a 10% incidence of disruptions and includes vapour shielding (see references in [22]) which reduces the energy actually reaching the plate to a few percent. The erosion by slow high power transients of attached operation (20 MW/m^2 for 10 s in 10% of the shots) is evaluated without mitigating impurity radiation. Erosion of metals (Be, W alloy) by both disruptions and slow transients depends strongly on melt layer loss - 10% to 50% loss per event is assumed. To maximise the lifetime, the PFCs are made as thick as possible consistent with a maximum surface temperature requirement at nominal power in detached operation (1080K for Be, 1780K for CFC and W at 5 MW/m^2).

The erosion lifetimes of the divertor plates in the strike point region are shown in Fig. 3. The Be lifetime is low and dominated by slow transients, the CFC lifetime is determined by all three processes, and the W alloy lifetime is dominated by disruptions. For Be, the lifetime is inadequate, 120 - 320 shots. For W alloy, it is 2400 - 7700 shots, depending on the melt layer loss, and for CFC it is 5800 - 8200 shots, depending on the incident power (T dependence of chemical sputtering). For higher power semi-detached operation, the PFCs must be thinner than for fully detached operation (surface temperature requirement); at the same time, sputtering increases since a larger fraction (less radiation) of the SOL power is carried by particles and the plasma temperature in front of the divertor plate is higher (~20eV). However, high power transients become relatively less important since the difference between transient and normal operation is then smaller. Whereas the Be lifetime drops below 100 shots at 10 MW/m^2, more than 2000 shots for CFC and 1500 - 4000 shots for W alloy are still obtained.

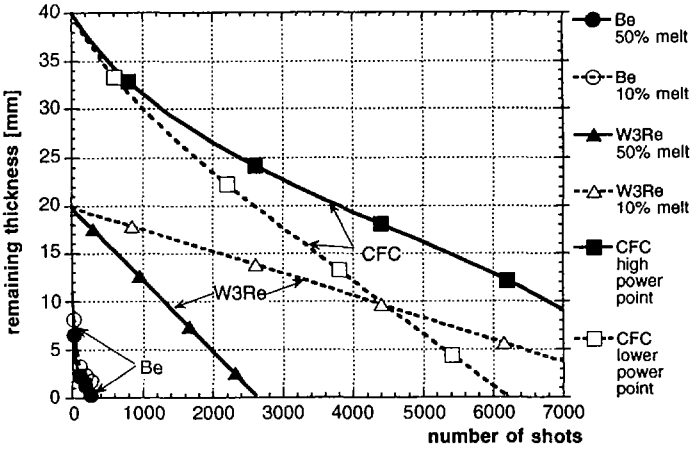

Fig. 3. Remaining thickness vs. shots for Be, CFC, and W alloy (W3Re used here) at nominal power of 5 MW/m^2 (90% redeposition). Melt loss varied for metals [22].

On the basis of this lifetime assessment and because a non-melting material is preferred at the strike zone for initial operation, CFC cladding 3-4 cm thick (depending on CFC type) has been chosen for the lower part of the vertical targets.

The erosion lifetime of the divertor side walls (upper part of vertical target, wings, dome, liner, baffle) is dominated by sputtering by neutrals, assumed to carry 0.5 MW/m^2 at average temperatures over 10 eV. The lifetime [22], is about 1000 shots for Be and several 1000 for CFC, too short for components (lower baffle) for which frequent replacement is not planned. In contrast, W has a lifetime of tens of thousands of shots at least, so that from lifetime considerations tungsten is chosen in this area.(The actual lifetime also depends on erosion and surface melting from the reradiated energy during a disruption thermal quench).

The first wall in the main chamber is clad with Be 1 cm thick. Since W displays bulk uptake of tritium 10 times lower than C or Be at a given impinging DT flux, its use in areas of high neutral flux will help to reduce the T inventory in the ITER vessel. In this context it is necessary to minimise the DT flux onto the Be-clad first wall (~2000 m^2), i.e. to maintain low neutral density in the main plasma chamber by providing an efficient neutral baffle at the divertor entrance.

6 DESIGN OF THE ITER DIVERTOR

The divertor must exhaust 150 MW (inboard) and 200 MW (outboard), corresponding to 300 MW conducted to the PFCs with allowance for variations in the in/out distribution. To this, 100 MW of neutron bulk heating is added.

A divertor assembly comprises 60 cassettes (each 5 m long, ~ 2 m high and 0.5 - 1.0 m wide, weighing 25 tons) installed on toroidal rails [23]. Each cassette assembly consists of a cassette body and high heat flux components, (Fig. 4) which are demountable in the Hot Cell.

Four vertical targets (VT), are attached to a cassette body, each having a water cooled > 100 mm thick stainless steel body onto which a water cooled copper alloy heat sink is mounted. The targets are clad with CFC monoblocks (30 mm thick) on the lower 600 mm and with W on the rest of the target. An advanced design consisting of a W brush (15 mm thick, 4.5x4.5 mm cross section) or a W lamella is under development in order to mitigate the otherwise excessive thermal stresses in

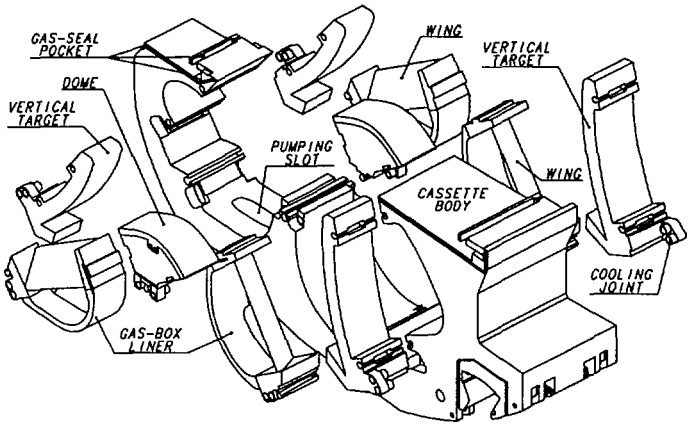

Fig.4. Exploded View of Divertor Cassette and PFCs.

operation (~ 5 MWm^{-2}) and during manufacture. The PFCs are designed for normal operation at < 5 MW/m^2 but the lower vertical target must accept 100 MJ/m^2 in 0.1 to 3 ms during disruptions, 10 MJ/m^2 during ELMs, and up to 20 MW/m^2 during slow transients (10 sec).

To mitigate degradation of the copper heat sink by neutron irradiation, the irradiation temperature must be kept within 150-350 °C (DSCu) and within 150-250 °C (CuCrZr), with tolerable excursions up to 350 °C for an hour. For the lower part of the vertical targets at 20 MW/m^2, this requires a monoblock or saddle block design. Therefore CFC monoblocks are used, brazed onto 10 mm Cu tubes with swirl tapes and a water velocity of 12 m/s, giving a critical heat flux of > 25 MWm^{-2}.

In the private region four tungsten clad (plasma sprayed) water cooled copper louvers or wings and gas box liners are mounted on the cassette body. The liners protect the SS cassette body and the wings improve momentum removal from the divertor plasma and thermalise the CX neutrals [1]. Two tungsten or beryllium clad domes below the X-point provide neutral baffling at the X-point and protect the wings from plasma contact. These HHF components are only required to withstand 5 MW/m^2. The wing nose design is similar to the vertical target design. The dome consists of a hypervapotron clad with a W brush or Be and mounted on a stainless steel dome block. A large R&D effort is underway to develop and assess the quality and reliability of the ~10^6 armour to heat sink joints in an ITER divertor [24], [25].

The overall coolant parameters adopted for the Heat Transfer System (HTS) dedicated to the divertor are: 140 °C inlet temperature, 1 m^3/s flow rate in each of four separate circuits, 4 MPa inlet pressure, and 1.5 MPa pressure drop in-vessel through the divertor. The CHF of the PFC heat sink designs with these parameters has been tested to be > 25 MW/m^2 for both swirl tapes and hypervapotrons [26].

The cassette body itself is a water-cooled rigid stainless steel structure to be built using either cast/HIP or powder/HIP technology. Internal cooling channels in the cassette body are optimised to reduce the temperature rise and thermal stress due to nuclear heating, to keep mechanical stresses within allowable limits for internal pressure and electromagnetic loads [27], to distribute the water flow to the HHF components, to allow rapid draining of the cooling water and to eliminate air pockets.

Because of their small angle to the field lines (as low as 1°), targets on adjacent cassettes must be well aligned and angled to shield the leading edges. A reasonable maximum step between targets on adjacent cassettes of 4 mm gives additional power load peaking factors of 1.35 outboard and 1.4 inboard. Normal manufacturing tolerances are sufficient for the cassette body, but precision machining of the dome and dump target support points and individual machining of the cassette support shoes is required to meet the 4 mm tolerance.

The attachment of the HHF-components and the design of the gas seals between the top of the divertor cassette and the vacuum-vessel outboard and inboard are described in [28]. The gas seals limit the gas leakage to the main chamber to < 5 $Pa \cdot m^3 \cdot s^{-1}$ or $1.35 \cdot 10^{21}$ particles/s at 1 Pa divertor pressure.

The cassette solution is fundamental to the remote maintenance concept, which is based on installation of a small number of integrated components inside the vessel to provide short RH times and high reliability. Connections to the cooling system and the locking mechanism are in an area of low neutron flux to permit frequent rewelding and bolting. The cassettes are mounted from the side (the last one from the port), avoiding access holes through the HHFC's. The divertor geometry (HHF-components) can be changed without modifying the interfaces to the machine.

Remote maintenance ([23]) is performed through four dedicated RH ports (one per quadrant) serving 15 cassettes each. Of these, 12 are 'standard' and two cassettes with diagnostic sensors are positioned on either side of a 'central' cassette carrying

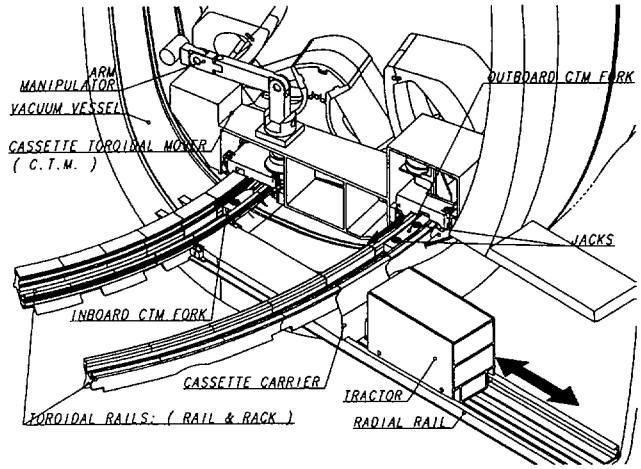

Fig 5. View of toroidal mover, the skid for standard cassettes or the toroidal mover and the radial tractor connected to the skid.

optical and/or micro-wave diagnostics. A Cassette Toroidal Mover (C.T.M.) handles the cassettes between their in-vessel location and the central position in front of the RH port. Not larger than a cassette, it is introduced in the vessel once the central cassette (in front of the RH port) and the second cassette (next to the central one) have been removed. It uses a dextrous manipulator arm which locks (bolting tool) the supports, earth-straps and gas seals, is guided by the toroidal rails and driven by two rack-and-pinion assemblies. It handles the cassette using three grips and two wheeled lifting forks inserted between toroidal rail grooves and the cassette bottom (Fig.5).

A Radial Tractor, driven by a rack-and-pinion and combined with a set of rolling carriers, handles the cassettes and the C.T.M. along the RH port radial rail, between the vessel and a transport cask outside the cryostat [23]. It includes a manipulator arm for RH operations inside the port (pipe handling, connections) and is supplied from the cask. This cask is also used to transport cassettes and tools between the Hot Cell and the machine.

Cutting and welding of the cassette water feeds (6 pipes per port connecting three cassettes) is performed in a parallel process . A set of hands-on assisted RH pipe tools cut, weld and inspect the pipe end caps outside the bio-shield (orbital tools) and the joints located inside the vessel (bore tools) between the cassette water-feeds and the fixed straight pipes inside the 20 ducts (Fig. 6). Due to radioactive corrosion products inside the pipework, the tools are confined in glove boxes or casks.

A preliminary assessment of replacement times for the whole divertor and for a single faulty cassette yielded less than 3 months and less than 2 month, respectively, times well below the required 6 months.

7 FUELLING AND PUMPING SYSTEM DESIGN

The fuelling / pumping system is designed to provide a range of fuelling rates based on the following considerations: replacement of the DT burnup requires 50 Pa-m^3/s assuming 10% He concentration in the core plasma, a He enrichment in the divertor of 0.2 (experimental; B2-Eirene gives 0.15) and a He production rate of 2

Pa-m^3/s for 1.5 GW of fusion power. The upper limit chosen for the fuelling rate is 200 Pa-m^3/s; a compromise between the need to generate some SOL flow for impurity entrainment (scaling from DIII-D based on SOL volume) and the pumping / T processing capability of the ITER plant. Up to 500 Pa-m^3/s are foreseen for up to 50 s for density ramp up as well as divertor and burn control actions. Control of the DT mix and of the divertor target power load requires the injection of up to three hydrogenic gases (D, T, DT) and of up to three impurity gases (e.g. Ne, Ar, He) at the same time. To mitigate local erosion of the first wall (0.2 mm Be after 10000 discharges) from CX sputtering five evenly spaced injection locations are provided around the torus at the top of the machine and in the divertor. An injection time response of ~ 0.5 sec, required for divertor and burn control, allows pipes 25 m long (10 mm diameter) from the injection valve to the plasma chamber.

The gas fuelling system consists therefore of 5 valve containers (6 injection valves each) evenly distributed around the torus inside the upper Heat Transfer vault and of 5 containers in the divertor level pit. Each valve container is connected through six gas fuelling lines (4 lines with 10 mm and 2 with 20 mm dia.) and a pumping flushing line (50 mm dia.) to a ring manifold at the equator. The gas supply lines are then routed into the gallery and through a vertical pipe shaft to the tritium plant. The valves inside each container are arranged for independent injection of 6 fuelling gases via a common 10 mm dia, discharge manifold (~20 m long) connected to the plasma chamber and the divertor volume, respectively. This manifold is also connected by a valve to the pumping /flushing line allowing flushing of gas injection lines as well as puffing tests. Two safety isolation valves controlled by the safety system can isolate the fuelling system from the torus in case of a pressure excursion, and can also stop fuelling of the plasma instantly to shut down the fusion power within ~ 10 sec. Two puffing valves also controlled by the safety system can bypass the flow controllers of two of the impurity injection lines to provide strong impurity puffing (~ 500 Pa-m^3/s) for an even faster fusion power shutdown (~ 3 sec) .

In addition to gas injection, a pellet fuelling system is provided to inject up to 100 Pa-m^3/s of hydrogenic species (3 to 8 mm pellets with 1.5 km/sec) for fuelling and also impurity pellets for physics experiments or wall conditioning. This pellet injection system consists of: (a) two centrifuge pellet injector drivers, (b) three extruders per injector, (c) a feed manifold for the gas supply (6 gas lines and a pumping/ flushing line), (d) a continuous regenerating cryopump per injector, (e) a flight tube per injector connected through an equatorial port to the plasma chamber, (f) a diagnostic, control & data acquisition system. The two pellet injector assemblies are installed inside a transport cask (6 m long x 4 m high x 3 m wide) located at the midplane. Each pellet injector is connected to the plasma chamber via a 5 cm diameter flight tube exiting in the gap between two blanket modules.

A stand alone "killer pellet" system (2 injectors) is also foreseen for rapid discharge termination as a part of the emergency shut down / disruption mitigation system. The requirement to provide a reliable and quick impurity pellet(s) based discharge termination leads to the choice of solid state pellets (Li, Be, B or C) and a simple injection system (e.g. pneumatic gun).

The primary pumping system for ITER comprises two major subsystems: the torus roughing system and the high vacuum system (cryo pumps). The former must perform two primary functions: to evacuate the torus to < 50 Pa from atmosphere in less than 60 hours with the torus back-filled with air, helium or nitrogen, and to regenerate the primary cryopumps to < 5% of their initial inventory in < 62.5 s during plasma burn. The latter requirement is the design driver for the roughing system (two mechanical pump sets, one for redundancy) located in the vacuum pump room [29].

The high vacuum system consists of 16 batch regenerating cryo sorption pumps designed to provide the required ~ 200 m^3/sec pumping speed in the divertor

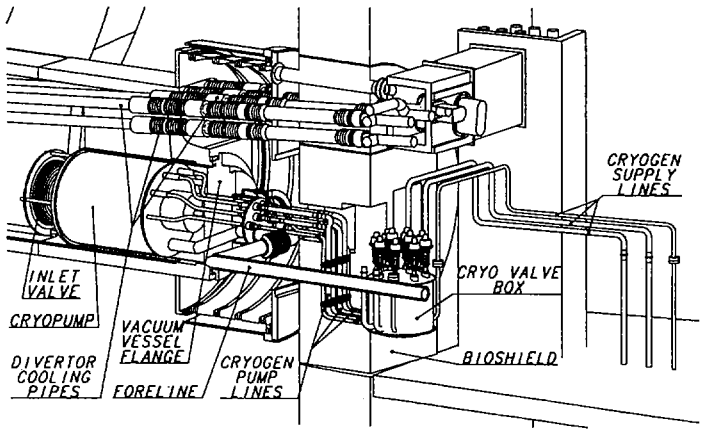

Fig 6. One of the 16 cryo pumps mounted in a divertor port. The divertor cooling pipes, the cryogenic lines and their routing through the bio shield as well as the cryogenic valve box and the roughing line can be seen.

private region (see section 2 to 4). The minimum gas throughput (D, T and He) of 50 Pa-m^3/s can thus be provided at ~ 0.3 Pa pressure in the divertor private region whereas the maximum throughput (200 Pa-m^3/s)requires 0.8 Pa. These or even higher pressures are readily observed during detached or semi-detached divertor operation in present day machines and when modelling the ITER divertor.

The cryo pumps are independently controlled to allow individual pumps to be regenerated, shut down in the event of failure, or to regulate the pumping speed. They consist of a cylindrical SS housing 1500 mm OD x 1500 mm long into which charcoal coated cryopanels (8 m^2 / pump) and an 80 K radiation shield are mounted. Each pump uses a pneumatically driven inlet valve to control the pumping speed and to isolate the pump from the torus during regeneration. The pumps are connected to a common ring manifold which in turn is connected to the torus roughing system for regeneration. Cooling is done with supercritical and gaseous helium at three inlet temperature levels: 4.5K for the cryopanels, 80K for the inlet gas baffle and radiation shields, and 300K for the inlet valve which receives heat by radiation and conduction from the 400K duct (see also [30]). Each cryopump is mounted to the inside of the vacuum vessel port closure flange within the divertor port duct (Fig. 6). The cryopump and port closure flange form an integral assembly which is installed and removed as one unit using a remote handling cask and tools similar to the one described for the divertor. Six cryogenic supply lines and a double contained 150 mm diameter foreline pipe which is connected to the regeneration ring manifold exit the back of the cryopump/flange assembly. The cryogenic lines are routed to a vacuum insulated valve box located on the back of the bioshield plug which provides flow and control of cryogens to the pump. The cryogen valve boxes are supplied by common cryogenic ring manifolds which run toroidally under the divertor pit floor.

To maintain the tritium inventory in the pumping system below the allowable 200g a rapid regeneration cycle is employed with a pump starting regenerating every 62.5 sec. At any given moment during the plasma discharge 12 pumps are in pumping mode and 4 pumps are in various states of regeneration: namely rapid warm-up to ~80K, gas desorption and evacuation and rapid cool down. Thus each

cryopump will pump for 750 s followed by a 250 s regeneration cycle. The tritium content in the 16 cryopumps thus reaches a maximum steady state value of 140 g after 750 sec. The total 4.5 K refrigeration required to operate the cryopumps is an estimated 20 kW and depends on the flowrate required for rapid cool down [30].

8 SUMMARY

The physics operation scenario for the ITER divertor and the chosen divertor geometry are in line with the present knowledge of SOL and divertor physics. Some uncertainties concerning the co- existence of divertor heatflux control and good main plasma confinement as well as the possible limitations of the plasma edge density are presently under investigation inside the JCT and in the home teams (expert groups). The design of the divertor HHF-components and of the remote maintenance approach is backed by initial R&D results with further results, in particular from the two large projects described in [24] and in [31], expected between now and the end of the EDA.

The fuelling and pumping system design can meet all the requirements for a burning plasma operation and provides enough flexibility for a wide range of physics investigations. The vigorous R&D program under way for both fuelling and pumping systems [30] has started to produce results guiding further refinements in the design.

REFERENCES

[1] JANESCHITZ, G., et al., J. Nucl. Mater. **220–222** (1995) 73.
[2] JANESCHITZ, G., et al., in Controlled Fusion and Plasma Physics (Proc. 20th Eur. Conf. Lisbon, 1993), Vol. 17C, Part II, European Physical Society, Geneva (1993) 559.
[3] POST, D.E., J. Nucl. Mater. **220–222** (1995) 143.
[4] KUKUSHKIN, A., et al., in Plasma–Surface Interactions (Proc. 12th PSI Conf. St. Raphaël, 1996), to appear in J. Nucl. Mater.
[5] KUKUSHKIN, A., IAEA-CN-64/FP-27, this volume.
[6] MATTHEWS, G.F., J. Nucl. Mater. **220–222** (1995) 104.
[7] PARKER, R., et al., in Plasma–Surface Interactions (Proc. 12th PSI Conf. St. Raphaël, 1996), to appear in J. Nucl. Mater.
[8] LIPSCHULTZ, B., et al., in Controlled Fusion and Plasma Physics (Proc. 22nd Eur. Conf. Bournemouth, 1995), Vol. 19C, Part III, European Physical Society, Geneva (1995) 325.
[9] FONCK, R.J., et al., J. Nucl. Mater. **128 & 129** (1984) 330.
[10] GRUBER, O., et al., Phys. Rev. Lett. **74** (1995) 4217.
[11] POST, D.E., et al., in Plasma–Surface Interactions (Proc. 12th PSI Conf. St. Raphaël, 1996), to appear in J. Nucl. Mater.
[12] MANDREKAS, J., et al., Nucl. Fusion **36** (1996) 917.
[13] LOARTE, A., et al., in Plasma–Surface Interactions (Proc. 12th PSI Conf. St. Raphaël, 1996), to appear in J. Nucl. Mater.
[14] VLASES, G., et al., in Plasma–Surface Interactions (Proc. 12th PSI Conf. St. Raphaël, 1996), to appear in J. Nucl. Mater.
[15] NAKAMURA, H., et al., Phys. Rev. Lett. **67** (1991) 2658.
[16] SUGIHARA, M., et al., in Plasma–Surface Interactions (Proc. 12th PSI Conf. St. Raphaël, 1996), to appear in J. Nucl. Mater.
[17] BOUCHER, D., et al., IAEA-CN-64/FP-22, this volume.
[18] LANG, P.T., et al., in Controlled Fusion and Plasma Physics (Proc. 22nd Eur. Conf. Bournemouth, 1995), Vol. 19C, Part II, European Physical Society, Geneva (1995) 449.
[19] BORRASS, K., et al., Rep. IPP 5/70, Institut für Plasmaphysik, Garching, Germany (in preparation).

[20] JET TEAM (presented by D. STORK), IAEA-CN-64/A1-1, these Proceedings, Vol. 1, p. 189.
[21] PERKINS, F.W., IAEA-CN-64/FP-23, this volume.
[22] PACHER, H.D., et al., in Plasma–Surface Interactions (Proc. 12th PSI Conf. St. Raphaël, 1996), to appear in J. Nucl. Mater.
[23] MARTIN, E., et al., in Fusion Technology (Proc. 19th SOFT Lisbon, 1996).
[24] ULRICKSON, M., et al., IAEA-CN-64/FP-4, this volume.
[25] VIELDER, G., et al., in Fusion Technology (Proc. 19th SOFT, Lisbon, 1996).
[26] SCHLOSSER, J., et al., ibid.
[27] CHIOCCHIO, S., et al., ibid.
[28] ANTIPENKOV, A., et al., ibid.
[29] LADD, P., et al., ibid.
[30] MURDOCH, D., et al., IAEA-CN-64/FP-5, this volume.
[31] MAISONNIER, D., et al., IAEA-CN-64/FP-16, ibid.

DISCUSSION

D.N. HILL: Given that present vertical target experiments show low density detachment at $q_{\parallel}$ power levels similar to those projected for ITER, and that ITER will run at high density, how do you plan to control the degree of detachment to maintain an adequate operating window?

G. JANESCHITZ: Extrapolation to ITER from present day machines for such detailed questions can only be done with 2-D edge models such as B2-Eirene. This kind of modelling predicts that we will always need moderate scaling of impurities to achieve detachment. Therefore, we do not expect to have a problem in controlling detachment.

A.GIBSON: Do your modelling calculations take account of the charge exchange interactions with the tungsten surfaces? If so, to what extent do you expect tungsten to contribute to the bulk plasma radiation loss?

G. JANESCHITZ: At present, the B2-Eirene modelling does not treat W production or transport. Independent assessment of W sputtering from charge exchange neutrals, and the assumption of a retention factor of 100, which is backed by experimental results, give less than 10^{-5} W concentration in the main plasma. A more detailed treatment may be possible in the future.

SAFETY CHARACTERISTICS OF ITER*

Y. SHIMOMURA, R. AYMAR, H. BARTELS, C. GORDON,
W. GULDEN[1], D. HOLLAND, H. IIDA, T. INABE[2], M. ISELI,
A. KASHIRSKI, B. KOLBASOV[3], M. KRIVOSHEEV[4], G. MARBACH[5],
K. McCARTHY[6], S. MOROZOV, A. NATALIZIO[7], D. PETTI[6], S. PIET,
A. POUCET, J. RAEDER, G. SAJI, Y. SEKI[2], L. TOPILSKI
ITER Joint Central Team

Abstract

SAFETY CHARACTERISTICS OF ITER.

The safety and environmental characteristics of ITER, with representative safety assessment results, are described. Fusion has built-in safety characteristics without depending on layers of "safety protection systems". Safety considerations are integrated into the design by making use of the intrinsic safety characteristics of fusion, which are adequate for the moderate hazardous inventories. A systematic nuclear safety approach has been applied to the design of ITER, and the safety assessment of the design shows how ITER will safely accommodate uncertainties, flexibility of plasma operations, and experimental components, all of which are fundamental in ITER, the first experimental fusion reactor.

1. INTRODUCTION

Magnetic fusion has basic favorable safety characteristics as follows:

• The reaction is self-limiting bounded by the ß-limit of the plasma. The conditions for maintaining an ignited plasma are so stringent that off-normal events will generally terminate the reaction. The total amount of fuel in the plasma is only a few tenths of a gram and the plasma cannot remain ignited for longer than about ten seconds without fueling. Under any failure conditions with any primary coolant or air leakage into the plasma vessel, the fusion reactions are physically impossible.

---

[1] NET Team, Max-Planck-Institut für Plasmaphysik, Garching, Germany.
[2] Japan Atomic Energy Research Institute, Ibaraki, Japan.
[3] Kurchatov Institute, Moscow, Russian Federation.
[4] Efremov Institute, St. Petersburg, Russian Federation.
[5] Idaho National Engineering Laboratory, Idaho Falls, Idaho, USA.
[6] Centre d'études de Cadarache, Saint-Paul-lez-Durance, France.
[7] Canadian Fusion Fuels Technology Project, Mississauga, Ontario, Canada.

• Fusion power density and radioactive decay heat densities are moderate. Therefore structural melting of the plasma vessel is physically impossible and fast acting emergency cooling systems are not required.

• The ultimate performance of confinement barriers that needs to be assured in accidents will be about one order of magnitude reduction for tritium and mobilizable metallic dust for ITER, whereas six to seven orders of magnitude reduction is required for iodine and rare gas in fission power reactors.

• Activation products are produced by the interaction by the neutron with structural materials surrounding the plasma; however, the quality and half-lives of these products are determined by the choice of materials.

The ultimate objectives of developing fusion energy undoubtedly include fulfilling its potential to be a safe and environmental benign energy source. Some safety issues are specific to the design choice of ITER as an experimental machine, e.g. relatively high activation of in-vessel components made of SS316LN, and are not necessarily representative of a future commercial fusion plant. It is, however, important to keep in mind that fusion has further advantageous safety characteristics, where safety can be improved by further development such as low activation material. Safe operation of ITER itself will help demonstrate fusion's safety and environmental potential in areas such as personnel exposure, effluent control, and machine control. Data gathered through the progressive stages of operation will provide validation of safety data and analyses. In addition, the test program will provide information to improve the safety design of future fusion devices.

ITER is a research facility. The experimental nature of ITER requires a design that permits uncertainties and flexibility of plasma operation, facilitates experimentation and accommodates changes. Changes for example could include testing of alternative divertor designs and different blanket designs. These needs drive the safety design to provide robust safety envelopes and to minimize the safety role and influence of plasma operations and experimental components; and this report presents how these safety considerations have been integrated in the ITER design by applying a well-established nuclear safety approach[1], and how ITER will be safe.

2. RADIOLOGICAL AND ENERGY SOURCE TERMS AND THEIR CONTROL

2.1. Radiological Source Terms

2.1.1. Tritium sources and their control

The total site inventory of tritium is limited to 3 kg excluding the long-term storage capability of 1 kg. Only a fraction can be mobilized at high temperature which may occur in the course of accidents.

Tritium inventory in each primary coolant loop is less than 0.01 kg and is well controlled by the detritiation system.

The total inventory in the tritium plant is about 0.5 kg. It is segregated into sub-inventories and the technology is well established. The tritium inventory in the cryopump system located inside the vacuum vessel is under 0.2 kg. This inventory is vulnerable to escape in the event of accident.

The plasma facing components are beryllium for the first wall, carbon for components subjected to very high heat flux such as the divertor targets, and tungsten for those subjected to very high neutral particle flux such as the divertor throats. Beryllium and carbon eroded by plasma-wall interaction form dust and co-deposited layers, which are rich in tritium. The tritium inventories co-deposited with carbon and beryllium and the inventory in loose dust could be mobilized in the event of steam or air ingress. Therefore, an administrative limit, currently 1 kg-T for safety analysis, was set which corresponds to about 1000 discharges, equivalent to about one year of operation. The total amount of tritium inventories of the bulk of the plasma facing material is also limited to 1.5 kg. Only a very small fraction of tritium in the bulk could be mobilized in an accident. In order to keep the inventories in the vacuum vessel within acceptable values, removing methods of tritium will have to be prepared for ITER operation and applied if the accumulation was found close to the limit after operation. Release of tritium from the vacuum vessel is controlled as follows: First, the amount of gaseous tritium is very small (<1 g-T) since the tritium in the vacuum vessel is mainly implanted in the in-vessel components or deposited with dust or on the cryopump. Therefore, only a fraction of this could be mobilized in accidents. It is conservatively assumed that 100% of the vulnerable tritium (1.5 kg) is at risk in an extreme situation. Second, there are natural confinement barriers available to confine these mobilizable inventories. Most notably, the vacuum vessels and the cryostat required for tokamak operation; these are woven into the confinement strategy. The plasma vacuum vessel is located inside the cryostat which comprises a part of the secondary confinement barrier. Third, the cryostat is housed in a tokamak building, part of this supplements the confinement barriers with active building ventilation systems.

2.1.2. Dusts and their control

For the safety analysis, dust is assumed to include 100 kg of tungsten, 100 kg of beryllium and 200 kg of carbon. These values are conservative but there are large uncertainties in dust products and therefore the quantity of dust will be monitored and removed if the accumulation of dust was found close to the limit after operation. Control of release of this dust is the same as that of tritium described in the previous sub-section (2.1). Oxidation-driven volatility of in-vessel metal, e.g. tungsten, is not significant at ITER accident temperatures since passive mechanisms limit temperatures to below 500°C for the first wall and 600°C for the divertor.

2.1.3. Active corrosion products and their control

There is uncertainty in the corrosion product inventory in copper alloy tubes which are used in the divertor loops and therefore intermediate loops are employed in this coolant system. In other systems, stainless steel is used and the corrosion product inventory is conservatively assumed to be 10 kg per loop in safety analysis. The amount of corrosion products and their release will be controlled by conventional methods.

Maximum mobilizable radiological inventory and relevant control strategies are summarized in Table I.

TABLE I. MAXIMUM MOBILIZABLE RADIOLOGICAL INVENTORY AND CONTROL STRATEGIES

"At risk" inventory	Maximum "at risk" inventory	Relevant control strategies
In-vessel co-deposited tritium	1 kg-T	Control layer buildup; provide confinement
In-vessel diffusively held tritium plus tritium in cryopumps	0.5 kg-T	Keep temperatures below ~600°C for short term, ~300°C for long term; keep oxidizers away; provide confinement
In-vessel dust	100 kg-W 100 kg-Be 200 kg-C	Keep mobilizing gases out; control dust inventory; provide confinement
Tritium in water coolant	100 g-T	Control inventory; provide confinement
Corrosion products in water coolant	10 kg metal	Control dissolved oxygen in water; control pH and water chemistry
Tritium plant circulating inventory	0.5 kg-T	Control inventories; provide confinement

2.2. Fusion Power, Plasma Energy and Their Control

Fusion reactions are easily terminated if necessary. Under any failure conditions with any primary coolant or air leakage into the plasma chamber, the reactions are physically impossible and therefore fusion reactions cannot aggravate the release. The conditions for maintaining ignited plasma are so stringent that off-normal events will generally terminate the reactions. The termination, however, frequently induces disruptions which could damage the first wall and its cooling pipes. There are uncertainties in the damage; therefore the vacuum vessel is designed to release leaked steam into the suppression tank and to keep accidental pressure less than 500 kPa in the case of in-vessel cooling water leakage. This design accommodates uncertainties of plasma-wall interactions due to disruptions and all possible damage of the in-vessel components (first wall, baffle, limiter, or divertor).

2.3. Nuclear Energy and Its Control

The decay heat comes mainly from in-vessel components and is a function of the operating scenario. A conservative calculation gives the total decay heat of 38 MW immediately after shutdown, 6 MW averaged during the first day and only 1.8 MW averaged during the first week. This decay heat is removed by the normal facility cooling systems or by the passive vacuum vessel cooling system of 3 MW heat removal capacity only with natural circulation and does not require emergency cooling systems, even for extremely unlikely events. The vacuum vessel heat transport system can remove decay heat via natural circulation indefinitely.

2.4. Chemical Energy: Beryllium-Steam Reaction and Its Control

Steam leaked in-vessel can chemically react with beryllium if the beryllium temperature is high, potentially generating hydrogen. Such a situation is avoided by controlling the temperatures of the first wall. The plasma will automatically passively terminate before the beryllium temperature reaches the breakoff point for self-sustained chemical reaction(2). Active plasma shutdown systems are provided to further minimize the beryllium temperature and the hydrogen generation immediately after plasma termination. The vacuum vessel cooling system can remove decay heat passively by natural circulation and prevent long-term, slow reactions.

3. EFFLUENTS AND WASTE DURING OPERATION

Effluents during normal operation come mainly from the coolant systems, from outgassing during maintenance operations and from the tritium plant, and can be estimated from tritium permeation through the first wall into the primary coolant and coolant losses scaled from operational experience data of CANDU plants to the ITER case. CANDU experience is used because the expected tritium level at ITER is compatible and similar technology would be applicable. Preliminary conservative extrapolation indicates that the ALARA principle is well integrated in the design, i.e. effluents are less than 1 g-T/a which is the ITER design release limit for HTO.

As to the wastes, since SS316LN is used, the waste streams are not representative for a future commercial fusion power reactor. The SS316LN generates long-lived induced activation, including ^{99}Tc, ^{94}Nb, ^{60}Co, and $^{192\text{-}192m}Ir$ from impurities. The major active wastes are from structural materials of the in-vessel components. The higher activity and more prone-to-wear portion of the in-vessel components are designed to be replaceable to implement waste volume minimization. Wastes emit gamma rays and further decay is needed prior to disposal. However, the necessary cool-off time is several tens to hundred years and not by any means the geological time scale typical for fission high level waste. These structural materials are not chemically active and their biological effects are in the category of moderate risk.

4. ANALYSIS OF REFERENCE EVENTS AND ULTIMATE SAFETY MARGINS

A set of ITER reference accident sequences is analyzed to assess whether the ITER design has adequately implemented top level safety and environmental criteria. The analysis of the reference events was carried out starting from Postulated Initiating Events to all consequential failures including environmental releases, if any.

4.1. Plasma

Malfunction of the plasma control is investigated by postulating increased fueling or sudden injection of all the auxiliary power available into an ignited plasma. An unexpected doubling of the confinement time is investigated as part of the uncertainties in plasma physics. Plasma density and ß-limits are assumed in an optimistic way to conservatively assess the maximum fusion power transients. Up to 3.5 GW of fusion power can be reached transiently but no damage to in-vessel components is expected from these transients. Plasma disruptions are included in the normal operational regime.

Large uncertainties exist in the estimation of the possible damage of the plasma facing components from worst case disruption. This fact is accommodated by a very robust design of the vacuum vessel pressure suppression system which can safely handle the maximum possible damage of plasma facing components. Consequently, no release is expected due to plasma transients.

4.2. Cooling System

A large family of accidents are grouped around the ITER cooling systems. Sequences starting with postulated loss of coolant or flow in various cooling loops and locations have been investigated. The pressure suppression system limits the maximum pressure within the vacuum vessel to below 500 kPa. The pressure suppression system also captures the majority of mobilized tritium and activated dust when actuated passively via rupture disk (at 200 kPa) or actively via bleed lines (at 110 kPa). This capability allows uncertainties of plasma wall interactions and any possible failures of the in-vessel components alone do not induce any radioactive release.

In case of ex-vessel coolant loss with continued plasma burn, the plasma facing components can potentially reach high temperatures and produce hydrogen by reacting with steam in cases of an additional failure of in-vessel components. There are two typical cases for a very large ex-vessel coolant loss: case 1 is for the divertor with very high heat flux and case 2 is for the normal shielding blanket with moderate heat flux. In case 1, the temperature of the divertor target increases rapidly. A temperature of about 1100°C in the coolant pipe will be reached within about 30 s and can melt coolant channels if the fast fusion shutdown does not work (Fig. 1). Even if the plasma is terminated, there is a possibility that the in-vessel divertor channels will undergo damage because of the fast disruption that could be caused by the shutdown. In this case with beryllium armors, hydrogen is produced by steam-Be reactions because of the high surface temperature of Be. The surface, however, is rapidly cooled because of

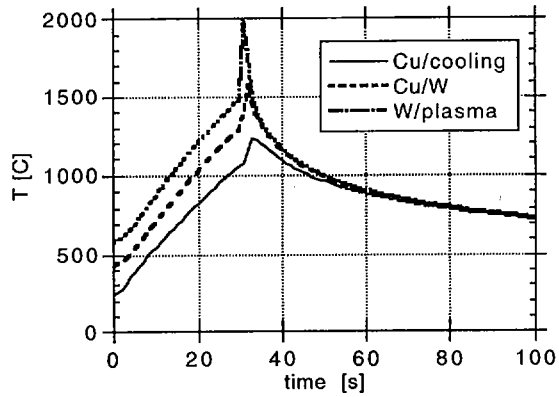

FIG. 1. Temperature transient for the divertor structure during coolant flow blockage event. The plasma heating is stopped when the copper structure in front of the coolant is completely melted. The thermal load due to a disruption at plasma shutdown was included in the analysis. (W/plasma: tungsten was assumed as armor in this calculation.)

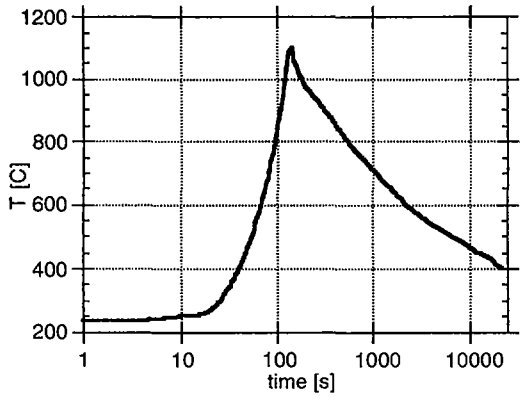

FIG. 2. Temperature transient of the first wall during large ex-vessel coolant leak. The plasma heating is stopped when the first wall reaches 1100°C.

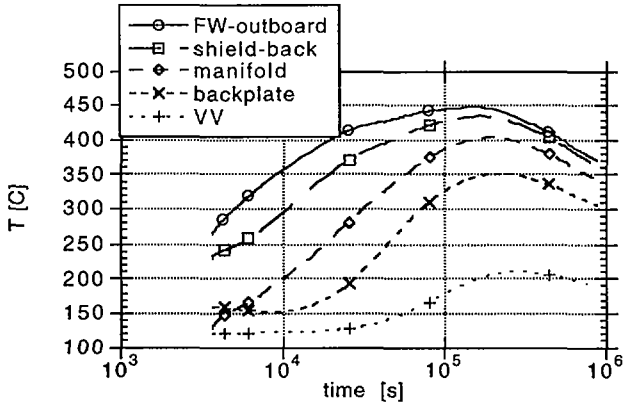

FIG. 3. Shielding blanket temperature increase due to decay heat after loss of coolant of in-vessel components. The vacuum vessel is assumed to be actively cooled. The heat transport is due to natural radiation, steam gap convection and heat conduction. (FW: first wall, VV: vacuum vessel.)

large temperature gradient and residual coolant (Fig. 1). Therefore the amount of produced hydrogen is only <0.1 kg and there is no safety concern. In case 2, the affected shield blanket coolant pipe temperature increases slowly and reaches about 1000°C after about 200 sec if the fusion power is not terminated. Then the plasma will be spontaneously terminated because of beryllium influx at about 1100°C which is low enough to prevent a self-sustaining chemical reaction, but failure of the coolant pipe may occur and the amount of hydrogen could be large because the surface temperature

decreases very slowly due to the small temperature gradient and small residual coolant (Fig. 2). Even here, for best-estimate chemical reaction rates, the hydrogen production is within the ITER design limit of 10 kg[3], i.e. 4.2 kg, but relatively large. For case 2, however, there is sufficient time (several minutes) to terminate softly fusion power. If the normal plasma control system does not work, the fast shutdown system of two trains terminates the power, the maximum temperature is about 800°C and the hydrogen production is only 0.15 kg. The long-term decay heat removal is assured by two independent methods to keep the maximum first wall temperature below 500°C and to avoid long and slow steam-beryllium reactions (Fig. 3). In conclusion, hydrogen production is always kept below tolerable limits that avoid deflagration in the vacuum vessel.

4.3. Vacuum Vessel Penetrations

Although all vacuum vessel penetrations are designed with care to supply two containment barriers, because of the large number of these penetrations it was considered prudent to postulate failure of a penetration line. A loss of vacuum event results from this. The eventual small leakage out of the vacuum vessel is truncated by planning for operator action to start the vacuum vessel pumping system (one hour after the accident is assumed in the analysis). This will allow clean-up of the contaminated vacuum vessel atmosphere. A small in-vessel coolant leak with failure of one vacuum vessel penetration line is also investigated. The vacuum vessel pressure suppression system limits the possible driving pressure for expulsion of in-vessel materials through the bypass. Several confinement options are investigated to show compliance with ITER design release limits.

4.4. Magnet and Cryostat

Several cases of failures in the magnet system are analyzed and their impact on other systems is found to be minimal. Possible damage to neighboring confinement barriers is investigated by postulating air, water and helium ingress into the cryostat. Environmental releases are small due to the small source term involved in cryostat accidents. Failures in the tritium plant are analyzed to demonstrate the adequacy of confinement.

4.5. Ultimate Safety Margins

Even in the most severe case of extremely unlikely events (Category IV, frequency = (10^{-4}-10^{-6}/a)[4]), the conservatively calculated tritium release due to the failure is less than the conservatively defined ITER design release limit (10 g ground release or 100 g elevated release) by a factor of about 10 and metallic dust release is also less than the release limit (50 g ground release) by a factor of about 5. In ITER, structure melting of the vacuum boundary is physically impossible since there would be no fusion power after such failures and due to the low decay heat. Therefore the safety functions degrade gracefully and the release cannot increase abruptly even beyond the extremely unlikely sequences i.e. in hypothetical sequences (Category V). For all other cases, it is also confirmed that there are no adverse edge effects of failures just outside the boundary of the extremely unlikely events.

For a "no-evacuation limit", 50 mSv early dose to the public is recommended by the "International Basic Standards for Protection against Ionizing Radiation and for the

TABLE II. TOLERABLE RELEASE FRACTIONS (%) TO MEET CATEGORY IV DOSE LIMIT AND CATEGORY V NO-EVACUATION OBJECTIVE

Event sequence category	Extremely unlikely sequences (Category IV)	Hypothetical sequences (Category V)	
Criteria	GSEDC dose limit [4]	50 mSv early dose, illustrative for siting and "no-evacuation"	
Weather	Worst case	Average	Average
Release height	Elevated	Elevated	Ground level
Tritium as HTO from in-vessel	7	100	30
Tritium as HTO from a single tritium plant system	30–100	100	100
Tritium as HT from either in-vessel or tritium plant	100	100	100
Metal from plasma-facing surfaces via dust	0.5	100	50
Metal from plasma-facing surfaces via volatility	100	100	100
Metal from steel/water corrosion products	5	100	50

Safety of Radiation Sources", IAEA Safety Series No. 115, 1996. This number at 1 km from the release point corresponds to the ground level release of 500 g tritium in HTO, which is about 30% of the maximum possible mobilized tritium in ITER and 50 times of the maximum possible release calculated in Category IV. Tolerable release fractions to meet Category IV dose limit and Category V No-Evacuation are summarized in Table II, which shows that only modest confinement capability or elevated release is required to preclude off-site evacuation.

5. CONCLUSIONS

(a) A high level of safety is integrated into the ITER design.

The design incorporates the well-established concepts of Defense in Depth and multiple lines of defense to attain high confidence in the reliability of critical safety features of the facility and ensure protection against postulated accidents.

(b) Radioactive effluents and emissions during normal operation are low.

Preliminary estimates show that these releases are well within ITER design release limits established in accordance with internationally accepted criteria and the principles of ALARA.

(c) The ITER design ensures protection of the public.

To assess the effectiveness of implementation of these safety functions in the ITER design, a comprehensive analysis of 25 different Reference Accident sequences has been performed using the best safety analysis computer programs available

worldwide. The analysis included conservative assumptions of initial facility operating and accident conditions. The results showed that radioactive releases for all 25 of these Reference Accidents are well within the conservative limits and there are no adverse edge effects of failure just outside the boundary of extremely unlikely events. It is also concluded that only modest confinement capability or elevated release is required to preclude off-site evacuation.

It is concluded that ITER could be constructed and operated without undue risk to the health and safety and without significant environmental impacts.

REFERENCES

[1] Technical Basis for the ITER Interim Design Report, Cost Review and Safety Analysis, ITER EDA Documentation Series No. 7, IAEA, Vienna (1996) IV-6.
[2] AMANO, T., Passive Shut-Down of ITER Plasma by Be Evaporation, Natl Inst. for Fusion Science, Nagoya (1996).
[3] Technical Basis for the ITER Interim Design Report, Cost Review and Safety Analysis, ITER EDA Documentation Series No. 7, IAEA, Vienna (1996) II-41.
[4] Ibid., p. II-29.
[5] Ibid., Appendix II-8.

DISCUSSION

R.J. GOLDSTON: A dose of 50 mSv seems rather high — under average weather conditions — to avoid the requirement for an evacuation plan. Have you determined that this level is acceptable to each of the ITER partners?

Y. SHIMOMURA: Some partners have no evacuation plan. Some partners have a higher value. Under the worst weather conditions and other most conservative conditions, the release limit would be an order of magnitude less than the reference case (IAEA recommendation). In any case, the requirement will be determined by the host party, but we have a margin and I don't expect any significant design change.

ITER MAGNETS AND PLASMA CONTROL*

ITER JOINT CENTRAL TEAM AND HOME TEAMS

Presented by M. Huguet[1]

Abstract

ITER MAGNETS AND PLASMA CONTROL.

The ITER magnet system comprises 20 Toroidal Field (TF) coils, a Central Solenoid (CS) and 7 Poloidal Field (PF) coils. The TF coils operate at a maximum field of 12.5 T with a total stored energy of about 100 GJ. The TF coils are bucked on the CS and enclosed in stainless steel cases that form the major part of an integrated mechanical structure. This structure resists the gravity, electromagnetic and seismic loads. The CS weighs about 1300 t and provides about 140 MA·turns with a maximum field of 13 T. The PF coil system comprises 7 coils for plasma shape and position control. The ITER magnets will require about 1200 t of Nb_3Sn strand for the TF coils, CS and two of the PF coils, and 650 t of NbTi strand for the other PF coils. A worldwide R&D programme is underway, the main activity of which is the manufacture of model coils. Construction of these coils has started and the initiation of the test programme is scheduled for mid 1998. The PF coil system provides adequate flexibility for the reference operation scenario at a plasma current of 21 MA and for a range of alternate scenarios. An alternate CS design is being considered to provide better control of the position of the divertor separatrix, improve the plasma shaping capability and expand the range of operational flexibility.

1. INTRODUCTION

The International Thermonuclear Experimental Reactor (ITER) is a tokamak with a nominal plasma major radius of 8.1 m, plasma minor radius of 2.8 m, elongation of about 1.6 and plasma current of 21 MA. The toroidal magnetic field at the major radius is 5.7 T. The project goals include the demonstration of controlled burn of DT plasmas for a duration of about 1000 s. The average neutron loading at the first wall will be about 1 MW/m^2 and a total fluence of at least 1 MWa/m^2 should be achieved for blanket and material tests [1].

---

[1] ITER Naka Joint Work Site, 801-1 Mukoyama, Naka-machi, Naka-gun, Ibaraki-ken 311-01, Japan.

The magnet system comprises 20 Toroidal Field (TF) coils, the Central Solenoid (CS), 7 Poloidal Field (PF) coils, and a mechanical structure. In addition, PF correction coils provide a small component (about 10^{-4} of the toroidal field) of magnetic field to correct some components of non-axisymmetric field errors. All ITER coils are superconducting and use either Nb_3Sn or NbTi superconducting material depending on the field value at the conductor. The magnet system is designed for up to 50,000 tokamak pulses. The magnets and structures are located within a cryostat which provides the vacuum for thermal insulation from the ambient heat load.

The paper will review the overall mechanical design of the magnet system, describe the designs of each type of coil and the conductor design. The magnet R&D programme is then briefly outlined. The paper concludes with an overview of plasma control aspects and the description of a segmented CS design option.

2. MECHANICAL DESIGN

Magnet systems are permanent components of the machine and must be designed to achieve maximum reliability and a fatigue life compatible with at least 50,000 tokamak pulses. At the same time, the space available for structures is limited for design efficiency and optimum tokamak performance.

These considerations have resulted in a strongly integrated mechanical design with mutually compensating force systems. As a result, the TF coils are bucked on the CS and the TF coil cases, which form the main structural component of the tokamak, integrate all coils and the Vacuum Vessel into a single mechanical system to contain and equilibrate the gravity, electromagnetic and seismic loads [2]. An elevation of the magnet systems is shown in Fig. 1.

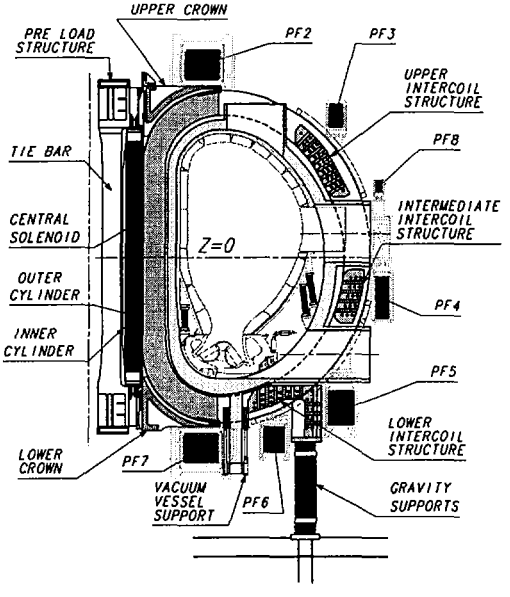

FIG. 1. ITER mechanical design.

2.1 Containment of in-plane loads acting on the TF coils

The tensile hoop loads in the D-shaped TF coils are contained partly by the radial plates that support the conductor and partly by thick coil cases described in section 3. The centripetal force acting on each of the TF coils is essentially reacted by the CS assembly. This is in accordance with the design philosophy of mutually compensating force systems and allows the CS to operate under compressive loads, suppressing fatigue crack growth in the conductor conduit. The CS assembly includes the 100 mm thick Outer Cylinder (OC), the CS winding pack itself and the 200 mm thick Inner Cylinder (IC). The primary function of the OC and IC is to increase the stiffness of the CS as a bucking structure and to keep the compressive hoop stress in the CS winding pack within allowable limits.

A fraction of the centripetal force of the TF coils is also reacted by Outer Intercoil Structures (OIS) linking the outboard legs of the TF coils. The OIS form three toroidally complete structural belts and are loaded in compression by leaving a clearance gap of 15 mm at assembly between the TF coils and OC. After cooling to the operating temperature of 4.5K and the TF coils are energized, this gap is closed and the OIS are pulled radially inwards by the TF coil centripetal forces. This reduces fatigue problems at the bolts and shear keys in the OIS.

When the TF coils are energized, their inboard legs stretch and vertical tensile strain can be transferred by friction to the CS assembly. To ensure that the CS operates under compressive stress, a preload structure is provided to compress the CS vertically at assembly and during cool-down of the machine.

2.2 Containment of out-of-plane loads acting on the TF coils

The out-of-plane (azimuthal) forces acting on the TF coils are due to the interaction between the current in the TF coils and the poloidal magnetic field. These forces are reacted entirely within the TF system by the OIS linking the outboard legs and by crowns in the upper and lower inboard regions of the TF coils. The OIS are integral parts of the TF coil cases and are linked in the meridian planes between coils so as to form toroidal shear belts. Shear load transmission at the links is accomplished with insulated bolts and shear keys. The crowns are also shear-resisting structures but, unlike the OIS, they are separate from the coil cases. Structural rails attached at the top and bottom of each of the coil cases engage in radial slots in the crowns. Azimuthal loads between TF coil case rails and crowns are transmitted by normal pressure. The crowns are each composed of 10 sectors connected by insulated bolts and shear keys.

Although the three OIS belts and the two crowns provide stiffness against shear deformations, this stiffness is provided only at five discrete locations along the contour of the TF coils. The overall torsional stiffness of the TF magnet assembly relies on the TF coil cases acting as beams linking the five shear structures. The stiffness of the TF coil cases to out-of-plane bending and torsion is therefore important.

The OC of the CS assembly also serves the purpose to locate the inboard straight legs of the TF coils. The OC is composed of 10 sectors joined into a complete cylinder by insulated bolts and shear keys. The nose of each TF coil, along the straight inboard leg, is machined as a cylindrical scallop that engages with a congruent fluted groove on the outer surface of the OC.

It is important to note that the out-of-plane support structures are decoupled from the in-plane support structures so that fatigue problems from cyclic out-of-plane forces are not compounded by static tensile in-plane loads. For example, shear keys and keyways where fatigue is potentially severe due to stress concentration effects and the cyclic load, have all been located in structures, or areas of structures, with little or no primary tensile stress.

2.3 PF coil and Vacuum Vessel supports

The PF coils carry their radial loads individually by hoop tension in the conductor conduit. Vertical loads are transferred to, and equilibrated by, the TF coil cases. Clamps on the PF coils transfer the loads through flexible members which allow relative radial displacements between TF and PF coils, but are rigid in the azimuthal direction. The supports have been designed for the largest vertical loads that can occur during Vertical Displacement Events (VDE). The largest load of 730 MN is expected on PF coil number 5 (PF5) during a VDE.

During plasma disruptions and VDEs, a large fraction of the plasma current can flow in the poloidal direction in First Wall components and generate large vertical forces (up to 150 MN) or radial forces acting on First Wall components [3]. The current distribution is not axisymmetric and the radial forces can generate a net horizontal force (up to 50 MN). These loads are transferred to the Vacuum Vessel (VV) and since they are balanced by forces acting on the plasma and the magnets, the VV is itself attached to the TF coils and the total force system is contained and equilibrated within the rigid TF coil cases.

To react the vertical forces, a support leg is welded at the bottom of each VV segment. This leg passes between the adjacent TF coil cases and is connected to them by a set of tension rods. The rods can flex or pivot at their attachment to allow relative radial displacements between the TF coils and the VV [4]. The horizontal loads acting on the vessel are contained by tension rods that provide a connection in the toroidal direction between the TF coil cases and the equatorial ports of the VV. These tangential rods are also designed to resist the horizontal loads generated by seismic events with an acceleration up to 0.2 g. The rods serve also the purpose to locate the VV with respect to the TF coils.

2.4 Gravity supports and seismic loads

The gravity supports (GS) must carry the weight of the tokamak and resist all horizontal and vertical loads during earthquakes. The GS must also accommodate the differential displacement due to the thermal contraction of the machine from room temperature down to 4.5 K. This is achieved by 20 columns (one per TF coil) each made of 20 steel plates oriented in the toroidal direction to give radial flexibility while retaining a high azimuthal rigidity [4]. The attachment of the columns to the TF coil cases is integrated with the lower OIS belt for increased rigidity. The lower ends of the columns are connected to a rigid ring which is an integral part of the cryostat. Seismic acceleration up to 0.2 g in the vertical and horizontal directions can be resisted without any yielding of the supports. Should the maximum ground acceleration to be considered at the ITER construction site be larger than 0.2g, it is intended to provide seismic isolation to the building so that the tokamak itself is not subjected to accelerations in excess of 0.2 g.

2.5 Analysis

Extensive stress analysis has been performed to support the design concept. This analysis has included the design sensitivity to gaps and friction effects at interfaces, in particular the IC-CS and CS-OC interfaces. Some preliminary conclusions on the effect of manufacturing and assembly tolerances on the critical stress levels are also available.

During normal pulsing, the TF coils experience a maximum out-of-plane dispacement of 35 mm. The peak stress in the case is close to 500 MPa whereas the allowable for fatigue loads is 570 MPa. The allowable assumes a 10 mm long and 1

mm deep pre-existent surface crack in this region. This type of crack is easily detectable by conventional quality inspection methods.

Within the CS, the conductor conduit stress is under 600 MPa (allowable is 800 MPa) and the bonding strength required from the insulation is 20 MPa (allowable is 25 MPa).

3. TF COILS

The number of the TF coils - 20 - was selected to obtain the maximum possible size of vacuum vessel ports to facilitate remote handling of In-Vessel components, in particular divertor modules [5], within given limitations on toroidal field ripple. This ripple is specified to be less than 2.5% at the First Wall contour to keep the loss of ripple trapped particles within acceptable limits [6]. The use of ferromagnetic inserts in the VV to lower the ripple is under evaluation.

As illustrated on Fig. 2, the TF coils are pancake wound and enclosed in thick vacuum tight stainless steel cases. A major feature of the TF coil design is the use of radial steel plates with machined grooves that support the conductor. These radial plates transfer the Lorentz forces acting on each conductor directly to the case without accumulation of forces on the conductor and its turn insulation. With this arrangement, the TF coil conductor can use a thin circular Incoloy 908 conduit, the function of which is only to support the local conductor forces and act as helium containment. Incoloy 908 has been selected because its thermal contraction coefficient matches that of Nb_3Sn giving a minimum of critical current degradation due to strain induced by thermal contraction.

Another advantage of the radial plates is that the turn insulation is mechanically decoupled and physically separated from the plate and ground insulations. The turn, plate, and ground insulations include an electrical barrier material such as a polyimide film. This requires the turn insulation to be applied after the reaction treatment of the Nb_3Sn superconductor. Tables I and II show some TF coil data.

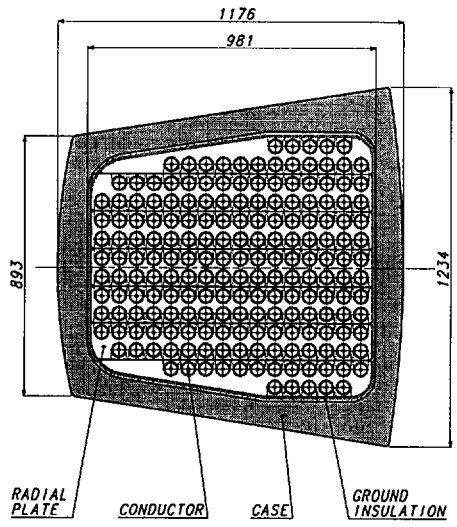

FIG. 2. TF coil inboard leg cross-section.

Table I. TF Coil - Geometrical Data

Overall Height/Width	18.7m/12m
Approximate Weights:	
Cable	64 t
Conduit	19 t
Insul. Miscl.	42 t
Radial Plates	145 t
Case + Structure	470 t
TOTAL per Coil	740 t
Average Turn Length	44 m

Table II. TF Coil - Electromechanical Data

Number of Turns per Coil	192
Current per Conductor	60.2 kA
Total Stored Energy	101 GJ
Max. TF at Conductor	12.3 T
Maximum Poloidal Field	2.6 T
Maximum Total Field	12.5 T
Centering Force per Coil	762 MN

4. CENTRAL SOLENOID (REFERENCE DESIGN)

The Central Solenoid is layer wound along its entire height with a cable in conduit conductor that uses a thick walled Incoloy 908 square conduit. The layer construction provides an axisymmetric and vertically uniform bucking structure for the TF coils. An advantage of the layer construction is that current leads and interlayer series connections are located about 1 m above and below the winding pack in regions where the field does not exceed 5.5 T, and well away from primary mechanical load paths. Tables III and IV show some CS data.

In the winding pack, each layer is wound with four conductors in hand to keep cooling channel lengths to about 1 km. These four in hand conductors are connected in parallel in order to minimize turn to turn and layer to layer voltages. As a result, the supply current is about 170 kA and some development is required for the circuit breakers that must interrupt this DC current.

Similar to the TF coil insulation, the turn, layer and ground insulations include an electrical barrier material such as a polyimide film. The CS is divided into three concentric modules corresponding to three conductor grades. This allows for modules to be fabricated separately and subjected to factory acceptance tests before the entire solenoid is nested. After nesting, the 5 mm radial clearance between adjacent modules must be filled with resin mixed with glass fiber or alumina powder to allow transmission of radial loads during machine operation.

Table III.
Central Solenoid - Geometrical Data

Height of Winding	12.12 m
Inner Radius of Winding	1.919 m
Outer Radius of Winding	2.700 m
Max. Conductor Length	1020 m
Approximate Weights:	
Cable	273 tons
Conduit	457 tons
Insulation	53 tons
Buffer zone, etc.	67 tons
Outer & Inner cylinders	600 tons
TOTAL	1450 tons
Preload Structure Weight	710 tons

Table IV.
Central Solenoid - Electromagnetic Data

Number of Turns	3,356
Maximum Field at Conductor	13 T
Current per Conductor	39 kA
Flux at Outer Radius at Mid-Plane	233 Wb
Total Stored Energy	14.3 GJ

5. PF COIL SYSTEM

The seven PF coils (PF2 to PF8) are built with cable in conduit conductors which use thick walled stainless steel square conduit. Conductors are wound in double pancake configuration. PF2 and PF7 which operate at fields up to about 8.5 T will use Nb_3Sn superconductors, while all other coils operate at fields not exceeding 5 T and will use NbTi superconductors to decrease the cost.

All PF coils are difficult to replace in the event of failure because of the need to disconnect many mechanical, electrical and cryo connections. Moreover, all coils, except PF2 and the CS, are either trapped under the machine or by VV ports or cooling water pipes for In-Vessel components. As a result, each PF coil consists of 4 identical modules which are designed to allow full ampere-turn operation with 3 modules only, but at reduced operating temperature (3.8 K). In the event of a failure in a module, the module would be disabled electrically or mechanically. Each module has ground insulation and a steel protector to prevent propagation of a short circuit burn from one module to the next. This redundancy renders the need to replace a coil very unlikely. Should, however, this need arise, schemes have been developed which allow the removal and replacement of each of the PF coils. In particular, a lower coil can be cut up and removed in pieces and a new coil can be rewound in a shielded cell under the cryostat and raised to its final location on the machine. The design of the lower part of the cryostat, the lay-out of the gravity support and the height of the cell under the cryostat are all compatible with this coil replacement scheme [7]. This scheme, if applied to PF7, would require a coil redesign and a reduced operating temperature to limit the loss of performance since the replacement coil would use NbTi instead of Nb_3Sn.

6. CORRECTION COILS

Resonant magnetic perturbations tend to create magnetic islands in the plasma region and can affect the plasma confinement and stability via plasma locked modes. The perturbations originate from non axisymmetric errors in the magnet manufacture and assembly, non axisymmetric configuration of current in winding packs and stray fields of bus bars. To avoid plasma locked-modes, the $m = 2$, $n = 1$ helical component of the error field normal to the magnetic surface (inside the plasma) defined by $q = 2$

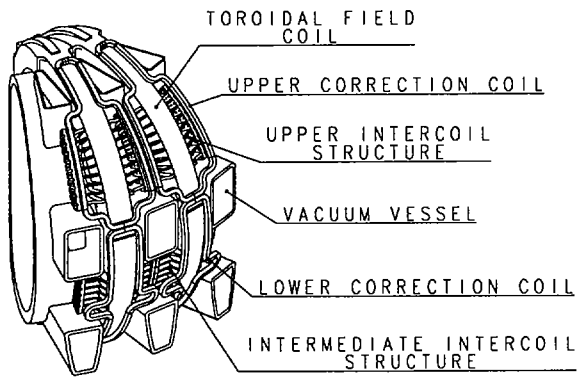

FIG. 3. Machine sector with correction coils.

must be limited to about 10^{-5} of the main toroidal field [8]. This requirement is very demanding and, if translated into positional accuracy of the ITER magnets, can be met only if winding packs are typically within 1 to 3 mm of their theoretical location. Such accuracy is clearly unrealistic and other means must be found to mitigate the effect of error fields. Plasma rotation, as can be induced by Neutral Beam Injection, inhibits locked modes and can relax the limitation on error field, perhaps by a factor up to 10. Correction coils will also be installed to decrease the amplitude of the most critical helical modes.

The superconducting correction coils will be saddle shaped and located outside of the TF coils as shown in Fig. 3. Four pairs of coils will be required to produce the desired helical field component. Coils are split into sub-coils for assembly and maintenance reasons. Estimates indicate a need for a capacity of about 0.4 MA.turns per coil to produce corrections of the order of 10^{-4} of the main toroidal field.

7. CONDUCTOR

7.1 Summary of operation conditions

The operating conditions of the conductor are severe for both TF coils and CS due to the high field and the relatively large energy deposition during operation. Energy deposition is due to nuclear heat, AC losses and friction forces.

In the case of the TF coils, a significant fraction of the energy deposition is due to nuclear heating but this heat is essentially deposited in the cases. In these coils, the dominating requirement is for a strand with high critical current, typically an internal tin type of strand. In the CS, the hysteresis losses are about 50% of the total losses and a low loss strand, typically a bronze type, is preferred. For all PF coils, AC losses resulting from plasma control actions are a significant fraction of the total AC losses. Since these control actions are relatively poorly specified in terms of frequency and amplitude, the PF coils require design margins on the conductor. For the PF2 and PF7 coils, the field does not exceed 8.5 T but still requires a Nb_3Sn superconductor in view of the high AC losses. NbTi can be used for the outer PF coils (PF3, 4, 5, 6, 8). A more complete description of the superconducting conductors for ITER magnets can be found in [9].

7.2 Heat loads and cooling

The total cold mass of the magnets and structures is about 25,000 t and cool-down is expected to take about 1 month. The ITER cryoplant supplies liquid helium to a number of cold boxes which provide forced flow cooling to the coils. The boxes contain helium circulation pumps and a cold bath to recool the circulating helium. Cooling of the conductors is achieved with helium at 4.5 K and 6 bar and a pressure drop of up to 2 bars giving a typical helium flow rate of 20-25 g/s and velocity of 1.3 m/s in the central channel. Table V shows the typical time-averaged heat loads during operation. In the table, other heat loads include resistive losses in joints, conduction,

Table V. Heat Loads (Heat loads in kW are averaged over a pulse cycle of 2200 s)

	TF Coils (excl. cases)	CS	PF	TF cases and structures
AC losses	4.8	3.3	6.3	20.9
Nuclear heat	2.2	0	1.2	6.1
Other heat loads	1.5	1.2	2.8	8.0

radiation and mechanical friction. During operation, the total timed averaged refrigeration heat load at 4.5 K from the magnets, bus-bars, structures and helium circulation pumps is about 95 kW. The cryoplant also supplies the helium that cools the current lead transitions from 4.5 K to room temperature. This helium returns to the cryoplant at room temperature. The helium liquefaction requirements for current lead cooling amounts to about 230 g/s in normal operation.

In the event of a fast discharge of the TF coils or a quench in any of the coils, the coil content of helium is vented through pressure relief valves to a helium recovery tank. A thermal shield cooled with 80 K gaseous helium is provided between the TF coils and the VV. This shield is attached by flexible straps to the TF coil cases. The entire cryostat inner surface is also covered by a thermal shield.

8. ITER MAGNET R&D PROGRAMME

The major tasks for a six year, coordinated, magnet R&D programme with all four ITER participants are in place with an estimated equivalent value of over 200 M$. This programme aims at developing basic components, production experience and Quality Assurance (QA) methods and culminates in the construction and testing of model coils that incorporate many design features of the full size ITER coils [10].

8.1 Conductor R&D

Conductors able to meet the ITER specifications, in terms of current capability, field and AC loss limitation during operation represent a new development. The bronze and internal tin types of ITER Nb_3Sn strand that fulfils ITER specifications have already been successfully produced by industries of the four ITER participants. For ITER construction, it is envisaged that multiple strand production facilities will be necessary to produce the nominal 1200 t of Nb_3Sn and 650 t of NbTi.

The strand-cable-conductor development provides conductors for the model coils which are identical to the full size conductors, except for the length. An experiment of jacketing (insertion of the cable in the conduit followed by compaction) of a 1 km long TF type conductor is being prepared to complete the demonstration of the full length ITER conductor fabrication.

Incoloy 908 is the selected conduit material for the TF coils and CS conductors. A feature of Incoloy 908, like other high nickel alloys, is a susceptibility to cracking if certain conditions of temperature, stress and oxygen concentration simultaneously occur. This cracking, also called SAGBO for Stress Accelerated Grain Boundary Oxidation, has been the subject of a comprehensive study since the reaction treatment for Nb_3Sn requires a temperature of about 700 C, inside the SAGBO range. The study showed that two parameters, namely stress and oxygen concentration, can be independently controlled to avoid SAGBO. For ITER conductors, both parameters are planned to be carefully controlled to give a high safety margin [11].

8.2 Basic component R&D

The design and evaluation of the performance of joints for Nb_3Sn conductors that combine high current, in the 40-60 kA range, with AC operation is a major area of development. Joints for ITER coils are to be tested up to 12 T in DC conditions at the SULTAN facility in the European Union (EU) and in AC conditions but at lower field (~5.5 T) in the Pulse Test Facility (PTF) in the United States (US).

Insulation systems have been irradiated using fission reactors in the EU and in the Russian Federation (RF) and tested in cold conditions. An important aspect which

requires more investigation is the gas formation in the insulation matrix during irradiation and the behaviour of this gas when coils are warmed up.

The TF coil case requires thick plates, forgings and thick plate welding. Full size portions of the case are planned to be manufactured.

8.3 Central Solenoid model coil

The central solenoid model coil is a 640 MJ solenoid of about 1.6 m inner diameter, 1.8 m height, and capable of reaching the nominal field of 13 T [12]. The weight of the model solenoid is about 100 t and the total weight of the assembly and mechanical structure is about 150 t. The CS model coil assembly is shown in Fig. 4. The model coil uses full size CS cable, is layer wound and has current leads and interlayer joint designs similar to that of the full size CS. The winding is composed of an inner module built in the US and an outer module built in Japan (JA).

The model coil will be subjected to a tensile hoop stress when energized, whereas the full scale CS operates in a compressive state. To simulate relevant operating conditions for the conductor, the model coil will be capable of accepting replaceable single layer inserts that can be operated in such a way to simulate the expected hoop compression, in the case of the CS conductor, or hoop tension for the TF coil conductor. Inserts will be made in JA (CS type) and the RF (TF type). The CS Model Coil is therefore not only a scaled model for manufacturing development but also a high field test facility for ITER conductors.

Testing of the model coil will be performed in a facility at the Japan Atomic Energy Research Institute, Naka. Testing will include pulsed operation with ramped current and field to demonstrate the ability to continuously operate with the expected level of AC losses in the conductor and surrounding structures.

8.4 TF model coil

The TF model coil is race track shaped with dimensions of about 2.7 m x 3.1 m [13]. The design and fabrication techniques will closely reflect those of the full scale coils. In particular the model will use full scale conductor supported in radial plates.

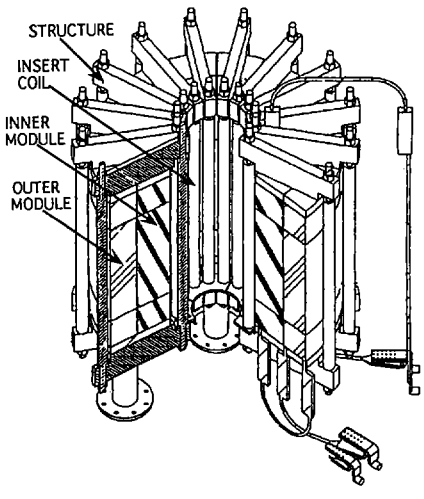

FIG. 4. CS model coil assembly.

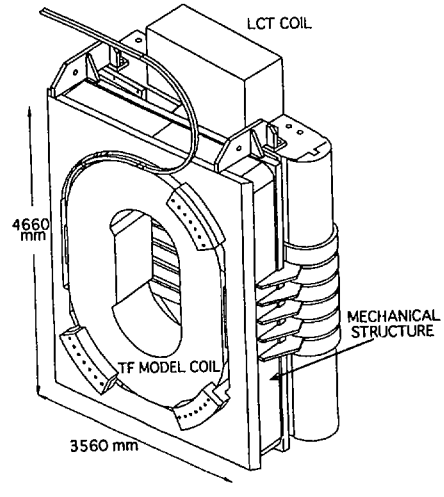

FIG. 5. TF model coil configuration.

The coil will be manufactured in the EU and tested in conjunction with the EU Large Coil Task (LCT) coil at FZK, Karlsruhe as illustrated in Fig. 5. The test arrangement allows for testing under various conditions, including the simulation of some in-plane and out-of-plane loading. Even in combination with the EU-LCT coil, the peak field in the model coil will be about 9.8 T, whereas the ITER TF coil will see a peak field of about 12.5 T. This difference in full field is the main rationale for also testing the TF conductor as an insert in the CS model coil.

9. POLOIDAL FIELD OPERATION SCENARIOS

The reference plasma scenario is a 21 MA, ignited, 1000 s burn duration pulse [14]. The total flux swing needed for the scenario is about 530 Wb. The PF system can provide about 540 Wb generated partly by the CS with a field variation from +13 T at initial magnetization to -12.5 T at the end of burn (EOB) and partly by the PF coils. For the reference scenario, the flux consumption is 427 Wb to the end of the current rise, 31 Wb during heating to ignition and 72 Wb during the 1000 s burn. The PF system can provide up to 82 Wb for burn.

9.1 Breakdown and plasma initiation

The PF coil system is able to produce a low magnetic field, $|B_{pol}| \leq 2$ mT, in a plasma initiation region of 1 m radius that is close to the outboard limiter and centered at R ~ 9.5 m and Z ~ - 1 m, below the equatorial plane. Breakdown is expected about 2 s after the application of the voltage to the PF coils. The delay is due to eddy currents in the passive structures and results in a loss of inductive flux of approximately 21 Wb. The passive structures are the vacuum vessel and the in-vessel components with a combined toroidal resistance of 4.3 mΩ. Additional electron-cyclotron heating power in the range 2-10 MW at 140 GHz will improve the reliability of gas breakdown and plasma initiation.

Coil voltages are highest during this phase and are typically 15 V/turn for the CS, 50 V/turn for PF2-3-7 and 30-40 V/turn for the other PF coils.

9.2 Plasma current pulse (reference scenario)

As illustrated on Fig. 6 the plasma shape is kept nearly circular up to 4 MA. Elongation is then gradually increased from 1 up to 1.6. The expansion of the plasma size (minor radius and vertical elongation) can be programmed to occur with a nearly constant edge q (safety factor) to minimize the resistive flux consumption and avoid MHD instability. The transition from a limiter to a divertor configuration occurs at a current of about 15 MA but can also be achieved at a lower current, about 10 MA, albeit at a higher q than in the reference scenario. Modeling and extrapolation of data from present experiments show that the optimal average rate of current rise should be about 0.15 MA/s leading to a total current rise time of about 150 s. This rate of rise is well within the capability of the PF system.

During the current flat top, the maximum PF current requirements have been evaluated by considering an operational space defined by a range of plasma current density profiles ($0.7 < l_i < 1.1$) and pressures ($\beta p < 1.2$). For the reference scenario with $l_i = 0.9$, the safety factor q_{95} varies from 2.8 at start of flat top (SOF) to 3 at end of burn (EOB).

After EOB the plasma current drops from 21 MA to 16 MA in 100 s. This is followed by the current ramp down phase with plasma aperture compression lasting 200 s.

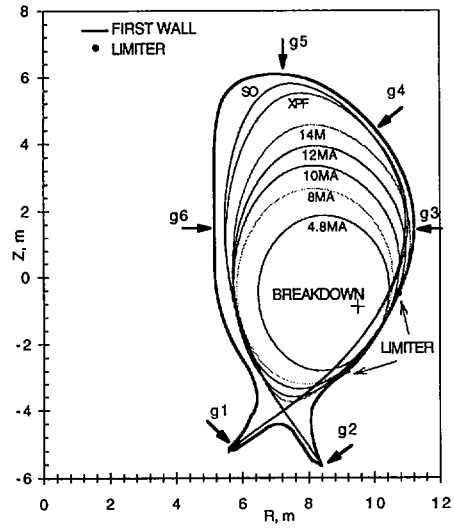

FIG. 6. Control gaps (g1 to g6) and plasma shape at various phases of the plasma pulse.

9.3 Flexibility of operation and alternate scenarios

In addition to the reference plasma scenario, the PF coil system is capable of a number of variations of this reference scenario which intend to cope with, or exploit, a range of physics conditions in relation for example to energy confinement. The PF system is also compatible with extended burn duration scenarios which employ reduced plasma current combined with either heating or non inductive current drive [15]. Table VI illustrates the main ITER PF scenarios.

Table VI. Main ITER plasma scenarios

Scenario	I_p (MA)	max. β_p	l_i	Burn duration (s)	Aux. power at burn (MW)
Reference, ignited	21	1.2	0.7~1.1	1000	0
High current, ignited	24	1	0.8~1.0	600	0
High neutron fluence	17	1.2	0.7~1.1	4000	100
Reverse shear	12	2.3	0.4	steady state	100

10. PLASMA SHAPE AND POSITION CONTROL

10.1 Control parameters

During the phase when the plasma is in a limiter configuration, the PF system will control the radial and vertical position of the plasma centroid and global shape parameters such as elongation and triangularity. Following divertor formation and attainment of a nearly full aperture plasma, the feedback control logic will shift to controlling certain gaps which are critical for plasma operation. The location of these gaps which define the clearance between the separatrix and the first wall or divertor is

shown on Fig. 6. Control of the vertical position is included in the control of the uppermost gap. The optimum method to implement the transition from shape control during the limiter phase to gap control during the divertor phase remains to be determined.

Since the control of plasma position, shape and vertical stabilization are closely coupled, an integrated multi-variable control concept and individual power supplies dedicated to each PF coil are chosen as the reference design concept.

10.2 Control response to plasma disturbances

Numerical simulations of the effect of control actions in case of plasma disturbances have been carried out using different control algorithms and different plasma models. Preliminary results have shown that control systems using different control methodology (Linear Quadratic Gaussian, Generalized PD or H∞ controllers) with the same power supply limitations, have similar plasma control capabilities.

The control response is illustrated in Fig. 7 which shows waveforms of some of the control gaps following typical plasma disturbances. In the two cases considered, vertical displacement and beta drop, adequate control is maintained.

One issue is that of AC losses in PF coils associated with low amplitude ($\delta\beta_p$ ~ δl_i ~ -0.03) but high frequency plasma disturbances such as sawteeth and ELMs. Regardless of which control action, if any, is taken by the control system, the disturbances induce currents in the PF coils and generate some AC losses. The strategy to mitigate these losses is under study.

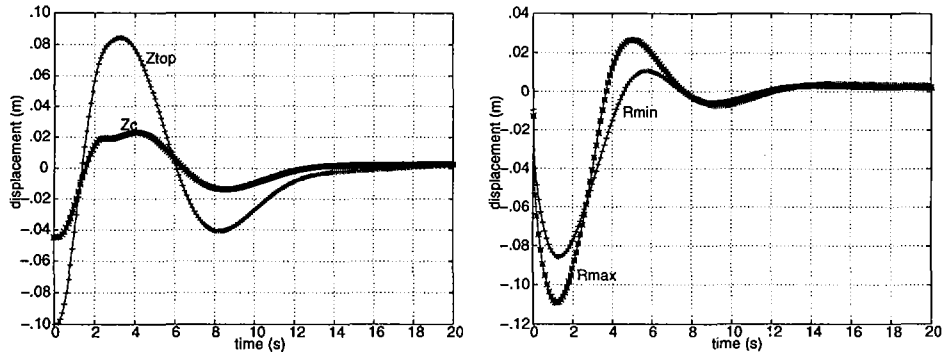

FIG. 7. Left: vertical displacement of plasma uppermost point (+) and current centre (*) after an initial downward shift ΔZ_{top} = –0.1 m. Right: radial displacement of plasma innermost (+) and outermost (*) points after a step-like beta drop $\Delta\beta p$ = –0.2.

11. ALTERNATE CENTRAL SOLENOID DESIGN

11.1 Rationale for a segmented CS design

In the layer-wound reference design CS, the current density is vertically uniform and all plasma shaping and control must be performed by the outer PF coils. A CS composed of several independently powered segments, along the vertical direction, should allow a more flexible and effective control of the plasma shape and position.

Another incentive to consider a segmented CS is brought by the reduction of current-carrying requirements in PF2 and PF7 which could then use the less expensive NbTi instead of Nb_3Sn. Using NbTi, PF7 could be rewound under the cryostat according to the replacement scheme described in section 5.

11.2 Preliminary design and plasma control features of a segmented CS

The CS is split into 5 independently powered segments. The central segment, CS0, is 9.5 m tall and subject to the radial compressive load from the TF coils. The upper and lower segments CS1U, CS2U, CS1L and CS2L are free standing coils with joints in low field regions. CS0 is layer wound, similarly to the reference design. To be able to locate the CS0 joints in regions where the field does not exceed 7 T (5.5 T for the reference design), a gap of about 1.5 m is provided between CS0 and CS1. CS1 and CS2 can be built with the same inner and outer radius as CS0 but there is also the option to build CS2 at a radius intermediate between CS1 and PF2 or PF7 to allow the use of NbTi in CS2.

Engineering issues of the segmented design that require further investigation include the design of the CS0 buffer zone, supports for CS2 and mechanical fatigue in the TF coil cases.

The plasma reference scenario described in section 9 can be produced with a segmented CS but with the following differences:

- Plasma shaping is improved. The upper plasma triangularity is increased (0.29 throughout the pulse) and as a consequence, the safety factor q_{95} can be maintained at about 3 throughout the plasma pulse.
- There is a wider range of available plasma shapes and separatrix to first wall distances that may result in improved performance. In particular, the operating range for steady state plasmas at 12 MA is widened in regard to the l_i values. Also, the ability to move the 12 MA plasma away from the outboard high TF ripple region is important for alpha particle confinement.
- The flux available for burn is slightly reduced to 72 Wb (down from 82 Wb).

For the response to plasma disturbances, the main advantage of the segmented CS design is an improved transient control of the separatrix position in the divertor channels. The required control power is smaller and the separatrix position settling time is shorter. This capability for a fast transient control is important for high power plasma operation and ensuring a long life of divertor plasma facing materials.

In summary, the segmented design offers some attractive plasma control features but cannot be adopted at this point due to the limited engineering study that has been carried out so far. The overall tokamak design and assembly approach are compatible for both the reference and segmented designs of the CS, so the reference CS will be retained pending more detailed analysis and design effort for the segmented options.

12. CONCLUSIONS

The ITER magnet design and R&D are making steady progress. The Model Coil programme is well underway. The conductor manufacture has identified and solved of a number of issues in relation to strand production, cabling, conduit material manufacture and jacketing. Winding of the CS Model coil has started. These development activities have already provided a technological data base which is essential for full size construction and is available to all ITER participants.

The ITER PF system has the capability to produce a range of plasma scenarios and to control the plasma shape and position for the expected plasma disturbances. A design option that offers the promise of improved plasma shape and position control is being evaluated for the Central Solenoid. The impact of this option on the design is however confined to the Central Solenoid itself and the two small Poloidal Field coils.

Progress achieved so far has developed great confidence that international collaboration for ITER can proceed successfully to full size construction.

ACKNOWLEDGEMENTS

Within the ITER Joint Central Team, magnet design and analysis is carried out by the Superconducting Coils and Structures Division under the leadership of Dr. R.J. Thome and plasma control analysis is carried out by the Plasma and Field Control Division under the leadership of Dr. P.L.Mondino. Home Teams of the four ITER participants have been key contributors to analysis and are responsible for R&D activities.

REFERENCES

[1] AYMAR, R., et al., these Proceedings, Vol. 1, p. 3.
[2] SBORCHIA, C., et al., "The mechanical structure of the ITER magnet system", Proc. 19th Symp. on Fusion Technology, Lisbon, 1996.
[3] WESLEY, J., et al., IAEA-CN-64/FP-25, this volume.
[4] GALLIX, R., et al., "ITER tokamak supports: initial sizing and design", Proc. 19th Symp. on Fusion Technology, Lisbon, 1996.
[5] HAANGE, R., et al., IAEA-CN-64/FP-14, this volume.
[6] CHENG, C.Z., et al., IAEA-CN-64/FP-23, ibid.
[7] TESINI, A., et al., "Remote operation for replacement of a lower PF coil in ITER", Proc. 19th Symp. on Fusion Technology, Lisbon, 1996.
[8] Technical Basis for the ITER Interim Design Report, Cost Review and Safety Analysis, ITER EDA Documentation Series No. 7, IAEA, Vienna (1996).
[9] MITCHELL, N., et al., IEEE Trans. Magn. **32** (1996) 2997.
[10] OKUNO, K., et al., "Status of the ITER Central Solenoid and Toroidal Field Model Coil programme", Proc. 19th Symp. on Fusion Technology, Lisbon, 1996.
[11] WONG, F.M., et al., "Selection of jacket materials for Nb_3Sn superconductor", ibid.
[12] JAYAKUMAR, R.J., et al., IAEA-CN-64/FP-12, this volume.
[13] SALPIETRO, E., et al., IAEA-CN-64/FP-13, ibid.
[14] GRIBOV, Y., et al., "The ITER Poloidal Field Configuration and Operation Scenario", Proc. 16th IEEE/NPSS Symp. on Fusion Engineering, Champaign, 1995, Vol. 2, p. 1514.
[15] BOUCHER, D., et al., IAEA-CN-64/FP-22, this volume.

THRESHOLD POWER AND ENERGY CONFINEMENT FOR ITER

ITER CONFINEMENT DATABASE
AND MODELLING EXPERT GROUP*
(Presented by T. Takizuka)

Abstract

THRESHOLD POWER AND ENERGY CONFINEMENT FOR ITER.

In order to predict the threshold power for L–H transition and energy confinement performance in ITER, databases have been assembled and are being analysed. The ITER threshold database includes data from ten divertor tokamaks. This database gives a scaling of the threshold power of the form $P_{thr} \propto B_t n_e^{0.75} R^2 (n_e R^2)^{\pm 0.25}$, which predicts $P_{thr} \approx 100 \times 2^{0 \pm 1}$ MW for ITER at $n_e = 5 \times 10^{19}$ m^{-3}. The ITER L mode confinement database has also been assembled from 14 tokamaks, and a scaling of the thermal energy confinement time in L mode and ohmic phases has been obtained: with the ITER parameters, $\tau_{th} \approx 2.3$ s. For ignition in ITER, more than 2.5 times this value will be required. The ITER H mode confinement database has been expanded from data of six to data of eleven tokamaks. A τ_{th} scaling for the ELMy H mode obtained by a standard regression analysis predicts an ITER confinement time of $\tau_{th} \approx 6 \times (1 \pm 0.3)$ s. No degradation of τ_{th} with increasing $n_e R^2$ (or decreasing ρ_*) is found for the ELMy H mode. An offset linear law scaling with a dimensionally correct form also predicts nearly the same τ_{th} value.

1. INTRODUCTION

In order to achieve its long time, high Q goal, improved confinement over L mode scaling with an H factor ($= \tau_E / \tau_E^{ITER89P}$) above 2 will be required for ITER. The ELMy H mode is considered to be the most suitable candidate for this purpose. Accurate predictions of the energy confinement as well as of the H mode transition threshold power are urgently required for the ITER EDA. This paper presents recent studies of threshold power and energy confinement for ITER and extends former publications by the H mode Database Working Group [1–5].

2. THRESHOLD POWER

The change of a confinement regime from L to H mode occurs when certain conditions for the plasma parameters are satisfied. A heating power exceeding a threshold, P_{thr}, is necessary for these conditions to be fulfilled. For the prediction of

* For the composition of this group see Appendix.

P_{thr} in ITER, the size dependence of P_{thr} is required, which can only be obtained from a multimachine database, e.g., the ITER threshold database [5]. Data from ten divertor tokamaks are included in the database: Alcator C-Mod, ASDEX, ASDEX Upgrade, COMPASS-D, DIII-D, JET, JFT-2M, JT-60U, PBX-M and TCV. Since the scattering in data points is rather large, it has, so far, been difficult to determine uniquely the size dependence of P_{thr}.

From a dimensional consideration, we obtain a P_{thr} scaling with uncertainties in the density and size dependences [5]. The total heat flux through the separatrix surface is assumed to be given by $P \propto n_e T^{1.5} R^2 F(\rho_*, \beta, \nu_*)$, where n_e is the electron density, T the temperature and R the major radius. A non-dimensional function $F(\rho_*, \beta, \nu_*)$ represents the transport process near the plasma edge, where $\rho_* \propto T^{0.5}/B_t R$ is the normalized Larmor radius, $\beta \propto T n_e/B_t^2$ the beta value and $\nu_* \propto n_e R/T^2$ the collisionality. If we consider, e.g., a Bohm diffusion, F is proportional to ρ_* and $P \propto n_e T^2 R/B_t$. The condition for the L–H transition is also assumed to be given by a non-dimensional equation of the form $G(\rho_*, \beta, \nu_*) = 1$. Since $F \propto T^f$ and $G \propto T^g$, we can eliminate T from P at the transition by dividing P by G^γ $(=1)$ with $\gamma_g = 1.5 + f$. The threshold power is then given as a function of R, B_t and n_e, $P_{thr} \propto B_t^Z n_e^X R^Y$, where a relation $8X - 4Y + 5Z = 3$ should hold. Although at present we do not know the exact forms of F and G, we can find the values of X, Y and Z from an analysis of the ITER threshold database.

As for the B_t dependence, a linear relation is clearly seen in the data of each tokamak with the density nearly constant, as shown in Fig. 1. The loss power in the

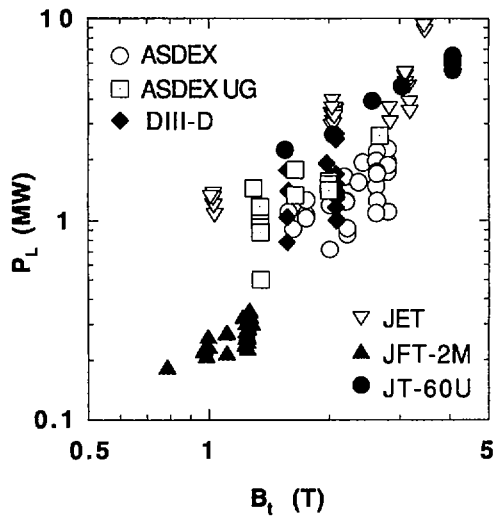

FIG. 1. Dependence of P_L on B_t. The density regions chosen are: (2.5–3.0) × 10^{19} m^{-3} for ASDEX, (4.0–5.5) × 10^{19} m^{-3} for ASDEX Upgrade, (3.0–3.5) × 10^{19} m^{-3} for DIII-D, (2.3–3.0) × 10^{19} m^{-3} for JET, (2.0–2.5) × 10^{19} m^{-3} for JFT-2M and (1.4–2.1) × 10^{19} m^{-3} for JT-60U.

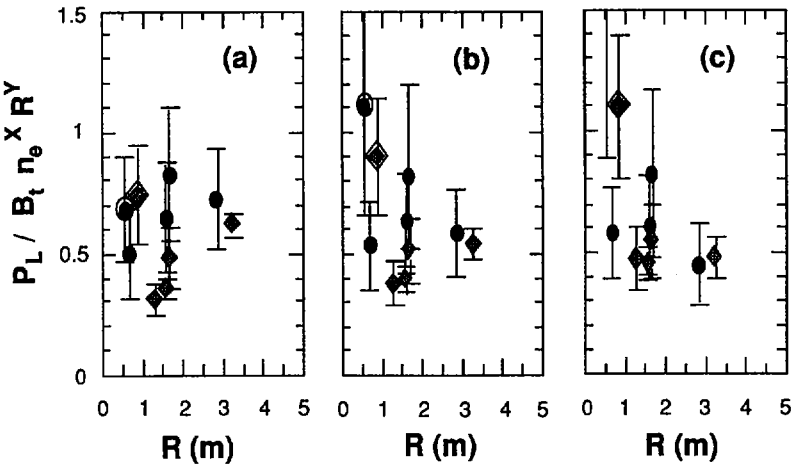

FIG. 2. Loss power P_L normalized by $B_t n_e^X R^Y$ versus major radius R. Black circles: average for a fat tokamak (R/a < 3.5); diamonds: average for a slender tokamak (R/a > 3.5). Data of COMPASS-D (double circle) and of TCV (double diamond) exhibit higher thresholds than other data, especially for P_L normalized by $B_t n_e R^{2.5}$. (a) x = 0.5; (b) x = 0.75; (c) x = 1.0.

figure is defined as $P_L = P_{NB} + P_{RF} + P_{OH} - dW/dt$, at the L–H transition (P_{NB} is the neutral beam heating power, P_{RF} the RF heating power, P_{OH} the ohmic heating power, and dW/dt is the time derivative of the stored energy). Using this linear B_t dependence (Z = 1), we obtain the following scaling with an arbitrary power α of $n_e R^2$:

$$P_{thr} = C(R/a, \kappa, q, \alpha)\, B_t n_e^{0.75} R^2 (n_e R^2)^{\alpha} \quad (1)$$

where C is a non-dimensional coefficient including aspect ratio R/a, elongation κ, safety factor q and α. Throughout this paper, the following notations and units are used: power P in MW, major radius R in m, minor radius a in m, line averaged density n_{20} in 10^{20} m^{-3} (n_{19} in 10^{19} m^{-3}), magnetic field B_t in T and plasma current I_p in MA.

The non-dimensional quantity $n_e R^2$ is proportional to β/ρ_i^2, and this value for ITER is much larger than its value for present tokamaks. Therefore, an uncertainty of the order of $(n_e R^2/\langle n_e R^2\rangle)^{\alpha}$ where $\langle n_e R^2\rangle$ represents the average of $n_e R^2$ in the ITER threshold database becomes quite large in ITER even for quite small values of α.

The limits of α are determined from a data analysis. Figure 2 shows the loss power P_L normalized by (a) $B_t n_e^{0.5} R^{1.5}$, (b) $B_t n_e^{0.75} R^2$ and (c) $B_t n_e R^{2.5}$. Black circles represent the average of the normalized P_L for a fat tokamak (R/a < 3.5) and diamonds correspond to the average for a slender tokamak (R/a > 3.5). Note that the lower half of the error bar region for a tokamak should be used for comparison when

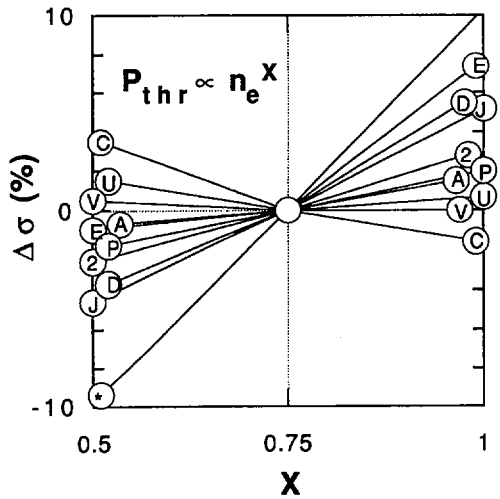

*FIG. 3. Change in standard deviation $\Delta\sigma$ with various n_e dependences of P_{thr}. C: Alcator C-Mod; U: ASDEX Upgrade; V: TCV; A: ASDEX; E: JET; P: PBX-M; 2: JFT-2M; D: DIII-D; J: JT-60U; *: COMPASS-D.*

the error bar of a tokamak is long. We see that the normalized P_L for case (a) increases with R, and the expression $P \propto B_t n_e^{0.5} R^{1.5}$ does not describe the scaling of P_{thr} properly. The data of COMPASS-D (double circle) and of TCV (double diamond) exhibit higher thresholds than other data, especially for P_L normalized by $B_t n_e R^{2.5}$. These data are, however, taken into account only weakly to determine the scaling at present because the number of data points is small and also because two devices are of small size, have open divertor configurations, and are therefore expected to be more sensitive to neutrals which are known to generally increase the threshold power. Neutral density measurements, which are not yet available in these devices, would be required to address this question quantitatively. Figure 3 shows the change of the standard deviation $\Delta\sigma$ with the variation of the n_e dependence of $P_{thr} \propto n_e^X$, where σ is defined as $\sigma^2 = N^{-1} \{\hat{P}_L/\langle\hat{P}_L\rangle - 1\}^2$, N is the number of data points, $\hat{P}_L \equiv P_L/B_t n_e^X R^Y$ and $\Delta\sigma = \sigma(X) - \sigma(X - 0.75)$. The standard deviation for the majority of tokamaks decreases at $X = 0.5$ and increases at $X = 1.0$, except for Alcator C-Mod. Therefore, the scaling of the form $P_{thr} \propto B_t n_e R^{2.5}$ is less reliable.

Using the results of Figs 2 and 3, the limits of α are evaluated as ± 0.25. Assuming that C is independent of R/a, κ, and q, for simplicity, the value of C is estimated from Fig. 2 as

$$C = (0.45 \pm 0.1) \times 0.6^{\alpha} \quad \text{with} \quad -0.25 \leq \alpha \leq 0.25 \tag{2}$$

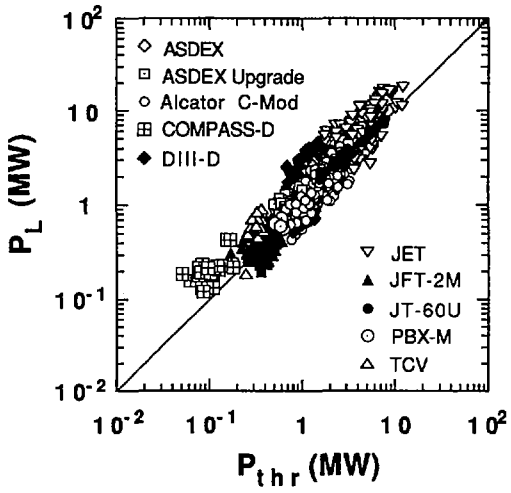

FIG. 4. Comparison of experimental data from ten tokamaks to a scaling $P_{thr} = 0.45\ B_t n_{20}^{0.75} R^2$.

where the unit of the line averaged density n_e is 10^{20} m^{-3}. A weak dependence of C on R/a and κ is seen in Fig. 2(a) for X = 0.5 and Y = 1.5, but is not particularly seen in Fig. 2(c) for X = 1.0 and Y = 2.5. As for the q dependence of C, a clear dependence $C \propto q^{0.5-1}$ is found in the JET data, while no clear dependence is observed in other tokamaks. Data from JT-60U suggest a very weak q dependence of C [6]. One of the possible reasons why P_{thr} decreases at smaller q is the fact that a sawtooth crash sometimes causes an L–H transition.

Regression analyses yield results similar to the above. Using equal weighting for all data, we obtain a relation: $P_{thr} \sim B_t n_e^{0.7} R^2$. When we use a $(1/N_{tok})$ weighting for each data point, we obtain another relation: $P_{thr} \sim B_t^{0.9} n_e^{0.75} R^{1.8}$, where N_{tok} is the number of data points from a tokamak; this method weights all machines equally. These analyses support the assumption that Eqs (1) and (2) reliably describe the scaling of the threshold power. Figure 4 shows a comparison of the experimental data from ten tokamaks to the scaling $P_{thr} = 0.45\ B_t n_{20}^{0.75} R^2$. This formula is found to fit the data well.

In predicting P_{thr} in ITER, the dependence of C on R/a, κ, and q is not so important because many data points cover the parameter region of ITER: R/a $\approx$ 3, $\kappa \approx 1.7$ and q $\approx$ 3. The predicted value of P_{thr} in ITER (B_t = 5.7 T and R = 8.1 m) at $n_e = 0.5 \times 10^{20}$ m^{-3} is obtained from Eqs (1) and (2) as $100 \times 2^{0\pm1}$ MW. A large uncertainty still remains: 50 MW $< P_{thr} <$ 200 MW.

The importance of radiation losses, edge plasma density and neutral density has prompted efforts to include these elements in the database. The analysis of this new version of the database, including a more physical approach to analysing the edge

data, is advancing towards a reduction of the prediction uncertainties. A data analysis on P_{thr} for the H–L backtransition is also in progress. It should be studied theoretically whether the condition for the L–H–L transitions is really determined by three parameters, ρ_*, β, ν_*, and is independent of other non-dimensional parameters such as the normalized mean free path, λ_{*cx}, against charge exchange reactions.

3. L MODE CONFINEMENT

A basis of the confinement performance has historically been given by a total energy confinement scaling for L mode plasmas. One of the well-known scalings for the total energy confinement time τ_E is the ITER89 power law scaling [7]:

$$\tau_E^{ITER89P} = 0.048\, M^{0.5} I_p^{0.85} R^{1.2} a^{0.3} \kappa^{0.5} n_{20}^{0.1} B_t^{0.2} P^{-0.5} \quad (3)$$

where τ is in units of seconds and M denotes the ion mass number.

It is more useful to have a scaling of the thermal energy confinement for evaluating the performance of ITER. For this purpose, the L mode confinement data (L) from 14 tokamaks have been assembled in the ITER L mode confinement database [4], where ohmic confinement data (OH, I mode data (I) and LHEP mode data (LHEP)) are also included: Alcator C-Mod (L, OH), ASDEX (L, OH), Doublet III (L), DIII-D (L), FTU (OH), JET (L, OH), JFT-2M (L), JT-60 (L, OH), PBX-M (L), PDX (L, OH), T-10 (L, OH), TEXTOR (L, I, OH), TFTR (L) and TORE SUPRA (L, LHEP, OH). The standard linear regression analysis of the L mode data yields the following scaling:

$$\tau_{th}^{L} = 0.023\, M^{0.2} I_p^{0.96} B_t^{0.03} \kappa^{0.64} R^{1.89} a^{-0.06} n_{19}^{0.4} P^{-0.73} \quad (4)$$

The root mean square error (RMSE) is 15.8%. The τ_{th}^{L} scaling expression has a rather strong density dependence and shows strong power degradation compared with the τ_E scaling. This difference is due to the effect of the high energy ion component in the total energy. The formula of Eq. (4) indicates that the L mode confinement is of the Bohm type, $\tau_{th}^{L} \sim \tau_{Bohm}(\nu_*^{0.18}/\beta^{1.34})$, i.e. has the same nature as the ITER89 power law scaling, $\tau_E^{ITER89P} \sim \tau_{Bohm}(1/\nu_*^{0.28}\beta^{0.56})$, where $\tau_{Bohm} \propto R^2 B_t/T$ denotes the Bohm confinement time.

The above scaling fits well not only the L mode data but also the ohmic confinement data, as is shown in Fig. 5. This scaling is similar to a dimensionally correct scaling, $\tau_{th}^{JT\text{-}60}$, based mainly on JT-60 data [8], except for the q dependence and the stronger power degradation. The present scaling gives a smaller RMSE against the total data points although it fits JT-60 data a little worse than the previous JT-60 scaling.

For the ITER parameters, M = 2.5, I_p = 21 MA, B_t = 5.7 T, κ = 1.7, R = 8.1 m, a = 2.8 m, $n_e = 1.3 \times 10^{20}$ m^{-3} and P = 190 MW, Eq. (4) predicts

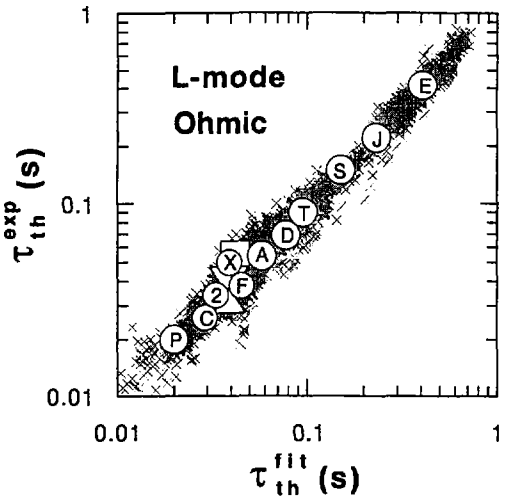

FIG. 5. Thermal energy confinement time τ_{th} for L mode and ohmic phases. The scaling expression τ_{th}^{fit} of Eq. (4) fits the experimental data well. Symbols represent averaged positions of data from tokamaks. E: JET; J: JT-60U; S: TORE SUPRA; T: TFTR; D: DIII-D; A: ASDEX; X: TEXTOR; F: FTU; 2: JFT-2M; C: Alcator C-Mod; P: PDX. The square corresponds to PBX-M, the reversed triangle to Doublet III and the triangle to T-10.

$\tau_{th}^{L} = 2.3$ s. This value is nearly the same as $\tau_E^{ITER89P} = 2.3$ s, and $\tau_{th}^{JT\text{-}60} = 2.4$ s when the Bohm type confinement criterion is imposed. Since a minimum confinement time of 5.6 s is required for ignition in ITER, an enhancement factor of about 2.5 over the L mode will be necessary. In the L mode phase at $n_e = 0.5 \times 10^{20}$ m^{-3} with an additional heating power of 100 MW, a fusion power of about 150 MW can be produced with $\tau_{th}^{L} \approx 2$ s and an average temperature of $\langle T \rangle \approx 5$ keV. Since the expected alpha heating power from an L mode plasma is less than 40 MW, the uncertainty in the prediction of P_{thr} should be reduced within this range.

4. H MODE CONFINEMENT

On the basis of the ITER H mode confinement database, a scaling of the thermal energy confinement time for the H mode has been given. A standard regression analysis of data, from ASDEX, DIII-D, JET, JFT-2M, PDX and PBX-M, gave the following scaling of τ_{th} for the ELM free H mode called ITER93-H [2, 3]:

$$\tau_{th}^{ELM\text{-}free} = 0.036\ M^{0.41} I_p^{1.06} B_t^{0.32} \kappa^{0.66} R^{1.9} a^{-0.11} n_{19}^{0.17} P^{-0.67} \qquad (5)$$

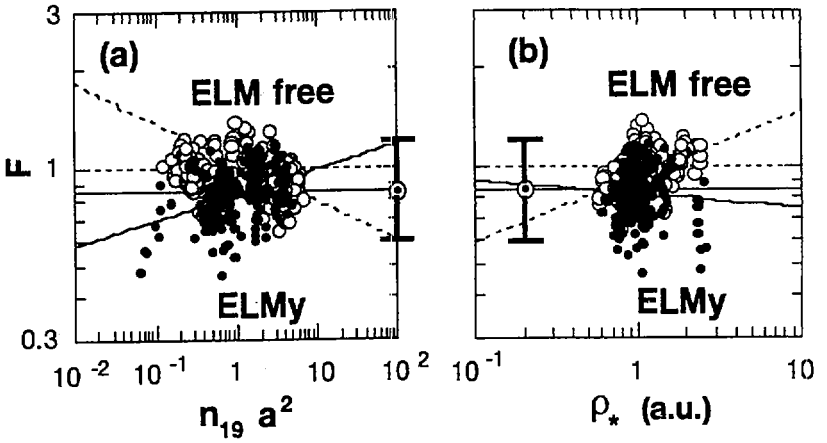

FIG. 6. Dependences of $F \equiv \tau_{th}^{experiment}/\tau_{th}^{ELM\text{-}free}$ *on (a)* $n_e a^2$ *and (b)* ρ_* *for the ELM free case (open circles and dashed lines) and ELMy case (closed circles and solid lines). The expected values for ITER are shown by dotted circles. The uncertainties in the predictions are estimated to be* $\pm 30\%$.

The RMSE for ELM free data is 12.2%. A scaling for the ELMy H mode, τ_{th}^{ELMy}, was also given in Refs [2, 3]; it can be simply evaluated as $\tau_{th}^{ELMy} = 0.85\tau_{th}^{ELM\text{-}free}$. This scaling of $\tau_{th}^{ELM\text{-}free}$ suggests a gyroBohm type transport in H mode plasmas, $\tau_{th}^{ELM\text{-}free} \sim \tau_{Bohm}(1/\rho_*^{0.8}\nu_*^{0.28}\beta^{1.19})$, in contrast to the L mode scaling (Bohm type). In ITER plasmas, β and ν_* will take almost the same values in present H mode plasmas. On the other hand, ρ_* will become smaller than the present values, and the H factor in ITER is expected to become larger than in present tokamaks, by a factor of $1/\rho_*^{0.74}$. The predicted value of τ_{th}^{ELMy} in ITER becomes up to 6 s (H factor ~ 2.5). With this value, ignition in ITER will be achieved. However, if τ_{th} is reduced by 30%, the fusion multiplication factor Q will decrease to around 10.

It is necessary to examine whether systematic degradation of τ_{th} from the above scaling is probable or not with the decrease of ρ_*. From the experimental viewpoint, ρ_* scaling experiments have been performed in DIII-D, JET, JT-60U and ASDEX Upgrade. Here, we study the ρ_* dependence of $F \equiv \tau_{th}/\tau_{th}^{ELM\text{-}free}$ in the database. Recently, many scalings have been proposed, describing the degradation with the increase of $n_e a^2 \propto \beta/\rho_*^2$. An example for such scaling expressions for the ELM free H mode is $\tau^{fit} = F_l \tau_{th}^{ELM\text{-}free}$, where $F_l = 1.3\ M^{-0.09}(a/R)^{0.11} \times (q_{eng}/n_{19}a^2g)^{0.17}(B_tR^{1.25})^{0.04}$ and $\ln g = (n_e a^2)^{-0.5} \ln(2q_{eng})$. The RMSE decreases a little to 12.0% for ELM free data. The scaling is more pessimistic as far as ITER performance is concerned (i.e. $F_l = 0.6$ for ITER parameters).

Figure 6 shows F of experimental data for ELM free (open circles) and ELMy (closed circles) H modes with $3 \leq q_{95} \leq 4$ as functions of (a) $n_e a^2$ and of (b) ρ_*, where q_{95} is the safety factor at the 95% flux surface and is about 1.4 times larger

than $q_{eng} \equiv 5\kappa a^2 B_t / R I_p$ for an ITER-like configuration. The value of ρ_* is evaluated from the thermal stored energy. Note that new data from Alcator C-Mod, ASDEX Upgrade and COMPASS-D are used in this figure. They have only recently been included in the database. Since the ratio $F_{ELMy}/F_{ELM\text{-}free}$ for the data with larger $n_e a^2$ (or smaller ρ_*) is nearly unity but is clearly less than unity for the other data, the dependences of F on $n_e a^2$ and on ρ_* are opposite between for the ELMy (solid line) and the ELM free (broken line) cases; $F_{ELMy} \propto (n_e a^2)^{0\text{-}0.08} \propto \rho_*^{-0.04\text{-}0}$, and $F_{ELM\text{-}free} \propto (n_e a^2)^{-0.12\text{-}0} \propto \rho_*^{0\sim 0.2}$. The value of F_{ELMy} becomes about unity for the ITER parameters in Fig. 6(a). This result supports the previous report that an ELMy H mode scaling predicts a slightly higher τ_{th}^{ELMy} than $\tau_{th}^{ELM\text{-}free}$ with the ITER parameters [2]. From this analysis, we find that the use of the scaling $\tau_{th}^{ELMy} = 0.85 F_{ELM\text{-}free} \tau_{th}^{ELM\text{-}free}$, where $F_{ELM\text{-}free}$ degrades with increasing $n_e a^2$ (or decreasing ρ_*) is not suitable for ITER prediction. The uncertainty in the ITER prediction (expected values are represented by dotted circles in Fig. 6) can be estimated to be $\pm 30\%$ in the present situation. This uncertainty corresponds to ± 26 for a simple power law scaling.

The H mode confinement scaling is re-examined from the viewpoint of the offset linear expression. It is found that the dependence of τ_{th} on P differs among tokamaks: $\tau_{th}^{ELM\text{-}free} \propto P^{-\alpha_P}$. Figure 7 shows results of DIII-D (I_p = 2 MA/B_t = 2.1 T), JET (3 MA/2.3 T), JFT-2M (0.25 MA/1.3 T) and PBX-M (0.34 MA/1.4 T), where $\alpha_P = 0.45 \pm 0.3$, 0.44 ± 0.12, 0.70 ± 0.13 and 0.76 ± 0.24 for DIII-D, JET,

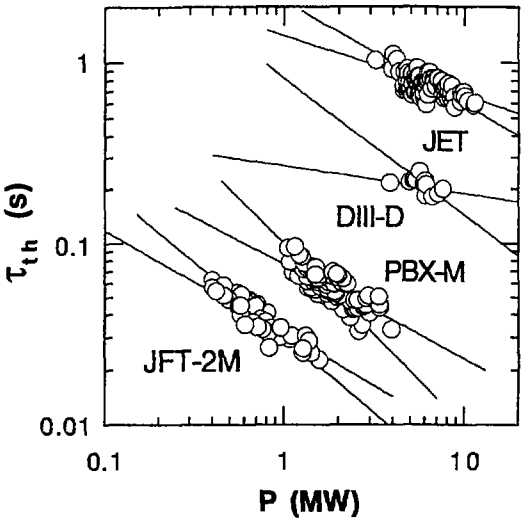

FIG. 7. Power dependence of τ_{th} for the ELM free H mode. The dependences differ among DIII-D (I_p = 2 MA/B_t = 2.1 T), JET (3 MA/2.3 T), JFT-2M (0.25 MA/1.3 T) and PBX-M (0.34 MA/1.4 T).

JFT-2M and PBX M, respectively. This fact indicates that a simple power law such as Eq. (5) is not best suited for the H mode confinement scaling expression. Several offset linear expressions have been proposed [9–11]. One of them gives a rather small RMSE (= 11.1%) against ELM free data [11]. These expressions are, however, dimensionally incorrect. A dimensionally correct form of the offset linear law scaling is the following:

$$\tau_{th} = C_0 I_p B_t R^2 (n_{19} R^2)^{x_0} (B_t R^{1.25})^{y_0} P^{-1} + C_1 I_p R^{1.5} (n_{19} R^2)^{x_1} (B_t R^{1.25})^{y_1} \quad (6)$$

where $B_t R^{1.25} \propto \beta^{0.25}/\rho_*^{1.5}\, \nu_*^{0.25}$. The simplest set of coefficients is given by $C_0 = 0.05$, $x_0 = y_0 = 0$, $C_1 = 0.04$, $x_1 = 0$ and $y_1 = -0.3$. These values are determined by using ELM free data of Alcator C-Mod, DIII-D and JET. This formula is similar to the previous offset linear expression given in Refs [9, 10], where $(B_t R^{1.25})$ is replaced by $R^{2.1}$. The predicted value of $\tau_{th}^{ELM\text{-}free}$ for ITER is 7.3 s, which is nearly the same as that predicted by the power law scaling of Eq. (5). A detailed study of the dependence on other non-dimensional parameters, R/a, κ, etc., is in progress.

In order to improve the reliablity of the ITER prediction, new data from DIII-D and JET have been included in the H mode database. Data from Alcator C-Mod, ASDEX Upgrade, COMPASS-D and JT-60U have also recently increased the range of the database. Data of the RI mode in TEXTOR in the new database will be used for comparison. A detailed analysis of this database is under way which specifically takes into account the effects of smaller ρ_* and higher density.

5. SUMMARY

Databases called the ITER threshold database, the ITER L mode confinement database and the ITER H mode confinement database have been developed and analysed to yield scalings for the prediction of ITER performance. A scaling of the threshold power of the form $P_{thr} \propto B_t n_e^{0.75} R^2 (n_e R^2)^{\pm 0.25}$, which predicts $P_{thr} \approx 100 \times 2^{0\pm1}$ MW for ITER at $n_e = 5 \times 10^{19}$ m^{-3}, has been given. This scaling is derived from experimental data and dimensional considerations, and has a large uncertainty at present. A scaling of the thermal energy confinement time in the L mode and the ohmic phases has been obtained. It has a rather strong density dependence and strong power degradation. For ITER parameters, it attains about 2.3 s, which is nearly equal to $\tau_E^{ITER89P}$. For ignition in ITER, more than 2.5 times this value will be required. The ITER H mode confinement database is expanded from data of six tokamaks to the data of 11 tokamaks. A τ_{th} scaling for the ELMy H mode has been obtained by a standard regression analysis and predicts an ITER confinement time of $\tau_{th} \approx 6 \times (1 \pm 0.3)$ s. No degradation of τ_{th} with increasing $n_e R^2$ (or decreasing ρ_*) is found for the ELMy H mode. An offset linear law scaling with a dimensionally correct form also predicts nearly the same τ_{th} value.

ACKNOWLEDGEMENTS

The databases used in the present analysis were supplied by tokamak teams all over the world: Alcator C-Mod, ASDEX, ASDEX Upgrade, COMPASS-D, Doublet III, DIII-D, FTU, JET, JFT-2M, JT-60, PBX-M, PDX, T-10, TCV, TEXTOR, TFTR and Tore Supra. The authors wish to express their sincere thanks to all members of these teams. They are indebted to the members of the ITER Confinement and Expert Group for continuous collaboration and useful suggestions.

REFERENCES

[1] H-MODE DATABASE WORKING GROUP (presented by KARDAUN, O., et al.), in Plasma Physics and Controlled Nuclear Fusion Research 1992 (Proc. 14th Int. Conf. Würzburg, 1992), Vol. 3, IAEA, Vienna (1993) 251.

[2] H-MODE DATABASE WORKING GROUP (presented by SCHISSEL, D., et al.), in Controlled Fusion and Plasma Physics (Proc. 20th Eur. Conf. Lisbon, 1993), Vol. 17C, Part I, European Physical Society, Geneva (1993) 103.

[3] ITER H-MODE DATABASE WORKING GROUP (presented by THOMSEN, K., et al.), Nucl. Fusion **34** (1994) 131.

[4] ITER CONFINEMENT DATABASE AND MODELING GROUP (presented by KAYE, S.), in Plasma Physics and Controlled Nuclear Fusion Research 1994 (Proc. 15th Int. Conf. Seville, 1994), Vol. 2, IAEA, Vienna (1995) 525.

[5] RYTER, F., H-MODE DATABASE WORKING GROUP, Nucl. Fusion **36** (1996) 1217.

[6] SATO, M., et al., "Threshold power for H-mode transition in JT-60U plasmas", paper presented at 5th H-mode Workshop, Princeton (1995); to be published in Plasma Phys. Control. Fusion.

[7] YUSHMANOV, P.N., TAKIZUKA, T., RIEDEL, K.S., KARDAUN, O.J.W.F., CORDEY, J.G., KAYE, S.M., POST, D.E., Nucl. Fusion **30** (1990) 1999.

[8] SHIRAI, H., et al., in Plasma Physics and Controlled Nuclear Fusion Research 1994 (Proc. 15th Int. Conf. Seville, 1994), Vol. 1, IAEA, Vienna (1995) 355.

[9] MIURA, Y., et al., J. Plasma Fusion Res. **67** (1992) 352.

[10] CHRISTIANSEN, J.P., et al., Nucl. Fusion **32** (1992) 291.

[11] H-MODE DATABASE WORKING GROUP (presented by KARDAUN, O., et al.), in Controlled Fusion and Plasma Physics (Proc. 21st Eur. Conf. Montpellier, 1994), Vol. 18B, Part I, European Physical Society, Geneva (1994) 90.

DISCUSSION

W.D. DORLAND: The ITER93-H expression fails to predict C-Mod and JT-60U H mode confinement by a factor of ~ 2. You estimate the uncertainty in the prediction for ITER as $\times 1.3$. How can you explain this apparent discrepancy?

T. TAKIZUKA: In the Alcator C-Mod data, the discrepancy of the data with $3 \leq q_{95} \leq 4$ from the ITER93-H scaling is < 1.5 rather than a factor of ~ 2, as can be seen from Fig. 6 of our paper.

As for the JT-60U data, one of the causes of the discrepancy is the ITER93-H scaling having a favourable aspect ratio dependence, which is mainly due to the good confinement of PBX-M. Though the ITER93-H scaling is not correct in the aspect

ratio scaling, ITER performance is predictable because the other dependences are determined mainly by the data from tokamaks with shapes similar to that of ITER.

R.J. HAWRYLUK: At this meeting, R.E. Waltz and also others have identified a difficulty in ρ^* scaling experiments, namely the Mach number. In the ρ^* scaling experiment, as well as in the ITER database, how is the toroidal rotation taken into account? Note that the isotopic mass scaling is not consistent with gyroBohm!

T. TAKIZUKA: In the ITER database, the direction of neutral beam injection is described but the rotation speed is not quantified. A difference in the confinement is found between co- and counter-injections although it is not large. As for the ρ^* scaling experiment, it is not within the scope of our present activity.

Appendix

COMPOSITION OF ITER CONFINEMENT DATABASE AND MODELLING EXPERT GROUP

D. Boucher*[10], G. Bracco[4], T.N. Carlstrom[6], J.G. Cordey*[7], J.W. Connor*[16], A.N. Chudnovskij*[15], J.C. DeBoo*[6], B. Dorland[9], Yu.V. Esipchuk[15], S.J. Fielding[16], T. Fukuda[8], R.S. Granetz[11], M. Greenwald[11], G.T. Hoang[2], W. Houlberg*[13], Y. Kamada[8], O.J.W.F. Kardaun[12], S.M. Kaye*[14], M. Kikuchi[8], A. Kus[12], Y. Martin[3], T. Matsuda[8], Y. Miura*[8], O. Naito[8], Y. Ogawa*[17], J. Ongena[1], M. Ossipenko*[15], F. Perkins[10], E. Righi[7], F. Ryter*[12], D.P. Schissel[6], J.A. Snipes[11], U. Stroth[12], H. Tamai[8], T. Takizuka*[8], K. Thomsen[7], M. Valovic[16]; Alcator C-Mod team[11], ASDEX team[12], ASDEX Upgrade team[12], COMPASS-D team[16], Doublet III team[6], DIII-D team[6], FTU team[4], JET team[7], JFT-2M team[8], JT-60 team[8], PBX-M team[14], PDX team[14], T-10 team[15], TCV team[3], TEXTOR team[5], TFTR team[14], TORE SUPRA team[2].

* Official member of the ITER Confinement Database and Modelling Expert Group (no mark: additional members of the Group).

[1] Association Euratom–Belgian State, ERM–KMS, Brussels, Belgium.

[2] Association Euratom–CEA sur la fusion, St. Paul-lez-Durance, France.

[3] Association Euratom–Confédération Suisse, Lausanne, Switzerland.

[4] Association Euratom–ENEA sulla Fusione, Frascati, Italy.

[5] Forschungszentrum Jülich GmbH, Jülich, Germany.

[6] General Atomics, San Diego, California, USA.

[7] JET Joint Undertaking, Abingdon, Oxfordshire, UK.

[8] Japan Atomic Energy Research Institute, Naka, Japan.

[9] Institute for Fusion Studies, Austin, Texas, USA.

[10] ITER Joint Central Team, San Diego, California, USA.

[11] Massachusetts Institute of Technology, Cambridge, Massachusetts, USA.

[12] Max-Planck Institut für Plasmaphysik, Garching, Germany.

[13] Oak Ridge National Laboratory, Oak Ridge, Tennessee, USA.

[14] Plasma Physics Laboratory, Princeton University, Princeton, New Jersey, USA.

[15] Russian Research Center, Kurchatov Institute, Moscow, Russian Federation.

[16] United Kingdom Atomic Energy Authority, Culham, UK.

[17] University of Tokyo, Tokyo, Japan.

ITER

(Poster Session FP)

DEVELOPMENT OF A FULL-SIZE DIVERTOR CASSETTE PROTOTYPE FOR ITER

M.A. ULRICKSON[1]
Sandia National Laboratories,
Albuquerque, New Mexico,
United States of America

G. VIEIDER, H.D. PACHER, I. SMID, C. WU
NET Team,
Max-Planck-Institut für Plasmaphysik,
Garching, Germany

A. PIZZUTO, B. RICCARDI, M. ROCCELLA
Centro Ricerche Energia Frascati,
Associazione Euratom–ENEA sulla Fusione,
Frascati, Italy

P. CHAPPUIS, G. LEMAROIS, J. SCHLOSSER
Centre d'études de Cadarache,
Association Euratom–CEA,
Saint-Paul-lez-Durance, France

M. RÖDIG
Forschungszentrum Jülich GmbH,
Jülich, Germany

L. PLÖCHL
Plansee,
Reutte, Austria

M. AKIBA
Japan Atomic Energy Research Institute,
Naka-machi, Naka-gun, Ibaraki-ken,
Japan

[1] Work supported by US Department of Energy contract DE-AC04-94AL85000.

I. MAZUL
Russian Federation Home Team,
Efremov Institute,
St. Petersburg, Russian Federation

R. TIVEY
ITER Garching Joint Work Site,
Garching, Germany

Abstract

DEVELOPMENT OF A FULL-SIZE DIVERTOR CASSETTE PROTOTYPE FOR ITER.

Production of a full-size divertor cassette for the International Thermonuclear Experimental Reactor (ITER) involves eight major components. All of the components are mounted on the cassette body. Inner divertor channel components for both the vertical target and the gas box design are being provided by the Japan Home Team. Outer divertor channel components for the vertical target design are being provided by the European and United States Home Teams. Gas box liners are being provided by the Russian Home Team. The full-size components manufactured by the four parties will be shipped to the US Home Team for assembly into a full-size divertor cassette. The techniques for assembly and maintenance of the cassette will be demonstrated during this process. The assembled cassette will be tested for proper flow distribution and proof of the filling and draining procedures. The testing will include vacuum leak, cyclic heating to 150°C, and verification of dimensional accuracy of the assembled components. The development of the divertor for ITER depends on successful R&D efforts on materials, joining and plasma–materials interactions. Results of the development program are presented. The scale-up of the processes developed in the basic R&D tasks is accomplished by producing medium and full-scale mock-ups and testing them at high heat flux. The design of these mock-ups is discussed.

1. Introduction

The divertor is one of the critical heat removal systems in the ITER machine. Steady-state high heat flux in a neutron environment coupled with erosion and very large transients due to plasma current disruptions create a very challenging environment. The divertor is composed of modules (cassettes) which permit easy maintenance (see Figure 1). Beryllium, carbon-fiber composite, and tungsten are being considered for the plasma facing materials (PFM). The heat removal structures are being designed with copper alloys while the structural supports are 316 stainless steel.

The divertor task will develop, test and demonstrate the fabrication technology for the divertor and its high heat flux and plasma facing components (PFC), with particular attention to the achievement of tolerances, reliability, and maintainability. The lifetime due to disruptions and realistic estimates of tritium retention and permeation will also be established within the scope of this project. A full-size divertor cassette, including support structure (body) and PFC, is to be developed and tested in the main design task (see Figure 1). Development of PFM and techniques for attaching the PFM to a water-cooled copper-alloy heat sink for full-size PFCs is essential for demonstrating the ability of the divertor to meet ITER heat loads. Erosion of the PFM due to normal operation or disruptions will determine the lifetime of the PFCs. The lifetime can be extended if the PFM can be repaired without removing the PFC. Development of plasma spray offers a method for such repair.

2. Design Requirements and Organization of the Work

The divertor components are to be designed for operation with 4 MPa water cooling at 140°C and a maximum flow rate of 4 m^3/s. The peak heat flux is 5 MW/m^2 on the vertical target with a peak off-normal flux of 20 MW/m^2[1]. The other components have a peak heat flux of between 2 and 6 MW/m^2. A total of 10,000 pulses of 1000 s duration are planned for the basic performance phase of operation. The divertor must be designed for halo currents and eddy currents due to disruptions. The forces exerted on the components are equivalent to about 5 MPa of pressure.

The development of the divertor cassette is being shared among teams from the United States (US), Japan (JA), the European Union (EU), and the Russian Federation (RF). Each party has responsibility for one of the major high heat flux components. The EU will supply one half of the outer vertical target and one wing assembly. JA will supply one half of the inner vertical target, two inner wings, and one set of dump targets for the gas box option. The RF will supply five gas box liners to be joined to the wings and the JA gas box option. The US will supply the cassette body, one outer wing, and one half of the outer vertical target. The US has the additional responsibility for determination of the tolerances, interface control, assembly of the completed cassette, and final testing. The final testing will include flow testing, leak testing, verification of assembly techniques and tolerances, and proof-of-principle for remote handling. The development of the cassette is closely tied to the research tasks in the parties. The results from the research tasks are scaled to the size of the cassette in order to complete the cassette manufacturing.

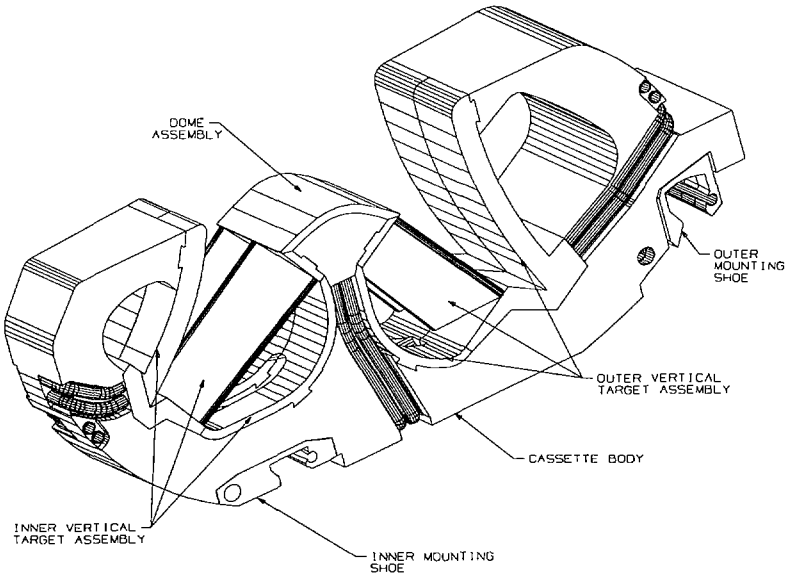

Figure 1. The ITER divertor cassette showing the subelements of the assembly, the shoes for mounting the cassette in the vacuum vessel, and some of the cooling lines.

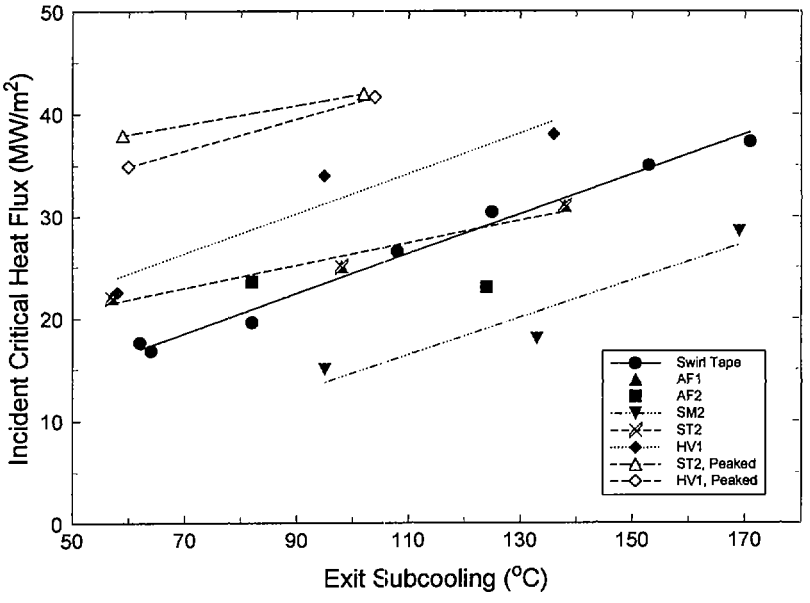

Figure 2. Results of measurements of incident critical heat flux as a function of exit subcooling (see [2]) for a variety of coolant channel designs. All the samples were 27mm wide and heated from one side with 100 mm of heated length except for the peaked profile with 23 mm. The flow velocity was 10 m/s. The samples are: (a) swirl tape is two 10mm dia. tubes with twist ratio 2; (b) AF1 annular flow channel OD=16mm, ID=11mm with twist ratio 2; (c) AF2 annular flow channel OD=22mm, ID=18.6mm with twist ratio 2; (d) SM2 is two 10mm dia. smooth tubes; (e) HV1 is a hypervapotron with a 4mm fin height and 5mm between the fin and the back of the channel and a 21mm width of fin.

3. Results of the Research and Development

3.1 European Union Home Team Results

Extensive thermohydraulics testing was performed by CEA Cadarache (FE-200) on five different heat sink schemes [2]. The results are summarized in Figure 2 for the selected ITER coolant conditions (10 m/s). For 10mm swirl tubes (ST) with a 2mm thick swirl tape, a good agreement was found with the existing CEA database for uniform heating and incident critical heat fluxes (ICHF) of 26 and 42 MW/m^2 for uniform (100 mm heated length) and peaked heat flux (100mm heated length with a full-width at half-maximum of 45mm, about one-half of the ITER peaked profile width), respectively. For hypervapotrons (HV), a 30% higher incident-critical heat flux was found compared with the ST, but the maximum critical heat flux may be limited by the copper operating temperature or stresses. We conclude that peak transient heat fluxes up to 30 MW/m^2 could be tolerated with a 50% margin to critical heat fluxes for divertor-like peaked profiles.

The industrial development of 3D-carbon fiber composites (CFC) with and without Si doping has been completed. Characterization is in progress. For the CFC with 10% Si [3],

a high thermal conductivity of 320 and 150 W/m K at room temperature and at 800°C has been measured. These materials are thermally stabile when heated to 1600°C for one hour. The Si containing CFC showed a reduction of chemical erosion by a factor two to three at 500°C and an order of magnitude reduction of tritium retention, outgassing, and water/air reactivity compared with CFC without Si.

More than 50 small-scale mock-ups of high heat flux components have been manufactured with CFC, Be and W-armor, CuCrZr and DS-Cu heat sinks, and several bonding techniques, primarily without silver. Brazing was mainly used for Be armor, where a monoblock mock-up survived ~150 cycles at about 10 MW/m^2 in the Joint European Torus (JET) neutral beam test facility and a flat tile mock-up survived 500 cycles at about 5 MW/m^2 in the 60 kW electron beam facility JUDITH at Kernforschungsanlage (KFA) [4, 5]. One of joining technique for the CFC tiles to the copper heat sink materials was already developed and tested on prototypes for TORE-SUPRA. These elements survived several thousand cycles of heat flux testing at 15 MW/m^2 on FE-200 [6]. "Active metal casting" of a Cu interlayer was applied to CFC and W armor with subsequent brazing or electron beam welding of the armor tiles to the Cu heat sink. Several CFC monoblock mock-ups survived 1000 cycles at 20 MW/m^2 without damage in JUDITH [7]. Hot isostatic pressing (HIP) and diffusion bonding is used for all armor materials. Completion is expected by October 1996 to provide the basis for the selection of the manufacturing technique. A neutron irradiation program has been carried out at High Flux Reactor (HFR) Petten[8]. Irradiation at 0.5 dpa at 350 and 700°C was completed for several different CFCs, Be and W-alloys as well as small mock-ups to be tested in JUDITH [9].

The European design of the vertical target features CFC-monoblocks in the high heat flux region for maximum lifetime and W-flat tiles on the remainder of the target. A 10mm swirl tube in DS-Cu is chosen as the heat sink in the CFC-monoblock region (ST2, see Figure 2). The target is made as an assembly of plate like modules consisting of plasma facing armor, heat sink and a thick stainless steel support.

3.2 Japanese Home Team Results

The Japanese Home Team has developed a saddle-shaped divertor mock-up with parallel cooling channels, and tested it in the Japan Atomic Energy Research Institute (JAERI). The armor tile was unidirectional CFCs and the cooling tube was made of OFHC Cu. The mock-up successfully withstood both a heat load of 5 MW/m^2 at 15 s for more than 10,000 cycles, and a heat load of 15 MW/m^2 at 15 s for more than 1000 cycles, which corresponded to heat load requirements for the normal operation and the slow transient condition of ITER, respectively [10]. Neither degradation of thermal response nor failure of the armor was found. In parallel, development of the bonding technique for 3-D CFCs brazed on a DS Cu swirl tube with a nonsilver braze has also been continued for this configuration to enhance thermal fatigue performance. Based on this encouraging result, a 1/4-width mock-up of the vertical target has been fabricated as shown in Figure 3.

Small CVD-tungsten-coated divertor mock-ups were fabricated and tested in an ion beam test facility in JAERI. The mock-up endured a heat load of 15 MW/m^2 at 0.3 s for more than 1000 thermal cycles without failure, which gives an equivalent thermal stress at the bonding interface under a steady-state heat load of 5 MW/m^2[11].

For the short dump target, the Japanese Home Team proposes to use a saddle-shaped configuration or a new configuration based on the thermal bond layer(TBL) concept proposed by the ITER Joint Central Team (JCT). A small mock-up was fabricated with a Pb-0.1Cu filler as the thermal bond layer. The mock-up endured up to 15 MW/m^2 for several cycles without degradation of thermal response[12].

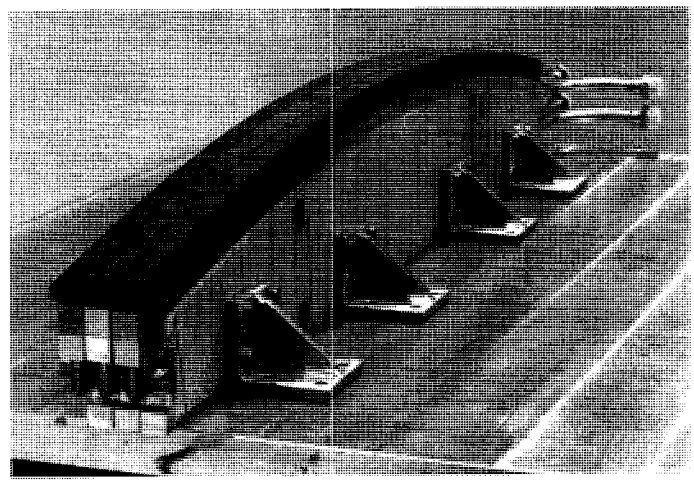

Figure 3. One-quarter-width mock-up of the vertical target. The length is 1.3 m, and the width is about 10 cm. The armor tile is unidirectional CFCs brazed on an OFHC Cu heat sink with a silver braze. The cooling tube is an OFHC Cu swirl tube.

3.3 Russian Federation Home Team Results

The gas box liners receive power from photon and particle flux that passes through the wing structures. The maximum heat load is about 1 MW/m^2. Since there are large holes in the gas box liners for the pumping ducts, they must be constructed to allow simple diversion of the coolant flow around the cutouts. The Russian Home Team is proposing the use of a structure composed of a SS backing plate covered by array of Cu-Cr-Zr rectangular beams with circular cooling channels. These beams are armored by Be-Cu or W-Cu bimetallic tiles. The coolant is routed around the cutouts by adding a duct to the edge of the panel at the cutout. Interface to wing foot is a stainless steel welded joint. Small and medium scale mock-ups will be tested to prove and optimize the choice of joining technology for Cu-Cr-Zr to Cu, Be to Cu and W to Cu.

Coating a smooth tube with a porous coating has been found to increase the critical heat flux [13]. Medium-scale mock-ups (about 1m long) are being produced with porous coatings. One sample has ribbed channels running the long direction in the heat sink with porous coating on the ribs. The second sample has two tubes with porous coating applied to the inside of the tubes. Both samples will be high heat flux tested. Samples of beryllium joined to copper have been high heat flux tested, and some samples survived for nearly 7000 cycles at 5 MW/m^2[14].

3.4 United States Home Team Results

The US has proposed that the cassette body, including the internal cooling channels, be fabricated using a cast and HIP process. Two prototype castings (475 kg each) have been fabricated using stainless steel 316LN-IG material. No porosity was detected in the castings.

The strength of the material was about 7% less than that of wrought 316 stainless steel (155 MPa vs. 166 MPa). The uniform elongation of the cast material is higher than wrought material (48% vs. 30%). Weld development for joints up to 100 mm thick is in progress. The next prototype will be approximately 2000 kg and contain internal coolant channels. The results thus far are very encouraging for this inexpensive method for fabricating the cassette body.

The joining of beryllium to copper alloys is particularly complicated because beryllium forms brittle berylides with most elements (including copper)[15]. Our studies have indicated the formation of copper berylides (BeCu and Be_2Cu) at temperatures as low as 350°C for times as short as 100 hrs. The use of diffusion barriers between the Be and Cu is being investigated[16]. Aluminum is one of the elements that does not form berylides. Aluminum that is explosion bonded to copper alloys and then joined to Be using an AlSi braze (including HIP) has produced very strong joints (>100 MPa) which are being tested at high heat flux. Graded layers of Al and Be are in development. They have the advantage of about three times the strength and a better thermal expansion match. High thermal conductivity and high density (>98%) beryllium coatings on copper have been made using the plasma spray method[17]. These coatings will be high heat flux tested in late 1996. The relative thermal fatigue resistance of several grades of beryllium has been measured[18].

Tungsten and copper have very different thermal expansions. Thin tapes (0.5 mm) containing 20, 40, 60, and 80% W in a soft copper matrix have been produced using either HIP or liquid-phase sintering. These tapes have been joined to each other and to W and Cu alloys using HIP at 450°C and 100 MPa. High-quality joints were found in micrographs made of the joints. Mechanical testing and high heat flux testing are in progress.

4. Conclusions

The four parties and the JCT are cooperating effectively on the design and development of the divertor for ITER. The preliminary design phase is nearing completion. Fabrication of the full-size components will begin in 1997. The supporting research is also progressing well. The development of joints between plasma facing materials (C, Be, or W) and the copper alloy heat sink is showing that joints suitable for ITER conditions can be produced, although the reliability of these joints under cyclic loading is not yet fully demonstrated. Irradiation effects on the joints are just beginning to be studied. The scale-up of the fabrication techniques to the full ITER size is just starting. While the schedule for producing the full-size divertor cassette is very ambitious, all of the parties still believe that the goal can be achieved during the Engineering Design Activity (by July 1998). Successful completion of this project will demonstrate that the four parties can cooperate on the construction of a very complex component for ITER. Such success will provide assurance that the machine can actually be built as an international project.

REFERENCES

[1] For additional details see the ITER Design Description Document for the Divertor, ITER Document G17DDD, ITER San Diego Joint Work Site, CA.

[2] SCHLOSSER, J., et al., "Comparison between various thermohydraulic concepts for the ITER divertor", Proc. 19th Symp. on Fusion Technology, Lisbon, 1996.

[3] WU, C.H., et al., "Evaluation of an advanced silicon doped CFC for plasma facing material", ibid.

[4] PEACOCK, A.T., et al., "Development of silverfree bonding techniques and the investigation of cadmium in silver brazes", ibid.

[5] FALTER, H.D., et al., High Heat Flux Exposure Tests on Beryllium Monoblocks Brazed to a Copper Swirltube, JET Joint Undertaking, Abingdon, Oxfordshire, UK.
[6] SCHLOSSER, J., et al., "Developments for an actively cooled toroidal pumped limiter for TORE-SUPRA", Proc. 19th Symp. on Fusion Technology, Lisbon, 1996.
[7] LINKE, J., et al., "High heat flux performance tests of divertor modules for ITER with beryllium and carbon armour", ibid.
[8] BONAL, J.P., WU, C.H., Neutron irradiation effects on the thermal conductivity and dimensional stability of carbon fibre composites, J. Nucl. Mater. **228** (1996) 155.
[9] RÖDIG, M., MEUSER, F., POTT, G., Neutron Irradiation HFR-D302 (PARIDE), Rep. KFA-IWE-TN 37/95, Forschungszentrum Jülich GmbH, Germany.
[10] SUZUKI, S., ARAKI, M., SATO, K., NAKAMURA, K., AKIBA, M., IAEA-CN-64/GP-12, these Proceedings, Vol. 3.
[11] SATO, K., et al., "High heat flux test of CVD-tungsten coated Cu heat sink divertor mock-up", Proc. 12th ANS Topical Mtg on Technology of Fusion Energy, Reno, NV, 1996.
[12] SUZUKI, S., et al., "High heat flux experiments on divertor mock-ups with a thermal bond layer", ibid.
[13] DIVAVIN, V.A., GRIGORIEV, S.A., TANCHUK, V.N., High heat flux experiments on mock-ups with porous coating on the inner surface of circular coolant channels, Proc. ASME Heat Transfer Division, HTD **317-1** (1995).
[14] GUINIATOULINE, R.N., et al., Analysis of a beryllium–copper diffusion joint after HHF test, J. Nucl. Mater. **233–237** (1996) 616.
[15] ODEGARD, B.C., A review of the joining techniques for plasma facing components in fusion reactors, J. Nucl. Mater. **233–237** (1996) 44.
[16] CADDEN, C.H., BONIVERT, W.D., ODEGARD, B.C., WATSON, R.D., in Proc. 16th IEEE/NPSS Symp. on Fusion Engineering, Champaign, IL, 1995, p. 377.
[17] CASTRO, R.G., et al., ibid., p. 381.
[18] WATSON, R.D., YOUCHISON, D.L., DOMBROWSKI, D.E., GUINIATOULINE, R.N., KUPRIYNOV, I.B., ibid., p. 214.

ITER PRIMARY VACUUM PUMPING CONCEPT DEVELOPMENT AND TESTING PROGRAMME

D.K. MURDOCH
NET Team,
Max-Planck-Institut für Plasmaphysik,
Garching, Germany

A. MACK
Forschungszentrum Karlsruhe,
Karlsruhe, Germany

J.-C. BOISSIN
L'air liquide,
Division des techniques avancées,
Sassenage, France

Abstract

ITER PRIMARY VACUUM PUMPING CONCEPT DEVELOPMENT AND TESTING PROGRAMME.

The demands on torus exhaust pumping of the ITER machine are very high, owing to the in-vessel primary pump location which requires high reliability and durability in a challenging environment, characterized by high magnetic and radiation fields and the potential for sudden pressurization with air and/or steam under accident conditions. To meet these exacting requirements, cryosorption pumps with cyclic regeneration have been selected for all modes of machine operation, following initial rough pumping by a mechanical pump train. For plasma burn duty, the combination of high gas throughput and low allowable tritium inventory limits the cryopump cycle time, necessitating fast regeneration and a large number of cycles in the projected lifetime of the machine. The pump concept proposed embodies a number of novel design principles to meet these conditions, and an integrated development programme is under way in order to test critical components and to design, build and test a model pump.

1. INTRODUCTION

The primary vacuum pumping system consists of sixteen identical batch regenerating cryosorption pumps, each located in one of the divertor ducts of the machine [1]. The performance requirements are exacting, in terms of versatility in handling broad ranges of gas composition and pressure, robustness to withstand the in-vessel environmental conditions and off-normal events, and reliability in order to minimize maintenance intervention.

The pump development programme comprises both design and supporting R&D activities. Within the constraints of the limited time available during the ITER EDA and the test facilities available (currently being upgraded), the goal is to maximize progress towards qualification of a full scale prototype pump. Accordingly, the decision was made to design, build and test a model pump with a total pumping surface of 50% of that proposed for the full scale version. Critical components, such as the inlet valve, and key dimensions, such as the cross-section and the pitch of the pumping panels, are being maintained at full scale so as to minimize any uncertainties in performance due to the scale-up of the design. The R&D includes both the qualification of critical components and the construction and testing of the reduced scale cryopump.

2. PERFORMANCE REQUIREMENTS

The pumps are designed to provide the specified vacuum conditions inside the machine during all phases of operation following roughing down by a separate, externally located, mechanical pump system. These phases include pumpdown to base pressure, bake-out, wall conditioning, leak detection and plasma operation (He, H_2, D_2, and DT pulses). The operating parameter ranges are specified in the ITER Vacuum Equipment Specification [2]. The main duties of the system are summarized in Table I.

TABLE I. PRIMARY PUMPING SYSTEM PARAMETERS

Pumping speed, m^3/s	1000
Maximum throughput, Pa·m3/s	245
Minimum pressure for maximum throughput, Pa	0.245
Base pressure, Pa	10^{-7}
Maximum tritium inventory, g	140
Maximum inlet gas temperature, K	475
Magnetic field (peak), T	3.0
Lifetime radiation dose, Gy	5×10^6
Nuclear heating, W/cm^3	4×10^{-3}
Design pressure, MPa	0.5

3. CONCEPT DESCRIPTION

The design (Fig. 1) is based on a cylindrically shaped cryopump of 1.5 m diameter, with a valved 1 m diameter inlet port, an ~80 K louver baffle cooled by gaseous helium (GHe), and laterally arranged 5 K cryosurfaces with a total area of 8 m^2/pump cooled by supercritical helium (SCHe) [3]. The pump is directly attached to the duct plug.

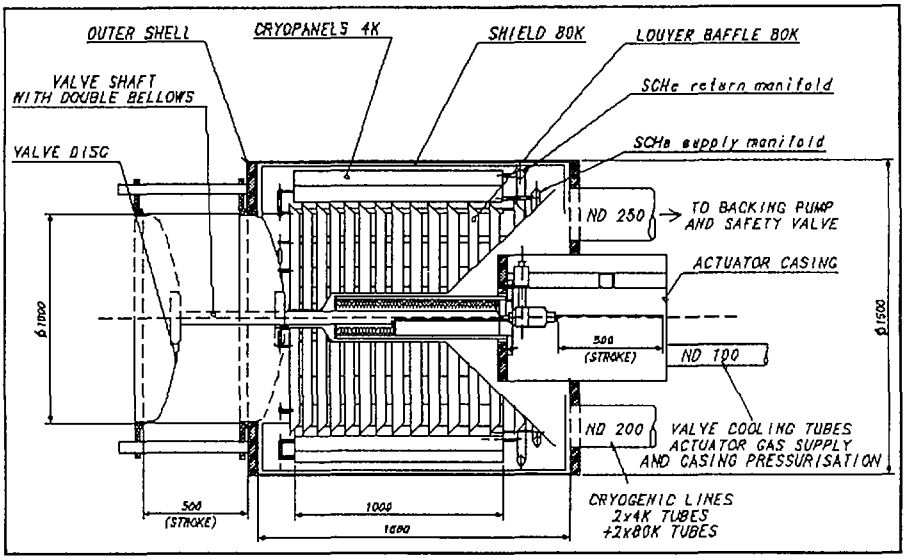

FIG. 1. ITER primary cryopump — preliminary design (dimensions in millimetres).

Impurity, fuel and helium ash fractions are cosorbed on a single set of activated charcoal coated panels maintained at ~5 K, eliminating the need for pumping stages between the pump inlet and the helium pumping panels, thereby maximizing the conductance through the pump to achieve the required pumping speed for helium [4]. Between the pump inlet and the pumping panels the gas passes through a single set of baffles at ~80 K, which, along with the shielding on the inside of the pump shell (also at 80 K), reduces the refrigeration requirements of the 5 K panels. The pump is designed to operate in the molecular flow regime which exists at pressures lower than 10^{-1}Pa at the pump inlet. Above this pressure, transition or viscous flow prevails, and heat conduction from ~80 K components to the 5 K panels would increase refrigerant consumption to unacceptable levels. During pumping, the inlet valve maintains the pressure inside the pump within the molecular/transition regime and controls the throughput and pumping speed of the pump. For regeneration, the valve is closed to isolate the pump from the torus.

4. DEVELOPMENT

4.1. Fast regeneration requirement

The combination of high throughput and low tritium inventory limit requires a very short operating cycle time (see Table II). At any chosen time during the reference DT plasma operation mode, twelve of the sixteen pumps will be in the pumping mode

TABLE II. PUMP OPERATING CYCLE (DT PLASMA)

Phase	Time (s)
Pumping	750
Regeneration steps	
Close inlet valve (torus isolation)	10
Warm up panels from 5 to 90 K	60
Desorb pumped gas	20
Pump out desorbed/evaporated gas	60
Cool down panels from 90 to 5 K	60
Reopen torus isolation valve	10
Subtotal	220
Contingency	30
Time available for regeneration phase	250
Overall pump cycle time	1000

and four in various stages of regeneration [3]. The individual pump cycles are staggered at equal 62.5 s (i.e. 1000 s/16) intervals to minimize the total system inventory.

Appropriate process parameters for quantitative release of the sorbed tritiated gas species are being determined so that a balance is struck between effective regeneration and avoidance of excessively severe heating and cooling methods. This determination is presently being carried out for the broad spectrum of gas compositions anticipated, and cryopanel warm-up temperatures of ~80–90 K for partial regeneration and up to ~300 K for complete regeneration are anticipated. The durations envisaged for the various steps in the operating cycle (as indicated in Table II) are being experimentally determined/confirmed.

4.2. Fast panel heating tests

Parametric tests of three heating methods for fast regeneration of cryopanels were carried out at the Forschungszentrum Karlsruhe (FZK), Germany [5]. Infrared radiation heating was tested, but the short heating times required could not be achieved because of the high thermal inertia of the heating rods. This is a generic drawback of methods where the heating source is not in contact with the panel, and no further investigation of such methods was undertaken.

As the second method, a forced flow of warm helium gas was passed through the flow channels of the test cryopanel, and the heating times for different mass flows were recorded. Significant temperature inhomogeneities across the panel surface were observed owing to a non-optimized panel geometry and the use of LHe (liquid helium) rather than SCHe as refrigerant. Nevertheless, heating times of less than 60 s were measured at positions on the panel surface representative of the ITER geometry.

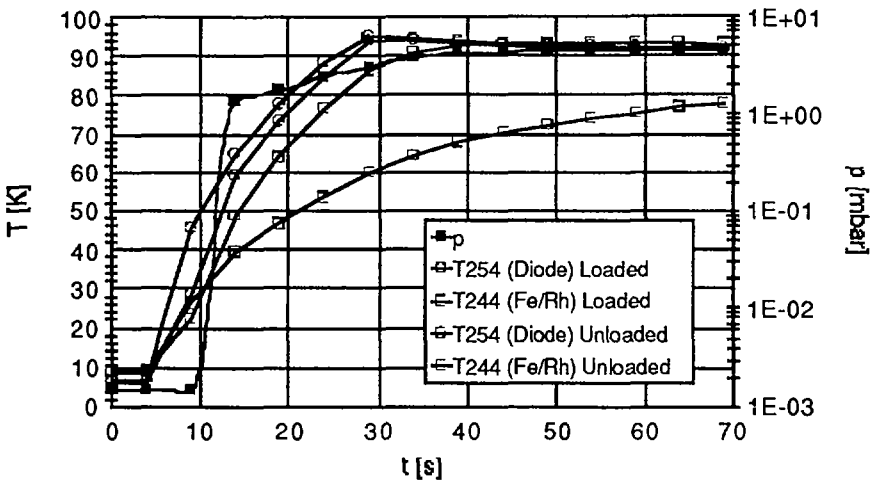

FIG. 2. Fast regeneration test of cryopanel (electrical resistance heaters).

The third heating method investigated was surface bulk heating with electrical resistance heating elements mechanically fastened to the panel substrate. By using this technique, heating times of less than 30 s were achieved without difficulty (Fig. 2). The technique can provide precise control of the panel temperature as well as a uniform temperature distribution over the panel surface.

On the basis of these tests, the required heat input for one full scale ITER cryopump (8 m^2 pumping surface) has been estimated to require a flow rate of 70 g/s GHe flow or about 30 kW electric heating power, respectively. By adjusting the warm-up period to ~60 s, which is the time interval between regenerations of successive pumps in plasma operation, one of the sixteen pumps would be in warm-up mode at any given time, and this heat input would, from the system perspective, be a steady state load.

A final selection of the heating process for ITER depends on confirmatory tests with a panel of optimized geometry, endurance tests, and engineering assessments of related safety, operational and economic aspects of the respective techniques.

4.3. Fast panel cooling tests

An initial series of tests indicates that recooling of the panels to ~5 K after regeneration can be achieved within the target time of 60 s. The precision of the test results was compromised by the cylindrical shape of the temperature sensors (Fe–Rh thermocouples) used and the fixation method (cement), which resulted in poor contact with the panel surface. A further series of tests using flat temperature sensors with inherently faster response times (silicon diodes) soldered on to a panel more representative of the geometry selected for the ITER pump is in progress.

4.4. Temperature cycling tests

During the ITER lifetime the cryopanels must withstand a large number of fast heating and cooling cycles without significant loss of pumping performance. It is estimated that approximately 200 000 cycles between 5 and 90 K (partial regeneration to recover helium, hydrogenic species and most impurity species) and 20 000 cycles between 90 K and room temperature (complete regeneration to recover trapped water vapour, etc.) will take place. Endurance tests comprising representative numbers of cycles over these temperature ranges are being conducted to ensure that the proposed panel design will meet this duty. Test panels will be examined and pumping speed measurements made periodically during the tests to determine if and when any performance degradation occurs.

4.5. Sorbent performance

Because of the low rate of transport of hydrogenic species into the bulk of the sorbent, which could limit pumping speed and/or capacity for these species, it may be preferable to use panels in which the side facing the axis of the pump is bare metal (stainless steel), to enable a large fraction of the hydrogenic species to be pumped by condensation, with more favourable kinetic characteristics than the sorption and desorption from an activated charcoal layer. This should enhance quantitative recovery of tritium during regeneration, which will contribute to tritium inventory minimization. There is a trade-off in sorption capacity and pumping speed for helium and protium (at lower pressures), and these conflicting requirements will be carefully evaluated as the design and supporting R&D proceed.

The most recent tests [6] of sorbent panel pumping speed and capacity for pure helium indicate that the specified system pumping speed and throughput (Table I) can just be achieved at gas loadings up to 0.2 $Pa \cdot m^3/cm^2$, which corresponds to the reference 750 s pumping period, provided both sides of the panel are coated with sorbent. For protium, the safety margin on pumping speed is more comfortable, but sorption capacity only just exceeds requirements. Further tests to investigate the poisoning effect of impurities, which would progressively degrade sorbent performance, are under way. The sorbent used for these tests consists of a ~1 mm thick layer of activated charcoal (Chemviron SCII), bonded to the stainless steel substrate by an inorganic cement (Thermoguss 2000) employing a process specially developed at the Forschungszentrum Karlsruhe in Germany [7].

The cryopanels are based on a quilted design, to minimize the length of the heat transfer path and, therefore, the temperature differential between the sorbent layer and the supercritical helium refrigerant. For the reference burn conditions, preliminary calculations of the temperature differentials between the refrigerant (bulk) and the sorbent pumping surface have been made [2] (Table III).

Thus the temperature rise through the sorbent layer dominates the overall differential. In addition, the longitudinal temperature rise along the panel as the

TABLE III. TEMPERATURE DIFFERENTIALS THROUGH PANEL ELEMENTS

Resistance	Temperature differential (K)
Film layer	0.08
Metal substrate	0.16
Sorbent	0.29
Frost interface	0.01
Frost layer	0.01
Total	*0.55*

refrigerant picks up heat will account for an additional ~0.2 K, resulting in a temperature of 5.1–5.3 K at the pumping surface of the panel, based on an SCHe refrigerant supply temperature of 4.5 K. Tests and calculations of sorbent performance, as well as benchmarking against data in the literature, will reflect these temperatures.

4.6. Tritium testing

The mechanical integrity of the sorbent/bonding agent/substrate system under tritium exposure is being verified by using small scale coupons. These tests, which are now in progress, consist of exposure of approximately 100 coupons representative of candidate sorption panel options to different combinations of tritium pressure, temperature and exposure time. This will determine the contributions of the various pump operating phases to any degradation in the physical properties of the sorbent/bond/substrate system, and enable material property evolution over the relatively short test periods to be extrapolated with confidence to the expected lifetime of ITER. First results show that accelerated exposures to tritium in line with ITER lifetime projections (~10^{10} Pa·s) give rise to a measurable, but acceptable, decrease in the microhardness of the sorbent used, but no degradation of the sorbent or bonding agent integrity was reported. In a second test series, the evolution of pumping/regeneration characteristics of a panel will be studied as a function of tritium exposure.

4.7. Valve development

The combined regeneration and throttling valve at the pump inlet is an integral part of the pump assembly. A travel time of 5–10 s is specified in order to adapt pump performance to fluctuations in divertor pressure and exhaust gas flow rate. The specified pressure range of approximately two orders of magnitude (0.245–10 Pa), over which pump throughput is to be held constant, may require the incorporation of a small supplementary valve which would be mounted on the main valve disc and

driven by the same actuator as the main valve. The same valve system is used to isolate the pump volume from the torus during regeneration.

The valve discs will be cooled by 300 K helium gas, and are sealed by metallic O-rings. The main valve stroke is 500 mm, in order to offer an opening of ~1.5 times the area of the 1 m diameter port, thereby minimizing the throttling effect when the valve is fully open.

Tests will be carried out to calibrate the throttling effect as a function of valve opening, and endurance tests will be conducted to verify that the required number of cycles (approximately 10^6 in the lifetime of the machine) can be achieved.

5. MAINTENANCE

As no in situ maintenance at the specified pump location is possible, all components of the pump are designed for maximum reliability and longevity. The pumps will be removed from the machine, transferred to a hot cell, refurbished and reinstalled on a planned, but infrequent, basis. Schemes for effecting these transfer operations, using a set of purpose-built casks, are being developed [7]. Occasional isolated pump failures will be accommodated by the modest redundancy margin inherent in the system, and, for some operational modes, an extension of operating times until a suitable machine outage provides an opportunity for replacement of the faulty pump(s).

6. CONCLUSIONS

The programme planned at present covers the remainder of the ITER EDA and will culminate with the completion of fabrication and preliminary performance testing of a model pump, which, although smaller than the full scale ITER duty by a factor of two in terms of pumping speed, embodies ITER relevant scale inlet valve and sorption panels and will therefore provide a sound basis for extrapolation to an ITER scale prototype pump design.

ACKNOWLEDGEMENTS

The collaboration of the members of the Vacuum Pumping Task Force at the Forschungszentrum Karlsruhe in providing the experimental data and in planning the future programme outlined in this paper is gratefully acknowledged.

REFERENCES

[1] JANESCHITZ, G., et al., IAEA-CN-64/F-2, this volume.
[2] LADD, P., et al., Vacuum Equipment Specification - Primary Cryopump, ITER Garching JWS (April 1996).
[3] BOISSIN, J.-C., ITER Model Pump Conceptual Design, Final Report, FZK Contract 315/20 002 214/HIT 1/8/95 (December 1995).
[4] PERINIC, D., et al., "Proposal of a torus pumping and fuel recycling system for ITER", Fusion Technology 1994 (Proc. 18th SOFT, 1994), Vol. 1, (1994) 1131.
[5] DAY, Ch., et al., Tests on Fast Heating for the Regeneration Process of ITER Cryopumps, Rep. FZK 5806, Forschungszentrum Karlsruhe, Germany (1996).
[6] DAY, Ch., Forschungszentrum Karlsruhe, personal communication, 1996.
[7] ÖZDEMIR, I., et al., "A comparison of thick and thin sorbent layers for plasma exhaust cryopumping", Fusion Technology 1994 (Proc. 18th SOFT, 1994), Vol. 1 (1994) 1123.
[8] HAINES, T., et al., Spar Aerospace/CFFTP, personal communication, 1996.

R&D ACTIVITY OF KAZAKHSTAN ON THE ITER PROJECT

V.S. SHKOLNIK
Ministry of Science,
Academy of Sciences
of the Republic of Kazakhstan,
Almaty

V.A. SHEMANSKY
National Joint Stock Company KATEP
of the Republic of Kazakhstan,
Almaty

Yu.S. CHEREPNIN
National Nuclear Center
of the Republic of Kazakhstan,
Kurchatov

E.Ya. SKOZ
Joint Stock Company UMZ,
Ust-Kamenogorsk

L.I. NAZARENKO
Mangyshlak Nuclear Energy Combine (MAEK),
Aktau

V.P. SHESTAKOV
Scientific Technical Center (CTF),
Almaty

I.L. TAZHIBAEVA
Scientific Research Institute of Experimental
and Theoretical Physics,
Kazakh State National University,
Almaty

Kazakhstan

Abstract

R&D ACTIVITY OF KAZAKHSTAN ON THE ITER PROJECT.

The paper discusses the R&D activity of the Republic of Kazakhstan on the ITER project. The main Kazakh participants in the ITER programme, their work sites and resources are described. The types of irradiation and research facility and the techniques used are presented. The main tasks ('Divertor' and 'Safety') of Kazakhstan are described. The principal directions of the Kazakh work under the ITER project are formulated and the main results of the work carried out so far are presented. This work includes: (1) irradiation testing in the BN-350 reactor; (2) study of the physical and mechanical properties of industrial grades of beryllium in the temperature range 200–800°C to determine its possible use in the ITER project; (3) microstructural characterization of polycrystalline beryllium material; (4) investigation of in-vessel component materials, including IVG.1M reactor experiments investigating the hydrogen permeability of stainless steel and of the vanadium alloys VCr6Ti5 and VCr4Ti4; (5) study of beryllium and graphite plasma facing components, including research on the changes in beryllium surface element composition caused by deuterium–hydrogen plasma interaction and on deuterium permeation through beryllium with surface element composition control, as well as the results of IVG.1M in-pile experiments on hydrogen–RGT–graphite interaction and hydrogen–beryllium interaction.

In July 1994 the Republic of Kazakhstan became an official participant of the ITER project.

The main collaborating institutions of the ITER project in Kazakhstan are the National Nuclear Center (NNC), the National Joint Stock Company of the enterprises for nuclear engineering and industry (KATEP), and the Scientific Research Institute of Experimental and Theoretical Physics of the Kazakh State National University (NIIETF KazGU).

NNC, located on the territory of the former Semipalatinsk testing site, has the following experimental facilities for carrying out work on the ITER project:

(a) The pulsing IGR reactor, on which were carried out the first reactor tests in the former USSR of fuel for nuclear rocket engines. At present IGR is used for materials studies and modelling of cooling loss emergencies in water–water type reactors. Use of the reactor for modelling an emergency involving loss of ITER divertor cooling is planned. The flow of neutrons in a pulse of 0.12 s is 0.7×10^{17} n·cm^{-2}·s^{-1}, and in a stationary mode 0.7×10^{16} n·cm^{-2}·s^{-1}; the maximum fluence of thermal neutrons is 3.7×10^{16} n/cm^2 (per reactor run).

(b) The IVG.1M and RA reactors were also intended for testing fuel for nuclear rocket engines. At present they are used to study, within the framework of the ITER project, the interaction of hydrogen isotopes with structural materials of the discharge chamber, divertor and blanket of a thermonuclear reactor (permeation and inventory). In IVG.1M the flow of thermal neutrons is 5×10^{14} n·cm^{-2}·s^{-1}, and of fast neutrons 2×10^{13} n·cm^{-2}·s^{-1}. The nominal power is 60 MW, and the time of operation at a nominal level is 2 h. In the RA reactor the flow of thermal neutrons is 2×10^{12} n·cm^{-2}·s^{-1} and of fast neutrons 3×10^{13} n·cm^{-2}·s^{-1}, and the operating time is 100 h.

The Institute of Nuclear Physics has the following irradiation devices:

(a) The isochronous cyclotron U-150, in which the energy of accelerated particles — protons, deuterons, helium ions, α particles — is adjustable between 7 and 60 MeV, with a current of 15–70 μA;
(b) The heavy ion accelerator UKP-2-1, which allows ions of all masses from hydrogen to uranium to be accelerated with an energy of up to 2 MeV, with a current of 0.1–60 μA;
(c) The VVR-K water–water type research reactor, with a density of thermal neutron flow of 2×10^{14} n·cm^{-2}·s^{-1} and power of up to 10 MW.

KATEP (ULBA plant) carries out:

(a) The manufacture of fuel pellets for nuclear power plants;
(b) The manufacture of beryllium, including all technological processes from the processing of concentrates to production of the final compact beryllium;
(c) The production of ceramics based on beryllium oxide;
(d) The production of beryllium alloys and of copper–beryllium and aluminium–beryllium alloy compositions;
(e) Industrial manufacture of superconducting materials for thermonuclear fusion installations.

Mangyshlak Nuclear Energy Combine (MAEK) is the owner of the BN-350 reactor, a fast neutron reactor that produces 125 MW of electric power and 1×10^5 t/d of purified water, and that at present is also used for irradiation of beryllium samples for the ITER programme. The BN-350 reactor has a thermal power of 1000 MW and a neutron flux density of 0.6×10^{16} n·cm^{-2}·s^{-1}.

NIIETF KazGU carries out experiments to study hydrogen isotope inventory and permeation in long range materials for the ITER first wall and divertor (graphite, beryllium, stainless steel, vanadium alloys). In-pile experiments are carried out in collaboration with NNC under the tasks 'Divertor' and 'Safety'. Out-of-pile experiments are devoted to the study of the interaction of hydrogen with beryllium, steels and vanadium alloys under temperature and chemical (active gases) influence, and also under the influence of a hydrogen–deuterium glow discharge plasma with simultaneous control of surface element composition changes by an Auger electron spectroscopy method. The principal directions of Kazakh work in 1996–1997 for the ITER project concern the following main areas of the R&D task agreement:

(1) Irradiation tests of materials on the BN-350 reactor;
(2) Continuation of in-pile experiments for determination of deuterium interaction parameters with beryllium samples manufactured by the ULBA plant of KATEP using the IVG.1M nuclear reactor (permeation and inventory);
(3) Conducting of in-pile experiments for determination of hydrogen isotope permeation parameters for vanadium alloys using the IVG.1M reactor, and of out-of-pile experiments with beryllium and with vanadium alloys;

(4) Investigation of beryllium structure and properties with respect to hydrogen in conditions simulating gas impurity inventory, and under thermal and neutron influence;
(5) Simulation of plasma disruption on the divertor;
(6) Simulation of water steam interaction with beryllium;
(7) Determination of hydrogen permeation parameters for various materials with in situ surface control by the Auger electron spectroscopy method;
(8) Development and manufacture of Be–Cu alloys.

MAIN RESULTS OF ITER R&D

(1) Irradiation testing in the BN-350 reactor

The in-pile assembly for irradiation of beryllium samples in the industrial reactor BN-350 has been developed, and irradiation of the samples is being carried out in the reactor. To prevent reactivity loss, the in-pile assembly is combined with antimony tubes in order to increase the neutron flux density in the active zone. This construction of the in-pile assembly allows samples to be irradiated up to a damage level of 10 dpa and the reactivity loss of the reactor to be compensated by the yield of photoneutrons from the antimony [1, 2]. At present, the assemblies are being prepared for determining tritium and helium production in beryllium and for investigating physical and mechanical properties of irradiated beryllium and duplex structure Be–Cu.

(2) Study of the physical and mechanical properties of industrial grades of beryllium in the temperature range 200–800°C to determine its possible use in the ITER project

HIP-56 grade beryllium has the best isotropism of physical and mechanical properties, owing to the absence of appreciable crystallographic texture in comparison with other beryllium grades. Deformed beryllium grades EHP-56 and BHP-56 have the highest strength and plastic properties at 20–500°C. This is explained by the formation of a crystallographic texture and linear oriented microstructure inherent to semifinished items during deformation (extrusion or forging). In the range 600–800°C, HIP-56 and HP-56 grades of beryllium have the highest strength properties, while deformed grades EHP-56 and BHP-56 have the highest plastic properties, which is explained by the change of deformation mechanisms during the tests. Mainly dislocation sliding at 20–500°C is being changed by sliding along grain boundaries. At present, the manufacture of duplex structure Be–Cu using a diffusion welding technique and brazing is being carried out.

(3) Microstructural characterization of polycrystalline beryllium material

The results show that sufficiently complete information about the microstructure of polycrystalline beryllium material can be obtained by means of transmission electron microscopy in combination with optical metallography and X ray diffraction. The material analysed in the present study is a polycrystalline beryllium with an average grain size of about 8.5 μm, with well formed grain boundaries and without cavities. The dislocation density in the grain matrix is 2×10^9 cm^{-2}, taking into account dislocation walls. A high content of BeO inclusions (about 1% by volume) with an average diameter of 400 nm was found in the material.

(4) Investigation of in-vessel component materials

IVG.1M reactor experiments investigating the hydrogen permeability of stainless steel

Pile irradiation was carried out to stimulate the process of hydrogen permeation in 08Cr18Ni10Ti steel. Radiation influence results in the increase of effective diffusion and permeation coefficients with decreasing solubility constants of hydrogen in austenite steel. For that steel, hydrogen effective diffusion and permeability coefficients at 773 K under irradiation were obtained to be 3 and 1.7 times greater than without irradiation, respectively. After irradiation, the effective diffusion and permeability coefficients did not reach their initial values [3].

IVG.1M reactor experiments investigating the hydrogen permeability of the vanadium alloys VCr6Ti5 and VCr4Ti4

Hydrogen gas driven permeation experiments for VCr6Ti5 have been carried out in the temperature range 423–1073 K with input pressures of 10^2–10^3 Pa [4]. The process of hydrogen permeation through the sample was shown to be limited by the surface processes. Sticking, recombination coefficients and solubility constants in the vanadium alloy have been taken from permeation experiments in the framework of the model for hydrogen permeation limited by adsorption and desorption processes without consideration of the rate constants, describing transfer from the surface into the bulk and emergence from the bulk to the surface. The diffusion assembly for in-pile experiments has been developed and manufactured. Preliminary experiments on the effect of reactor irradiation on hydrogen interaction with the vanadium alloy VCr4Ti4 have been carried out. The study of the effect of reactor irradiation on hydrogen mass transfer through vanadium alloys will be continued.

(5) Study of beryllium and graphite plasma facing components

Research on the changes in beryllium surface element composition caused by deuterium–hydrogen plasma interaction

The investigations have shown that, with total vacuum conditions of about 5×10^{-7} Pa before the entry of hydrogen into the research chamber, a beryllium surface free of oxide film could not be obtained using a glow discharge. After exposure to the glow discharge the beryllium surface appeared to be covered with carbon. The most reasonable explanation for this phenomenon is carbon segregation on the surface along microcracks formed near the surface owing to the glow discharge [5].

Deuterium permeation through beryllium with surface element composition control

The deuterium penetration rates through a beryllium membrane were measured in the temperature range 673–873 K with surface element composition control. The experimental results were processed to determine the effective diffusivity and permeability constants in the beryllium samples. Using multipenetration theory, the deuterium diffusion coefficient in FP-56 grade beryllium was calculated as $D_0 = 9.0 \times 10^{-12}$ m^2/s; E = 14.9 kJ/mol. Study of surface samples in a wide temperature range using the Auger electron spectroscopy technique showed beryllium oxide presence only on the surface. No changes of surface element composition were observed below 1273 K [6].

Results of IVG.1M in-pile experiments on hydrogen–RGT–graphite interaction

Experiments on thermally stimulated hydrogen release from irradiated and control samples of RGT–graphite were carried out. Processing of two thermal desorption spectrometry (TDS) peaks at temperatures near 770 and 1100 K in a framework of a second order desorption model gives values of activation energy of 2.8 and 4.0 eV/H_2. Processing of a third peak at 1300 K, which appears only for graphite samples irradiated in hydrogen, allows hydrogen diffusivity in graphite grains to be obtained as $D = 1.8 \times 10^{-4} \exp(-2.5 \text{ eV/kT})$ m^2/s. It was also shown that the influence of simultaneous reactor irradiation and exposure to hydrogen could increase hydrogen retention in graphite [7].

Results of IVG.1M in-pile experiments on hydrogen–beryllium interaction

Experiments on gas release from reactor irradiated beryllium samples in comparison with control samples were carried out. The influence of simultaneous reactor irradiation and exposure to hydrogen results in more hydrogen retention in beryllium than in the case of beryllium initially irradiated and then exposed to hydrogen. The

appearance of low temperature peaks (460 and 540 K) with calculated second order desorption energies of 0.71 and 0.84 eV/atom is mainly responsible for the increase in hydrogen content.

The appearance of low temperature peaks in TDS spectra of samples charged with hydrogen at 1150 K in-pile conditions can be explained by intensive microcrack formation along the grain boundaries near the surface of the beryllium samples. Thus, the extended surface area produces a large amount of new adsorption centres effectively trapping hydrogen. In the framework of such an assumption, the TDS peak at 1100 K was presumed to result from hydrogen diffusion from the beryllium grains located near the surface with $D = 6.7 \times 10^{-9} \exp(-0.286 \text{ eV/kT}) \text{ m}^2/\text{s}$ [8].

A study of neutron flux intensity and spectrum influence on hydrogen release parameters from irradiated beryllium has been carried out. The irradiation was implemented in the RA reactor, and the results of the study of gas release from the beryllium samples irradiated at different neutron fluxes but similar fluences (2.5×10^{18} n/cm^2) showed that the irradiation effect on gas release depends on dose accumulation rate. There is no difference between the initial samples and samples irradiated in a hydrogen atmosphere with a neutron flux of 2.0×10^{12} n·s^{-1}·cm^{-2} (thermal) and 3.0×10^{13} n·s^{-1}·cm^{-2} (fast) in the RA reactor [9].

The irradiation of beryllium samples of different grades (HP-56, HIP-56, EHP-56, FHP-56, FP-56) manufactured at the ULBA production plant is carried out in the RA reactor. The study of gas release from the samples is planned for the future.

REFERENCES

[1] Report on Scientific Research Work on the Kazakhstan ITER Programme, Rep. NTP-0009, Scientific Technical Center, Almaty (1995) 151 pp. (in Russian).

[2] KARAULOV, V.N., BLYNSKIJ, A.P., YAKOVLEV, I.L., "Beryllium irradiation in the fast neutron reactor BN-350", Nuclear Power Engineering in the Republic of Kazakhstan. Perspectives of Development (Abstracts of Reports of the Int. Scientific-Practical Conf. Aktau, 1996), Sigma, Kurchatov, Kazakhstan (1996) 103.

[3] TAZHIBAEVA, I.L., et al., Hydrogen permeability technique in situ reactor irradiation for ITER structural materials, Fusion Technol. **28**, Part 2 (1995) 1290.

[4] TAZHIBAEVA, I.L., et al., "Hydrogen diffusion parameters in vanadium alloys", Proc. 7th Int. Conf. on Fusion Reactor Materials, Obninsk, 1995, abstracts, 115.

[5] CTF Report on Los Alamos Natl Lab. Agreement 54620015, Almaty (1995).

[6] TAZHIBAEVA, I.L., et al., "Deuterium permeation through beryllium with surface element composition control", Proc. 18th Symp. on Fusion Technology, Karlsruhe, 1994, Elsevier, Amsterdam (1995) 427.

[7] TAZHIBAEVA, I.L., et al., Hydrogen release of reactor irradiated RGT graphite, J. Nucl. Mater. **233–237**, Part B (1996) 1198.

[8] KLEPIKOV, A.Kh., et al., Hydrogen release from reactor irradiated beryllium, J. Nucl. Mater. **233–237**, Part B (1996) 837.

[9] KLEPIKOV, A.Kh., et al., "Study of neutron flux intensity and spectrum influence on hydrogen release from irradiated beryllium", Nuclear Power Engineering in the Republic of Kazakhstan. Perspectives of Development (Abstracts of Reports of the Int. Scientific-Practical Conf. Aktau, 1996), Sigma, Kurchatov, Kazakhstan (1996) 105.

ITER VESSEL AND BLANKET*

K. IOKI[1], A. CARDELLA[1], W. DÄNNER[2], F. ELIO[1], Y. GOHAR[1], G. JOHNSON[1], K. KOIZUMI[3], E.G. KUZMIN[4], D. LOUSTEAU[1], R. MATTAS[5], K. MOHRI[1], B. NELSON[6], R. PARKER[1], R. RAFFRAY[1], Y. STREBKOV[7], K. SHIMIZU[1], N. TACHIKAWA[1], H. TAKATSU[3], C. VALLONE[2], D WILLIAMSON[1], M. YAMADA[1]

[1] ITER JCT Garching
[2] EU Home Team, NET
[3] JA Home Team, JAERI
[4] RF Home Team, Efremov Institute
[5] US Home Team, ANL
[6] US Home Team, ORNL
[7] RF Home Team, RDIPE

Abstract

ITER VESSEL AND BLANKET.

In ITER, the Vacuum Vessel (VV) most not only provide a high quality vacuum boundary for plasma, but also must act as the first safety confinement boundary. The blanket system (BLS) removes the majority of the neutron power at an average neutron wall loading of ~1 MW/m^2 and a substantial fraction of the alpha power from the plasma. The blanket and the divertor provide shielding for the VV and all three provide shielding for the coils. The VV is a water cooled all-welded 316 LN stainless steel double wall toroidal structure approximately 13 m in outer radius and 15 m high. It is sized for combinations of off-normal pressure and electromagnetic loads, including those on the in-vessel components in supports. Natural convection cooling occurs during a loss of fuel accident (LOFA). The blanket system is composed of first wall (FW)/shield modules supported from a toroidally continuous backplate and interconnected by manifolds. The FW section consists of a plasma facing armour bonded to an actively cooled Cu alloy layer. The shield section is a water cooled 316 LN stainless steel block. The shielding blanket installed for the Basic Performance Phase (BPP) can be replaced by a ceramic breeding blanket for the Enhanced Performance Phase (EPP). A net tritium breeding ratio ≥0.8 can be produced while maintaining the tritium inventory in the breeder at ≤100 g.

---

1. VACUUM VESSEL

The Vacuum Vessel provides the primary high vacuum and tritium boundary for the plasma while supporting the in-vessel components. The VV is comprised of a main vessel, a 316 LN (0.06 to 0.08 % nitrogen) double wall structure, port assemblies, and supports for in-vessel components. Its overall thickness of 0.45-0.82 m is formed by inner and outer shells, 40 to 60 mm thick, joined by welded stiffening ribs. The VV is curved in the poloidal direction and faceted in the toroidal direction. It is divided toroidally into 20 sectors which are joined by field welding at the central plane of the ports. TIG Welding is the preferred process for welding the vessel and ports. An 18° sector of the VV is shown in Fig. 1. Twenty horizontal midplane ports, 3.0 m tall by 1.8 m wide, and lower horizontal ports, 2.5 m tall by 1.0 to 1.75 m wide, are provided [1,2].

Approximately 65 % of the volume between the shells is filled with plate or block inserts to provide the required nuclear shielding. These inserts will be attached to the ribs such that the total toroidal electrical resistance of the vacuum vessel limits the induced eddy current flow while allowing magnetic field penetration. The toroidal resistance of the VV is 10.4 μΩ, while the total resistance of the VV plus BLS is 4.3 μΩ. Water flows in the space around the inserts to remove the 3 MW of nuclear heat deposition.

The BLS is supported from the VV at twenty inboard and forty outboard positions. The supports are formed by sets of leaf plates providing flexibility in the radial direction to accommodate differential thermal expansion between the VV and BLS while providing large vertical and toroidal stiffness to support the BLS weight, imposed electromagnetic loads, and possible seismic accelerations.

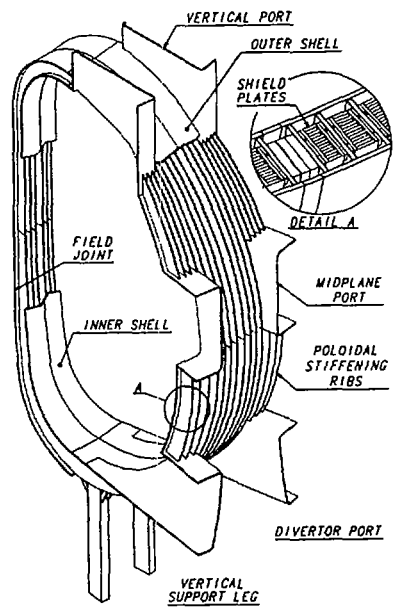

FIG. 1. Vacuum vessel (18° sector)

1.1. Power handling

The total heat deposition in the VV during in the BPP is 3 MW with a maximum nuclear heating rate due to radiation streaming of ~0.12 MW/m^3. The heat deposition after installation of the breeding blanket is increased to 11 MW. Water is used for both cooling and baking. Two independent cooling loops are used. Ten sectors (every other one) are connected in parallel to each loop. The main cooling parameters are shown in Table I.

The basic flow arrangement was selected to provide a reliable system with maximum natural convection cooling during a LOFA. The coolant enters through the wall of the divertor port and is routed to an internal manifold at the bottom of the vessel. The manifold distributes coolant to channels on both the inboard and outboard sides of the vessel. The coolant is recollected into an internal manifold at the top of the vessel and then routed through a channel in the upper port wall to an exit point. This configuration maximizes the elevation difference between the supply and return connections on the vessel and maintains the forced convection flow in the same direction as the natural convection flow path. The water will be used to bake the VV at a temperature of 200° C.

1.2. Loads and structural analysis

During normal operation, the vessel will be subjected to gravity forces, coolant pressure, nuclear heating, and loading due to temperature differences between the vessel and in-vessel components. Plasma disruptions will result in directly applied electromagnetic loads as well as reaction forces from in-vessel components. Off-normal events may also produce internal or external torus pressure, electromagnetic forces, or seismic loading . A pressure suppression system is used to limit the maximum vessel pressure during an off-normal event. Four 1 m^2 ducts located on the bottom of divertor ports connect the VV to a large pressure suppression tank. These ducts contain rupture discs which isolate the tank from the vessel during normal operation.

TABLE I. VACUUM VESSEL OPERATING CONDITIONS

Cooling (normal)	
Nominal wall temperature	~120°C (BPP)/~160°C (EPP)
Maximum wall temperature	200°C
Inlet/outlet pressure	~2.0/1.999 MPa
Inlet/outlet temperature	~100°C ± 10°C/111°C ± 10°C
Coolant velocity	~0.001–0.005 m/s
Total flow rate	~32.5 kg/s per loop (0.033 m^3/s)
Cooling (LOFA condition)	
Total flow rate estimate (natural convection ΔZ ~50 m)	~16.5 kg/s per loop (0.017 m^3/s)
Inlet/outlet temperature	~100°C/122°C
Coolant velocity	~0.0005–0.0025 m/s
Maximum vessel wall temperature	<300°C

Stress analysis to date has focused on operating states that are perceived to be the worst cases for the vessel. Stress limits for these cases were set consistent with the service limits defined in the ASME Pressure Vessel code. Load combinations have been evaluated for three scenarios: 1) normal plasma operation 2) off-normal operation with severe VDE and 3) off-normal operating with a pressure pulse of 0.5 MPa in the vessel . During 1996, design modifications, such as increasing the outer and inner vessel walls in the lower part of the vessel from 40 to 60 mm and changing the rib layout, were required to reduce stresses to allowable levels for these three cases.

During normal operation, vessel loads include gravity loads of in-vessel components, water pressure, and thermal loads due to temperature gradients. With these loading conditions, vessel deformation is about 6 mm and stress levels are about 75 MPa (50 MPa membrane) with some stress peaking up to 160 MPa in the region around the vessel support. In the case of a VDE, additional loads from the blanket and divertor supports are imposed on the vessel. For the symmetric VDE, these additional loads result in maximum deformations of 10-15 mm and stresses of approximately 104 MPa (85 MPa membrane). For the asymmetric case, the maximum stress is approximately 140 MPa (110 MPa membrane) and occurs in the vertical support legs. Additional stress concentrations of up to 190 MPa and 200 MPa are found around the square corners of the divertor duct and in the support legs respectively. For the pressure pulse in-vessel condition, the maximum displacement is about 4 mm in the torus and stress intensity is 130 MPa (90 MPa membrane). These calculated stresses are below the allowable limits for the respective load combinations considering the classification of the load category allowed by the code.

1.3. Vessel fabrication and quality

Typical fabrication tolerances for the vessel height and width are ± 20 mm, and ± 5 mm for the vessel sector wall thickness. The fabrication of the inner shell is completed first to ensure its best possible quality because it will form the first confinement boundary on the plasma side. The weld joints for the inner shell can be accessed from both sides minimizing deformations and making inspection easier. Access is also very good when welding the ribs to the inner shell. Welding on both sides of the ribs helps keep the ribs straight and in alignment.

The vacuum vessel is built in the factory as 20 right hand and 20 left hand segments, each spanning 9° in the toroidal direction from the port midplane to the center of the TF coil. After being received at the site, the vessel half sectors are leak tested and inspected before being mated with the TF coils. Leak testing is performed of the between-shell volume, and dimensions are performed after joining of the vessel half sectors. As adjacent sectors are installed, vessel field joints splice plates are installed, welded, and leak checked.

2. FIRST WALL/BLANKET (Table II)

The first wall/blanket system is composed of 740 blanket modules supported from a toroidally continuous 100 mm thick back plate and interconnected by manifolds supplying cooling water at 140°C and 4 MPa as shown in Fig 2. The blanket system is being designed for remote maintenance. Each module piping and structural connections can be (dis)connected and the modules moved through the midplane ports by a manipulator which moves in the vessel on a toroidal rail. The system is designed to accommodate test blanket modules in the midplane ports for development of power-reactor technology [2,3].

TABLE II. DESIGN SPECIFICATIONS FOR THE FIRST WALL/BLANKET SYSTEM

Fusion power			1.5 GW
Maximum fusion power excursions			+20%, ~10 s
Total number of pulses			1.3×10^4 (BPP), 4×10^4 (EPP)
Pulse duration			1000 s
Total number of full current disruptions			1000 (BPP)
Total blanket thermal power			~2.2 GW
Heat flux, average (maximum)			
	PW		0.25 (0.5) MW/m^2
	Limiter during startup/shutdown		~2.4 (~5) MW/m^2
	baffle		~1 (~3) MW/m^2
Energy deposition during VDE			20–60 MW/m^2
Neutron wall loading: average/maximum			0.92 MW/m^2/1.2 MW/m^2
Average neutron fluence (MW·a/m^2)			0.3 (BPP), 1 (total)
Number of modules PW/limiter/baffle			520/120/100
First wall surface area			~1200 m^2
Weight	Blanket modules		~2900 t
	backplate and manifolds		~1200 t
	total		~4100 t
Typical module dimensions (No. 4 module)			1800 mm × 810 mm × 370 mm
First Wall Materials			
	PFM	(PW)	Be
		(limiter)	Be or CFC
		(baffle)	Be or CFC (upper), W (lower)
	heat sink		copper alloy
	cooling tube	(PW)	316 LN
		(limiter and baffle)	copper alloy with SS liner
Coolant conditions			
	coolant		water
	inlet pressure/temperature		4 MPa/140°C
	nominal $\Delta T/\Delta P$/flow rate		
		(PW and inner baffle)	51°C/0.5 MPa/6700 kg/s
		(outer baffle and limiter)	34°C/0.7 MPa/3500 kg/s

2.1. Power handling

The total thermal power in the blanket for operation at a nominal 1.5 GW is ~ 2.2 GW. The FW/shield modules are classified as three types: primary, limiter, and baffle - according to the function of their FW. The primary FW will be subjected to an assumed maximum heat flux of 0.5 MW/m^2; the limiter is subjected to ~ 5 MW/m^2 during plasma start-up and shut-down; and the baffle will receive ~ 3 MW/m^2 from neutral-plasma interactions near the entrance to the divertor. In the primary wall, 10 mm SS cooling tubes, 1 mm thick, are embedded in the copper (see Figure 3). The plasma facing material for the primary modules will be beryllium. The thickness of the SS tubing is reduced in the limiter and baffle FW and the armour and copper layers are segmented to accommodate the higher heat fluxes and associated thermal stresses. Beryllium is also the primary

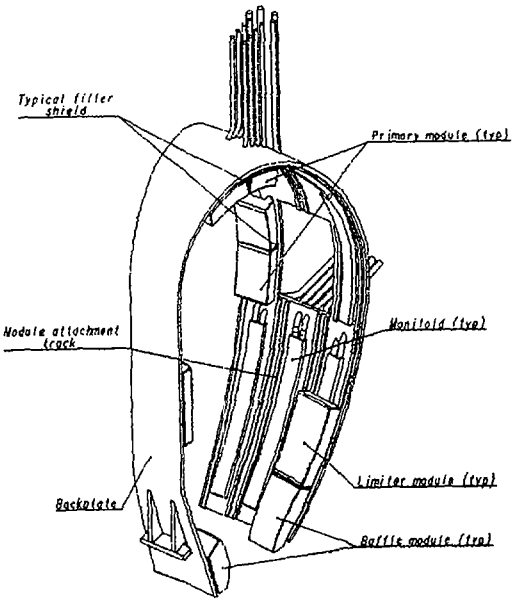

FIG. 2. Sector of blanket system.

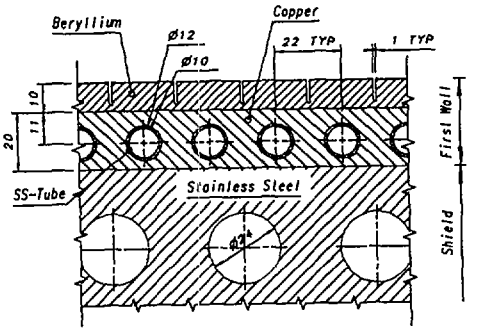

FIG. 3. Detail of primary first wall

candidate FW material for the limiters; however, carbon fiber composite which has superior thermal properties is being considered as an alternate. Tungsten will be used in the lower region of the baffles subject to erosion by charge-exchanged neutrals [4].

The copper alloy FW will be joined to the shield block by Hot Isostatic Pressing (HIP) to obtain good thermal contact and structural integrity. The coolant water pressure of 4 MPa was chosen as a compromise between minimizing primary coolant stresses in the FW and providing a subcooled margin to critical heat flux during limiter operation. This pressure also allows FW conditioning at temperatures up to 240°C without use of steam. The inlet temperature of 140°C mitigates copper embrittlement from irradiation.

2.2. Thermal responses of first wall to VDE heat loads

The FW armor thickness was determined by detailed analyses of the armour and heat sinks response to VDE's (~ 60 MJ/m^2 over 0.3 s). Figure 4 shows the Be temperature at 5 MW/m^2 and the ratio of coolant heat flux, to critical heat flux (CHF) with and without a 0.2 mm SS liner, following a VDE as a function of the Be thickness. As can be seen in the figure, a minimum Be thickness of ~ 5.5/6.0 mm (with/without insert) is required for a ratio < 1. Assuming an allowable Be temperature of ~1000 K, a value which needs to be verified by R&D, the maximum thickness of Be would be 5.9 /7.3 mm. The effect of erosion, vaporization, and melting on the small design window may result in the need for a plasma shutdown method to limit the number of events and/or the development of an in-situ method of refurbishing the Be layer on the limiter.

For the primary first wall design load of 0.5 MW/m^2, a minimum Be thickness of ~ 8 mm is required to avoid severe degradation of the coolant heat removal. The maximum thickness is set by manufacturing and cost considerations. For the baffle, the armour design window is also small (~8 – 10 mm) and allows a limited number of VDE's [5,6].

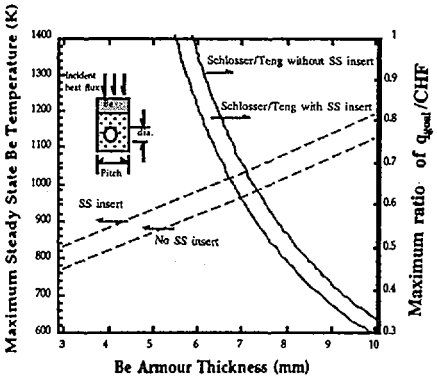

FIG. 4. Thermal analysis of Be FW.

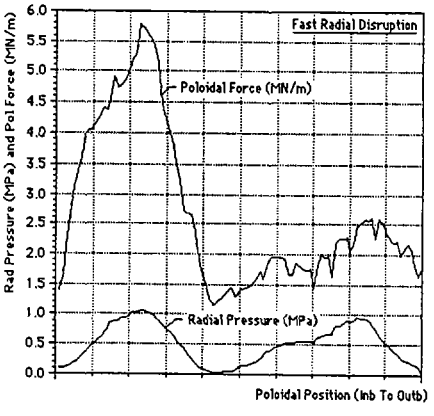

FIG. 5. Distribution of EM loads.

2.3. Disruption/VDE electromagnetic loads and structural analysis

Design of the blanket system is strongly influenced by the magnitude of plasma disruption forces. During a disruption the plasma current of 21 MA is assumed to decay linearly to 0 MA in 10 ms. When this occurs, almost all of the initial plasma current is induced toroidally in the blanket system. The interaction of the induced toroidal current with poloidal field results in a maximum radial pressure of 1.1 MPa on the modules. The largest electromagnetic loads are developed when these currents flow radially along the side wall of the modules across toroidal field lines. The maximum sidewall poloidally directed force of ~5.5 MN per meter of module poloidal length occurs at the inboard midplane. A plot of the radial and side wall loads as a function of poloidal position is included as Fig. 5 [7,8].

The modules and back plate system are designed to accommodate the EM loads from centered disruptions and for halo currents of 10 to 40 % of the initial plasma current with corresponding toroidal asymmetry of 3.0 to 1.2. A principal function of the back plate is to minimize the loads that are transmitted to the VV, the first safety barrier. The back plate is sized to react the main loads on the modules, the radial and twisting forces due to eddy currents during disruption. Only vertical loads and horizontal force due to toroidal asymmetry in the loading are transmitted through the blanket supports to the vessel. Back plate stresses at a combination of loads from blanket weight and a downward VDE with halo current and toroidal peaking have been calculated. The calculated stresses are less than but close to those allowable [8].

2.4. Structural arrangement of the first wall/blanket

The cross-section of an inboard module is shown as Fig. 6. Both welded and mechanically joined methods are being considered for joining the modules to the back plate and it has been shown that each approach can meet design requirements. The welded option offers a robust method for transmitting the FW pressure and module side wall shear loads to the back plate. It also provides a predictable heat transfer and eddy current path between the modules and back plate. A maximum leg/weld thickness of approximately 90 mm is required for the inboard modules near the horizontal centerline. The mechanically attached

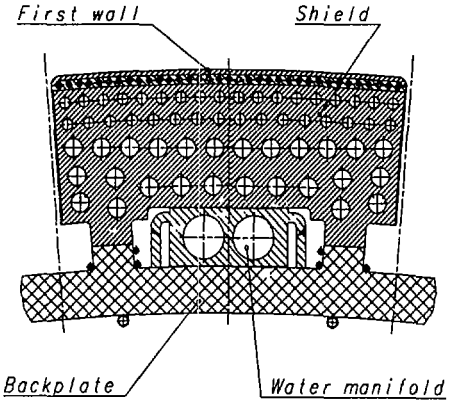

FIG. 6. Cross-section of blanket.

options are attractive from a maintenance perspective. The shear loads are reacted by keys machined into the module and the backplate surfaces. The radial pressure is taken by prestressed studs or other type of mechanical connectors. The concepts require accurate machining of the mating parts prior to installation. Design issues with this type connection include adequate cooling of mechanical elements and electrical connection/insulation between the modules and back plate. The major concerns are related to the stresses and deformations in the attachment elements due to EM loads and differential thermal expansion in the system for both the welded and mechanical options.

3. BREEDING BLANKET

The breeding blanket provides all the functions of the BPP blanket while providing tritium for EPP operation. It has the same radial build, modularity, structural material, cooling water, installation, support, and replacement methods as the shielding blanket but does not have a copper alloy heat sink in the FW. Helium loops are incorporated for tritium removal. A highly enriched lithium zirconate ceramic is used with a beryllium neutron multiplier to obtain a tritium breeding ratio ≥ 0.8 [9].

4. RESEARCH AND DEVELOPMENT

Major R&D projects are being conducted to provide needed input for design of the VV and Blanket Systems. An R&D program has been established to fabricate and test a full scale model of an 18° sector of the VV. The R&D program will demonstrate the required tight manufacturing tolerances [10]. For the Blanket System, small size subcomponents will first be used in the selection between copper alloys, FW bonding methods. Intermediate size modules will address fabrication issues and will also be used for performance testing. Prototype modules, back plate sections, and manifolds will be produced and assembled into a full size sector mock-up to address fabrication, cost, assembly, and integration issues [11].

REFERENCES

[1] IOKI, K., et al., Fusion Eng. Des. **27** (1995) 39.
[2] PARKER, R.R., et al., Fusion Eng. Des. **30** (1995) 119.
[3] IOKI, K., et al., in Fusion Engineering (Proc. 16th IEEE Symp. 1995), Urbana–Champaign (1995).
[4] IOKI, K., et al., Phys. Scri. **T64** (1996) 53.
[5] RAFFRAY, R., et al., "RACLETTE: A model for evaluating the thermal response of plasma facing components to slow high power plasma transients — Part I: Theory and description of model capabilities", J. Nucl. Mater. (in press).
[6] FEDERICI, F., et al., "RACLETTE: A model for evaluating the thermal response of plasma facing components to slow high power plasma transients — Part II: Analysis of ITER plasma facing components" (in preparation).
[7] IOKI, K., et al., Fusion Eng. Des. **30** (1995)351.
[8] CHIOCCHIO, S., et al., in Fusion Techonolgy (Proc. 19th SOFT, Lisbon, 1996), Centro de Fusão Nuclear (1996) 243.
[9] GOHAR, Y., et al., IAEA-CN-64/FP-10, this volume.
[10] KOIZUMI, K., et al., IAEA-CN-64/FP-8, ibid.
[11] DÄNNER, W., et al., IAEA-CN-64/FP-9, ibid.

DEVELOPMENT OF DOUBLE WALLED VACUUM VESSEL FOR ITER*

K. KOIZUMI, M. NAKAHIRA, Y. ITOU,
N. KANAMORI, K. KITAMURA, E. TADA
Japan Atomic Energy Research Institute,
Naka-machi, Naka-gun, Ibaraki-ken,
Japan

G. JOHNSON, K. SHIMIZU, G. SANNAZZARO,
T. TAKAHASHI, Yu. UTIN, K. IOKI
ITER Joint Central Team,
Garching Joint Work Site,
Garching, Germany

E.G. KUZMIN, V. KRYLOV
Efremov Institute,
St. Petersburg,
Russian Federation

Abstract

DEVELOPMENT OF DOUBLE WALLED VACUUM VESSEL FOR ITER.

Fabrication and testing of the vacuum vessel full scale sector model have been initiated in 1995 as one of the Seven ITER Large R&D Projects to finalize the fabrication process and to demonstrate the required performance of the ITER vacuum vessel before ITER construction. The full scale sector model corresponds to an 18° toroidal sector composed of two sectors, Sector-A and Sector-B, which are spliced and welded at the port centre according to the current ITER design. On the basis of the partial model fabrication, manufacturing procedures and welding methods have been defined so as to satisfy tight manufacturing tolerances of full poloidal sector and structural integrity. A combination of TIG/EB and TIG/MIG weldings has been adopted for Sector-A and Sector-B, respectively. On adopting the segmented configuration of Sector-A and Sector-B, furthermore, remote cutting, rewelding and weld inspection can be verified for the sector-to-sector connection required for replacement of a toroidal field magnet. The fabrication of the full scale sector model including Sector-A and Sector-B connection will be completed by the end of 1997, and thereafter performance tests on mechanical and hydraulic characteristics are scheduled until the end of ITER EDA. The integration with the midplane port extension fabricated by the Russian Home Team is also planned as a post-EDA activity.

---

1. INTRODUCTION

The ITER vacuum vessel is a large torus structure with a D shaped cross-section of around 15 m vertical height and 9 m radial width. In order to meet several design requirements to be mentioned below, the vacuum vessel is designed as a double walled structure reinforced with poloidal ribs and filled with nuclear shields and water beetween the walls [1]:

— to keep the toroidal resistance over 4 $\mu\Omega$, together with in-vessel components;
— to support gravity and disruption loads acting on in-vessel components;
— to assure the structural integrity of the tritium barrier under accidental pressure;
— to provide nuclear shielding for protection of magnets from irradiation damage;
— to remove decay heat of in-vessel components by natural convection cooling.

In addition to these requirements, the vacuum vessel is to be segmented into 20 toroidal sectors at the port centre between the adjacent TF magnets according to the current assembly procedure. Thus, cutting and rewelding at the port centre are required for reassembly of a vessel sector when a TF magnet is replaced. For assembly and reassembly of the vacuum vessel, therefore, tight dimensional tolerance of each vessel sector is specified to be within ± 20 mm for total vertical height and radial width, and ± 5 mm for total wall height. Because of its large size, tight manufacturing tolerances for assembly and reassembly and large mechanical loads, fabrication and testing of a prototype vacuum vessel are essential to ensure the structural integrity of the ITER vacuum vessel. For this requirement, a prototype programme, full scale vacuum vessel sector model project has been initiated as one of the Large Seven R&D Projects. This paper describes the outline, work plan and latest status of the vacuum vessel full scale sector model project.

2. OUTLINE OF THE PROJECT

The major technical objectives of the project are: (1) to develop and demonstrate the fabrication technologies required to assure the high quality full scale sector and (2) to perform the testing of the full scale sector to investigate mechanical and hydraulic characteristics for the validation of analyses employed for the ITER design. In order to achieve these objectives, the project is being conducted with the joint effort of the ITER Joint Central Team (JCT), and the Japanese and Russian Home Teams. The two main parts of the project are fabrication and testing of the full scale sector model being performed by the Japan Home Team and the full scale midplane port extension being carried out by the Russian Home Team; they are integrated into a demonstration test at the Japan Atomic Energy Research Institute (JAERI). In parallel with these activities, the R&D work required for the development of remotized welding, cutting and inspection systems for sector-to-sector connection is conducted as related R&D tasks.

3. WORK PLAN

3.1. Design of full scale sector model

Figure 1 shows the configuration of the full scale sector model designed for the project. The full scale model is composed of an inner skin, an outer skin and poloidal ribs of 40 mm thickness. The sector model has six and fourteen poloidal ribs in the inboard and outboard sections, respectively, for the reinforcement of the double walled structure. In addition to this rib arrangement, the thickness of both sinks and ribs is partially increased up to 60 mm to assure high mechanical integrity against the gravity and electromagnetic loads of the in-vessel components. Structural materials specified for the fabrication are stainless steel SS316L and SS316L+N ($0.06 \leq N \leq 0.08$wt%). As is shown in the figure, the full scale sector model is

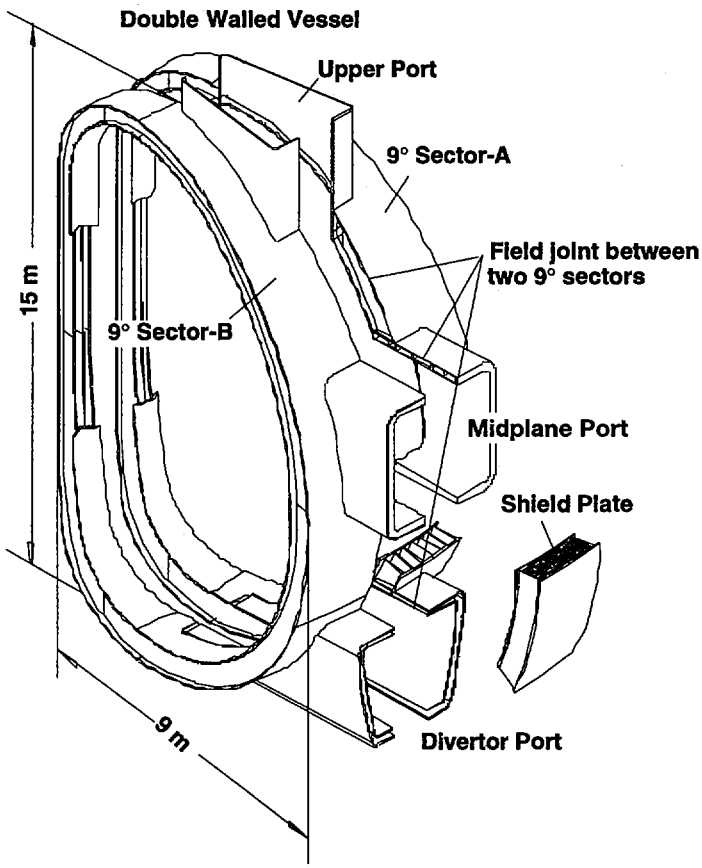

FIG. 1. Full scale sector model designed for prototype fabrication and testing.

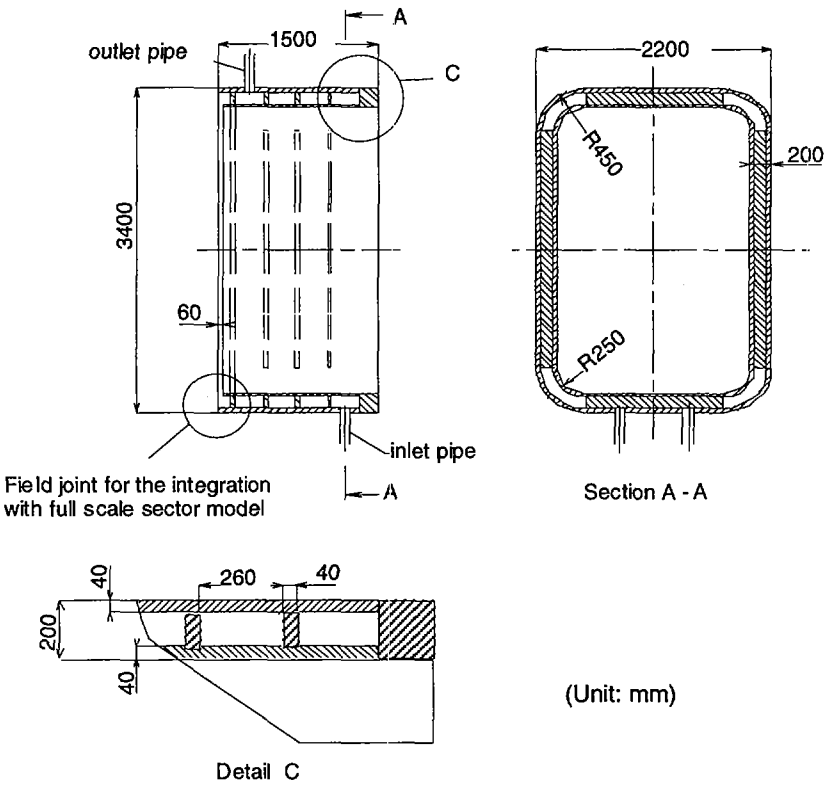

FIG. 2. Full scale midplane port extension designed for prototype fabrication and testing.

composed of two 9° sectors, Sector-A and Sector-B, which are spliced and welded at the port centre according to the current ITER design. This segmentation enables the first demonstration of the field joint welding. In the design of Sector-A, shield plate assemblies, which are attached to the poloidal ribs by welding and insulated bolts, are designed to be installed in the inboard upper sections and around the upper and lower ports.

Figure 2 shows the structure of the full scale midplane port extension designed by the Russian Home Team. The model is a full scale double walled assembly of 2.2 m toroidal width and 3.4 m vertical height. The dimensions of port opening and total wall height are consistent with the current ITER design.

3.2. Fabrication procedure

On the basis of the technical database obtained by partial model fabrication performed in 1994 [2], the manufacturing procedures and welding methods of the sector model have been specified so as to satisfy the tight manufacturing tolerances of full

TABLE I. TEST ITEMS SPECIFIED FOR THE FULL SCALE SECTOR MODEL

Test items planned within ITER EDA	
I.	Full scale sector model
(1)	Feasibility test
	• Initial welding, non-destructive inspection and dimension test of sector-to-sector field joints by automatic narrow gap-TIG and ultrasonic/PT
(2)	Performance test
	• Leak and pressure test of full scale sector at 0.5 MPa
	• Coolant flow test for vessel sector
	— Measurement of pressure drop by using upper inboard section of Sector-A
(3)	Validation test
	• Deformation measurement of full scale sector due to gravity loads
	• Measurement of flow distribution by subscale model
II.	Mid plane port extension
	• Vacuum leak test of inner volume and cooling channels
	• Pressure test of double walled structure at 3.44 MPa and inner volume at 0.5 MPa
	• Coolant flow test to measure flow distribution

poloidal sector and structural integrity. In order to allow the assessment of two candidate techniques for the fabrication of the ITER vacuum vessel, a combination of TIG (tungsten arc inert gas)/EB (electron beam) welding and TIG/MIG (metal inert gas) welding has been adopted for Sector-A and Sector-B, respectively.

3.3. Test plan and expected results

The test items specified for the full scale sector model and for midplane port extension are summarized in Table I. From these tests, the following results are expected within the ITER/EDA period:

The cutting and rewelding test of field joints between two 9° sectors and the integration with sector model and midplane port extension are also planned as post-EDA activites:

(1) Full development and demonstration of fabrication technology of the full scale sector including dimensional tolerance.
(2) Demonstration of feasibility of the automatic welding of field joints located at the centre line of the port.
(3) Demonstration of leak tightness and structural integrity.
(4) Sufficient database for the validation of the models employed for detailed design of the ITER vacuum vessel relating to the mechanical behaviour of double walled sector and flow distribution and hydraulic characteristics.

4. LATEST STATUS OF THE PROJECT

Following the design completion in November 1995, the fabrication of the upper inboard poloidal sections of both Sector-A and Sector-B began in December 1995. Since SS 316L is more readily available than SS 316L+N, these sections were fabricated by using this material to keep to the tight fabrication schedule. The inboard upper sections of Sector-A and Sector-B, completed in March 1996, are shown in Figs 3 and 4, respectively. Both upper inboard sections are successfully completed within dimensional errors of ± 5 mm to the nominal values. All major design and

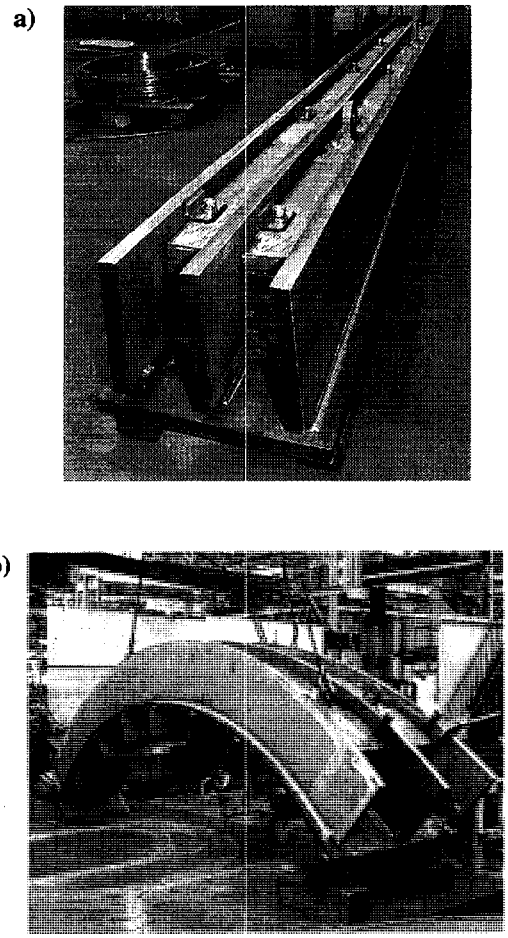

FIG. 3. Upper inboard section of Sector-A completed in March 1996: (a) upper inboard straight section; (b) upper curved section.

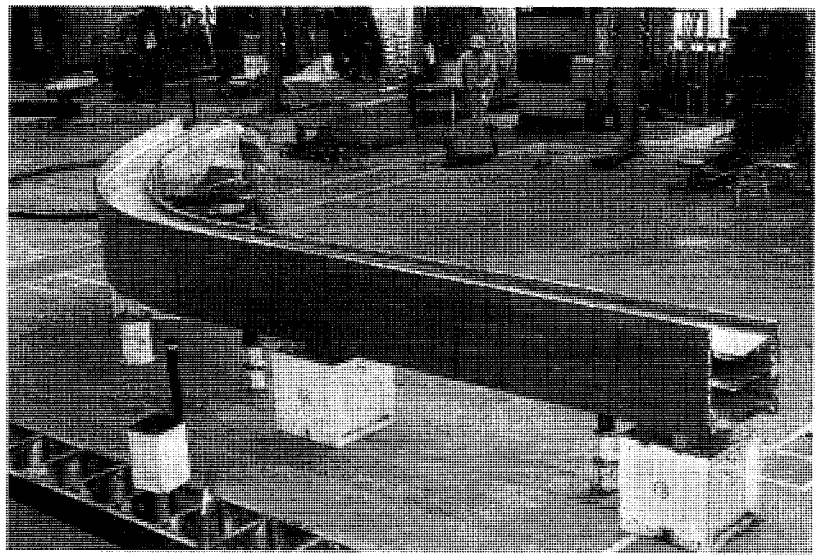

FIG. 4. Upper inboard section of Sector-B completed in March 1996.

fabrication issues have been resolved through discussions between the JCT and the Japanese Home Team, and the fabrication of the remaining poloidal sections of Sector-A and Sector-B began on schedule in July 1996 by using SS 316L+N. The full scale sector model fabrication including the sector-to-sector connection will be completed by the end of 1997, and thereafter performance tests on mechanical and hydraulic characteristics are scheduled up to the end of ITER EDA. The fabrication and testing of midplane port extension are scheduled to be completed in mid-1997 and in December 1997, respectively.

5. SUMMARY

On the basis of the specifications of the ITER vacuum vessel, a work plan of the project has been established. The two main parts of the project are shared with the Japanese and Russian Home Teams and are, with joint effort, integrated into a demonstration test at JAERI. The fabrication of the full scale sector model was started in December 1995, and the upper inboard sections of two 9° sectors, Sector-A and Sector-B, were successfully completed in March 1996, with a dimensional tolerance within ± 5 mm. The fabrication of the remaining poloidal sections is continuing on schedule, and the fabrication, including the sector-to-sector connection, will be completed by the end of 1997. Thereafter, performance tests are scheduled up to the end of ITER EDA.

ACKNOWLEDGEMENTS

The authors would like to express their sincere appreciation to Drs S. Shimamoto, S. Matsuda, M. Ohta and R. Parker for continuous encouragement in this work. They are grateful to the members of the Home Teams, JCT, Hitachi Ltd. and Toshiba Co., who co-operated in this development.

REFERENCES

[1] IOKI, K., et al., IAEA-CN-64/FP-7, this volume.

[2] KOIZUMI, K., et al., "Fabrication of double-walled section models for the ITER vacuum vessel", in Fusion Engineering (Proc. 16th Symp. 1995), Vol. 1, IEEE/NPSS, Piscataway, NJ (1995) 198.

THE ITER "L-4" BLANKET PROJECT*

W. DÄNNER[1], K. IOKI[2], P. LORENZETTO[1], A. CARDELLA[2], G. KALININ[2], R.T. SANTORO[2], Y. GOHAR[2], R. MATTAS[3], Y. STREBKOV[4], H. TAKATSU[5], F. TAVASSOLI[6], P. BATISTONI[7], M. HELLER[8], G. VIEIDER[1], C. VALLONE[1], E. RODGERS[1], M. FERRARI[7]

[1] NET Team,
Max-Planck Institut für Plasmaphysik,
Garching, Germany

[2] ITER Joint Central Team,
Garching Joint Work Site,
Garching, Germany

[3] Argonne National Laboratory,
Argonne, Illinois,
United States of America

[4] Research and Development Institute
of Power Engineering,
Moscow, Russian Federation

[5] Japan Atomic Energy Research Institute,
Naka-machi, Naka-gun, Ibaraki-ken,
Japan

[6] CEA, Centre d'études de Saclay,
Gif-sur-Yvette, France

[7] ENEA, Frascati Research Centre,
Frascati, Italy

[8] Siemens AG Unternehmensbereich KWU,
Erlangen, Germany

Abstract

.THE ITER "L-4" BLANKET PROJECT.

The "L-4" Blanket Project embraces the R&D of the ITER Shielding Blanket and is oriented towards the fabrication of prototype components as its main objective. The paper gives an overview of the present status of those activities from which conclusions are required to be fed into the prototype specifications. These include the R&D on copper alloys, copper to stainless steel joining techniques, shield block fabrication and module to backplate attachment systems. It is shown that this R&D is well on schedule. Pending design decisions, however, might delay completion.

1. Introduction

The "L-4" Blanket Project is one of the Seven Large Projects the ITER Joint Central Team is organizing together with the four Home Teams. It includes all R&D activities related to the Shielding and the Breeding Blanket to be installed in the ITER machine for the Basic and the Enhanced Performance Phase, respectively.

The Project objectives are to develop and fabricate prototype components for the Shielding Blanket, to assemble them in a single place inside the EU, to demonstrate the performance by testing representative parts of the components under relevant operation conditions, and to obtain confirmation of design choices by results from accompanying generic R&D by the end of the ITER EDA.

All Project R&D has been defined such as to support the ITER Shield Blanket design as described in [1,2,3]. The initial Breeding Blanket R&D has just recently been identified, and is not fully implemented yet. The rationale of the Blanket Project, the activities included, the main achievements obtained so far, and the organizational structure have been described in [4]. This paper intends to give a more detailed summary of the present status.

2. Project Phases

In general terms, the L-4 Project is subdivided into two major phases. The first phase coincides with the development of the conceptual design. The R&D conducted during this period is mainly of generic nature, but includes also technological development activities which are required to select the optimum approach among various engineering solutions. The selected options will then be implemented in the second phase in which the emphasis is placed on the fabrication of prototype components, and the performance testing of appropriately sized test pieces. The transition from the first to the second phase is anticipated for early 1997.

3. Prerequisites for Prototype Fabrication

The prototype components include modules of the Primary Wall, Limiter, and Baffle type. They consist of a massive 316 LN-IG stainless steel shield block and an integrated multilayered First Wall made of stainless steel (as structural material), a copper alloy (as heat sink), and beryllium as protection material. The protection of Baffle modules is partially made of tungsten or a carbon fiber composite (CFC). In addition to the modules, the prototype components include also representative pieces of the Blanket Backplate, and of the coolant manifold.

Before the prototype module fabrication can be initiated, the proper copper alloy has to be decided, and the best techniques have to be identified for joining the copper alloy to the stainless steel, and the three candidate protection materials to the copper alloy. Furthermore, the technically and economically most convincing fabrication route for the shield block has to be found, and the suitability of means to attach the modules to the backplate, and to connect them to the manifolds has to be experimentally confirmed. All activities except those related to the protection materials are subjects of the L-4 Project. The latter ones are covered by the L-5 Divertor Project.

Tab. I: Main Characteristics of ITER Grade (IG) Copper Alloys

Properties	**PH Cu (CuCrZr-IG)**	**DS Cu (Glidcop Al25-IG0)**
Availability	Is industrially produced by many companies	Is produced by SCM (USA) and similar material is produced by SPEZSPLAV (RF)
Weldability	Can be welded by TIG, EB	Not weldable
Thermal stability	Stable up to ~ 450°C (ageing temperature)	Stable up to ~ 950°C
Tensile properties	Similar to DS Cu up to 450°C	Similar to PH Cu for low temperatures
Fracture toughness	No data	Decreases with increasing temperature to relatively low values
Fatigue	Superior strain vs. life	Lower fatigue resistance than PH Cu
Physical properties	Similar to DS Cu up to 450°C	Similar to PH Cu at low temperatures

In the following, a brief description of those activities performed under the L-4 project is presented which are the major R&D elements entering the decision process on the prototype manufacturing.

4. Status of Copper Alloy R&D

Since the beginning of the ITER EDA, various precipitation hardened (PH) and dispersion strengthened (DS) copper alloys were under consideration, and subjected to screening tests [5]. Properties before and after irradiation up to ~0.3dpa have been measured in a temperature range from Room Temperature up to about 350°C. The samples had been subjected to a heat treatment which the material will experience during the module fabrication procedure (see Sect.6).

Currently, two cooper alloys, i.e. PH CuCrZr-IG and DS-Cu (GlidcopAl25-IG0), are under investigation. Their characteristics are summarized for comparison in Tab.I.

The CuCrZr-IG is easily weldable. However, it is sensitive to the heat treatment, which includes sensitivity to the temperature changes during operation, and to irradiation which leads to softening of the material. The DS-Cu instead is thermally very stable, and largely unaffected by heat treatment, and as a result is less sensitive to thermal treatments during component manufacturing. For First Wall application, weldability is not required. The low ductility which additionally exhibits an anisotropic behaviour has been substantially enlarged by improving the fabrication process. Recently, the specification of an ITER grade material (IG0) has been settled. For the next step in the L-4 Project, the Glidcop Al25-IG0 has been selected as the preferred material.

5. Copper Alloy to Stainless Steel Joining Techniques

An assessment procedure conducted early in the EDA had revealed joining technologies based on the process of Hot Isostatic Pressing (HIP) as the best suiting the modular Shield Blanket design. An extensive effort was done over about a two year period of time to find out the peculiarities of the various procedures depending on the type of copper alloy, and the physical form of the starting product. Plate to plate bonding ("solid HIP"), powder/powder HIP, and powder-to-solid HIP with and without pre-solidification of the powder have been tried. The most promising of them have then been optimized with respect to the process conditions, and the resulting bonds have been characterized and tested. Some data are summarized in Tab. II. The same was done for the process of Explosion Bonding which was found optimum if followed by a HIP treatment as well.

Tab. II: Tensile Properties of Copper Alloys to Stainless Steel Joints

Joining Tech-niques	Materials	HIPing Parameters		Test Temp.	Tensile Properties		
					UTS	YS	EL
		T, °C	p, MPa	°C	MPa	MPa	%
Solid HIP	Elbr.G/FN42/316LN	920	120	20	385	267	22
				300	290	216	7
	Al-25/316LN	980	100	20	408	253	16
				300	188	178	1
	Al25-IG0/316LN	930	100	20	420	263	16
				300	295	202	2
	Al25/316L	1050	150	20	401	335	23
				200	357	306	24
				300	318	283	5
				400	241	185	2
Powder HIP	DS-Cu Al-15/316LN	930	100	20	332	261	2
				300	207	165	1
	Cu0.7Cr0.2Zr/316LN	950	140	20	264	113	26
	Cu0.7Cr0.2Zr/316LN	800	140	20	297	157	24
Expl. welding	CuCr1Zr/316LN-IG			20	412	364	13
				300	311	285	9

The status of this R&D is soon mature for a decision which is scheduled for early 1997. It seems today that the preferred copper alloy (DS-Cu) is best joined by the Solid HIP process. A similar conclusion is expected for the CuCrZr alloy for which Solid HIP is already a fully industrialized process.
HIPing of CuCrZr powder to solid steel leads to acceptable bond properties as well, but it seems more difficult to achieve the required geometrical tolerances. A process with powder pre-solification (CIP-HIP) may solve the tolerance problem, but has then to compete with the Solid HIP option. The same holds for the Explosive Bonding followed by HIP for which additional difficulties are foreseen to transfer the technology to the specific application on a final Shield module.

The performance capability of the DS-Cu Solid HIP approach was recently demonstrated on a small mock-up under cyclic heat load conditions. The mock-up was exposed to a heat load of 1 MW/m^2 (4 times the nominal heat load) for 1000 cycles, followed by a few cycles with heat loads up to $9.6MW/m^2$, showing no visible cracks after testing. The detailed examination is still in progress.

The next step in the Project Work Plan is the fabrication and testing of a number of larger, but still small scale First Wall mock-ups which are partially equipped with the protection materials as well. Two examples are shown in

Figs. 1 and 2. Both Primary Wall, Limiter, and Baffle type mock-ups will be tested under high heat fluxes up to disruption like loads, and for long term thermal fatigue. For the latter tests, also mock-ups with artificial defects are foreseen. A series of mock-ups will also be devoted to experimentally optimize the geometry of the beryllium protection. It is expected that some test results will be available early next year as well to support the selection of a Reference.

So far, the development of joining techniques had to be done in absence of any indications about the irradiation behaviour of joints. In 1997, the first results from screening tests will become available. To be safe against any surprises from these tests, a few additional mock-ups will be tested that use CuCrZr joined by alternative techniques.

6. Shield Block Fabrication

A couple of fabrication routes for manufacturing the shield block are under investigation and development with Industry. Preferred methods are again based on the Solid and the Powder HIP technology. Alternative methods are steel casting with and without HIP treatment afterwards. Solid HIP offers excellent controllability of tolerances if done in several steps, but it entails grain coarsening with each step. Powder HIP could guarantee a fine grain

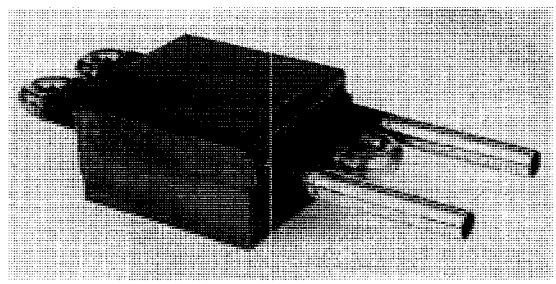

FIG. 1. Be/Cu/SS mock-up (European Union).

structure, but, if done in a single step, is difficult to inspect with present day Ultrasonic probes. It is clearly more difficult for Powder HIP to achieve the required tolerances.

Both HIP fabrication routes have successfully been demonstrated on mock-ups of the size of about 400x200x200 mm. While the Solid HIP route ended up with a perfect product as far as geometry is concerned, the Powder HIP one showed still some important tube deformations. Two Solid HIP

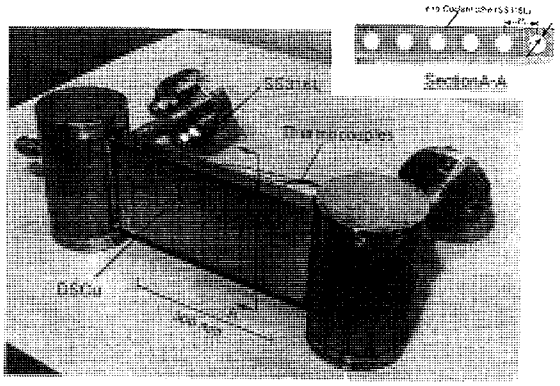

FIG. 2. Cu/SS mock-up (Japan).

demonstrators are shown in Figs. 3 and 4. Whether or not such deformations would be tolerable is still open. A powder HIP mock-up of about 1.2 tons has been fabricated as well. It includes curved surfaces and a representative internal tubing system. The examination of this piece is still pending. A mock-up based on the Cast/HIP technology has also successfully been completed in the frame of the L-5 Project. The results should be readily transferable to the shield block fabrication.

As far as copper and stainless steel Solid HIP is concerned, there is still a discrepancy in the Home Team opinions about the necessary total number of steps, and the optimum process conditions. Therefore, it is intended to continue these fabrication developments until early 1997 as well, and then to draw conclusions for the fabrication of the prototypes.

7. Module Attachment

The ways how to attach a module to the backplate and to connect it to the coolant manifold are essential details for the specification of the module, manifold, and backplate prototype components to be fabricated in the second phase of the Project. For the module-to-backplate attachment, a mechanical concept is preferred, while attachment by welding is to be followed as a backup. For both concepts, significant issues have been identified, and R&D results addressing some of them have already been obtained. Results on the branch pipe connection are still missing.

The main elements of a mechanical attachment system are pre-stressed bolts or studs, and shear keys. Comparative tests between bolts and studs resulted in a preference for studs because it is easier to achieve the required

preload. In the course of repeated cold and hot tests under vacuum conditions, valuable information about the preload behaviour was collected, and coatings for the prevention of seizing were qualified. Mechanical tests of the connection in which the shear loads occurring during a disruption were

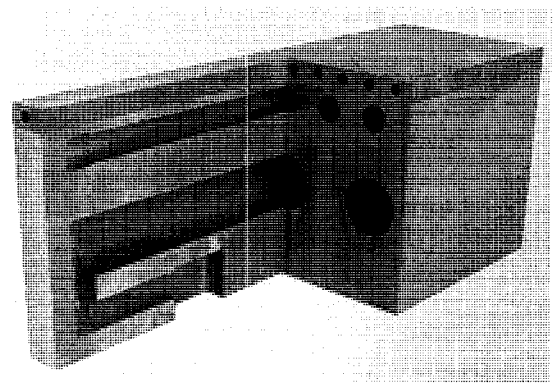

FIG. 3. Solid HIP demonstrator (European Union).

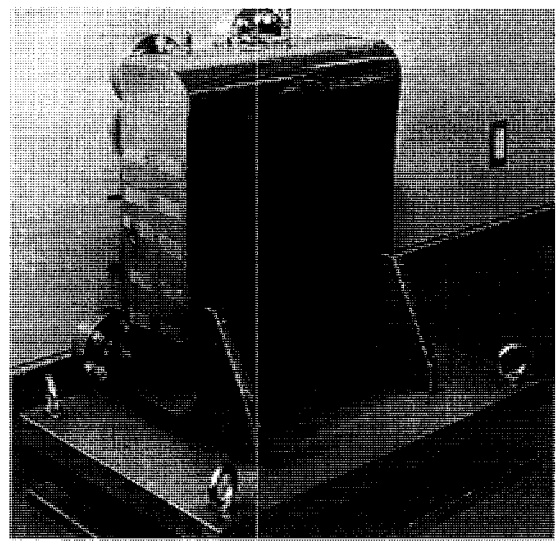

FIG. 4. Solid HIP demonstrator (Japan).

simulated on a mock-up shown in Fig. 5, showed plastic deformation of the steel even below the yield strength which, however, is smaller than the fabrication tolerances. Further tests are planned as soon as the design will be frozen.

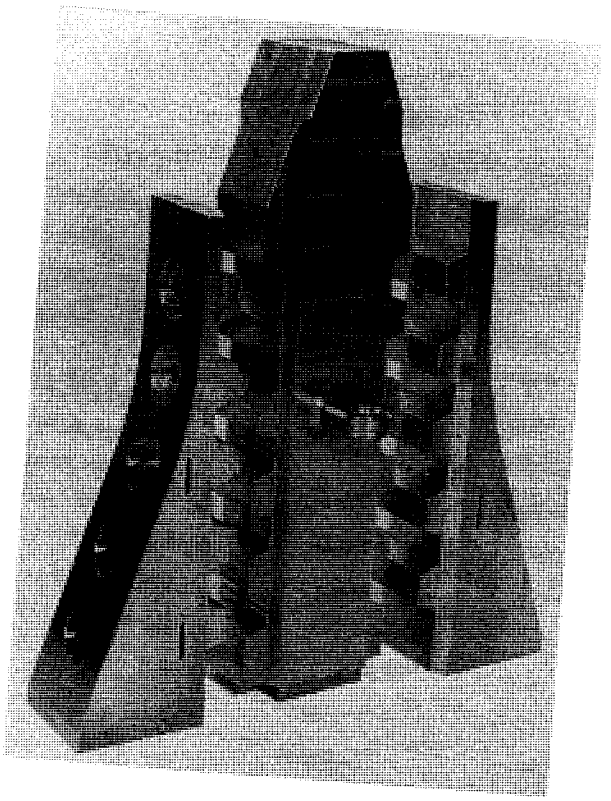

FIG. 5. Mechanical attachment mock-up.

Welding trials with narrow gap TIG for the backup option were done on full scale pieces. They gave essential practical information about the weld shrinkage (half the gap width) and the distortion at the First Wall level (~1 mm) which is encouraging for meeting the tolerance requirements during assembly and replacement. The plasma cutting process was also successfully demonstrated including an efficient system for collecting the cutting debris. Further R&D will in future be focused on the miniaturization of the equipment, and on solving the many practical problems inherent for this approach.

The selection between the two attachment approaches is an important element for launching the prototype fabrication and their assembly in a way as is visualized in Fig. 6.

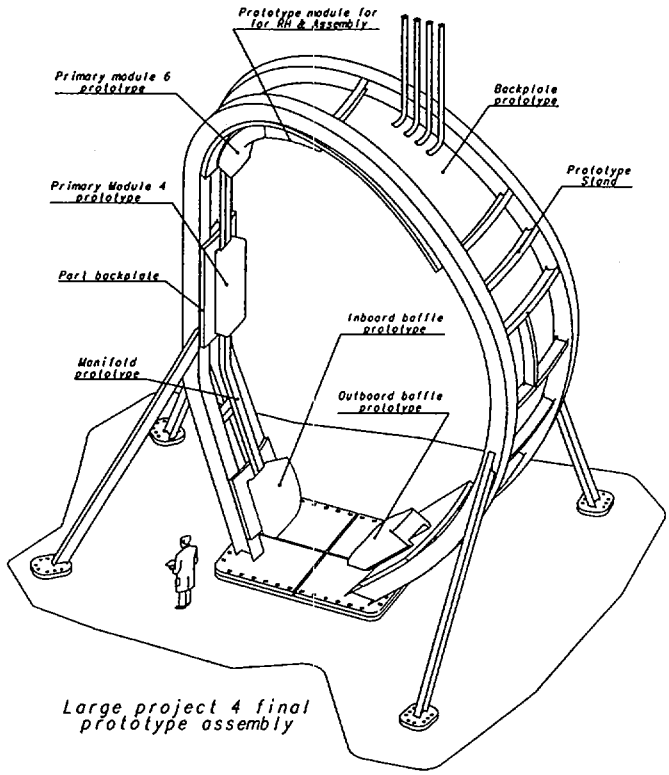

FIG. 6. Prototype assembly.

8. Conclusions

The L4 Project is entering the stage where medium scale test objects and prototype components will be manufactured, assembled, and/or tested. Maintaining project schedules requires the timely release of technical specifications for these task. Decisions on a few key outstanding design issues such as module attachment are required prior to the release of these specifications.

REFERENCES

[1] Technical Basis for the ITER Interim Design Report, Cost Review and Safety Analysis, ITER EDA Documentation Series No. 7, IAEA, Vienna (1996).
[2] IOKI, K., et al., in Proc. 19th Symp. on Fusion Technology, Lisbon, 1996.
[3] IOKI, K., et al., IAEA-CN-64/FP-7, this volume.
[4] DÄNNER, W., et al., in Proc. 19th Symp. on Fusion Technology, Lisbon, 1996.
[5] KALININ, G., et al., "Structural materials for in-vessel component design", Proc. 7th Int. Conf. on Fusion Reactor Materials, Obninsk, 1995.

ITER BREEDING BLANKET AND DEMO RELEVANT BLANKET TEST PROGRAM*

Y. GOHAR[1], R. PARKER[1], R. AYMAR[2], R. HAANGE[3], K. MOHRI[1], G. SAJI[2], S. BOOTH[4], M. DALLE DONNE[5], E. PROUST[6], H. TAKATSU[7], T. KURODA[7], S. TANAKA[8], Y. STREBKOV[9], I. KIRILLOV[10], V. KAPYCHEV[11], M. ABDOU[12], T. HUA[13], L. WAGANER[14]

[1]ITER Joint Central Team,
Garching, Germany
[2]ITER Joint Central Team,
San Diego, California,
United States of America
[3]ITER Joint Central Team,
Naka, Japan
[4]CEC Programme Fusion,
Brussels, Belgium
[5]Forschungszentrum Karlsruhe,
Karlsruhe, Germany
[6]Commissariat à l'énergie atomique,
Saclay, France
[7]Japan Atomic Energy Research Institute,
Naka, Japan
[8]University of Tokyo,
Tokyo, Japan
[9]Research and Development Institute of Power Engineering,
Moscow, Russian Federation
[10]D.V. Efremov Institute of Electrophysical Apparatus,
St. Petersburg, Russian Federation
[11]Bochvar Research Institute of Inorganic Materials,
Moscow, Russian Federation

[12] University of California Los Angeles,
Los Angeles, California,
United States of America
[13] Argonne National Laboratory,
Argonne, Illinois,
United States of America
[14] McDonnel Douglas Aerospace,
St. Louis, Missouri,
United States of America.

Abstract

ITER BREEDING BLANKET AND DEMO RELEVANT BLANKET TEST PROGRAM.

One of the main objectives of the International Thermonuclear Experimental Reactor (ITER) is to test fusion blanket designs relevant to demonstration power plants (DEMO) which are developed in the Four Parties national programs. Demonstration of a breeding capability that would lead to tritium self-sufficiency in a power plant, extraction of high grade heat, and electricity generation are the main goals of the tests. The test blanket modules will be installed in the ITER horizontal (equatorial) ports. To achieve the different objectives of ITER, the ITER operation is divided into two phases, the Basic Performance Phase (BPP) and the Enhanced Performance Phase (EPP). The BPP has a few thousand hours of DT operation of ~ 0.3 MW·a/m^2 integrated DT neutron fluence over ten years. During this phase, test campaigns of three to six days will be dedicated to functional blanket tests. The EPP is also expected to last about ten years with integrated DT neutron fluence of at least 1 MW·a/m^2. Continuous test campaigns of one to two weeks will be dedicated to blanket tests. A breeding blanket will be installed for this phase replacing the shielding blanket of the BPP to provide the majority of the required tritium fuel with the expected external resources of 1.5 kg/year. A net tritium breeding ratio greater than 0.84 will be necessary to achieve a neutron fluence of at least 1 mW·a/m^2 during the EPP. Four different DEMO blanket concepts are under consideration for testing in ITER: solid breeder blanket with water coolant, solid breeder blanket with helium coolant, lithium-lead breeder blanket with water coolant, and self-cooled liquid lithium blanket. Also, the ITER breeding blanket will be tested during the BPP to confirm its performance for the EPP. Neutronics tests will be performed at the start of the DT operation to characterize the nuclear environment and to verify the neutronics design tools. Material testing will be done during the EPP to calibrate the fission reactor test results for fusion environment and to confirm the material performance in the ITER fluence range of 1 to 3 MW·a/m^2.

1. INTRODUCTION

One of the main objectives of ITER is to test blanket designs relevant to DEMO power plants. The tests foreseen on blanket modules include the demonstration of a breeding capability that would lead to tritium self-sufficiency in a power plant, extraction of high-grade heat, and electricity generation. The test blanket modules will be installed in 4 to 5 horizontal ports of about 1.8 m wide and 3 m high. To achieve the different objectives of ITER, the ITER operation is divided into two phases, the BPP and the EPP. The BPP has a few thousand hours of DT operation of ~0.3 MW.a/m^2 integrated DT neutron fluence over ten years. This phase will address the issues of controlled ignition, extended burn, near steady state operation, blanket testing. During this phase, test

campaigns of 3-6 days will be dedicated for functional blanket tests. The tritium requirements for this phase will be provided from external resources. The EPP is also expected to last about ten years with integrated DT neutron fluence of at least 1 MW.a/m^2. This phase will address high availability operation, near steady state mode of plasma operation, material testing, and blanket testing. Continuous test campaigns of 1-2 weeks will be used for these blanket tests. A breeding blanket will be installed for this phase replacing the shielding blanket of the BPP to provide the majority of the required tritium fuel. Assessment of the ITER tritium requirements including the expected external tritium resources available at the time of operation, the ITER operational scenario, the total tritium inventory in the different ITER components, and the blanket replacement time between the two phases shows the need for a breeding blanket with a tritium breeding ratio in the range of 0.84 to 0.95 to achieve a neutron fluence in the range of 1 to 3 MW.a/m^2 during the EPP.

At present, the four parties are focusing on a limited number of blanket design options for fusion power plants. Five different blanket concepts are under consideration for testing in ITER, a breeding blanket for the second phase of ITER for tritium production, solid breeder blanket with water coolant, solid breeder blanket with helium coolant, lithium-lead breeder blanket with water coolant, and self cooled liquid lithium blanket. Neutronics tests will be performed at the start of the DT operation to characterize the nuclear environment of ITER and to verify the neutronics design tools. Also during the EPP, material testing will be done in ITER to calibrate the fission reactor test results for fusion environment and confirm the material performance in the fluence range of 1 to 3 MW.a/m^2. In preparation for testing these blankets in ITER and the development of the ITER breeding blanket, it is now essential to implement comprehensive R&D programs in each party. These programs should include the following: a) Breeder and multiplier materials development and testing in fission reactors and non-nuclear facilities, b) Structural material development and testing for operation in fusion environment, c) Functional blanket module testing in non nuclear facilities, d) Small blanket module testing in fission reactors, and e) Supporting R&D activities including tritium control and safety aspects. Elements of these programs are underway in the four parties.

The main objectives of the ITER blanket test program can be summarized as follows: 1) Evaluation of nuclear responses under fusion environment including nuclear heating and tritium production, 2) Demonstration/verification of the on-line tritium recovery and control system, 3) Demonstration of high-grade heat extraction and electricity generation, 4) Validation and calibration of design codes and data base used for the design of the blanket modules including neutronics, electromagnetic, heat transfer, hydraulics, and stress codes, 5) Confirmation and calibration of the test results obtained from fission reactors and non-nuclear facilities, 6) Demonstration of blanket module integrity and performance under thermal and electromagnetic loads, and 7) Observation of possible irradiation effects in the performance of the blanket modules.

2. ITER DESIGN FEATURES FOR BLANKET TESTING

Blanket testing has been included in the ITER design process as a fundamental design objective. This objective impacts the design configuration and the main operating parameters of ITER as can be seen in this section. ITER has twenty sectors corresponding to the number of the toroidal field coils. Each

sector has a horizontal port on the outboard side between the outer legs of the toroidal field coils. These ports provide access from the outside to the plasma as shown in fig. 1. Maintenance, plasma heating, diagnostics, and services are provided through these ports. About four to five of these ports are dedicated for blanket testing. The port size is ~ 1.6 x 2.6 m at the first wall. The blanket test articles will be inserted through these ports where it will be attached to the back plate. The coolant system and the tritium recovery system of these test articles are independent from the basic machine systems except for the ITER breeding blanket of the EPP, which is designed to use the basic machine systems. Most of the ancillary equipments are accommodated behind the test port to minimize the system response time for operational control and data collection. About 100 m^2 x

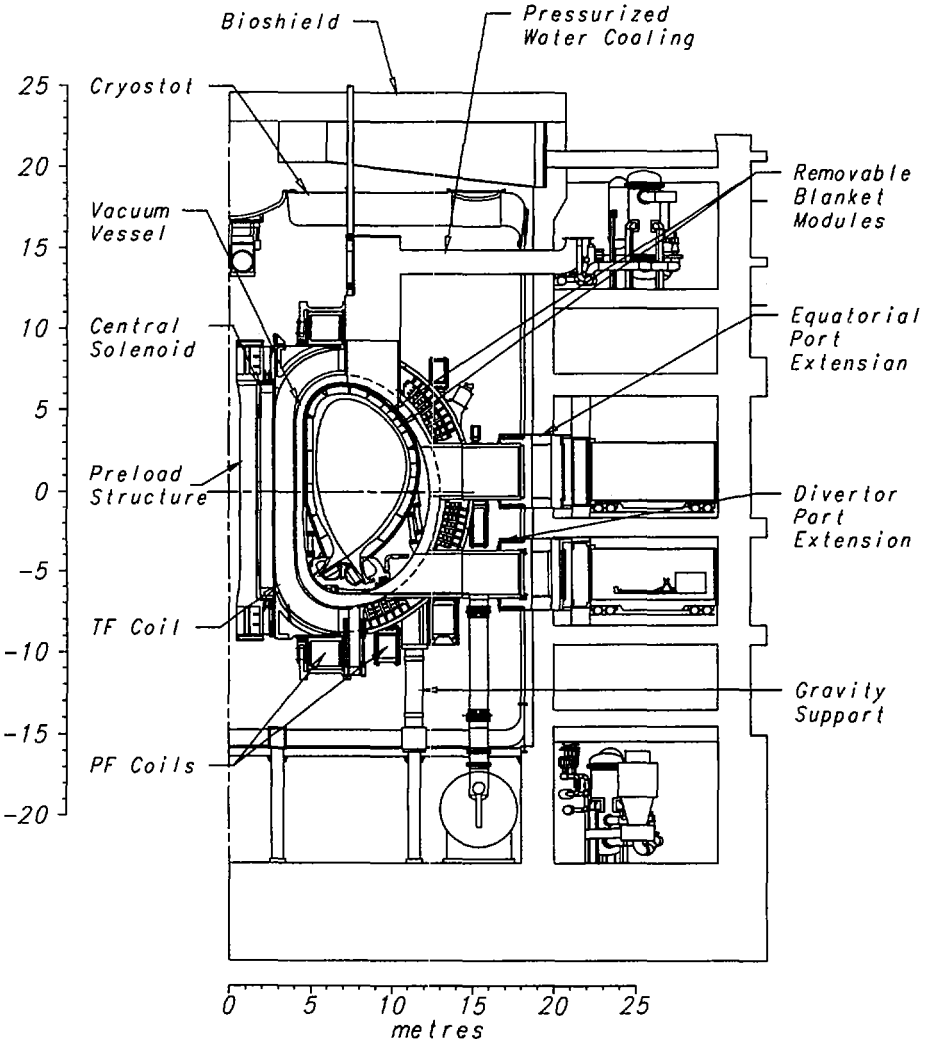

FIG. 1. ITER vertical cross-section.

4 m space is allocated for this purpose and extra space for the large equipments is located in the reactor building. Installation, replacement, and maintenance are performed by a transfer cask. The cask has the necessary remote handling equipments and some ancillary equipments.

To perform blanket testing at relevant conditions for fusion power plants, an average neutron wall loading of about 1 MW/m^2 and an average DT neutron fluence at the first wall of at least 1 $MW.a/m^2$ are specified for ITER. However, the design of the ITER permanent components does not preclude achieving fluence levels up to 3 $MW.a/m^2$ for extensive blanket testing including blanket segment demonstration. The test ports are poloidally located where the neutron wall loading has its peak value of 1.2 MW/m^2. On the first wall of the test port, the neutron wall loading is almost constant at the peak value and the peak surface heat flux is 0.5 MW/m^2. ITER has several operating modes including pulse and near steady state operation. The reference pulse mode has a flat burn duration of 1000 seconds and dwell time of 1200 seconds. This burn time is adopted to permit the temperature of the test articles to reach and operate at thermal equilibrium conditions during each pulse. During the BPP, test campaigns of 3-6 days will be dedicated for functional blanket tests. For most of the blanket concepts, this period will be adequate for the tritium systems to reach equilibrium conditions. These test campaigns will be 1-2 weeks during the EPP.

3. ITER TRITIUM BREEDING BLANKET

A breeding blanket is designed to provide the necessary tritium fuel during the EPP. It uses a ceramic breeder and water coolant for compatibility with the ITER machine design of the BPP. Li_2ZrO_3 is the selected ceramic breeder based on the current data base with enriched lithium and beryllium neutron multiplier. Both forms of beryllium material, blocks and pebbles are used at different blanket locations based on thermo-mechanical considerations and beryllium thickness requirements. As for the shielding blanket, Type 316LN austenitic steel is used as structural material and the water coolant parameters are the same for the two phases. The breeding blanket performance parameters have been checked against the ITER design requirements. The results indicate that the breeding blanket can be accommodated within the reference ITER configuration and satisfy the design requirements with adequate safety factors. Its breeding capability permits ITER to operate for a fluence goal in the range of 1 to 3 $MW.a/m^2$. This blanket and its support systems including the heat transport system, tritium processing system, and any special maintenance equipment will be tested in one of the ITER horizontal ports during the BPP.

The inboard blanket modules have two breeder zones embedded in beryllium with three coolant panels. The first wall has the first coolant panel to remove the surface heat flux and the nuclear heating from the front section of the breeding blanket. The second panel is located between the two breeder zones separated by beryllium. The last coolant panel is located at the back section of the module to remove the nuclear heating from the back section of the breeding blanket and the module structure. The outboard blanket module is similar to the inboard except it has three breeder zones instead of two to obtain a net tritium breeding ratio ≥ 0.8. The first wall consists of 13 mm thick Type 316LN stainless steel plate with built in rectangular coolant channels and a 5 mm beryllium coating for protection against plasma interaction. Tritium will be recovered by a helium purge gas (He + 0.1 to 1% H_2) during operation.

4. EUROPEAN DEMO RELEVANT BLANKET TEST PROGRAM [1,2]

The first phase of the European research and development program to identify the four most promising DEMO blanket concepts was started in 1989 and it was completed in 1995 by a comparative assessment of the four concepts. Two blanket concepts, a water-cooled lead lithium blanket (WCLL) and a helium-cooled pebble bed blanket (HCPB), were selected for the second phase of the program based on this assessment. Developments of these two blankets for fusion power plants and the delivery of blanket modules for testing in ITER are the main objectives of the second phase. The current scenario is to complete the development of the materials and technologies required for these blankets, and the detailed engineering design of the modules and their ITER interfaces by the year 2005. Fabrication and pretesting of the modules and ancillary systems will follow to start testing in ITER by the year 2010.

The WCLL blanket has liquid eutectic of lead-lithium (83Pb-17Li) as a tritium breeder and neutron multiplier. A single-steel box is used as a container for the liquid metal with radial and toroidal stiffeners. An independent pressurized water loop is used to cool the blanket box. The cooling tubes are inserted and soft brazed in toroidal channels. Also, pressurized water coolant flows in double-walled U-tubes within the lead-lithium pool. The water coolant parameters are based on the PWR systems. The water pressure is 15.5 MPa with inlet/outlet temperatures of 265/325 and 300/325 °C for the eutectic pool and the first wall, respectively. The selected structural material is ferritic martensitic steel to accommodate DEMO operating parameters. The lead-lithium eutectic is circulated slowly outside the blanket (< 0.005 m/s) for on-line tritium recovery. The HCPB blanket uses a lithium ceramic breeder and beryllium neutron multiplier in pebble form. Helium is used as a coolant with ~ 8 MPa pressure and 250/450 °C inlet/outlet temperature. Two independent coolant loops are used to cool the first wall and the blanket internals. The ceramic breeder and the neutron multiplier are separated by radial toroidal cooling plates. The tritium is recovered during operation by helium purge gas at 0.1 MPa. The current reference breeder material is lithium orthosilicate; lithium zirconate and lithium titanate are also under consideration. The selected structural material is also ferritic martensitic steel.

At present, the European long term technology program has an average budget of 19 MECU/year for the period of 1995-1998, 50 MECU for blanket and 26 MECU for structural materials. The minimum estimate for the development of the two concepts is 300 MECU over 15 years. This gives an average budget of ~ 20 MECU/year, which is comparable to the current average budget of the ongoing 1995-1998 development program.

5. JAPANESE DEMO RELEVANT BLANKET TEST PROGRAM [3]

Development of DEMO blankets in Japan has concentrated on the solid breeder blanket concepts with beryllium neutron multiplier. Li_2O is the first candidate breeder in pebble form. Other ceramic breeders (Li_2ZrO_3 and Li_2TiO_3) are under consideration. As for the structural material, ferritic steel, F82H, is selected to accommodate the expected DEMO operating conditions. Heat load capability, low swelling due to neutron irradiation, and industrial experience are the main reasons for this selection. Breeder out of tubes design with beryllium pebbles is the selected concept. Ceramic breeder and beryllium multiplier are separated by steel structure or coolant panels to avoid material interaction.

Two coolants, water and helium, are under consideration for different reasons. Water has a good materials compatibility data base, excellent heat transfer characteristics, and very low cost. Conventional PWR technology for power conversion is well established. However the thermal energy conversion is modest and high pressure containment is required. Helium coolant overcomes some of these difficulties and offers other advantages. Its chemical inertness, transparency to neutrons, and purity control are the main advantages. However its commercial deployment is much less than that of water-cooled technology. Therefore both coolants are being pursued.

A long term research and development program for DEMO relevant blankets has been proposed by Japan Atomic Energy Research Institute. The main objective of this program is to develop and construct test modules for the water- and helium-cooled ceramic blankets. The estimated cost is 10 GYen for the period of 1997-2008. This program is being reviewed by the Fusion Council of Japan.

6. RUSSIAN FEDERATION DEMO RELEVANT BLANKET TEST PROGRAM [4]

The Russian Federation program has two blanket concepts under development, a self-cooled lithium blanket with vanadium structure and a helium-cooled ceramic breeder blanket with ferritic steel structure. The first concept uses lithium as coolant and breeder material with beryllium multiplier and vanadium alloy structure. An electrical insulation is utilized to reduce the MHD pressure drop. Tritium is recovered from the lithium outside the blanket during operation. The second concept uses solid breeder material (Li_2ZrO_3 or Li_2TiO_3) with beryllium multiplier. Separate helium loops are used for heat removal and tritium recovery during operation.

For the self-cooled blanket, the vanadium alloy development has concentrated on two alloys (V-4Cr-4Ti and V-5Cr-10Ti). Baseline mechanical properties, compatibility with liquid lithium, industrial fabrication and joining methods, and irradiation effects on the mechanical properties are the main elements for this development. Several electrical insulator coatings on vanadium structure have been tested in contact with liquid lithium. Purification methods to remove impurities and corrosion products from lithium loop have been tested. MHD pressure drop and heat transfer studies have been carried out for the test module design. Beryllium multiplier fabrication tests and characterization are under way for the solid breeder blanket concept.

At present, the key Russian Federation Institutes are finishing a long term plan for the development and manufacture of blanket modules for testing in ITER. The budget for this program will be determined after its approval. The current year budget for this development is 2 GRub.

7. UNITED STATES DEMO RELEVANT BLANKET TEST PROGRAM [5]

The United States fusion program has concentrated on the development of two blanket concepts since the late 1980s, a self-cooled lithium vanadium blanket and a helium-cooled solid breeder blanket with reduced low-activation structure material. The self-cooled blanket concept utilizes electrical insulator (CaO or

AlN) coatings to reduce the MHD pressure drop with V-4Cr-4Ti alloy as the structural material. The solid breeder blanket concept utilizes Li_2TiO_3 as the breeder material, beryllium as the neutron multiplier material, and reduced low-activation ferritic steel as the structural material. Also, SiC is under consideration as low activation structural material for future testing. A development program for the two concepts, in collaboration with other parties, is under way aiming at module testing in ITER.

At present, the United States is spending 4.1 M$/year on the development of the self-cooled lithium-vanadium concept. A 78% of this budget is directed toward vanadium structural material development. For the helium-cooled solid breeder with ferritic steel structure, the current spending is 1.4 M$/year where the ferritic steel development uses 78% of this budget. A similar effort of 1.3 M$ is allocated for the development of the silicon carbide based materials. These developments are aiming for submodule or module testing in ITER at different time-scale. The testing of the first self-cooled blanket module may start prior to the first plasma because valuable data can be obtained concerning liquid metal MHD effects related to the electrical insulator coating. Following the last year restructuring of the United States fusion program, there could be modest budget growth beyond the current level of spending if the fusion program funding is not reduced from the current level.

8. Conclusions

The development of the DEMO blanket modules and ITER breeding blanket design are progressing, which satisfy the programmatic objectives of ITER. R&D programs in the four parties have been started to provide the necessary data required for the DEMO relevant blanket modules and ITER breeding blanket for testing in ITER.

REFERENCES

[1] S. J. Booth, W. Dietz, and S. Paidassi, "The European Breeding Blanket Development Programme", JAHRESTAGUNG KERNTECHNIK '96, Deutsches Atomforum e.V., Bonn, INFORUM GmbH, Bonn, Juni 1996.

[2] Ch. Maisonnier, European Fusion Programme Director "Coordination Between the Parties' Blanket R&D Plans for Testing in ITER", A letter to Dr. E. Proust, Chairman, ITER Test Blanket Working Group, May 1996.

[3] M. Yoshikawa, ITER Programme Director of Japan, "Coordination Between the Parties' Blanket R&D Plans for Testing in ITER", A letter to Dr. E. Proust, Chairman, ITER Test Blanket Working Group, June 1996.

[4] E. Velikhov, Russian Federation Program Director, "Coordination Between the Parties' Blanket R&D Plans for Testing in ITER", A letter to Dr. E. Proust, Chairman, ITER Test Blanket Working Group, June 1996.

[5] N. Anne Davies, Associate Director for Fusion Energy Sciences, Office of Energy Research of The United State "United State Plans for Blanket R&D and Testing in ITER", A letter to Dr. E. Proust, Chairman, ITER Test Blanket Working Group, May 1996.

THE ITER CS MODEL COIL PROJECT

R.J. JAYAKUMAR[1], H. TSUJI[2], O. OHSAKI[3], J. WOHLWEND[4], R. THOME[5], D.B. MONTGOMERY[1], J. MINERVINI[1], D. GWINN[1], R. RANDALL[1], C.Y. GUNG[1], W. BECK[1], R. CHILDS[1], B. SMITH[1], T. HRYCAJ[1], S. SHIMAMOTO[2], T. ANDO[2], T. HIYAMA[2], Y. TAKAHASHI[2], H. NAKAJIMA[2], T. KATO[2], M. SUGIMOTO[2], T. ISONO[2], N. KOIZUMI[2], K. KAWANO[2], K. HAMADA[2], M. NOZAWA[2], J. HARADA[2], T. HONDA[2], K. MATSUI[2], T. ITO[2], A. TERASAWA[2], I. WATANABE[2], K. TANEDA[2], S. SEKIGUCHI[2], M. OSHIKIRI[2], H. HANAWA[2], S. SEKI[2], H. WAKABAYASHI[2], K. TAKANO[2], Y. UNO[2], T. NAGASHIMA[2], M. OHTA[2], T. FUJIOKA[3], A. OZAKI[3], D. PAGANINI[4], P. GERTSCH[4], B. OHEA[4], R. McCOOL[4], J. DALESSANDRO[4], L. HAWLEY[4], G. MIYATA[4], N. MARTOVETSKY[6], J. ZBASNIK[6], R. REED[7], K. OKUNO[5], R. VIEIRA[5], N. MITCHELL[5], D. BESSETTE[5], P. BRUZZONE[5], Z. PIEC[5]

[1] Massachusetts Institute of Technology,
Cambridge, Massachusetts,
United States of America

[2] Japan Atomic Energy Research Institute,
Naka-machi, Naka-gun, Ibaraki-ken,
Japan

[3] Toshiba Corporation,
Kanagawa, Japan

[4] Lockheed–Martin,
San Diego, California,
United States of America

[5] ITER Joint Central Team,
Naka Joint Work Site,
Naka-machi, Naka-gun, Ibaraki-ken,
Japan

[6] Lawrence Livermore National Laboratory,
Livermore, California,
United States of America

[7] Cryogenic Materials Inc.,
Boulder, Colorado,
United States of America

Abstract

THE ITER CS MODEL COIL PROJECT.

The International Thermonuclear Experimental Reactor (ITER) Engineering Design Activities (EDA) include the development, fabrication and testing of a Central Solenoid Model Coil. The results of R&D and manufacturing efforts during this project will be used to confirm design criteria and to develop detailed design of components, manufacturing procedures and materials for the ITER coils. The fabrication of this large coil has also spurred the development of high-current density and low AC loss superconductors and joints satisfying ITER specifications. The coils will be layer wound two in hand, with turn, layer and ground insulation incorporating polyimide films. The modules will be epoxy impregnated. They will have praying hand or butt welded joints and will be supported by a structure which applies axial compression on the modules. The coil will be mounted on gravity supports and housed in a cryostat and will be energized with pulsed mode power supplies at a ramp rate of up to 1 T/s to produce a maximum field at the conductor of 13 T at 46 kA. Additional single layer insert coils with independent support structure, cooling and power supplies will be placed in the bore of the magnet to test conductors. The coil and the structures will be cooled and maintained at operating temperature using a 5 kW/4.5 K refrigerator. The conductor, the model coil and the insert coils are being fabricated by an international collaboration among the ITER Home Teams and will then be tested in a facility at the Japan Atomic Energy Research Institute.

Introduction

ITER has an extensive superconducting magnet R&D program, under which a high priority project is to design, fabricate and test a Model Coil for the ITER Central Solenoid. The model coil (CSMC) program will confirm the design criteria and performance of the ITER conductor, develop and verify manufacturing tooling and processes, and verify material performance following fabrication processes. The CS Model Coil [1] will be constructed using specially developed superconducting ITER CS conductors. These cable-in-conduit conductors (CICC) will employ Niobium Tin strands which are cabled and inserted into a jacket which is then compacted to produce the required void fraction in the cable space. The superconducting strands and cables are fabricated by all 4 Home Teams, jacket material is produced by the US Home Team (USHT) and the jacketing (welding of jacket lengths, cable insertion and compaction) is carried out by the European Home Team (EUHT). The CS Model Coil is composed of an inner module and outer module with parameters as shown in Table I. The USHT is responsible for the fabrication of the inner module, the model coil support structures and busbars. The Japanese Home Team (JAHT) is responsible for the fabrication of the outer module and for the construction of the CS Model Coil Test Facility. The JAHT and Russian Federation Home Team (RFHT) are producing insert coils for testing of TF coil and CS conductors. The Joint Central Team (JCT) monitors the activities at various sites and coordinates requirements and communications. The model coil and the interfaces between the modules, the insert and the facility were designed with the combined effort of the JCT, JAHT and USHT, with the RFHT providing key information for the design.

TABLE I. KEY PARAMETERS OF THE CSMC

	Inner module	Outer module
Number of layers	10	8
Number of turns/layer	31–34	34
Total number of turns	328	272
Inner radius, including ground insulation (m)	0.79	1.367
Outer radius, including ground insulation (m)	1.357	1.800
Height of winding (m)	1.775	1.775
Height, including ground insulation (m)	2.795	2.795
Conductor length, including joints (m)	2288	2687
Total module weight (t)	46	52.6
Operating current (kA)	46	46
Operating field (T)	13	7.3
Self-inductance	606 mH	
Stored energy at 13 T	641 MJ	
Ground insulation thickness	10 mm	

Coil Design

The inner module coil is wound two-in-hand and the turn insulation [2] consists of 2 half-lapped layers of 25 mm wide TGDM epoxy impregnated glass prepreg (0.23 mm thickness) and 200 HA Kapton (0.05 mm thickness-Kapton layer on the outside of the prepreg) and an additional overwrap of half-lapped layer of prepreg. The layer insulation will consist of 1 to 3 mm thick sheets of epoxy insulated glass.

The outer module coil[3] is also wound two-in-hand. The turn insulation consists of 3 parts. The inner part is composed of 25 mm wide 200 HA Kapton (0.025 mm thickness) sandwiched with DGEBA epoxy impregnated glass prepreg (0.11 mm thickness) (GKG), and the middle part is the same prepreg as the inner layer and Kapton (GK), and the outer part is dry glass tape. Each part is fabricated with 2 half-lapped layers.

Winding the model coil with multiple conductors in hand will develop the tooling required to apply this technique to the full scale coil which requires a four in hand winding. The tooling for fabrication must form the approximately 50 mm square, Incoloy 908 conductor with an accuracy of ~ 2 mm, taking into account the linear change in dimensions of -0.001% during the reaction of the conductor at about 650 C for 240 hours to form the Nb3Sn superconductor.

Buffer Zone

The buffer zone houses and supports the joints and transmits the axial preload applied by the support structure to the coil. It is fabricated from cylindrical segments spanning about 90 degrees and having a thickness equal to the conductor width. The material is fiberglass reinforced epoxy (FRP) which has an anisotropic thermal contraction, the lower contraction direction is chosen to be the axial (preload) direction to minimize preload loss during cool down. However, this creates a radial mismatch relative to the top of the coil, which shrinks less than the buffer zone. To minimize shear stresses due to this mismatch, the cylindrical segments are not bonded together or to the coil and are instead

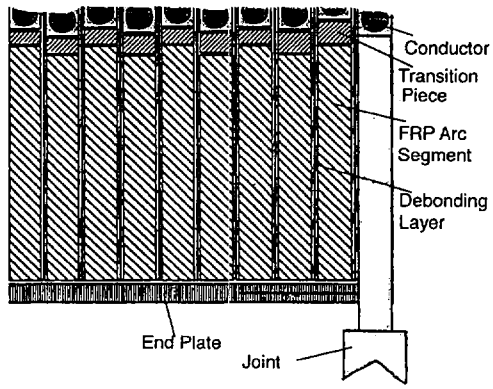

FIG. 1. Buffer zone arrangement. The debonding layer between the individual cylindrical segments and the locking of the segments in the transition pieces are shown.

locked radially by the transition pieces which supports the turns near the joints. The joints and the cylindrical segments are also held in place by an end FRP plate (Fig.1).

Tooling and Fabrication

Winding Machine

The winding machine for the inner module is shown in Fig. 2 (a) and has a 3 roll bender with the central roller fixed and adjustable side rolls to obtain the desired radius. In addition there are 3 pinch rollers mating with the bending rollers and the flanges of these rollers form the cavity which controls the keystoning of the conductor during bending. The bending and pinch rollers (which correspond to the forming radius) are controlled by precision actuators and the bending force is applied by hydraulic arms. One arm mounted on a movable frame supports the 4 m diameter conductor and another arm takes up the wound conductor. The machine is symmetric from the two ends and therefore can be used for reverse bending for accurate forming. The winding machine for the outer module has an uncoiler, a straightening bender, a correction roller, a 3 roll bender, a shot peening device and a winding mandrel whose diameter is the same as its final diameter, taking account of shrinkage after heat reaction. These are operated under synchronous control and the layer winding is performed in the vertical direction(Fig. 2 (b)).

Layer Assembly and Lead Forming

For fabrication of the inner module, each hand of the two-in-hand coils will be formed and then the two will be corkscrewed together in a machine by feeding one hand through alternate bogies on a machine and then feeding the other hand through the remaining intermediate bogies. In the case of the outer module, the two-in-hand layer will be assembled during the winding process on the same mandrel by first winding one hand with a space between turns and then winding the other hand into the space. The turns will be clamped together before removing from the mandrel and transferring to a turn insulation machine.

(a)

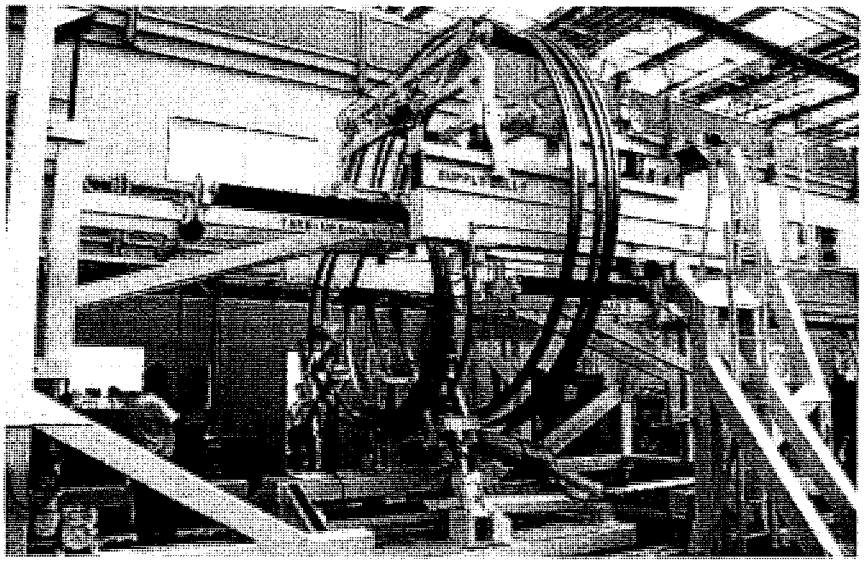

(b)

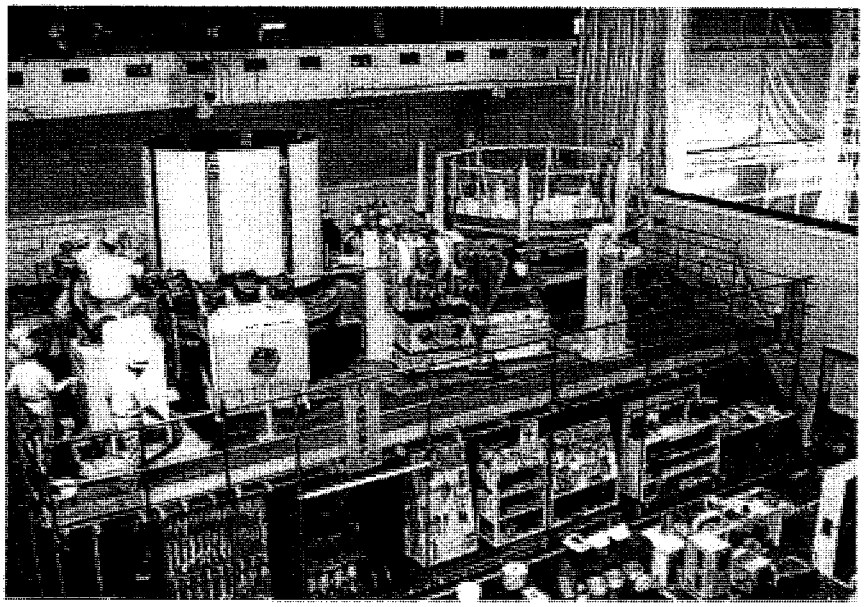

FIG. 2. Winding machine systems for (a) the inner module (axis horizontal) and (b) the outer module (axis vertical).

The leads will be made by first straightening the conductor with one tool. A second tool will then make a 90 degree bend and a third tool then will form the conductor so that it lies on the cylindrical surface of the coil.

Heat Treatment

Incoloy 908® is a material which is susceptible to SAGBO (Stress Accelerated Grain Boundary Oxidation) and therefore the conductor has to be heat treated in a low oxygen environment or tensile stresses should be minimized on exposed jacket surfaces [4]. For the outer surface of the jacket, both these conditions will be provided as follows. For the inner module---by heat treating the coil in a 2.9 m dia x 3.8 m tall vacuum furnace maintaining a vacuum of 0.1 mTorr or better. For the outer module---in a 4.2 m dia x 5.3 m tall retort maintaining high purity argon atmosphere with the oxygen and water vapor concentrations below 1 ppm at 1 atm. In addition, the conductor outer surfaces and all the welds will be shot peened to assure compressive stresses on the surface. The ID of the conductor, which is mostly in surface compression and where the cable itself acts an effective getter, will be thoroughly purged with high purity argon. An argon purge gas stream with 200 scc/sec will be continuously maintained and the oxygen and water vapor concentrations will be monitored and kept below 1 ppm at 1 atm.

The specifications for these processes were developed as part of the manufacturing R&D program and have been successfully proven on successively larger sections of conductor up to a full size dummy winding.

Coil Assembly and VPI

After turn insulating, each successive layer is lowered vertically around the previous layers held on a mandrel and compressed radially. The leads at one end are fixed and the length of conductor in each layer is controlled accurately throughout the fabrication process such that with some shimming on the radius, the leads at the other end will be positioned correctly, and overall dimensional requirements are also met. The coil will be impregnated with axis vertical and epoxy will be fed from the bottom through holes lined up with the layer parting regions. The epoxy chosen has a very low viscosity to permit wicking up to the full height.

Conclusion

The results in the CS Model Coil program to date are: Approximately 20 tonnes of Nb_3Sn Strand have been produced in all four Parties and most of the balance of about 5 tonnes will be produced during 1996. Cabling is underway. A 300 m jacketing line has been set up for the CS type of conductor. Five 100 m lengths of dummy and six approximately 150 m lengths of actual cable have been jacketed. About 1100 m of the Incoloy 908 jacket material for the CSMC has been delivered to the jacketing line and the balance of about 4600 m will be delivered in 1996. Major items of tooling for the CSMC manufacture have been procured. Trial winding and heat treatments of the dummy conductors have been done and actual winding has started. The result will demonstrate full-scale coil manufacturing processes and produce a 13 T, 640 MJ coil, and insert coil program capable of simulating performance in the full-scale CS. The test facility for the CSMC is ready at the Japan Atomic Energy Research Institute. The ITER collaboration has resulted in significant strides in establishing the R&D program that has essentially been successful.

REFERENCES

[1] HUGUET, M., et al., "Model coils for the central solenoid and toroidal field coils in ITER", paper presented at ANS 12th Topical Mtg on Technology of Fusion Energy, Reno, NV, 1996.

[2] JAYAKUMAR, R., et al., "Testing of ITER central solenoid coil insulation in an array", paper presented at 16th IEEE/NPSS Symp. on Fusion Engineering, Champaign, IL, 1995, Rep. UCRL-JC-122228, US Govt Printing Office, Washington, DC (1995).

[3] ANDO, T., et al., "Design of the ITER CS model coil — outer module", paper presented at 16th Int. Cryogenic Materials Conf. Kitakyushu, 1996.

[4] WONG, F.M.G., "Residual stresses in superconducting jackets after compaction", paper presented at 16th Int. Cryogenic Materials Conf. Kitakyushu, 1996.

TOROIDAL FIELD MODEL COIL PROGRAMME FOR THE ITER TOKAMAK

E. SALPIETRO, R.K. MAIX, G. BEVILACQUA
NET Team,
Garching, Germany

N. MITCHELL
ITER Joint Central Team,
Naka, Japan

B. TURCK, P. LIBEYRE
Center d'études de Cadarache,
France

A. ULBRICHT, G. ZAHN
Forchungszentrum Karlsruhe,
Karlsruhe, Germany

M. SPADONI, A. DELLA CORTE
ENEA,
Frascati, Italy

Abstract

TOROIDAL FIELD MODEL COIL PROGRAMME FOR THE ITER TOKAMAK.

The ITER toroidal field coil (TFC) system is made of 20 toroidal field coils, each consisting of a winding pack enclosed in a vacuum tight case, about 17 m high and 12 m wide. The winding pack is pancake wound and uses a circular conductor embedded in radial plates. Each turn is insulated from the enclosing plate, and the plates are insulated from each other. These radial plates transfer the forces acting on each conductor directly to the casings without accumulation of forces on the turn insulation. The winding pack is wrapped in a ground insulation, the outer surface of which is matched to the case. There is no bond between winding pack and case. The in-plane hoop forces of the coil are carried by the combined structure of plates and case, and the case provides most of the bending and torsional rigidity. The conductor jacket is thin and only provides a containment for helium.

1. GENERAL

The toroidal field model coil (TFMC) is a 'racetrack' shaped coil about 4 m high and 3 m wide, scaled with respect to the full size ITER TF coils and including the key technical features and manufacturing approaches foreseen for the full size ITER TF coils. In addition to the coil, in some areas extra R&D is planned to ensure that all the manufacturing problems of the full size coil are adequately addressed. The main operating conditions of the coil are summarized in Table I.

TABLE I. ITER TF COIL AND TFMC OPERATING CONDITIONS

	Coil/TFMC		Coil/TFMC
Maximum field, T	12.5/9.8	Average winding hoop stress, MPa	294/63
Conductor current, kA	60/80	Peak interplate shear, MPa	35/30
Coil MAT	11.5/7.8	Average nose pressure, MPa	90/25

2. INTRODUCTION

The ITER TF model coil consists of five double pancakes (DPs). Figure 1 shows the coil cross-section in the straight leg, compared to the full size coil [1]. Each DP consists of a radial plate with machined grooves on both sides, in which the round conductor is placed. The insulated conductor is pressed and held in place by covers which are welded at the corners of the groove. The two single pancakes of a DP are connected by a joint at the inner circumference. The five DPs are each impregnated with epoxy resin and are then assembled and insulated to ground with a combination of glass fabric and polyimide tapes and again impregnated with epoxy resin. The DPs are then connected by joints at the outer circumference. The impregnated coil is placed in a welded stainless steel case. The main parameters of the coil are summarized in Table II.

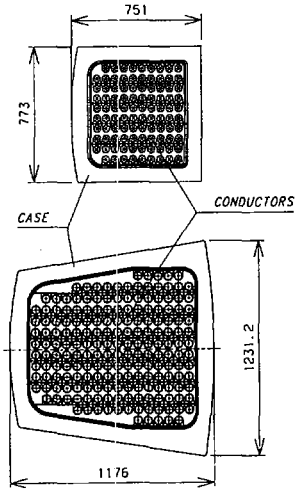

FIG. 1. Coil cross-sections (in millimetres).

TABLE II. MAIN PARAMETERS OF THE TFMC

Length of conductor, m	860	Weight of winding pack, t	16
Weight of Nb_3Sn strand, t	4	Weight of case, t	15
Weight of jacket, t	1.3	Stored energy (+ LCT), MJ	370

The TFMC will be tested in the TOSKA test facility, coupled by means of a supporting steel structure to the existing large superconducting coil (LCT) [2] that provides the background field to locally generate mechanical loads on the TFMC, comparable to the ones predicted for the ITER TF coil (Table I).

The TFMC will interface with the LCT background coil in a parallel configuration (Fig. 2), where the TFMC is located on the side of the LCT coil, with a small angle between the two coils (roughly the same configuration of two adjacent TF coils in the ITER tokamak). This arrangement allows testing of the coil under various conditions simulating the TF coil in-plane and out-of-plane loadings. The TFMC is not aligned concentrically with the LCT coil so that a resultant in-plane force is generated to simulate better the ITER coil conditions [1]. The TFMC rests inside a supporting framework and is connected to it through four U shaped wedges at the corners that allow the TFMC to develop both in- and out-of-plane bending without transmitting extra stresses to the LCT coil (Fig. 2). The supporting framework extends between the coils to react the forces between them.

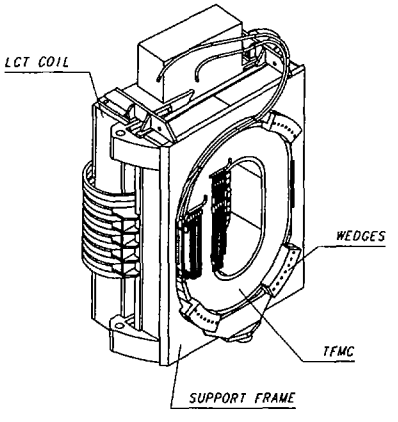

FIG. 2. TFMC in test configuration.

3. OBJECTIVES

The TFMC programme objectives are distributed throughout the manufacturing programme, and the final test in TOSKA is by no means the sole target of the work. High field testing of the ITER TF coil conductor under both steady and pulsed conditions will be a part of the high field central solenoid model coil test, with a single layer TF conductor insert [3]. This facility gives a much more convenient configuration for conductor testing, with great lengths (up to 100 m) at fields of up to 13 T. The TFMC programme concentrates on the manufacturing issues of the TF coils for a wind, react and transfer process:

- techniques for winding the conductor and clamping it during the Nb_3Sn reaction heat treatment so that the 0.5 mm tolerance fit to the grooves can be achieved;
- closure of the plate groove with a welded cap without distorting the plate or damaging the insulation;
- application of insulation to the conductor during transfer and epoxy penetration into the groove during impregnation;
- design of joint region to avoid local stress concentrations;
- flatness achievable on radial plates after completion of the plate insulation layer;
- case manufacture (both welding assembly from plates and final tolerances);
- winding pack assembly into case (gap filling and case closure welding).

In several cases, both the development of cost effective techniques and a resolution of various technical problems are required. The development of quality assurance procedures that will be applicable to the full size coils is an important consideration at all steps.

4. MANUFACTURING FEATURES OF THE TF MODEL COIL

The ITER TFMC incorporates the following features and will use the following critical manufacturing steps:

— The superconducting strands are cabled with a multistage arrangement around a central cooling tube formed from a spiral. A pullthrough process followed by compaction is used to insert the cable into the pre-assembled oversize jacket. In the TFMC, copper strands are incorporated into the cabling layout by replacing one of the superconducting strands in the first stage triplet (in the ITER TF coils, because of the higher field, a slightly different pattern is used). In the ITER TF coils, the jacket is Incoloy 908 with 2 mm wall thickness since the thermal contraction matches that of Nb_3Sn and does not cause degradation of the critical current and temperature [4]. In the TFMC, a 316LN stainless steel jacket with a 1.6 mm wall thickness is being used.

— The conductors are wound on a rigid frame that holds them in the position suitable for their transfer to the grooves in the radial plates. The joint terminations are prepared, and the conductor is then put through the reaction heat treatment for the strand. In the TF coils, the use of the Incoloy jacket requires strict control of oxygen levels both inside and outside the jacket during this process [5]; the frame and/or the grooves must also allow possible dimension changes that can arise from the precipitation hardening of the Incoloy. As the TFMC uses a different conductor jacket material, problems specific to the Incoloy will be addressed in a separate R&D action. This runs in parallel with the TFMC manufacture and will lead to the fabrication and electrical tests (at 4 K) of a DP made with a dummy conductor with an Incoloy jacket. The parallel programme will allow manufacturing trials without affecting the TFMC schedule.

— The radial plates are made of stainless steel with grooves machined on either side. Although for the TFMC the plates are made as a single unit and then machined (Fig. 3), a very large machining centre would be required for the actual coils. The machining of the grooves in segments of the plates, followed by welding assembly of the finished plate, will be investigated in a separate R&D action. In this action, a significant proportion of a full size radial plate will be made from segments; the tolerance that can be obtained on the flatness is a critical input to the full size coil design.

— The conductors are transferred one turn at a time to the groove on either side of a radial plate. The transfer process requires control to avoid strain damage to the superconducting strands. During the transfer operation, the conductor is wrapped

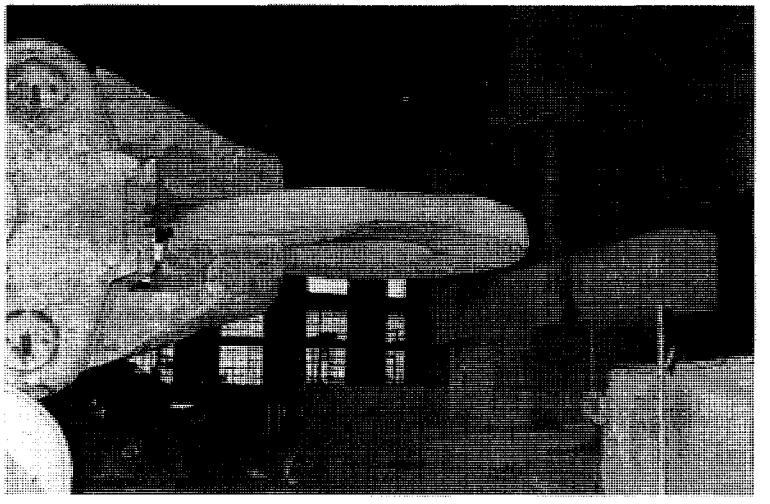

FIG. 3. Radial plate forging.

with insulation. The conductor grooves are closed by welding a stainless steel cover so that the conductor and the turn insulation are totally enclosed in steel which then serves as the primary path for loads accumulating across the winding pack section. A joint is made between the pancakes on each side of the plate. The turn insulation is sized at a thickness of 2.5 mm including 0.5 mm for an allowance for tolerances on groove and conductor dimensions in order to assure insertion without insulation damage. The insulation is to include multiple wraps of an electrical barrier material such as a polyimide film. A bond of the turn insulation to the surface of the grooves in the radial plates is not required. The filler material around the conductor is provided by a vacuum impregnation with epoxy resin made after the steel cover has been applied.

— Each radial plate is enclosed in insulation 1–1.5 mm thick, with an extra layer of insulation between the plates. A bond of the insulation to the surface of the plate and between plates is desired, but the integrity of the structure does not require bonding. The five plates are then stacked together to form the coil, the interpancake joints are completed and the stack is wrapped with ground insulation and impregnated/cured. Because of different thermal expansion between jacket and case, the local conductor insulation stresses are substantially different with a steel or an Incoloy jacket. Mechanical testing, at 4 K, of DP sections with an Incoloy jacketed dummy conductor will be used to confirm the satisfactory behaviour of Incoloy.

— The winding pack is inserted in a stainless steel coil case. The case is formed from plate stock with full penetration welds at the corners of the section. The closure weld in the full size coil is located at the midplane because this is a region of lower stresses where partial penetration and/or mechanical property degradation can be tolerated and the symmetric location provides easier control of geometric distortion. The TFMC will use the same insertion, closure and filling procedures but the case itself is substantially lighter (the thickness is about 10 cm, whereas that of the ITER coil reaches 30–40 cm). To obtain the necessary manufacturing information, two or three full size sections of the case will be made in a separate R&D action. Each of these will weigh about 20 t and will represent the most critical sections of the case (the upper curved region and the outside, where the outer intercoil structure is attached). The space between the coil and the case is to be filled with glass reinforced resin either in a final impregnation process or with inflatable bladders, and a slip surface is included in the winding pack/case interface.

— In the nose region, the coil insulation is subject to nuclear radiation, with a cumulative lifetime dose of 10^7 Gy. Samples of the coil insulation will be tested in a fission reactor [4] as a confirmation of the results from preliminary screening.

5. STATUS

Both the detailed manufacturing drawings of the TFMC and the stress analysis of the test configurations are nearly completed. About one third of the total of 4 t

TABLE III. PROJECT MILESTONES

Main coil	Parallel R&D	Date
Finalize design and analysis		8/96
	Atmosphere control with Incoloy jacket, absence of SAGBO [5]	6/97
Demonstrate steel jacket transfer process to radial plate with dummy		5/97
	Demonstrate Incoloy jacket transfer process with dummy	2/98
Start radial plate machining		9/96
	Fabrication of full scale radial plate	5/98
Demonstrate cover plate closure on grooves		6/97
Demonstrate performance of turn insulation		7/97
Complete conductor manufacture		2/97
Demonstrate s/c joint [8]		2/97
Qualify case winding filling		2/97
Complete first double pancake (wind, react and insulate)		8/97
Complete fifth double pancake		12/97
Complete case		3/98
	Fabrication of full scale case sections	5/98
Complete coil		5/98

of Nb_3Sn strand is complete and the conductor jacketing line is operational. Two 50 m long dummy lengths of conductor for pre-production trials have been finished. The forgings for the radial plates (Fig. 3) have been done, and final machining is under way. Table III identifies the main R&D and manufacturing steps.

6. TEST PROGRAMME

The TOSKA test programme will contain the following major items:

- Pressure drop will be measured on each cooling circuit of the TF model coil for mass flow rates from 0 to 18 g/s per channel.
- The TF model coil and the LCT coil will be separately and jointly charged in steps toward the maximum current of the TF model coil. Changes in outlet temperature, flow rate, stress levels and displacements of the TF model coil will be measured.
- The current sharing temperature of individual pancakes will be measured by heating the inlet helium at constant current with a slow rate of temperature rise, at conditions of maximum current in the TFMC and the LCT coil.
- Quench performance (rate of the helium expulsion and resistance increase) of the TF model coil, with and without delayed discharge, will be measured to examine pancake to pancake propagation and heat transfer effects from radial plates. The quench detection system will be characterized [6].
- The TFMC will be ramped down from high to intermediate current values, and the transient electromagnetic behaviour of the winding will be measured.
- The TFMC will undergo cyclic charging 1000 times, with the LCT coil at a constant level of current. The DC performance parameters will then be remeasured with and without the LCT coil.
- The state of the TFMC insulation will be periodically minitored by the partial discharge diagnostic procedure [7].

7. CONCLUSIONS

The manufacturing techniques of the ITER TF coils are being defined and qualified in an extensive R&D programme over the next two years. One of the programme elements, the TFMC, will be tested under mechanical loading conditions approaching those of the full size coil to provide a final confirmation of the design.

ACKNOWLEDGEMENTS

The authors gratefully acknowledge the contributions of their colleagues both in their own institutes and in Ansaldo Energia, Noell, ACCEL and GEC-ALSTHOM.

REFERENCES

[1] HUGUET, M., The ITER magnet system, Fusion Technology (Proc. 19th SOFT, Lisbon, 1996).
[2] AUGENSTEIN, A., et al., Test results of the cryogenic supply system of the upgraded TOSKA facility and of the EURATOM LCT cooled with forced flow supercritical superfluid helium, ibid.

[3] OKUMO, K., Status of the ITER CS and TF model program, ibid.
[4] GERSTENBERG, H., et al., Shear Compression Strength of Organic Insulation System at 4 K, Rep. ICEC16, Kitakyushu, Japan (1996).
[5] WONG, F., et al., Selection of jacket materials for Nb_3Sn superconductors, Fusion Technology (Proc. 19th SOFT Lisbon, 1996).
[6] MARINNUCCI, C., Performance of the Quench Detection System for ITER, paper presented at 1996 Applied Superconductivity Conference, Pittsburgh, PA, USA (1996).
[7] IRMISCH, M., Hochspannungs-Isolationsdiagnostik an supraleitenden Grossmagneten, Rep. FZKA 5615, Forschungszentrum Karlsruhe, Germany (1995).
[8] BRUZZONE, P., et al., Design and R&D results of the joints for the ITER conductor, paper presented at 1996 Applied Superconductivity Conference, Pittsburgh, PA, USA (1996).

MAINTENANCE CONCEPTS FOR ITER*

ITER JOINT CENTRAL TEAM and ITER HOME TEAMS

Presented by R. Haange[1]

Abstract

MAINTENANCE CONCEPTS FOR ITER.

Neutron activation of structural materials will preclude human access into the ITER vacuum vessel soon after the start of the operations. As a result, all maintenance operations inside the vacuum vessel will have to be carried out remotely. Because of attenuation of neutrons by the shield blanket and vacuum vessel, the activation levels inside the cryostat will build up slowly, and restricted, short term human access for inspection and repair operations may remain feasible. Tasks of longer duration will, however, have to be undertaken remotely. Maintenance concepts for in-vessel and ex-vessel (inside cryostat) components are described in the paper.

1. GENERAL APPROACH

The present state of the art concerning remote operations in a highly radioactive environment is not sufficiently advanced for in-situ repair. Therefore, with a few exceptions, the maintenance procedures are based on replacement of faulted components [Ref. 1]. The faulted components are removed from the vessel and sent to a hot cell facility for refurbishment or preparation for waste disposal.

The large inventory of tritium and activated material inside the vessel is confined within two safety barriers: the vacuum vessel and the cryostat vessel. Remote handling (RH) operations that breach the existing barriers must therefore be done with extensions to these barriers. For this reason, regular in-vessel inspections will be done such that the external parts of the probes outside the vessel are surrounded by two confinement enclosures. This allows the probes to be inserted soon after a plasma pulse.

---

[1] ITER Joint Work Site, Naka, Japan, for ITER Joint Central Team and Home Teams.

For in-vessel maintenance operations, the releasable radioactive inventory and stored energy are reduced by a sufficient amount so that one safety barrier only has to be maintained throughout an intervention. An in-vessel maintenance operation is therefore preceded by a detritiation campaign that may involve non-tritium plasma pulses, glow discharge cleaning, baking or other procedures that reduce the tritium inventory inside the vessel. This is followed by lowering of the temperatures of the water cooled in-vessel components and the vessel itself, and subsequent decrease of the coolant loop pressures to near ambient. Before opening, the vessel is vented with dry nitrogen and a purge is maintained through a detritiation system inside the tritium plant. Removal of dust from inside the vessel at the start of the intervention further reduces the releasable active inventory.

Opening of the ports giving access to the vessel is done from within permanent hot cell type structures that enclose the maintenance ports or from transfer casks that are hermetically docked to the port before opening. The maintenance cell or the cask then form the extended single safety barrier for the confinement of tritium and activated dust.

Components that are installed inside the ports of the vacuum vessel, including cryopumps, additional heating components, plasma confining structures, diagnostics, test blanket modules, etc. must be designed such that the components can be pretested to the maximum practical extent prior to installation. By doing so, essential parts do not have to be disassembled and remotely reconnected during installation. In practise, this requirement cannot always be fully complied with due to weight, size and handling constraints.

Interventions inside the cryostat that require venting must be preceded with warming of the coils and cold structures to ambient temperature. Together with the subsequent cooldown, this adds approximately two months to the overall maintenance time. Given the fact that many ex-vessel components are very large and costly so that keeping spares is impractical, the approach is to design these components such that they should last the life of the ITER machine. Moreover, to lower further the likelihood of requiring replacement of large components involving difficult and lengthy RH procedures, redundancy has been introduced in the design of components where practical. For example, all poloidal field(PF) coils have been designed to include four winding packs such that if a fault were to develop in one of them, the current in the remaining three could be increased to match the required ampere turns. Actively cooled thermal shields that cover very large areas inside the cryostat have been designed to have two independent cooling circuits, one being adequate for the removal of the thermal energy. The general approach is therefore to make ex-vessel interventions very unlikely. Provisions are made in the design and layout to accommodate RH. Operations will be planned in detail but equipment not procured until needed. Furthermore, should repair or inspection inside the cryostat be necessary, human access is under consideration.

Remote handling procedures take a large amount of effort to develop and generally require complex, specialised equipment and tools. It is therefore important on the one hand to standardise as much as practical the operations, tooling, etc , and on the other hand to optimise hands-on or hands-on assisted operations in support of the fully remote activities. This is achieved in ITER in two ways:

(i) by surrounding the frequently used RH maintenance ports with shielding walls so that hands-on operation can be carried out in parallel in adjacent locations, and

(ii) by using hands-on procedures for preparatory operations for prior to removing all shielding from port ducts and finishing operations after reinstallation of shielding.

2. MAINTENANCE OF IN-VESSEL COMPONENTS

Towards the end of the BPP, the gamma dose rate inside the vacuum vessel one week after the last plasma pulse is expected to be approximately 5 E4 Sv/hr. Therefore all maintenance inside the vacuum vessel has to be carried out remotely.

The plasma is surrounded by 740 shield blanket modules and shield plugs in the port openings. The divertor consists of 60 cassettes. Other main components inside the vacuum vessel are either integrated with the shield plugs (RF antennae, EC waveguides, test blanket modules), or are mounted inside the port ducts (diagnostics, cryopumps).

Plasma-wall interaction will lead to erosion of materials facing the plasma. As a result, it is estimated that divertor cassettes must be replaced several times during the lifetime of the machine, whereas the ITER first wall shield blanket modules will only be replaced once when breeding blanket modules are installed at the end of the basic performance phase (BPP). Realistically, one should also assume that, due to the experimental nature of ITER operations, local damage may occur leading to the need to replace a number of the first wall shield modules or divertor cassettes. Cryopumps and diagnostics should generally be designed to not require replacement. However, novel designs combined with changing requirements could lead to the replacement of a number of these components.

Shield blanket replacement will be undertaken by deploying inside the vessel a monorail system that is normally stored in two diametrically opposite maintenance cells. Two additional dedicated RH ports at the equatorial level, each at a position half-way between the rail deployment cells, are used to insert a rail support device and to transfer components in and out of the vessel. In the reference design, the transfer cells are enclosed by permanent shield walls. However, the feasibility of replacing the permanent cell structures with moveable casks that dock directly to the RH port interface is being studied. The cask would then be located inside radial side walls, which provide shielding together with doors in the opening of the pit wall, allowing human access in the adjacent areas when the port is fully open and active components are loaded in the cask. Up to four remote vehicles can travel on the rail system, one operating in each quadrant. Each vehicle may carry a telemanipulator suitable for pay loads up to five tonnes to handle individual modules for positioning and removal. Additional equipment is required to effect the attachment to the back plate by either welding or bolting. The connection to the water cooling manifolds is made by bore welding equipment based on YAG laser technology that is also used for cutting of the pipe connection. This equipment is introduced in the cooling pipework from outside the bioshield in a hands-on assisted mode [Ref. 2]. Reinstallation of modules involves the reverse procedure but includes measurement of the position of critical surfaces to check whether the specified alignment has been attained. A frequency modulated laser radar system that is expected to measure to submillimetre accuracy in the ITER vessel environment is under development for this purpose.

Transfer of the radioactive components to the hot cell is done inside sealed RH casks. To provide gamma shielding would add hundreds of tonnes of weight to the casks. It has therefore been decided not to shield the casks but to seal them for confinement of tritium and other active contaminants. The use of unshielded casks requires that during transfer of active components, all personnel are excluded from the transfer route. To do this in a safe way, it has been proposed to bar all personnel from the pit, gallery and transfer route between hot cell and lift by having dedicated transfer shifts, possibly during silent hours. The undocking and docking operations at

the cryostat (direct docking case) and the hot cell are designed to retain confinement during all stages of the operations. This is possible through the use of so-called double seal doors. Their design is based on the sealing of a cask to the port, followed by the clamping together of the port and cask "doors", and the subsequent opening of the double door unit by raising it inside a vertical enclosure that forms part of the cask/port interface. The clamped sides of the doors are sealed against each other and thereby protected from contamination so that when the doors part after the transfer operation, the sides exposed to the outside remain free of contamination. The vertical moving section of the door frame attached to the port is of thick stainless steel providing sufficient shielding to allow personnel access into the shielded cell in the closed condition.

Upon undocking, the loaded cask is remotely driven and guided on railway tracks to the hot cell. The route to the hot cell involves passage from the pit area to the circumferential gallery, where the lift is located. After raising the loaded cask to the hot cell level, the cask continues its journey to the hot cell and docks to transfer ports having an interface identical to the vessel ports. After docking, the active component is unloaded and replacement components may be loaded for transfer to the machine.

The interface at the four RH ports at the divertor level for divertor cassette transfer is of very similar design to the one described for the equatorial RH transfer ports, allowing quick docking and undocking operations. This arrangement allows for maintenance operations to be carried out through four ports simultaneously at the divertor level, as at the equatorial level. The coolant pipework to individual cassettes is routed through all ports such that six lines for three cassettes penetrate through each port. The pipework, after draining, can be opened from outside the bioshield and, in a hands-on assisted mode, the bore tooling is introduced and operated for cutting, rewelding and inspection operations. After cutting the pipework and opening the RH ports, the central cassettes can be radially extracted using a special transporter (mover) guided on rails through the port duct into the cask. After transfer to the hot cell, the second, adjacent cassettes can be toroidally moved, via rollers on the toroidal rails, to which the cassettes are securely fastened, onto an extraction vehicle introduced in the central position and extracted. This is repeated for the remaining 13 cassettes in the case of complete exchange. Additional operations are necessary for unlocking and unclamping of the cassettes from the rails and detachment of current leads, etc. The reverse procedure is used for reinstallation but this will involve a final check to ensure that the specified alignment has been achieved, using the same equipment as mentioned for the blanket modules. The shielding configuration around the divertor RH ports is similar to that described for the equatorial RH ports.

Should replacement of a cryopump be required, it will be performed using a special cask. As this is not expected to be a frequent event, the docking interface is not as highly developed as for the RH ports at the equatorial and divertor level. The removal of all the service lines that penetrate the port, which is necessary to allow cask access, is done in a hands-on mode. Those lines that are internally contaminated will be handled in locally applied temporary contamination protection "sleeves". The removal of the bioshield plug will also be a hands-on operation. If possible, that plug will be stored inside the pit, near the port. The attachment of handling equipment to the cryostat cover plate will also be a hands-on assisted operation. Before withdrawal, however, a transfer cask with RH equipment will be docked to the port to disassemble the pumps mounting flange and extract the cryopump into the cask.

Similar procedures are under development in conjunction with port layout for the equatorial ports holding RF antennae, EC waveguides and test blanket modules.

3. MAINTENANCE OF EX-VESSEL COMPONENTS

While all components inside the cryostat should be designed to last the life of ITER, failure of components can, of course, never be fully ruled out. The most likely components to require repair or replacement are the coils, including the central solenoid (CS), and the thermal shields. Due to segregation of the cryofeed and current lines, and external and internal manifolding of the thermal shield cooling lines, the affected coil or group of thermal shields should be identifiable when failure is discovered. If the extent of the failure exceeds any built-in redundant capacity or operation with reduced capacity is not viable, then the component will have to be repaired or replaced. Coil failure could include the following [Ref. 3]:

(i) helium leakage, e.g., electrical insulation break,
(ii) internal short circuit, and
(iii) ground insulation short circuit.

Some faults, e.g. a leak at an electrical break, can be repaired locally inside the break boxes that contain these insulators. Other faults require a bypass of the faulty winding module, or the complete replacement of a coil. Repair operations that have to be performed within the electrical break boxes inside the cryostat have been investigated and remote repair concepts have been developed. However, the required delicate remote operations will always remain difficult. Man access to the break boxes for such repair work is therefore considered of great advantage. The component activation and resultant dose rate levels inside the cryostat have been calculated for BPP and extended performance phase (EPP) operation. The accuracy of the predicted levels is, naturally, not expected to be very good at this stage of the project. However, the indications are that the dose rates may remain below the mSv/hr level during the whole BPP, after 30 days of cooldown. It seems reasonable to assume that a fraction, of the presently assumed maximum yearly dose for radiation workers in ITER of 20 mSv, could be allocated for hands-on repair and inspection activities, provided, of course, that this can be supported along the guiding ALARA principles. On this basis, particularly when additional local shielding can be introduced inside the cryostat, man access for times that appear reasonable for the execution of repair work seems feasible.This could greatly benefit repair activities inside break boxes as well as leak localisation in thermal shields after the area had been narrowed down to a certain segment.

Initial calculations have shown that some areas inside the cryostat that are well-shielded from the plasma are expected to have lower dose rates than the bulk of the cryostat volume. This includes the space inside the CS and the areas just above and below the CS. Again considerable benefit would be gained by having, albeit limited, man access for repair work or preparatory and finishing operations in connection with CS replacement.

CS removal is possible through an inner port inside the cryostat cover. An additional ring of material (built accordingly) can be cut from the cover to allow vertical removal of the PF2 coil. To replace the PF3 or PF8 coil not only involves the removal of the complete cover, but also the removal of all coolant lines to the vertical ports. In all this would include some 1000 pipe cutting and rewelding and associated handling and inspection operations. The cryostat cover and top shield can be removed, but for limited time only in order to prevent a significant dose rate at the site boundary.

Coils PF4, 5, 6, and 7 are replaceable by lowering to the basemat, where they will be sectioned and moved in transfer casks to the hot cell or another active storage area. The design of the lower cryostat includes the possibility of removal of a ring

section and refitting by welding (of new sections). This does require the clearing of the area underneath the cryostat, i.e., the large coolant storage tanks and pressure suppression device will have to be sectioned into transportable pieces and taken to a temporary storage site. After clearing and decontaminating the area following removal of the faulty coil, a temporary ceiling providing gamma shielding is installed and a new coil is rewound in the area underneath the machine, followed by installation into the cryostat.

As described, removal of any PF coil out of the cryostat for repair or rewinding and its replacement is feasible, but a very large process, not mentioning the time to procure a large amount of new conductor, even if a significant amount is already available. This difficult perspective completely justifies the decision to provide built-in redundancy in PF coil ampere-turns.

Replacement of toroidal field (TF) coils has been studied by the Joint Central Team and Home Teams. The presently envisaged method involves simultaneous removal of the associated vacuum vessel sector, after the internal components and back plate of that sector and a fraction of the components of adjacent sector have been extracted from the vessel and stored in the hot cell. One TF coil, as well as one segment of the VV and the backplate from the initial procurement, will be available as spares. It is intended to shift the PF3 coil sufficiently sidewards to allow vertical throughpassage of the faulty coil. This avoids having to cut and remove all the pipework routed to the upper vertical ports. The main problem associated with this difficult remote handling procedure is that in this case the complete removal of the upper shield is not allowed when a segment of VV is removed. This therefore requires an additional, temporary large-scale shield on top of the cryostat, which is to be studied in more detail in Home Team tasks.

4. RH DEVELOPMENT

Because the remote replacement of divertor cassettes and blanket modules is expected to be required several times during the lifetime of ITER, the RH development programs are focused on these areas. For both operations test platforms are under construction by Home Teams with the objective to demonstrate and optimize the remote replacement of divertor cassettes and blanket modules, as an important R&D activity [Ref. 2,4,5]. The test platforms will not only demonstrate the remote handling aspects, including transfer through the port ducts, but also the cutting and welding of the pipework. To this end, prototype transporters, telemanipulators and tools are under development for use in the tests. Further development of equipment is directed towards in-vessel inspection systems and metrology equipment, and testing of small components for radiation hardness. It is expected that following establishment of more detailed port layouts and component design, a large amount of additional testing will have to be carried out, using the test platforms as mock-up facilities, before design of components and their RH equipment can be frozen.

5. CONCLUSION

Remote maintenance of in-vessel components mainly involves replacement of faulty components. Removed components are transported to the hot cell in sealed casks on a railway system. Double door devices are used to avoid the release of radioactivity during docking and undocking operations. Dedicated large scale RH transporters, telemanipulators and tools are being developed and crucial RH operations will be tested during the next few years.

For ex-vessel components redundancy has been incorporated in the design where practical so that a single failure does not lead to the need for replacement. However, gross failure cannot be totally ruled out and hence replacement scenarios for the coils and other ex-vessel components are under development. The provision for eventual coil replacement has had a profound influence on the overall layout of the building and design of the cryostat.

REFERENCES

[1] SHIBANUMA, K., et al., "Remote handling in ITER", WAC/ISRM '96 (Proc. Symp. Montpellier, 1996).

[2] KAKUDATE, S., et al., IAEA-CN-64/FP-15, this volume.

[3] TESINI, A., et al., "Remote operations for the replacement of a poloidal field coil in ITER", Fusion Engineering (Proc. 17th IEEE Symp. Lisbon, 1996).

[4] MAISONNIER, D., et al., "Divertor remote handling test facilities", WAC/ISRM '96 (Proc. Symp. Montpellier, 1996).

[5] MAISONNIER, D., IAEA-CN-64/FP-16, this volume.

DEVELOPMENT OF A REMOTE MAINTENANCE SYSTEM FOR ITER BLANKETS*

S. KAKUDATE[1], K. OBARA[1], K. OKA[1], M. NAKAHIRA[1],
S. NISHIO[1], K. TAGUCHI[1], A. ITOH[1], S. FUKATSU[1],
N. KANAMORI[1], E. TADA[1], K. SHIBANUMA[2], R. HAGER[2],
T. BURGESS[2], A. TESINI[2], N. MATSUHIRA[2],
C. HOLLOWAY[2], R. HAANGE[2]

[1] Japan Atomic Energy Research Institute

[2] ITER Joint Central Team,
Naka Joint Work Site

Naka-machi, Naka-gun, Ibaraki-ken,
Japan

Abstract

DEVELOPMENT OF A REMOTE MAINTENANCE SYSTEM FOR ITER BLANKETS.

In ITER, remote maintenance is a key technology since in-vessel components such as the blanket require scheduled maintenance under severe γ radiation. For this purpose, a rail mounted vehicle type maintenance system has been developed to handle the heavy blanket modules with the required accuracy. Its applicability to ITER blanket handling has been verified through use of a prototypical vehicle manipulator and rail transporter. In addition, bore tools using a YAG laser for welding and cutting of blanket cooling pipes, and a radiation hard periscope for viewing the blanket and first wall, have been developed. On the basis of the development of this technology, a blanket remote handling test platform composed of full scale remote handling equipment and tools is being fabricated as one of the Seven Large R&D Projects to demonstrate the remote maintainability of the ITER blanket prior to ITER construction. The paper describes the status of these programmes.

1. INTRODUCTION

The ITER tokamak components inside the cryostat will be activated by DT operation, so that maintenance of the components will have to be conducted with remote handling technology. Maintenance of the blanket is especially critical since scheduled maintenance is foreseen, including the complete replacement of the shielding blanket with the breeding blanket. A modular type blanket structure has been chosen for ITER to allow individual module replacement consistent with a multilevel maintenance philosophy. In this concept, handling of a 4 t blanket module in a confined space with accurate positioning, welding and cutting of branch pipes, and in-vessel viewing for inspection and monitoring are essential technologies to be developed.

In accordance with the ITER technology development programme, a rail mounted vehicle type remote handling system [1] has been developed to handle the heavy blanket modules within the limited space and with the required precision. In addition, associated critical technologies such as YAG laser bore tools for welding and cutting of branch pipes and a 15 m long periscope for in-vessel viewing have also been developed. Full scale remote handling equipment and tools are being fabricated for construction of a blanket remote handling test platform to demonstrate the remote maintainability of the ITER blanket modules.

2. FULL SCALE BLANKET REMOTE HANDLING TEST PLATFORM

2.1. Design requirements

In the current ITER design, it is anticipated that blanket module replacement will be carried out several times during the life of the machine, including the complete replacement of the shielding blanket with the breeding blanket at the end of the Basic Performance Phase (BPP). To facilitate replacement, the blanket is segmented into 740 modules within a dead weight limitation of around 4 t. The maintenance time for replacing one module is specified to be two months and for replacing all modules two years. The installation tolerance for module replacement is specified to be 2 mm as a step gap between modules. The blanket remote handling test platform has been designed to meet these design requirements.

2.2. Outline of the test platform

Figure 1 shows the general layout of the blanket remote handling test platform, which is composed of module handling equipment, port handling equipment, auxiliary remote handling tools and a blanket mock-up structure to reproduce the physical environment of a 180° ITER in-vessel region.

A vehicle/manipulator with a payload capacity of over 4 t is installed as the main module handling equipment. The vehicle can be moved toroidally along the rail using

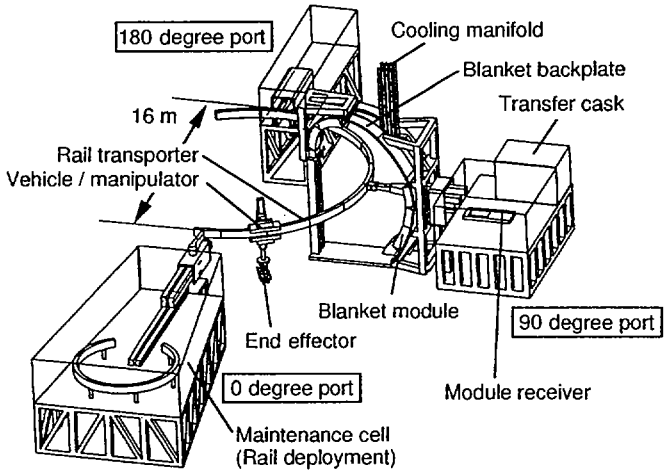

FIG. 1. Full scale test platform for blanket remote maintenance.

a rack and pinion mechanism. The manipulator is composed of a two stage telescopic arm whose total length is about 6 m so as to access all of the blanket modules. The manipulator, which is connected to the rotating mechanism of the vehicle, can rotate around and along the rail in order to minimize the port opening space for deployment and to maximize the flexibility for in-vessel maintenance operation.

A maintenance cell located at the 0° port is to deploy and store the 180° articulated rail. The rail is formed in the vessel in a circular configuration with a major radius of 8 m and is supported from the 90° and 180° ports. The rail supports include a radial movement mechanism for fixing the rail and a positioning mechanism for compensating rail deflection. A module receiver is installed at the 90° port to receive a blanket module from the vehicle/manipulator and to transport it to a transfer cask for delivery to a hot cell.

Remote handling tools include bore tools for welding and cutting of blanket cooling pipes and for weld inspection. A YAG laser transmitted through a flexible optical fibre is chosen for welding and cutting of branch pipes and cooling manifolds with several bends. The blanket mock-up structure is composed of a blanket backplate, blanket modules and cooling pipes so as to demonstrate remote operation for the blanket module replacement.

2.3. Main milestones and schedule

Following design completion in March 1996, fabrication of the module handling equipment and tools has begun. So far, the 90° and 180° rail supports have been completed. All the other remote handling equipment and tools are scheduled to be fabricated by the end of March 1997, including basic function tests and inspection at the factory. Thereafter, fabricated equipment and tools will be delivered to the Japan

Atomic Energy Research Institute (JAERI) for installation of the blanket remote handling test platform. The integrated performance test of blanket module replacement using remote handling procedures will be performed by the end of June 1998.

3. DEVELOPMENT OF REMOTE HANDLING EQUIPMENT AND TOOLS

3.1. Vehicle/manipulator and end effector for module handling

A prototypical vehicle/manipulator with a payload capacity of 1.2 t has been fabricated and tested [2] to verify its structural integrity and handling capability. The manipulator is composed of telescopic arms with a maximum arm length of 6 m. It has been demonstrated that the vehicle/manipulator provides sufficient stiffness and precision to handle heavy components within a 1 mm tolerance. A position feedback control has also been developed to compensate for relative displacement to achieve reliable gripping.

Following the manipulator experiments, an end effector with gripper for handling the dummy blanket module has been fabricated and attached to the 1.2 t

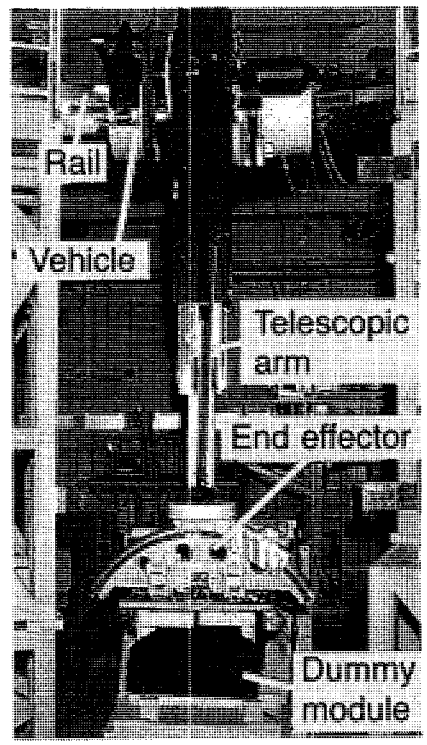

FIG. 2. Vehicle/manipulator with end effector and module gripper.

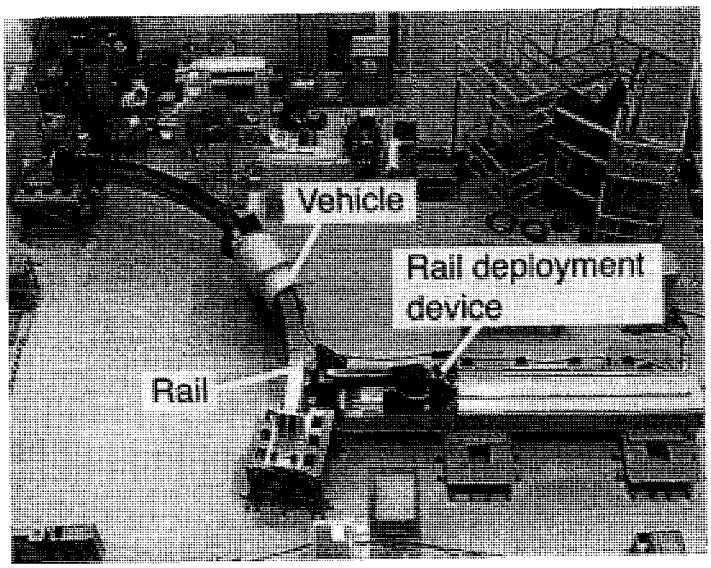

FIG. 3. Articulated rail transporter.

vehicle/manipulator as shown in Fig. 2. Preliminary experiments to replace the dummy module have been performed using a teaching playback control. This includes essential operations for module replacement such as gripping, lifting, transporting, positioning and fixing the module, as well as screwing and unscrewing bolts. The test results have shown high repeatability within a 0.5 mm tolerance in all directions. Further experiments including cooling pipe alignment and position sensing are being prepared.

3.2. Articulated rail and rail deployment/storage

A prototypical rail transporter and rail deployment/storage [3] as shown in Fig. 3 have been fabricated to verify the rail deployment/storage procedure and to qualify the mechanical stiffness of the rail joint for cyclic operation. As a result, it has been verified that the articulated rail can be sequentially deployed using a teaching playback control. In addition, the rail joints with hook type locks are stiff and reliable enough for cyclic operation and the maximum differential step gap at the rail joint is less than 1 mm in the worst loading conditions.

3.3. YAG laser welding and cutting of blanket cooling pipe

Figure 4 shows a full scale YAG laser welder/cutter fabricated for branch pipe welding and cutting. This system can move inside the 100 mm manifold with a minimum bend radius of 400 mm and weld a 50 mm branch pipe with a thickness of

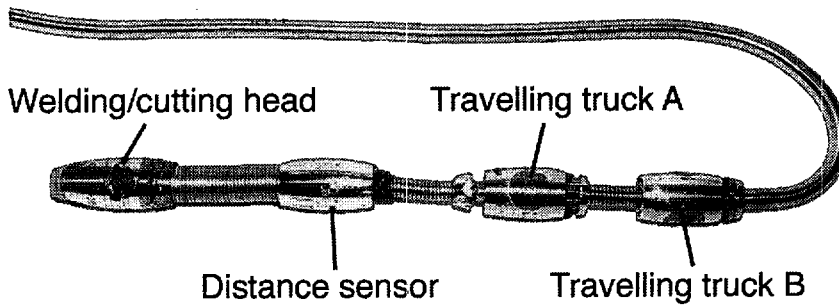

FIG. 4. YAG laser welder/cutter for blanket branch pipes.

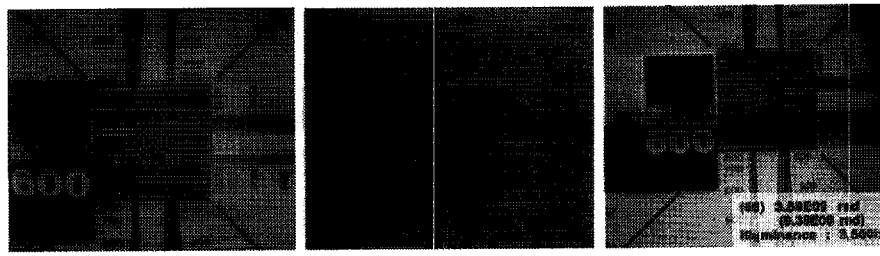

FIG. 5. Viewing performance of standard and radiation hard type periscopes. Left: before irradiation; middle: standard periscope after 2 h irradiation; right: radiation hard periscope after 3870 h irradiation.

3 mm. The measured axial movement speed is around 0.5 m/min, which meets the design requirements. In parallel with the tool development, welding and cutting experiments have been conducted using a YAG laser with a capacity ranging from 1 to 4 kW, corresponding to a 3 mm thick branch pipe and a 6 mm thick cooling manifold, so that a technological database on YAG laser welding, cutting and rewelding has been accumulated.

3.4. Radiation hard periscope for in-vessel viewing

An in-vessel viewing system is quite essential not only to detect any damage of in-vessel components but also to monitor and assist in-vessel maintenance operation. Specifically, radiation hardness of the in-vessel viewing system is the most critical requirement to ensure viewing performance for a sufficient length of time under intense γ radiation of around 30 kGy/h.

A periscope type viewing system has been chosen as a reference in ITER because of its clear and wide viewing capability. Three types of radiation hard lenses — alkaline barium glass and lead glass containing CeO_2, and OH doped synthetic

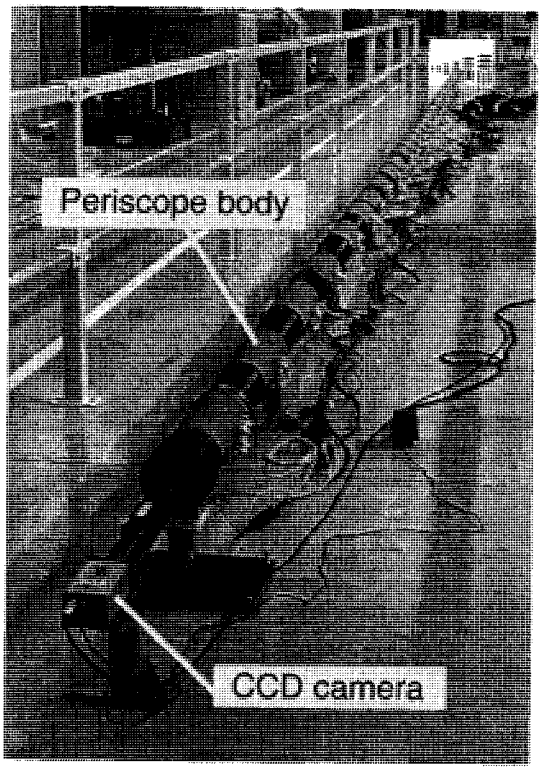

FIG. 6. The 15 m long radiation hard periscope.

quartz — have been developed through γ irradiation experiments [4]. Using these radiation hard lenses, a 6 m long periscope has been fabricated and irradiated at a dose rate of around 10 kGy/h. Figure 5 shows typical views observed by the radiation hard periscope and a standard periscope for comparison. The viewing performance of the radiation hard periscope is not degraded up to an accumulated dose of 36 MGy (3870 h). In contrast, a commercial base standard periscope cannot be used for more than 2 h at this dose rate. As a final step of development, a full scale radiation hard periscope with a length of 15 m has been fabricated for further integrated performance tests, as shown in Fig. 6.

4. CONCLUSION

The current ITER remote handling design for blanket maintenance has been proven through fabrication and experiments of the main remote handling equipment and tools such as the vehicle/manipulator, rail transporter, YAG laser bore tools and

periscope. On the basis of this experience, fabrication of a full scale blanket remote handling test platform is in progress for verification of ITER blanket maintainability prior to ITER construction.

ACKNOWLEDGEMENTS

The authors would like to express their sincere appreciation to M. Ohta, S. Matsuda and M. Huguet for their guidance and encouragement, and to members of Toshiba Corporation, Mitsubishi Heavy Industries Ltd, Ishikawajima–Harima Heavy Industries Co. Ltd and Minoruta Corporation for their co-operation in this work.

REFERENCES

[1] TADA, E., et al., Fusion Eng. Des. **29** (1995) 249.

[2] KAKUDATE, S., et al., Fusion Technol. (1994) 1411.

[3] OKA, K., et al., "Mock-up test of rail-mounted vehicle type in-vessel transporter/manipulator", Proc. 16th IEEE/NPSS Symp. on Fusion Engineering, Champaign, IL, 1995, Vol. 1 (1995) 224.

[4] OBARA, K., et al., Irradiation Test of Critical Components for Remote Handling System in Gamma Radiation Environment, Rep. JAERI-TECH-96-011, Japan Atomic Energy Research Inst., Ibaraki (1996).

STATUS OF DEVELOPMENT OF REMOTE MAINTENANCE OF ITER DIVERTOR CASSETTES

D. MAISONNIER[1], G. CERDAN[1], A. TIMPERI[1], C. DAMIANI[2], L. PIERAZZI[2], C. CALVARESI[2], P. GAGGINI[3], M. SIUKKO[4], A. TURNER[5], C. PROCTER[5], G. JANESCHITZ[6], R. TIVEY[6], S. CHIOCCHIO[6], E. MARTIN[6], A. ANTIPENKOV[6], E. TADA[7], S. FUKATSU[7], J. SHEPPARD[8], J. MILLARD[8], J. BLEVINS[9], I. ERCE[10], P. HERRERO[10], C. PASCUAL[10], A. TESINI[11], J. F. DAGENAIS[12], R. BOSSU[12]

[1] NET Team, Garching, Germany
[2] ENEA, Centro Richerche Brasimone, Camugnano, Italy
[3] ENEA, Centro Richerche E. Clementel, Bologna, Italy
[4] Tampere University of Technology, Tampere, Finland
[5] NNC Ltd., Knutsford, Cheshire, UK
[6] ITER Joint Central Team, Garching, Germany
[7] JAERI Naka, Naka-machi, Naka-gun, Ibaraki-ken, Japan
[8] SPAR Aerospace, Brampton, Ontario, Canada
[9] CFFTP, Mississauga, Ontario, Canada
[10] IBERTEF SENER, Bilbao, Spain
[11] ITER Joint Central Team, Naka-machi, Naka-gun, Ibaraki-ken, Japan
[12] COMEX Nucléaire, Marseille, France

Abstract

STATUS OF DEVELOPMENT OF REMOTE MAINTENANCE OF ITER DIVERTOR CASSETTES.

The ITER divertor assembly consists of 60 cassettes located in the bottom region of the vacuum vessel. Because of erosion and damage, their replacement is expected to be required eight times during the machine lifetime. The cassettes will be withdrawn from the vessel through dedicated ducts and will be transported to a hot cell for refurbishment. To demonstrate the feasibility of these operations and to optimize the maintenance scenario and the handling equipment design, two test facilities will be set up in Europe, at the ENEA Research Centre of Brasimone. The divertor test platform will allow simulation, in full scale, of all handling operations inside the vacuum vessel. The divertor refurbishment platform will allow simulation, also in full scale, of the most critical operations to be realized in the hot cell. The paper describes the proposed objectives, test programme and layout of both test facilities.

1. INTRODUCTION

Activation of the ITER structure by neutrons requires that all interventions inside the cryostat be performed remotely. Maintenance operations inside the primary vacuum vessel will be carried out in a particularly hostile environment: approximately

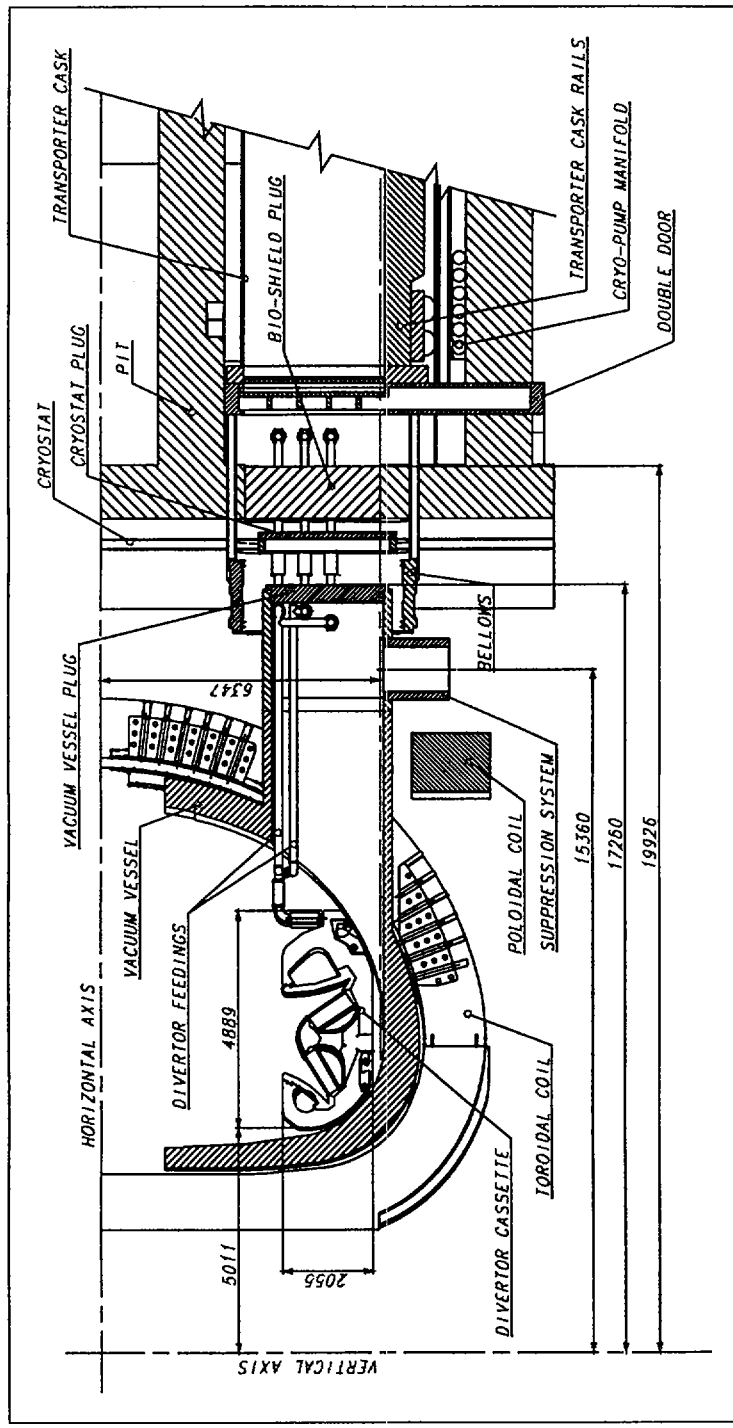

FIG. 1. Cross-section of the divertor region (dimensions in millimetres).

10^6 rad/h (gamma), contaminated dust (beryllium, carbon and steel), high temperature (around 100°C) and inert atmosphere (presumably nitrogen).

The most frequent operation to be performed is expected to be the replacement of the divertor cassettes.

2. DIVERTOR MAINTENANCE

2.1. Divertor assembly

The divertor assembly consists of 60 cassettes, each weighing approximately 25 tons, located in the bottom region of the vacuum vessel (Fig. 1). There are three cassettes in each machine sector which are cooled by water supplied by pipes that are routed through the divertor ducts. Four of these ducts, 90° apart, are dedicated to cassette insertion (withdrawal) into (from) the vessel. Cassettes removed from the vessel are evacuated to the hot cell, for refurbishing or final disposal, via contained transfer casks.

Each cassette is made of a rigid stainless steel body to which the high heat flux components (HHFCs) are attached mechanically (Fig.2). To minimize radiative waste,

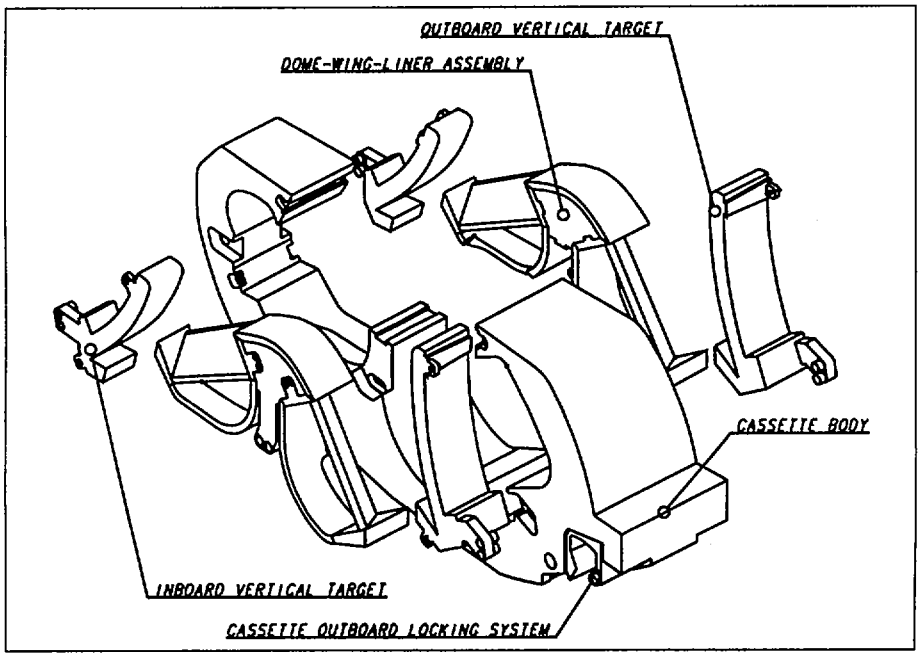

FIG. 2. Components to be refurbished.

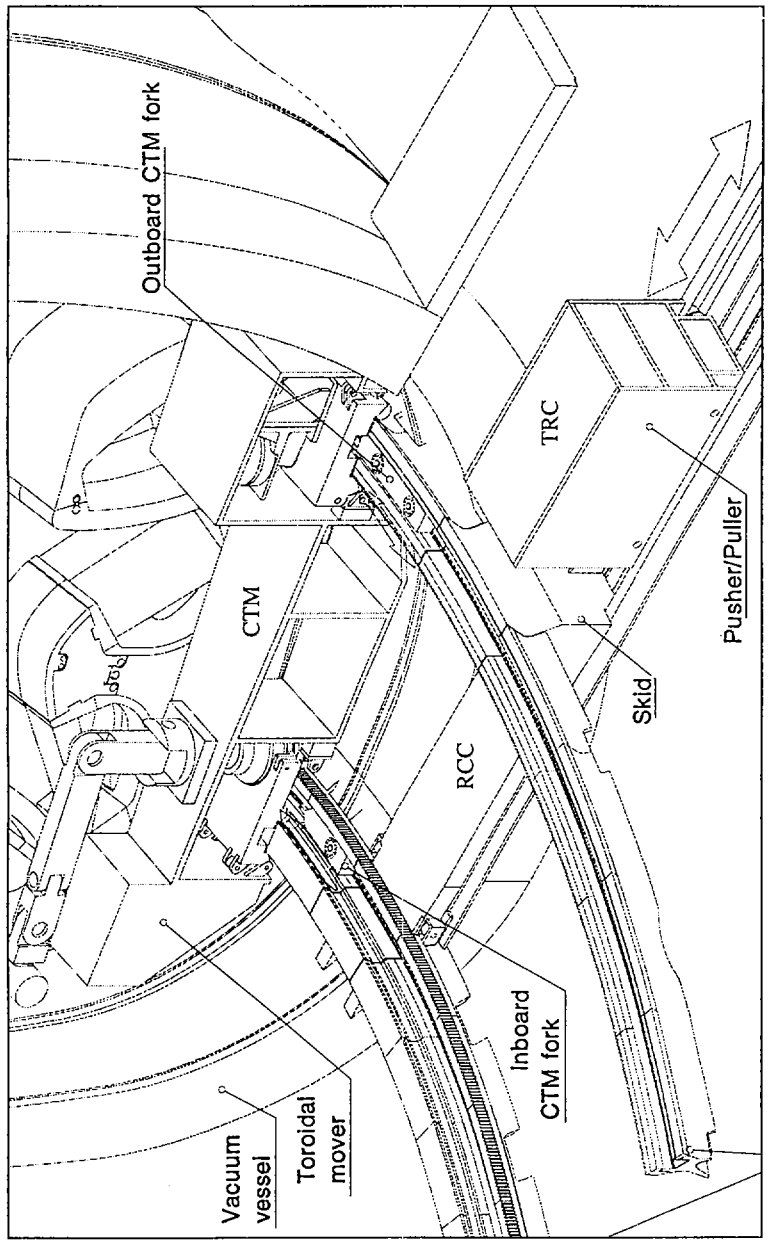

FIG. 3. Tree dimensional view of the CTM, RCC and TRC during in-vessel handling.

it is planned to refurbish, whenever possible, the cassettes in a hot cell. Because of erosion and/or local damage, it is expected that all HHFCs will have to be replaced. Similarly, the cassette locking system (CLS) and the electrical earth straps (ESs) will also be replaced.

2.2. Maintenance requirements

All ITER components are classified according to their remote handling (RH) requirements. RH class 1 components are those that require scheduled maintenance or repair (e.g. the divertor) and whose duration must be minimized. RH class 2 components are those requiring unscheduled or very infrequent maintenance (e.g. shield/blanket). The feasibility of RH class 1 and class 2 operations, which may involve the use of mock-ups, must be demonstrated during the ITER Engineering Design Activity. RH class 3 components are those not expected to require maintenance during the lifetime of ITER (e.g. coils). RH class 4 components are those that will not require remote maintenance or repair [1].

The replacement of all cassettes, expected to be required eight times during ITER lifetime, should not take more than six months whereas the replacement of one faulty cassette is expected to be required 16 times during ITER lifetime. The refurbishment of a complete set of divertor cassettes should be completed in less than 12 months while it shall be possible to store two complete sets of cassettes in an appropriate storage area.

2.3. Handling and refurbishment concepts

2.3.1. In-vessel handling

The cassettes are divided into three types: the central cassettes (four off), located in front of each handling port; the second cassettes (eight off), adjacent to the central cassettes (one on each side) and the standard cassettes (48 off), i.e. all the remaining ones. Cassette handling is carried out by dedicated 'movers' (some of which are shown in Fig. 3); each of these is dedicated to a specific set of operations [2].

The central cassette carrier (CCC) is used to translate a central cassette radially along the divertor duct (travel length: ~20 m) up to its final location and to lock it to the vacuum vessel.

The installation of a second cassette is carried out by a sequence of two operations: a radial translation along the duct (travel length: ~20 m), followed by a toroidal translation along the vessel toroidal rails (travel length: 6°). The second cassette carrier (SCC) is able to execute both operations. The toroidal translation is executed by deployable forks which are equipped with hydraulic jacks for lifting the cassette. The final positioning and locking of the cassette to the vessel is carried out by a manipulator arm installed on a dedicated vehicle, which is inserted after withdrawal of the SCC.

The installation of a standard cassette also requires a combination of radial and toroidal translations. The radial cassette carrier (RCC), which is similar to the SCC but for the absence of the forks, allows the cassette to be translated along the duct. The cassette toroidal mover (CTM), which must previously have been inserted into the vessel by the RCC, picks up the cassette from the RCC and translates it along the toroidal rails up to its final position (travel length: between +12° and +72°). Cassette locking to the vessel is carried out by a manipulator arm installed on board the CTM.

The radial tractor (TRC) is a device able to push/pull any cassette carrier along the radial duct.

2.3.2. Hot cell handling

The sequence of operations inside the hot cell for cassette refurbishment includes the following steps: decontamination; overall survey and visual inspection; dismantling of the HHFCs, i.e. the inner and outer vertical targets, the dome, the inner and outer wing liner assemblies, and of the CLS; detailed metrological survey of the cassette body; machining of the mating surfaces of the new HHFCs, ESs and CLS; reassembly, onto the cassette body, of new HHFCs, ESs and CLS; final inspection [3].

The definition of the refurbishment cycle is based on the following assumptions:

— Movements of the cassettes inside the hot cell are ensured by ad hoc carriers relying on conventional technology.
— Decontamination of a cassette is necessary before its refurbishment. The decontamination station will be located close to the cassette entry port into the hot cell. No feasibility issue is related to the decontamination process.
— Through-the-wall manipulators, assisted by heavy duty handling equipment (power manipulators, cranes), are used for the refurbishment and will be available at each work station.
— Although macrodeformations of a cassette body cannot be excluded, it is assumed that no machining of the body will be required during the refurbishment cycle (local machining of mating surfaces excluded). Should a cassette body be deformed more than a given value, it will be disposed off as radiative waste. Deformations of a cassette body, unless excessive, will be compensated for by adequate machining of the HHFCs/CLS mating surfaces.

3. TEST FACILITIES

3.1. Divertor test platform

3.1.1. Test objectives

The procedure for divertor cassette replacement and the related remote handling equipment have been devised by considering the initial assembly, positioning and

manufacturing tolerances of the ITER components ('nominal' conditions). Deviations from the initial tolerances ('limit' conditions), resulting from deformations of the components to be handled or of their supports, will be unavoidable after several years of machine operation.

Remote maintainability of divertor cassettes will be demonstrated after checking the performance of the movers under 'nominal' and 'limit' conditions. Engineering judgement will then be required to assess whether their operational limits are adequate.

Tests foreseen during the EDA can, therefore, be summarized as follows:

— commissioning of prototypes;
— validation of mover operations and auxiliary RH systems in nominal conditions;
— assessment of operational limits of movers.

Further tests will be required to validate rescue procedures in case of difficulties (e.g. jamming) or single point failure of any RH equipment and to optimize the handling equipment. Although not required to demonstrate the feasibility of divertor handling, these tests are necessary to validate the overall procedure before finalization of the RH equipment and the components design. They can, however, be postponed to after the EDA.

3.1.2. Divertor test platform

To execute the test programme outlined above, an experimental test site, the divertor test platform (DTP), will be set up. The DTP includes the following sub-systems (Fig. 4).

The *platform proper*, which represents a 72° sector of the lower region of the vacuum vessel and four radial ducts. To allow for parallel testing, it shall be possible to simulate RH operations from any of these four ducts.

Mock-ups of the components to be handled and *prototypes* of the handling equipment, including: one central cassette and three standard cassettes with all their specific RH interfaces (ES, CLS, water feeds, grappling points); one vacuum plug and, possibly, one shield plug; all items that will be located in the ducts but are not yet defined; one set of prototypical handling equipment for handling the cassettes (CTM, TRC, RCC, SCC, CCC) and other auxiliary RH equipment and tools (e.g. for pipe cutting and welding).

All mock-ups will be made of steel with their overall dimensions, assembly tolerances, mass distribution and structural characteristics as close as possible to those of the real components. The most relevant RH interfaces (toroidal and radial rails together with the racks, cassette support and locking systems, mover pinions, roller bearings for the movers, etc.), which have a strong impact on the feasibility of the

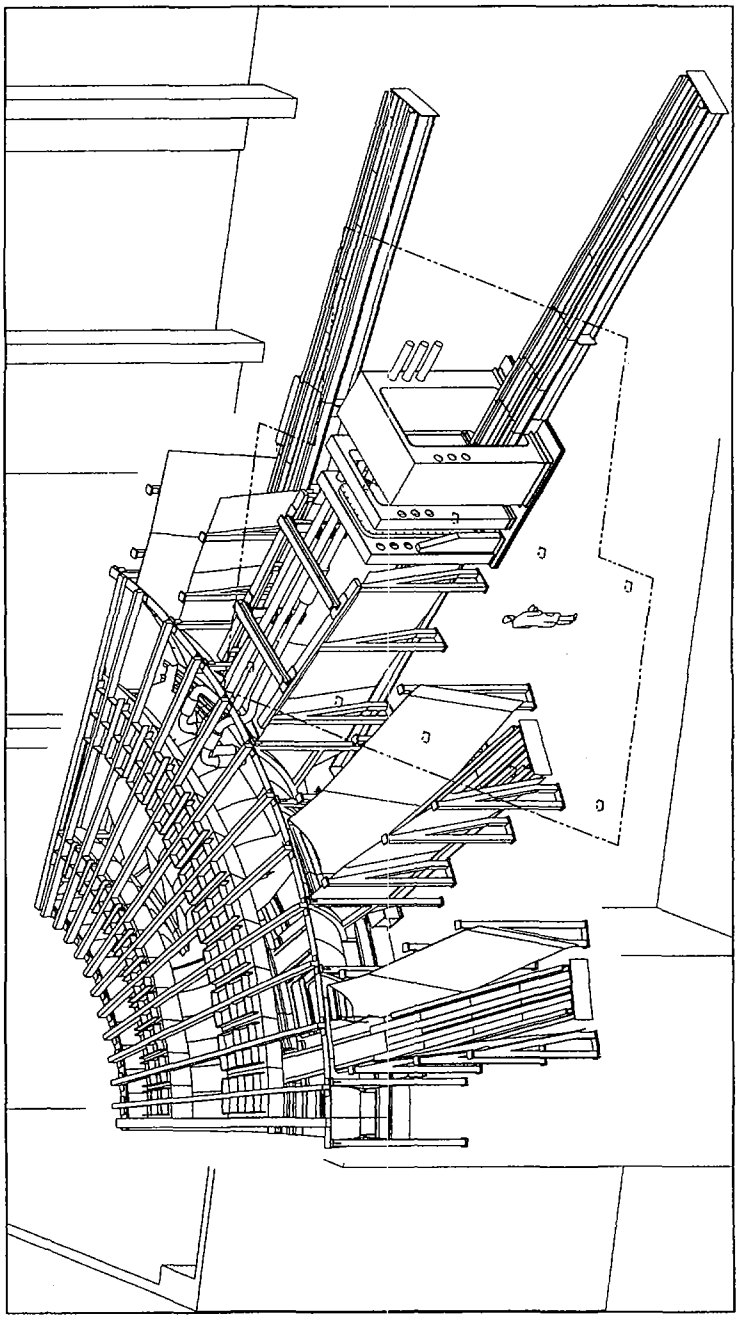

FIG. 4. DTP layout.

operations, will be made from the same materials as the real components (e.g. a special, non-magnetic nickel alloy).

Test equipment, including sensors (range, acceleration, inclination, force, etc.), installed on the platform, the mock-ups and the prototypes, and the relevant data acquisition system. With respect to the real operating conditions some degree of redundancy is foreseen to allow better understanding of the interactions between the components handled, their interfaces and the handling equipment. This will also allow a determination of the minimum set of sensors to be installed on the real handling equipment, which must be adequate to proper monitoring of the operations under all circumstances.

Each prototype is equipped with its individual low level control system (PLC, servo-amplifiers, etc.), by means of which local control of the device is possible. The high level control system (remote handling workstation, data acquisition system, kinematics simulator, Ethernet network, etc.) interfaces with each individual low level control system and supervises the operations.

Several cameras will be installed in the field, some on the movers, others in fixed locations, to allow remote monitoring and control. Image processing and synthetic viewing will be implemented at a later stage, after the EDA.

3.2. Divertor refurbishment platform

3.2.1. Test objectives

The operations to be validated in the DRP are the following (see also Fig. 2):

— Metrological survey of the cassette. In particular, the impact on the selected processes resulting from their implementation in a hot cell shall be assessed.
— HHFCs and CLS reassembly. The experimental validation shall be limited to the most complex components to be reassembled, presumably the outer target and wing liner assembly. Validation of one CLS assembly could also be required.
— Qualification of special tools (e.g. 'extractors') for the disassembly of HHFCs and CLS. To provide the required efforts while satisfying the cleanliness requirements, a number of tools powered by demineralized water hydraulics are being considered.

Tests foreseen during the EDA can therefore be summarized as follows:

— commissioning of prototypes;
— validation of key refurbishment operations in nominal conditions;
— validation of the most critical rescue procedures.

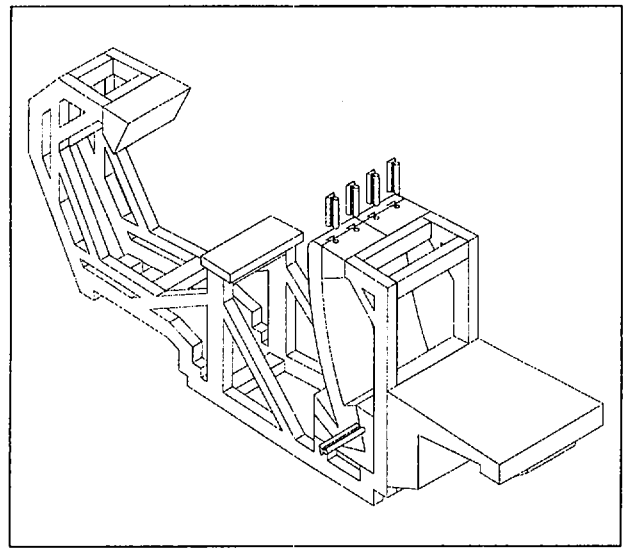

FIG. 5. Cassette mock-up for DRP.

3.2.2. *Divertor refurbishment platform*

The design of the mechanical attachments between the HHFCs and the cassette body is the most critical one for the success of the refurbishment operation. In addition to the RH requirements, the attachments must be able to resist the divertor operating loads induced by electromagnetic forces, halo currents and nuclear heating. A close co-operation with the divertor designers is mandatory but, to allow testing of different attachment schemes, a modular design of the cassette mock-ups has been adopted (Fig. 5).

The DRP includes the following subsystems (Fig. 6):

Conventional *hot cell equipment*, i.e. two pairs of through-the-wall manipulator, a heavy duty manipulator (100 kg) and an overhead crane (5 t).

Two *cassette mock-ups*, one for testing the assembly/disassembly of any HHFCs and CLS in nominal conditions of misalignment, the second to test the assembly/disassembly of the outer vertical target in off-nominal conditions of misalignment (to simulate macrodeformations of the cassette body). Mock-ups of the HHFCs and CLS to be handled will also be procured.

Prototypes of the mechanical attachments, of the assembly/disassembly tools and of the metrology tools.

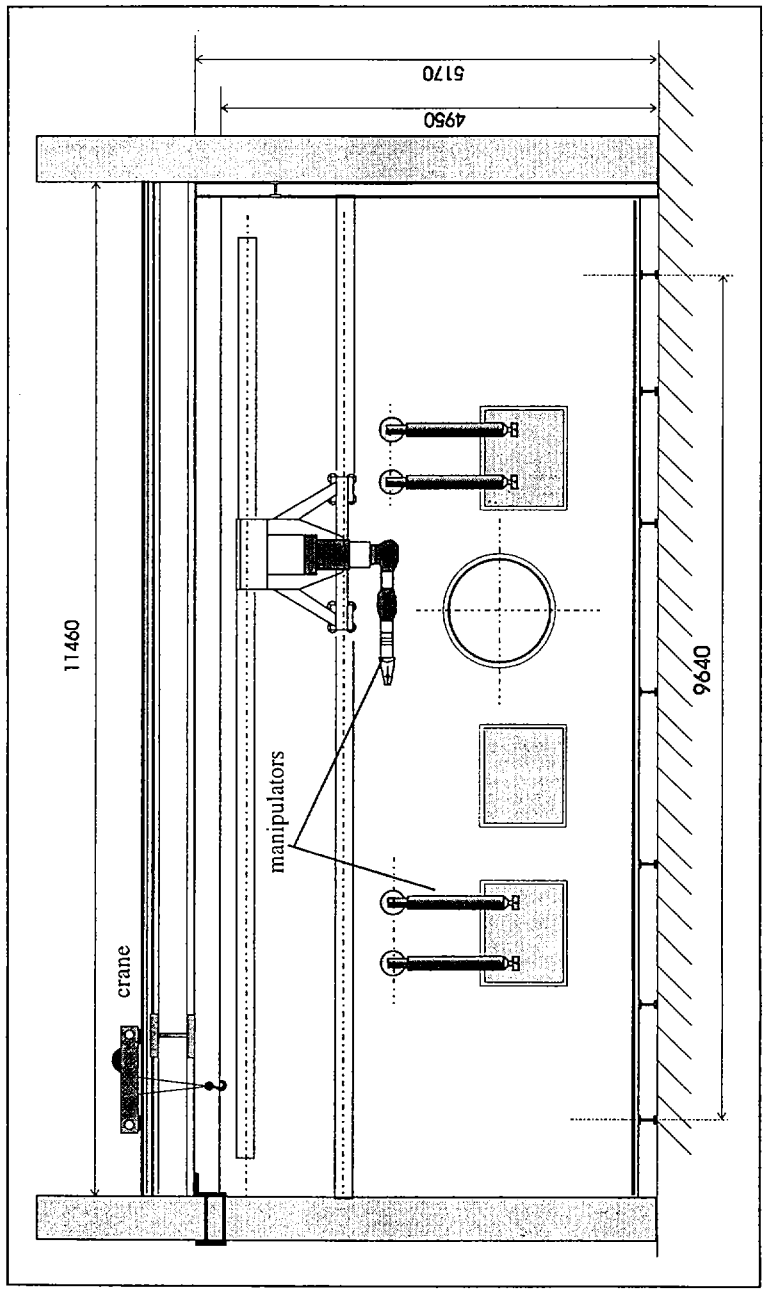

FIG. 6. DRP hot cell equipment (dimensions in millimetres).

4. CONCLUSIONS

The decision to set up large test facilities for the full scale demonstration of critical RH operations was reached in June 1995, simultaneously with the publication of the ITER Interim Design Report. The facilities to be set up in Europe should allow, before the end of the EDA (July 1998), the feasibility of divertor maintenance to be demonstrated. The main challenge is the short time available for this purpose, but the excellent co-operation between the various institutions involved in this work, within and outside Europe, allows us to be confident that the main objectives will be achieved in time.

REFERENCES

[1] SHIBANUMA, K., et al., "Remote handling in ITER", WAC/ISRM '96 (Proc. Symp. Montpellier, 1996).

[2] TADA, E., et al., "The blanket and divertor maintenance concept for ITER" (Proc. 16th Symp. Fusion Engineering 1995, USA).

[3] MAISONNIER, D., et al., "Divertor remote handling test facilities," WAC/ISRM '96 (Proc. Symp. Montpellier, 1996).

ION CYCLOTRON, ELECTRON CYCLOTRON AND LOWER HYBRID HEATING AND CURRENT DRIVE IN ITER

G. BOSIA, R. ELIO, M. MAKOWSKI, G. TONON,
ITER JOINT CENTRAL TEAM, ITER HOME TEAMS

Abstract

ION CYCLOTRON, ELECTRON CYCLOTRON AND LOWER HYBRID HEATING AND CURRENT DRIVE IN ITER.

An auxiliary power of ~100 MW is required to heat ITER and to control the plasma burn as well as to drive a fraction of the plasma current for profile control and, ultimately, for steady state operation in high bootstrap fraction discharges. The auxiliary power could be shared among different heating methods, as there are advantages in using multiple systems to satisfy ITER operation requirements. A (negative ion) neutral beam injection (NBI) and two RF heating and current drive (H&CD) systems — ion cyclotron (ICRF) and electron cyclotron (ECRF) range of frequencies — are under conceptual development as co-ordinated by the ITER JCT, while a lower hybrid wave (LHW) system is being developed by the European Home Team. Together, these three radio frequency (RF) H&CD systems offer a range of features and services capable of fully satisfying all ITER requirements.

1. INTRODUCTION

The primary function assigned to ITER heating and current drive systems is to induce an H mode confinement state in a low density plasma ($n \sim 0.3 \times 10^{20}$ m^{-3}) and to maintain it through the path towards sustained plasma burn. An overall auxiliary power flow of 100 MW through the separatrix is required to achieve ignition with an H mode multiplier > 1.8. A driven burn of 300 MW of alpha particle heating can be obtained with the same power with an H mode multiplier as low as $H \approx 1.4$ [1]. These two possibilities provide, therefore, a range of high fusion power operation.

For steady state operation, ITER H&CD systems should produce an on-axis seed current density $j(0) > 0.3$ MA/m^2 as needed by high bootstrap fraction operation, corresponding to $q(0) < 4.0$ and a total current $I_{seed} \leq 0.5$ MA. According to present modelling, an off-axis current drive capability of 2–3 MA at $n \sim 1.0 \times 10^{20}$ m^{-3} should also be induced in order to support shear inversion [2] in a 12 MA total plasma current.

H&CD systems are also required to provide plasma control functions such as: (i) to induce plasma rotation in order to suppress error field instabilities; (ii) to provide auxiliary power (typically, a heat flux of 10 MW/m^2) to commission ITER divertor during initial operations; (iii) to assist in burn control; and (v) to sustain plasma temperature and current profiles in the termination phase of ITER discharges,

thereby avoiding density limit disruptions. Additional functions include startup of the plasma with low toroidal electric fields; stabilization of MHD activity; wall conditioning; and tritium removal from plasma facing components.

The majority of the present day tokamaks rely on two or more heating systems. In ITER, H&CD functions can be shared among different methods. Providing the total auxiliary power out of more than one system allows a greater degree of flexibility to accommodate present physics uncertainties as well as future progress in more than one field.

The three RF H&CD systems together offer a range of features and services capable of satisfying all ITER requirements: the ion cyclotron range of frequencies (ICRF) features the capability of central ion heating, central electron heating and current drive at minimum development cost. The electron cyclotron range of frequencies (ECRF) provides electron heating with precise power localization needed for an efficient off-axis CD, non-evanescent propagation at the plasma edge and auxiliary services such as startup and wall conditioning. Lower hybrid waves (LHWs) specialize in an off-axis current drive function, where they have the highest demonstrated current drive efficiency.

A uniform approach has been adopted in the design of the RF systems: all launchers can be accommodated within standard ITER equatorial ports, feature an all metal construction, have a very limited impact on the torus layout and do not significantly modify its vacuum and tritium boundaries. They are removable through the port with similar manual and remote handling (RH) operations. This approach is intended to facilitate a later implementation of the most convenient combination.

2. ION CYCLOTRON RANGE OF FREQUENCY

The ITER ICRF system has evolved from an in-blanket to an in-port concept, which requires a lower impact with the ITER blanket and allows simpler maintenance.

The design changes have not significantly modified the operating scenarios. The principal heating scheme is at the $2\Omega_T = \Omega_{He^3}$ resonance (57 MHz at full B_T), successfully tested in D–T plasmas in TFTR, with Ω_D (42 MHz at full B_T) as an alternative. Fast wave current drive (FWCD) is proposed in the frequency window between $2\Omega_T$ and Ω_{He^4}, where the electron absorption is high. A maximum CD efficiency of $\eta = (0.15\text{–}0.2)$ $A \cdot W^{-1} \cdot m^{-2}$ is predicted at 62.5 MHz. Operation at lower B_T is simply obtained by lowering the operating frequency, which can be varied in the range of 40–70 MHz.

The system uses four midplane ports. Each array consists of eight current straps (Fig. 1) fed by one coaxial transmission line and tuned by two variable reactances at the two ends. The feeder is asymmetrically connected close to the centre of symmetry of the strap, at a point where the capacitive admittance of the long section is compensated by the inductive admittance of the short section. A resonant $\lambda/2$

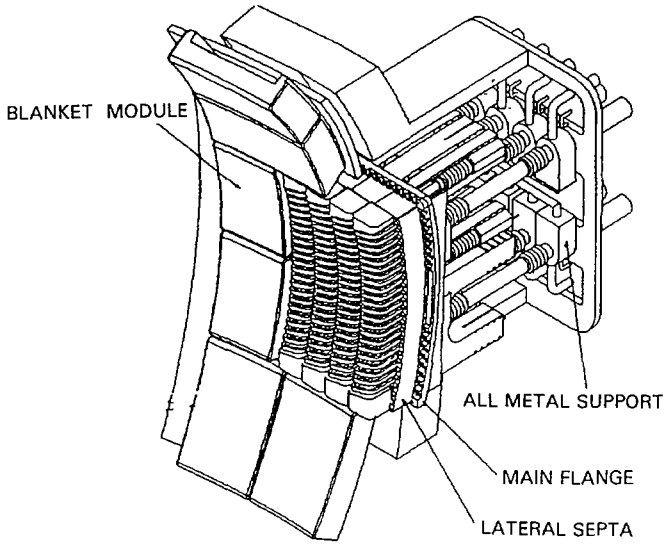

FIG. 1. ICRF array assembly.

double loop antenna results, whose electrical length can be adjusted to different frequencies. The (resistive) input impedance is matched to the nominal characteristic impedance by the feeder acting as a coaxial $\lambda/4$ transformer.

A nominal power of 2 MW/strap (or a total of 64 MW) is available. The maximum operating voltage depends on the plasma coupling (typically, 3 Ω/m). Present estimates show that, in unfavourable conditions, a total of 50 MW can be applied at an operating voltage of < 42 kV [3].

An important design issue is the array sensitivity to plasma edge density fluctuations (such as those due to ELMs), which cause fast variations in the antenna coupling and may reduce the RF power flow. A pretuned antenna design is proposed in order to achieve the maximum tolerance to such variations. Computations show that, once prematched to a given frequency, plasma load variations in the range 2 to 8 Ω (or the whole range expected in ITER operation) can be accepted with input voltage standing wave ratio (VSWR) variations of <2. The array pretuning requires small mechanical adjustments of the strap's electrical length whenever the operating frequency is changed. Practical methods of performing these adjustments are being developed within the ICRF R&D programme.

The array assembly is electrically and mechanically connected to the blanket backplate. There is no mechanical connection between the array assembly and the vacuum vessel (VV) in order to accommodate the relative displacements between blanket and vessel due to thermal expansions and mechanical deformations. All components are cooled by pressurized water.

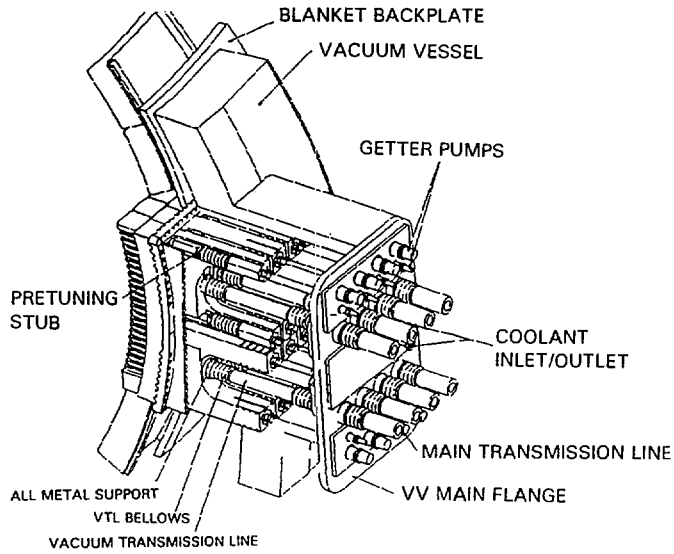

FIG. 2. ICRF VTL system.

The antenna feeders are connected to the pressurized main transmission lines by evacuated coaxial lines (vacuum transmission lines (VTLs), see Fig. 2). The vacuum/tritium boundary is provided by a ceramic (double) vacuum window assembly. The VTL runs in the VV port, through the main VV port flange, in its extension to the cryostat, and exits from the cryostat port.

The VTLs are pumped by getter pumps to maintain a specified base pressure independent of the torus vacuum conditions ($P_{base} < 10^{-2}$ Pa). In the coaxial VTL, the inner conductor is used as a coolant duct for the array components and is positioned and supported by all metal wide band coaxial supports [4], which, among other advantages, allow direct coolant transfer from the inner to the outer conductor.

The ICRF array offers substantial neutron sheilding. 3-D calculations realistically including all antenna voids show maximum heating rates in the toroidal coils in the range of 1/10 to 1/3 of the maximum allowed in the coil steel and winding pack. They also show that at the location of the ceramic window (VV flange), the neutron flux (1.8×10^{12} n·cm^{-2}·s^{-1}) would not cause important dielectric degradation in BeO ceramic, although Al_2O_3 windows would be close to their end of life fluence at the end of the basic performance phase.

3. ELECTRON CYCLOTRON RANGE OF FREQUENCIES

Central heating for ECRF requires a frequency in the range of 150–170 GHz and allows ordinary mode propagation up to peak densities of $>3 \times 10^{20}$ m^{-3}.

Simulations show that full single pass absorption can be obtained even during the initial ohmic phase of the discharge. At a central temperature of only 5 keV and a central density of 3×10^{19} m^{-3}, the optical depth is already 30 and increases to ~300 as ignition is approached.

Useful frequencies for current drive lie in the range of 160–220 GHz, the higher frequencies being associated with higher current drive figures of merit. Heating and current drive can be accomplished over a wide range of temperatures, central magnetic fields (4.0–5.7 T), and densities ($(0.2–2.0) \times 10^{20}$ m^{-3})), using fixed frequency sources. The predicted off-axis current ($\rho < 0.7$) drive efficiency at $B_T = 5.7$ T is $\eta \sim 0.16–0.19$ $A \cdot W^{-1} \cdot m^{-2}$. At reduced magnetic fields, current drive efficiencies of up to $\eta \sim 0.3$ are achievable.

ECRF has been used successfully for preionization and startup in many tokamak experiments, and its use can broaden the conditions under which reliable breakdown can occur, for the small loop voltage typical of ITER. A few MW of power should be adequate for this purpose.

The highly localized nature of heating and current drive possible with EC waves can be used to control MHD and other types of activity in a plasma. Sawtooth instability has been stabilized through the application of ECRF power with careful placement of the EC resonance relative to the $q = 1$ surface. Similarly, heating near the $q = 2$ surface has been shown to suppress $m = 2$ oscillations which can lead to a disruption [5]. Local ECRF power deposition very near the separatrix can strongly decrease the frequency of ELMs in H mode plasmas. Locked modes have also been suppressed through ECRF.

The feasibility of the ECRF system relies on the development of 170 GHz, 1 MW, steady state, high efficiency sources and windows. The demonstration of a long pulse 170 GHz tube is expected by the end of the EDA. The remaining task is to develop a tube which simultaneously demonstrates all the required performance parameters. Two main developments toward a high efficiency ECRF system have been made. One is the introduction of depressed collectors on gyrotrons. With a single stage depressed collector, efficiencies of 50% are now current, and up to 65% has been achieved. Another development is the availability of highly efficient (~97%) solid state, high voltage power supplies and switches.

Windows are the second critical technology, which has made significant progress during the last year. A single disk, polycrystalline diamond, edge cooled window was tested at long pulse and high power. The results show that a 1 MW, 170 GHz, steady state window is likely to be feasible with the material available at present. Alternative MW window concepts under development are: cryogenic windows, Au doped (high resisitivity) silicon windows and the distributed window (slotted grill-like structure made of alternating thin sapphire bars brazed to niobium microchannel cooled heat sinks) [6].

ITER physics requirements can be met by ECRF by using either frequency tunable sources or fixed frequency sources with an adjustable injection angle. The latter option has been chosen for the design, based on the current development of

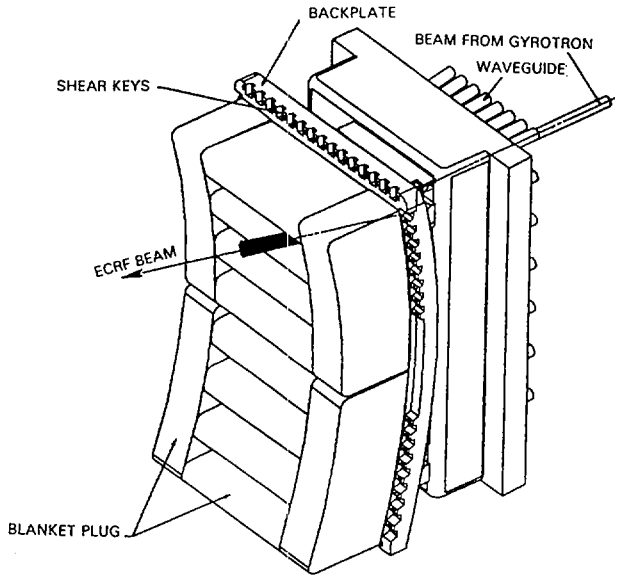

FIG. 3. ECRF launcher.

fixed or step tuned frequency gyrotron sources. The ITER system has been designed to provide a modest toroidal steering capability of $\sim 30°$. Current profile control is also possible by using the same angular steering range, because of the localized nature of the absorption.

The ECRF system uses two ports. In addition to the main heating and current drive system, two startup and wall conditioning systems, one per port and each supplying 3 MW of power at a single frequency in the range 90–140 GHz, are also provided. As there is sufficient space, within a single port, for up to 56 waveguides, up to 94 MW could be launched through two ports, 88 MW for H&CD and 6 MW for startup and wall conditioning. All systems are designed for steady state operation.

An array of steerable mirrors, one per waveguide, injects the ECRF power into the plasma through a slotted shield/blanket segment as shown in Fig. 3. The mirrors can be rotated about a vertical axis in an angular range of 15°–45° from the perpendicular direction. The injection geometry is such that there is no direct neutron streaming through the port (Fig. 4).

4. LOWER HYBRID WAVES

According to predictive simulations, now based on models validated by experiments, the lower hybrid wave (LHW) system can provide non-inductive assist and current profile control during ramp-up, off-axis current profile control during

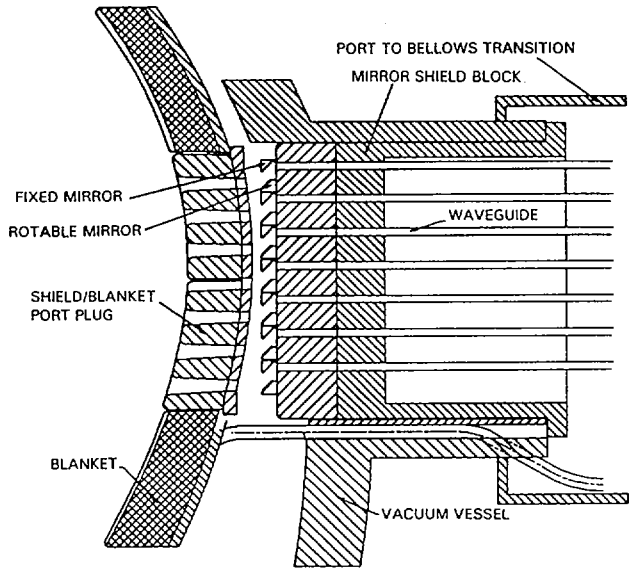

FIG. 4. ECRF rotating mirror system.

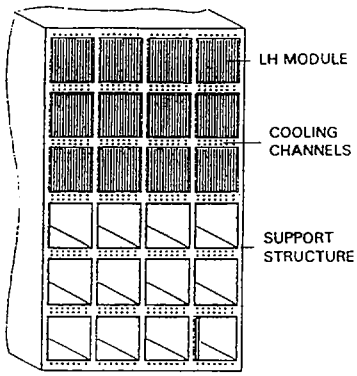

FIG. 5. Front view of LHW launcher.

burn (nominal operation scenario) and a main contribution to the non-inductive current generation in the advanced tokamak scenarios. A CD efficiency of $\eta = 0.3 \times 10^{20}$ A·W^{-1}·m^{-2} is currently predicted.

The LHW system operates at 5 GHz; this frequency is a trade-off between power absorption by alpha particles and RF source (klystron) technology. It consists of several similar subsystems which contain the same basic elements: antenna modules, transmission line, RF source, power supply, RF monitoring and controls, auxiliaries. A more detailed description of the LHW system is given in Ref. [7].

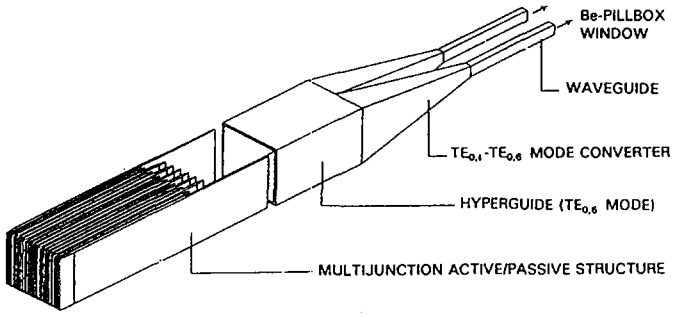

FIG. 6. LHW splitting network.

The LH antenna is an in-port RF plug, the launcher mouth being flush to (or slightly recessed from) the first wall. The antenna (Fig. 5) consists of 24 identical modules (six rows by four columns) located inside the support structure and facing the plasma. It forms an integral part of the shield and is in good electrical contact with the first wall. The LH antenna is designed to the same thermal and mechanical specifications as the shield/blanket.

The LH module design is based on the multijunction active–passive (MAP) launcher concept which provides a high structural strength in the plasma facing components as well as good coupling properties. The version shown in Fig. 6 is able to inject a fixed $N_{\parallel} = 2$ spectrum. An alternative launcher providing an improved flexibility in the launched spectrum ($1.3 \leq N_{\parallel} \leq 2.1$) by electronic phase steering in a slightly modified splitting network is under study.

The size of each RF plug module is 326 mm × 321 mm and consists of an assembly of active and passive waveguides acting as reflectors [8]. The active waveguide is 9.25 mm wide, and the wall thickness between the waveguides (13.25 mm) has been chosen to minimize plasma erosion and enable active cooling at the launcher mouth. The front ends of the walls are grooved to form short passive waveguides acting as reflectors. The LH module mouth will be fabricated from copper alloy with beryllium coating.

On the basis of the JET and Tore Supra results achieved at 3.7 GHz and taking also into account the reduction in the reflection coefficient due to cross-coupling with the passive guides, it appears possible in ITER to couple up to 35 MW per port, well above the previous estimate of 25 MW.

As shown in Fig. 4, the plug incorporates the RF splitting network. The multijunction principle is used with E plane dividers designed to split the incoming power from the hyperguide into 14 guides. Built-in 270° phase shifters between active waveguides provide a central $N_{\parallel}$ of 2, and the directivity is typically 65%.

A hyperguide operating in the $TE_{0,6}$ mode is chosen to couple power to the plug in order to simplify the mechanical design, to reduce RF losses and outgassing and to improve pumping where the electron multipactor resonance is expected.

Two $TE_{0,1}$ - $TE_{0,6}$ mode converters are used to excite the $TE_{0,6}$ mode inside the hyperguide. The conversion efficiency is estimated to be ~99%.

The LH module is connected through hyperguide and mode converters to two beryllium pillbox windows, based on the existing 3.7 GHz technology (JET).

A hyperguide couples about 1 MW, supplied by two 0.7 MW klystrons in line with existing technology. The global efficiency for the system is estimated to be ~50%.

5. CONCLUSIONS

ITER is likely to use more than one H&CD system in order to allow a greater degree of flexibility to accommodate physics needs as well as future progress in more than one field. A parallel development of the RF H&CD systems is taking place in ITER, and a standardized approach has been adopted in their design in order to facilitate their integration. The proposed systems are an application of tested operating scenarios and a modest extrapolation of existing systems; hence, they offer the prospect of reliable operation without need for extensive development.

REFERENCES

[1] BOUCHER, D., et al., in Controlled Fusion and Plasma Physics (Proc. 21st Eur. Conf. Monlpellier, 1994), Vol. 18B, Part II, European Physical Society, Geneva (1994) 524.

[2] NEVINS, W.M., et al., in Plasma Physics and Controlled Nuclear Fusion Research 1994 (Proc. 15th Int. Conf. Seville, 1994), Vol. 2, IAEA, Vienna (1995) 543.

[3] BATCHELOR, D., et al., Contribution to First ITER Expert Group on Energetic Particles, Heating and Current Drive (Moscow, Oct. 1995).

[4] KIMURA, H., et al., Rep. 95 070 JAERI (1996).

[5] HOSHINO, K., et al., in Plasma Physics and Controlled Nuclear Fusion Research 1994 (Proc. 15th Int. Conf. Seville, 1994), Vol. 1, IAEA, Vienna (1995) 697.

[6] HEIDINGER, R., in Millimeter Waves (Digest 19th Int. Conf. Sendai, JSAP) Catalogue No. AP 941 228 (1994) 277.

[7] Rep. EUR-CEA-FC 1529, Association Euratom-CEA, Centre d'études nucléaires de Cadarache (Nov. 1994).

[8] BIBET, P., et al., Nucl. Fusion 35 (1995) 1213.

ITER NEUTRAL BEAM INJECTOR DESIGN*

R. HEMSWORTH, E. DI PIETRO,
M. HANADA, A. KRYLOV
ITER Joint Central Team,
ITER Joint Work Site,
Naka, Japan

E. ALEXANDROV, M. BARINOV, E. DLOUGACH,
V. KULYGIN, V. NAUMOV,
A. PANASENKOV, V. PETROV
Russian Federation Home Team

Y. FUJIWARA, T. INOUE, K. MIYAMOTO,
N. MIYAMOTO, Y. OHARA, Y. OKUMURA,
K. WATANABE, K. SHIBATA, M. TANII
Japan Home Team

J.-H. FEIST, B. HEINEMANN, E. KÜSSEL,
J. PAMÉLA, P. LOTTE, P. MASSMANN, M. WATSON
European Union Home Team

Abstract

ITER NEUTRAL BEAM INJECTOR DESIGN.

The ITER neutral beam injection system consists of three 17 MW, 1 MeV D^0 injectors attached to three adjacent tokamak ports, arranged to produce beams tangential to the toroidal field at a radius of 6.5 m. The paper describes the 'physics' design of the injectors which will heat, drive current in, and induce plasma rotation of, the ITER plasma. Each injector uses a single, large, caesiated volume arc discharge ion source and an electrostatic accelerator. The D^- beam is neutralized in a gas neutralizer and the remaining charged fraction is separated from the neutral beam in an electrostatic residual ion dump (RID). The pressure at the exit of the accelerator and downstream the neutralizer is kept low by a cryopump surrounding the neutralizer and the RID. A calorimeter located downstream the RID allows the injectors to be commissioned independently of ITER.

---

1. OVERVIEW AND BACKGROUND

The ITER neutral beam (NB) system must be able to heat the plasma, to drive current in the plasma for pulse lengths of up to 10 000 s and to induce plasma rotation [1]. The system will deliver 50 MW of 1 MeV D^0 to the ITER plasma from three identical injectors attached to three adjacent tokamak ports, which are arranged so that the beams are tangential to the toroidal field at a radius of 6.5 m. The basic components of the injector can be seen in Fig 1.

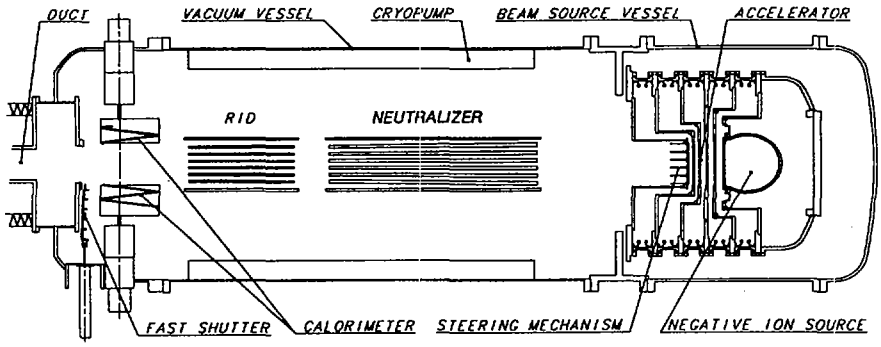

FIG. 1. Plan section through an ITER injector.

TABLE I. SIGNIFICANT RESULTS FROM ITER NB R&D

Accelerator	
1 MeV without beam	EU home team
910 keV, ≈40 mA, H^- beam	EU home team
805 keV, ≈50 mA, H^- beam	JA home team
Ion source	
Scale model ITER ion source built and operated:	JA (H^-) & EU (D^-)
>30 mA/cm^2 H^- at 0.24 Pa, >20 mA/cm^2 D^- at 0.35 Pa,	home teams
< one electron extracted per negative ion accelerated	in collaboration
Insulator	
Model, 480 mm diameter, ceramic insulator built by a new forming technology (slip casting and 'ultra moulding')	JA home team
Flange alumina insulator vacuum seals by spring energized metal O rings successfully tested	JA home team

The 1 MeV D^0 beam is produced by the neutralization, in a simple gas target, of 1 MeV D^-, the efficiency of which is ≈60%. Allowing for neutralization efficiency, transmission losses and reionization losses, injection of 17 MW requires that a 40 A, 1 MeV D^- beam be produced [2]. ITER is supporting R&D on the ion source, the accelerator and the accelerator insulator by the JA and EU Home Teams. The most significant results achieved so far are listed in Table I.

2. INJECTOR DESIGN

The design of the main injector components is described below, with the exception of the ion source and the extractor/accelerator, which are described elsewhere [3–6]. Experimental data on the beam optics of the ITER source are not yet available. Therefore, to determine the power and power density on the various components and, thus, to allow their design to be carried out, various possible beam optics were assumed. The beam is considered to be described by a bi-Gaussian power density distribution, consisting of 'core' and 'halo' fractions. The 'standard' case has 85% of the power in the core fraction and 15% in the halo fraction, the core divergence, ω_c, is 5 mrad, and the halo divergence, ω_h, is 15 mrad. Other cases considered have all been combinations of ω_c = 3, 5 and 7 mrad, ω_h = 10, 15 and 100 mrad, halo fraction = 15% or 0%. The power to the ITER plasma was kept at 17 MW per injector. It was also considered that the beams could be misaligned by up to 2 mrad in the horizontal plane.

2.1. Neutralizer

The neutralizer is 3 m long and subdivided into five vertical channels, 70 mm wide × 1.6 m high. The apertures of the extractor/accelerator are arranged so that the five 'column beams' are produced, matching the channels of the neutralizer. This

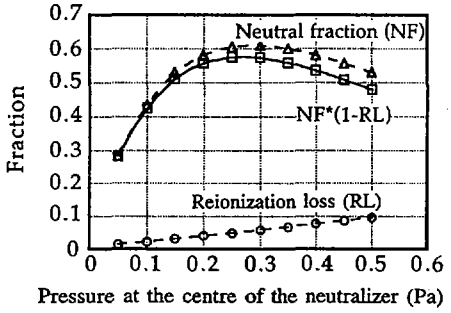

FIG 2. Neutral beam efficiency and reionization loss as a function of the neutralizer pressure.

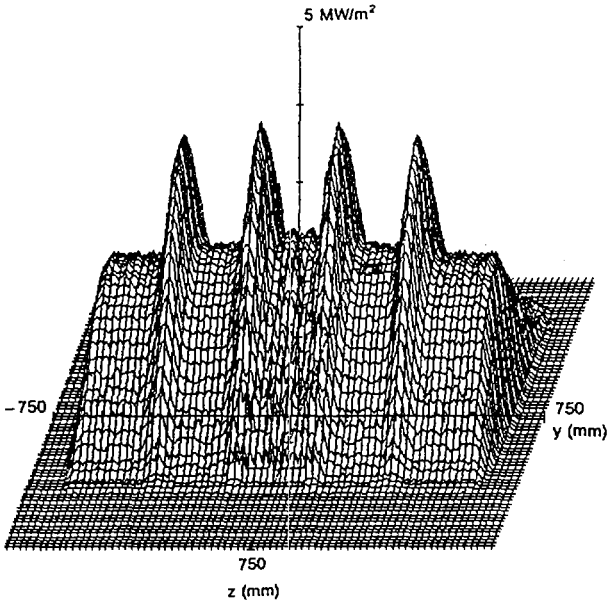

FIG. 3. Beam footprint for D^+ on the residual ion dump with no magnetic field.

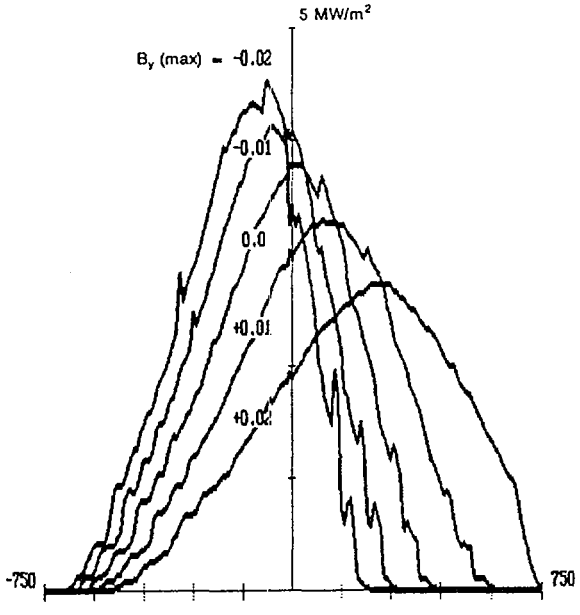

FIG. 4. Power density along the RID for different values of the vertical magnetic field.

subdivision of the neutralizer reduces the gas flow required to produce the neutralization target. Figure 2 shows the reionization loss, neutralization efficiency and the product of those as a function of the neutralizer pressure. This shows that the optimum pressure in the neutralizer is 0.25 Pa. At this pressure, the gas flow is 11 $Pa \cdot m^3 \cdot s^{-1}$.

The maximum power to be intercepted by the neutralizer is <7 MW, and the power density on the neutralizer walls is <0.4 MW/m^2. The channel walls are formed from copper panels, 10 mm thick, with serpentine cooling pipes brazed on the rear face. Two such panels, separated by spacers, form one of the inner walls; 10 mm thick mu-metal plates, fixed to the sides, top and bottom of the neutralizer, form part of the passive magnetic shielding (see Section 2.5).

2.2. Residual ion dump

The charged components of the beam emerging from the neutralizer, 1 MeV D^+ and D^-, will be removed from the beam by the electrostatic residual ion dump (RID) to provide controlled ion beam power interception. The RID consists of six vertical plates forming five channels in line with the channels of the neutralizer. Half the RID plates are at ~20 kV and half at ground potential.

The length of the RID plates, 1.5 m, is chosen to provide reliable ion beam interception and acceptable power density deposition with the foreseen range of NB operating conditions. A typical beam footprint for D^+ is shown in Fig. 3. Figure 4 shows the effect on the footprint of a vertical magnetic field increasing linearly from zero at the exit of the neutralizer to the exit of the RID, which approximates the expected residual field.

As the electric fields in adjacent channels are of opposite signs, on one side of a plate the magnetic field deflects ions in the same direction as the electrical field does, whereas on the other side the deflection is in the opposite direction to the electrical deflection. This causes beam 'focusing' on one side and 'defocusing' on the other. To avoid unequal power loading on either side of an RID panel and the consequent thermal stress and bending, the magnetic field must be $<5 \times 10^{-3}$ T at the exit of the RID.

Secondary electrons from the ground potential plates are accelerated across the gap and deposit their energy, 20 keV, on the opposing panel, with a power density footprint similar to that of the negative ions. The total power to the RID will be <17.8 MW, and the peak power density is calculated to be <8 MW/m^2. An array of 60 vertical swirl tube elements are connected together to form one flat RID panel.

2.3. Calorimeter

The calorimeter consists of two sets of water cooled panels, on either side of the beam path, which can be moved such that each panel intercepts one of the column beams exiting the RID (Fig 1). This allows injector operation and commissioning independent of ITER operation. The main design consideration is the high power

density, which could be up to 15 MW/m^2. To reduce the power density on the panels, they are set at 8° with respect to the beam axis. Arrays of rectangular cross-section vertical swirl tube elements are connected together to form the flat panels.

2.4. Cryopump and reionization

A 3-D Monte Carlo code has been used to determine the gas density profile in the injector. In particular, the density along the beam path determines the neutralization efficiency and the beam loss from reionization. The gas is horizontally collimated when it leaves the neutralizer (Fig. 5(b)), which increases the gas density in the beam path and, thus, the loss due to reionization.

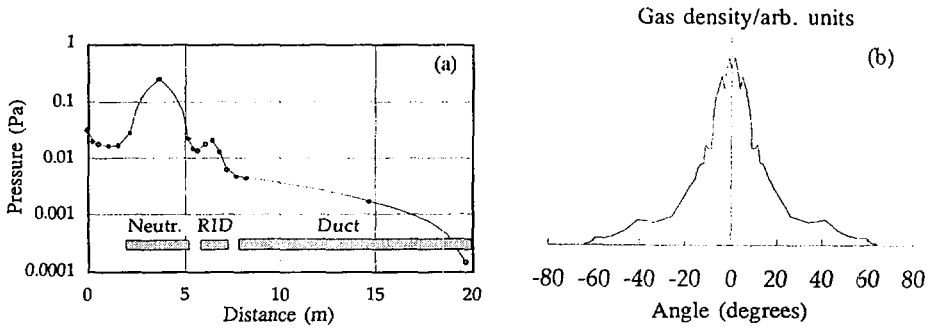

FIG. 5. (a) Gas pressure along the beam path; (b) normalized horizontal particle flow from a neutralizer channel.

Calculations as a function of cryopump speed and beamline geometry have been used to determine the required pumping speed, position and length of the cryopump. The cryopump is quasi-cylindrical, with a pumping speed of $\approx 2.8 \times 10^3$ m^3/s for D_2. It fits close to the walls of the injector vacuum vessel from the entrance of the neutralizer to the exit of the RID and covers all but the lower section of the vessel, where the support structure for the other beamline components and coolant and gas supply lines are located. The design is quite conventional, using a liquid helium filled stainless steel panel with a liquid nitrogen cooled chevron baffle. The reionization loss is calculated to be $\approx 4.5\%$.

2.5. Magnetic field reduction system

In the region of the injectors, the stray magnetic field from ITER is between 0.08 and 0.04 T, and it is necessary to reduce this substantially, principally to ensure good operation of the negative ion source ($B < 0.001$ T) and to avoid undue deflection of the D^- beam before neutralization ($B < 10^{-4}$ T). The magnetic field reduction system consists of a layer of mild steel 200 mm thick around the injector, a 10 mm layer of mu-metal around the beam path and three active field compensation coils. Two of

these coils (rectangular, 5 × 12 m^2, 200 kA turns) are located above and below the injector. The third coil (5.4 m diameter, 350 kA turns) is located around the injector duct. This combination is found to reduce the field within the injectors to the design values and not to produce unacceptable error fields in the tokamak.

3. SUMMARY

A reference design of a neutral beam system has been evolved which meets all the requirements of ITER. The 'physics design' has evolved to the state that all critical parameters have been defined, and engineering solutions have been proposed. R&D has concentrated on the ion source and the 1 MeV extractor/accelerator and its associated ceramic insulator. This has progressed to the stage that the basic specifications of the ITER ion source have been achieved in a model source, and H^- beams in excess of >900 keV have been generated, which gives confidence that the ITER NB system can be realised.

REFERENCES

[1] INTERNATIONAL ATOMIC ENERGY AGENCY, Technical Basis for the ITER Interim Design Report, Cost Review and Safety Analysis, Ch. I, "ITER general design requirements", and Ch. V, "ITER physics performance assessment", ITER EDA Documentation Series, No. 7, IAEA, Vienna (1996).

[2] HEMSWORTH, R.S., et al., Neutral Beams for ITER, Rev. Sci. Instrum. **67** (1996) 1120.

[3] WATANABE, K., et al., in Plasma Physics and Controlled Nuclear Fusion (Proc. 14th Int. Conf. Würzburg, 1992), Vol. 3, IAEA, Vienna (1993) 371.

[4] WATANABE, K., et al., "Recent progress of high power ion beam development for fusion plasma heating", Advances in Nuclear Energy Research (Proc. 7th Int. Symp. Takasaki, Japan, 1996) (in preparation).

[5] KRYLOV, A., et al., General design of the neutral beam injection system and integration with ITER, Fusion Technology (Proc. 19th SOFT Lisbon, 1996) (in preparation).

[6] SIMONIN, A., Electrons in the Accelerator (MAMuG & SINGAP), paper presented at ITER R&D and Design Review Meeting, Cadarache, France (1996).

VALIDATION OF 1-D TRANSPORT AND SAWTOOTH MODELS FOR ITER*

J.W. CONNOR[1], M. ALEXANDER[2], S.E. ATTENBERGER[3], G. BATEMAN[4], D. BOUCHER[5], N. CHUDNOVSKIJ[6], Yu.N. DNESTROVSKIJ[6], W. DORLAND[7], A. FUKUYAMA[8], G.T. HOANG[9], D.M.G. HOGEWEIJ[10], W.A. HOULBERG[3], S.M. KAYE[11], J.E. KINSEY[4], J.A. KONINGS[12], M. KOTSCHENREUTHER[7], A.H. KRITZ[4], V.M. LEONOV[6], M. MARINUCCI[13], D.R. MIKKELSEN[11], J. ONGENA[14], A.R. POLEVOJ[6], F. ROMANELLI[13], D.P. SCHISSEL[12], H. SHIRAI[15], P.M. STUBBERFIELD[16], T. TAKIZUKA[15], A. TARONI[16], M.F. TURNER[1], G. VLAD[13], R.E. WALTZ[12], J. WEILAND[17]

ITER Confinement Database and Modelling Working Group

[1] UKAEA, Culham, UK.
[2] Max-Planck-Institut für Plasmaphysik, Garching, Germany.
[3] Oak Ridge National Laboratory, Oak Ridge, Tennessee, USA.
[4] Lehigh University, Lehigh, Pennsylvania, USA.
[5] ITER San Diego Joint Work Site, San Diego, California, USA.
[6] Russian Research Center, Kurchatov Institute, Moscow, Russian Federation.
[7] Institute for Fusion Studies, University of Texas at Austin, Austin, Texas, USA.
[8] Okayama University, Okayama, Japan.
[9] Association Euratom-CEA, Centre d'études de Cadarache, France.
[10] FOM Institute for Plasma Physics Rijnhuizen, Nieuwegein, Netherlands.
[11] Plasma Physics Laboratory, Princeton University, Princeton, New Jersey, USA.
[12] General Atomics, San Diego, California, USA.
[13] ENEA, Frascati, Italy.
[14] Ecole royale militaire/Koninglijke Militaire School, Association Euratom-Belgian State, Brussels, Begium.
[15] Japanese Atomic Energy Research Institute, Naka, Japan.
[16] JET Joint Undertaking, Abingdon, Oxfordshire, UK.
[17] Chalmers University of Technology, Göteborg, Sweden.

Abstract

VALIDATION OF 1-D TRANSPORT AND SAWTOOTH MODELS FOR ITER.

Progress on validating a number of local transport models by comparing their predictions with relevant experimental data from a range of tokamaks in the ITER profile database is described. This database, the testing procedure and the results are discussed. In addition, a model for sawtooth oscillations is used to investigate their effect in an ITER plasma with alpha particles.

1. INTRODUCTION

Assessments of the ignition capability of ITER usually rely on the extrapolation of empirical scaling laws for the global energy confinement time [1]. Reliable local transport models would allow more precise predictions. In this paper, we describe progress on validating a number of local transport models [2] by comparing their predictions with relevant experimental data from a range of tokamaks in the ITER profile database. This database is described in Section 2, the testing procedure is explained in Section 3, and the results are discussed in Section 4. In Section 5, a model [3] for sawtooth oscillations is used to investigate their effect in an ITER plasma with alpha particles.

2. ITER PROFILE DATABASE

The profile database is organized through the Confinement Modelling and Database expert group which collects inputs from data providers and users. The structure adopted for the profile database is that all the information required for detailed transport analysis is supplied for each discharge in the form of four text files:

(1) a file containing comments and a discharge description;
(2) a file containing a list of global quantities (such as plasma composition, neutral beam energy, etc.) at a selected time point during a discharge;
(3) a file containing 1-D time traces such as plasma current, line average density or heating power; and, finally,
(4) a file containing profiles of quantities such as electron and ion temperatures, densities, safety factor and heat deposition at the specified time point (and as a function of time, where possible).

Profile information is given as a function of the 'minor radius' ρ, the square root of the normalized toroidal flux; geometrical quantities such as the surface averaged quantities $\langle|\nabla\rho|\rangle$ or $\langle|\nabla\rho|^2\rangle$ are also provided. All energy and particle sources are given as a function of ρ and time to allow detailed transport analysis.

A standard file format has been agreed upon. All sets of files for each available discharge are on an ftp server which also contains the profile database manual listing all the details for the file format, as well as the lists and definitions of the physics quantities to be included for each discharge. The database used for this validation

exercise contains fully documented discharges from DIII-D, JET, TFTR, JT60-U, ASDEX-U, T-10, TEXTOR, Tore Supra and RTP. The experimental data in the database include data from a wide experimental regime: ohmic, L mode, H mode (ELMy and ELM free), hot ion modes, and ECH heated hot electron as well as high power DT discharges. Of particular interest are series of discharges over which various parameters were individually varied: scans over current, shaping, isotope, ρ_*, ν_* and β.

3. MODEL TESTING PROCEDURE AND SIMULATIONS DATABASE

Eleven transport models [2] are being tested by twelve modellers (Table I). These models have been made available on the profile database server by their authors so that other modellers can also use them.

Various tools are being used to test the transport models: these range from fully predictive codes that self-consistently model heating and particle sources and predict both temperature and density profiles, to power balance codes that use the heat and particle sources as well as density profiles from the profile database to predict the temperature profiles for a given transport model. A benchmarking exercise, using a simple transport model, has been carried out to test the basic elements of the power balance codes and the way the data are read. A similar procedure is under way among

TABLE I. MODELS AND MODELLERS

Model	Modeller	Physics
Turner	M.F. Turner (EU), S.E. Attenberger (US)	Semi-empirical
Turner-IFS/PPPL	M.E. Turner (EU), S.E. Attenberger (US)	Semi-empirical
Itoh	A. Fukuyama (Japan), S.E. Attenberger (US) D.R. Mikkelsen (US), R.E. Waltz (US)	Current diffusive ballooning modes
T11/SET	A.R. Polevoj (RF)	Semi-empirical
RLW-Bohm	D.R. Mikkelsen (US), D. Boucher (JCT)	Semi-empirical
Waltz	R.E. Waltz (US)	ITG
Mixed	A. Taroni (EU)	Semi-empirical
Mixed shear	G. Vlad/M. Marinucci (EU)	Semi-empirical
IFS/PPPL	M.F. Turner (EU), S.E. Attenberger (US), B. Dorland (US), D.R. Mikkelsen (US), R.E. Waltz (US)	ITG
Weiland	J. Weiland (EU), D.R. Mikkelsen (US), R.E. Waltz (US)	ITG
Multimode	J.E. Kinsey (US)	Drift waves RBM

predictive codes but is not yet completed because of the larger range of potential differences between these codes. Therefore, we emphasize the model testing by using validated power balance codes. The simulations from power balance and predictive codes are recorded by using the same format as the experimental data and centrally stored on the ftp server. This allows modellers to compare their simulations and to apply comparison tests between simulations and experiments in a fully automated and rigorously identical fashion.

A number of tests have been chosen to compare simulations and experiment:

(1) Ratio of total stored energies (s stands for 'simulation', x for 'experiment'): W_s/W_x, where $W = \Sigma(3/2)(n_eT_e + n_iT_i)dV$;

(2) W_{es}/W_{ex} and W_{is}/W_{ix} (same as (1) but separating electron and ion contributions);

(3) $(n_{i,\rho=0.3}T_{i,\rho=0.3}W)_s/(n_{i,\rho=0.3}T_{i,\rho=0.3}W)_x$;

(4) $\chi^2 = \Sigma(T_s - T_x)^2/N\sigma^2$, where σ is the experimental error;

(5) $\beta_s^{*2}/\beta_x^{*2}$, where $\beta^{*2} = \Sigma n_i^2T_i^2dV$;

(6) $\text{STD} = \sqrt{\Sigma(T_s - T_x)^2}/\sqrt{\Sigma T_x^2}$, $\text{OFF} = \Sigma(T_s - T_x)/\sqrt{\Sigma T_x^2}$.

Measures (1) to (5) are over the range $0.2 < \rho < 0.9$; measure (6) over three intervals: $0.2 \leq \rho \leq 0.9$, $0.2 \leq \rho \leq 0.5$, $0.5 \leq \rho \leq 0.9$.

Since the simulations use the experimental edge temperature as an input boundary condition, we remove this 'pedestal' contribution in the comparison of the energies W, W_e and W_i. These 'incremental' values of W are used in Section 4.

4. SIMULATION RESULTS

It is only possible to present here a few examples of the analysis of the modelling results that has been carried out with the data and software on the server. In Fig. 1, as illustrations of temperature profile modelling, we compare results for the T_i profile for two JET shots. Figure 1(a) shows the agreement between the results for a number of different codes using the IFS/PPPL model; Fig. 1(b) shows the results obtained for a number of different models by their authors. In Fig. 2 we show the values of W_s/W_x for a number of models using the same power balance code (RW); this figure indicates L and H mode simulations.

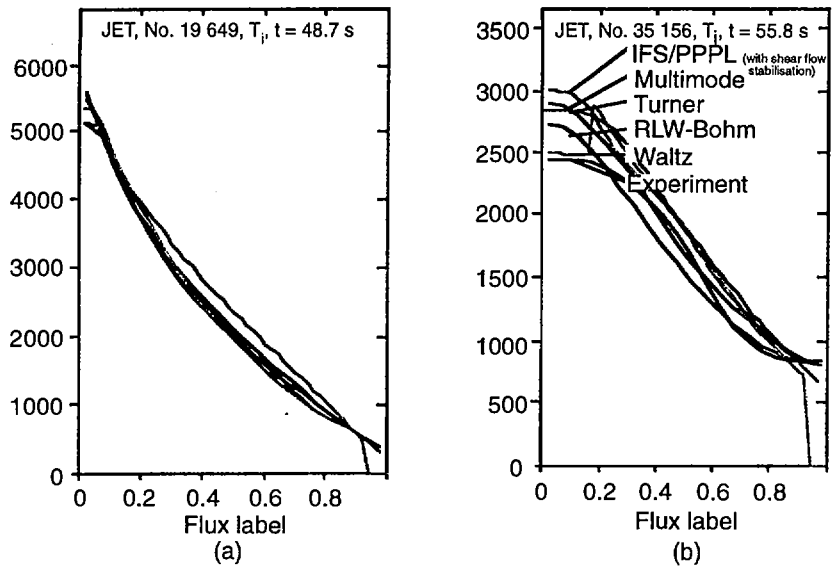

FIG. 1. Various predictions for ion temperature profiles for two JET shots: (a) No. 19 649, an L mode (codes by Waltz, Dorland, Turner and Mikkelsen and experiments were used); (b) No. 35 156, a member of an H mode ρ_* scan.

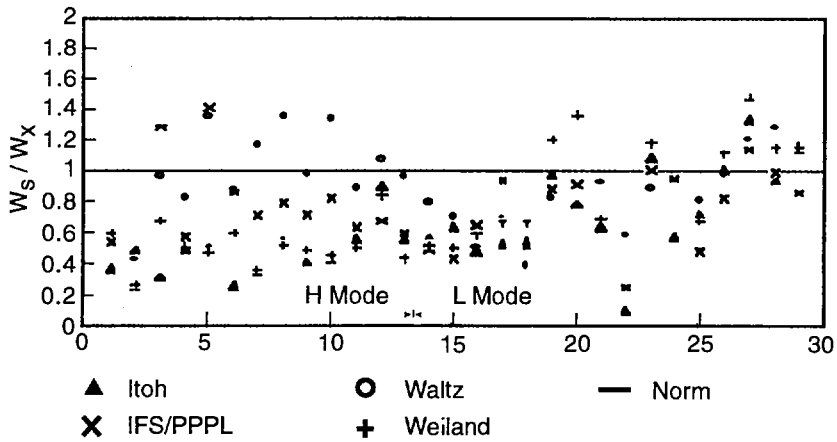

FIG. 2. Power balance code modelling results for W_s/W_x from various models. (These preliminary results use models taken from the literature rather than the server.)

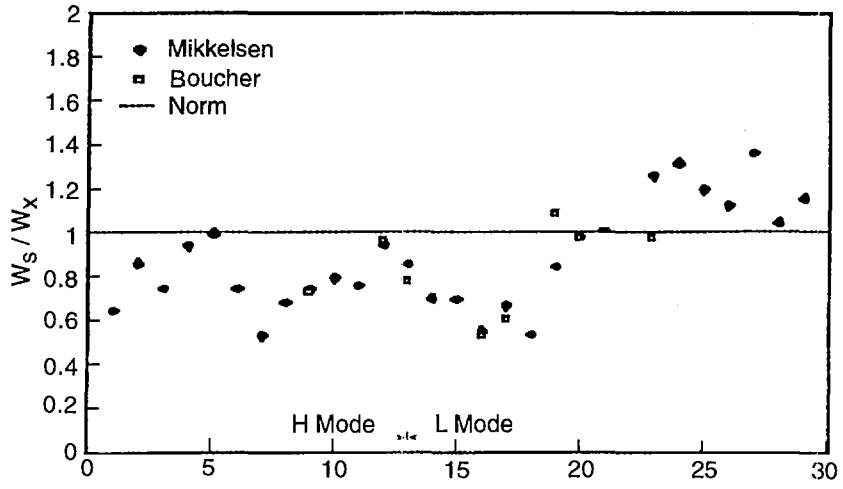

FIG. 3. RLW-Bohm model predictions for W_s/W_x using a predictive (DB) and a power balance (DM) code.

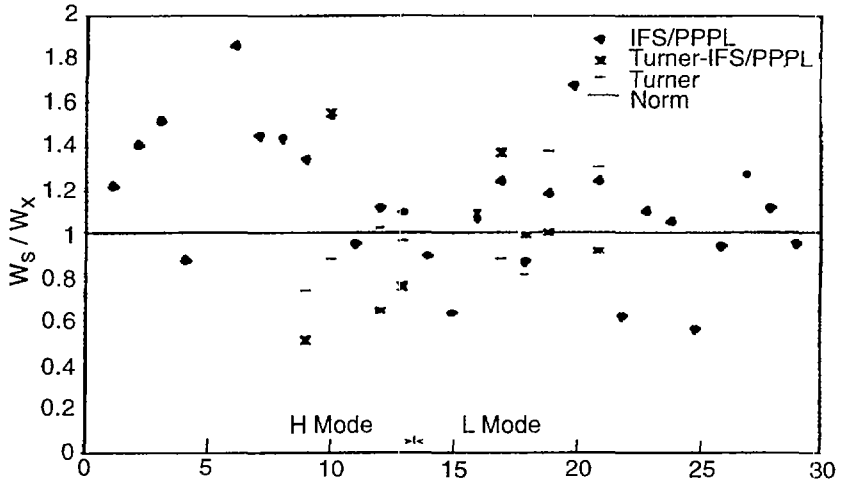

FIG. 4. Results for W_s/W_x from the semi-empirical Turner and Turner–IFS/PPPL models and the physics based IFS/PPPL model with an estimate of shear flow stabilization.

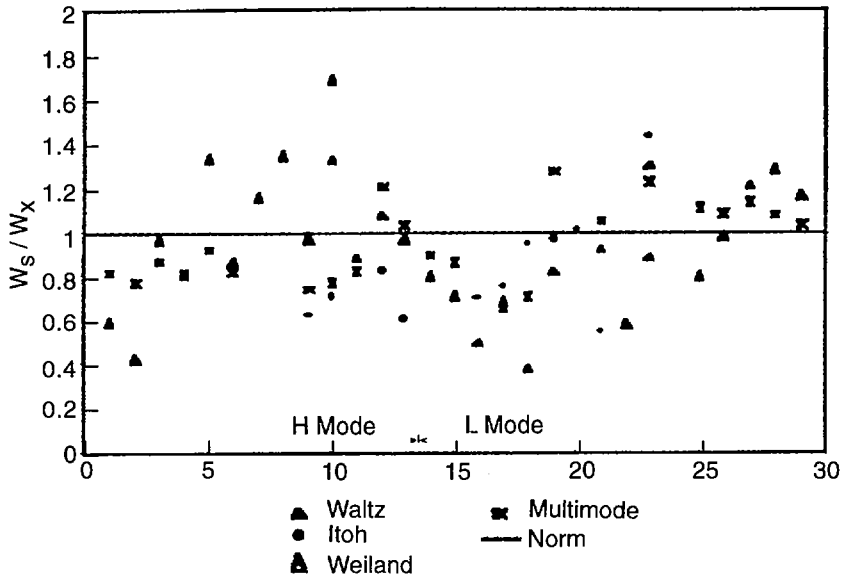

FIG. 5. Results for W_s/W_x from some physics based Itoh, Waltz, Weiland and multimode models.

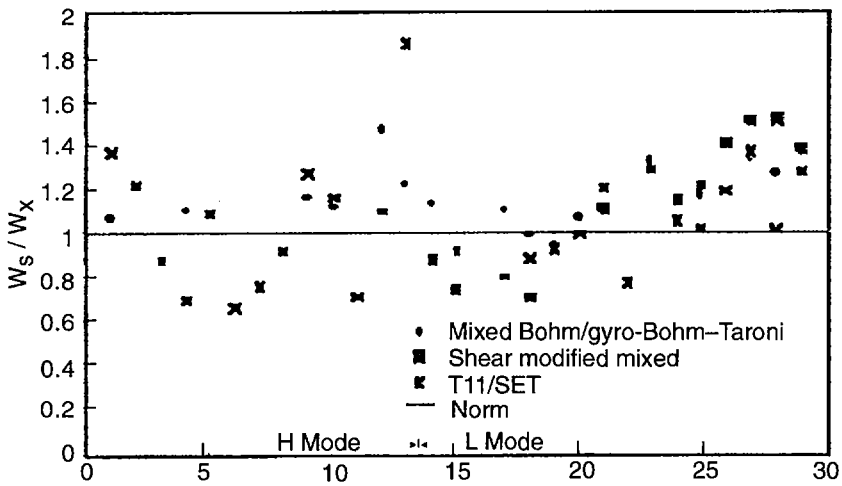

FIG. 6. Results for W_s/W_x from some semi-empirical models: the mixed Bohm/gyro-Bohm model (these simulations use a different edge prescription) and its modification to account for magnetic shear and T11/SET models.

Figure 3 illustrates the variability arising from using the two different types of code to calculate W_s/W_x, with the RLW-Bohm model as an example. Figures 4, 5 and 6 show the results for W_s/W_x for a number of modellers using their own models. Figure 4 shows the semi-empirical Turner and Turner–IFS/PPPL models and the physics based IFS/PPPL model with an estimate of the shear flow stabilization; Fig. 5 illustrates the physics based Itoh, Waltz, Weiland and multimode models; and Fig. 6 shows the semi-empirical mixed Bohm/gyro-Bohm model, and its modification to take account of magnetic shear and the T11/SET models.

The standard deviations on the incremental W_e and W_i over the discharges in the database for a number of models and modellers have been analysed. This shows that for these measures of performance, few models achieve better than 30% success in fitting the data, which is competitive with the performance of global scaling laws. A number of the models perform comparably well. It is thus difficult, at this point, to identify a 'best' model on the basis of these particular comparisons. It is, however, worth while to use a number of them in predictive codes to establish a range of predictions for ignition in ITER. Some models (e.g. IFS/PPPL) can be very sensitive to edge boundary conditions, and the significance of this fact for ITER needs quantifying.

The true importance of the work reported here is that, for the first time, an open and systematic procedure for assessing the performance of transport models against well documented data is available to all user. It can be anticipated that (i) continuing work on improving the completeness and consistency of the information in the profile database, and (ii) further developments of models (e.g. including effects of sheared rotation) and their subsequent testing will help to discriminate between transport models. Non-steady-state situations could also be particularly helpful in this regard. A transport model that performs satisfactorily can provide the capability to predict non-stationary scenarios in ITER and to explore profile effects and new regimes (e.g. internal transport barriers), which are beyond the power of global scaling laws.

5. SAWTOOTH MODELLING

Experimentally, sawteeth are often triggered as a result of the peaking of the pressure profile inside the mixing radius that follows the sawtooth reconnection event. The resulting sawtooth period is therefore related to the energy confinement time which determines how fast the temperature profile recovers after flattening. There is, however, a different class of sawteeth where the temperature and density profiles can reach their equilibrium value without triggering a reconnection process. For such sawteeth, known as monster sawteeth, the period between successive crashes is much longer than the energy confinement time or the slowing-down time of energetic particles. The subsequent sawtooth reconnection can only occur as a consequence of the current profile evolution. The monster sawtooth period is therefore related to the characteristic current penetration time which scales like $a^2T^{3/2}/Z_{eff}$.

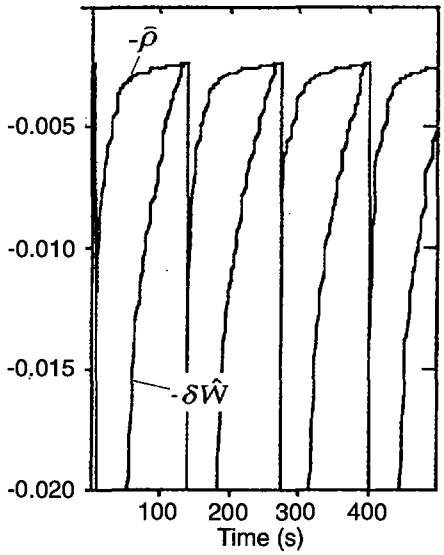

FIG. 7. Sawtooth crash triggered for $-\delta\hat{W} = -\hat{\rho}$.

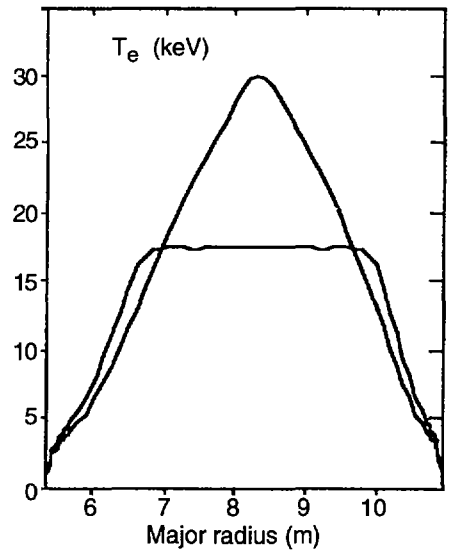

FIG. 8. Electron temperature profile before and after reconnection.

For example, in JET discharge No. 33 127, which is an ITER demonstration discharge, the monster period was about 0.8 s with a = 0.9 m, $T_e(0)$ = 6.2 keV, $Z_{eff} \sim 1.5$. Assuming that the same relative current variation would trigger a crash in ITER (a = 2.8 m, $T_e(0) \sim 30$ keV, $Z_{eff} \sim 1.5$), the sawtooth period would be ~80 s. A model has been implemented [3] to study the stabilization of the internal kink instability in ITER by the fusion produced fast alpha particles. The potential energy $\delta\hat{W}$ of the internal kink is estimated including the modification coming from high energy particles and thermal trapped particles. A criterion for the sawtooth crash including layer physics (represented by $\hat{\rho}$) is derived in the model and has been implemented in a local transport code that involves these quantities using ITER parameters. The predicted sawtooth period varies between 50 and 100 s, depending on the current reconnection model used. Figures 7 and 8 show an example of the sawtooth oscillation and resulting T_e profiles for full Kadomtsev reconnection.

REFERENCES

[1] ITER CONFINEMENT DATABASE AND MODELLING GROUP, in Plasma Physics and Controlled Nuclear Fusion Research 1994 (Proc. 15th Int. Conf. Seville, 1994), Vol. 2, IAEA, Vienna (1995) 525.

[2] CONNOR, J.W., Plasma Phys. Control. Fusion **37** (1995) A119; papers presented at workshops of the Confinement and Database Expert Group: Seville, 1994; San Diego, 1995; Naka, 1995; Moscow, 1996.

[3] PORCELLI, F., BOUCHER, D., ROSENBLUTH, M.N., Model for the sawtooth period and amplitude, Plasma Phys. Control. Fusion (in press).

ITER SCENARIOS INCLUDING NON-INDUCTIVE STEADY STATE OPERATION

D. BOUCHER[1], Y. BARANOV[2], B. FISCHER[2],
X. LITAUDON[3], D. MOREAU[3], W. M. NEVINS[4], V. PARAIL[2],
F. X. SÖLDNER[2], I. VOITSEKHOVITCH[2], ITER JOINT CENTRAL TEAM,
ITER HOME TEAMS

[1] ITER Joint Central Team

[2] JET Joint Undertaking,
Abingdon, Oxfordshire,
United Kingdom

[3] Association Euratom – CEA/DRFC,
Centre d'études de Cadarache,
France

[4] Lawrence Livermore National Laboratory,
Livermore, California,
United States of America

Abstract

ITER SCENARIOS INCLUDING NON-CONDUCTIVE STEADY STATE OPERATION.

A new divertor model has been added to a 1½-D transport code (PRETOR V4.8) to self-consistently predict the helium removal rate and the argon level in the main ITER plasma. With standard confinement, a fully ignited scenario is presented showing fusion power ramp-up, flat-top and ramp-down while demonstrating simultaneous control of the power to the divertor target plates by using an appropriate feedback control of the argon injection rate. Next, the possibility to operate in reversed shear configuration is studied, and a number of configurations that can be controlled in the ITER device are proposed. Finally, thte full time dependent evolution of these scenarios in reversed shear is investigated by adding local transport constraint and simulating the generation of current drive by lower hybrid waves.

1. INTRODUCTION

The reference physics rules for ignited and driven scenarios are shown in Table I.

2. DIVERTOR COUPLING MODEL

A 1-D reduced model of the divertor plasma solving the energy balance along the field lines and a 0-D model for particle and momentum balance in the divertor [1] have been implemented as a boundary condition for the 1½-D transport code PRETOR V4.8 to compute self-consistently the helium removal rate and the argon level required in the divertor and the main plasma to limit the power reaching the divertor target plates to below 50 MW. Typically, helium levels ranging from $\tau^*_{He}/\tau_E = 3.5–7$ and argon levels around 0.2% are projected for ITER.

3. TIME DEPENDENT SCENARIOS

Simultaneous control of the fusion power and of the power to the divertor plates while maintaining the H mode operation and keeping the plasma density within an acceptable range is required in ITER. To demonstrate the feasibility of such an operation and to develop an appropriate strategy for achieving this simultaneous control, transport simulations have been carried out with the following feedback schemes:

— The argon injection rate is controlled by feedback to protect the divertor target plate by limiting the target power to 50 MW while minimizing the injected amount.
— The fuel injection rate is controlled to keep the fusion power at a required preprogrammed value.

TABLE I. REFERENCE PHYSICS RULES FOR IGNITED AND DRIVEN SCENARIOS[a]

Quantity	Reference
Confinement	0.85 × ITER93H
L → H power thresholds	Upper limit: $P \sim 0.037\ NE_{19}\ B_t\ R^{2.5}$
	Nominal: $P \sim 0.080\ NE_{19}^{0.75}\ B_t\ R^2$
	Lower limit: $P \sim 0.17\ NE_{19}^{0.5}\ B_t\ R^{1.5}$
Auxiliary heating	100 MW

[a] P in MW, NE_{19} in 10^{19} m^{-3}, B_t in T, R in m.

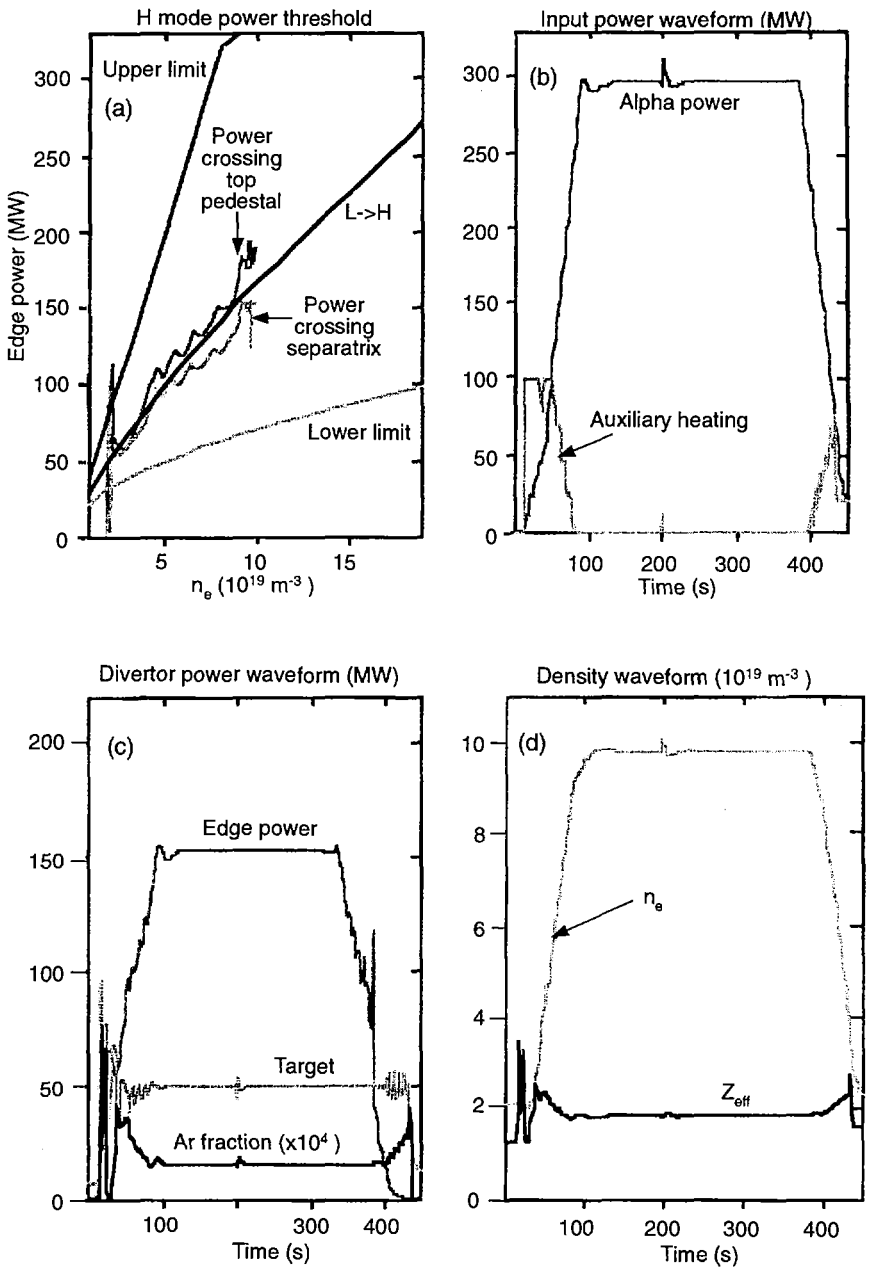

FIG. 1. (a) Trajectory in edge power versus density; (b) auxiliary heating and fusion power waveforms; (c) argon fraction required to limit the power to the target plates below 50 MW; (d) density and Z_{eff} waveforms.

— The amount of auxiliary heating is controlled — in the order of decreasing priority — to maintain the plasma in the H mode, to maintain the plasma density below a maximum value and to assist fusion power control.

All these feedback schemes must react appropriately as the Ar level is independently changed for divertor protection and the helium removal rate varies with the divertor conditions. The waveforms for the time dependent scenario showing successful control are plotted in Fig. 1.

4. NON-INDUCTIVE STEADY STATE OPERATION

Non-inductive operation in ITER will create the opportunity to develop ultra-long pulse operating modes for ITER's nuclear testing mission and to develop the physics database for a steady state demonstration reactor. Operating parameters for three example steady state operating modes are shown in Table II.

It appears that these demanding requirements for steady state ITER operation can be met by reversed shear modes. Figure 2 shows the pressure and current profiles for a 12 MA steady state operating scenario that is projected to produce 1500 MW of fusion power. Ideal MHD calculations show that this pressure profile is stable to both kink and ballooning modes with a conducting wall at 1.3 times the plasma minor

TABLE II. OPERATING PARAMETERS FOR THREE STEADY STATE OPERATING MODES

Parameter	Fully optimized	H mode-like density profile	Low density reversed shear
P_{fusion}/P_{CD} (MW)	1500/100	1500/100	1500/100
f_{BS} (%)	94	79	71
γ_{cd} ($\times 10^{20}$A·W^{-1}·m^{-2})	0.06	0.21	0.21
$\beta_N/\beta_{toroidal}$	2.9%/2.8%	3.8%/3.7%	3.6%/3.5%
$\langle T_e\rangle_n/T_{e0}$ (keV)	10.2/18.1	12.5/25.9	15.8/32.9
$\langle n_e\rangle/n_{e0}$ ($\times 10^{20}$ m^{-3})	1.0/1.7	1.0/1.1	0.71/0.78
$\langle n_e\rangle/n_{GR}$	1.4	1.4	1.0
τ_E (s)	2.35	2.46	2.84
$\tau_E/\tau_{ITER93\text{-}H}$	1.05	1.22	1.26
$\tau_E/\tau_{ITER89\text{-}P}$	2.0	2.26	2.38

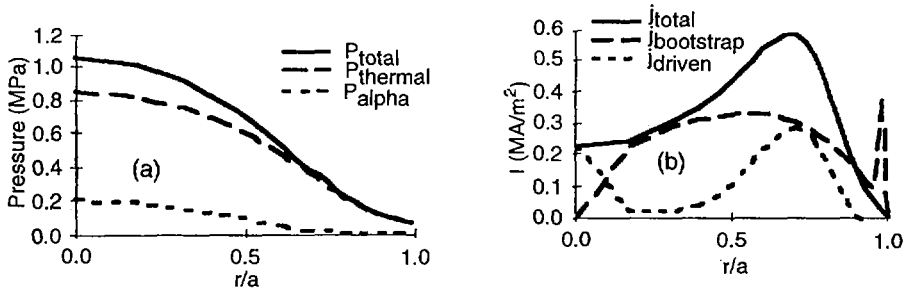

FIG. 2. Pressure and current profiles for ITER reversed shear steady state operating scenario.

radius for $\beta_N \leq 5$ (the desired operating points from the table have $\beta_N \leq 3.8$) although there exist uncertainties regarding the stability with respect to resistive wall modes.

High β operation in these reversed shear scenarios assumes a strongly shaped plasma with high elongation ($\kappa_{95\%} \geq 1.85$) and high triangularity ($\delta_{95\%} \geq 0.4$). This can be achieved with the ITER poloidal field system using the monolithic central solenoid of the Interim Design Report, the pancake wound segmented central solenoid design, or the hybrid variant design (which combines a short layer wound central solenoid with two additional PF coils both above and below this shortened solenoid). The allowed operating window is greatly expanded with the additional shape flexibility afforded by either the segmented or the hybrid central solenoid design as shown in Fig. 3.

In addition to current, B field and force limits on the ITER PF coils, we have considered limitations on the allowed operating space from both passive and active control of the plasma position. We find an adequate passive structure for passive position control (on the MHD time-scale) over the full ($\kappa_{95\%}$, a) space allowed by the segmented or hybrid central solenoid. Active control of dispacements up to $\Delta z = 1$ cm is possible to the right of the line in Fig. 3(a) labelled '$\Delta z = 1$ cm', while active control of 10 cm displacements (ITER design specifications) is possible to the right of the line labelled '$\Delta z = 10$ cm'.

In addition to axisymmetric magnetic limits, we have considered limitations on the steady state operating space due to the drift of fast alpha particles (produced by fusion reactions) in the toroidal field ripple. We find this to be a serious problem, with 16% of the fast alpha power lost to the first wall in the nominal ITER steady state equilibria. Since the toroidal field ripple is largest in the upper, outboard corner of the plasma chamber, the fast alpha power losses can be brought to within the first wall design limits (no more than 5% of the fast alpha power) by choosing a shorter plasma, a plasma with smaller minor radius, or by combining inward and downward displacements of the plasma (Fig. 3(b) with 0.3% fast alpha power losses).

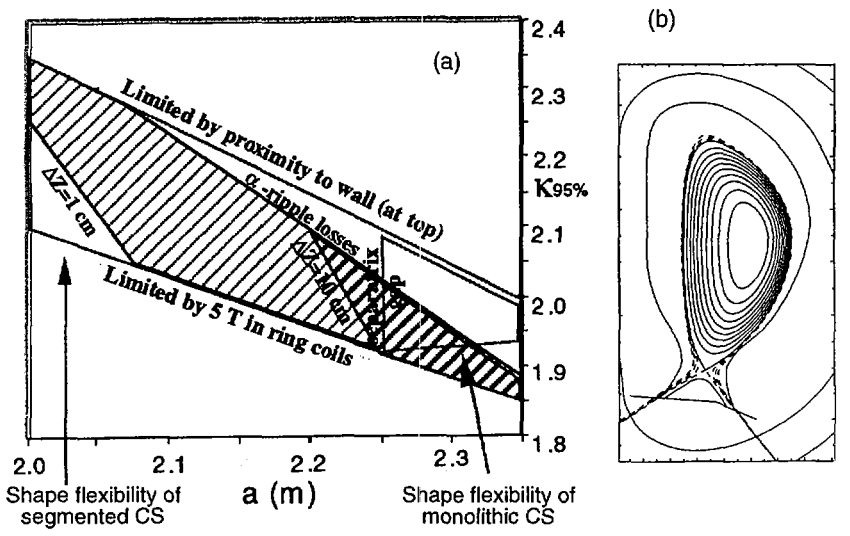

FIG. 3. (a) Approximate ITER reversed shear operation limits; (b) example of plasma equilibrium.

5. NON-INDUCTIVE CURRENT DRIVE MODELLING

This section studies the physics merits of current generation in ITER by means of lower hybrid (LH) waves. It does not address the design issues associated with operation, maintenance or control of such a system in ITER. These issues are addressed in Ref. [2].

Non-inductive current drive and profile control in ITER can be efficiently obtained with LH waves and, for steady state operation, with a high bootstrap current fraction and a seed current in the plasma centre generated, for example, by fast wave current drive (FWCD). Appropriate scenarios have been studied with the transport codes JETTO and ASTRA. The transport code results are analysed with the MHD stability code CASTOR, to study the behaviour of ballooning, kink and infernal modes. The LHCD deposition profiles are determined with codes validated on existing experimental results (BARANOV, BANDIT3D, WDFP). Practical means of controlling the current density profile and fusion power by appropriate feedback loops are also investigated with ASTRA and CRONOS.

Three types of scenario have been investigated, with the following results:

(i) In the first low activation phase of ITER, the pulse length can be considerably prolonged by non-inductive current drive with the lower hybrid current drive (LHCD) system proposed in Ref. [2]. High current drive and heating efficiency can be provided by LHCD in this operation regime where the heating power density is low in the absence of alpha particle heating. Profile control scenarios for the subsequent high performance operation can therefore be conveniently tested in this phase.

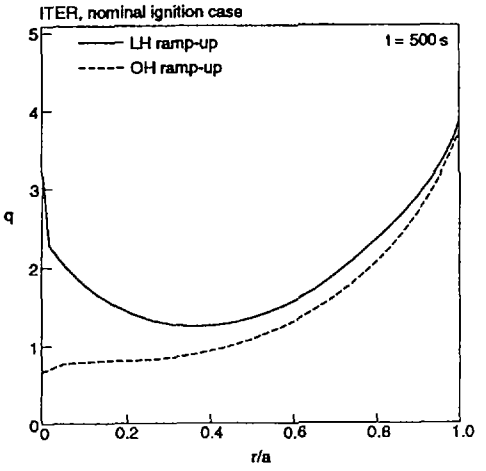

FIG. 4. Safety factor profiles at t = 500 s for ohmic current ramp-up and LH assisted current ramp-up.

(ii) In the standard ITER case with pulsed operation at 21 MA plasma current, current profile optimization throughout the discharge can be achieved by supplementing non-inductive current drive with LH waves. Ramping up the LH power to 50 MW during a 0.15 MA/s current rise phase provides non-monotonic q(r) profiles with a wide central region of flat shear at the beginning of the flat-top phase. Then, over the long resistive diffusion time in the burning phase, the magnetic shear zone shrinks slowly and the current profile reverts to a monotonic shape, but q values can be kept above 1 over the whole plasma cross-section up to 1000 s. Sawteeth are therfore avoided throughout the whole discharge duration. The q profiles during flat-top at t = 500 s are compared in Fig. 4 for ohmic ramp-up only and LH assisted ramp-up, both with 50 MW ICRH heating started at the beginning of the current flat-top.

The primary power supply during ramp-up is significantly reduced with LHCD, thanks to the large enhancement of the current drive efficiency from the electric field in the outer half of the plasma. A total of about 70 V·s is saved in the ohmic flux consumption. Consistent operation of the poloidal field (PF) system is required in order to account for changes in the primary flux consumption, but to maintain the PF coil currents compatible with X point formation and plasma control (appropriate premagnetization, etc.).

(iii) In an advanced steady state scenario at 13 MA, off-axis LHCD in the region r/a = 0.5–0.8 is used to create a wide magnetic shear reversal zone and to provide full current drive together with the bootstrap current. The transport model used in the JETTO calculations links the heat conductivities to the magnetic shear, reducing transport in the region of flat or negative shear. A fusion power output of order 1 GW is produced in steady state.

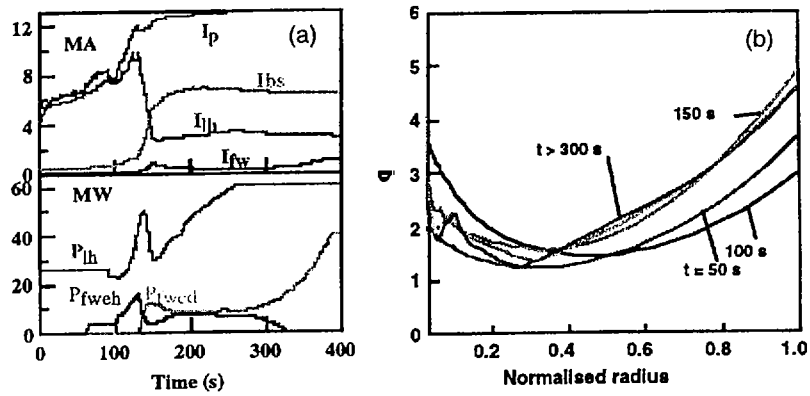

FIG. 5. (a) Time evolution of plasma current, non-inductive currents, and LH and FW powers; (b) q profile for steady state, feedback controlled, 1500 MW burn. (I_p: plasma current; I_{bs}: bootstrap current; I_{lh}: LH driven current, I_{fw}: fast wave driven current; P_{lh}: lower hybrid power; P_{fweh}: fast wave electron heating power; P_{fwcd}: fast wave current drive power.)

The sensitivity of these results to various assumptions on the models is studied by running similar time dependent scenarios on codes such as ASTRA and CRONOS. With a slightly different dependence of heat transport on shear, consistent with Tore Supra results [3] and a somewhat deeper penetration of the LH waves, the duration of the sawtooth free period ($q > 1$) is found to be reduced to about 650 s in the standard case (ASTRA). For steady state scenarios, access to optimized MHD stable profiles and prescribed fusion yields will require simultaneous control, on the resistive timescale, of the off-axis (LH) current generation, of the central heating and current drive power, and of the plasma fuel density. Assuming that real time estimates of the internal loop voltage can be made from magnetic reconstruction, appropriate feedback loops on the heating and current drive systems would possibly allow the plasma to be controlled and maintained in the desired steady state high Q equilibrium. An example for such a scenario is shown in Fig. 5 (CRONOS).

REFERENCES

[1] SUGIHARA, M., AMANO, T., BOUCHER, D., IGITKHANOV, Y., JANESCHITZ, G., PACHER, H.D., POST, D., YUSHMANOV, P., J. Nucl. Mater. (in press).

[2] BOSIA, G., et al., IAEA-CN-64/FP-17, this volume.

[3] LITAUDON, X., et al., IAEA-CN-64/AP1-11, these Proceedings, Vol. 1, p. 669.

ENERGETIC PARTICLE PHYSICS ISSUES FOR ITER*

C.Z. CHENG[1], H.L. BERK[2], D. BORBA[3], R.V. BUDNY[1], R.H. BULMER[4], J. CANDY[2], D.S. DARROW[1], A. FASOLI[3], E.D. FREDRICKSON[1], G.Y. FU[1], R.J. GOLDSTON[1], N.N. GORELENKOV[1], G.T.A. HUYSMANS[3], W. KERNER[3], H. KIMURA[5], S.V. KONOVALOV[6], Y. KUSAMA[5], J. MANICKAM[1], R. NAZIKIAN[1], G.H. NEILSON[1], W.M. NEVINS[4], T. OZEKI[5], L.D. PEARLSTEIN[4], S. PUTVINSKI[7], M.H. REDI[1], F. ROMANELLI[8], M.N. ROSENBLUTH[7], S.E. SHARAPOV[3], D.A. SPONG[9], K. TOBITA[5], J.W. VAN DAM[2], G. VLAD[8], R.B. WHITE[1], K.L. WONG[1], V. WONG[2], F. ZONCA[8], S.J. ZWEBEN[1]

[1] Plasma Physics Laboratory,
Princeton University,
Princeton, New Jersey,
United States of America

[2] Institute for Fusion Studies,
University of Texas,
Austin, Texas,
United States of America

[3] JET Joint Undertaking,
Abingdon, Oxfordshire, United Kingdom

[4] Lawrence Livermore National Laboratory,
Livermore, California,
United States of America

[5] Japan Atomic Energy Research Institute,
Naka-machi, Naka-gun, Ibaraki-ken,
Japan

[6] Kurchatov Institute,
Moscow, Russian Federation

[7] ITER Joint Central Team,
La Jolla, California,
United States of America

[8] Associazione Euratom–ENEA sulla Fusione,
Frascati, Italy

[9] Oak Ridge National Laboratory,
Oak Ridge, Tennessee,
United States of America

Abstract

ENERGETIC PARTICLE PHYSICS ISSUES FOR ITER.

The paper summarizes the present understanding of the following energetic/alpha particle physics issues for the 21 MA, 20 TF coil ITER Interim Design configuration and operational scenarios: (a) toroidal field ripple effects on alpha particle confinement, (b) energetic particle interaction with low frequency MHD modes, (c) energetic particle excitation of toroidal Alfvén eigenmodes, and (d) energetic particle transport due to MHD modes. TF ripple effects on alpha loss in ITER under a number of different operating conditions (L-mode, H-mode, and post-sawtooth) are found to be small, with a maximum loss of 1%. With careful plasma control in ITER reversed-shear operation, TF ripple induced alpha loss can be reduced to below the nominal ITER design limit of 5%. Fishbone modes are expected to be unstable for $\beta_\alpha > 1\%$, and sawtooth stabilization is lost if the ideal kink growth rate exceeds 10% of the deeply trapped alpha precessional drift frequency evaluated at the $q = 1$ surface. However, it is expected that the fishbone modes will lead only to a local flattening of the alpha profile owing to small banana size. MHD modes observed during slow decrease of stored energy (as much as 20% in 50–100 msec) after fast partial electron temperature collapse (in about 100 μsec) in JT-60U reversed-shear experiments may be resonant type instabilities; they may have implications for the energetic particle confinement in ITER reversed-shear operation. From the results of various TAE stability code calculations, ITER equilibria appear to lie close to TAE linear stability thresholds. However, the prognosis depends strongly on q profile and profiles of alpha and other high energy particle species. If TAEs are unstable in ITER, the stochastic diffusion is the main loss mechanism, which scales with $(\delta B_r/B)^2$, because of the relatively small alpha particle banana orbit size. For isolated TAEs the particle loss is very small, and TAEs saturate via the resonant wave–particle trapping process at very small amplitude. If a wide range of overlapping medium- to high-n TAEs do prove to be linearly unstable, then a global quasilinear, possibly bursty, flattening of the alpha profile, resulting from an explosive "domino" effect due to enhanced wave energy release, is possible. Finally, theoretical calculations for energetic/alpha particle physics issues have made much progress. Critical energetic/alpha physics experimental input is expected in the near future from JET DT, TFTR DT, and JT-60U negative ion beam experiments.

Introduction

The study of energetic particle transport and effects on MHD modes is important for ITER design and operation. In particular, the behavior of alpha particles produced in DT fusion reactions and that of energetic ions produced by auxiliary ICRF and N-NBI heating planned for ITER should be well understood. Any unanticipated loss of energetic/alpha particle power could result in reduction of plasma beta, serious wall damage, impurity influx, major operational control problems, or even a failure to sustain ignition. NBI and ICRF experiments in large tokamaks have shown that collective MHD modes such as the fishbone and TAE modes can be strongly unstable and cause the loss of up to half of the fast beam ions. Our present understanding of the following critical energetic particle physics issues for the ITER design configuration and operational scenarios is addressed.

1. TF Ripple Effects on Alpha Particle Confinement

Toroidal field ripple breaks the symmetry of any tokamak and can result in the loss of a significant fraction of the fast α heating power. The toroidal field ripple is defined as $\delta \equiv (B_{max} - B_{min})/(B_{max} + B_{min})$, where B_{max} and B_{min} are toroidal magnetic fields calculated at two points having the same radial and vertical coordinates in the meridional cross section but different toroidal coordinates — one under the TF coil and another midway between two neighboring coils. The ITER device has been designed such that the maximum ripple at the plasma separatrix is about 2% and, in the reference ignited operating mode, TF ripple losses of fast α-particles are negligible. However, the situation is less favorable in the high-q (low plasma current) operating modes envisioned for steady-state operation. In high-q operation ripple wells can cover a substantial fraction of the plasma cross-section. Ripple wells occur when $n\ \delta(R,Z) \geq |B_R/B_{\phi 0}|\ (|B|^2/B_\phi{}^2) - 1/2\ (R/F_0F^2)\ [\partial\psi/\partial Z\ \partial|\nabla\psi|^2/\partial R - \partial\psi/\partial R\ \partial|\nabla\psi|^2/\partial Z]$, where n is the number of toroidal field coils, B_R is the radial component of the magnetic field, $B_{\phi 0}$ is the vacuum toroidal field, B_ϕ is the toroidal field (including equilibrium corrections), $F_0 \equiv RB_{\phi 0}$, $F \equiv RB_\phi$, and ψ is the poloidal flux, and the second term on the right hand side of this inequality is a small correction due to poloidal variations in the poloidal field strength. The leading terms are approximately $\delta(R,Z) \geq \varepsilon/qN$ (where we have used the estimate $B_R/B_\phi \approx \varepsilon/q$, $\varepsilon = r/R$).

Guiding center particle orbit following code calculations have been made to study ripple-induced alpha loss in ITER, under a number of different operating conditions for the 21 MA, 20 TF coil ITER Interim Design [1]: L-mode, H-mode, post-sawtooth, and reversed-shear configurations. In all cases except for reversed-shear operation, alpha loss is below 1% [2]. Alpha loss is substantially higher in a reference 12 MA ITER reversed-shear equilibrium (96015-01) with $q(0) = 5$, $q_{min} = 3.5$, and $q(a) = 6$ at the 95% flux surface, localized near the outer wall. This result is also supported by JT-60U experimental results that the confinement of 1 MeV tritons in reversed-shear plasmas is inferior to that in normal shear plasmas, causing an enhanced heat load on the first wall [3]. The stochastic loss is predicted to be negligible, but the TF ripple asymmetry gives large losses due to ripple well drift. The ripple well domain is quite large. The up-down asymmetry causes it to extend to the edge of the plasma in the upper half plane. Much of the plasma core lies within the ripple well region, and essentially all alpha particles born with banana tips outboard of the magnetic axis will drift to the first wall, while the upper banana tip never leaves the ripple well region.

Collisionless losses predicted by ORBIT [2] and GIBRID [4] Monte Carlo orbit simulations and a novel accelerated method [5] are about 15-16%, which may produce unacceptable peak heat loads on the first wall (several MW/m^2).

To mitigate the ripple loss in ITER reversed-shear operations, three operational scenarios are proposed: 1) use of the plasma shape control system to hold the plasma away from the high ripple region, 2) operation with lower values of q at mid plasma radius, and possibly 3) reduction of the magnitude of the toroidal field ripple. For example, a shorter ITER reversed-shear equilibrium (96015-02) with reduced elongation to make the plasma more nearly centered within the TF coil set, is found to lose less than 3% of alpha particles, below the nominal ITER design limit of 5%. Since it fits the outer wall less snugly, it may present increased problems of vertical control. Hence, it appears that ripple losses of fast α in reversed-shear modes can be held to acceptable values through control of the plasma shape. For a maximum alpha ripple loss of 3% for the 21 MA case we estimate that the heat load gives roughly 0.08 MW/m^2. However, the wall heat load may be increased by MHD and TAE enhanced losses, in addition to toroidal peaking factors.

2. Energetic/Alpha Particle Interaction with Low Frequency MHD Modes

Energetic trapped particles can significantly affect the stability of low frequency MHD modes such as internal kink modes, fishbone modes, and ballooning modes, which in turn can cause energetic particle transport. Recent DT experiments on TFTR have shown a substantial redistribution of partially thermalized alphas by sawtooth crashes [6]. A similar sawtooth-induced alpha redistribution in ITER would cause a change in the alpha heating profile, and possibly an increase in TF ripple loss. Increased alpha particle loss due to the kinetic ballooning mode and various other types of coherent MHD have also been seen on TFTR.

For low frequency MHD modes with frequency below the energetic trapped particle bounce-averaged magnetic drift frequency ω_d, the particle dynamics is no longer governed by the ExB drift, but rather by the magnetic drift. For $\omega << \omega_d$, if the energetic particle diamagnetic drift frequency ω_* has the same sign as ω_d, the MHD modes will be stabilized because the energetic trapped particles precess rapidly and their motion becomes too rigid to release its pressure gradient free energy to the MHD waves. On the other hand, resonant type MHD modes such as fishbone ($n = 1$ internal kink type) modes and kinetic ballooning modes (KBM) with $\omega = \omega_d$ can resonate with the energetic trapped particles and be destabilized if the hot trapped particle beta β_h is larger than a threshold value. The stability of higher frequency KBM can also be affected by the drift-bounce resonance with energetic particles. Since ω_d is a function of particle velocity, pitch angle, aspect ratio, plasma beta, and plasma shaping, the magnetic drift reversal domain in the pitch angle and minor radius space can be significantly enlarged in ITER. Alpha particles have a uniform velocity pitch angle distribution, and their averaged magnetic drift frequency can be significantly reduced so that the theoretical β_α threshold for the fishbone instability becomes much lower than previously thought.

Calculations for ITER parameters [7], with $q = 1$ at $r = a/3$, show that fishbone modes can be excited for $\beta_\alpha \geq 1\%$, where β_α is the volume averaged alpha particle

beta within the q = 1 surface. Internal kink stabilization is lost if the ideal growth rate exceeds 10% of the deeply trapped alpha precessional drift frequency evaluated at the q = 1 surface. This is mainly because the drift reversal effect reduces the average trapped alpha precessional drift so that low frequency MHD modes can more easily resonate with trapped alphas and release the alpha pressure gradient free energy. The stable window in the β vs. β_α domain for both sawteeth and fishbone modes is further reduced when the core ion diamagnetic drift effect is included. However, it is expected that the fishbone modes (localized mainly within the q =1 surface) will lead only to a local flattening of the alpha profile due to small banana size. To eliminate the possibility of exciting fishbone modes, ITER can be operated with q(0) > 1. However, kinetic ballooning modes may still be excited when the plasma β is below MHD marginal stability.

Recent JT-60U reversed-shear experiments have found very fast (in about 100 μsec) partial collapse of electron temperature in the NBI and ICRF heated plasmas [8]. Following this fast collapse of electron temperature the total stored energy can decrease slowly by as much as 20% in about 50 - 100 msec. Accompanying this slow decrease of the stored energy is MHD activity with frequency in the range of 2 to 7 kHz. The cause of the slow decay of the stored energy has not been clearly identified. Besides the possible cause of the redistribution of the thermal and fast ion pressures and the modification of the current profile after the fast electron temperature collapse, the MHD activity may play some role in the slow stored energy decay. These MHD modes may be resonant type MHD instabilities because their frequencies are on the order of the beam ion precessional drift frequency. These MHD modes, if excited in ITER reversed-shear operation, may have important effects on energetic particle confinement. The stability calculation of these MHD modes is yet to be performed for both JT-60U and ITER.

3. Energetic Particle Excitation of TAE Modes

The Toroidal Alfvén Eigenmodes (TAE) [9] have been shown to exist with discrete frequencies located inside the shear Alfvén continuum gaps created by toroidal coupling of different poloidal harmonics. The frequency of the TAE mode in the lowest continuum gap is roughly given by $\omega \approx V_A/2qR$ for all toroidal mode numbers. The existence of TAE modes depends on the plasma density and q profiles, plasma β, plasma shaping, aspect ratio, and wall boundary. Energetic particles with velocity near the Alfvén speed can resonate with TAE modes and destabilize them if the expansion free energy associated with the energetic particle pressure gradient can overcome velocity space and collisional damping effects due to all particle species.

Alpha driven TAE modes have recently been observed in TFTR DT plasmas with reduced central shear (< 0.2) out to r/a = 0.6 and elevated central safety factor q(0)=1.5-3.0 [10]. TAE modes are observed within 80-100 msec (D and T beam ion slowing down time) following neutral beam injection. The dominant mode is an n = 3 core localized TAE mode with frequency within 10% of the TAE frequency predicted by the NOVA-K code [11]. The threshold fusion power for exciting the n = 3 TAE mode is very low (=1.5 MW for q(0)=3.0 and =2.5 MW for q(0)=1.5 corresponding to =300 kW and = 500 kW alpha heating power, respectively). NOVA-K code calculates that the threshold $\beta_\alpha(0)$ is consistent with experiment in the range 0.01-0.02%. The mode amplitude is very weak with $\delta B/B=10^{-8}$ on the Mirnov coils while

the reflectometer measurements indicate a mode amplitude $\delta n/n = 10^{-4}$ at $r/a = 0.4$ with no observable density fluctuations at larger radii. No alpha loss due to this TAE mode has been observed.

TAE modes have also been observed in JT-60U experiments [8] with high power ICRF and NBI. TAE modes with n=1, 2 are observed in low positive shear (q(0)=1.6) plasmas, but not in reversed-shear plasmas with strong ITB (internal thermal barrier) formation. However, weak TAE modes with n=5-8 have been observed in reversed-shear plasmas (q(0) = 3-4, $q_{min} = 2$ (at r/a =0.7), and q(a)=3.5) after partial collapse of the stored energy (weak ITB plasmas). The results have also been confirmed by the NOVA-K code calculation. Due to different radial wave structure, TAE modes do not access as much hot ion drive in strong ITB cases than in weak ITB cases. These JT-60U results indicate that TAE modes will probably be unstable in ITER weak normal shear or reversed-shear plasmas

For ITER the increased size shifts the spectrum of unstable TAE modes towards medium- to high-n modes. Linear TAE stability in ITER has been examined for ITER reference (PRETOR 1) pressure and q profiles which have very flat regions in the center ($r/a < 0.7$) due to assumed rapid sawtoothing and sharp gradients outside the q = 1 surface. Code calculation results from NOVA-K [11] and TAE/FL [12] codes show that TAE modes are stable up to at least n = 50. However, using relatively more realistic peaked pressure profiles for TAE stability calculation we find that TAE modes can be more easily destabilized in ITER than in the TFTR D-T experiments. One reason is because ITER has lower $q(a)$ (≈ 3.5) and its plasma beta is below the Troyon limit so that TAE modes can exist with more global radial structure. Another reason is that the expected $<\beta_\alpha>$ is about one order of magnitude larger than in TFTR D-T experiments. The existence of core-localized TAE modes [13,14] has been predicted in the low-shear region, where the population of destabilizing fusion alpha particles is peaked for normal ITER operation. In reversed-shear operations the low-shear region is moved outward but these modes can still be unstable due to their enlarged mode width. For more peaked pressure profiles in ITER, core localized TAE modes are expected to be unstable. In the following we summarize the present status of TAE stability in ITER as predicted by various codes.

(a) NOVA-K Code Results

To study the medium-n TAE stability for ITER experiments using the NOVA-K code [11] we consider a series of equilibria with varying plasma beta. The fixed parameters of the ITER equilibrium are taken to be the major radius R = 8.1 m, the minor radius a = 2.8 m, the ellipticity κ = 1.6, the triangularity δ = 0.25, the toroidal field B = 5.7 T. The pressure profile is chosen as $P = P(0)\,(1-\psi)^{1.2}$, where ψ is the normalized poloidal flux. The q-profile is chosen with q(0) = 1.0, q(1) = 3.78, q'(0) = 0.5, q'(1) = 13. The plasma is assumed to consist of thermal electrons, thermal D-T ions and alpha particles. The electron density profile is given by $n_e = n_e(0)\,(1 - 0.8\,\psi^2)$. The thermal ions are assumed to consist of an equal mixture of D and T with equal temperature. We assume $n_i = n_e$ and $T_i = T_e$. The alpha pressure profile is chosen to be proportional to $P(r)^{3.5}$. The TAE stability is studied in the $n_e(0)$-$T_e(0)$ space with self-consistent equilibria and alpha pressure profiles for $n \leq 30$. Both global TAE and core localized TAE are considered. The main damping mechanisms are the ion Landau damping, which increases rapidly with $<\beta_i>$, and the radiative

damping. But, the alpha drive also increases with $<\beta_i>$. The global TAEs tend to have large amplitude near the plasma edge and are found to be stable up to $n = 10$. On the other hand high-n ($n = 15$ - 30) core localized TAEs tend to be unstable due to large alpha drive. Without the radiative damping, the core localized mode is unstable below a critical density; the $n = 25$ core localized TAE mode is stabilized for $n_e(0) > 2\times10^{14}$ cm^{-3} by the ion Landau damping. Higher n TAE modes will have higher density threshold. However, the radiative damping stabilizes TAE modes in the low density domain. Based on an analytical radiation damping formula the $n = 25$ core localized TAE mode is stabilized for $n_e(0) < 7\times10^{13}$ cm^{-3}. Nonetheless, the radiative damping is sensitive to plasma profiles, especially the q profile, and thus, the exact stability boundary depends on details of the profiles. Because ITER is expected to operate in the range 2×10^{14} $cm^{-3} \geq n_e(0) \geq 5\times10^{13}$ cm^{-3} and 30 keV $\geq T_e(0) \geq$ 10 keV, TAE modes may be destabilized in ITER experiments. Operations at lower temperature and higher density would put ITER below TAE instability thresholds.

(b) TAE/FL Code Results

The α-particle effect on the stability of TAE modes has been studied for ITER by using the TAE/FL gyro-fluid simulation code [12] for an equilibrium with peaked profiles, which occurs just before a sawtooth event. The equilibrium is obtained from the TRANSP analysis code with $q(0) = 0.9$, $q(a) = 3.7$, $n_e(0) = 1.67\times10^{14}$ cm^{-3}, $T_e(0) = 22$ keV, $T_i(0) = 20$ keV. The alpha pressure gradient is finite over a significant domain of the plasma radius ($0 < r/a < 0.6$). At $<V_\alpha>/V_A(0) = 1$, two core localized TAE modes ($n = 2$ and 5) are found to be unstable for the TRANSP calculated value of $\beta_\alpha(0) = 0.95\%$. At higher $\beta_\alpha(0) = 1.2\%$ (above that predicted by TRANSP) four core localized TAE modes ($n = 2$, 3, 5, and 6) are unstable. At higher $\beta_\alpha(0)$ (say at 2%) a range of high-n ($n = 20$ - 30) global TAE modes are unstable.

(c) CASTOR-K Code Results

The α-particle effect on the stability of kinetic toroidal Alfvén eigenmodes (KTAE) has also been studied for ITER by using the CASTOR-K code [15]. The frequencies of KTAE modes are near the upper Alfvén continuum gap boundary. The α drive is usually smaller for KTAE modes than for TAE modes due to higher frequency and narrower radial wave structure. However, the thermal plasma damping effects on KTAE modes can be smaller than on TAE modes. We consider the α pressure profile $P_\alpha = P_\alpha(0)\,(1-\psi)^s$, where $s > 1$, and the plasma pressure profile is chosen as $P = P(0)\,(1-\psi)$. The fixed parameters of the ITER equilibrium are taken to be the major radius $R = 8$ m, the minor radius $a = 2.6$ m, the ellipticity $\kappa = 1.6$, the triangularity $\delta = 0.25$, the toroidal field $B = 6$ T. The central electron density is set at $n_e(0) = 10^{14}$ cm^{-3}. The CASTOR-K code results show that for $s < 4$, KTAE modes are stable for $n < 10$. For $s > 2$, high-n KTAE modes can be unstable and with $s = 4$, $n > 10$ KTAE modes are unstable with $\gamma/\omega \approx <\beta_\alpha>$.

(d) High-n TAE Modes

All global TAE eigenvalue stability codes are based on a perturbative approach and due to limitation of computing power are quite inefficient to calculate high-n TAE stability. For high-n TAE modes, the core ion FLR effects are as important as other damping mechanisms in determining the TAE stability. Therefore, 2D high-n TAE

stability codes based on 2D WKB-ballooning formalism, such as the HINT code [16] and a semi-analytical 2D WKB code developed at Frascati [17], have been developed to take into account full core ion FLR effects as well as wave-particle resonance on a nonperturbative basis. Results for the peaked alpha profiles show that resonant TAE modes (also called Energetic Particle Modes) can be destabilized. The calculation assumes all deeply trapped alpha particles and is based on a large aspect ratio s-α equilibrium with circular shifted circular flux surfaces. For example unstable modes (n = 5-20) are found near the peak gradient at $r/a = 0.4$. The most unstable mode has n = 10, $\omega_r/\omega_A \approx 0.32$, and $\gamma/\omega_A \approx 3.5 \times 10^{-3}$. However, using a more realistic uniform pitch angle alpha distribution but an analytical local (1D) dispersion relation the Frascati semi-analytical 2D calculation indicates that the $n = 10$ mode is stable for expected β_α values in ITER [17].

To summarize from the above TAE stability calculations, ITER equilibria appear to lie close to TAE linear stability thresholds. The prognosis is not yet clear due to the complexity of mode structures and damping mechanisms, the strong dependence on alpha profiles, and additional free energy sources due to other high energy particle species such as ICRH minority tail ions and high energy NBI and N-NBI beam ions, which can contribute additional TAE instability drive and lower the instability threshold. On the other hand, q(r) and $n_e(r)$ profiles can be controlled so that the radial gap structure does not line up across the minor radius, and the TAE mode will experience continuum damping and can be stabilized. Another way is to increase plasma β. As the plasma β exceeds the ballooning mode β limit or the magnetic shear decreases to zero, the TAE frequency will move downward into the lower continuum and suffer continuum and radiation damping to provide continuum damping and stabilize the TAE modes. In addition, plasma rotation can have a strong stabilizing effect on the TAE stability as shown in the JT-60U ICRF experiments. Therefore, TAE stability in ITER needs to be investigated further by considering more realistic plasma profiles and more particle species.

4. Energetic Particle Transport due to TAE Modes

TAE modes can lead to energetic particle transport as high as 80%, as has been found both experimentally and theoretically in present tokamaks. Two main MHD mode induced transport mechanisms have been identified [18]: (1) near-boundary transient loss, which affects mainly particles near the prompt loss boundary, and (2) stochastic diffusion loss across the prompt loss boundary in the phase space of particle energy, pitch angle, and toroidal angular momentum, which arises from overlapping of particle drift orbit islands. For particles trapped inside a well-defined resonant drift orbit island intersecting with the prompt loss boundary, their loss rate scales as $(\delta B_r/B)^{1/2}$. If the particle loss is due to distorted orbits close to the resonant drift orbit island, the transient loss rate scales as $(\delta B_r/B)$. The stochastic diffusion loss will last longer and it arises from the overlap of particle drift orbit islands. The stochastic diffusion loss rate scales as $(\delta B_r/B)^2$, and the loss rate can be drastically increased in case of multiple modes. The stochastic threshold is $(\delta B_r/B) \approx 10^{-3}$ for a single global TAE mode which can produce multiple drift orbit islands. When multiple global TAE modes are present, the orbit stochasticity threshold can be substantially reduced to $(\delta B_r/B) \approx 10^{-4}$.

In tokamak experiments, the loss rate scaling with the TAE mode amplitude will be a mixture of these three scalings and will strongly depend on the plasma equilibrium, the TAE mode structure, and the duration of TAE activity. For bursting TAE activity, it is more likely that the total energetic particle loss scales linearly with the wave amplitude, as observed experimentally. However, it is expected that the diffusive loss mechanism can be more important for saturated large amplitude TAE modes with amplitudes exceeding the stochastic threshold for a longer duration. Because of the relatively small banana orbit size in ITER only the stochastic diffusion loss mechanism is expected to be important, in contrast with many present experiments.

Nonlinear simulations of the TAE mode saturation mechanisms and related fast ion transport have been carried out with the use of hybrid kinetic-MHD models. Without a strong and steady energetic/alpha particle source, quasi-linear profile modification is found to be the most efficient means of achieving TAE mode saturation. Resonant particles trapped in the wave produce flattening of the local pressure gradient. Also, the particle energy gradient becomes steeper because high energy particles lose energy whereas low energy particles do not interact with the mode, so the mode further loses drive due to increased velocity space Landau damping and eventually saturates. As in previous studies of TAE mode induced particle loss, the dominant loss process is that of barely counter-passing particles losing energy to the wave, transferring into fat banana orbits, and then hitting the outside wall in the co-moving direction. The losses are very effective for particles with large banana width. For ITER the particle loss is very small due to small banana width, and the alpha particles remain in the device and contribute to mode damping so that TAE modes saturate at very small amplitude. The time scale for the profile modification is orders of magnitude shorter than the time scale for alpha replenishment, so the additional new alpha particles would not modify this result. The nonlinear response may be a superposition of single mode responses when there is no resonance overlap. If a wide range of overlapping medium- to high-n TAE modes does prove to be linearly unstable, then a global quasilinear, possibly bursty, flattening of the alpha profile, resulting from an explosive, avalanche-like "domino" effect due to enhanced wave energy release, is possible [19]. For multiple-n TAE modes, resonance overlap among different modes is expected for linearly unstable profiles. On the other hand, a flattened alpha pressure profile such as might evolve quasilinearly could be stable to TAE modes even without actual loss of alphas.

5. Conclusion

Alpha/energetic particle loss due to MHD modes and TF ripple is an important issue for ITER. MHD modes are expected to be destabilized by alpha/energetic particles in ITER. However, the prognosis depends strongly on q(r) profile and profiles of alpha and other high energy particles. Finally, alpha/energetic particle loss can be reduced to a manageable level by controlling plasma profiles to reduce MHD activity and by careful control of plasma shape to reduce TF ripple well.

REFERENCES

[1] ITER Physics Design Description Document, Part II.
[2] WHITE, R.B., et al., Phys. Fluids **27** (1984) 2466.
[3] TOBITA, K., et al., these Proceedings, Vol. 1, p. 497.

[4] KONOVALOV, S.V., ITER Physics Design Report (1996).
[5] REDI, M.H., BUDNY, R.V., McCUNE, D.C., MILLER, C.O., WHITE, R.B., Phys. Plasmas **3** (1996) 3037;
WHITE, R.B., GOLDSTON, R.J., REDI, M.H., BUDNY, R.V., Phys. Plasmas **3** (1996) 3043.
[6] PETROV, M.P., et al., these Proceedings, Vol. 1, p. 261.
[7] WU, Y., CHENG, C.Z., WHITE, R.B., Phys. Plasmas **1** (1994) 3369.
[8] KIMURA, H., et al., IAEA-CN-64/E-6, these Proceedings, Vol. 3.
[9] CHENG, C.Z., CHANCE, M.S., Phys. Fluids **29** (1986) 3695;
CHENG, C.Z., CHEN, L., CHANCE, M.S., Ann. Phys. (N.Y.) **161** (1985) 21.
[10] NAZIKIAN, R., et al., these Proceedings, Vol. 1, p. 281.
[11] CHENG, C.Z., Phys. Rep. **211** (1992) 1;
FU, G.Y., CHENG, C.Z., WONG, K.L., Phys. Fluids B **5** (1993) 4040.
[12] SPONG, D.A., CARRERAS, B.A., HEDRICK, C.L., LEBOEUF, J.-N., WELLER, A., in Plasma Physics and Controlled Nuclear Fusion Research 1994 (Proc. 15th Int. Conf. Seville, 1994), Vol. 3, IAEA, Vienna (1996) 567.
[13] FU, G.Y., et al., Phys. Rev. Lett. **75** (1995) 2336.
[14] BERK, H.L., et al., Phys. Plasmas **2** (1995) 3401;
CANDY, J., BREIZMAN, B.N., VAN DAM, J.W., OZEKI, T., Phys. Lett. A **215** (1996) 299.
[15] BORBA, D., CANDY, J., KERNER, W., SHARAPOV, S., in Proc. Joint Varenna–Lausanne Int. Workshop on Theory of Fusion Plasmas, Varenna, 1996 (in press).
[16] HSU, C.T., et al., in Proc. Sherwood Fusion Theory Conf. (1996) paper 1D33.
[17] VLAD, G., ZONCA, F., ROMANELLI, F., Nucl. Fusion **35** (1995) 1651.
[18] CHENG, C.Z., et al., in Plasma Physics and Controlled Nuclear Fusion Research 1994 (Proc. 15th Int. Conf. Seville, 1994), Vol. 3, IAEA, Vienna (1996) 373.
[19] BERK, H.L., et al., IAEA-CN-64/D2-5, this volume.

ITER OPERATIONAL LIMITS*

F.W. PERKINS, D. POST, M.N. ROSENBLUTH, O. SAUTER[1],
K. BORRASS[2], D. CAMPBELL[3], J.G. CORDEY[3], M.J. GREENWALD[4],
T.C. HENDER[5], Y. KAMADA[6], R. LaHAYE[7], M.A. MAHDAVI[7],
A.W. MORRIS[5], V. MERTENS[2], J. NEUHAUSER[2], T.S. TAYLOR[7],
H.R. WILSON[5], R. YOSHINO[6], H. ZOHM[2],
ITER JOINT CENTRAL TEAM

Abstract

ITER OPERATIONAL LIMITS.

Operational limits for density and β play a key role in determining whether ITER can meet its goal of about 1 MW/m^2 neutron flux onto the first wall. This goal corresponds to roughly 1500 MW of fusion power and is equivalent to $\langle\beta\rangle \approx 0.032$. Given the optimum temperature $\langle T\rangle \approx 10$ keV vor achieving ignition power blance, a line-average density of $\bar{n} = 1.5n_{GR}$ is required, where $n_{GR} = I_p/\pi a^2$ denotes the empirical Greenwald limit. Recent experiments have obtained steady state ELMing H modes with line average densities exceeding the Greenwald limit, thereby documenting that the limit is empirical, not fundamental. Models for the occurrence of a density limit are discussed. Even though they are safely below the ideal MHD β limits, long pulse ITER-like tokamak discharges exhibit β limits arising from spontaneously generated magnetic island structures, which have been interpreted as arising from neoclassical bootstrap current. Prospects for ECH stabilization of these islands appear favourable, theoretically.

1. INTRODUCTION

Operational limits on density and plasma pressure bound the plasma performance of present tokamaks as well as the projections of ITER performance. Two limits — the β limit on plasma pressure and the empirical Greenwald limit on line average density [1] — are especially important. Because the DT thermonuclear reaction rate varies as $\langle\sigma v\rangle \propto T^2$ in the temperature range

[1] European Union Home Team.
[2] IPP–Garching, Germany.
[3] JET, Abingdon, Oxfordshire, UK.
[4] Plasma Fusion Center, MIT, Cambridge, Massachusetts, USA.
[5] UKAEA, Abingdon, Oxfordshire, UK.
[6] JAERI, Naka-machi, Naka-gun, Ibaraki-ken, Japan.
[7] GA, San Diego, California, USA.

foreseen for fusion reactors, the fusion power output of a reactor scale scales as β^2 — $P_{fusion} \propto \beta^2 B^4 R a^2 \kappa$ — and the limit on β translates directly into limits on fusion power and neutron wall flux. To obtain 1500 MW of fusion power which corresponds to a neutron wall flux of 1 MW/m^2, ITER requires $<\beta>=0.032$ (equivalently $\beta_N = \beta(\%)\ (I_{MA}/a\ B_T)^{-1} = 2.4$). While this β value lies safely below ideal MHD limits, β saturation has been observed in the range $2.0<\beta_N<3.0$ for ITER-like plasmas, depending on density and toroidal field strength. The phenomenology and physics of this beta limiting process is clearly of importance to ITER and tokamak reactors.

The density limit bears on ITER projections because tokamak transport losses increase with both β and T. The relationship $P_{loss} \propto \beta^{2.5} T^{0.5} B^{0.86} R^{0.5}$ resulting from the ITER93H scaling relation [2] is representative. In this case for fixed β, a balance between transport losses and fusion power —ignition— is most readily obtained at a relatively low plasma temperature $<T> \approx 10$ keV and corresponding density of $n=1.3\cdot10^{20}m^{-3}$, which exceeds the Greenwald limit of $n20 = I_{MA}/\pi a_m^2 = 0.85$ by 50%. If ITER is constrained to operate below the Greenwald density limit, then the temperature must be increased to maintain β and fusion power. Consequently, driven burn results [3]. The issue of whether the Greenwald density limit is fundamental or can be transcended by appropriate design and operation is of evident importance to ITER and future tokamak reactors.

2. LONG PULSE BETA LIMITS

In recent years, it has been recognized experimentally that, while a tokamak can sustain β values close to ideal MHD limits for many characteristic MHD (Alfvén) times, on longer time-scales rotating magnetic island structures appear which prevent increases in energy content with increasing heating power. Moreover, the β saturation level varies with density and toroidal field, indicating a physics process different from that of ideal MHD. It is desirable to carry out ITER relevant β limit experiments at the same collisionality as ITER and hence the same relative bootstrap current levels. Because $\nu^* \propto n^3 R(\beta^2 B^4)^{-1}$ modest deviations from the requisite scaled density can lead to appreciable differences in collisionality.

At densities above the scaled ITER density, experiments have shown that β_N values adequate to ITER needs can be sustained with ELMy H mode confinement. For example, experiments on DIII-D [4] have achieved a sustained ELMy H mode discharge at $\beta_N=3.5$. The density in this shot was $n_e = 4\cdot10^{19}m^{-3}$ compared to the scaled ITER density of $1.5\cdot10^{19}m^{-3}$, leading to a collisionality a factor-of-20 larger than the value foreseen for ITER. In ASDEX-U [5], soft β limits in the range $\beta_N=2.7$-2.9 were obtained for $q_{95}=3.0$-3.5, under conditions where, because of lack of explicit density control, the density exceeded the scaled ITER density by typically 50%.

At densities comparable to and below scaled ITER densities, soft β limits have been found on DIII-D [6] and JT-60U [7] that lie close to the minimum β_N values for acceptable ITER operation. For those plasmas, as well as the ASDEX-U plasmas cited above, the β limiting physics appears to be the appearance of low (m,n) magnetic islands which cause a beta saturation. Moreover, the DIII-D results show the β limit decreases systematically with decreasing density. The JT-60U results, on the other hand, are achieved at low densities ~40% of the scaled ITER density — a very collisionless plasma. Plasma shape apparently plays a role as JT-60U β limits increased with increasing triangularity as do results from

ASDEX-U [5]. JET experiments [8] indicate a β saturation occurring in ITER-like discharges (q_{95}=3.1) at β_N =3.8. However, fast particle accounted for 40% of the energy so that $\beta_{N,th}\approx 2.3$. For these experiments, the density was quite close to the ITER scaled density. For some discharges in JET and JT-60U, ELMs rather than low (m,n) modes limit β.

Summarizing, a common feature of long duration β limit experiments is the spontaneous creation of magnetic islands and confinement degradation at values $\beta_N \approx 2.5$, just the value needed to fulfill ITER performance requirements. ITER performance projections needs a physics understanding of the β limiting process.

The emerging model for low (m,n) magnetic islands is that of neoclassical tearing modes wherein the reduction of the usual toroidal bootstrap current around the island O-points by flattening of density and temperature gradients within the island provides the current density configuration needed to establish the island configuration in the first place. A number of authors have contributed to the development of neoclassical island theory [9-13] and TFTR [14] as well as COMPASS experiments [15] have confirmed the expression for saturated island width.

It does seem clear that, once a threshold island size has been established via interaction with ELMs or sawteeth, that in the collisionless limit $\nu^* \ll 1$, magnetic islands develop according to [11]

$$(1)\quad 0.8\,\frac{\mu_o}{\eta_{neo}}\,\frac{d}{dt}w = \Delta' + 4.4\, f_t(\nu^*)\,\mu_o\, n_e\, B_\theta^{-2}\,\hat{s}^{-1}\left(\frac{d}{dr}T_e\right)\frac{r_s\, w}{\left(w_D^2 + w^2\right)}$$

where w denotes the island full width, n the toroidal mode number, $f_t(\nu^*)$ the effective trapped particle fraction $f(\nu^*) = f\,(1+\sqrt{\nu^*}+0.25\nu^*/Z^2)$,and f_t is the collisionless trapped particle fraction This equation differs in numerical factors from that of [11] in that only the bootstrap current arising from electron temperature gradient enters because it is the electron temperature that equilibrates most readily in an island. Here, w_D describes a threshold island size arising from electron temperature equilibration within the island [11]:

$$(2)\qquad w_D = 5.1\,\frac{r_s}{\sqrt{\varepsilon\,\hat{s}\,n}}\left(\frac{\kappa_\perp}{\kappa_\parallel}\right)^{1/4}$$

Additional terms arising from polarization drifts as well as mode frequency are matters of current theoretical research [12,15]. If one adopts a gyroBohm formula for the cross field electron thermal conductivity $\kappa_\perp = (T^{3/2}M^{1/2}c^2 n)/(e^2B^2R)$, parallel Spitzer electron thermal conductivity for $\kappa_\parallel$, as well as expected ITER flat density profiles and $dT_e/dr \approx 2T_e(0)/a$ near q=2 [3,15], one can arrive at an expression for the threshold central electron β-value needed for neoclassical island to develop

$$(3)\qquad \beta_e(0) = \frac{(\Delta' a)}{2.2}\left(\frac{\varepsilon^{3/2}\,\hat{s}}{q^2}\right)\frac{w_D}{r_s}$$

At this threshold, the seed island must have a width $w=w_D$.Let us define $\rho^* = (TM)^{1/2}(eBa)^{-1}$ and manipulate (2) into the form

$$(4)\qquad \frac{w_D}{r_s} = 3.8\,\sqrt{\rho^*}\left(\frac{m_e}{M_i}\right)^{1/8}(\nu^*)^{1/4}\left(\frac{\varepsilon^{3/2}}{\hat{s}^2\, q\, n^2}\right)^{1/4}$$

which is small (a few cm for DIII-D). For this island size, the use of collisional, Spitzer parallel thermal conductivity is generally justified.

The threshold β value deduced by combining (3) and (4) is readily exceeded by present experiments and ITER. It follows that neoclassical islands can spontaneously arise for β values anticipated for ITER (and most research tokamaks) with rather modest requirements on the seed island size. Since the threshold β values are readily exceeded, one concludes that the density dependence of β saturation observed in ASDEX-U, COMPASS-D, and DIII-D could be explained in terms of the collisionality dependence of the effective trapped particle fraction $f_t(\nu^*)$, emphasizing the importance of performing experiments at ITER collisionality values. For DIII-D experiments, one evaluates $\nu^* \approx 0.1$, just the value for which collisionality begins to play a role. JT-60U, on the other hand, should be well into the collisionless limit and does not exhibit a density dependence of the saturated β value. A theory of β saturation via neoclassical islands is just beginning [10].

Consideration of the polarisation current contribution [15] to Eq(1) leads to an alternate picture. A seed island whose width is of order the ion banana width is required to trigger a tearing mode in the collisionless regime ($\nu_i/\varepsilon\omega_{*pe}<<1$), while in the collisional regime a larger seed island ($\sim\varepsilon^{-3/4}$ bigger) is needed; this may explain the observed stability to neoclassical tearing modes of higher density plasmas. The collisionality dependence of this threshold provides an alternative interpretation for the experimentally observed density dependence of the β limit, since the transition from the collisional to collisionless regime occurs at lower β as the density decreases.

Neoclassical magnetic islands develop because of lack of bootstrap current at the O-points. Replacing this current by electron cyclotron current drive, modulated to deposit current only near the O-point of a rotating island, provides a method for ameliorating or potentially eliminating neoclassical island limitations on β. The required driven current within the island is

$$(5) \qquad I_{CD} \approx \frac{4r_s}{m} \sqrt{\frac{1+\kappa^2}{2}}\, w\, j_{bs} = \frac{1.3\ MA}{m}\, w_m$$

where the practical formula is evaluated for (2,1) islands in ITER and w_m is in meters. Equating this to the usual expression for the current drive efficiency $I_{MA} = \gamma P_{MW}\,(m\, R_m\, n_{20})$, one finds for ITER that $P_{MW} = (10MW)\, n_{20}\, w_m/\gamma$. For anticipated values of $\gamma \approx 0.2$, 50 MW of power suffices to stabilize islands of even 1m full width.

The scaling of the threshold β via Eqs. (3,4) implies that neoclassical islands will be present in reactor scale tokamaks. However, electron cyclotron current drive stabilization requires only rather modest powers, both for ITER and present experiments. But ECCD can be expected to stabilize only low (m,n) modes and further research is needed to determine whether this suffices to prevent or reduce β saturation. We note also that in reverse shear regions neoclassical islands will not grow and that, in some theoretical formulations [12,15], negative bootstrap currents arising from ion temperature gradients can stabilize neoclassical island growth in the large aspect ratio limit and taking the flat density profiles expected for ITER. Since density gradients contribute more than temperature gradients to bootstrap current, one could expect β limits arising from neoclassical island to be more severe if density gradients occur near major rational surfaces. Experimentally, ECCD stabilization is just beginning[16-18].

3. DENSITY LIMIT

The density dependence of the β limit as well as ignition power balance point to the advantages to operating ITER at density of $n_e=1.3\cdot10^{20}m^{-3}$, a value 50% above the standard Greenwald density limit. While the bulk of tokamak experiments do obey the empirical Greenwald limit $(\bar{n}_{20})_{GR} = I_{MA}/\pi a_m^2$, which, in the case of ohmically heated plasmas, can be understood as a radiation limit [19,20], auxiliary heated experiments dedicated to transcending this limit have been successful, indicating that this limit is not fundamental. ASDEX-U [21] has used combined pellet injection and gas puffing to achieve H modes at $\bar{n}_e = 1.5\ (\bar{n})_{GR}$. In this experiment, pellets eventually reached the central region, leading to a peaked density profile while the edge density remained below the Greenwald limit. A modest confinement degradation was noted. Similarly, with pellet fueling, DIII-D has reached $\bar{n}_e = 1.5\ (\bar{n})_{GR}$ [22], while maintaining confinement at the level of JET/D3D scaling [23] . Again, observations indicate peaked density profiles and edge densities below the limit. TFTR has had similar success [24]. With strictly gas puff fueling, JET [25,26] attained discharges with densities exceeding $1.3\ (\bar{n})_{GR}$ at low current I_p=1MA but lacked the power to perform similar demonstrations at higher currents. A consistent interpretation is that a limit on edge density just inside the transport barrier does exist, and that peaked density profiles, made possible by pellet injection fueling, are needed to surpass simple Greenwald limit.

What physics can limit the edge density? In an H mode plasma, a transport barrier exists just inside the separatrix. Pressure gradients within the barrier region must be limited by ideal MHD considerations. Results from JT-60U confirm that the extent of the transport barrier scales with poloidal gyroradius and is given by $\Delta r=4\varepsilon^{1/2}\rho_\theta$ [27]. One can combine this result with the definition of the α, the limiting MHD gradient

$$\alpha = -\left(\frac{dP}{dr}\right)\left(\frac{2\mu_o R q^2}{B_t^2}\right) \tag{6}$$

and $B_\theta=\mu_o I_p\ \{\pi a\ (2+2\kappa^2)^{1/2}\}^{-1}=\varepsilon B_T q^{-1}((1+\kappa^2)/2)^{1/2}$ to reach a relation between the density and temperature at the top of the pedestal

$$n = \left(\frac{\alpha}{2}\right)\left(\frac{R}{a}\right)^{1/2}\left(\frac{M_i}{T}\right)^{1/2}\left(\frac{I_p}{e\,\pi\,a^2}\right)\left(\frac{2}{1+\kappa^2}\right)^{3/2}$$

$$n_{20} = \left(\frac{\alpha}{2}\right)\frac{I_{MA}}{\pi a_m^2}\left(\frac{R}{3\,a}\right)^{1/2}\frac{\sqrt{A}}{\sqrt{T_{100}}}\left(\frac{2}{1+\kappa^2}\right)^{3/2} \tag{7}$$

where T_{100} is the pedestal temperature in units of 100 eV. Measurements of α in JT-60U show that α≈2 and increases significantly with triangularity. Thus to reach densities consistent with the Greenwald limit, edge pedestal temperatures of less than 100 eV are required. At these temperatures, MARFES on closed field lines will provide a lower limit on plasma temperature and hence in combination with (7) place an upper limit on the plasma density. Approximately, the criterion for MARFE formation is

$$(8) \qquad n_{20} > \frac{30\,(T_{100})^{7/4}}{(L_{33})^{1/2}} \left(\frac{Z^2 - Z}{Z_{eff}\,(Z_{eff} - 1)} \right)^{1/2} \frac{1}{Rq}$$

where Z is the impurity ion charge state and L_{33} the radiation rate for the impurity ion in question [28]. In coronal equilibrium, the radiation rate for carbon has a secondary peak of $L_{33} \sim 1$ at $T_{100} \sim 1$. For present machines, Eq.(8) implies that a coronal equilibrium MARFE on a closed field line is difficult to produce. Nonetheless, ASDEX-U results [21] indicate that MARFES are associated with the density limiting process. The resolution may well lie in the substantial enhancement above coronal equilibrium radiation rates which result from charge exchange recombination [28] associated with gas puff fueling. Main chamber neutral gas pressures are in the 10^{-5}millibar range corresponding to neutral densities ~ 10^{17}-$10^{18}m^{-3}$, sufficient to cause important increases over coronal equilibrium. The power conducted into the separatrix region does not directly enter these arguments but it is clear power is needed to support radiative losses in the pedestal region. Excess power will serve to raise the pedestal temperature, resulting in a lower density limit via (8).

K. Borass [29] has recently proposed a model for a scrape-off-layer density limit based on the occurrence of complete detachment and shown that weak power scaling and almost inverse q_ψ scaling result. Magnetic field and current scaling enter through the assumed (Bohm) dependence of the cross-field diffusivity. Since a core plasma MARFE is close to complete detachment (within considerable uncertainties regarding radiating impurity concentrations, charge exchange enhancement of radiation rates, etc.) MARFES appear to be a common element of density limit models.

While the interpretive models proposed above are clearly not definitive, they do suggest approaches to increasing the density limit in ITER. (1) Increased triangularity (or generally improved edge magnetic configurations) will increase α in Eq.(8) and possibly ameliorate ELMs as well [7]. (2) Methods for central fueling which will peak the density profile. Compact torus fueling [30] is a new, but relatively unexplored, possibility. (3) Much reduced main chamber neutral pressure resulting from ITER's highly baffled divertor should minimize charge-exchange enhancement of radiation and hence inhibit MARFES.

4. CONCLUSION

Research over the last two years has elucidated new physics concerning two key operational limits for tokamaks in general and reactors in particular. Fortunately, relatively simple physics models are in accord with the general trend of observation and point to steps with a potential to improve the limits.

REFERENCES

[1] GREENWALD, M., et al., Nucl. Fusion **28** (1988) 2199.

[2] ITER CONFINEMENT DATABASE AND MODELING GROUP, in Plasma Physics and Controlled Nuclear Fusion Research 1994 (Proc. 15th Int. Conf. Seville, 1994), Vol. 2, IAEA, Vienna (1995) 525.

[3] BOUCHER, D., et al., IAEA-CN-64/FP-22, this volume.

[4] TAYLOR, T.S., et al., in Plasma Physics and Controlled Nuclear Fusion Research 1990 (Proc. 13th Int. Conf. Washington, 1990), Vol. 1, IAEA, Vienna (1991) 177.

[5] ZOHM, H., et al., "β-limiting phenomena in ASDEX Upgrade", Controlled Fusion and Plasma Physics (Proc. 23rd Eur. Conf. Kiev, 1996), Vol. 20C, European Physical Society, Geneva (1996).
[6] La HAYE, R.J., et al., Nucl. Fusion **37** (1997) 397.
[7] KAMADA, Y., et al., in Plasma Physics and Controlled Nuclear Fusion Research 1994 (Proc. 15th Int. Conf. Seville, 1994), Vol. 1, IAEA, Vienna (1995) 651; KAMADA, Y., et al., IAEA-CN-64/A1-6, these Proceedings, Vol. 1, p. 247.
[8] CHALLIS, C.D., et al., in Controlled Fusion and Plasma Physics (Proc. 22nd Eur. Conf. Bournemouth, 1995), Vol. 19C, Part II, European Physical Society, Geneva (1995) 69.
[9] CARRERA, R., et al., Phys. Fluids **29** (1986) 899.
[10] HEGNA, C.C., CALLEN, J.D., Phys. Fluids B **4** (1992) 1855.
[11] FITZPATRICK, R., Phys. Plasmas **2** (1995) 825.
[12] WILSON, H.R., et al., Phys. Plasmas **3** (1996) 248.
[13] ZABIÉGO, M., GARBET, X., Phys. Plasmas **1** (1994) 1890.
[14] CHANG, Z., et al., Phys. Rev. Lett. **74** (1996) 4663.
[15] WILSON, H.R., et al., The Collisionality Dependence of Tokamak β-Limits, Rep. UKAEA-FUS 336, Culham Lab., UK (1996).
[16] HOSHINO, K., et al., in Plasma Physics and Controlled Nuclear Fusion Research 1994 (Proc. 15th Int. Conf. Seville, 1994), Vol. 1, IAEA, Vienna (1995) 697.
[17] MORRIS, A.W., et al., in Controlled Fusion and Plasma Physics (Proc. 19th Eur. Conf. Innsbruck, 1992), Vol. 16C, Part I, European Physical Society, Geneva (1992) 423.
[18] MORRIS, A.W., et al., in Plasma Physics and Controlled Nuclear Fusion Research 1990 (Proc. 13th Int. Conf. Washington, 1990), Vol. 1, IAEA, Vienna (1991) 797.
[19] PERKINS, F.W., HULSE, R.A., Phys. Fluids **28** (1985) 1837.
[20] ASHBY, D.E.T.F., HUGHES, M.H., Nucl. Fusion **21** (1981) 91.
[21] MERTENS, V., "High density operation in auxiliary heated ASDEX Upgrade discharges", Controlled Fusion and Plasma Physics (Proc. 23rd Eur. Conf. Kiev, 1996), Vol. 20C, European Physical Society, Geneva (1996).
[22] MAHDAVI, M.A., et al., IAEA-CN-64/A4-3, these Proceedings, Vol. 1, p. 397.
[23] SCHISSEL, D.P., et al., Nucl. Fusion **31** (1991) 73.
[24] BELL, M.G., et al., Nucl. Fusion **32** (1992) 1585.
[25] CAMPBELL, D.J., et al., in Controlled Fusion and Plasma Physics (Proc. 21st Eur. Conf. Montpellier, 1994), Vol. 18B, Part I, European Physical Society, Geneva (1994) 2.
[26] SAIBENE, G., et al., "Influence of active pumping on density and confinement behavior of JET plasmas", Controlled Fusion and Plasma Physics (Proc. 23rd Eur. Conf. Kiev, 1996), Vol. 20, European Physical Society, Geneva (1996).
[27] HATAE, T., et al., Review of JT-60U Experimental Results from Fegruary to October 1995, Rep. JAERI-96-018, Japan Atomic Energy Research Inst. (1996).
[28] POST, D.E., J. Nucl. Mater. **220–222** (1995) 143.
[29] BORRASS, K., et al., A Scrape-Off-Layer Based Model for Hugill–Greenwald Type Density Limits, Rep. IPP 5/70, Max-Planck-Institut für Plasmaphysik, Garching (1996).
[30] RAMAN, R., et al., Phys. Rev. Lett **73** (1994) 3101.

DISRUPTION, VERTICAL DISPLACEMENT EVENT AND HALO CURRENT CHARACTERIZATION FOR ITER

J. WESLEY, N. FUJISAWA, S. ORTOLANI[1], S. PUTVINSKI,
M.N. ROSENBLUTH, ITER JOINT CENTRAL TEAM

Abstract

DISRUPTION, VERTICAL DISPLACEMENT EVENT AND HALO CURRENT CHARACTERIZATION FOR ITER.

Characteristics, in ITER, of plasma disruptions, vertical displacement events (VDEs) and the conversion of plasma current to runaway electron current in a disruption are presented. In addition to the well known potential of disruptions to produce rapid thermal energy and plasma current quenches and theoretical predictions that show the likelihood of ~50% runaway conversion, an assessment of VDE and halo current characteristics in vertically elongated tokamaks shows that disruptions in ITER will result in VDEs with peak in-vessel halo currents of up to 50% of the predisruption plasma current and with toroidal peaking factors (peak/average current density) of up to 4:1. However, the assessment also shows an inverse correlation between the halo current magnitude and the toroidal peaking factor; hence, ITER VDEs can be expected to have a product of normalized halo current magnitude times toroidal peaking factor of ≤75%.

1. INTRODUCTION

Plasma disruptions, vertical displacement events (VDEs) and the conversion of plasma current to runaway electron current in the current quench phase of a disruption, VDE or pellet injection initiated plasma shutdown pose a challenging and interconnected set of thermal, structural and lifetime design issues for the ITER in-vessel plasma facing components and their supporting structures. Design of these components and evaluation of their performance require specification of disruption, VDE and runaway conversion parameters. To promote the fusion community's involvement in collecting data on these effects and developing such design specifications, the ITER Joint Central Team and the ITER Expert Group on Disruptions, Plasma Control and MHD (S.V. Mirnov, J. Wesley, N. Fujisawa, O. Gruber, T.C. Hender, N. Ivanov, S. Jardin, J. Lister, F.W. Perkins, M.N. Rosenbluth, N. Sauthoff, T.S. Taylor, S. Tokuda, K. Yamazaki, R. Yoshino) have reviewed past and present physics R&D data on disruptions, VDEs and runaway electrons and have compiled disruption related design basis specifications and a database on halo current characteristics. This paper presents a summary of this work, with emphasis on analysis

[1] Present address: Istituto Gas Ionizzati, Euratom-ENEA-CNR Association, Padua, Italy.

of data on halo current magnitude and toroidal asymmetry. Disruption and VDE related R&D areas where more experimental or theoretical work is needed are also noted.

2. DESIGN BASIS SPECIFICATION FOR DISRUPTIONS

The basis used herein for assessing ITER disruption and VDE related design issues is an ignited DT plasma, with an initial current of I_{p0} = 21 MA, as will be obtained at q_{95} = 3.0 with a single null divertor, R = 8.14 m, a = 2.8 m, B = 5.7 T, κ_{95} = 1.60 and δ_{95} = 0.25. This plasma produces 1.5 GW fusion power at $\beta_N = \langle\beta\rangle aB/I \approx 2.4$; thermal and magnetic energies, W_{th} and W_{mag}, are, respectively, about 1.1 and 1.2 GJ. Here, W_{mag} includes the ex-plasma magnetic energy within the nuclear shield backplate. This backplate and the torus vacuum vessel, which have a combined toroidal resistance of $\approx 4\ \mu\Omega$ and an effective toroidal L/R time constant of ~1 s, determine the passive stability of the plasma with respect to n = 0 modes (and, hence, the time-scale of the VDE evolution) and also limit the magnetic energy dissipation from the disruption or VDE current quench to $\sim W_{mag}$.

Specifications for ITER disruptions are summarized in Table I. The basis for these specifications is presented in Ref. [1]. For design purposes, the most important parameters are the durations of the thermal and magnetic energy quenches and the partitioning of the corresponding energies among the divertor and first wall (FW) surfaces. The thermal quench duration is estimated to be 1–10 ms; the range reflects uncertainty in the extrapolation of the data to ITER size and plasma temperature and also the observation that thermal quenches are sometimes single step and sometimes

TABLE I. DESIGN BASIS SPECIFICATION FOR ITER DISRUPTIONS[a]

Parameter	Value (range)	Comment
Thermal quench duration	1–10 ms	Single or multistep; see text
Fraction of W_{th} to divertor	80–100%	By conduction
Fraction of W_{th} to FW (baffle)	≤30%	By radiation (FW) or conduction (baffle)
In-divertor partitioning (inside/outside target)	2:1–12	Significant uncertainty; see text
Current quench duration[b]	25 (10–300) ms	Duration >10 ms will result in appreciable VDE
Maximum current decay rate[b]	2 MA/ms	
Fraction of W_{mag} to FW	80–100%	By radiation, with poloidal peaking factor of ~2
Fraction of W_{mag} to FW or baffle	0–20%	By conduction and localized radiation, during VDE

[a] For component design and lifetime assessment purposes: specifications are not self-consistent with respect to total energy accountability.

[b] In the absence of thermal to runaway electron current conversion, see Section 4.

multistep, wherein energy loss occurs in two or more rapid steps separated by a period that extrapolates to ~10 ms for ITER parameters.

The location of the thermal quench deposition will normally be within the divertor channels. The 80–100% range reflects the possibility that up to ~20% W_{th} may be deposited on the divertor entrance baffle and/or the FW, since SOL widening of up to ten times is sometimes seen in present experiments. Partitioning of the in-divertor energy between the inside and outside channels is relatively uncertain; however, data typically show more energy to the inside channel.

Dissipation of W_{mag} (80–100%) in the current quench phase will be primarily by radiation to the FW, with a poloidal peaking factor of ≤2. More localized deposition of the magnetic energy on the FW can also be expected if significant plasma motion (VDE) occurs during a slow (≥100 ms) current quench. Dynamic equilibrium evolution models that self-consistently include ex-plasma halo current must be used to predict this evolution and the resulting magnitude of such deposition for ITER. The resulting energy loadings are, at present, relatively uncertain, but are estimated to be as high as 60 MJ/m^2.

3. VDE AND HALO CURRENT CHARACTERISTICS

Disruptions and/or loss of plasma vertical position control in ITER will result in the onset of a VDE, with subsequent onset of plasma–wall contact and ex-plasma ('halo') current flow, I_h, that will close poloidally through conducting in-vessel components with resulting $\mathbf{I}_h \times \mathbf{B}_T$ forces on these components and their supporting structures. For design assessment purposes, the key parameters needed are the maximum magnitude and the toroidal distribution of the in-vessel halo current. To support empirical assessment of these design parameters for ITER, we have compiled a database of the magnitude and toroidal distribution of in-vessel halo currents observed during VDEs in vertically elongated tokamaks. Our evaluation of this database shows that: (1) the maximum halo current magnitude ($I_{h,max}$) to be expected in ITER with a full size $q_{95} = 3$ plasma can be as high as 50% of the initial predisruption or pre-VDE plasma current (I_{p0}); (2) the toroidal peaking factor (TPF = $j_{max}/\langle j \rangle$, where $\langle\ \rangle$ denotes a toroidal average) can be as high as 4; (3) there is a general inverse correlation between $I_{h,max}/I_{p0}$ and TPF; and (4) the resulting magnitude of $I_{h,max}/I_{p0}$ within a given experiment itself exhibits an apparently random variation that is likely to reflect an underlying variance in the post-disruption or pre-VDE plasma current and safety factor profiles and/or the plasma equilibrium and profile evolution during the VDE.

Table II summarizes the overall parameters of the database, which comprises 2382 data sets from six tokamaks. Each data set includes measurements of B, I_{p0}, $q_{95}(0)$, $\kappa_x(0)$ and $I_{h,max}$ and, when available, TPF evaluated at (near) the time of $I_{h,max}$ (four tokamaks). The data sets from each experiment encompass an appreciable range of I_{p0} and q_{95} and, for JET and Alcator C-Mod, also an appreciable range of κ_x.

TABLE II. HALO CURRENT DATABASE SUMMARY

Experiment	N_{total}	N_{κ}[a]	N_{TPF}	$N^{a}_{TPF,\kappa}$	κ_x	q_{95}	I_{p0}(MA)
ASDEX-U	78	40	78	40	1.01–1.78	3.1–6.5	0.37–1.18
C-Mod	1477	561	552	301	0.95–1.96	2.2–10.1	0.18–1.16
COMPASS-D	53	53	20	20	1.6	2.9–7.2	0.10–0.19
DIII-D	18	18	18	18	1.62–1.92	2.7–5.6	0.96–1.49
JET	708	207	0	0	1.02–1.92	2.4–12.5	1.00–6.96
JT-60U	48	0	0	0	1.25–1.52	2.0–11.0	0.44–1.53

[a] The subscript κ denotes $\kappa_x \geq 1.6$.

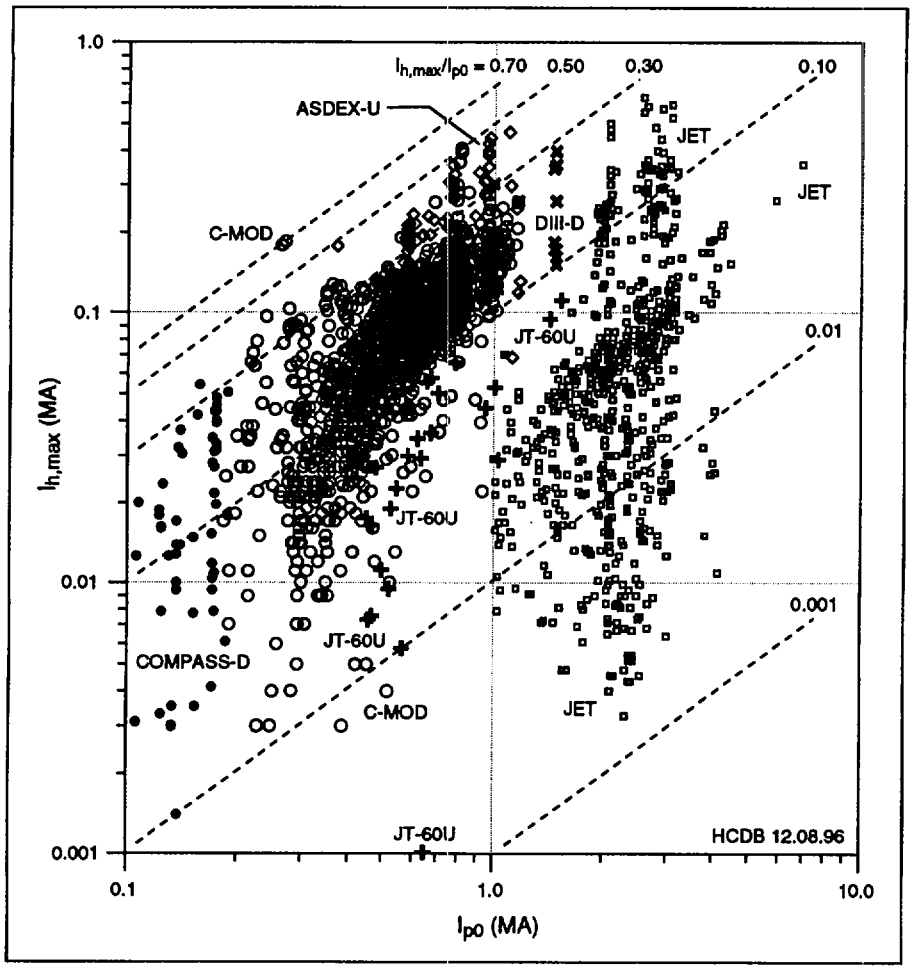

FIG. 1. Halo current database: maximum halo current magnitude versus initial plasma current.

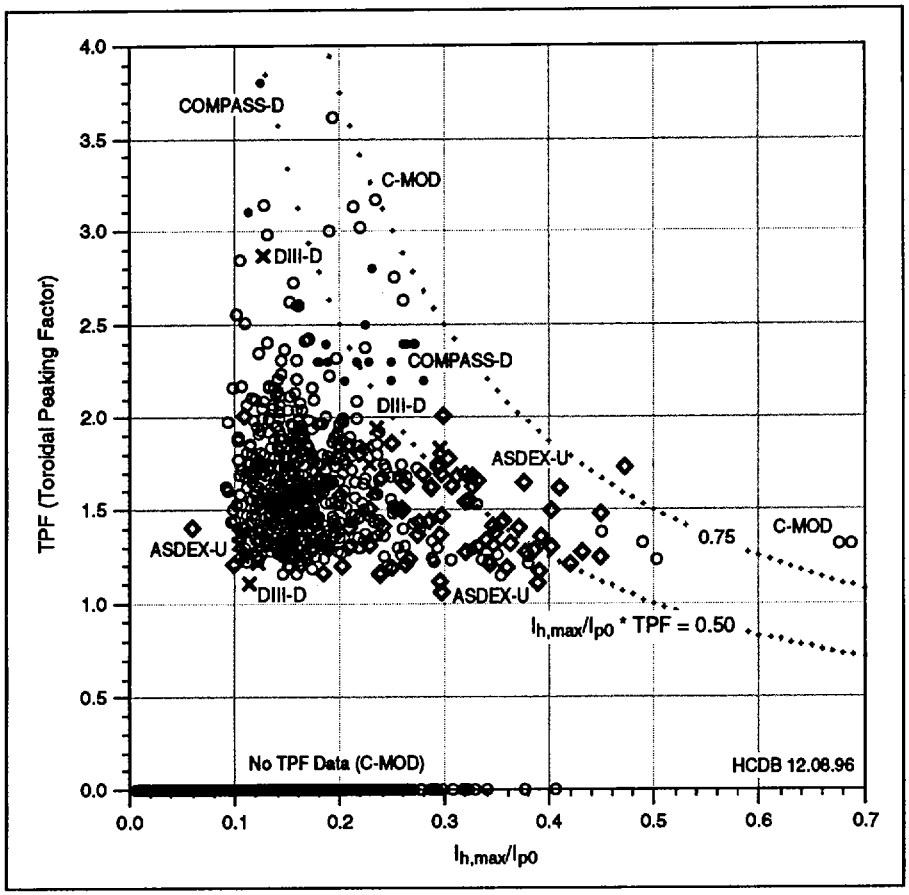

FIG. 2. Halo current database: toroidal peaking factor (TPF) versus normalized halo current magnitude.

Figures 1 and 2 show some of the key features of the database. Figure 1 shows that, while $I_{h,max}$ generally increases with I_{p0}, $I_{h,max}$ in a given device at fixed I_{p0} can typically vary by a factor of ~10 (C-Mod and COMPASS-D) and in some cases (JET) by a factor of nearly 100.

We have examined the scaling behaviour of the data from each experiment and conclude that some of the single experiment variances reflect the effects of the ranges of q_{95} and/or κ_x (elongation at the plasma surface or separatrix). Here, an experiment specific analysis of the dependence of $I_{h,max}/I_{p0}$ on q_{95} and/or κ_x shows two scalings. In the C-Mod data, the mean value of $q_{95}I_{h,max}/I_{p0}$ averaged over a finite q_{95} interval is essentially constant (±10%) and independent of κ_x. Accordingly, $I_{h,max}/I_{p0}$ scales as q_{95}^{-1}. This scaling has previously been reported in Ref. [2]. In contrast, in ASDEX-U

TABLE III. HALO CURRENT MAGNITUDE SCALING AND VARIANCE

Experiment	$I_{h,max}/I_{p0}$ scaling versus q_{95}	$I_{h,max}/I_{p0}$ scaling versus κ_x	$I_{h,max}/I_{p0}$ and $q_{95} = 3$, $\kappa_x \geq 1.6$	Maximum $I_{h,max}/I_{p0}$	Maximum $I_{h,max}/I_{p0}$ [$\kappa_x \geq 1.6$]
ASDEX-U	constant	no data	0.31 ± 0.08	0.47	0.45
C-MOD	q_{95}^{-1}	constant	0.20 ± 0.03	0.68	0.31
COMPASS-D	$q_{95}^{-1} \rightarrow$ constant	no data	0.20 ± 0.12	0.34	0.34
DIII-D	$q_{95}^{-1} \rightarrow$ constant	no data	0.16 ± 0.06	0.30	0.30
JET	$q_{95}^{-1} \rightarrow$ constant	increases for $\kappa_x \geq 1.4$	0.09 ± 0.07	0.24	0.24
JT-60U	constant	no data	0.11 ± 0.06	0.23	no data

and JT-60U data, $I_{h,max}/I_{p0}$ is essentially independent of q_{95}. These data sets have only a limited κ_x variation, so we cannot determine the κ_x dependence. However, we find no indication of a strong κ_x effect.

Data from COMPASS-D, DIII-D and JET are consistent with either scaling, and the scatter in the data is sufficiently large to preclude distinguishing between the two scalings. For JET data, there is sufficient range in κ_x to show a clear elongation effect: the average $I_{h,max}/I_{p0}$ is a rapidly increasing function of κ_x for $\kappa_x \geq 1.4$. In Fig. 1, this κ_x dependence is responsible for the cluster of JET data points with $I_{h,max}/I_{p0} \geq 0.1$ at $2 \text{ MA} \leq I_{p0} \leq 3 \text{ MA}$.

Table III summarizes the q_{95} and/or κ_x scaling behaviour inferred from our analysis and the corresponding extrapolation of the data to 'ITER-like' conditions of $q_{95} = 3$ and $\kappa_x \geq 1.6$. The mean value and the corresponding standard deviation (1σ) are presented. For COMPASS-D, DIII-D and JET data, where the q_{95} scaling is ambiguous, we use the q_{95}^{-1} scaling for the extrapolation, which results in a ~20% increase in magnitude of $I_{h,max}/I_{p0}$. The actual maximum values of $I_{h,max}/I_{p0}$ for both the full data set and with selection of only $\kappa_x \geq 1.6$ cases are presented. With the single exception of the full C-Mod data set, the observed maximum halo currents fall within the mean plus a (2–3)σ error bar, and hence we conclude that the mean scaling plus variance provides a valid way to compare normalized $I_{h,max}$ among experiments. Here, the data fall into three relatively distinct groups: high (ASDEX-U), medium (C-Mod, COMPASS-D, DIII-D) and low (JET and JT-60U).

Figure 2 shows a plot of TPF versus $I_{h,max}/I_{p0}$: there is a general inverse correlation between these quantities. Except for two high $I_{h,max}/I_{p0}$ C-Mod points ($\kappa_x \approx 1.5$) and the single ASDEX-U point at $I_{h,max}/I_{p0} = 0.48$ (kx ≈ 1.0), all data fall within a domain bounded by $\text{TPF} \times I_{h,max}/I_{p0} = 0.75$, $I_{h,max}/I_{p0} \leq 0.50$ and $\text{TPF} \leq 4$. We recommend this domain as a 'worst case' specification for ITER in-vessel component design. In Fig. 2, we also show a contour for $\text{TPF} \times I_{h,max}/I_{p0} = 0.50$. While our choice of the precise magnitude of this contour is somewhat subjective, we propose that it is representative of a 'typical' VDE.

The inverse correlation between $I_{h,max}/I_{p0}$ and TPF is qualitatively consistent with a VDE/halo current model where the shrinking plasma generates near surface helical currents so as to remain in force free equilibrium as the safety factor at the last closed flux surface in the plasma core falls to or below unity. Erosion ('scrape-off') of the resulting n = 0 and n = 1 current distribution results in the observed toroidally asymmetric current distribution and inverse TPF correlation: either a low q force free dynamic equilibrium is achieved with a large poloidal current and nearly n = 0 symmetry, or larger helical perturbations are driven by the deviations from the stable profiles. In principle, such behaviour can be modelled with a 3-D MHD code, and we note the urgent need for application of such modelling to both experimental data and ITER design studies.

We also note that our recommended design domain is determined by data from COMPASS-D, DIII-D and C-Mod and from ASDEX-U, respectively, filling in the low and high $I_{h,max}/I_{p0}$ portions of the domain. Given the high electromagnetic loads that this domain implies, and also given that peak $I_{h,max}/I_{p0}$ seen in JET and JT-60U is significantly lower than our worst case prediction, we conclude that future experimental and/or theoretical R&D is needed to narrow the range of uncertainty about maximum halo current magnitude and toroidal peaking and the relationship of these parameters to predisruption or pre-VDE plasma parameters. In addition, as we shall describe below, an 'integrated' disruption/VDE/runaway modelling capability will ultimately be needed to make definitive self-consistent design basis predictions for ITER.

4. RUNAWAY CURRENT CONVERSION

In ITER, the high electric fields produced in either disruptions or the proposed use of high Z impurity pellet injection to effect a fast fusion power and current shutdown are predicted to produce substantial conversion of plasma current to runaway electron current. Here, knock-on avalanche multiplication of minute levels of pre-shutdown superthermal electrons will result in wholesale ($\geq$ 50%) conversion of the initial plasma current to runaway current (up to 16 MA, with E ~10 MeV) [3]. Similar runaway conversion can be expected during 'natural' disruptions and, possibly, during the current collapse phase of a VDE. While our conclusions about runaway conversion in ITER are subject to caveats about prompt loss of runaways owing to MHD instabilities and open flux surfaces, our modelling suggests that runaway effects must be accounted for in the prediction of ITER disruption, VDE and fast shutdown characteristics. We also note that the predicted levels of runaway current conversion will modify the current quench and VDE/halo current characteristics of ITER high current disruptions ($I \geq$ ~10 MA) relative to the characteristics that we have inferred above from disruptions and/or VDEs in existing lower current experiments where wholesale runaway conversion is absent. Accordingly, we caution that aspects of disruptions and halo current formation that depend on current quench dynamics are

likely to be significantly modified when runaway conversion effects are present. Given that appreciable runaway conversion can be expected only for plasma currents ≥10 MA, we also find that definitive prediction of ITER disruption, fast shutdown and VDE characteristics will require a predictive simulation model that incorporates all relevant physics effects — including 3-D MHD equilibrium, halo current and runaway conversion — involved. Development and validation of such an 'integrated' disruption/VDE model is identified as an urgent and yet incomplete ITER physics R&D requirement.

ACKNOWLEDGEMENTS

The ITER Engineering Design Activities are conducted by the European Atomic Energy Community, Japan, the Russian Federation and the United States under the auspices of the IAEA. Much of the work presented herein took place during the 1994–1996 meetings of the ITER Expert Group on Disruptions, Plasma Control and MHD. The contributions of the Group Members and additional participants in these Meetings and the special help of the Alcator C-Mod, ASDEX-U, COMPASS-D, DIII-D, JET and JT-60U experimental teams and their respective disruption data co-ordinators — R.S. Granetz, G. Pautasso, A.W. Morris, A.G. Kellman, M. Johnson and R. Yoshino — for data and collaboration during the course of our halo current database analysis are gratefully acknowledged.

REFERENCES

[1] SCHÜLLER, F. C., Plasma Phys. Control. Fusion **37** (1995) A135.
[2] GRANTEZ, R., et al., Nucl. Fusion **36** (1996) 545.
[3] ROSENBLUTH, M., IAEA-CN-64/FP-26, this volume.

RUNAWAY ELECTRONS AND FAST PLASMA SHUTDOWN*

M.N. ROSENBLUTH, P.B. PARKS[1], D. POST,
S. PUTVINSKI, N. PUTVINSKAYA[3], H.A. SCOTT[2],
ITER JOINT CENTRAL TEAM

[1] General Atomics,
San Diego
[2] Lawrence Livermore National Laboratory,
Livermore
[3] Science Applications International Corporation,
San Diego

California, United States of America

Abstract

RUNAWAY ELECTRONS AND FAST PLASMA SHUTDOWN.

In high current tokamaks such as ITER, a primary problem is the ability to withstand disruptions. While the prompt heat load (primarily on the divertor) during the thermal quench is of some concern, a more significant worry are the electromechanical stresses induced by the subsequent current quench with its attendant vertical displacement event (VDE), which leads to the current channel hitting the wall, the development of asymmetric halo currents, etc., on a time-scale of about one second (the L/R time of the first wall). These stresses would limit the number of disruptions which could be tolerated. It would be desirable to ensure that the current decays rapidly on a time-scale of 0.1 to 1 s to lessen such interactions. This has led to the concept of the 'killer pellet', which could enhance radiative energy loss, lead to a low plasma temperature and, hence, a rapid decay. However, the situation is greatly complicated by the prospect that with the high voltages induced in a rapid current decay a large number of runaway electrons will be produced — in fact, the discharge may be converted to a long lived runaway discharge. In this paper, aspects of the runaway physics and the potential for fast plasma shutdown are considered. Avoiding runaway generation with assurance appears to require a high density injection of deuterium.

---

* This paper is an account of work undertaken within the framework of the ITER EDA Agreement. Neither the ITER Director, the parties to the ITER EDA Agreement, the IAEA or any agency thereof, or any of their employees, makes any warranty, express or implied, or assumes any legal liability or responsibility for the accuracy, completeness, or usefulness of any information, apparatus, product, or process disclosed, or represents that its use would not infringe privately owned rights. Reference herein to any specific commercial product, process or service by tradename, trademark, manufacturer, or otherwise, does not necessarily constitute its endorsement, recommendation, or favouring by the parties to the ITER EDA Agreement, the IAEA or any agency thereof. The views and opinions expressed herein do not necessarily reflect those of the parties to the ITER EDA Agreement, the IAEA or any agency thereof.

1. PHYSICS OF RUNAWAYS

In the presence of a parallel electric field, the acceleration of an electron to higher energies will exceed the plasma drag for an electron moving parallel to $\mathcal{E}$ if $\hat{\mathcal{E}} = \mathcal{E}/\mathcal{E}_0 > (1 + 1/p^2)$. When pitch angle scattering is neglected, such an electron will run away to very high energies. Here, p is electron momentum in units of mc and the critical field $\mathcal{E}_0 \equiv 4\pi n_e e^3(\ln \Lambda)/mc$.

We note that the high energy electrons of interest will be slowed down by both free plasma electrons and bound electrons such as will be present at high Z and low T, although for the latter the Coulomb logarithm will be smaller. A useful approximation is $n_e = n_f + n_{b/2}$. Numerically, $\mathcal{E}_0 \approx 0.1\ n_e(v/M)$ with n_e in units of 10^{14} cm^{-3}. For $\mathcal{E} < \mathcal{E}_0$, no runaways are possible. We will show that for $\mathcal{E} > \mathcal{E}_0$ a large runaway formation may be expected. We note that if we wish to dissipate the 200 V·s ITER flux in 1/2 s to lessen the wall interaction, then we would have $\mathcal{E} \approx 400/2\pi R = 8(v/M)$. Hence, avoiding runaways requires densities of the order of 10^{16} cm^{-3} (somewhat less when pitch angle scattering is considered). Sustaining ITER currents requires $10^3\ Z_{eff}/T_{eV}^{3/2} = \mathcal{E}(v/M)$; thus, large electric fields are initially generated. If a runaway discharge is produced, the electric field can be expected to asymptote to $\mathcal{E}_0$ to sustain the current; hence, lifetimes of about $40/n_{14}$ s are predicted.

We have identified four possible sources of runaways: (a) Dreicer source: boiling off the tail of the thermal distribution. Non-relativistically, the runaway energy is $mc^2/2\hat{\mathcal{E}}$, and we expect runaway production proportional to $\exp(-mc^2/4\hat{\mathcal{E}}T)$. This is the predominant source of runaways in present experiments. It is difficult to estimate because of the strong dependence on rapidly evolving disruption quantities. For ITER killer pellet and plausible disruption scenarios, it appears quite negligible. (b) Tail source: electrons which are magnetically trapped when the field lines open during the thermal quench are not initially lost [1] and could serve as an initial source of runaway electrons. Similarly, with a large, high Z killer pellet a very rapid (< 10 ms) thermal quench allows survival of a high energy tail. However, such rapid thermal quenches would in any event lead to first wall damage by surface heating and should be avoided [2]. Again, we estimate for ITER thermal quench times > 20 ms so that high energy tails will slow down well before the electric field exceeds the runaway thresholds. However, it is difficult to be certain that some rapid localized disruption might not produce an adequate source. (c) In ITER, some fast electrons are produced by tritium decay. These can provide a runaway source for $\hat{\mathcal{E}} > 15$. A source of higher energy electrons is available from Compton scattering of the γ rays emitted by the wall [3]. The estimated flux is 3×10^{12} cm$^{-2}\cdot$s^{-1}. (There is also a large source of β decay electrons which cannot, however, cross the field.) This source dominates in most ITER scenarios. Even though it is quite small it is exponentially amplified by: (d) Avalanching [4]: a relativistic electron makes finite angle collisions with plasma (or bound) electrons. The cross-section for producing a secondary of energy $\gamma = E/mc^2 \equiv \sqrt{1 + p^2}$ is easily found to be

$\sigma = 2\pi(e^2/mc^2)^2 d\gamma/(\gamma - 1)^2$. The secondary can also be seen from kinematical considerations to be emitted nearly perpendicularly to the primary momentum (and hence the magnetic field), i.e. $p_\perp^2/2 = \gamma - 1$. Accounting for this, we find that secondaries will run away for $p^2 > 2(\hat{\mathcal{E}} - 1)^{-1}$ so that the runaway density (or current) exponentiates with growth $(n_r)^{-1}\partial n_r/\partial t = e\mathcal{E}/2mc \ln \Lambda\, a(Z)$, where $a(Z)$ represents the effect of pitch angle scattering, magnetic trapping and relativistic effects as discussed below. Note that, except for this rather weak dependence, the number of e-foldings to be expected is independent of the plasma properties and only depends on the volt-seconds. For ITER, $N = 80/a(Z)$. Hence, even the very weak radioactive sources are in many cases able to exponentiate so as to produce a runaway current of about 70% of the initial current. Since the electric field is highest on the axis, the current distribution produced is essentially the initial current density over the inner two thirds of the discharge area.

For a more quantitative calculation, it is necessary to solve the bounce averaged relativistic Fokker–Planck equation. The equation may be solved in two limits: (1) neglecting the pitch angle scattering, and (2) regarding pitch angle scattering as large (i.e., a large Z expansion). An approximate joining formula that fits both limits is:

$$\frac{1}{n_r}\frac{\partial n_r}{\partial t} = \frac{e\mathcal{E}(\hat{\mathcal{E}} - 1.2)}{mc \ln \Lambda} = \sqrt{\frac{f_c}{\bar{Z} + 5}}\left\{\hat{\mathcal{E}}^2 + 3(\bar{Z} + 1)^2/(\bar{Z} + 5)\right\}^{-1/2} \quad (1)$$

Here, $\hat{\mathcal{E}} = \mathcal{E}/\mathcal{E}_0$ as defined earlier, f_c is the fraction of untrapped particles (at low aspect ratio, $f_c \approx 1 - 1.5\sqrt{\varepsilon}$), and $\bar{Z}$ is roughly Z_{eff} as determined from the bare nuclear charges, with the Coulomb logarithm for high Z replaced by $5 - 0.33 \ln(Z)$ as predicted for a Thomas–Fermi atom. The growth and saturation of the avalanche and the evolution of the distribution function are being studied by Monte Carlo and Fokker–Planck codes [5].

The physics outlined in this section seems fairly robust. The principal assumption is that following the thermal quench, with its consequent removal of the pressure and current gradient driving forces for instability, good and quiescent flux surfaces re-form on which runaway can occur. The principal evidence that this is true are the runaways observed in many disruption and 'killer pellet' experiments [6]. Unfortunately, there are no experiments well enough diagnosed to permit evaluation of the very sensitive Dreicer source. Such well diagnosed experiments are needed for the ITER design, especially high density injection into high current discharges where substantial avalanching could be studied.

2. SIMULATIONS

In order to study runaway evolution and current quench, a simple 1-D time evolution cylindrical model was set up consisting of:

(1) Faraday's law: $\nabla^2\mathcal{E} = 4\pi\frac{\partial}{\partial t}\left[\sigma\mathcal{E} + j_r\right]$, with a circuit equation for the wall.

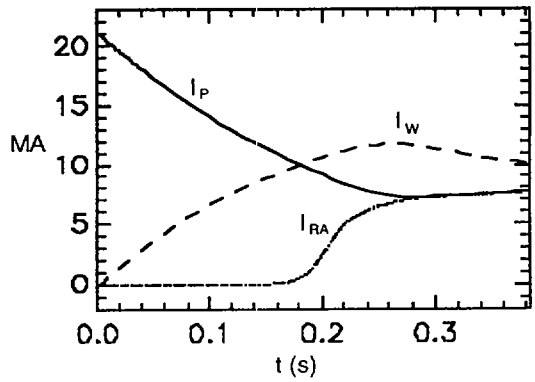

FIG. 1. Plasma, wall and runaway currents after injection of 10^{18} m^{-3} Xe into 10^{20} m^{-3} ITER DT plasma.

(2) A temperature evolution equation including ohmic heating and coronal equilibrium radiation with preliminary estimates of line trapping effects. The temperature, of course, determines resistivity and hence electric field, current decay and runaway production. A crude treatment of MHD introduces large thermal diffusion locally whenever $q < 1$, which occurs in some cases near the edge of the shrinking pre-runaway current profile.

(3) Equation (1), with the addition of the sources described above, was used to describe the runaway evolution. In most of the simulations, fixed impurity and density profiles were assumed; since the emphasis was on killer pellet simulations, it was assumed that initially the plasma pressure and current profiles were those present before the disruption.

The results of a typical simulation are shown in Fig. 1 for a xenon injection (uniform profile) of $n_{xe} = 0.01 n_D$, with $nD = 10^{14}$ cm^{-3}. Initially, radiative cooling occurs with the plasma cooling down to about 15 eV in 50 ms. This cooling is in the form of a 'wave' proceeding in from the initially cool edge towards the centre. The runaway avalanche then begins until by 250 ms the residual plasma current (8 MA) is completely carried by runaways with 12 MA in the wall. The runaway current then gradually increases to about 12 MA as the wall current decays and would persist for another 20 s, if discharge motion and the wall interaction to be expected on this long time-scale were neglected. The plasma temperature with lessened ohmic heating falls to about 1 eV in this latter phase. At very low ($< 10^{-5}$) Xe concentration the temperature in the nearly pure hydrogen discharge is high enough so that the electric field remains below critical and no runaways occur. As the concentration increases so does the runaway current up to about 15 MA until above 10^{-3}, when pitch angle scattering lowers the avalanche growth. Finally, above 10^{-2} the thermal quench is rapid enough to bring in the tail source and lead to high (20 MA) runaway currents, even with weak avalanching. It should be noted that about 25 e-foldings are required

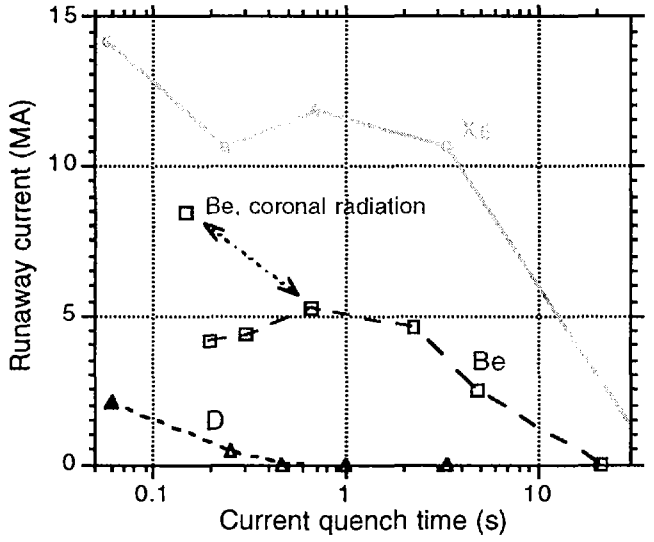

FIG. 2. Magnitude of runaway current as function of current quench time for additions of varying amounts of D, Be and Xe to a 10^{20} DT discharge.

for the weak gamma source to build up while the internal flux decay can provide about 40 e-foldings on-axis.

Other injected elements showed a similar behaviour with the evolution of large runaway currents, except for H (or D), where the radiative loss was low enough to allow the temperature to stabilize at 30 eV where $\mathcal{E} < \mathcal{E}_0$, even at densities as high as 5×10^{15} cm^{-3}. This was possible because the strong line radiation in H is trapped so that, in effect, only the continuum radiation leads to cooling. We note that by keeping the electric field below critical we remove uncertainties connected with the sources. We are investigating whether line trapping would allow low Z injection (e.g. Be or He) to avoid runaway formation with fast shutdown, but this seems unlikely. Figure 2 is a summary of our results, plotting the expected peak runaway current as a function of the current quench time, defined as the time at which the Ohmic current falls to half its initial value. This time should be longer than about 0.1 s to avoid wall damage from too rapid a thermal quench and less than 1 s to lessen wall forces by a factor of two. As noted earlier, high Z material such as Xe gives rise to very high runaway levels at all concentrations, while D has few or no runaways, even at densities high enough to produce current quenches in the desired time range. Our results for Be are provisional since there is considerable sensitivity to the radiation transport model employed. The curve is for an ad hoc model assuming that most of the line radiation is trapped, except for the one coronal equilibrium point indicated. Detailed transport calculations using the CRETIN code are in progress. We have not, as yet, attempted to model possible direct losses of runaways to the boundary during MHD activity.

3. INSTABILITIES

While instabilities could possibly inhibit runaway formation by increasing effective pitch angle scattering and possibly inducing ripple loss, they also increase the prospect of uncontrolled localized deposition and damage. A prevalent form of MHD activity to be expected with shrinking current channels is the tearing mode. However, we find that enhanced avalanching in the magnetic islands actually leads to stabilization of the islands at about 1 cm width for $q > 1$. The condition $q < 1$ is not expected to develop in the runaway discharge until after the current channel strikes the wall. High frequency modes such as the fan instability have the potential to be driven unstable by beam anisotropy, $T_\perp \ll T_\parallel$. Such instabilities can occur at the Doppler cyclotron resonance, $k_\parallel c = \omega + \Omega_{0\gamma}$, where $\Omega_0 = eB/m_0c$. Solving the cold plasma dispersion relation, we find the most dangerous mode to be the upper hybrid mode for which $\omega^2 = \omega_p^2 + \Omega_0^2/(1 + \omega_p^2/k_\perp^2c^2)^2$, when the resonance condition is satisfied. To determine stability we must compare the stabilization by means of background plasma electron–ion collisions with the beam destabilizing term. For a beam distribution given by $f = \exp[-\sqrt{1 + \bar{p}^2}/\bar{\gamma} - p_\perp^2/\bar{p}^2]$, the stability condition for the most dangerous perpendicular wavelength ($k_\perp = \Omega/\bar{p}$) is:

$$\frac{\nu_{ei}}{\omega_{pe}} > 0.1 \frac{\omega_{pr}^2 \bar{\gamma}}{\Omega_0^2(1 + \bar{p}^2\omega_{pe}^2/2\Omega_0^2)} \tag{2}$$

where $\omega_{pr}^2 = 4\pi n_r e^2/m_e$. With the expected ITER current densities (100 A/cm^2), and energies of $\bar{\gamma} = 20$, this yields the stability condition $Z_{eff}\sqrt{n_{14}}/T^{3/2} > 10^{-2}$, even for $\bar{p} = 0$. This would clearly be well satisfied for most likely post-disruption or killer pellet scenarios, where $T \sim 1$–10 eV is typical. Finally, we note that the field ripple resonance $k_\parallel c = \Omega_0/\gamma$, which has been found to limit the runaway energy in TEXTOR and ASDEX [7], is not important for ITER, since short wavelength field ripple components fall off rapidly with the radius.

4. EFFECT OF RUNAWAYS ON THE WALL

First, we estimate the energy spectrum to be expected for the runaways during avalanching. Comparing the avalanche growth rate with the electron acceleration $d\gamma/dt \equiv e\mathcal{E}/mc$, we predict an exponential spectrum, $\exp(-\gamma/\bar{\gamma})$, with $\bar{\gamma} = 2 \ln \Lambda\, \alpha(Z)$. For $\alpha(Z) = 1$, this implies 15 MeV electrons. Considering that electrons strike the wall almost tangentially, a few millimetres of penetration depth is indicated, allowing for pitch angle scattering in the wall. Hence, this represents an enhanced surface deposition. The total energy of the runaway electrons in a full 20 MA ITER discharge is about 40 MJ. The full magnetic energy supported by the current is about ten times as large. Since the damage threshold is about 10 MJ/m^2

[8], we can expect that a smooth deposition, e.g. toroidally symmetric rubbing against the inner wall, while moving vertically 1 m, could be tolerated. The runaway–wall interaction is complex and has not yet been analysed. Studies of the evolution of the electron spectrum after avalanching has been completed are now in progress. In view of the uncertainties, there is a strong motivation to use dense hydrogen injection to avoid runaway formation. Assessing the viability of a high density runaway discharge which decays rapidly requires MHD simulation of the discharge motion. Preliminary DINA code results [9] indicate that fast current quench (<5 s) vertical displacement events (VDEs) cannot be controlled, but that forces on the wall are reduced by about a factor of two for either runaway discharges or high density ($n = 5 \times 10^{15}$ cm^{-3}) deuterium 'killer pellets' or jets.

5. HIGH DENSITY INJECTION

For a deuterium pellet of radius r, the Parks ablation model, in reasonable agreement with experiment, predicts $dr/dx \approx -10^{-8}\, n_e^{1/3} Te^{1.64}/r^{2/3}V$, where V is the pellet velocity and n_e and T_e are plasma parameters (cgs, eV). Because of the strong temperature dependence, it does not appear practical to penetrate to the centre of ITER with a single killer pellet. However, a train of pellets can readily penetrate by cooling successive plasma layers. Simulations show that a train of about 40 pellets of 1 gram mass and a velocity of 0.7 km·s^{-1} would produce densities of 5×10^{15} cm^{-3} with fairly uniform profiles. An alternative could be the use of a liquid deuterium jet. Owing to the ablation instability it can be expected, in the plasma, to break up into droplets of approximately the initial jet radius, and hence to approximate a continuous pellet stream. An extension of Parks' ablation model to the cylindrical case shows that a jet of radius 4 mm, velocity 700 m·s^{-1} and length 3 m could penetrate to the ITER core and produce the desired plasma density of 5×10^{15} cm^{-3}. It would appear feasible to produce such a jet (about 500 atm pressure), but questions arise concerning its propagation in vacuum. We have looked at boiling and turbulent spreading and conclude that several metres propagation from the nozzle may be feasible [10]. However, R&D is clearly needed if this is to be considered seriously.

6. CONCLUSIONS

In order to terminate an ITER discharge rapidly enough (<1 s) to mitigate VDEs and to avoid, with some certainty, the conversion of the discharge to a runaway discharge, it appears that an injection of D to produce a high density ($>3 \times 10^{15}$ cm^{-3}) plasma may provide a unique solution. This could, in principle, be done with a multiple pellet train or, perhaps, a liquid jet. R&D is clearly required as to both the feasibility of such delivery systems and the plasma response to such high density injection.

REFERENCES

[1] JAYAKUMAR, R., FLEISCHMANN, H.H., ZWEBEN, S., Phys. Lett. A **172** (1993) 447. We are strongly indebted to Professor Fleischmann for bringing the whole issue of avalanching runaways to our attention.

[2] WESLEY, J., et al., IAEA CN-64/FP-25, this volume, for survey of disruption issues.

[3] BARTELS, H.-W. (ITER), personal communication, 1996.

[4] This mechanism was originally predicted by Yu. SOKOLOV in 1979 and observed in TEXTOR by FINKEN, K.H., et al., Nucl. Fusion **30** (1990) 859; see also Ref. [2].

[5] CHIU, S.C., et al., paper presented at the meeting of the American Physical Society, Denver, CO, 1996.

[6] Observations of runaways from disruptions and killer pellets have been reported by JET, DIII-D, JT-60U, ASDEX and TFTR at the Disruption Expert Group Meeting at Naka (1996).

[7] JASPERS, R., et al., in Controlled Fusion and Plasma Physics (Proc. 22nd Eur. Conf. Bournemouth, 1995), Vol. 19C, Part IV, European Physical Society, Geneva (1995) 930; KURZAN, B., Doctoral Thesis, Rep. IPP-1/287, Garching, Germany (1996); SCHITTENHELM, M. (ASDEX-Upgrade Team, Garching, Germany), personal communication, also concludes that ripple effects on ITER are not important.

[8] TOPILSKI, L.N. (ITER), personal communication, 1996.

[9] KHAYRUTDINOV, R., LUKASH, V. (ITER), personal communications, 1996.

[10] ROSENBLUTH, M.N., PARKS, P.B., PUTVINSKI, S., ITER Rep. S 19 RE I 96-07-21 F1.

ANALYSIS OF ITER DIVERTOR PERFORMANCE AND ITER TOKAMAK EDGE PARAMETER DATABASE*

A. KUKUSHKIN, H.D. PACHER[1], V. ABRAMOV[2], M. BAELMANS[3], S. BOSCH[4], D. BOUCHER[5], B. BRAAMS[6], D.P. COSTER[4], Yu. IGITKHANOV, H. ITAMI[7], G. JANESCHITZ, D. KNOLL[8], B. LIPSCHULTZ[9], A. LOARTE[10], J. MANDREKAS[11], P. McHUGH[8], J. NEUHAUSER[4], T. OSBORNE[12], G. PORTER[13], D. POST[5], V.A. POZHAROV[2], D. REITER[3], M. RENSINK[13], T. ROGNLIEN[13], R. SCHNEIDER[4], M. SHIMADA[7], R. SIMONINI[10], W. STACEY[11], M. SUGIHARA, A. TARONI[10], R.A. VESEY[14], G.C. VLASES[10], F. WISING[9, 15], ITER DIVERTOR MODELLING and DATABASE EXPERT GROUP FOR ITER JOINT CENTRAL TEAM and HOME TEAMS

ITER Joint Central Team,
Garching Joint Work Site,
Garching, Germany

[1] NET Team, Garching, Germany.
[2] Russian Research Center, Kurchatov Institute, Moscow, Russian Federation.
[3] Forschungszentrum Jülich, Jülich, Germany.
[4] Max-Planck-Institut für Plasmaphysik, Garching, Germany.
[5] ITER JCT, San Diego Joint Work Site, San Diego, California, USA.
[6] New York University, New York, N.Y., USA.
[7] JAERI, Naka-machi, Naka-gun, Ibaraki-ken, Japan.
[8] Idaho National Engineering Laboratory, Idaho Falls, Idaho, USA.
[9] Massachusetts Institute of Technology, Cambridge, Massachusetts, USA.
[10] JET, Abingdon, UK.
[11] Georgia Institute of Technology, Atlanta, Georgia, USA.
[12] General Atomics, San Diego, California, USA.
[13] Lawrence Livermore National Laboratory, Livermore, California, USA.
[14] Plasma Physics Laboratory, Princeton University, Princeton, New Jersey, USA.
[15] Chalmers University of Technology, Göteborg, Sweden.

Abstract

ANALYSIS OF ITER DIVERTOR PERFORMANCE AND ITER TOKAMAK EDGE PARAMETER DATABASE.

The ITER power balance in the core plasma is analysed. 2-D divertor modelling results are given, showing the total power and peak power to the plate in semi-detached and detached operation. The helium removal is estimated. First results from an analysis of the ITER edge database are given.

Introduction

The ITER divertor is designed to exhaust the ITER alpha heating power of 300 MW and the associated helium ash [1]. The ITER divertor concept is based on using impurity radiation losses to reduce the peak heat loads on the divertor plates by transferring most of the heating power to the main chamber and divertor side walls before it reaches the divertor plate. While this type of divertor operation has been demonstrated in divertor experiments [2], it has been achieved only for power levels less than those expected in ITER. It is thus necessary to use models and simple scalings to extrapolate from present experiments to ITER. These models include the 1-1/2 dimensional tokamak transport codes GTWHIST and PRETOR, and the 2-dimensional divertor modelling codes B2/EIRENE, B2, EDGE2D/NIMBUS and UEDGE. These codes are being validated against divertor experiments. Modelling can provide guidance for such issues as the impurity concentrations needed to achieve the necessary level of impurity radiation losses in the main and divertor plasma, the choice for the optimum impurity to be injected, the operational range in density, power level, etc., the optimum divertor configuration (especially with regard to the confinement of neutrals in the divertor chamber) and the neutral pressure in the divertor chamber. A key question is the divertor operational regimes (attached, partially attached and detached) that will be accessible in ITER. Databases of the experimental divertor edge plasma parameters are being assembled and analysed to characterise divertor operation for code validation and to develop scalings for divertor parameters.

The limit for the power on the divertor plates set by engineering considerations is about 50 MW. For 300 MW of alpha heating power, reducing

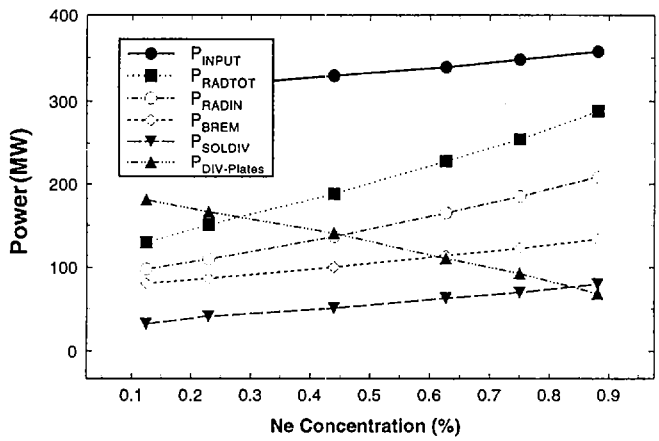

FIG. 1. Power levels radiated from the main plasma as a function of the peak neon concentration from a GTWHIST calculation.

the heat load on the divertor plate to 50 MW requires that 250 MW be radiated from the main plasma and divertor plasma. This radiation would be from hydrogen ions, ~ 10% He ash, a few percent of low Z wall materials (Be, C,..) and a fraction of a percent of a recycling impurity such as Ne, Ar or Kr.

1. Power balance in the core plasma

Bremsstrahlung losses from the main plasma and line radiation losses from the mantle (defined here as the region between the q=2 surface at r/a ~ 0.83 and the separatrix) have been calculated with analytic models and with the 1-1/2D GTWHIST transport code. Maximum seeded impurity concentrations were limited by the core power balance constraints $Q>25$ and $|\delta P_\alpha/P_\alpha|<5\%$. Bremsstrahlung losses with intrinsic impurity levels of ~10% He and ~2% Be or C and with seeded Ne levels in the range 0.12 to 0.88% are 80-135 MW; for seeded Ar levels in the range 0.012 to 0.16% they are 75-100 MW, and for seeded Kr levels in the range $2.4\ 10^{-3}$ to $1.3\ 10^{-2}$% they are ~75 MW. Impurity line radiation losses from the mantle for seeded Ne, Ar and Kr impurity levels in the above ranges are 20-65 MW, 20-110 MW, and 25-145 MW, respectively. Thus, the total possible radiation losses from inside the separatrix, without significant detriment to the core power balance, are ~100-200 MW with seeded Ne (Fig. 1) and ~100-260 MW with seeded Ar or Kr, but enough power must be tranferred to the SOL to exceed the H/L power threshold.

2. Divertor performance and power transfer to the walls and targets

2-D divertor modelling codes and analytic models are being used to assess the performance of the ITER divertor. First estimates with analytic models and simplified two-dimensional divertor model calculations (simpler impurity

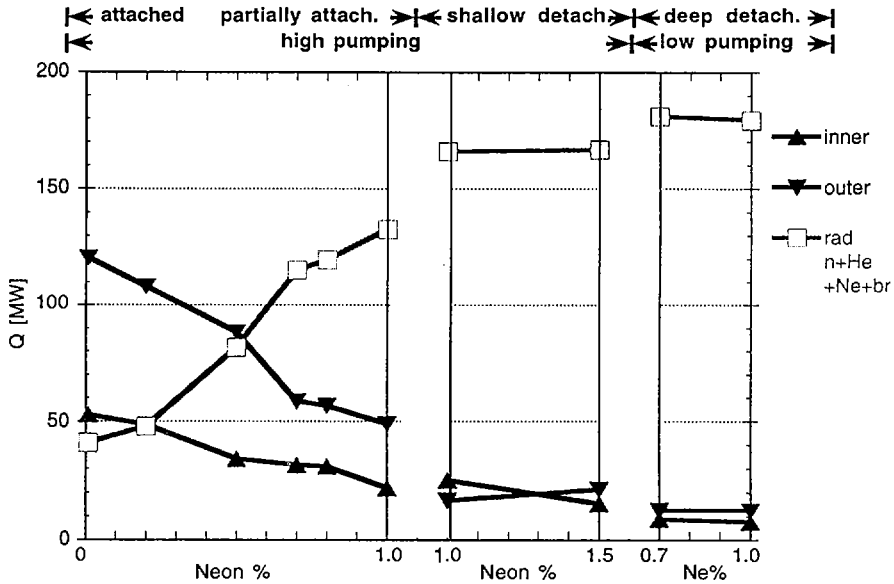

FIG. 2. Total power to targets including plasma plus neutrals (conduction, ion convection, surface recombination, neutral convection, molecular dissociation) and radiation (neutral, ion, bremsstrahlung (br)) for the three types of divertor operation.

transport models, simpler geometries, and/or simple neutral transport models) indicate that impurity levels of about 0.3 % Ne or 0.1% Ar will be adequate to achieve as much as 100 MW of radiation losses in the divertor plasma for main plasma edge densities of about 5 10^{19} m^{-3} [3]. The 100 MW of radiation losses include about 25 MW of charge exchange and radiation losses from hydrogen and low Z impurities such as He and Be. These calculations indicate that the radiation is from an extended region along the separatrix so that the radiated power will be spread out along the length of the divertor channel.

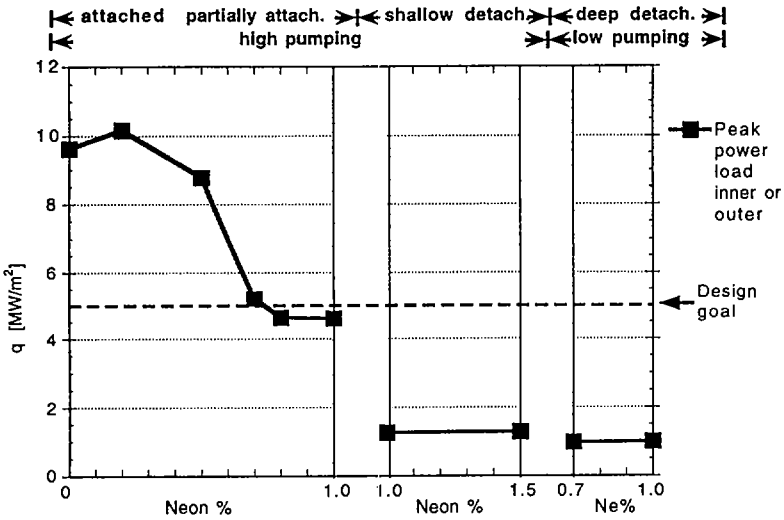

FIG. 3. Peak power load on the targets from plasma and neutrals (conduction, ion convection, surface recombination, neutral convection, molecular dissociation) and radiation (neutral, ion, bremsstrahlung) versus neon fraction.

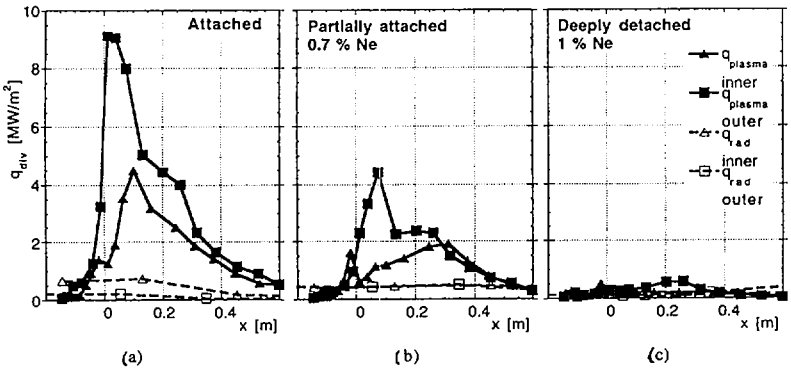

FIG. 4. Profiles of power load on the divertor targets (particles and radiation) for (a) attached plasma, 0.01% Ne; (b) partially attached plasma, 0.7% Ne; and (c) deeply detached plasma, 1% Ne.

More complete calculations done for the real ITER geometry with full multispecies impurity transport algorithms produce however somewhat less optimistic results regarding impurity radiation. The impurity transport is strongly dominated by the thermal force and the plasma flow pattern, causing the distribution of impurities in the edge plasma to be far from optimum. UEDGE and B2-EIRENE calculations indicate that the impurity concentration is peaked near the edge reducing the total radiation. On the contrary, allowance for the volumetric recombination together with more accurate atomic physics result in higher power losses due to line radiation from neutral hydrogen. Moreover, under certain conditions, the plasma detaches from most of the target surface, and intense internal recycling occurs in the divertor volume due to strong recombination and ionisation [4].

Fig. 2 shows calculated variation of the total power delivered to the targets and radiated from the divertor plasma with the neon concentration in the core, and similar variation of the peak power loads is given in Fig. 3. Here three kinds of divertor operation regime – attached, shallow detached and deeply detached plasma – are presented. Transition from one regime to another can be accomplished by changing the pumping rate. The profiles of the divertor target load for three operation points are shown in Fig. 4.

Although detached operation seems more attractive from the design point of view, current modelling indicates that the particular regimes shown here could be transient with a time scale of a fraction of a second to several seconds – that is, fast on the ITER operation time scale and extremely slow on the time scale of modelling capabilities. At the extremes of the range (in upstream density, impurity concentration, or pumping rate), the plasma will either relax to the normal semi-attached state, or collapse, forming an x-point MARFE. The size of the operating window and the possibility of stabilising the operating point via feedback on the neutral pressure in the private flux region remains to be investigated. Even without full detachment, semi-attached operation with 0.7% Ne is found to yield peak power levels of 5 MW/m^2 , i.e. falls within the acceptable range with some further optimisation, as also demonstrated by the value of 7 MW/m^2 found in [5] using EDGE2D/NIMBUS.

3. Helium removal

The helium concentration and neutral pressure in the divertor are strongly dependent on the divertor operating regime and divertor configuration. Helium ions, like other impurities, are subject to the thermal force in the SOL. This force impedes the helium flow to the target in the hot zone adjacent to the separatrix, making the helium diffuse outwards and recombine on the outboard part of the target. Given the present ITER geometry, for which pumping is from the private flux region (PFR), the helium atoms have to traverse the divertor plasma to reach the pumping duct, and this can make their removal quite inefficient [6]. The 2-dimensional divertor model calculations with He and H plasmas indicate that the helium gas pressure in the divertor does not increase as rapidly as the hydrogen pressure when the recycling level is increased. With attached operation, the helium concentration is higher in the outer portion of the scrape-off layer than near the separatrix by a factor as high as 10 or more.

The efficiency of helium exhaust can be discussed in terms of the helium enrichment factor η, which is the ratio of relative helium concentration in the pumped-out gas to that in the core plasma, and of the neutral pressure in the pumping duct P_{neut}. Since the required helium exhaust rate is determined by the fusion power, these two parameters give the relation between the helium concentration in the core and the pumping speed. The variation of the reference parameters with neon concentration in the core is given in Fig. 5. Simple

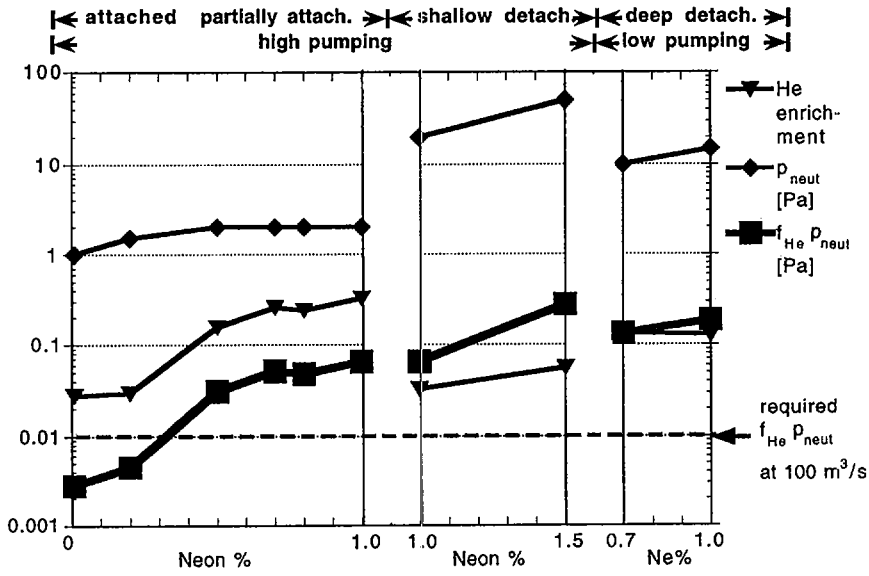

FIG. 5. Helium fraction, helium enrichment, deuterium neutral pressure and helium 'partial pressure' (helium fraction times deuterium pressure) versus neon fraction. He fraction is helium flux over deuterium flux at pump surface, He enrichment is this helium fraction over ratio of helium and deuterium densities at core. Deuterium pressure is measured at plasma edge in private flux region.

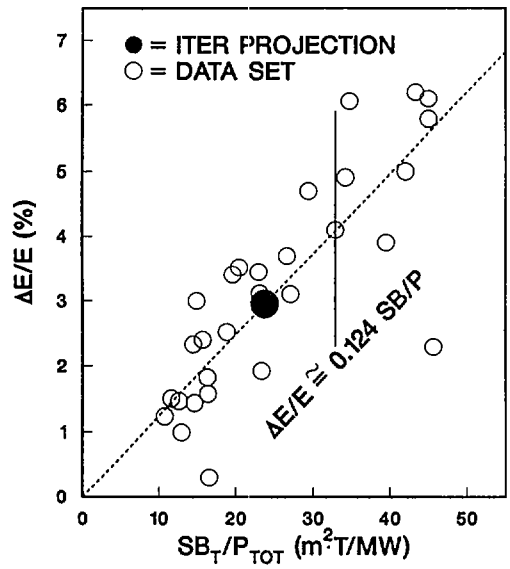

FIG. 6. Scaling of energy loss associated with ELMs.

estimates show that the neutral gas in the PFR must be collisional, whereas our Monte-Carlo package used for the neutral transport calculations does not treat neutral-neutral collisions. Therefore the neutral pressure in the PFR (at the duct entrance) is estimated here to be equal to the average neutral pressure at the plasma boundary in the PFR. Whenever the helium pressure of 0.01 Pa at the entrance of the pump duct is attained, the pumping system of ITER as designed presently can remove the necessary amount of helium to ensure steady-state operation. Our calculations indicate that this goal could be achieved even in the regime of semi-detached plasma, and that the helium exhaust conditions become more favourable with transition to detached operation.

4. Edge database analysis

A database for tokamak edge parameters from divertor experiments on Alcator C-Mod, ASDEX Upgrade, DIII-D, JET and JT-60/U has been assembled and is being analysed and checked for consistency. The 434 data sets contain τ_p, $n_{sep}/\langle n \rangle$, peak heat flux, f_{rad}, λ_{SOL} and the ELM characteristics as a function of 119 discharge parameters. A preliminary analysis of the data indicates that the JT-60/U scaling of the peak heat flux ~ $q^{0.5}$ is consistent with the data from JET and DIII-D (with H-mode operation). However, the dependence on input power and the plasma density in the core for JET and DIII-D is different from JT-60/U. Based on an analysis of the ELM data, the energy content, ΔW_{ELM} of type 1 ELMs of the form $\Delta W_{ELM}/W_{plasma}$ is proportional to $S\ B_T / P_{tot}$ where S is the plasma surface area. The projected value for ITER is $\Delta W_{ELM}/W_{plasma} = 0.03$ (Figure 6). This projected value will necessitate significant spatial spreading of the ELM energy loss compared to the time averaged value to reduce the energy to the divertor plates to the 1% required for ITER. Further analysis of the database is underway.

5. Conclusions

The transport analysis of the core plasma shows that 100 to 250 MW of the heating power could be dispersed via radiation from inside the separatrix without unacceptable deterioration of the plasma performance, but H-mode threshold requirements may limit this to 100-150 MW. Further reduction of the power transferred by the plasma particles to the divertor structures down to approximately 100 MW by impurity radiation and radiation from neutrals requires impurity seeding and an adequate fuelling and pumping arrangement. The operation in semi-detached mode, though less attractive with respect to the target loading, may be easier to achieve than fully detached operation. This regime still provides acceptable power loads and conditions for helium removal. Given the attractiveness of detached operation, more effort should be devoted to assess the feasibility of stable operation of ITER in this regime.

The first results of the edge database indicate possible significant impact of the ELMs on the ITER design. The database activity is underway to provide an adequate basis for projection of current experiments to ITER conditions.

REFERENCES

[1] JANESCHITZ, G., et al., J. Nucl. Mater. **220–222** (1995) 73; IAEA-CN-64/F-2, this volume.

[2] MATTHEWS, G., J. Nucl. Mater. **220–222** (1995) 104.

[3] PARKER, R., et al., in Plasma–Surface Interactions (Proc. 12th PSI Conf. St. Raphaël, 1996).

[4] KUKUSHKIN, A., et al., ibid.

[5] VLASES, G.C., et al., ibid.

[6] KRASHENINNIKOV, S.I., KUKUSHKIN, A.S., SOBOLEVA, T.K., Nucl. Fusion **31** (1991) 1455.

THE ITER DIAGNOSTIC SYSTEM*

A.E. COSTLEY, K. EBISAWA, G. JANESCHITZ, L.C. JOHNSON, S. KASAI[1], L. DE KOCK, V. MUKHOVATOV, D. ORLINSKI[2], P.E. STOTT[3], G. VAYAKIS, C. WALKER, S. YAMAMOTO, K.M. YOUNG[4], V. ZAVERIAEV[2, 3], ITER JOINT CENTRAL TEAM, ITER HOME TEAMS

Abstract

THE ITER DIAGNOSTIC SYSTEM.

The ITER diagnostic system is outlined. The most critical design areas are identified and the solutions being adopted are described. A brief assessment of the present design is included and areas which require further work are identified.

1. INTRODUCTION

In order to achieve its operational and programmatic goals, ITER [1] requires an extensive set of plasma diagnostics. In terms of the number and type of measuring instruments, the diagnostic system will be similar to those existing on today's large tokamaks such as JET, TFTR and JT60U. On the other hand, the demands on the diagnostic system will be enhanced: in particular, more measurements will be used in real-time control of the plasma and so will have to be made at very high levels of reliability and availability. Moreover, the implementation of the diagnostics is especially demanding because of the high levels of radiation, the limited access, and the stringent requirements for vacuum integrity and tritium containment. Together these requirements constitute a substantial design challenge and generate a need for dedicated R&D.

The overall specifications of the ITER diagnostic system have been determined [2], and the role plasma measurements will play in the ITER physics programme has been summarised [3, 4]. Individual diagnostic systems are now

---

[1] Japan Atomic Energy Research Institute, Naka-machi, Naka-gun, Ibaraki-ken, Japan.

[2] Kurchatov Institute, Moscow, Russian Federation.

[3] JET Joint Undertaking, Abingdon, Oxfordshire, UK.

[4] Plasma Physics Laboratory, Princeton University, Princeton, New Jersey, USA.

being designed by a combined effort of the ITER Joint Central Team and design teams within the four ITER Parties. Underpinning the design work is an R&D programme which thus far has concentrated on the effects the high levels of neutron and gamma radiation will have on materials used in diagnostic construction but is planned in the near future to examine prototypes of key diagnostic components.

In this paper, the ITER diagnostic system is outlined. The most critical design areas are identified and the solutions being adopted are described. A brief assessment of the overall performance of the present design is included.

2. SYSTEM DESCRIPTION AND KEY DESIGN AREAS

The diagnostic system comprises about 40 individual measurement systems which can be conveniently grouped into seven generic groups:

- magnetic diagnostics
- neutron diagnostics
- optical/IR systems
- bolometric system
- spectroscopic and neutral particle analyser (NPA) systems
- microwave diagnostics
- plasma facing component diagnostics and operational systems

2.1. Magnetic Diagnostics The magnetic diagnostics consist of several individual sub-systems: pick-up coils, saddle loops and voltage loops mounted on the inner wall of the vacuum vessel; coils and saddle loops mounted on the plasma side of the back plate in gaps between blanket shield modules and/or inside pockets in the shield modules; coils mounted in the divertor diagnostic cassettes; four continuous poloidal (Rogowski) loops mounted on the outside of the vacuum vessel; four poloidal diamagnetic loops; and Rogowski coils around earth straps in the divertor region for measurements of 'halo' currents. The system will provide the measurements necessary for determining the plasma shape and position, plasma current, loop voltage, stored plasma energy and will permit the study of MHD modes and fluctuations.

The pick-up coils mounted on the inner wall of the vacuum vessel are coils of mineral insulated (MI) cable wound on a stainless steel former with a protective cover. They are cooled by conduction. The saddle loops are formed from small diameter MI cable and the voltage loops are metallic rods supported by ceramic insulators. Both are mounted on the vessel wall. Irradiation tests have shown that these components can withstand a dose of 1 dpa without deterioation and so in this location they will survive for the lifetime of ITER. This magnetic sensor set will provide the plasma shape and position on a time-scale ~ 1 s. The coils and saddle loops mounted on the back plate and/or in the blanket modules and in the divertor cassettes will provide the plasma shape and position on a faster time-scale (~ 10 ms), and information on MHD modes. Providing this fast response is the most critical area in the design. The high frequency coils must be well coupled to the plasma to achieve a high frequency response (up to 200 kHz) but must be shielded from the high levels of radiation. Parts of this subsystem may have to be replaced if the blanket modules and/or divertor cassettes are replaced.

2.2. Neutron Diagnostics The principal neutronic systems are a radial neutron camera, a vertical neutron camera, neutron spectrometers, neutron flux monitors, and a neutron activation system.

The radial neutron camera consists of a fan-shaped array of flight tubes, viewing the ITER plasma through slots in the blanket/shield, intersecting at a common aperture defined by a specialized shielding plug in a midplane port, and penetrating the vacuum vessel, cryostat, and biological shield through thin stainless steel "windows". A cross section of the camera is shown in figure 1. Each flight tube culminates in a set of detectors chosen to provide the required range of sensitivity and temporal and spectral resolution. The detectors are housed in an auxiliary shielded enclosure outside the biological shield, and additional shielding along and between flight tubes provides necessary collimation. All electronics are situated outside the biological shield. The vertical neutron camera viewing from above has a similar configuration but is installed on a top port. The cameras provide the measurement of the total neutron flux and emission profile from which the fusion power and power density and the alpha particle source profile are derived.

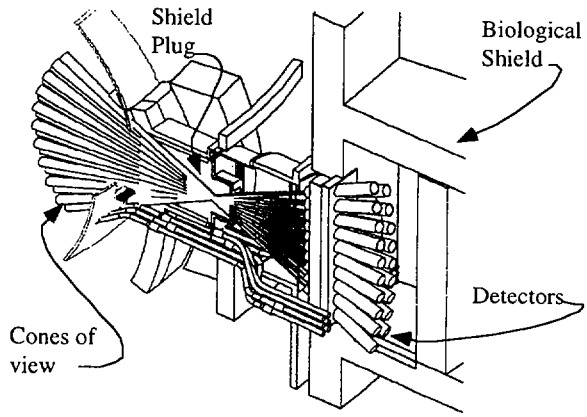

FIG. 1. Isometric cutaway view of the radial neutron camera.

Several types of neutron detectors and spectrometers are being considered. These range in size from compact natural diamond detectors to magnetic proton recoil (MPR) and time of flight spectrometers. The present design of the radial neutron camera is sufficiently flexible to accommodate many possible instruments and this is the preferred arrangement for the installation of the spectrometers. From the measurements, the ion temperature would be determined and possibly the tritium-to-deuterium ion density ratio in the core, n_T/n_D.

The neutron flux monitors consists of a number of fission chambers containing ^{235}U or other isotopes, situated in various locations around the tokamak inside the biological shield. The system measures the global neutron source strength from which the total fusion power is obtained.

The neutron activation system uses pneumatic transfer methods to place a sample of material close to the plasma where it is irradiated by neutrons. The system will provide a robust relative measure of fusion power and allows an absolute calibration of fusion power production.

The most critical design area is the access for the radial and vertical neutron cameras. The cameras need a wide angle view in order to be able to measure the neutrons from the full plasma cross-section and this has to be obtained simultaneously with maintaining high levels of radiation and thermal shielding of the tokamak. Modifications to the standard midplane and vertical ports are being designed, and additional shielding will be installed outside the biological shield and on the ceiling above the tokamak.

2.3. Optical/Infra-red systems Two multipulse Thomson scattering systems and an equatorial plane interferometer are among the principal optical systems. One of the Thomson scattering systems is optimised for making measurements in the core region while the other is optimised for making measurements in the edge region. The core system operates on the time-of-flight (LIDAR) principle. Light from a high power laser is transmitted to the plasma using a folded mirror system inside a shielded labyrinth located in a mid-plane port. The plasma-facing mirror is an actively cooled metal mirror. The scattered radiation returns along the same path to spectrometers and detectors sited remotely. The system provides the spatial profile of the electron density and temperature.

A LIDAR type system will not provide the spatial resolution necessary for measurements in the edge region where high gradients are expected. Hence, the design of the edge system is being based on a conventional Thomson scattering arrangement.

A vibration-compensated interferometer employing Faraday rotation techniques will be used to measure the line-integrated density for use in the feedback control of the plasma density. The measurements will be made in the equatorial plane. The probing beams will have wavelengths of 10.6 μm and 3.39 μm. The radiation will be transmitted to and from the plasma through shielding labyrinths in an equatorial port and small (~ 100 mm diameter) retroreflectors mounted in other equatorial ports will return the radiation. The lasers and detectors will be sited remotely.

The most critical design issue is the survivability of the first mirrors: these must maintain a good optical quality in the presence of the nuclear heating, plasma radiation and neutral particle bombardment. For the Thomson scattering systems, the mirrors also have to handle the high level of laser power. The mirrors will be actively cooled metallic mirrors possibly protected with shutters. Key tests are being pursued in the diagnostic R&D programme.

2.4. Bolometers There will be bolometer arrays with multiple lines of sight covering the main plasma and the divertor regions. The bolometer arrays will be mounted in the mid-plane and vertical ports and in the divertor diagnostic cassettes. Additional locations for bolometer arrays are under consideration. The aim is to obtain the two dimensional distribution of the total radiated power in the poloidal cross-section in both the main plasma and divertor regions through tomographic reconstruction. Existing bolometer heads meet many of the design requirements but R&D is required to establish their radiation resistance.

2.5. Spectroscopic and Neutral Particle Anaysis Systems An extensive array of spectroscopic instrumentation will be installed on ITER covering the X-ray to visible range: both passive and active measurement techniques will be employed. The four main regions of the plasma - the core, the radiation mantle, the scrape off layer (SOL) and the divertor - will be probed. The measurements can potentially provide impurity species identification, ion densities, ion temperature, electron temperature, Z_{eff}, plasma rotation, internal magnetic field, impurity transport coefficients, and information on MHD phenomena.

The specific instruments to be employed have not yet been finalized. However, for the X-ray region it is probable that there will be two spectrometers: a medium resolution survey instrument providing full coverage in the wavelength range 0.1 - 10 nm and a high resolution (crystal) instrument with narrow coverage in the range between about 0.1 - 0.2 nm. For the UV and XUV region the spectrometers and detectors will have to be directly coupled to the tokamak vacuum because it is not possible to use windows. However, mirrors can be used at low angles of reflection and so it is possible to shield the detectors from neutron and gamma radiation by using labyrinthine optical systems imbedded in shielding blocks. Passive spectral measurements in the visible wavelength range are of limited value for probing the core because of the high plasma temperatures. However, active measurements employing charge exchange recombination spectroscopy with beams of energetic neutrals are a rich source of information. For several of the important measurements, the optimum beam energy is ~ 100 keV/amu which is significantly below the energy of the heating beams (1 MeV). This generates a requirement for a dedicated diagnostic neutral beam (below). The beams are viewed through labyrinthine optical systems imbedded in shielding blocks. Motional Stark Effect measurements of the current profile, however, benefit from the higher energy of the heating beams and so an optical system to view one of these beams is also planned.

Measurements in the divertor region will be made through folded optical paths in special divertor diagnostic cassette modules which will be located at each of the four divertor remote handling (RH) ports (figure 2). The wavelength range is presently limited to wavelengths > 200 nm due to absorption in the quartz windows. The light will be transported with mirrors, lenses and optical fibres to the spectrometers sited outside the biological shield. Mirror damage due to the deposition of target plate material during a major disruption is a potentially serious problem which is presently being investigated.

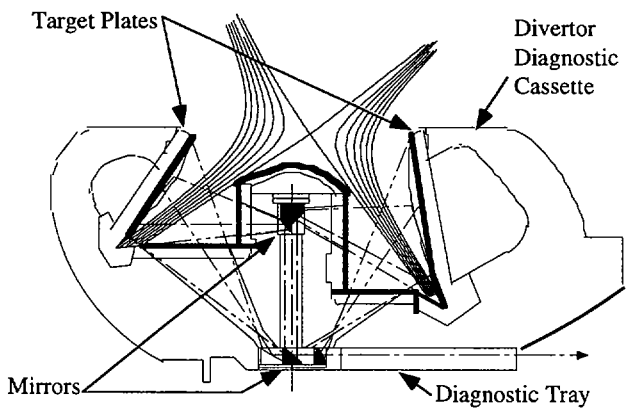

FIG. 2. Folded optical paths in the special divertor cassette modules.

The spectroscopic diagnostics will be supplemented by two neutral particle analyzers, both viewing radially through an equatorial port along the same line of sight. One will be used for monitoring the n_T/n_D ratio in the plasma edge ($r/a > 0.7$) and the other will provide the fast alpha particle distribution function in the energy range 0.5-4 MeV.

2.6. Microwave Diagnostics The principal microwave diagnostics will be a system to measure the electron cylotron emission (ECE) from the main plasma, and three reflectometery systems for probing the main plasma, the divertor plasma, and for measuring the plasma position. Additional systems under study are an electron cyclotron absorption system for use in the divertor region, a fast wave reflectometery system and two microwave scattering systems.

The ECE system consists of an array of antennas mounted in a radial port plug, a transmission system which carries the radiation through the vacuum vessel, cryostat and shield, and the spectrometers and detectors which are located remote from the tokamak in one of the diagnostic areas. A calibration source will be built into the radial port plug. The system will measure the electron temperature with good spatial and temporal resolutions.

The reflectometer for the main plasma has three sub-systems: a system which utilizes the upper cutoff (extraordinary mode) from the low-field side of the plasma to provide measurements of the density profile in the scrape-off layer (SOL); a system which utilizes the plasma frequency cutoff (ordinary mode) from both the low-field and high-field sides of the plasma to provide the inboard and outboard density profile in the gradient region; and a system which utilizes the lower cutoff (extraordinary mode) launched from the high-field side of the plasma to provide the core profile. The low-field-side systems share an array of broad-band antennas of typical diameter 100 mm, mounted on a diagnostic block in an equatorial port and viewing the plasma through apertures in the blanket/shield. Broad-band, overmoded, corrugated, circular transmission lines couple the front ends to the system electronics.

The plasma position reflectometer provides the location of particular density layers which occur in the vicinity of the separatrix. This system is intended as a stand-by reference to the plasma position and shape control system for very long ITER pulses (> 3000 s), so reliability is of the highest priority. The divertor reflectometer is intended to provide density profiles across the divertor plasma.

For all systems, dog-leg structures in the transmission lines reduce neutron streaming outside the vacuum vessel and bioshield. Double vacuum windows of fused quartz directly bonded to metal structures provide the necessary pressure boundaries.

The critical design area is the installation of the antennas and waveguides on the high-field side, and at various locations in the poloidal cross-section, necessary for some of the reflectometry systems. The solution being adopted is to mount the antennas within specially modified blanket modules and to route the radiation to these systems using small bore (typically 25 mm) rectangular or circular corrugated waveguides depending on the frequency range. These waveguides are routed either in the interspace between the backplate and the vacuum vessel, or alongside the blanket/shield cooling water conduits. The waveguides are brought out through an upper port and the cryostat to electronics located on top of the bioshield.

2.7. Plasma Facing Component Diagnostics and Operational Systems The condition of the high heat flux components in the main chamber and in the divertor will be monitored using IR/visible cameras and thermocouples. Langmuir probes will be used to determine the parameters of the divertor plasma near the target plates. The critical design issues for these systems are achieving the required views of the high heat flux components, the survivability of the optical elements and the connections and cabling between the diagnostic sensors and the remote processing electronics. Special divertor cassettes are being designed for the divertor diagnostic measurements and will incorporate the diagnostic sensors

and optical and microwave transmission lines. Finally, many diagnostics such as pressure gauges, residual gas analysers, hard X-ray monitors and 'halo' current monitors will be installed to aid the protection and operation of the tokamak.

2.8. Diagnostic Neutral Beam The optimum beam energy for the diagnostic neutral beam is ~100 keV [5]. Two options are being considered for the beam design. In the first case, the design would be based on the design of the main heating beams; in particular, it would require only minor modifications of the high cost and high technology components developed for these beams and adopt the same RH and maintenance procedures. In order to achieve the required measurement performance, the beam would have to have a power of about 5 MW, a narrow beam divergence, a small beam footprint and be capable of modulation at frequencies of a few Hz. An alternative approach is to use a very short pulse (1 μs), intense (5 GW) beam which can be pulsed at a repetition rate of about 100 Hz [6]. Such a beam would have an average beam power requirement of about 500 kW, would be significantly smaller than the conventional beam and would give an improved measurement performance. However, it is at a much earlier state of development and is a subject of on-going R&D.

3. BRIEF ASSESSMENT OF PRESENT DESIGN AND REQUIRED FURTHER WORK

The design and supporting R&D work that has been undertaken so far have shown that it will be possible to implement many of the diagnostic systems and thereby make many of the required plasma meaurements on ITER, although many details have yet to be worked out. Measurements of the plasma shape and position, plasma current and beta on a moderate time-scale (~1s); the neutron emission profile, plasma density and temperature, impurity species, edge fuelling ratio n_T/n_D, total radiated power, and MHD activity appear feasible and for these parameters it should be possible to meet or exceed the measurement requirements. The implementation of the fast magnetic measurements will not be settled until the interface of the coils with the blanket modules is concluded. Measurements of the condition and temperature of the divertor plates, and measurements of the parameters of the plasma in the divertor region, are less certain because of the difficulties of access and the possible damage to the diagnostic components during disruptions. Measurements which derive from the diagnostic neutral beam - primarily the density of light impurities including the He ash, the ion temperature and plasma rotation, are also less certain because of the difficulties and cost of implementing the beam. Existing techniques for measuring the core n_T/n_D ratio, confined and escaping fast ions including alpha particles, and the internal current profile appear difficult to implement on ITER and so the development of novel approaches for these parameters is encouraged.

REFERENCES

[1] AYMAR, R., et al., these Proceedings, Vol. 1, p. 3.

[2] COSTLEY, A.E., et al., "Requirements for ITER diagnostics", Workshop on Diagnostics for ITER, Varenna, 1995, Plenum Press, New York, p. 23.

[3] YOUNG, K.M., et al., "An overview of ITER diagnostics", Proc. 11th Annu. Conf. on High Temperature Plasma Diagnostics, Monterey, 1996, Rev. Sci. Instrum. (in press).

[4] MUKHOVATOV, V., et al., Rev. Sci. Instrum. **68** (1997) 1250.
[5] MARMAR, E., et al., "Diagnostic neutral beam spectroscopy requirements", Proc. 11th Annu. Conf. on High Temperature Plasma Diagnostics, Monterey, 1996.
[6] OLSON, J., et al., "Progress towards a microsecond duration, repetitive, intense ion beam for active spectroscopy measurements on ITER", ibid.

CHAIRPERSONS OF SESSIONS

Session C1	F. WAGNER	Germany
Session C2	E.P. KRUGLYAKOV	Russian Federation
Session D1	M.N. ROSENBLUTH	ITER
Session D2	T. SATO	Japan
Session D3	D. BALDWIN	United States of America
Session F	K. LACKNER	Germany

SECRETARIAT OF THE CONFERENCE

T.J. DOLAN	Scientific Secretary
U. SCHNEIDER	Scientific Secretary
E. PILLER	Conference Organizer
J. WEIL	Editor
M. SPAK	Editor
I. WARDELL	Records Officer

HOW TO ORDER IAEA PUBLICATIONS

No. 5, May 1997

☆ ☆ **In the United States of America and Canada**, the exclusive sales agent for IAEA publications, to whom all orders and inquiries should be addressed, is:

Bernan Associates, 4611-F Assembly Drive, Lanham,
MD 20706-4391, USA

☆ ☆ **In the following countries** IAEA publications may be purchased from the sources listed below, or from major local booksellers. Payment may be made in local currency or with UNESCO coupons.

AUSTRALIA	Hunter Publications, 58A Gipps Street, Collingwood, Victoria 3066
BELGIUM	Jean de Lannoy, 202 Avenue du Roi, B-1060 Brussels
BRUNEI	Parry's Book Center Sdn. Bhd., P.O. Box 10960, 50730 Kuala Lumpur, Malaysia
CHINA	IAEA Publications in Chinese: China Nuclear Energy Industry Corporation, Translation Section, P.O. Box 2103, Beijing
CZECH REPUBLIC	Artia Pegas Press Ltd., Palác Metro, Narodni tř. 25, P.O. Box 825, CZ-111 21 Prague 1
DENMARK	Munksgaard International Publishers Ltd., P.O. Box 2148, DK-1016 Copenhagen K
EGYPT	The Middle East Observer, 41 Sherif Street, Cairo
FRANCE	Office International de Documentation et Librairie, 48, rue Gay-Lussac, F-75240 Paris Cedex 05
GERMANY	UNO-Verlag, Vertriebs- und Verlags GmbH, Dag Hammarskjöld-Haus, Poppelsdorfer Allee 55, D-53115 Bonn
HUNGARY	Librotrade Ltd., Book Import, P.O. Box 126, H-1656 Budapest
INDIA	Viva Books Private Limited, 4325/3, Ansari Road, Darya Ganj, New Delhi-110002
ISRAEL	YOZMOT Literature Ltd., P.O. Box 56055, IL-61560 Tel Aviv
ITALY	Libreria Scientifica Dott. Lucio di Biasio "AEIOU", Via Coronelli 6, I-20146 Milan
JAPAN	Maruzen Company, Ltd., P.O. Box 5050, 100-31 Tokyo International
MALAYSIA	Parry's Book Center Sdn. Bhd., P. O. Box 10960, 50730 Kuala Lumpur
NETHERLANDS	Martinus Nijhoff International, P.O. Box 269, NL-2501 AX The Hague Swets and Zeitlinger b.v., P.O. Box 830, NL-2610 SZ Lisse
POLAND	Ars Polona, Foreign Trade Enterprise, Krakowskie Przedmieście 7, PL-00-068 Warsaw
SINGAPORE	Parry's Book Center Pte. Ltd., P.O. Box 1165, Singapore 913415
SLOVAKIA	Alfa Press Publishers, Križkova 9, SQ-811 04 Bratislava
SPAIN	Díaz de Santos, Lagasca 95, E-28006 Madrid Díaz de Santos, Balmes 417, E-08022 Barcelona
SWEDEN	Fritzes Customer Service, S-106 47 Stockholm
UNITED KINGDOM	The Stationery Office Books, Publications Centre, 51 Nine Elms Lane, London SW8 5DR

☆ ☆ Orders (except for customers in Canada and the USA) and requests for information may also be addressed directly to:

Sales and Promotion Unit
International Atomic Energy Agency
Wagramerstrasse 5, P.O. Box 100, A-1400 Vienna, Austria

Telephone: +43 1 2060 22529 (or 22530)
Facsimile: +43 1 2060 29302
Electronic mail: sales.publications@iaea.org

INTERNATIONAL ATOMIC ENERGY AGENCY
VIENNA
ISBN 92-0-102997-7
ISSN 0074-1884